PROCEEDINGS OF THE 26TH INTERNATIONAL FREE ELECTRON LASER CONFERENCE & 11TH FEL USERS WORKSHOP

RENÉ BAKKER
LUCA GIANNESSI
MARINO MARSI
RICHARD WALKER

EDITORS

FEL2004

Proceedings of the
26th International Free Electron Laser Conference and 11th FEL Users Workshop

August 29 to September 3, 2004
Stazione Marittima, Trieste, Italy

René Bakker
Luca Giannessi
Marino Marsi
Richard Walker
Editors

Published by
Comitato Conferenze Elettra
S.S. 14 – km 163.5 in Area Science Park
I-34012 Trieste
Italy

PROCEEDINGS OF THE
26TH INTERNATIONAL FREE ELECTRON LASER CONFERENCE AND
11TH FEL USERS WORKSHOP

ISBN: 88-87992-02-9

Printed in Italy by Graphart ts

Foreword

The 26th International Free Electron Laser Conference and 11th FEL Users Workshop were held between August 29th and September 3rd, 2004 at the beautiful seafront location of the Stazione Marittima congress centre in Trieste, Italy. The Conference and Workshop, known as FEL2004, was organised by Sincrotrone Trieste, home of the third generation synchrotron light source ELETTRA, the EU funded storage ring free electron laser (EUFELE), and the VUV single-pass FEL project FERMI. A total of 287 participants from 18 different countries attended the conference, making this one of the biggest ever conferences. A total of 62 talks and 158 posters were presented and 184 papers were accepted for publication in these proceedings.

FEL2004 marks the 25th Anniversary of the International FEL Conference, and incidentally 20 years since the first FEL conference held in Italy, in Castelgandolfo. This marked an appropriate moment look back on the achievements since then, and to consider the future prospects for the field as well as the FEL conference itself.

At the time of the first international FEL meeting held at Stanford in 1979, later classified as the first of the International FEL Conference series, only one FEL had actually operated, namely the Stanford oscillator, which first lased in 1977. Since then remarkable progress has been made in the power and spectral range of operating FELs as well as in their scientific applications. The programme of FEL2004 reflected the very active nature of the field, and we thank the members of the International Programme Committee for putting together a balanced program highlighting both the current activity and the exciting prospects ahead. We also thank Mike Poole for a lively personal summary of the FEL field over the last 25 years in the concluding session.

The social programme of the conference included an excursion to the Roman ruins and the magnificent 11th Century basilica with its impressive floor mosaics in Aquileia, and to the town of Grado with its sandy beaches, its old historic centre, and picturesque harbour. The excursion was followed by a banquet in the Savoia Excelsior Hotel opposite the conference centre. Following tradition, the FEL Prize was awarded during the banquet and this years recipients were Hiroyuki Hama and Vladimir Litvinenko for their fundamental and pioneering contributions in Storage Ring Free Electron Lasers (SRFELs).

We would like to express our sincere gratitude to Sincrotrone Trieste for hosting the Conference and to the members of the Local Organising Committee, and in particular the Local Organising Coordinator Carlo Bocchetta, for their hard work in taking care of the many organisational aspects of the conference. Special thanks are due also to Ivan Andrian of Sincrotrone Trieste and his team for organising the abstract and paper submission as well as the new electronic proceedings.

On behalf of the International Executive Committee (IEC) and local organising committee we would also like to express our thanks for the generous financial support received from the following institutions: Area Science Park, Italy, the Council for the Central Laboratory of the Research Councils (CCLRC), UK, Consiglio Nazionale delle Ricerche (CNR), Italy, Deutsches Elektronen-Synchrotron (DESY), Germany, Ente per le Nuove Tecnologie, l'Energia e l'Ambiente (ENEA), Italy, the Istituto Nazionale di Fisica Nucleare (INFN), Italy, the Regione Autonoma Fiuli Venezia Giulia. The conference also benefited from the financial support of the 12 industrial exhibitors, listed elsewhere. All of this helped to balance the conference budget as well as to provide financial support for 10 young researchers who would not otherwise have been able to attend the conference.

This year sees an end to a 20 year old tradition to publish the Conference Proceedings in the journal Nuclear Instruments and Methods in Physics Research. This decision was reached after an intense debate over several months amongst the members of the IEC, taking into account the opinion of the FEL community who had responded in November 2003 to a questionnaire on publication policy with a 2:1 vote in favour of changing to electronic publication on the Joint Accelerator Conference Website (JACoW). The organisers of FEL2004

hope that the rapid publication and the benefits of being included in the JACoW group of conferences will serve the FEL community well in future years.

In keeping with the usual policy, only those papers presented at the conference, either orally or as a poster, are included in these Proceedings. The change in publication policy has also implied a significant change in the refereeing of the papers. Since the proceedings do not have refereed status, the decision has been taken to only perform a light refereeing by members of the International Program Committee to ensure that minimum standards of readability and content are met. At the same time, authors have been encouraged to submit extended articles to the online refereed journal Physical Review Special Topics Accelerators and Beams (PRST-AB), which has agreed to publish a Special Edition of FEL Conference related papers.

Another issue that causes continuing debate amongst the FEL community, which surfaced also at this years conference, was the question of whether to maintain annual conferences or change to conferences in alternate years. This year the IEC debated the issue at length and found itself closely divided. To resolve the issue, a poll of the conference attendees was organized in the form of a show of hands. This indicated an approximate 2:1 majority in favour of the *status quo*, which subsequently swayed the IEC to vote in favour of retaining annual conferences. Having received and considered bids for FEL2007, the decision was then taken to award the organisation of FEL2007 to the Budker Institute of Nuclear Physics in Novosibirsk, Russia.

On its 25th anniversary, this years International FEL Conference therefore marks a significant change in the way its proceedings are published. Other important aspects of the conference remain the same for some time at least: for example, the traditional annual conference, a testimony to the fact that there is no lack of interest in hosting or attending FEL conferences and of the exciting times ahead for the FEL field.

René Bakker
Luca Giannessi
Marino Marsi
Richard P. Walker

FEL Prize

The International Free Electron Laser Prize is awarded each year to recognize individual researchers for their outstanding contribution to the field. At the 26th International Free Electron Laser Conference the prize for 2004 was awarded to Hiroyuki Hama (Tohoku University) and Vladimir Litvinenko (Brookhaven National Laboratory), in recognition of their fundamental and pioneering contributions to Storage Ring Free Electron Lasers (SRFELs).

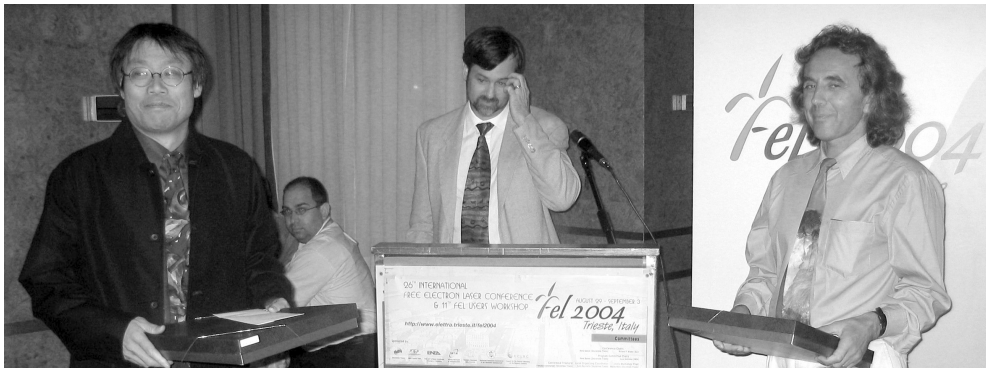

Hiroyuki Hama (left) and Vladimir Litvinenko (right) receiving the 2004 FEL Prize from the FEL Prize Committee Chairman, Stephen Benson (centre)

Vladimir Litvinenko and Hiroyuki Hama have performed fundamental and pioneering contributions in Storage Ring Free Electron Lasers (SRFELs). Thanks to their deep understanding of the FEL and to their achievements, they have promoted the use of SRFELs in a broad scientific community, from synchrotron radiation to nuclear physics.

They have both worked innovatively at the frontiers of SRFELs. V. Litvinenko installed the electromagnetic optical klystron OK4 on the by-pass of VEPP3 at Akadiemgorodok (Russia) in 1988, and H. Hama installed the first optical klystron with adjustable planar-to-helical field in 1996 on UVSOR in Okazaki (Japan). These improvements produced new short wavelength records for FELs: 240 nm for VEPP3 SRFEL in 1988, 238 nm for the UVSOR SRFEL in 1996. Then, after a move by Litvinenko to Duke University, 226 nm in 1998, and to 193 nm in 1999.

They have both been very active in advancing the understanding of storage ring FEL dynamics, H. Hama performed very early systematic sophisticated experimental analysis of the FEL micro-pulse temporal and spectral distribution versus time for different operating conditions starting in 1994. He also carried out detailed studies on FEL performances for different momentum compaction factors. V. Litvinenko developed a complete theoretical model of giant and super pulses whose findings are in good agreement with measurements performed on the DUKE FEL, and used super pulses to produce strong coherent harmonics.

They have developed technological improvements to SRFELs that improve the device for users. Hama developed a feedback system to maintain the FEL pulse at perfect synchronism, leading successful pump-probe two-color experiments in gas phase using FEL light and synchrotron radiation for the first time. A transverse feedback system was developed in Duke FEL to stabilize beam operation.

A very important contribution of their work has been the production of monochromatic gamma-rays by Compton Back-Scattering with SRFELs. Hama performed the first experimental demonstration at UVSOR

in 1996 in the MeV range. At Duke University, Litvinenko developed a high intensity gamma ray user facility (HIGS), leading to new discoveries in Nuclear Resonant Fluorescence and near-threshold break-up of Deuterium. This has broadened the use of FELs into the field of nuclear physics.

Besides their leading role in FELs, they continue to make important contributions to the field of physics as a whole. They have trained many graduate students and have assisted in the commissioning of numerous synchrotron light sources. Both operated FEL user facilities providing hundreds of hours of FEL light to users each year. Litvinenko is now working on electron-ion colliders. Hama is involved in the design of the next generation of storage rings in Japan.

The FEL Prize Committee

Previous FEL Prize Winners

2004 (Trieste) Vladimir Litvinenko and Hiroyuki Hama

2003 (Tsukuba) Li-Hua Yu

2002 (Argonne) H. Alan Schwettman and Alexander F.G. van der Meer

2001 (Darmstadt) Michel Billardon, Marie-Emmanuelle Couprie, and Jean-Michel Ortega

2000 (Durham) Stephen V. Benson, Eisuke J. Minehara, and George R. Neil

1999 (Hamburg) Claudio Pellegrini

1998 (Williamsburg) John Walsh

1997 (Beijing) Kwang-Je Kim

1996 (Rome) Charles Brau

1995 (New York) Richard Pantell and George Bekefi

1994 (Stanford) Alberto Renieri and Giuseppe Dattoli

1993 (The Hague) Roger Warren

1992 (Kobe) Robert Phillips

1991 (Santa Fe) Phillip Sprangle and Nikolai Vinokurov

1990 (Paris) Todd Smith and Luis Elias

1989 (Naples, FL) William Colson

1988 (Jerusalem) John Madey

A Tribute to Professor Emeritus Haruo Kuroda

Professor H. Kuroda will be remembered by the free-electron laser (FEL) community for his enthusiastic building of the mid-infrared (MIR) wavelength region FEL users facility as one of the most advanced and leading in the world at Noda campus, Science University of Tokyo in 1999 - 2003. He designed and prepared many users experimental laboratories dedicated to FEL applications in chemistry, physics, material and medical science and so on, and he started the experimental programs and proposals. After he started routine operation of the mid-infrared region free-electron laser, another FEL in the far-infrared (FIR) wavelength region was just ready to start up, and many experiments were planned using both of the MIR and FIR free-electron lasers.

It has been extremely regrettable that Professor H. Kuroda and his followers did not have the possibility to add their new and fruitful findings using the FELs to his famous, pioneering work in the early history of synchrotron radiation sciences because he passed away so suddenly, after contracting interstitial pneumonia, on the 4th May, 2004. On behalf of the FEL community in Japan, I would like to ask you, all of his friends and his acquaintances in the world, that now we would share the deep sense of loss and pray for the soul of the late Professor H.Kuroda.

After his Buddhist funeral ceremony in the 7th May 2004, the Japanese Government decided to confer a decoration from His Majesty the Japanese Emperor for his great academic contributions. His conferment is named The Order of the Sacred Treasure, Gold Rays with Neck Ribbon.

Professor H.Kuroda's biographical outline is briefly described below. As one of the heartful tributes given by his old friends in the synchrotron radiation community records (The Independent, England, 27th May 2004) "Haruo Kuroda was one of the world's foremost experts on the design and application of synchrotron radiation to the elucidation of a wide range of scientific problems. Haruo Kuorda was a humble, almost self-effacing individual, short in physical stature, but towering in his intellectual energy and authority". He will be sadly missed by all who knew him.

Eisuke John Minehara

Haruo Kuroda, Chemist, biographical outline

- Born in Tokyo, 28 June1931;
- Research Associate, Department of Chemistry, University of Tokyo 1960-1968,
- Associate Professor, University of Tokyo 1968-1971,
- Professor, University of Tokyo 1971-1977,
- Department Chairman, University of Tokyo 1977-1979,
- Chairman of the Library Council, University of Tokyo 1988-1991;
- Chairman of the Advisory Council, Photon Factory, KEK, Japan 1980-2003;
- Chairman of the Library Council, National University of Japan 1988-1991;
- Professor, Science University of Tokyo 1992-2003,
- And Director of Infrared Free-Electron Laser Center 1999-2003;
- Married 1958 to Hiroko Fujimoto (two sons);
- Died in Tokyo, 4 May 2004.

CONFERENCE ORGANISATION

Organised by

Sincrotrone Trieste, Italy

Conference Chairs

René Bakker (Sincrotrone Trieste)
Richard Walker (DLS)

Programme Committee Chairs

René Bakker (Sincrotrone Trieste)
Luca Giannessi (ENEA)

Users Workshop Chair

Marino Marsi (Sincrotrone Trieste)

Local Organizing Coordinator

Carlo Bocchetta (Sincrotrone Trieste)

Conference Treasurer

Francesco Antonangeli (Sincrotrone Trieste)

International Executive Committee

I. Ben-Zvi (BNL)
W.B. Colson (NPGS)
M.-E. Couprie (LURE)
A. Gover (Tel Aviv University)
H. Hama (Tohoku University)
K.-J. Kim (ANL & University of Chicago)
Y. Li (IHEP)
V.N. Litvinenko (BNL & Duke University)
G.R. Neil (TJNAF)
C. Pellegrini (UCLA)
M.W. Poole (Daresbury)
A. Renieri (ENEA)
C.W. Roberson (ONR)
J. Rossbach (Hamburg University)
T. Smith (Stanford University)
A.F.G. van der Meer (FOM)
N.A. Vinokurov (BINP)
R.P. Walker (DLS)

International Programme Committee

S. Biedron (ANL and MAX-Laboratory)
J. Clarke (ASTeC, Daresbury Laboratory)
M.E. Couprie (CEA)
J. Dai (BFEL)
G. Edwards (Duke U.)
J. Feldhaus (DESY)
M. Ferrario (INFN)
J. Galayda (SLAC)
R. Hajima (JAERI)
H. Hama (Tohoku U.)
T. Hara (RIKEN)
D. Krämer (BESSY)
I. Lindau (SLAC)
A. Lumpkin (APS/ANL)
P. Michel (FZ Rossendorf)
D. Nölle (DESY)
J.S. Oh (PAL)
Y. Pinhasi (The College of Judea and Samaria)
R. Prazeres (LURE)
S. Reiche (UCLA)
M. Shinn (JLAB)
T. Tanaka (RIKEN)
X. Shu (IAPCM)
T. Smith (Stanford U.)
N. Tolk (Vanderbilt U.)
N. Vinokurov (BINP)
Y. Wu (Duke U.)
T. Yamazaki (Kyoto U.)
L.H. Yu (BNL)

Local Organising Committee

A. Accettulli
I. Andrian
L. Biecker
C.J. Bocchetta
D. Bulfone
G. D'Auria
G. De Ninno
S. Deiuri
B. Diviacco
C. Fiandra
C. Grubissa
P. Michelini
M. Nadalin
G. Risicato
E. Save
R. Skabar
M. Trovò

Organising Secretariat

the office
via San Nicolò 14, 34121 Trieste, Italy
e-mail: *theoffice@theoffice.it*
web: *http://www.theoffice.it*

EDITORIAL TEAM

Paper Reception Desk

M. Antonetti
R. Duimich
C. Garettini
C. Grubissa
M. Nadalin
E. Save

Proceedings Office

I. Andrian
M. Bressan
P. Craievich
S. Deiuri
R. De Monte
V. Forchì
R. Passuello
G. Penco
C. Roberti
M. Trovò
L. Zambon

Posters

S. Di Mitri
G. Risicato
M. Trovò

Presentations

M. Folla
I. Gregori

Information Technology

C. Allocchio
I. Andrian
A. Cipolat
E. Cocolo
S. Deiuri
M. Stolfa

INSTITUTIONAL SPONSORS

Area Science Park
Consiglio Nazionale delle Ricerche (CNR)
Council for the Central Laboratory of the Research Councils (CCLRC)
Deutsches Elektronen Synchrotron in der Helmholtz Gemeinschaft (DESY)
Ente per le Nuove tecnologie, l'Energia e l'Ambiente (ENEA)
Istituto Nazionale di Fisica Nucleare (INFN)
Regione Autonoma Friuli Venezia Giulia
Sincrotrone Trieste (ELETTRA)

INDUSTRIAL SPONSORS AND EXHIBITORS

Accel Instruments
Advanced Energy Systems
C.A.E.N. – Costruzioni Apparecchiature Elettroniche Nucleari
CINEL – Strumenti Scientifici
Cinquepascal
CPI – Communications & Power Industries International Inc.
Danfysik
Instrumentation Technologies
Lecroy
MBE – Mediterranean Broadcasting Equipment
Micos Italia
RMP – Meccanica Progettazione Prototipi
Thales Electron Devices

Contents

Preface

FEL Prize Talk and New Lasing

FEL Theory

Single-Pass FELs

FEL Oscillators

FEL Experimental Results

FEL Technology

New Concepts

FEL Users Workshop

Tables of Operating and Proposed FELs

Indexes

R&D EXPERIMENTS AT BNL TO ADDRESS THE ASSOCIATED ISSUES IN THE CASCADING HGHG SCHEME

Li Hua Yu, 725C, BNL, Upton , NY11973, USA

Abstract

Several experiments that can be carried out at BNL's DUVFEL are discussed to address issues associated with cascaded HGHG FELs. These include: Chirped Pulse Amplification (CPA), HGHG with seed shorter than electron bunch length, 8th harmonic HGHG (from 800 nm to 100 nm), regenerative synchronization of seed pulse and electron bunch, tuning of HGHG without changing seed, and cascading from 400 nm to 100 nm to 50 nm using NISUS and VISA undulators. These experiments may have important impact on the development of multi-stage cascaded HGHG FELs.

INTRODUCTION

The proof-of-principle HGHG experiment at 5 μm [1,2] and recent HGHG experiment at the DUVFEL [3] have generated significant interests in the FEL community. The more relaxed requirement on electron beam current and emittance to generate coherent deep UV output with much narrower bandwidth and high pulse energy stability, as exhibited by the recent experiment, and its potential to be generalized to soft-x-ray FEL, have attracted much attention. Several labs[4], including BESSY [5], ELETRRA [6], LBL [7], MIT [8], and SSRF [9] proposed the development of UVFEL based on HGHG principle or soft-x-ray FEL based on the cascaded HGHG principle [10,11,12]. Among them SSRF has already started the construction of an FEL system based on the HGHG principle. Hence it would be a contribution to be able to carry out a first proof-of principle experiment of cascaded HGHG at the DUVFEL. In this paper, we discuss this experiment and several associated experiments that can be carried out at BNL before this experiment and may also have important impact on the development of multi-stage cascaded HGHG FELs.

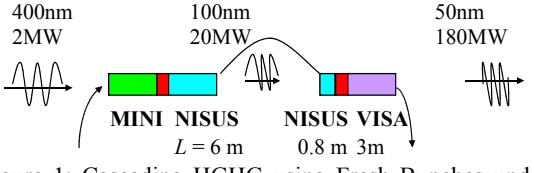

Figure 1: Cascading HGHG using Fresh Bunches under the present e-beam conditions, see Table 1, and a seed pulse with a duration of 200 fs.

THE CASCADED HGHG DEMONSTRATION EXPERIMENT AT DUVFEL

The analysis of recent experiment at DUVFEL shows that it is possible to realize a proof-of-principle cascaded HGHG experiment with existing system parameters and with reasonable cost, as we shall show in the following. This suggested experiment is a cascaded HGHG with two stages. In the future it is possible to generalize it to several stages by other labs. We will also show that even though the DUVFEL is a small facility, with present electron beam parameters and without significant increment of hardware, we can carry out experiments to address several important issues associated with the cascaded HGHG FEL.

Table 1: Present electron beam conditions.

Peak current	I	300	A
Bunch duration	σ_t	1	ps
Beam energy	E	288	MeV
Energy spread	σ_γ/γ	1×10^{-4}	
Norm. emittance	$\varepsilon_{n,xy}$	2.7	π mm mrad

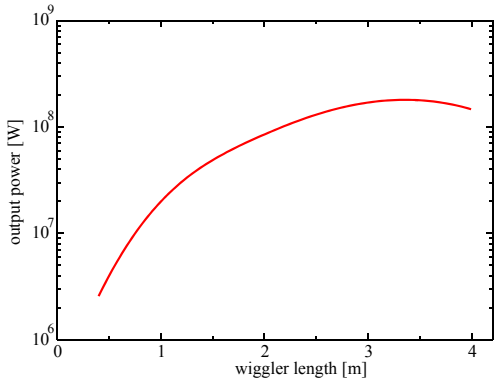

Figure 2: TDA simulation of the last stage of a cascading HGHG from 400 nm, to 100 nm, to 40 nm for a beam current of 500 A and a seeding at 100 nm of 20 MW.

A cascaded HGHG FEL with two stages is schematically shown in Figure 1. More detailed description of the principle of the cascaded HGHG is given in [10]. In this experiment we propose to use the first 6 meters of the existing NISUS undulator to achieve output at 100 nm using a 400 nm seed into the existing MINI undulator. When compared with the recent published PRL paper [3], it is easy to see that the parameters in the proposed experiment, electron beam current (300 A), energy spread (1×10^{-4}), pulse length (1ps), and emittance (2.7 μm) are the same as we have already established by the recent results [3]. The electron beam energy is to be increased from the present 200 MeV to 288MeV. Simulation shows that when seeded with a 2-MW 400-nm 200-fs laser-pulse, the 100 nm stage will reach beyond 20MW with this set of parameters in 6 m (the recent experiment show saturation to 100MW in 5 m, at 266 nm), but we can always control the output at the desired 20MW level, for example by tuning the dispersion

magnet before the NISUS away from maximum bunching, or use a part of the electron bunch with less current than 300 A. Following the 6 m NISUS is a shifter chicane (about 0.3-0.4 m long), which will shift the 100 nm output 200 fs pulse to a "fresh" part of the electron bunch. This is followed by a 0.8 m long NISUS section as a modulator for the next stage of HGHG, and then by a dispersion magnet (about 0.3-0.4 m long). The dispersion magnet will transform the 100 nm energy modulation into micro-bunching, which will generate coherent radiation at 50 nm and will be exponentially amplified to saturation at 180 MW power in the 3-m long VISA undulator following this dispersion magnet.

Here we assume 300 A for the beam current, so the saturation is at 3 m in the VISA undulator. Within 2 meters the output is only about a factor 2 from saturation, as shown by Figure 2. Recently a tomography [13] at our DUVFEL has shown that after compression the peak current is more than 400 A, as is shown in Figure 3 (see the current profile at the right side of the figure). In near future, we will improve the peak current to more than 500 A, and the saturation can be reached at 2 meters in VISA. At the present, we have already the parts for a 2-m long VISA undulator, hence this will significantly lower the cost of the project.

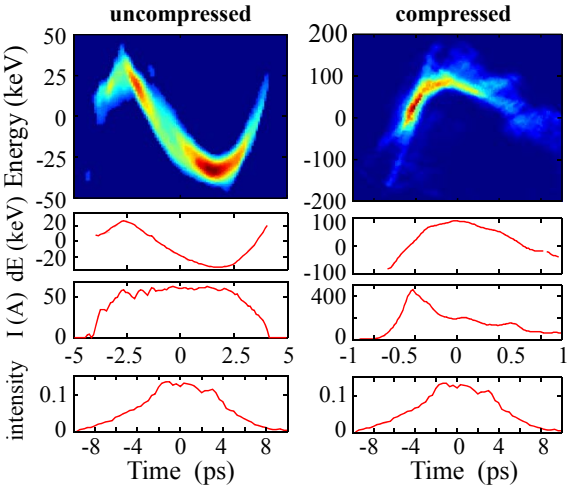

Figure 3 Tomography of the electron bunch distribution for a uncompressed (left) and compressed (right) bunch [13].

Another important issue in the cascading scheme is the time jitter between the electron bunch and the seed laser. It is important that the jitter should be much less than the electron bunch length. As a recent experiment using electro-optical method [13] showed, the jitter is about 300 fs FWHM. To see the relation between the cascaded FEL laser pulse and the electron pulse, we plot them in Figure 4 against the background of the current profile obtained by the tomography in Figure 3. This figure shows that with the jitter about 300 fs, it is still possible to arrange the seed pulse and the cascaded pulse so that the first HGHG operates at about 200 A while the second HGHG stage uses the peak of more than 400 A. Therefore our analysis shows clearly the feasibility of this experiment, which is based on the existing system parameters.

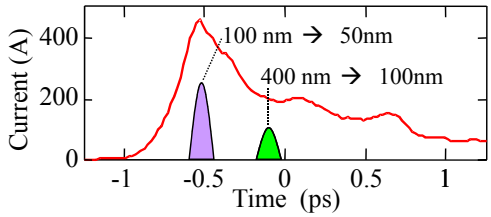

Figure 4: Illustration on double use of an electron bunch in a cascaded HGHG setup.

It is also clear that the space needed by this experiment is available because we only need 6 meters NISUS for the first HGHG stage. The present NISUS is 10 m long, hence leaving 4 meters room for the second stage. In addition, the most important hard ware, the VISA parts, is already in our possession. So the main works for the implementation of this experiment is the removal of the 4 m NISUS and assembly and installation of the 2-m VISA. Hence the total cost is significantly reduced.

Not only the success of the cascaded HGHG experiment provides a first proof-of-principle demonstration, the output of the cascaded HGHG at 50 nm with 180 MW peak power also provides an unprecedented high intensity coherent new light source at this wavelength.

SEVERAL EXPERIMENTS ADDRESSING THE ISSUES ASSOCIATED WITH THE CASCADED HGHG SCHEME

In addition to the cascaded HGHG proof-of-principle experiment, there is also a series of FEL experiments closely associated with it, but in smaller scale, hence can be carried out at DUVFEL earlier. These experiments will significantly improve and advance the multi-staged cascaded scheme. In the following, we shall discuss these experiments: their significances, and their present status.

Chirped Pulse Amplification (CPA)

CPA in FEL can be used to generate high peak power short pulse (bellow 10-20 fs), which will have wide applications in physics and chemistry and also can be used as seed for the multi-staged cascaded HGHG. Because of the high efficiency and wide bandwidth of FEL, CPA using FEL can generate unprecedented short radiation pulses in short wavelength region (bellow 100 nm) [14]. After the recent success of the HGHG experiment at DUVFEL, we have carried out the first step towards a first demonstration of CPA in FEL at 266 nm [15]. As shown in Figure 5, the green bars in the lower part of the figure represent chirped seed with the tail at shorter wavelength, while the blue curved bar represent the electron bunch with three different chirping of energy (with tail at higher beam energy). The three curves in the top figure are the output spectrum for these three settings. The middle one (blue curve) has the largest bandwidth. In the latter setting the electron beam energy chirp matched

to the seed with best overlap in the time-energy phase space. In the other two cases there is less matching, which results in a narrower bandwidth. Due to RF curvature, the best overlap occurs at different part of the seed for each case, hence the wavelength is also shifted.

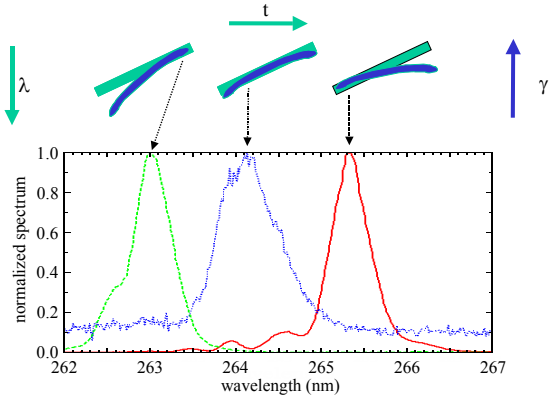

Figure 5: Several CPA HGHG Spectra (bottom). The top part illustrates the explanation for the different spectrums as an effect or the RF curvature. See text for details.

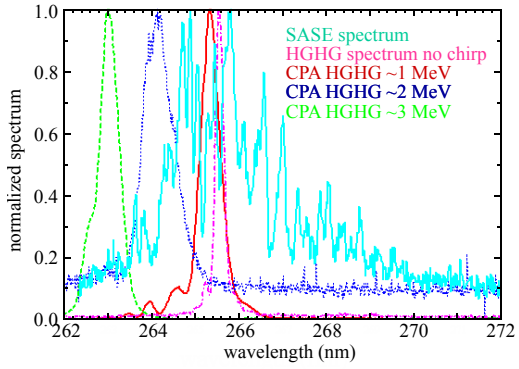

Figure 6: Chirped and unchirped HGHG spectra.

In Figure 6 we plot the 3 spectra with the spectrum of SASE and HGHG without chirp (the pink curve with minimum bandwidth has nearly fourier transform limited bandwidth). It clearly shows the significant increase of the bandwidth for CPA, and the smooth profile of the CPA spectra, compared with the SASE spectrum indicate the well preserved coherence for the CPA output, which is essential for later compression to generate short pulses.

Figure 7 shows the measured bandwidth as a function of the energy chirp of the electron bunch. Since the seed laser bandwidth is 5.5 nm, we expect the CPA with bandwidth of 1.8 nm in idealized situation (our current experiment is carried out in 3rd harmonic of the seed at 800 nm with output at 266 nm, hence the bandwidth is divided by 3 for a perfect CPA condition). The actually achieved bandwidth is 1.5 nm, with future potential of further improved bandwidth more close to 1.8 nm. Based on this data, the expected compressed CPA output pulse length would be about 50 fs or larger, depends on the quality of the preservation of the phase linearity in the HGHG process.

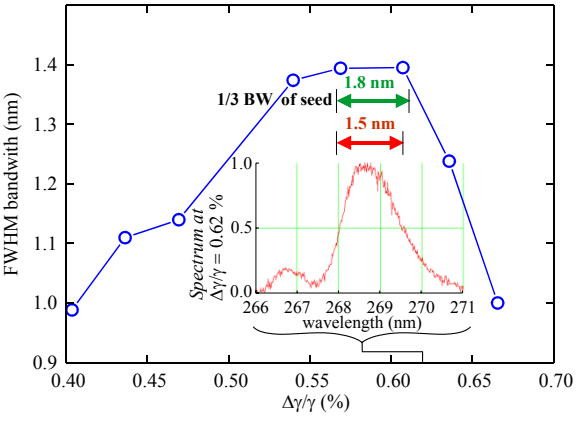

Figure 7: Spectral bandwidth vs Chirp. The inset shows the recorded spectrum at a chirp of 0.62 %.

The next steps in this direction will be the measurement of the preservation of the phase chirp linearity by a method called Spectral Interferometry for Direct Electric Field Reconstruction (SPIDER) [16] and actually carry out the compression as a first demonstration of CPA in FEL. This is now in advanced stage of preparation.

In Figure 8 we show the basic principle of the SPIDER. The 266 nm output pulse is split into two temporarily spaced pulses and mixed with a longer 800 nm chirped pulse and creates two 400 nm pulses. Since the 800 nm pulse is chirped, these two 400 nm pulses not only are spatially separated, but also have their wavelength shifted relative to each other. Hence, when they are sent to a

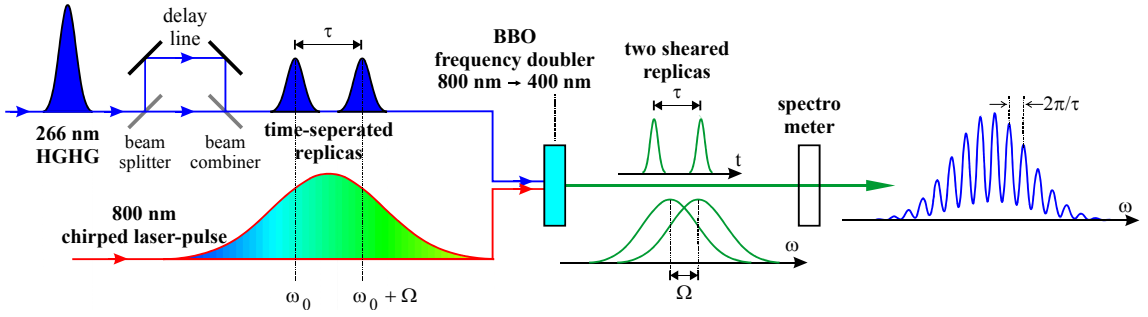

Figure 8: Principle of the SPIDER (Spectral Interferometry for Direct Electric-Field Reconstruction) setup [10].

spectrometer, their spectrum form a interference pattern as show in the upper right corner of the figure. The fringes give information about the relation between the phase and frequency, thus can be used to reconstruct the electric field of the 266 nm pulse.

A first SPIDER measurement result for an unchirped HGHG pulse is shown in Figure 9. It is clear the phase change within the bandwidth is negligible. The measurement on chirped pulse is still under way.

In the future works, it would be challenging and exciting to develop CPA bellow 200 nm, which would be an unprecedented achievement, in particular below 100 nm once our electron beam energy is upgraded to 300MeV.

A first SPIDER measurement result for an unchirped HGHG pulse is shown in Figure 9. It is clear the phase change within the bandwidth is negligible. The measurement on chirped pulse is still under way, some preliminary results are presented in the reference in these proceedings [16].

In the future works, it would be challenging and exciting to develop CPA bellow 200 nm, which would be an unprecedented achievement, in particular below 100 nm once our electron beam energy is upgraded to 300MeV.

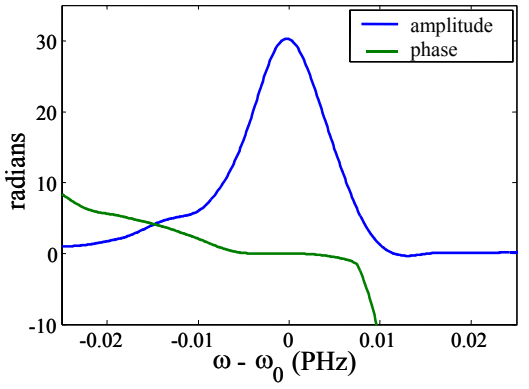

Figure 9: First SPIDER measurement of an unchirped HGHG pulse.

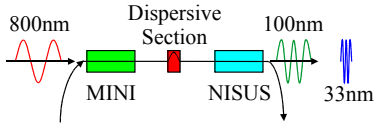

Figure 10: Experimental setup for lasing at the 8th harmonic.

8th harmonic HGHG at DUVFEL

Our present HGHG is in 3rd harmonic, as we have mentioned before. The design was based on data from 10 years ago, and was a conservative one: it was based on the assumption of local energy spread of 1.5×10^{-3}, while our recent experiment showed it is bellow 1×10^{-4}. Based on our new data obtained during the HGHG experiment, we propose to carry out new 8th harmonic HGHG experiment with seed still at 800 nm, but output directly shorten to 100 nm instead of the present 266 nm, as shown in the schematic of Figure 10. The output reaches saturation to 100MW at about 8 m in NISUS, as shown in Figure 11. There will be non-linear harmonic output at 33 nm of about 1 MW, which will have significant applications in chemistry too.

As we mentioned before, the local energy spread is found to be less than 1×10^{-4} during the recent experiment. Actually there are indications that this can be as small as 0.3×10^{-4}. Theory of HGHG predicts that the highest harmonic number is determined by the local energy spread. Hence it means it is possible to reach even higher than 8 for the harmonic number in the future (ours will be limited to 8 by the 300 MeV electron beam energy we plan to upgrade to).

The significance of higher harmonic number in HGHG is that for a cascaded HGHG scheme it means we need fewer stages of HGHG to achieve shorter wavelength. Hence the demonstration of 8th harmonic HGHG will have important impact on future development.

The proposed 8th harmonic HGHG requires only the reduction of vacuum chamber of the present MINI undulator (the 0.8 m modulator before the NISUS) from the present about 4 cm to 2.1 cm, and a minor modification of the corresponding supporting mechanical structure of the undulator. Hence the cost associated with this advance is very low, the required man-power is also very limited.

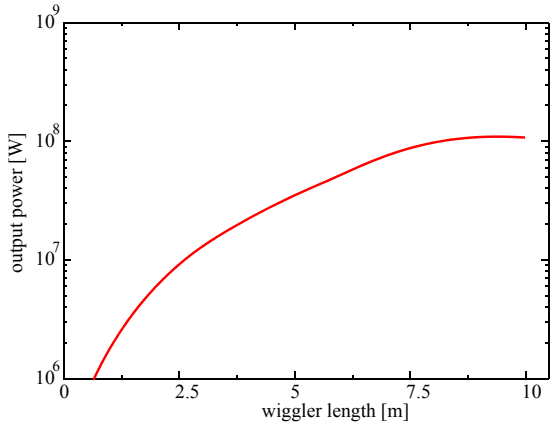

Figure 11: TDA simulation of the power vs distance for 100 nm in HGHG from 800 nm.

Short pulse HGHG

In the present HGHG experiment the electron bunch length is 1 ps, while the seed laser pulse length is 9 ps, as described in the PRL paper [3]. In a cascaded HGHG experiment the pulse length should be much shorter than the electron bunch length. In the proposed cascaded HGHG experiment, we shall use a seed length of 200 fs long. Hence as a first step towards the cascaded HGHG experiment, we shall test one stage of HGHG with 200 fs seed pulse. When the time jitter between the seed and the electron bunch is negligible compared with the electron bunch length, the measurement of the HGHG output

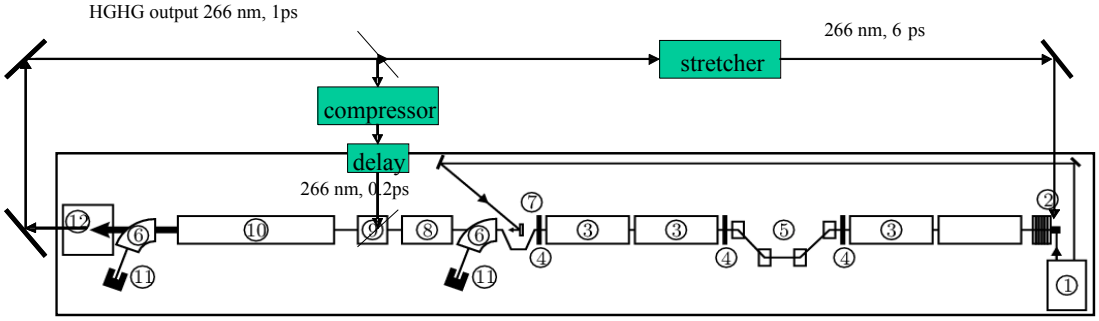

Figure 12: Regenerative synchronization of a seed pulse and electron bunches [ref].

power as a function of the relative delay between the seed and the electron bunch can be used to characterize the electron beam parameters as a function of time within the electron bunch length. This information is very important for the understanding of the properties of the electron beam.

However, there is a time jitter of about 300 fs FWHM, as we have mentioned before. This will give an error bar about the current profile obtained by the scanning of the short pulse HGHG. Hence a statistical analysis of the measured scanning data should be carried out to compare with theory to see if this error bar profile is consistent with the 300 fs jitter, measured by the electro-optical method.

This experiment does not need new hardware, and has already been in an early stage of study. The success of this experiment will confirm the feasibility of the proposed cascaded HGHG experiment. In particular, it will confirm the theoretical prediction of the relation between the output pulse energy fluctuation and the time jitter.

Regenerative synchronization of a seed laser with the electron bunch

As we mentioned before, it is important that the time jitter between the seed laser pulse and the electron bunch should be much smaller than the electron bunch length. This condition is roughly satisfied in our proposed cascaded HGHG experiment: the jitter is 300 fs FWHM while the electron bunch is 1ps. However, further reduction of this jitter is desirable: it will reduce the fluctuation caused by the time jitter. Furthermore, in the future possible multi-staged cascaded HGHG FEL, we may need to use more than two "fresh" parts of the electron bunch, and to achieve much shorter wavelength, we may need higher current so the electron bunch should be further compressed, thus the electron bunch length may be shorter (e.g., 400 fs bunch length for a 750 A current with the same electron bunch charge of 300 pC for our case to achieve 2 nm soft-x-ray FEL). Both of these will require the time jitter to be further reduced.

Our recent analysis provides a new scheme to reduce the time jitter from 300 fs to below 50 fs [17]. In this scheme, as shown in Figure 12, the HGHG output at 266 nm is sent back to the photo-cathode of the RF gun to generate a second electron bunch. In the mean time, a beam splitter will divert a small fraction of the HGHG output to seed the next HGHG stage. In the specific example as described in detail in the reference [17], using the present DUVFEL as a demonstration of the basic principle of this regenerative synchronization scheme, the 1 ps output of the HGHG pulse will be stretched by a pulse stacking method to the desired photo-cathode pulse length of 8 ps, while the split seed pulse for the next HGHG stage is compressed to 200 fs or less. The first cathode drive laser pulse may have a time jitter relative to the RF phase of the order of 300 fs, however, since the first seed pulse is a few ps long, and the electron bunch is 1ps long, the jitter will not cause any significant fluctuation in the first HGHG output.

Since the first HGHG output pulse length is completely determined by the 1ps electron bunch length, it is exactly synchronized with the electron bunch. The electron bunch at the exit of the RF gun has a time jitter of about 300 fs, i.e., the same as the time jitter of the photo-cathode laser, which is exactly synchronized with the seed laser pulse. However, since the electron bunch is compressed from 6 ps to 1 ps, the time jitter of the electron bunch after the compressor is also reduced by the compression ratio of 6, i.e., reduced from 300 fs to 50 fs. Hence, the jitter of the HGHG output is also reduced to 50 fs relative to the RF system. Thus the second electron bunch at the exit of the RF gun jitters also less than 50 fs.

Much more detailed and lengthy analysis as given by reference [17] shows that the time jitter between the second seed pulse and the second electron bunch is reduced by the compression ratio when compared with the jitter between the first electron bunch and the external laser, i.e., it is reduced from 300 fs to 50 fs. As a by-product, the electron beam energy fluctuation of the second electron bunch is also reduced by the same compression ratio, which in our DUVFEL case is about 5 to 6. Due to the high stability of HGHG process, the operation condition of HGHG can be arranged to fully explore the slow varying nature of the peak of the Bessel function in the micro-bunching process [18] so that if the seed intensity is higher then the output of HGHG will be slightly lower and vise versa. Like negative feedback, this further reduces the intensity fluctuation HGHG output.

As we can see from this brief discussion and as described in detail in reference [17], the required hardware for this synchronization experiment mainly consists of an optical transport line, an optical compressor, and a pulse stretcher, all the rest is the existing DUVFEL system. Hence the cost is also very low.

Once this synchronization is achieved, a detailed study of the temporal structure of the electron bunch in the time resolution of about 50 fs can be realized, and a much more stable output in the cascaded HGHG output can be expected, making it much easier to generalize the cascaded scheme to more stages and reach much shorter wavelength. This would be a significant advance in the field.

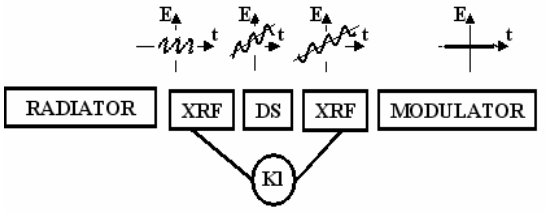

Figure 13: Scheme to tune the HGHG output wavelength without changing the seed wavelength [19]

Tunable HGHG without changing seed wavelength

A new practical scheme to tune the HGHG output wavelength without changing the seed wavelength has been proposed recently [19]. The scheme uses the fact that the dispersion section slightly compresses the electron bunch if it is energy chirped. As shown in Figure 13, after passing the modulator the electron bunch is chirped by a first RF cavity ("XRF"), and then, after passing through the dispersion section "DS" the chirp is removed by the second RF cavity. The energy modulation impressed upon the electron beam in the modulator is converted into micro-bunching in the dispersion section as in the usual HGHG process. However, the electron bunch is slightly compressed too, resulting also the slight compression of wavelength (if the chirp is positive, i.e., the tail of the bunch has higher energy). If the chirp is negative, it is obvious that the wavelength will become longer.

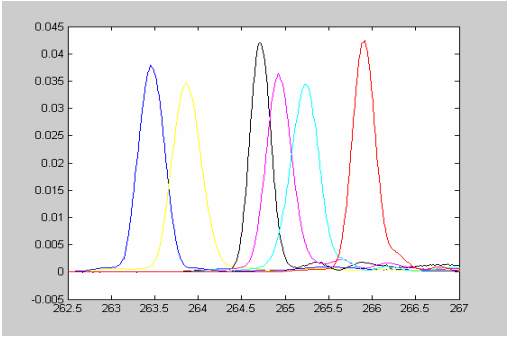

Figure 14: The spectrum of several HGHG output with different chirp but for a fixed seed wavelength.

Recent experiment at DUVFEL has used the chirp generated in the last section of the accelerator to confirm a 1% tuning. The spectrum of several HGHG output with different chirp but for a fixed seed wavelength are shown in Figure 14. With increased dispersion section we can verify larger tuning range. An analysis shows that it is possible to tune 20% wavelength when the two RF cavities shown in Figure 14 are used. It is obvious that this will greatly simplify the tuning of the HGHG process, and will have wide applications.

Summary

Based on the previous analysis, and the impact and scale of the several experiments, we can summarize these experiments in the order of a suggest time sequence as follows:

- Chirped Pulse Amplification
- HGHG with seed shorter than electron bunch length
- 8th harmonic HGHG (800nm→100nm)
- Regenerative synchronization of seed pulse and electron bunch
- Tuning of HGHG without changing seed
- Cascading using NISUS + VISA: 400nm →100nm→50nm.

It is seen that the cascading experiment requires the removal of the last 4 meters of NISUS and the installation of the VISA section, which will be a significant interruption of the DUVFEL schedule. Also the assembly and measurement of the VISA system will take time. Therefore, even though the cascading will have the most important impact, it is suggested to be implemented after the completion of the first five experiments. We emphasize that, as we have explained, this cascading experiment design is based on the existing beam parameters and existing parts, the experiment is not only very important, it is also rather realistic and cost effective.

REFEREENCES

[1] L.-H. Yu, M. Babzien, I. Ben-Zvi, L. F. DiMauro, A. Doyuran, W. Graves, E. Johnson, S. Krinsky, R. Malone, I. Pogorelsky, J. Skaritka, G. Rakowsky, L. Solomon, X.J. Wang, M. Woodle, V. Yakimenko, S.G. Biedron, J.N. Galayda, E. Gluskin, J. Jagger, V. Sajaev, I. Vasserman, Science, 289 (2000) 932

[2] A. Doyuran, M. Babzien, T. Shaftan , S.G. Biedron, L. H. Yu, I. Ben-Zvi, L.F. DiMauro, W. Graves , E. Johnson, S. Krinsky, R. Malone, I. Pogorelsky, J. Skaritka, G. Rakowsky, X.J. Wang, M. Woodle, V. Yakimenko, J. Jagger, V. Sajaev, I. Vasserman , Phys. Rev. Lett. 86, 5902 (2001)

[3] L.H. Yu, A . Doyuran, L. DiMauro, W. S. Graves, E. D. Johnson, R. Heese, S. Krinsky, H. Loos, J.B. Murphy, G. Rakowsky, J. Rose, T. Shaftan, B. Sheehy, J. Skaritka, X.J. Wang, Z. Wu, PRL, 91, 7, 074801 (2003)

[4] Workshop on the Physics of Seeded FELs ,MIT http://mitbates.mit.edu/xfel/conference.htm. (6/2004)

[5] D. Krämer, "A Multistage HGHG-Scheme for the BESSY Soft X-ray Multi User FEL Facility", these proceedings (2004).
[6] S. Di Mitri, R.J. Bakker, P. Craievich, G. D'Auria, G. De Ninno, B. Diviacco, L. Tosi, V. Verzilov, "Start-to-end simulations for the FERMI project at ELETTRA", these proceedings.
[7] J. Corlett, W. Fawley, G. Penn, W. Wan, and A. Zholents, M. Reinsch and J. Wurtele, contribution THPOS51, in these Proceedings
[8] http://mitbates.mit.edu/xfel/
[9] Zhao Zhentang, private communication (2004)
[10] Juhao Wu, and Li Hua Yu, Nucl. Instru. Meth., A475, (2001) 104
[11] S.G. Biedron, S.V. Milton, H.P. Freund, Nuclear Instruments and Methods in Physics Research, **A475** (2001) 401
[12] F. Ciocci, G. Dattoli, A. De Angelis, B. Faatz, F. Garosi, L. Giannessi, P. L. Ottaviani, A. Torre, IEEE J. of Quant. Electron., **31-7** (1995), 1242
[13] H. Loos, A. Doyuran, J. B. Murphy, J. Rose, T. Shaftan, B. Sheehy,Y. Shen, J. Skaritka, X.J. Wang, Z. Wu, L.H. Yu, PAC 2003
[14] L.H.Yu, E.Johnson, D.Li, D.Umstadter, Phys. Rev. E, Phys. Rev. E, 49, 4480 (1994)
[15] A. Doyuran, L. Di Mauro, R. Heese, E.D. Johnson, S. Krinsky, H. Loos,, J.B. Murphy, G. Rakowsky, J. Rose, T. Shaftan, B. Sheehy, Y. Shen, J. Skaritka, X. Wang, Z. Wu, L.H. Yu, Proceedings of FEL2003, Tuskuba , Japan (2003)
[16] Z. Wu, E. Johnson, S. Krinsky, H. Loos, J. Murphy, T. Shaftan, B. Sheehy, Y. Shen, X. Wang, L.H. Yu, "Spectral Phase Modulation and chirped pulse amplification in HGHG", these proceedings
[17] L.H.Yu, Proceedings of FEL2003, Tuskuba , Japan (2003) BNL-71194-2003-IR
[18] Juhao Wu, L. H. Yu, BNL report 67732, (2000)
[19] T. Shaftan, S. Krinsky, H. Loos, J. Murphy, J. Rose, B. Sheehy, J. Skaritka, X. Wang, Z. Wu, L.H. Yu, "Experiments on the HGHG Wavelength Tuning at the DUV FEL", these proceedings (2004)

FIRST LASING OF THE ELBE MID-IR FEL

P. Michel, F. Gabriel, E. Grosse, P. Evtushenko, T. Dekorsy, M. Krenz, M. Helm,
U. Lehnert, W. Seidel, R. Wünsch, D. Wohlfarth, A. Wolf
Forschungszentrum Rossendorf, Germany

Abstract

First lasing of the mid-infrared free-electron laser at ELBE was achieved on May 7, 2004. The Radiation Source ELBE at the Forschungszentrum Rossendorf in Dresden is currently under transition from commissioning to regular user operation. Presently the electron linac produces an up to 18 MeV, 1 mA (cw) electron beam which is alotted to generate various kinds of secondary radiation. After the successful commissioning of the bremsstrahlung and channeling-X-ray facilities during 2003 stable lasing has now been observed in the IR range (15 to 22 μm). The oscillator FEL is equipped with two planar undulator units, both consisting of 34 hybrid permanent magnets with a period of 27.3 mm ($K_{rms} = 0.3 \ldots 0.8$). The distance between the two parts is variable and the gaps can be adjusted and tapered independently. At 19.6 μm an optical power of 3 W was outcoupled in a macro pulse of 0.6 ms duration using an electron beam energy of 16.1 MeV and an energy spread of less than 100 keV. The micropulse charge was 50 pC and its width slightly above 1 ps. With the installation of a second acceleration module for additional 20 MeV shorter wavelengths will become available in the near future.

INTRODUCTION

At Forschungszentrum Rossendorf a superconducting Electron Linac with high Brilliance and low Emittance (ELBE) has been constructed which can deliver a 1 mA cw beam at 40 MeV [1]. The electron beam is used to generate infrared light (Free Electron Lasers), X-rays (electron channelling), MeV-Bremsstrahlung, fast neutrons and positrons. Table 1 gives an overview of the secondary beams at the ELBE facility and the associated fields of science.

Table 1: Secondary radiation sources at ELBE and their scientific application

0...20 MeV γ-radiation	-nuclear physics -astrophysics
10...100 keV X-rays	-radiation damage of cells -study of phase transitions in liquid metals
5...150 μm infrared FEL	-semiconductor physics -radiochemical and biological experiments
0...30 MeV neutrons	-materials studies for fusion reactors
0...30 keV positrons	-defect studies in solids

OVERVIEW OF THE ELBE FEL

The ELBE accelerator is fed by a grid-pulsed thermionic gun operating at 250 keV. The gun can deliver 450 ps long pulses and bunch charges up to 77 pC at 13 MHz or 4 pC at 260 MHz. A macro pulser chops the electron beam with adjustable duty cycle and allows to generate a very flexible time structure. By means of two RF buncher cavities operating at 260 MHz and 1.3 GHz the pulses are compressed down to 10 ps upon injection into the first accelerator module.

The Linac uses standing wave RF cavities (1.3 GHz) designed for the TESLA test facility at DESY [2]. Two 9-cell superconducting niobium cavities are contained in a cryomodule cooled with superfluid helium at about 2 K. Each cavity has its own RF coupler and is driven by a 10 kW CPI klystron amplifier. The standard accelerating gradient amounts to 10 MeV/m and the beam energy after acceleration is 20 MeV. Downstream the first cryomodule a magnetic chicane is used for bunch length variation. After the installation of the second LINAC module in near future the full energy of ELBE of 40 MeV will be available.

Infrared radiation in the 5–25 μm range will be produced at ELBE in the undulator U27 [3]. It consists of two 34-pole sections with a length of 0.98 m each. The undulator structure has a period of λ_u=27.3 mm and consists of NdFeB permanent magnets and poles of decarburized iron (hybride type; the units were test modules for the TTF-Facility at DESY [4] and are modified for use as a "passive" undulator). The sections are mounted on carriages (delivered by DANFYSIK) such that the distance between the two sections is adjustable for phase-matching. The gaps (minimum=13.8 mm, corresponding to K_{rms}=0.70) of both sections can be varied independently. For high-gain lasing it is possible to introduce a taper of the field. Both sections were scanned and adjusted using a calibrated Hall probe setup at DESY. After installation at ELBE the field distribution was checked using the pulsed wire method [5]. The inner dimension of 10 x 34 mm^2 of the stainless steel vacuum chamber in the undulator required a well designed resonator. The cavity requirements are summarized in the following Table 2.

To optimize the extraction ratio over the whole wavelength range we use 5 mirrors with different hole sizes in

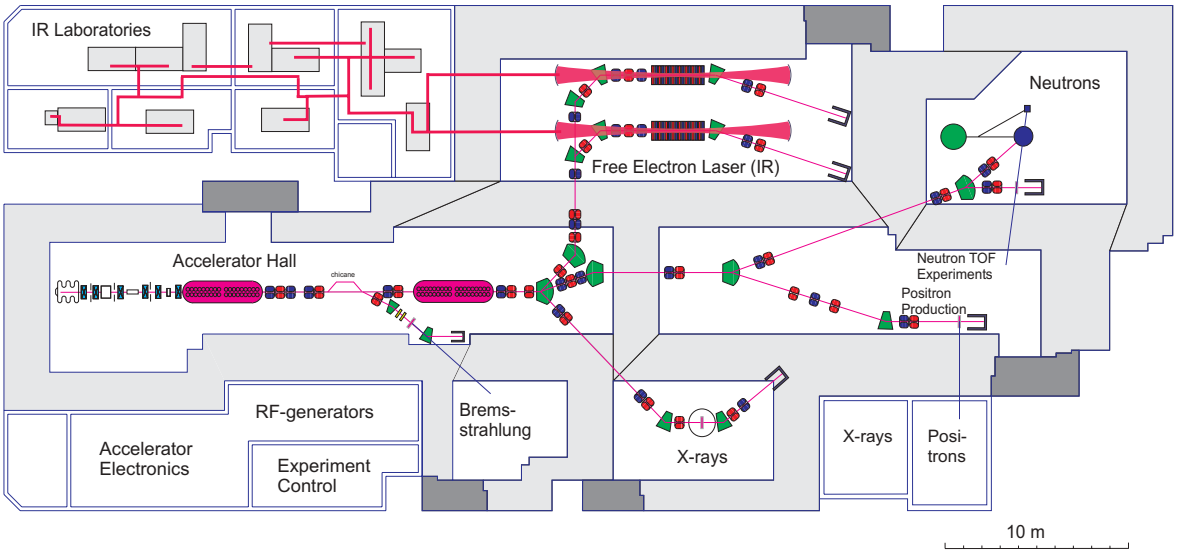

Figure 1: Layout of the radiation source ELBE.

Table 2: Design parameters of the U27 resonator

resonator type	stable, near concentric, symmetric
cavity length	11.53 m, stabilized < 0.5 μm
tilt stability	< 6 μrad
Rayleigh range	1 m
mirror diameter	7.5 cm
radii of curvature	5.94 m
g^2	0.88
diameter of the outcoupling holes	1.5, 2.0, 3.0 and 4.5 mm

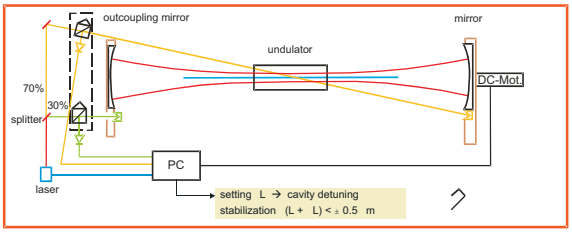

Figure 2: Schematic view of the resonator length control system. Its time constant is one Hz and hence fast in comparison to the thermal time constant of the resonator.

the upstream mirror chamber. The Au-coated Cu-mirrors are mounted on a revolvable holder (wheel), which is fixed to a high-precision rotational stage. Angular adjustment of the mirror wheel is performed using piezoelectric inchworm UHV motors, which provide both coarse and fine adjustments. A similar construction with 3 mirrors of different curvature is used in the downstream chamber. Here, the angular as well as longitudinal adjustment are designed with micrometers and a flexible bar for fine tuning driven by DC-motors outside the vacuum. The translation stage of this mirror will be used to adjust the cavity length to <5 μm accuracy.

To ensure the stability of the resonator at wavelengths down to 3 μm we require the mirror angular adjustment to have a resolution and stability in the order of 6 μrad. For the initial alignment of the mirror angles an accuracy in the order of 20 μrad is required. To achieve this accuracy we built an alignment system consisting of two collinear He-Ne lasers using insertable adjustment apertures inside the cavity.

A Hewlett-Packard interferometer system is used to monitor and stabilize the resonator length (see Fig. 2). The interferometer beam is split into two beams (70% and 30%). The low-intensity beam monitors the position of the upstream mirror using one of five retro reflectors installed adjacent to each outcoupling mirror. The high intensity beam passes through the same resonator chamber as the main laser and the electron beam. However, constraints on the width of the vacuum chamber do not leave enough space in the cavity for a separate parallel interferometer beam. Therefore, the latter will pass diagonally from one side of the upstream cavity mirror to a retro reflector on the other side of the downstream mirror. The control electronics for the two interferometer arms include a servo system to control and stabilize the relative distance between the two cavity mirrors using the motorized micrometer drive on the translation stage of the downstream chamber. There is no active tilt stabilization.

Estimating the maximum intracavity laser power, up to 15 W (cw regime) can be absorbed in the mirrors despite

their high reflectivity of more than 99% . To stabilize the mirror wheel temperature we installed a heater in the center of the wheel. Independently of whether the laser is working or not all components are at the same equilibrium temperature slightly above the expected saturation temperature. The mirror wheel is made of Cu to reduce mechanical tension between the mirrors and the surrounding material but thermally isolated from the high-precision rotational stage. The heat is dissipated directly to the outside of the vacuum chamber (Peltier element or air cooling).

Behind the out coupling hole the divergent IR beam passes through a CVD diamond vacuum window (thickness 320 μm; useable aperture 8 mm) mounted at Brewster angle. The adjacent optical transport system [6] guides the beam to the diagnostic station using 4 (3 toroidal and 1 flat) gold plated copper mirrors. The optics of the system was aligned by monitoring the spatial intensity profiles of a He-Ne guide laser which in turn is aligned to the resonator axis. The same laser will be used for indicating the position of the IR beam in each user laboratory with an accuracy better than 200 μm. Therefore, all optical components of the transport system have to be transparent for IR radiation and for 632 nm as well. Spot size and position of the waist at the diagnostic table are independent of the wavelength. Linear polarization is conserved. The transport system and the diagnostic station [7] both are purged with dry nitrogen to avoid absorption in air. From the main beam, approximately 10. . . 40 percent of the total power are extracted by different beam splitters for wavelength measurement and power monitoring.

FEL COMMISSIONING

Electron beam parameters measurements and diagnostics

One of the first steps in the FEL commissioning was the electron beam characterization done at a beam energy of 16 MeV. The transverse emittance was measured in the injector with the multislit method, while the emittance of the accelerated beam was measured with the quadrupole scan. At the maximum design bunch charge of 77 pC the emittance is measured to be 8 mm mrad. The gain reduction factor due to the finite emittance was 0.97 at first lasing, i.e., is almost negligible.

Since the FEL gain is linearly proportional to the beam peak current it is highly desirable to minimise the electron bunch length in the vicinity of the undulator. Previously, the bunch length was measured to 1.5 ps (rms) immediately at the accelerator exit using a Martin-Puplett interferometer (MPI). At the undulator with the beam tuned for lasing this value is however different. One can groupe the beam line elements, which influence the bunch length, between the accelerator exit and the undulator in three groups. These are the magnetic chicane, the "S"–shaped part of the beam line and drift spaces. The chicane can be used to adjust the R_{56} of the FEL beam line. For the FEL commissioning

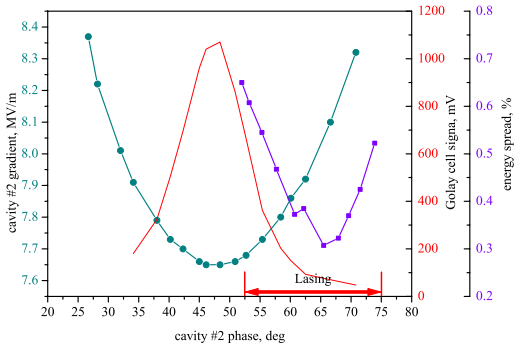

Figure 3: Electron beam parameters dependence on the second cavity phase (dots show the cavity gradient needed for constant energy, squares the energy spread and the line the bunchlength signal).

the MPI was installed right downstream of the undulator. Additionally a single Golay cell detectors was installed upstream of the "S" shaped part of the beam line to measure the total power of the coherent transition radiation, which is in the first approximation inversely proportional to the bunch length. Note that the two Golay cells installed at the interferometer can be used in the same way for the bunch length minimisation without scanning the interferometer. One of the key elements to tune the longitudinal phase space is the second accelerator cavity. Adjusting the cavity phase one changes the electron beam energy spread and the bunch length in the undulator vicinity because of the non-zero R_{56} of the beam line. For that reason the energy spread and the Golay cell signals were measured as a function of the second cavity phase. Fig. 3 shows results of the measurements. The bunch length at its minimum can be measured with the help of the interferometer. Here the FWHM of the interferogram is about of 2.5 ps.

The most important observation to note is the following: adjusting the cavity phase to have minimum energy spread drastically increases the bunch length in the undulator . In fact at the energy spread minimum the bunch length is so long that it cannot be measured with the MPI. It turnes out, however, that for lasing at the used (rather long) wavelength it is more critical to minimize the energy spread of the beam than to minimize the bunchlength.

The electron beam profile and position in the undulator are measured with the help of OTR view screens. They are made of beryllium and have a prism shape. The prism has a 1 mm diameter hole with is precisely aligned to the magnetic axis of the undulator. The view screens are used for the optical cavity alignment as well, which is important to ensure the overlap between the electron beam and the optical mode. It is noteworthy that the view screens are extremely long-term reproducible and reliable, which means that every time an inserted view screen takes the same po-

sition with a 10 μm accuracy.

ELBE is equipped with a strip-line beam position monitor (BPM) system. The resolution of the system is about 10 μm. There are two phenomena, which make this system very useful during the FEL operation. First, there is an energy drift observed for the first 2–3 hours every time the linac is switched on. A BPM located in a dispersive region is used to monitor the electron beam energy and to compensate the drift. The second phenomenon is the dependence of the R_{56} of the "S" shaped beam line on the electron beam path through it. Both phenomena are to be investigated more detailed in the future.

Observation of the spontaneous radiation

The general idea for the first FEL turn–on was to observe the spontaneous undulator radiation and to maximize it by systematic adjustment of the optical cavity and the electron beam parameters. First, the spontaneous radiation was observed downstream of the undulator so that the optical cavity was not incorporated in the measurements. For that purpose a mirror was inserted in to the beam line behind the last dipole deflecting the beam to the dump. The spontaneous radiation was outcoupled off the beam line through a KRS–5 window and focused by a parabolic mirror on a liquid nitrogen cooled MCT detector. An accurate alignment of the setup was essential for the spontaneous radiation measurements. For the first observation of the spontaneous radiation we had to use an extremely strong averaging of the data, however, that was an important step for the commissioning, since once the spontaneous radiation was observed we could optimize the machine using it as a tune signal.

Setting the optical cavity length

The adjustment of the FEL cavity to the correct length is an important prerequisite for the achievement of lasing. The cavity length of the FEL has been determined by employing an external frequency stabilized fs mode-locked Ti:sapphire laser (Femtolasers, Austria) [8]. The fs laser is operated at 78.0 MHz, i.e. the 6^{th} harmonic of the FEL. A 390 MHz reference signal is derived from the RF electronics of the gun, which is used for stabilizing the repetition rate of the fs laser with a phase-lock loop at its 5^{th} harmonic. This synchronization scheme reduces the timing jitter of the fs laser to 500 fs. The pulse train of the fs laser operating at 800 nm with 15 fs pulse duration is directed through the outcoupling hole into the FEL cavity. The light re-emitted through the outcoupling hole is detected via a beam splitter and a fast photodiode. When perfect synchronism of the fs laser and the FEL cavity is achieved, the detected optical pulse is enhanced due to constructive superposition of pulses circulating in the cavity. This results in an increase of the detected pulse intensity by a factor of five. The correct cavity length is determined by this method with an accuracy of some μm, i.e. a relative accuracy of 10^{-7}. Since the expected FEL operation covers a cavity detuning range of several 10 μm, this accuracy was sufficient to start lasing at the preset cavity length.

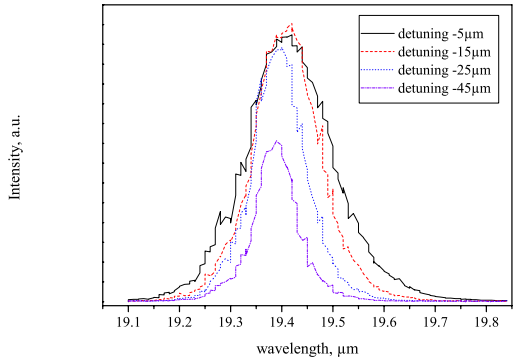

Figure 4: FEL spectra measured at different optical cavity detuning.

FIRST RESULTS

First lasing of the mid-infrared free-electron laser at ELBE was achieved on May 7, 2004. At 19.6 μm an optical power of 3 W was outcoupled using an macro-pulsed electron beam with anenergy of 16.1 MeV and an energy spread of less than 100 keV. The bunch charge charge was 50 pC.

The optical spectrum of the FEL

The FEL spectra were measured with a Czerny-Turner type spectrometer (SpectraPro-300i from ARC) which contains a turret with three different gratings (75 l/mm, blazed at 8 μm; 60 l/mm, blazed at 15 μm; 30 l/mm, blazed at 30 μm). For these measurements we used the side exit slit equipped with a single MCT detector. Fig. 4 shows how the spectral width decreases with the detuning of the cavity length.

Detuning curves

Up to now we operate the FEL in a pulsed mode only using an MCT detector to measure the FEL power as a function of time. In that mode the small signal gain is measured by fitting an exponential function to the rising slope of the MCT signal in its very beginning. The amplitude of the MCT detector close to the macropulse end is associated with the saturated power. The saturation power as well as the small signal gain are measured as a function of the optical cavity detuning. Typical results of such measurements are shown in Fig. 5.

Such measurements are made in the beginning of every FEL run, since the active cavity length stabilization is not yet commissioned and the cavity length may change between the runs. The measured detuning curve appears in

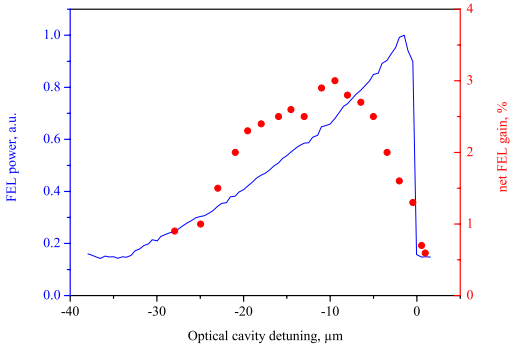

Figure 5: The saturation power (line) and the FEL net gain (dots) vs. optical cavity detuning.

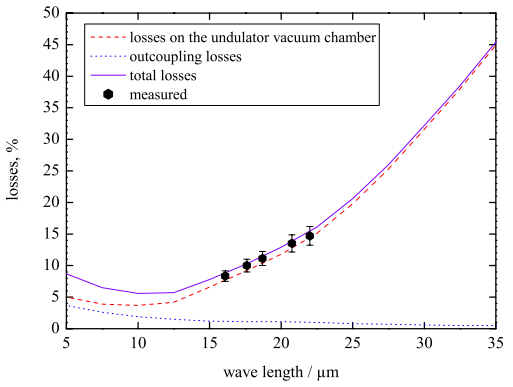

Figure 6: Optical cavity losses.

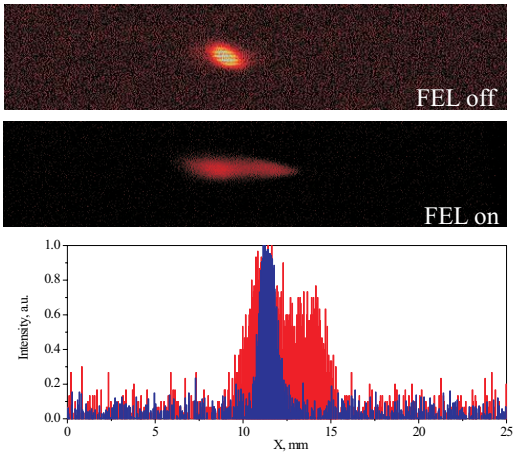

Figure 7: Electron beam spectrum change when the FEL turns on.

correspondence with the shape predicted by theory. It is also clearly observed that the detuning which optimizes the FEL gain differs from the detuning that optimizes the saturated power, which is also expected according to the theory.

Optical cavity loss measurements

The optical cavity losses can be measured similar to the small signal gain. At the end of the macropulse the electron beam is turned off instantaneously. Then, the characteristic decay time of the MCT signal carries the information on the cavity losses, which includes diffraction losses at the undulator vacuum chamber as well as the losses on the mirrors and the outcoupled beam. Thus, the total cavity losses were measured as a function of the FEL wavelength. The losses were also calculated using numerical code GLAD. The measurements are in reasonable agreement with the calculations. However, one has to note that the calculations are also limited in accuracy, probably of the same order of magnitude as the measurement accuracy. In the code there is no element like a tube which could simulate the vacuum chamber. For that reason a set of apertures was used to that purpose, which also causes some systematic error. More detailed numerical calculations of the cavity losses are in progress. Results of both the measurements and the calculations are shown in Fig. 6.

Electron beam energy spectrum

After the electron beam passes the undulator it is deflected to the beam dump by a dipole. There is a quadrupole doublet between the dipole and the dump, which is normally adjusted to have maximum transmission of the electron beam to the dump. However, it can also be also adjusted to image the electron beam energy spectrum on a view screen. Fig. 7 shows both the electron beam energy spectra when the FEL is off and when the FEL turns on. An increase of the energy spread is observed as predicted by Madey's second theorem. The change of the electron beam mean energy is measured as well, which allows one to estimate the amount of energy transferred from the electron beam to the optical beam.

Autocorrelation IR pulse length measurements

To characterize the ultrashort pulses generated by the FEL we built a non-collinear background-free autocorrelator. As SHG medium we use a CdTe crystal [9]. CdTe is transparent for a wide wavelength range in the FIR, thus, a good candidate for SHG of the FEL radiation.

In Fig. 8 we present the autocorrelation function measured at the maximum-power point of the detuning curve. From the measured autocorrelation we calculate a pulse duration of 2.1 ps, assuming a Gaussian temporal pulse shape. The FWHM of the spectrum is approx. 220 nm. The calculated time-bandwidth product is 0.46 which indicates Fourier-transform limited operation.

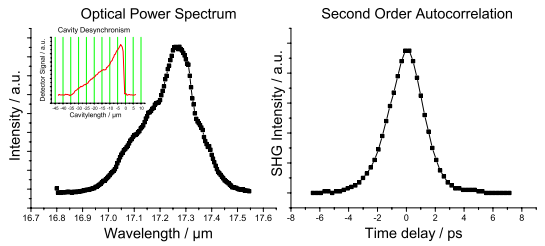

Figure 8: Power spectrum (left) and corresponding SHG autocorrelation (right) at the maximum power point of the cavity detuning curve shown in the insert (left).

FURTHER DEVELOPMENT

The ELBE far-IR FEL

To produce IR radiation in the THz region (up to 150 μm) an electromagnetic undulator with an undulator period of 12 cm is envisaged. In this region the FEL constitutes a unique radiation source. Radiation quanta with this energy are appropriate for the spectroscopy of low-energy elementary and collective excitations in solid-state quantum structures and in complex biomolecules as well (e.g. in DNA molecules).

Restricting the electron beam of ELBE to energies above 20 MeV, where the energy spread is better than at lower energies, an undulator with 50 periods guarantees a laser gain of 30%. This undulator should be supplied with a rectangular waveguide which is 10 mm high and extends from the undulator entrance to the downstream resonator mirror. Appropriate mirror curvatures minimize the resonator losses to values below 10%.

The ELBE FEL as a user facility

It is the intention that by the year 2005, the FEL operates as a user facility, being open to users worldwide, provided their scientific proposals have been favorably evaluated by the panel responsible for distribution of beamtime. Under the name “FELBE” the facility is member of the EC funded “Integrating Activity on Synchrotron and Free Electron Laser Science (IA-SFS)”, which comprises most synchrotron and FEL facilities in Europe and provides financial support to users from EC and associated states.

The relevant user facilities at FELBE comprise 6 laboratories. Some of these are also used by in-house groups, mainly in the areas of semiconductor physics, biophysics, and radiochemistry, and experiments there will require a certain level of collaboration with the in-house researchers. In particular noteworthy is the fact that a number of other optical sources from the visible to the THz frequency range are available, e.g. for two-color pump-probe experiments. These sources (Ti:sapphire laser and amplifer, OPO, OPA, broad-band THz generator) are all based on Ti:sapphire oscillators which are synchronized with the FEL with an accuracy better than a ps. Two laboratories are intended to provide users with utmost flexibility for their own experiments, also in scientific areas not covered by in-house groups (e.g., surface physics, molecular physics).

Instructions for beamtime applications will be available on the FELBE website (www.fz-rossendof.de/FELBE) by the end of 2004.

ACKNOWLEDGEMENTS

The authors would like to thank the colleagues from HEPL Stanford University, DESY Hamburg, Jlab Newport News and FELIX Nieuwegein for strong help and useful discussions. Special thanks to Prof. Todd Smith, A.F.G. van der Meer and Kevin Jordan.

REFERENCES

[1] F. Gabriel et al., NIM B 161–163 (2000), 1143–1147

[2] TESLA Test Facility Linac – Design Report (Ed. D.A. Edwards), DESY print TESLA 95–01

[3] P. Gippner et al., Contribution to the 23rd Int. Free Electron Laser Conf. Darmstadt, Germany, 2001, Nucl. Instr. and Meth. A483 (2002) II–55

[4] B. Faatz, J. Pflüger and Y.M. Nikitina, Nucl. Instr. Meth. A 375 (1996) 618

[5] P. Evtushenko et al., Contribution to the 25th Int. Free Electron Laser Conf. Tzukuba, Japan, 2003

[6] Th. Dekorsy et al., Contribution to the 24th Int. Free Electron Laser Conf. Argonne, USA, 2002, Nucl. Instr. and Meth. A507 (2003) II–35

[7] W. Seidel et al., Annual Report 2001, FZR–341 (2002) 34

[8] K.W. Berryman, P. Haar, and B.A. Richman, Nucl. Inst. Meth. A 358 (1995) 260–263

[9] J. Xu, G.M.H. Knippels, D. Oepts, and A.F.G. van der Meer, Opt. Comm. 197 (2001) 379–383

BACKWARD WAVE EXCITATION AND GENERATION OF OSCILLATIONS IN DISTRIBUTED GAIN MEDIA AND FREE-ELECTRON LASERS IN THE ABSENCE OF FEEDBACK

Yosef Pinhasi, Asher Yahalom, Yuri Lurie, Gad A. Pinhasi

Faculty of Engineering
The College of Judea and Samaria
P.O. Box 3, Ariel 44837, Israel

Abstract

Quantum and free-electron lasers (FELs) are based on distributed interactions between electromagnetic radiation and gain media. In an amplifier configuration, a forward wave is amplified while propagating in a polarized medium. Formulating a coupled mode theory for excitation of both forward and backward waves, we identify conditions for phase matching, leading to efficient excitation of backward wave without any mechanism of feedback or resonator assembly. The excitations of incident and reflected waves are described by a set of coupled differential equations expressed in the frequency domain. The induced polarization is given in terms of an electronic susceptibility tensor. In quantum lasers the interaction is described by two first order differential equations, while in high-gain free-electron lasers, the differential equations are of the third order each. Analytical solutions of reflectance and transmittance for both quantum lasers and FELs are presented. It is found that when the solutions become infinite, the device operates as an oscillator, producing radiation at the output with no field at its input, entirely without any localized or distributed feedback.

INTRODUCTION

Conventional (quantum) lasers, microwave tubes and free-electron lasers (FELs) are based on distributed interactions between electromagnetic radiation and gain media. When such devices are operating in an amplifier configuration, a forward wave is amplified while propagating in a polarized medium, in a stimulated emission process [1]. In an oscillator configuration a resonator [2]-[4] or a distributed feedback [5] are employed to circulate the radiation, which is excited and amplified by the gain medium. If the single-pass gain is higher than the total losses, the radiation intensity inside the cavity increases and becomes more coherent. After several round trips, the radiation is built up until arriving at the nonlinear regime and saturation.

In this paper we suggest a mechanism of generation of laser oscillations, without any feedback means. It is shown that under conditions of phase-matching, both forward and backward waves can be excited in a distributed gain medium as illustrated schematically in Figure 1. The excitation of incident and reflected waves is described by a set of two differential equations coupled by the induced polarization of the gain media. The coupling coefficient is given in terms of the electronic susceptibility tensor.

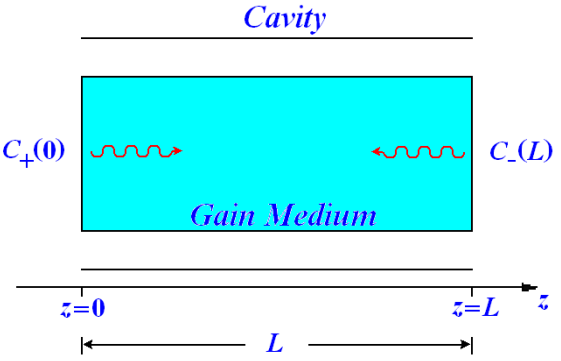

Figure 1: Schematic illustration of incident and reflected waves in a distributed gain medium.

Two cases are discussed: In quantum lasers, which are characterized by isotropic, homogeneous gain media, the interaction is described by two first order differential equations. In high-gain free-electron lasers, where the susceptibility is space dependent, the set includes two differential equations of the third order each. The coupled equations sets are solved analytically for both cases. Oscillation conditions are identified from the derived reflectance and transmittance coefficients.

EXCITATION OF FORWARD AND BACKWARD MODES

The total electromagnetic field is given by the time harmonic wave vector:

$$\mathbf{E}(\mathbf{r},t) = \Re\left\{\widetilde{\mathbf{E}}(\mathbf{r})e^{-j\omega t}\right\} \qquad (1)$$

where $\widetilde{\mathbf{E}}(\mathbf{r})$ is the phasor of the wave oscillating at an angular frequency ω. The vector $\mathbf{r}$ stands for the (x,y,z) coordinates, where (x,y) are the transverse coordinates and

z is the axis of propagation. In the case of excitation of forward and backward modes, the phasor can be written as the sum [6]:

$$\widetilde{\mathbf{E}}(\mathbf{r}) = \left[C_+(z)\, e^{+jk_z z} \;+\; C_-(z)\, e^{-jk_z z}\right] \widetilde{\mathcal{E}}(x,y) \qquad (2)$$

$C_+(z)$ and $C_-(z)$ are scalar amplitudes of forward and backward modes respectively, with profile $\widetilde{\mathcal{E}}(x,y)$ and axial wavenumber k_z. The evolution of the amplitudes of the excited modes is described by a set of two coupled differential equations:

$$\frac{d}{dz}C_\pm(z) = \mp\frac{1}{2\mathcal{N}} e^{\mp jk_z z} \int\int \widetilde{\mathbf{J}}(\mathbf{r}) \cdot \widetilde{\mathcal{E}}^*(x,y)\, dx\, dy \qquad (3)$$

The normalization of the mode amplitudes is made via the complex Poynting vector power:

$$\mathcal{N} = \int\int \left[\widetilde{\mathcal{E}}_\perp(x,y) \times \widetilde{\mathcal{H}}^*_\perp(x,y)\right] \cdot \hat{\mathbf{z}}\, dx\, dy \qquad (4)$$

The total power carried by the forward and backward (propagating) modes is:

$$\begin{aligned} P(z) &= \frac{1}{2}\Re \int\int \left[\widetilde{\mathbf{E}}(\mathbf{r}) \times \widetilde{\mathbf{H}}^*(\mathbf{r})\right] \cdot \hat{\mathbf{z}}\, dx\, dy \\ &= \frac{1}{2}\left[|C_+(z)|^2 - |C_-(z)|^2\right] \cdot \Re\{\mathcal{N}\} \end{aligned} \qquad (5)$$

When the interaction takes place in a polarized gain medium, the driving current density $\widetilde{\mathbf{J}}(\mathbf{r})$ is given in terms of the induced polarization (dipole moment per unit volume) $\widetilde{\mathbf{P}}(\mathbf{r})$. In the time domain, the current density is the time derivative of the induced polarization. Thus, the phasor representation of the driving current density is given by:

$$\widetilde{\mathbf{J}}(\mathbf{r}) = -j\omega\widetilde{\mathbf{P}}(\mathbf{r}) = -j\omega\varepsilon_0\, \chi(\mathbf{r},\omega) \cdot \widetilde{\mathbf{E}}(\mathbf{r}) \qquad (6)$$

where $\chi(\mathbf{r},\omega)$ is the electronic susceptibility tensor at the frequency ω (in a homogeneous isotropic medium it is a scalar). Using (6) in (3) results in:

$$\frac{d}{dz}C_\pm(z) = \pm j\frac{\omega\varepsilon_0}{2\mathcal{N}} e^{\mp jk_z z} \int\int \widetilde{\mathbf{E}}(\mathbf{r}) \cdot \chi(\mathbf{r},\omega) \cdot \widetilde{\mathcal{E}}^*(x,y)\, dx\, dy \qquad (7)$$

Substitution of the field expansion (2) in the excitation equations (7), the mode amplitudes $C_\pm(z)$ are described by a set of two coupled differential equations, that can be presented in a matrix form:

$$\frac{d}{dz}\begin{bmatrix} C_+(z) \\ C_-(z) \end{bmatrix} = \begin{bmatrix} +\kappa(z) & +\kappa(z)e^{-j2k_z z} \\ -\kappa(z)e^{+j2k_z z} & -\kappa(z) \end{bmatrix} \begin{bmatrix} C_+(z) \\ C_-(z) \end{bmatrix} \qquad (8)$$

The coupling parameter:

$$\kappa(z,\omega) \equiv j\frac{\omega\varepsilon_0}{2\mathcal{N}} \int\int \widetilde{\mathcal{E}}(x,y) \cdot \chi(\mathbf{r},\omega) \cdot \widetilde{\mathcal{E}}^*(x,y)\, dx\, dy \qquad (9)$$

is in general a complex, space-frequency dependent quantity.

QUANTUM LASER

We relate first to gain media, where the electronic susceptibility does not change along the axis of propagation z. This situation occurs in quantum lasers, where the atomic susceptibility of the gain medium is uniform [1]. In that case the coupling parameter is not yet space (z) dependent and can be presented in the form $\kappa(\omega) = \gamma(\omega) + j\beta(\omega)$, where $\gamma(\omega)$ is the field gain factor. Consequently, the set (8) can be written as two coupled first order linear differential equations:

$$\frac{d}{dz}\begin{bmatrix} C_+(z) \\ C_-(z) \end{bmatrix} = \begin{bmatrix} +\kappa & +\kappa e^{-j2k_z z} \\ -\kappa e^{+j2k_z z} & -\kappa \end{bmatrix} \begin{bmatrix} C_+(z) \\ C_-(z) \end{bmatrix} \qquad (10)$$

Analytical solution of the coupled set (10) for a given forward mode amplitude $C_+(0)$ at the input $z = 0$, while the backward mode amplitude at the exit of the interaction region ($z = L$) is $C_-(L) = 0$, leads to the solution of incident and reflected wave amplitudes:

$$\begin{aligned} \frac{C_+(z)}{C_+(0)} &= \frac{(\kappa + jk_z)\sinh\left[S(L-z)\right] - S\cosh\left[S(L-z)\right]}{(\kappa + jk_z)\sinh(SL) - S\cosh(SL)}\, e^{-jk_z z} \\ \frac{C_-(z)}{C_+(0)} &= \frac{-\kappa\sinh\left[S(L-z)\right]}{(\kappa + jk_z)\sinh(SL) - S\cosh(SL)}\, e^{+jk_z z} \end{aligned} \qquad (11)$$

where $S \equiv \sqrt{(\kappa + jk_z)^2 - \kappa^2}$ is a complex parameter. The evolution of incident and reflected wave amplitudes along the gain medium are shown in Fig. 2. It is assumed that the interaction takes place in the vicinity of the resonance frequency, where $\kappa(\omega_0)$ is real.

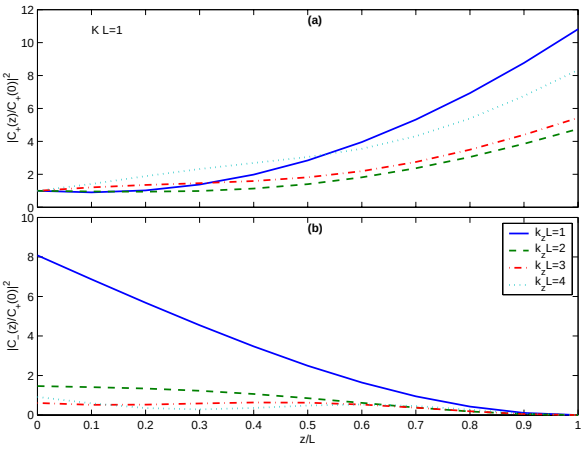

Figure 2: The evolution of (a) incident and (b) reflected wave amplitudes along the gain medium.

The transmission gain is defined by:

$$\frac{C_+(L)}{C_+(0)} = \frac{-SL}{(\kappa + jk_z)L\sinh(SL) - SL\cosh(SL)}\, e^{-jk_z L} \quad (12)$$

Respectively, the reflection gain is:

$$\frac{C_-(0)}{C_+(0)} = \frac{-\kappa L\sinh(SL)}{(\kappa + jk_z)L\sinh(SL) - SL\cosh(SL)} \quad (13)$$

Contour plots of the transmission and reflection power gain in the $(k_z L, \kappa L)$ plane are shown in Figure 3. An infinite gain singularities are inspected when the denominator of the gain dispersion relations given in (12) and (13) vanishes. This happens when:

$$\tanh(SL) = \frac{SL}{\kappa L + jk_z L} \quad (14)$$

In that case the forward and backward modes will be excited in the absence of an input signal, resulting in excitation and buildup of oscillations. Equation (14) expresses the oscillation condition, determining the threshold gain factor required for excitation of oscillations and their resultant frequencies at steady-state.

HIGH GAIN FREE-ELECTRON LASER

In free-electron lasers, the accelerated electrons serve as a gain medium and the interaction with the electromagnetic field takes place along the e-beam axis. Coupled mode theory for multi transverse mode excitation was developed previously, deriving an expression for the gain-dispersion relation in the linear regime of the FEL operation [7]. Set of equations (3) for the different modes were solved together with the small-signal moment equations describing the evolution in the driving current modulation. In the high gain limit the amplitudes of the forward and backward waves is described by two coupled third order linear differential equations:

$$\frac{d^3}{dz^3}\begin{bmatrix} C_+(z) \\ C_-(z) \end{bmatrix} = \begin{bmatrix} +\kappa & +\kappa e^{-j2k_z z} \\ -\kappa e^{+j2k_z z} & -\kappa \end{bmatrix}\begin{bmatrix} C_+(z) \\ C_-(z) \end{bmatrix} \quad (15)$$

where the coupling parameter:

$$\kappa = j\frac{\epsilon_0\zeta_q}{4\mathcal{N}}\frac{\omega_p^2}{v_{z0}^2}(k_z + k_w) \times \int\int f(x,y)\,\widetilde{\mathcal{E}}^{pm}(x,y)\,\widetilde{\mathcal{V}}_\perp^w \cdot \widetilde{\mathcal{E}}_\perp^*(x,y)\,dx\,dy \quad (16)$$

where $\widetilde{\mathcal{E}}_q^{pm}(x,y)$ is the pondermotive field, $f(x,y)$ is the transverse profile of the e-beam and ω_p is the plasma frequency of a relativistic beam with average axial electron velocity v_{z0}.

We solved the coupled set (15) analytically. The amplitude of the forward wave can be written as:

$$C_+(z) = e^{-jk_z z}\sum_{i=1}^{6} c_i e^{\lambda_i k_z z} \quad (17)$$

and the backward wave's amplitude is:

$$C_-(z) = e^{+jk_z z}\sum_{i=1}^{6}\frac{(j-\lambda_i)^3}{(j+\lambda_i)^3}c_i e^{\lambda_i k_z z} \quad (18)$$

where the six eigenvalues λ_i appear in the above solutions are found from a characteristic equation of the sixth order. Fortunately it can be written in a third order form:

$$\gamma^3 + 3\gamma^2 + 3\gamma(1-jw) + 1 + jw = 0 \quad (19)$$

in which $\gamma = \lambda^2$ and $w = \frac{2\kappa}{k_z^3}$, enabling analytical solution of λ_i. The properties of the eigenvalues λ_i are discussed in the Appendix. The constants c_i are determined by the boundary conditions. Assuming that there is no prebunching in the electron beam, an initial amplitude $C_+(0)$ is assumed for the forward mode at $z = 0$ and all the other boundary conditions are $C'_+(0) = C''_+(0) = C_-(0) = C'_-(0) = C''_-(0) = 0$ (here $'$ denotes first order derivative $\frac{d}{dz}$). The analytical results were verified using a numerical algorithm solving the boundary condition problem. Figure 4 presents contour plots of the transmission and reflection power gain in the $(k_z L, \kappa L^3)$ plane. Oscillations are expected where an infinite gain is obtained.

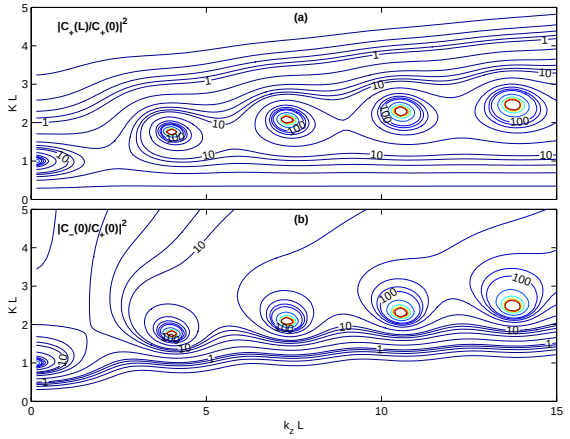

Figure 3: (a) Transmission and (b) reflection contours in the $(k_z L, \kappa L)$ plane for atomic laser.

ACKNOWLEDGMENTS

The research was supported by the Israel Science Foundation.

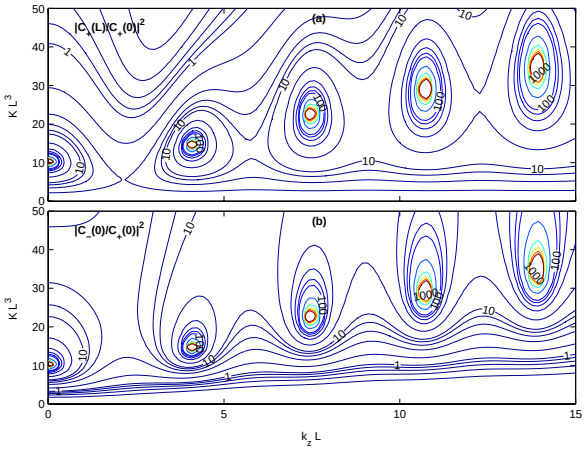

Figure 4: (a) Transmission and (b) reflection contours in the ($k_z L$, κL^3) plane for free-electron laser.

REFERENCES

[1] A. Yariv, *Nucl. Optical Electronics*, Holt Rinehart and Winston (1991)

[2] A. L. Schawlow and C. H. Towens, em Phys. Rev. **112**, 1940 (1958)

[3] V. L. Bratman, N. S. Ginzburg and M. I. Petelin, *Optics. Comm.* **30**, 409 (1979)

[4] T. M. Antonsen and B. Levush, *Phys. Fluids B* **1**, 1097 (1989)

[5] H. Kogelnik and C. V. Shank, em J. Appl. Phys. **43**, 2328 (1972)

[6] Y. Pinhasi, Yu. Lurie, A. Yahalom, A. Abramovich, *Nucl. Instr. Methods Phys. Res.* A **483**, 510 (2002)

[7] Y. Pinhasi and A. Gover, *Phys. Rev. E.* **51**, 2472 (1995)

APPENDIX

The six eigenvalues calculated from equation (19) come in positive-negative pairs $\lambda = \pm\sqrt{\gamma}$. Taking complex conjugate of equation (19) (assuming that w is real):

$$\gamma^{*3} + 3\gamma^{*2} + 3\gamma^*(1+jw) + 1 - jw = 0 \qquad (20)$$

reveals that the solutions satisfy the relation:

$$\gamma_m^*(-w) = \gamma_n(w) \qquad (21)$$

in which m, n are the solution indices. However, since we have a total of three roots to equation (19) , at least one of the roots, say γ_1, satisfies the relation:

$$\gamma_1^*(-w) = \gamma_1(w) \qquad (22)$$

that is its real part is even with respect to w and its imaginary part is odd.

Equation (19) can be readily solved and the solutions are:

$$\begin{aligned}
\gamma_1 &= -1 + ba - \frac{a^2}{b} \\
\gamma_2 &= \frac{1}{2}[-\gamma_1(1+\sqrt{3}j) - 3 - \sqrt{3}j + 2\sqrt{3}jab] \\
\gamma_3 &= \frac{1}{2}[-\gamma_1(1-\sqrt{3}j) - 3 + \sqrt{3}j - 2\sqrt{3}jab] \qquad (23)
\end{aligned}$$

where:

$$a = (-jw)^{\frac{1}{3}} \quad b = (2 + \sqrt{4 - jw})^{\frac{1}{3}} \qquad (24)$$

We see that:

$$\gamma_3(w) = \gamma_2^*(-w) \qquad (25)$$

Hence one can deduce the behavior of the roots for negative w values from their behavior for positive values.

In the case $w \to 0$ we obtain $\lim_{w\to 0}\gamma_i = -1$ for $i \in [1,2,3]$. This is obviously a degenerate case in which the solution is not of an exponential type. Inserting the condition $w \to 0$ into equation (15) one is left with the trivial equation $\frac{d^3}{dz^3}\begin{bmatrix} C_+(z) \\ C_-(z) \end{bmatrix} = 0$ with the solution:

$$\begin{aligned}
C_+(z) &= \frac{1}{2}z^2 c_+^{(2)} + z c_+^{(1)} + c_+^{(0)} \\
C_-(z) &= \frac{1}{2}z^2 c_-^{(2)} + z c_-^{(1)} + c_-^{(0)} \qquad (26)
\end{aligned}$$

In the opposite limit in which $w \to \infty$ we obtain the following results:

$$\begin{aligned}
\lim_{w\to\infty}\gamma_1 &= \frac{1}{3} \\
\lim_{w\to\infty}\gamma_2 &= \sqrt{3}e^{\frac{5}{4}\pi j}w^{\frac{1}{2}} \\
\lim_{w\to\infty}\gamma_3 &= \sqrt{3}e^{\frac{1}{4}\pi j}w^{\frac{1}{2}} \qquad (27)
\end{aligned}$$

Since non of those are negative real numbers this means that we have three growing exponents and three decaying exponents in the case of large w those are:

$$\begin{aligned}
\lim_{w\to\infty}\lambda_1 &= \frac{1}{\sqrt{3}} \\
\lim_{w\to\infty}\lambda_2 &= -\frac{1}{\sqrt{3}} \\
\lim_{w\to\infty}\lambda_3 &\cong 3^{\frac{1}{4}}(-0.383 + 0.924j)w^{\frac{1}{4}} \\
\lim_{w\to\infty}\lambda_4 &\cong 3^{\frac{1}{4}}(0.383 - 0.924j)w^{\frac{1}{4}} \\
\lim_{w\to\infty}\lambda_5 &\cong 3^{\frac{1}{4}}(0.924 + 0.383j)w^{\frac{1}{4}} \\
\lim_{w\to\infty}\lambda_6 &\cong 3^{\frac{1}{4}}(-0.924 - 0.383j)w^{\frac{1}{4}} \qquad (28)
\end{aligned}$$

For large w, λ_5 is clearly the most dominant exponent. Although λ_1 & λ_2 asymptotically approach a finite number, the other eigenvalues continue to grow without limit.

CSRtrack: FASTER CALCULATION OF 3-D CSR EFFECTS

M. Dohlus, T. Limberg, DESY, Hamburg, Germany

Abstract

CSRtrack is a new code for the simulation of Coherent Synchrotron Radiation effects on the beam dynamics of linear accelerators. It incorporates the physics of our previous code, TraFiC4 [1], and adds new algorithms for the calculation of the CSR fields. A one-dimensional projected method allows quick estimates and a greens function method allows 3-D calculations about hundred times faster than with the 'direct' method for large particle numbers.

The tracking code is written in standard FORTRAN77 and has its own parser for comfortable input of calculation parameters and geometry. Phase space input and the analysis of the traced particle distribution is done with MATLAB interface programs.

INTRODUCTION

In usual optics and tracking codes for accelerator development the bunch self fields due to synchrotron radiation and changes of the bunch shape are neglected. Therefore special CSR tracking codes have been developed (e.g., TraFiC4 [1], CSRtrack, R.Li's code [2]) and existing codes have been expanded (e.g., Elegant [3,5], TREDI [4]). Essentially two types of approaches are presently used for the self-consistent calculation of particle distributions on curved trajectories. Both are available in CSRtrack.

The 1-D approach uses a simplified model for the calculation of longitudinal forces [6]. It neglects transverse forces as well as transverse beam dimensions and assumes that the longitudinal distribution is unchanged at retarded times. A 'renormalized' Coulomb term is used to extract the field singularity in the 1-D beam.

The sub-bunch approach uses a set of 3-D charge distributions*, e.g., time-independent Gaussian, to approximate the source distribution. The physical model of the sub-bunch method is complete, but the resolution of phase space modelling is severely limited by the numerical effort for the field calculation of all point to point interactions. Even with parallel computing particle numbers above 10^3 are difficult to handle (CPU time on a cluster is many days).

TraFiC4 and CSRtrack ease that problem by using a convolution method [8] to reduce the field calculation of 3-D sources to 1-D integrations (for each interaction), gaining about a factor of ten in manageable particle numbers.

Further improvement is possible with a pseudo Green's function approach; it uses the discretized field of one reference sub-bunch to calculate all interactions. This method is implemented in CSRtrack and allows tracking calculations with 10^4 particles on one CPU in a few hours, up to $4 \cdot 10^4$ particles have been tracked on 20 CPUs.

For the tracking of even bigger numbers of particles, the disadvantage that the effort scales quadratic with the number of particles could be avoided by calculating the electromagnetic fields on a mesh. With a combination of mesh field calculation and pseudo Green's function method, $>10^5$ particles in less then one day (using 20 CPUs in parallel) seem to be in reach.

NUMERICAL ASPECTS OF DIFFERENT CSR FIELD CALCULATION METHODS

In the following we discuss different algorithms and their relative computation time consumption, which are summarized in Fig. 2.

A word of warning: if the initial bunch density is modulated, for instance to study CSR induced instability, the computation time depends quadratically on the ratio of the bunch length to its fine structure – in any approach. We will discuss that further in a paper to come.

One Dimensional Approach – Projected Method

The particle distribution is projected to the reference trajectory and a smooth one dimensional charge density $\lambda(s)$ is calculated by binning or filtering. The smoothing is crucial for the stability and accuracy of the simulation because the micro bunch instability is sensitive to high frequency components in the charge density.

The longitudinal field $E^{(\lambda)}$ can be calculated by one dimensional integration

$$E^{(\lambda)}(s_0,t_0) = \int \lambda'(u + s_0 - vt_0) K(s_0,u) du\,,$$

with the kernel function $K(s_0,u)$ that depends on the geometry of the trajectory. This integral is a convolution in time. It can be solved efficiently by FFT methods if $E^{(\lambda)}$ is required for a time interval.

The longitudinal field is calculated on a mesh and interpolated to the projected particle positions. The particle tracking takes into account external fields and the longitudinal self field. The effort for the field calculation depends linearly on the number of particles.

Sub-Bunch Approach

The distribution of source particles is described by a set of sub-bunches with well defined shape. The individual trajectory of each sub-bunch has to be known in absolute coordinates back in time. This defines the 3-D source distribution $\rho(\mathbf{r},t)$ so that potentials and electromagnetic fields can be calculated by an integration of retarded sources.

A disadvantage of the sub-bunch approach is the large numerical effort. For M test particles and N source distributions (sub-bunches) $M \times N$ three-dimensional integrations have to be performed for every time step.

* 2-D sub-bunches in R.Li's code

Source Distributions and Test Particles

For **self consistent tracking** the trajectory of each source is defined by the motion of an associated test particle. Therefore $M=N+M_t$ test particles are needed, with M_t the number of additional particles that can be used for more detailed explorations e.g. of the transverse phase space. The effort for self consistent tracking is at least proportional to N^2. Additional test particles need the computation of $N\times M_t$ interactions.

If the bunch shape is weakly deformed due to self forces a **perturbation approach** can be used. The self forces to the test particles are calculated for unperturbed motion of source distributions and test particles. These forces are used in a second step to calculate the perturbed motion. The initial condition of test particles can be set as required (e.g. to investigate an individual slice) but at least some test particles should be used to verify the perturbation approach.

3-D Sub-Bunches, Convolution Method

Since the field of each source sub-bunch has to be calculated for every test position by a 3-D integration of retarded sources, the full field computations is quite time consuming. For spherical Gaussian sub-bunches this integration can be reduced to a 1-D integral [7].

The codes TraFiC4 and CSRtrack adopt a calculation method that was developed in [8]. A certain type of 3-D distribution can be represented by the convolution of a longitudinal 1-D profile $\lambda(s,t)$ with a transverse 2-D density function $\eta(x,y)$.

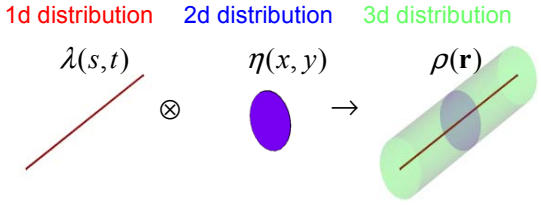

Fig 1: *Schematic of the Convolution Method*

Then the 3-D electromagnetic fields can also calculated by a convolution of fields $\mathbf{E}^{(\lambda)}$, $\mathbf{B}^{(\lambda)}$ caused by the 1-D source with the 2-D density function. $\mathbf{E}^{(\lambda)}$ and $\mathbf{B}^{(\lambda)}$ are split into singular parts $\mathbf{E}^{(\lambda,s)}$ and $\mathbf{B}^{(\lambda,s)}$, which are dominated by local effects, and non-singular parts $\mathbf{E}^{(\lambda,ns)}$ and $\mathbf{B}^{(\lambda,ns)}$. The asymptotic behaviour of the singular part is analytically known so that its convolution with certain transverse density functions can be computed efficiently.

As the non singular parts depend mainly on long range interactions, their transverse dependency is weak and the convolutions $\mathbf{E}^{(\lambda,ns)}\otimes\eta$, $\mathbf{B}^{(\lambda,ns)}\otimes\eta$ can be approximated by $\mathbf{E}^{(\lambda,ns)}$, $\mathbf{B}^{(\lambda,ns)}$ for sufficiently small transverse dimensions ($<<\sqrt[3]{R_0\sigma_\lambda^2}$, with R_0 the curvature radius and σ_λ the bunch length). Therefore the numerical effort E_c is determined by the 1-D integration for the non singular parts. The total effort for all source to test-point interactions is $M\times N\times E_c$.

Pseudo Green's Function Approach

The fields $\mathbf{E}^{(0)}(\mathbf{r},t_0)$, $\mathbf{B}^{(0)}(\mathbf{r},t_0)$ of a reference sub-bunch (charge q_0) that travels along a reference trajectory $\mathbf{r}_0(t)$ are used to approximate the fields of other sub-bunches (charge q_ν, trajectory $\mathbf{r}_\nu(t)$). This approach neglects vertical forces. At the observation time t_0 the trajectory of sub-bunch ν is approximated by

$$\mathbf{r}_\nu(t) \approx \mathbf{r}_\nu(t_0) + \mathbf{R}\cdot\left(\mathbf{r}_0(t)-\mathbf{r}_0(t_0)\right).$$

This shift-rotation-transformation (with rotation operator $\mathbf{R}$) is used to calculate

$$\mathbf{E}^{(\nu)}(\mathbf{r},t_0) \approx \frac{q_\nu}{q_0}\mathbf{R}\cdot\mathbf{E}^{(0)}\left(\mathbf{r}_0(t_0)+\mathbf{R}^{-1}(\mathbf{r}-\mathbf{r}_\nu(t_0)),t_0\right)$$

and $\mathbf{B}^{(\nu)}(\mathbf{r},t_0)$ in the same way. The pseudo Green's functions $\mathbf{E}^{(0)}(\mathbf{r},t_0)$, $\mathbf{B}^{(0)}(\mathbf{r},t_0)$ are calculated once for every time step on a 2-D mesh in the horizontal plane with M_g points:

$$\mathbf{E}^{(0)}(\mathbf{r},t_0) = E_x(x,y)\mathbf{u}_x + E_y(x,y)\mathbf{u}_y$$

$$\mathbf{B}^{(0)}(\mathbf{r},t_0) = B_z(x,y)\mathbf{u}_z$$

The numerical effort for the calculation of all self forces is $M_g\times E_c+M\times N\times E_{i,g}$ with $E_{i,g}$ the effort for the interpolation on the mesh. The approach is effective for $N\times M > M_g$. Simulations with many particles ($>10^4$) are not limited by the effort for the field calculation ($M_g\times E_c$) but by the effort for the interpolation ($M\times N\times E_{i,g}$).

Meshed EM Fields

If the density of particles is large compared to the fine structure of the particle distribution (and the self-fields) it is more efficient to calculate electromagnetic fields on a mesh with M_{em} points and to interpolate them to the test points. The numerical effort is $M_{em}\times N\times E_c+M\times E_{i,em}$ with $E_{i,em}$ the effort for the interpolation on the field mesh. The total effort is not longer proportional to the squared number of particles ($M\times N$ with $M \geq N$ for self consistent tracking)!

Reasonable EM meshes need at least $M_{em} > 10^4$ points and therefore the method gets efficient for M, $N > 10^4$. The effort for such particle numbers is still too large (even with parallel computing) for routine investigations.

This is different if the meshed fields approach is combined with the pseudo Green's function approach: the total effort is $M_g\times E_c+M_{em}\times N\times E_{i,g}+ M\times E_{i,em}$. This method is still in preparation.

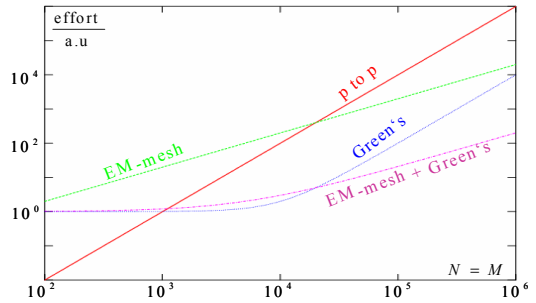

Fig. 2: *Numerical effort of different CSR field calculation methods vs. # of tracked particles*

Iterative Tracking

For tracking, self-forces have to be calculated for particles on phase space coordinates that depend on the unknown forces. If the track step is sufficiently small the forces can be approximated for phase space positions calculated without self contributions. To avoid the numerical effort for very many small steps iterative tracking with medium step size is used: estimated self forces are calculated for estimated particle positions and are used to improve the position estimation. The iteration is repeated until an error criterion is fulfilled.

The numerical integration of the equation of motion in CSRtrack uses sub-steps that are (much) smaller than the steps of the iterative force calculation. The forces at sub-steps are linearly interpolated between the force at the start point of an iterative step and at its end point. The error due to this linear interpolation and due to too big iterative steps is not reduced by iterative tracking.

CSRtrack provides two possibilities to determine the size of iterative steps: by a recursive algorithm that is based on the bunch length and curvature radius of the trajectory and by external definition. Like in all self-field applying tracking codes, the result has to some extent to be interpreted and justified by the user (e.g. convergence tests or the inspection of the forces observed by some selected test particles).

CSRtrack 1.0

Particles Definition

Position, momentum and charge of each particle of the distribution are defined in an absolute Cartesian coordinate system with the horizontal plane as *xy*-plane. Particles with nonzero charge are source particles that create self-fields that affect the motion of test particles. In the present versions all particles have the source and test property.

Lattice

CSRtrack supports magnetic dipole- and multipole-fields that are defined in Cartesian coordinates. The range of the fields of one element is limited by two field boundaries perpendicular to the horizontal plane. The **dipole** field between two field boundaries is constant and parallel to the vertical *z*-axis. Together with the dipoles a reference trajectory is defined that consists of arcs and lines.

To take into account vertical edge focussing at the hard edges of dipoles the tracking algorithm applies discrete kicks proportional to the vertical offset. The magnetic **multipole** field is defined in a local coordinate system (longitudinal, horizontal, vertical) with its origin in the intersection point of the reference trajectory and the field boundary.

The magnetic multipole field between field boundaries depends only on transverse coordinates. It is characterized by its strength, azimuthal order, transverse offset and skew angle.

Shielding

CSRtrack provides shielding as of now with parallel ideal conducting plates with constant distance to the beam. The user has to specify the maximum distance to the beam up to which mirror charges will be taken into account.

Parallel Computing

CSRtrack is available as a parallel processing code using the MPI protocol with the MPICH package. Only the sub-bunch methods are calculating parallel.

# of particles	calc. steps	Method	CPU	Running time
10000	~200	Point to point	20x1GHz	~ 10 d
10000	~200	Greens funct.	1x1GHz	~0.5 d
41000	~200	Greens funct.	20x1GHz	~0.5 d

Table 1: *CPU time consumption of CSRtrack runs for TTF2 and XFEL magnet chicanes*

COMPARING RESULTS FOR DIFFERENT METHODS

CSRtrack is well suited to explore the applicability of different CSR calculation methods. An example is a calculation for the European XFEL bunch compression system (see Fig. 4).

The beam is tracked from the gun into the linac up to about the 100 MeV point with a space charge code (ASTRA). For the remaining injector linac up to the two magnetic chicanes for bunch compression a linac tracking code (elegant) is used. In the chicanes, where the beam dynamics is dominated by CSR effects, we need to employ CSRtrack.

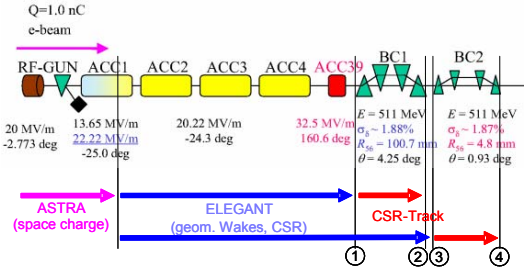

Fig. 4: *Start-to-end calculation for the European XFEL*

In Fig. 5 the longitudinal phase space at the end of the beam line is shown; calculated with the 1-D and a 3-D method of CSRtrack. The RMS bunch length is about 20 μm, the peak current 5 kA.

The longitudinal tails of the initial distribution have been over-compressed back towards the center of the distribution. They have to be excluded from any meaningful evaluation of beam parameters vs. longitudinal bunch position such as transverse slice emittance or, as shown here, slice energy spread. In the graphs, these particles are color coded.

The 1-D model underestimates the growth in slice energy spread in the center of the bunch due to CSR effects by a factor of 5-10.

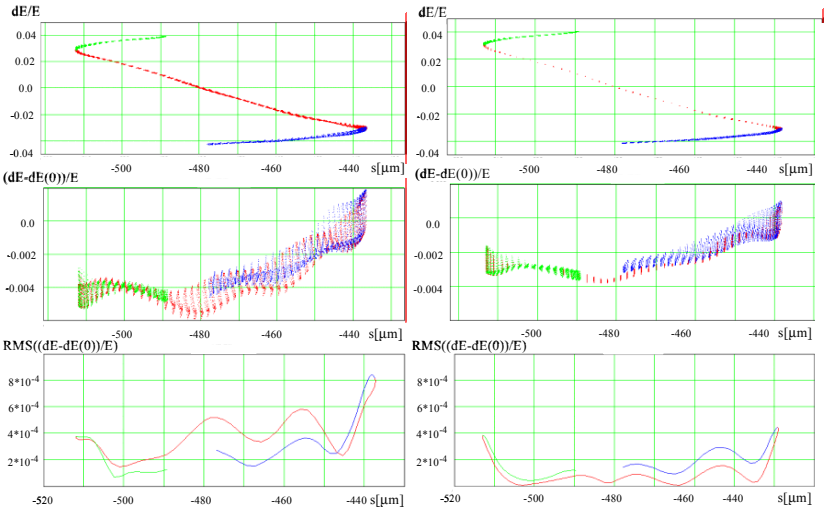

Fig. 5: *Longitudinal Phase Space at the end of the bunch compression system calculated with the 3-D Greens function method (left) and the projected 1-D method (right).*

The lower graphs show the difference in particle energies due to compression and the RMS of that value vs. longitudinal bunch position.

The particles in the energy distribution tails are shown in blue and green.

POSTPROCESSING

We use MATLAB tools on a XP PC to administrate and manipulate the data files and to run the tracking codes on both the local (XP) computer and a Linux PC cluster, in single CPU or parallel processing mode (see Fig. 6).

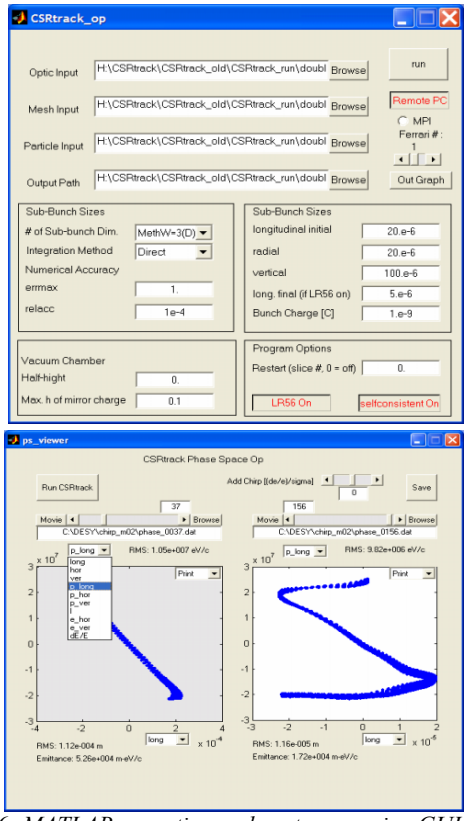

Fig.6: *MATLAB operating and post-processing GUIs*

Input and output phase space data files can be inspected, changed and plotted.

User options are made invisible if they do not make sense; for example the option to display beam current (I) on the vertical axis disappears if something else than the longitudinal coordinate is chosen for the horizontal axis.

File formats are checked and detected automatically to avoid mistakes. Saving data in files works via the standard XP 'save as' window, also the file formats (e.g., elegant or ASTRA) can be chosen with the familiar pull-down menu.

FURTHER PLANS, CONCLUSION

Soon a web page will be ready to download a CSRtrack executable and a user's guide with input examples. The program has to be developed further to incorporate the mesh option described above.

REFERENCES

[1] T.Limberg, A.Kabel, M.Dohlus: Numerical Calculation of CSR Effects Using TraFiC4. Nucl. Instrum.Meth. A455 (2000) 185-189.

[2] R.Li: Self-Consistent Simulation of the CSR Effect. EPAC1998, Stockholm, Sweden June 1998.

[3] M.Borland: Simple Method for Particle Tracking with Coherent Synchrotron radiation. Phys.Rev. ST AB 4(070701), July 2001.

[4] L.Giannessi, P.Musumeci, M.Quattromini: TREDI. NIM A 436, pp. 443-444, Nov. 1999.

[5] P.Emma: private communication

[6] E. Saldin, E.Schneidmiller, M.Yurkov: Radiative Interaction of Electrons in a Bunch Moving in an Undulator. NIM A417 (1998) 158-168.

[7] M. Dohlus: Two Methods for the Calculation of CSR Fields. TESLA-FEL-2003-05.

[8] M. Dohlus, A. Kabel, T. Limberg: Efficient Field Calculation of 3-D Bunches on General Trajectories. NIM A445 (2000) 338-342.

A 3D SELF-CONSISTENT, ANALYTICAL MODEL FOR LONGITUDINAL PLASMA OSCILLATION IN A RELATIVISTIC ELECTRON BEAM

Gianluca Geloni, Evgeni Saldin, Evgeni Schneidmiller and Mikhail Yurkov
Deutsches Elektronen-Synchrotron (DESY), Notkestrasse 85,
22607 Hamburg, Germany

Abstract

Longitudinal plasma oscillations are becoming a subject of great interest for XFEL physics in connection with LSC microbunching instability [1] and certain pump-probe synchronization schemes [2]. In the present paper we developed the first exact analytical treatment for longitudinal oscillations within an axis-symmetric, (relativistic) electron beam, which can be used as a primary standard for benchmarking space-charge simulation codes. Also, this result is per se of obvious theoretical relevance as it constitutes one of the few exact solutions for the evolution of charged particles under the action of self-interactions.

INTRODUCTION

Longitudinal space-charge oscillations have been treated, so far, only from an electrodynamical viewpoint, or using limited one-dimensional models: in this paper we report a fully self-consistent solution to the initial value problem for the evolution of a relativistic electron beam under the action of its own fields in the (longitudinal) direction of motion. In our derivation the beam is accounted for any given radial dependence of the particle distribution function. For a more detailed description of our work and references see [1].

An initial condition is set so that the beam, which is assumed infinitely long in the longitudinal direction, is modulated in energy and density at a given wavelength. When the amplitude of the modulation is small enough the evolution equation can be linearized. An exact solution can be found in terms of an expansion in (self-reproducing) propagating eigenmodes.

Our findings are, in first instance, of theoretical importance since they constitute one of the few exact solutions known up to date to the problem of particles evolving under the action of their own fields.

Yet, particle accelerator and FEL physics make large use of simulation codes in order to obtain the influence of space-charge fields on the beam behavior and these codes are benchmarked against exact solutions of Poisson equation only; recently partial attempts have been made to benchmark them against some analytical model accounting for the system evolution. However, such attempts are based on one-dimensional theory which can only give some incomplete result. On the contrary, we claim that our findings can be used as a standard benchmark for any space-charge code from now on.

Our results are of relevance to an entire class of practical problems arising in state-of-the-art FEL technology when (optically) modulated electron beams are feed into an FEL. For instance, optical seeding is a common technique for harmonic generation. Moreover, two-color pump-probe schemes have been proposed which rely on the passage of an optically modulated electron beam through an X-ray FEL and an optically tuned FEL: given the parameters of the system, plasma oscillations turn out to be a relevant effect to be accounted for. It is also important to mention, here, the relevance of plasma oscillation theory in the understanding of practical issues like longitudinal space-charge instabilities in high-brightness linear accelerators which may lead to beam microbunching and break up.

THEORY

We are interested in developing a theory to describe longitudinal plasma waves in a relativistic electron beam. We do this assuming that transverse coordinates enter purely as parameters in the description of the fields and of the particle distribution. Our beam is initially modulated at some wavelength λ_m, in density and energy. It is natural to define the phase $\psi = \omega_m \left(z/v_z(\mathcal{E}_0) - t\right)$, where $v_z(\mathcal{E}_0) \sim c$ is the longitudinal electron velocity at the nominal beam kinetic energy $\mathcal{E}_0 = (\gamma - 1)mc^2$, $\omega_m = 2\pi v_z/\lambda_m$, t is the time and z the longitudinal abscissa. It is then appropriate to operate in energy-phase variables (P, ψ), P being the deviation from the nominal energy.

Under the assumption of a small energy deviation P, the equations of motion for our system can be interpreted as Hamilton canonical equations corresponding to the Hamiltonian $H(\psi, P, z) = e\int d\psi E_z + \omega_m P^2/(2c\gamma_z^2\mathcal{E}_0)$. The bunch density distribution will be then represented by the density $f = f(\psi, P, z; \boldsymbol{r}_\perp)$. Linearization of the evolution equation for f is possible when $f(\psi, P, z; \boldsymbol{r}_\perp)_{|_{z=0}} = f_0(P; \boldsymbol{r}_\perp) + f_1(\psi, P, z; \boldsymbol{r}_\perp)_{|_{z=0}}$, f_0 being the unperturbed solution of the evolution equation with $f_1 \ll f_0$ for any value of dynamical variables or parameters. Moreover we assume $f_0(P; \boldsymbol{r}_\perp) = n_0(\boldsymbol{r}_\perp)F(P)$, where the local energy spread function $F(P)$ is considered normalized to unity. The initial modulation can be written as a sum of density and energy modulation terms: $f_1(\psi, P, z; \boldsymbol{r}_\perp)_{|z=0} = f_{1d}(\psi, P; \boldsymbol{r}_\perp) + f_{1e}(\psi, P; \boldsymbol{r}_\perp)$ where $f_{1d}(\psi, P, z; \boldsymbol{r}_\perp) = a_{1d}(\boldsymbol{r}_\perp)F(P)\cos(\psi)$ and $f_{1e}(\psi, P, z; \boldsymbol{r}_\perp) = a_{1e}(\boldsymbol{r}_\perp)dF/dP\cos(\psi + \psi_0)$. Here

[1] E. Saldin et al. Longitudinal Spacs Charge Driven Michrobunching instability in TTF linac, TESLA-FEL-2003-02, May 2003

[2] J. Feldhaus et al. Two-color FEL amplifier for femtosecond-resolution pump-probe experiments with GW-scale X-ray and optical pulses DESY 03-091, July 2003

ψ_0 is an initial (relative) phase between density and energy modulation. Finally it is convenient to define complex quantities $\tilde{f}_{1d} = a_{1d}F$, and $\tilde{f}_{1e} = a_{1e}(dF/dP)e^{i\psi_0}$ so that $f_{1_{|z=0}} = (\tilde{f}_{1d} + \tilde{f}_{1e})e^{i\psi} + CC$. Further definition of $\tilde{E}_z = \tilde{E}_z(z; \boldsymbol{r}_\perp)$ in such a way that $E_z = \tilde{E}_z e^{i\psi} + \tilde{E}_z^* e^{-i\psi}$ allows one to write the Vlasov equation linearized in $\tilde{f}_1$:

$$\frac{\partial \tilde{f}_1}{\partial z} + i\frac{\omega_m P}{c\gamma_z^2 \mathcal{E}_0}\tilde{f}_1 - e\tilde{E}_z\frac{\partial f_0}{\partial P} = 0\,. \tag{1}$$

Let us now introduce the longitudinal current density $j_z(z; \boldsymbol{r}_\perp) = -j_0(\boldsymbol{r}_\perp) + \tilde{j}_1 e^{i\psi} + \tilde{j}_1^* e^{-i\psi}$, where $j_0(\boldsymbol{r}_\perp) \simeq ecn_0(\boldsymbol{r}_\perp)$ and $\tilde{j}_1 \simeq -ec\int_{-\infty}^{\infty} dP\tilde{f}_1$. From Eq. (1) follows

$$\tilde{j}_1 = -ec\int_{-\infty}^{\infty} dP\left(a_{1d}F + a_{1e}\frac{dF}{dP}e^{i\psi_0}\right)e^{-i\frac{\omega_m P z}{c\gamma_z^2\mathcal{E}_0}} - ej_0\int_0^z dz'\left[\tilde{E}_z\int_{-\infty}^{\infty} dP\frac{dF}{dP}e^{i\frac{\omega_m P}{c\gamma_z^2\mathcal{E}_0}(z'-z)}\right]. \tag{2}$$

The next step is to present the equation for the electric field $\tilde{E}_z$ which, coupled with Eq. (2), will describe the system evolution in a self-consistent way.

Starting with the inhomogeneous Maxwell equation for the z-component of the electric field, passing to complex quantities and assuming that the envelope of fields and currents vary slowly enough over the z coordinate (this simply means that we can neglect retardation effects) we have

$$\nabla_\perp^2\tilde{E}_z - \frac{\omega_m^2\tilde{E}_z}{\gamma_z^2c^2} = \frac{4\pi i\omega_m}{\gamma_z^2c^2}\tilde{j}_1\,, \tag{3}$$

which forms, together with Eq. (2), a self-consistent description for our system.

Combining Eq. (2) with Eq. (3) and using properly normalized quantities we obtain an integro-differential equation for the field evolution:

$$\hat{\nabla}_\perp^2\hat{E}_z - q^2\hat{E}_z = iq^2\int_{-\infty}^{\infty} d\hat{P}\left(\hat{a}_{1d}\hat{F} + \hat{a}_{1e}\frac{d\hat{F}}{d\hat{P}}\right)e^{-i\hat{P}\hat{z}} - iq^2S_0\int_0^{\hat{z}} d\hat{z}'\left[\hat{E}_z\int_{-\infty}^{\infty} d\hat{P}\frac{d\hat{F}}{d\hat{P}}e^{i\hat{P}(\hat{z}'-\hat{z})}\right]. \tag{4}$$

Definitions of naturally normalized quantities in Eq. (4) are as follows: $\hat{\boldsymbol{r}} = \boldsymbol{r}_\perp/r_0$, $\hat{E}_z = \tilde{E}_z/E_0$, $q = k_m r_0/\gamma_z$, $\hat{P} = P/(\rho\mathcal{E}_0)$, $\hat{a}_{1d} = -eca_{1d}/J_0$, $\hat{a}_{1e} = -ece^{i\psi_0}a_{1e}/(J_0\rho\mathcal{E}_0)$, $\hat{z} = \Lambda_P z$; $\hat{F}(\hat{P})$ is normalized to unity and S_0, the transverse profile function of the beam, obeys $S_0(\mathbf{0}) = 1$. Parameters are the typical transverse size of the beam r_0 , $J_0 = I_0\left[\int S(\boldsymbol{r}_\perp/r_0)d\boldsymbol{r}_\perp\right]^{-1}$, $E_0 = 4\pi J_0/\omega_m$ (where I_0 is the beam current), the plasma wave number $\Lambda_P = \left[4I/(I_A r_0^2\gamma\gamma_z^2)\right]^{1/2}$ ($I_A = mc^3/e$ being the Alfven current), $\rho = \Lambda_p\gamma_z^2/k_m$. Moreover the rms energy spread $\langle(\Delta\mathcal{E})^2\rangle$ can be measured by the dimensionless parameter $\hat{\Lambda}_T^2 = \langle(\Delta\mathcal{E})^2\rangle/\rho^2\mathcal{E}_0^2$ and the dimensionless current densities can be written as $\hat{j}_0 = j_0/J_0 \equiv S_0(\boldsymbol{r}_\perp/r_0)$ and $\hat{j}_1 = \tilde{j}_1/J_0$.

An equivalent description of the evolution of our system in terms of $\hat{j}_1$ can be obtained using the following result:

$$\hat{E}_z = -\frac{iq^2}{2\pi}\int d\hat{\boldsymbol{r}}_\perp^{(s)}\hat{j}_1 K_0\left(q \mid \hat{\boldsymbol{r}}_\perp - \hat{\boldsymbol{r}}_\perp^{(s)} \mid\right), \tag{5}$$

where K_0 indicates the modified Bessel function of the second kind. Then, substitution in Eq. (2) yields (using dimensionless quantities):

$$\hat{j}_1 = \int_{-\infty}^{\infty} d\hat{P}\left(\hat{a}_{1d}\hat{F} + \hat{a}_{1e}\frac{d\hat{F}}{d\hat{P}}\right)e^{-i\hat{P}\hat{z}} + \frac{iq^2}{2\pi}S_0\int_0^{\hat{z}} d\hat{z}'\left[\int d\hat{\boldsymbol{r}}_\perp^{(s)}\hat{j}_1 K_0\left(q \mid \hat{\boldsymbol{r}}_\perp - \hat{\boldsymbol{r}}_\perp^{(s)} \mid\right)\times\int_{-\infty}^{\infty} d\hat{P}\frac{d\hat{F}}{d\hat{P}}e^{i\hat{P}(\hat{z}'-\hat{z})}\right]. \tag{6}$$

The description in terms of the fields is particularly suitable for analytical manipulations, while the description in terms of currents is advisable in case of a numerical approach.

MAIN RESULT

After introduction of the Laplace transform of $\hat{E}_z$, $\bar{E}(p, \hat{\boldsymbol{r}}_\perp)$, with $Re(p) > 0$, it follows from Eq. (4) that

$$\mathcal{L}\bar{E} = f \quad \text{with :} \tag{7}$$

$$\mathcal{L} = \hat{\nabla}_\perp^2 + \hat{g}(\hat{\boldsymbol{r}}_\perp, p)\,, \tag{8}$$

$$f(\hat{\boldsymbol{r}}_\perp, p) = iq^2\left(\hat{D}_0\hat{a}_{1d} + \hat{D}\hat{a}_{1e}\right), \tag{9}$$

$$\hat{g}(\hat{\boldsymbol{r}}_\perp, p) = -q^2(1 - i\hat{D}S_0)\,, \tag{10}$$

$$\hat{D}_0 = \int_{-\infty}^{\infty} d\hat{P}\frac{\hat{F}}{p + i\hat{P}}\,, \quad \hat{D} = \int_{-\infty}^{\infty} d\hat{P}\frac{d\hat{F}/d\hat{P}}{p + i\hat{P}} \tag{11}$$

with the boundary conditions $\bar{E} \longrightarrow 0$ for $|\hat{\boldsymbol{r}}_\perp| \longrightarrow \infty$ and $\partial\bar{E}/\partial\hat{\boldsymbol{r}}_\perp \longrightarrow 0$ for $|\hat{\boldsymbol{r}}_\perp| \longrightarrow \infty$. Solution is found if we can find the inverse of the operator $\mathcal{L}$, namely a Green function $\bar{G}$ obeying the given boundary conditions; in this case we simply have $\bar{E} = \int d\hat{\boldsymbol{r}}'_\perp\bar{G}(\hat{\boldsymbol{r}}_\perp, \hat{\boldsymbol{r}}'_\perp)f(\hat{\boldsymbol{r}}'_\perp)$.

Assuming, without prove, completeness and discreteness of the spectrum of $\mathcal{L}$ (we ascribe to alternative theoretical approaches and numerical techniques the assessment of the validity region of this assumption) we can expand $\bar{G}$ using the eigenfunction of $\mathcal{L}$ defined by $\mathcal{L}\Psi_j = \Lambda_j\Psi_j$ thus getting

$$\bar{E} = \sum_j \frac{\Psi_j(\hat{\boldsymbol{r}}_\perp)}{\Lambda_j}\int d\hat{\boldsymbol{r}}'_\perp\Psi_j(\hat{\boldsymbol{r}}'_\perp)f(\hat{\boldsymbol{r}}'_\perp)\,. \tag{12}$$

To find $\hat{E}_z$ we use the inverse Laplace transformation and we perform the integration analytically with the help of Jordan lemma. Although we write results in a general form, this method is straightforward only in the case of a cold beam $\hat{F} = \delta(\hat{P})$ that will be the only one considered here. Then our final result is written as follows:

$$\hat{E}_z(\hat{z}, \hat{\boldsymbol{r}}_\perp) = \sum_j u_j\Phi_j(\hat{\boldsymbol{r}}_\perp)e^{\lambda_j\hat{z}}\,, \tag{13}$$

$$u_j = \frac{\int d\hat{\boldsymbol{r}}'_\perp \Phi_j(\hat{\boldsymbol{r}}'_\perp) f(\hat{\boldsymbol{r}}'_\perp, \lambda_j)}{\left[\int d\hat{\boldsymbol{r}}'_\perp \left(\frac{\partial g}{\partial p}\right) \Psi_j^2\right]_{p=\lambda_j}} . \quad (14)$$

The modes Φ_j are not orthogonal. Appropriate initial conditions can be chosen to obtain a single propagating mode. In order to excite a single mode at *fixed* values of j one must impose:

$$\frac{\hat{a}_{1e}}{\hat{a}_{1d}} = -i\lambda_j \ , \quad \hat{a}_{1d} = (\hat{\nabla}_\perp^2 - q^2)\Phi_j . \quad (15)$$

From now on we will deal with case of an axis-symmetric beam described with a cylindrical (normalized) coordinate system $(\hat{r}, \phi, \hat{z})$, with obvious meaning of symbols. It is convenient to discuss azimuthal harmonics of $\hat{j}_1$, $\hat{E}_z$ and f which will be indicated with $\hat{j}_1^{(n)}(z, \hat{r})$, $\hat{E}_z^{(n)}(\hat{z}; \hat{r})$ and $f^{(n)}(\hat{r}, p)$. Our results Eq. (13) and Eq. (14) take the simpler form:

$$\hat{E}_z^{(n)}(\hat{z}, \hat{r}) = \sum_j u_{nj} \Phi_{nj}(\hat{r}) e^{\lambda_j^{(n)} \hat{z}} , \quad (16)$$

$$u_{nj}(\hat{r}) = \frac{\int_0^\infty d\hat{r}' \hat{r}' \Phi_{nj} f^{(n)}(\hat{r}', \lambda_j^{(n)})}{\left[\int_0^\infty d\hat{r}' \hat{r}' \left(\frac{\partial g}{\partial p}\right) \Psi_{nj}^2\right]_{p=\lambda_j^{(n)}}} . \quad (17)$$

We give here some explicit calculations for several profile cases.

Stepped profile - In this case $S_0 = 1$ for $\hat{r} < 1$ and $S_0 = 0$ for $\hat{r} \geq 1$. Putting $\alpha_j^2 = -q^2(1 + 1/\lambda_j^{(n)\,2})$ we obtain the eigenvalue equation:

$$\alpha_j J_{n+1}(\alpha_j) K_n(q) - q K_{n+1}(q) J_n(\alpha_j) = 0 . \quad (18)$$

It turns out that $\lambda_j^{(n)}$ are imaginary and such that $-1 < Im(\lambda_j^{(n)}) < 1$. The solution for the evolution equation is:

$$\hat{E}_z^{(n)}(\hat{z}, \hat{r}) = \begin{cases} \sum_j u_{nj} J_n(\alpha_j \hat{r}) e^{\lambda_j^{(n)} \hat{z}} & \hat{r} < 1 \\ \sum_j u_{nj} \frac{J_n(\alpha_j)}{K_n(q)} K_n(q\hat{r}) e^{\lambda_j^{(n)} \hat{z}} & \hat{r} \geq 1 \end{cases} , \quad (19)$$

$$u_{nj} = \frac{K_n(q) \int_0^1 d\xi J_n(\alpha_j \xi) \xi f^{(n)}(\xi)}{J_n(\alpha_j) \frac{d}{dp} \left[\alpha J_{n+1}(\alpha) K_n(q) - q K_{n+1}(q) J_n(\alpha)\right]_{p=\lambda_j^{(n)}}} , \quad (20)$$

where $\alpha_j^2 = -q^2(1 + 1/p^2)$.

Parabolic profile - In this case $S_0(\hat{r}) = 1 - k_1^2 \hat{r}^2$ for $\hat{r} < 1/k_1$ and $S_0 = 0$ for $\hat{r} \geq 1/k_1$. Solution for the homogeneous problem defined by $\mathcal{L}$ can be found in literature (see [1] for references). We can use that solution in order to solve our eigenvalue problem, and to write the expressions for the eigenfunctions Ψ_{nj} to be inserted in Eq. (13). Let us introduce the following notations: $\mu^2 = i\hat{D}q^2 - \Lambda_j^{(n)}$, $\delta^2 = i\hat{D}K_1^2$, $d^2 = \Lambda_j^{(n)}$, $\epsilon = (n+1)/2 - \mu^2/(4\delta)$. After some calculation we find:

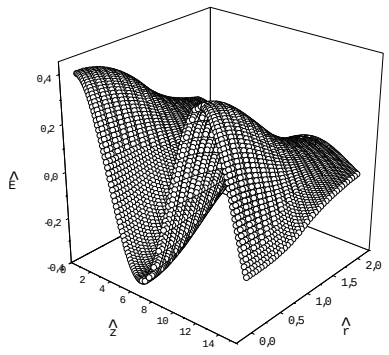

Figure 1: $\hat{E} = Re(\hat{E}_z)$ vs. $\hat{z}$ and $\hat{r}$. $q = 1$, $n = 0$; gaussian transverse profile case with $\sigma = 2.0$.

$$\Psi_{nj}(\hat{r}) = \begin{cases} \hat{r}^n e^{-\delta\hat{r}^2/2} \, {}_1F_1(\epsilon, n+1, \delta\hat{r}^2) & \hat{r} < 1 \\ e^{-\delta/2} \, {}_1F_1(\epsilon, n+1, \delta) \frac{K_n(d\hat{r})}{K_n d} & \hat{r} \geq 1 \end{cases} . \quad (21)$$

where ${}_1F_1$ is the confluent hypergeometric function, and the eigenvalue equation analogous of Eq. (18) is now

$$\delta K_n(d) \left[2\epsilon(n+1)^{-1} \, {}_1F_1(\epsilon+1, n+2, \delta) - {}_1F_1(\epsilon, n+1, \delta)\right] + d K_{n+1}(d) \, {}_1F_1(\epsilon, n+1, \delta) = 0 . \quad (22)$$

Multilayer method approach - An arbitrary gradient axisymmetric profile can be approximated by means of a given number of stepped profiles, or layers, superimposed one to the other. Results for the stepped profile case can be then used to construct an algorithm to deal with any profile (see [1] for more details).

ALGORITHM FOR NUMERICAL CALCULATIONS

The linear regime assumption is not too restrictive but it would be interesting to provide a solution for the full problem. As a first step towards this goal we present here a numerical solution of the evolution equation in the case of an axis-symmetric beam, that we will cross-check with our main result, Eq. (13). In order to build a numerical solution it turns out convenient to make use of Eq. (6).

After some manipulations Eq. (6) yields:

$$\frac{d^2 \hat{j}_1^{(n)}}{d\hat{z}^2} = -q^2 S_0 \int_0^1 d\hat{r}' \hat{r}' G^{(n)} \hat{j}_1^{(n)} , \quad (23)$$

where

$$G^{(n)}(\hat{r}, \hat{r}') = \begin{cases} I_n(q\hat{r}) K_n(q\hat{r}') & \hat{r} < \hat{r}' \\ I_n(q\hat{r}') K_n(q\hat{r}) & \hat{r} > \hat{r}' \end{cases} , \quad (24)$$

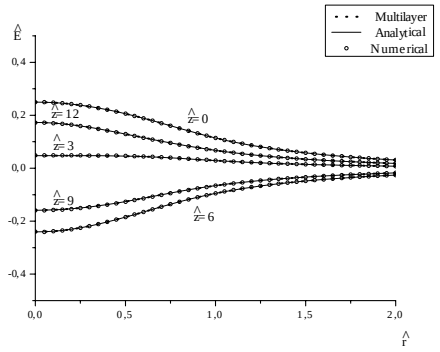

Figure 2: Analytical (solid), 15 layers (dotted) and numerical (circles) method. $\hat{E} = Re(\hat{E}_z)$ is plotted vs. $\hat{r}$. $q = 1$, $n = 0$; parabolic transverse profile with $k_1 = 1.0$.

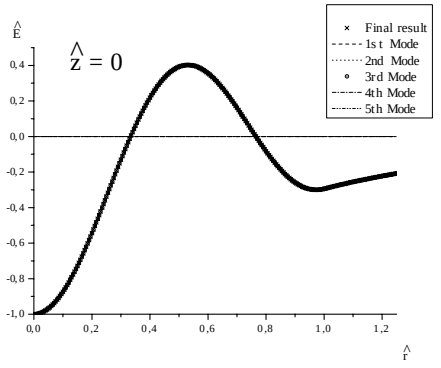

Figure 3: Selective excitation of the third mode. Here $n = 0$. $\hat{z} = 0$

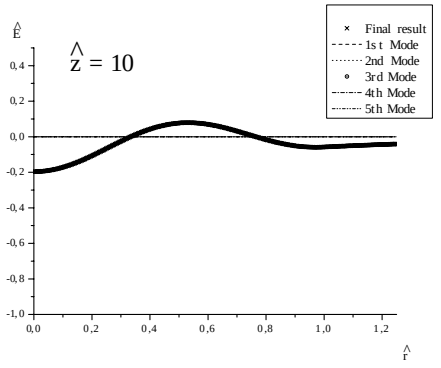

Figure 4: Selective excitation of the third mode. Here $n = 0$. $\hat{z} = 10$

Eq. (23) is to be considered together with proper initial conditions for $\hat{j}_1$ and its z-derivative at $z = 0$. The interval $(0, 1)$ can be then divided into an arbitrary number of parts so that Eq. (23) is transformed in a system of the same number of 2nd order coupled differential equations to be solved numerically. This gave us the solution of the evolution problem in terms of the beam current. Then we calculated back $\hat{E}_z$ and we compared obtained results with Eq. (13) for different choices of transverse profiles. The real field E_z should be recovered but all relevant information is included in $Re(\hat{E}_z)$. In Fig. 1 we present $Re(\hat{E}_z)$ as a function of $\hat{z}$ and $\hat{r}$ in the case of stepped, profile. The initial conditions are proportional to the transverse distribution function (stepped), and $n = 0$; moreover $\hat{a}_{1e} = 0$. Consistency with the perturbation theory approach requires $\hat{a}_{1d} \ll 1$ but using $\hat{a}_{1d} = \rho$ will simply multiply our results by an inessential factor ρ so, for simplicity, we chose $\rho = 1$. Comparison with the Runge-Kutta integration program are shown for example in 2 for the parabolic case. Finally we may actually select a single mode by fixing appropriate initial conditions as described in Eq. (15). For instance, if we fix $\hat{a}_{1e} = 0$ and we excite only the $j = 2$ mode for the azimuthal harmonic $n = 0$, then, in the case $S_0 = 1$ and $q = 1$ we obtain the results presented in Fig. 3 at $\hat{z} = 0$ and in Fig. 4 at $\hat{z} = 10$. As it can be seen by inspection only the third mode is excited and evolves, as it should.

CONCLUSIONS

In this paper paper we presented one of the few self-consistent analytical solutions for a system of charged particles under the action of their own electromagnetic fields. Namely, we considered a relativistic electron beam under the action of space-charge at given initial conditions for energy and density modulation and we developed a fully analytical, three-dimensional theory of plasma oscillations in the direction of the beam motion in the linear regime. We specialized the general method to the important cases of stepped and parabolic transverse profiles, which are among the few analytically solvable situations. In particular, the stepped profile case could be used to develop a semi-analytical technique to solve the evolution problem for the field using an arbitrary transverse shape. We also developed an algorithm able to solve the evolution problem in terms of the beam currents. Numerical and analytical or semi-analytical solutions for the fields were then compared and gave a perfect agreement. Finally we showed how to build up initial conditions in such a way that a single mode is excited and propagates through and we checked our prescription by setting up particular initial conditions and looking at the propagation of various eigenmodes.

REFERENCES

[1] G. Geloni, E. Saldin, E. Schneidmiller and M. Yurkov, DESY 04-112, see http://xxx.lanl.gov/abs/physics/0407024

BENCHMARK OF ASTRA WITH ANALYTICAL SOLUTION FOR THE LONGITUDINAL PLASMA OSCILLATION PROBLEM

Gianluca Geloni, Evgeni Saldin, Evgeni Schneidmiller and Mikhail Yurkov
Deutsches Elektronen-Synchrotron (DESY), Notkestrasse 85,
22607 Hamburg, Germany

Abstract

During the design of X-FELs, space-charge codes are required to simulate the evolution of longitudinal plasma oscillation within an electron beam in connection with LSC microbunching instability [1] and certain pump-probe synchronization schemes [2]. In the paper [3] we presented an analytical solution to the initial value problem for longitudinal plasma oscillation in an electron beam. Such a result, besides its theoretical importance, allows one to benchmark space-charge simulation programs against a self-consistent solution of the evolution problem. In this paper we present a comparison between our results [3] and the outcomes of the simulation code *ASTRA*.

INTRODUCTION

Start-to-end simulations of X-FEL systems require the use of several codes, able to deal with different parts of the setup. In particular, at low energies, simulations must account for space-charge interactions. These codes are also used in connection with LSC microbunching instability problems [1] and certain pump-probe synchronization schemes [2]: benchmarking them correctly is of critical importance since it is the only way to build up confidence in their outcomes.

In this paper we present first results of an ongoing benchmark of the space-charge code *ASTRA*. Our work takes advantage of the first three-dimensional, analytical model for the description of plasma oscillations within a relativistic electron beam, which has been described in [3] and [4]. This is the first time that such an analytical, self-consistent model is used to benchmark space-charge codes, which are usually compared with solutions of the Poisson equation for specific charge distributions. We claim that our method should be considered as a standard for benchmarking these codes from now on. In the following we describe how the simulation is set up, how it is compared with analytical results and we report the outcomes of this comparison as regards the estimation of a typical evolution parameter.

ANALYTICAL STUDY

We consider a radially uniform electron beam with transverse dimension $r_0 = 1.0$ mm and length $l_b = 2.2$ cm propagating with kinetic energy $E_k = 6.0$ MeV and current $I = 44.97$ A. Longitudinal and transverse beam emittances are set to zero. A $\rho = 5\%$ density modulation is considered at a wavelength $\lambda_m = 1$ mm in the longitudinal direction. This modulation is uniform in the transverse direction.

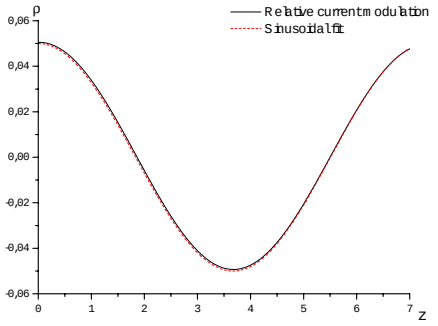

Figure 1: Relative current modulation level as a function of position inside the beam line (in m) and sinusoidal fit - analytical results. Parameters are given in the text.

Our analytical theory [4] deals with the longitudinal dynamics of the system, so it is applicable, roughly speaking, when the beam does not evolve, transversely, during the characteristic plasma oscillation length λ_p. This can be implemented in a simulation by focusing the beam using as we did, for instance, a longitudinal magnetic field B_z (compare with the next Section).

In our theory we describe the system evolution equivalently in terms of fields or currents. The former description is suitable, as has been remarked in [4] for numerical manipulations, while the latter gives us back a fully analytical model: the results out of these descriptions, of course, coincide. Our theory provides the longitudinal field $E_z(z,r)$ and current density $J_z(z,r)$ as a function of the longitudinal z and radial position r. As a first investigation, nevertheless, we were interested in how these quantities, averaged over the transverse beam distribution, compare with the analogous ones from *ASTRA*. Averaging J_z over the transverse distribution of the beam we get back the beam current $I(z) = \int_0^{r_0} J_z r dr$, while integrating E_z over z and averaging as for J_z we get back the momentum $p_z(z) = -2e/(cr_0^2)\int_0^r(\int_0^z E_z dz')rdr$.

In our theory the fields are presented as a superposition of propagating eigenmodes. The parameters described above correspond to a region where the one-dimensional asymptotic treatment of plasma oscillation is not applicable, and care was taken to choose them such that the

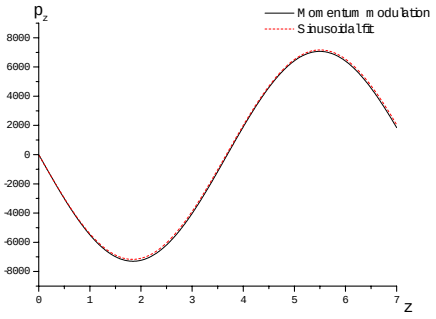

Figure 2: Momentum modulation (in eV/c) as a function of position inside the beam line (in m) and sinusoidal fit - analytical results. Parameters are given in the text.

first eigenmode is dominant with respect to the others. In this case the beam current and the longitudinal momentum, considered as functions of z, are nearly sinusoidal and therefore can be easily fitted [1] giving back, in both cases, the same estimation for the wavelength of plasma oscillations, $\lambda_p = 7.34$ m. In Fig. 1 we present the modulation level as a function of z, while in Fig. 2 we plot $p_z(z)$ as from our theory. Both figures also include sinusoidal fits. An alternative estimation of the plasma wavelength can be obtained, in the approximation when only the first eigenfunction is important, using the following equation (compare with [4]):

$$\lambda_p = \left[4I/(I_A r_0^2 \gamma\gamma_z^2)\right]^{1/2} /\Lambda_0 \simeq 7.31\mathrm{m}\,. \qquad (1)$$

Here $I_A = mc^3/e$ is the Alfven current, $\gamma = \gamma_z = 12.7417$ corresponds to a kinetic energy of 6 MeV and the first eigenvalue $\Lambda_0 = 0.3804$ is obtained from our analytical method: note that Λ_0 is sensibly different from unity, which is a clear signature of the fact that the one-dimensional theory cannot be applied.

Together with the benchmark for the full program, one can obtain, as a sort of by-product, a separate benchmark for the electromagnetic solver of *ASTRA* alone. In fact, at a short distance $z \ll \lambda_p$ the beam has not yet appreciably evolved so that E_z is the solution to the electrostatic problem of the initial charge distribution. Our analytical technique gives, at $z = 0.1$ m, an electric field on axis ($r = 0$) $E_z = 7235$ V/m. We checked that one can recover roughly the same value (with an accuracy of order 10^{-3}) from the well-known expression for the impedance per unit length of drift:

$$Z = \frac{4}{k_m r_0^2}\left[1 - \frac{k_m r_0}{\gamma} K_1\left(\frac{k_m r_0}{\gamma}\right)\right]\,, \qquad (2)$$

where $k_m = 2\pi/\lambda_m$ and K_1 is the modified Bessel function of the second kind of order 1. In fact $(I/I_A)Zm_e = 7242$ V/m, m_e being the electron mass in eV.

The maximum field on axis, multiplied by $ez/c = 0.1$ e m/c is the maximum momentum modulation at $z = 10$ cm, which may be compared with *ASTRA* results. Indeed, we preferred to average $E_z(z, r)$ at $z = 10$ cm over the transverse beam distribution and compare with the analogous averaged value of p_z from *ASTRA*.

ASTRA SIMULATION

For our purposes we used a modified version of *ASTRA* [5] using dynamic memory allocation, which allowed us to set the number of macroparticles $N_{ptc} = 12 \cdot 10^6$ and we used the customary *Generator* program to produce a uniform, cold beam with no modulation. No particular option for noise reduction was used. A 5% modulation was then subsequently introduced by rearranging the z positions of the particles using a short code written $ad\ hoc$: this allowed to overcome numerical noise problems in the z direction, related with the *Generator* program, but not with *ASTRA* itself. A solenoidal field $B_z = 7$ T has been used to decouple the longitudinal from the transverse dynamics. The question obviously arises if the transverse particle motion is truly negligible. Because of B_z, particles undergo small circular trajectories in the transverse plane with Larmor frequency $\omega_L = qB_z/(\gamma m_e)$, q being the macroparticle charge. The radius of these circles are related to the transverse velocities of the particles which are altered though, during the beam evolution, by the transverse space charge force. A quick estimation shows that the particle-tracker maximal integration step (which was set to 10 ps, corresponding to about 3 mm) is too long to sample the Larmor motion correctly. Yet, if the effect of Larmor motion is negligible at any point in the z direction, this fact is not of concern. We checked that this is the case analyzing the transverse rms angular spread as a function of the z-position, and the maximal transverse momentum also as a function of the z-position. We set the beam line length $L = 7$ m, which is about one full plasma oscillation length, according to our analytical estimations. A simple and conservative estimate shows that, at $z = L = 7$ m, every particle moved, transversely, $6.5 \cdot 10^{-5}$ m $at\ most$. This distance should be compared with the smaller transverse dimension typical of our system. *ASTRA* divides the beam in several radial slices for the calculation of the space-charge interactions. In our simulations we used 10 radial rings, with a difference of a factor 2 in thickness between the outer and the inner ring. Given the beam dimension $r_0 = 1.0$ mm we have that throughout all the evolution a particle can move, at most, the dimension of the thinner ring. Moreover, one should account for the fact that the transverse motion of the particles introduce a small change in the longitudinal projected motion of order $(p_\perp/p_z)^2$; however this can be estimated to be less than 10^{-10} or, on a length of 7 m, less than 1 nm, which is completely negligible.

The previous discussion allows us to consider the transverse particle motion negligible and to compare *ASTRA*

[1] For this purpose we used the program *ORIGIN*.

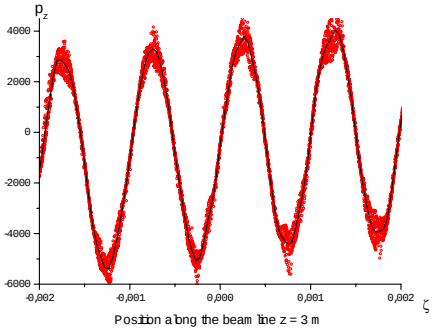

Figure 3: Particle longitudinal momenta p_z (in eV/c) as a function of the position inside the beam (in m) at 3 m inside the beam line. The solid line represents the momentum averaged over r. $N_{bin} = 400$.

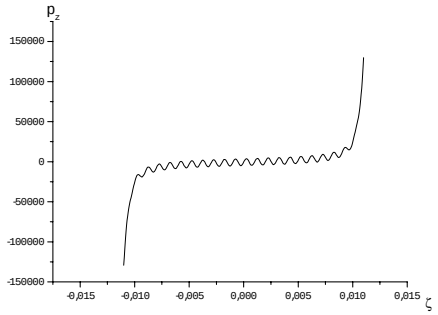

Figure 4: Average particle longitudinal momentum p_z (in eV/c) as a function of the position inside the beam (in m) at 3 m inside the beam line. $N_{bin} = 400$.

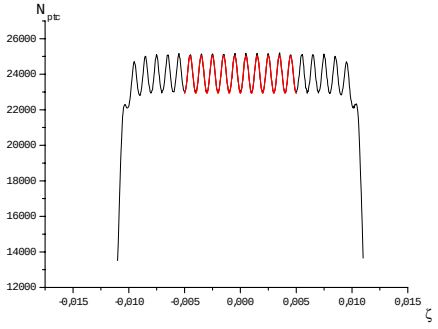

Figure 5: Particle density distribution normalized to N_{ptc} as a function of the position inside the beam (in m) at 3 m inside the beam line. $N_{bin} = 400$.

results with our analytical results.

In order to calculate the space-charge fields, *ASTRA* divides the beam also in a number N_{bin} of longitudinal slices, or bins: this is a critical parameter which should be studied to obtain correct results. A right estimation of the fields will occur only when a sufficiently large number of bins is chosen: considering a modulation wavelength λ_m, an intuitive guideline is that the number of bins per radiant should be larger than unity. At the same time, the number of particles in each bin should be large. We ran several *ASTRA* simulations with different longitudinal bins. The maximum number of bins was $N_{bin} = 800$, for a 2.2 cm-long bunch modulated at $\lambda_m = 1$ mm, which means that, when $N_{ptc} = 12 \cdot 10^6$, about 10^3 particles can be expected, roughly, to be present in each longitudinal slice for each radial ring.

The *ASTRA* output file consists of several information, among which the phase-space state of every particle. To give an example, in Fig. 3 we plot the particles longitudinal momentum p_z as a function of the longitudinal coordinate inside the bunch at 3 m down the beam line for $N_{bin} = 400$ [2]. We wrote a short code to get the average p_z and position (see the solid line in Fig. 3) of particles as a function of the longitudinal coordinate from *ASTRA* output: this program divides the bunch length (2.2 cm) in 500 parts, then the raw data from the simulation is read by the code and the average momentum and position is calculated for each slice. Results for the same example case in Fig. 3 are shown in Fig. 4 and Fig. 5.

The data in Fig. 4 and Fig. 5 and their analogous for every simulation run at any position down the beam line have been subsequently fit. The particle momenta have been fit with a tilted sinusoidal function $A + B\sin(2\pi z/\lambda_m) + Cz$, where the tilting is due to the fact that the tail of the bunch is decelerated, while the head is accelerated by the space-charge fields. The particle density distribution, instead, has been fitted using $A + B\sin(2\pi z/\lambda_m + \pi/2)$, B/A giving the relative modulation level. Only the inner 10 periods have been used in the fits (nearer the bunch center, in the longitudinal direction) since, as the bunch progresses through the beam line, spurious edge effects get more and more important.

For every *ASTRA* run (with a fixed number of longitudinal slices N_{bin}) we could plot the current modulation level and the absolute energy modulation and fit them, as before, using a sinusoidal function.

The results in the case of $N_{bin} = 400$ are shown in Fig. 6 and Fig. 7, from which we have two estimation for the plasma wavelength, $\lambda_p = 7.32$ m and $\lambda_p = 7.44$ m respectively, which differ of about 1.6%.

As said before several *ASTRA* runs were performed with different numbers of longitudinal slices N_{bin}. This allowed us to plot the plasma wavelength as a function of

[2] actually only one particle in 500 was selected for the plot, in order to make the figure file more easily manageable.

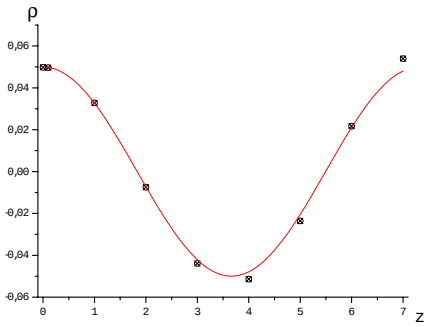

Figure 6: Averaged relative current modulation level as a function of the position in the beam line (in m) and sinusoidal fit. $N_{bin} = 400$.

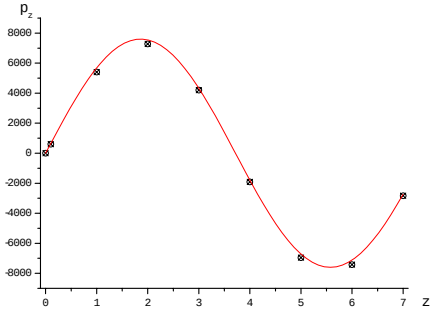

Figure 7: Average momentum modulation (in eV/c) as a function of the position in the beam line (in m) and sinusoidal fit. $N_{bin} = 400$.

the number of bins per modulation wavelength and to compare the results with analytical estimations. This result is presented in Fig. 8. As one can see at least 20 bins per wavelength are required in order to obtain acceptable results. Finally, to benchmark separately *ASTRA* electromagnetic solver, we plotted the electromagnetic fields estimated from the average momenta at $z = 10$ cm, as a function number of bins per wavelength and we compared these data with our analytical expectations. The result is shown in Fig. 9. It can be seen that results in Fig. 8 and Fig. 9 are in agreement: as the number of bins decreases, the fields are underestimated and the plasma wavelength is then badly overestimated.

CONCLUSIONS

We benchmarked *ASTRA* simulation by means of an analytical, self-consistent three-dimensional model developed by us in [4]. Results show a very good agreement between analysis and simulations, provided that critical parameters like the number of longitudinal bins for space-charge calculations are chosen correctly.

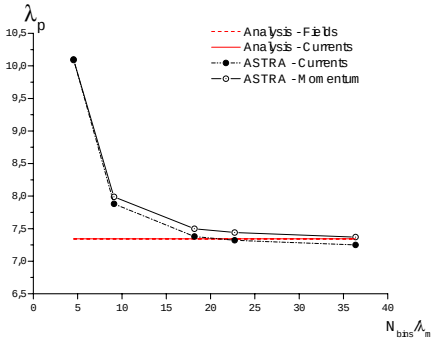

Figure 8: Benchmark of ASTRA - self-consistent problem: comparison between λ_p (in m) as a function of N_{bin}/λ_m calculated by ASTRA and with our analytical method.

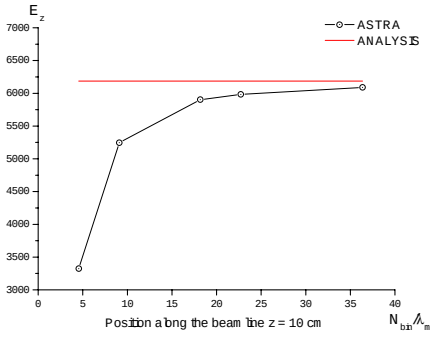

Figure 9: Benchmark of ASTRA - electromagnetic problem: comparison between the fields at 10 cm down the beam line (in V/m) as a function of N_{bin}/λ_m calculated by ASTRA and with our analytical method.

REFERENCES

[1] E. Saldin et al., TESLA-FEL-2003-02

[2] J. Feldhaus et al., DESY 03-091

[3] G. Geloni, E. Saldin, E. Schneidmiller and M. Yurkov, MOPOS08, this conference

[4] G. Geloni, E. Saldin, E. Schneidmiller and M. Yurkov, DESY 04-112, see http://xxx.lanl.gov/abs/physics/0407024

[5] http://www.desy.de/ mpyflo/

OFF-AXIS ORBITS IN REALISTIC HELICAL WIGGLERS: FIXED POINTS AND TIME AVERAGED DYNAMICAL VARIABLES

J.T. Donohue, Centre d'Etudes Nucléaires de Bordeaux-Gradignan, BP 120, 33175 Gradignan, France
J. L. Rullier, CEA CESTA, BP 2, F-33114 Le Barp, France

Abstract

Many years ago Fajans, Kirkpatrick and Bekefi (FKB) studied off-axis orbits in a realistic helical wiggler, both experimentally and theoretically. They found that as the distance from the axis of symmetry to the guiding center increased, both the mean axial velocity and the precession frequency of the guiding center varied. They proposed a clever semi-empirical model which yielded an excellent description of both these variations. We point out that a approximate model proposed by us several years ago can be made to predict these delicate effects correctly, provided we extend our truncated quadratic Hamiltonian to include appropriate cubic and quartic terms. We develop an argument similar to the virial theorem to compare time averaged and fixed-point values of dynamical variables. Illustrative comparisons of our model with numerical calculation are presented.

INTRODUCTION

In 1985 Fajans, Kirkpatrick and Bekefi performed an experiment with a low-energy free electron laser (FEL) operating in the amplifier mode in the microwave region[1]. The wiggler was helical, and a uniform axial field was present. The electron beam was furnished by a pulse-line diode in single shot operation. Among other studies, they investigated what happened when the beam was injected off axis, simply by displacing their wiggler in the transverse direction. Both beam and FEL measurements were carried out. In general, they found that for small displacements, the FEL operation remained satisfactory. Two properties of the beam were measured quantitatively as a function of the off-axis injection distance. The mean axial velocity was observed to satisfy a simple quadratic law

$$\langle \beta_z(y) \rangle = \beta_z(0) + K_\beta y^2 + \cdots$$

where K_β is a number which depends on the FEL parameters, and y denotes the displacement of the beam centroid from the wiggler axis at injection. The symbol $\langle\ \rangle$ denotes the time average of the corresponding dynamical quantity Throughout this paper we shall use only dimensionless quantities with mc as the unit of momentum, $1/k_w$ the unit of length and ck_w the unit of frequency. A second important property was the precession of the displaced quasi-circular FEL orbits. Again, for small displacements, a simple quadratic behavior was found for the precession frequency ω_P.

$$\omega_P(y) = \omega_P(0) + K_P y^2 + \cdots$$

where K_P denotes another constant. Since the quantities $\beta_z(0)$ and $\omega_P(0)$ are just the values on the ideal orbit, they may be considered as known. The real task is to compute the quantities K_β and K_P.

The authors analyzed the wiggler magnetic field in detail, and proposed two formulas to describe the modification of the mean axial velocity and the precession frequency. The former is described by

$$\langle \beta_\perp \rangle = \frac{\langle \beta_z \rangle \Omega_w I_0(k_w y_g)(I_0(\lambda) - I_2(\lambda))}{\gamma \langle \beta_z \rangle - \Omega_0 - 2\Omega_w I_0(k_w y_g) I_1(\lambda)}$$

$$\text{subject to } \gamma = \frac{1}{\sqrt{1 + \langle \beta_z \rangle^2 + \langle \beta_\perp \rangle^2}}$$

where γ is the dimensionless energy. The quantities Ω_0 and Ω_w are eB_0/mc^2k_w and eB_w/mc^2k_w, respectively, y_g denotes the off-axis injection distance, and λ is $\pm k_w\rho$, where ρ is the radius of the FEL motion. A somewhat simpler expression had been proposed by Freund and Ganguly [2],

$$\langle \beta_\perp \rangle = \frac{\langle \beta_z \rangle \Omega_w I_0(k_w y_g)}{\gamma \langle \beta_z \rangle - \Omega_0}$$

$$\text{subject to } \quad \gamma = \frac{1}{\sqrt{1 + \langle \beta_z \rangle^2 + \langle \beta_\perp \rangle^2}}$$

For the precession, FKB proposed the formula

$$\omega_p = ck_w \frac{\langle \beta_\perp \rangle \Omega_w (I_0(k_w y_g) - I_2(k_w y_g))}{\Omega_0 - 2\Omega_w I_0(k_w y_g) I_1(\lambda)}.$$

In the three cases investigated by FKB, their formula were remarkably successful. That of Freund and Ganguly for the diminution of the mean axial speed was somewhat less precise, but adequate.

Given the success of these formulas at describing the data, one might well consider the problem solved. However, having proposed an analytic (but approximate) method of calculating the trajectories in a helical wiggler with axial guide field [3], we felt challenged to show that our model could be used to generate equally successful

expressions, perhaps in a more systematic way. We don't know the details of the adiabatic magnetic field used by FKB to inject into the wiggler, so we address a related but slightly different problem. Suppose that an electron is on the ideal axially centered helical trajectory, and then displace the electron by a small amount in a transverse direction, leaving its velocity vector unchanged. We remind the reader that the ideal orbit satisfies two conditions:

$$\psi = \phi - z = \begin{pmatrix} 0 & \text{Group II} \\ \pi & \text{Group I} \end{pmatrix},$$

$$\gamma\beta_z = \Omega_0 - 2\Omega_w I_1(\rho)\left(\frac{1}{\rho^2}+1\right)\cos\psi,$$

where ρ denotes the constant radius of the helix. The notation Group I corresponds to $\gamma\beta_z > \Omega_0$ and Group II to $\gamma\beta_z < \Omega_0$. There is also the reversed field configuration, studied by Conde and Bekefi [4], where the axial velocity is anti-parallel to the axial field, or $\gamma\beta_z\Omega_0 < 0$. If one chooses the z-direction such that $\Omega_0 > 0$, then the reversed field is a special case of Group II, typically with a very small radius. The effect of a small displacement is then calculated by linearizing the equations of motion around the ideal helix. This procedure is described in detail in the monograph of Freund and Antonsen [5]. The electron then has two independent normal modes of oscillation, whose frequencies are well-known. It turns out that one of these two frequencies is numerically close to the unperturbed constant axial velocity β_z.

In our approach to calculating the trajectories, the key role is played by the Helical Invariant, P_z, a conserved quantity which is a consequence of the screw symmetry of the wiggler field [6]. We find the fixed point of the Hamiltonian (where the first derivatives with respect to our chosen dynamical variables vanish), expand to second order in our variables, and then find the normal modes of oscillation of the resulting quadratic system. If we denote the complex normal mode amplitudes in our model by A_+ and A_-, with the Poisson brackets $\{A_\alpha, A_\beta^*\} = i\delta_{\alpha\beta}$, our Hamiltonian may be written as

$$H = H_{fp} + \Omega_+ |A_+|^2 + \Omega_- |A_-|^2 + O(A^3).$$

Neglecting the cubic and higher order terms, we find the simple dynamics,

$$A_\alpha(t) = A_\alpha(0)\, e^{i\Omega_\alpha t}.$$

With our rather complicated choice of dynamical variables the transformation to normal modes was straightforward, and we obtained a quantitatively accurate description of the transverse motion as a Ptolemaic superposition of three independent circular motions. One is the projection of the standard FEL helix, the second, driven mainly by the mismatch in transverse velocity, occurs at a frequency near the relativistic cyclotron field Ω_0/γ, while the third is a very slow motion, whose effective frequency is $\langle\beta_z\rangle - \Omega_\beta$, where Ω_β denotes that oscillation frequency which is close to β_z. It is this slow motion that is the precession seen by FKB.

In terms of our model, the calculation of the effects observed by FKB is straightforward. Displacing the electron from the ideal helical orbit produces a change in the Helical Invariant that is second order in the displacement. The resulting changes in the axial velocity and frequency are readily computed, and can be compared to experiment. Proceeding in this way, we find extremely **poor** agreement between our calculations and experiment.

TIME AVERAGES AND FIXED POINTS

The difficulty encountered in attempting to calculate the mean axial velocity was traced to the source, the fact that the time average of a dynamical variable in the neighborhood of a fixed point is not its value at the fixed point. The time averages of our normal modes of oscillation, which we had assumed to be zero, were in fact different from zero. If our quadratic approximation to the Hamiltonian were exact, this would not occur. However, the cubic terms in the Hamiltonian generate such non-zero time average values. While the inclusion of the cubic terms into our model makes it non-soluble, it is possible by using a perturbation approach to obtain the lowest order corrections by calculating third derivatives at the fixed point. The required labor is greatly facilitated by using symbolic manipulators such as MAPLE or *Mathematica*. If one is interested in calculating the dependence of the precession frequency on the displacement, some fourth derivatives at the fixed point are also needed. We present below a sketch of our method.

The essential tool in our approach is a proposition similar to the virial theorem in classical mechanics. Given a general Hamiltonian, and a complex dynamical variable $A(t)$ of the sort we use, we consider the time average of the following quantity

$$\left\langle \frac{d}{dt}\left(A(t)\, e^{i\omega t}\right)\right\rangle = \lim_{T\to\infty} \frac{A(T)\, e^{i\omega T} - Q(0)}{T} = 0$$

provided the variable is $A(t)$ bounded. But by Hamilton's equations

$$\left\langle \frac{d}{dt}\left(A(t)\, e^{i\omega t}\right)\right\rangle = i\left\langle \left(\omega A(t) + \frac{\partial H}{\partial A^*}\right) e^{i\omega t}\right\rangle.$$

For technical reasons, it is more convenient to compute the higher order terms using the squared Hamiltonian, and we arrive the following result

$$(\omega+\Omega_\alpha)\left\langle A_\alpha(t)e^{i\omega t}\right\rangle = -\frac{1}{2H}\left\langle \frac{\partial\left(H^2\right)_{cubic}}{\partial A_\alpha^*}e^{i\omega t}\right\rangle$$

where represents the cubic and higher order terms in the multi-variable Taylor series expansion of the squared Hamiltonian at the fixed point. For our purposes, we keep only the cubic terms, and find non-vanishing contributions only for the nine following values of the arbitrary frequency ω,

$$\omega_j = \left\{0, \pm 2\Omega_+ \pm 2\Omega_-, (\Omega_+ \pm \Omega_-), -(\Omega_+ \pm \Omega_-)\right\}.$$

This means we may write, correct to second order in the displacement,

$$A_+(t) = A_+(0)e^{i\Omega_+ t} + \sum_{j=1}^{9} a_{j+}e^{-i\omega_j t}$$

with a similar expression for $A_-(t)$. Here the quantities a_{j+} are second order in the displacement. We find

$$\left(\omega_j+\Omega_+\right)a_{j+} = \frac{-1}{2H}\left\langle \frac{\partial\left(H^2\right)_{cubic}}{\partial A_\alpha^*}e^{i\omega_j t}\right\rangle_{A(t)=A(0)e^{i\Omega t}}$$

where on the right-hand-side only the first approximation to the variables is to be used.

HIGHER ORDER TERMS

In order to compute the quantities a_{j+}, we need the cubic part of the squared Hamiltonian, which we write as

$$H^2_{cubic} = -iK_+\left|A_+^2\right|\left(A_+ - cc\right) - iL_+\left|A_-^2\right|\left(A_+ - cc\right) - iR_+\left(A_+^3 - cc\right)$$
$$- iS_+\left(A_+^2A_- - cc\right) - iT_+\left(A_+^2A_-^* - cc\right) + (+\leftrightarrow -)$$

where cc denotes complex conjugate. The ten quantities K_+ etc. may be computed most easily if we write the squared Hamiltonian in cylindrical coordinates, as in ref. [7],

$$H(\rho,\psi,z,p_\rho,p_\psi,P_z) =$$
$$\sqrt{1+\left(p_\rho+A_\rho(\rho,\psi)\right)^2+\left(\frac{p_\psi}{\rho}+A_\phi(\rho,\psi)\right)^2+\left(P_z-p_\psi\right)^2}$$

The complex dynamical variables A_+ and A_- are linearly related to the usual variables,

$$A_\pm = a_\pm p_\rho + ib_\pm\left(\rho-\rho_f\right) + ic_\pm\left(p_\psi-\left(p_\psi\right)_f\right) + d_\pm\left(\psi-\psi_f\right)$$
$$p_\psi = \left(p_\psi\right)_f + id_+\left(A_+ - cc\right) + id_-\left(A_- - cc\right)$$

where ρ_f, ψ_f and $\left(p_\psi\right)_f$ denote the values of the variables at the fixed point. The time averaged axial velocity is then

$$\left\langle\beta_z\right\rangle = \frac{P_z-\left\langle p_\psi\right\rangle}{H}$$
$$= \frac{P_z-\left(p_\psi\right)_f}{H} - \frac{2i\left(d_+\left\langle A_+\right\rangle + d_-\left\langle A_-\right\rangle\right)}{H}$$

Explicit calculation yields

$$\left\langle A_+\right\rangle = \frac{-i\left(2K_+\left|A_+^2\right| + L_+\left|A_-^2\right|\right)}{2\Omega_+H}$$

and similarly for $\left\langle A_-\right\rangle$. In these expressions the amplitudes are linear in the displacement y, and we thus can calculate the coefficient of y^2 in $\left\langle\beta_z\right\rangle$, K_β.

CHANGES IN TIME AVERAGED FREQUENCIES

In order to calculate the slope of the FKB precession frequency, we must calculate the change in the time average of the oscillation frequencies caused by the higher order terms in the Hamiltonian. The relevant equation is

$$\left\langle\Omega_+\right\rangle = \left\langle\frac{d\Im\ln A_+}{dt}\right\rangle = \frac{1}{4H}\left\langle\frac{\partial H^2}{A_+\partial A_+^*}+cc\right\rangle.$$

This receives contributions from both the cubic part and from three of the many quartic contributions. These may be written as

$$H^2_{quartic} = M_+\left|A_+^4\right| + M_-\left|A_-^4\right| + N\left|A_+^2\right|\left|A_-^2\right| + \cdots$$

The details of the explicit calculation are too long to be given in this paper, and we give only the final result: $\left\langle\Omega_+\right\rangle = \Omega_+ + C_{++}\left|A_+\right|^2 + C_{+-}\left|A_-\right|^2$,

$$C_{++} = \frac{M_+}{H}$$
$$-\frac{1}{2H^2}\left(\frac{3\left(K_+^2+R_+^2\right)}{\Omega_+}+\frac{L_-^2}{\Omega_-}+\frac{S_+^2}{2\Omega_++\Omega_-}-\frac{T_+^2}{2\Omega_+-\Omega_-}\right),$$

$$C_{+-} = \frac{N}{2H}-\frac{1}{H^2}\left(\frac{K_+L_+}{\Omega_+}+\frac{K_-L_-}{\Omega_-}\right)$$
$$-\frac{1}{H^2}\left(\frac{S_+^2}{2\Omega_++\Omega_-}+\frac{T_+^2}{2\Omega_+-\Omega_-}+\frac{S_-^2}{2\Omega_-+\Omega_+}+\frac{T_-^2}{2\Omega_--\Omega_+}\right),$$

For the quantity $\left\langle\Omega_-\right\rangle$ a similar expression holds provided one makes the substitution $+\leftrightarrow-$ throughout. Note that $C_{+-} = C_{-+}$.

COMPARISON WITH NUMERICAL SIMULATIONS

At this point we can calculate K_β and K_P. However, in order to verify this analysis, we carried out numerical calculations of the trajectories using solvers of differential

equations available on MAPLE and Mathematica. Our approach is simple. We start with an electron on the ideal trajectory suited to its energy. We then displace the position of the electron tangentially through a distance y, keeping the velocity unchanged. We then calculate the trajectory of the electron for long times, typically 100 periods, in order to obtain reliable numerical estimations of the time averaged axial velocity and the precession frequency. We performed this calculation for the three cases studied by FKB. In each of these, the frequency concerned by the precession was Ω_+ so we added two more, for which the relevant frequency was Ω_-. These include a Group II configuration with a large axial field, which we label low-ρ, and a reversed field configuration, of the sort investigated by Conde and Belkefi. The results are summarized in the Table, which indicates various properties of the trajectory, the frequencies, the precession frequency intercept $\omega_P(0)$ (in the FKB units of $10^8 s^{-1}$). The last eight lines show comparisons of our theory (denoted by T) with the simulations (S). The agreement between these is quite good.

	FKB a group I	FKB b group II	FKB c group II	low ρ, Group II	reversed $\beta_z B_0 < 0$
B_0 (T)	0.16	1.312	0.4	1.8	1
B_w (T)	0.025	0.05833	0.025	0.063	0.147
V (MeV)	0.16863	1.2264	0.16863	0.750	0.750
λ_w (cm)	3.30	3	3.30	3.18	3.18
k_w (cm^{-1})	1.904	2.094	1.904	1.97584	1.97584
γ	1.33	3.4	1.33	2.46771	2.46771
ρ_f	0.22461	0.31543	0.21602	0.06073	0.08433
$(\beta_z)_f$	0.64327	0.911498	0.644436	0.912532	-0.9110
ψ_f	π	0	0	0	0
Ω_+	0.65416	0.90481	0.640016	1.25171	2.10919
Ω_-	-0.23792	0.19576	0.286011	0.91155	-0.90526
$\omega_P(0)$	-6.217	4.199	2.523	0.5812	-3.389
d_+	-0.00110	-0.00304	-0.00230	-0.0991	-0.1018
d_-	-0.11976	-0.38085	-0.16418	0.00047	-0.0008
$\frac{\langle \Im A_+ \rangle}{y^2}$ T	-1.580	-3.290	-2.793	-13.46	-7.133
$\frac{\langle \Im A_+ \rangle}{y^2}$ S	-1.575	-3.292	-2.795	-13.15	-7.128
$\frac{\langle \Im A_- \rangle}{y^2}$ T	-1.085	-1.246	-1.525	-20.68	-10.69
$\frac{\langle \Im A_- \rangle}{y^2}$ S	-1.085	-1.247	-1.524	-20.88	-10.76
K_β T	-0.00952	-0.0165	-0.0076	-0.00094	0.0017
K_β S	-0.0095	-0.0165	-0.0076	-0.00094	0.0017
K_P T	-2.4868	1.3272	0.89201	0.2112	0.07146
K_P S	-2.56	1.31	0.88	0.20	0.072

TABLE

Comparison of theoretical (T) and simulation (S) values for various quantities. Five different configuration were studied FKB a, b and c, low ρ Group II, and reversed field.

CONCLUSION

We may thus conclude that our approach of calculating the contributions of the higher perturbatively is successful. However, one word of caution is necessary. The generally small values we find for K_P, especially in columns 5 and 6, are the result of cancellations of much greater changes in the separate pieces. Indeed, the change in the fixed point frequency due to the displacement is almost exactly cancelled by the contribution of the higher order cubic and quartic terms. This suggests that in a yet more sophisticated approach such cancellations could be avoided.

REFERENCES

1 J. Fajans, D.A. Kirkpatrick, and G. Bekefi, Phys. Rev. A 32 (1985) 3488.
2 H. P. Freund, A. K. Ganguly, IEEE J. Quantum Electron., **QE-21** (1985) 1073
3 J. T. Donohue, J.L. Rullier, Phys. Rev. E 49 (1994) 766.
4 M. E. Conde, G. Bekefi, Phys. Rev. Lett. 67, (1991) 3082.
5 H. P. Freund and T. M. Antonsen, Jr., *Principles of Free-electron Lasers*, 2nd Edition, Chapman and Hall, London .
6 R. D. Jones, Phys. Fluids 24 (1981) 564.
7 J. T. Donohue, J. L. Rullier, Nucl. Instr. And Meth. A 507 (2003) 56.

ANALYTIC ELECTRON TRAJECTORIES IN AN EXTREMELY RELATIVISTIC HELICAL WIGGLER: AN APPLICATION TO THE PROPOSED SLAC E166 EXPERIMENT

J. T. Donohue, Centre d'Etudes Nucléaires de Bordeaux-Gradignan, BP 120, 33175 Gradignan, France

Abstract

The proposed experiment SLAC E166 intends to generate circularly polarized gamma rays of energy 10 MeV by passing a 50 GeV electron beam through a meter long wiggler with approximately 400 periods. Using an analytic model formulated by Rullier and me, I present calculations of electron trajectories. At this extremely high energy the trajectories are described quite well by the model, and an extremely simple picture emerges, even for trajectories that that fail to encircle the axis of the wiggler. The calculations are successfully compared with standard numerical integration of the Lorentz force equations of motion. In addition, the calculation of the spectrum and angular distribution of the radiated photons is easily carried out.

PROPOSED EXPERIMENT AND ITS RELATION TO FELS

The experiment E-166 at SLAC proposes to produce circularly polarized photons of energy 10 MeV by sending a beam of electrons of energy 50 GeV through a helical undulator one meter long [1,2]. The wiggler period is 2.4 mm. The aim is to convert the polarized photons into longitudinally polarized positrons by pair production on a Ti target. Polarized leptons enable one to perform high precision tests of the Standard Model of weak and electromagnetic interactions, and the experiment is intended as a demonstration of principle. A key feature of the experiment is the helical wiggler Its properties, along with some beam properties are summarized in Table 1. Much information can be is found in the detailed report of Mikhailichenko [3], who designed the wiggler.

Table 1: Beam and Wiggler and Specifications

Energy	50 GeV
N_e/bunch	1×10^{10}
σ_x, σ_x	40 μm
$\gamma\varepsilon_x = \gamma\varepsilon_x$	3×10^{-5} m rad
Type	Helical
Period	0.24 cm
Length	1 m
Field on axis	0.76 T
Inner diameter	0.89 mm
Ω_w	0.1704
k_w	26.18 cm^{-1}

Although the wiggler is too short for any substantial bunching to occur, and consequently the system can't be classed as a Free Electron Laser (FEL), it does resemble many FELs that operated at much lower energy. . It also will be the highest energy photon source available, and may be seen as a test –bed for ultra high energy FELs. In particular, the FEL experiments performed at the CEA_CESTA facility [4] used helical wigglers and low energy (a few MeV) electron beams. Rullier and I developed a model to simulate the trajectories of the electrons in those experiments [5]. Our much earlier work on the analytic but approximate calculation of trajectories had been successful in describing trajectories in helical wigglers with an axial guide field [6], but was inapplicable in the absence of an axial field. A key advantage of our older approach is its ability to describe trajectories which don't encircle the axis of the wiggler. Our second approach is also capable of describing such trajectories. Now the radius of the SLAC E-166 beam (40 μm) is much greater than the radius of the ideal helical trajectory (0.665 nm), which implies that most electrons will be following trajectories that do not encircle the axis. While there is no major problem in calculating such trajectories by numerical integration of the Lorentz force equations of motion (I use both the NDSolve procedure in *Mathematica*, and the dsolve procedure in MAPLE), it is of interest to see what our model predicts. In fact, the conditions of the experiment are favorable, since the high energy limit of our model is quite simple. One can write simple closed form expressions for the position and velocity variables as functions of time.

An important experimental issue is the emission pattern of the radiation generated by the electrons during their passage through the wiggler. For the ideal helical trajectory, one may compute this most easily in the co-moving Lorentz frame, where the electron has only transverse motion. The resulting relative velocity is only 0.17, which means that the radiation is mainly at the fundamental frequency, with a small admixture of the second harmonic. Standard formula may be found, for example, in Jackson's book [7], where the problem 14.8 addresses the question (and provides the answer). A simple generalization furnishes the amplitudes for positive and negative helicity radiation. A straightforward Lorentz transformation then produces the angular distribution of the radiation in the laboratory frame. As might be expected the emission occurs mainly in a cone of half angle $1/\gamma_z$, where γ_z denotes the quantity

$\gamma_z = \left(1-\beta_z{}^2\right)^{-1/2}$ where β_z is the axial velocity of the electron in the laboratory. Both the photon energy and the polarization are highly correlated with the laboratory (lab) emission angle. The relations among the lab frequency ω, co-moving fundamental frequency $\tilde{\omega}_0$, on-axis wiggler field $\Omega_w = eB_w / mc^2 k_w$, lab emission angle θ, longitudinal rapidity y, and circular polarization P are:

$$\omega = \frac{\tilde{\omega}_0 e^y}{\cos^2\frac{\theta}{2} + e^{2y}\sin^2\frac{\theta}{2}}$$

$$\tilde{\omega}_0 = \frac{ck_w\gamma\beta_z}{\sqrt{1+\left(k_w\rho\gamma\beta_z\right)^2}} \cong \frac{ck_w\gamma\beta_z}{\sqrt{1+\Omega_w{}^2}}$$

$$\Omega_w = \frac{eB_w}{mc^2 k_w} \cong 0.934 B_w\lambda_w$$

$$\beta_z = \tanh y$$

$$P \cong \frac{1-e^{2y}\tan^2\frac{\theta}{2}}{1+e^{2y}\tan^2\frac{\theta}{2}}$$

The relation between the radius of the ideal helix and the axial momentum is

$$\gamma\beta_z = 2\Omega_w I_1\left(k_w\rho\right)\left(1/\left(k_w\rho\right)^2+1\right) \cong \Omega_w / k_w\rho$$

In order to obtain both high photon polarization and energy, the emitted photons must make an angle of less than 5 μ radians with the axis. The conversion target is placed 10 m downstream from the wiggler, which means that its diameter must be about 100 μm .

THE MODEL

The model presented in ref. 5 is based on finding the fixed point of the Hamiltonian, making a series expansion keeping only quadratic terms, and then a transformation to two normal modes. The dynamics is simply that of two uncoupled harmonic oscillators. The squared frequencies of the oscillations were known from much earlier work; they may be found in the monograph of Freund and Antonen [8]. According to our model, the frequency of greater magnitude is positive, while, for zero axial field, that of lesser magnitude is negative. In fact, for small radius (In the remainder of this paper we shall use only dimensionless quantities with *mc* as the unit of momentum, $1/k_w$ the unit of length and ck_w the unit of frequency), one finds

$$\Omega_\pm \cong \pm\left(\beta_z\right)_f\left(1\pm\tfrac{1}{\sqrt{2}}\rho_f - \tfrac{1}{2}\rho_f{}^2\right)$$

where ρ_f denotes the radius and $(\beta_z)_f$ the axial velocity at the fixed point. The dynamical variables are two conjugate coordinate and momentum pairs called (u,q) and (v,k). The key equation needed is the following, which is valid in the high energy limit:

$$x(t)+iy(t) = -\rho_f e^{iz(t)} + e^{i\left(z(t)-(\Omega_+-\Omega_-)t/2\right)}\times$$
$$\left\{\left(u+iv\right)_0\cos\left(\frac{\left(\Omega_-+\Omega_+\right)t}{2}\right)+\frac{\sqrt{2}}{\Omega_w}\left(k+iq\right)_0\sin\left(\frac{\left(\Omega_-+\Omega_+\right)t}{2}\right)\right\}$$

where

$$\left(u+iv\right)_0 \equiv u(0)+iv(0)$$
$$= x(0)+iy(0)+\rho_f \cong x(0)+iy(0)$$

Similarly,

$$\left(k+iq\right)_0 \equiv k(0)+iq(0)$$
$$\cong \gamma\left(\beta_x(0)+i\beta_y(0)\right)+i\Omega_w$$

Since the quantity $\left(\Omega_-+\Omega_+\right)t/2 \simeq \rho_f z/\sqrt{2}$ is always small in a one-meter-long wiggler, one may replace the cosine by 1, and the sine by its argument. I find to a good approximation

$$x(t)+iy(t) \cong -\rho_f e^{iz(t)} + x(0)+iy(0)+z\left(\frac{\gamma\left(\beta_x(0)+i\beta_y(0)\right)+i\Omega_w}{\gamma\beta_z}\right)$$

This espression shows that the transverse position is a superposition of the FEL helix, with the period of the wiggler, an initial constant displacement, and a drift at constant velocity . The time derivative of this expression yields the transverse velocity,

$$\beta_x(t)+i\beta_y(t) \cong -i\beta_z\rho_f e^{iz(t)} + \beta_x(0)+i\beta_y(0)+i\Omega_w/\gamma$$

The resulting transverse motion is quite simple, consisting only of the ideal FEL helix and a constant drift. What turns out to be essential is matching the initial velocity as closely as possible to the ideal value,

$$\beta_x = 0, \quad \beta_y = -\Omega_w/\gamma$$

It will be essential to the success of the experiment that these conditions be realized as closely as possible.

COMPARISON WITH SIMULATION

In order to verify that the simple motion found above is indeed correct, we have calculated numerically some trajectories using the NDSolve package in *Mathematica*. The trajectories were calculated with high precision, and a typical 400 period trajectory took about 90 seconds on a PC.

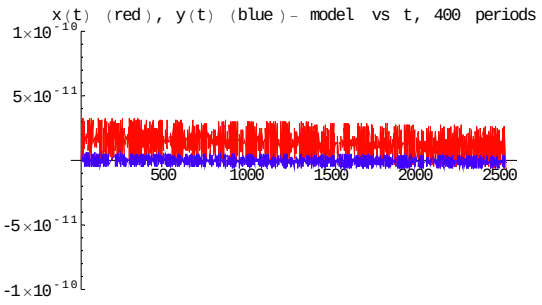

Figure 1. Difference between numerical solution and model keeping sine and cosine. Red is for $x(t)$, blue $y(t)$.

In figure 1 I show the differences between a numerically calculated trajectory and the model in which the sine and cosine are retained. The x-difference is shown in red, the y difference in blue. For this trajectory

$$x(0) = -1.7415\times10^{-6}, \qquad y(0) = 0.005,$$
$$\beta_x(0) = 1.7415\times10^{-8},\ \beta_z(0) = -1.7414\times10^{-6},$$
$$\beta_z(0) = 1 - 1.02\times10^{-10}, \qquad z = 0$$

For comparison the ideal injection would have $y(0) = 0$ and $\beta_x(0) = 0$. The initial y value is about 2 μm from the axis. In general the agreement between the model and the numerical calculation is excellent.

In Figure 2 I show the difference between the same numerical calculation and the simplified version of the model, in which the cosine is replaced by 1, and the sine by its argument.

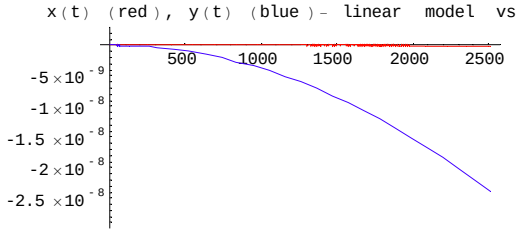

Figure 2. Difference between numerical solution and the simplified model with sine replaced by its argument and cosine by 1. Red is for $x(t)$, blue $y(t)$. Note change of scale compared to Figure 1.

Here the agreement remains surprisingly good for the x-coordinate, and slightly less so for the y-coordinate. However, the true value of the y-coordinate is approximately 0.005 throughout the trajectory, so the relative error remains small.

EFFECT ON RADIATION EMISSION

Without going into detail, one sees that for electrons that are injected with the ideal velocity, the resulting motion is basically the standard helix, except that it is not centered on the axis. For such trajectories, the radiation pattern is the same as the ideal one, except that the axis of the cone must be taken over the true axis of the helix. This necessarily leads to some "smearing" of the radiation pattern. A more serious problem occurs for those electrons whose injection velocity is not ideal. If the transverse drift is sufficiently large, the radiation pattern might be strongly affected. Further study is needed to settle this.

CONCLUSION

While we have not considered all the possible trajectories that are likely to occur in the proposed experiment, we are confident that the major part of them will be correctly described by our analytic approach. The even simpler approximation appears to be adequate for most purposes.

REFERENCES

1 http://www.slac.stanford.edu/exp/e166/
2 G. Moortgat-Pick, Eur. Phys. J. C 33 s1047 (2004).
3 A. A. Mikhailichenko, Report CBN 02-10, (2002). Available at site indicated in ref. [1].
4 T. Lefevre et al, Phys Rev. Lett. 1188 (2004).
5 J. T. Donohue, J. L. Rullier, Nucl. Instr. And Meth. A 507 (2003) 56.
6 J. T. Donohue, J. L. Rullier, Phys Rev. E 49 766 (1994).
7 J. D. Jackson Classical Electrodynamics, 2nd Edition, John Wiley & Sons, Inc. 1975.
8 H. P. Freund and T. M. Antonsen, Jr., Principles of Free-electron Lasers, 2nd Edition, Chapman and Hall, London .

HARMONIC GENERATION AND LINEWIDTH NARROWING IN SEEDED FELS

L. Giannessi, ENEA Via E. Fermi 45, 00044, Frascati, Italy

Abstract

The process of harmonic generation in a seeded, single pass, Free Electron Laser, are studied in the time/frequency domain following the evolution of the harmonics within a self consistent time dependent model. The first and second order correlation functions of the fundamental and of the higher order harmonics fields are studied as a function of the input seed amplitude.

INTRODUCTION

Single pass Free Electron Lasers (FEL) operated in Self Amplified Spontaneous Emission (SASE) configuration are amplifiers of the natural shot noise of the driving electron beam. The spectral properties of the output radiation are the result of the amplification of the wide bandwidth noise arising from the stochastic distribution of the electron beam current, in the narrow bandwidth FEL amplifier. The properties of the output radiation, in terms of temporal coherence and intensity stability, have been extensively studied in literature [1][2][3] and reflect the stochastic nature of the electron beam shot noise. In a recent experiment at BNL[4] it has been shown that seeding a single pass FEL with an external laser allows to improve the spectral properties and the temporal stability of the laser source. In the same experiment it has been demonstrated that these properties are transferred to the higher order harmonics generated by the FEL. There is a widespread interest in this process, because emission on high order harmonics represents a significant resource to extend the wavelength tunability of an FEL and several recent proposals of FEL facilities rely on schemes based on seeding an harmonic generation[5]. The input seed, in order to be effective, must be characterized by enough intensity to overcome the intensity associated to the beam shot noise. The equivalent input intensity associated to a bunched beam is given by [6],

$$I_0 = \left|\left\langle \exp(\zeta_i)\right\rangle\right|^2 \frac{\rho P_e}{\Sigma_b} \tag{1}$$

where Σ_b is the electron beam cross section and $P_e = I_{peak} m_0 c^2 \gamma / e_0$ is the e-beam peak power. The parameter

$$\rho = \frac{1}{2\gamma}\left(\frac{\left[\lambda_u K\left(J_0(\xi) - J_1(\xi)\right)\right]^2}{4\pi\Sigma_b}\frac{I}{I_A}\right)^{\frac{1}{3}} \tag{2}$$

is the Pierce parameter, with $\xi = K^2/\left[4\left(1+K^2/2\right)\right]$, and $\zeta_i = \left(k+k_u\right)z_i - \omega t + \varphi_{0,i}$ are the electron phases in the ponderomotive potential associated to an undulator of period λ_u (with $k_u = 2\pi/\lambda_u$) and strength *K,* and to an optical field $E(z,t) = \widetilde{E}(z,t)\exp\left(i(\omega t - kz)\right)$, being $\widetilde{E}(z,t)$ the slowly varying field component. In the specific case of randomly distributed electrons, the average $\left\langle \exp(\zeta_i)\right\rangle$ is the normalized sum of n_e independent phasors, i.e.,

$$\left|\left\langle \exp(\zeta_i)\right\rangle\right| = 1/\sqrt{n_e} \tag{3}$$

We estimate the number of interfering electrons n_e with the following naïve procedure. We define as

$$n_{1,e} = I_{peak}\lambda_0 / e_0 c \tag{4}$$

the number of electrons contained in a single resonant wavelength. Interference effects between electrons contained in contiguous wavelengths must be estimated. The field generated in a given longitudinal "slice" slips along the bunch and is amplified while the bunch travels along the undulator. This amplification must be considered in evaluating the interference between the fields emitted by electrons from different slices. The field evolution in presence of gain is given by [6],

$$\widetilde{E}(z) = \frac{E_0}{3}\left[e^{\left(\frac{i}{\sqrt{3}}+1\right)\frac{z}{2L_g}} + e^{\left(\frac{i}{\sqrt{3}}-1\right)\frac{z}{2L_g}} + e^{-i\frac{z}{\sqrt{3}L_g}}\right] \tag{5}$$

where $L_g = \lambda_u / \left(4\pi\sqrt{3}\rho\right)$ is the FEL gain length. We can use eq. (5) as a function of the longitudinal coordinate, to weight the electron number in each slice. Adding up the weighted number of electrons contained in all the slices, in a portion of the bunch of length $L\lambda_0/\lambda_u$, we get

$$n_e = n_{1,e}\int_0^L \left|E_0/\widetilde{E}(z)\right| dz = \; f(L) I_{peak} L_g \lambda_0 / \lambda_u e_0 c \tag{6}$$

The dimensionless function $f(L)$ grows linearly with L for the first gain lengths, then converges rapidly to the constant ~ 4.3. Assuming $n_e \approx 4.3\, I_{peak} L_g \lambda_0 / \lambda_u e_0 c$ as the total number of interfering electrons, we get from eq.(1)

$$I_0 \approx \lambda_u e_0 c / \left(4.3 I_{peak} L_g \lambda_0\right)\frac{\rho P_e}{\Sigma_b} \tag{7}$$

The equivalent input seed intensity I_0 can be estimated more accurately by considering the gain length corrections associated to diffraction/inhomogeneous effects [8][9]. In this paper we will study with a time dependent numerical model, the coherence properties of

an FEL amplifier seeded with an input seed of amplitude varying across the "threshold" eq. (7).

TEST CASES AND NUMERICAL MODEL DESCRIPTION

The analysis of longitudinal coherence in a single pass FEL amplifier has been developed by implementing a 1D time dependent model of an FEL amplifier in PERSEO [10]. PERSEO is a library of FEL dedicated functions available in the Mathcad environment. The basic element of PERSEO is a FEL pendulum-like equation solver for the particle dynamics, coupled with the field equations in the slowly varying envelope approximation (SVEA). The integrator includes self consistently the higher order harmonics. Transverse effects, as inhomogeneous broadening due to emittances, are accounted for by introducing an equivalent energy spread. In order to include time dependency, both the slowly varying field distribution and the electron phase space distributions are sampled longitudinally. At each time step the longitudinal slippage of radiation over the electron beam is applied shifting the radiation parameters array over the electron parameter arrays by an interpolation procedure. The implementation is capable of simulating the FEL interaction process for any profile of the input field/e-beam current, satisfying the SVEA approximation. In the cases studied, a continuous current distribution/input seed distribution, with a periodic boundary condition in the simulation window, has been considered. This choice allowed to minimize the number of parameters affecting the results. In table 1 the main simulation parameters are shown.

Table 1: Main simulation parameters.

Case label	***A***	***B***	***C***
λ_0 (nm)	50	15	5
Undulator K (peak)	2.2	2.2	2.2
Energy (MeV)	500	900	1550
En. spread (MeV)	0.4	0.4	0.4
I_{peak}(A)	500	800	1500
N. emitt.(mm-mrad)	1	1	1
Σ_b (mm^2)	3.2×10^{-2}	1.8×10^{-2}	1.04×10^{-2}
Pierce parameter ρ	2.86×10^{-3}	2.26×10^{-3}	1.94×10^{-3}
I_0, eq.(1) (W/cm^2)	4.4×10^{4}	2.9×10^{5}	1.9×10^{6}
Sim. window (μm)	250	200	200
Sampl. period (μm)	0.625	0.5	0.5
Sim. bandwidth	4%	1.5%	0.52%

We have selected three configurations with the operating wavelength in the VUV. This choice is driven by the general interest in seeding FELs with very high order harmonics of the Ti-Sa laser, generated in gases[11]. These sources span the VUV region of the spectrum with a considerable level of peak power and constitute interesting candidates for seeding FEL amplifiers[5]. From the numerical representation point of view, at these wavelengths diffraction effects in the FEL dynamics are less severe. This mitigates the lack of accuracy due to the one dimensional FEL model implemented in PERSEO.

RESULTS

The statistics of radiation and its coherence properties are studied with the first and second order correlation functions. In the time domain, the first order classical correlation function is defined by [12]

$$g_1(\tau)=\frac{\left\langle \tilde{E}(t)\tilde{E}^*(t+\tau)\right\rangle}{\sqrt{\left\langle\left|\tilde{E}(t)\right|^2\right\rangle\left\langle\left|\tilde{E}(t+\tau)\right|^2\right\rangle}} \tag{8}$$

An estimation of the coherence length can be obtained by the relation [12]

$$z_c = c\int_{-\infty}^{+\infty}\left|g_1(\tau)\right|^2 d\tau \tag{9}$$

In the hypothesis of a SASE FEL operating in the exponential growth regime, the coherence length (9) is a monotonic growing function of the longitudinal coordinate z in the undulator, and reads [3],

$$z_c = \frac{1}{6}\frac{\lambda_0}{\rho}\sqrt{\frac{z}{2\pi L_g}} \tag{10}$$

In fig.1, the coherence length evaluated according to eq.(10) has been compared with the values calculated from the simulation data,

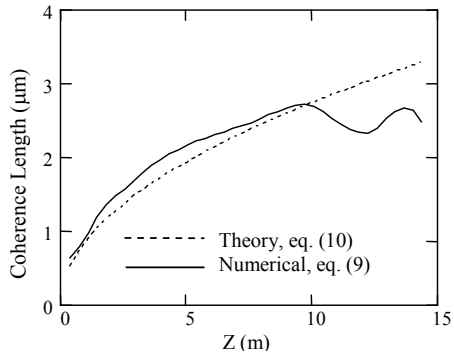

Fig. 1. Coherence length as given by eq. (10) (dashed line) and as calculated from the simulation data, according to eq.(9) (continuous line)

The plot in fig. 1 has been obtained simulating the configuration in column A of table 1, starting from the natural shot noise (no input seed). The beam energy spread has been set to zero in order to preserve the homogeneous conditions in which eq.(10) has been

derived. The agreement is reasonable until saturation, which is occurring at z~10m, is reached.

In fig. 2 the growth of the laser intensity as a function of the longitudinal coordinate is shown. The parameters are those of tab.1, col. *A,* with an input seed represented by a perfectly uniform classical wave of intensity I_s=3.1x10^5 W/cm^2.

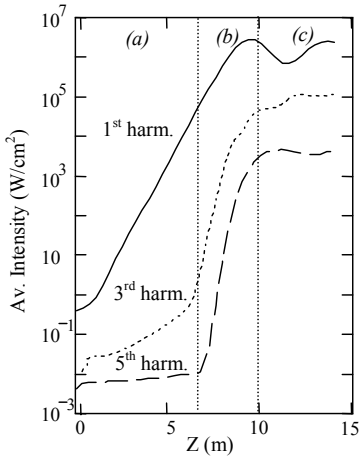

Fig. 2. Laser intensity vs. the longitudinal coordinate for the first three odd harmonics. The regions of exponential growth *(a)*, harmonics generation *(b)* and saturation *(c)* have been indicated in the figure.

In fig. 2 we can distinguish the region, labeled with *(b)*, where the growth of the third/fifth harmonic intensity is driven by the beam bunching due to the ponderomotive potential relevant to the first harmonic field.

The typical spectra for the third harmonic field, as calculated in regions *(a)* and *(b)* are shown in figs. 3.a,b respectively. In fig. 3.a the third harmonic field is not yet locked in phase to the bunching induced by the fundamental. The situation changes in fig. 3.b, where the phase of the third harmonic field is determined by the bunching on the fundamental and the coherence properties of the seed are transferred to the third harmonic. A similar behaviour is observed for the fifth harmonic.

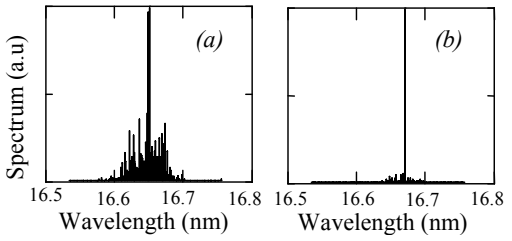

Fig.3. Third harmonic spectrum in the region *(a)* (at z~4.7m) and in the region *(b)* (at z~7.2m). The relative r.m.s. linewidth is ~0.174 % in *(a)* and ~0.076 % in *(b)*.

In fig.4 it is shown the behaviour of the maximum coherence length reached along the undulator, as a function of the input seed intensity. The parameters are those of table 1, column *A*. At 500μm the coherence length saturates because of the limited extension of the simulation window (250μm). The value of the intensity calculated according to eq.(1) is shown as a vertical dashed line. In figs. 5 and 6 are shown the equivalent plots obtained with the parameters listed in columns *B* and *C* of table 1 respectively.

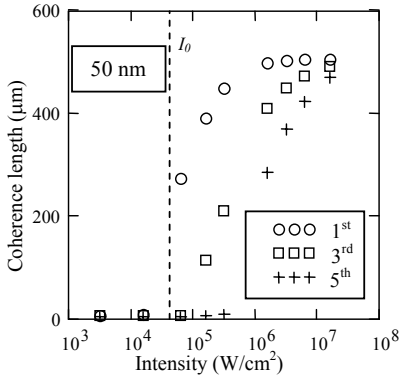

Fig. 4. Maximum coherence length reached along the undulator, as a function of the input seed intensity in the test case *A*. The dashed line indicates the threshold intensity I_0 evaluated according to eq. (7).

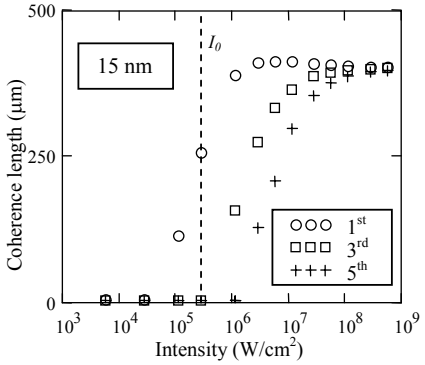

Fig. 5. As in fig.4 with the parameters of tab.1, col. *B*.

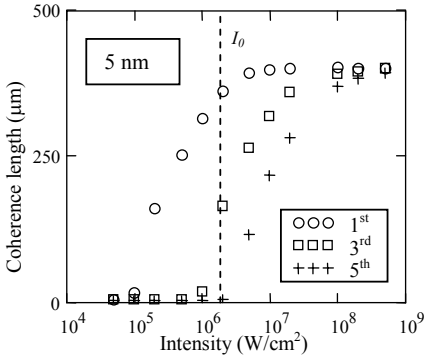

Fig. 6. As in fig.4 with the parameters of tab.1, col.*C*

As expected the power level required to ensure coherence on the higher order harmonics grows with the harmonic order. Comparing figs. 4, 5 and 6 it appears that the equivalent seed I_0 obtained according to eq.(7),

slightly overestimates the intensity required to establish coherence on the fundamental harmonic, as the wavelength decreases (parameters of col. C, fig.6). It must be stressed that the intensity of eq.(1) still matches quite well the intensity that can be obtained by extrapolating the laser intensity at z=0 from the simulation data.

The intensity fluctuations have been studied calculating the second order correlation function $g_2(\tau)$ [12]:

$$g_2(\tau) = \frac{\left\langle \left|\widetilde{E}(t)\right|^2 \left|\widetilde{E}(t+\tau)\right|^2 \right\rangle}{\left\langle \left|\widetilde{E}(t)\right|^2 \right\rangle \left\langle \left|\widetilde{E}(t+\tau)\right|^2 \right\rangle} \qquad (11)$$

as a function of the longitudinal coordinate along the undulator. From the definition (11), and assuming $I(t) \propto \left|\widetilde{E}(t)\right|^2$, it follows that

$$\sqrt{g_2(0)-1} = \left[I/\langle I\rangle\right]_{RMS} \qquad (12)$$

In figs.7, 8 and 9 it is shown the minimum along the undulator of the r.m.s. intensity (12), as a function of the seed intensity, in the cases *A*, *B* and *C* respectively. The averages in (12) are taken over the temporal extension of simulation window.

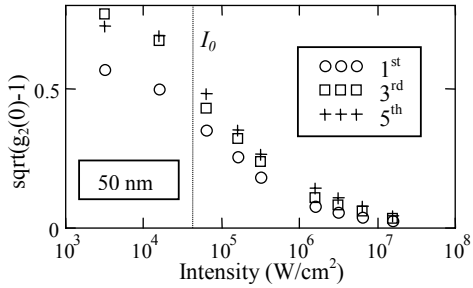

Fig. 7. Standard deviation of the intensity fluctuations vs. the seed intensity with the parameters of tab.1, col. *A*

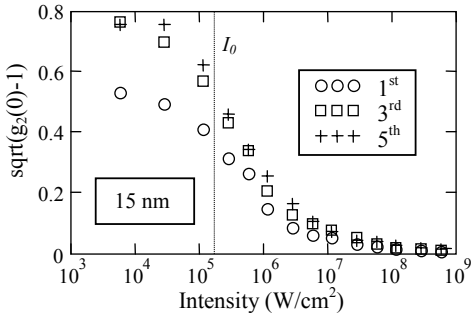

Fig. 8 As in fig. 7, with the parameters of tab.1, col. *B*

In a SASE FEL in the exponential growth regime, we have $\sqrt{g_2(0)-1} = 1$ [3]. As expected the effect of the seed is that of suppressing the intensity fluctuations but this transition is smoother than the one observed in establishing the temporal coherence (figs. 4,5 and 6).

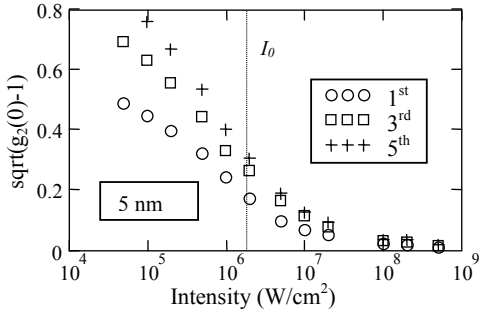

Fig. 9. As in figs. 7,8 with the parameters of tab.1, col. *C*

Fluctuations of the higher order harmonics are larger than fluctuations on the fundamental. The amplitude of the seed required for suppressing the fluctuations exceeds by orders of magnitude the intensity provided by eq.(7).

CONCLUSIONS

We have analysed the coherence properties of a seeded FEL amplifier as a function of the seed amplitude. The equivalent intensity associated to the beam shot noise, eq.(7), has been compared to the transition to coherence induced by the presence of a seed. The results obtained so far constitute a preliminary analysis which gives an indication about the power requirements of the input seed, in order to be effective in improving the coherence properties of a single pass FEL.

REFERENCES

[1] R. Bonifacio, L. De Salvo, P. Pierini, N. Piovella, C. Pellegrini, Phys. Rev. Lett. 73 (1994) 70 and references therein.
[2] P. Pierini, W. M. Fawley, Nucl. Instrum. & Meth. A 375 (1996) 332-335
[3] E.L. Saldin, E.A. Schneidmiller, M.V. Yurkov, Optics Communications 148, (1998) 383–403
[4] L. H. Yu et al., Phys. Rev. Lett. 91 (2003) 74801
[5] Workshop on the Physics of Seeded Free Electron Lasers, 17-19 June 2004, MIT campus, Cambridge, MA http://mitbates.mit.edu/xfel/conference.htm
[6] G. Dattoli, P.L. Ottavini, Journal of Appl. Phys. 86 (1999) 5331
[7] See e.g. G. Dattoli, A. Renieri, A. Torre, Lectures on the Free Electon Laser Theory, World Scientific ed. (1993) p. 493
[8] M. Xie, in *Proceedings of the Particle Accelerator Conference, Dallas, TX, 1995* (IEEE, Piscataway, NJ, 1996), p. 183. Sect. A **483**, 101 (2002).
[9] G. Dattoli, L. Giannessi, P.L. Ottaviani, C. Ronsivalle, Journal of Appl. Phys. 95 (2004) 3206
[10] http://www.enea.perseo.it
[11] P. Salières et al., Science **292** (2001) 902
[12] See e.g. R. Loudon, Quantum Theory of Light, Oxford Univ. Press (2000), chapter 3.

ANALYTICAL SOLUTION OF PHASE SPACE EVOLUTION OF ELECTRONS IN A SASE FEL

N. Nishimori*, JAERI, Ibaraki, Japan

Abstract

I present an analytical solution for the phase space evolution of electrons in a self-amplified spontaneous emission Free Electron Laser (FEL) operating in the linear regime before saturation, by solving the one dimensional FEL equation together with the solution of the cubic equation, which represents the evolution of the FEL power. The analytical solutions for the phase space evolution are complementary to the solution for the optical evolution and hold until the optical amplitude grows greater than one-tenth of the amplitude in saturation. The amplitude in saturation obtained from a time dependent numerical calculation in which the analytical solutions are used as the initial values is shown to be equal to that obtained in the conventional theories.

INTRODUCTION

A self-amplified spontaneous emission (SASE) free electron laser (FEL) has been developed worldwide as an intense coherent x-ray radiation source [1, 2, 3]. The development has been supported by extensive theoretical studies [4, 5, 6], which can account for various types of experimental results such as the exponential increase of SASE power with the undulator length [1]. However, those studies have mainly focused on the property of the radiation field, and the phase space evolution of electrons of a SASE FEL has been studied only in numerical simulations so far [6].

In this paper, I present an analytical solution for the phase space evolution of electrons in a SASE FEL operating in the linear regime before saturation, by solving the one dimensional (1D) equations of electron motion together with the solution of the cubic equation, which represents the evolution of SASE power. The solutions for the energy and phase changes of electrons are respectively represented by sum of three independent terms similarly to the solution of the cubic equation; an exponentially growing term, an exponentially decaying term and an oscillating term. The 1D Maxwell equation results in the same field gain as the solution of the cubic equation, when the solution for the electron phase is substituted into the Maxwell equation. The solutions for the phase space evolution are thus complementary to the solution for the optical evolution. The present solutions hold until the optical amplitude grows greater than one-tenth of the amplitude in saturation. The field in non-linear regime near saturation is obtained from a numerical calculation which uses the analytical solutions as the initial values and solves the 1D FEL equations. The peak amplitude in saturation obtained in the calculation agrees well with those obtained in conventional theories [5, 6].

* nisi@milford.tokai.jaeri.go.jp

1D FEL EQUATIONS

The present study starts with the Colson's dimensionless FEL equations under the slowly varying envelope approximation (SVEA) [7]. Some of the variables used in the present study are however defined differently from those of Colson's variables, as described later in this section. The simplest situation is considered in the present study where the electron pulse has a rectangular shape with density of n_e and an initial energy of $\gamma_0 mc^2$ with no energy spread. The electron pulse length is assumed to be longer than the slippage distance $N_w\lambda$. Here N_w is the number of undulator periods, $\lambda = \lambda_w(1 + a_w^2)/(2\gamma_0^2)$ is the resonant wavelength, $\lambda_w = 2\pi/k_w$ is the period of the undulator and a_w is the undulator parameter. The fundamental FEL parameter in MKSA units is given by

$$\rho = \frac{1}{\gamma_0}[ea_wF\sqrt{n_e/(\epsilon_0 m)}/(4ck_w)]^{2/3}, \qquad (1)$$

where F is unity for a helical undulator or Bessel function $[JJ]$ for a planar undulator [5]. The dimensionless time is defined by $\tau = ct/\lambda_w$, so that $\delta\tau = 1$ corresponds to the transit time of light through the undulator period. The longitudinal position of the ith electron is defined by $\zeta_i(\tau) = [z_i(t) - ct]/\lambda$, so that $\delta\zeta = 1$ corresponds to λ. The dimensionless field envelope is defined by

$$a(\zeta,\tau) = \frac{2\pi e a_w \lambda_w F}{{\gamma_0}^2 mc^2} E(\zeta,\tau)\exp[i\phi(\zeta,\tau)], \qquad (2)$$

with phase $\phi(\zeta,\tau)$, which is equivalent to the Colson's dimensionless field envelope [8] divided by $2N_w^2$ and to the Bonifacio's envelope [5] multiplied by $(4\pi\rho)^2$. Here $E(\zeta,\tau)$ is the rms optical field strength. The dimensionless energy and phase of the ith electron are respectively defined by $\mu_i(\tau) = 4\pi[\gamma_i(t) - \gamma_0]/\gamma_0$ and $\psi_i(\tau) = (k_w + k)z_i(t) - \omega t$, where $k = 2\pi/\lambda$ is the wave number of the resonant wavelength λ.

In the present definition, evolutions of $a(\zeta,\tau)$, $\mu_i(\tau)$ and $\psi_i(\tau)$ are respectively given by [8]

$$\frac{d\mu_i(\tau)}{d\tau} = a[\zeta_i(\tau),\tau]\exp[i\psi_i(\tau)] + \text{c.c.}, \qquad (3)$$

$$\frac{d\psi_i(\tau)}{d\tau} = \mu_i(\tau), \qquad (4)$$

$$\frac{\partial a(\zeta,\tau)}{\partial\tau} = -(4\pi\rho)^3\langle\exp[-i\psi_i(\tau)]\rangle_{\zeta_i(\tau)=\zeta}. \qquad (5)$$

The angular bracket indicates the average of all the electrons in the volume V around ζ.

PHASE SPACE EVOLUTION

The lasing process in FELs starts with formation of a uniform field in time and space. This process is known as the spectrum narrowing in the frequency domain [4] or as the longitudinal phase mixing in the time domain [9]. The evolution of the uniform field before saturation is represented by three complex roots of the cubic equation [5, 8]. The field in τ for the steady-state region where $\zeta < -\tau$ is given by

$$a(\tau) = \frac{|a(0)|e^{i\phi(0)}}{3}[\exp(4\pi\rho\tau e^{i\pi/6}) + \exp(-4\pi\rho\tau e^{-i\pi/6}) + \exp(4\pi\rho\tau e^{-i\pi/2})] \quad (6)$$

The ith electron interacts with the field in the steady-state region due to the slippage, and the energy modulation at τ' during $\delta\tau'$ is given from Eq. (3) by $\delta\mu_i(\tau') = [a(\tau')e^{i\psi_i(\tau')} + \text{c.c.}]\delta\tau'$. Here the linear regime before saturation is defined as the regime where the electron phase remains almost unchanged due to the weak FEL field, i.e., $\psi_i(\tau') \approx \psi_i(0)$. The energy modulation in the linear regime is expressed by $\delta\mu_i(\tau') \approx [a(\tau')e^{i\psi_i(0)} + \text{c.c.}]\delta\tau'$. The energy change of the ith electron at time τ, $\mu_i(\tau)$, is given by the sum of those modulations during τ:

$$\mu_i(\tau) = \int_0^\tau \{a(\tau')\exp[i\psi_i(0)] + \text{c.c.}\}d\tau'. \quad (7)$$

The integration of Eq. (7) after substitution of Eq. (6) yields

$$\mu_i(\tau) = \frac{2|a(0)|}{3(4\pi\rho)} \times \{e^{2\pi\sqrt{3}\rho\tau}\cos[\psi_i(0) + \phi(0) + 2\pi\rho\tau - \pi/6] - e^{-2\pi\sqrt{3}\rho\tau}\cos[\psi_i(0) + \phi(0) + 2\pi\rho\tau + \pi/6] + \cos[\psi_i(0) + \phi(0) - 4\pi\rho\tau + \pi/2]\}. \quad (8)$$

The first term in the right hand side of Eq. (8) is the exponentially growing term, the second is the exponentially decaying term, and the third is the oscillating term.

The phase modulation at τ' during $\delta\tau'$ is given from Eq. (4) by $\delta\psi_i(\tau') = \mu_i(\tau')\delta\tau'$. The phase change of the ith electron at time τ is given by the sum of those modulations during τ:

$$\Delta\psi_i(\tau) = \psi_i(\tau) - \psi_i(0) = \int_0^\tau \mu_i(\tau')d\tau'. \quad (9)$$

The integration of Eq. (9) after substitution of Eq. (8) yields

$$\Delta\psi_i(\tau) = \frac{2|a(0)|}{3(4\pi\rho)^2} \times \{e^{2\pi\sqrt{3}\rho\tau}\cos[\psi_i(0) + \phi(0) + 2\pi\rho\tau - \pi/3] + e^{-2\pi\sqrt{3}\rho\tau}\cos[\psi_i(0) + \phi(0) + 2\pi\rho\tau + \pi/3] + \cos[\psi_i(0) + \phi(0) - 4\pi\rho\tau + \pi]\}. \quad (10)$$

Equation (10) has the exponentially growing term, the exponentially decaying term and the oscillating term, similarly to Eq. (8). Equations (8) and (10) are the analytical expressions for the phase space evolution in a SASE FEL operating in the linear regime; only numerical solutions for those have been obtained previously [6].

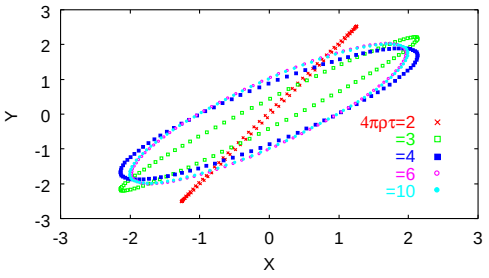

Figure 1: Electron distributions in a phase plane of $X = \Delta\psi_i(\tau)(4\pi\rho)^2/[|a(0)|\exp(2\pi\sqrt{3}\rho\tau)/3]$ and $Y = \mu_i(\tau)(4\pi\rho)/[|a(0)|\exp(2\pi\sqrt{3}\rho\tau)/3]$ derived from Eqs. (8) and (10) for $4\pi\rho\tau = 2, 3, 4, 6, 10$. The center of the electron microbunch is located at $(X, Y) = (0, -1)$ when $4\pi\rho\tau \geq 4$.

Using Eqs. (8) and (10), one can study the distribution of electrons in a longitudinal phase space. The electrons contained in the resonant wavelength at $\tau = 0$ are numbered from the front to back along the propagating direction in the present study. The relative position between two adjacent electrons is represented by $\zeta_i(0) - \zeta_{i+1}(0) > 0$, and the relative phase between two adjacent electrons is given by $\psi_i(0) > \psi_{i+1}(0)$, since $\psi_i(\tau) = 2\pi\zeta_i(\tau) + k_w z_i(t)$ by definition. One can calculate the values of Eqs. (8) and (10) for each i and plot the point in a phase space of $\Delta\psi_i(\tau)$ and $\mu_i(\tau)$. The point rotates counterclockwise in the phase space, as i increases. The distribution of the electrons at time instant τ in a longitudinal phase space of

$$X = \Delta\psi_i(\tau)\frac{3(4\pi\rho)^2}{|a(0)|e^{2\pi\sqrt{3}\rho\tau}} \quad (11)$$

and

$$Y = \mu_i(\tau)\frac{3(4\pi\rho)}{|a(0)|e^{2\pi\sqrt{3}\rho\tau}} \quad (12)$$

is elliptical as shown in Fig. 1. The shape of the distribution gradually changes when $4\pi\rho\tau < 4$ and remains almost constant when $4\pi\rho\tau \geq 4$.

The gain of the steady state field in the linear regime before saturation where $|\Delta\psi_i(\tau)| \ll 1$ is obtained by substitution of Eq. (10) into Eq. (5) as follows:

$$\frac{\partial a(\tau)}{\partial\tau} = \frac{4\pi\rho|a(0)|e^{i\phi(0)}}{3}[\exp(4\pi\rho\tau e^{i\pi/6} + i\pi/6) - \exp(-4\pi\rho\tau e^{-i\pi/6} - i\pi/6) + \exp(4\pi\rho\tau e^{-i\pi/2} - i\pi/2)]. \quad (13)$$

Equation (13) is the same as $\partial a(\tau)/\partial\tau$ obtained from differentiation of Eq. (6). This means that Eqs. (8) and (10) are complementary to Eq. (6). The magnitudes of the gain and phase shift are almost constant when $4\pi\rho\tau \geq 4$.

EVOLUTION IN HIGH GAIN REGIME

In this section, the field and electron phase space evolutions are studied in the high gain regime, which is defined by $4\pi\rho\tau \geq 4$ where the exponentially growing terms only survive in Eqs. (6), (8) and (10). In this case, the field is given by

$$a(\tau) \sim \frac{|a(0)|}{3} e^{2\pi\sqrt{3}\rho\tau} e^{i\phi(\tau)}, \qquad (14)$$

where $\phi(\tau) = 2\pi\rho\tau + \phi(0)$, and the energy and phase changes of the ith electron are respectively given by

$$\mu_i(\tau) \sim \frac{2|a(0)|e^{2\pi\sqrt{3}\rho\tau}}{3(4\pi\rho)} \cos\big[\psi_i(0) + \phi(\tau) - \frac{\pi}{6}\big], \quad (15)$$

$$\Delta\psi_i(\tau) \sim \frac{2|a(0)|e^{2\pi\sqrt{3}\rho\tau}}{3(4\pi\rho)^2} \cos\big[\psi_i(0) + \phi(\tau) - \frac{\pi}{3}\big]. \quad (16)$$

The shape of the distribution in a longitudinal phase space of X and Y is simply represented by the ellipse $X^2 + Y^2 - \sqrt{3}XY = 1$. The ellipse rotates clockwise as $\phi(\tau)$ increases linearly with τ. The electrons are lined along the ellipse counterclockwise as the identification number i increases. The electron at the microbunch center satisfies the condition of $\Delta\psi_i(\tau) = 0$. The electron just in front of the electron at the microbunch center satisfies the condition of $\Delta\psi_{i-1}(\tau) < 0$ for the bunch to be formed. Thus the microbunch center in the high gain regime is located at $(X, Y) = (0, -1)$ in Fig. 1 and the electrons inside the microbunch are concentrated around $\psi_i(0) + \phi(\tau) - \pi/3 = \pi/2$ when $4\pi\rho\tau \geq 4$.

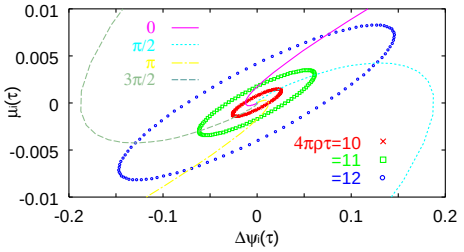

Figure 2: Electron distributions in a phase plane of $\Delta\psi_i(\tau)$ and $\mu_i(\tau)$ derived from Eqs. (8) and (10) when $4\pi\rho\tau$ = 10 (crosses), 11 (open squares), 12 (open circles). The time evolution of four different electrons, initial phases of which are $\psi_i(0)$ (solid line), $\psi_i(0) + \pi/2$ (dotted line), $\psi_i(0) + \pi$ (dash-dotted line) and $\psi_i(0) + 3\pi/2$ (dashed line), are also shown. The FEL parameter $\rho = 0.00447$ and $|a(0)| = 7.1 \times 10^{-5}\rho^{3/2}$ are used.

The evolution of the electron distribution in a longitudinal phase space of $\Delta\psi_i(\tau)$ and $\mu_i(\tau)$ is shown in Fig. 2, where $\rho = 0.00447$ and $|a(0)| = 7.1 \times 10^{-5}\rho^{3/2}$ are used. Those values are typical parameters in JAERI FEL [10]. The crosses are the distribution when $4\pi\rho\tau = 10$, the open squares when $4\pi\rho\tau = 11$ and the open circles when $4\pi\rho\tau = 12$. The figure also shows the time evolution of four different electron particles, initial phases of which are $\psi_i(0)$ (solid line), $\psi_i(0) + \pi/2$ (dotted line), $\psi_i(0) + \pi$ (dash-dotted line) and $\psi_i(0) + 3\pi/2$ (dashed line). One can find that the ellipse expands exponentially in size due to the exponential increase of $|a(\tau)|$ and rotates clockwise due to the linear increase of $\phi(\tau)$. The intersection of the ellipse and the line $\Delta\psi_i(\tau) = 0$ where $\mu_i(\tau) < 0$ is the location of the microbunch center. The exponential decrease of the energy of the microbunch center corresponds to the exponential decrease of the energy of the microbunch as a whole. The energy radiated by the microbunch is used for the field amplification.

The field gain in the linear regime where $|\Delta\psi_i(\tau)| \ll 1$ is given by Eq. (13). However, the gain deviates from Eq. (13) in the non-linear regime near saturation where the amplitude grows and $|\Delta\psi_i(\tau)| \ll 1$ does not hold any more for some electrons. The threshold amplitude for the non-linear regime can be roughly estimated from Eq. (5) in which Eqs. (14) and (16) are substituted as follows:

$$\frac{\partial \frac{|a(\tau)|}{(4\pi\rho)^2}}{\partial(4\pi\rho\tau)} = -\langle\cos\{\psi_i(0) + \phi(\tau) + 2\frac{|a(\tau)|}{(4\pi\rho)^2} \times \cos[\psi_i(0) + \phi(\tau) - \pi/3]\}\rangle_{\zeta_i(\tau)=\zeta}, \quad (17)$$

$$\frac{\partial\phi(\tau)}{\partial(4\pi\rho\tau)} = \frac{(4\pi\rho)^2}{|a(\tau)|}\langle\sin\{\psi_i(0) + \phi(\tau) + 2\frac{|a(\tau)|}{(4\pi\rho)^2} \times \cos[\psi_i(0) + \phi(\tau) - \pi/3]\}\rangle_{\zeta_i(\tau)=\zeta}. \quad (18)$$

One can calculate the values of the right hand sides of Eqs. (17) and (18) as a function of the value of $|a(\tau)|/(4\pi\rho)^2$ and find that Eq. (13) begins to deviate from Eqs. (17) and (18) around $|a(\tau)|/(4\pi\rho)^2 = 0.15$. In the calculation the value of $\psi_i(0) + \phi(\tau)$ is uniform over 2π.

SATURATION

One can calculate the efficiency and amplitude in the non-linear regime near saturation by solving the time dependent 1D FEL equations together with the initial values given by Eqs. (14), (15) and (16). In the high gain and linear regime, where $4\pi\rho\tau_x \geq 4$ and $|a(\tau_x)|/(4\pi\rho)^2 = x$ for $x \leq 0.15$, Eq. (14) is rewritten by

$$\frac{a(\tau_x)}{(4\pi\rho)^2} \sim \frac{|a(0)|}{3(4\pi\rho)^2} e^{2\pi\sqrt{3}\rho\tau_x} e^{i\phi(\tau_x)} = xe^{i\phi(\tau_x)}. \quad (19)$$

The energy and phase of the ith electron at τ_x are derived from substitution of Eq. (19) into Eqs. (15) and (16) and are respectively given by

$$\frac{\mu_i(\tau_x)}{4\pi\rho} \sim 2x\cos\{\psi_i(0) + \phi(\tau_x) - \frac{\pi}{6}\}, \quad (20)$$

$$\psi_i(\tau_x) \sim \psi_i(0) + 2x\cos\{\psi_i(0) + \phi(\tau_x) - \frac{\pi}{3}\}. \quad (21)$$

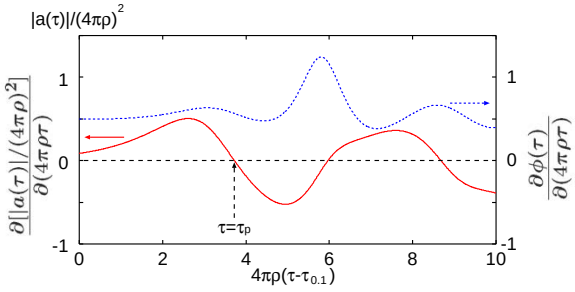

Figure 3: The amplitude gain $\partial[|a(\tau)|/(4\pi\rho)^2]/\partial(4\pi\rho\tau)$ (solid line) and phase shift $\partial\phi(\tau)/\partial(4\pi\rho\tau)$ (dotted line) calculated numerically from the 1D FEL equations given by Eqs. (22), (23), (24) and (25) as a function of $4\pi\rho(\tau - \tau_{0.1})$. The initial values for the calculation are derived from Eqs. (19), (20) and (21).

Solving the 1D FEL equations numerically with the initial values given by Eqs. (19), (20) and (21), one can calculate the phase space evolution of electrons and the field evolution. The equations for $\tau \geq \tau_x$ are written as follows:

$$\frac{d\frac{\mu_i(\tau)}{4\pi\rho}}{d(4\pi\rho\tau)} = 2\frac{|a(\tau)|}{(4\pi\rho)^2}\cos[\psi_i(\tau)+\phi(\tau)], \quad (22)$$

$$\frac{d\psi_i(\tau)}{d(4\pi\rho\tau)} = \frac{\mu_i(\tau)}{4\pi\rho}, \quad (23)$$

$$\frac{\partial\frac{|a(\tau)|}{(4\pi\rho)^2}}{\partial(4\pi\rho\tau)} = -\langle\cos[\psi_i(\tau)+\phi(\tau)]\rangle_{\zeta_i=\zeta}, \quad (24)$$

$$\frac{\partial\phi(\tau)}{\partial(4\pi\rho\tau)} = \frac{(4\pi\rho)^2}{|a(\tau)|}\langle\sin[\psi_i(\tau)+\phi(\tau)]\rangle_{\zeta_i=\zeta}. \quad (25)$$

Figure 3 shows $\partial[|a(\tau)|/(4\pi\rho)^2]/\partial(4\pi\rho\tau)$ and $\partial\phi(\tau)/\partial(4\pi\rho\tau)$ as a function of $4\pi\rho(\tau - \tau_x)$ when $x = 0.1$. It is found that $\partial[|a(\tau)|/(4\pi\rho)^2]/\partial(4\pi\rho\tau)$ decreases down to 0 when $4\pi\rho(\tau_p - \tau_{0.1}) = 3.7$. Here τ_p is the time when the efficiency and amplitude reach their peaks and the amplitude gain turns to negative.

Integration of $\partial|a(\tau)|/\partial(4\pi\rho\tau)$ from $4\pi\rho\tau_{0.1}$ to $4\pi\rho\tau_p$ yields

$$\int_{4\pi\rho\tau_{0.1}}^{4\pi\rho\tau_p}\frac{\partial|a(\tau)|}{\partial(4\pi\rho\tau)}d(4\pi\rho\tau) = 1.08(4\pi\rho)^2.$$

The peak amplitude is thus given by

$$|a(\tau_p)| = 1.18(4\pi\rho)^2, \quad (26)$$

which agrees well with the peak amplitude of the SASE in the steady-state regime obtained in a numerical calculation [5]. Equation (26) does not depend on x.

CONCLUSION

The phase space evolution of electrons in a SASE FEL operating in the linear regime before saturation where $|\Delta\psi_i(\tau)| \ll 1$ has been solved analytically from the 1D FEL equation. The evolutions of $\Delta\psi_i(\tau)$ and $\mu_i(\tau)$ are represented by sum of three independent analytical solutions similarly to the evolution of the SASE field; an exponentially growing term, an exponentially decaying term and an oscillating term. The distribution in a longitudinal phase space of $\Delta\psi_i(\tau)$ and $\mu_i(\tau)$ expands exponentially with time in size, rotating clockwise linearly in the high gain regime where $4\pi\rho\tau \geq 4$. These expansion in size and clockwise rotation corresponds to the exponential increase of the amplitude and linear increase of the phase of the radiation field, respectively. The microbunch center is located where $\Delta\psi_i(\tau) = 0$ and $\mu_i(\tau) < 0$, and the energy of the microbunch center decreases exponentially, which corresponds to the exponential increase of the SASE power. The analytical solutions hold until the optical amplitude grows greater than one-tenth of the amplitude in saturation. A numerical calculation which solves the 1D FEL equations together with initial values given by the present analytical solutions results in the peak amplitude in saturation $|a(\tau_p)| = 1.18(4\pi\rho)^2$, which agrees well with the conventional theories.

ACKNOWLEDGEMENTS

The author would like to acknowledge valuable discussions with S. Hiramatsu at KEK, H. Hama at Tohoku univ and E. Minehara at JAERI.

REFERENCES

[1] V. Ayvazyan et al., PRL **88**, 104802 (2002).

[2] C. Limborg, NIM A **507**, 378 (2003).

[3] T. Shintake et al., NIM A **507**, 382 (2003).

[4] Kwang-Je Kim, PRL **57**, 1871 (1986); NIM A **250**, 396 (1986); Kwang-Je Kim and Ming Xie, NIM A **331**, 359 (1993).

[5] R. Bonifacio et al., Riv. Nuovo Cimento **13**, 9 (1990).

[6] E.L. Saldin, E.A. Schneidmiller and M.V. Yurkov, in *The Physics of Free Electron Lasers*, (Springer, Berlin, 2000), pp. 48–54.

[7] W.B. Colson and S.K. Ride, Phys. Lett. **76**A, 379 (1980).

[8] W.B. Colson, in *Laser Handbook*, edited by W.B. Colson, C. Pellegrini, and A. Renieri (North Holland, Amsterdam, 1990), Vol.6, pp. 115–193.

[9] N. Nishimori, R. Hajima, R. Nagai and E.J. Minehara, NIM A **507**, 79 (2003).

[10] N. Nishimori, R. Hajima, R. Nagai, and E.J. Minehara, PRL **86**, 5707 (2001); NIM A **483**, 134 (2002).

BEHAVIOUR OF ELECTRON BEAM IN COMBINED A SELF-GENERATED FIELD AND A REVERSED GUIDE FIELD IN THE HELICAL WIGGLER

Soon-Kwon Nam * and Ki-Bum Kim
Department of Physics, Kangwon National University, Chunchon 200-701, Republic of Korea

Abstract

We have studied behaviour of electron beam in combined a self-generated field and a reversed axial-guide field in the tapered helical wiggler. The divergence of electron beam is caused by three-dimensional effects on the electron beam loss, we employ a tapered and reversed axial-guide field magnetic field. Evolution of energy spread and emittance of electron beam are investigated using three dimensional simulation. Beam cross-section, transverse momentum variation and cross-section view of electron beam are also calculated along z axis. The electron beam loss is reduced by optimizing the magnetic field strength and tapering parameter of reversed axial guide field.

INTRODUCTION

In free-electron laser(FEL), the gain increases when the beam current and the wiggler field amplitude are increased. When the free-electron laser experiments operate at the high-current regime and the intense wiggler field regime to get the sufficiently large gain, the axial-guide field make us to steer the electron beam in the axial direction [1–4] and the electron motion can be altered by the axial-guide field and self-field effects [5–11] .

In this work, we study the behaviour of electron beam in combined a self-generated field and a reversed axial-guide field in the tapered helical wiggler. Cross-section, profile and density of electron beam are investigated using three dimensional simulation.

THE SELF-GENERATED FIELD AND EXTERNAL FIELD

The space charge and current of electron beam generate the self-electric and self-magnetic fields. The Maxwell's equations in steady state are

$$\nabla \cdot \mathbf{E} = 4\pi\rho_0 \ , \ \nabla \times \mathbf{B} = \frac{4\pi}{c}\mathbf{J} \tag{1}$$

We assume that equilibrium properties (electron density and velocity) are uniform in the z-direction with $\partial n_b/\partial z = 0$ and $\partial v_b/\partial z = 0$. There is no equilibrium electric field parallel to z-direction with $\mathbf{E} \cdot \hat{\mathrm{e}}_z = 0$. Where n_b is electron density and v_b is mean velocity of electron. The radial density and velocity profiles are assumed to be azimuthally symmetric about the z-axis. Therefore the density and velocity profiles can be written as only function of r, that is,

$$n_b(r,\theta,z) = n_b(r),\ v_b(r,\theta,z) = v_{b,\theta}(r)\hat{e}_\theta + v_{b,z}(r)\hat{e}_z$$

The self-generated electric field $\mathbf{E_r}(\mathrm{r})$ induced by the space charge, azimuthal self-magnetic field induced by the axial current $\mathbf{J_z}(\mathrm{r})$, and axial self-magnetic field induced by the azimuthal current $\mathbf{J}_\theta(\mathrm{r})$. One can find the self-generated field from the steady state Maxwell equations.

Within above assumptions, the equilibrium self-generated field components are

$$\begin{aligned} \mathbf{E}(r,\theta,z) &= E_r(r)\hat{e}_r \\ \mathbf{B}^s(r,\theta,z) &= B_\theta(r)\hat{e}_\theta + B_z(r)\hat{e}_z \end{aligned} \tag{2}$$

Therefore the self-generated fields are determined from the steady-state Maxwell's equations

$$\begin{aligned} \nabla \cdot \mathbf{E}(\mathbf{r}) &= \frac{1}{r}\frac{\partial}{\partial r}\big(rE_r(r)\big) = 4\pi\rho_0(r) \\ \nabla \times \mathbf{B}(\mathbf{r}) &= -\frac{\partial B_z(r)}{\partial r}\hat{e}_\theta + \frac{1}{r}\frac{\partial B_\theta(r)}{\partial r}\hat{e}_z \\ &= \frac{4\pi}{c}\big(J_\theta(r)\hat{e}_\theta + J_z(r)\hat{e}_z\big) \end{aligned} \tag{3}$$

where $\rho_0(r) = -ef_b(r)$ is charge density, $J_z(r) = -f_b(r)ev_z$ is axial current density, $J_\theta(r) = -f_b(r)ev_\theta$ is azimuthal current density and $f_b(r)$ is electron beam profile function. The axial velocity and azimuthal velocity of electron beam are $v_z = \beta_b c$ and $v_\theta = r\omega_r$, where $\beta_b = v_b c$ is the normalized axial velocity, ω_r is the angular velocity.

The self-generated field amplitude depends on the electron beam profile. We consider Gaussian shape electron beam. The profile function $f_b(r)$ for the Gaussian density is

$$f_b(r) = \frac{c_n n_b}{\sqrt{2\pi r_b^2}} \exp\left(-\frac{r^2}{2r_b^2}\right) \tag{4}$$

where $c_n = \pi r_b^2$ is the normalized factor and the self electric and magnetic field are

$$\begin{aligned} \mathbf{E_r^s}(\mathbf{r}) &= -\frac{2\alpha r_b^2}{r}\left[1 - \exp\left(-\frac{r^2}{2r_b^2}\right)\right]\hat{e}_r \\ \mathbf{B_\theta^s}(\mathbf{r}) &= -\frac{2\alpha\beta_b r_b^2}{r}\left[1 - \exp\left(-\frac{r^2}{2r_b^2}\right)\right]\hat{e}_\theta \\ \mathbf{B_z^s}(\mathbf{r}) &= -\frac{2\alpha\omega_r r_b^2}{c}\left[\exp\left(-\frac{r^2}{2r_b^2}\right) - \exp\left(-\frac{r_w^2}{2r_b^2}\right)\right]\hat{e}_z \end{aligned} \tag{5}$$

* snam@kangwon.ac.kr; Tel:+82-33-250-8463; fax:+82-33-257-9689

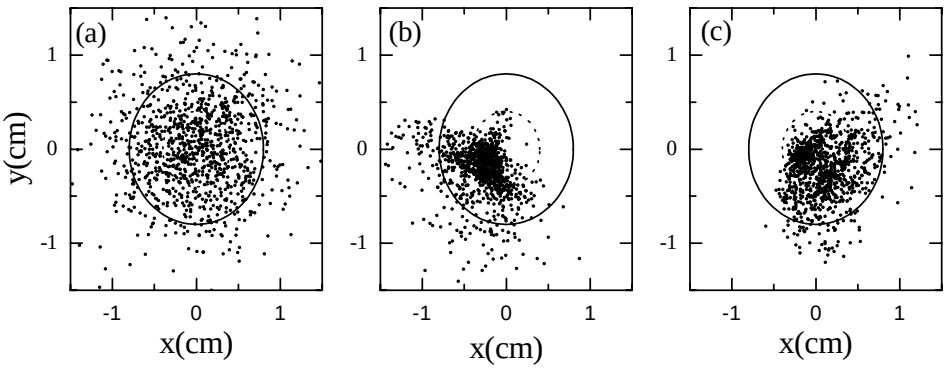

Figure 1: Cross section views of electrons at (a) the entrance of wiggler and (b) the end of wiggler for $\kappa_s = 2$, a_g=0 and (c) $\kappa_s = 2$, a_g=-2, ϵ_t=0. Dotted(solid) line indicate $r = r_b(2r_b)$.

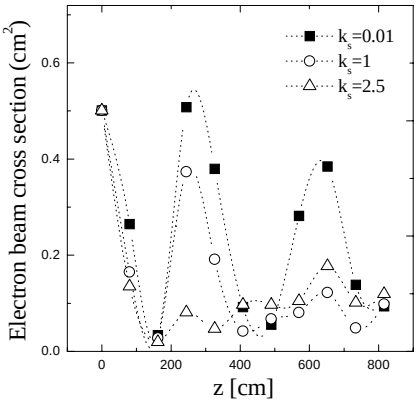

Figure 2: The electron beam cross section along z-axis of the wiggler for various self-field parameters.

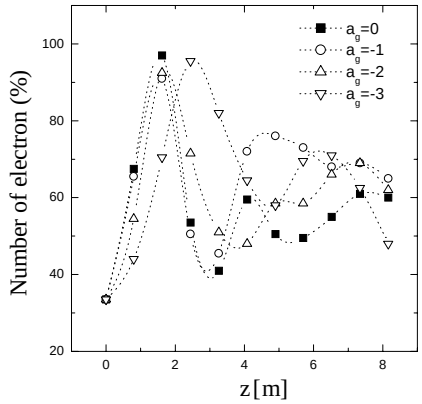

Figure 3: Number of electron along z-axis of the wiggler in r_b for various reversed axial guide field strength.

where $\alpha = \pi e n_b$, $\omega_p = (4\pi n_b e^2/m_e)^{1/2}$ is plasma frequency of electron beam, $\omega_r = k_w c\beta$ is the angular velocity, r_b is the electron beam radius and r_w is the cylindrical waveguide radius.

The scalar potential and vector potential of the self-generated field which satisfies $\mathbf{E_s} = -\nabla\Phi_s$ and $\mathbf{B^s} = \nabla \times \mathbf{A^s}$ are

$$\begin{aligned}
\Phi_s &= \alpha r_b^2 \left[\Gamma - \mathrm{Ei}\left(-\frac{\mathrm{r}^2}{2\mathrm{r}_\mathrm{b}^2}\right) - \log\left(\frac{\mathrm{r}^2}{2\mathrm{r}_\mathrm{b}^2}\right)\right] \\
\mathbf{A}_\theta^\mathbf{s} &= \mathbf{\Phi_s}\beta_b\hat{e}_z \\
\mathbf{A_z^s} &= \frac{\alpha\omega_r r_b^2}{cr}\left[2r_b \exp\left(-\frac{r^2}{2r_b^2}\right)\right. \\
&\qquad \left. +(r^2 + 2r_b^2 - r_w^2)\exp\left(-\frac{r_w^2}{2r_b^2}\right)\right]\hat{e}_\theta
\end{aligned} \tag{6}$$

where $\mathrm{Ei(x)} = \int_{-\infty}^{\mathrm{x}} \frac{\mathrm{e}^{-\mathrm{u}}}{\mathrm{u}}\mathrm{du}$ is exponential integrate function, and $\Gamma = \lim_{m\to\infty}\left(\sum_{k=1}^{m}\frac{1}{k} - \log m\right) \approx 0.577$ is Euler-Mascheroni constant.

The vector potential of helical wiggler magnetic field in Cylindrical coordinate system is defined as

$$\begin{aligned}
\mathbf{A_w} &= \frac{B_w}{k_w}\Big[\big(I_0(k_w r) + I_2(k_w r)\big)\cos(k_w z - \theta)\Big]\hat{e}_r \\
&+ \frac{B_w}{k_w}\Big[\big(I_0(k_w r) - I_2(k_w r)\big)\sin(k_w z - \theta)\Big]\hat{e}_\theta
\end{aligned} \tag{7}$$

and vector potential of axial-guide field $\mathbf{B_g} = B_g\hat{e}_z$ which steer the electron to axial direction is $\mathbf{A_g} = \frac{1}{2}B_g r\hat{e}_\theta$.

HAMILTONIAN FORMALISM AND THE TAPERING PROFILE OF GUIDE MAGNETIC FIELD

The Hamiltonian of relativistic test electron is

$$\mathbf{H} = \sqrt{(c\mathbf{P} + e\mathbf{A})^2 + m_e^2 c^4} - e\Phi_s \equiv \gamma m_e c^2 - e\Phi_s \tag{8}$$

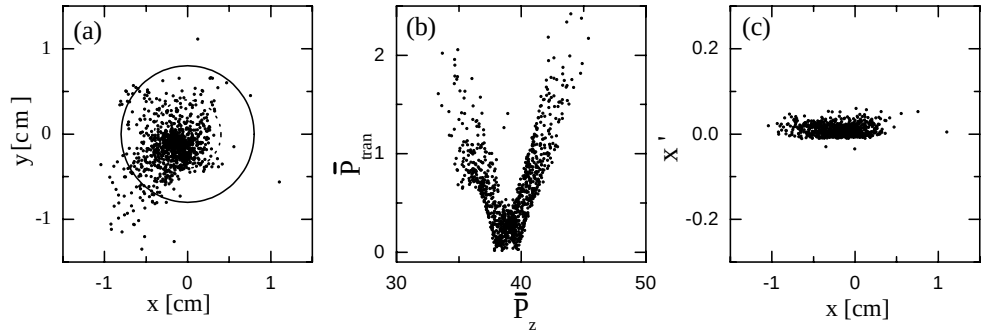

Figure 4: Electron beam profiles at the exit of the wiggler for $a_w = 3$, $\kappa_s = 2$, $a_g = -2$, $\epsilon_t = 0.6$. Dotted(solid) line indicate $r = r_b(2r_b)$.

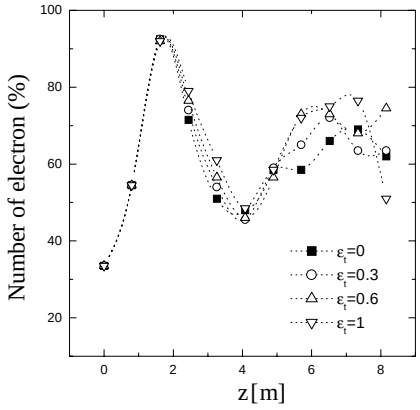

Figure 5: Number of electron along the z-axis of wiggler in r_b for various tapering parameters.

where $\mathbf{P}$ is the canonial momentum, $\mathbf{p} = \mathbf{P} + e\mathbf{A}/c$ is the mechanial momentum, $\gamma = \sqrt{1 + (\mathbf{p}/m_e c)^2}$ is the relativistic mass factor, m_e is the electron rest mass, e is the electron charge and total vector potential is $\mathbf{A} = \mathbf{A_w} + \mathbf{A_g} + \mathbf{A^s_\theta} + \mathbf{A^s_z}$.

Conveniently, we introduce the dimensionless potentials, canonical momentum, and Hamiltonian defined by

$$\bar{\mathbf{A}} = \frac{e\mathbf{A}}{m_e c^2 k_w},\ \bar{\mathbf{\Phi}}_s = \frac{e\mathbf{\Phi}_s}{m_e c^2 k_w},\ \bar{\mathbf{P}} = \frac{\mathbf{P}}{m_e c},\ \bar{\mathbf{H}} = \frac{\mathbf{H}}{m_e c^2} \quad (9)$$

In the dimensionless scalar and vector potential of self-field, the constant α becomes $\alpha = \kappa_s k_w^2/4$, where $\kappa_s = \omega_p^2/c^2 k_w^2$ is the dimensionless strength of the self-field.

Therefore the dimensionless Hamiltonian is

$$\begin{aligned}
&\bar{\mathbf{H}} = \sqrt{1 + (\bar{\mathbf{P}} + \bar{\mathbf{A}})^2} - \bar{\Phi}_s = \sqrt{1 + \Sigma h_i^2} - \bar{\Phi}_s \\
&h_1 = \bar{P}_r + a_w(I_0(\bar{r}) - I_2(\bar{r}))\cos(\bar{z} - \theta) \\
&h_2 = \frac{\bar{P}_\theta}{\bar{r}} + \frac{a_g \bar{r}}{2} + \bar{A}^s_\theta + a_w(I_0(\bar{r}) + I_2(\bar{r}))\sin(\bar{z} - \theta) \\
&h_3 = \bar{P}_z + \bar{A}^s_z
\end{aligned} \quad (10)$$

where $a_g = eB_g/m_e c^2 k_w$ is a dimensionless axial-guide field strength, $a_w = eB_w/m_e c^2 k_w$ is a dimensionless wiggler field amplitude, and $\bar{r} = k_w r$, $\bar{z} = k_w z$.

The tapered guide magnetic field $a_g(z) = a_g(0) f_t(z)$, where $f_t(z)$ is the tapering profile function.

$$f_t(z) = \begin{cases} 1 & \text{for } 0 \le z < z_t \\ 1 + c_n \epsilon_t (z - z_t) & \text{for } z > z_t \end{cases} \quad (11)$$

where z_t is the starting position of the tapering, ϵ_t is tapering parameter, and c_n is constant which satisfy $f_t(z = z_f, \epsilon_t = 1) = 2$. The electron orbits can be calculated from the equation of motions which derived from the Hamiltonian of Eq. 10.

We make the incident electron beam using the beam parameters such as electron beam energy E_b = 3 MeV, energy spread E_s = 5 %, emittance $\epsilon_{x,y} = 10\ \pi\mathrm{mm} \cdot \mathrm{mrad}$. Fig. 1(a) shows the cross section view of the incident electron beam which is the initial state of the Gaussian random distribution. Fig. 1(b) shows the cross section views at the exit of the wiggler for self-field parameters $\kappa_s = 2$ without axial guide field, and (c) with uniform axial guide field $a_g = -2$ for $a_w = 3$. Those parameters correspond to the wiggler magnetic field strength B_w = 2.67 kG, the guide magnetic field strength B_w = 1.78 kG and the electron beam current $I_b = 368$ A for wiggler period λ_w = 12 cm and electron beam radius $r_b = 0.4$ cm.

Fig. 2 shows the electron beam cross section area along z-axis of the wiggler for various self-field parameter stength. The cross section area is reduced by increasing self-field parameter. Number of electron in r_b along z-axis

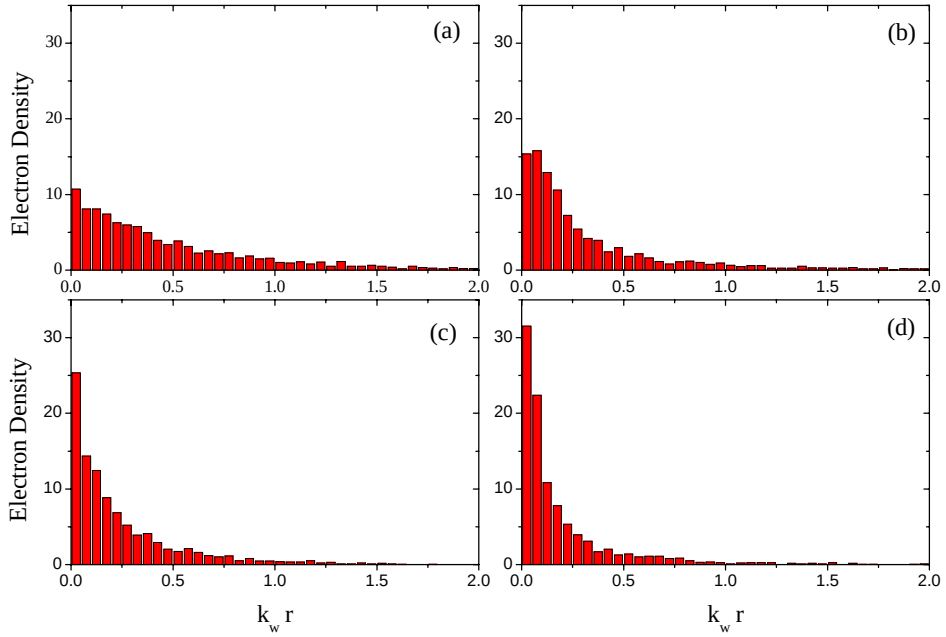

Figure 6: Electron beam density versus $k_w r$; (a) incident electron beam, (b) $\kappa_s = 2$ and $a_g = 0$, (c) $\kappa_s = 2$, $a_g = -2$ and $\epsilon_t = 0$, (d) $\kappa_s = 2$, $a_g = -2$ and $\epsilon_t = 0.6$.

of the wiggler for various reversed axial guide field strength is shown in Fig. 3.

Fig. 4 shows the cross section view, transverse momentum variation and x versus x' phase space for $\kappa_s = 2$, $a_g = -2$ and $\epsilon = 0.6$. The number of electron in r_b along z-axis of the wiggler for various tapering parameters is shown in Fig. 5. The electron densities versus $k_w r$ are shown in Fig. 6. The electron density with tapered and reversed axial guide field is increased by about twice correspond to that of without axial guide field case in center of electron beam.

CONCLUSION

We studied behaviour of electron beam in combined a self-generated field and a reversed axial-guide field in the helical wiggler. Evolution of energy spread and emittance of electron beam were investigated by using three dimensional simulation. Beam cross-section, transverse momentum variation and cross-section view of electron beam were also calculated along z axis. The electron beam loss was reduced by optimizing the magnetic field strength and tapering parameter of reversed axial guide field.

ACKNOWLEDGEMENTS

This work was supported by a Korea Research Foundation grant.

REFERENCES

[1] L. Friedland, Phys. Fluids. **23** (1980) 2376.

[2] P. Diament, Phys. Rev. **A23** (1981) 2537.

[3] H. P. Freund and A. T. Drobot, Phys. Fluids. **25** (1982) 736.

[4] H. P. Freund, Phys. Rev. **A27** (1983) 1977.

[5] C. Chen and R. C. Davidson, Phys. Fluids. **B2** (1990) 171.

[6] C. Chen and R. C. Davidson, Phys. Rev. **A43** (1991) 5541.

[7] L. Michel, A. Bourdier and J. M. Buzzi, Nucl. Instri. and Meth. **A304** (1991) 465.

[8] S. Spindler and G. Renz, Nucl. Instri. and Meth. **A304** (1991) 492.

[9] L. Michel-Lours, A. Bourdier and J. M. Buzzi, Phys. Fluids. **B5** (1993) 965.

[10] A. Bourdier and L. Michel-Lours, Phys. Rev. **E49** (1994) 49.

[11] R. C. Davidson, *Physics of Nonneutral Plasmas* (Addison Wesley, 1990).

EVOLUTION OF ELECTRON BEAM IN THE TAPERED PLANAR WIGGLER

Soon-Kwon Nam * and Ki-Bum Kim
Department of Physics, Kangwon National University, Chunchon 200-701, Republic of Korea

Abstract

We have investigated the evolution of electron beam in the tapered planar wiggler field with a self-electric field and self-magnetic fields. In order to suppress the divergence of emittance and spread of the electron beam by the three-dimensional effects on the off-axis electron and a self-generated field effects, the tapered and bent wiggler field is applied. We calculate the emittance, transverse trajectories and Fourier transformation of electron beam using three dimensional simulation by optimizing the magnetic field strength, a tapering parameter and self-field parameters. This method could be expected to enhance the efficiency compared to those of a untapered wiggler in a free-electron laser.

INTRODUCTION

The free-electron laser which the new electromagnetic generation source have been active areas of research due to their attractive properties, such as high efficiency, tunable frequency from microwave to X-ray, and powerfule output. The quality of the electron beam plays an important role and limits the operating wavelength, gain, and efficiency.

Free-electron laser operation often requires sufficiently large gain, which increase when the beam current is increased. In the high-current regime, the electron motion can be altered by the self-generated field effects [1, 2, 3, 4, 5, 6, 7].

In this work, we study the evolution of electron beam in the tapered planar wiggler field with self-electric and self-magnetic fields. To suppress the divergence of emittance and spread of the electron beam, we apply the tapered and bent wiggler field.

The emittance, transverse trajectories and Fourier transformation of electron beam are calculated using three dimensional simulation by optimizing the magnetic field strength, a tapering parameter and self-field parameters.

THE SELF-GENERATED FIELD AND EXTERNAL MAGNETIC FIELD

The scalar potential of planar wiggler magnetic field with bent pole face is

$$\phi = -\frac{B_w}{k_w}\cosh(k_x x)\sinh(k_y y)\cos(k_w z) \qquad (1)$$

* snam@kangwon.ac.kr; Tel:+82-33-250-8463; fax:+82-33-257-9689

and if $k_x x \ll 1$ and $k_y y \ll 1$, the wiggler magnetic field is derived from Eq. 1.

$$\mathbf{B}_w = B_w \begin{pmatrix} \left(1 + \frac{k_x^2 x^2}{2} + \frac{k_y^2 y^2}{2}\right)\cos(k_w z) \\ k_x^2 xy\cos(k_w x) \\ -k_w y \sin(k_w x) \end{pmatrix} \qquad (2)$$

In order to fulfill Maxwell's equations the scalar potential must be a solution of the Laplace equation $\nabla^2\phi = 0$. Therefore we can find the relation such as $k_x^2 + k_y^2 = k_w^2$, and we choose the case as $k_x = k_y = k_w/\sqrt{2}$.

The vector potential of planar wiggler magnetic field which satisfy $\mathbf{B_w} = \nabla \times \mathbf{A_w}$ defined as

$$\begin{aligned} \mathbf{A_w} = &-\frac{B_w}{k_w} k_x^2 xy \sin(k_w x)\hat{e}_x \\ &+ \frac{B_w}{k_w}\left(1 + \frac{k_x^2 x^2}{2} + \frac{k_y^2 y^2}{2}\right)\sin(k_w z)\hat{e}_y \end{aligned} \qquad (3)$$

The space charge and current of electron beam generate the self-electric and self-magnetic fields. The Maxwell's equations in steady state are

$$\nabla \cdot \mathbf{E} = 4\pi\rho_0 \ , \ \nabla \times \mathbf{B} = \frac{4\pi}{c}\mathbf{J} \qquad (4)$$

The self-generated electric field $\mathbf{E_r}(\mathrm{r})$ induced by the space charge, azimuthal self-magnetic field induced by the axial current $\mathbf{J_z}(\mathrm{r})$. One can find the self-generated field from the steady state Maxwell equations.

We assume that equilibrium properties (electron density and velocity) are uniform in the z-direction with $\partial n_b/\partial z = 0$ and $\partial v_b/\partial z = 0$. And there is no equilibrium electric field parallel to z-direction with $\mathbf{E} \cdot \hat{\mathrm{e}}_z = 0$. Where n_b is electron density and v_b is mean velocity of electron. The radial density and velocity profiles are assumed to be azimuthally symmetric about the z-axis. Therefore the density and velocity profiles can be written as only function of r, which means $n_b(r,\theta,z) = n_b(r)$ and $v_b(r,\theta,z) = v_{b,z}(r)\hat{e}_z$.

There is no equilibrium electric field parallel to z-direction with $\mathbf{E} \cdot \hat{\mathrm{e}}_z = 0$.

$$\begin{aligned} \nabla \cdot \mathbf{E}(\mathbf{r}) &= \frac{1}{r}\frac{\partial}{\partial r}\big(rE_r(r)\big) = 4\pi\rho_0(r) \\ \nabla \times \mathbf{B}(\mathbf{r}) &= \frac{1}{r}\frac{\partial B_\theta(r)}{\partial r}\hat{e}_z = \frac{4\pi}{c}J_z(r)\hat{e}_z \end{aligned} \qquad (5)$$

where $\rho_0(r) = -ef_b(r)$is charge density, $J_z(r) = -f_b(r)ev_z$ is axial current density, $f_b(r)$ is electron beam

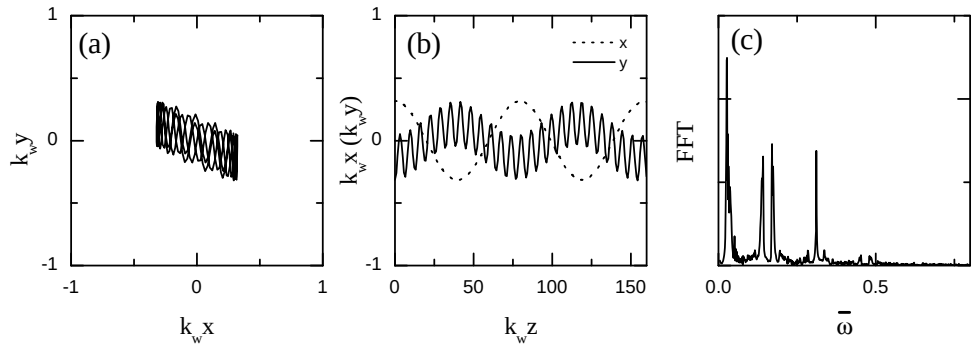

Figure 1: Electron trajectories and Fourier transformation $a_w = 1$, $\Theta = 90^\circ$ and $\kappa_s = 2$.

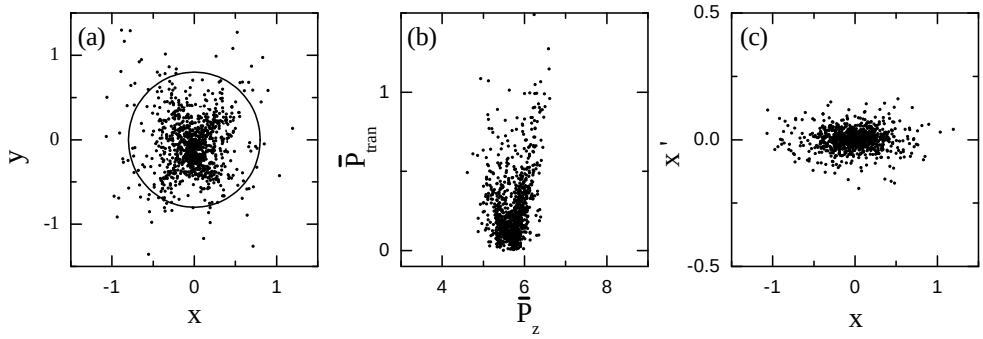

Figure 2: Electron beam profiles at the exit of the wiggler with (a) electron beam cross section, (b) transverse momentum variation and (c) x versus x' phase space. Other electron beam parameter are $a_w = 1$, $\Theta = 90^\circ$ and $\kappa_s = 2$. Dotted(solid) line indicate $r = r_b(2r_b)$.

profile function and $\beta_b = v_b c$ is the normalized axial velocity of electron.

The self-generated field amplitude depend on the electron beam profile. We consider Gaussian shape electron beam. The profile function $f_b(r)$ for the Gaussian density is

$$f_b(r) = \frac{c_n n_b}{\sqrt{2\pi r_b^2}} \exp\left(-\frac{r^2}{2r_b^2}\right) \tag{6}$$

where n_b is electron density, $c_n = \pi r_b^2$ is the normalized factor and the self electric and magnetic field are

$$\begin{aligned} \mathbf{E}^{\mathbf{s}}_{\mathbf{r}}(\mathbf{r}) &= -\frac{2\alpha r_b^2}{r}\left[1 - \exp\left(-\frac{r^2}{2r_b^2}\right)\right]\hat{e}_r \\ \mathbf{B}^{\mathbf{s}}_{\theta}(\mathbf{r}) &= -\frac{2\alpha\beta_b r_b^2}{r}\left[1 - \exp\left(-\frac{r^2}{2r_b^2}\right)\right]\hat{e}_\theta \end{aligned} \tag{7}$$

where $\alpha = \pi e n_b$, $\omega_p = (4\pi n_b e^2/m_e)^{1/2}$ is plasma frequency of electron beam, $\omega_r = k_w c\beta$ is the angular velocity, r_b is the electron beam radius and r_w is the cylindrical waveguide radius.

The scalar potential and vector potential of the self-generated field which satisfies $\mathbf{E_s} = -\nabla\Phi_s$ and $\mathbf{B^s} = \nabla \times \mathbf{A^s}$ are

$$\begin{aligned} \Phi_s &= \alpha r_b^2\left[\Gamma - \mathrm{Ei}\left(-\frac{\mathrm{r}^2}{2\mathrm{r}_\mathrm{b}^2}\right) - \log\left(\frac{\mathrm{r}^2}{2\mathrm{r}_\mathrm{b}^2}\right)\right] \\ \mathbf{A}^{\mathbf{s}}_{\theta} &= \mathbf{\Phi_s}\beta_b\hat{e}_z \end{aligned} \tag{8}$$

where $\mathrm{Ei(x)} = \int_{-\infty}^{\mathrm{x}} \frac{\mathrm{e}^{-\mathrm{u}}}{\mathrm{u}}\mathrm{du}$ is exponential integrate function, and $\Gamma = \lim_{m\to\infty}\left(\sum_{k=1}^{m}\frac{1}{k} - \log m\right) \approx 0.577$ is Euler-Mascheroni constant.

HAMILTONIAN FORMALISM

The Hamiltonian of relativistic test electron is

$$\mathbf{H} = \sqrt{(c\mathbf{P} + e\mathbf{A})^2 + m_e^2 c^4} - e\Phi_s \equiv \gamma m_e c^2 - e\Phi_s \tag{9}$$

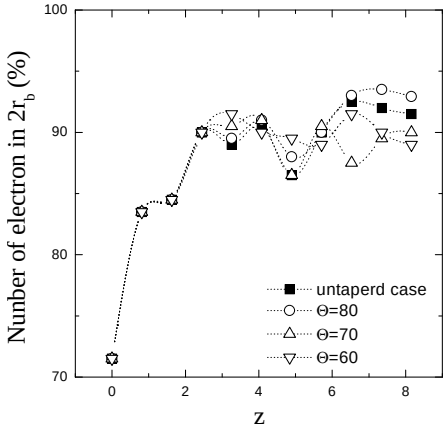

Figure 3: Number of electron along the z-axis of wiggler in $2r_b$ for various tapering parameter Θ of wiggler field. Other parameters are $a_w = 1$ and $\kappa_s = 2$.

where $\mathbf{P}$ is the canonial momentum, $\mathbf{p} = \mathbf{P} + e\mathbf{A}/c$ is the mechanial momentum, $\gamma = \sqrt{1 + (\mathbf{p}/m_e c)^2}$ is the relativistic mass factor, m_e is the electron rest mass, e is the electron charge and total vector potential is $\mathbf{A} = \mathbf{A_w} + \mathbf{A}^{\mathbf{s}}_{\theta} + \mathbf{A}^{\mathbf{s}}_{\mathbf{z}}$.

Conveniently, we introduce the dimensionless potentials, canonical momentum, and Hamiltonian defined by

$$\bar{\mathbf{A}} = \frac{e\mathbf{A}}{m_e c^2 k_w},\ \bar{\mathbf{\Phi}}_s = \frac{e\mathbf{\Phi}_s}{m_e c^2 k_w},\ \bar{\mathbf{P}} = \frac{\mathbf{P}}{m_e c},\ \bar{\mathbf{H}} = \frac{\mathbf{H}}{m_e c^2} \quad (10)$$

In the dimensionless scalar and vector potential of self-field, the constant α becomes $\alpha = \kappa_s k_w^2/4$, where $\kappa_s = \omega_p^2/c^2 k_w^2$ is the dimensionless strength of the self-field. Therefore the dimensionless Hamiltonian is

$$\begin{aligned} \bar{\mathbf{H}} &= \sqrt{1 + (\bar{\mathbf{P}} + \bar{\mathbf{A}})^2} - \bar{\Phi}_s = \sqrt{1 + \Sigma h_i^2} - \bar{\Phi}_s \\ h_1 &= \bar{P}_x + k_x^2 xy \sin(k_w x) \\ h_2 &= \bar{P}_y + \big(1 + \frac{k_x^2 x^2}{2} + \frac{k_y^2 y^2}{2}\big) \sin(k_w z) \\ h_3 &= \bar{P}_z + \bar{A}_z^s \end{aligned} \quad (11)$$

where $a_w = eB_w/m_e c^2 k_w$ is a dimensionless wiggler field amplitude. To correct the electron energy loss in wiggler, the wiggler magengtic field is tapered as $a_w(z) = a_w(0) f_t(z)$, where $f_t(z)$ is the tapering profile function

$$f_t(z) = \begin{cases} 1 & \text{for } 0 \le z < z_t \\ 1 + c_n(z - z_t)\cos\Theta & \\ \quad + (z - z_t)^2 \cos^2\Theta & \text{for } z > z_t \end{cases} \quad (12)$$

where z_t is the starting position of wiggler tapering, Θ is taper parameter, and c_n is constant which satisfy $f_t(z = z_f, \Theta = 45^\circ) = 1/2$.

The electron orbits can be calculated from the equations of motion which are derived from the Hamiltonian of Eq. 11. Fig. 1 shows the electron trajectories in (a) the $(k_w x, k_w y)$ plane and (b) $(k_w x(k_w y), k_w z)$ plane, and (c) the Fourier transformation for a single electon and untapered wiggler case. Other parameters are $a_w = 1$ and $\kappa_s = 2$ which correspond to the wiggle magnetic field strength B_w = 1.78 kG and the electron beam current $I_b = 1.47$ kA for wiggler period λ_w = 6 cm and electron beam radius $r_b = 0.4$ cm. In the planar wiggler with bent pole face, the electrons move periodically not only y direction but x direction.

We made the incident electron beam using the beam parameters such as electron beam energy $E_b = 3$ MeV, energy spread E_s = 5 %, emittance $\epsilon_{x,y} = 10\ \pi\mathrm{mm} \cdot \mathrm{mrad}$.

Fig. 2 shows the electron beam cross section, transevers momentum variation and x versus x' phase space at the exit of the wiggler with $a_w = 1$, $\Theta = 90^\circ$ and $\kappa_s = 2$.

The number of electron along z-axis of the wiggler in $2r_b$ for the various wiggler parameter Θ is shown in Fig. 3. The number of electron for the case of the tapered wiggler is increased about 1.6 $\%$ compared to that of untapered case. The wiggler tapering parameter of $\Theta = 80^\circ$ was used.

STEADY-STATE SOLUTION

Assume that y component of canonical momentum $\bar{P}_y = p_y - eA_y/c$ is exact constant of the motion. Therefore, we assume that $\bar{P}_y = 0$ (i.e. $p_y = eA_y/c$) and interest the (x, z) plane only. The Hamiltonian of Eq. 11 become

$$\begin{aligned} \bar{\mathbf{H}} = &\Big(1 + \bar{P}_x^2 + \big((1 + k_x^2/2)\sin(k_w z)\big)^2 \\ &+ \big(\bar{P}_z + \bar{A}_z^s\big)^2\Big)^{1/2} - \bar{\Phi}_s \end{aligned} \quad (13)$$

We can find the steady-state solution $\bar{P}_z = 0, k_w z = \pi/2$ which satisfy $\bar{r}\,' = \psi\,' = \bar{P}_r\,' = \bar{P}_\psi\,' = 0$ from the equations of motion derived from the Hamiltonian.

$$\gamma = \Big(1 + \big(1 + \frac{k_x^2 x^2}{2}\big)^2 + \big(\bar{P}_z + \bar{A}_z^s\big)^2\Big)^{1/2} \quad (14)$$

One can find the $k_w x_0$ from Eq. 14.

Fig. 4 shows Poincarè surface of section plot in $(k_w z, \bar{P}_z)$ plane at $\bar{p}_x = 0$ for various tapering parameters and $k_w x_0$. In the strong wiggle field regime, the electron orbits for tapered wiggler $\Theta = 80^o$ are more stable than those of a untapered wiggler case.

CONCLUSION

We investigated the evolution of electron beam in the tapered planar wiggler field with a self-electric field and self-magnetic fields. To suppress the divergence of emittance and spread of the electron beam by the three-dimensional effects on the off-axis electron and a self-generated field effects, the tapered and bent wiggler field was applied. We calculated the emittance, transverse trajectories, Fourier

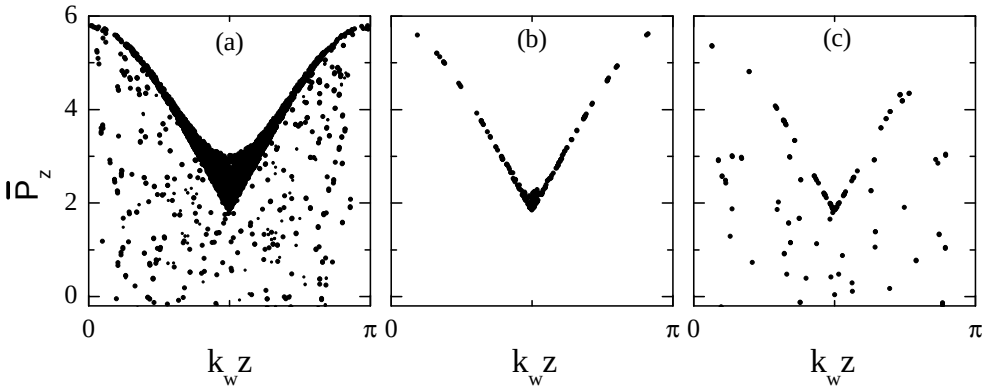

Figure 4: Poincarè surface of section plot in the $(k_w z, \bar{P}_z)$ plane at $\bar{p}_x = 0$ for (a) $\Theta = 80^o$ and the various $k_w x_0$, (b) $\Theta = 80^o$ and $k_w x_0$=0.615 and (c) $\Theta = 90^o$ and $k_w x_0$=0.615. Other parameters are $a_w = 5$, $k_w r_b$=0.4 and E_b=3 MeV.

transformation and Poincarè surface of section of electron beam using three dimensional simulation by optimizing the magnetic field strength and a tapering parameter of axial guide field. This method could be expected to enhance the efficiency compared to those of a untapered wiggler in a free-electron laser.

ACKNOWLEDGEMENTS

This work was supported by a Korea Research Foundation grant.

REFERENCES

[1] C. Chen and R. C. Davidson, Phys. Fluids. **B2** (1990) 171.

[2] C. Chen and R. C. Davidson, Phys. Rev. **A43** (1991) 5541.

[3] L. Michel, A. Bourdier and J. M. Buzzi, Nucl. Instri. and Meth. **A304** (1991) 465.

[4] S. Spindler and G. Renz, Nucl. Instri. and Meth. **A304** (1991) 492.

[5] L. Michel-Lours, A. Bourdier and J. M. Buzzi, Phys. Fluids. **B5** (1993) 965.

[6] A. Bourdier and L. Michel-Lours, Phys. Rev. **E49** (1994) 49.

[7] R. C. Davidson, *Physics of Nonneutral Plasmas* (Addison Wesley, 1990).

THE EFFECT OF LINER INDUCED PHASE FLUCTUATIONS ON THE GAIN OF A CERENKOV FEL

Peter van der Slot, Isabel de la Fuente*, Klaus Boller
Laser Physics and Non-Linear Optics Group,
Department of Science and Technology, University of Twente, The Netherlands

Abstract

In a Cerenkov FEL (CFEL), the phase velocity of an EM wave is determined by geometry (i.e., waveguide radius and inner liner radius) and by material parameters (i.e., the dielectric constant of the liner). Changes or fluctuations in any of these parameters induce changes (or fluctuations) in the phase velocity of the EM wave and thus can degrade the gain of the CFEL. To investigate the effect of such fluctuations on the gain, a method is developed to describe the effect of a slowly varying inner liner radius on the EM wave propagation and consequently on the gain of the CFEL. As an example, results for a low gain, 800 mA Cerenkov FEL operating at a frequency of 50 GHz and a maximum beam voltage of 100 kV are presented.

INTRODUCTION

It is well known that errors in the magnetic field of an undulator can result in (serious) degradation of the gain of an undulator based Free-Electron Laser (FEL) [1, 2]. These errors couple to the electron motion and manifest themselves as fluctuations in the phase of the electron with respect to the ponderomotive potential. As the gain is based on longitudinal phase-bunching of the electrons, these phase fluctuations will in general lower the gain of the device. The effect of the undulator errors is wavelength dependent and this leads to increasingly stringent tolerances on the undulator to avoid significant reduction in the gain at shorter wavelength [2].

In a Cerenkov FEL (CFEL), an electron beam interacts with an electromagnetic (EM) field as they co-propagate through an axial-symmetric, lined cylindrical waveguide. The longitudinal wavenumber of the EM wave is determined by geometry (waveguide radius and inner liner radius) and by material parameters (dielectric constant of the liner). Coherent amplification of EM waves takes place when the phase velocity of the waves approximately equals the electron beam velocity and the EM-wave has a longitudinal electric field component. Therefore, variations or fluctuations in the dielectric constant or in the geometry of the liner result in changes of the longitudinal wavenumber and consequently in the relative phase between the EM-wave and the co-propagating electrons. As the EM wave is the ponderomotive potential in a CFEL, it can be expected that these fluctuations will influence the gain of a CFEL as well. However, here the errors in the liner are coupled to the radiation field whereas in the undulator based FEL the errors of the undulator are coupled to the electron motion.

To our knowledge, we are the first to investigate liner induced phase fluctuation in the ponderomotive potential and their effect on the gain of a Cerenkov FEL. This information is especially important for the design of low gain Cerenkov FEL devices (see e.g., [4]) as liners made from commercial tubes have variations in the inner radius ranging from a few hundred microns down to a few tens of microns (e.g., for precision tubes). Low gain devices are usually designed as an oscillator and have a low net-gain per pass such that any degradation of the gain seriously effects the performance of the device.

The organization of the remainder of this work is as follows. We will consider an axial-symmetric lined waveguide for which the inner radius of the liner $r_d(z)$ varies slowly with axial distance z and is otherwise constant. We first discuss, in the limit of no electron beam, the influence of the liner fluctuations on the propagation of an EM wave in such a waveguide. Then we will use the SVAP approximation to derive the fundamental FEL equations from Maxwell's equations. We continue with applying the set of equations to a low gain CFEL that uses an 800 mA electron beam with a maximum energy of 100 kV to generate more than 1 kW in continuous wave mode, to study the effect of liner irregularities on the performance of the device. By applying a linear change of r_d with distance z the formulation can also be used to model a tapered version of the CFEL.

WAVE PROPAGATION IN AN IRREGULAR LINED WAVEGUIDE

Consider an axial-symmetric waveguide lined with a dielectric that has a varying inner radius $r_d(z)$ and is otherwise constant. Let r_g be the radius of the waveguide, which is also equal to the outer radius of the liner. As for the case of constant r_d, it is sufficient to solve Maxwell's equations for the longitudinal field components alone, since they completely specify the electromagnetic wave. As $\vec{\nabla}\epsilon = 0$ within the vacuum and dielectric region separately, and assuming a $e^{i\omega t}$ dependence for the fields, the wave equation can be written as

$$\left(\vec{\nabla}_\perp^2 + \frac{\partial^2}{\partial z^2} + \frac{\omega^2}{c^2}\right)\left\{\begin{array}{c} E_z(r,z) \\ B_z(r,z) \end{array}\right\} = 0 \qquad (1)$$

for each region. Here $c = c_0$ in the vacuum region, $c = \frac{c_0}{\sqrt{\epsilon_r}}$ in the liner region, and c_0 is the speed of light in vacuum. As observed above, the longitudinal wavenumber is a function of z due to the longitudinal variation of

* i.delafuentevalentin@utwente.nl

$r_d(z)$. Assuming that the longitudinal wavenumber, $k(z)$ will be slowly varying with distance z, we will follow the WKB approximation [3] and make the ansatz that the fields have a longitudinal variation according to

$$E_z(r,z) = \frac{g(r)}{\sqrt{k(z)}} \exp\left(i\int_0^z k(z')dz'\right). \quad (2)$$

In agreement with the WKB approximation, we neglect the second order derivative in $k(z)$. Substituting (2) into the wave equation (1) gives

$$\left(\vec{\nabla}_\perp^2 - k^2(z) + \frac{\omega^2}{c^2}\right) g(r) = 0, \quad (3)$$

which is Bessel's equation. However, eq. 3 still has an implicit dependence on the distance z through the longitudinal wavenumber $k(z)$ and this would in general violate the assumption that $g(r)$ is a function of r alone. However, we assume that the variations in $k(z)$ are slow and small, i.e., $\Delta k(z) = k(z) - k_0 << k(z)$, where k_0 is the wavenumber corresponding to a constant r_d equal to the average liner radius r_{d0}. Thus, we find, in first approximation, $k_z \approx k_0$ and the transverse profile of the EM-wave remains unaffected by the slowly varying inner radius. On the other hand, a small value of $\Delta k(z)$ may give an appreciable value in the phase factor $\exp\left(\int_0^z (k_0 + \Delta k(z'))dz'\right)$. Thus $\Delta k(z)$ will be retained in the phase factor. The phase $\alpha(z,t)$ of the electromagnetic wave is given by

$$\alpha(z,t) = \int_0^z k(z')dz' - \omega t, \quad (4)$$

where the slowly varying longitudinal wavenumber is given by

$$k(z) = k_0 + \int_0^z \frac{\partial k}{\partial z'}dz' \approx k_0 + \left.\frac{\partial k}{\partial r_d}\right|_{r_{d0}} \int_0^z \frac{\partial r_d}{\partial z'}dz'. \quad (5)$$

It is assumed here that the inner radius of the liner is equal to the mean radius at $z = 0$. To summarize, the transverse mode pattern is not influenced by the slowly varying inner boundary of the liner which only influences the phase of the propagating EM-wave through k_z. Variations in $r_d(z)$ are considered slow if they are slow compared to a radiation wavelength, because the SVAP approximation, used to derive the dynamical FEL equations, includes an average over one ponderomotive wavelength (i.e., a radiation wavelength).

To find the fields, within these approximations, eq. (3) is solved and the usual boundary conditions are applied. The solution consists of axial-symmetric, propagating EM-waves that can be divided into two classes. These are the well known TE_{0n} and TM_{0n} modes with respectively $E_z = 0$ and $B_z = 0$. Only modes with $E_z \neq 0$ are of interest, as these modes are responsible for the bunching of the electrons in a Cerenkov FEL. Limiting ourselves to the interesting case of a phase velocity less then c_0, the expressions for the fields, used to derive the dynamical CFEL equations, are as follows. The transverse wavenumbers κ_n and κ'_n for the vacuum respectively liner region are given by

$$\kappa_n = \sqrt{k_{0n}^2 - \frac{\omega^2}{c_0^2}} \qquad \kappa'_n = \sqrt{\epsilon_r \frac{\omega^2}{c_0^2} - k_{0n}^2}, \quad (6)$$

whereas the components for the TM_{0n} are given by

$$\vec{E}_{0n}(\vec{r},t) = \omega\left(iI_1(\kappa_n r)\hat{e}_r - \frac{\kappa_n}{k_{0n}} I_0(\kappa_n r)\hat{e}_z\right) A_{0n}(z,t) \quad (7)$$

and

$$\vec{B}_{0n}(\vec{r},t) = ik_{0n}\left(1 - \frac{\kappa_n^2}{k_{0n}^2}\right) I_1(\kappa_n r) A_{0n}(z,t)\hat{e}_\theta \quad (8)$$

in the vacuum region and by

$$\begin{aligned}\vec{E}_{0n}(\vec{r},t) &= \\ &= \omega\left(i\frac{\kappa_n}{\kappa'_n}\left[a_n J_1(\kappa'_n r) + b_n Y_1(\kappa'_n r)\right] A_{0n}(z,t)\hat{e}_r - \right. \\ &\quad \left. - \frac{\kappa_n}{k_{0n}}\left[a_n J_0(\kappa'_n r) + b_n Y_0(\kappa'_n r)\right] A_{0n}(z,t)\hat{e}_z\right) \end{aligned} \quad (9)$$

and

$$\begin{aligned}\vec{B}_{0n}(\vec{r},t) &= \\ &= ik_{0n}\left(1 + \frac{\kappa_n'^2}{k_{0n}^2}\right)\frac{\kappa_n}{\kappa'_n}\left[a_n J_1(\kappa'_n r) + \right. \\ &\quad \left. + b_n Y_1(\kappa'_n r)\right] A_{0n}(z,t)\hat{e}_\theta \end{aligned} \quad (10)$$

in the liner region. In these equations,

$$A_{0n}(z,t) = a_{0n}\frac{1}{\sqrt{k_n(z)}} e^{\imath\alpha_n(z,t)}. \quad (11)$$

DYNAMICAL EQUATIONS FOR CFEL

In this section a non-linear formulation is given for a Cerenkov FEL with an irregular liner. As usual, we start with expressing the total field as a sum over the TM_{0n} waves (eqs. (7) to (10)) found for the irregular, axially symmetric, lined waveguide with no electron beam present [5]. The amplitude of each mode is $z-$dependent such that the wave can be amplified by the electron beam. This total field is substituted into Maxwell's equations with the electron beam as the driving term for the field. Using the orthogonality property of the modes, a single mode amplitude is filtered out from Maxwell's equation by multiplying it with the transverse profile of that mode and integrate Maxwell's equation over the cross-section of the waveguide. Then the slowly varying amplitude and phase (SVAP) approximation is applied to obtain the final dynamical equation that describes the amplification of the mode amplitude. The set of equations is closed by complementing it with Lorentz's equation that describes the motion of the electrons within the beam under influence of the electromagnetic fields and

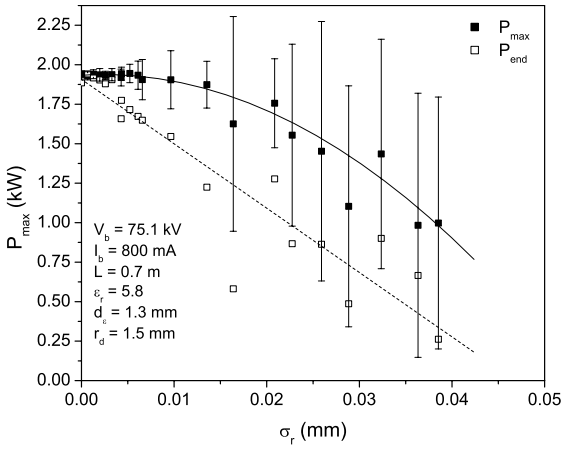

Figure 1: Calculated power as a function of the standard deviation of the liner irregularities. See the text for more details. The lines are for guidance only.

the axial magnetic guide field present. As the derivation is straightforward and very similar to [5] we only present the final result for the mode amplitude,

$$2\sqrt{k_n(z)}(1-\frac{\kappa_n^2}{k_{0n}^2})\frac{\partial a'_{0n}}{\partial z} = \\ = -4\frac{\omega_p^2}{c_0^2}\frac{\beta_{z0}}{A_n r_{d0}^2}\int_0^{r_{d0}} drr\left[iI_1(\kappa_n r)\langle\frac{\beta_r}{|\beta_z|}e^{i\alpha_n}\rangle + \right. \\ \left. +\frac{\kappa_n}{k_{0n}}I_0(\kappa_n r)\langle e^{-i\alpha_n}\rangle\right] \quad (12)$$

where A_n is a normalization constant, ω_p is the plasma frequency and $a'_{0n}(z) = \frac{e}{mc}a_{0n}(z)$ with $a_{0n}(z)$ the complex z-dependent amplitude of (11). Here, $\langle\ldots\rangle$ is an average over all electrons within one ponderomotive wavelength, i.e., one radiation wavelength. Note that with the electron beam present, the phase of the TM_{0n} mode is not solely given by $\alpha_{0n}(z,t)$ as the dynamical CFEL equation (eq. (12)) also drives the phase of the complex amplitude a'_{0n}. Therefore the total relative phase of an electron with respect to the ponderomotive potential is given by the sum of these two phases.

LINER IRREGULARITIES

The above given formulation is used to investigate the effect of irregularities in the inner radius of an otherwise constant liner used in a low gain CFEL operating at a nominal frequency of 50 GHz [4]. The CFEL uses a 800 mA electron beam with a radius r_b of 1mm and a maximum beam voltage V_b of 100 kV to generate an output power in excess of 1 kW. Using a liner with the following parameters, ϵ_r=5.8, r_{d0}=1.5 mm, length L=0.7 m and thickness d_ϵ=1.3 mm, the CFEL requires a beam voltage V_b of 75.1 kV to obtain maximum output power at 50 GHz. The liner fluctuations are generated using a uniform random distribution between $-\delta r_d$ and δr_d that is filtered with a low-pass spatial filter. The filter has a cut-off distance of 0.1 m and removes fast fluctuations. To estimate the influence on the maximum power, 20 different realizations of the fluctuations are generated for each maximum amplitude δr_d. For each realization the maximum power P_{max} or, if not saturated, the power P_{end} at the end of the liner, and the standard deviation σ_r of the fluctuations are calculated. The average of these values are plotted in fig. 1 for a liner length of 70 cm. The error bar in P_{max} represent the average standard deviation of P_{max} (P_{end} has a similar standard deviation). With no fluctuations, the laser has a saturated power of P_{max} = 1.9 kW at a distance $z_{sat} = 67 \pm 1$ cm. From the simulations it follows that both P_{max} and z_{sat} decrease with increasing σ_r and at the same time the spread in both increases, i.e., $z_{sat} = 55 \pm 8$ cm at $\sigma_r = 40$ μm. It follows from fig. 1 that a rms fluctuation of approx. 40 μm is already sufficient to lower the maximum power, on average, by a factor of 2. On the other hand, fig. 1 also shows that a particular realization of the liner fluctuations can also enhance the saturated power and this will be investigated in the next section.

TAPERED LINER

In the previous section we considered a dielectric liner with an inner radius that fluctuates slowly but randomly with distance z and found that even small fluctuations can seriously degrade the gain of a CFEL. If, on the other hand, we were to apply a linear taper starting at some distance, we expect to enhance the gain and obtain a higher output power. The latter is the result of keeping the bunch away from reaching the bottom of the ponderomotive potential well by changing the phase velocity of the EM wave. As the average electron velocity decreases, the phase velocity of the EM wave must be reduced as well to avoid saturation. Because dk_{0n}/dr_{d0} is negative, one has to reduce the inner liner radius to avoid trapping. This will reduce the gap between the electron beam and liner and will thus have limited applicability. However, it is interesting to find out if a negative taper on $r_d(z)$ improves the performance and by how much.

We consider the same CFEL as in the previous section. The growth of the power as a function of z is shown in fig. 2 where the length of the liner has been extended to L = 3 m to allow for some distance for the taper. As the CFEL has initially a gap of 0.5 mm between the electron beam and the liner, the length of the taper is limited and the maximum liner length depends on the slope of the taper. Fig. 2 shows the power as a function of z for different, negative, slopes of a taper that starts at z = 60 cm. If the slope is not large enough, the laser will not reach saturation within a liner length of 3 m. The output of the laser increases with increasing slope of the taper up to the point where the liner diameter is such that the gap with the electron beam is reduced to zero and electrons start to hit the liner before the

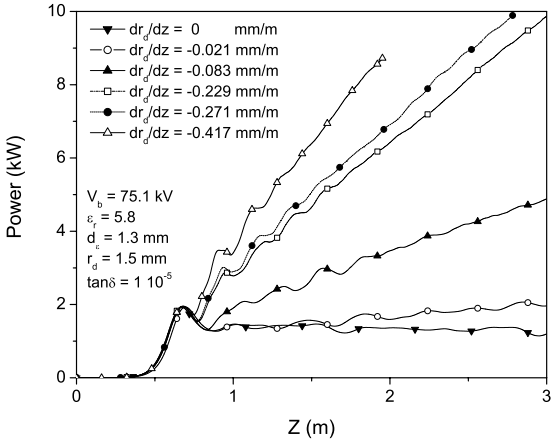

Figure 2: Calculated power as a function of distance z for different slopes of the taper. The taper starts at z=0.6 m.

end is reached. At this point the output power is close to 10 kW (dr_d/dz = -0.229 mm/m). A still larger slope results in a shorter distance to reach the point of zero gap and a gradual decrease of the maximum power; for a slope of -0.417 mm/m the maximum power is already reduced to 8.7 kW at z = 1.95 m. For a slope of -0.188 mm/m we extended the liner length and found a maximum power of 10.4 kW at a distance of 3.65 m where, again, the gap was reduced to zero. It should be pointed out that although the decrease in gap as a result of the negative taper increases the coupling strength between electrons and EM wave, it is the change in phase velocity that prevents the laser from reaching saturation. To conclude, for this particular CFEL, it is found that a negative taper on r_{d0} increases the maximum attainable power with a factor of 5 before the gap is reduced to zero. Note that at that point the laser was not saturated.

Therefore, further improvements are to be expected by using different methods of tapering that avoid reducing the gap. These methods are changing the dielectric constant or the outer waveguide radius. This is currently under study.

CONCLUSIONS

We have demonstrated that, in first approximation, the transverse mode profile of a CFEL is not influenced by a slowly varying inner radius of the liner. However the liner does effect the phase velocity of the propagating wave. We derived the dynamical CFEL equation and applied it to investigate the influence of liner fluctuations and a taper of the inner liner radius on the performance of the CFEL. It was found that an rms fluctuation that is approximately 3 % of r_{d0} is already sufficient to decrease the maximum power by a factor of 2, at least for the configuration investigated. Note that this rms fluctuation is comparable to the manufacturing accuracy of commercially available (quartz) tubes. By applying a negative taper to r_{d0} the maximum power can be increased by a factor of 5 before the gap between electron beam and liner becomes zero. At this point the laser is not yet saturated, so other methods of tapering may still further improve the performance.

ACKNOWLEDGEMENT

This research is supported by the EU, contract G5RD-CT-2001-00546.

REFERENCES

[1] A. Friedman, S. Krinsky, L.H. Yu, FEL gain reduction due to wiggler errors. IEEE J. of Quantum Elec, **30**, 1295 (1994)

[2] R. Tatchyn et.al. Research and development toward a 45 - 1.5 Å linac coherent light source (LCLS) at SLAC. Nucl. Instr. and Meth. in Phys. Res. A **375**, 274 (1996)

[3] W. Elmore and M. Heald, Physics of Waves, New York, Dover (1985)

[4] I. de la Fuente, P.J.M. van der Slot, K-J. Boller, A mm-wave, table top Cerenkov Free-Electron Laser. This proceedings.

[5] H.P. Freund, A.K. Ganguly, Nonlinear Analysis of the Cerenkov Maser, Physics of Fluids B **2**, 2506, (1990)

SIMULATION INVESTIGATION OF THE DETUNING CURVE

Xiaojian Shu, Yuhuan Dou, Yuanzhang Wang, Institute of Applied Physics and Computational Mathematics, P. O. Box 8009, Beijing 100088, P. R. China

Abstract

The detuning curves of free-electron laser oscillators are calculated with the help of our three-dimensional code, which are compared with those from one-dimensional simulations and super-mode theory, and the experiments. The influence of the optical guiding and other three-dimensional effects on the detuning curve is studied. It is found that the length of the detuning curve from three-dimensional simulations is shorter than that from one-dimensional simulations and super-mode theory.

INTRODUCTION

An obstacle to the development of a short pulse free-electron laser (FEL) oscillator is the slippage that occurs between the electron beam and radiation duo to their different velocities, which results in lack of overlapping between the electron and the optical pulses and a reduction in gain, and so is called the laser lethargy effect [1]. This effect can be overcome by slightly shortening the length of the optical cavity from synchronism so to keep the overlapping between the electron and the optical pulses [1, 2]. The FEL power as a function of cavity length, which is named the detuning curve, has been studied abundantly both theoretically and experimentally. The detuning curves are usually calculated by one-dimensional (1D) simulations due to the simplicity and little consumption of the computer time, which in general are good agreement with super-mode theory [3] and experiments. To our knowledge there is almost no detuning curve calculated from three-dimensional (3D) simulations. However, recently it is found that the length of the detuning curve seems to be shorter than possible assuming a one-dimensional super-mode theory when the gain is high in the experiments of an infrared FEL oscillator [4, 5]. On the other hand, the lethargy effects is more severe in a far-infrared FEL such as the CAEP FIR FEL [6] because the slippage length which is proportional to the optical wavelength is large compared to the short electron pulse produced by an RF linac. It is of interesting and necessary to obtain more exact detuning curve from 3D simulations to study it more carefully.

In this paper, the detuning curves of the CAEP FIR FEL [6] and the Jefferson Lab IR Demo FEL [4, 5] are calculated with the help of our 3D code [6-8], which are compared with those from 1D simulations and super-mode theory, and the experiments. The influence of the optical guiding and other three-dimensional effects on the detuning curve is studied. It is found that the length of the detuning curve from 3D simulations is shorter than that from 1D simulations and super-mode theory.

CAEP FIR FEL

Firstly, as usual, the detuning curves are calculated by using our one-dimensional time-dependent code GOFELP [9, 10]. In simulations, the distribution functions of the electrons and optical pulses are assumed as Gaussian. The transverse overlap factor between Gaussian mode of TE_{00} of the optical cavity and the electron beam with a parabolic transverse density profile is considered in the code [11].

In Fig. 1 we show the output power as a function of cavity length with the parameters of CAEP FIR FEL [6] as listed in Table 1. In simulations, the current is adjusted to obtain the same gain as 3D simulations and the loss of the cavity is given the result of 3D simulations. The range of the detuning curve is from about –70 μm to –360 μm and the length is about 290 μm.

Table 1: CAEP FIR FEL Parameters

Electron beam	
Energy (MeV)	6.5
Energy spread (%)	1
Peak current (A)	8
Micro bunch (ps FWHM)	15
Wiggler	
Period (cm)	3
Peak field strength (kG)	3
Number of periods	50
Optical	
Wavelength (μm)	110.7
Cavity length (m)	2.536
Mirror curvature (m)	1.768

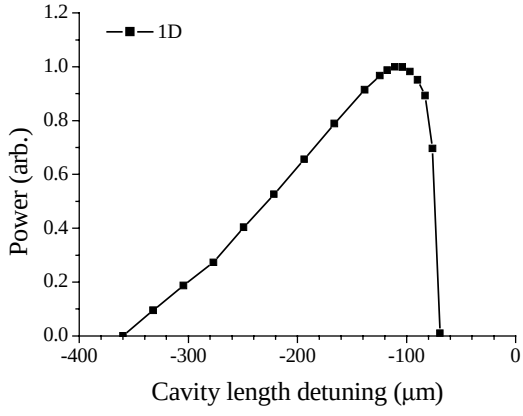

Figure 1: Detuning curve of CAEP FIR FEL from 1D simulations.

Then the detuning curve is calculated by using our 3D code OSIFEL [6-8]. As shown in Fig. 2, the curve has almost same shape as Fig. 1 but moves toward zero point, i.e. synchronism point, which cannot be observed and fixed in experiments. The range of the detuning curve is from about –25 μm to –330 μm and the length is about 300 μm, which approach the result of 1D of 290 μm. The reason is that the gain and loss are almost same in 1D and 3D simulations and the net gain is small [6].

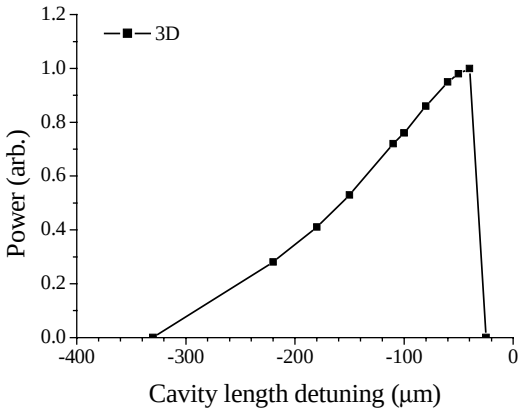

Figure 2: Detuning curve of CAEP FIR FEL from 3D simulations.

JLAB IR DEMO FEL

Fig. 3 shows the detuning curve calculated by using our 1D code with Jlab IR Demo FEL parameters [4, 5] listed in Table 2. In the simulations, the energy spread is zero in order to cut down on the computer time. The range of the detuning curve is from about –0.2 μm to –31 μm and the length is about 30 μm. Note that the curve is very sharp, which is totally different to Fig. 1 and results from experiments [4, 5], due to high small signal gain of more about 150% in the 1D simulations without energy spread.

Table 2: Jlab Demo FEL Parameters Used in Simulations

Electron beam	
Energy (MeV)	47.8
Energy spread (% FWHM)	0.5
Emittance (mm.mrad rms)	8.7
Peak current (A)	58.8
Micro bunch (ps FWHM)	1
Wiggler	
Period (cm)	2.7
Peak field strength (kG)	5.61
Number of periods	40.5
Optical	
Wavelength (μm)	3.1
Cavity length (m)	8.0105
Mirror curvature (m)	4.05
Loss (%)	9.63575

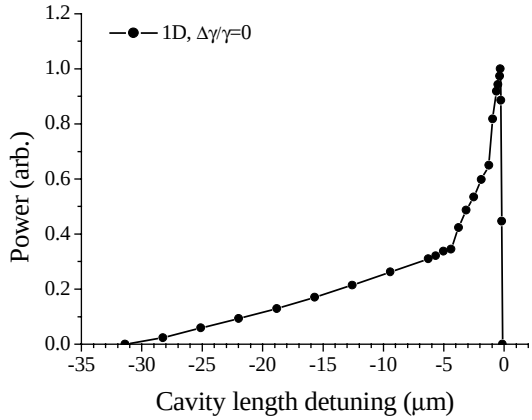

Figure 3: Detuning curve of Jlab IR Demo FEL from 1D simulations without energy spread.

Fig. 4 shows the detuning curve calculated by using our 3D code. The shape of curve becomes gently, not so sharp, since the small signal gain is about 100% in the 3D simulations, which approaches the gain in the experiments. The range of the detuning curve is from about 0 μm to –20 μm and the length is about 20 μm, which is shorter than 30 μm obtained from the 1D simulations without energy spread, but little longer than 16μm of that from the experiments [5] and in good agreement with experiments. The 3D simulations give better results than the 1D calculations and super-mode theory.

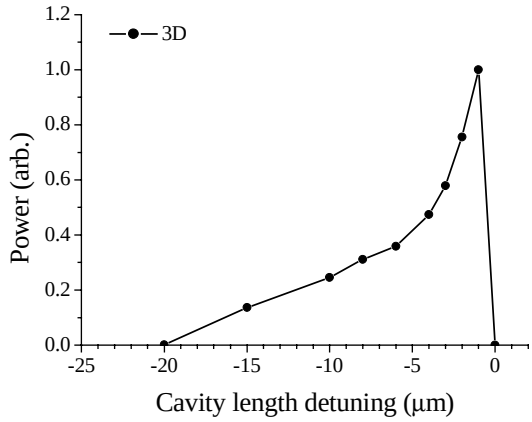

Figure 4: Detuning curve of Jlab IR Demo FEL from 3D simulations.

Then the energy spread of the electron beam is considered in 1D simulations. Fig. 5 shows the detuning curve from the 1D simulation with the energy spread of 0.5%. Fig. 4 and 5 are remarkably similar to each other. The range of the detuning curve is from about 0 μm to –22 μm and the length is about 22 μm, which is little

longer than 20 μm that obtained from the 3D simulations and in better agreement with the experiments than the 1D simulations without the energy spread. The small signal gain is about 80%, which is smaller than that from the 3D simulations. The optical guiding effects result in an increase in the gain. Note, however, that the length of detuning curve from the 3D simulations and experiments seems to be shorter than possible assuming a higher gain.

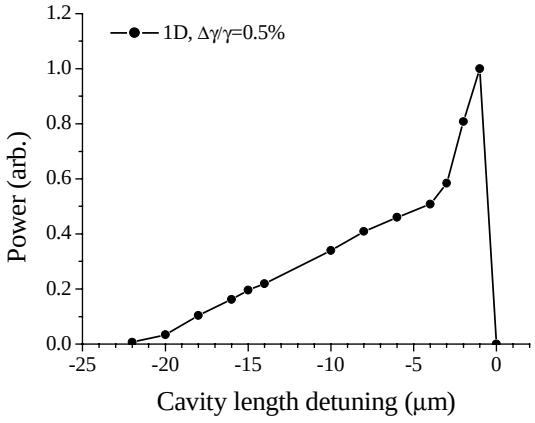

Figure 5: Detuning curve of Jlab IR Demo FEL from 1D simulations with energy spread.

CONCLUSION AND DISCUSSION

In this paper, the detuning curves of the CAEP FIR FEL and the Jefferson Lab IR Demo FEL are calculated with the help of our 3D code, which are compared with those from 1D simulations and the experiments. The influence of the optical guiding and other three-dimensional effects on the detuning curve is studied. It is found that the length of the detuning curve from 3D simulations is shorter than that from 1D simulations when the gain is high and in better agreement with experiments. The 3D non steady-state simulations give better results than the 1D calculations and super-mode theory. The 1D non steady-state simulations with TE_{00} mode and energy spread can give good results due to the facts that the emittance of the electron beam is very small and the optical cavity is a stabile.

The optical guiding effects cause an increase in the gain in the 3D simulations. In general the increase in the gain results in an increase in the length of the detuning curve. It is found, however, that the length of detuning curve from the 3D simulations and experiments seems to be shorter than possible with a higher gain. Does it hint that the optical guiding effects can shorten a detuning curve even though the gain is increased in the case of a high gain FEL oscillator? It is the subject of a future work.

ACKNOWLEDGMENTS

This work is supported by High Power Radiation Laboratory under National 863 RD Program and National Laser Technology Committee, China.

REFERENCES

[1] H. Al-Abawi et al., Optics Comm. 30 (1979) 235.
[2] W.B. Colson and A. Renieri, J. Phys. Colloq. 44 (1983) 11.
[3] G. Dattoli et al., Nucl. Instr. and Meth. A 285 (1989) 108.
[4] S. Benson et al., Nucl. Instr. and Meth. A 429 (1999) 27.
[5] G.R. Neil et al., Nucl. Instr. and Meth. A 445 (2000) 192.
[6] Xiaojian Shu and Yuanzhang Wang, Nucl. Instr. and Meth. A 483 (2002) 205.
[7] Wang Taichun and Wang Yuanzhang, High Power Laser and Particle Beams, 7 (1995) 25, (in Chinese).
[8] Xiaojian Shu et al., Optical Engineering, 39 (2000) 1543.
[9] Xiaojian Shu, Optics Comm. 105 (1994) 188.
[10]Xiaojian Shu et al., J. Appl. Phys. 77 (1995) 426.
[11]D.C. Quimby et al., IEEE J. Quantum Electron. QE-21 (1985) 979.

HARMONIC AMPLIFIER FREE ELECTRON LASER

Jia Qika
National Synchrotron Radiation Laboratory, University of Science and Technology of China
Hefei, Anhui, 230029, China

Abstract

The harmonic optical klystron (HOK) in which the second undulator is resonant on the higher harmonic of the first undulator is analysed as a harmonic amplifier. The optical field evolution equation of the HOK is derived analytically for both CHG mode (Coherent Harmonic Generation, the quadratic gain regime) and HGHG mode (High Gain Harmonic Generation, the exponential gain regime), the effects of energy spread, energy modulation and dispersion in the whole process are considered.

INTRODUCTION

One way of free electron laser (FEL) developing toward short wavelength is using harmonic. In the coherent harmonic generation (CHG) [1,2] scheme an optical klystron(OK) has been used, an external laser pulse is focused into the first undulator, the wavelength of the laser is resonated with the fundamental radiation of the optical klystron, with optimized system parameters the harmonic radiation in the second undulator is coherently enhanced. Analyze shown that if make second undulator of OK resonant on the higher harmonic, namely the wavelength of fundamental radiation of the second undulator matches with *n*th harmonic optical field in the first undulator, it will be more beneficial to the harmonic generation [3]. To distinguish it from the normal optical klystron, we temporarily call such optical klystron the "harmonic optical klystron"(HOK). A similar configuration was proposed and used for high gain harmonic generation (HGHG) [4].the scheme evolved from many earlier ideals (e.g. ref. [5]). In the HGHG mode the optical power grows exponentially while in the CHG mode the optical power grows quadratically, both modes are harmonic amplifier. Cascaded optical klystron [6,7] and cascaded harmonic optical klystron [8-9] for X-ray FEL are also proposed and discussed.

So far the theory of optical klystron amplifier has all approximated it as the scheme with separate functions: the energy modulation only be considered in the first undulator, the dispersive effect only occur in dispersive section, and the gain section generate radiation. In Ref [4] the HGHG problem is solved for the small energy spread limit, in the second undulator the electron beam is assumed be mono-energetic and dispersive effect is ignored. The amplifying process of optical klystron (and harmonic optical klystron) have been analysed mostly by calculating the bunching factor at the entrance of the second undulator (the techniques developed for microwave klystron). But such approximation treatments are not always appropriate. In this paper I derive the optical field evolution equation complete analytically for HOK, the energy spread effect and the dispersive effect in the whole process will be considered in the derivation.

OPTICAL FIELD EVOLUTION EQUATIONS

We use the one-dimensional FEL theory and start from the paraxial optical field equation and the electron phase equation:

$$\frac{d\tilde{a}_s}{dz} = \lambda_s r_e a_u \delta_p n_e \left\langle \frac{e^{-i\phi}}{\gamma} \right\rangle \tag{1}$$

$$\frac{d^2\phi}{dz^2} = -\frac{2k_u k_s a_u \delta_p}{\gamma^2} \mathrm{Re}(\tilde{a}_s e^{i\phi}) \quad , \tag{2}$$

where $\tilde{a}_s = a_s e^{i\varphi_s}$, $a_s=eE_s/(mc^2k_s)$ and $a_u=eB_u/(mc^2k_u)$ are dimensionless vector potential of the *rms* radiation field E_s and undulator field B_u, respectively; $k_s=2\pi/\lambda_s$, $k_u=2\pi/\lambda_u$ are the corresponding wave number; φ_s is the phase of radiation field; $\phi=(k_s+k_u)z-\omega_s t$ is the pondermotive phase of electron, r_e is the classical electron radius; n_e and γ is the density and energy of electrons; the angular bracket represents the average over the electron's initial phases and initial phase velocities. δ_p is the polarization modify factor: for circularly polarized helical undulator $\delta_p=1$; for linearly polarized planar undulator with even *n*th harmonic radiation δ_p =0, and with odd *n*th harmonic $\delta_p=[J,J]_n$,

$$[J,J]_n = (-1)^{\frac{n-1}{2}} [J_{\frac{n-1}{2}}(\frac{na_u^2}{2(1+a_u^2)}) - J_{\frac{n+1}{2}}(\frac{na_u^2}{2(1+a_u^2)})]$$

J is integer order Bessel function.

The electron phase in the second undulator is

$$\phi_2 = \phi_{20} + \phi_{20}' z_2 + \Delta\phi_2 \quad . \tag{3}$$

The first term of the right hand side of eq.(3) is the electron phase at the entrance of the second undulator

$$\phi_{20} = n\phi_1(z_{20}) + (k_{u2} - nk_{u1}) z_{20} \quad . \tag{4}$$

The second part in the right hand side of eq.(4) is a constant for all electrons. $\phi_1(z_{20})$ is the electron phase referenced to the first undulator valued at the entrance of the second undulator and given by

$$\phi_1(z_{20}) = \phi_{10} + \phi_{10}' l_1 + \Delta\phi_1 + \Delta\phi_d \, , \tag{5}$$

where ϕ_{10} and ϕ_{10}' is the initial phase and phase velocity (detuning parameter), $\Delta\phi_1$ is the phase change due to interaction with optical field of the seed laser in the first undulator and given from eq.(2)

$$\Delta\phi_1 = -2k_{s1}k_{u1}a_{u1}\delta_{p1}\,\mathrm{Re}\int_0^{l_1}(l_1 - z_1)\frac{\widetilde{a}_{s1}e^{i\phi_1}}{\gamma^2}dz_1 . \quad (6)$$

k_{s1} and a_{s1} are the wave number and the dimensionless vector potential of the seed laser field (*rms*) , respectively. $\Delta\phi_d$ is phase change in the dispersive section

$$\Delta\phi_d = \int_0^d k_s(1-\frac{1}{\beta_{II}})dz = -\frac{k_s}{2}\int_0^d(\frac{1}{\gamma^2}+\beta_\perp^2)dz = -\frac{k_s}{2\gamma^2}L_d \quad (7)$$

$$L_d = d + (\frac{e}{mc^2})^2\int_0^d(\int_0^z B_d dz')^2 dz$$

is equivalent drift length, d and B_d are the lengths and magnetic field of the dispersive section, respectively. Using resonant relation of FEL and the phase velocity expression $\phi' \cong k_u(1-\gamma_r^2/\gamma^2)$, eq.(7) can be written as

$$\Delta\phi_d = -\frac{k_u L_d \gamma_r^2}{(1+a_u^2)\gamma^2} = N_d\lambda_u\phi_1'(l_1) - 2\pi N_d \quad (8)$$

$$N_d = \frac{1}{\lambda_u(1+a_u^2)}[d + (\frac{e}{mc^2})^2\int_0^d(\int_0^z B_d dz')^2 dz], \quad (9)$$

where γ_r is the resonant energy, N_d is the dispersive section parameter, it is the scale parameter of optical klystron itself and independent on the electron beam. The physical meaning of N_d is that it is number of wavelengths of the light passing over the resonant electron in the dispersive section. For electrons with different energy N_d also can be expressed as

$$N_d = \frac{\gamma}{4\pi}\frac{\delta\Delta\phi_d}{\delta\gamma} , \quad (10)$$

obviously N_d describe the dispersive strength

The second term of eq.(3) ϕ_{20}' is electron phase velocity at the entrance of the second undulator

$$\phi_{20}' = k_{u2}(1-\frac{\gamma_r^2}{\gamma_{20}^2}) = \frac{k_{u2}}{k_{u1}}\phi_1'(l_1) \quad (11)$$

$$\phi_1'(l_1) = \phi_{10}' + \Delta\phi_1' ,$$

$$\Delta\phi_1' = -2k_{s1}k_{u2}a_{u1}\delta_{p1}\,\mathrm{Re}\int_0^{l_1}\frac{\widetilde{a}_{s1}e^{i\phi_1}}{\gamma^2}dz_1 . \quad (12)$$

The third term of eq.(3) is phase variation due to the interaction with the radiation field in the second undulator

$$\Delta\phi_2 = -2k_{s2}k_{u2}a_{u2}\delta_{p2}\,\mathrm{Re}\int_0^{z_2}(z_2 - z_2')\frac{\widetilde{a}_{s2}e^{i\phi_2}}{\gamma^2}dz_2' \quad (13)$$

Therefore the electron phase in the second undulator (we drop the constant term) is

$$\phi_2 = n\phi_{10} + \phi_{10}'[n(l_1 + N_d\lambda_{u1}) + z_2\lambda_{u1}/\lambda_{u2}] -$$
$$-2k_{u1}k_{s1}a_{u1}\delta_{p1}\,\mathrm{Re}\int_0^{l_1}[n(l_1 - z_1 + N_d\lambda_{u1}) + z_2\frac{\lambda_{u1}}{\lambda_{u2}}]\frac{\widetilde{a}_{s1}e^{i\phi_1}}{\gamma^2}dz_1$$
$$+\Delta\phi_2 \quad (14)$$

The harmonic generation problem of HOK including the electron beam quality effects and dispersive effects for whole process from beginning to saturation can be numerically solved by substituting above expression into eq.(1).

SUPERRADIANCE REGIME(CHG MODE)

Owing to the short length of first section undulator (modulator) the optical field in the modulator is approximately constant. The third term of the right hand side of eq.(14) is phase variation due to the interaction with the seeding optical field. The integral function in the term varied approximately linearly with z_1, so taking its median in the integral is a reasonable approximation

$$-\frac{2k_{u1}k_{s1}a_{u1}\delta_{p1}a_{s1}}{\gamma^2}\int_0^{l_1}[l_1 - z_1 + N_d\lambda_{u1} + \frac{\lambda_{u1}z_2}{n\lambda_{u2}}]\cos(\phi_{10}+\phi_{10}'z_1)dz_1$$
$$\approx n\Delta\xi\cos(\phi_{10}+\phi_{10}'\frac{l_1}{2}) \quad (15)$$

where

$$\Delta\xi = 4\pi(\frac{N_1}{2} + N_d + \frac{z_2}{n\lambda_{u2}})\frac{\Delta\gamma_m}{\gamma} \quad (16)$$

$$\frac{\Delta\gamma_m}{\gamma} = 4\pi N_1\frac{a_{u1}\delta_{p1}a_{s1}}{(1+a_{u1}^2)} . \quad (17)$$

$\Delta\gamma_m/\gamma$ is the maximum energy modulation induced in the first section undulator.

In coherent harmonic generation (CHG) mode, the electron beam current is low and the length of the gain section of HOK (or OK) is short, while the N_d may be very large. It have $L_2 < 3L_g$ (L_g: the power gain length) and $N_d + N_1/2 >> N_2/n \geq z_2/n\lambda_{u2}$. Therefore the z_2 in $\Delta\xi$ can be approximated with its median:

$$\Delta\xi = 4\pi(\frac{N_1}{2} + N_d + \frac{N_2}{2n})\frac{\Delta\gamma_m}{\gamma} ,$$

and the phase variation due to interaction with the radiation field (the last term of the right hand side of eq.(14)) can be neglected. Thus the optical field in CHG mode for HOK is

$$\widetilde{a}_{s2} = -\frac{r_e\lambda_{s2}a_{u2}\delta_{p2}n_e}{\gamma}J_n(n\Delta\xi)$$
$$\times\left\langle i^n e^{-i\phi_{10}'\lambda_{u1}[n(\frac{N_1}{2}+N_d)+\frac{N_2}{2}]}l_2\sin c\frac{\phi_{02}'l_2}{2}\right\rangle \quad (18)$$

For a Gaussian initial energy distribution of the electron beam the corresponding radiation intensity is

$$\widetilde{a}_{s2}^2 = (\frac{r_e\lambda_{s2}a_{u2}\delta_{p2}n_e l_2}{\gamma})^2 J_n^2(n\Delta\xi)f_\gamma^2$$
$$f_\gamma = \exp\{-\frac{1}{2}[4\pi n(N_d + \frac{N_1 + N_2/n}{2})\frac{\sigma_\gamma}{\gamma}]^2\} \quad (19)$$

where $\delta_{p2}=[J,J]_1$. For given energy spread and energy modulation (i.e. given seed laser) we can give the optimal dispersive parameter

$$N_d^{opt.} = \frac{1}{4\pi n}\min[\frac{\sqrt{n}}{\sigma_\gamma/\gamma}, \frac{n+1}{\Delta\gamma_m/\gamma}] - \frac{N_1+N_2/n}{2} \quad (20)$$

If we do following substitution in eq.(19)

$a_{u2}\rightarrow a_u$, $\delta_{p2}\rightarrow\delta_p=[J,J]_n$, $N_2/n\rightarrow N_2$,

then we have the *n*th harmonic radiation intensity for OK configuration. The advantage of HOK over OK for CHG is obvious: the energy spread effect is reduced, the radiation is also enhanced by proper selecting undulator parameters to make $(a_{u2}[J,J]_1)^2 >>(a_u[J,J]_n)^2$ [6]. Moreover besides the odd harmonic the HOK also can operated at the even harmonic of the seed laser.

EXPONENTIAL GAIN REGIME (HGHG MODE)

For the HGHG mode, the electron beam current is relatively high, the length of the second undulator must be sufficiently long to reach the exponential gain regime: $L_2>3L_g$. Therefore the condition $N_d+N_1/2>>N_2/n$ may not be satisfied. Substituting eq.(14) into eq.(1) and linearizing it, after averaging over a uniform initial phase distribution of electrons, the optical field evolution equation in linear region for HOK is given by

$$\begin{aligned}\frac{d\tilde{a}_{s2}}{dz_2} &= \frac{8k_{u2}^2\gamma^2\rho_2^3}{k_{s2}a_{u2}\delta_{p2}}\left\langle e^{-i[n\phi_{10}'(\frac{l_1}{2}+N_d\lambda_{u1})+\phi_{02}'z_2]} i^n J_n(n\Delta\xi)\right\rangle \\ &-(2k_{u2}\rho_2)^3\left\langle\frac{\partial}{\partial\phi_{02}'}\int_0^{z_2} J_0(2k_{u2}(z_2-z_2')\frac{\Delta\gamma_m}{\gamma})\right. \\ &\left.\times a_{s2}e^{-i\phi_{02}'(z_2-z_2')}dz_2'\right\rangle \\ &+(2k_{u2}\rho_2)^3\left\langle ie^{-i2n\phi_{10}'(\frac{l_1}{2}+N_d\lambda_{u1})}\int_0^{z_2}(z_2-z_2')\right. \\ &\left.\times J_{2n}(n(\Delta\xi+\Delta\xi'))\tilde{a}_{s2}e^{-i\phi_{02}'(z_2+z_2')}dz_2'\right\rangle\end{aligned} \quad (21)$$

where ρ is Pierce parameter, ϕ_{02}' is the electron phase velocities (referenced to the second undulator) at the entrance of the first undulator (note it is different with ϕ_{20}'):

$$\phi_{02}' = \frac{k_{u2}}{k_{u1}}\phi_{10}' = k_{u2}(1-\frac{\gamma_r^2}{\gamma_0^2}) \quad (22)$$

In the right hand side of equation (21), the first term correspond to the coherent enhancement process, we can see that the dispersion effect ($\Delta\xi$) and energy-spread effect (the exponential factor) include the contribution not only from dispersive section, the modulation section, but also from gain section. The formula (18) can be obtained from this term. The second term corresponds to the usual gain process, it gives usual gain results when the seed laser is off, the Bessel function in it indicates the effect of the additional energy spread due to energy modulation. The third term contributes small and can be neglected for many cases.

For mono-energetic electron beam and weak modulation we can obtain [10]

$$a_{s2}(z_2) \approx \frac{4k_{u2}\gamma^2\rho_2^2}{3k_{s2}a_{u2}\delta_{p2}} J_n(n\Delta\xi^*)e^{\sqrt{3}k_{u2}\rho_2 z_2} \quad (23)$$

where $\Delta\xi^* = \Delta\xi(z_2^*)$, $Z_2^*: 0<Z_2^*<l_2$

$$\int_0^{l_2} J_n(n\Delta\xi(z_2))e^{-i\phi_{02}'z_2}dz_2 = J_n(n\Delta\xi(z_2^*))\int_0^{l_2} e^{-i\phi_{02}'z_2}dz_2$$

DISCUSSION

From eq.(18) and eq.(23) the division of the CHG mode and HGHG mode for mono-energetic electron beam can be estimated: $z_2\approx 3.73L_g$, therefore the length of the second undulator for HGHG mode should be at least four time longer than the power gain length: $N_2>4N_g$. Figure 1 is a numerical result of equation (21) compared with the result given by numerically solving the equation (1) and eq.(14). It shows that the linear approximation is valid from start up to near saturation (linear region). It also shows that the quadratic gain regime (the CHG mode) is for $z_2<4L_g$.

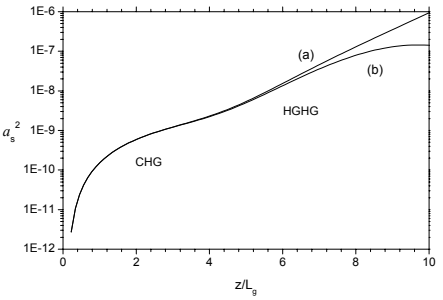

Figure 1, (a) the linear approximation (equation (21)) (b) the result given by numerically solving the equation (1) and (14)

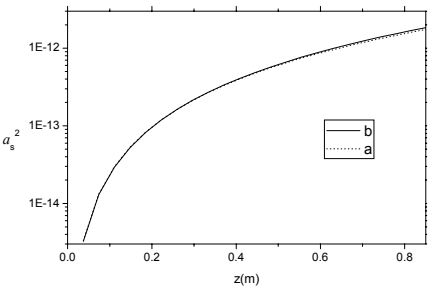

Figure 2, CHG (a) a result of analysis formula (eq. (19)) (b) the result of the linear theory (eq.((21))

Figure2 is a result of analytical formula (equation (19)) compared with the result of the linear theory (the

equation (21) for the CHG. It can be seen that the agreement between them is very well.

From eq.(21) we noted that for the linear region the additional energy spread due to energy modulation only affects usual gain term but not the coherent enhancement term. Therefore, for CHG scheme, in which the coherent enhancement term is dominant, one should chose seeding laser filed a_{s1} and despersive field N_d to make $n\Delta\xi \cong n+1$ so that $J_n=J_{n\max}$, and at the same time a large a_{s1}(strong modulation) and a small N_d (weak dispersion, to reduce the effect of energy spread) are preferred. For HGHG scheme, the additional energy spread effect due to energy modulation must be considered, this gives the up limit for seeding laser filed a_{s1}:

$$\Delta\gamma_m/\gamma < \rho, \quad a_{s1} < \frac{(2+K_1^2)}{4\pi N_1 K_1 \delta_{p1}}\rho \qquad (24)$$

For high harmonic, the optimal $\Delta\xi=(n+1)/n$ not changed much so does the energy modulation $\Delta\gamma_m/\gamma$ and the seeding optical filed (a_{s1}). But as harmonic number increase, the energy spread effect factor and the Bessel function term J_n decrease, both them make the gain degradation. The energy spread factor is more important by comparison. To reduce the energy spread effect we can reduce the dispersive field strength (N_d), but that $J_n(\Delta\xi)$ may also be decreased. The best way is reducing the energy spread itself, this can be achieved by adopting the local (slice) energy spread of electron bunch, namely adopting ultra-short pulse of seeding laser.

In summary we have derived optical field evolution equations complete analytically for harmonic optical klystron. By numerically solving the equation (1) and (14) the harmonic generation problem including the effects of energy spread, energy modulation and the dispersion in whole process can be easily described. Both CHG mode and HGHG mode are analysed as harmonic amplifier. The linear theory is given and analysed for HGHG mode. For CHG mode the analytical formula is given and the advantages of HOK over OK were demonstrated. The optimal parameters for harmonic amplifier are discussed briefly.

REFERENCES

[1] R.Coisson and F. De martini, “Free-electron coherent relativistic scatter for UV generation”, Physics of Quantum Electronics(Addison-Welsley,1982) Vol.9,p939

[2] J.M.Ortega, et al., “Ultraviolet Coherent Generation from an Optical Klystron”, IEEE **QE-21**, pp909-919,1985

[3] Q.K. Jia, “Coherent harmonic generation using the non-symmetric optical klystron”, High Power Laser and Particle Beams,Vol.6, No.3, pp450-454,1994.(In Chinese); “Optimization of optical klystron for coherent harmonic generation FEL”, Nucl. Instr. Meth. A**407**, pp246-250, 1998

[4] L.H.Yu, "Generation of intense uv radiation by subharmonically seeded single-pass free-electron laser", Phys.Rev.A**44**,pp5178-5193,1991

[5] R.Bonofacio, *et.al*, “Generation of XUV light by resonant frequency tripling in a two-wiggler FEL amplifier”, .Nucl.Instr. & Meth. A**296**, pp787-790,1990

[6] V.N.Litvinenko, “High gain distributed optical klystron”, Nucl.Instr. & Meth. A**304**, pp463-464,1991

[7] G.R.Neil,H.P.Freund, "Dispersively enhanced bunching in high-gain free-electron lasers", Nucl.Instr. & Meth. A**475**,pp381-384,2001

[8] J.Wu, L.H.Yu, “Coherent hard X-ray production by cascading stages of High Gain Harmonic Generation", Nucl.Instr. & Meth. A**475**,pp104-111,2001

[9] E.L.Saldin *et.al.*, “Study of a noise degradation of amplification process in a multistage HGHG FEL”, Optics Comm.**202**, pp169-187,2002

[10] Jia Qika,,“One-dimensional theory of high gain harmonic generation free electron laser” Nucl.Instr. & Meth. A**519**,pp489-492,2004

PARAMETER ANALYSIS FOR A HIGH-GAIN HARMONIC GENERATION FEL BY NUMERICAL CALCULATION BASED ON 1D THEORY

Li Yuhui, Jia Qika, Zhang Shancai
National Synchrotron Radiation Laboratory University of Science and Technology of China
Hefei, Anhui, 230029, China

Abstract

High-gain harmonic generation (HGHG) free-electron laser (FEL) is an important candidate for fourth-generation light source. Lots of research works about it have been done all along. Recently a further 1D theory about HGHG FEL has been developed. It considers the effects of different parameters for the whole process. An initial program based on this theory has been made. In this paper, a brief compare of the results from this 1D program and from TDA (3D code) is discussed and it also analyses the parameters for Shanghai deep ultra violate free electron laser source (SDUV-FEL), including electron beam energy spread, seed laser power, strength of dispersion section etc.

INTRODUCTION

The high-gain harmonic generation (HGHG) scheme is one of leading candidates for VUV to X-ray FELs. Ordinarily, a modified TDA3D code, which takes into account the effect of dispersive section, is used to simulate the process of HGHG-FEL.

Recently, a 1D theory about HGHG-FEL has been developed [1]. Different from the previous theories, it accounts for the energy modulation and density modulation (bunching) for a whole process. In this paper, we present some analysis about the choice of seed laser power and dispersive strength based on it.

BRIEF REVIEW OF THE 1D THEORY

The 1D paraxial optical field equation and the election phase equation are:

$$\frac{d\tilde{a}_s}{dz} = \lambda_s r_e a_u \delta_p n_e \left\langle \frac{e^{-i\phi}}{\gamma} \right\rangle \tag{1}$$

$$\frac{d^2\phi}{dz^2} = -\frac{2k_u k_s a_u \delta_p}{\gamma^2} \mathrm{Re}(\tilde{a}_s e^{i\phi}) \tag{2}$$

The symbols in the equations express the common meaning. Especially, δ_p is the polarization modify factor: for circularly polarized helical undulator $\delta_p=1$; for linearly polarized planar undulator with even nth harmonic radiation $\delta_p=0$, and with odd nth harmonic $\delta_p=[J_n J]_n$.

As well known, the process of HGHG-FEL is the three steps: the electron beam first pass an undulator (modulator) with a resonant seed laser for energy modulation. Next, the beam travels through a dispersive section, to form spatial bunch. Finally the beam enters a second undulator (radiator), which is tuned in resonance to the harmonic wavelength of seed laser, to achieve coherent radiation at this higher. The pondermotive phase of electron in the second undulator can be calculated by the equation below[1]:

$$\phi_2 = n\phi_{10} + \phi_{10}'[n(l_1 + N_d\lambda_{u1}) + z_2\lambda_{u1}/\lambda_{u2}] - 2k_{u1}k_{s1}a_{u1}\delta_{p1}\,\mathrm{Re}\int_0^{l_1}[n(l_1 - z_1 + N_d\lambda_{u1}) + z_2\lambda_{u1}/\lambda_{u2}]\frac{\tilde{a}_{s1}e^{i\phi_1}}{\gamma^2}dz_1 + \Delta\phi_2 \tag{3}$$

where ϕ_{10} and ϕ_{10}' is the initial phase and phase velocity; k_{s1} and a_{s1} are the wave number and the dimensionless vector potential of the seed laser field (*rms*) , respectively; z_1 , z_2 are the coordinate in the two section undulator; $\Delta\Phi_2$ is phase variation due to the interaction with the radiation field (a_{s2}) in the radiator:

$$\Delta\phi_2 = -2k_{s2}k_{u2}a_{u2}\delta_{p2}\,\mathrm{Re}\int_0^{z_2}(z_2 - z_2')\frac{\tilde{a}_{s2}e^{i\phi_2}}{\gamma^2}dz_2' \tag{4}$$

From equations (1)-(4), the optical field evolution equation for linear region can be given by:

$$\begin{aligned}\frac{d\tilde{a}_{s2}}{dz_2} = {} & \frac{8k_{u2}^2\gamma^2\rho_2^3}{k_{s2}a_{u2}\delta_{p2}}\left\langle e^{-i[n\phi_{10}'(\frac{l_1}{2}+N_d\lambda_{u1})+\phi_{02}'z_2]} i^n J_n(n\Delta\xi)\right\rangle \\ & -(2k_{u2}\rho_2)^3\left\langle \frac{\partial}{\partial\phi_{02}'}\int_0^{z_2} J_0(2k_{u2}(z_2 - z_2')\frac{\Delta\gamma_m}{\gamma}) \right. \\ & \left. \times a_{s2}e^{-i\phi_{02}'(z_2-z_2')}dz_2'\right\rangle \\ & +(2k_{u2}\rho_2)^3\left\langle ie^{-i2n\phi_{10}'(\frac{l_1}{2}+N_d\lambda_{u1})}\int_0^{z_2}(z_2 - z_2') \right. \\ & \left. \times J_{2n}(n(\Delta\xi+\Delta\xi'))\tilde{a}_{s2}e^{-i\phi_{02}'(z_2+z_2')}dz_2'\right\rangle\end{aligned} \tag{5}$$

Where

$$\Delta\xi = 4\pi(\frac{N_1}{2} + N_d + \frac{z_2}{n\lambda_{u2}})\frac{\Delta\gamma_m}{\gamma} \tag{6}$$

$\Delta\gamma_m/\gamma$ is the energy modulation induced by interacting with the seed laser:

$$\frac{\Delta\gamma_m}{\gamma} = 4\pi N_1 \frac{a_{u1}\delta_{p1}a_{s1}}{(1+a_{u1}^2)} \tag{7}$$

The radiation power in the radiator can be described by eqs (1)-(4). But from the equations, analytical results are difficult to get without various approximations and simplifications. Therefore, a program is written to give us a numerical calculation.

The angular bracket in eq (1) represents the average over the electron's initial phase (Φ_0) and initial phase velocities (Φ_0'). The program calculates it by means of numerical integration. We assume Φ_0 has a uniform

distribution and Φ_0' has a Gauss distribution (Gaussian beam). The integrate region of Φ_0' is set between $-6\sigma \sim 6\sigma$, σ is the standard deviation. The seed laser is assumed to be a Gaussian wave.

RESULT COMPARE WITH TDA3D

First, to check the program, we make a comparison between the results from the program and from the simulation code TDA3D. Three set of parameters are used in this comparison, including the Shanghai deep ultraviolet FEL source (SDUV) [2], the Accelerator Test Facility at BNL [3] and the Sincrotrone Trieste (ELETTRA) [4].

To simplify the program, we directly use a numerical integration for the process of average Φ_0 and Φ_0'. The energy spread is taken into account but the emittance is ignored to save computation time. To compare the results under same condition, we set the emittance a very small value for TDA3D.

From Figs1-3, the computation by our program gives a good agreement with the simulation by the code TDA3D.

Table 1: Parameters for SDUV

Electron beam parameters for HGHG:
γ:538.117 Peak current : 400*A*
Energy spread : 0.05%
Seed laser beam parameters:
Wavelength: 266*nm*
Input seed power: 16*MW*
Rayleigh range: 0.8*m*
Magnet parameters:
Modulative section
Length : 0.98*m*
Undulator period: 3.5*cm*
Number of periods: 28
Peak magnetic field: 0.8*T*
Dispersive section
Induced dispersion : 0.75 (dψ/dγ)
Radiative section
Undulator Period: 2.5*cm*
Peak magnetic: 0.62*T*

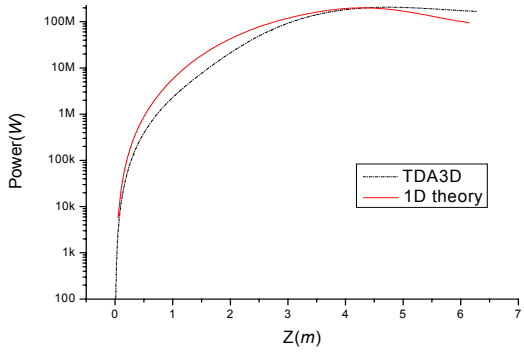

Fig1 Results of the program and TDA3D for SDUV

Table 2: Parameters for the BNL FEL

Electron beam parameters for HGHG:
γ 82
Peak current 110*A*
Energy spread 0.043%
Seed laser beam parameters:
Wavelength 10.6*μm*
Input seed power 0.7*MW*
Rayleigh range 0.76*m*
Magnet parameters:
Modulative section
Length 0.684*m*
Undulator period 7.2*cm*
Number of periods 9
Peak magnetic field 0.202*T*
Dispersive section
Induced dispersion 1.5(dψ/dγ)
Radiative section
Undulator Period 3.3*cm*
Peak magnetic 0.494*T*

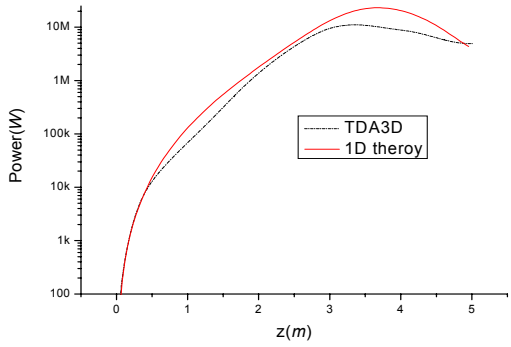

Fig2 Results of the program and TDA3D for the BNL FEL

Table 3: Parameters from ELETTRA

Electron beam parameters for HGHG:	
γ	1956.947
Peak current	600*A*
Energy spread	0.05%
Seed laser beam parameters:	
Wavelength	200*nm*
Input seed power	150*MW*
Rayleigh range	3*m*
Magnet parameters:	
Modulative section	
Length	2.964*m*
Undulator period	5.7*cm*
Number of periods	52
Peak magnetic field	1.35*T*
Dispersive section	
Induced dispersion	0.4(dψ/dγ)
Radiative section	
Undulator Period	4*cm*
Peak magnetic	0.977*T*

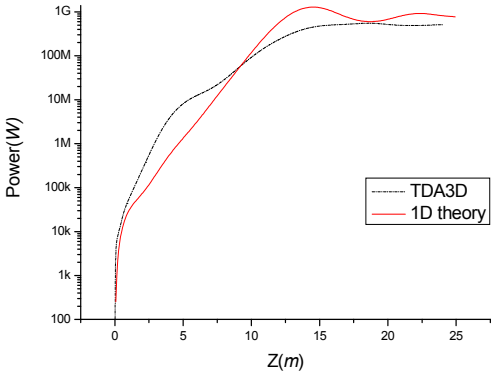

Fig3 Results of the program and TDA3D for ELETTRA

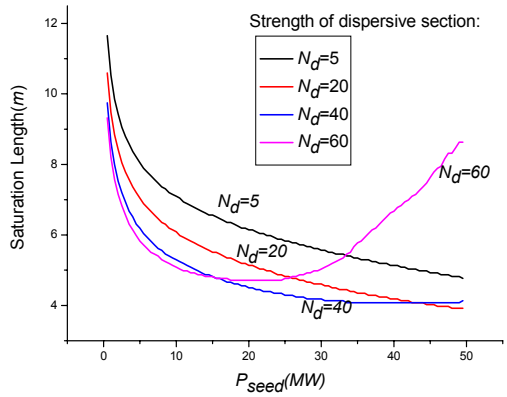

Fig4 Saturation length as function of seed laser power for different N_d

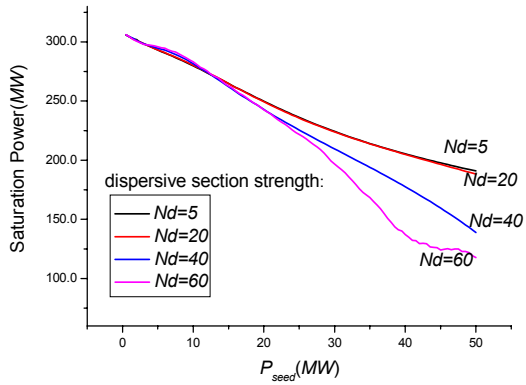

Fig5 Saturation energy as function of seed laser power for different N_d

PARAMETER OPTIMIZING FOR SDUV

The HGHG-FEL experiment involves lots of parameters, which are relevant to the magnet field, the electron beam and the seed laser. Among them only few ones are tuneable during the experiment. The seed laser power and the strength of dispersive section are most important of all.

Energy modulation term $\Delta\gamma_m/\gamma$ is relevant to the seed laser power, it represents an additional energy spread and should be less than the Piece parameter. This gives an upper limit for the seed laser power. For the case considered here, it is about 50*MW*.

Using the parameters listed in Table 1, we calculate the variation of the saturation length and the saturation power with seed laser for different N_d. The results are given in Fig4 and Fig5.

From Fig 4, with increase of the input power, the saturation length drops dramatically initially for low input power and then the descending speed slows down. For a given input power, the saturation length also drops off with increase of N_d. But when N_d becomes sufficiently large, the saturation length ascends instead of dropping. For N_d = 60, saturation length has minimum value when the seed laser power is about 20*MW*.

Fig5 shows, as seed laser power increases, the saturation power decreases. For a given laser power less than 15*MW*, the saturation power has little difference for different N_d.

Therefore, we choose 15*MW* seed laser power and dispersive strength N_d=40 for SDUV. To illustrate this choice clearly, we give the power development along radiator with seed laser to be 15*MW* for different N_d (Fig6) and the power development with N_d=40 for different seed laser power (Fig7) respectively:

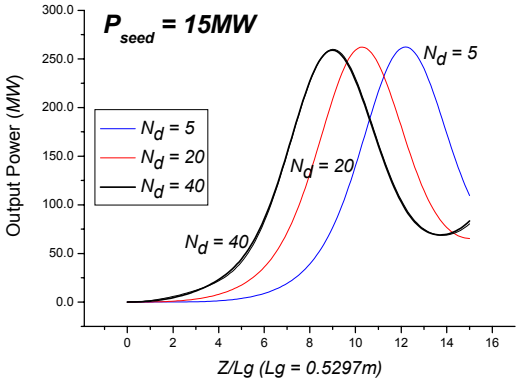

Fig6 Power development along radiator for different N_d (P_{seed} =15MW)

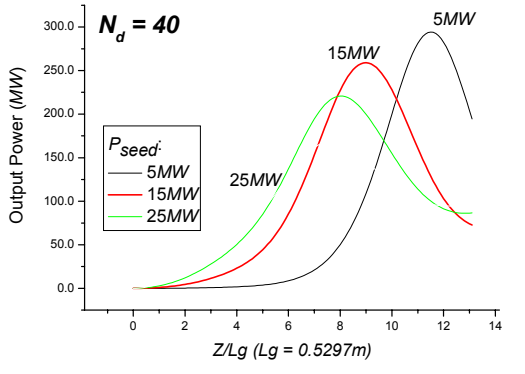

Fig7 Power development along radiator for different seed laser power (N_d=40)

As mentioned above, for N_d = 60, the saturation length reaches a minimum value when laser power is about 20MW (Fig4), Here we make some analysis for the phenomena.

In the right hand side of linear approximate equation (5), the first term denotes the coherent enhancement process, the Bessel function $J_n(n\Delta\xi)$ is important to it; the second term denotes the usual exponential gain process and the energy modulation $\Delta\gamma_m/\gamma$ affects it greatly; the contribution of the third term is small, can be neglect. Therefore, $J_n(n\Delta\xi)$ and $\Delta\gamma_m/\gamma$ should be emphasized to this problem.

It has been mentioned that we constrain the seed laser less than 50MW to guarantee the energy modulation $\Delta\gamma_m/\gamma$ less than the Piece parameter (ρ=0.217%). Therefore the additional energy spread induced by energy modulation is relatively small (at 20MW seed laser, $\Delta\gamma_m/\gamma$ =0.14%) that it shouldn't be the leading reason for the increase of saturation length. Thus the Bessel function $J_n(n\Delta\xi)$ should be dominant for this phenomena. We calculate the variation of Bessel function $J_n(n\Delta\xi)$ with seed laser power for N_d = 60. $\Delta\xi$ denotes the total dispersion that consists of the contribution from the modulator, the dispersive section, as well as the radiator. So it is function of radiator distance z_2. Because the coherent enhancement process is dominant in the first four gain length of the radiator [5], z_2 in $\Delta\xi$ is approximated with its median over $4L_g$ i.e.2 L_g .

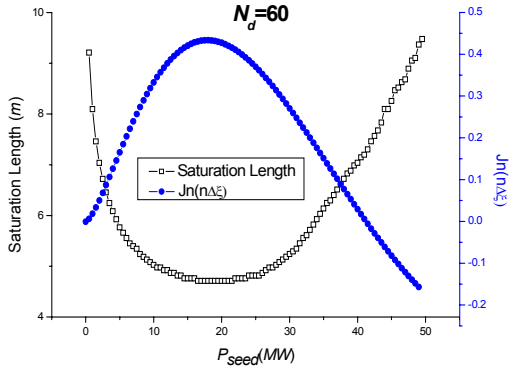

Fig8 Saturation length and $J_n(n\Delta\xi)$ as function of different seed laser power.

From Fig8, we can see that when seed laser power is about 20MW, where the saturation length has the minimum value, the Bessel function $J_n(n\Delta\xi)$ just reaches its maximum value. The coincidence verifies our analysis above.

SUMMARIZING

A program based on a 1D HGHG theory is introduced. First, the program is checked with modified code TDA3D. Then the seed laser power and the dispersive strength are optimized for SDUV. Finally the affect of the seed laser power and the dispersive strength to the saturation length and saturation power are analyzed and discussed. For a further work, we can add in the effect of emittance as an equivalent energy spread. And use a Monte Carlo process for the numerical integration to save the computation time.

REFERENCES

[1] Jia Qika,,"One-dimensional theory of high gain harmonic generation free electron laser" Nucl.Instr. & Meth. A**519**,pp489-492,2004

[2] Z.T.Zhao *et.al,* "The Shanghai High Gain Harmonic Generation DUV Free Electron Laser" Nucl.Instr. & Meth.A528, p591-594, 2004

[3] S.G.Biedron, H.P.Freund, L.-H. Yu, "Parameter analysis for a high-gain harmonic generation FEL using a recently developed 3D polychriomatic code" Nucl.Instr.&Meth. A445. pp95-100,2000

[4] Li Hua Yu, Juhao Wu, "Simulations for the FERMI@ELETTRA proposal to generate 40- and 10-nm coherent radiation using the HGHG scheme" Nucl.Instr.&Meth. A507. pp455-458,2003

[5] Jia Qika,"harmonic amplifer free electron laser" ,this proceeding

IMPROVING SELECTIVITY OF 1D BRAGG RESONATOR USING COUPLING OF PROPAGATING AND TRAPPED WAVES

N.S.Ginzburg #, A.M.Malkin, N.Yu.Peskov, A.S.Sergeev, IAP RAS, Nizhny Novgorod, Russia
A.V.Elzhov, A.K.Kaminsky, A.P.Sergeev, S.N.Sedykh, JINR, Dubna, Russia

Abstract

In the paper FEM oscillator operation based on coupling of quasi cut-off mode with propagating wave, which is amplified by the electron, is considered. The coupling is realized by periodical corrugation of sidewall of microwave system. The cut-off mode provides the feedback while the efficiency in steady-state regime of generation is almost completely determined by the propagating mode, synchronous to the beam. The main advantage of a discussed scheme is provision of higher selectivity over transverse index than traditional scheme of FEM with a Bragg resonator. The novel feedback scheme should be tested on a JINR- IAP FEM as a method of increasing operating frequency.

INTRODUCTION

A number of oscillator schemes based on the interaction between propagating and locked waves are known in microwave electronics. One of them is a scheme of a gyrotron with an electron beam that excites a quasi cut-off mode while the output of radiation is provided by the propagating wave coupled with the locked one via corrugation of the waveguide side walls. Another example is a scheme [1] of CARM or FEM in which the electron beam interacts both with a propagating wave (at the first harmonic) and a quasi-cutoff wave (at the second harmonic). In this case direct coupling of the waves is absent and the waves interact by modulating the beam.

In this paper we discuss one more variant of such a device that uses a beam of electrons interacting only with a propagating wave, and the latter is coupled with a quasi cut-off trapped mode. This coupling is realized by either helical or azimuthally symmetric corrugation. The quasi cut-off mode provides the feedback in the system leading to the self-excitation of the whole system while the efficiency in steady-state regime of generation is determined by the propagating wave, synchronous to the electrons. The main advantage of above scheme is provision of higher selectivity over transverse index than traditional scheme of FEM with Bragg resonators. The novel feedback scheme should be tested at a JINR-IAP FEM as a method of increasing operating frequency for fixed transverse size of interaction space.

MODEL AND BASIC EQUATIONS

Let us consider a model of a FEM oscillator based on coupling of a synchronous wave propagating forward to the direction of the electron beam motion

$$\vec{E} = Re\left(A_+(t,z)\vec{E}_A(r_\perp)e^{-ihz-im_A\varphi}e^{i\omega_c t}\right) \qquad (1a)$$

and a trapped feedback mode

$$\vec{E} = Re\left(B(t)\vec{E}_B(r_\perp)f(z)e^{-im_B\varphi}e^{i\omega_c t}\right) \qquad (1b)$$

Here ω_c is a carrier frequency, which is chosen equal to the eigenfrequency of the cut-off mode, $\vec{E}_{A,B}(r_\perp)$ functions specify the transverse structure of the modes. Assuming that the Q-factor of the cut-off mode is high, one can consider its longitudinal structure $f(z)$ fixed, as the longitudinal structure of the propagating mode $A(z)$ is changed under influence of the electron beam.

Helical corrugation

$$r = r_0 + r_1\cos\left(\bar{h}z + \bar{m}\varphi\right) \qquad (2)$$

(r_0 is a mean radius of the waveguide, $\bar{h} = 2\pi/d$, d and r_1 are the period and the depth of the corrugation correspondingly) under the Bragg conditions

$$h \approx \bar{h},\ \bar{m} = m_1 - m_2 \qquad (3)$$

provides the coupling of the propagating and trapped modes. Dispersion diagrams, showing the coupling of partial waves are presented in Fig.1.

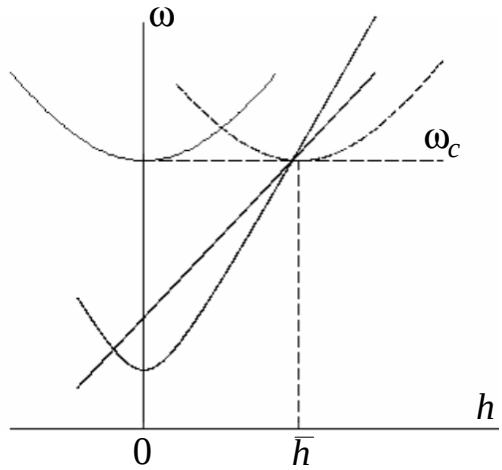

FIGURE 1

Operating frequency is close to eigenfrequency of the trapped mode $\omega_c = \frac{c\nu_B}{r_0}$, hence we obtain a relation on the geometrical parameters

#ginzburg@appl.sci-nnov.ru

$$\frac{2\pi}{d} \approx \frac{\sqrt{\nu_B^2 - \nu_A^2}}{r_0} \quad (4)$$

where $\nu_{A,B}$ are the roots of Bessel functions (or their derivatives) corresponding to the modes of a regular waveguide.

Forward wave $A(z)$ is synchronous to the electron beam moving in the $+z$ direction. Corresponding synchronism condition can be represented as

$$\omega - h v_{||} = \Omega, \quad (5)$$

where Ω is the frequency of oscillations of particles in a spatially periodic wiggler field or in homogenous guiding magnetic field. A system of equations describing both the process of amplification of synchronous wave and its scattering to the trapped mode under assumption that the time Q/ω_c of the changing of the amplitude of the cut-off mode is substantially exceeds the electron transit time can be presented in the form:

$$\frac{\partial \hat{A}}{\partial Z} = i\alpha \hat{B} f(Z) e^{i\delta z} + J \quad (6a)$$

$$\frac{\partial \hat{B}}{\partial \tau} + \frac{1}{2Q}\hat{B} = -i\alpha \int_0^L \hat{A}_+(Z) e^{-i\delta Z} f^*(Z) dZ \quad (6b)$$

where $J = \frac{1}{2\pi}\int_0^{2\pi} e^{-i\theta(Z)} d\theta_0$ is an amplitude of RF current, which is determined by the electron motion equations

$$\frac{\partial^2 \theta}{\partial Z^2} = \mathrm{Re}\left(\hat{A}_+(Z) e^{i\theta}\right) \quad (7)$$

In Eqs. (6), (7) we have used the following dimensionless variables and parameters: $Z = zC\bar{h}$, $\tau = \bar{\omega}t$, $\theta = \bar{\omega}t - hz - \int \Omega \mathrm{d}t$ is electron phase in the field of the synchronous wave, $\hat{A}_\pm = e\kappa\mu A_\pm / mc\omega\gamma_0 C^2$, $\hat{B} = e\kappa\mu B\sqrt{N_A} / mc\gamma_0 C^2 \sqrt{\omega N_B}$,

$$C = \left(\frac{eI_0}{mc^3}\frac{c\lambda^2 K^2 \mu}{4\pi^2 \gamma_0 N_A}\right)^{1/3}$$

is a Pierce parameter, I_0 is an unperturbed beam current, μ is a parameter of inertial bunching, K is a parameter of the coupling between the wave and electrons proportional to the amplitude of the electrons transverse oscillation, α is the coupling coefficient of waves on the Bragg grating which is proportional to the depth of the grating r_1, $N_{A,B}$ are the norms of the propagating and the trapped modes correspondingly, Q is the Q-factor of the trapped mode, $\delta = (\bar{\omega} - \omega_c)/C\bar{\omega}$ is the normalized detuning of the Bragg frequency $\bar{\omega} = \bar{h}c$ from the cut-off frequency.

Initial and boundary conditions of the equations (6), (7) are given by:

$$\hat{A}\big|_{Z=0} = 0, \hat{B}\big|_{\tau=0} = \hat{B}_0,$$

$$\theta\big|_{Z=0} = \theta_0 \in [0, 2\pi), \left.\frac{\partial\theta}{\partial Z}\right|_{Z=0} = \Delta \quad (8)$$

where L is the normalized length of the resonator and Δ is initial detuning of synchronism between the electrons and the wave at the carrier frequency.

Obviously, when the coupling between modes is absent ($\alpha = 0$) Eqs. (6), (7) describe the convective mechanism of instability, and self-excitation of the oscillations is impossible. Thus, the self-excitation of the system is provided by the coupling with the cut-off mode ($\alpha \neq 0$). To obtain starting conditions we linearize the equations of motion. In the assumption that the length of the interaction space is large ($L >> 1$) the main contribution to excitation factor in the right hand of Eq. (6a) related with exponentially growing wave having for $\Delta = 0$ the longitudinal wavenumber $g = -\frac{1}{2} - \frac{i\sqrt{3}}{2}$. As a result for amplitude of trapped wave we get

$$\frac{\partial B}{\partial \tau} + \frac{1}{2Q}B = -\frac{\alpha^2 B}{3} e^{\frac{\sqrt{3}L}{2}} \varphi(\delta, L) \quad (9)$$

$$\varphi(\delta, L) = \left(\frac{1}{\delta - g + \pi/L} - \frac{1}{\delta - g - \pi/L}\right)^2 \mathrm{e}^{-\frac{iL}{2} - i\delta L}$$

The self-excitation condition can be presented in a form:

$$\frac{1}{2Q} < -\frac{\alpha^2}{3} e^{\frac{\sqrt{3}L}{2}} Re\,\varphi(\delta, L) \quad (10)$$

Self-excitation of the generator is possible if the function $\mathrm{Re}\,\varphi(\delta, L)$ presented in Fig.2 is negative.

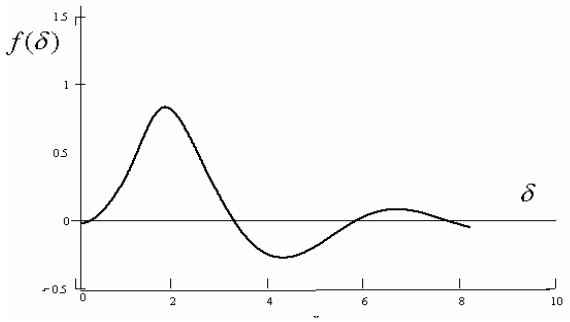

FIGURE 2

RESULTS OF THE SIMULATIONS

Establishment of a stationary regime of generation found from numerical simulation of the nonlinear equations (6), (7) are shown in Fig.3. Efficiency is rather high $\hat{\eta} \sim 3$. It is important to note that in optimal conditions the main part of the energy extracted from electron beam transforms into the radiation of the propagating mode A but not dissipated with the trapped wave B.

According to estimations based on above feedback mechanism it is possible to decrease effective coupling parameter sufficient for an oscillator self-excitation in comparison with traditional Bragg FEM schemes, where a feedback wave possesses rather high group velocity [2]. Correspondingly in oversized microwave system where Bragg conditions are satisfied for a large number of couples of modes with different transverse indices it is possible to provide selective excitation of a single couple consisting of a cut-off mode and operating wave which is amplified by the electron beam. Above method of mode control should be tested in JINR-IAP FEM at Ka band and then used as a method of increasing operating frequency for fixed transverse size.

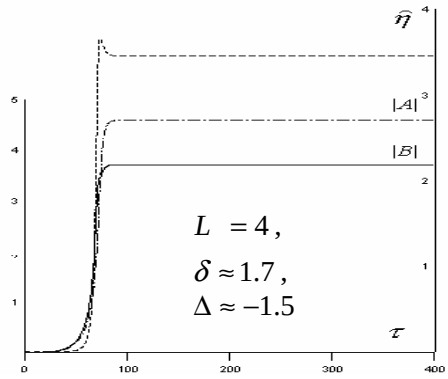

FIGURE 3

REFERENCES

[1] Savilov, A.V. et al., Phys. Rev. E58, 1002 (1998).
[2] Bratman V.L., Denisov G.G., Ginzburg N.S., Petelin M.I., *IEEE J. Quant. Electr.* QE-19, 282 (1983).

ANALYTIC MODEL OF HARMONIC GENERATION IN THE LOW-GAIN FEL REGIME*

G. Penn, M. Reinsch, J.S. Wurtele†, LBNL, Berkeley, CA 94720, USA

Abstract

Harmonic generation using free electron lasers (FELs) requires two undulators: the first uses a seed laser to modulate the energy of the electron beam; the second undulator uses the subsequently bunched beam to radiate at a higher harmonic. These processes are currently evaluated using extensive calculations or simulation codes which can be slow to evaluate and difficult to set up. We describe a simple algorithm to predict the output of a harmonic generation beamline in the low-gain regime based on trial functions for the output radiation. Full three-dimensional effects are included. This method has been implemented as a Mathematica script which runs rapidly and can be generalized to include effects such as asymmetric beams and misalignments. This method is compared with simulation results using the FEL code GENESIS, both for single stages of harmonic generation and for the LUX project, a design concept for an ultrafast X-ray facility, where multiple stages upshift the input laser frequency by factors of up to 200.

INTRODUCTION

There is growing interest in using seeded electron beams to drive a free electron laser (FEL), rather than relying on amplification of noise. This allows for controlled timing and pulse structure. The seed can be a laser field which is then amplified by the FEL instability, or it can be an initial current variation (bunching) in the electron beam. The second method allows for harmonic generation, where the output wavelength can be at a harmonic of the initial perturbation [1]. The possible use of multiple stages of such harmonic generation is an area of active study, for example in the LUX [2] project, which is an R&D project in ultrafast X-ray production. Here, an analytic model for predicting and optimizing the FEL output from an idealized, prebunched electron beam is presented, with emphasis on harmonic generation. While previous examinations of seeded electron beams either assume the laser field structure in advance [3, 4], or rely on summations over single-particle radiation fields [5], this formalism uses a trial-function approach to obtain simple analytic prescriptions for determining the output laser field. These expressions only apply to FELs in the low-gain regime, but include the full 3-dimensional dynamics. A set of scripts implemented in Mathematica allows for rapid calculation of the dominant mode produced by a seeded electron beam, as well as a means to rapidly optimize FEL and beam parameters.

* Work supported by the Director, Office of Science, U.S. Dept. of Energy under Contract DE-AC03-76SF0098.

† also at UC Berkeley, Berkeley, CA 94720, USA

ANALYTIC MODEL

The output from the radiating undulator, or radiator, is here approximated as a simple Gaussian mode, but is otherwise kept arbitrary:

$$E_y = \Re\mathrm{e}\; E_0 \mathrm{e}^{\mathrm{i}\Phi_0} G(x,y,s)\exp(\mathrm{i}ks - \mathrm{i}\omega t), \qquad (1)$$

where

$$G(x,y,s) \equiv \frac{Z_R}{Z_R + \mathrm{i}(s-s_0)} \exp\left[-\frac{1}{2}\frac{k(x^2+y^2)}{Z_R+\mathrm{i}(s-s_0)}\right] \qquad (2)$$

characterizes the structure of the mode. The laser wavelength is $\lambda = 2\pi/k$, the frequency $\omega = ck$, and Z_R is the Rayleigh length. The longitudinal coordinate s represents the position along the undulator, and at $s = s_0$ the laser is at its waist with spot size $(Z_R/2k)^{1/2}$. It is possible to generalize this to include higher-order transverse modes. Note that this field only characterizes the output from the radiator, and so will be described by vacuum field solutions.

The particle motion due to the undulator is

$$v_u \simeq \frac{\sqrt{2}\,c}{\gamma} a_u \sin(k_u s), \qquad (3)$$

where the undulator period is $\lambda_u = 2\pi/k_u$, the normalized field strength is $a_u = eB_0/mck_u$, and B_0 is the RMS dipole field on axis from the undulator. The dipole field on axis is taken to be $B_x = -\sqrt{2}\,B_0\cos(k_u s)$. For a single particle, the forward motion satisfies

$$t = t(s=0) + \frac{s}{v_z} - \frac{a_u^2}{4ck_u\gamma^2}\sin(2k_u s), \qquad (4)$$

where v_z is the average forward velocity, and the last term arises from the motion in a planar undulator.

The change in energy of a particle is given by

$$\begin{aligned}\frac{\mathrm{d}\gamma}{\mathrm{d}s} &= -\frac{e}{mc^2}\frac{E_y v_u}{v_z} \qquad (5)\\ &\simeq -\Re\mathrm{e}\; k a_L G(x,y,s)\mathrm{e}^{\mathrm{i}(ks-\omega t)}\frac{\sqrt{2}\,a_u}{\gamma}\sin(k_u s),\end{aligned}$$

where the normalized (complex-valued) laser field is

$$a_L = \frac{eE_0}{mc^2 k}\mathrm{e}^{\mathrm{i}\Phi_0}. \qquad (6)$$

Averaging over an undulator period yields

$$\frac{\mathrm{d}\gamma}{\mathrm{d}s} = -\Im\mathrm{m}\;\frac{\sqrt{2}\,k}{2\gamma} a_u a_L G(x,y,s)\mathbb{JJ}(\xi)\mathrm{e}^{\mathrm{i}\Psi}, \qquad (7)$$

where $\mathrm{JJ}(\xi) \equiv J_0(\xi) - J_1(\xi)$, $\xi \equiv ka_u^2/4k_u\gamma^2$, and the ponderomotive phase $\Psi \equiv ks - \omega t + k_u s$. To leading order in $1/\gamma^2$, this phase evolves according to

$$\frac{\mathrm{d}\Psi}{\mathrm{d}s} = k_u + k(1 - c/v_z) \simeq k_u - \frac{k}{2}(1/\gamma^2 + v_\perp^2/c^2), \quad (8)$$

where $v_\perp^2$ is also averaged over an undulator period.

The undulator field increases with strength off-axis. For an undulator with equal focusing in both planes, and taking into account the slight transverse dependence of a_u in Eq. (3), the average of $v_\perp^2/c^2$ over an undulator period is roughly given by

$$\frac{v_\perp^2}{c^2} = \frac{a_u^2}{\gamma^2} + \frac{2(J_x + J_y)}{\gamma\beta_u}, \quad (9)$$

where $\beta_u \equiv \sqrt{2}\gamma/a_u k_u$ is the matched beta function for the undulator, and J_x, J_y are the transverse actions for this value of the beta function:

$$J_x \equiv \frac{\gamma}{2}\left[\frac{x^2}{\beta_u} + \beta_u\left(\frac{\mathrm{d}x}{\mathrm{d}s}\right)^2\right], \quad (10)$$

and similarly for J_y. If external focusing is used, however, then J_x and J_y will no longer be constants of the motion.

Now we can expand out the equation for Ψ,

$$\begin{aligned}\frac{\mathrm{d}\Psi}{\mathrm{d}s} \;\simeq\; & k_u\Big[-\frac{\delta k}{k_r} + 2\frac{\gamma-\gamma_r}{\gamma_r} - \frac{2a_u\delta a_u}{1+a_u^2} \\ & -\sqrt{2}\,\frac{a_u}{1+a_u^2}k_u(J_x+J_y)\Big], \quad (11)\end{aligned}$$

where we define $k = k_r + \delta k$, and the resonant wave vector is

$$k_r \equiv \frac{2\gamma_r^2}{1+a_u^2}k_u. \quad (12)$$

The detuning can be expressed equivalently in terms of δk or as a shift in undulator strength δa_u. Using the resonance condition, the argument of the Bessel functions in Eq. (7) is $\xi = (1/2)a_u^2/(1+a_u^2)$.

Finally, there is the expression for the laser field, assuming the power given up by the electron beam goes into a single mode. For the mode defined by Eq. (2), the power is

$$P_L = \frac{1}{2}c\epsilon_0 E_0^2 \pi\frac{Z_R}{k} = \frac{1}{8}kZ_R\frac{mc^3}{r_e}|a_L|^2, \quad (13)$$

where $r_e = e^2/(4\pi\epsilon_0 mc^2)$. By conservation of energy, the change in power is given by $dP_L/ds = -(I/e)mc^2\langle(d\gamma/ds)\rangle$, where I is the peak current and $\langle d\gamma/ds\rangle \equiv \int \mathrm{d}\bar{X} f(\bar{X})(d\gamma/ds)$. The term $\bar{X}$ is used as a shorthand to represent the full set of 6D phase space variables, and the distribution function $f(\bar{X})$ is normalized so that $\int \mathrm{d}\bar{X} f(\bar{X}) = 1$. Noting that P_L scales as $|a_L|^2$, we have

$$\frac{\mathrm{d}|a_L|}{\mathrm{d}s} = \frac{I}{\mathrm{I_A}}\frac{2\sqrt{2}\,a_u}{\gamma Z_R}\mathrm{JJ}(\xi)\,\Im\mathrm{m}\left\langle \mathrm{e}^{\mathrm{i}\Phi_0}G(x,y,s)\mathrm{e}^{\mathrm{i}\Psi}\right\rangle, \quad (14)$$

where $\mathrm{I_A} \equiv 4\pi\epsilon_0 mc^3/e \simeq 17$ kA. This is the electric field generated by the net bunching of the electron beam, and we wish to generalize this to include the possibility of having no seed pulse, but a pre-bunched beam. Using the relation that $d|a_L|/ds = \Re\mathrm{e}(\mathrm{e}^{-\mathrm{i}\Phi_0}da_L/ds)$, Eq. (14) can be generalized to

$$\frac{\mathrm{d}a_L}{\mathrm{d}s} = \mathrm{i}\frac{I}{\mathrm{I_A}}\frac{2\sqrt{2}\,a_u}{\gamma Z_R}\mathrm{JJ}(\xi)\left\langle G^*(x,y,s)\mathrm{e}^{-i\Psi}\right\rangle. \quad (15)$$

The above average is a correction to the usual bunching parameter, $b \equiv \langle\exp(-\mathrm{i}\Psi)\rangle$. The generalized bunching parameter will be defined as

$$B(s) \equiv \left\langle G^*(x,y,s)\mathrm{e}^{-\mathrm{i}\Psi}\right\rangle. \quad (16)$$

Harmonic generation, for example in the LUX design concept, uses a seed laser to generate an energy modulation in one undulator, which is then converted into microbunching by means of a chicane. The additional slippage which results from the chicane is characterized by the parameter R_{56}, defined by $c\Delta t = R_{56}(\gamma-\gamma_0)/\gamma_0$. Following this, the bunched beam produces radiation while passing through a second undulator. Because the bunching includes Fourier components at harmonics of the initial laser seed, this second, radiating undulator can be tuned to a higher harmonic of the laser seed. Here, we consider a simplified case where the modulator applies an energy modulation which depends solely on the phase Ψ of the electrons. The energy distribution after modulation then takes the form

$$f(\bar{X}) \propto H[(\gamma-\gamma_0-\kappa_x J_x-\kappa_y J_y+\gamma_M\sin\Psi)/\Delta_\gamma]. \quad (17)$$

We will consider both Gaussian and uniform energy profiles, where Δ_γ is equal to the RMS energy spread and maximum deviation, respectively. This energy distribution includes the possibility for "beam conditioning", where there is a correlation between energy and transverse amplitude. The transverse component of the distribution function is $\exp(-J_x/\epsilon_x - J_y/\epsilon_y)$, where ϵ_x is the normalized emittance in the x-plane. The wave vector in the following radiator will be a harmonic, n, of the resonant wave vector in the modulator. Thus, we will want to look at the quantity $\exp(-\mathrm{i}n\Psi)$ instead of the bunching at the first harmonic.

After the modulator, the beam passes through a dispersive section with a resulting phase shift $\Delta\Psi = k_0 R_{56}(\gamma - \gamma_0)/\gamma_0$, where k_0 is the wave vector corresponding to the modulator. After this dispersive section, the higher harmonic bunching will be given by

$$|\langle\mathrm{e}^{-\mathrm{i}n\Psi}\rangle| = J_n(kR_{56}\gamma_M/\gamma_0)F_\gamma(kR_{56}\Delta_\gamma/\gamma_0), \quad (18)$$

where $k = nk_0$ is the wave vector of the higher harmonic. The function F_γ depends on the form of the energy distribution:

$$F_\gamma(x) = \begin{cases} \exp(-x^2/2), & \text{Gaussian} \\ (\sin x)/x, & \text{uniform.}\end{cases} \quad (19)$$

The averages over particle energy and ponderomotive phase within the radiator yield the same F_γ and Bessel

function as above for the initial bunching parameter, but with kR_{56} replaced with $kR_{56} + 2k_u s$. In addition to $G^*(x, y, s)$, there are extra phase terms which depend on transverse coordinates which must be considered. Below, we assume that the beam has the properly matched beta function for the undulator. The final result for the generalized bunching at the higher harmonic is

$$\begin{aligned} B(s) = & \exp\left[\mathrm{i}k_u s\left(\frac{\delta k}{k_r} - 2\frac{\gamma_0 - \gamma_r}{\gamma_r}\right)\right] \\ \times & \quad J_n\left[(kR_{56} + 2k_u s)\frac{\gamma_M}{\gamma_0}\right] \\ \times & \quad F_\gamma\left[(kR_{56} + 2k_u s)\frac{\Delta_\gamma}{\gamma_0}\right]\frac{Z_R}{Z_R - \mathrm{i}(s - s_0)} \\ \times & \quad F_\epsilon(\epsilon_x, c_x(s), s)F_\epsilon(\epsilon_y, c_y(s), s), \end{aligned} \tag{20}$$

where

$$\begin{aligned} F_\epsilon(\epsilon, c, s) \quad = \quad & (1 - \mathrm{i}c\epsilon)^{-1/2} \\ & \times \left(1 - \mathrm{i}c\epsilon + \frac{k_r\beta_u\epsilon/\gamma_0}{Z_R - \mathrm{i}(s - s_0)}\right)^{-1/2}. \end{aligned} \tag{21}$$

The quantity

$$c_x(s) \equiv 2k_u s\left(\frac{\sqrt{2}}{2}k_u\frac{a_u}{1 + a_u^2} - \frac{\kappa_x}{\gamma_r}\right) - \frac{\kappa_x}{\gamma_r}kR_{56} \tag{22}$$

is related to the slippage due to transverse emittance, and similarly for $c_y(s)$. If it is the strength of the undulator which is being tuned, the detuning term $\delta k/k_r$ can be replaced with $2a_u\delta a_u/(1 + a_u^2)$.

The laser field at the end of the radiator is then given by

$$a_L = \mathrm{i}\frac{I}{\mathrm{I_A}}\frac{2\sqrt{2}\,a_u}{\gamma Z_R}\mathrm{JJ}(\xi)\int_0^L B(s)\mathrm{d}s, \tag{23}$$

and the laser power is given by Eq. (13).

TRIAL FUNCTIONS

The result is still not fully defined because Z_R and s_0 are free parameters. In general, after fixing Z_R and s_0, any radiation field can be described using a sum of normal modes, but here we are restricting attention to a single, Gaussian mode. Because the exact result will include the power contained within all these modes, the analytic result is expected to always fall below the correct value. This suggests varying the free parameters to maximize the output power, yielding a greatest lower bound to the correct result.

This method is essentially a trial function approach, and any trial function which is a valid vacuum laser field can be used. The closer the trial function is to the exact result, the more accurate this estimate for the power will be. Furthermore, the prediction for the laser power is expected to be second-order accurate compared to the optimized trial function; in other words, even a poor approximation to the laser field can result in a good estimate for the output power. In the configurations being considered, a pure Gaussian mode is expected to be a reasonable approximation to the FEL output except in the emittance-dominated regime, $\epsilon/\gamma_0 \gtrsim \lambda/(4\pi)$. In this paper, only a simplified FEL configuration is considered, but the trial function method applies to more general cases as well.

The resulting integrals are simple enough to implement as a Mathematica script, which allows for rapid optimization. Because the optimization procedure is to maximize the output power, any additional constraints (undulator field, R_{56}, or energy modulation) can be simultaneously optimized to obtain the largest possible output power. Thus any optimizations performed on the beamline can occur simultaneously with the trial function optimization for Z_R and s_0, greatly reducing the computational time required.

SIMULATION RESULTS

FEL simulations using the GENESIS code [6] have been compared with this analytic theory. Two cases are considered, the first stage of a cascade which converts 200 nm wavelength to 50 nm, and the final stage which converts 3.13 nm wavelength to 1.04 nm. All sections are assumed to use planar undulators.

For a given set of trial functions, the analytic model finds the closest fit to the actual radiation, and predicts a lower bound on the total output power. Even if the trial function does not accurately represent the radiation field produced by the FEL, the prediction for the output power may still serve as a good estimate.

Table 1: Comparison between analytic model and simulations using GENESIS for two case studies.

Case	Results	Analytic Theory	GENESIS: $M^2 \equiv 1$	GENESIS: fit M^2
50 nm	P_L (MW)	130.3	134.2	134.2
	Z_R (m)	1.12	0.94	0.97
	s_0 (m)	1.20	1.19	1.21
	M^2	$\equiv 1$	$\equiv 1$	1.04
1.04 nm	P_L (MW)	35.1	39.0	39.0
	Z_R (m)	52.7	49.0	33.0
	s_0 (m)	-10.4	-14.6	0.73
	M^2	$\equiv 1$	$\equiv 1$	1.72

The electron beam parameters are: $I = 500$ A, $\gamma_0 = 6067$, and the normalized emittances are $\epsilon_x = \epsilon_y = 2$ μm. Results for the two cases considered are given in Table 1. The transverse mode structure of the output radiation is described in terms of the M^2 parameter, which is the ratio of the emittance of the laser to the minimum emittance, $\lambda/4\pi$. This parameter can also be described as the ratio of the idealized Rayleigh length for the given waist diameter to the observed Rayleigh length. In terms of power flux, the RMS width of the laser at the waist is $(\lambda M^2 Z_R/4\pi)^{1/2}$. For the first stage, producing radiation at 50 nm by going to

the fourth harmonic, the energy modulation is $\gamma_M = 2.68$, and the chicane is set to an optimized value of $R_{56} = 92$ μm. The radiating undulator has an 8 cm period and is 2.4 m long. The electron beam is taken to be matched to the undulator, with $\beta = 16.28$ m. The resonant undulator strength is $a_u = 6.709$, but optimal performance occurs at $a_u = 6.686$. An analysis of the GENESIS results show that 7.8 MW of power lies outside the predicted Gaussian mode. The analytic theory underestimates the total power by 3.9 MW, a relative error of 3%. For the final stage, producing radiation at 1.04 nm by going to the third harmonic, the energy modulation is $\gamma_M = 1.10$, and the idealized chicane uses $R_{56} = 3.2$ μm. The radiating undulator has a 2.8 cm period and is 8.4 m long. The electron beam is taken to be matched to the undulator, with $\beta = 29.00$ m. The resonant undulator strength is $a_u = 1.3186$, but optimal performance occurs at $a_u = 1.3181$. In the simulation results, 2.3 MW of power lies outside the predicted Gaussian mode. The analytic theory underestimates the total power by 3.9 MW, a relative error of 10%. A generalization to trial functions having two or more transverse modes would be desirable for more accurate results.

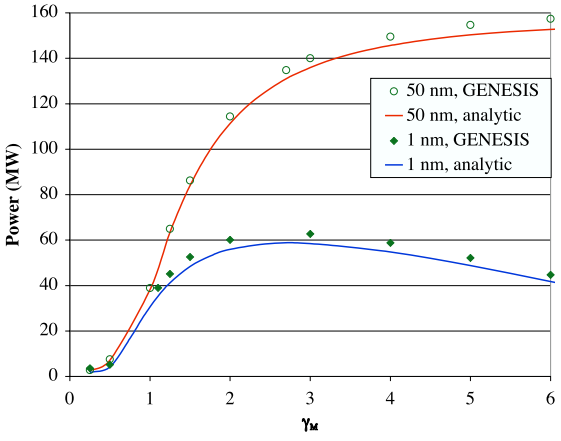

Figure 1: Comparison of analytic theory with simulations using GENESIS. Results for harmonic generation at 50 nm and 1.04 nm, as the energy modulation γ_M is varied.

The dependence of the output radiation on the energy modulation is shown in Figure 1, and also shows good agreement between the analytic model and numerical simulations. The value of R_{56} is re-optimized for each case. For short wavelengths, FEL performance is more sensitive to the energy spread, as slippage along the length of the undulator leads to debunching of the electron beam. The optimal power of 60 MW can only be increased either by using a different undulator design or by lowering the harmonic number.

The agreement between theory and simulations only falters for the 1.04 nm case, when the magnetic fields are tuned below the resonant value, as shown in Figure 2. Far from resonance, there is roughly 5 MW of power in

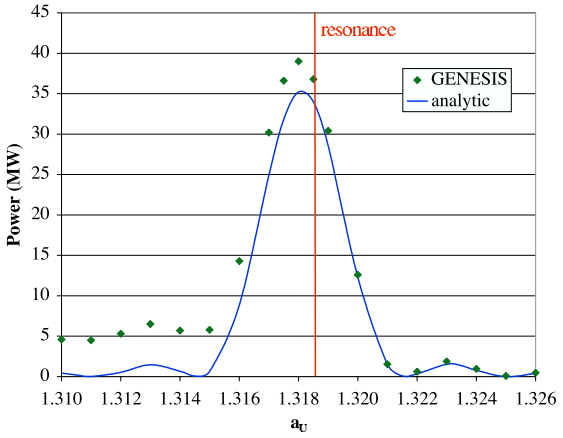

Figure 2: Comparison of analytic theory with simulations using GENESIS. Results for harmonic generation at 1.04 nm, as dipole field strength (a_u) is varied.

the form of higher-order transverse modes, with values of $M^2 \sim 10$. This radiation is generated by particles having large transverse amplitude, which also move forward more slowly. When the magnetic field is too high these higher-order modes do not appear, because there are no particles moving fast enough to be in resonance. For earlier stages which are not emittance-limited, the analytic calculations are in much closer agreement with numerical simulations.

Other sources of error are the nonlinearity of the interaction, where the FEL instability or trapping may increase the output power; the neglect of betatron motion and betatron phase mixing, which may decrease the output power; and an oversimplification of the geometry of each stage of harmonic generation. In the above examples, the FEL instability is unimportant. For example, in the 1.04 nm case, simulations at low beam current, when the FEL gain length is much longer than the total length of the system, would scale to a total output power of 38.9 MW at 500 A. However, for larger values of the applied energy modulation, nonlinear effects become important for reducing particle slippage and maintaining a large bunching parameter.

REFERENCES

[1] L.H. Yu et al., Science **289** (2000) 932–934.

[2] W.A. Barry et al., Report LBNL-51766, LBNL (2002).

[3] M. Arbel et al., Nucl. Instr. Methods A **445** (2000) 247–252.

[4] L.H. Yu and J. Wu, Nucl. Instr. Methods A **483** (2002) 493–498.

[5] V.N. Litvinenko, Nucl. Instr. Methods A **359** (1995) 50–56.

[6] S. Reiche, Nucl. Instr. Methods A **429** (1999) 243–248.

SHORT RAYLEIGH LENGTH FREE ELECTRON LASER SIMULATIONS IN EXPANDING COORDINATES

R. L. Armstead, W.B. Colson, and J. Blau
Physics Department, Naval Postgraduate School
333 Dyer Road, Monterey, CA 93943

Abstract

For compact short-Rayleigh length free electron lasers (FELs), the area of the optical beam can be thousands of times greater at the mirrors than at the beam waist. A fixed numerical grid of sufficient resolution to represent the narrow mode at the waist and the broad mode at the mirrors would be prohibitively large. To accommodate this extreme change of scale with no loss of information, we employ a coordinate system that expands with the diffracting optical mode. The simulation using the new expanding coordinates has been validated by comparison to analytical cold-cavity theory, and is now used to simulate short-Rayleigh length FELs.

INTRODUCTION

A short-Rayleigh length optical cavity may give several advantages for a high-power FEL, including reduced mirror damage and improved beam quality [1]. However, such a design poses difficult numerical problems. Since the mode area expands within the cavity many thousands of times, a very large grid is required to accurately represent the mode at both the waist and the mirrors. For example, assume a Rayleigh length of $z_0 = 0.1$ and a cavity length of $S = 30$, both normalized to the undulator length, L. Then the mode radius will expand by a factor of $(1 + (S/2)^2/z_0^2)^{1/2} = 150$. If we assume 100 gridpoints in each dimension are needed to accurately represent the mode at the waist, then 15000 gridpoints are needed at the mirrors. A two-dimensional complex, double-precision array of that size requires about 4 GB of RAM, beyond the limits of many computers. Furthermore, the simulation runtime increases as the square of the number of gridpoints. For the typical parameters given above, we estimate it would require about 4 hours for each pass through the optical cavity, running a three-dimensional simulation in (x, y, t) on a 2 GHz IBM G5 processor. For some sets of parameters, several hundred passes are needed to reach steady-state operation, implying that the program would take many weeks to run. Furthermore, if we wish to include a 4th dimension in the simulation (z) to study longitudinal modes and pulse effects, we would need at least 100 slices in the z direction. In addition, steady-state in 4D requires thousands of passes. The memory requirements would then grow to 100's of GB and the simulation runtime would increase to many years. One solution to this numerical problem is to abandon a fixed Cartesian grid, and instead use a coordinate system that expands with the diffracting optical mode. This approach [2], [3] is explained below for the FEL.

PARAXIAL EQUATION

As usual, the equation to be solved for the complex electric field a is the paraxial wave equation expressed in dimensionless coordinates,

$$[\partial_x^2 + \partial_y^2 - (4/i)\partial_\tau]a(x, y, \tau) = 0. \quad (1)$$

The dimensionless coordinates $x, y,$ and τ are, in terms of the dimensioned coordinates $X, Y,$ and Z: $x \equiv X(\pi/\lambda L)^{1/2}, y \equiv Y(\pi/\lambda L)^{1/2}$, and $\tau \equiv Z/L$,where L is some characteristic length (which in FEL simulations will be the undulator length), and λ is the optical wavelength. The paraxial equation follows from the usual four-dimensional second-order partial differential wave equation on the assumption that deviations from plane-wave behavior in the longitudinal (Z axis) direction are slow, a reasonable condition for a laser. Eq. 1 has been studied extensively [4], and is solved reliably by the application of an FFT, except for the numerical difficulty of the expanding beam due to diffraction.

Adopting the convention that a subscript in $x, y,$ or τ stands for the derivative with respect to that variable, Eq. 1 becomes

$$a_{xx} + a_{yy} - (4/i)a_\tau = 0. \quad (2)$$

TRANSFORMING THE COORDINATES

In order to see the motivation for a coordinate transformation, consider the exact fundamental-mode solution to Eq. 2:

$$a(x, y, \tau) = a_0(\pi z_0/A)^{1/2} \exp(-\pi r^2/A)e^{i\phi}, \quad (3)$$

where z_0 is the dimensionless Rayleigh length Z_0/L, and where the dimensionless beam area is

$$A = \pi z_0[1 + \tau^2/z_0^2], \quad (4)$$

so that the $1/e$ beam radius is

$$w = w_0[1 + \tau^2/(z_0)^2]^{1/2}, \quad (5)$$

where $w_0 = {z_0}^{1/2}$, and

$$\phi(r, \tau) = -\arctan(\tau/z_0) + \pi r^2\tau/(Az_0). \quad (6)$$

Thus, for the case that $\tau \gg z_0$, $A \approx \pi\tau^2/z_0$ and $\phi \approx -\pi/2 + r^2/\tau$, so that

$$a(r,\tau) \approx a_0(z_0/\tau)\exp(-r^2 z_0/\tau^2)\exp(ir^2/\tau) \quad (7)$$

to within a constant phase factor. It is clear from Eq. 7 that for large τ the radius of the beam expands linearly with τ, which suggests that we define the new "expanding" independent variables by

$$x' \equiv z_0^{1/2} x/\tau, \quad (8)$$

$$y' \equiv z_0^{1/2} y/\tau, \quad (9)$$

and a new dependent variable $v(x', y', \tau')$ such that

$$a(x,y,\tau) = (1/\tau)v(x',y',\tau')\exp(ir^2/\tau), \quad (10)$$

where $r^2 \equiv x^2 + y^2$.

The phase factor $\exp(ir^2/\tau)$ characterizing an expanding spherical wave, as well as the spherical amplitude expansion factor $1/\tau$, are explicitly factored out from a, so the remaining function v has to account only for the small diffraction effects not contained in the solution for the Gaussian fundamental mode. In addition, the inverse dependence of x' and y' on τ means that the dimensions of the primed numerical grid decrease with increasing τ, i.e. in precisely the region where the physical beam (represented on the unprimed grid x and y) becomes large by diffraction.

Then some algebra, outlined below, shows that $v(x', y', \tau')$ itself does indeed satisfy exactly the same paraxial wave equation as does $a(x, y, \tau)$.

First, evaluate $a_x = (v_{x'}x'_x/\tau + i2xv/\tau^2)\exp(ir^2/\tau)$, by the chain rule applied to Eq. 10. But $x'_x = z_0^{1/2}/\tau$ by Eq. 8. So $a_x = (v_{x'}z_0^{1/2}/\tau^2 + i2xv/\tau^2)\exp(ir^2/\tau)$. One more derivative with respect to x yields

$$a_{xx} = \exp(ir^2/\tau)[v_{x'x'}z_0/\tau^3 + i4v_{x'}z_0^{1/2}x/\tau^3 \quad (11)$$
$$+i2v/\tau^2 - 4vx^2/\tau^3].$$

In the same fashion, we find that

$$a_{yy} = \exp(ir^2/\tau)[v_{y'y'}z_0/\tau^3 + i4v_{y'}z_0^{1/2}y/\tau^3 \quad (12)$$
$$+i2v/\tau^2 - 4vy^2/\tau^3].$$

Furthermore,

$$a_\tau = \exp(ir^2/\tau)[v_{x'}x'_\tau/\tau + v_{y'}y'_\tau/\tau + v_{\tau'}\tau'_\tau/\tau \quad (13)$$
$$-v/\tau^2 - ir^2v/\tau^3].$$

Substituting Eqs. 11, 12, and 13 into Eq. 2 yields

$$v_{x'x'} + v_{y'y'} = 4\tau^2 v_{\tau'}\tau'_\tau/(iz_0). \quad (14)$$

This can be written as the paraxial wave equation in the primed coordinates,

$$v_{x'x'} + v_{y'y'} - (4/i)v_{\tau'} = 0, \quad (15)$$

if $\tau'_\tau = z_0/\tau^2$. Integrating this first order differential equation for τ' with respect to τ yields

$$\tau' = z_0[1/\tau_1 - 1/\tau], \quad (16)$$

where the constant of integration is written z_0/τ_1 so that $\tau' = 0$ when $\tau = \tau_1$. The well-understood FFT method may then be applied to Eq. 15, without the numerical difficulty of following a rapidly-expanding wavefront.

The solution for the optical field a in the near field ($\tau < \tau_1$) is calculated in the conventional coordinates x, y, and τ, then connected (using Eq. 10) onto the expanding-coordinate solution in the far field ($\tau \geq \tau_1$). Remember that $\tau = \tau_1$ corresponds to $\tau' = 0$.

Notice that for the special case of the fundamental mode in expanding coordinates,

$$v(r',\tau') = (a_0 z_0)\exp[-(r')^2], \quad (17)$$

which is independent of τ'. This trivial outcome will not apply when the fundamental mode is modified by the presence of electrons in the FEL, but does provide an opportunity to compare a numerical simulation to an exact solution. In the simulation of an actual FEL, there may be a mixture of modes rather than just the fundamental mode, but the transformation can handle the general case as well with no modification.

The schematic representations in Fig. 1 and Fig. 2 show $|a|$ expanding as a function of τ and $|v|$ as a function of τ' respectively, to illustrate the effect of the coordinate transformation. In an actual numerical simulation, we calculate $|a|$ in the region $\tau = 0$ to $\tau = \tau_1$ in (x, y, τ), then switch to the primed system (x', y', τ') to calculate $|v|$ for $\tau > \tau_1$, corresponding to $\tau' > 0$. Then we apply the transformation to recover $a(\tau)$ for $\tau > \tau_1$. The dashed lines in the diagrams remind us of the relative size of the integration steps in the primed and unprimed systems.

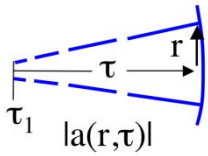

Figure 1: Contours of constant optical field amplitude $|a|$ as a function of Cartesian coordinates (r, τ) for free-space diffraction of a spherical wavefront.

In terms of the numerical integration using the expanding coordinates, constant time steps $\Delta\tau'$, correspond to time steps in the unprimed coordinates which increase quadratically with τ, so that $\Delta\tau = \tau^2\Delta\tau'/z_0$. This is a consequence of the Eq. 16, and the effect shows clearly in the progression of integration "slice" size in Fig. 3.

FREE-SPACE DIFFRACTION

The upper left picture in Fig. 3 shows a cross-section of the optical field amplitude $|a|$ in terms of the unprimed co-

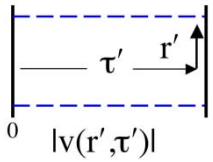

Figure 2: Contours of constant virtual field amplitude $|v|$ as a function of expanding coordinates (r', τ') for free-space diffraction of a spherical wavefront.

ordinates (x, τ) as τ goes from 0 to 3 with $\tau_1 = 1$, for the propagation of a spherical wavefront in free space. The color scale, shown in the lower-right, goes from blue (small amplitude) to yellow (large amplitude). Integration for τ between 0 and 1 is performed in the conventional coordinate τ in ten steps with $\Delta\tau = 0.1$. The interval $\tau = 1 \rightarrow 3$ corresponds to expanding coordinate $\tau' = 0 \rightarrow 0.2$. This is also integrated in ten equal steps, with $\Delta\tau' = 0.02$, and is displayed in the lower picture as the "virtual" field amplitude $|v|$ in the primed coordinates. In this calculation the Rayleigh length $z_0 = 0.3$ corresponds to initial waist size $w_0 = z_0^{1/2} \approx 0.55$. Notice that the virtual field amplitude $|v|$ appears not to change with τ' for the fundamental mode, which is precisely what Eq. 17 predicts. Also note that, compared to τ, the range of τ' is much diminished by the transformation Eq. 16. The optical field a for $\tau \geq \tau_1 = 1$ is then given in terms of the transformation Eqs. 8, 9, 16, and 10. The ratio of the beam area at $\tau = 3$ to the beam area at the waist is 100.

The right-hand pictures in Fig. 3 are both end-on cross-sections at $\tau = 3$. The upper is the optical field amplitude $|a(x, y)|$, and the lower is the virtual field amplitude $|v(x', y')|$, also at $\tau = 3$, corresponding to $\tau' = 0.2$.

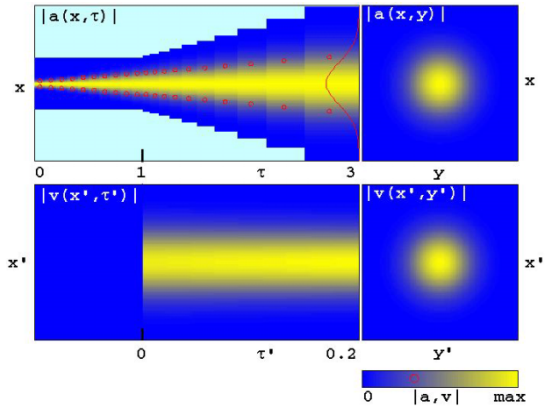

Figure 3: Free-space diffraction of a fundamental Gaussian mode in Cartesian coordinates $|a(x, \tau)|$ (top), and expanding coordinates $|v(x', \tau')|$ (bottom) for $z_0 = 0.3$, $\tau_1 = 1$, and $\tau = 0 \rightarrow 3$.

LARGER RANGE

Another calculation, shown in Fig. 4, spans a much larger range, $\tau = 0 \rightarrow 30$, with $z_0 = 0.1$. Conventional coordinates are used for for $\tau = 0 \rightarrow 1$ and primed coordinates for $\tau = 1 \rightarrow 30$, for which $\tau' = 0 \rightarrow 0.1$. Ten equal steps $\Delta\tau'$ suffice to take the field all the way to $\tau = 30$ and preserve its Gaussian shape. The ratio of the beam area at $\tau = 30$ to that at its waist is $(1 + 30^2/0.1^2) = 90,000$, and is much too large for integration in conventional coordinates. Using the coordinate transformation method, there are no distortions in the outcome, which is the same as the exact analytical result.

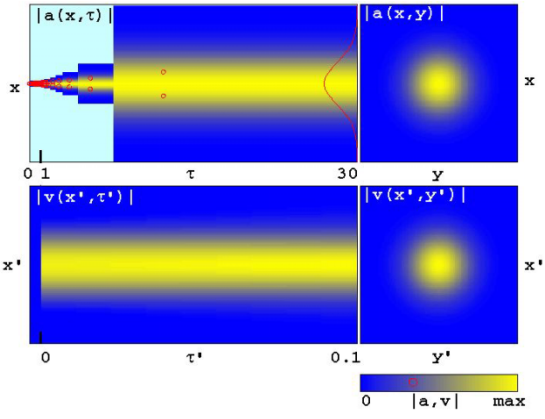

Figure 4: Free-space diffraction of a fundamental Gaussian mode in Cartesian coordinates $|a(x, \tau)|$ (top), and expanding coordinates $|v(x', \tau')|$ (bottom) for $z_0 = 0.1$, $\tau_1 = 1$, and $\tau = 0 \rightarrow 30$.

Furthermore, multiple transverse modes have been accurately propagated over this range.

ACKNOWLEDGMENTS

The authors are grateful for the support from NAVSEA, ONR, and the JTO.

REFERENCES

[1] D.W. Small, R.K. Wong, W.B. Colson, R.L. Armstead, "Free electron lasers with short Rayleigh length", Nuclear Instruments and Methods in Physics Research A393 (1997) 262.

[2] E.A. Sziklas and A.E.Siegman, "Diffraction calculations using fast Fourier transform methods,", Proc. IEEE 62, 410 (March 1974).

[3] E.A. Sziklas and A.E. Siegman, "Mode calculations in unstable resonator with flowing saturable gain. 2: Fast Fourier transform method," Appl. Opt. 14,1873-1889 (August 1975).

[4] W.H. Press et. al., "Numerical Recipes in C", 2nd Edition, Cambridge University Press, New York, 1992.

OPTICAL MODE DISTORTION IN A SHORT RAYLEIGH LENGTH FREE ELECTRON LASER

J. Blau, W.B. Colson, B.W. Williams, S.P. Niles and R.P. Mansfield
Physics Department, Naval Postgraduate School
333 Dyer Road, Monterey, CA 93943

Abstract

A short-Rayleigh length free electron laser (FEL) will operate primarily in the fundamental mode with a Gaussian profile that is narrow at the waist and broad at the mirrors. The gain medium will distort the optical wavefront and produce higher-order modes that will expand more rapidly than the fundamental. Wavefront propagation simulations are used to study optical mode distortion, as electron beam, undulator, and optical cavity parameters are varied.

INTRODUCTION

A proposed design for a high-power free electron laser calls for a short-Rayleigh length optical cavity [1]. This design has several advantages. The strongly-focused optical mode is narrow at the waist, enhancing the interaction with the electron beam. The small interaction volume should improve optical beam quality, encouraging the development of a fundamental Gaussian mode. The rapidly-expanding mode will reduce the peak intensity on the cavity mirrors, lessening the possibility of mirror damage.

The narrow, high-current electron beam will distort the optical mode, as new light is created due to spontaneous and stimulated emission along the length of the undulator. Higher-order modes may develop, and propagate to the cavity mirrors. Some power may be lost outside the mirrors, but the portion that remains within the cavity will produce a combined wavefront that no longer has a simple Gaussian profile.

SHORT-RAYLEIGH LENGTH FEL PARAMETERS

A proposed high-power FEL has electron beam energy $E_b = 80$ MeV, bunch charge $q = 200$ pC and bunch length $l_b = 0.15$ mm, yielding a peak current of $\hat{I} = 400$ A. The normalized emittance is $\epsilon_n = 3$ mm-mrad, with a beam radius of $r_b = 60$ μm. The undulator consists of $N = 22$ periods, each of length $\lambda_0 = 2.36$ cm, for a total length of $L = 52$ cm, with a peak magnetic field $\hat{B} = 0.7$ T. The undulator parameter is $K = 1$. The optical cavity is $S = 18$ m long, with Rayleigh length $Z_0 = 6$ cm, and quality factor $Q_n = 4$, corresponding to 25% power transmission per pass. The optical wavelength is $\lambda = 1$ μm.

Our simulations use dimensionless parameters [2]. Longitudinal distances are normalized to the undulator length L, and transverse distances are normalized to $(L\lambda/\pi)^{1/2}$. The dimensionless current density is given by

$$j = \frac{8N(e\pi KL)^2\rho_e}{\gamma^3 mc^2}, \qquad (1)$$

where $\rho_e \propto \hat{I}$ is the electron particle density, $\gamma = E_b/mc^2$ is the Lorentz factor, e and m are the electron charge and mass, and c is the speed of light. For the above parameters, $j = 200$. The dimensionless electron beam radius is $\sigma = r_b/(L\lambda/\pi)^{1/2} = 0.15$ and the dimensionless Rayleigh length is $z_0 = Z_0/L = 0.12$. The dimensionless cavity length is $\tau_{mirr} = S/L = 35$.

SIMULATION METHOD

Our wavefront propagation program has been described elsewhere [3]. At each time step, it uses the relativistic Lorentz force equations to determine the electron motion in the presence of the undulator and optical fields, and the parabolic wave equation to evolve the optical wavefront in (x, y, t). The simulation can follow multiple and arbitrary transverse optical modes, as they interact with the electron beam and bounce back and forth in the optical cavity, including mirror transmission and edge losses. We typically start the simulation in weak optical fields, and allow it to evolve over many passes through the cavity until the FEL reaches steady-state.

Recent improvements to our program include a faster Fourier transform algorithm [4], a more accurate integration method that uses next-nearest neighbors in the propagation of the wavefront matrix, and an expanding coordinate system to follow the rapidly-diffracting optical mode with a reasonable grid size [5].

SIMULATION RESULTS

For each set of simulation runs described below, we start with the nominal parameters given above. Then we vary some of the parameters to determine the effect on FEL performance and optical beam quality.

Fig. 1 shows the steady-state extraction for many simulations as the current density j is varied while emittance is held constant. Extraction is defined as the fraction of electron beam power converted to optical power on a single pass through the undulator. A theoretical curve, discussed below, is also shown for reference.

Since the weak-field gain is proportional to j, there is a minimum threshold value of $j \approx 20$ below which there is no extraction, because the cavity losses exceed the gain. For larger values of j, the power will grow over each pass

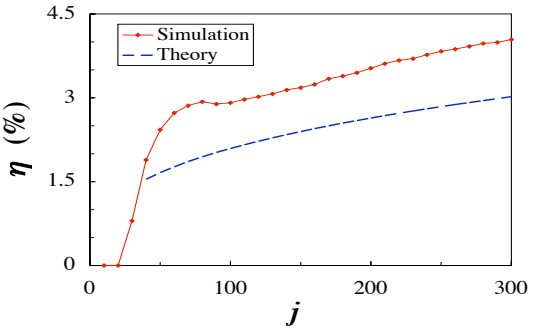

Figure 1: Extraction η versus current density j, for a series of simulations (solid red line), compared to theory (dashed blue line).

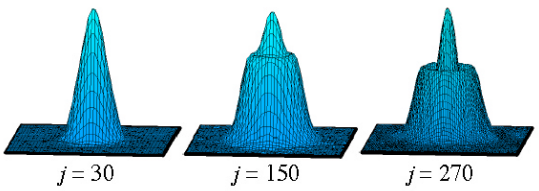

Figure 2: Optical field amplitude $|a(x, y)|$ at the output mirror for several values of current density j.

until the laser reaches saturation in strong optical fields. Basic FEL theory [2] predicts that for high gain, $j \gg 1$, the extraction should grow as

$$\eta \approx \frac{(j/2)^{1/3}}{8N}. \qquad (2)$$

Eq. 2 is plotted as a dashed blue line in Fig. 1. The similar slope of the two curves confirms the $j^{1/3}$ dependence, but the theory curve is well below the simulation curve. However, Eq. 2 is only an approximation, and doesn't include the effects of mode distortion.

Fig. 2 shows the steady-state optical wavefront profile at the output mirror for several values of j. For low current, $j = 30$, the laser appears to be operating close to the fundamental mode. For moderate current, $j = 150$, the mode is beginning to distort. For high current, $j = 270$, there is at least one higher-order Laguerre-Gaussian mode evident. This series clearly shows the effect of the FEL gain medium on mode distortion.

Fig. 3 shows the results of many simulations as the electron beam radius σ is varied. The beam angular spread is also varied to keep the emittance constant. For small beam radii, the corresponding large angular spread reduces overlap with the optical beam over the length of the undulator, hence lowering extraction. For large beam radii, many electrons are outside the strongly focused optical beam at the waist, again reducing extraction. The simulations predict that the optimal beam radius is at $\sigma = 0.12$.

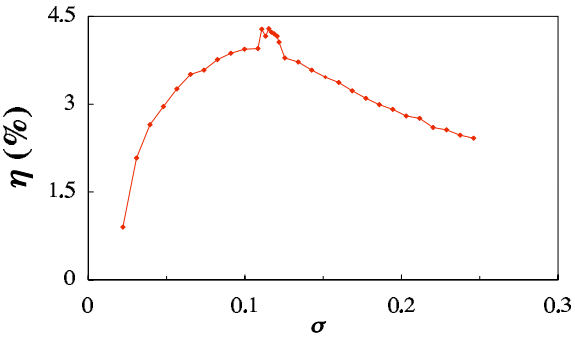

Figure 3: Simulation results for extraction η versus electron beam radius σ.

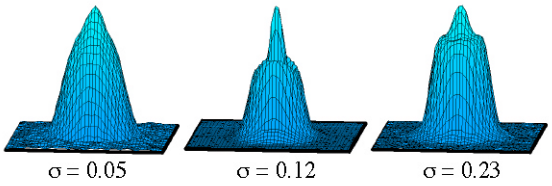

Figure 4: Optical field amplitude $|a(x, y)|$ at the output mirror for several values of electron beam radius σ.

There is a curious feature in the center of Fig. 3, around $\sigma \approx 0.12$, where the extraction appears to briefly rise a bit higher than the overall trend. This may be due to optical mode distortion around that value. Fig. 4 shows the output wavefront for several values of σ.

We also consider varying the electron beam focus point from $\tau_\beta = 0-1$, normalized to the undulator length L. The simulations give a fairly constant extraction over the entire range, as shown in Fig. 5, predicting that the short-Rayleigh length FEL should be fairly insensitive to fluctuations in the electron beam focal point. The optical mode profiles (not shown) do not change much over this range.

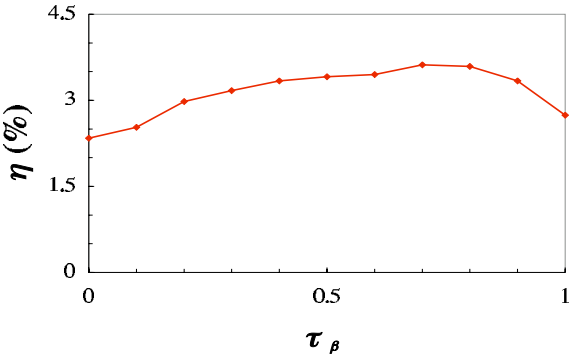

Figure 5: Simulation results for extraction η versus electron beam focus position τ_β within the undulator.

Next, we look at the effects of varying the number of

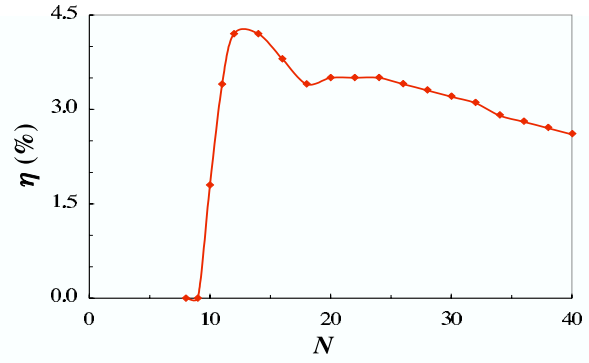

Figure 6: Simulation results for extraction η versus number of undulator periods N.

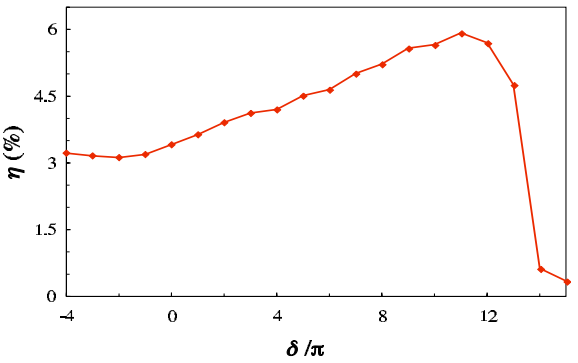

Figure 8: Simulation results for extraction η versus undulator taper strength δ.

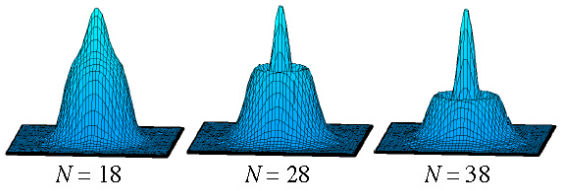

Figure 7: Optical field amplitude $|a(x,y)|$ at the output mirror for various number of undulator periods N.

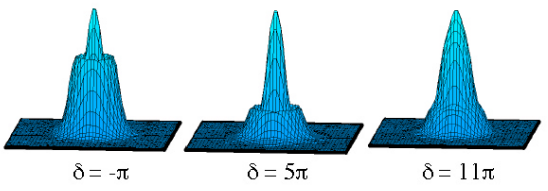

Figure 9: Optical field amplitude $|a(x,y)|$ at the output mirror for several values of undulator taper strength δ.

undulator periods N, keeping the undulator period λ_0 constant. The simulation results are plotted in Fig. 6. Note that changing N affects many other dimensionless parameters; for example, the electron current density $j \propto N^3$. Consequently, if there are too few periods, the gain will be below threshold, and the simulation results indeed show that there is no extraction for $N < 10$, corresponding to $j < 20$. Above that, the extraction increases rapidly, until $N \approx 14$. For larger values of N, even though j continues to increase, the extraction drops off. The optical wavefronts in Fig.7 predict the development of higher-order modes as N increases.

The results for undulator length motivate consideration of tapering the undulator, to extend saturation and enhance extraction. Fig. 8 shows simulation results as the undulator taper rate is varied. The taper rate is defined by

$$\delta \approx -4\pi N \left(\frac{K^2}{1+K^2}\right)\frac{\Delta K}{K}, \qquad (3)$$

where $\Delta K/K$ is the change in the undulator parameter. The simulations confirm that a positive taper could significantly improve FEL performance. A taper rate of $\delta = 11\pi$ produced an extraction of 5.9%, compared to the untapered value of 3.4%. Tapering also seems to improve the beam quality. Fig. 9 shows the output wavefront for several taper values; at $\delta = 11\pi$ it is close to the fundamental mode.

Next we show a series of simulations varying the Rayleigh length from $z_0 = 0.05 - 0.85$, normalized to the undulator length L. The results are shown in Fig. 10.

The extraction changes very little over this entire range, confirming that a short-Rayleigh length FEL can maintain good extraction while reducing optical intensity on the mirrors. Fig. 11 shows the output wavefronts at several values of z_0. Note that these are not all drawn to the same scale since the beam width expands as z_0 decreases.

Finally, we vary the cavity length over the range $\tau_{mirr} = S/L = 5 - 35$. The mirror curvature is also changed to keep z_0 constant. Again there is little variation in the extraction, as shown in Fig. 12, although the optical mode profiles, shown in Fig. 13 become increasingly distorted as the cavity is lengthened. Again, these are not all drawn to the same scale; the beam width expands dramatically as τ_{mirr} increases.

ACKNOWLEDGMENTS

The authors are grateful for the support from NAVSEA, ONR, and the JTO.

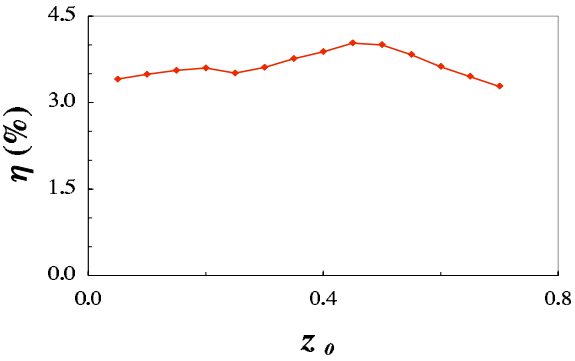

Figure 10: Simulation results for extraction η versus Rayleigh length z_0.

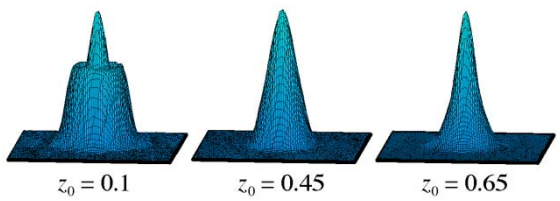

Figure 11: Optical field amplitude $|a(x, y)|$ at the output mirror for several values of Rayleigh length z_0.

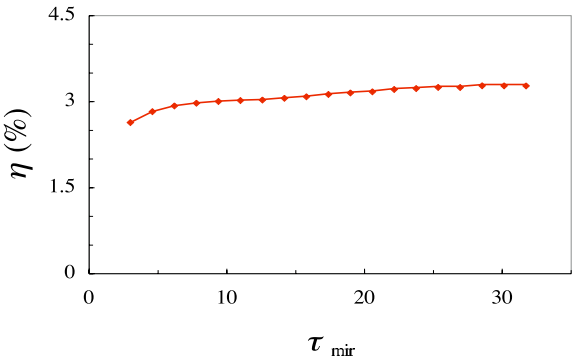

Figure 12: Simulation results for extraction η versus cavity length τ_{mirr}.

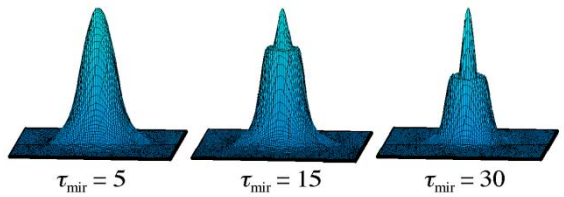

Figure 13: Optical field amplitude $|a(x, y)|$ at the output mirror for several values of cavity length τ_{mirr}.

REFERENCES

[1] W.B. Colson, "Short Rayleigh length free electron lasers", Proc. FEL2004.

[2] W.B. Colson, in: W.B. Colson, C. Pellegrini, A. Renieri (Eds.), Laser Handbook, Vol. 6, North Holland, Amsterdam, 1990.

[3] J. Blau, Ph.D. Dissertation, Naval Postgraduate School, http://handle.dtic.mil/100.2/ADA401739 (2002).

[4] Frigo, Matteo and Johnson, "FFTW: An adaptive software architecture for the FFT", Proc. 1998 Intl. Conf. Acoustics Speech and Signal Processing, 1381 (1998).

[5] R.L. Armstead, J. Blau, and W.B. Colson, "Short Rayleigh length free electron laser simulations in expanding coordinates", Proc. FEL2004.

WIGGLER EFFECTS ON THE GROWTH RATE OF A RAMAN FREE-ELECTRON LASER WITH AXIAL MAGNETIC FIELD OR ION-CHANNEL GUIDING

B. Maraghechi,[1,2,*] H. Aghahosseini,[1] and A. A. Kordbacheh[1,2]
[1]Department of Physics, Amirkabir University of Technology, Tehran, Iran
[2] Institute for Studies in Theoretical Physics and Mathematics (IPM),
P.O. Box 19395-5531, Tehran, Iran*

Abstract

A relativistic theory for Raman backscatteing in the beam frame of electrons is used to find the growth rate of a free-electron laser (FEL), in the Raman regime. First, a one dimensional helical wiggler and an axial magnetic field are considered. The wiggler effects on the linear dispersion relations of the space-charge wave and radiation are included in the analysis. A numerical computation is conducted to study the the growth rate of the excited waves. It was found that the wiggler effects on the growth rate decreases the growth rate on both group I and group II orbits. Next, the growth rate under an ion-channel guiding, instead of an axial magnetic field, under similar condition is calculated and is studied numerically.

INTRODUCTION

Lab-frame analysis of a FEL with a one dimensional helical wiggler and an axial magnetic field was first presented by Kwan and Dawson [1] using fluid model. In linearizing the relativistic factor, they included the energy exchange between the beam and the space-charge wave but neglected the exchange of energy between the beam and the radiation. The fully relativistic treatment of this problem, in the lab-frame, was first presented by Bernstein and Friedland [2] but they did not analyze the wiggler effect on the dispersion relations of the growing waves. Mehdian *et al.* [3] derived a nonlinear dispersion relation, with the wiggler effects on the dispersion relation of the excited waves included, but they did not find the growth rate. Ion-channel guiding of the electron beam in a FEL has been proposed as an alternative to guiding by a solenoid (or quadrupole) magnetic field [4]. This type of guiding involves the formation of a positive ion core by expulsion of electrons from a preionized plasma channel into which the electron beam is injected. Jha and Kumar [5] have calculated the growth rate with the higher order relativistic terms neglected.

BEAM-FRAME ANALYSIS WITH AXIAL MAGNETIC FIELD

A relativistic and cold electron beam is passed through a uniform static axial guide magnetic field, and a static helical (wiggler) magnetic field, which is periodic along the guide axis. In the beam frame of reference, the wiggler field comprises a propagating electromagnetic (pump) wave, which undergoes stimulated Raman backscattering. This process is characterized by the parametric decay of the pump wave (ω_1, k_1) into a forward-scattered space-charge wave (ω_2, k_2) and a backscattered electromagnetic wave (ω_3, k_3). The transverse and longitudinal components of the velocity are treated as relativistic. The unperturbed state in the beam frame is characterized by $n^{(0)} = n_0/\gamma_{||}$, and

$$\mathbf{E}^{(0)} = \frac{-\gamma_{||} v_{||} B_w}{2c}(\widehat{\mathbf{x}} - i\widehat{\mathbf{y}})exp[i(k_1 z + \omega_1 t)] + c.c., \quad (1)$$

$$\mathbf{B}^{(0)} = \Big(\frac{-i\gamma_{||} B_w}{2}(\widehat{\mathbf{x}} - i\widehat{\mathbf{y}})exp[i(k_1 z + \omega_1 t)] + c.c.\Big) + \widehat{z} B_0, \quad (2)$$

$$\mathbf{V}^{(0)} = \frac{i\gamma_{||} v_w}{2}(\widehat{\mathbf{x}} - i\widehat{\mathbf{y}})exp[i(k_1 z + \omega_1 t)] + c.c., \quad (3)$$

$$v_w = \frac{\Omega_{wL} v_{||}}{(\Omega_{0L} - \gamma_0 k_w v_{||})}.$$

Perturbation composed of a longitudinal plasma wave (ω_2, k_2) and a transverse backscattered electromagnetic wave (ω_3, k_3) are considered. The frequencies and wave numbers satisfy the phase matching conditions, $\omega_3 = \omega_2 - \omega_1$ and $k_3 = k_2 - k_1$. These waves are assumed to vary as $exp[i(k_2 z + \omega_2 t)]$, and $exp[i(k_3 z + \omega_3 t)]$. The amplitudes of the longitudinal space-charge wave are E_2, V_2, and n_2 and the x and y components of the radiation are E_3, B_3, and V_3.

The relativistic momentum equation in the beam frame

$$m\gamma d\mathbf{V}/dt + m\mathbf{V}d\gamma/dt = -e\mathbf{E} - ec^{-1}\mathbf{V} \times \mathbf{B}, \quad (4)$$

with $d\gamma/dt = -e/(mc^2)\mathbf{V}.\mathbf{E}$ and with the use of the linearized relativistic factor, can be linearized as follows

$$m\gamma_0\gamma_{||}^{-1}\Big[\frac{\partial \mathbf{V}^{(1)}}{\partial t} + \big(\mathbf{V}^{(0)}.\nabla\mathbf{V}^{(1)} + \mathbf{V}^{(1)}.\nabla\mathbf{V}^{(0)}\big)\Big]$$
$$+mc^{-2}\gamma_0^3\gamma_{||}^{-3}\Big(\frac{\partial \mathbf{V}^{(0)}}{\partial t}\mathbf{V}^{(0)}.\mathbf{V}^{(1)}$$

* Electronic mail: behrouz@aut.ac.ir

$$+\mathbf{V}^{(0)}.\mathbf{V}^{(1)}\mathbf{V}^{(0)}.\nabla\mathbf{V}^{(0)}\big) - ec^{-2}\big(\mathbf{V}^{(0)}\mathbf{V}^{(0)}.\mathbf{E}^{(1)} +\mathbf{V}^{(0)}\mathbf{E}^{(0)}.\mathbf{V}^{(1)} + \mathbf{V}^{(0)}.\mathbf{E}^{(0)}\mathbf{V}^{(1)}\big) = -e\big(\mathbf{E}^{(1)} +c^{-1}\mathbf{V}^{(0)}\times\mathbf{B}^{(1)} + c^{-1}\mathbf{V}^{(1)}\times\mathbf{B}^{(0)}\big). \quad (5)$$

After substituting the first order quantities in Eq. (5), and making use of the phase matching-conditions in the coupling terms, the terms corresponding to (ω_2, k_2) and (ω_3, k_3) phases will give equations for the longitudinal space-charge wave and the transverse wave (radiation), respectively. The fluid-Maxwell equations will be

$$m\gamma_0\gamma_{||}^{-1}\omega_2 V_2 = ieE_2 - ec^{-1}\gamma_{||}V_w B_3 + ec^{-1}\gamma_{||}B_w V_3 \quad (6)$$

$$m\gamma_0\gamma_{||}^{-1}\big(2\omega_3 V_3 - k_1\gamma_{||}V_w V_2\big) - mc^{-2}\omega_1\gamma_0^3\gamma_{||}^{-1} \times V_w^2 V_3 - ec^{-2}\big(\gamma_{||}^2 V_w^2 E_3 - c^{-1}\gamma_{||}^2 V_{||}V_w B_w V_3\big) = -2eE_3 - 2ec^{-1}B_0 V_3 + e\gamma_{||}B_w V_2, \quad (7)$$

$$\omega_2 n_2 + k_2 n_0 V_2 = 0, \quad (8)$$

$$4\pi e n_0 V_2 = i\omega_2 E_2, \quad (9)$$

$$k_3 c E_3 = -\omega_3 B_3, \quad (10)$$

$$-k_3 c B_3 = 4\pi e n_0 V_3 - 2\pi e\gamma_{||}V_w n_2 + \omega_3 E_3. \quad (11)$$

Equations (6)-(11) form a system of linear homogenious algebraic equations. The necessary and sufficient condition for a nontrivial solution is the dispersion relation

$$\Big(\omega_2^2 - \omega_p^2\Phi\Big)\Big(k_3^2c^2 - \omega_3^2 + \frac{\omega_p^2\omega_3}{\omega_c+\omega_3} + \Psi\Big) = -\frac{\omega_w^2 k_2\omega_1\omega_p^2}{2k_w^2\Big(\omega_1-\omega_c\Big)}\Big[\frac{k_3\omega_1}{\omega_1-\omega_c} + \frac{k_1\omega_3(1-a_1)}{\omega_c+\omega_3-a_1a_2}\Big] \times\Big[1 - \frac{k_1\omega_2\omega_c}{k_2\omega_1\big(\omega_c+\omega_3\big)} - \frac{a_1a_2}{\omega_c+\omega_3}\Big]. \quad (12)$$

The wiggler effects on the linear dispersion relations of the space-charge wave and radiation are contained in Φ and Ψ, respectively. For zero wiggler, they reduce to an ordinary longitudinal plasma oscillations and a transverse electromagnetic wave in a magnetized plasma. If coupling to the radiation is removed Φ becomes unity and the wiggler has no effect on the space-charge wave. On the other hand, if coupling to the space-charge wave is removed Ψ becomes nonzero, which shows the direct effect of wiggler on the radiation.

The real parts of the frequencies and wave numbers satisfy the linear dispersion relations for the space-charge wave and radiation, respectively, with all of the effects of the wiggler and guide magnetic fields included. The imaginary parts of the complex frequencies and wave numbers of the growing waves may be expressed in terms of the lab-frame growth rate Δ_L. This will give the lab-frame spatial growth rate of the space-charge wave and radiation with the lab-frame temporal growth rate taken to be zero;

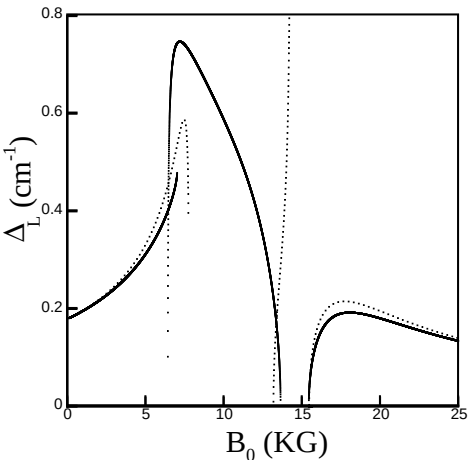

Figure 1: Lab-frame spatial growth rate Δ_L as a function of axial magnetic field B_0. With wiggler effects (solid line); without wiggler effects (dotted line).

$$\Delta_L^2 = \frac{\omega_w^2 k_2\omega_p^2}{8k\gamma_{||}\Big(\omega_1-\omega_c\Big)}\Big[\frac{k_3\omega_1}{\omega_1-\omega_c} + \frac{k_1\omega_3(1-a_1)}{\omega_c+\omega_3-a_1a_2}\Big] \times\Big[1 - \frac{k_1\omega_2\omega_c}{k_2\omega_1\big(\omega_c+\omega_3\big)} - \frac{a_1a_2}{\omega_c+\omega_3}\Big]\Big[k_3c^2 - v_{||}\omega_3 + \frac{\omega_p^2 v_{||}\omega_c(1-a_1)}{2\big(\omega_c+\omega_3\big)^2} - \frac{a_1a_2k_3c^2}{\omega_c+\omega_3} + \frac{a_1a_2\omega_c\omega_c v_{||}}{2(\omega_c+\omega_3)^2} + \frac{a_1a_2v_{||}(k_3^2c^2+\omega_3^2)}{2(\omega_c+\omega_3)^2}\Big]^{-1}\Big[\omega_2 - \big(k_1^2c^2a_1\omega_c(\omega_c - \omega_1)\big)\frac{(\omega_c-\omega_1-a_1a_2)}{2\omega_1^2(\omega_3+\omega_c-a_1a_2)^2}\Big]^{-1}. \quad (13)$$

The wiggler effects, through Φ and Ψ, on Δ_L are shown in Fig. 1 (solid lines). Dotted lines show Δ_L when the wiggler effects are neglected. Lab-frame values for the unperturbed electron density, wiggler wavelength(period), and Lorentz factor were taken to be $n_0 = 10^{12}\ cm^{-3}$, $\lambda_w = 2\ cm$, and $\gamma_0 = 2.5$, respectively. The wiggler is assumed to be $B_w = 1500\ G$. It can be observed that the wiggler effects on the growth rate decreases the growth rate on both group I and group II orbits.

FEL WITH ION-CHANNEL GUIDING

As an alternative to guiding by an axial magnetic field, focusing of the electron beam can be accomplished by an

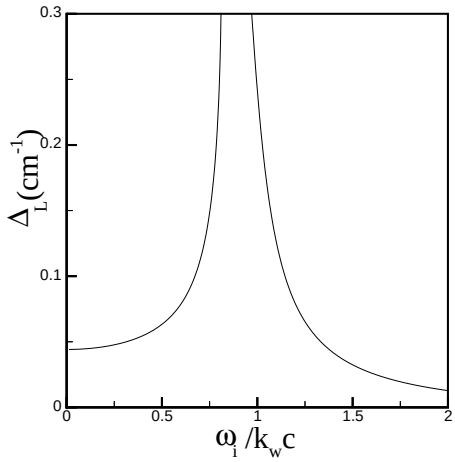

Figure 2: Lab-frame spatial growth rate Δ_L as a function of ion-channel frequency $\omega_i/k_w c$ with wiggler effects included.

ion-channel. The transverse electrostatic field generated by the ion-channel is

$$\mathbf{E}_i = 2\pi e n_i \big(\widehat{\mathbf{x}} x + \widehat{\mathbf{y}} y\big), \tag{14}$$

and the wiggler induced velocity will be given by Eq. (3) with v_w given by

$$v_w = \frac{\Omega_{wL} k_w v_{||}^2}{(\omega_i^2 - \gamma k_w^2 v_{||}^2)}, \tag{15}$$

where $\omega_i^2 = 2\pi n_i e^2/m$ is the betatron frequency squared. With similar procedure as in the axial magnetic field case, the dispersion relation can be found as

$$\Big(\omega^2 - \omega_p^2\Phi\Big)\Big(k_3^2c_3^2 - \omega_3^2 + \omega_p^2 + \Psi\Big) = \frac{-k_2 k_w^2 \omega_w^2 \omega_p^2 v_{||}^3}{2\Big(\omega_i^2 - k_w^2 v_{||}^2\Big)^2}\Big[k_3 v_{||} - \frac{\omega_3(1-a_1)\Big(\omega_i^2 - k_1^2 v_{||}^2\Big)}{k_1 v_{||}\Big(\omega_3 - a_1 a_2\Big)}\Big] \times\Big[1 - \frac{a_1 a_2}{\omega_3} - \frac{\omega_2 \omega_1^2}{k_1 k_2 \omega_3 v_{||}^2}\Big]. \tag{16}$$

Expressing imaginary parts of the complex frequencies and wave numbers of the growing waves in terms of the lab-frame growth rate Δ_L will give the lab-frame spatial growth rate of the space-charge wave and radiation

$$\Delta_L^2 = \frac{k_2 k_w^2 \omega_w^2 \omega_p^2 v_{||}^3}{8\gamma_{||}^2 \omega_2 \Big(\omega_i^2 - k_w^2 v_{||}^2\Big)^2}\Big[1 - \frac{a_1 a_2}{\omega_3} - \frac{\omega_2 \omega_1^2}{k_1 k_2 \omega_3 v_{||}^2}\Big] \times\Big[k_3 v_{||} - \frac{\omega_3(1-a_1)\Big(\omega_i^2 - k_1^2 v_{||}^2\Big)}{k_1 v_{||}\Big(\omega_3 - a_1 a_2\Big)}\Big]\Big[\omega_2 + a_1\omega_i^2 c^2 \times\frac{\big(\omega_i^2 - k_1^2 v_{||}^2\big)\big(\omega_2 + a_1 a_2\big)}{2k_1^2 v||^4\big(\omega_3^2 - a_1 a_2\big)^2}\Big]^{-1}\Big[k_3 c^2 - \omega_3 v_{||} + \frac{a_1 a_2 v_{||}}{2\omega_3^2}\big(\omega_2 + a_1 a_2\big)\Big]^{-1}. \tag{17}$$

Variation of the growth rate Δ_L with the ion-channel guiding frequency $\omega_i/k_w c$ is shown in Fig. 2 with wiggler effects on the excited waves included. Growth rate in both group I and group II orbits increase sharply as the resonance is approached.

REFERENCES

[1] T. Kawn and J. M. Dawson, Phys. Fluids **22**, 1089 (1979).

[2] I. B. Bernstein and L. Friedland, Phys. Rev. A **23**, 816 (1981).

[3] H. Mehdian, J. E. Willett, and Y. Aktas, Phys. Plasma **5**, 4079 (1998).

[4] K. Takayama and S. Hiramatsu, Phys. Rev. A, **37**, 730 (1988).

[5] P. Jha and P. Kumar, Phys. Rev. E, **57**, 2256 (1998).

THE EUROPEAN X-RAY FREE ELECTRON LASER PROJECT AT DESY

A.S.Schwarz, Deutsches Elektronen-Synchrotron, Hamburg, Germany
for the XFEL Group

Abstract

The X-ray Free Electron Laser XFEL is a 4th generation synchrotron radiation facility based on the SASE FEL concept and the superconducting TESLA technology for the linear accelerator. In February, 2003, the German Federal Ministry of Education and Research decided that the XFEL, proposed by the International TESLA Collaboration, should be realized as a European project and located at DESY/Hamburg. The ministry also announced that in view of the locational advantage, Germany is prepared to cover half of the investment and personnel costs for the XFEL. In the course of the last year work has concentrated on the following areas: setting up of an organizational structure at DESY for the preparation of the project, discussions with potential European partners on several levels, selection of a new site for the XFEL facility and the preparation of the 'project approval procedure'. The present status of the technical layout of the Linear Accelerator, the SASE Undulator and Photon Beam lines and the experiment stations will be presented.

BASIC DESIGN CONSIDERATIONS

The basic idea underlying the XFEL is the extension of the principle of linear accelerator based Self Amplification of Spontaneous Emission (SASE) Free Electron Lasers (FELs) to the hard X-ray (~1Å wavelength) regime. The ultra-high brilliant laser pulses with sub-100-fs pulse length and a large degree of coherence will allow to probe the dynamic state of matter with atomic resolution in space and time and to study non-equilibrium states and very fast transitions between different states of matter [1]. Compared to 3rd generation synchrotron sources the gain factors for the peak brilliance for the SASE lines and the spontaneous radiation exceed 10^9 and 10^4, respectively. Using superconducting Rf technology for the linear accelerator allows for a large flexibility in the electron bunch patterns.

TECHNICAL LAYOUT

The principle layout for the first stage of the XFEL facility is shown in Fig.1 [2], [3]. The electron beam is accelerated in a linear accelerator using superconducting Rf technology to approx. 20GeV and then distributed into several beam lines, This allows to use the electron beam for several FELs and spontaneous radiators and facilitates parallel operation of many experiments, including R&D on the light generation process and beam line hardware.

The SASE FELs cover the photon energy range between 200eV and ≤15keV in a continuous way. The emphasis is on the production of hard X-rays such that 1Å wavelength can safely be reached with conservative assumptions on the beam parameters.

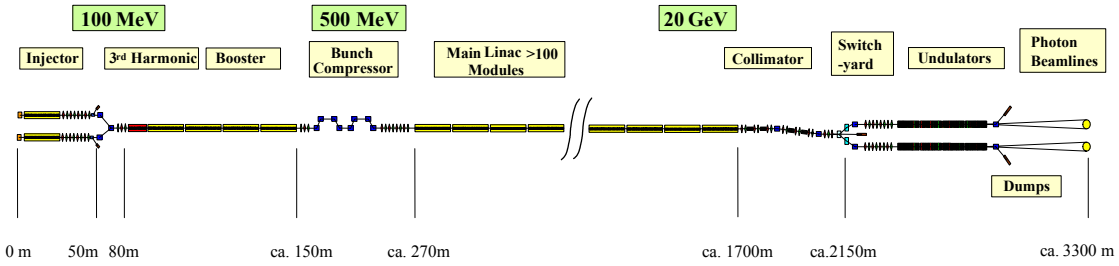

Figure 1: The principle layout of the XFEL facility

The overall length of the facility is 3.3km (2.15km for the linear accelerator complex including the beam collimation section and 1.15km for the undulator and photon beam lines). The length scales are largely determined by

- the required electron beam energy and the available accelerating gradient of the superconducting Rf structures
- the requirements of the machine optics in the beam distribution sections,
- the saturation length of the undulators

- provisions for spare space for future options (e.g. laser- or self-seeding) and
- the photon diagnostics and transport lines.

The XFEL is laid out as a multi-user facility. In its 1st stage, it will have 5 undulator beam lines, 3 of which are SASE-FELs (two for the Å wavelength regime, one for softer X-rays), the other two for hard X-ray spontaneous radiation. Initially, 10 experimental stations are foreseen. The underground experimental hall has a floor space of 50×90m^2 and more stations can be added later. The site allows to extend the user facility for more beam lines in a later stage (see Figure 2).

Table 1: XFEL Design Parameters

Performance Goals for the Electron Beam	
Beam Energy	10 - 20 GeV
Emittance (norm.)	1.4 mrad × mm
Bunch Charge	1 nC
Bunch Length	80 fs
Energy spread (uncorrel.)	<2.5 MeV rms
Main Linac	
Acc. Gradient @ 20 GeV	23 MV/m
Linac Length	approx. 1.5 km
Inst. Accelerator Modules	116
Installed Klystrons	29
Beam Current (max)	5 mA
Beam Pulse Length	0.65 ms
# Bunches p. Pulse (max)	3250
Bunch Spacing (min)	200 ns
Repetition Rate	10 Hz
Max. Avg. Beam Power	650 kW
Performance Goals for SASE FEL Radiation	
photon energy	15 – 0.2 keV
wavelength	0.08 – 6.4 nm
peak power	24 – 135 GW
average power	66 – 800 W
number photon per pulse	1.1 – 430 × 10^{12}
peak brillance	5.4 – 0.06 ×10^{33} *
average brillance	1.6 – 0.03 ×10^{25} *
* in units of photons / (s mrad^2 mm^2 0.1% b.w.)	

An overview of the main XFEL parameters is given in Table 1. The undulator parameters have been optimised for one Å wavelength at a beam energy of 17.5 GeV. This implies that at the nominal maximum beam energy from the linac of 20GeV at 23MV/m accelerating gradient, the ^{57}Fe line at 0.08nm, of interest for certain experiments, will be accessible.

ELECTRON BEAM DISTRIBUTION

The XFEL linac can accelerate more than 3,000 bunches per RF pulse, serious beam dynamics problems related to higher order modes in the cavities are not expected [4]. User requirements regarding beam time structure will vary over a large range, from single or few bunches to partial or full trains per RF pulse. Generation of such patterns is possible at the source, at the end of the linac or by a combination of both. From the point of view of maximum flexibility a system using programmable fast kickers appears to be the optimum solution. Beam loading conditions in the linac could be quasi static, i.e. the same from pulse to pulse, and bunches could be distributed to different beam lines according to the needs of the respective experiments.

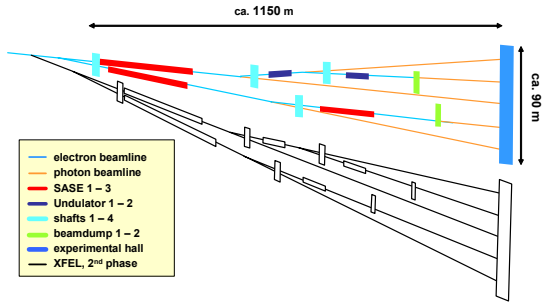

Figure 2: The 1st stage user beam line layout (coloured) and the possible extension.

The required switching devices are demanding, though, regarding jitter tolerances and reliability. In addition to switching the electron beam, it is also possible to switch the FEL process on and off by phase shifters, such that different photon pulse time structures can be generated in a beam line with a sequence of several undulators [5].

The beam transport lattice from the end of the linac to the undulators includes sections for diagnostics and collimation to protect the undulators from potentially large amplitude halo or mis-steered beam. A large momentum acceptance is foreseen so that energy modulation with a bunch train by up to 3% is possible. The lattice layout and the civil construction in the beam distribution region for the 1st phase of the user facility will also already take into account the possibility of later adding more beam lines.

PHOTON BEAM LINES

The generic layout for the undulator and photon beam lines is shown in Fig.3. Following the light generation in the undulator sections, a gasfilter section with photon monitoring is added that allows to tune the intensity of the photon beam. This is followed with a photon diagnostic section. Before entering the experimental hall, the photons pass through a mirror system, with e.g. a double crystal monochromator. After the monochromator, the photon beam is split into several beams that are transferred to a range of experiments in the experimental hall.

The undulator sections have a maximum total length of 250m. Variable gap (min. 10mm) type 5m long undulator segments are foreseen, which not only permits to independently adjust the photon energy within certain limits, but also facilitates the precise steering of the electron beam for optimum overlap with the photon beam [6]. Typical Distances are ~650m between the exit of the undulator and the optical elements and ~200m between the optics and the experiment.

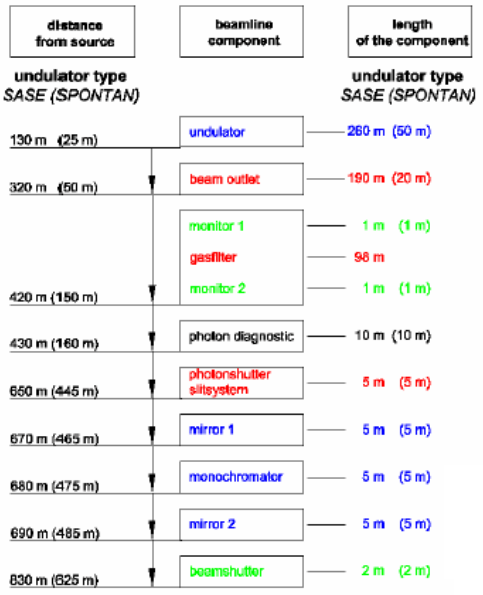

Figure 3: The generic layout for the undulator and photon beam lines

A generic layout of the experimental area at the end of a given photon beam line is shown in Fig.4. The area available for experiments is approximately 750 square meters for each of the five photon beam lines of the first stage of the XFEL facility.

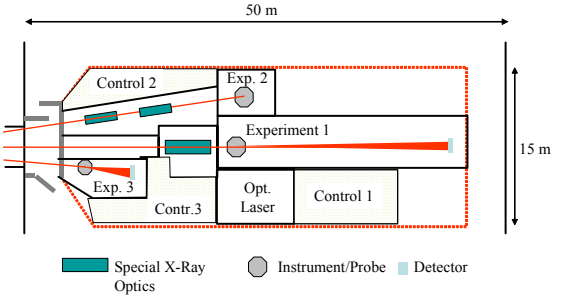

Figure 4: A generic layout of the experimental area at the end of one of the five photon beam lines of the first stage of the European XFEL facility

PARAMETER FLEXIBILITY

With conservative assumptions for the slice energy spread of the electron bunch (2.5MeV), the slice emittance (1.4mm mrad) and the size of the undulator gap (10mm) a wavelength of 1Å can be reached at a beam energy of 17.5GeV with a saturation length of approx. 140m. Improvements in the slice emittance or the energy spread at a given beam energy would allow a reduction of the saturation length or a reduction of the photon wavelength below 1Å at the same undulator length.

Furthermore, the expected higher performance of the superconducting cavities of the linear accelerator will permit to operate at even shorter wavelength, provided that the electron beam quality can also be further improved to guarantee saturation in the SASE FEL process.

The required klystron power per station is 4.8MW, well below the maximum power of 10MW of the multi-beam klystrons developed in industry for the TESLA project. This will not only cover the power needs for an operation at higher energies, but also allow to operate the linac at higher repetition rates (and duty cycles) at lower energy (the main limitation then being the *average* power of the RF system).

In contrast to conventional linacs, with the superconducting accelerator technology even a continuous wave (CW, 100% duty cycle) operation of the linac is conceivable [3], although only at reduced energy/accelerating gradient in order to avoid excessive cryogenic load into the Helium at 2K. Such an option is not viewed as being part of the initial stage of the facility, but could become attractive if lower-emittance, high duty cycle beam sources become available [7], possibly in combination with advanced FEL concepts.

The superconducting linac allows for a wide flexibility in the generation of bunch train patterns. The

nominal beam pulse length is 0.65ms with max. 3250 bunches per pulse at a spacing of min. 200ns. Depending on the requirements of the user community, single bunches or few bunches per pulse train are possible as well as bunch trains with varying bunch spacing.

PRESENT ACTIVITIES/STATUS

The XFEL was originally proposed as integral part of the TESLA project together with a 500 – 800 GeV e^+e^- Linear Collider based on superconducting RF (SRF) technology [8]. In a later update [9], the proposal was modified such as to build the XFEL with its own, separate linac for the benefit of flexibility regarding construction, commissioning and operation of the facility, maintaining the SRF technology identical to the collider linac and a common experimental site 16km northwest from the DESY site in Hamburg.

The German government decision in 2003 to go ahead with the XFEL as a European project and to postpone the decision on the collider led to a revision of the site. The new site layout, sketched in Fig.5, has the XFEL linac starting on the DESY site, permitting to make optimum use of existing infrastructure, and the user facility in a rural area about 3km west-northwest from DESY south of the city of Schenefeld.

Project Approval Procedure

In Germany, the legal procedure necessary to prepare the civil construction and operation for such a large scale facility as the XFEL is the 'Project Approval Procedure'. The legal basis for such a procedure is a treaty between the Bundesländer Hamburg and Schleswig-Holstein which has been signed by the respective governments in July, 2004.

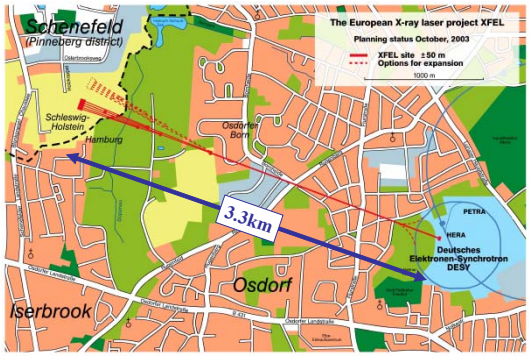

Figure 5: Sketch of the XFEL site near DESY

For the Project Approval Procedure a relatively detailed planning of the various underground and surface buildings and the construction and operation phases of the facility has to be performed. After the decision for the site in October 2003, the planning for the Project Approval Procedure has started. It is foreseen to prepare all necessary material describing the project by spring 2005. The examination of the planning information by a public authority will then take likely until the end of 2005 such that construction of the European X-Ray Laser Laboratory XFEL can start in the year 2006.

Towards a European XFEL

The project organisation at the European level is ongoing. A steering committee and two working groups, one on scientific-technical (STI) and one on administrative and financial issues (AFI), have been established early in 2004, with members from all European countries which are interested in participating in the project. The main task of these groups is to prepare the documents required for the technical definition and organisational structure of the project by 2005. The final decision to move into the construction phase is expected for 2006. The construction time until beam operation will be 6 years. The total project cost is estimated at 684 M€ (year 2000 price level), of which Germany will cover 50%.

A Memorandum of Understanding (MoU) regulating the preparatory phase for the construction of the European XFEL has been prepared by the presently participating countries and is expected to be signed before the end of the 2004.

The XFEL Project Group at DESY

In the summer of the year 2003 a project group was established at DESY in order to organise the preparatory work towards start of construction of the facility in 2006. The charge of this group thus covers the present intermediate phase of the project during which the organisation at the European level is in progress. The main tasks are the further optimisation of the overall design of the XFEL, starting from the supplement [9] of the TESLA Technical Design Report [8], the specification, prototyping, etc. of major technical components towards industrial production and the preparation of the site for the facility near the existing DESY site in Hamburg. While the group has at the start been formally arranged purely within the DESY laboratory, it is also thought to serve as an organisational structure to facilitate and integrate participation from outside collaborators in this intermediate phase, for the time being until a European project group has been established.

The DESY XFEL group is managed by a project leader, a deputy project leader and an administrative project coordinator. In order to structure the work, in total 37 work packages (WPs) have been defined. The WPs are grouped into 6 main topics as listed in Table 2.

Table 2: Work Package Groups for the organization of the preparatory work for the XFEL at DESY

WP group	Topic
01	Linear Accelerator
02	Accelerator Sub-systems
03	Photon Beam Lines
04	General Issues
05	Infrastructure
06	Site and Buildings

For each of the 37 WPs a person has been nominated as the coordinator in charge for this part of the work within the DESY laboratory. It is expected that responsibility for part of or entire WPs will be taken over by persons from outside DESY, once the project organisation develops from its present stage to the European level.

The project group holds regular weekly meetings. Participation via video by external groups can be easily arranged and has occasionally been used. In addition to the main weekly project meeting, a considerable number of other sub-group meetings, either on a regular basis or when required, take place (examples: preparations for the Project Approval Procedure for legal permission of construction, accelerator module group, beam dynamics group). A web site has been set up to serve as information platform among the participating groups and institutes [10].

CONCLUSION

The European X-Ray Free Electron Laser Laboratory will provide unprecedented opportunities for basic research with photons in the 1Å regime. The baseline design offers a conservative approach to reach this wavelength. It offers a considerable amount of flexibility and allows later incorporation of further developments in the photon generation scheme. The preparatory work for the XFEL is well underway at DESY and on the European level.

With the R&D work progressing towards industrial production of major components and the preparations for the site and the legal procedure (project approval procedure) well under way, the project should be ready to go into the construction phase in ~2 years from now such that the facility could be commissioned in 2012.

ACKNOWLEDGEMENTS

The author wishes to thank all members of the XFEL Group as well as the TESLA collaboration who have provided the basis for this report. Special thanks go to Reinhard Brinkmann, Thomas Tschentscher and Hans Weise.

REFERENCES

[1] H. Dosch, “Advanced Analysis in Nanospace: Research with the XFEL”; LINAC04, XXII International Linear Accelerator Conference, Lübeck, Germany, August 16-20, Paper MO101; see also http://www.linac2004.de/

[2] R. Brinkmann, “Accelerator Layout of the XFEL”, LINAC04, XXII International Linear Accelerator Conference, Lübeck, Germany, August 16-20, Paper MO102; see http://www.linac2004.de/

[3] H. Weise, “The TESLA XFEL Project“, 9th European Particle Accelerator Conference, EPAC'04, July 5-9, Lucerne, Switzerland; see http://www.epac04.ch/

[4] N. Baboi, “Multi-Bunch Beam Dynamics Studies in the TESLA XFEL”, LINAC04, XXII International Linear Accelerator Conference, Lübeck, Germany, August 16-20, Paper TUP57; see also http://www.linac2004.de/

[5] E. L. Saldin, E. A. Schneidmiller and M. V. Yurkov, DESY-TESLA-FEL-2004-02, May 2004.

[6] M. Tischer et al., Nucl. Instr. Meth. A483(2002)418.

[7] M. Ferrario, J.Sekutowicz and J. Rosenzweig, “An Ultra-High Brightness, High Duty Factor, Superconducting RF Photoinjector”, EPAC2004, Lucerne, MOPKF043.

[8] F. Richard et al. (eds.), “TESLA Technical Design Report“, DESY 2001-011, March 2001; http://tesla.desy.de

[9] R. Brinkmann et al. (eds.), “Supplement to the TESLA XFEL TDR“, DESY 2002-167, October 2002; http://xfel.desy.de

[10] Information Portal of the XFEL Group for the preparation of the XFEL project at DESY: http://xfel.desy.de/

OVERVIEW OF SINGLE PASS FEL DESIGNS TECHNICAL SUGGESTIONS FOR STABILITY IMPROVEMENT

Tsumoru Shintake, RIKEN/SPring-8, Japan

Abstract

The single pass FEL based SASE is only one realistic candidate to generate intense coherent radiation at X-ray wavelength. To achieve high gain amplification of FEL signal, we need to provide a high density electron beam with low transverse emittance and maintain its trajectory in precisely straight line along the fairly long undulator, typically, 100 m or even longer. To do beam based alignment or simply guide the beam, the machine has to be very stable, with low pulse-to-pulse jitter and slow drift. This paper will provide some technical suggestions to improve today's linear accelerator to meet the above demand.

INTRODUCTION

The FEL: free electron laser using a high energy electron beam running in an undulator as an active media has been realized and used for various applications in infrared wavelength. However, when the requested wavelength becomes short, the interaction of the electron beam with the undulator radiation becomes weaker, since the energy exchange is performed through transverse motion of the beam along sinusoidal trajectory in the undulator, and its amplitude is inversely proportional to the beam energy, thus FEL becomes harder to be realized in shorter wavelength. Additionally, bellow 200 nm wavelength, no efficient mirror material is available as the cavity reflector, and all mirror material becomes weaker against intense radiation circulating in the FEL resonator.

To avoid this difficulty, the X-ray free-electron laser (FEL) based on linear accelerator technology using the principle of self-amplified spontaneous emission (SASE) appears to be the most promising approach. SASE does not require the resonator, instead it amplifies the spontaneous signal associated with the incoming electron beam, for several decade of magnitude, until it reaches to saturation condition along a fairly long undulator.

To realize this type of new FEL, we have to establish the following two major technologies.

(1) Generation of high density electron bunch with a peak intensity at a few kA, at the same time the beam emittance has to be very low, typically 1 π.mm.mrad for transverse, and 10^{-4} energy spread.

(2) Transport above electron bunch fairly straight trajectory in the long undulator line. The alignment tolerance is typically 10 to 50 micron-meter for each Q-magnet in X-ray FELs.

To perform these requirements, in many accelerator laboratories, new R&D programs for X-ray FEL have been started in these years. Up to now, R&D's are mostly focused on the development of low-emittance electron-source using photo-cathode RF-gun, or HV gun using thermionic cathode. Recently, very promising results are reported from those R&D's at FEL2004 conference.

To achieve the high peak current in a bunched beam, we currently believe the magnetic chicane type bunch-compressor will be capable of handling the low emittance beam without emittance dilutions. There are a large number of studies on this subject, and can be found elsewhere.

However, on the second issue, not many studies have been carried out, because this is not a single subject and the target cannot be clearly specified, since it varies on boundary conditions of each detail designs. The issue is widely cross-related between, undulator technology, beam optics, electron beam monitoring, and X-ray beam detection.

In this paper, the author wishes to illuminate machine stability issues behind each of these technical details. To perform the beam based alignment on undulator beam line, machine has to provide fairly stable beam during iteration process: measuring beam position carefully with changing the beam energy. Also on tuning the chicane magnet, we need careful measurement on bunch length v.s. energy or CSR noise radiation from the beam line. Every tuning and beam study will request stable beam and quiet environment (low electro-magnetic radiation from power supplies).

In this paper, we compare machine stability of the linear accelerators with storage ring and discuss various aspects of machine stability. The author will also try to provide some technical suggestions on improving the machine stability.

STABILITY COMPARISON

Table-1 compares various aspects related to the machine stability of the storage ring and linear accelerator (pulse mode). In the storage ring, machine runs mostly in steady state condition, while the pulse mode linear accelerator runs in transient condition, this cause the major difference of the machine stabilities in two types.

The electron beam trajectory in a storage ring is a "closed orbit", which is an eigen vector of the wave-function (ring optical matrix). Therefore, even with different initial conditions, in practice with beam injection errors, beam converges to unique closed orbit (eigen vector) after damping. On the other hand, in the linear accelerator, the trajectory is not an eigen vector, it is an open single-pass trajectory, which varies with initial conditions, in practice, injection error. Therefore, the stability of the electron source is very important in the linear accelerator.

In the storage ring, there is a synchrotron damping effect, which is a combined effect of synchrotron phase stability phenomena on rf-voltage and radiation damping effect. Thanks to this effect, the initial condition error or some temporal error excitations are damped, and the

beam trajectory approaches to the steady state closed-orbit. But, in the linear accelerator, there is no phase-stability phenomena, therefore no negative feedback acts on the beam in natural, and also there is no synchrotron radiation damping. Thus, we do not have any helpful phenomena on beam stabilization in the linear accelerator, and the beam accumulates error during its acceleration from the electron source to the undulator, until it is damped.

According to the beam quality issue, i.e., shape of the beam distribution function, in the storage ring, beam tails are cleaned up during many turns by quantum excitation due to the synchrotron radiation, and by limited rf-bucket height or collision to the beam aperture, finally it approaches to the Gaussian shape. In the linear accelerator, there is no such natural beam cleaning effect. Additionally, we have the dark-current emission from metallic surface in high-field at the rf-gun and also in the linear accelerating structure. In order to clean up and avoid contamination, we have to prepare beam collimators in proper locations, where we carefully need to study the wakefield effect associated to non continuous change in beam aperture.

The state of the art achievement on stability has been made recently in storage rings after introducing the "Top-up mode" operation[1]. The beam intensity (or beam current) stability reached to 2 x 10^{-4} level, and the beam energy stability is in the range of 10^{-5} to 10^{-6}. for period of a day(the beam energy spread is 10^{-3}). There is no question to all synchrotron radiation users being satisfied with these beam stabilities. For example, protein crystallography, can be smoothly performed if the beam energy stability at $<10^{-3}$ level.

On the other hand, today's linear accelerator has much poorer performance, unfortunately. The charge stability from electron gun and after acceleration is in the order of 10^{-2} in single bunch mode. The energy stability is about 10^{-3}, which depends on the power supply stability, especially the line-type pulse modulator power supply stability is in 10^{-3} level. The author believes that there is much rooms of improvement on the machine performance.

The super conducting accelerator technology will solve a part of the jitter problem.

The X-ray FEL based on SASE mode will be used for very wide applications, among them; unique applications will be the basic study on high field phenomena in condensed matter, and imaging of single molecular or nano-structure by single shot. In such applications the intensity stability of 10^{-2} level and 10^{-3} energy stability will be good enough. However, the beam trajectory inside the undulator line has to be stable within 10 to 50 micron-meter (depends on design choice) for 100 m long undulator line in X-ray FELs.

Change in energy will cause trajectory deviation with dispersion in focusing system, or bunch compression factor change in chicane magnet. The charge variation will cause energy variation through beam loading effect, and bunching ratio change through space charge repulsive force, or betatron phase shift through radial space charge force. Those parameters are closely related in complex manner, so it is not simple to specify the beam stability requirement, and not be described further in this paper. The author instead will try to provide suggestions on improving the machine stability by introducing today's advancing technology in industries.

JITTER AND DRIFT SOURCES

The possible jitter sources of pulse-to-pulse change in intensity, energy, timing, etc., and sources of long-term parameter change are listed below.

(1) AC line voltage and phase fluctuation.
(2) Power supply fluctuation (due to temperature, or other reasons).
(3) Switch-tube pulse-to-pulse jitter. Residual ON-voltage and delay time variation of thyratron tube in pulse modulator power supply for the high power klystron.
(4) EM noise interfere from switching power supply of modulator and inverter type power supply.
(5) AD, DA digitising and quantized resolution noise.
(6) Temperature fluctuation on all hardware components.
(7) Ground motion of natural and human activity.

We need to cure all these sources of fluctuation. In an ideal machine, thermal noise will define all the residual

Table-1. Stability comparison.

	Storage Ring Machine	Linear Accelerator (Pulse Mode Machine)
Machine condition	All hardware are in the steady state condition.	Transient condition (less stable)
Trajectory	Closed-Trajectory (Eigen-vector)	Open-Trajectory (Not Eigen vector)
Damping	Synchrotron damping	No Damping Effect
Beam cleaning	During many turns, synchrotron excitation and beam tail loss make Gaussian beam.	Single pass. No natural beam cleaning exists. Dark-current contamination is a big problem.
Noise bandwidth	~ 1 kHz Narrow tune resonance.	~GHz. Bunched electron beam samples all the noise in wide frequency spectrum.
Energy and intensity stability	$10^{-5} \sim 10^{-6}$	$10^{-2} \sim 10^{-3}$

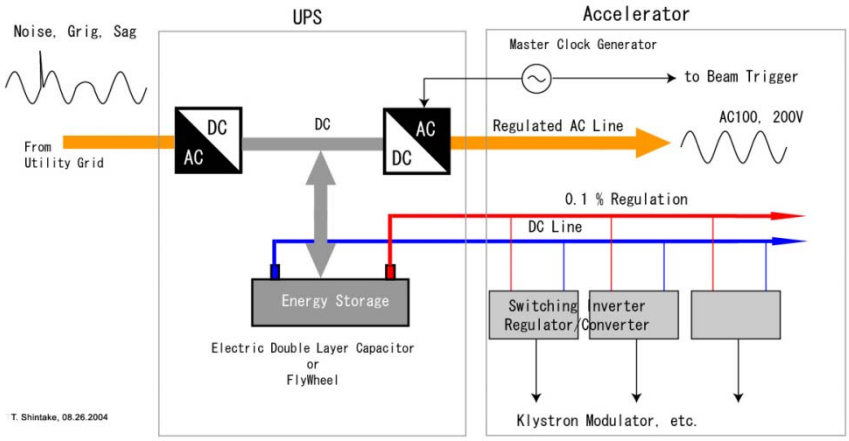

Fig. 1. UPS as an energy storage and power regulation.

fluctuations, however practical machine is far from such ideal conditions. From the following section, possible cure to these fluctuations will be discussed.

AC Line stabilization

AC line provides all the energy to the accelerator, thus it is one of the most important fluctuation source. Today's power generator plants form a network connection and exchange energy to compensate variation of energy consumption in a day or a week, and also regional unbalance between a city and industrial zone. Therefore, voltage and phase are always changing (AC phase is artificially used to control power flow in the network).

Also, in spring and summer seasons, lightning in thunderstorm causes short-term power glitches, sags or power down, resulting in beam loss, or vacuum pump down. On the other hand, in pulse mode operation of the normal conducting accelerator, machine runs at 10 to a few hundred pps, in which, after firing each pulse, the power supplies need to be re-charged within a cycle, thus system creates pulse power loading to external power grid.

In order to avoid the power down, and also prevent the system to sending the pulse loading to external site, the accelerator should be equipped with UPS (uninterruptible power supplies). A small UPS system has been used to backup the computer power in important network servers, where mostly the small size chemical batteries were used. For large scale application, such as in a hospital or semiconductor fabrication line, a diesel engine was used, but it runs limited time only after the AC power down, and can not be used continuously. An advanced system using flywheel energy storage [2] and IGBT switching power controller can be found in large scale applications, such as semiconductor fabrication line.

UPS system using lead acid battery also used in a large system, however, it needs frequent maintenance on the battery with careful treatment of acid. The lead acid battery is also massive.

In electric car development, a new type of energy storage using "double layer capacitor" appears to be the most promising battery [3]. The energy to mass ratio is ten times higher than the lead acid battery, and does not use the chemical process to store the electric charge, therefore the life time is much longer. The USP system capable of handling 400 kW using this type of capacitor is already on market [4].

Fig. 2 shows a possible UPS power regulation system. The key points are

(1) The double layer capacitor store energy for UPS function.
(2) The switching inverter converts DC power to AC power with high regulation and its cycle is locked to a clock generator in the accelerator.
(3) The AC power from external grid is converted to DC power through active rectifier on the double layer capacitor, and regulated.
(4) The DC power is also directly distributed to accelerator, and used for various voltage through switching converter. In this scheme, we can simplify each power supply by eliminating AC-DC converter parts.
(5) Pulse loading effect in the linear accelerator is almost perfectly compensated by the energy storage in UPS.

Detail information of the double layer capacitor can be found in ref. [3].

EM NOISE

The traditional design of the line type pulse power supply (modulator) generates strong EM noise. The rush current in thyratron switch is usually 1000A or more, the voltage swing across the switch is 20 to 50 kV, and the switching speed exceeds order of 10 kV/100 ns. If the circuit is not properly designed, the switching circuit will radiate EM noise in wide frequency spectrum at DC to a few tens MHz. Once this radiation spreads out to envi-

Fig. 2. Klystron pulse modulator for SCSS project. All HV components are installed in metallic shield tank, and filled with oil.

ronment of accelerator system, its runs along the power line or control line, finally cause various effects on the system. Most sensitive part is the beam diagnostics, and user experiments.

In order to cure this noise, we have to design the noise source not to radiate to outside, or to keep the rush current within the closed circuit. To do this, the Faraday cage concept provides best guideline on hardware design. As shown in Fig. 2, if the switching circuit is perfectly surrounded by a closed metallic boundary, no EM field will can leak out. But weed to make holes to provide in and out power feeds, or control lines. We can stop the noise leakage through these holes and wires by properly choosing filter, so called, common-mode choke. Today, such filters can be easily found in market.

Fig. 3 shows the klystron power supply developed in SCSS project based on Faraday-cage concept. All of the switching device and high voltage components of the modulator are installed into a metallic shield box made by stainless panels, and filled with oil to prevent the circuit from high voltage discharge. The stainless panels are standard components designed for water supply, so it is not expensive. This design is also desirable to isolate high voltage circuit from the environmental change, i.e., the humidity, temperature, or dust contamination.

The same guideline can be applied to all the circuit components in liner accelerators.

ASIC DEVICE

ASIC: Application Specific Integrated Circuit is widely used in rf, wireless and optical fiber communications, and also electrical test equipments [5]. This technology is based on silicon and germanium integrated circuit, which suitable to design frequency up- and down- converting mixer and amplifier in rf-detector and modulator, or BPM detector. In linear accelerators, rf: radio-frequency power is used as the energy source of particle acceleration, or beam monitoring signal. There are basic functions of

(1) Signal modulation of rf-carrier and de-modulation.
(2) Frequency up and down conversion.
(3) Local frequency generation using PLL.
(4) Level adjustment according to the beam intensity.

All of those functions can be integrated into a chip based on ASIC technology. We may also realize those circuits via traditional design like circuit boards in a shielding box. With ASIC, we may eliminate shielding box, since the chip size is much smaller than the typical wavelength of signal, thus it is in-sensitive to noise environment. Also it is easy to utilize the laser trimming technique to adjust the balance of mixers, or the amplifier gain, thus it is fairly easy to produce repeatable parameter for many number of circuit in mass production, which resulting in reducing the fabrication cost.

Additionally, standardization of basic functions listed above by means of ASCI design will make easier to share the circuit design between each accelerator design groups, which will enhance the R&D efficiency.

THE MECHANICAL STRUCTURE

Mechanical support structure of accelerator component is also important subject for stability issue. Since the X-FEL requires very small electron beam emittance: 1 π.mm.mrad, the beam size in the undulator becomes about 100 micron-meter or smaller. We need to keep overlapping of the electron beam and X-ray radiation through undulators, therefore, the position stability of focusing component has to be very stable.

Traditionally we use a support structure made by steel framework to support Q-magnet, and position of the beam pipe is about 1 m high from floor. Since the heat capacitance of the steel framework usually not so big, the framework temperature always follows the air temperature. If the room temperature changes 1 deg.C, the steel framework will expand 12 micron-meter, which is already close to the tolerance limit of the alignment.

If the temperature distribution around the steel framework is not uniform, it will cause transverse displacement. If there is forced air flow inside tunnel, or a heat source located nearby (a lump or cooling water), this type of displacement becomes not negligible.

The author would like to suggest the following design for support structure in X-FEL.

(1) Locate beam height as low as possible. Lower structure makes vertical and transverse displacement due to thermal expansion smaller, and also provides higher stiffness.
(2) Use low thermal expansion material.
(3) Use massive volume structure rather than frame work. Larger heat capacity makes sensitivity to ambient temperature change smaller. Larger mass makes vibration amplitude from external force smaller.

Table-2. Material Properties for Support Structure

	Units	Steel	Alumina	Granite	Concrete	Anocast™	Cordierite	Fused Silica
Chemical formula		Fe(C)	Al_2O_3			Epoxy resin quartz	$2MgO\text{-}2Al_2O_3\text{-}5SiO_2$	SiO_2
Thermal expansion	10^{-6} /C	6~15	7	5 ~ 15	7 ~ 13	17	1~0.1 * 1.7 **	0.45**
Thermal conductivity	W cm/°C	0.8~2	0.17~0.29	0.02	0.01	0.24	0.03	0.014
Specific heat	Cal/g°C	0.1	0.19	0.2	0.24~0.3	0.23~0.26	0.35	0.16
Density	g/cm^3	7.8	3.8	2.6~2.7	2.4	2.32	2.6	2.2
Compressive strength *	MPa	1000-2000	~2000	130	30~100	110-117	350	650-1100
Tensile strength *	MPa	1800	260-300		-	15.2	25.5	48

* room temperature - **~25ºC through ±1000ºC

Table 2 compares several materials for support structure. Among them, candidates for the support structure will be cordierite ceramic or fused silica. In industrial ceramic factory, the cordierite has been used as high-voltage bushing operating at high temperature in a dust cleaning chamber at the power generation plant. Therefore, technology to fabricate meter-size cylinder with cordierite and fixing to metal flange exists in ceramic factory [6]. We may employ the cordierite ceramic tube as the stable support with reasonable cost. Fig. 3 shows our ceramic support for SCSS project, on which focusing Q-magnet and BPM will be installed in the undulator line. The outer surface of the ceramic is covered by soft polymer sponge (black color) for protection. Inner volume is filled with sand to damp mechanical vibration. With careful measurement, we found the thermal expansion ratio was $1.9x10^{-6}$ (1/C).

The same concept can be applied to large scale magnetic device, such as the undulator. In the undulator, linear arrays of permanent magnet generate periodic transverse field. Since the field is fairly uniform in transverse plane, we do not need precise positioning of the undulator. However, the field intensity is a strong function of the gap size of two magnet arrays, we need to precisely maintain the relative position of the gap, tolerance is order of 1 micron-meter.

In the undulator design, steel structure have been used to hold the magnetic array. However, as mentioned above, the steel frame work does not have enough heat capacity, thus it changes the dimension with ambient temperature change.

The author would like to suggest the granite table as the support structure for the magnet array of the undulator. From the thermal expansion point of view, cordierite will

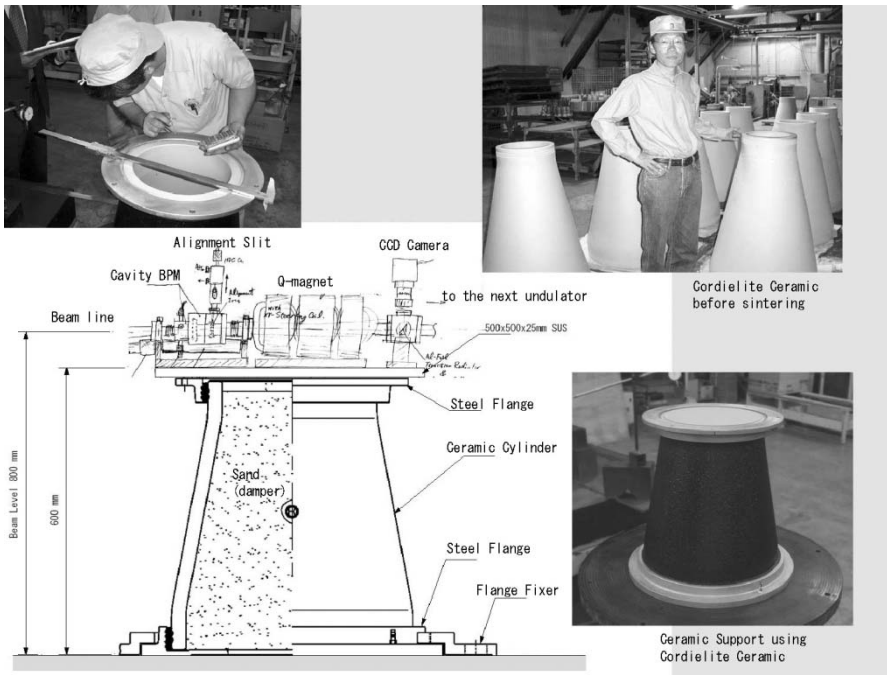

Fig. 3. Ceramic material is suitable to stable support for accelerator component.

Fig. 4. Granite table as the support structure of the undulator magnet. Massive granite will provide high rigidity against various deformation forces. In-situ field measurement will be performed by movable probe, whose linear guide has to be integrated into the chamber.

be the best choice, but ceramic factory can not handle a few meter long structure. If we chose granite, we can find a few meter long solid block with reasonable cost. Casted concrete, with steam heat treatment, may be alternative candidate, but we need a careful study on slow dimension change with drying for few years.

Fig. 4 shows illustration of the idea. Massive granite will provide high rigidity against various deformation forces. The assembly and field tuning will be made in a laboratory, the we transport the undulator to the tunnel. During this transport, various external forces will be applied and also internal force due to temperature change will cause deformation. Therefore, the support structure has to have high rigidity.

In the X-ray FEL, since the field tolerance is very tight, while the beam quality will not be good as one in the storage ring, and also dark-current emission from the linear accelerator cause degradation of magnetic property.

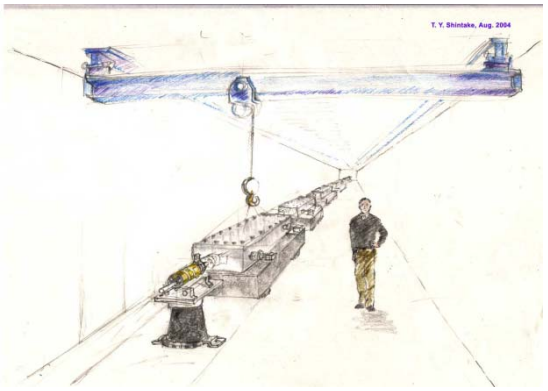

Fig. 5. Accelerator tunnel image. Focusing elements sit on the ceramic cylinders, and undulators are on the granite table.

Therefore, in-situ field measurement will be non evitable process and scheduled measurement has to be repeated once per year, for example. As shown in the figure, in-situ field measurement will be performed by a movable probe, whose linear guide will be integrated into the chamber.

When we install the focusing elements and undulators, the tunnel becomes as Fig. 5. Beam line height will be 1m or lower, the undulator will be accessible from top cover. The total length of undulator line will be 100m or longer in X-FEL.

CONCLUSION

The X-ray FEL based on SASE mode request revolutionary improvement on accelerator performance. The super conducting accelerator technology will solve a part of the jitter problem, but at the same time it may introduce new type of difficulties. Now, the X-FEL is a big challenge to the accelerator community. Continuous persevering efforts in each detail will be requested.

REFERENCES

[1] Hitoshi Tanaka et. al., "Top-up Operation at SPring-8 - Towards Maxmizing the Potential of a 3rd Generation Light Source", EPAC2004.
[2] Active Power Inc., http://www.activepower.com/
[3] Okamura Laboratory Inc., http://www.okamura-lab.com/index.htm
[4] Shizuki electric Co., http://www.shizuki.co.jp/electric/v_lineup.html
[5] for example, Maxim Integrated Products, Inc., http://www.maxim-ic.com/asics.cfm
[6] for example, Daito Co., http://www.daito-otk.co.jp/frame15.htm

SCHEME FOR GENERATION OF SINGLE 100 GW 300-AS PULSE IN THE X-RAY SASE FEL WITH THE USE OF A FEW CYCLES OPTICAL PULSE FROM TI:SAPPHIRE LASER SYSTEM

E.L. Saldin, E.A. Schneidmiller and M.V. Yurkov
Deutsches Elektronen-Synchrotron (DESY), Hamburg, Germany

Abstract

Femtosecond optical pulse interacts with the electron beam in the two-period undulator and produces energy modulation within a slice of the electron bunch. Then the electron beam enters the first part of the X-ray undulator and produces SASE radiation with 100 MW-level power. Due to energy modulation the frequency is correlated to the longitudinal position, and the largest frequency offset corresponds to a single-spike pulse in the time domain which is confined to one half-oscillation period near the central peak electron energy. After the first undulator the electron beam is guided through a magnetic delay which we use to position the X-ray spike with the largest frequency offset at the "fresh" part of the electron bunch. After the chicane the electron beam and the radiation enter the second undulator which is resonant with the offset frequency where only a single (300 as duration) spike grows rapidly. The final part of the undulator is a tapered section allowing to achieve maximum output power 100-150 GW in 0.15 nm wavelength range.

INTRODUCTION

With the realization of the fourth-generation light sources operating in the X-ray regime [1, 2], new attoscience experiments will become possible. In its initial configuration the XFEL pulse duration is about 100 fs, which is too long to be sufficient for this class of experiments. The generation of subfemtosecond X-ray pulses is critical to exploring the ultrafast science at the XFELs. The advent of attosecond X-ray pulses will open a new field of time-resolved studies with unprecedented resolution. X-ray SASE FEL holds a great promise as a source of radiation for generating high power, single attosecond pulses. Recently a scheme to achieve pulse duration down to attosecond time scale at the wavelengths around 0.1 nm has been proposed [3]. It has been shown that by using X-ray SASE FEL combined with terawatt-level, sub-10-fs Ti:sapphire laser system it will be possible to produce GW-level X-ray pulses that are reaching 300 attoseconds in duration. In this scheme an ultrashort laser pulse is used to modulate the energy of electrons within the femtosecond slice of the electron bunch at laser frequency. Energy-position correlation in the electron pulse results in spectrum-position correlation in the SASE radiation pulse. Selection of ultra-short X-ray pulses is achieved by using the monochromator. Such a scheme for production of single attosecond X-ray pulses would offer the possibility for pump-probe experiments, since it provides a precise, known and tunable interval between the laser and X-ray sources.

In this paper we propose a new method allowing to increase output power of attosecond X-ray pulses by two orders of magnitude. It is based on application of sub-10-fs laser for slice energy modulation of the electron beam, and application "fresh bunch" techniques for selection of single attosecond pulses with 100 GW-level output power. The combination of very high peak power (100 GW) and very short pulse (300 as) will open a vast new range of applications. In particular, we propose visible pump/X-ray probe technique that would allow time resolution down to subfemtosecond capabilities. Proposed technique allows to produce intense ultrashort X-ray pulses directly from the XFEL, and with tight synchronization to the sample excitation laser. Another advantage of the proposed scheme is the possibility to remove the monochromator (and other X-ray optical elements) between the X-ray undulator and a sample and thus to directly use the probe attosecond X-ray pulse.

Operation of 100 GW attosecond SASE FEL is illustrated for the parameters close to those of the European XFEL operating at the wavelength 0.15 nm [1]. Optimization of the attosecond SASE FEL has been performed with the three-dimensional, time dependent code FAST [5] taking into account all physical effects influencing the SASE FEL operation (diffraction effects, energy spread, emittance, slippage effect, etc.).

HIGH POWER ATTOSECOND FACILITY

A basic scheme of the high-power attosecond X-ray source is shown in Fig. 1. An ultrashort laser pulse is used to modulate the energy of electrons within the femtosecond slice of the electron bunch at laser frequency. The seed laser pulse will be timed to overlap with the central area of the electron bunch. It serves as a seed for modulator which consists of a short (a few periods) undulator. Following the energy modulator the beam enters the baseline (gap-tunable) X-ray undulator. In its simplest configuration the X-ray undulator consists of an uniform input undulator and nonuniform (tapered) output undulator separated by a magnetic chicane (delay) as it is shown in Fig. 2.

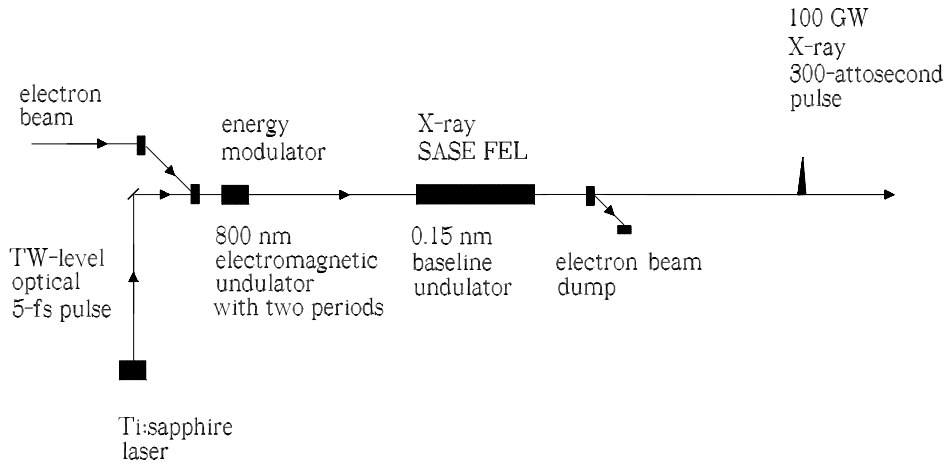

Figure 1: Schematic diagram of high power attosecond X-ray source.

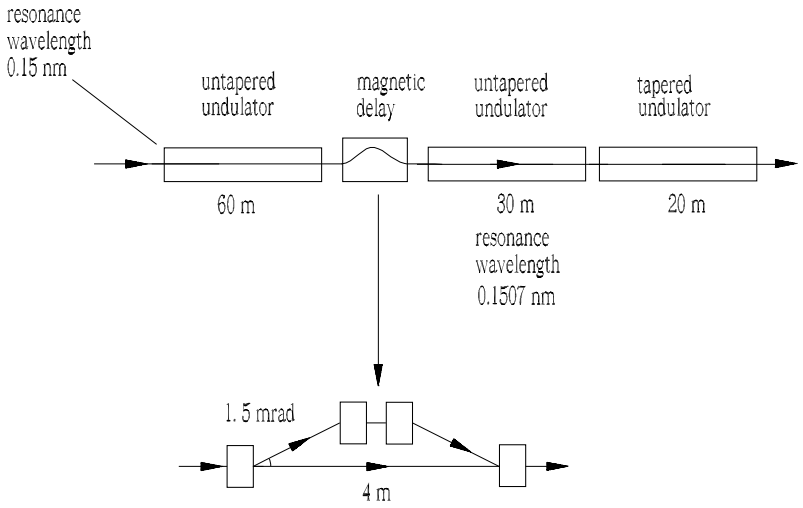

Figure 2: Design of undulator system for high power attosecond X-ray source.

The process of amplification of radiation in the input undulator develops in the same way as in conventional X-ray SASE FEL: fluctuations of the electron beam current serve as the input signal. When an electron beam traverses an undulator, it emits radiation at the resonance wavelength $\lambda = \lambda_w(1 + K^2/2)/(2\gamma^2)$. Here λ_w is the undulator period, $mc^2\gamma$ is the electron beam energy, and K is the undulator parameter. In the proposed scheme the laser-driven sinusoidal energy chirp produces a correlated frequency chirp of the resonant radiation $\delta\omega/\omega \simeq 2\delta\gamma/\gamma$.

Our concept of attosecond X-ray facility is based on the use of a few cycle optical pulse from Ti:sapphire laser system. This optical pulse is used for modulation of the energy of the electrons within a slice of the electron bunch at a wavelength of 800 nm. Due to extreme temporal confinement, moderate optical pulse energies of the order of a few mJ can result in electron energy modulation amplitude higher than 30-40 MeV. In few-cycle laser fields high intensities can be "switched on" nonadiabatically within a few optical periods. As a result, a central peak electron energy modulation is larger than other peaks (see Fig. 3). This relative energy difference is used for selection of SASE radiation pulses with a single spike in time domain. Single-spike selection can effectively be achieved when electron bunch passes through a magnetic delay and output undulator operating at a shifted frequency.

Operation of proposed attosecond facility is illustrated with Figs. 4-6. The input undulator is a conventional 0.15 nm SASE FEL operating in the high-gain linear regime. This undulator is long enough (60 m) to reach 100 MW-level output power (see Fig. 2). After the input undulator the electron beam is guided through a magnetic delay (chi-

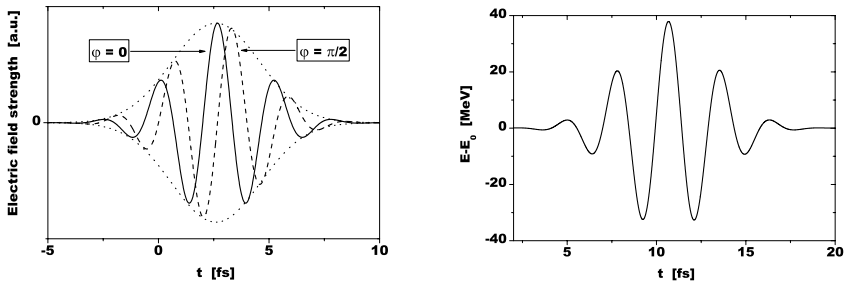

Figure 3: Left plot: electric field strength within femtosecond laser pulse. Right plot: energy modulation of electron bunch at the exit of the modulator.

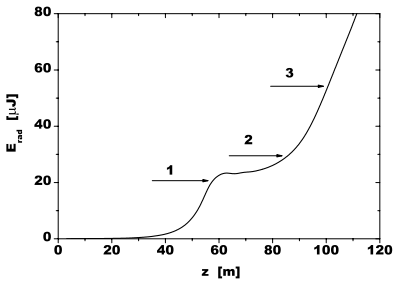

Figure 4: Energy in the radiation pulse versus undulator length. Marks 1, 2, and 3 show the end points of the 1st, 2nd, and 3rd undulator sections, respectively.

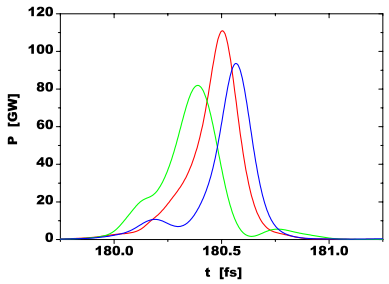

Figure 6: Shot-to-shot fluctuations of the radiation pulse after monochromator with 0.5% linewidth tuned to the frequency of the main maximum. Undulator length is 100 m.

cane). The trajectory of the electron beam in the chicane has the shape of an isosceles triangle with the base equal to L. The angle adjacent to the base, θ, is considered to be small. Parameters in our case are: $L = 4$ m, $\theta = 1.5$ mrad, compaction factor $L\theta^2 = 8\mu$m, extra path length $L\theta^2/2 = 4\mu$m, horizontal offset $L\theta/2 = 3$ mm. In the present design we have only 4 μm extra path length for the electron beam, while the FWHM length of electron bunch is about 50 μm. Calculations of the coherent synchrotron radiation effects show that this should not be a serious limitation in our case.

Passing the chicane the electron beam and seed SASE radiation enter the output undulator operating at an offset frequency. We use a magnetic delay to position the offset frequency radiation at the "fresh" part of the electron bunch. This seed single spike at an offset frequency starts interacting with the new set of electrons, which have no energy modulation, since they did not participate in the previous interaction with optical laser pulse. This is the essence of the "fresh bunch" techniques which was introduced in [4].

In the output undulator seed radiation at reference frequency plays no role. However, single spike at an offset frequency is exponentially amplified upon passing through the first (uniform) part of the output undulator. This part is long enough (30 m) to reach saturation. The power level at saturation is about 20 GW. The most promising way to extend output power is the method of tapering the magnetic field of the undulator. Tapering consists in slowly reducing the field strength of the undulator field to preserve the resonance wavelength as the kinetic energy of the electrons changes. The strong radiation field produces a ponderomotive well which is deep enough to trap the particles. The radiation produced by these captured particles increases the depth of the ponderomotive well, and they are effectively decelerated. As a result, much higher power can be achieved than for the case of a uniform undulator. At the total tapered undulator length of 20 m, the single-spike power is enhanced by a factor of five, from 20 GW-level to 100 GW-level. Figure 6 shows temporal characteristics of the radiation pulse at the exit of the undulator after monochromator with 0.5% linewidth. It is seen that the method proposed in this paper allows direct production from XFEL of single 100 GW-level X-ray pulses with FWHM duration of 300 as.

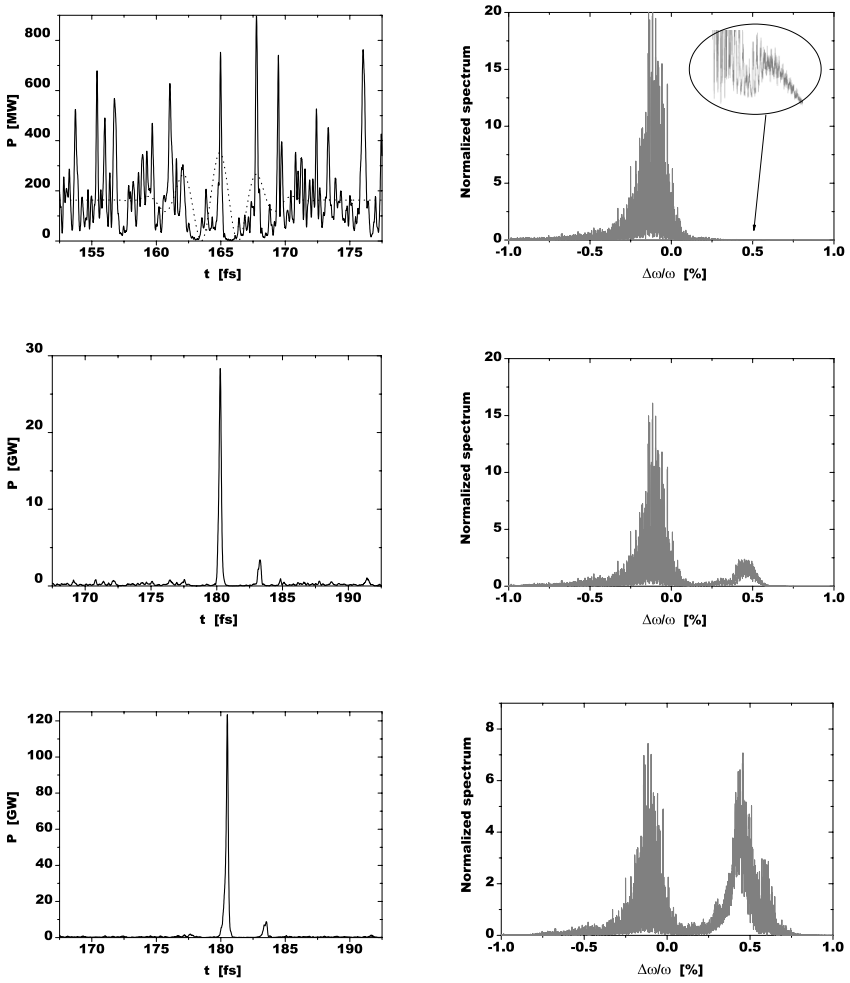

Figure 5: Temporal (left column) and spectral (right column) evolution of the radiation pulse along the undulator. Upper, middle, and lower plots correspond to the undulator lengths of 57, 85, and 100 m. Dashed line shows energy modulation of the electron bunch.

CONCLUSION

Today there are at least two possible attosecond X-ray sources for light-triggered, time-resolved experiments associated with the X-ray SASE FEL: the "attosecond X-ray parasitic" [3] and the "attosecond X-ray dedicated" source mode proposed in this paper. The simplest way to obtain attosecond X-ray pulses from XFEL is to use "parasitic" technique which is proposed in [3]. It also would offer the possibility of providing a beam to a pump-probe experiments with the XFEL that has a precise, known and tunable time interval between the laser and X-ray sources. More power of attosecond pulse could be obtained using the XFEL for dedicated attosecond X-ray pulse production as described in this paper.

REFERENCES

[1] P. Audebert et al., "TESLA XFEL: First stage of the X-ray laser laboratory – Technical design report (R. Brinkmann et al., Eds.)", Preprint DESY 2002-167.

[2] The LCLS Design Study Group, LCLS Design Study Report, SLAC reports SLAC- R521, Stanford, 1998.

[3] E.L. Saldin, E.A. Schneidmiller and M.V. Yurkov, Optics Communications 237(2004)153.

[4] L. H. Yu and I. Ben-Zvi, Nucl. Instrum. and Methods A393(1997)96.

[5] E. L. Saldin, E. A. Schneidmiller and M. V. Yurkov, Nucl. Instrum. and Methods **A 429**(1999)233.

AN EXPERIMENTAL STUDY OF THE BEAM-STEERING EFFECT ON THE FEL GAIN AT LEUTL'S SEGMENTED UNDULATORS*

Y.-C. Chae#, A.H. Lumpkin, M. Erdmann, J.W. Lewellen, and S.V. Milton
Advanced Photon Source Argonne National Laboratory Argonne, Illinois 60439 USA

Abstract

The electron trajectories at the low-energy undulator test line (LEUTL), a self-amplified spontaneous emission (SASE) free-electron laser (FEL) facility at Argonne, were routinely corrected during the user run in order to deliver maximum radiation power to the user. Even though we knew from experience that SASE gain at the segmented undulators was dependent on the trajectory, the quantitative understanding of steering effects associated with the specific trajectory was lacking. Recently Tanaka et al. [1] proposed an analytical model for the single-kick error (SKE) effect. Since the LEUTL has eight segmented undulators, we performed the first measurement of SKE on the FEL gain. In the experiments we varied the corrector strength up to the critical angle, and the gain over the undulator was measured for each corrector setting. The results were compared with the analytical model and GENESIS simulations. We also measured the e-beam positions and SASE intensities over the undulators. The experimental data were analyzed and their results were reproduced by GENESIS simulation. The simulation condition, including the measured not-so-ideal trajectory, was used to predict performance enhancements that could be achieved by upgrading e-beam current, e-beam emittance, or trajectory control.

EXPERIMENTAL SETUP

The low-energy undulator test line (LEUTL) is the Advanced Photon Source's self-amplified spontaneous emission (SASE) free-electron laser (FEL) facility, which has shown high gain and saturation near 530 nm and 385 nm, as reported elsewhere [2]. The schematic of the facility is shown in Fig. 1, which includes a photocathode rf-gun, a 650-MeV linac, 3-screen emittance measurement area, and undulators with diagnostic stations between them.

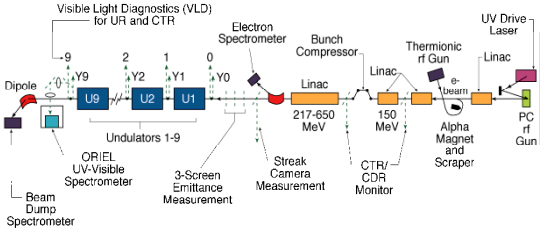

Figure 1: Schematic of APS SASE FEL experiment.

*Work supported by the U.S. Department of Energy, Office of Basic Energy Sciences, under Contract No.W-31-1090-ENG-38.
#chae@aps.anl.gov

The experiments were performed around the fifth undulator ID-5, which also includes a horizontally focusing quadrupole, a steering coil, and a reflecting mirror that transports the radiation to VUV cameras, as shown in Fig. 2.

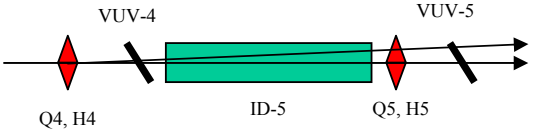

Figure 2: Schematic of a segmented undulator used for single-kick-error (SKE) measurement; shown are quadrupoles Q4 and Q5 with steering coils H4 and H5, mirror and cameras VUV-4 and VUV-5, and the fifth undulator ID-5 over which we measure the gain of SASE radiation.

During experiment we steered the orbit by using the H4 corrector. For a given H4 strength we record the radiation images by using cameras VUV-4 and VUV-5 before and after undulator ID-5. The undulator radiation by SASE was used to measure the gain over the undulator. The coherent transition radiation (CTR) was used not only to measure the electron beam's microbunching but also to measure the beam's position in order to estimate the steering angle. The CTR is generated by interaction of a 6-μm-thick Al foil and the beam, as describe in Ref. [3]. The angle estimate is based on the fact that in the horizontal plane the undulator is a drift space where the e-beam's trajectory is straight. For each radiation type, SASE or CTR, we took near-field and far-field imaging. Because of the statistical nature of the SASE process, we took 100 images of each type of radiation for a given steering angle.

At the beginning of the experiment we established a reference orbit that should provide exponential gain over ID-5 but should not be saturated there. The experimental conditions were radiation wavelength λ=130 nm, beam energy E=439 MeV, charge Q=250 pC, FWHM pulse length σ_t=250 fs, energy spread σ_E=0.15%, and normalized emittance $\varepsilon_x/\varepsilon_y$=4.5/3.5 π mm-mrad, respectively. The measured SASE intensity along the undulators is shown in Fig. 3, where two results from processing near-field and far-field images are presented. The horizontal axis refers to the location after the n^{th}-undulator.

Radiation power or intensity shown in Fig. 3 was estimated by integrating the intensities of image as follows: 1) project 100 images into the horizontal or vertical axis in order to obtain the profile in either

plane, 2) take the average of 100 profiles to make a single profile representing the average state of the measurement condition, 3) set the baseline of the profile to zero as a background removal, and 4) integrate the profile in order to obtain the total intensity. Thus this total intensity represents the averaged power of 100 radiation pulses resulting from a given experimental condition. Since the background of the profile is different in the horizontal and vertical planes, the resultant intensities I_x and I_y are not necessarily the same. In order to have a unique quantity, we take the average of the two quantities $I=(I_x+I_y)/2$. The unit of intensity obtained this way is arbitrary, but the real radiation power is proportional to this quantity so that we can estimate the gain.

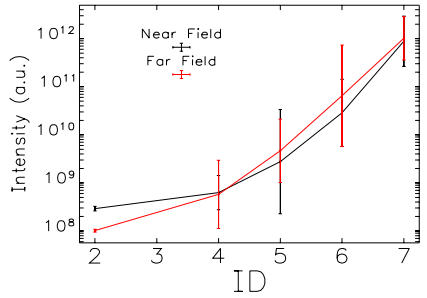

Figure 3: The z-dependent SASE power measurements at ID-2,4,5,6,7; both far-field and near-field results are included for comparison.

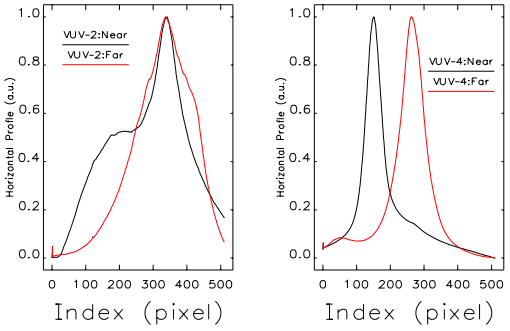

Figure 4: Horizontal profiles of undulator radiation images at two different locations at ID-2 and ID-4. The images from ID-2 in small-gain are displayed on the left and the ones from ID-4 in exponential gain are compared on the right. The far-field images in red provide better-defined profiles than the near-field images in black which have broader shoulders.

Far-field and near-field images were examined in order to explain the discrepancies shown in Fig. 3. We found that radiation profiles from near-field images have a broader shoulder than the far-field images shown in Fig. 4, which were taken at VUV-2 and VUV-4. Whether this shoulder resulted from the variation in trajectory or from the reflection in the light tube due to the limited acceptance is yet to be determined. We observed that the far-field images in general provide better-defined profiles with higher intensities. Thus we decided to use far-field images in measuring the intensity of the SASE pulse in the SKE experiment where we vary the steering angle.

SINGLE-KICK ERROR (SKE) EXPERIMENT

According to Tanaka's model [1] the gain will be degraded by the SKE due to two effects: 1) the mismatch between incoherent radiation with angle of incidence and coherent radiation with its wave-front normal in the z-direction and 2) the smearing of micro-bunching. Since the analysis of microbunching is incomplete when providing the results in bounded form, we only refer to the first case where we compare the experiment and the theory. The model predicts that the gain will be degraded according to

$$L_g' = \frac{L_g}{1-x^2}, \qquad (1)$$

where $x = \theta/\theta_c$. The critical angle is defined as $\theta_c = \sqrt{\lambda / L_g}$, where λ is the radiation wavelength and L_g is the gain length of ideal trajectory, and θ is the steering angle.

After we established the reference trajectory described in the previous section we adjusted the angle of trajectory by varying the corrector H4. A calibration was performed on H4 and found that it can steer 0.34 mrad/A. Since the critical angle of this experiment was estimated to be 0.4 mrad we decided to vary H4 by ±1 A with the respect to the currently set -0.7 A. For each H4 setting we measured the intensities at VUV-4 and VUV-5. Even though VUV-4 measurements shouldn't depend on the H4s, the repeated measurements were necessary in order to make sure that we could detect drift of beam condition while we were taking data for five hours.

The intensities as a function of H4 are shown at the top of Fig. 5. The black curve represents the intensity at VUV-4 showing we maintained steady beam operation, and the red curve gives the results at VUV-5 showing the significant variation on average power over the H4s. We also note large fluctuations at VUV-5, a characteristic of exponential gain regime. The ratio of average power between VUV-4 and VUV-5 is the gain to be compared with the SKE model of Eq. (1). At the same time we also acquired CTR images. The centroids of images representing the e-beam positions are also shown in Fig. 5 as a function of H4.

Data shown in Fig. 5 were processed in terms of gain and steering angle. The result is fitted by Eq. (1) with two parameters, the offset angle θ_0 in slightly generalized $x=(\theta_0-\theta)/\theta_c$ and the gain length L_g. We found θ_0 close to zero and L_g equal to 1.6 m. The comparison between the experiment and theory is

shown in Fig. 6. Since the critical angle with λ=130 nm and L_g=1.6 m is 0.28 mrad, two data points whose steering angles are greater than 0.3 mrad are out of range but still had small gain. One data point near 0.1 mrad, whose gain is far smaller than theory predicts, corresponds to the corrector setting H4=-0.2 A where the beam position didn't respond to the setting, as was revealed in Fig. 5. Thus we are suspicious about this data point, and we may disregard its validity in its gain. Other than that we have good agreement between the measurement and the model prediction.

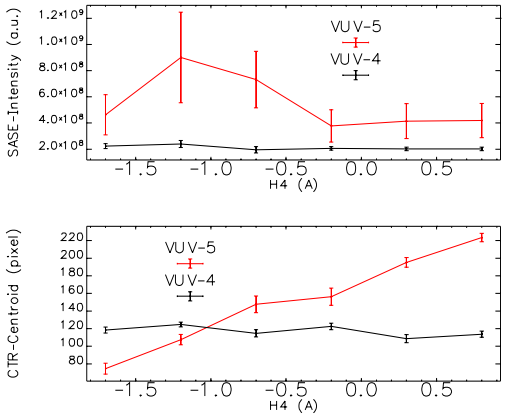

Figure 5: SASE radiation intensities measured by cameras VUV-4 and VUV-5 as a function of H4 (top) and electron beam position estimated by CTR images as a function of H4 (bottom)

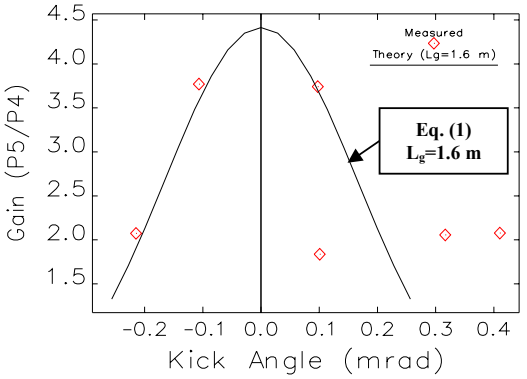

Figure 6: Measured gains as a function of steering angle compared with theory (Eq. (1)).

COMPARISON WITH SIMULATION

We used the GENESIS program [4] in order to compare the experimental results with simulation. The simulation conditions were the same as the experimental condition specified in the previous section. In the simulation we needed to vary the beam current in order to find the condition resulting in the gain length equal to 1.6 m. In the steady-state simulation we found the solution at 380 A, and in the SASE simulation the solution was 550 A for a given 250-fs pulse length.

Once we settled on the beam parameters, we varied the corrector in the GENESIS simulations in a segmented undulator configuration; both steady-state and SASE simulations were performed. All results, including experiment, theory, and simulations, are included in Fig. 7 and show good agreement with each other. We note that the theory and steady-state simulations have better agreement because the analytical model assumed DC beam. The results by pulsed beam, which represents a more realistic situation, indicates that the ideal gain length should be slightly shorter than 1.6 m in order to have a better fit.

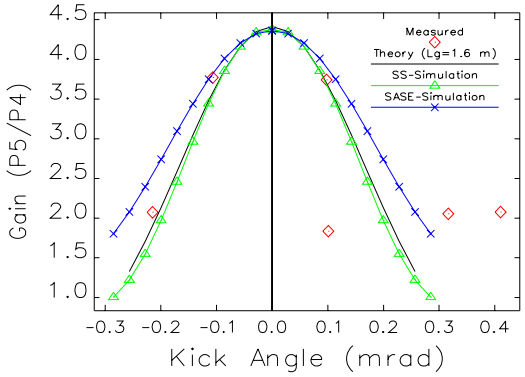

Figure 7: Gain vs. steering angle: experiment (diamond symbol), theory (black line), steady-state (SS) simulation (green line with symbol), time-dependent (SASE) simulation (blue line with symbol).

TRAJECTORY ANALYSIS

As we verified the steering effect quantitatively, we gained a better understanding of the importance of trajectory control in the segmented undulators. However, we questioned how much we could improve the FEL performance by correcting the trajectory. With this as motivation, we tried to reproduce by simulations the measured trajectory and z-dependent gains. Then, the simulation conditions found this way could be used to benchmark the effectiveness of trajectory control vs. upgrading other beam parameters such as beam current and beam emittances.

The first requirement for trajectory analysis is to determine the trajectory. Instead of relying on beam position monitors (BPMs) installed in the LEUTL tunnel, we used CTR images for determining e-beam positions. As usual, 100 shots of images were taken at the camera stationed between the undulators.

The trajectory responsible for the gain shown in Fig. 3 has been determined experimentally, and its results are depicted in Fig. 8, which includes the centroid coordinates of the e-beam and the alignment laser on the viewing screen. The difference between the two will be the beam position with respect to the alignment

laser; this trajectory is shown at the bottom of Fig. 8. Since not all stations have VUV or diagnostic cameras, we could only measure positions at VUV-2,4,5,6,7. Even though we measured both horizontal and vertical positions, we only took the horizontal trajectory into account in our simulation.

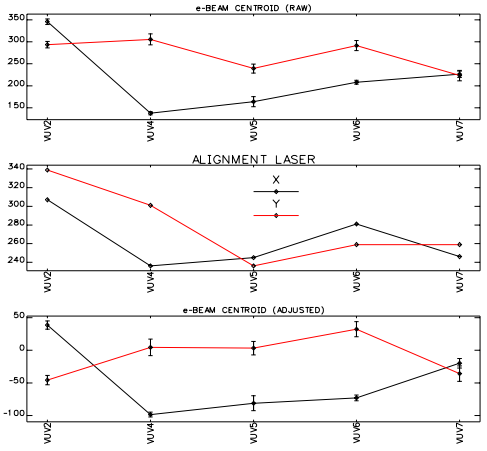

Figure 8: Trajectory measurement along the undulators by using CTR images: (top) electron beam centroid, (middle) alignment laser beam, (bottom) electron beam positions with respect to the alignment laser at VUV-2,4,5,6,7.

Since our measured trajectories were limited, we tried several simulated trajectories with right betatron oscillations. The most successful "guesstimate" is depicted in Fig. 9 together with measured beam positions. With these simulated trajectories we could reproduce the z-dependent gain quite accurately, as shown in Fig. 10. Because of this good agreement in gain measurement, we use this simulated trajectory testing in several performance upgrading scenarios.

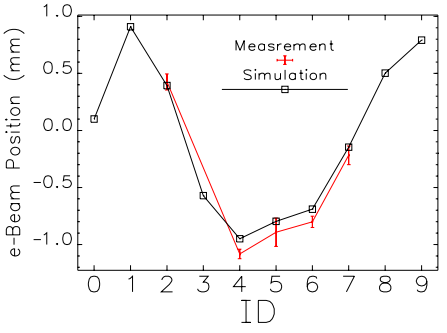

Figure 9: Measured beam positions and their simulated trajectories used in the GENESIS simulation.

For definite comparison we put three upgrade scenarios into one picture: 1) increase the beam current from 950 A to 1250 A, 2) reduce the beam emittance from 4.5/3.5 π mm-mrad to 3/3 π mm-mrad, and 3) correct trajectory to an ideal trajectory. The assumed amount of current and emittance improvement are arbitrary but within an achievable envelope in the near future as gun technology develops. Trajectory control requires improving BPM electronics in terms of sensitivity and gain bandwidth. The combination of improvements in both beam and trajectory is the ideal upgrade path, but we emphasize controlling trajectory could be easy and its effect would be immediate as evidenced by the simulation study shown in Fig. 11.

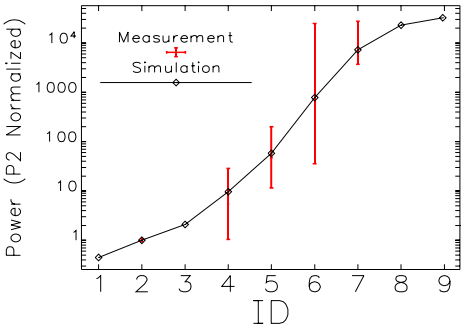

Figure 10: Measured gain at ID-2,4,5,6,7 and the corresponding simulation results. Power is normalized by the power at ID-2 or VUV-2.

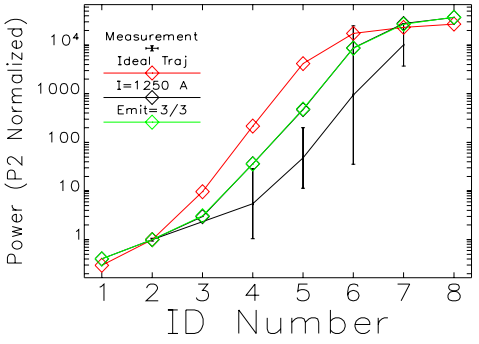

Figure 11: Comparison of performance upgrade options: 1) trajectory correction, 2) current increase, 3) emittance reduction.

SUMMARY

We measured the SKE effect for the first time, and we obtained good agreement between theory, experiment, and simulation. We also analyzed a measured trajectory to show that improving trajectory could be as important as improving the beam qualities.

REFERENCES

[1] T. Tanaka et al., "Consideration on an Alignment Tolerance of BPMs for SCSS Undulator Line," Proc. 25th International FEL Conference, September 9-12, 2003, Japan
[2] S. V. Milton et al., Science 292, 2037 (2001).
[3] A. H. Lumpkin et al., Phys. Rev. Lett. 86, 79 (2001).
[4] S. Reiche, Nucl. Instrum. Methods Phys. Res. A 429, 243 (1999).

START-TO-END INJECTOR AND LINAC TOLERANCE STUDIES FOR THE BESSY FEL*

M. Abo-Bakr†, M.v. Hartrott, J. Knobloch, B. Kuske, A. Meseck, BESSY, Berlin, Germany

Abstract

BESSY is proposing a soft X-ray FEL user facility in Berlin, delivering short and stable photon pulses in the wavelength range of 62 nm $\leq \lambda \leq$ 1.2 nm by utilizing up to four cascaded High Gain Harmonic Generation (HGHG) stages [1]. To optimize the FEL performance of the cascaded HGHG stages extensive Start-to-End (S2E) simulations have been carried out. To test the quality of the chosen configuration with respect to the sensitivity towards various error sources tolerance studies from the injector to the linac end have been performed. Procedures and results of these studies are presented.

INTRODUCTION

Based on it's experiences in operating high brilliant synchrotron light sources the Berliner Elektronenspeicherring-Gesellschaft für Synchrotronstrahlung (BESSY) is proposing a 2.3 GeV linac-based single-pass Free-Electron Laser (FEL) user-facility for the wavelength range from 62 nm $\leq \lambda \leq$ 1.2 nm. To generate very short photon pulses of $\leq$ 20 fs duration and to ensure stable radiation output a cascaded High Gain Harmonic Generation (HGHG) scheme has been designed. A detailed description of the BESSY FEL can be found in the recently completed Technical Design Report [1].

Due to the FEL process the quality of the seeded part of the electron bunch, mainly the energy spread, after one HGHG stage is significantly reduced and no longer suitable for further stages. For that reason the "fresh bunch technique" [2] is applied, providing a fresh part of the electron bunch to to all HGHG stages and the final amplifier. Taking timing jitter sources and synchronization limits into account, a flat top pulse of about 700 fs duration is required. In combination with the requested 1.8 kA peak current a total bunch charge of 2.5 nC will be needed.

To deliver such an electron beam to the FEL lines, a very long bunch of 40 ps FWHM duration is generated in the photo-injector. By means of two magnetic bunch compression stages at energies of 220 MeV and 750 MeV in combination with an energy-position correlation in the longitudinal phase space (chirp) the longitudinal bunch density and thus the peak current is increased to the requested values.

Aim of this studies was to verify that compression, timing and energy variations at the linac end due to the expected "shot-to-shot" errors stay within tolerable limits. For that purpose, start-to-end simulations have been performed, beginning at the injector cathode and ending at the first HGHG undulator entrance.

* Funded by Bundesministerium fr Bildung und Forschung, the state of Berlin and the Zukunftsfonds Berlin

† Michael.Abo-Bakr@bessy.de, Albert-Einstein-Strasse 15, 12489 Berlin, Germany

ERROR SOURCES AND THEIR EFFECTS

In the simulations, errors in the injector and linac part are investigated, that influence mainly the dynamics of the longitudinal phase space. Nevertheless, the horizontal emittance can also be affected due to the peak current dependency of wake field and CSR effects.

Injector: for the injector (rf gun and first, eight-cavity "booster" module), timing errors and intensity variations of the photo cathode laser are considered as well as phase and amplitude errors of the rf fields in the injector gun and the booster cavities.

For the main linac tolerance studies, phase and amplitude rf field errors are considered. No error correlation between neighbouring linac cavities is assumed. Vibrations and field strength variations of the magnets on a "shot-to-shot" time level haven't been considered as well as vibrations of the rf modules, which would cause the electron bunches to scan "off axis" transverse electric field components in the cavities. Mechanical vibrations of the cavities are considered within the microphonics simulations, incorporated into our assumptions on cavity phase and amplitude errors.

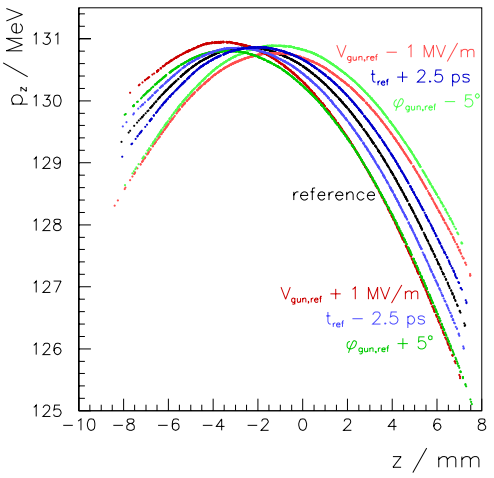

Figure 1: Single error simulations for the BESSY FEL injector: longitudinal phase space at the booster module end for $\pm$2.5 ps timing jitter (blue), $\pm$1 MV/m gun amplitude (red) and $\pm 5^\circ$ gun phase errors (green). The reference curve is also plotted (black).

At the end of the booster module, all injector errors result in a time and energy jitter of the bunch center with respect to the undisturbed bunch. In addition, the momentum position correlation (chirp) is changed, when the bunch passes the booster module with a time or, equivalently, a phase jitter. All injector error sources couple by "time of flight" effects in the non-relativistic part of the injector. Thus the resulting time, energy or chirp jitter at the injector end can not be easily associated to a single error source.

In Figure 1 longitudinal phase space distortions at the end of the booster module due to injector errors are shown. For demonstration exemplary single error types such as ± 2.5 ps timing jitter, ± 1 MV/m gun amplitude and $\pm 5°$ gun phase have been applied. In all cases the mean energy and z-position (for a fixed time of flight) changes as well as the momentum chirp. The effects of gun amplitude and phase errors dominate at the chosen error weighting, while the changes due to the timing jitter are small.

Main linac: the effect of injector errors on the final longitudinal phase space at the linac end are illustrated in Figure 2. Both a mean energy jitter and a time jitter of the bunch are investigated.

The main effect of an energy jitter from the injector is the transformation into a time jitter in the bunch compressors and thus at the linac end (upper graph of Figure 2). For an HGHG FEL with several "fresh bunch" stages this causes two problems: to ensure, that the seeding laser hits the electron bunch always in its flat top, high current part, the flat top length has to be increased at both ends by the expected time jitter. If the jitter exceeds the expectations, either the initial seed for the first HGHG stage or the last seed for the final amplifier interacts with a lower current region on the bunch edges. In both cases the final radiation output might be significantly reduced.

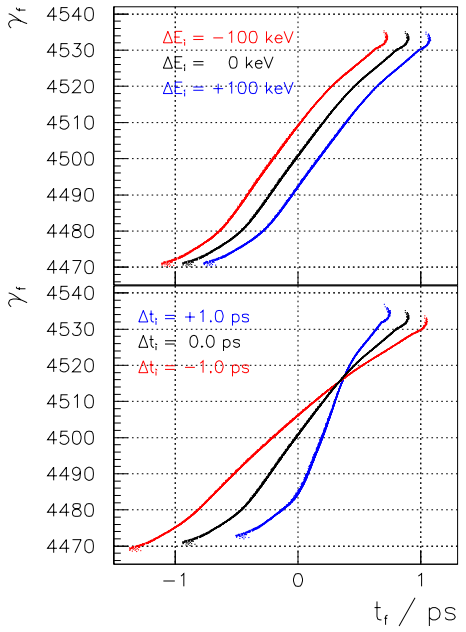

Figure 2: BESSY HGHG FEL: variations of the final longitudinal phase space (high energy beamline) due to energy (top) and timing (bottom) jitter from the injector.

A second problem is a variation of energy looking to a fixed longitudinal bunch position, just like the HGHG seeds do. It is caused by the the time jitter at the linac end in connection with the momentum chirp, which was required for the bunch compression. As every HGHG stage is optimized for a special energy this leads to a mismatch of the seeding and the insertion device resonant wavelength. The energy modulation and, later on, the bunching and the radiator output is reduced.

A time jitter from the injector not only leads to a time jitter at the linac end, with all the drawbacks just mentioned. It also strongly influences the bunch compression, by modifying the momentum chirp (lower graph in Figure 2), which can cause a significant output power degradation of a cascaded HGHG FEL.

To little compression results in a lower peak current with a longer flat top. The smaller peak current reduces the radiator output of the first HGHG stage, which acts as seed for the second one. Clearly the reduced seed power produces less momentum modulation in the second modulator. Thus the output power of the second radiator is not only reduced by the lower peak current but also by the smaller bunching.

Too much compression leads to a higher peak current with a shorter flat top. If the flat top becomes too short, again either the first or the last seed hits the edges of the flat top with less peak current. Even if this is not the case, too high peak currents can be disadvantageous: the increased output of the first radiator produces a stronger momentum modulation in the second modulator. Of course the strength of the dispersive section, converting the momentum into a current density modulation, is fixed, and one will end up with an over-compressed bunch. This reduces the output of the second radiator, but is counteracted to a certain degree by the higher peak current.

Finally, also in the case of an injector time jitter the sliced energy varies, leading again to a mismatch of seeding and resonant wavelength, as already described above.

TOLERANCE BUDGET

Assumptions on the error sizes arise from experiences, made with PITZ at DESY/Zeuthen, the FZ Rossendorf and the Max Born Institute (MBI) and result from RF control simulations.

Two cases have been investigated: "case 1" with errors as they are presently already reached in the mentioned laboratories and "case 2" with decreased errors, as they are assumed to be in reach within the next few years. Listed in Table 1 are the considered (rms) errors of the longitudinal "shot-to-shot" tolerance budget.

The limited synchronization between the photo-cathode laser and the rf system determines the timing jitter. A 500 fs rms-jitter can be assumed today, with future state-of-the-art systems this value could be further reduced by 50% or

		case 1	case 2
cath. laser	jitter / ps	0.5	0.25
	bunch charge (rel.)	1×10^{-2}	
injector gun	phase / °	1.0	0.2
	amplitude (rel.)	5×10^{-3}	2×10^{-3}
linac cav.	phase / °	0.1	
	amplitude (rel.)	3×10^{-4}	

Table 1: BESSY FEL: longitudinal tolerance budget.

more. For the integrated laser intensity stability, defining bunch charge fluctuations, an rms error of 1% was recently measured at PITZ [3].

Phase and amplitude errors have also been adopted from measurements at PITZ. A 1° phase error and a 3×10^{-3} relative amplitude error has been deduced [4], limited by the thermal stability of the normal conducting cavity. With an extended cooling scheme and a direct measurement of the rf amplitude and phase in the gun, allowing for fast rf feedback, a further reduction to the values used for "case 2" seems to be feasible.

Values of 1×10^{-4} and 0.1° for the relative stability of the rf amplitude and for the phase errors of the superconducting linac cavities are based on measurements at Rossendorf [5] and on rf feedback simulations [6].

SIMULATION TECHNIQUES

Two codes have been used for the tolerance studies: ASTRA [7] for the injector and ELEGANT [8] for the linac part. To get a sufficient statistics, 100 runs were performed for each of the two cases. With ASTRA 25000 macro-particles were tracked, taking space charge forces into account. The output particle distribution in the 6D phase space is converted to the ELEGANT input format. With ELEGANT the particle distributions were tracked under the influence of wake and CSR fields. To reduce noise in the longitudinal density distribution, the number of particles was raised to 100 000, keeping the characteristic bunch parameters unchanged.

SIMULATION RESULTS

Injector: in Figure 3 histograms of the ASTRA injector simulation results at the injector end ($E = 130$ MeV) are shown.

For "case 1" the arrival time jitter is about 1.2 ps while the energy variation is 85 keV (rms). Comparing the rms time jitter with the "single error case", even stronger modifications of the bunch compression have to be expected as presented in Figure 2. Also for the energy variation, the rms value is close to the assumptions for the "single error case" example. Thus disturbances of the longitudinal phase space have to be expected in an order as shown in Figure 2, which would represent a severe distortion of the electron bunch parameters.

There is one effect, that will reduce the arrival time variations at the linac end: in contrast to the simple examples in Figure 2, the real time and energy variations from the injector are correlated. This correlation is produced by the off crest passage trough the booster module, adjusted to produce the bunch compression chirp. For that reason the time jitter is compressed just like the bunches them self. In the frame of the simple examples, shown in Figure 2, the final arrival time variations caused by injector time and energy jitter have opposite signs and will cancel partially.

For "case 2" arrival time and energy variations reduce significantly to about 0.4 ps and 30 keV, respectively (rms). In this case much smaller disturbances of bunch timing and shape are expected.

Main linac: the results of the ELEGANT linac simulations are shown in Figure 4. Histograms of the central bunch arrival time and energy are plotted in Figure 4a and 4b. Compared to the injector values, the time variations are strongly reduced due to the correlation of the injector jitter. No significant difference between the two error cases occurs for the arrival time variation, which indicates a nearly full compression of the correlated injector time jitter. In contrast the rms value of the energy variation is strongly reduced for the "case 2" scenario, compared to the "case 1" value.

In Figure 4c and 4d histograms of the distribution of the horizontal emittance and energy spread are shown. Both values are averaged over all slices, weighted by the slice current. The variation of the horizontal emittance is less than 20% and 10% for "case 1" and "case 2", respectively. For the energy spread, there is no big difference between the two error scenarios, most of the bunches have values around 1×10^{-4}.

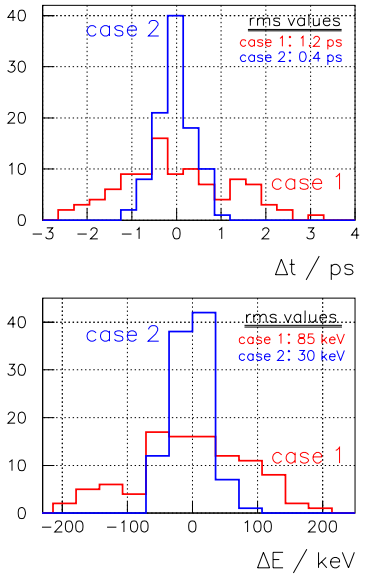

Figure 3: Injector simulation results: histograms of the central bunch arrival time (top) and energy (bottom) variation at the injector end (case 1: red, case 2: blue).

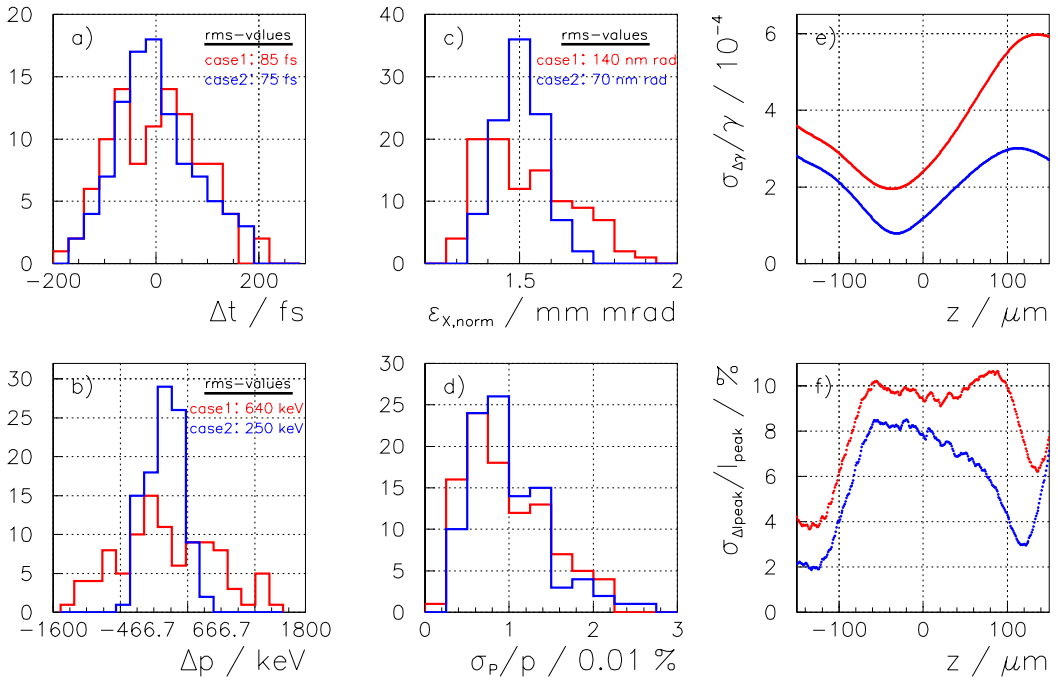

Figure 4: Linac simulation results: histograms of the variations of the central bunch arrival time (a), energy (b), the sliced horizontal emittance (c) and the sliced energy spread (d) at the linac end. The relative rms values of the momentum (e) and peak current (f) variations as function of the longitudinal position are drawn. (case 1: red, case 2: blue)

In Figure 4e and 4f the rms values for the sliced mean energy and peak current variations of all runs of each case are plotted versus the longitudinal position. This is of major importance for the HGHG process, as it describes the bunch parameter changes for every HGHG stage. The maximum energy variations occur in the head of the bunch and reach 6×10^{-4} for "case 1" and 3×10^{-4} for the second scenario. The momentum acceptance of the final amplifier of the most critical four stage HGHG is about 1×10^{-3}, which is about 2σ even with "case 1". The maximum peak current variations do not strongly differ for "case 1" and "case 2" and amount 11% and 8% respectively.

Simulations on the FEL radiation performance under the influence of single error sources (energy, current, emittance, energy spread) show relative output variations on the order of the assumed relative errors compared to the ideal case, but no drastic decrease [9].

CONCLUSION

S2E simulations for the BESSY FEL injector and linac have been performed. Final distortions of the longitudinal phase space are dominated by error sources in the injector. Time and energy jitters at the injector end are transformed by the bunch compressors and yield tolerable values for both investigated error cases, where "case 2" with smaller error assumptions clearly delivers smaller final distortions.

A reliable proof of FEL power losses due to the estimated bunch distortions can only be done, using the simulated realistic bunches to perform S2E FEL simulations, where all variations of the sliced bunch parameters are taken into account.

REFERENCES

[1] "The BESSY Soft X-ray Free Electron Laser, Technical Design Report", March 2004, eds.: D. Krämer, E. Jaeschke, W. Eberhardt, ISBN 3-9809534-0-8, BESSY, BERLIN (2004).

[2] L. H. Yu, I. Ben-Zvi, "High-Gain Harmonic Generation of Soft X-Rays with the Fresh Bunch Technique", NIM-A 393, 96 (1997).

[3] J. H. Han, et al., "Conditioning and High Power Test of the RF Guns at PITZ", Proc. of the 8^{th} EPAC, Swiss (2004).

[4] D. Lipka, PhD thesis, Berlin (2004).

[5] A. Büchner, et al., "Noise Measurements at the RF System of the ELBE Superconducting Accelerator", FZR, Dresden, Germany, Proc. the 7^{th} EPAC, France (2002).

[6] A. Neumann, J. Knobloch, "RF Control of the Superconducting Linac for the BESSY FEL", Proc. of the 8^{th} EPAC, Swiss (2004).

[7] K. Floettmann, "ASTRA user's manual", http://www.desy.de/ mpyflo

[8] M. Borland, "elegant: A Flexible SDDS-Compliant Code for Accelerator Simulation", Advanced Photon Source LS-287 (2000).

[9] B. Kuske, et al., "Impact Studies of Bunch Parameter Variations on the Performance of the BESSY HGHG FEL", this proceedings.

A MULTISTAGE HGHG-SCHEME FOR THE BESSY SOFT X-RAY FEL MULTIUSER FACILITY*

D. Krämer# on behalf of the BESSY Soft X-ray FEL Design Team,
BESSY, Albert-Einstein-Strasse 15, 12489 Berlin, Germany

Abstract

2nd generation FEL facilities in the VUV to soft X-ray range delivering reproducible ultra short photon pulses at an energy level of mJ/pulse will open up new physical frontiers. Tuneability of photon-wavelength and variable beam polarization as well as synchronization to external lasers will be essential for the future ultra-fast time-resolved pump-probe experiments utilizing these novel FEL base synchrotron light sources. Furthermore, using a RF photoinjector in combination with a CW superconducting (s.c.) linac, free selectable pulse repetition rates and pulse pattern can be realized. Distributing the electron bunches to different FEL-lines allows effective multi-user operation.

Following this approach BESSY proposes a soft X-ray HGHG-FEL multi-user facility for the VUV to soft X-ray range.

INTRODUCTION

Ultra-short pulses from free electron lasers will be *the* tool in future time-resolved fs-physics experiments. However there is an on-going debate on the best FEL scheme how to derive intrinsic stable photon beam as is mandatory for any future multi-user FEL facility. The cascaded High-Gain-Harmonic-Generation (HGHG)-FEL scheme as pioneered by BNL [1], is the most promising scheme in achieving high performance reproducible and stable fs-photon pulses in the soft X-ray wavelength range $\lambda \leq 1.2$ nm, i.e. photon energies up to 1 keV.

In the HGHG approach a seed from an external high power fs-laser co-propagates with the electron bunch through an undulator (modulator), modulating the electron energy if the resonance condition

$$\lambda_L = \frac{\lambda_U}{2\gamma^2}\left(1 + K^2\right)$$

is met, where λ_L denotes the laser wavelength, λ_U is the undulators period, γ is the electron Lorentz factor and K the undulator field parameter. The imprinted energy modulation has a period length equal to the laser wavelength λ_L and an envelope corresponding to the seed pulse, increased by the slippage of electrons relative to the laser field over the N_U undulator periods.

In a following dispersive section the energy modulation is transferred into a spatial density modulation. The bunching structure reflects the laser fundamental wavelength and its harmonics $h \cdot \lambda_L$. In a second undulator (radiator), tuned to be in resonance to a specific harmonic $n \cdot \lambda_L$, the micro-bunches will emit coherently when the modulation depth $\Delta\gamma$ fulfills the condition $\Delta\gamma \geq n\sigma_\gamma$, where σ_γ is the electron beam energy spread. The resulting photon output is used as the seed field of a next HGHG stage.

Thus the stages consist of a sequence of modulator - dispersive section - radiator, the last stage followed by a final amplifier. In this long undulator, the FEL amplification process is brought to saturation at the desired wavelength.

Generation of stable ultra-short photon pulses thus is the result of the high-quality characteristics of the external optical fs-seed pulse in the first HGHG-stage dominating the statistical noise features from self amplified spontaneous emission.

Two to four HGHG stages are needed to down-convert the seed laser wavelength from the tunable frequency multiplied high power fs-Ti:Sa laser ($\lambda \approx 230$ - 460 nm) to the desired range in the FEL-lines.

To avoid degradation of the FEL process in the various HGHG stages of the cascade, the "fresh bunch technique" [2] is applied, i.e. the photon field and the interacting electrons are delayed with respect to each other. Thus there is always a new, "unused" part of the

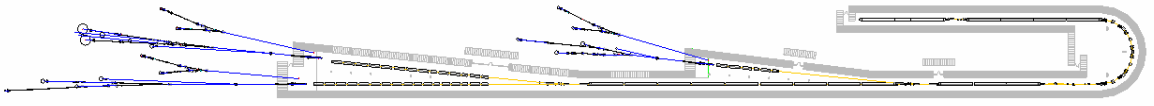

Fig. 1: Foot print of the BESSY soft X-ray user facility with three independent FEL-lines serving three beam lines each. The total length of the facility is approximately 400 m.

*Funded by the Bundesministerium für Bildung und Forschung, the State of Berlin and the Zukunftsfonds des Landes Berlin
#kraemer@bessy.de

electron bunch interacting with the electromagnetic field from the preceding HGHG-stage.

THE BESSY SOFT X-RAY USER FACILITY

The Technical Design Report for the BESSY Soft X-ray FEL based on the multi-staged HGHG scheme was published recently [3]. This FEL-user facility will operate three FEL-lines in parallel, spanning the photon energies 24 eV – 120 eV, 100 eV – 600 eV and 500 eV– 1000 eV, delivering pulses of ≤ 20 fs (fwhm) duration at variable beam polarization. Fig. 1 gives a foot print of the machine layout.

A superconducting 2.3 GeV CW-linac is used as driver in the FEL process. In combination with an injector (1 kHz repetition rate, to be replaced by a superconducting photoinjector at a later stage of the project) high flexibility is achieved with respect to pulse repetition rate and pulse pattern, providing the opportunity to adjust to the experimenters specific needs.

FEL Output Simulations

To derive detailed information on the photon beam properties, time-dependent simulations have been performed in a start-to-end approach [4,5], using a modified version of GENESIS 1.3 [6]. Typical results of time resolved power distribution and spectral power distribution as calculated for the low-energy and medium-energy FEL-lines are depicted in figure 2.

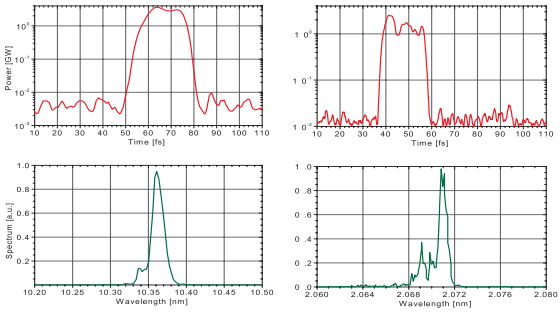

Figure 2: Time-resolved power distribution (top) and spectral power distribution (bottom) calculated for the low-energy and medium energy FEL at wavelength of 10 and 2 nm .

The calculations correspond to the high energy end of the two and three fold staged FEL-lines, corresponding to a wavelength of 10.3, and 2.0 nm. In all cases a 17 fs (rms) Gaussian seed pulse of 500 MW peak power was assumed.

The simulation results show a constant power level and a reasonable clean spectrum for the FEL photon beam. However, as the interacting electrons experience a non-constant seed due to the seed pulse shape and the slippage effect, the energy modulation imprinted in the modulators differs along the interacting part of the electron beam. Optimizing for maximum photon beam brilliance, those electrons corresponding to the seed pulse center typically will be overbunched when having passed the dispersive section and thus perform synchrotron oscillations in the ponderomotive bucket. As a result sidebands are generated in the spectral distribution. These sidebands which are pronounced only at the low energy part of the spectrum due to the slippage effect. This effect repeats in the following HGHG-stages. Thus the higher the number of stages the sideband structure becomes more and more complex and pronounced. Means to suppress the effect are described elesewhere [7].

Based on the simulation results the main performance parameters of the BESSY-FEL are listed in table 1. Comparing the FEL parameters to a 3rd generation light source as BESSY II, the gain in peak brilliance is more than 10 orders in magnitude.

Table 1: Main performance parameters of the BESSY X-FEL. Values in brackets refer to an s.c. injector as planned at a later phase of the project.

Parameter	Value	Unit
No. of FEL lines	3	
No of beamlines	9 (15)	
Electron energy	2.3	GeV
Emittance	1.5	π mm mrad
Bunch length	290	µm
Peak current	1.75	kA
Beam power	18 (150)	kW
Wavelength range	51 – 1.24	nm
Photon peak power	1.5 – 14	GW
Ave. Power	0.26 – 0.02	W
Beam size	14 – 160	µm
Divergence	27 – 140	µrad
Pulse duration	< 20	fs
No. of pulses in train	3 (1)	
Repetition rate	1 (25)	kHz
No of photons/pulse	$2\cdot10^{11} – 7\cdot10^{13}$	
Peak brilliance	$6\cdot10^{29} – 1.3\cdot10^{31}$	(s mrad^2 mm^2 0.1% bw)$^{-1}$

The RF-Photoinjector

Operation of the BESSY-FEL is planned at a 1 kHz repetition frequency at the three FEL-lines. Thus the injector has to deliver bunch trains containing three single bunches. The spacing of bunches will be 3 µs, a compromise between an acceptable duty cycle of the

room-temperature gun cavity and the demands on the linac RF-system with respect to beam loading.

To generate the electron bunches at a charge of 2.5 nC a RF photoinjector based on the PITZ design [8] is intended to be used. Calculations show that with a short rise and decay time of about 3 ps and a 40 ps "flat-top" intensity profile photocathode laser-pulse a normalized slice emittance of less than 1.5 π mm mrad can be achieved [9]. Thus the PITZ-type photogun modified to higher repetition rates will be the technical starting point for the BESSY-FEL.

However, a superconducting RF-gun, as is presently under construction by a FZR-BESSY-MBI-DESY consortium, will replace the injector later on.

The CW-Linac

The superconducting acceleration structures are based on the TESLA linear collider modules that have demonstrated reliable operation at TTF [10]. The TESLA modules consist of eight niobium 9-cell cavities, each module being 12 m long. 18 modules are needed for the 220 m long 2.3 GeV linac. The operation field of ~16 MV/m CW is the economical optimum with respect to investments and long-term operation costs. Minor modifications are required to adapt the (pulsed) TESLA technology for CW. The changes are due to the increased He-flux from the cavities (20.5 W/cavity) requiring a modest enlargement of the two-phase He supply line.

To confirm the basis for a reliable CW operation an detailed qualification program started at BESSY. Test of couplers and tuners, optimization of cryogenic parameters such as bath temperature are performed. For this purpose a Horizontal Bi-Cavity Test facility (HoBiCaT) has been set up [11].

Tests of new concepts for damping microphonics - most important in our CW operation - are under preparation. The test bench also will allow optimization at realistic conditions during RF source development, allowing for a cost-optimized specification for the 144 units of 1.3 GHz-power sources. Commissioning of the bench is in progress. 1.8 K LHe is provided from an existing Linde TCF50 cryogenic plant connected to a pumping station.

Two 9-cell cavities completely manufactured and processed by industry have been delivered and are available now for testing.

The Beam Delivery System

A kicker system will be used to extract single bunches from the main linac into the low and medium energy FEL-lines at beam energies of 1.0 and 2.3 GeV respectively. Extreme tight tolerances in the order of $\Delta\theta/\theta \approx 5\cdot10^{-5}$ are required on the relative stability and reproducibility of the extraction angle θ.

As the kicker stability is determined primarily by the power converter, a pulser design was developed based on IGBT power semiconductors.

After careful design of the pulser geometry to minimize intrinsic inductivities and optimization of grounding, the measurements revealed a peak to peak stability of $\Delta\theta/\theta \leq 5\cdot10^{-5}$ of the system over a time scale of hours[12]. Figure 3 depicts a single kicker pulse as generated by the new pulser. The pulser repetition rate is 1 kHz, the pulse width less than 3 µs, compatible with the bunch spacing.

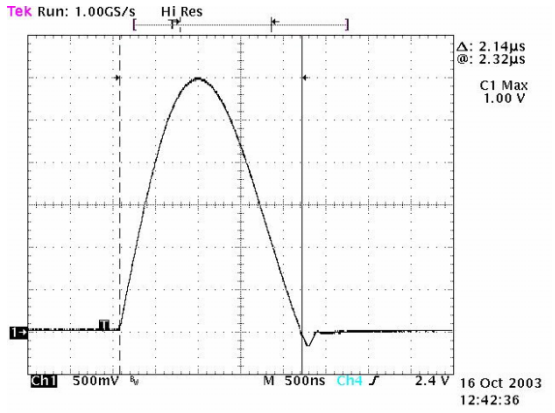

Figure 3: Single pulse as achieved with the new high stability pulser.

The Beam Collimation

Beam collimation to protect the undulators modules from electron losses and dark-current will be achieved by a compact 43 m long dedicated beamline between linac and undulators sections. The collimator acts as transverse and longitudinal phase space filter avoiding degradation of the radiation sensitive NdFeB undulator structures. For transverse collimation round apertures in absorber blocks are used. Particles outside the tolerable transverse acceptance intercept the absorbers.

Energy collimation is achieved with apertures located in a closed dispersion bump in a dogleg structure. The present system[13] is optimized for an acceptance bandwidth of 5% in energy spread.

The Undulator Sections

For the three FEL-lines in total 120 m of undulators of different period lengths is needed to ensure a proper matching between modulator and radiator of the various stages, ranging from λ_u = 122 mm to 28.5 mm. A minimum gap of 10 mm is sufficient to cover the full wavelength range. In each case the undulators are variable gap devices, the radiators of the last HGHG-stage and the final amplifier undulators will follow the elliptical permanent magnet design now known as APPLE III design.

The modulators are very short undulators (< 3 m each). The radiators and final amplifiers however will be built up from segments of typically 3.5 m in length. These segments are spaced by 0.95 m long intersections equipped with phase shifters, focusing quadrupole magnets, steering elements, vacuum pumps and a variety of diagnostic elements as OTR, wire scanner and beam position monitors for beam characterization and manipulation, see figure 4.

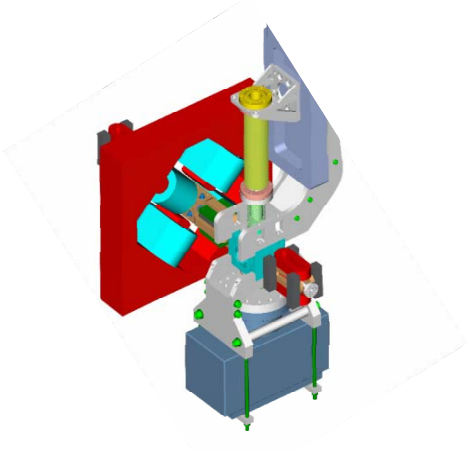

Figure 4: 3-D model of the compact intersection region with components for beam focusing, steering, diagnostics and vacuum pumps.

Special attention has been paid to the undulator vacuum chamber to avoid beam degradation arising from wakefields. An all Cu-vacuum chamber with a beam duct of surface roughness < 100 nm (rms) is favored for the design.

Beamlines

The three FELs will be equipped with three beamlines each: optimized for high resolution experiments, a "white light" beamline without any monochromatization and a high intensity station conserving the short pulse structure of the FEL beam. Table 1 gives the main parameters for the high-energy (HE) FEL beamlines as an example. Data were calculated from detailed ray-tracing.

Dedicated undulators using the spent beam from the FEL are planned at a later phase of the project.

Table 1: Main parameters for the HE-FEL beamlines.

Beamline	Bandwidth (meV)	Pulse length (fs)	Pulse energy (nJ)	Energy density (mJ/cm^2)
High resolution	20 - 33	650 – 120	2.4 – 10	0.23 – 1.4
White light	2000	10	11000	120000
Short pulse	800	11	600	250
FEL output	2000	10	15000	1000

CONCLUSIONS AND OUTLOOK

The proposed seeded soft X-ray FEL facility ideally will complement the 3rd generation synchrotron light source BESSY II. The machine is based on existing technology making use of hardware developments for high energy physics colliders and/or hard X-ray FELs.

Future options such as seeding with future intense short-wavelength High Harmonic Generation (HHG) lasers (λ ~ 30 nm) as well as options to expand the number of FEL-lines from three to five have been incorporated into the design of the soft X-ray FEL.

The flexibility of the CW-accelerator together with features as continuous wavelength tuning, variable beam polarization, will efficiently open-up the field of ultra-fast time resolved spectroscopy allowing to take advantage of the specific characteristic of seeded FELs, i.e. transverse and longitudinal coherence of ultra-short pulses at highest peak brilliance.

ACKNOWLEDGEMENTS

The author acknowledges the contributions from the BESSY staff as well as the help from many colleagues at BNL, Cornell, DESY, MBI-Berlin, TU Dresden and Forschungszentrum Rossendorf in preparing the BESSY Soft X-ray FEL TDR.

REFERENCES

[1] I. Ben-Zvi, F. Di Mauro, S. Krinsky, L.H. YU, Nucl. Instrum. and Meth., **A304** (1991)181.
[2] L.H. Yu, I. Ben-Zvi, Nucl. Instrum. and Meth. **A393** (1997)96.
[3] The BESSY Soft X-ray Free Electron Laser, TDR BESSY March 2004, eds.: D. Krämer, E. Jaeschke, W. Eberhardt, ISBN 3-9809534-0-8, BESSY, Berlin (2004).
[4] M. Abo-Bakr, M.v. Hartrott, J. Knobloch, B. Kuske, A. Meseck, Start-to-End Tolerance Studies for the BESSY FEL, this proceedings.
[5] B. Kuske, M. Abo-Bakr, A. Meseck, Impact Strudies of Bunch Parameter Variation on the Performance of the BESSY HGHG FEL, this proceedings.
[6] S. Reiche, Nucl. Instrum. and Meth. **A429**(1999)243.
[7] A. Meseck, M. Abo-Bakr, B. Kuske, The Influence of the Seed Pulse Shape on the Output Performance of the BESSY Multi-stage HGHG-FEL, these proceedings.
[8] F. Stephan et al., Recent Results and Perspectives of the Low Emittance Photo Injector at PITZ, these proceedings.
[9] F. Marhauser, Photoinjector Studies for the BESSY Soft X-ray FEL, EPAC 2004.
[10] R. Brinkmann, K. Flöttmann, J. Rossbach, P. Schmüser, N. Walker, H. Weise (editors), TESLA Technical Design Report, Part II – The Accelerator, DESY-2001-011 (2001).
11] J. Knobloch, W. Anders, A. Neumann, D. Pflückhahn, M. Schuster, Status of the HoBiCaT Test Facility at BESSY, EPAC 2004.
[12] O. Dressler, J. Feikes, J. Kuszynski, Kicker Pulser with High Stability for the BESSY FEL, EPAC 2004.
[13] T. Kamps, Collimation System for the BESSY FEL, this proceedings.

IMPACT STUDIES OF BUNCH PARAMETER VARIATIONS ON THE PERFORMANCE OF THE BESSY HGHG FEL*

B. Kuske †, M. Abo-Bakr, A. Meseck, BESSY, Berlin, Germany

Abstract

In the recent past interest has grown in FEL designs offering alternatives to the SASE principle. BESSY proposed a High Gain Harmonic Generation (HGHG) soft X-ray FEL, composed of three independent FEL-lines utilising 2 to 4 HGHG stages. Modulators and radiators in such a scheme are kept short, to stay away from the exponential regime of the FEL process and only the final amplifier (FA) reaches saturation. Therefore, the mechanisms of how the electron beam properties generated by the gun and the linac influence the radiation output differ from what is known in SASE devices. Shot to shot variations and the influence of realistic bunch profiles are considered, as well as requirements arising from the use of the fresh bunch technique.

INTRODUCTION

BESSY recently presented the technical design report for a linac-based soft X-ray FEL, designed as a multi-user facility [1]. Three independent beamlines are planed and will supply photons in the spectral range from $0.02\,keV \leq \hbar\omega \leq 1\,keV$. The FEL is designed as a High Gain Harmonic Generation (HGHG) structure, to avoid the known restrictions of a SASE device and in lack of high-power short-wavelength seeding lasers that could be used for seeding at the desired wavelength. As in every beam based radiation source, the achieved bunch parameters, such as energy, energy spread, emittances, current, and the like, determine the radiation quality. Different to storage rings, not only deviations from design parameters have to be investigated. Due to jitter, mainly in the gun, but also in the linac, bunch properties will vary shot to shot. In addition, as the fresh bunch technique is applied, the longitudinal profile of the bunch is of major importance. In an HGHG cascade, only the final amplifier takes the FEL process to saturation, whereas all other undulators stay in the linear regime. Consequently, the mechanisms of how varying bunch parameters influence the final performance differ strongly from those in the SASE case. Performance improvements in one stage might be lost in the following stage, while minor bunching or less seed power might still lead to adequat output one stage later. The paper will cover different aspects of bunch parameter deviations. All calculations are performed for the two stage low energy FEL line, using the time-dependent computer code GENESIS [2]. Even in this comparatively short set up (the other lines cover three and four stages) the computational efforts are considerable.

*Funded by the Bundesministerium für Bildung und Forschung (BMBF), the State of Berlin and the Zukunftsfond Berlin

† Bettina.Kuske@bessy.de

DEVIATION FROM CONSTANT BUNCH PARAMETERS

In the design of the BESSY FEL it was assumed, that the bunch parameters do not vary along the bunch. The design values of the bunch parameters are listed in Table 1.

Table 1: Nominal bunch parameters.

bunch parameter	design value	
energy spread	2.0×10^{-4}	
emittance$_{x,y}$	1.5×10^{-6}	m rad
peak current	2.1	kA
gamma (low energy)	1996.09	
beam size$_{x,y}$	$< 1.0 \times 10^{-4}$	m

When the energy spread, the emittance or the current of the bunch differ from their design values at the end of the linac, it is not possible to retune the FEL in order to improve its performance. These cases will be discussed first. In case of an offset in the central electron energy, it is possible to change the gap of the undulators and restore the design output. Deviations in the central energy will be treated in the next paragraph. Beam sizes and trajectory offsets can be corrected using the optics in front of the FEL and between the HGHG stages, and will not be considered. After a short reminder of how these parameters determine the HGHG process, the effect of their deviations from the design values will be discussed.

Energy spread: The energy spread of the bunch at the end of the linac, σ_γ, is modified during the passage through the undulators due to spontaneous emission of synchrotron radiation. Furthermore, an additional energy modulation is introduced to the bunch by the interaction with the seeding field. For harmonic generation, the imprinted modulation depth $\Delta\gamma$, has to fulfill $\Delta\gamma \geq n\sigma_\gamma$, with n the harmonic number sought in the modulator. Therefore, the larger the energy spread the weaker the bunching on the seeding frequency after the dispersive section. In the radiators, a smaller energy spread supports the amplification process as more particles fulfill the resonance condition.

Emittance: When the transverse emittances, $\varepsilon_{x,y}$, are reduced, the radiation power is concentrated on axis, and the amplification process in the radiators is enhanced. Additionally, the energy spread induced to the bunch during the passage through the undulator is linked to the transverse emittances, as longitudinal energy is tranfered to the transverse velocities. This effect depends on ε_n/λ_s, where ε_n is the normalised emittance and λ_s is the resonant wavelength, i.e. its importance grows with every stage, resp. wavelength reduction.

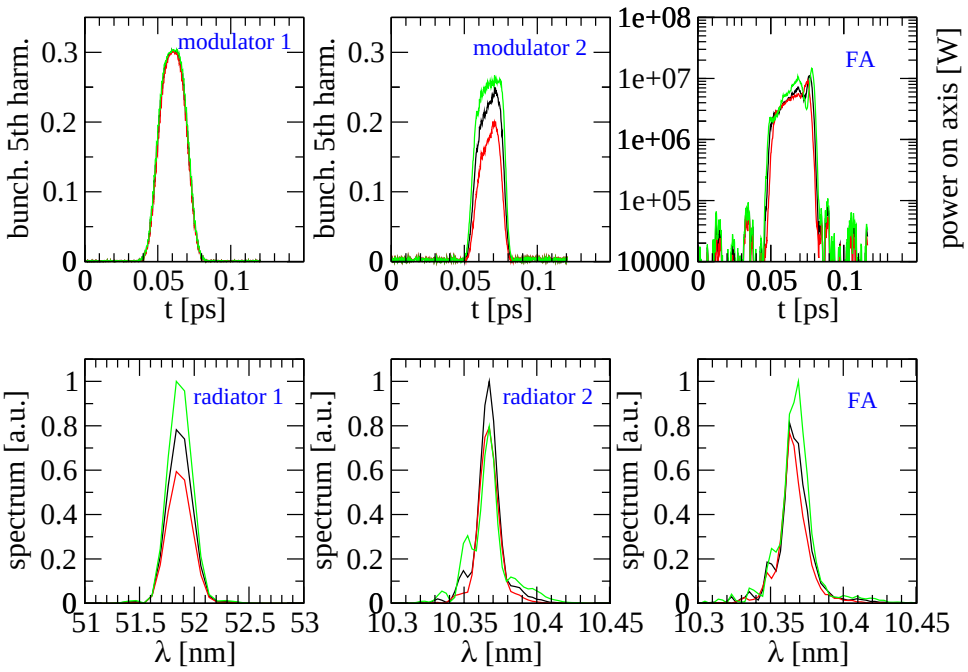

Figure 1: Development of the bunching in the modulators and the spectral power of the radiators and the FA, when the average bunch current is altered by $\pm 10\%$.

Current: The higher the bunch current, the higher is the radiation power emitted by the bunch even far away from exponential gain. The bunching in the modulators is slightly enhanced by the additional radiation. The dominant effect of current changes shows in the radiators, where a higher bunch current directly leads to an increased spectral power.

Fig. 1 shows the development of the bunching in the modulators, and the spectral power of the radiators and the final amplifier for the 2 stage low energy FEL line. The three curves depict the reference case with the design current (black) and two cases with a reduced (green) and a enhanced bunch current (red). A 10% deviation in the bunch current hardly influences the bunching rate created in the first modulator (upper left), but leads to a 30% increase in spectral power emitted by radiator 1 (lower left). The bunching rate produced in the second modulator (center top) reflects the different seed powers of radiator 1. In the case of the higher seeding power, though, the particles are already overbunched, as can be detected from the reduced flat top of the green curve. This overbunching leads to the rise of side maxima and a reduction of the peak power in the spectrum of radiator 2 (center bottom). The peak power in the case of the reduced bunching is similiar, and both lie 20% below the design current. In the final amplifier (right bottom), the reduced current case still reaches the reference spectral power by saturating at a later point in the undulator. The higher current case shows an increase of the spectral peak power by 20% due to the extra current.

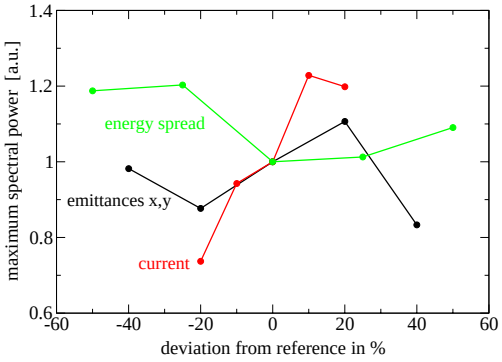

Figure 2: Peak spectral power as a function of bunch parameter offsets in percent.

Fig. 2 shows relatice changes in the peak spectral power at the end of the final amplifier as a function of offsets in the bunch parameters in percent. Clearly, the output power depends strongest on the bunch current. This differs from the SASE experience, where f.e. the emittance has a stronger influence on the power. When the bunch current increases, overbunching limits the performance.

Changes in the energy spread can be large according to start-to-end simulations. The energy spread plays a mayor role in the modulators, in the interaction between the seed radiation and the bunch. The output of the radiators corresponds to the bunching rates created in the previous modu-

lators. While the spectra of radiator 2 still reflect the changing energy spread, the output of the FA increases slightly for deviating σ_γ. The overall change in spectral power is small.

It should be pointed out, that for the design values the saturation point of the final amplifier was chosen well inside the device, leaving space for fluctuations of whatever kind. As a result, a slower amplification process, due to minor parameters might still saturate at a later point, and even at higher power than the reference. An excess of power, due to advantageous bunch parameters might get lost, when the amplification process saturates too early, and overbunching sets in. As the final amplifier consists of 3 undulators only, opening gaps will be too crude to compensate this effect. In a sense this is a stabilising mechanism that reduces the output fluctuations.

In the case of small emittance changes, the results are dominated by the point of saturation in the FA rather then by the emittance value. For growing emittances the expected power reduction sets in. For smaller emittances, overbunching dominates the positive effects, the reduction in spectral peak power is below 20% for $\pm 40\%$ emittance changes.

SHOT TO SHOT VARIATIONS

Jitter in the gun and linac parameters will lead to unavoidable shot to shot variations in the parameters of the bunches reaching the FEL. Start-to-end tolerance simulations [3] predict typical shot to shot rms deviations for the emittance of $0.14 mm\,mrad$, for the energy spread of 0.8×10^{-4} for the low energy FEL line and for the current of $\leq\ 200\,A$. The studies presented in the previous paragraph cover $\geq 2\sigma$ of the expected variations, so the expected fluctuations in the FA output seem to be tolerable, as long as single error sources are concidered.

Effects leading to shot to shot variations in the transverse size and position of the bunches have not yet been studied.

Whereas constant offsets in the central bunch energy, γ can be counteracted by adjusting the undulator gaps, shot to shot variations of γ could well be problematic, as the resonant wavelength will be shifted, or worse, particles might run out of the resonance condition, and the FEL process might not get started. Start-to-end simulation show, that the expected gamma variations depend on the position inside the bunch and are largest at the head and the tail of the bunch, where rms values of up to 6×10^{-4} can be reached. The resonance condition predicts shifts of the resonant wavelength of

$$\frac{\Delta\lambda}{\lambda} = -2\,\frac{\Delta\gamma}{\gamma} \qquad (1)$$

Fig. 3 shows spectra of the final amplifier of the low energy FEL line, for bunches with the design γ (black) and with central energies shifted by $\pm 1 \times 10^{-3}$ and $\pm 2 \times 10^{-3}$ (solid and dashed lines). As expected, the central wavelength is clearly shifted, but it is shifted by only 6×10^{-4}, about $1/4$ of the expected value. The reason is, that, as long as the seed laser wavelength stays within the bandwidth of the modulator, the energy modulation on the seeding frequency will be enhanced and the following radiator is seeded with the respective harmonics. During the passage through the radiator the central frequency of the spectrum slowly drifts from the harmonics of the seeding frequency towards the resonant wavelength of the radiator. The shorter the radiator, the smaller the wavelength shift. Also in this respect, the HGHG setup is more relaxed than a SASE device. The effects of jitters in the seeding wavelength, though, yet have to be investigated, as well as the influence of shot to shot variations in the beam sizes and trajectories.

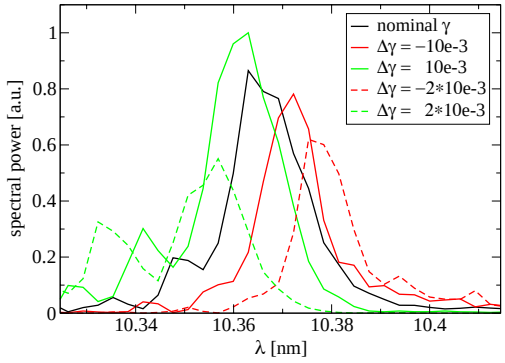

Figure 3: Spectra of the final amplifier for bunches with offsets in the central energy of $\pm 1 \times 10^{-3}$ (solid line) and $\pm 2 \times 10^{-3}$ (dashed line).

REALISTIC BUNCH PROFILE

In order to study the effects of a realistic bunch profile, a bunch with $1.4\,ps$ total length, extracted from start-to-end simulations [3] has been tracked through the low energy FEL line. In such a bunch, all parameters vary slice to slice, f.e. there is an energy chirp needed for the bunch compression and the current distribution approaches a flat top profile. As only small parts of the bunch are used in each HGHG stage, the bunch has been cut into twelve $120\,fs$ long pieces for the simulations. This corresponds roughly to the spacing sought for the fresh bunch technique. As the properties of the seeded part of the bunch spoil during the passage through a HGHG stage, the seeding radiation for the next stage has to be shifted to a fresh, unperturbed part of the bunch. In the two stage HGHG-FEL, f.e., three consecutive parts of the bunch are used. The averaged properties of each of the twelve bunch parts are depicted in Fig. 4. While the central energies (top) vary around the design value (line), the design current of $2100A$ is only approached by the central four bunch parts (center). The emittances and the energy spread stay well below the design values (bottom). The beam size is twice the design value horizontally, and the first three parts have a consider-

able horizontal offset (not shown).

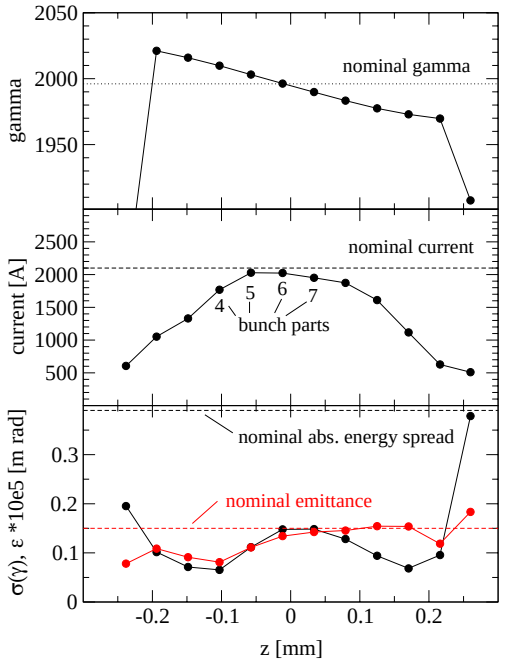

Figure 4: Bunch properties deduced from start-to-end simulations. Above: gamma, center: current, below: absolut energy spread (black) and emittance (red).

In an first attempt, these bunch parts have been tracked through the first HGHG stage, without any readjustment. Fig. 5 shows the resulting spectra of the first radiator. Clearly, the frequency shift due to the energy slope in the bunch is detectable. As above, Eq. 1 is not fulfilled. The achieved peak power basically reflects the current distribution. Part 5 radiates best, but still the peak power is only 60% of the design value, since the resonance condition is not met anymore.

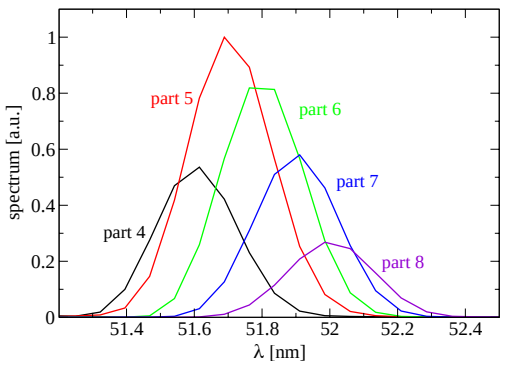

Figure 5: The power spectra of different bunch parts are dominated by the respective current and gamma.

In a second step, the K parameters of the modulators and radiators have been adjusted, each stage to the gamma of the bunch part that is actually used. Although the averaged bunch parameters of part 5 are close to, and better than the design values, it reaches only 80% of the required power in radiator 1. For part 4, the nominal values are reached. Both parts have a $50\mu m$ horizontal offset that has not been compensated. The even smaller emittance of part 4 apparently over compensates the lack of current and the trajectory mismatch.

Although the radiation generated by part 4 is comparable to the reference case, only 80% of the bunching is achieved, when it is used to seed part 5 in the second modulator. In radiator 2, the power rises only slowly for part 5, and finally reaches 1/3 of the expected value. In addition, the central wavelength of the spectrum is shifted by 1×10^{-3} to lower frequencies. This shift is caused by the energy ramp of the bunch, despite the adjustment of the undulators. Due to the ramp, the dispersion sections following the modulators not only transform the energy modulation into bunching, but, in addition compress the bunch, and thus shift the impressed wavelength to lower values. The optimisation of the second stage under these circumstances requires further investigations.

CONCLUSION

The effects of deviant bunch parameters have been studied for the BESSY low energy FEL line. Due to certain 'self stabilizing' effects of HGHG structures, offsets in the averaged bunch parameters are tolerable in the order of magnitude, that is expected from start-to-end simulations. Reductions in the bunching factor or spectral power that occure in the early HGHG stages are at least partly compensated in the final amplifier, by a shifted saturation point. When the early stages function too well, overbunching will limit the final output. First studies using bunches extracted from start-to-end simulations were presented. Unexpected effects like a shift in the resonant wavelength caused by the dispersive sections in combination with the energy chirp of the bunch have to be included in further optimization procedures. Due to the fresh bunch technique, the bunch parameters vary for every HGHG stage, making the analysis of performance limitations and the definition of acceptable parameter tolerances extremely difficult. In further studies the three and four stage FEL lines will be investigated.

REFERENCES

[1] The BESSY Soft X-ray Free Electron Laser, Technical Design Report, March 2004, eds.: D. Krämer, E. Jaeschke, W. Eberhardt, ISBN 3-9809534-0-8, BESSY, BERLIN (2004)

[2] GENESIS 1.3: A Full 3D Time Dependent FEL Simulation Code, S. Reiche, Nuclear Instruments and Methods A429 (1999) p. 243

[3] Start-to-End Injector and Linac Tolerance Studies for the BESSY FEL, M. Abo-Bakr, M. v. Hartrott, J. Knobloch, B. Kuske, A. Meseck, BESSY, Berlin, Germany, this proc.

THE INFLUENCE OF THE SEED PULSE SHAPE ON THE OUTPUT PERFORMANCE OF THE BESSY * MULTI-STAGE HGHG-FEL

A. Meseck, M. Abo-Bakr, B. Kuske, BESSY, Berlin, Germany

Abstract

The BESSY soft X-ray FEL is planned as a High Gain Harmonic Generation (HGHG) FEL multi-user facility. Three independent FEL-lines, fed by a superconducting CW linac, will be provided to cover the VUV to soft X-ray spectral range. In the HGHG scheme, the properties of the radiation output are dominated by the characteristics of the laser seed. In this connection, the influence of the laser pulse shape on the output characteristics, in particular on the output spectrum is of high interest. We present simulation studies for the BESSY-HGHG-FELs and discuss the output performance for different shapes of the laser pulse.

INTRODUCTION

Based on the experience with its third generation light-source, BESSY proposes a linac-based cascaded HGHG-FEL multi-user facility. The target photon energy ranges from 24 eV to 1 keV with a peak-brilliance of about 10^{31} photons/sec/mm^2/mrad^2/0.1% BW, i.e. a peak power of up to a few GW for pulse lengths less than 20 fs (rms). The polarization of the output radiation will be variable. The technical design report for the BESSY soft X-ray FEL was published recently [1].

The BESSY HGHG multi-user FEL facility will consist of three undulator lines to cover the target photon energy range. Each line is seeded by a tunable laser covering the spectral range of 230 nm to 460 nm. The pulses are assumed to have a Gaussian profile, a peak power of 500 MW, and a pulse duration of about 15 fs (rms).

Two to four HGHG stages are necessary to reduce existing laser wavelengths to the desired range of the BESSY FEL. Each stage consists of a modulator - dispersive section - radiator structure, for more details on the HGHG-stages see [1, 2]. The last radiator is followed by the so-called final amplifier. It is seeded at the desired wavelength and the amplification process is brought to saturation.

For a Gaussian-shaped seed, only a part of the interacting electrons experience the full power due to the seed shape and the slippage effect. The impressed energy modulation mirrors the Gaussian profile of the seed. The strength of the dispersion section can be adjusted for the peak energy modulation at the center of the seeded part or for a somewhat lower energy modulation including the flanks. The second case provides the maximum output power of the following radiator, since more electrons are optimally bunched. In this case the electrons at the center, which experience the full power of the seed are somewhat overbunched. The overbunched electrons perform synchrotron oscillations in the ponderomotive bucket. The resulting modulation of the emitted radiation frequency causes the side spikes (sidebands) [3]. The more electrons are overbunched the stronger is the growth of the sidebands. This effect is repeated in the following stages. In this way the number of sidebands in the spectrum adds up from stage to stage. Due to the slippage in the radiators and final amplifier, the sidebands are shifted to one side.

The sidebands can be avoided by optimizing the dispersion sections for the peak energy modulation, as described in [4]. In this case the bunching is of more Gaussian shape. The resulting radiation power and pulse length are reduced compared to the overbunched case, since less flank-electrons are optimally bunched. The losses in the integrated power are due to the reduction of the pulse length, i.e. the peak power suffers only slightly. Nevertheless the loss of integrated power and the reduction of the pulse length which inhere in this approach might be undesirable. Therefore other possibilities to avoid the sidebands are of interest.

The sidebands are due to the overbunched electrons in the seeded part of the bunch. The shape of the impressed energy modulation in connection with the strength of the dispersion section determines whether the electrons are overbunched or not. Therefore the sidebands can also be avoided by adjusting the shape of the energy modulation instead of reducing the dispersion strength. In this case one would expect that the integrated power and pulse length do not suffer in spite of more spectral purity. As the shape of the impressed energy modulation is mainly determined by the profile of the laser seed, the shape of the seed pulse can be adjusted to optimize the shape of the energy modulation. Note that, due to the slippage, the impressed energy modulation is not an one-to-one copy of the seed shape.

In this paper, we present simulation studies for different laser-pulse shapes for the BESSY-HGHG-FELs and discuss the output performance in terms of power and spectrum purity. The calculations have been performed with the time-dependent 3-D-simulation code GENESIS [5]. The different laser seed profiles in the time domain are generated with a modified version of the GENESIS output routine. Note, that the chosen seed-pulse shapes should demonstrate the influence of the seed shape in a HGHG-FEL rather than represent realistic laser radiation profiles.

SIMULATION STUDIES

Seed Pulse Shapes

In order to avoid the overbunching and ensure the maximum output power of the radiator a constant energy modulation in the interacting part of the bunch seems to be ben-

* Funded by the Bundesministerium für Bildung, und Forschung, the state of Berlin and the Zukunftsfonds Berlin.

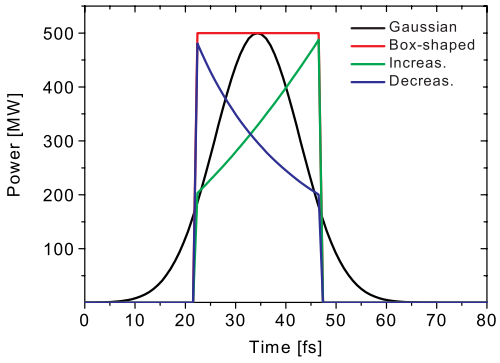

Figure 1: The different shapes of the seed pulses used in the simulation studies.

eficial. Using a box-shaped seed a nearly constant energy modulation of the interacting electrons can be achieved. As the slippage of the seed in the modulator as well as the slippage of the emitted photons in the radiator have to be taken into account, the expected output of the radiator is not box-shaped.

Figure 1 shows the different shapes of the seeds used for the present simulation studies. In addition to the simulations with the Gaussian and the box-shaped seeds, also simulations with increasing and decreasing seed power are performed to investigate the slippage effects.

First Stage

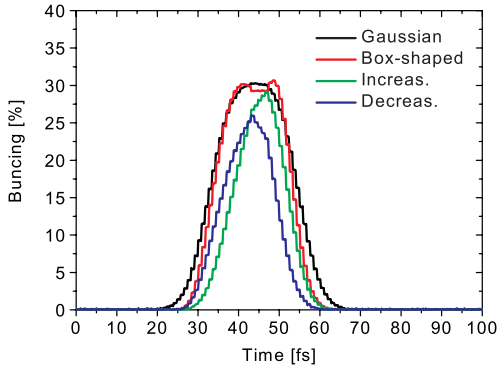

Figure 2: The resulting bunching factors on the fifth harmonic after the first dispersion section of the two-stage HGHG-FEL for different seed cases.

The resulting bunching factors of the fifth harmonic after the first dispersive section for the two-stage HGHG-FEL [1] are shown in figure 2. The dispersion strength is adjusted to maximum radiator power and for retaining pulse

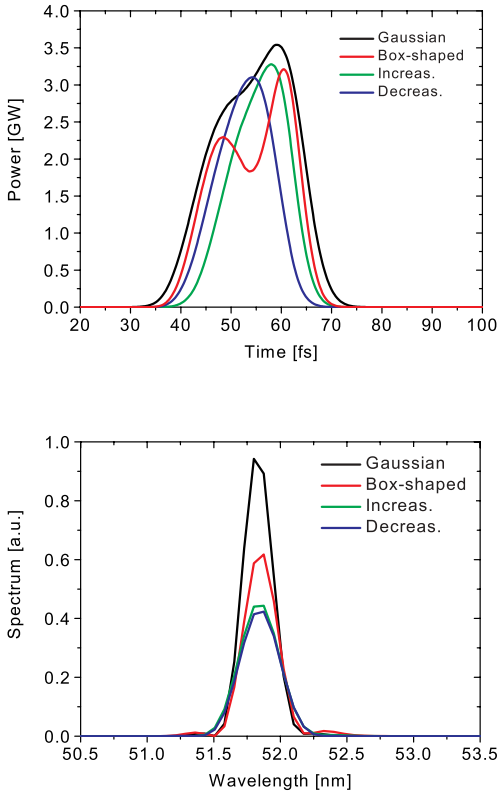

Figure 3: The power distribution (top) and the spectrum (bottom) of the first radiator of the two-stage HGHG-FEL for different seed-pulse shapes.

lengths if procurable. As expected, the bunching caused by the box-shaped seed is not fully box-shaped. Due to the slippage, there exist electrons in the interacting part, which do not experience the peak power during the whole passage through the modulator. For the maximum power of the following radiator, the strength of the dispersion section has to be adjusted such that these edge electrons are bunched optimally. In this case the central electrons experience a to high dispersion strength, which leads to an over bunching of them. The flanks of the bunching caused by the box-shaped seed are steeper than those of the Gaussian shaped seed, while the flanks of the increasing-power and decreasing power seeds are roughly as steep as those of the Gaussian seed in spite of the upright edges of the corresponding seed shapes.

The bunching maxima of the increasing- and decreasing power cases are shifted relative to each other but this shift is much smaller than the shift by the seed shapes itselfs. The slippage effect seems to mitigate these seed characteristics. Due to the fact that the integrated seed powers for these both shapes are lower than for the Gaussian and box-shaped cases, the resulting maximum bunching factors are

also lower.

The power distributions and the spectra of the first radiator for different seeds, shown in figure 3, point at the effects of the slippage and overbunching. The higher peaks at the right side of the power distributions for the Gaussian and box-shaped cases are caused by the slippage. The dips in the power profiles originate from the overbunching, which increases during the passage through the radiator. The maxima for the other two seed cases are shifted according to the bunching factors. For these cases, the electrons are not yet overbunched but the radiator outputs are far from the maximum results.

Second Stage

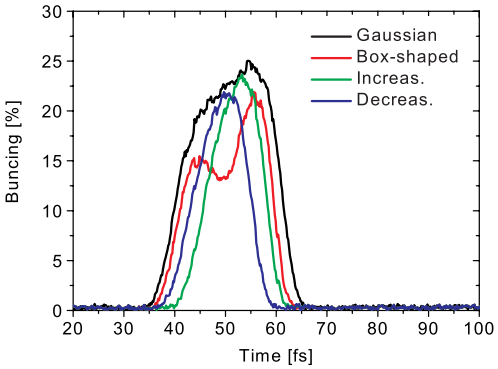

Figure 4: The Bunching on the fifth harmonics after the second dispersion section of the two-stage HGHG-FEL for different seed cases.

The output of the first radiator is used as a seed for the second stage. Figure 4 shows the bunching factors on the fifth harmonics after the second dispersive section for the two-stage HGHG-FEL. The dip in the bunching for the box-shape case is not an overbunching effect but rather it mirrors the shape of the seed radiation, i.e. the output of the first radiator. This can be concluded from the spectrum of the second radiator, figure 5b, where the sidebands are very small. The flanks of the bunching profile for the box-shaped case are no more steeper than the Gaussian case.

Although the peaks of the power distributions for the different seeds, figure 5a, have roughly the same values, the spectral distributions differ strongly. The high sideband in the spectrum of the Gaussian case points to a strong overbunching which is also indicated by the deep dip in the corresponding power distribution. The spectrum of the box-shaped case is pure and its maximum is roughly as high as the Gaussian case. The spectrum of the increasing- and decreasing power cases are also pure but the maximum spectral powers suffer from the reduced pulse length similar to the purity-optimized case described in [4]. The relative shift between the spectral maxima is not only reduced but

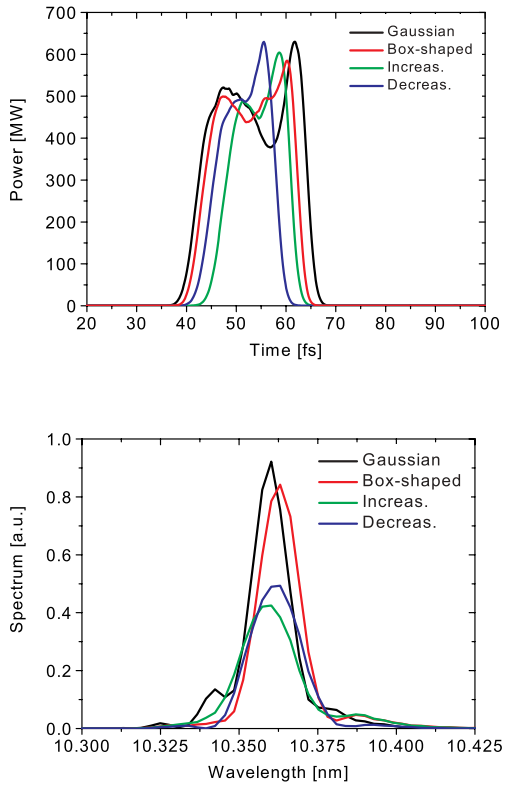

Figure 5: a)The power (top) and b) spectrum (bottom) of the second radiator for different seed-pulse shapes.

also the order of the maxima is changed compared to the spectra of the first radiator.

Final Amplifier

Using the output radiation of the second radiator as seed for the final amplifier, one would expect, that the properties of the radiator outputs dominate the output characteristics of the amplifier. Figures 6a and 6b show that this is true only for the Gaussian and box shaped case. For the increasing- and decreasing power cases, the properties of the radiator outputs are not fully retained during the amplification process. The spectral purity is reduced compared to the radiator output and the shift between the maxima of the spectrum seems to increase.

A comparison of the results of the final amplifier for the Gaussian, box-shaped, and purity-optimized case [4], figure 7, shows that a box-shaped seed leads to a spectral purity as high as a purity-optimized case, i.e. reduced dispersion strengths, while the output power is roughly as high as for a Gaussian seed. Although the pulse duration of the box-shaped case is longer than of the purity-optimized case, it is not as long as the Gaussian case. This might be

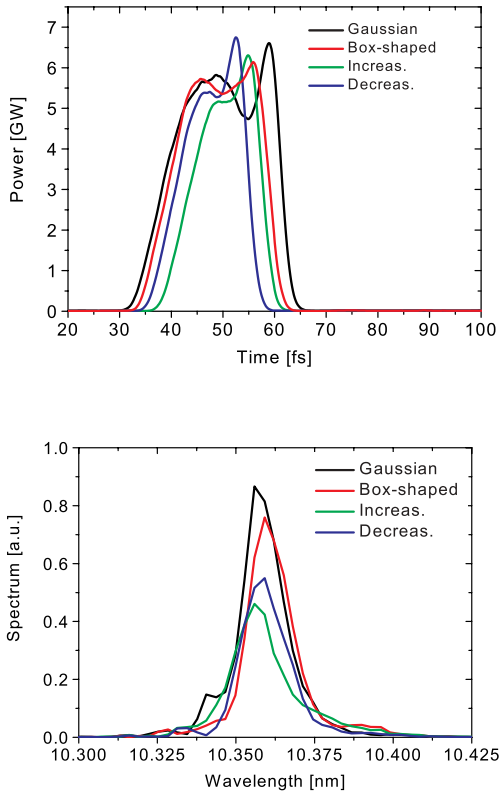

Figure 6: The power and spectrum of the final amplifier for different seed-pulse shapes.

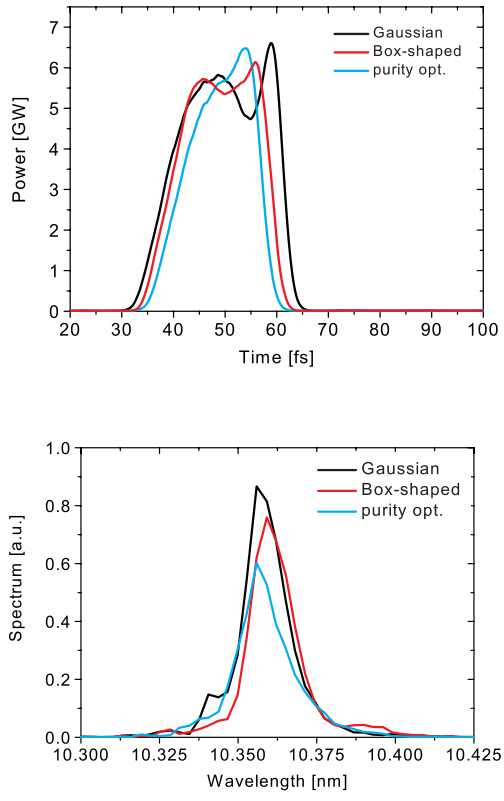

Figure 7: A comparison of the temporal and spectral power of the final amplifier for the Gaussian, box-shaped, and purity-optimized case [4] is shown.

originate from the flanks of the Gaussian distributed seed pulse.

CONCLUSION

The simulation studies show that the performance of a HGHG-FEL can be further optimized by adjusting the seed pulse shape. For the BESSY two-stage HGHG-FEL a box-shaped seed pulse can be used to achieve notable more spectral purity with only a minor loss of power compared with the FEL output for a Gaussian seed. Nevertheless the simulations with the increasing and decreasing seed power show also that due to the slippage, the shape of the radiation pulse changes during the passage through the FEL-line. Therefore the seed pulse shape should be adjusted for each of the three BESSY FEL-lines separately, in order to preserve the benefits of a well adjusted seed.

ACKNOWLEDGEMENT

The authors would like to thank A. Gaupp for very fruitfull discussions concerning the physics of the free electron lasers and the HGHG scheme.

REFERENCES

[1] The BESSY Soft X-ray Free Electron Laser, Techniacal Design Report March 2004, eds.: D.Krämer, E. Jaeschke, W. Eberhardt, ISBN 3-9809534-08, BESSY, Berlin (2004)

[2] L.H. Yu, J. Wu, Nucl. Instrum. and Meth. **A 483** (2002) 493

[3] E.L. Saldin, E.A. Schneidmiller, M.V. Yurkov, The physics of free electron lasers, Springer-Verlag Berlin Heidelberg, 2000

[4] A. Meseck, M. Abo-Bakr, B. Kuske, Output Variability of the BESSY Soft X-Ray FEL, EPAC 2004

[5] S. Reiche, Nucl. Instrum. and Meth. **A 429** (1999) 243

VELOCITY BUNCHING SIMULATIONS FOR THE DESY VUV-FEL

J.-P. Carneiro*, B. Faatz, K. Floettmann
DESY, Hamburg, Germany

Abstract

The TESLA Test Facility is currently being upgraded to reach in its final stage as a user facility SASE radiation at a wavelength of 6 nm. After a brief description of the layout and status of the VUV-FEL, this paper presents start-to-end simulations studying velocity bunching as a scenario for the first operation of the accelerator.

INTRODUCTION

The injector of the VUV-FEL consists of a 1.5 cell RF gun operating at 1.3 GHz surrounded by 2 solenoids (a bucking and a main) and followed by a cryomodule (ACC1) containing eight TESLA type superconducting cavities. A high quantum efficiency Cs_2Te photo-cathode is inserted into the half-cell of the RF gun and allows the production of high charge bunches when illuminated by the UV light of a laser pulse (20 ps FWHM) with a wavelength of 262 nm. The optimal operation of the injector requires, for emittance compensation purposes, that the four first cavities of the cryomodule operate with a lower accelerating field ($\sim$12.5 MV/m) than the four others ($\sim$20 MV/m). The RF-induced curvature of the longitudinal phase space is corrected by the use of a third harmonic cavity installed at the exit of ACC1. Five cryomodules and two magnetic compressors will then accelerate the beam to 1 GeV and compress it down from $\sigma_z \simeq 2$ mm to $\sigma_z \simeq 62$ μm. Under optimal operation, the beam peak current at the entrance of the undulator is expected to be $\sim$2.5 kA, for a slice emittance $<$1.5 mm-mrad (in the radiation part) and a total energy spread of $\sigma_E \leq 1$ MeV. The radiation pulse is then expected to be in the order of $\sim$200 fs FWHM for a peak power in the GW level.

In the present status of the VUV-FEL, a shorter laser pulse length ($\sim$10 ps FWHM measured with a streak camera) is available and the last cryomodules have not yet been installed. Furthermore, the third harmonic cavity is under development ([1]) and will not be available for use in the VUV-FEL within 2 to 3 years. Without this element, only a short part of the electron bunch can present at the undulator entrance the required beam properties (peak current, emittance and energy spread) to induce SASE radiation. Reference [2] indicates that a possible way to operate the VUV-FEL under these starting conditions is to use a low charge beam (0.5 nC) together with both magnetic compressors. At the entrance of the undulator, the bunch presents then a slice with a peak current of 1.3 kA, a normalized emittance $<$1.5 mm-mrad and a local energy spread of about 300 keV inducing a SASE radiation pulse of 15 to 50 fs at a wavelength of 30 nm. In this paper, we study an alternative option for the start-up of the VUV-FEL based on velocity bunching and on which no magnetic compression is used.

* Jean-Paul.Carneiro@desy.de

VELOCITY BUNCHING PRINCIPLE

The velocity bunching is based on the phase slippage between the electrons and the RF wave for a non-relativistic beam [3]. Reference [4] suggests, for the VUV-FEL, to use the first cavity of the first cryomodule (located $\sim$2.5 meters from the photo-cathode) to compress the bunch by velocity bunching.

This scenario, presented in Figure 1, shows ASTRA [5] simulations of the RMS bunch length as a function of the phase of the first cavity of ACC1 (relative to an acceleration on crest) keeping the phase of the other cavities to a maximum energy gain.

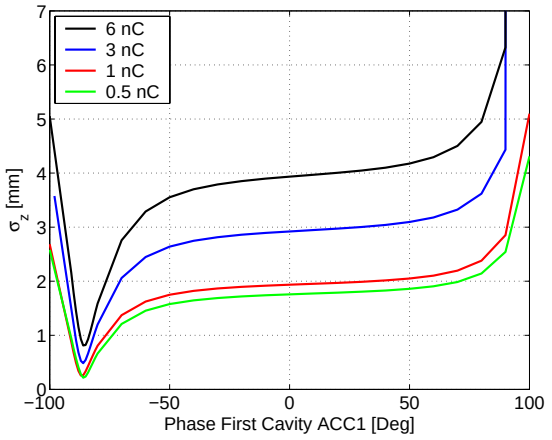

Figure 1: ASTRA [5] simulation of the RMS bunch length versus the phase of the first cavity of ACC1 (relative to acceleration on crest) for different charges. Outputs at the exit of ACC1 (z=13.6 m).

Four different bunch charges Q are studied and the outputs are taken at the exit of ACC1, at z=13.6 m. The main parameters of the injector used for these simulations were determined from measurements during the conditioning: field on the gun of 40 MV/m and accelerating field on the cavities of ACC1 of $\sim$12 MV/m. The beam enters

Q [nC]	Nominal			Velocity Bunching		
	I_n [kA]	ϵ_n [μrad]	ΔE_n [MeV]	I_n [kA]	ϵ_n [μrad]	ΔE_n [MeV]
0.5	0.03	1.3	0.13	0.65	3.2	0.58
1.0	0.05	2.0	0.15	1.2	5.1	0.72
3.0	0.10	5.3	0.33	1.8	8.6	0.91
6.0	0.16	9.9	0.57	2.1	15.6	1.35

Table 1: Main beam characteristics for nominal and velocity bunching operations and for different charges. From ASTRA [5]. Outputs at z=13.6 m.

the first cavity with a total energy of ∼4.7 MeV and exits the cryomodule with an energy of ∼107 MeV. Figure 1 indicates that a minimum bunch length is obtained for a phase of -86°. Table 1 presents the beam characteristics from ASTRA simulations at z=13.6 m for an optimized (laser diameter on the photo-cathode and solenoid field) operation of the injector under nominal (all cavities on crest) and velocity bunching (-86°) cases. The table shows that the use of velocity bunching enables a significant increase of the peak current (from 50 A to 1.2 kA for Q=1 nC) but it also degrades the projected emittance and the energy spread. The charge Q=6 nC corresponds to the maximum charge extractable from the RF gun using a laser diameter of 5 mm at 40 MV/m (maximum available, from [6]).

DISTRIBUTION AT Z=203 METERS

ELEGANT [7] has been used to track the compressed bunch obtained by velocity bunching from the exit of ACC1 to the entrance of the undulator (z=203 m). The four charges studied in the previous paragraph were transported along the VUV-FEL linac, taking both bunch compressors as drifts. The field on the cryomodules ACC2, ACC3 and ACC4 was ∼14 MV/m in order to get a total energy of ∼440 MeV. Figure 2 shows the beam current and slice emittance distributions at the entrance of the undulator for Q=0.5 nC, 1 nC and 3 nC. It is clear from these figures that first, the velocity bunching induces a sharp peak (∼100 μm) at the head of the bunch and second, that the slice emittance in the peak keeps reasonable values (∼5 mm-mrad for ∼1 kA). The slice energy spread in the peak (which has not been plotted) stays below 200 keV.

SASE FEL OUTPUTS

The ELEGANT outputs were tracked in the undulator using the FEL code GENESIS [8]. The transverse distribution of the beam has been taken as gaussian with the appropriate emittance and the longitudinal one as given by ELEGANT. The peak of the current distribution has been matched into the undulator focusing structure.

The undulator of the VUV-FEL is made of six segments (of 4492 mm each) separated with doublet focusing and diagnostics blocks between. The undulator period is set at

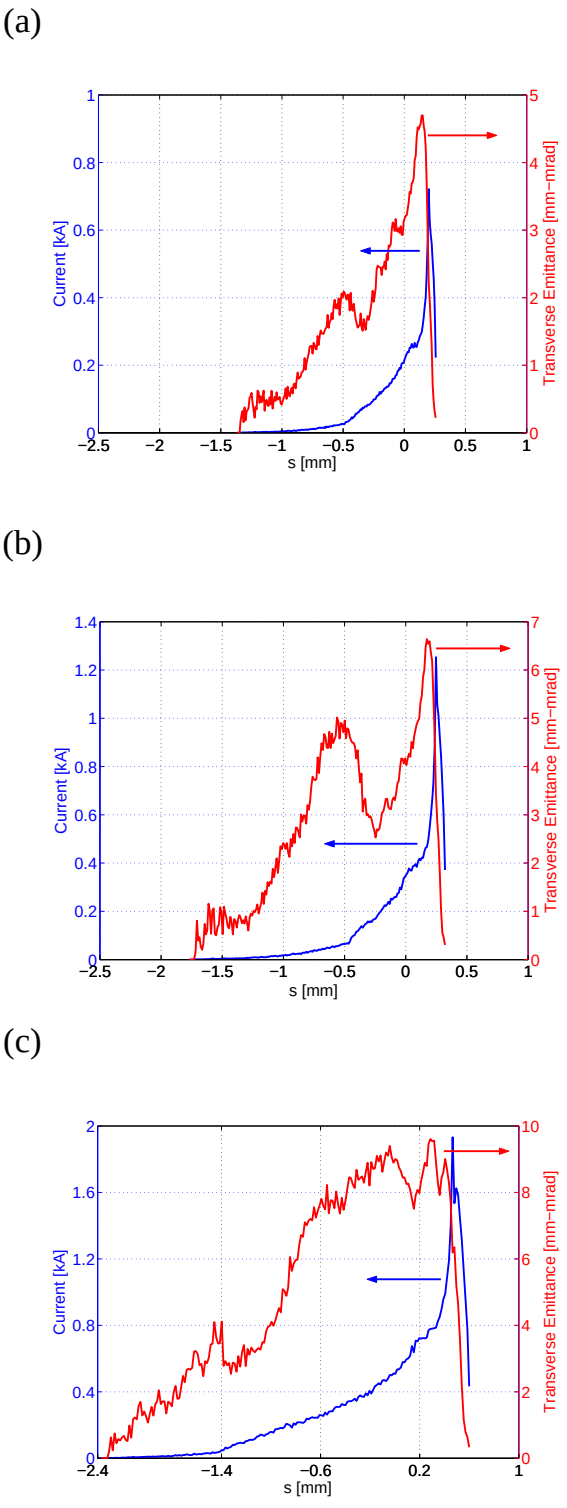

Figure 2: Current and slice emittance distributions at the entrance of the undulator (z=203 m) for bunch charges of (a) 0.5 nC, (b) 1.0 nC and (c) 3 nC. Bunch head for s>0. From ELEGANT [7].

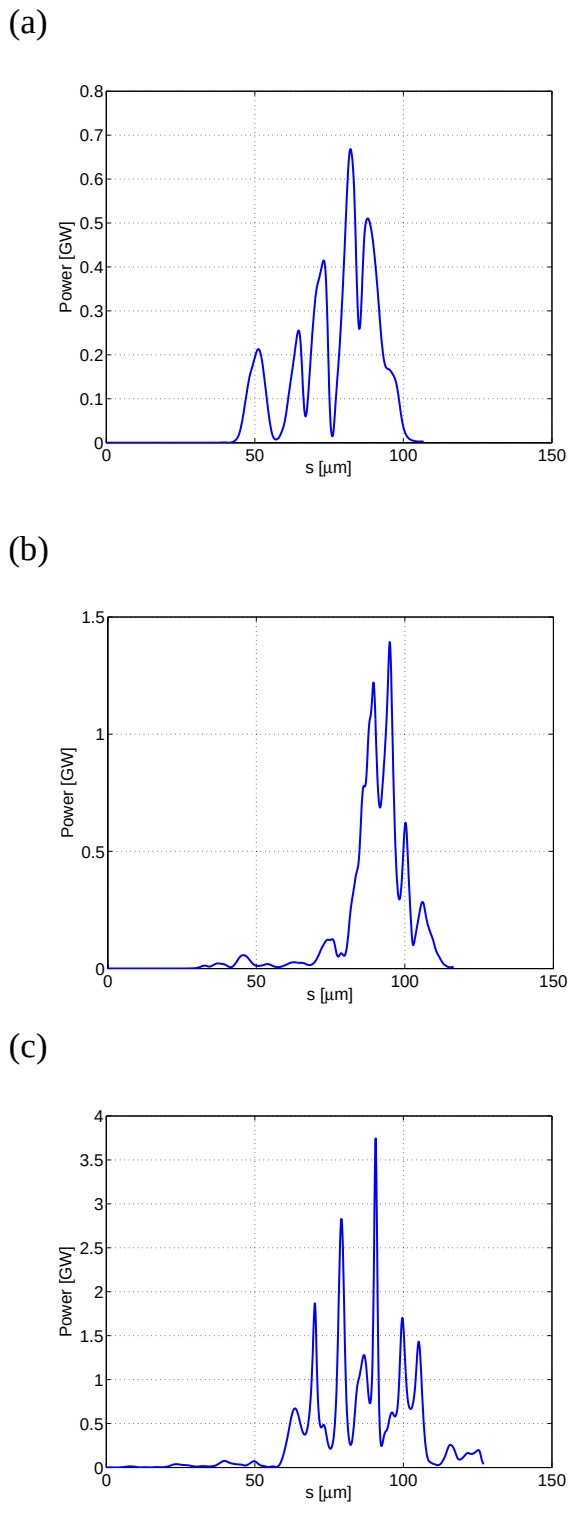

Figure 3: Radiation power at position of minimum spectral bandwidth for bunch charges of (a) 0.5 nC, (b) 1.0 nC and (c) 3 nC. From GENESIS [8].

Q [nC]	Saturation length [m]	Pulse duration FWHM [fs]	Mean power [GW]
0.5	15.233	80	0.2
1.0	13.268	65	0.5
3.0	15.233	100	1.0
6.0	19.165	500	1.0

Table 2: Main radiation power characteristics.

27.3 mm with an undulator parameter of K=1.23. GENESIS outputs of the radiating part of the distributions, corresponding to the peak in the current distribution shown in Figure 2, are shown in Figure 3 for the cases 0.5 nC, 1 nC and 3 nC. They show the power distributions at a position where the first peak reaches saturation, corresponding approximately to minimal spectral bandwidth. Table 2 shows the main characteristics of the radiation at the same positions, together with the 6 nC case.

CONCLUSION

The simulations presented in this paper show that the velocity bunching applied to the VUV-FEL produces bunches whose characteristics enable the SASE process in the undulator. However, it is important to notice that the space charge effects along the linac (mainly the longitudinal ones) have not been taken into consideration and can have a significant impact on the beam dynamics, especially for the high charge cases (3 nC and 6 nC). These effects should be studied in the future. First experimental studies of velocity bunching at the VUV-FEL began in June 2004 where the compression of the bunch has been observed with a pyrodetector located downstream of ACC1 for a phase of the first cavity of about -90°. More experiments on this subjects are foreseen in the VUV-FEL in the next months.

REFERENCES

[1] T. Kabibouline *et al.*, TESLA-FEL-2003-01, May 2003.

[2] E. Saldin, E. Schneidmiller and M. Yurkov, TESLA-FEL-04-06, to be published.

[3] L. Serafini and M. Ferrario, "Velocity Bunching in Photo-Injectors", AIP conference proceeding 581, p. 87-106, 2001.

[4] Ph. Piot and K. Floettmann, " An upgraded injector for the TTF FEL user facility", EPAC2002, Paris, France.

[5] K. Floettmann, ASTRA User Manual, see http://www.desy.de/∼mpyflo/Astra_dokumentation/.

[6] S. Schreiber, private communication.

[7] M. Borland, Advanced Photon Source LS-287, Sept. 2000.

[8] S. Reiche and B. Faatz, TESLA-FEL-2001-09.

THE POTENTIAL FOR THE DEVELOPMENT OF THE X-RAY FREE ELECTRON LASER: GENERATION OF SASE RADIATION

E.L. Saldin, E.A. Schneidmiller, and M.V. Yurkov
Deutsches Elektronen-Synchrotron (DESY), Hamburg, Germany

Abstract

We present a concept of a universal FEL beamline covering continuously wavelength range from 0.1 to 1.6 nm at a fixed energy of the electron beam. FEL beamline accommodates three undulators (SASE1-3) installed one after another. The first undulator, SASE1, is optimized for operation at the wavelength range 0.1-0.15 nm. Our study shows that such tunability range almost does not affect operation at the shortest wavelength of 0.1 nm. Operation of two other FELs (SASE2 and SASE3) is not so critical, and nominal tunability range is chosen to be by a factor of two (2-4 nm, and 8-16 nm, respectively). The length of the undulators is chosen such that continuous wavelength tunability can be provided by means of extra opening the undulator gaps, or by tuning to the frequency doubler mode of operation. Changing of undulator gaps in different parts of SASE2 and SASE3 undulators allows one to tune the modes with high output power (sub-TW level), or for effective generation of the second harmonic. The latter feature might be important for future pump-probe experiments. Also, recently proposed attosecond SASE FEL scheme is foreseen for implementation.

INTRODUCTION

For the design of the XFEL laboratory and the undulators the requirements with respect to photon energy range and tunability are important. The FEL laboratory will provide intense photon beams in the X-ray regime. Within the upper limit for generation of XFEL radiation at about 15 keV (0.08 nm) a wide range of photon energies has to be provided [1, 2, 3]. The lower energy cutoff is practically determined by the availability of the other sources, in particular the DESY TTF soft X-ray FEL facility which is foreseen to deliver FEL radiation with wavelength down to 2 nm in its third harmonic [4].

The superconducting linac is capable of supplying the pulse rate needed to support a farm of X-ray undulators. The proposed XFEL source will consist of three FEL beam lines. All together we expect that up to a hundred experimental stations can be distributed among the three undulator beam lines according to the needs of the user community.

LAYOUT OF XFEL

The accelerator will be operated at 10 Hz repetition rate providing bunch trains of up to 4000 electron bunches within one bunch train. All electron bunch trains will be guided into one electron beamline and dump. The electron beam transport line takes every bunch train and delivers it to the 1st SASE undulator (see Fig. 1). The performance of the FEL depends critically on the parameters of the electron beam. The optics between the undulators is especially designed to ensure the desired beam quality. The two bending magnets with a 10 mrad bending angle provide the parallel shift of the beam axis by a distance of 0.5 m, then the electron beam reaches the entrance of the 2nd SASE undulator. To bend the beam into the undulator, magnets operate in a DC mode with improved field stability. The photon beams of the 1st and 2nd SASE undulators have to be separated by a distance of 2 m in the experimental hall, which is realized by a deflection angle of about a one mrad. After passing all three undulators, the electrons are stopped in the beam dump. All three photon beamlines can be operated in parallel.

At a fixed electron energy the magnet gap of the FEL undulator can be varied mechanically for wavelength tuning. The wavelength range 0.1-1.6 nm at a fixed electron energy of 17.5 GeV can be covered by operating the XFEL with three undulators which have different periods. These SASE undulators can be placed behind each other assuming that the subsequent undulator radiates at longer wavelength. It is a great advantage that accelerator and electron beam transport line in new scheme of multi-user facility operate at fixed parameters and that a fast "electron switchyard" is not required. In order to avoid the need for a costly additional tunnels and shafts, the XFEL source is designed such that accelerator, all three SASE undulators, electron beamline, and three photon transport beamlines are installed inside the same (5 m diameter) tunnel.

Table 1: Specification of undulators

	λ_r nm	λ_u mm	gap mm	B_w T	L_w m
SASE1	0.1-0.15	39	10-12	0.8-1	150
SASE2	0.1-0.4	47.9	10-19	0.6-1.3	150
SASE3	0.4-1.6	64.8	10-20	0.8-1.7	110

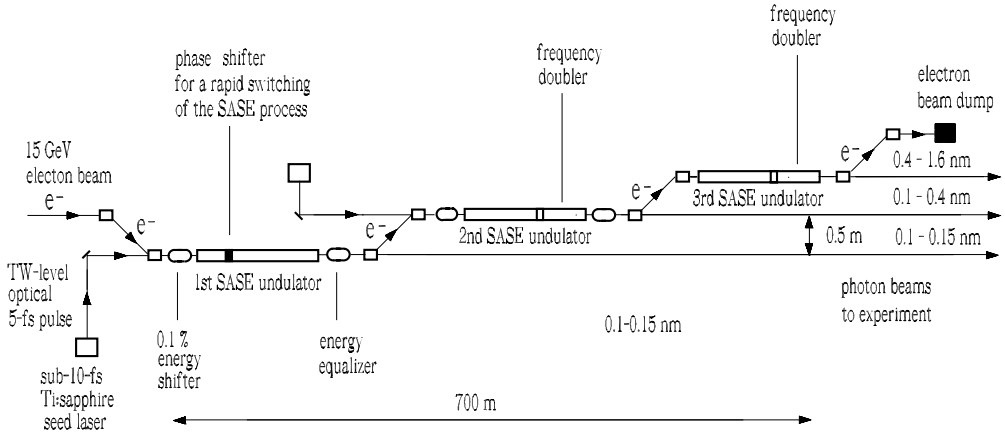

Figure 1: Sketch of a X-ray SASE FEL source.

Table 2: Specification of photon beam properties*

	Units	SASE1	SASE2	SASE3
Wavelength range	nm	0.1-0.15	0.1-0.4	0.4-1.6
Photon energy range	keV	12.4-8.3	12.4-3.1	3.1-0.8
Peak power	GW	10	20	20
Average power	W	40	80	80
Photon beam size (FWHM)	μm	90	60	60
Photon beam divergence (FWHM)	μrad	1.1	2.2	6.6
Coherence time	fs	0.22	0.25	0.5
Spectrum bandwidth (FWHM)	%	0.08	0.14	0.3
Pulse duration (FWHM)	fs	100	100	100
Number of photons per pulse	#	5×10^{11}	2×10^{12}	4×10^{12}
Average flux of photons	#/sec	2×10^{16}	8×10^{16}	2×10^{17}
Peak brilliance	B	2.5×10^{33}	1.4×10^{33}	8×10^{31}
Average brilliance	B	1×10^{25}	6×10^{24}	3×10^{23}

*Parameters are calculated for nominal electron energy of 17.5 GeV and middle of tunability range (see section 4 for more details). Average characteristics are calculated for 10 Hz repetition rate, and 4000 pulses per one train. Brilliance is calculated in units of photons/sec/mrad^2/mm^2/(0.1% bandwidth).

CONTROL OF THE AMPLIFICATION PROCESS WITH SASE SWITCHERS

Although the electron beam leaving the 1st SASE undulator has acquired some additional energy spread, it is still a good "active medium" for the 3rd SASE undulator at the end. In this scheme it will be possible to provide in parallel hard (around 0.1 nm) and soft (around 1 nm) X-rays for two photon beamlines (after-burner mode of operation). Normally if a SASE FEL operates in saturation, the quality of the electron beam is too bad for the generation of SASE radiation in a subsequent undulator which is resonant at a few times longer wavelength. On the other hand, to operate XFEL at the requested radiation wavelengths, three undulators are needed. The new method of SASE undulator-switching based on a rapid switching of the SASE process proposed in this paper is an attempt to get around this obstacle. This approach could be a very interesting alternative to the SASE undulator-switching based on "electron beam switchyard". The same goal, rapid switching between different SASE undulators, can be achieved in a more technically reliable way at less expenses.

There are two approaches to solving the problem of rapidly switched FEL. The first one focuses on the development of electromagnetic phase shifter embedded in the other components needed inside the undulator insertion. Second, electron energy shifter, can also be used. The technique of using a phase shifter as a switch relies on the fact that dependence of the FEL gain on the phase between the electron beam modulation and the radiation field, acting on the electrons is very strong. It is apparent that the electron's relative position within a radiation wavelength will determine whether it consistently gains or loses energy as it trav-

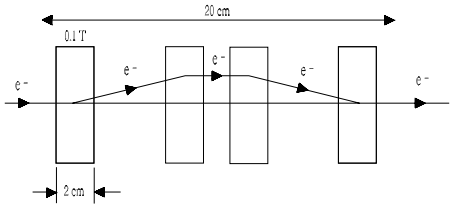

Figure 2: Electromagnetic phase shifter for a rapid switching of the SASE process in the 0.1 nm undulator.

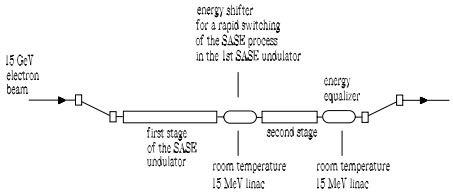

Figure 3: The second way to a rapid switching of the SASE process in the 0.1 nm undulator. Conceptual layout of the electron (photon) energy shifter.

els through the undulator. Optimal suppression is obtained when phase shift is such that most of electrons fall into accelerating phase and after passing through the phase shifter the electrons start to absorb power from electromagnetic wave. For the purpose of phase switching, electron beam has to be slightly delayed (about of Angstrom) as compared to the radiation beam. This is done by a suitably designed magnetic chicane called a phase shifter [5] (see Fig. 2). It consists of three horizontal magnets. The length of the center one is doubled because it needs twice the strength. The total length of phase shifter is about 20 cm. It uses electromagnets at an excitation level which is low enough, so that water cooling is not needed. For trapezoidal mode a frequency of 1 Hz is specified with a switching time of less than 10 ms. This kind of insertion device can be embedded between two neighboring undulator segments.

Another interesting approach is that of photon (electron) energy shifter. This method of beamline switching is based

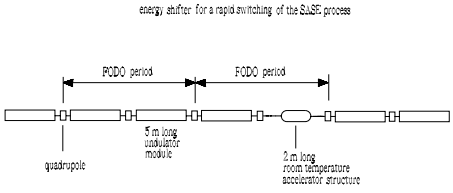

Figure 4: Installation of an energy shifter for a rapid switching of the SASE process. The quadrupole separation of a FODO lattice is large enough so that an accelerator structure of length 2 m can be installed.

on the accelerator technique. In this case the SASE undulator beamline consists of an input undulator, and an output undulator separated by an accelerator module (see Fig. 3). The typical FEL amplification bandwidth in the X-ray wavelength range is of the order of 0.1%. The offset photon energy 0.2% corresponds to electron energy shift of 15 MeV. By shifting the energy of the electron beam, one can effectively switch output undulator off. So the effective length of the undulator system can be rapidly varied. The RF switch consists of RF accelerator module with total voltage $V_0 \simeq 15$ MeV. We select 1.3 GHz structure based on standing-wave room temperature cavities with gradient of 8 MV/m. The quadrupole separation of an undulator FODO lattice is large enough so that relatively short (2 m) accelerator structure can be installed (see Fig. 4). Each RF switch would require one klystron TH 2104. This klystron is used for the TTF RF gun. The RF switch is operated with full beam loading and with design beam parameters. The average heat load of the accelerator cavity amounts to 20 kW which has to be removed by the cooling water. DESY is now developing similar room temperature accelerator structure for research unit PITZ at DESY Zeuthen [6].

EXTENDED POSSIBILITIES BEYOND STANDARD (SASE) MODE OF OPERATION

The developments discussed in this paper concern also the increased FEL output radiation power. The most promising way to achieve the goal is the method of tapering the magnetic field of the undulator. Tapering consists in slowly reducing the field strength of the undulator field to preserve the resonance wavelength as the kinetic energy of the electrons changes. Figure 5 shows the design principle of a high-power undulator. The first stage is a conventional X-ray SASE FEL. The gain of the first stage is controlled in such a way that the maximum energy modulation of the electron beam at the FEL exit is about equal to the local energy spread, but still far away from saturation. When the electron bunch passes through the dispersion section this energy modulation leads to effective compression of the particles. Then the bunched electron beam enters the tapered undulator, and from the very beginning produces strong radiation because of the large spatial bunching. Radiation field produces a ponderomotive well which is deep enough to trap the particles, since the original beam is relatively cold. The radiation produced by these captured particles increases the depth of the ponderomotive well, and they are effectively decelerated. As a result, much higher power can be achieved than for the case of a uniform undulator. At the total undulator length of 150 m, the FEL output at 0.2 nm is enhanced by a factor of 8, from 20 GW to 150 GW. With the proposed variable gap undulator design this option would require only installation of a dispersion section. Our study has shown that the required net compaction factor of the dispersion section is about a fraction

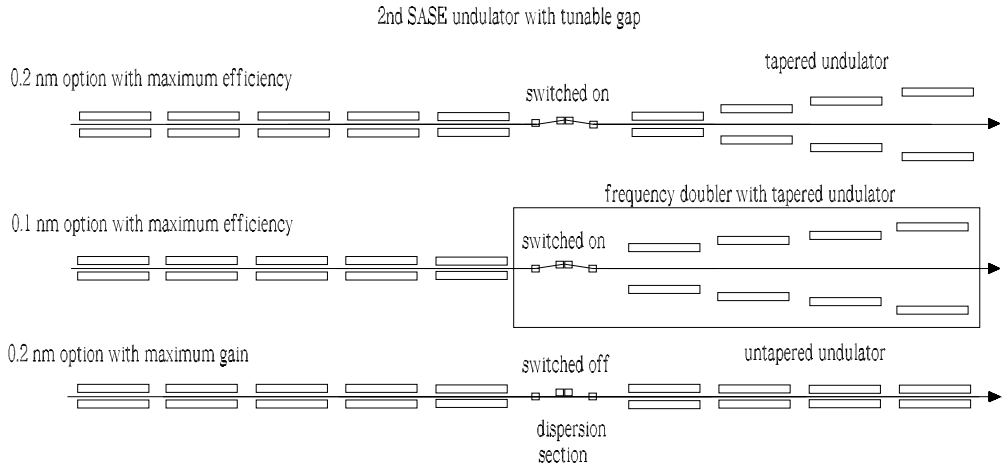

Figure 5: Three schemes for 2nd SASE undulator. Only one type of undulator magnet structure is needed. The radiation wavelength will be tuned by changing the gap. The total magnetic length is 150 m

of μm. The quadrupole separation of an undulator FODO lattice is large enough so that relatively short (4 m) dispersion section can be installed. An undulator taper could be simply implemented as a step taper from one undulator segment to the next.

The specification of the 2nd SASE undulator in uniform mode of operation gives a range of wavelengths between 0.2 and 0.4 nm. It was concluded that most experiments which are not interested in particular resonance effects will benefit from using photon energies close to 0.1 nm. A design was conceived that enables to obtain XFEL radiation at a close to 0.1 nm wavelength at two of the three SASE undulators simultaneously. The problem to be solved is how to extend the higher photon energy cutoff of the 2nd SASE undulator up to 12 keV. In this paper we propose to use an efficient frequency doubler for the 2nd and 3rd SASE FELs [7]. In its simplest configuration the frequency doubler consists of an input undulator, and an output undulator separated by a dispersion section. After passing through the dispersion section the bunched beam has not only a fundamental radiation frequency component, but also has considerable intensity in its harmonics. It is possible to have an input undulator operating at one frequency, and an output undulator operating at double of this frequency (see Fig. 5). The radiation in the output undulator will then be excited by the harmonic component in the electron beam, and the FEL will operate as a combination of frequency multiplier and amplifier.

Another perspective development is an attosecond mode of operation. A technique for the production of attosecond X-ray pulses is based on the use of X-ray SASE FEL combined with a femtosecond laser system [8]. It is important that this attosecond scheme is based on the nominal XFEL parameters, and operates in a "parasitic" mode not interfering with the main mode of the XFEL operation. It can be realized with minimum additional efforts. The machine design should foresee the space for installation of modulator undulator and a viewport for input optical system. Many of the components of the required laser system can be achieved with technology which is currently being developed for applications other than the attosecond X-ray source.

REFERENCES

[1] "Conceptual Design of 500 GeV e^+e^- Linear Collider with Integrated X-ray Facility" (Edited by R. Brinkmann et al.), DESY 1997-048, ECFA 1997-182, Hamburg, May 1987.

[2] TESLA Technical Design Report, DESY 2001-011, edited by F. Richard et al., and http://tesla.desy.de/.

[3] P. Audebert et al., "TESLA XFEL: First stage of the X-ray laser laboratory – Technical design report (R. Brinkmann et al., Eds.)", Preprint DESY 2002-167.

[4] "A VUV Free Electron Laser at the TESLA Test Facility at DESY. Conceptual Design Report", DESY, TESLA-FEL 95-03, Hamburg, June, 1995.

[5] J. Pflueger and M. Tischer DESY Print TESLA FEL 2000-08, DESY, Hamburg, 2000.

[6] V. Paramonov, private communication.

[7] J. Feldhaus et al., Preprint DESY 03-092, 2003. Nucl. Instrum. and Methods A, in press.

[8] E.L. Saldin, E.A. Schneidmiller and M.V. Yurkov, Preprint DESY 04-013, 2004. Opt. Commun., in press.

ATTOSECOND X-RAY SOURCE FOR LIGHT-TRIGGERED TIME-RESOLVED EXPERIMENTS ASSOCIATED WITH THE X-RAY SASE FEL

E.L. Saldin, E.A. Schneidmiller, and M.V. Yurkov
Deutsches Elektronen-Synchrotron (DESY), Hamburg, Germany

Abstract

We describe a technique for the production of attosecond X-ray pulses which is based on the use of X-ray SASE FEL combined with a femtosecond laser system. A few-cycle optical pulse from a Ti:sapphire laser interacts with the electron beam in a two-period undulator resonant to 800 nm wavelength and produces energy modulation within a slice of the electron bunch. Following the energy modulator the electron beam enters the X-ray undulator and produces SASE radiation. Due to energy modulation the frequency is correlated to the longitudinal position within the few-cycle-driven slice of SASE radiation pulse. The largest frequency offset corresponds to a single-spike pulse in the time domain which is confined to one half-oscillation period near the central peak electron energy. The selection of single-spike pulses is achieved by using a crystal monochromator after the X-ray undulator. Our studies show that the proposed technique is capable to produce 300-attoseconds long single pulses with GW-level output power in the 0.1 m wavelength range, and is applicable to the European X-Ray Laser Project XFEL and the Linac Coherent Light Source at SLAC.

INTRODUCTION

Brilliance, coherence, and timing down to the femtosecond regime are the three properties which have the highest potential for new science to be explored with an XFEL. In its initial configuration the XFEL pulse duration is about 100 femtoseconds [1, 2]. Even though this is a few hundreds times shorter than in third generation light sources, it can probably be further reduced to about 10 femtoseconds [3, 4, 5]. A novel way to generate sub-10-fs x-ray pulses – the slotted spoiler method has been proposed recently [6]. This method is based on spoiling the beam phase density in a part of the electron bunch so that this part will not lase, while preserving lasing in a short length of the bunch. The FEL performance of the spoiled beam approach was computed using the time-dependent GENESIS simulation. It has been shown that it is possible to produce X-ray pulses with duration of 3-4 fs FWHM for nominal LCLS bunch compression parameters [6, 7].

Recently an approach for the generation of attosecond pulses combining fs quantum laser and harmonic cascade (HC) FEL scheme was proposed in [8]. The HC FEL scheme has the potential to produce coherent light down to wavelengths of a few nm in an undulator sequence [9]. The analysis presented in [8] shows that this technique has potential to produce 100 as long radiation pulses with MW-level of output power down to 1 nm wavelength.

The shortest possible X-ray pulse duration generated by XFEL is limited by the intrinsic bandwidth of the SASE process. In the case of the European XFEL and the LCLS, the FWHM bandwidth near saturation (at 0.1 nm) is about 0.1%, indicating a 300-as coherence time determined by the bandwidth product. Recently a scheme to achieve pulse durations down to 400-600 attoseconds at a wavelength of 0.1 nm has been proposed [10]. It uses a statistical property of SASE FEL high harmonic radiation. The selection of a single 10-GW level attosecond pulses is achieved by using a special trigger in data acquisition system. A promising scheme for attophysics experiments using this approach has been studied and could be implemented in the XFEL design [1].

In this paper we describe a new method to allow reducing the pulse length of the X-ray SASE FEL to the shortest conceptual limit of about 300 as [11]. It is based on the application of a sub-10-fs laser for slice energy modulation of the electron beam, and application of a crystal monochromator for the selection of single attosecond pulses with GW-level output power. Optimization of the attosecond SASE FEL has been performed with the three-dimensional, time dependent code FAST [12] taking into account all physical effects influencing the SASE FEL operation (diffraction effects, energy spread, emittance, slippage effect, etc.).

GENERATION OF ATTOSECOND PULSES FROM XFEL

A basic scheme of the attosecond X-ray source is shown in Fig. 1. An ultra short laser pulse is used to modulate the energy of electrons within the femtosecond slice of the electron bunch at the seed laser frequency. The seed laser pulse will be timed to overlap with the central area of the electron bunch. It serves as a seed for a modulator which consists of a short (a few periods) undulator. Following the energy modulator the beam enters the X-ray undulator. The process of amplification of radiation in this undulator develops in the same way as in a conventional X-ray SASE FEL: fluctuations of the electron beam current serve as the input signal. The proposed scheme for the generation of attosecond pulses is based on frequency-chirping

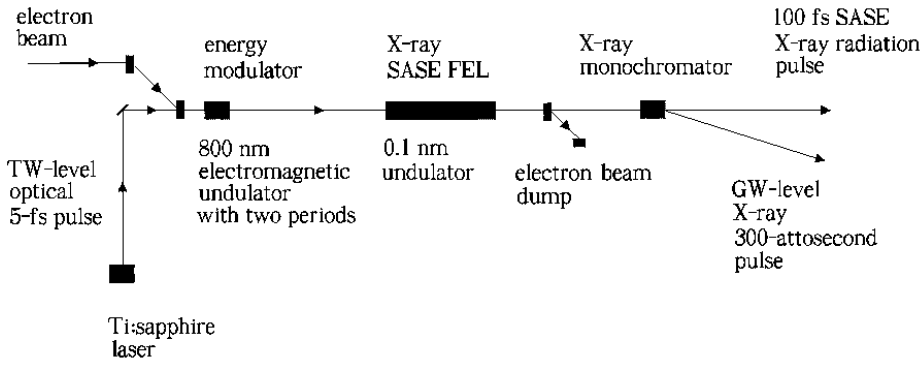

Figure 1: Schematic diagram of attosecond X-ray source.

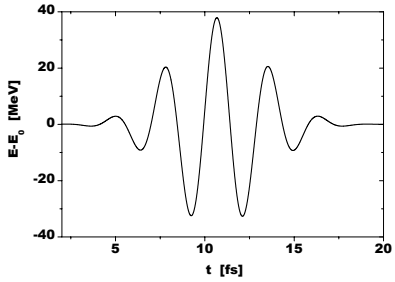

Figure 2: Energy modulation of electron bunch at the exit of the modulator.

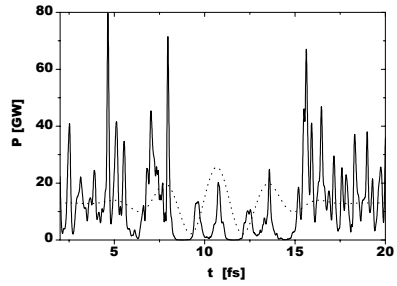

Figure 3: Temporal structure of the central part of the radiation pulse (single shot). Undulator length is 120 m. Dotted line shows energy modulation of the electron bunch (see Fig. 2).

the SASE radiation pulse. When an electron beam traverses an undulator, it emits radiation at the resonance wavelength $\lambda = \lambda_w(1 + K^2/2)/(2\gamma^2)$. Here λ_w is the undulator period, $mc^2\gamma$ is the electron beam energy, and K is the undulator parameter. The laser-driven sinusoidal energy chirp produces a correlated frequency chirp of the resonant radiation $\delta\omega/\omega \simeq 2\delta\gamma/\gamma$. After the undulator, the radiation is passed through a crystal monochromator which reflects a narrow bandwidth. Since the radiation frequency is correlated to the longitudinal position within the beam, a short temporal radiation pulse is transmitted through the monochromator.

In the following we illustrate the operation of an attosecond SASE FEL for the parameters close to those of the European XFEL operating at the wavelength 0.1 nm [1]. The parameters of the electron beam are: energy 15 GeV, charge 1 nC, rms pulse length 25 μm, rms normalized emittance 1.4 mm-mrad, rms energy spread 1 MeV. Undulator period is 3.4 cm.

In the present scheme an electron beam with slice modulation of the energy passes through the undulator and produces SASE radiation. Since only a small fraction of the bunch is modulated (10 fs versus 200 fs of FWHM electron pulse duration, see Fig.2), the total energy in the radiation pulse remains approximately the same as in the case of non-modulated electron beam, and saturation is achieved at an undulator length of about 120 m. Figure 3 shows a view of the central part of the radiation pulse. The dotted lines in this figure show the initial energy modulation of the electron beam. The temporal structure of the radiation pulse has a clear signature of the slice energy modulation. The FEL process is strongly suppressed in the regions of the electron bunch with large energy chirp, and only regions of the electron bunch with nearly zero energy chirp produce radiation.

The plots in Fig. 4 show the spectrum of the radiation pulse. A signature of the slice energy modulation is reflected by the tails of the spectrum. Each of three clearly visible bumps in the averaged spectrum corresponds to a local extremum of the energy offset shown in Fig. 2. The bump marked as M_1 corresponds to the central peak energy offset. The bump M_2 corresponds to the neighboring two positive energy offsets. The bump M_3 comes from the areas of the electron bunch with negative energy offset. The single-shot spectrum (shown as grey line) exhibits an oscillatory behavior near bumps M_2 and M_3. That is due to an

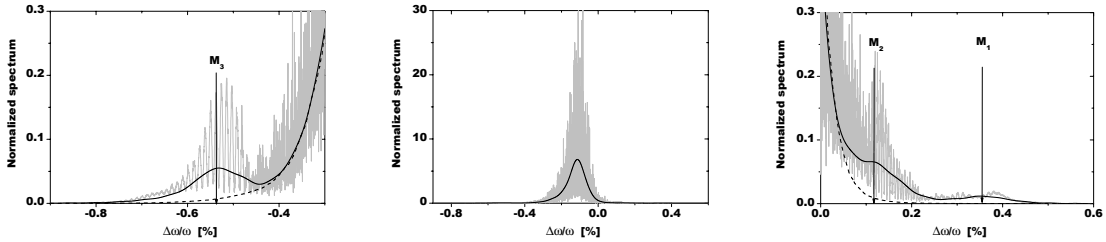

Figure 4: Spectrum of the radiation pulse produced by modulated electron bunch. Undulator length is 120 m. Middle: complete spectrum. Left and right plots show enlarged tails of complete spectrum. Solid line is averaged spectrum. Dashed line is averaged spectrum of non-modulated electron beam. Mark M_1 shows tuning of monochromator for single pulse selection. Marks M_2 and M_3 show tuning of the monochromator for selection of two pulse sequence (see Fig. 5).

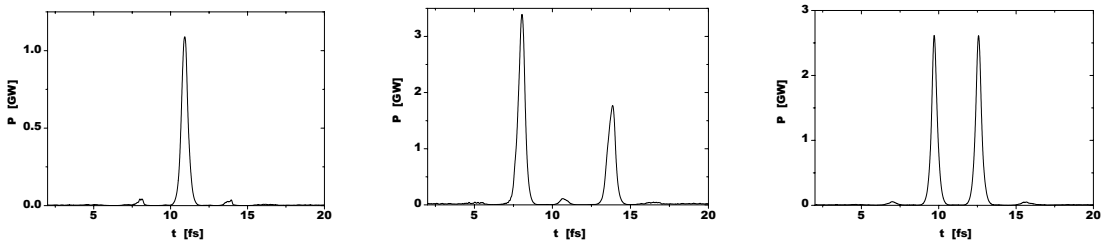

Figure 5: Averaged temporal structure of the radiation pulse behind monochromator tuned to single spike (left plot) and two pulse sequence selection (middle and right plots).

interference of two radiation wave packets with close frequencies coming from different parts of the electron bunch. Other maxima can be hardly distinguished, since they are located within the bandwidth of the main spectrum.

Figure 4 gives a clear idea about separation of the attosecond radiation pulses. Positioning of the monochromator to different maxima of the spectrum allows us to select single pulse, or a two pulse sequence of attosecond duration. The calculation involves the following steps. The FEL simulation code produces 3-D arrays for the radiation field in the near zone. This field is recalculated into the far field zone, and is subjected to the Fourier transform. The latter result is convoluted with the reflectivity function of Ge(111) monochromator, and is subjected to inverse Fourier transform giving temporal structure of the radiation pulse behind the monochromator.

By selecting the frequency offset of the monochromator to the position marked as M_1 in Fig. 4, we select single pulses. Their properties are illustrated with Figs. 5 and 6. An analysis of single pulses shows that their pulse duration is about 300 as, the average power has GW-level, and the radiation pulse energy is about a μJ. The larger width of the averaged curve is partially due to shot-to-shot fluctuations of the position of the radiation pulse (a fraction of coherence time). Note that shot-to-shot fluctuations of the radiation energy after monochromator are suppressed significantly due to ultra short duration of the lasing fraction

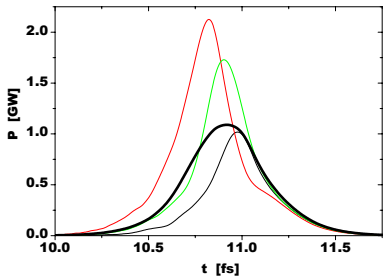

Figure 6: Temporal structure of the radiation pulse behind monochromator tuned to single spike selection (mark M_1 in Fig. 4). Thin curves are single shots, and bold curve is average over many pulses.

of the electron bunch [13]. An advantage of single-pulse selection is the small background from the main radiation pulse due to a large offset from the resonant frequency.

By positioning of the monochromator central frequency to the spectrum bumps M_2 or M_3 one can select a two pulse sequence as illustrated in Fig. 5. Two pulses are separated by two or one oscillation period of optical laser depending on the choice of the monochromator tuning. Note that due to the statistical nature of the SASE process the time

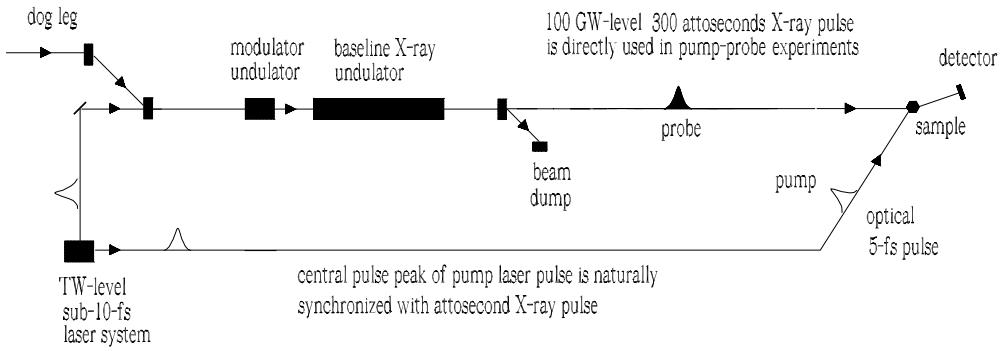

Figure 7: Scheme for femtosecond resolution pump-probe experiments based on the generation of the 100 GW-level attosecond X-ray pulses directly from X-ray SASE FEL.

jitter between two pulses is about 200 as, a fraction of the coherence time. One should not wonder that pulse amplitudes differ visibly for the case of pulse separation by one laser oscillation period. This is a typical nonlinear effect related to the sensitivity of the FEL process to the sign and the value of the energy chirp. Although the energy modulation amplitude is the same in both maxima, the shape of the energy chirp is asymmetric.

CONCLUSION

Attosecond X-ray FEL described here is an ideal tool for organization of pump-probe experiments (see Fig. 7) [11, 14]. Indeed, attosecond X-ray pulse is naturally synchronized with its fs optical pulse, and time jitter is cancelled. Usual optical elements are used for seed laser beam splitting and tunable delay. It should be possible to achieve a timing accuracy close to duration of the half period of the seed laser pulse (1 fs), allowing an unprecedented insight into the dynamics of electronic excitations, chemical reactions, and phase transitions of matter, from atoms, through organic and inorganic molecules, to surface, solids and plasma.

It is important that proposed attosecond scheme is based on the nominal XFEL parameters, and operates in a "parasitic" mode not interfering with the main mode of the XFEL operation. It can be realized with minimum additional efforts. The machine design should foresee the space for installation of modulator undulator and a viewport for input optical system. Many of the components of the required laser system can be achieved with technology which is currently being developed for applications other than the attosecond X-ray source. As a result, a laser system could be developed over the next few years and can meet the XFEL requirements well in advance of XFEL construction schedule.

REFERENCES

[1] TESLA Technical Design Report, Supplement, DESY2002-167, edited by R. Brinkmann et al., and http://tesla.desy.de.

[2] The LCLS Design Study Group, LCLS Design Study Report, SLAC reports SLAC-R-593 (2002), and http://www-ssrl.slac.stanford.edu/lcls/CDR.

[3] C.B. Schroeder et al., Nucl. Instrum. and Methods A483(2002)89.

[4] E.L. Saldin, E.A. Schneidmiller and M.V. Yurkov, Opt. Commun. 205(2002)385.

[5] S. Reiche, P. Emma, and C. Pellegrini, Nucl. Instrum. and Methods A507(2003)426.

[6] P. Emma et al., Phys. Rev. Lett. 92(2004)074801.

[7] M. Cornacchia, et al., SLAC-PUB-10133, December 2003.

[8] A. Zholents and W.M. Fawley, Preprint LBNL-54084, LBNL, Berkeley, 2003.

[9] E.L. Saldin, E.A. Schneidmiller and M.V. Yurkov, Opt. Commun. 202(2002)169.

[10] E.L. Saldin, E.A. Schneidmiller and M.V. Yurkov, Opt. Commun. 212(2002)377.

[11] E.L. Saldin, E.A. Schneidmiller and M.V. Yurkov, Opt. Commun. 237(2004)153.

[12] E.L. Saldin, E.A. Schneidmiller and M.V. Yurkov, Nucl. Instrum. and Methods A429(1999)233.

[13] E.L. Saldin, E.A. Schneidmiller and M.V. Yurkov, Nucl. Instrum. and Methods A507(2003)101.

[14] E.L. Saldin, E.A. Schneidmiller and M.V. Yurkov, Opt. Commun. 239(2004)161.

THE POTENTIAL FOR THE DEVELOPMENT OF THE X-RAY FREE ELECTRON LASER: MULTI-USER PHOTON DISTRIBUTION SYSTEM FOR XFEL LABORATORY

E.L. Saldin, E.A. Schneidmiller, and M.V. Yurkov
Deutsches Elektronen-Synchrotron (DESY), Hamburg, Germany

Abstract

X-ray photon beam from a SASE FEL undulator is in principle a single user tool, just like an optical laser. Therefore, the operation and amortization cost cannot be easily spread over many simultaneous experiments. To avoid prohibitive cost for each experiment, a new XFEL laboratory scheme is proposed. A photon beam distribution system based on movable multilayer X-ray mirrors can provide an efficient way to generate a multi-user facility. Distribution of photons is achieved on the basis of pulse trains and it is possible to partition the photon beam among a few tens independent beamlines thereby obtaining many users working in parallel. The second way to increase the number of simultaneous experiments is based on the working with a series of perfect crystals in transmission (Laue) geometry. The later concept is the basic idea of the Troika beamline at ESRF. In principle, a hundred of photon beamlines with different experiments can be served by a single XFEL source.

INTRODUCTION

The preferred layout of a SASE FEL is a linear arrangement in which the injector, accelerator, bunch compressors and undulators are nearly collinear, and in which the electron beam does not change the direction between accelerator and undulators. On the other hand, a X-ray FEL laboratory should serve several tens, may be up to a hundred experimental stations which should operate independently according to the needs of the user community. The present paper describes a beam distribution system which allows to switch the FEL beam quickly between many experiments in order to make efficient use of the source. Many applications require only very high peak brilliance. Such experiments for which average brilliance and wavelength are not critical, could operate simultaneously at the same radiation wavelength.

Each FEL source emits only one photon beam. Therefore, the operation and amortization costs cannot be easily spread over many simultaneous experiments. To avoid prohibitive cost for each experiment, new photon beam distribution scheme is proposed. It would specifically partition the photon beam among a few tens independent beamlines thereby obtaining many users working in parallel. Our analysis shows that proposed mult-user photon distribution schemes may be implemented at future upgrades of XFEL facilities [1, 2, 3].

MULTI-USER DISTRIBUTION SYSTEM BASED ON MULTILAYERS

The technical approach adopted in this variant of XFEL laboratory design makes use of movable multilayer X-ray mirrors. Layered synthetic materials – multilayers – are layered structures with usually two alternating materials: a low and high density materials. They play an important role in synchrotron X-ray optics [4, 5, 6, 7]. They provide less energy resolution but correspondingly more flux and keep the angular beam divergence constant (in the ideal case). Typical multilayers used as optical elements at third generation synchrotrons provide a spectral bandwidth of 1 to 5%. Typical glancing angles are of the order of a degree and thus lie between the mrad wide angles of X-ray mirrors and the much bigger 10 degree wide Bragg angles of single crystals. The angular acceptance of X-ray multilayer mirror is of the order of one mrad (for a bandwidth 1%). As a rule, from 100 to 400 periods participate in effective reflection in such mirrors. About 90% peak reflectivity was achieved for wavelengths around 0.1 nm. Computer simulations are in very good agreement with experimental results in all cases so that efficiencies can be safely predicted.

The concept of photon beam distribution system is very simple. Figure 1 shows relevant photon beamline configuration. The distribution of pulse trains among the different user stations can be done by movable deflectors. A schematic diagram of a movable deflector is shown in Fig. 2. Its key components include rotating multilayers and multifacet reflector. The advantages of multilayer as movable photon beam deflector are based on two factors: the larger deflection angle compared to X-ray mirrors; and the larger angular acceptance compared to crystals. The multilayer mirror angular acceptance is of the order of one mrad, and is well matched to the natural opening angle, (from one to a few μrad), of an XFEL source. In order to achieve stable photon beam deflection the alignment accuracy of multilayer deflectors must be less than 0.1 mrad. It is believed that technology, presently in advanced development for applications other than XFEL, will enable rotating multilayers to satisfy these requirements. The initial photon beam is transformed into 5 beams. The switching mirrors need to rotate at a frequency of 1 Hz such that each user actually receives one train of pulses with a full duration of

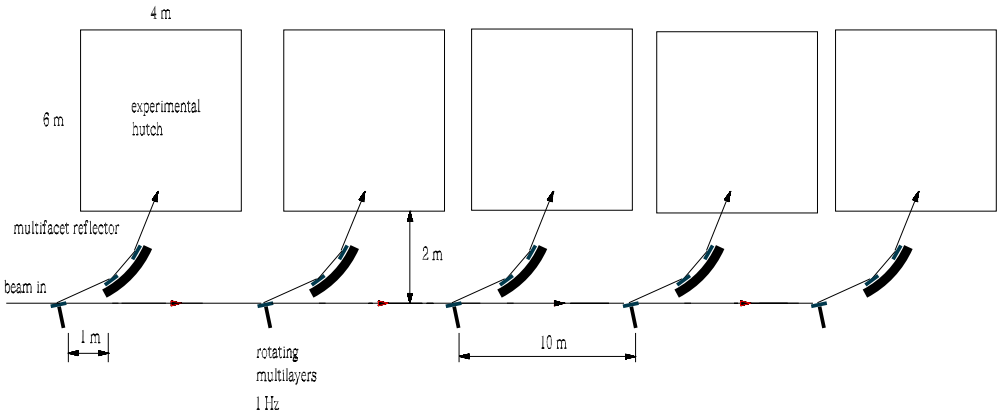

Figure 1: Proposed SASE undulator beamline for studies with maximum X-ray flux. The distribution of photons is achieved on the basis of pulse trains and it is possible to serve 5 user stations with repetition rate 1 Hz.

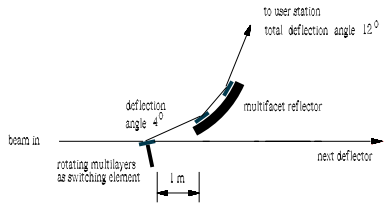

Figure 2: Concept of the photon beam deflector based on multilayer X-ray mirror. Using rotating multilayer mirrors as switching elements between the multifacet reflectors makes it possible to provide X-ray radiation for many user stations.

1 ms per second. Note that even if the photon beam is distributed among many users, the peak flux per user remains untouched (apart from the losses in the deflector system). Such a scheme, which adopts multilayer deflector concept, allows one to increase the total number of user stations by using standardized X-ray optical components.

An attractive feature of the distribution system based on movable multilayers is the absence of no apparent limitations which would prevent operation at even hundred user stations (per SASE undulator) simultaneously. All users will receive the photon beam of identical (and high) quality. Every time deflection process happens only once during one pass of the photon beam through the deflector unit with only three multilayers, and the problem of the absorption of the radiation in the distribution system does not exist at all. Another advantage comes from small (one to a few μrad) angular divergence of the FEL radiation. As a result, in an extended sequence of deflectors (say, a few tens of meters), photon beam properties (spot size) remain unchanged. The larger number of beamlines, the smaller is the macropulse repetition rate per user station. Note also that even if the beam is distributed among 50 users, the macropulse repetition rate per user will still be 0.1 Hz. It is important to note that for many experiments this may not be a difficulty and the macropulse (4000 pulses) per 10 seconds is more than sufficient. Photon intensity integrated over macropulse is equivalent to an intensity integrated per an hour at synchrotron radiation sources today. Another attractive feature of the proposed photon system is a high degree of flexibility: if some user will request a full photon flux for a while, this can be done simply by means of "freezing" motion of the multilayers for a while such that full photon flux is directed to dedicated user station.

MULTI-USER DISTRIBUTION SYSTEM BASED ON CRYSTAL DEFLECTORS

Photon beam distribution system based on movable multilayers is one of the alternatives under consideration to extend the XFEL capability to a few tens users working in parallel. The second potential candidate for the XFEL laboratory to progress into multi-user facility class is that distribution system based on (fixed) crystal deflectors. Figure 3 shows a schematic layout of the photon distribution

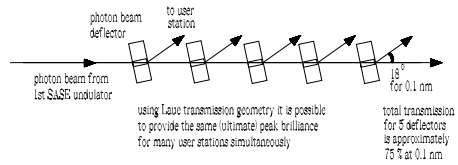

Figure 3: Photon beam distribution system setup based on crystal deflectors for simultaneous multi-user mode of operation at 0.1 nm

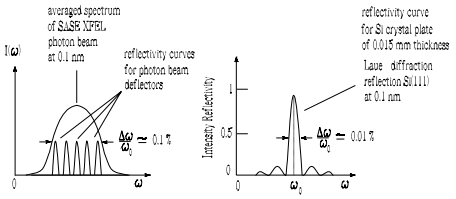

Figure 4: Basic principle of the XFEL multi-user distribution system. Using Laue diffraction in Si crystals as a method of photon beam deflection it is possible to provide X-ray radiation for many user-station simultaneously.

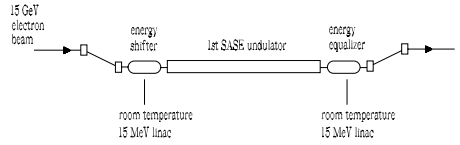

Figure 5: Electron (photon) energy shifter as a switching element between 3 beamline clusters. Conceptual layout.

system. This is a farm of multi-station SASE undulator beamlines, working with a series of transmission crystal deflectors. Advantage of this scheme is the possibility of using not only the diffracted photon beam, but also the transmitted "broadband" SASE beam for downstream experimental stations operating at different photon energies (see Fig. 4). The latter concept is the basic idea of the Troika beamline at ESRF [8, 9, 10]. Note that even if the photon beam is distributed among a few tens of users, the peak brilliance per user remains untouched (apart from the losses in the deflector system). In the case of end stations the direct photon beam is used.

The relative spectral bandwidth for Laue reflection is independent of the wavelength or glancing angle of X-rays and is given merely by properties of the crystal and the reflecting atomic planes. In particular, it implies that the choice of a crystal and reflecting atomic planes determines the spectral resolution. For example, one can consider Si(111) crystals, which have FWHM bandwidth of $\Delta\lambda/\lambda \simeq 1.2 \times 10^{-4}$ in Laue transmission geometry. Deflectors at photon beam lines are fabricated from silicon. The main advantage of the silicon is the availability of almost perfect synthetic monocrystals, with high transparency. The reason is that semiconductor industry has created a huge demand for defect-free, perfect single crystal. In order to maintain a high transmission through the deflectors for the downstream stations, it is necessary to limit the absorption in the 10 deflectors to about 50% at 0.1 nm. The thickness of the one crystal must therefore not exceed 15 μm. The angular acceptance of silicon deflector is of the order of 20 μrad for a wavelength of 0.1 nm, and is well matched to the natural opening angle, (one μrad), of an XFEL source.

The use of a Laue deflector can be extremely advantageous in the case of high thermal loads, because the beam is almost entirely transmitted, and only a small part is absorbed. At 0.1 nm an average power of 40 W (2 mJ$\times$ 5 trains/s $\times$ 4000 pulse/train) at the 1st SASE undulator exit corresponds to a normal incidence power density of 50 W/mm^2 at the distance of 1000 m from the undulator for a beamsize (FWHM) of 1 mm. The absorbed power per one deflector is about 2 W.

Silicon has the advantage of a high heat conductivity and high damage threshold, thus achieving good performance at high power load. It is well known that when crystal plate is cooled, the thermal deformation results in a slope error composed of a bending and bump component. Briefly, the thermal deformation of the crystal induced by heat load depends on the ratio α/k, where α and k are the thermal expansion coefficient and the thermal conductivity of the crystal, respectively. This ratio is strongly temperature dependent for silicon. The ratio α/k is zero at 125 K, and about 50 times smaller at liquid-nitrogen temperature (77 K) than at room temperature.

The time-averaged power and power density at large distance from the SASE undulator are comparable to those of the third generation synchrotron radiation sources. For example, the brightest X-ray beams at ESRF facility are produced by in-vacuum undulators. These undulators emit about 0.5 kW of X-ray power in the central cone and the power density, at the position of the silicon monochromator 30 m from the source, is about 200 W/mm^2. Cooling techniques such as cryogenic cooling of Si have become standard at the third generation sources. The thermal deformation of the silicon crystal, which is indirectly cooled by liquid nitrogen, was studied experimentally and by finite-element analysis. Excellent agreement between the experimental measurements and theoretical results was observed. There is the best high-power working point for the crystal, when the power is raised to the point where the maximum temperature reaches 125 K. At this temperature the ratio between the thermal expansion and the thermal conductivity is zero [11].

The advantage of operating single-crystal-silicon deflector at cryogenic temperatures is obvious. Lowering the temperature of silicon from room temperature to liquid-nitrogen temperatures improves the so-called figure of merit, k/α, by 50-fold. A thin crystal is desired so that a large fraction of the incident beam would be transmitted, hence reducing the absorbed power in the deflector that has to be removed by the liquid nitrogen.

Although XFEL sources are designed primarily to generate brilliant X-rays with moderate energy 5-15 keV, high-energy X-rays are of great usefulness. In particular, high-energy focused beam is quite attractive for structural studies of amorphous solids and liquids and for diffraction studies of crystalline materials because of its extinction-free nature. The analysis shows that strong harmonic growth can

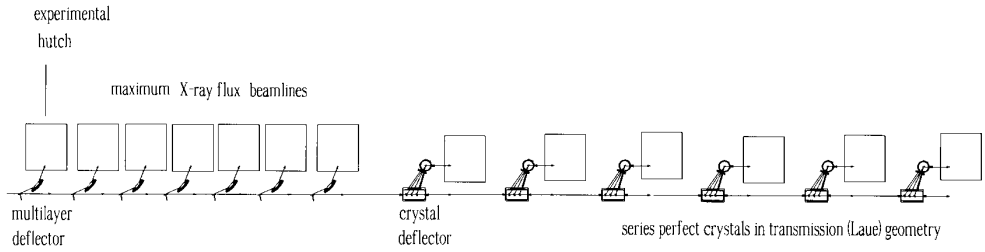

Figure 6: 1st SASE undulator beamline. A photon beam distribution system based on combination movable multilayers and crystals in transmission (Laue) geometry can provide efficient way to generate a multi-user facility.

be expected in SASE XFELs. When a beam is strongly bunched in the sinusoidal ponderomotive potential formed by the undulator field and the radiation field of fundamental frequency, the electron beam density spectrum develops rich harmonic contents. Coherent radiation at the odd harmonics can be generated in a planar undulator and significant power levels for the third harmonic can be reached before the FEL is saturated. Explicit calculations show that the power of the transversely coherent third-harmonic radiation can approach a fraction of a per cent of the fundamental power level.

In this paper we propose to utilize the third harmonic radiation from the XFEL. Four upstream transparent deflectors, which adopt so-called "Laue transmission geometry" concept, enable us to perform five different experiments simultaneously. High-energy X-rays are associated with a large penetration power, which makes it possible to use relatively "thick" silicon deflectors. The thickness of one crystal is 0.1 mm. The other main difference between diffraction at high energies and at conventional energies is the smaller Bragg angles. In particular for the 1st order Si(111) reflection at 0.03 nm the deflection angle is about 0.1 rad.

The distribution of pulse trains among the different beamline clusters can be done by a photon (electron) energy shifter pulsed at 5 Hz. It directs every other photon pulse train into a second cluster of photon beamlines. This method of pulse train distribution is based on the accelerator technique. In this case the SASE undulator beamline consists of an input energy shifter, SASE undulator, and output energy equalizer (see Fig. 5). Using photon energy shifter as switching element between 3 clusters of photon beamlines makes it possible to provide simultaneously X-ray radiation for $5 \times 3 = 15$ user station. Distribution of photons is achieved on the basis of pulse trains. Each user station actually receives one, two, or three pulse trains of full length at 1 Hz repetition rate.

It should be noted that crystal deflector performances are complementary to those of multilayer deflectors, whose bandwidth is much wider but whose photon flux is much higher. Crystal deflectors have a band-pass of the order of 10^{-4}, which is unnecessary narrow in many experiments. On the other hand, the fundamental SASE radiation has an energy peak-width of 10^{-3} and thus, using the whole SASE radiation peak, the flux is more than 10 times higher than that obtained with crystal deflector.

Both types of deflectors are important, their roles are complementary, and one type cannot replace the other. Figure 6 shows the optimal beamline configuration. The first 20 beamlines are planned to be multi-purpose beamlines for experiments with maximum X-ray flux. In this case 21st ... end-stations use the photon beam distribution system working with transmission crystal deflectors.

REFERENCES

[1] TESLA Technical Design Report, DESY 2001-011, edited by F. Richard et al., and http://tesla.desy.de/.

[2] P. Audebert et al., "TESLA XFEL: First stage of the X-ray laser laboratory – Technical design report (R. Brinkmann et al., Eds.)", Preprint DESY 2002-167.

[3] The LCLS Design Study Group, LCLS Design Study Report, SLAC reports SLAC- R521, Stanford (1998) and http://www-ssrl.slacstanford.edu/lcls/CDR.

[4] D. Windt, Appl. Phys. Lett. 74(1999)2890.

[5] E. Majkova et al., "Nanometer-scale period multilayers: thermal stability study", report at the 7th International Conference on the Physics of X-ray Multilayer Structures, Sapporo, Japan, 2004.

[6] P. Deschamps et al., J. Synchrotron Rad. 2(1995)124.

[7] Ch. Morawe et al., SPIE Proc. 4145(2000)61.

[8] G. Grübel et al., J. Phys. IV C9(1994)27.

[9] G. Grübel et al., Rev. Sci. Instrum. 67(1996)1.

[10] M. Mattenet, T. Schneider, and G. Grübel, J. Synchrotron Rad. 5(1998)651.

[11] Lin Zhang et al., J. Synchrotron Rad. 10(2003)313.

SUB-TERAWATT MODE OF OPERATION OF X-RAY SASE FEL

E.L. Saldin, E.A. Schneidmiller, and M.V. Yurkov
Deutsches Elektronen-Synchrotron (DESY), Hamburg, Germany

Abstract

Application of dispersion section in combination with undulator tapering is an effective tool for achieving extremely high output power of XFEL. In the first part of the undulator the gap is fixed, and amplification process is developed as in usual SASE FEL. When energy modulation of the electron beam becomes to be comparable with local energy spread, the electron bunch passes via dispersion section resulting in an effective compression of the electron bunch. Then bunched electron beam enters the second half of the undulator where the gap is tapered for effective extraction of the energy from the electron bunch. Our studies show that output radiation power can reach a sub-TW level in Angstrom wavelength range.

INTRODUCTION

Baseline design of present XFEL projects [1, 2, 3, 4] assumes only standard (SASE FEL) mode for production of radiation. Recent developments in the field of FEL physics and technology form a reliable basis for perspective extensions of the XFEL facilities. Relevant study for possible perspective developments of LCLS within next ten years since its commissioning has been presented in [5].

The first stage of the European XFEL facility assumes installation of five radiators, and three of them are SASE undulators. Present concept of an XFEL facility assumes to cover continuously wavelength range from 0.1 to 1.6 nm at a fixed energy of the electron beam. This is achieved with three undulators (SASE1-SASE3) [6]. A VUV option (SASE4) is under consideration, too [7]. Optimization of undulator parameters (see Table 1) has been performed for the electron beam parameters presented in the Supplement to TESLA XFEL Technical Design Report: peak current 5 kA, rms normalized emittance 1.4 mm-mrad, and initial energy spread of 1 MeV. All undulators are planar, variable-gap devices with an identical mechanical design. The first undulator, SASE1, is optimized for operation at the wavelength range 1-1.5 nm. Our study shows that such tunability range almost does not affect operation at the shortest wavelength of 0.1 nm. Operation of two other FELs (SASE2 and SASE3) is not so critical, and nominal tunability range is chosen to be by a factor of two (2-4 nm, and 8-16 nm, respectively). The length of the undulators is chosen such that continuous wavelength tunability can be provided by means of extra opening the undulator gaps, or by tuning to the frequency doubler mode of operation. It should be noted that wide wavelength tunability range of the proposed XFEL concept is not the only important feature. Changing of undulator gaps in different parts of SASE2 and SASE3 undulators allows one to tune the modes with high output power (sub-TW level), or for effective generation of the second harmonic (see Fig. 1). The latter feature might be important for future pump-probe experiments. Also, recently proposed attosecond SASE FEL scheme is foreseen for implementation [8, 9].

Table 1: Specification of undulators

	λ_r nm	λ_u mm	gap mm	B_w T	L_w m
SASE1	0.1-0.15	39	10-12	0.8-1	150
SASE2	0.1-0.4	47.9	10-19	0.6-1.3	150
SASE3	0.4-1.6	64.8	10-20	0.8-1.7	110
VUV	1.6-6.4	110	19-37	0.7-1.6	80

The developments discussed in this paper concern the increased FEL output radiation power.

STANDARD SASE MODE OF OPERATION

In this section we present main characteristics of XFEL source operating in a standard mode, i.e. conventional SASE mode. Figure 2 shows evolution of the averaged radiation power along undulator length. Saturation occurs at the undulator length of about 100 m. Figures 3 shows temporal and spectral structure of the radiation pulse at saturation. Increase of the undulator length results in moderate growth of the radiation power, but this happens mainly due to the growth of the sidebands. As a result, radiation spectrum spreads, and brilliance drops down.

HIGH-POWER MODE OF OPERATION

Application of dispersion section in combination with undulator tapering is an effective tool for achieving extremely high output power of XFEL and avoiding problems of sideband growth in the nonlinear regime. Tapering consists in slowly reducing the field strength of the undulator field to preserve the resonance wavelength as the kinetic energy of the electrons changes. Figure 1 shows a concept of a universal undulator allowing implementing different modes of XFEL operation: standard SASE, frequency doubler, and high power. The first stage is a conventional X-ray SASE FEL. The gain of the first stage is controlled in such a way that the maximum energy modulation of the electron beam at the FEL exit is about equal to the local

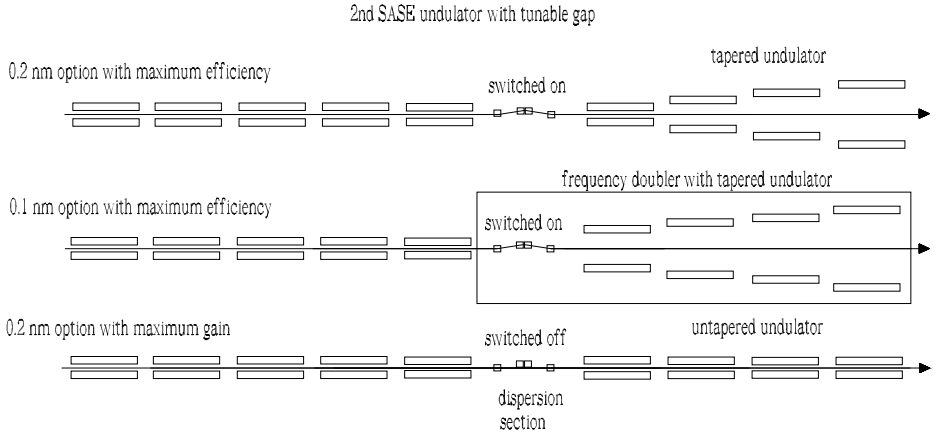

Figure 1: Three schemes for 2nd SASE undulator. Only one type of undulator magnet structure is needed. The radiation wavelength will be tuned by changing the gap. The total magnetic length is 150 m.

energy spread, but still far away from saturation. The left plot in Fig. 4 shows the phase space distribution of particles in a slice of the bunch. Such a picture is typical for every spike. The modulation amplitude is small, but there is visible energy modulation with an amplitude of about the value of the local energy spread. When the electron bunch passes through the dispersion section this energy modulation leads to effective compression of the particles as it is illustrated the right plot in Fig. 4. Then the bunched electron beam enters the tapered undulator, and from the very beginning produces strong radiation because of the large spatial bunching. Radiation field produces a ponderomotive well which is deep enough to trap the particles, since the original beam is relatively cold. The radiation produced by these captured particles increases the depth of the ponderomotive well, and they are effectively decelerated. As a result, much higher power can be achieved than for the case of a uniform undulator.

At the total undulator length of 150 m, the FEL output

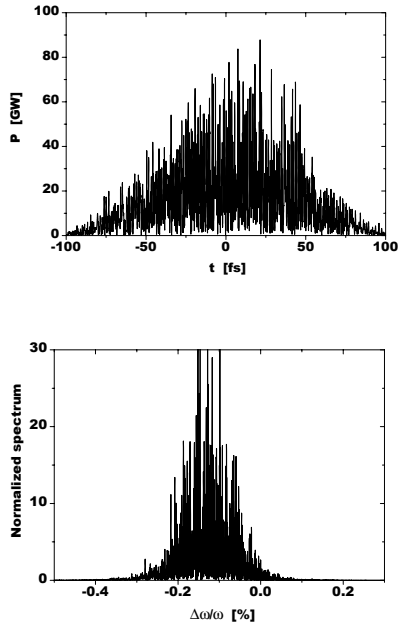

Figure 3: Temporal and spectral structure of the radiation pulse at saturation. Undulator length is 100 m. SASE FEL operates in a standard SASE mode.

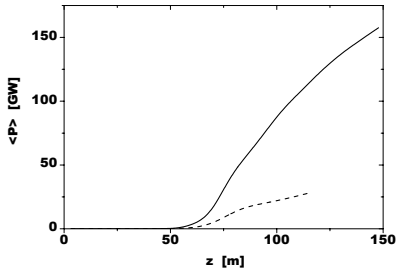

Figure 2: Average radiation power versus undulator length. Solid line: high power mode of operation. Dashed line: standard SASE mode. Radiation wavelength is 0.2 nm.

at 0.2 nm is enhanced by a factor of 8, from 20 GW to 150 GW (see Fig. 2). Figure 5 shows time structure of the radiation pulse at the undulator exit. It is seen that tapering procedure provides extremely high power of individual spikes, up to sub-TW level. Such features of the radiation may be useful for applications studying nonlinear processes. Figure 6 shows spectral structure of the radiation pulse. One can see that it does not contain a signature of

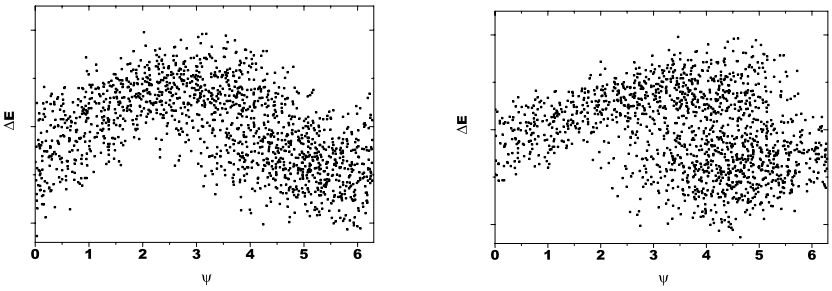

Figure 4: Phase space distribution of the particles in a slice before (left plot) and after (right plot) the dispersion section.

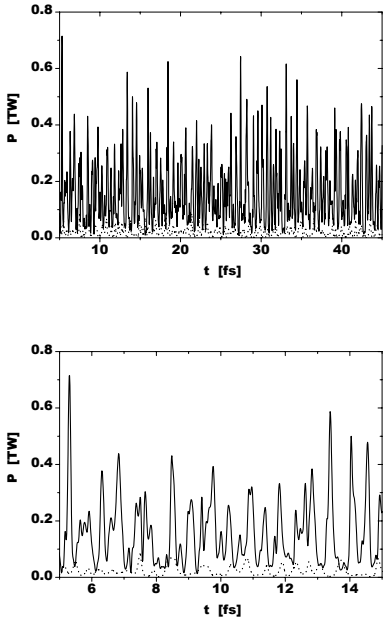

Figure 5: Temporal structure of the radiation pulse for SASE2 tuned for high power mode of operation. Lower plot shows enlarged view of the upper plot. Radiation wavelength is 0.2 nm, undulator length is 150 m. Dashed line shows power level of standard SASE FEL at saturation.

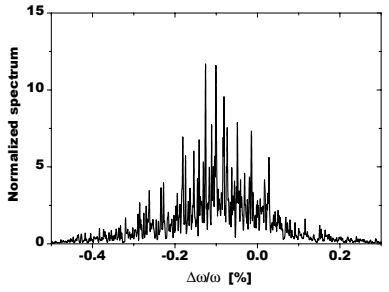

Figure 6: Spectral structure of the radiation pulse for SASE2 tuned for high power mode of operation. Radiation wavelength is 0.2 nm, undulator length is 150 m.

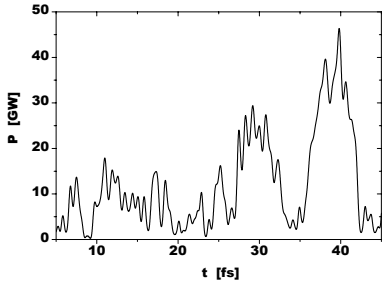

Figure 7: Temporal structure of the radiation pulse (see Fig. 5) reflected by thin Si (111) crystal. Central frequency corresponds to $\Delta\omega/\omega = -0.1\%$ (see Fig. 6). SASE2 tuned for high power mode of operation. Radiation wavelength is 0.2 nm, undulator length is 150 m.

sidebands, and the spectrum width does not differ from that of conventional SASE, while peak radiation power is much higher. The radiation filtered through a crystal (Si (111)) monochromator (see Fig: 7) has high peak power comparable with standard SASE level, but with much less spectrum width.

REFERENCES

[1] "Conceptual Design of 500 GeV e^+e^- Linear Collider with Integrated X-ray Facility" (Edited by R. Brinkmann et al.), DESY 1997-048, ECFA 1997-182, Hamburg, May 1987.

[2] TESLA Technical Design Report, DESY 2001-011, edited by F. Richard et al., and http://tesla.desy.de/.

[3] P. Audebert et al., "TESLA XFEL: First stage of the X-ray laser laboratory – Technical design report (R. Brinkmann et al., Eds.)", Preprint DESY 2002-167.

[4] The LCLS Design Study Group, LCLS Design Study Report, SLAC reports SLAC- R521, Stanford (1998) and http://www-ssrl.slacstanford.edu/lcls/CDR.

[5] M. Cornacchia et al., SLAC-PUB-10133, December, 2003.

[6] E.L. Saldin, E.A. Schneidmiller and M.V. Yurkov, DESY Print TESLA FEL 2004-02.

[7] E.L. Saldin, E.A. Schneidmiller and M.V. Yurkov, DESY Print TESLA FEL 2004-04.

[8] E.L. Saldin, E.A. Schneidmiller and M.V. Yurkov, Opt. Commun. 237(2004)153.

[9] E.L. Saldin, E.A. Schneidmiller and M.V. Yurkov, Opt. Commun. 239(2004)161.

[10] J. Feldhaus et al., Preprint DESY 03-092, 2003. Nucl. Instrum. and Methods A, in press.

DESIGN FORMULAS FOR VUV AND X-RAY FELS

E.L. Saldin, E.A. Schneidmiller, M.V. Yurkov
Deutsches Elektronen-Synchrotron (DESY), Hamburg, Germany

Abstract

Simple formulas for optimization of VUV and X-ray SASE FELs are presented. The FEL gain length and the optimal beta-function are explicitly expressed in terms of the electron beam and undulator parameters. The FEL saturation length is estimated taking into account energy diffusion due to quantum fluctuations of the undulator radiation. Examples of the FEL optimization are given. Parameters of a SASE FEL, operating at the Compton wavelength, are suggested.

INTRODUCTION

At the first stage of a SASE FEL (self-amplified spontaneous emission) [1] design one looks for the dependence of the FEL saturation length on the wavelength, electron beam parameters, undulator parameters, and beta-function. Usually the parameters are optimized for the shortest design wavelength since the saturation length is the largest in this case. The saturation length is proportional to the gain length (e-folding length) of the fundamental transverse mode (see [2] for more details). The gain length can be found by the solution of the FEL eigenvalue equation.

The eigenvalue equation for a high-gain FEL, including diffraction of radiation, emittance, and energy spread, was derived in [3, 4]. There exist approximate solutions [5, 6] of this equation. The exact solution was presented in [7] as well as an approximate solution (with a limited validity range). The latter solution was fitted [7] using 3 dimensionless groups of parameters, and 19 fitting coefficients. An approximate solution, that fits the exact solution in the entire parameter space with high accuracy (better that 1 %), was presented in [8]. A numerical algorithm for finding this approximate solution is very fast and robust. It was used to obtain the main results of this paper.

In this paper we present the fitting formula for the FEL gain length written down explicitly in terms of the beam and undulator parameters. This formula is not universal, but it provides a good accuracy (better than 5 %) in a typical parameter range of VUV and X-ray FELs. We present the formula without derivation since it was not derived analytically. In some sense the parametric dependencies were guessed, and then the fitting coefficients were found from the solution of the eigenvalue equation. For instance, we used only 2 fitting coefficients for the gain length with the optimized beta-function. The formulas of this paper allow one to quickly estimate FEL saturation length, including the effect of energy diffusion in the undulator due to quantum fluctuations of the undulator radiation. In addition, we present two practical examples of using our design formulas: optimization of SASE FEL with negligible energy spread, and the limitation on SASE FEL wavelength taking into account quantum diffusion. In particular, we suggest for the first time the set of parameters for a SASE FEL operating at the Compton wavelength.

GAIN LENGTH FOR THE OPTIMIZED BETA-FUNCTION

Let us consider an axisymmetric electron beam with a current I, and a Gaussian distribution in transverse phase space and in energy [7, 8]. The focusing structure in the undulator is a superposition of the natural undulator focusing and an external alternating-gradient focusing. The eigenvalue equation [7, 8] is valid under the condition [8]:

$$\frac{L_{\rm f}}{2\pi\beta} \ll \min\left(1,\, \frac{\lambda_r}{2\pi\epsilon}\right)$$

where $L_{\rm f}$ is the period of the external focusing structure, β is an average beta-function, ϵ is the rms emittance of the electron beam, and λ_r is the FEL resonant wavelength. The resonance condition is written as:

$$\lambda_r = \frac{\lambda_{\rm w}(1+K^2)}{2\gamma^2}\,. \qquad (1)$$

Here $\lambda_{\rm w}$ is the undulator period, γ is relativistic factor, and K is the rms undulator parameter:

$$K = 0.934\;\lambda_{\rm w}[{\rm cm}]\;B_{\rm rms}[{\rm T}]\,, \qquad (2)$$

$B_{\rm rms}$ being the rms undulator field.

In what follows we assume that the beta-function is optimized so that the FEL gain length takes the minimal value for given wavelength, beam and undulator parameters. Under this condition the solution of the eigenvalue equation for the *field* gain length can be approximated as follows:

$$L_g \simeq L_{g0}\,(1+\delta)\,, \qquad (3)$$

where

$$L_{g0} = 1.67\left(\frac{I_A}{I}\right)^{1/2}\frac{(\epsilon_n\lambda_{\rm w})^{5/6}}{\lambda_r^{2/3}}\;\frac{(1+K^2)^{1/3}}{KA_{JJ}}\,, \qquad (4)$$

and

$$\delta = 131\;\frac{I_A}{I}\;\frac{\epsilon_n^{5/4}}{\lambda_r^{1/8}\lambda_{\rm w}^{9/8}}\;\frac{\sigma_\gamma^2}{(KA_{JJ})^2(1+K^2)^{1/8}}\,. \qquad (5)$$

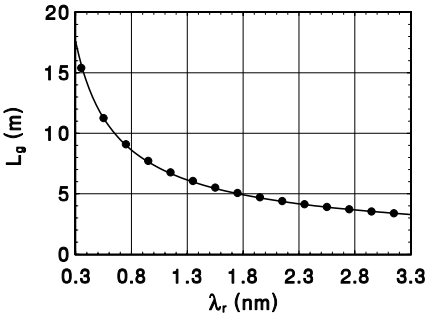

Figure 1: Gain length versus resonant wavelength for the following set of parameters: $\lambda_{\rm w} = 3$ cm, $K = 1$, $I = 2.5$ kA, $\epsilon_n = 2$ μm, $\sigma_\varepsilon = 1$ MeV. Undulator is planar, resonance is maintained by tuning electron beam energy, beta-function is optimized for each case. Line is the solution of the eigenvalue equation [8], and the circles are calculated using formula (3).

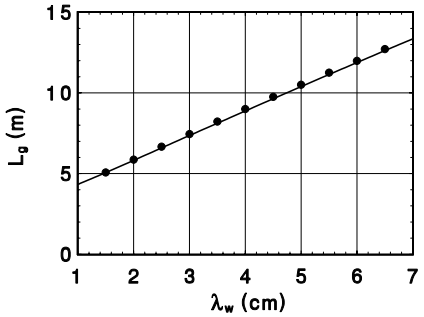

Figure 2: Gain length versus undulator period for the following set of parameters: $\lambda_r = 1$ nm, $K = 1$, $I = 2.5$ kA, $\epsilon_n = 2$ μm, $\sigma_\varepsilon = 1$ MeV. Undulator is planar, resonance is maintained by tuning electron beam energy, beta-function is optimized for each case. Line is the solution of the eigenvalue equation [8], and the circles are calculated using formula (3).

The following notations are introduced here: $I_A = 17$ kA is the Alfven current, $\epsilon_n = \gamma\epsilon$ is the rms normalized emittance, $\sigma_\gamma = \sigma_\varepsilon/mc^2$ is the rms energy spread (in units of the rest energy), $A_{JJ} = 1$ for a helical undulator and $A_{JJ} = J_0(K^2/2(1+K^2)) - J_1(K^2/2(1+K^2))$ for a planar undulator, J_0 and J_1 are the Bessel functions of the first kind.

The formula (3) provides an accuracy better than 5 % in the domain of parameters defined as follows

$$1 < \frac{2\pi\epsilon}{\lambda_r} < 5 \qquad (6)$$

$$\delta < 2.5 \left\{ 1 - \exp\left[-\frac{1}{2} \left(\frac{2\pi\epsilon}{\lambda_r} \right)^2 \right] \right\} \qquad (7)$$

Note that the condition (6) is usually satisfied in realistic designs of VUV and X-ray FELs when one does optimization for the shortest wavelength (defining the total undulator length). The condition (7) is practically not a limitation. To illustrate the accuracy of the formula (3) we present a numerical example. The following nominal operating point is chosen: $\lambda_r = 1$ nm, $\lambda_{\rm w} = 3$ cm, $K = 1$, $I = 2.5$ kA, $\epsilon_n = 2$ μm, $\sigma_\varepsilon = 1$ MeV, energy is 2.8 GeV, undulator is planar. We scan over different parameters and compare the gain length calculated with formula (3) and by solving the eigenvalue equation [8]. The results are presented in Figs. 1-6. We have carefully checked the accuracy of formula (3) for different combinations of dimensional parameters entering (4) and (5). The deviation of the approximate formula (3) from the solution of the eigenvalue equation [8] is indeed defined only by the parameters $2\pi\epsilon/\lambda_r$ and δ, and is within 5 % in the above specified domain.

We also present here an approximate expression for the optimal beta-function (an accuracy is about 10 % in the above mentioned parameter range):

$$\beta_{\rm opt} \simeq 11.2 \left(\frac{I_A}{I} \right)^{1/2} \frac{\epsilon_n^{3/2} \lambda_{\rm w}^{1/2}}{\lambda_r K A_{JJ}} \, (1 + 8\delta)^{-1/3} \qquad (8)$$

Note that dependence of the gain length on beta-function is rather weak when $\beta > \beta_{\rm opt}$.

Finally, let us note that the saturation length cannot be directly found from the eigenvalue equation. However, with an accuracy 10-20 % one can accept the following estimate:

$$L_{\rm sat} \simeq 10 \, L_g \qquad (9)$$

EFFECT OF QUANTUM DIFFUSION IN AN UNDULATOR

Energy spread growth due to the quantum fluctuations of the spontaneous undulator radiation can be an important effect [1, 10] in future SASE FELs. The rate of the energy diffusion is given by [11]:

$$\frac{d\sigma_\gamma^2}{dz} = \frac{14}{15} \lambda\!\!\!^{-}_{\rm c} r_{\rm e} \gamma^4 \kappa_{\rm w}^3 K^2 F(K) \, , \qquad (10)$$

where $\lambda\!\!\!^{-}_{\rm c} = 3.86 \times 10^{-11}$ cm, $r_{\rm e} = 2.82 \times 10^{-13}$ cm, $\kappa_{\rm w} = 2\pi/\lambda_{\rm w}$, and

$$F(K) = 1.42K + (1 + 1.50K + 0.95K^2)^{-1} \quad \text{for helical undulator}$$

$$F(K) = 1.70K + (1 + 1.88K + 0.80K^2)^{-1} \quad \text{for planar undulator} \qquad (11)$$

To estimate the FEL saturation length, we accept the following scheme. First, we neglect energy diffusion and find a zeroth order approximation to the saturation length from

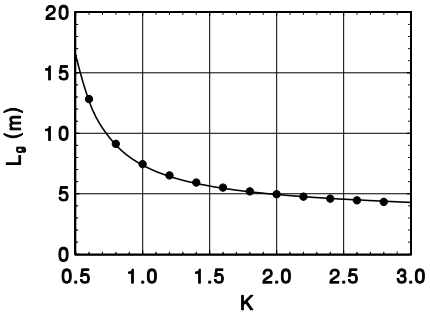

Figure 3: Gain length versus undulator parameter K for the following set of parameters: $\lambda_r = 1$ nm, $\lambda_{\rm w} = 3$ cm, $I = 2.5$ kA, $\epsilon_n = 2$ μm, $\sigma_\varepsilon = 1$ MeV. Undulator is planar, resonance is maintained by tuning electron beam energy, beta-function is optimized for each case. Line is the solution of the eigenvalue equation [8], and the circles are calculated using formula (3).

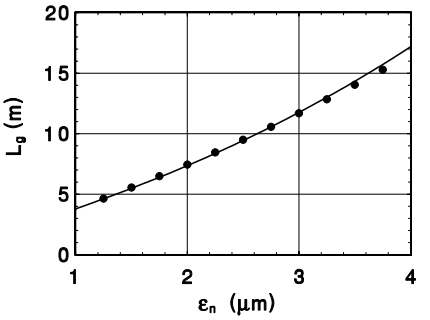

Figure 4: Gain length versus normalized emittance for the following set of parameters: $\lambda_r = 1$ nm, $\lambda_{\rm w} = 3$ cm, $K = 1$, $I = 2.5$ kA, $\sigma_\varepsilon = 1$ MeV. Undulator is planar, beta-function is optimized for each case. Line is the solution of the eigenvalue equation [8], and the circles are calculated using formula (3).

(9), (3)-(5). Then we calculate an induced energy spread in the middle of the undulator from (10), add it quadratically to the initial energy spread, and find a new expression for δ. Then, using (9), (3)-(5), we find the first approximation to the saturation length. Then we do the next iteration, etc. The saturation length is then proportional to a series $\sum_{n=0}^{\infty} \delta_q^n$ and is given by

$$L_{\rm sat} \simeq 10\, L_{g0}\, \frac{1+\delta}{1-\delta_q}\,, \qquad (12)$$

where

$$\delta_q = 5.5\times 10^4 \left(\frac{I_A}{I}\right)^{3/2} \frac{\lambda\!\!\!^{-}_c r_{\rm e}\epsilon_n^2}{\lambda_r^{11/4}\lambda_{\rm w}^{5/4}}\, \frac{(1+K^2)^{9/4}F(K)}{KA_{JJ}^3} \qquad (13)$$

Note that in the latter formula the powers are somewhat simplified. Comparing Eqs. (9) and (12), we can introduce an effective parameter

$$\delta_{\rm eff} = \frac{\delta+\delta_q}{1-\delta_q}\,, \qquad (14)$$

which should be used instead of δ in (7) to check the applicability range and in (8) to estimate the optimal beta-function.

Although formula (12) is rather crude estimate, it can be used for quick orientation in the parameter space with *a posteriori* check using a numerical simulation code.

OPTIMIZED FEL WITH A NEGLIGIBLE ENERGY SPREAD

Formulas, presented in the previous Sections, can be used for the optimization of undulator parameters as soon as a specific type of the undulator is chosen. We demonstrate such a possibility with the planar NdFeB undulator of which magnetic field can be described by the following formula [9]:

$$B_{\rm max}[{\rm T}] = 3.694\, \exp\left[-5.068\frac{g}{\lambda_{\rm w}} + 1.52\left(\frac{g}{\lambda_{\rm w}}\right)^2\right] \quad \text{for} \quad 0.1 < g/\lambda_{\rm w} < 1 \qquad (15)$$

where g is the undulator gap. The rms value of the parameter K is given by Eq. (2) with $B_{\rm rms} = B_{\rm max}/\sqrt{2}$.

We assume that the energy spread effect on the FEL operation can be neglected ($\delta\ ,\ \delta_q \to 0$). Then, using (3), (2) and (15), we minimize the gain length for a given undulator gap. The optimal undulator period is independent of λ_r, I and ϵ_n and is found to be

$$(\lambda_{\rm w})_{\rm opt}[{\rm cm}] \simeq 1 + 2\,g\,[{\rm cm}] \qquad \text{for} \quad g > 0.5\ {\rm cm} \qquad (16)$$

The optimal value of K is then defined from (15) and (2), the electron beam energy - from (1), and the optimal beta-function - from (8). The minimal gain length can be expressed (in practical units) as follows:

$$(L_g)_{\rm min}[{\rm m}] \simeq 20\, \frac{\epsilon_n^{5/6}[\mu{\rm m}]\, g^{1/2}[{\rm cm}]}{I^{1/2}[{\rm kA}]\, \lambda_r^{2/3}[{\rm \AA}]} \qquad (17)$$

Using estimate of the saturation length (9), we find the minimal wavelength at which SASE FEL can saturate within the given undulator length $L_{\rm w}$:

$$(\lambda_r)_{\rm min}[{\rm \AA}] \simeq 3\times 10^3\, \frac{\epsilon_n^{5/4}[\mu{\rm m}]\, g^{3/4}[{\rm cm}]}{I^{3/4}[{\rm kA}]\, L_{\rm w}^{3/2}[{\rm m}]} \qquad (18)$$

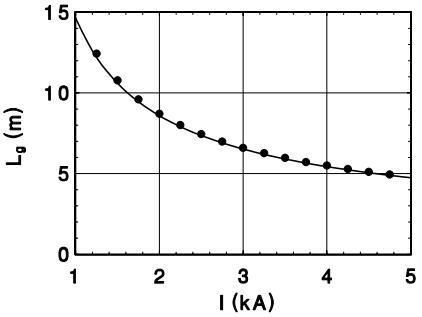

Figure 5: Gain length versus current for the following set of parameters: $\lambda_r = 1$ nm, $\lambda_w = 3$ cm, $K = 1$, $\epsilon_n = 2$ μm, $\sigma_\varepsilon = 1$ MeV. Undulator is planar, beta-function is optimized for each case. Line is the solution of the eigenvalue equation [8], and the circles are calculated using formula (3).

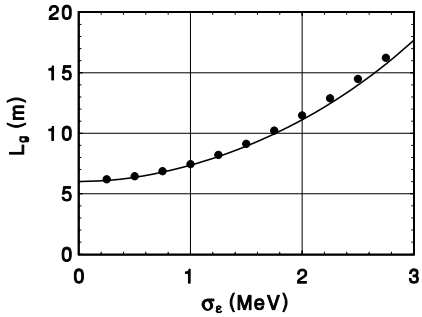

Figure 6: Gain length versus energy spread for the following set of parameters: $\lambda_r = 1$ nm, $\lambda_w = 3$ cm, $K = 1$, $I = 2.5$ kA, $\epsilon_n = 2$ μm. Undulator is planar, beta-function is optimized for each case. Line is the solution of the eigenvalue equation [8], and the circles are calculated using formula (3).

SASE FEL AT THE COMPTON WAVELENGTH

Another example is the optimization of sub-Angstrom FELs for which the effect of quantum diffusion in the undulator can play an important role. We consider the case when the energy spread is dominated by the quantum diffusion, and neglect initial energy spread ($\delta \to 0$). Optimizing undulator period and parameter K in (12), we get the following estimate for the minimal wavelength[1]:

$$(\lambda_r)^{\rm q}_{\rm min}[\text{Å}] \simeq \frac{4\,\epsilon_n[\mu\text{m}]}{I^{3/5}[\text{kA}]\,L_{\rm w}^{2/5}[\text{m}]} \qquad (19)$$

Note that in some cases the optimal undulator parameters can be impractical. In any case, the estimate (19) gives a lower limit. The following numerical examples show that one can be close to this limit with technically feasible undulator parameters.

Let us consider the electron beam parameters (peak current and emittance) assumed in [12]. One of the examples, considered in [12], is a SASE FEL operating at $\lambda_r = 0.28$ Å with $I = 5$ kA and $\epsilon_n = 0.3\,\mu$m. Another example is even more ambitious: $\lambda_r = 0.12$ Å with $I = 5$ kA and $\epsilon_n = 0.1\,\mu$m.

We try to push the wavelength closer to the extreme given by Eq. (19). In our first example we assume $I = 5$ kA and $\epsilon_n = 0.3\,\mu$m. With these parameters the wavelength $\lambda_r = 0.1$ Å can be reached at the electron beam energy 23 GeV in a planar undulator with $\lambda_w = 2$ cm and $K = 1$ (with the gap $g = 0.7$ cm according to (15) and (2)). The optimal beta-function is about 40 m, and the saturation length is estimated at 160 m.

The second example is a SASE FEL operating at the Compton wavelength, $\lambda_r = \lambda_c = 0.0234$ Å (photon energy is 0.5 MeV). We assume the electron beam with $I = 5$ kA and $\epsilon_n = 0.1\,\mu$m, the energy is 40 GeV. We choose a helical undulator with $\lambda_w = 2$ cm and $K = 0.7$. The optimal beta-function is about 35 m, and the saturation is reached within 200 m. Our estimates show that quantum effects, other than energy diffusion, give small corrections to the classical description and can be neglected.

[1] One can notice the difference with more crude estimate presented in [10]

REFERENCES

[1] Ya.S. Derbenev, A.M. Kondratenko and E.L. Saldin, Nucl. Instrum. and Methods **193**(1982)415

[2] E.L. Saldin, E.A. Schneidmiller and M.V. Yurkov, "The Physics of Free Electron Lasers", Springer, Berlin, 1999

[3] K.J. Kim, Phys. Rev. Lett. **57**(1986)1871

[4] L.H. Yu and S. Krinsky, Physics Lett. **A129**(1988)463

[5] L.H. Yu, S. Krinsky and R.L. Gluckstern, Phys. Rev. Lett. **64**(1990)3011

[6] Y.H. Chin, K.J. Kim and M. Xie, Nucl. Instrum. and Methods **A318**(1992)481

[7] M. Xie, Nucl. Instrum. and Methods **A 445**(2000)59

[8] E.L. Saldin, E.A. Schneidmiller and M.V. Yurkov, Nucl. Instrum. and Methods **A 475**(2001)86

[9] TESLA Technical Design Report, DESY 2001-011 (2001); TESLA XFEL, Supplement, DESY 2002-167 (2002)

[10] J. Rossbach et al., Nucl. Instrum. and Methods **A 374**(1996)401

[11] E.L. Saldin, E.A. Schneidmiller and M.V. Yurkov, Nucl. Instrum. and Methods **A 393**(1997)152

[12] M. Cornacchia et al., SLAC-PUB-10133 (2003)

THE FREE ELECTRON LASER KLYSTRON AMPLIFIER CONCEPT

E.L. Saldin, E.A. Schneidmiller, and M.V. Yurkov
Deutsches Elektronen-Synchrotron (DESY), Hamburg, Germany

Abstract

We consider optical klystron with a high gain per cascade pass. In order to achieve high gain at short wavelengths, conventional FEL amplifiers require electron beam peak current of a few kA. This is achieved by applying longitudinal compression using a magnetic chicane. In the case of klystron things are quite different and gain of klystron does not depend on the bunch compression in the injector linac. A distinguishing feature of the klystron amplifier is that maximum of gain per cascade pass at high beam peak current is the same as at low beam peak current without compression. Second important feature of the klystron configuration is that there are no requirements on the alignment of the cascade undulators and dispersion sections. This is related to the fact that the cascades, in our (high gain) case, do not need the radiation phase matching. There are applications, like XFELs, where unique properties of high gain klystron FEL amplifier are very desirable. Such a scheme allows one to decrease the total length of magnetic system. On the other hand, the saturation efficiency of the klystron is the same as that of conventional XFEL.

INTRODUCTION

High gain FEL amplifiers are of interest for a variety of potential applications that range from X-ray lasers [1, 2] to ultraviolet MW-scale industrial lasers [3]. There are various versions of the high gain FEL amplifier. A number of high gain FEL amplifier concepts may prove useful for XFEL applications. Two especially noteworthy ones are the FEL amplifier with a single uniform undulator [1, 2] and the distributed optical klystron [4, 5, 6, 7]. The high gain cascade klystron amplifier described in this paper is an attractive alternative to other configurations for operation in the X-ray wavelength range (see Fig. 1).

Electron bunches with very small transverse emittance and high peak current are needed for the operation of conventional XFELs. This is achieved using a two-step strategy: first generate beams with small transverse emittance using an RF photocathode and, second, apply longitudinal compression at high energy using a magnetic chicane. Although simple in first-order theory, the physics of bunch compression becomes very challenging if collective effects like space charge forces and coherent synchrotron radiation forces (CSR) are taken into account. Self-fields of bunches as short as 10-100 μm have never been measured and are challenging to predict.

The situation is quite different for klystron amplifier scheme described in our paper. A distinguishing feature of the klystron amplifier is the absence of apparent limitations which would prevent operation without bunch compression in the injector linac. As we will see, the gain per cascade pass is proportional to the peak current and inversely proportional to the energy spread of the beam. Since the bunch length and energy spread are related to each other through Liouville's theorem, the peak current and energy spread cannot vary independently of each other in the injector linac. To extent that local energy spead is proportional to the peak current, which is usually the case for bunch compression, the gain will be independent of the actual peak current. We see, therefore, that klystron gain in linear regime depends only on the actual photoinjector parameters. This incipient proportionality between gain and I_0/σ_γ (I_0 is a current and σ_γ is a local energy spread in units of the rest electron energy) is a temptation, in designing an XFEL, to go to very high values of I_0/σ_γ and very long values of bunch length. Starting with this safe scenario, one may gradually increase compression factor getting shorter FEL pulses with higher peak power (brilliance). Note that the average power (brilliance) is almost independent of the compression factor. It is also worth mentioning that there is a possibility [8] to get short (10 fs) radiation pulses for the pump-probe experiments, having long (10 ps) electron bunches. To illustrate further possible advantages of the klystron amplifier, we describe a multi-user facility having a ring geometry, and thus being similar to the 3rd generation synchrotron radiation facilities.

THE GAIN OF A KLYSTRON AMPLIFIER

A detailed theoretical analysis of a klystron amplifier with a high gain per cascade can be found in [8]. Here we present some results of that analysis.

The principle of klystron operation is simple and is very similar to that of a multi-resonator microwave klystron. A modulated electron beam radiates in a first undulator, and the radiation modulates the beam in energy. Then the beam passes a dispersion section where the energy modulation is converted into the density modulation which is much higher than the original one. In the second undulator the beam with the enhanced density modulation radiates pro-

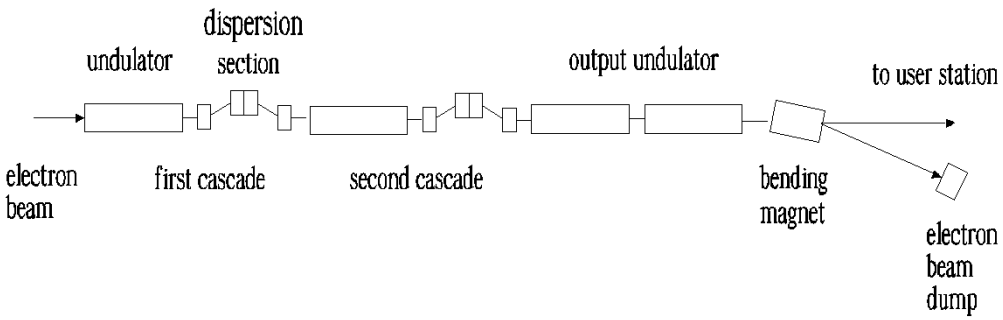

Figure 1: Schematic diagram of high gain cascade klystron amplifier

ducing much higher energy modulation etc. The process can continue in several cascades up to saturation in the last (output) undulator. Since the gain per cascade is high, the phase matching (on the scale of the radiation wavelength) between the beam and the radiation is obviously not required. An initial signal for such a device in VUV and X-ray spectral range is the shot noise in electron beam.

We present here the expressions for a gain per cascade for two different regimes of the klystron amplifier operation. In the first case the geometrical emittance of the electron beam ϵ is small as compared to $\lambda/(2\pi)$, where λ is the resonant wavelength. In this case the beta-function in the undulators can be chosen in such a way that the diffraction parameter, $2\pi\sigma^2/(\lambda L_{\rm w})$, is small (here σ is transverse size of the beam and $L_{\rm w}$ is the length of an undulator segment). At the same time the effect of velocity spread due to emittance on FEL operation can be neglected. After optimization of the strength of the dispersion section one gets the amplitude gain per cascade [8]:

$$G_0 \simeq 4\frac{A_{\rm JJ}^2 K^2}{(1+K^2)}\frac{N_{\rm w} I_0}{\sigma_\gamma I_{\rm A}}\,, \qquad (1)$$

where K is the rms undulator parameter, $N_{\rm w}$ is the number of undulator periods per an undulator, $I_{\rm A} = 17$ kA is the Alfven current, $A_{\rm JJ} = 1$ for a helical undulator and

$$A_{\rm JJ} = [J_0(Q) - J_1(Q)]$$

for a planar undulator. Here $Q = K^2/(2+2K^2)$ and $J_n(Q)$ is a Bessel function of nth order.

In the opposite limit, $2\pi\epsilon/\lambda \gg 1$, after optimizing beta-function and the strength of dispersion section one gets:

$$G_0 \simeq 2\frac{A_{\rm JJ}^2 K^2}{(1+K^2)}\frac{N_{\rm w} I_0}{\sigma_\gamma I_{\rm A}}\left(\frac{\lambda}{2\pi\epsilon}\right)^2\,. \qquad (2)$$

In the latter case the diffraction parameter is big, and the velocity spread due to emittance should be carefully taken into account. Note that in contrast with a conventional SASE, the effects of emittance and energy spread on longitudinal dynamics are separated in a klystron amplifier: emittance (energy spread) is important in undulators (dispersion sections). The noticeable feature of the results (1) and (2) is that the gain depends on the ratio I_0/σ_γ and is, therefore, independent of compression factor in the beam formation system. It is also interesting to note that in the case of a small emittance the gain is defined by the longitudinal brightness of the electron beam, while for a large emittance - by total brightness (particles density in 6-D phase space).

Let us present an example for the case when the emittance is below diffraction limit and the undulator is planar. With the numerical values $\lambda_{\rm w} = 3$ cm, $K = 1$, $\gamma = 10^3$, the resonance value of wavelength is $\lambda = 30$ nm. If the number of the undulator period is $N_{\rm w} = 100$, normalized transverse emittance $\epsilon_{\rm n} = 2\mu$m, and betatron function is equal to the undulator length, the diffraction parameter is about 0.4. For a peak current of 100 A and a local energy spread of 5 keV, appropriate substitution in (1) shows that the gain per cascade pass is about $G_0 \simeq 10^2$ (or, intensity gain $G_0^2 \simeq 10^4$). In order to reach saturation in a klystron amplifier, starting up from the shot noise, the total intensity gain should be of the order $N_\lambda N_{\rm w}$ [8], where N_λ is the number of electrons per radiation wavelength. Thus, for the considered set of parameters, one needs two cascades of amplification and the output undulator as shown in Fig. 1.

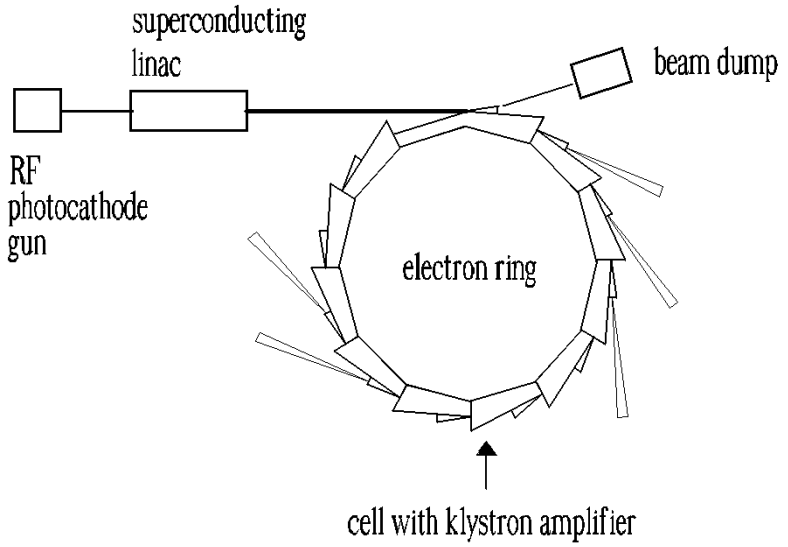

Figure 2: Diagram of a possible fourth-generation synchrotron facility using free-electron laser klystron amplifiers

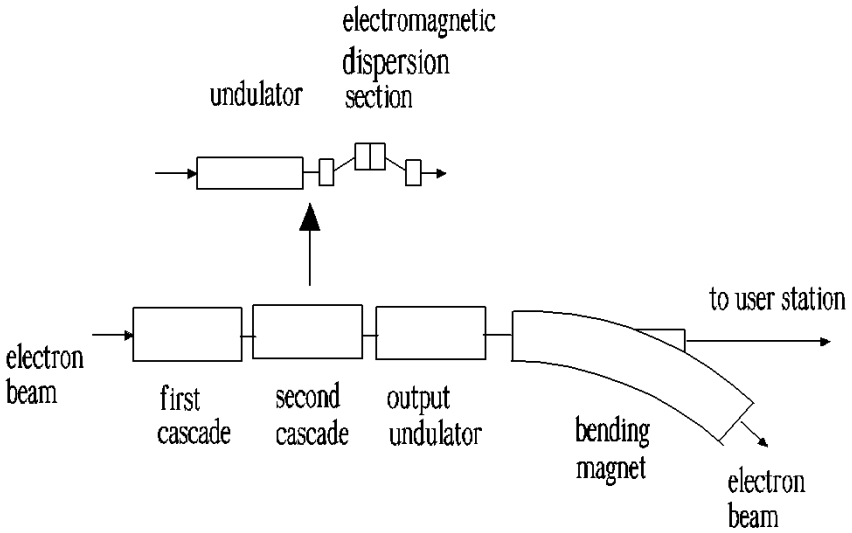

Figure 3: Electron ring cell design. Using a klystron electromagnetic dispersion section as a switching element it is possible to quickly switch off (on) the cell klystron amplifier thus providing multi-user capability. This design makes it possible to make various wavelengths available in the XFEL laboratory quasi-simultaneously

MULTI-USER DISTRIBUTION SYSTEM FOR XFEL LABORATORY

An X-ray laboratory should serve several, may be up to ten experimental stations which can be operated independently according to the needs of the user community. On the other hand, the multi-user distribution system has to satisfy an additional requirement. Passing the electron bunch through the bending magnets must avoid emittance dilution due to coherent synchrotron radiation (CSR) effects. For very short bunches and very high peak current, CSR can generate energy spread in the bending magnets and thus dilute the horizontal emittance. As a result, the preferred layout of a conventional SASE FEL is a linear arrangement in which the injector , accelerator, bunch compressors and undulators are nearly collinear, and in which the electron beam does not change direction between accelerator and undulators.

The situation is quite different for the klystron amplifier scheme proposed in our paper. Since it operates without bunch compression in the injector linac, the problem of emittance dilution in the bending magnets does not exist. An electron beam distribution system based on uncompressed electron beam can provide efficient ways to generate a multi-user facility - very similar to present day synchrotron radiation facilities. A possible layout of a soft X-ray FEL laboratory based on an electron ring distribution system is shown in Fig. 2. The layout of the laboratory follows a similar approach as that used for synchrotron light sources. The FEL user facility consists of an injector linac and electron beam distribution system. The injector is composed of a RF gun with photocathode and a main (superconducting) linac. In order to make efficient use of the new source it is proposed to segment the full circumference of a distribution system into arcs which are repeated a number of times to form a complete ring. Each cell includes a two-cascade klystron and a bending magnet. A specific realization of the electron ring cell is sketched in Fig. 3. The electron beam transport line guiding electrons from the injector linac to the experimental hall is connected tangentially to one of the straight sections of the electron ring. In order to obtain a useful separation between the experimental areas behind the photon beam lines, an angle of 36 degrees between two neighboring lines would be desirable. Thus, ten beam lines can be installed on a complete electron ring. Using klystron (electromagnetic) dispersion sections in each cell as switching elements it is possible to quickly switch the FEL photon beam from one experiment to the other, thus providing multi-user capability. Users can define the radiation wavelength for their experiment independently of each other to a very large extent, since they use different undulators. Injector linac and electron beam transport lines operate at fixed parameters. At a fixed electron energy the magnet gap of the klystron undulators can be varied mechanically for wavelength tuning. This design makes it possible to make various wavelengths available in the XFEL laboratory quasi-simultaneously. It is a great advantage that injector and electron beam transport lines in the new scheme of multi-user facility operate at fixed parameters and that an "electron switchyard" is not required.

When a relativistic electron beam passes through the undulator, it emits incoherent radiation. This process leads to an increase of the energy spread in the beam due to quantum fluctuations of the undulator radiation. This effect grows significantly with an increase in electron beam energy, strength field and length of the undulator. This effect should be carefully taken into account when designing multi-user distribution system. The expression for the rate of energy diffusion can be found in [9]. The next numerical example illustrates the amplitude of the effect. If $\gamma = 10^3$, $K = 1$, $\lambda_{\rm w} = 3$ cm, and the total length of the undulator system is equal to 100 m, then the energy spread increase due to quantum fluctuations is about 1 keV at the end of the 10th klystron amplifier, and has a negligible effect on the klystron performance.

CONCLUSION

The high-gain klystron amplifier described in this paper is an attractive alternative to other FEL configurations for operation in short wavelength range. A distinguishing feature of the klystron amplifier, operating in the VUV and soft X-ray range, is the absence of apparent limitations which would prevent operation without bunch compression in the injector linac. The scheme can also be adapted for generation of hard X-ray radiation. In this case one should take into account quantum diffusion in the undulator. A consequence would be that some moderate compression would be needed (which could still be more safe than the agressive compression required for conventional SASE FELs [1, 2]).

REFERENCES

[1] TESLA Technical Design Report, DESY 2001-011, edited by Richard et al., and http://tesla.desy.de

[2] The LCLS Design Study Group, LCLS Design Study Report, SLAC reports SLAC-R521, Stanford (1998) and http:www-ssrl.slacstanford.edu/lcls/CDR

[3] C. Pagani et al., Nucl. Instrum. Methods A 455(2000)733

[4] J.C. Gallardo, C. Pellegrini, Nucl. Instrum. Methods A 296(1990)448

[5] V.N. Litvinenko, Nucl. Instrum. Methods A 304(1991)463

[6] V.A. Bazylev, M.M. Pitatelev, Nucl. Instrum. Methods A 358(1995)64

[7] G.R. Neil, H.P. Freund, Nucl. Instrum. Methods A 475(2001)381

[8] E.L. Saldin, E.A. Scheidmiller, M.V. Yurkov, "The Free Electron Laser Klystron Amplifier Concept", preprint DESY 03-108, August 2003

[9] E.L. Saldin, E.A. Scheidmiller, M.V. Yurkov, Nucl. Instrum. Methods A 381(1996)545

THE POTENTIAL FOR EXTENDING THE SPECTRAL RANGE ACCESSIBLE TO THE EUROPEAN X-RAY FREE ELECTRON LASER IN THE DIRECTION OF LONGER WAVELENGTHS

E.L. Saldin, E.A. Schneidmiller, and M.V. Yurkov
Deutsches Elektronen-Synchrotron (DESY), Hamburg, Germany

Abstract

The baseline specifications of European XFEL give a range of wavelengths between 0.1 nm and 2 nm. This wavelength range at fixed electron beam energy 17.5 GeV can be covered by operating the SASE FEL with three undulators which have different period and tunable gap. A study of the potential for the extending the spectral range accessible to the XFEL in the direction of longer wavelengths is presented. The extension of the wavelength range to 6 nm would be cover the water window in the VUV region, opening the facility to a new class of experiments. There are at least two possible sources of VUV radiation associated with the X-ray FEL; the "low (2.5 GeV) energy electron beam dedicated" and the " 17.5 GeV spent beam parasitic" (or "after-burner") source modes. The second alternative, "after-burner undulator" is the one we regard as most favorable. It is possible to place an undulator as long as 80 meters after 2 nm undulator. Ultimately, VUV undulator would be able to deliver output power approaching 100 GW. A beam from this device could be run in pump-probe mode with X-ray FEL.

INTRODUCTION

Baseline design of present European XFEL project [1] assumed only standard (SASE FEL) mode for production of radiation. Recent developments in the field of FEL physics and technology form a reliable basis for perspective extensions of the XFEL facility. In [2] we proposed a concept of XFEL laboratory which will allow to implement perspective features from the very beginning of operation. These extra features include delivery of X-ray pulses in the attosecond regime, increasing of the FEL power (up to sub-TW level), simultaneous multi-undulator capability. The further development discussed in this paper concerns the expanded photon energy range to VUV range. This study will consider two possibilities: the first is based on "electron switchyard" technique (see Fig. 1). The electron beam (at energy of 2.5 GeV) is . The electron beam (at energy of 2.5 GeV) is extracted from the main linac and enters transport line, which guides it to the VUV undulator located near the experimental hall. The beam distribution system consists of two transport lines. The first beamline (2.5 GeV) directs one bunch train, coming to the "water window" undulator. The second beamline (17.5 GeV) takes every other bunch train and delivers it to X-ray undulators.

Figure 2 illustrates the second (baseline energy) option. This alternative is the one we regard as most favorable. The second option holds the energy at the baseline value (17.5 GeV) and chooses the undulator period length to match the water window wavelengths. This alternative is the one we regard as most favorable. Tables and present optimized parameters of undulator and FEL performance applied to "water window" wavelength range with the electron energy of 2.5 GeV, and for the case of the maximum available energy (17.5 GeV). If the electron energy is that of the upper limit of the range of the baseline design (17.5 GeV) the undulator period length increases, for the resonant wavelength of 6 nm, from 4 to 11 cm. The FEL peak power is a factor of 10 higher for baseline energy (17.5 GeV). The saturation length of "water window" undulator at 17.5 GeV is 80 m, against the 30 m of the low energy undulator.

The second option is the simplest way to obtain VUV radiation from the European XFEL. This is XFEL parasitic mode. All electron bunch trains will be guided into one electron beamline and dump. The wavelength range 0.1-6 nm at fixed electron beam energy of 17.5 GeV can be covered by operating the SASE FEL with four undulators which have different period and tunable gap. These SASE undulators can be placed behind each other assuming that the subsequent undulator radiates at longer wavelength. It is a great advantage that accelerator and electron beam transport line in this scheme operate at fixed parameters and that a fast "electron switchyard" is not required. In order to avoid the need for a costly additional tunnels and shafts, the XFEL source is designed such that accelerator, all four SASE undulators, electron beam line, and photon transport beamlines are installed inside the same (5 m diameter) tunnel.

OPERATION OF FEL SOURCE AT LONGER WAVELENGTH

Present concept of an XFEL facility assumes to cover continuously wavelength range from 0.1 to 6 nm at a fixed (17.5 GeV) energy of the electron beam. This is achieved with four undulators installed in a series in one electron beamline. Optimization of undulator parameters has been performed for the electron beam parameters presented in [1]: peak current 5 kA, rms normalized emittance 1.4 mm-mrad, and initial energy spread of 1 MeV. All undulators are planar, variable-gap devices with an identical mechani-

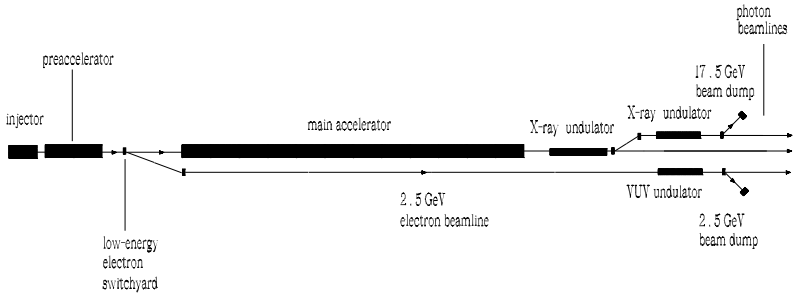

Figure 1: Schematic layout of the first possible strategy for VUV radiation. This scheme is based on the ”electron switchyard” technique

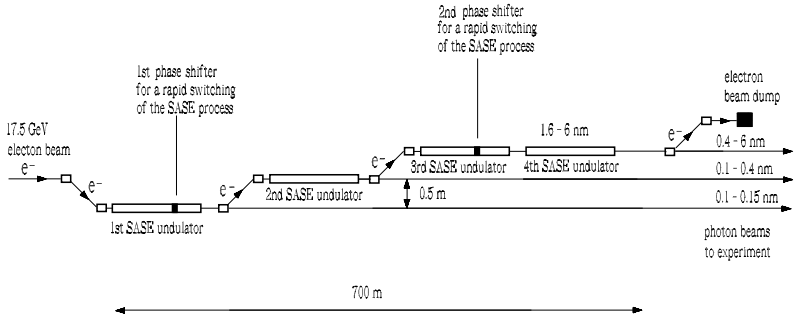

Figure 2: Schematic layout of the most favorable strategy for VUV radiation. In this scheme it will be possible to provide simultaneously hard X-ray and VUV radiation beams (”after-burner” mode of operation)

Table 1: Specification of soft X-ray undulators for XFEL laboratory

	Energy GeV	λ_u mm	gap mm	B_u T	L_u m
Nominal option	17.5	110	19-37	0.7-1.6	80
Low energy option	2.5	38	10-20	0.4-1	35

Table 2: Specification of soft X-ray FELs for XFEL laboratory

	Units	Nominal*	Low energy**
Energy	GeV	17.5	2.5
Wavelength range	nm	1.6/6.4	1.6/6.4
Peak power	GW	100/100	10/20
Average power	W	400/400	40/80
Photon beam size (FWHM)	μm	60/90	90/90
Photon beam divergence (FWHM)	μrad	11/27	11/30
Saturation length	m	70/80	18/32

*Operation in after-burner regime with rms energy spread of 8 MeV
**Operation with nominal energy spread of 1 MeV

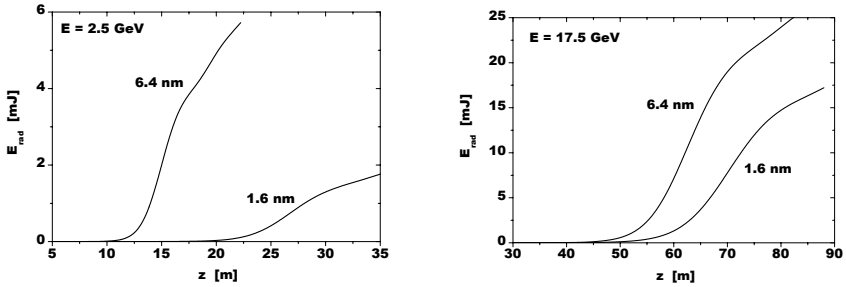

Figure 3: Energy in the radiation pulse versus undulator length. Left plot: low energy option (2.5 GeV). Right plot: nominal energy option (17.5 GeV).

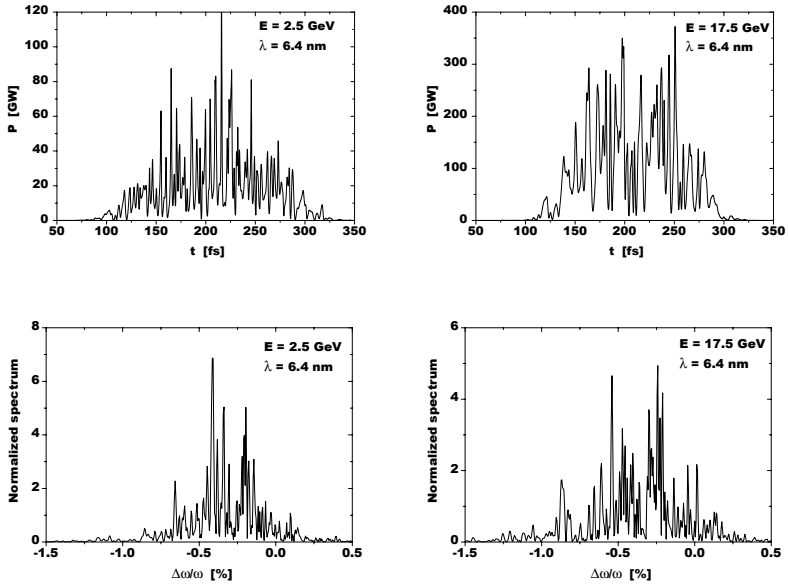

Figure 4: Temporal and spectral structure of the radiation pulse in saturation regime. Radiation wavelength is 6.4 nm. Left column: low energy option (2.5 GeV). Right column: nominal energy option (17.5 GeV).

cal design. Optimized parameters of the undulator for both cases are presented in Table . Calculations of the FEL characteristics are performed with time-dependent FEL simulation code FAST [3].

In this section, some examples will be given that shed light on the differences between the undulator applied to the VUV wavelengths with the electron energy of 2.5 GeV and an undulator that is modeled for the baseline energy 17.5 GeV (after-burner undulator). The build-up of the radiation pulse energy along the undulator is shown in Fig. 3. Requirements for FEL saturation at the shortest wavelength (1.6 nm) defines the undulator length: 35 m for dedicated 2.5 GeV option, and 80 m for 17.5 GeV after-burner option. Typical temporal and spectral structure of the radiation pulse from the VUV FEL operating at saturation are presented in Figs. 4 and 5. For both options these structures are very similar, while peak power is much larger for the after-burner option. At the wavelength around 1.6 nm all key parameters of SASE FEL (peak power, photon flux, brilliance) are by an order of magnitude higher for the after-burner option. This is an evident advantage for using high-energy electron beam to drive long-wavelength SASE FEL.

CONCLUSION

In this paper we performed direct comparison of two possible options to extend wavelength range of European XFEL towards 6 nm. The first option assumes to use electron beam extracted from the XFEL linac at the energy of 2.5 GeV. This beam is then transported via separate beam transport line, passes through the undulator, and is dumped

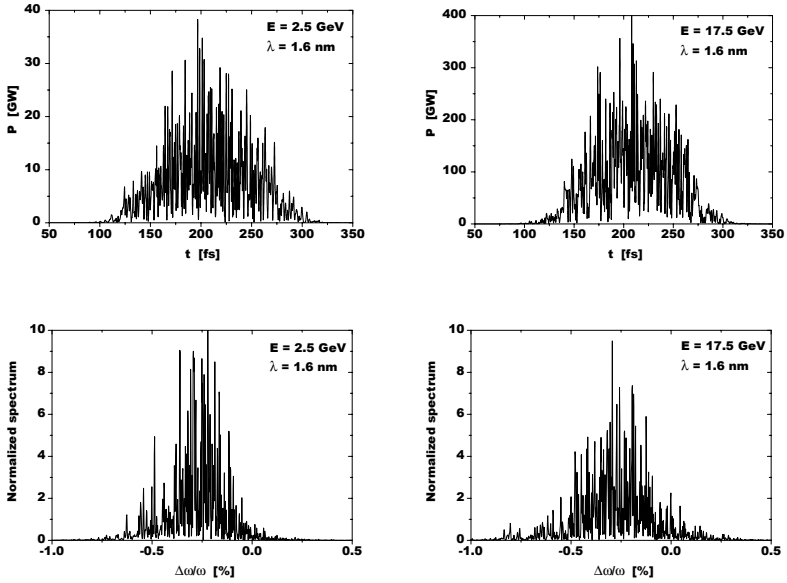

Figure 5: Temporal and spectral structure of the radiation pulse in saturation regime. Radiation wavelength is 1.6 nm. Left column: low energy option (2.5 GeV). Right column: nominal energy option (17.5 GeV).

into the beam dump. Extra expenses for this option are as follows. First, it requires to interfere XFEL linac in order to put extraction devices. Second, long beam transport line (of about two km long) is required. Third, it requires separate beam dump. These evident disadvantages can not be justified by relatively short undulator required (of about 35 meters). The second option, after-burner undulator is the one we regard as the most favorable. It uses electron beam with nominal energy of 17.5 GeV, and can be implemented in a parasitic mode of operation. It is possible to place an undulator as long as 80 meters after 2 nm undulator. Ultimately, VUV undulator would be able to deliver output power approaching 100 GW level (by an order of magnitude higher than for 2.5 GeV dedicated option). One should also keep in mind the problem of the overall efficiency of the XFEL laboratory, i.e. increasing the number of simultaneously working user stations. It is evident that 2.5 GeV option reduces the number of simultaneously working user stations: when electron beam is directed into the VUV branch, hard X-ray users need to wait. 17.5 GeV VUV option works in a parasitic mode: VUV pulse is produced by the electron bunch which was used for production of X-ray pulse in the previous undulator. Finally, in some modes of operation, VUV FEL radiation could be used with X-ray FEL radiation to do pump-probe experiments with precise intervals between the sources.

REFERENCES

[1] P. Audebert et al., "TESLA XFEL: First stage of the X-ray laser laboratory – Technical design report (R. Brinkmann et al., Eds.)", Preprint DESY 2002-167.

[2] E. L. Saldin, E. A. Schneidmiller and M. V. Yurkov, DESY Print TESLA FEL 2004-02, DESY, Hamburg, 2004.

[3] E. L. Saldin, E. A. Schneidmiller and M. V. Yurkov, Nucl. Instrum. and Methods A429(1999)233.

START-TO-END SIMULATIONS FOR PAL XFEL PROJECT

Yujong Kim*, DESY, D-22603 Hamburg, Germany
J. S. Oh, M. H. Cho, I. S. Ko, and W. Namkung, PAL, POSTECH, Pohang 790-784, Korea
D. Son and Y. Kim, The Center for High Energy Physics, Daegu 702-701, Korea

Abstract

At the Pohang Accelerator Laboratory (PAL), there is a 2.5 GeV S-band linac which is under operating as a full energy injector for the Pohang Light Source (PLS) storage ring. By installing a new S-band photoinjector, a new 0.7 GeV linac, and two new bunch compressors, the PLS linac can be operated as an FEL driver for the PAL XFEL project. To generate ultrashort, ultrabright, and coherent X-ray FEL sources, we should supply high quality electron beams to a long undulator. In this paper, we describe design concepts of the new injector, bunch compressors, linac layout optimization, and various start-to-end (S2E) simulations on linac optimization and jitter.

INTRODUCTION

During the nominal operation of the PLS storage ring, 2.5 GeV PLS linac is operated as a full energy injector for the ring, and its total injection time is within about 20 minutes a day. Since the PLS linac does not have any other special dedicated service, the linac can be ideally converted into the FEL driver for an X-ray FEL facility. To supply femtosecond (fs) hard X-ray FEL sources, recently, Korean government approved the PLS linac upgrade for the PAL XFEL project. Under the fundamental mode operation of the PAL XFEL facility, its tunable shortest wavelength is 3 Å, and FEL sources with more shorter wavelength can be also available by various higher harmonic generation technologies [1]. Detail FEL related parameters for the PAL XFEL project can be found in references [2] and [3], and its required electron beam parameters for 3 Å and 1 Å FEL sources are summarized in Table 1. Generally, FEL source properties strongly depend on the electron beam parameters such as slice and projected normalized rms emittances, slice rms relative energy spread, and peak current. And these parameters are mainly determined by the injector system and bunch compressors (BCs) in the FEL driving linac. Since the current 80 kV DC gun can not generate high quality electron beams, a new gun, two bunch compressors, and a new injector linac should be added to the existing PLS linac to supply required electron beams for the PAL XFEL project. However its overall modification must be minimized to reoperate the PLS storage ring within a limited period. In this paper, we propose one possible linac layout for the PAL XFEL project and describe various S2E simulation results with ASTRA and ELEGANT codes.

* E-Mail : Yujong.Kim@DESY.de, URL : http://www.desy.de/∼yjkim

Table 1: Main parameters for PAL XFEL project.

Parameter	Unit	3 Å / 1 Å
beam energy E	GeV	3.0 / 3.0
single bunch charge Q	nC	1.0 / 1.0
slice normalized rms emittance ϵ_{ns}	μm	1.5 / 1.0
slice rms relative energy spread $\sigma_{\delta s}$	10^{-4}	2.0 / 2.0
peak current I_{pk}	kA	4.0 / 4.0
undulator length for fundamental mode	m	60 / 37
undulator length for the 3rd harmonic	m	· / 23

INJECTOR FOR PAL XFEL PROJECT

Recently, by the help of a flat-top laser profile with about 9 ps (FWHM) length and about 1.5 ps rising and falling time, one BNL/SLAC/UCLA type S-band RF gun with a 14 MeV booster linac had generated high quality electron beams with a projected normalized rms emittance of about 1.2 μm for 1 nC singe bunch charge [4]. After considering two facts that slice normalized rms emittance should be smaller than 1.0 μm to generate 1 Å FEL source, and projected and slice emittances can be diluted at bunch compressors due to the microbunching instability and CSR, we determined that the PAL XFEL injector should supply much higher quality electron beams with a smaller projected normalized rms emittance [5]-[7].

This required higher quality electron beams can be generated by upgrading the BNL/SLAC/UCLA type S-band RF gun with following steps [4]: First, transverse laser profile will be improved to have a good homogeneous intensity, and longitudinal laser profile will be improved to have a good uniform flat-top shape with a shorter rising and falling time. These improvements will help in reducing emittance growth at head and tail regions due to the nonlinear space charge force [5]. Second, the maximum gradient at the cathode will be increased from current 100 MV/m to 120 MV/m which will also help in reducing space charge force effects [8]. Third, we will align laser on the cathode and correct solenoid misalignments by the beam based alignment. Fourth, several fine optimizations will be done under 120 MV/m gradient: gun RF phase optimization to get the maximum energy gain, laser pulse length optimization to control longitudinal space charge force, laser spot-size optimization at the cathode to control transverse space charge force and thermal emittance, solenoid current optimization to compensate emittance growth in gun region due to space charge force and to reduce emittance growth due to the none-zero magnetic field on the cathode [8], [9].

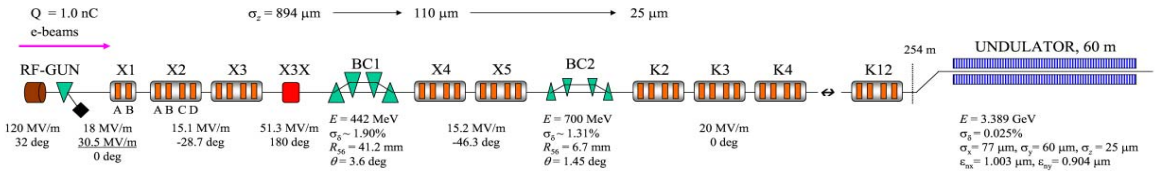

Figure 1: One possible linac layout (21JUL04 version) for PAL XFEL project.

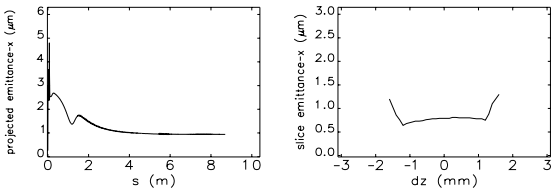

Figure 2: ASTRA simulation results on PAL XFEL injector: (left) projected normalized rms horizontal emittance up to the end of X1B, and (right) slice normalized rms horizontal emittance at the end of X1B. Here the entrance of X1A and X1B are located at 1.4 m and 5.4 m downstream from the cathode, respectively.

Fifth, we will re-compensate the second emittance growth due to space charge force in the drift space between gun and the booster linac by installing the first S-band accelerating column (X1A) at the so-called *Ferrario matching point* as shown in Figs. 1 and 2 [10]. Here, X1A has a lower gradient to satisfy the *Ferrario matching condition* and the second accelerating column (X1B) has a higher gradient to get a higher beam energy and to control Twiss parameters in X1B [10]. According to our ASTRA simulations for the PAL XFEL injector, we may generate higher quality electron beams with a projected normalized rms emittance of around 0.94 μm by following above optimization steps. Its simulation results are shown in Fig. 2, and its detail simulation conditions are summarized in Table 2.

Table 2: S2E simulation results for PAL XFEL project.

Parameter	Unit	Value
RF frequency of gun and linac	MHz	2856
repetition rate	Hz	60
gun cell number	cell	1.6
laser spotsize at cathode $\sigma_{x,y}$	mm	0.60
laser pulse length (FWHM)	ps	10
laser pulse rising and falling time	ps	0.7
normalized thermal emittance	μm	0.60
maximum longitudinal solenoid field	T	0.272
maximum gradient at the cathode	MV/m	120
gun phase from zero crossing	deg	32
accelerating gradient in X1A	MV/m	18
accelerating gradient in X1B	MV/m	30.5
X1A and X1B phase from on crest	deg	0.0
projected emittance before BC1 / BC2	μm	0.94 / 0.99
slice emittance before BC1 / BC2	μm	0.81 / 0.81
bunch length before BC1 / BC2	μm	894 / 110
beam energy before BC1 / BC2	MeV	442 / 700
projected energy spread before BC1 / BC2	%	1.90 / 1.31
slice energy spread before BC1 / BC2	10^{-5}	0.92 / 4.30
projected emittance after BC2 / LINAC	μm	1.08/ 1.00
slice emittance after BC2 / LINAC	μm	0.81 / 0.81
bunch length after BC2 / LINAC	μm	24.6 / 24.6
beam energy after BC2 / LINAC	GeV	0.70 / 3.39
projected energy spread after BC2 / LINAC	%	1.27/ 0.03
slice energy spread after BC2 / LINAC	10^{-4}	2.44 / 0.29

BC FOR PAL XFEL PROJECT

Basic bunch compressor design concepts are well described in references [7] and [11]. The same concepts are used in designing bunch compressors for the PAL XFEL project. Since dispersion is reversed inside of the S-type chicane, the chicane is generally useful in compensating the projected emittance growth [12]. But its overall CSR strength is much higher than that of the normal chicane with four dipoles because S-type chicane has two additional dipoles [12]. Specially, if current density profile and/or energy profile have a modulation before the S-type chicane, its CSR microbunching instability is stronger than that of the normal chicane [12].

To avoid slice parameter dilution due to the microbunching instability in BCs, we have adopted followings in our linac layout as shown Fig. 1: First, to reduce overall CSR strength, we choose only two bunch compressors with the normal chicane instead of S-type chicane. Second, to keep the slice rms relative energy spread at the entrance of BC2 large, we put BC2 at a low beam energy of around 700 MeV. In this case, BC2 has still a large projected rms relative energy spread of around 1.31%. Third, during compression in BCs, slice energy spread generally becomes larger to conserve the normalized longitudinal emittance. Therefore slice rms relative energy spread before BC2 can be further increased up to 4.3×10^{-5} by compressing bunch length at BC1 strongly. Since the compression factor at BC1 is high, we put BC1 at 442 MeV to avoid any beam dilution due to space charge force. Note that our linac layout can be also operated as the double chicane mode only by turning off two S-band accelerating sections (X4 and X5) and by rematching optics [5], [7]. In this case,

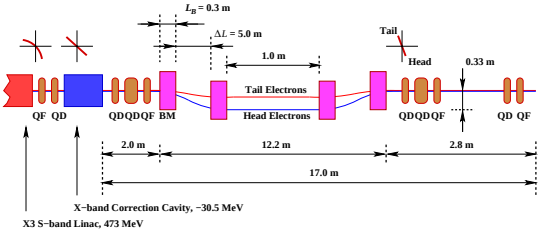

Figure 3: BC1 layout for PAL XFEL project. BC2 chicane has the same layout.

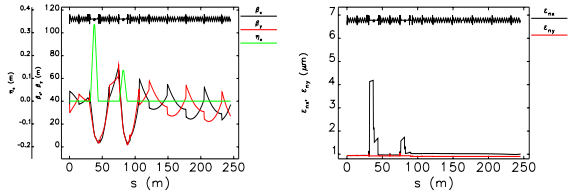

Figure 4: Twiss parameters (left) and projected emittances (right) along PAL XFEL linac.

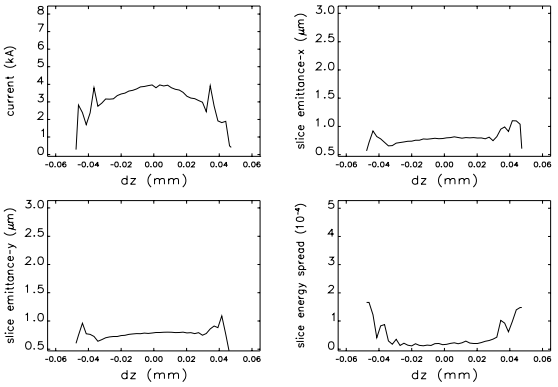

Figure 5: Slice parameters at the end of PAL XFEL linac.

microbunching instability will be effectively damped [5].

To avoid projected emittance dilution due to CSR in BCs, we have adopted followings in the PAL XFEL linac layout as shown in Figs. 1 and 3: First, to reduce CSR, we should choose a smaller momentum compaction factor R_{56} of chicane. This is possible by choosing a somewhat larger projected rms relative energy spread σ_δ [11]. After considering the emittance growth due to chromatic effect, we choose 1.90% at BC1. Second, we choose short quadrupoles around BCs to reduce emittance growth due to chromatic effect. Third, for a required R_{56}, we can reduce dipole bending angle (hence, CSR) further by using a longer drift space ΔL between the first dipole and the second one as shown in Fig. 3 [11]. Fourth, generally, CSR is weaker at BC1, and CSR becomes stronger at BC2 as bunch length is compressed. Hence, we choose a higher compression factor at BC1 and a lower compression factor at BC2 to reduce overall CSR effects in our two BCs. Fifth, we reduce CSR further by installing a 4th harmonic X-band accelerating column (X3X) before BC1 to compensate nonlinearities in the longitudinal phase space as shown in Fig. 3 [11]. Sixth, if we use a long linac between BCs, the longitudinal short-range wakefield in the linac induces a small change in the longitudinal-phase-space chirping slope at head and tail regions, where charge is low. In this case, projected emittance is increased due to overcompression at head and tail regions in BC2 [10]. Therefore we reduce the length of S-band linac between BCs to reduce the projected emittance growth at BC2. Seventh, the projected emittance dilution due to CSR can be reduced further by forcing the beam waist close to the last dipole where α-functions are zero, and β-functions are their minimum as shown in Fig. 4 [11]. Since chromatic effects become smaller at BC2 due to smaller σ_δ, we choose much higher β-functions at the upstream of BC2 to give strong focusing in BC2 as shown in Fig. 4(left) [11]. In this case, the projected emittance growth due to CSR can be effectively reduced at BC2.

To check performance of our linac layout, we have performed S2E simulations with ASTRA and ELEGANT codes as shown in Figs. 1 and 4(right), and as summarized in Table 2. Here emittance, energy spread, and bunch length are estimated in *normalized rms*, *rms relative*, and *rms*, respectively, and slice parameters before BC2 (after BC2) are estimated at ± 0.1 mm (± 0.02 mm) core region. In these simulations, we have included all important impedances such as space charge force in gun and X1 accelerating section, CSR and incoherent synchrotron radiation (ISR) in BCs, and short-range wakefields in all accelerating sections. According to our S2E simulations, all obtained slice parameters at the end of the linac are much better than our requirements as summarized in Table 2 and shown in Fig. 5. Here small spikes in current are generated by the weak over-compression at head and tail regions.

S2E SIMULATIONS ON JITTER

To relax jitter tolerance, we have adopted followings in PAL XFEL linac layout as shown in Fig. 1, where each accelerating section from X2 to K12 has four S-band accelerating columns: First, tight jitter tolerance can be improved by operating more klystrons in one accelerating section. Therefore one klystron will be dedicated to two sequent S-band accelerating columns from X1 to X5 sections to relax tight jitter tolerance there. Since X2AB (= X2A + X2B), X2CD, X3AB, and X3CD will be operated by their own klystrons under the same RF conditions, X2AB, X2CD, X3AB, and X3CD have the same jitter sensitivity [5]. Since jitter tolerance is loose at the downstream of BC2, one klystron will be dedicated to four sequent S-band accelerating columns from K2 to K12 sections. Second, tight jitter tolerance can be looser by operating S-band accel-

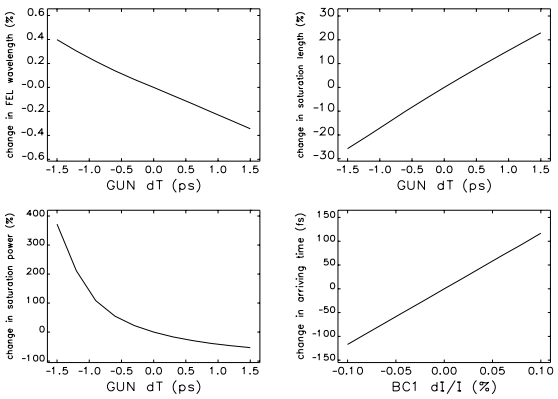

Figure 6: The most sensitive jitter sources in PAL XFEL linac: (top left) wavelength of FEL source versus gun timing jitter, (top right) saturation length versus gun timing jitter, (bottom left) saturation power versus gun timing jitter, and (bottom right) photon beam arriving time versus current error in BC1 magnet power supply.

erating columns around BCs with a low gradient of about 15 MV/m. To investigate the jitter sensitivity J_s and jitter tolerance J_t at the PAL XFEL linac, we have performed S2E simulations with ASTRA and ELEGANT codes. By applying an artificial jitter or error to each component, then by monitoring its impact on FEL performances, we can determine the jitter sensitivity of the component. In this paper, we assume that jitter is uncorrelated, and all components do not have any misalignment.

After considering users' requirements on photon beam stability, we have used following four constrains in determining the jitter sensitivity: First, peak-to-peak (p2p) change in wavelength of FEL source should be within $\pm 0.25\%$. Second, p2p change in saturation length should be within $\pm 5.0\%$. Third, p2p change in saturation power should be within $\pm 20.0\%$. Fourth, p2p change in bunch arriving time should be within ± 25 fs. The most sensitive jitter source in wavelength, saturation length, and saturation power is the gun timing jitter, and the most sensitive jitter source in bunch arriving time is the current error of magnet power supply for BC1 as shown in Fig. 6. Here the Ming Xie model is used in estimating FEL performances, which are averaged in 80% core slices.

By repeating above processes, we have determined jitter sensitivities and jitter tolerances of all linac components, which satisfy a relation of $\sqrt{\sum_{i=1}^{n}(J_{t,i}/J_{s,i})^2} < 1$, where n is the total number of all considered linac components. Investigated bunch-to-bunch jitter sensitivities and jitter tolerances are summarized in Table 3. Here Tol. (p2p) and Tol. (rms) are jitter tolerances which are estimated in *p2p* and *rms* respectively.

Recently, it was reported that gun timing jitter can be controlled within several tens of fs by newly developing laser-RF synchronizing and timing technologies, and by the help of newly developing advanced RF low level control system, rms phase error and rms voltage error can be controlled within 0.01 deg and 0.01%, respectively [13]. Therefore we expect that the PAL XFEL facility can supply stable FEL sources to users.

Table 3: Jitter sensitivity and tolerance at PAL XFEL.

Jitter parameter	Unit	Sensitivity	Tol. (p2p)	Tol. (rms)
gun timing ΔT	ps	-0.24	0.24	0.08
charge $\Delta Q/Q$	%	-3.00	3.00	1.00
X1AB $\Delta\phi$	deg	-0.14	0.06	0.02
X1AB $\Delta V/V$	%	-0.06	0.06	0.02
X2AB $\Delta\phi$	deg	-0.10	0.06	0.02
X2AB $\Delta V/V$	%	-0.11	0.06	0.02
X3X $\Delta\phi$	deg	+0.17	0.06	0.02
X3X $\Delta V/V$	%	+0.29	0.06	0.02
BC1 $\Delta I/I$	%	+0.02	0.02	0.007
X4AB $\Delta\phi$	deg	-0.64	0.06	0.02
X4AB $\Delta V/V$	%	-1.17	0.06	0.02
BC2 $\Delta I/I$	%	+0.11	0.02	0.007
K2 $\Delta\phi$	deg	-83.3	0.06	0.02
K2 $\Delta V/V$	%	+1.70	0.06	0.02

SUMMARY

By putting BC2 at a lower energy region, by using a short linac between BCs, and by choosing high compression factor at BC1, slice energy spread before BC2 is about 4.3×10^{-5}, which is large enough to control microbunching instability at BC2. In this case, optimized beam parameters at the end of PAL XFEL linac are also much better than our requirements, and growths of slice and projected normalized rms horizontal emittances in BCs are only 0.0 μm and 0.14 μm, respectively, even though peak current is about 4.0 kA. We expect that the PAL XFEL facility can supply stable FEL sources to users if jitter sources are controlled by newly developing advanced technologies.

REFERENCES

[1] L. H. Yu, Phys. Rev. A **44,** 5178 (1991).
[2] J. S. Oh, *et al*., Nucl. Instr. and Meth. A **528,** (2004) 582.
[3] J. S. Oh, *et al*., in these proceedings.
[4] J. Yang *et al*., J. Appl. Phys. **92,** 1608 (2002).
[5] Yujong Kim *et al*., in *Proc. EPAC2004*, 2004.
[6] Yujong Kim *et al*., Nucl. Instr. and Meth. A **528,** (2004) 427.
[7] Yujong Kim *et al*., in these proceedings.
[8] C. Travier, Nucl. Instr. and Meth. A **340,** (1994) 26.
[9] B.E. Carlsten, Nucl. Instr. and Meth. A **285**, (1989) 313.
[10] LCLS CDR, SLAC-R-593, 2002.
[11] Yujong Kim *et al*., Nucl. Instr. and Meth. A **528,** (2004) 421.
[12] http://www.desy.de/∼yjkim/TESLA_S2E_2003_10.pdf
[13] S. Simrock, in *Proc. LINAC2004*, 2004.

SEEDING HIGH GAIN HARMONIC GENERATION WITH LASER HARMONICS PRODUCED IN GASES

G. Lambert*, B. Carré, M. E. Couprie, D. Garzella, Y. Mairesse, P. Salières, CEA, DSM/SPAM, 91 191 Gif-sur-Yvette, France, A. Doria, L. Giannessi, ENEA C.R. Frascati, Italy,
T. Hara, H. Kitamura, T. Shintake, SPring-8/RIKEN Harima Institute, Hyogo 679-5148, Japan

Abstract

Free electron Lasers employing High Gain Harmonic generation (HGHG) schemes are very promising coherent light sources in the soft X-ray range. They offer both transverse and longitudinal coherence, while Self Amplified Spontaneous Emission schemes have a limited longitudinal coherence. We propose here to seed a HGHG experimental setup with high harmonics produced by a Ti:Sa femtosecond laser focused on a gas jet in the 100-10 nm spectral region. The implementation of this particular laser harmonics source as a seed for HGHG is investigated. Semi analytical and numerical 1D calculations are given, for the cases of the SCSS, SPARC and ARC-EN-CIEL projects.

INTRODUCTION

In order to reach very short wavelengths in systems based on Free Electrons Laser (FEL) [1,2], and to have more compact and fully temporally coherent sources, a High Gain Harmonics Generation (HGHG) configuration [3] is studied here, in which an external laser source is seeded into a modulator, thus allowing a strong prebunching of the e-beam. The use of a long radiator section can lead to the consistent emission of radiation at high order harmonics of the seeding source while reproducing its longitudinal and transverse coherence. A very promising scheme is the one where the seeding source is already in the XUV range, provided by the harmonics of the Ti:Sa laser generated in gas. Intense, ultra-short laser harmonics can be now generated down to 10 nm [4]. We propose to use these laser High Harmonics (HH at λ wavelength) as the seed for a high gain FEL amplifier radiating at λ or λ/3 and to extract its third and fifth non linear harmonics [2,5]. This scheme is considered for different installations: first on SCSS (Spring-8 Compact Sase Source, Japan) [6] and SPARC (Sorgente Pulsata e Amplificata di Radiazione Coerente, Italy) [7] for demonstration experiments, second on ARC-EN-CIEL (Accelerator-Radiation Complex for ENhanced Coherent Intense Extended Light, France) [8] and BATES (MIT, USA) [9] for efficient X-ray generation. SCSS and SPARC are projects of linac-based FEL, providing a compact SASE source with high brightness in the X-ray range. ARC-EN-CIEL (AEC) is a proposal for an innovative HGHG in the XUV range (Phase 1 is a first step towards VUV). In this paper, we discuss the prototype experiments on SCSS, AEC and SPARC, including a brief description of the experimental setup and theoretical estimate of the performances, the latter based on analytical formulae [1, 10] and 1D simulations using PERSEO code [11].

*guillaume.lambert@lure.u-psud.fr

THEORY OF HIGH ORDER HARMONICS PRODUCED IN GASES

The high harmonic generation in rare gas (Xe, Ar, Ne, He) results from the strong non linear polarisation induced by the strong laser field E_{Laser}, at intensity 10^{14}-10^{15} W/cm^2. The process is qualitatively described in the semi-classical "three-step" model [12, 13]. Close to laser focus, for E_{Laser} comparable to the intra-atomic field, atoms ionize in the tunnelling regime [4] (step 1). The ejected electrons are then accelerated by the laser field and gain a kinetic energy (step 2). Those which are driven back close to the core may recombine to the ground state, emitting a burst of XUV photons (step 3). This three-step process reproduces every half- optical cycle.

EXPERIMENTAL SET UP

Characteristics of High Harmonics in gases

A typical harmonic spectrum generated in Ne is displayed in fig. 1, illustrating the characteristic distribution of the odd harmonics into the "plateau" region, where the conversion efficiency is almost constant, and the "cut-off" region where the conversion efficiency rapidly drops down. The conversion efficiency for high harmonic (HH) generation remains relatively weak, typically varying from 10^{-4} in the plateau to 10^{-7} in the cut-off.

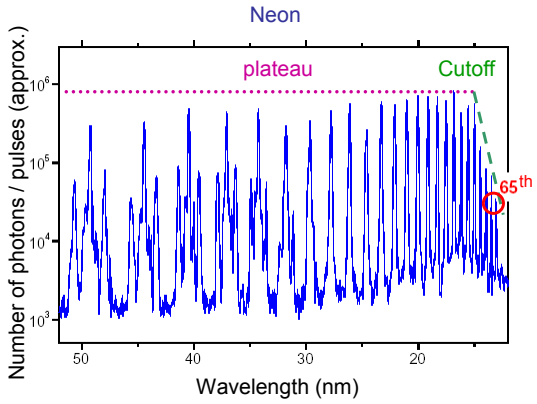

Fig. 1: High Harmonic spectrum in Ne.

The upper spectral limit is given by the "cut-off law" [5, 14]. It states that the lighter the gas, i.e. the higher the ionization potential and the laser intensity to which atom

can be submitted without ionizing, the higher the cut-off energy. The HH therefore cover the 100^{-3} nm range (12-400 eV). They have remarkable properties of ultra-short duration (of a few 10 fs down to sub-fs), longitudinal [15] and transverse [16] coherence, good beam quality (small divergence ~ 1mrad on laser axis), easily rotatable linear polarization [17] and can be produced at relatively high repetition rate (up to KHz). Finally it is possible to continuously tune the HH, e.g. by manipulating the spectral phase of the driving laser or by starting from two driving frequencies [18].

Beams and undulators parameters

For the seed experiment, a HGHG configuration is foreseen with two undulators: the modulator (mod), which is chosen according to the wavelength of the seeded radiation, and the "radiator" (rad), providing a high gain. In SCSS and SPARC projects, the radiator emitted wavelength is matched on the fundamental of the modulator ($\lambda_{rad}=\lambda_{seed}$). In AEC and AEC Phase 1 projects it is matched on the third harmonic ($\lambda_{rad}=\lambda_{seed}/3$). The table 1 shows the electron beam parameters, where I_P is the peak current, the undulators parameters, where N_P is the number of periods per section and N_S the number of section, and the seeding parameters, where E_H is the harmonic energy per pulse, P_H the harmonic power and D the harmonic spot diameter.

Table 1: electron beam, undulator, and seeding characteristics.

Projects	AEC PhI	AEC	SCSS	SPARC
Electron Beam Characteristics				
E (GeV)	0.22	1	0.25	0.21
σ_γ	0.001	0.001	0.0002	0.002
Q (nC)	1	1	1	1
ε (π mm-mrad)	1.7	1.5-2	1.5	1
I_P (kA)	0.8	0.6	0.2	0.15
Undulators Characteristics (Mod/Rad)				
λ_R (nm)	267/89	14/4.64	60	160
λ_U (nm)	38.9/20	30/20	15	28
K	1.76/1.14	2.27/1.26	1.39	1.36
N_P	34/450	160/1000	300	487
N_S	1/1	1/1	2	6
Seeding Characteristics				
λ_{seed} (nm)	H3=267	H57=14	H13=60	H5=160
E_H (μJ)	5	1	5	5
P_H (MW)	50	10	50	50
D (μm)	250	250	250	250

Layout of the HGHG configuration seeded by harmonics produced in gases

A Ti:Sa laser system delivers pulses at 800 nm (E_{ph}=1.55eV), which are converted into harmonics in the gas jet vessel. The harmonic pulses are then injected into the modulator. In SCSS and ARC-EN-CIEL projects, a magnetic chicane is inserted on the electron bunch path to superimpose the bunch and the XUV pulse at entrance of the modulator (Fig. 1).

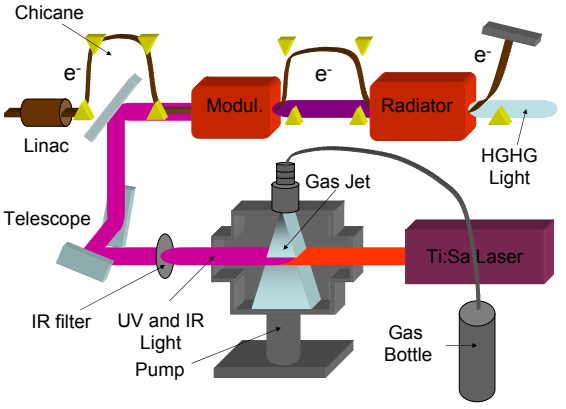

Fig. 1: Layout of the seeding system with a chicane.

A small size mirror serves to inject the XUV beam in the FEL cavity and to adjust its position. The advantage in this scheme is that all the XUV beam (~mm in diameter) is injected; the constraint is that enough room should be available to accommodate the magnetic elements. So, another arrangement, where the chicane is replaced by a holed mirror on the XUV beam, is envisaged in the SPARC project (Fig. 2).

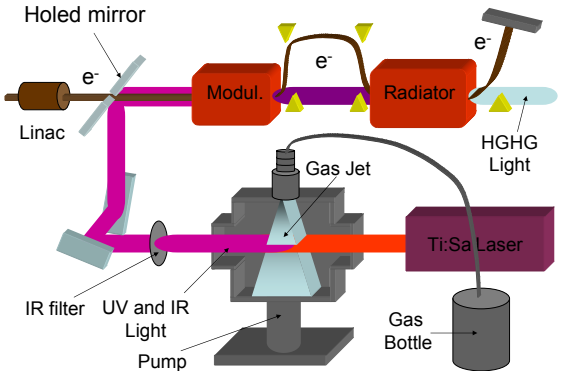

Fig. 2 : Layout of the seeding system with a holed mirror.

The constraint is now that the hole should be sufficiently small so that a high enough XUV energy is reflected.

In both schemes, the laser beam is eliminated using various metallic filters which further select a finite spectral range in the harmonic spectrum. Then the XUV beam should be collimated to a small diameter (mm) by means of a telescope (spherical mirrors in afocal geometry). The different mirrors should also improve, if needed, the spectral selection of a particular harmonic component, e.g. Mo/Si multilayer optics to select high orders in SCSS [19, 20]. The required multiple reflections should not reduce the XUV energy by more than 50%. Thus, if we consider a harmonics injection system based on five optics the global reflectivity falls around 3%.

CODES AND SIMULATIONS

One dimensional code PERSEO

Perseo [11] is a library of functions reproducing the main properties of the desired FEL configuration in a 1D simulation. The basic idea consists in the integration of the pendulum equation coupled to the fields equations. A typical simulation is shown in fig. 4.a,b where the growth of the output peak power on the fundamental and on the higher order non-linear harmonics is represented as function of the longitudinal coordinate in the radiator. The implementation of Perseo considered in this study allows to inspect the energy modulation (fig. 5a) and the associated bunching factor evolution (fig. 5b), during the parameters optimization. Finally in fig.6, the evolution of the output peak power on the harmonics is shown as a function of the seed power and the radiator length.

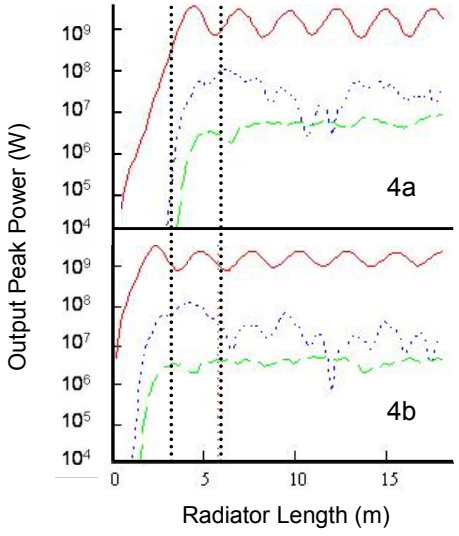

Fig. 4a, 4b: Evolution of the AEC SASE (a) and AEC Seeding HGHG (b) output peak power at 6.5nm (—) and at their third (…) and fifth (---) non linear harmonics.

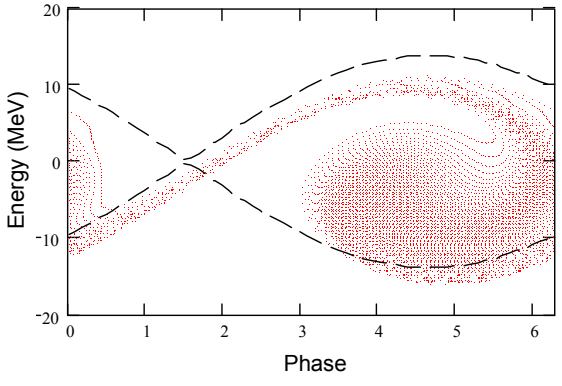

Fig. 5a: Evolution of the energy modulation before the drift section for SPARC project.

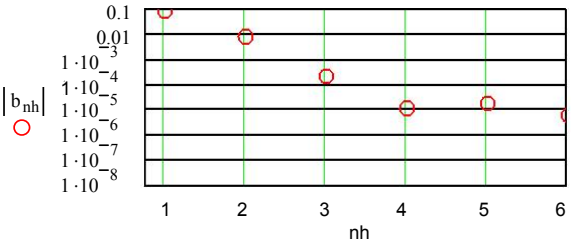

Fig. 5b: Evolution of the harmonics bunching factor (b_{nh}) before the drift section for SPARC project versus the order of harmonics (nh=1 is the fundamental).

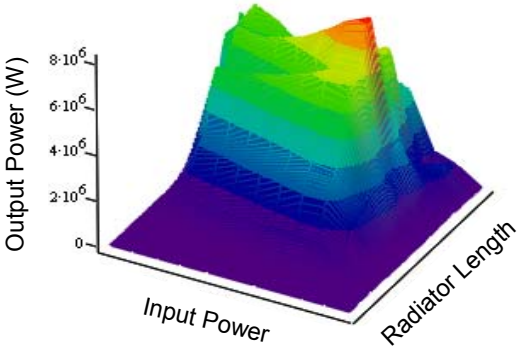

Fig. 6: Evolution of the SPARC Seeding HGHG output peak power for the third non linear harmonics (53.3 nm) versus input power and radiator length.

Analytical simulation

These simulations are based on an analytical 0D approach in static mode, that is to say, with an average on the transverse and longitudinal coordinates. The used FEL formula come from G. Dattoli and P. L. Ottaviani [10]. The simulations allow to investigate the exponential growth of the fundamental output peak power as a function of the radiator length.

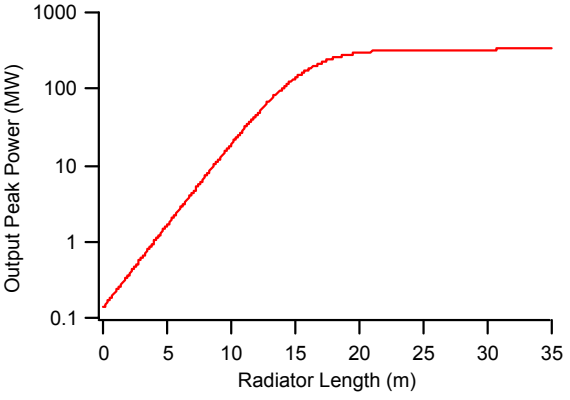

Fig. 7: Evolution of the AEC Seeding HGHG output peak power at 6.5nm.

EXPECTED PERFORMANCES

We can see in table 2 that seeding HGHG configuration allows the saturations lengths to be reduced from a factor of 1.5 to 2.

Table 2: Saturation length (m) comparison with Perseo: Seeding HGHG/SASE.

Projects	Fundamental Output Radiation (nm)	Saturation Length (Seeding/SASE) (m)
ARC-EN-CIEL	9.2	2/7.5
	6.5	3.5/7.5
	5.5	7/12
ARC-EN-CIEL Phase 1	88.9	3.5/5.5
	66.7	4.5/7
	53	6/12
SCSS	60	4/7.5
SPARC	260	4/6
	160	6/8.5

Figure 8 shows the expected results in terms of output power made with Perseo.

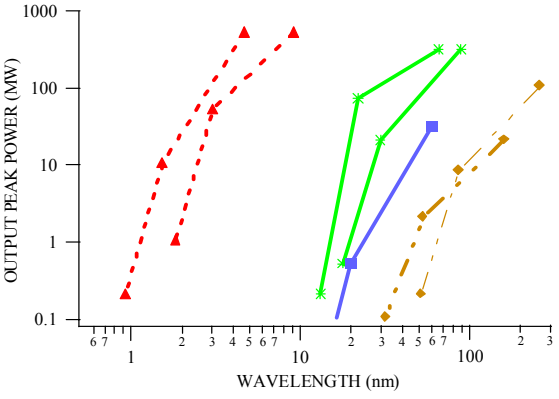

Fig. 8: Output peak power of λ_{rad}, its third and fifth non-linear harmonics for AEC (--▲--), AEC phase 1 (-*-), SCSS (-■-), SPARC (-♦-), and, for seed powers up to 1MW. $<P_{Rrad}>\approx$0.1-0.5 W.

As we can see on the figure 4a and 4b, the output peak power is lower by a factor of ~ 5 for a Seeding HGHG configuration than for a SASE configuration. However, it remains high and now corresponds to fully coherent XUV pulses. For instance, if we seed the SPARC experiment at 260 nm, the fifth harmonic at 52 nm is generated at 0.25 MW output level, whereas seeding at 160 nm gives a fifth harmonic at 32 nm of 0.15 MW peak power.

Figure 9 shows the expected results in terms of output power obtained by the analytical simulations.

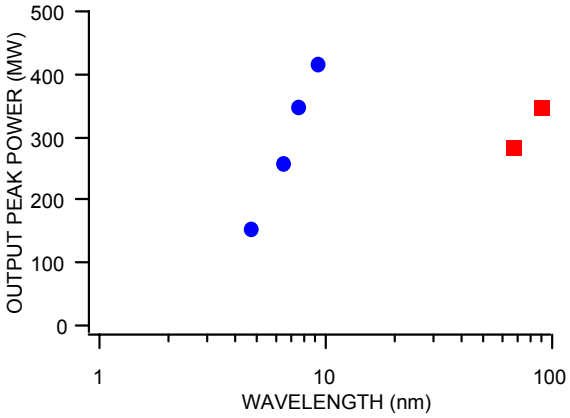

Fig. 9: Output peak power of the $\lambda_{seed}/3$ harmonics performances with a 1MW seed power and with beam parameters coming from Table 1, for AEC (●), and AEC phase 1 (■). $<P_{seed}>\approx$0.1-0.5 W.

CONCLUSIONS

Using high laser harmonics generated in gas for seeding High Gain FEL amplifiers appears very interesting, since the seed radiation is fully coherent, of ultra-short duration and tuneable in the XUV range. The seeding can reduce the saturation length, leading to a more compact source. The calculated performances roughly agree between 0 and 1D analysis. They show that high peak power (> MW) could be obtained with this scheme.

REFERENCES

[1] F. Ciocci et al, IEEE Jour. Quant. Elec. 31 (1995) 1242.
[2] S. G. Biedron et al., Nucl. Inst. Meth. A 475 (2001) 401.
[3] L. H. Yu, I. Ben-Zvi, Nucl. Inst. Meth. A 393 (1997) 96.
[4] K. Midorikawa, Phys. Rev. Lett. 82 (1999) 1422.
[5] D. Garzella et al., Nucl. Inst. Meth. A 527 (2004).
[6] http://www-xfel.spring8.or.jp/scss/.
[7] Sparc Collaboration, Nucl. Inst. Meth. A 507 (2003) 345.
[8] ARC-EN-CIEL www.lure.u- psud.fr/congres/femto/.
[9] http://mitbates.mit.edu/xfel/.
[10] G. Dattoli, P. L. Ottaviani J. Appl. Phys., 95, (2004).
[11] www.perseo.enea.it.
[12] P. B. Corkum, Phys. Rev. Lett. 71 (1993) 1994.
[13] M. Lewenstein et al., Phys. Rev. A 49 (1994) 2117.
[14] G. Lambert et al., to be published in Jacow.
[15] P. Salières et al., Science 292 (2001) 902.
[16] L. Le Déroff et al., Phys. Rev. A 61 (2000) 043802.
[17] P. Salières et al., Adv. At., Mol., Opt. Phys. 41 (1999) 83.
[18] H. Eichmann et al., Phys. Rev. A 51 (1995) R3414.
[19] Yu. A. Uspenskii, Nucl. Inst. Meth. A448 (2000) 147.
[20] T. Feigl et al., Nucl. Inst. Me

ELECTRON BEAM SIMULATIONS FOR THE FERMI PROJECT AT ELETTRA

S. Di Mitri*, R.J. Bakker, C.J. Bocchetta, P. Craievich, G. D'Auria, G. De Ninno, B. Diviacco, L. Tosi, V. Verzilov (Sincrotrone Trieste S.C.p.A., Area Science Park, 34012 Basovizza, Trieste, ITALY)

Abstract

FERMI at ELETTRA is a project aiming at the construction of a single-pass user facility for the spectral range from 100 nm to 10 nm. Starting point is the existing 1.2 GeV, 3 Ghz linac. Downstream of the linac two undulator beamlines will serve the wavelength range from 100 nm to 40 nm and from 40 nm to 10 nm, respectively. The former beamline will be based on a single-stage High Gain Harmonics Generation (HGHG) scheme, while for the latter a double stage HGHG scheme is foreseen.

In this paper we present the results of both numerical and analytical studies aimed to optimize the electron beam characteristics for the 100-40 nm HGHG. In particular, care has been taken to include realistic models for the injector.

INTRODUCTION

The FEL-I phase of the Fermi at Elettra project involves the construction of a single-pass FEL user facility for the spectral range of 100 nm to 40 nm. The laser will be driven by the existing normal conducting 1.2 GeV linac [1].

Studies on a reliable representation of the linac sections and of their influence on the beam dynamics are here presented; these topics are essential for realistic start-to-end simulations, as well as to guarantee the final desired beam quality (Table 1) [2].

LAYOUT

Fig.1 and Fig.2 show the scheme for the linac layout and for the undulators line, respectively. As for the linac, a new rf photo-cathode gun [3] provides a high quality electron beam (see Table 2).

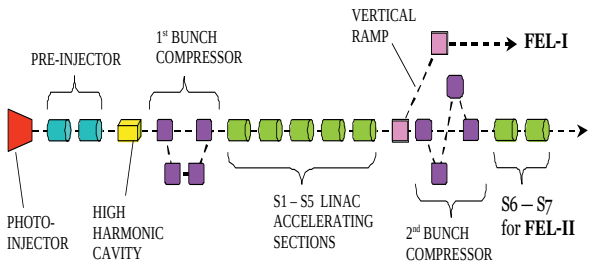

Fig.1 Schematic layout of the linac configuration for the FEL-I and FEL-II stages.

simone.dimitri@elettra.trieste.it

A 100 MeV pre-injector of two (2/3) π travelling wave accelerating sections (TWs) gets the beam out of the space-charge energy domain and creates an energy-position correlation suitable for the following bunch compression.

An X-band harmonic cavity (HC) linearizes the compression process in order to permit a uniform charge density in the bunch and to remove excessive current spikes which may drive the coherent synchrotron radiation (CSR) instability.

After the chicane, five (3/4)π backward travelling wave sections (BTWs) allow the beam to reach the fixed target energy of 700 MeV. Quadrupole triplets between the sections provide the necessary transverse focusing.

Table 1. Electron beam target parameters at the end of the linac for FEL-I stage.

	FEL-I	
Wavelength target	100 40	nm
Beam energy	0.70	GeV
Bunch charge	1.0	nC
Peak current	0.8	kA
Bunch duration (σ_t)	500	fs
Energy spread (σ_δ)	0.7	MeV
Emittance	1.5	μm rad
Repetition rate	50	Hz

The electron beam is taken to the surface undulator hall through a dogleg, which is achromatic and nearly isochronous: its 5° bending angle avoid a further beam quality degradation due to the CSR.

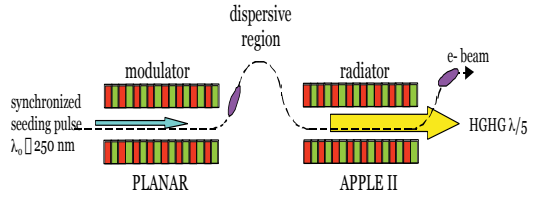

Fig.2 Set-up of the FEL-I undulators line based on a single-stage HGHG mode of operation.

HGHG using an external laser as input seed is foreseen for FEL-I. Such a technique allows the optimization of the stability and of the flexibility of the system, as well as the spectral properties of the output signal. The undulators line consists of sections of about 2.5 m, separated by drift sections 0.75 m long dedicated

to diagnostics and quadrupole focusing (FODO lattice). Planar undulators will be used in the upstream areas, where mainly the electron-bunching process is important. APPLE-II type of undulators, allowing the control of the polarization of the output signal, will be used to produce the final radiation [1].

RF PHOTO-INJECTOR

Simulations have been performed with a maximum of 10^5 macro-particles for 1 nC of total charge.

The ASTRA tracking code [4] simulates the beam generation in the rf photo-cathode gun and its transport to the end of the first section of the pre-injector. It takes into account 1D space-charge effects.

The new gun for the Fermi at Elettra project is a re-scaled version of the LCLS gun model [3]; it comprises an external solenoidal field of 0.3 T. Ferrario's working point [5] defines the distance from the cathode at which the total emittance (geometric and thermal) reaches a minimum; here the emittance is freezed by the solenoid [6]. Table 2 lists the parameters of the electron beam at the exit of the gun [3,6], in agreement with the specifications for FEL-I (see Table 1).

Table 2. Electron beam parameters at the exit of the rf photo-cathode gun. Simulations by ASTRA code.

Beam parameter	Gun field [MV/m]		Units
	140	120	
Beam size rms	340	330	μm
Normal. emittance rms	0.57	0.63	μm rad
Electron energy (E)	8	6	MeV
Bunch length (σ_z)	900	930	μm
Energy spread (σ_δ)	0.21	0.27	%
Peak current (I)	0.104	0.102	kA

BUNCH COMPRESSION

The beam distribution generated by ASTRA is transported by ELEGANT [7] to the magnetic chicane. The appropriate energy-position correlation is created by the "out of crest" acceleration in the second section of the pre-injector.

The following HC is described by a π-mode standing wave pill-box. It linearizes the longitudinal phase space in order to increase the compression efficiency. Its parameters are estimated by means of analytical formulas [8] and refined through an optimization in ELEGANT.

The bunch compressor is a symmetric structure of 4 rectangular bending magnets. The optics limits the effects of CSR, mainly the transverse emittance growth and the micro-bunching in the energy distribution. CSR has been taken into account also in the drifts following the dipoles.

A compression factor of 7 produces a peak current of 1 kA in a symmetric charge distribution, which may be modified at occurrence by a proper setting of the HC and of the bunch compressor. The beam parameters before and after the compression are listed in Table 3. The present scheme provides $R_{56} = -1.1 \times 10^{-2}$ m and $T_{566} \times \sigma_{\delta,i} = 1.8 \times 10^{-5}$ m. The emittance growth is limited to 10% in both planes by the optics arrangement.

Table 3. Electron beam parameters before and after the compression.

Beam parameters	Before	After	Units
Electron energy (E)	78.1	68.3	MeV
Bunch length (σ_z)	907	128	μm
Energy spread (σ_δ)	3.2	3.5	%
Peak current (I)	0.1	1.0	kA

LINAC

Wakefield in the BTW sections

The accomplishment of the FEL-I phase foresees the beam acceleration in 5 linac sections, each giving a maximum energy gain of 150 MeV (conservative value).

The Green functions for the transverse and longitudinal wakefield in the Elettra linac sections have been studied and well defined through numerical calculations [9]. The longitudinal wakefield interacts with the charged particles changing their energy. Thus it perturbs the bunch energy distribution inducing a correlated energy spread. The FEL-I electron beam simulations presented here include the longitudinal wakefield only, which is expected to be much stronger with respect to the SLAC-type [10] and TESLA [11] cases (Fig.3).

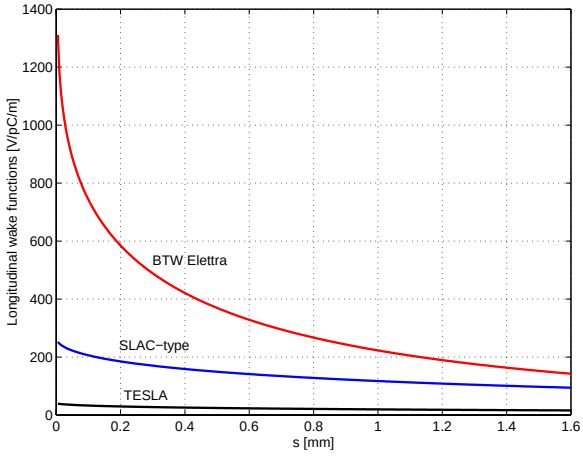

Fig.3 Wake function (in V/pC/m unit) vs. longitudinal coordinate behind the electron bunch in the ELETTRA, TESLA and SLAC-type accelerating sections. The origin s=0 coincides with the unit charge position generating the wakefield.

Studies on the reliability of the ELEGANT tracking in presence of wakefields have been carried out through a comparison with results obtained from an analytical treatment of the wake potential [12,13]. The beam transport has been investigated both for the case of a single section (i) and for the whole linac (ii). A gaussian distribution has been used as input, with initial central

energy and energy spread negligible with respect to the total energy gain.

In the analytical treatment the beam is propagated through (3/4)π TW sections. The ELEGANT simulation is performed using analogous π-mode SW sections, instead [7]. Simulations show that the particle distribution is practically unmodified by the propagation in one accelerating section.

Fig.4 for case (i) and Table 4 for the case (ii) permit a comparison of the final correlated energy spread obtained with the two methods. In both cases the agreement is quite good; the discrepancies are in the tolerances of the different wakefield implementations (few percent).

It is worth pointing out that there exists a minimum for the correlated energy spread induced by the simultaneous interaction of the accelerating field and of the wakefield with the electron beam. In particular, larger amplitudes of the rf voltage (that is larger energy gains) counteract the wakefield effect, thus reducing the growth of energy spread.

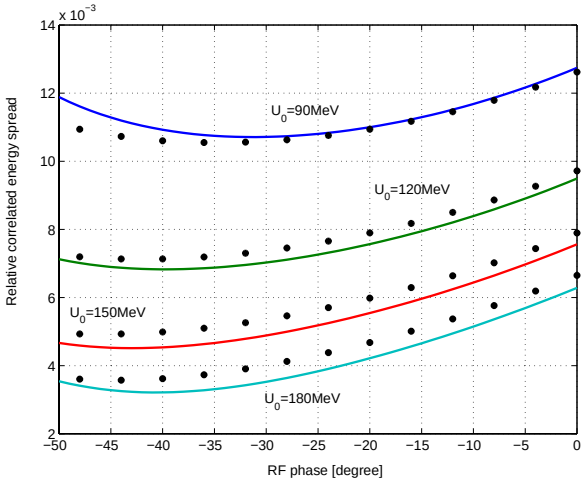

Fig.4 Relative correlated energy spread as function of the rf phase, at different energy gains in one accelerating section of the Elettra linac. Comparison of results from the analytical treatment of the wake potential (solid lines) and from ELEGANT tracking (dots).

Table 4. Results from the analytical method and ELEGANT tracking along 5 linac sections.

	Analytical Method	ELEGANT
Central Energy [MeV]	699.6	699.3
Relative Correlated Energy Spread (rms)	0.44%	0.45%

Arbitrary initial conditions in the energy and charge distributions cannot be described analytically in a satisfactory way. However, such distributions have been approximated by means of known functions in the analytical treatment. In these cases the two methods produce results differing to 30% as maximum, but the qualitative behaviour of the curves is still very similar.

Wakefield compensation

The evolution of phase space along the linac shows that the wakefields enhance a nonlinear region in the bunch energy-position correlation, producing a minimum at $\delta \approx -0.2\%$ for the correlated energy spread (corresponding to the highest peak in Fig.5); it is located in the bunch tail ($t > 0$ in Fig.6).

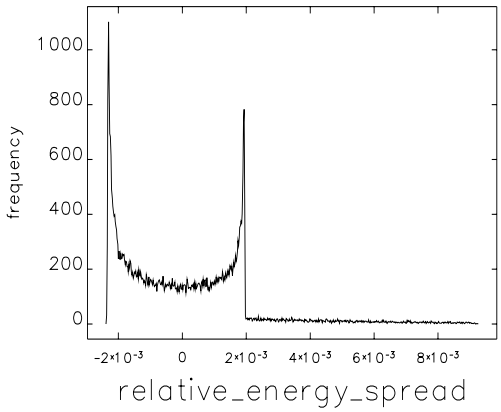

Fig.5 Frequency histogram of the relative correlated energy spread in the elecron bunch at the exit of the FEL-I linac. A large amount of the particles assumes an energy spread $\delta \approx -0.2\%$, as shown by the highest peak.

The minimization of the correlated energy spread can be performed in a similar way both by the analytical treatment and by ELEGANT: the rf phases are forced to the minimum, accordingly with the constraint of a final beam energy of 700 MeV. This condition requires thus maximum peak voltages.

A very simple linac optimization foresees identical parameters for the 5 sections, with maximum peak voltage (150 MeV energy gain) and -31^{o} rf phase for an "out of crest" bunch acceleration. The optimization provides $\sigma_z = 128$ μm and $\sigma_\delta = 0.2\%$, at a central energy of 699.5 MeV.

However, the FEL performance is determined by the uncorrelated slice-energy spread at the maximum current, i.e., the total energy spread over a cooperation length of the FEL [14]. In our case the typical cooperation length (L_c) is less than 2 μm. From Fig.6 and Fig.7 it follows that at the peak of the bunch-current the correlated energy spread is linear. Hence, the total energy spread within a cooperation length can thus easily be estimated by $L_c \cdot \sigma_\delta / 2\sigma_z = 1.6 \cdot 10^{-5}$, well below the limit stated in Tab.1. We also note that the estimated peak current of ~ 1 kA for FEL-1 fully satisfies the condition quoted in the table.

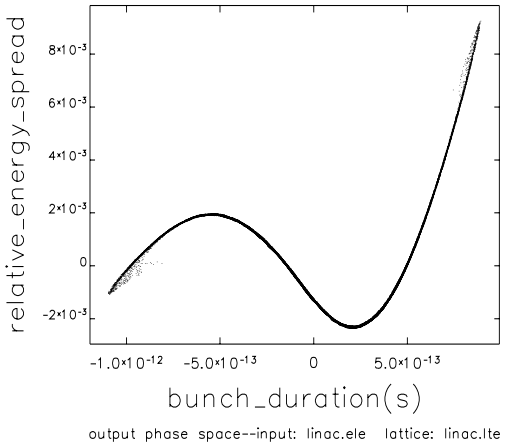

Fig.6 Longitudinal phase space (relative correlated energy spread vs. time) of the bunch at the exit of the FEL-I linac. The rf phases of the accelerating sections have been set for the wakefield compensation.

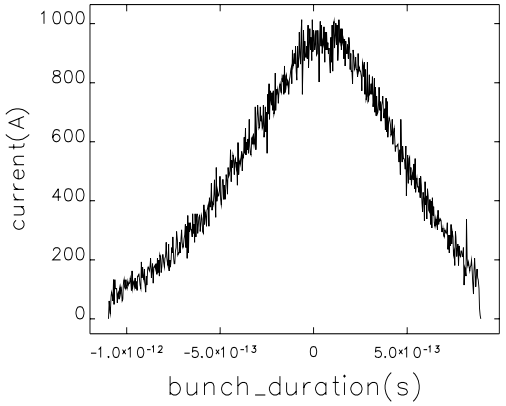

Fig.7 Current distribution along the bunch at the exit of the FEL-I linac.

CONCLUSIONS

Electron beam simulations for the FEL-I phase [1] of the Fermi at Elettra project [2] have been performed. Special care has been taken in the study of the longitudinal dynamics in the Elettra linac sections.

A fast analytical algorithm has been developed [12,13] to evaluate the evolution of the correlated energy spread in presence of longitudinal wakefields [9], as well as to optimize the rf phases for the wakefield compensation. The algorithm provides the same results obtained by the ELEGANT tracking on analytical beam distributions. It allows qualitative estimations in more realistic cases.

The strong longitudinal wakefield in the Elettra linac sections does not result to be critical for the FEL-I phase: the correlated energy spread has been minimized to the 0.2% rms value. It provides slice features in full agreement with the specifications [1,2]. Moreover, a wide fraction of the electron bunch is compatible with the seeded mode of operation; in this case, the central energy deviation may be easily compensated by the tuning of the wavelength through the gap variation of the undulator.

REFERENCES

[1] R.J.Bakker et al., "Fermi at Elettra: 100 nm – 10 nm single pass fel user-facility", presented at EPAC04 (July 2004, Lucerne, Switzerland).

[2] Fermi@Elettra Machine Project Update, Sincrotrone Trieste (2003, Trieste, Italy).

[3] V.A.Verzilov et al., "Photo-injector study for the ELETTRA linac FEL", presented at FEL-2003 (September 2003, Tsukuba, Japan).

[4] K.Flottman, "ASTRA, A Space Charge Tracking Algorithm", http://www.desy.de~/mpyflo/

[5] M.Ferrario, SLAC-PUB 8400, 2000.

[6] P.Craievich, V.Verzilov, ST/M-03/02, Elettra (May 2003, Trieste, Italy).

[7] M.Borland, http://www.aps.anl.gov/asd/oag/

[8] P.Emma, LCLS-TN-01-1 (November 2001, SLAC).

[9] P.Craievich, T.Weiland and I.Zagorodnov, "The short range wakefield in the BTW accelerating structure of the Elettra linac", presented at 8TH ICAP (June 2004, St.Petersburg, Russia).

[10]T.Weiland, I.Zagorodnov, "The short range transverse wake function for TESLA accelerating structure", TESLA Report 2003 – 11 (2003).

[11]C.J.Bocchetta et al., "Overview of FERMI@ELETTRA a Proposed Ultra Bright Coherent X-ray Source in Italy", presented at FEL2002 (9-13 September 2002, Argonne, Illinois, USA).

[12] A.Novokhatski, M.Timm and T.Weiland, "Single Bunch Energy Spread in the TESLA Crymodule" (September 1999, TH Darmstadt, Germany).

[13] P.Craievich, G.D'Auria, S.Di Mitri, "Energy spread in BTW accelerating structures at Elettra", presented at LINAC 2004 (August 2004, Lubeck, Germany).

[14] P.Emma, "Accellerator physics challenges of X-Ray FEL SASE Sources", Proc. of the EPAC2002, Paris, France, p. 49 (2002).

STATUS REPORT ON SPARC PROJECT

A. Renieri*, M. Carpanese, F. Ciocci, G. Dattoli, A. Di Pace, A. Doria, F. Flora, G.P. Gallerano, L. Giannessi, E. Giovenale, G. Messina, L. Mezi, P.L. Ottaviani, S. Pagnutti, G. Parisi, L. Picardi, M. Quattromini, G. Ronci, C. Ronsivalle, E. Sabia, M. Sassi, A. Zucchini, ENEA, Centro Ricerche Frascati, C.P. 65, 00044 Frascati, Italy

D. Alesini, M. Bellaveglia, S. Bertolucci, M.E. Biagini, C. Biscari, R. Boni, M. Boscolo, M. Castellano, A. Clozza, G. Di Pirro, A. Drago, A. Esposito, M. Ferrario, D. Filippetto, V. Fusco, A. Gallo, A. Ghigo, S. Guiducci, M. Incurvati, C. Ligi, F. Marcellini, M. Migliorati, C. Milardi, L. Palumbo, L. Pellegrino, M. Preger, P. Raimondi, R. Ricci, C. Sanelli, M. Serio, F. Sgamma, B. Spataro, A. Stecchi, A. Stella, F. Tazzioli, C. Vaccarezza, M. Vescovi, C. Vicario, M. Zobov, INFN-Frascati, Italy

F. Alessandria, A. Bacci, I. Boscolo, F. Broggi, S. Cialdi, C. De Martinis, D. Giove, C. Maroli, V. Petrillo, M. Romè, L. Serafini, INFN-Milano, Italy

D. Levi, M. Mattioli, G. Medici, P. Musumeci, INFN-Roma1, Roma, Italy

L. Catani, E. Chiadroni, S. Tazzari, INFN-Roma2, Roma, Italy

C.J. Bocchetta, M. Danailov, G. D'Auria, M. Ferianis, Elettra, Trieste, Italy

A. Cianchi, A. D'Angelo, R. Di Salvo, A. Fantini, D. Moricciani, C. Schaerf, Università di Roma Tor Vergata, Roma, Italy

S. Reiche, J.B. Rosenzweig, G. Travish, UCLA, Los Angeles, CA, USA

D.H. Dowell, P. Emma, C. Limborg, D. Palmer, SLAC, Stanford, CA, USA

Abstract

We review the status of FEL source activity of the ongoing SPARC FEL experiment, developed within the framework of a collaboration among ENEA, CNR, INFN, INFM, Sincrotrone Trieste and University of Rome Tor Vergata. The project is aimed at realising a SASE-FEL source, operating in the visible (around 500 nm), with an extended range of tunability down to the VUV (100 nm) by the use of the mechanism of non-linear harmonic generation. The development of the relevant activities foresees the realisation of an advanced 150 MeV photo-injector source, aimed at producing a high brightness electron beams, needed to drive a SASE-FEL experiment, and a 14 m long undulator. We present the status of the design and construction of SPARC FEL device. In particular we discuss the choice of the project parameters, their optimisation and the sensitivity of the SPARC performance to any parameter variation. We will show, using start-to-end simulations, what is the impact of the e-beam and of the undulator parameters on the characteristics of the output laser field and in particular on the amount of the non-linearly generated power at higher harmonics.

* Renieri@frascati.enea.it

INTRODUCTION

The *SPARC* project, funded by the Italian Government in 2003 with a 3 year time schedule, is an R&D activity aimed to develop a high brightness photoinjector for self-amplified spontaneous emission free-electron laser (SASE-FEL) experiments. The installation of the machine at LNF will start on September 2004, and the first beam is expected on June 2006. The SPARC [1] complex is composed of an RF gun driven by a Ti:Sa laser producing 10 ps flat top pulses that hit on a photocathode. The out coming beam is injected into three SLAC accelerating sections to feed a 14 m long undulator (Fig. 1).

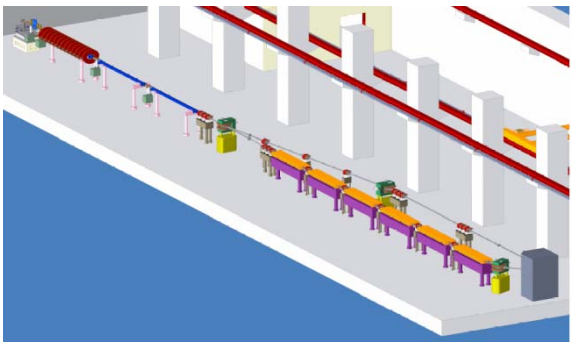

Figure 1: SPARC project layout.

The main goals of the project are:

1. the generation of a high brightness electron beam able to drive a SASE-FEL experiment in the green visible light and higher harmonics generation;
2. the development of an ultra-brilliant beam photoinjector needed for the future SASE-FEL based X-ray sources.

WORKING POINT OPTIMIZATION

The beam current required by the FEL experiment pushes the injector design towards the limits of the state-of-the-art for what concerns pulse charge and pulse shape. The design goal of the SPARC accelerator is to provide a 155 MeV bunch with projected emittance lower than 2 μm and slice emittance lower than 1 μm. The SPARC FEL operates in the diffraction dominated range and peak current is a key parameter for shortening the FEL gain length. Once including possible errors in the undulator system (see next section), the analysis of the SPARC FEL operation shows that, in order to leave a significant contingency margin to ensure full saturation and testing of harmonic generation, a safer parameter set requires a beam having 100 A in 50% of the slices with a slice emittance ≤1 μm. For this purpose a new optimization was performed, with start-to-end simulations and parametric sensitivity studies aiming to reduce the FEL saturation length. The best result was obtained with a scaling approach [2] in which more charge is launched from the cathode. The configuration that gives the minimum emittance corresponds to a working point with 1.1 nC and a pulse length of 10 ps. The overall result is the reduction of the SASE-FEL saturation length from 12 to 9 m at 500 nm wavelength. The beam characterization is shown in Fig. 2, while FEL power as a function of z as obtained with the GENESIS code is reported in Fig. 3. In Tab. 1 and 2 the final parameter sets are reported.

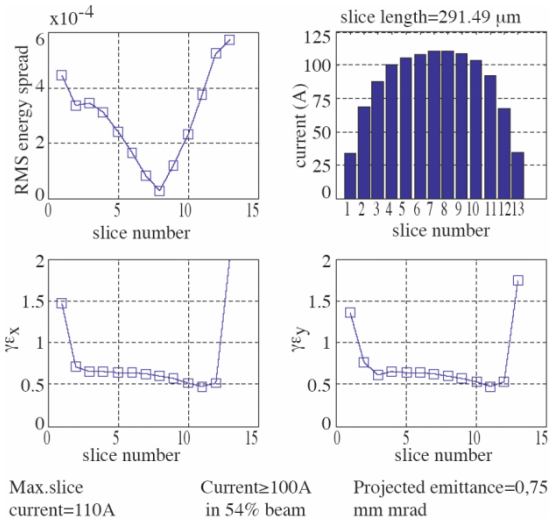

Figure 2: "Slice" electron beam energy spread, peak current, x and y emittances (PARMELA code).

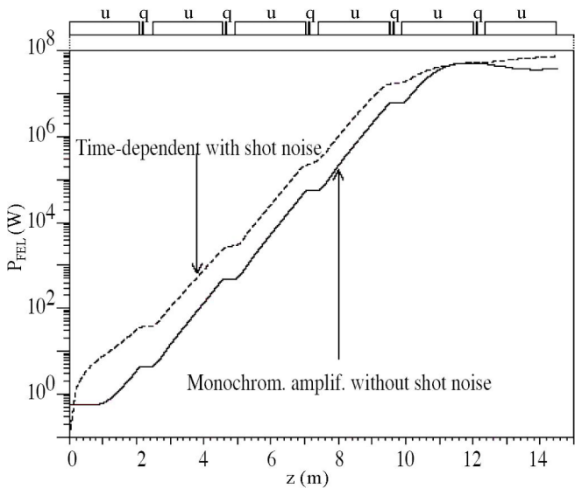

Figure 3: FEL power longitudinal evolution (λ_u = 2.8 cm, K = 2.1413, I = 110 A).

Table 1: Injector parameters.

ELECTRON BEAM	
Electron beam energy (MeV)	155
Bunch charge (nC)	1.1
Repetition rate (Hz)	1-10
Cathode peak field (MV/m)	120
Peak solenoid field @ 0.19 m (T)	0.273
Laser spot size, hard edge radius (mm)	1.13
Central RF launch phase (deg)	33
Laser pulse duration, flat top (ps)	10
Laser pulse rise time 10%→90% (ps)	1
Bunch energy @ gun exit (MeV)	5.6
Bunch peak current @ linac exit (A)	100
RMS normalized transverse emittance @ linac exit (mm-mrad); includes thermal comp. (0.3)	< 2
RMS slice norm. emittance (300 μm)	< 1
RMS longitudinal emittance (deg.keV)	1000
RMS total correlated energy spread (%)	0.2
RMS uncorrelated energy spread (%)	0.06
RMS beam spot size @ linac exit (mm)	0.4
RMS bunch length @ linac exit (mm)	1

Table 2: FEL parameters.

UNDULATOR & FEL	
Undulator period (cm)	2.8
No. of undulator sections	6
Undulator parameter	2.16
Undulator field on axis (T)	0.83
Undulator gap (mm)	9.25
Undulator section length (m)	2.13
Drifts between undulator sections (m)	0.36
FEL wavelength (nm)	500
Saturation length, geometrical (m)	< 14
FEL pulse length (ps)	8
FEL power @ saturation (MW)	> 80
No. of photons/pulse	10^{15}
FEL power @ saturation, 3rd harm. (MW)	> 10
FEL power @ saturation, 5th harm. (MW)	> 0.7

The SPARC project foresees the possibility of extending the tunability range by exploiting the non-linear generation of higher order harmonics. The understanding of the mechanism underlying such a process has required a strong effort involving analytical and numerical means [3] and, as to the SPARC proposal, it has been shown that it is possible to obtain a significant amount of coherent power at higher order harmonics, which guarantees a brightness of third (170 nm) and fifth (100 nm) harmonic two orders of magnitude only below the fundamental.

UNDULATOR SYSTEM

In this type of FEL one of the most significant problems is that of reaching a good level of mechanical precision along the whole length of the undulator, which is a flexible structure. It is therefore evident that one of the first effects to be included in the optimization of the device is that of bending of the undulator section due to the magnetic and gravitational forces (Fig. 4). The variations of the longitudinal profile will be in turn responsible of magnetic field variations, which will provide a kind of inhomogeneous broadening and thus a gain reduction along with an increase of the saturation length.

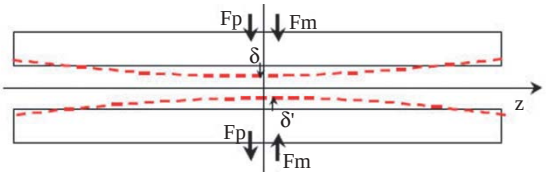

Figure 4: Flexure of the undulator upper and lower faces induced by the attractive magnetic forces and the gravity.

The problem of understanding the undulator bending effects on the SASE-FEL dynamics has been considered by merging two different points of view:

a) a typical engineering approach [4], according to which we have defined the maximum bending as a function of the attractive forces and of the Young modules of the relevant materials;
b) a method based on dynamical simulations [5][6], which have been able to evaluate the effects of a given flexure on the laser performances.

An example of the effects due to the profile variations on the final laser power and on the subharmonics is given in Fig. 5, which shows how such an effect may become significant for values of the maximum deflection above 10 μm. This example yields just an idea of the problems arising within the study of the optimization of the device. There are indeed other effects which cannot be considered by their own and should be combined with the others, as e. g. those associated with the fact that the surface of the undulator poles assembly may not be perfectly parallel.

This fact may combine with possible misalignments between undulator sections and it may induce a further gain reduction (Fig. 6), which has been accurately modelled [6].

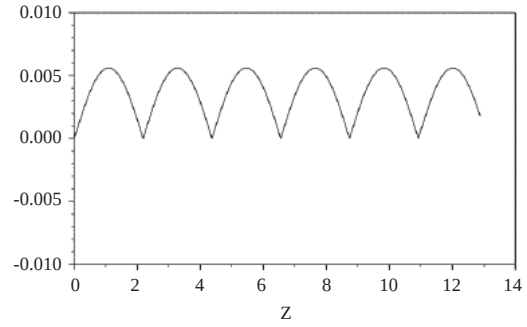

Figure 5a: Longitudinal on axis field variation along the six undulator sections due to the induced flexure.

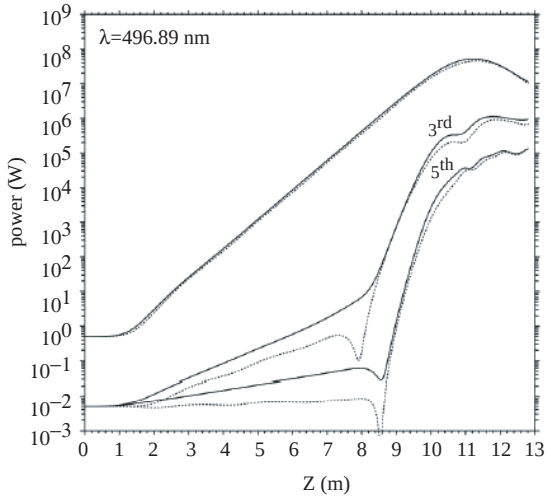

Figure 5b: Effect of the induced flexure on the power evolution of the fundamental and higher order harmonics (solid: no flexure, dots: 10 μm maximum flexure in the centre; Prometeo code).

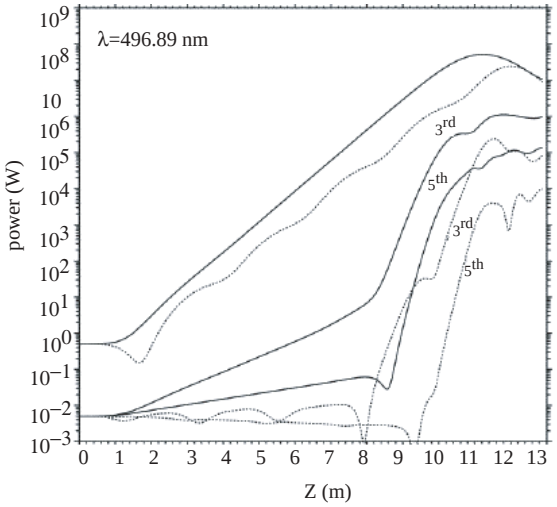

Figure 5c: As in Fig. 5b for 50 μm maximum flexure (Prometeo code).

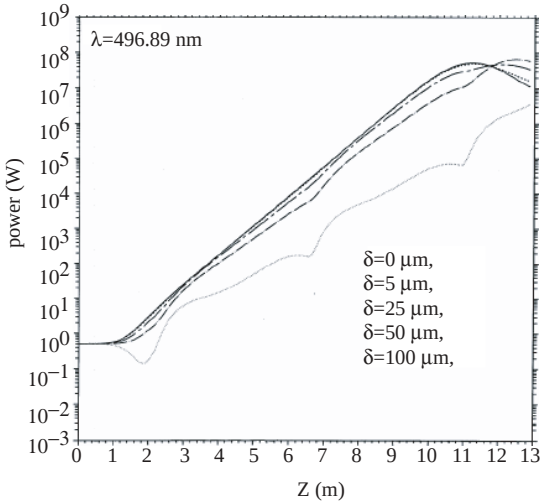

Figure 6: Effect of undulator faces misalignment on the laser power for different values of the maximum flexure δ (Prometeo code).

OPTICAL DIAGNOSTICS

The diagnostic layout is shown in Fig. 7; a diagnostic chamber is positioned in correspondence of each undulator section. Through these chambers the FEL radiation is extracted and transported up to a measurement station placed at the ending part of the FEL.

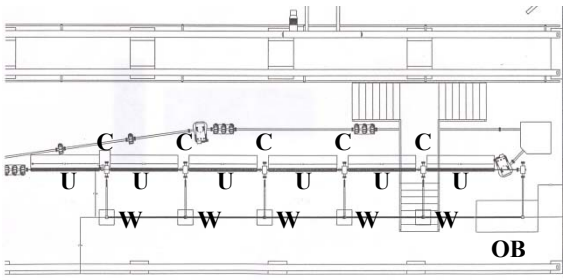

Figure 7: Diagnostic layout. U: undulator sections; C: diagnostic chambers; W: workstations for the analysis of the radiation from each undulator; OB: optical bench.

The study and the design of the diagnostic chamber foresee a series of conditions to be fulfilled. Among them the most significant one is due to the reduced space available for its installation. The distance between the different undulator sections is about 36 cm and within such a space it will be necessary to allocate, along with the diagnostic chamber, the quadrupoles for the electron focusing on the horizontal plane. The schematic layout of the diagnostic chamber is shown in Fig. 8. The diagnostic chamber will host "pop-up" mirrors to extract the FEL radiation as well as electron diagnostics, alignment screens based on transition radiation and all necessary ports to connect to the vacuum pumping system.

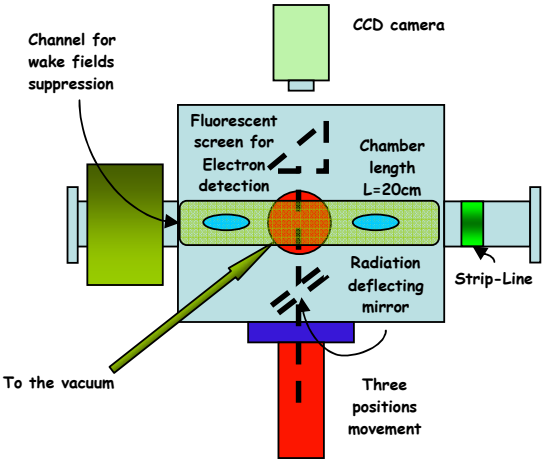

Figure 8: Diagnostics chamber.

A non-interceptive diagnostics, which will be tested at a later stage of the SPARC project, is based on the interaction between the electron beam and a metal grating. It has been shown that such a device is capable of providing quantitative information about the longitudinal bunch profile from the power spectrum of the emitted coherent spontaneous radiation [7].

CONCLUSIONS

The SPARC project has been approved by the Italian Government and funded in June 2003 with a schedule of three years. After the first year the project has been fully defined and the major components have been ordered.

REFERENCES

[1] SPARC Project Team, "SPARC Injector TDR", (www.lnf.infn.it/acceleratori/sparc).
[2] J.B. Rosenzweig and E. Colby, "Advanced Accelerator Concepts", AIP Conf. Proc. 1995, Vol. 335, p. 724.
[3] G. Dattoli, L. Giannessi, P.L. Ottaviani and A. Torre, J. Appl. Phys. (2004); G. Dattoli, these proceedings.
[4] A. Zucchini, "Considerazioni relative alla flessione del supporto e dei magneti a causa del campo magnetico", SPARC Tech. Note 03/007 (www.sparc.it).
[5] F. Ciocci, G. Dattoli, L. Mezi and P.L. Ottaviani, "The effect of the magnetic deflection on the FEL evolution:a dynamical point of view", SPARC Tech. Note 03/005 (www.sparc.it).
[6] F. Ciocci, G. Dattoli, L. Mezi and P.L. Ottaviani, "Angular Tolerances in the SPARC undulator", SPARC Tech. Note 03/008 (www.sparc.it).
[7] G. Doucas, M.F. Kimmitt, A. Doria, G.P. Gallerano, E. Giovenale, G. Messina, H.L. Andrews, J.H. Brownell, "Determination of longitudinal bunch shape by means of coherent Smith-Purcell radiation", Phys. Rev. Special Topics – Accelerators and Beams Vol. 5, 072802 (2002).

ANALYSIS OF INTENSITY FLUCTUATIONS OF SASE USING THE AR MODEL

R. Kato#, S. Kashiwagi, S. Isaka, C. Okamoto, T. Yamamoto, S. Suemine, G. Isoyama,
ISIR, Osaka University, Mihogaoka, Ibaraki, Osaka 567-0047, Japan

H. Sakaki,
J-PARC, Japan Atomic Energy Research Institute, Tokai, Naka, Ibaraki 319-1195, Japan

Abstract

Using the auto-regressive model analysis, we have analyzed the intensity fluctuation of the SASE produced with the L-band linac and the FEL system at the Institute of Scientific and Industrial Research, Osaka University. It has been found that the fluctuation of the SASE intensity is affected by the beam current in the frequency region less than 0.1 Hz and that the contribution ratio of the beam current to the intensity fluctuation of SASE is evaluated to be 18 % in the period longer than 100 seconds.

INTRODUCTION

We are conducting experimental studies on Self-Amplified Spontaneous Emission (SASE) in the infrared region using the L-band linac at the Institute of Scientific and Industrial Research (ISIR), Osaka University [1-3]. The intensity of SASE fluctuates intrinsically because the number of coherent optical pulses generated in an electron bunch changes statistically. In the actual system, however, another factor producing intensity fluctuations also shows up, namely instability of the linac. Generally speaking, it is difficult to distinguish contributions of these two factors in measured intensity fluctuations. We have applied the auto-regressive (AR) model, which is one of the techniques of statistical analysis and has been successfully applied to analysis of instability of rf linacs [4,5], to evaluate the contribution of beam instability in the measured data. In the AR model, the present data can be expressed with a linear combination of the past data plus white noise. By using the AR model analysis, contribution ratios of the beam fluctuations to the intrinsic fluctuations of SASE in measured data can be evaluated. In this paper, we will report results of the analysis of intensity fluctuations of SASE measured at ISIR, Osaka University, using the AR model.

LINAC AND MEASUREMENT SYSTEM

The L-band linac is equipped with a three-stage sub-harmonic buncher (SHB) system composed of two 1/12 and one 1/6 SHBs in order to produce an intense single-bunch beam with charge up to 91 nC/bunch. For the single-bunch operation mode, the electron beam with a peak current up to 28 A (typically 18 A in our experiments) and a duration of 5 ns is injected from a thermionic gun (EIMAC, YU-156) into the SHB system. After being compressed to a single-bunch, the electron beam is accelerated to 11 - 32 MeV in the 1.3 GHz accelerating tube. The electron beam is transported via an achromatic beam transport line to the wiggler for the FEL system. It is the 32 period planar wiggler with the period length of 60 mm. The K-value can be varied from 0.01 to 1.47. The main characteristics of the electron beam and the wiggler are listed in Table 1. Light emitted by the single-bunch beam passing through the wiggler was reflected with a downstream mirror, and led to the measurement room via a 10 m long optical transport line, which was evacuated with a rotary pump. The high vacuum in the beam transport line and the low vacuum in the optical transport line were separated by a 0.2 mm thick, 20 mm in diameter synthetic diamond window. The optical light was detected with a Ge:Ga photoconductive detector cooled with liquid-helium.

We measured the SASE intensity over a period of approximately 12 minutes with an interval of 0.73 s, together with the beam current measured at the entrance of the wiggler. The measured data are shown in Figure 1. The SASE intensity shown by the red lines in the lower part of the figure contains higher frequency components due to the intrinsic fluctuations of SASE, as well as the long-period variations, which are similar to those of the beam current shown by the blue lines in the upper part of the figure.

Table 1: Main parameters of the electron beam and the wiggler

Electron beam	
Accelerating frequency	1.3 GHz
Energy	12.8 MeV
Energy spread (FWHM)	1.97 %
Charge/bunch	10-20 nC
Bunch length	20-30 ps
Peak current	0.5 – 1.0 kA
Normalized emittance	150-200 π mm mrad
Repetition	60 Hz
Mode	Single-bunch
Wiggler	
Total length	1.92 m
Magnetic period	60 mm
No. of periods	32
Magnet gap	120-30 mm
Peak field	0.37 T
K-value	0.013-1.472

#kato@sanken.osaka-u.ac.jp

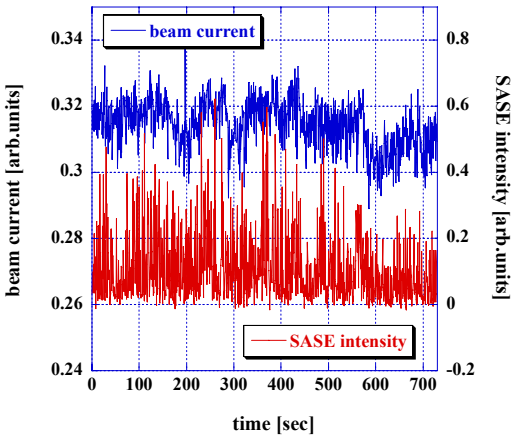

Figure 1: Beam current measured at the entrance of the wiggler (upper) and the SASE intensity (lower) over a period of approximately 12 minutes with an interval of 0.73 s.

AR MODEL

The AR model is a method for time series analysis [6]. It may be applicable to analysis of the feedback structure in a complicated system consisting of mutually interacting elements. For the AR model analysis of the feedback system with two parameters, the present data *X(n)* can be expressed by the linear combination of the past data *X(n-m)*, *Y(n-m)* and the white noise $e_x(n)$:

$$\begin{bmatrix} X(n) \\ Y(n) \end{bmatrix} = \sum_{m=1}^{M} \begin{bmatrix} a_{xx}(m) & a_{xy}(m) \\ a_{yx}(m) & a_{yy}(m) \end{bmatrix} \cdot \begin{bmatrix} X(n-m) \\ Y(n-m) \end{bmatrix} + \begin{bmatrix} e_x(n) \\ e_y(n) \end{bmatrix}, \quad (1)$$

where M is a regressive number. The optimum regressive number M is derived with FPE (Final prediction error)[7] or AIC (Akaike information criterion) [8]. Fitting the eq. (1) to a set of time series data, we obtain the factor a_{ij} and the noise e_i. These factors and noises show the feedback system modelled on the computer.

Assuming that the noises $e_x(n)$ and $e_y(n)$ are equal to zero, the system will either converge or diverge. When an impulse noise is applied to the feedback system in the stationary state without noise, it will attenuate soon for the stable system. By analysing the impulse response of the system, it is possible to know how the perturbation propagates with time among the components, and whether the system is stable or not. This method is called "impulse response analysis" and gives a physical image of the feedback structure in the time domain. Although a delta function impulse is applied to a component, its response is not like the delta function, but has a tail, since the component is influenced by its own past values and the other components.

The power spectrum is defined as the Fourier transform of an auto-covariance of the fluctuation data. Fractional factors of the influences due to the each intrinsic noise power contributing to the power spectrum are called the noise power contribution ratios. By analyzing the noise power contribution ratios, we can know which is the most influential component in the system.

ANALYSIS WITH THE AR MODEL

Impulse response

The SASE intensity and the beam current shown in Figure 1 are analysed with the impulse response analysis

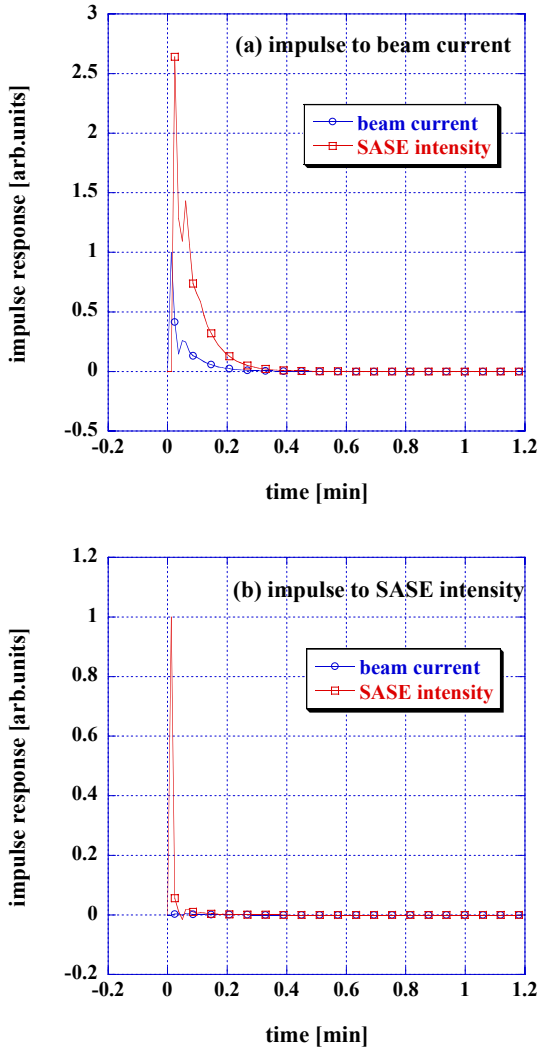

Figure 2: Impulse responses of the system for (a) impulse given to the beam current and (b) to the SASE intensity. The blue and the red lines indicate temporal responces of the beam current and the SASE intensity, respectively. The impulse given to the beam current influences the SASE intensity, but that to the SASE intensity does not affect the beam current.

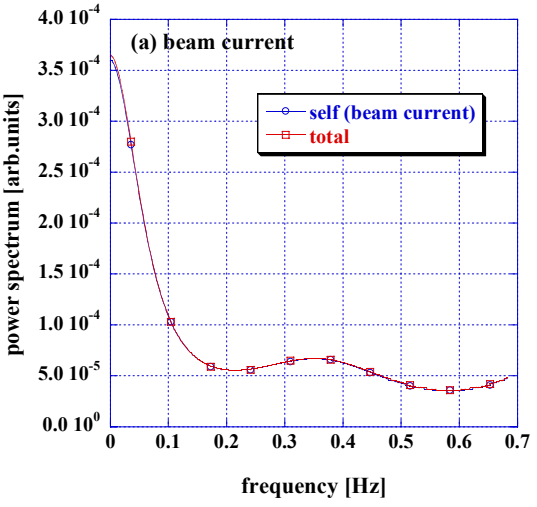

Figure 3: Power spectra (a) of the beam current and (b) of the SASE intensity. The red lines indicate the power spectra. The blue ones show spectra due to the own intrinsic noise power contributing to the power spectrum.

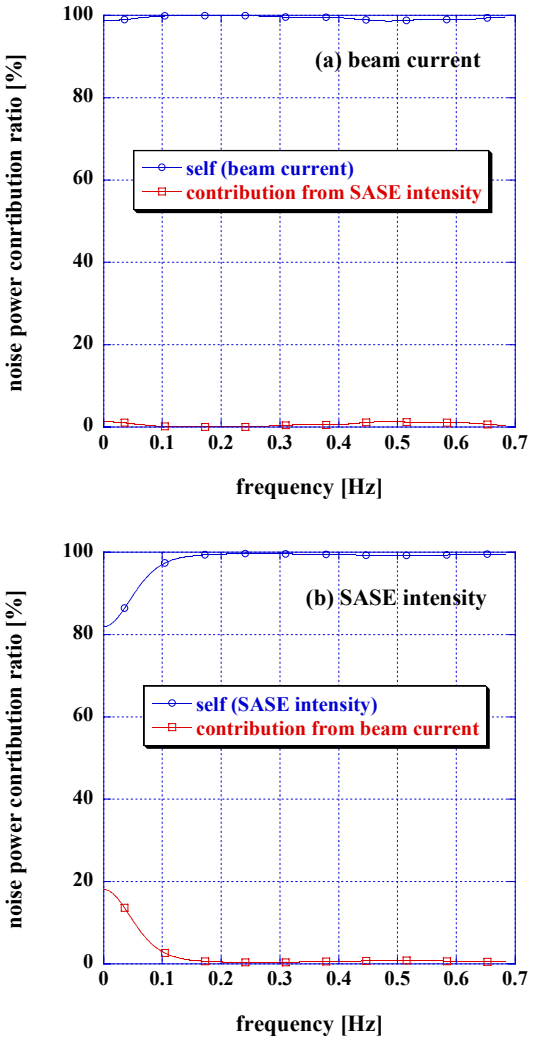

Figure 4: Noise contribution ratios (a) of the beam current and (b) of the SASE intensity. The blue and the red lines indicate the ratio of the power contribution due to the beam current to the power spectrum and that of the SASE intensity to the power spectrum, respectively.

method. Results of the analysis are shown in Figure 3, in which the order of the regressive number M is chosen to be 4 with the AIC for the measured data. The upper panel (a) shows the response of the system when the impulse is given to the beam current and the lower panel (b) to the SASE intensity. The vertical units in the figure are volts and the horizontal ones are minutes. When the beam jumps up from zero, SASE is generated and the intensity goes down gradually as the beam current decreases, but with a delay as shown in the panel (a). The result of the analysis is, (a): impulse to the beam current influences the SASE intensity, (b): impulse to the SASE intensity does not affect the beam current. The result is quite reasonable and does not contradict physical understanding. It shows that the AR model can be successfully applied to the measured data.

Power spectrum

Figure 3 shows results of the power spectrum analysis. The power spectrum of the beam current in the panel (a) shows that the frequency component less than 0.1 Hz is dominant and that the total spectrum is filled up with the power spectrum of the beam current, which indicates that the beam current is not influenced by the SASE intensity. On the other hand, the power spectrum of the SASE intensity in the panel (b) shows no significant peaks, and

it is flat and constant over the frequency range shown in Figure 3. The total power spectrum in the panel (b), however, shows a peak centred at zero frequency, which indicates the contribution of the other component, or the beam current. This means that fluctuations of the measured SASE intensity is composed of the lower frequency component due to the beam current and the white component due to the intrinsic fluctuation of SASE.

Noise power contribution ratio

Figure 4 shows noise power contribution ratios of the power spectra shown in Figure 3. The beam current is not affected by the SASE intensity, but the SASE intensity is affected by the beam current in the frequency region lower than 0.1 Hz. The contribution ratio is about 18 % at the frequency of 0.01 Hz.

SUMMARY

In order to evaluate the contribution of the beam current to the intensity fluctuation of the SASE numerically, we measured the beam current and the SASE intensity simultaneously and analysed the measured data with the AR model. The results of the analysis show that the power spectrum due to the SASE intensity alone has no frequency dependence, while the peak shows up due to fluctuation of the beam current in the frequency region lower than 0.1 Hz, of the total power spectrum of the measured SASE intensity. The noise power contribution ratio of the beam current to the intensity fluctuation of SASE was evaluated to be 18 % in the period longer than 100 seconds.

REFERENCES

[1] R. Kato, et al., Nucl. Instr. and Meth. in Phys. Res. A 445 (2000) 164.
[2] R. Kato, et al., Nucl. Instr. and Meth. in Phys. Res. A 475 (2001) 334.
[3] R. Kato, et al., Nucl. Instr. and Meth. in Phys. Res. A 483 (2002) 46.
[4] H. Sakaki et al., T.SICE Vol.35, No.10 (1999) 1283-1291.
[5] R. Kato, et al., Nucl. Instr. and Meth. in Phys. Res. A 528 (2004) 244.
[6] H. Akaike, Ann. Inst. Statist. Math., Vol. 20 (1968) 425-439.
[7] H. Akaike, Ann. Inst. Statist. Math., Vol. 23 (1971) 163-180.
[8] H. Akaike, IEEE Trans. Vol. AC-19 (1974) 716-723.

LINAC LATTICE AND BEAM DYNAMICS FOR X-RAY FEL AT PAL

E.-S. Kim*, M. Yoon, D.-E. Kim and S.-J. Park
Pohang Accelerator Lab., POSTECH, Pohang, KyungBuk, 790-784 KOREA

Abstract

The PAL-XFEL is a fourth generation light source project to produce soft and hard X-rays which is based on the self-amplified spontaneous emission (SASE) free-electron laser. The XFEL facility consists of a new photoinjector, a 1 GeV new linac, a 2.0 GeV existing linac, with two bunch compressors and long undulators to generate intense radiation. In this paper, we present lattice design of the linacs, bunch compressors, beam transport line, tuneable matching sections for the 3 GeV soft X-ray FEL facility and show results of start-to-end beam simulations that have performed to estimate FEL performance in the designed lattice.

INTRODUCTION

A 2.0 GeV linac in PLS had been used as an injector for 2.5 GeV PLS storage ring which is a third generation light source since 1994. Furthermore from September 2002, the linac has being used for full energy injection of the 2.5 GeV storage ring[1]. For this purpose operating time of the linac is less than 10 %. With the requirement for next generation light sources, the linac is being intensively considered as a facility for soft[3] and hard X-ray FEL, which will include the extension of the linac to achieve the energy of 3.0 GeV.

In this paper, we present concept of designed lattice and show the results on the first start-to-end simulations for an option of the soft X-ray FEL. For this simulation, injection beam in LCLS with energy of 135 MeV, emittance of 0.97 μm rms and bunch length of 870 μm rms and bunch charge of 1 nC was utilized for the particle tracking[2]. Code ELEGANT[4,5,6,7] was used up to 3.0 GeV at undulator entrance to estimate the FEL performance in the designed FEL lattice. Figure 1 shows a designed schematic for 3 GeV soft X-ray FEL in PAL.

LATTICE DESIGN

The designed PAL-XFEL facilities are composed of a 1 GeV new linac that will be constructed, one X-band section, two bunch compressors, a 2GeV existing linac, a beam transport linac, four matching sections and undulator beam lines. The Figure 2 shows Twiss parameters for the PAL-XFEL from end of the injector to undulator entrance. The gun and injector linac are excluded in Figure 2. In the following subsections, we will give investigations on design concept, and beam and machine parameters in the designed lattice.

* eskim1@postech.ac.kr

1 GeV new linac

Six quadrupole magnets just after the injector are used to match the beta functions into the new linac. The 0.6 m long X-band rf section is inserted just prior to the first bunch compressor to obtain the better linearity of the energy-time correlation along the bunch. The X-band section is set to the off-crest phase of -175 degree and the beam energy is reduced by 19 MeV from 370 MeV to 351 MeV in the section, which has the gradient of 31 MV/m. L1 linac in the new linac accelerates the beam from 135 MeV to 350 MeV with off-crest angle of -25 degree and provides the linear energy-time correlation that is required in the first bunch compressor. The L1 linac consists of 4 3-meter S-band rf structures. Because of the large off-crest rf phase angle and relatively long bunch length, the rms energy spread in L1 linac increases from 0.19 % to 1.41 %. L2 linac in the new linac accelerates the beam from 350 MeV to 1.05 GeV with off-crest angle of -25 degree and provides the linear energy-time correlation that is also required in the second bunch compressor. The L2 linac consists of 16 3-meter S-band rf structures and the rms energy spread in L2 linac decreases from 1.5 % to 0.74 %.

Two bunch compressors

Figure 3 shows the bunch compressors which exist in the 1 GeV new linac. Dispersion and beta functions around the first bunch compressor with R_{56}=16.3 mm are shown in Figure 4.

X-band rf structure is upstream of the first bunch compressor. The first bunch compressor is designed compress a 870μm rms bunch to 198 μm rms. Results of longitudinal beam simulations were used to set the bunch length of 198 μm rms in incoming second bunch compressor. Dispersion and beta functions through second bunch compressor with R_{56}=22.4 mm are shown in Figure 5.

The second bunch compressor is designed compress a 198 μm rms bunch to 35 μm rms. The parameters of the first and second bunch compressors are listed in Table 1. The bunch length after second bunch compressor can be varied by controlling parameters of R_{56} in second bunch compressor. Accordingly, the R_{56} of the second bunch compressor is adjustable to satisfy requirements of the different bunch lengths for the option of the soft and hard X-ray. Beta functions are kept to low values at the exit of the bunch compressors to minimize degradation of emittance due to coherent synchrotron radiation. Each bunch compressor has also a short length of about 6 m to reduce the effects of coherent synchrotron radiation.

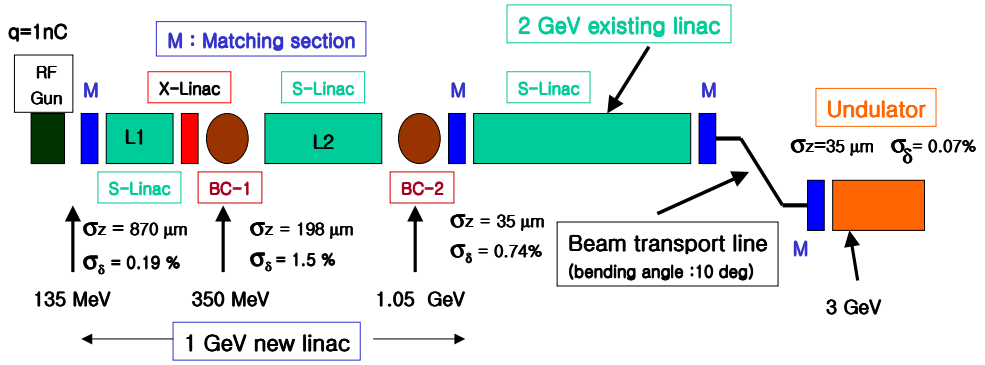

Figure 1: Schematic for a 3.0 GeV soft X-ray FEL in PAL.

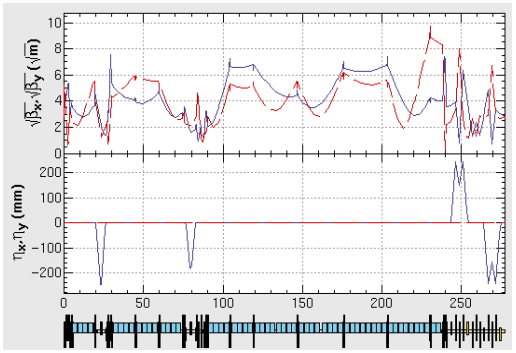

Figure 2: Twiss parameters for PAL soft X-ray FEL from injector exit to undulator entrance.

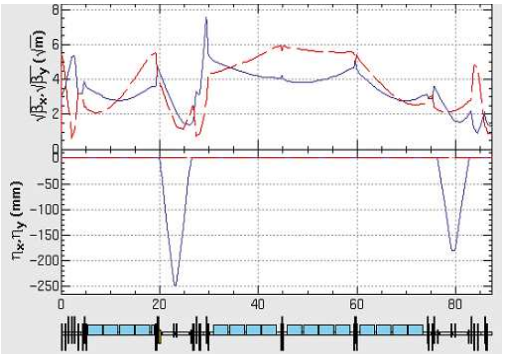

Figure 3: Twiss parameters for the 1 GeV new linac. It includes two bunch compressors, 16 accelerating structures and two matching sections. Matching sections are inserted for matching of optics between injector and L1 linac, and between second bunch compressor and the existing linac. Injector is excluded in this figure.

Existing linac

The existing linac begins at 90 m and ends at 235 m. It includes 42 3-meter rf structures and they will be used for the energy acceleration of 2 GeV for FEL facility. Newly designed lattice for the existing linac is shown in Figure 6. The short bunch of 35 μm rms in the linac effectively eliminates transverse wakefields as a source of emittance growth and the rms energy spread decreases from 0.74 % down to 0.07 % in the linac. The rf phase angle in the linac is set to -10 degree to improve energy stability.

Matching sections

Four matching sections are inserted in order to provide adjustable beta-matching in each system of the designed lattice. First matching section is located at the position between injector exit and L1 linac. Second one is inserted to match optics between the 1 GeV new linac and the existing linac. Third one is inserted to match optics between the existing linac and the beam transport line. The optics matching at the undulator entrance is performed by fourth one to obtain average beta funtions of $\sim$10-meter in the undulator. All matching sections are composed of six quadrupoles. Figure 7 shows the beta functions in the matching section between the new linac and the existing linac.

Beam transport line

Figure 8 shows dispersion and beta functions along 3 GeV beam transport line. The system with four dipole magnets is used for beam transport between the existing linac and undulator beam line, and a quadrupole triplet exists between dipole magnets. The net R_{56} in the four dipole system is designed to have almost zero by making the dispersion function to be reverse sign in the center of the four bending magnets. Each bending angle in the bending magnets with 1 m long is given by +5, +5, -5, -5 degree, respectively.

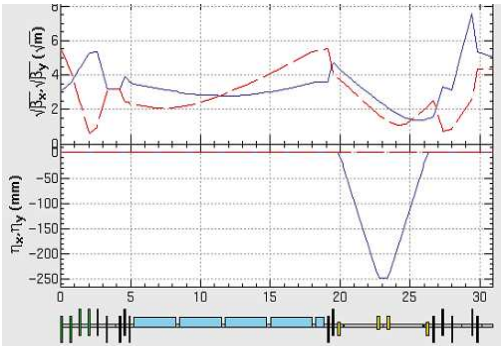

Figure 4: Beta function and dispersion functions around first bunch compressor. A X-band rf is located at upstream of first bunch compressor. 12 S-band rf structures with off-crest phase of -25 degree are located at upstream of the X-band rf section.

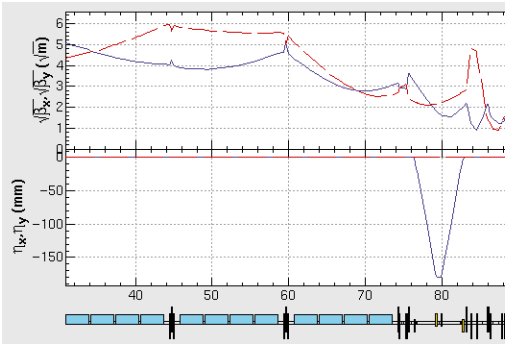

Figure 5: Beta function and dispersion functions around second bunch compressor. 12 S-band rf structures with off-crest angle of -25 degree are located at upstream of the second bunch compressor.

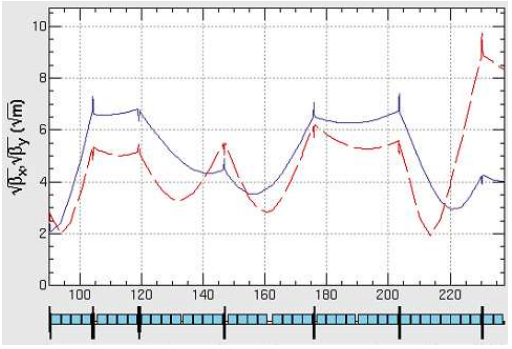

Figure 6: Newly designed beta functions along the existing linac. RF phase angle and energy acceleration for the FEL schematic are set to 10 degree and 2 GeV, respectively.

RESULTS ON START-TO-END BEAM SIMULATION

A start-to-end simulation using the code ELEGANT has been performed to optimize beam parameters for soft X-ray FEL. Our full simulation uses the beam that comes from the LCLS photoinjector which produces charge of 1 nC, bunch length of 2.9 ps rms, relative energy spread of 0.19 % rms and emittance of 0.97 μm rms. The L1 linac is used for energy chirp before the beam enters the X-band rf section. A bunch compression factor of 23.7 and a peak current of 10 KA in the bunch length of 105 fs rms were obtained by the simulation. The bunch compression occurs at beam energy of 350 MeV and 1.05 GeV. Voltage and phase downstream the bunch compressor were also optimized to reduce the energy spread. Table 2 shows the beam parameters at the undulator entrance in the beam energy of 3 GeV.

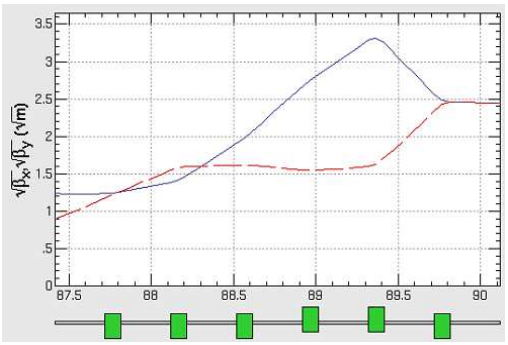

Figure 7: Beta functions in the tuneable matching section between second bunch compressor in the new linac and the existing linac.

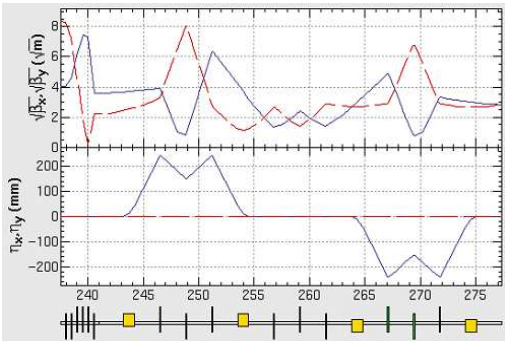

Figure 8: Beta and dispersion functions in the beam transport line with four bending magnets. Each bending angle in the bending magnets is +5, +5, -5, -5 degree, respectively. First bending magnet corresponds to BAS2.

CONCLUSIONS

We have performed lattice design for the 3 GeV PAL-XFEL project and optics was designed to minimize degradation of the emittance and energy spread due to the CSR and wakefields. Start-to-end beam simulations based on the parameters for soft X-ray FEL were also performed. These designed works have demonstrated the beam param-

Table 1: Parameters of first and second bunch compressors.

Parameter	**1st BC**	**2nd BC**
Beam energy	350 MeV	1.05 GeV
Ini. rms bunch length	870 μm	198 μm
Final rms bunch length	198 mm	35 μm
Ini. rms relative energy spread	1.41 %	0.74 %
Final rms relative energy spread	1.5 %	0.74 %
Magnetic field	0.5 T	0.36 T
R_{56}	16.3 mm	22.4 mm
T_{566}	-9.4 mm	-33.8 mm
Bending angle	5.04^o	3.66^o
Maximum dispersion	-250 mm	-180 mm
Length of bending magnet	203 mm	203 mm

Table 2: Beam parameters in the entrance of the undulator.

Parameter	**Units**	**Values**
Beam energy	GeV	3
RMS bunch length	μm	35
RMS relative energy spread	%	0.07
Norm. trans. emittance(H/V)	μm	1.2/1.3
Bunch charge	nC	1

eters and feasibility of soft X-ray FEL with wavelength of around 30 Angstron in PAL.

REFERENCES

[1] E.-S. Kim et. al, Proc. Particle Accelerator Conf., Portland, p.3114 (2003).

[2] LCLS Design Study Report, SLAC-R-521 (1998).

[3] M. Borland, APS LS-287, Sept. 2000. http://www.aps.anl.gov/techpub/IsnotesTOC.html.

[4] M. Borland, XX International Linac Conf., Minterey, p. 833 (2000).

[5] S. Reiche, et. al., SLAC-PUB-9369 (2002).

[6] P. Emma, LCLC-TN-o1-1, Nov. (2001).

[7] M. Yoon, et. al., In these proceedings.

DESIGN STUDY ON 0.3-NM PAL XFEL

J. S. Oh, I. S. Ko, and W. Namkung, PAL/POSTECH, Pohang 790-784, Korea
Y. Kim, DESY, D-22603 Hamburg, Germany

Abstract

PAL is operating a 2.5-GeV electron linac as a full-energy injector to the PLS storage ring. The PAL linac can be converted to a SASE-XFEL facility (PAL XFEL) that supplies coherent X-rays down to 0.3-nm wavelength. It requires a 3-GeV driver linac and a 60-m long in-vacuum undulator with a 3-mm gap and a 12.5-mm period to realize a hard X-ray SASE-FEL. The linac should supply highly bright beams with emittance of 1.5 mm-mrad, a peak current of 4 kA, and a low energy spread of 0.02%. FEL performance is very sensitive to electron beam parameters. The beam quality is degraded along the undulator trajectory due to the energy loss and the wake field. Also the FEL gain is reduced by errors in the undulator fields and beam trajectories. The preliminary design details for the 0.3-nm PAL-XFEL are presented with parametric analysis.

INTRODUCTION

PAL operates a 2.5-GeV electron linac, the 3rd largest in the world, as a full-energy injector to the PLS storage ring [1]. The PAL 2.5-GeV linac can be converted to an X-ray free electron laser (XFEL) facility driven by a self-amplified spontaneous emission (SASE) mode, which supplies coherent X-rays down to 0.3-nm wavelength. The undulator length has to be less than 60 m considering available site area and reasonable cost. Table 1 shows the comparison of single bunch specifications between the PLS linac and PAL XFEL. The linac should supply highly bright 3-GeV beams of which emittance of 1.5 mm-mrad, a peak current of 4 kA, and a low energy spread of 0.02% [2]. Normalized emittance should be improved 100 times, which requires a low emittance gun and high gradient acceleration at low energy region to preserve the emittance. A suitable bunch compression technique is important to realize the high peak current. The performance and stability of the 2.5-GeV linac is also challenging to meet the strict SASE requirements.

Table 1: Bunch specifications of PLS linac and XFEL

Parameter	PLS Linac	PAL XFEL
Beam energy	2.5 GeV	3.0 GeV
Normalized emittance	150 μm	1.5 μm
FWHM bunch length	13 ps	0.23 ps
RMS energy spread	0.26%	0.02%
Bunch charge	0.43 nC*	1.0 nC
Peak current	33 A*	4 kA
Repetition rate	10 Hz	60 Hz

* 2-A gun current and 62% transmission

0.3-NM PAL XFEL

The fundamental radiation wavelength λ_x of an undulator is given by

$$\lambda_x = \frac{\lambda_u}{2\gamma^2}(1 + K^2/2), \quad \gamma = E_o / 0.511, \quad K = 0.934 B_u \lambda_u ,$$

where E_o is the beam energy in MeV, B_u is the peak magnetic field of the undulator in Tesla, and λ_u is the undulator period in cm. Either a short-period undulator or a high-energy beam can provide short-wave radiation. A short-period undulator is preferred for a compact FEL machine. It is important to keep a reasonably large undulator parameter K to obtain a short saturation length. An in-vacuum mini-gap undulator can meet this requirement. This idea was introduced by T. Shintake for the SCSS project at SPring-8 [3].

Each curve in Fig. 1 shows the undulator parameters of the 0.3-nm PAL XFEL for saturation lengths of 40, 50, 60 m and beam energy of 2.5, 3.0, 3.5 GeV, respectively. The possible solution that is reasonably economic, to meet the saturation length of 50 m, is to use an undulator with a 3-mm gap, 12.5-mm period and a 3-GeV beam. For the saturation length of 50 m, the largest gap is 3.4 mm with 16-mm period at the beam energy of 4 GeV.

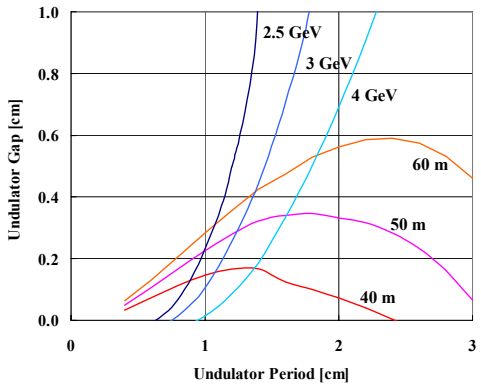

Figure 1: Undulator period and gap length for 0.3-nm SASE for saturation lengths (40, 50, 60 m) and beam energy (2.5, 3, 4 GeV).

Table 2 summarizes the FEL parameters for a 0.3-nm PAL XFEL. The undulator beta value is adjusted to obtain as short a saturation length as possible. Undulator saturation length is approximately 20 times the 3D gain length L_g. The peak brilliance of the PAL XFEL is 10^{12} time higher than the U7 undulator radiation from the PLS 3rd generation storage ring. The hard X-ray spontaneous

radiation from the undulator of the PAL XFEL is also 10^{10} times brighter than the synchrotron radiation from the PLS bending magnet.

Table 2: FEL parameters for 0.3-nm PAL XFEL

Undulator period [mm]	12.5
Undulator gap [mm]	3.0
Peak magnetic field [T]	0.97
Undulator parameter, K	1.14
Beta [m]	15
1D FEL parameter	4.3e-4
1D gain length [m], L_{1d}	1.35
3D gain length correction, η*	0.97
3D Gain length [m], L_g	2.67
Effective FEL parameter	2.2e-4
Cooperation length [nm]	63
Saturation length [m]	52
Peak power [GW]	2.1
Peak brightness [x 10^{32}]**	1.4

* $L_g = (1+\eta)\, L_{1d}$
** photons/sec-mm^2-mrad^2-0.1%BW

Figure 2 shows 3D gain length correction and 3D gain length according to normalized emittance, which are calculated according to M. Xie [4]. An electron beam has to match the transverse phase space for a diffraction-limited photon beam to get the minimum 3D gain correction. The gain correction factor of the PAL XFEL is larger than the LCLS and the TESLA XFEL due to a rather large normalized emittance relative to the natural radiation emittance. However, due to the small periodic length of an undulator, the gain length is smaller than others. Therefore, it is possible to realize a compact X-ray FEL by using an in-vacuum undulator with small period and a low energy linear accelerator.

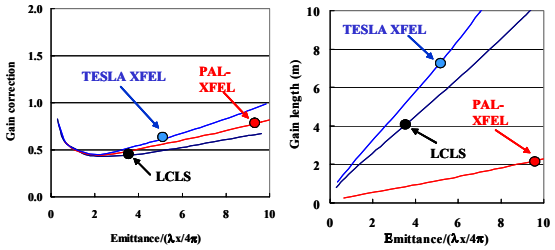

Figure 2: 3D gain correction factor and 3D gain length.

XFEL LINAC DESIGN

The existing 2.5-GeV S-band PLS linac can be converted to X-ray FEL driver by adding a new S-band FEL injector linac. Figure 3 shows the layout of the PAL linac including a new undulator system. The FEL injector linac consists of a laser-driven photo-cathode gun, three S-band accelerating modules (X1, X2, X3), and two bunch compressors (BC1, BC2). The S-band photo-injector consists of a copper cathode and a 1.6-cell S-band RF cavity. The photoelectron beam is generated by 10-ps, 500-μJ, and 260-nm UV laser. It is accelerated to 7 MeV by a high gradient of 120 MV/m.

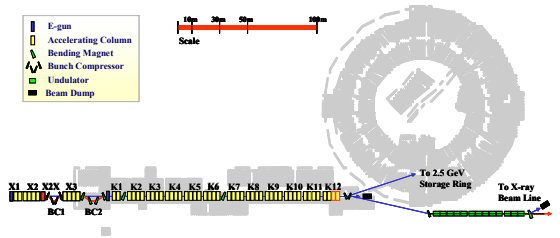

Figure 3: 3-GeV Linac for PAL XFEL.

The injector layout presented in FEL2003 is improved in this work [2]. Instead of the dog-leg layout, the new injector is aligned to the center line of the existing linac to suppress as far possible as emittance degradation due to CSR. All bunch compressors are included in the new injector area to preserve the existing layout of PLS 2.5-GeV linac. Figure 4 shows the layout of the new FEL injector linac and gives details of BC1 which is almost the same as the BC2 design. A suitable energy spread for bunch compression is provided by the modulator unit X2. The 4th harmonic cavity X2X linearizes the non-linear energy spread due to the RF curvature caused by the S-band modulator. The net chicane length is 12.2 m. The total chicane length becomes 17 m including focusing quadrupoles. The maximum beam offset in the middle of the bunch compressor is 33 cm.

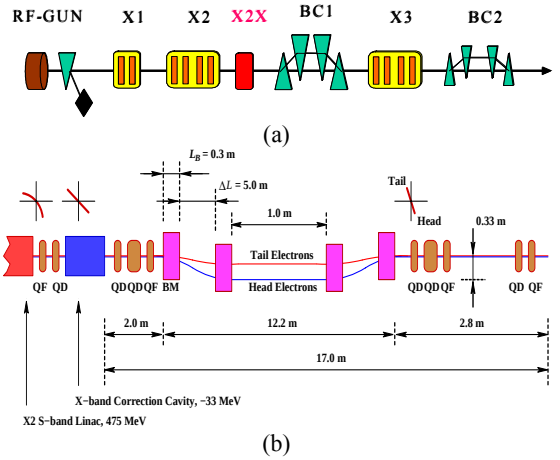

Figure 4: New injector layout (a) and details of BC1 (b).

The lattice design of two bunch compressors is shown in Fig. 5. The lattice is optimised by the following equation for the relative emittance growth [5]. The optimum condition is given at the alpha value of about 0 and beta function of about 3.

$$\frac{\Delta\varepsilon}{\varepsilon} = \sqrt{1 + \frac{(0.22)^2}{36}\frac{\gamma_e^2 N^2}{\gamma\varepsilon_N\beta}\left(\frac{|\theta|^5 L_B}{\sigma_z^4}\right)^{\frac{2}{3}}\left[L_B^2(1+\alpha^2) + 9\beta^2 + 6\alpha\beta L_B\right]}$$

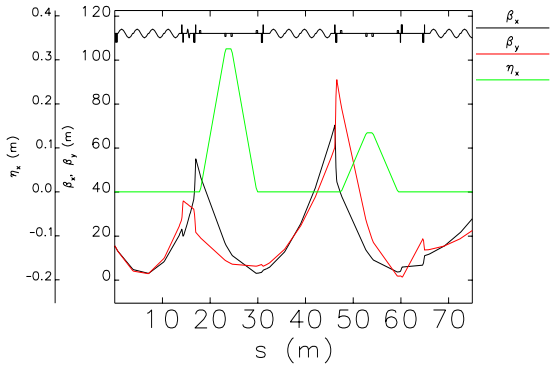

Figure 5: Lattice profile of two bunch compressors.

Against projected parameter dilution due to CSR and chromatic effect, adopted lattice design concepts are as follows: long drift space to reduce bending angle for a required R56, small bending angle at a large energy spread, large compression factor at BC1 and small compression factor at BC2. Strong focusing lattice around BCs to reduce CSR induced emittance growth, small quadrupole length around BCs to reduce the chromatic effects, smaller maximum beta-function of ~ 60 m at the entrance of BC1, larger maximum beta-function at the entrance of BC2 after reducing energy spread are also effective. Against slice parameter dilution due to the micro-bunching instability, the following design concepts are adopted: normal 4-bend chicane instead of S-type chicane, large relative uncorrelated energy spread at BC2 by putting BC2 in the low energy region, no laser beam heater or superconducting wiggler. Table 3 shows the design parameters of the bunch compressor BC1 and BC2.

Table 3: Design parameters of bunch compressors

Parameter	**BC1**	**BC2**
BC type	Two stage	Two stage
Bending angle	3.50°	1.45°
Momentum compaction R56	38.9 mm	6.70 mm
Chicane length	12.2 m	12.2 m
Dipole length	0.3 m	0.3 m
Drift length ΔL	5.0 m	5.0 m

SIMULATION

We examined beam parameters using the ASTRA code from the photo-injector to the X1 booster unit considering strong space charge effects in this region. The code ELEGANT is used to design the main linac lattice from the X2 unit to the end of the existing linac. This code includes CSR effects in the bunch compressor and geometric wake field effects in the accelerating section. Table 4 summarizes the simulated beam parameters for BC1 and BC2. All uncorrelated energy spread is estimated at ± 0.1 mm core region. Initial uncorrelated energy spread at BC2 is increased after compression by BC1. The uncorrelated energy deviation at BC2 is larger than the $1x10^{-5}$ that is required to suppress the micro-bunching instability.

Table 4: Beam parameters of bunch compressors

Parameter	**BC1**	**BC2**
Beam energy	442 MeV	700 MeV
Relative energy spread	1.84%	1.31%
Uncorrelated energy spread	$9.2x10^{-6}$	$4.3x10^{-5}$
Initial rms bunch length	820 μm	114 μm
Final rms bunch length	114 μm	26 μm
Compression factor	7.2	4.38
Initial projected emittance	0.90 μm	1.01 μm
Final projected emittance	1.01 μm	1.12 μm

Figure 6 shows the energy spread and beam size before BC1 and at the end of the linac, respectively. The energy spread along the bunch length is well linearized by the X-band section (X2X) before BC1. At the entrance of BC1, energy spread is 1.835% and the beam size is 230 μm (σ_x). At the end of the linac the energy spread is 0.033% and beam size is 68.1 μm (σ_x). The longitudinal short-range wake-field damps the energy spread so that the energy spread becomes flatter and uniform.

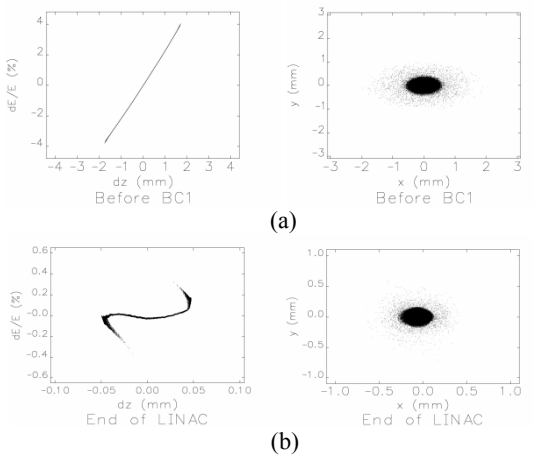

Figure 6: Energy spread and beam size before BC1 (a) and at the end of linac (b).

Figure 7 shows the variation of the projected energy spread and the bunch length along the linac. The relative energy spread is continuously increased to 1.84% until the entrance of BC1 by the modulator unit to fit the necessary compression factor at the BC1. The variation of energy spread in BC2 is mainly caused by CSR effects and kept reasonably low, which means the CSR is not so high in BC2. Increasing the beam energy, the energy spread is continuously decreased to 0.033% at the end of the linac. The large compression at BC1 and small compression at BC2 are clearly shown in the figure. The bunch length is compressed down to 26 μm after BC2.

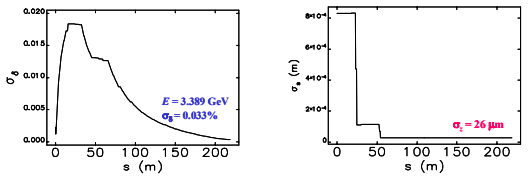

Figure 7: Energy spread and bunch length along linac.

Figure 8 shows the beam quality at the end of linac. The required beam parameters for FEL lasing at the undulator entrance correspond to dotted lines for the peak current of 4 kA, normalized emittance of 1.5 μm, and energy spread of 0.02%. The normalized emittance, that is the most sensitive FEL parameter, is well below the requirement along the bunch, which gives reasonable margin for saturation within a 60-m long undulator. The lowest peak current along the bunch is about 20% less than 4 kA. The slice emittance is also 20% lower than the nominal value of 1.5 μm. Because the saturation length is more sensitive to the emittance, it is possible to have saturation along the whole bunch.

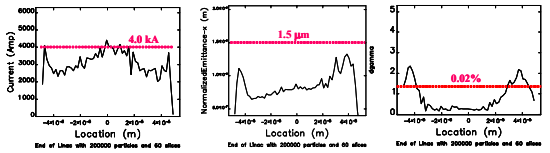

Figure 8: Beam quality at the end of linac.

DISCUSSION

The bunch compressor design can be tuned to provide a suitable beam heating effect. Figure 9 shows the distribution of uncorrelated energy spread along the bunch length before BC1 and after BC1, respectively. The uncorrelated energy deviation within ± 1.0 mm bunch core is 4 keV at the entrance of BC1. It is increased to 30 keV at the entrance of BC2 due to the high compression factor at the BC1. Considering space charge forces, it will be increased further, which helps to suppress micro-bunching instabilities.

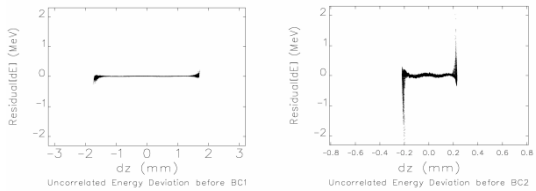

Figure 9: Uncorrelated energy spread at the entrance of BC1 and BC2.

In order to smoothly transfer the beam induced wall current, nickel foil, plated with copper, is attached on the pole surface using the magnetic attractive force. The practical smooth surface on commercially available metal plate has a high aspect-ratio of surface roughness, which makes the energy spread due to the surface roughness negligibly small enough. The energy spread due to the resistive wake field on the electron beams in the undulator can be estimated by assuming the radius being equal to half of the gap and energy spread being half of the pipe radius [3]. With the bunch charge of 1-nC, and the gap size of 3 mm, undulator length of 60 m, the projected energy spread due to the resistive wall wake is 0.07% for the bunch length of 26 μm. As the slippage length is 1.26 μm, the contribution to the slice energy spread is negligible. The emittance growth due to transverse resistive wall wake is less than 1% if the random oscillation is kept less than 20 μm with a Gaussian beam according to reference [6]. The gap size of each undulator can be tapered to adjust the resonant condition for the reduced average beam energy due to the incoherent synchrotron radiation loss.

The length of each undulator has to be at least $2xL_g$ in order to release the tight tolerance of longitudinal and transverse misalignment [7]. The achievable radiation power is reduced to 50% if the phase slip is π over the drift section between the adjacent segments or the radiation is cut off at the drift section. As the saturation length is $20xL_g$, the maximum number of segments is 10 and the minimum length of an undulator is 6 m for the PAL XFEL.

The jitter and sensitivity analysis on the combined parameter space is extensively studied in reference [8]. It is still necessary to analyse the hardware upgrade scheme and the stability requirements with related technical parameters.

ACKNOWLEDGMENTS

This work is supported by POSCO and the Ministry of Science and Technology (MOST) of Korea.

REFERENCES

[1] http://pal.postech.ac.kr/
[2] J. S. Oh, et al., "0.3-nm SASE FEL at PAL," Nuclear Instruments and Methods in Physics Research A528, 582 (2004)
[3] T. Shintake, et al., "SPring-8 Compact SASE Source (SCSS)," in Proc. the SPIE2001, San Diego, USA, 2001; http://www-xfel.spring8.or.jp
[4] M. Xie, "Design Optimization for an X-ray Free Electron Laser Driven by SLAC Linac," LBL Preprint No-36038, 1995
[5] T. Limberg, "Emittance Growth in the LCLS due to Coherent Synchrotron Radiation," SLAC internal note, Oct. 1997
[6] LCLS CDR, SLAC-R-593 (2002)
[7] T. Tanaka, et al., "Misalignment effects of segmented undulator in self-amplified spontaneous emission," PRST-AB, 5(2002)040701
[8] Y. Kim, et al., "Start-To-End Simulation of the PAL XFEL Project," 26th International FEL Conference and 11th FEL Users Workshop, Trieste, Italy, 2004

DESIGN STUDY OF LOW-EMITTANCE INJECTOR FOR SASE XFEL AT POHANG ACCELERATOR LABORATORY*

S. J. Park#, J. S. Oh, E. S. Kim, J. Y. Huang, D. E. Kim, J. H. Park, S. H. Nam, M. H. Yoon, I. S. Ko, S. G. Baik, and W. Namkung
Pohang Accelerator Laboratory, POSTECH, Pohang 790-784, Korea

Abstract

We report on the design study of the low-emittance injector for the SASE-XFEL that is being considered as the possible choice for the next-generation light sources at the Pohang Accelerator Laboratory (PAL), POSTECH. The PAL XFEL will utilize existing 2.5-GeV linac combined with a new 700-MeV linac, and aims to achieve the SASE saturation at 3 Å with 3-GeV beam energy and mini-gap in-vacuum undulators. Requirements imposed on the beam quality are tight, e.g., the normalized rms emittance at the entrance of the undulator should be less than 1.5 μm rad. Since the basic beam quality of the linac is determined by its injector system, the injector system should be developed as soon as possible, well before the start of the machine construction, which would greatly help to find and solve potential obstacles in achieving the required beam qualities. In this article, we report on our preliminary design work on the injector system and scheme for the development of the system.

INTRODUCTION

The PLS (Pohang Light Source) in the PAL/POSTECH is the 2.5-GeV light source with the full-energy injection linac. The PLS linac uses 44 SLAC-style accelerating structures powered by 80-MW klystrons and 200-MW modulators. While it is the world 3rd in its beam energy, it has been under-utilized with beam injections into the storage ring only two times a day. Utilization of the PLS linac as the 4th generation light source (PAL XFEL) has been one of the hot issues in the PAL since last year, and relevant design work has been performed. [1] As shown in Ref. 1, the PAL XFEL aims to achieve 3-Å lasing with 3-GeV beam energy. This implies it requires very high-quality beams at the entrance of the undulator. For the 4th generation light source, we are going to add a new 700-MeV linac, with a low-emittance electron gun and two bunch compressors, to the head of the main linac. In this way, we could lessen the modification and shutdown period for the main linac. The successful construction of the new linac and the conversion of the main linac into the 4th generation light source would require its electron source be prepared as soon as possible with required beam qualities. Due to these reasons, we have already started to construct the RF photo-injector system and will test its performance in a dedicated test-stand.

DESIGN CONSIDERATION

In Table 1, we summarize requirements imposed to the injector for the PAL XFEL.

Table 1: Injector requirements for PAL XFEL

Charge	1 nC
Beam Energy	150 MeV
Repetition Rate	30 Hz
Emittance (normalized, rms)	< 1.2 μm rad
Energy Spread (rms)	< 0.1 %

There are two representative schemes for XFEL injectors. One is the LCLS-style injector based on the RF photo-cathode gun and the emittance compensation by the generalized Brillouin flow (Invariant Envelope). Many laboratories are demonstrating the practicability of this scheme. [2][3][4] There is another unique approach at the SCSS (SPring-8 Compact SASE Source) in the SPring-8. The SCSS adopts thermionic DC gun with a single-crystal cathode. The DC Gun is followed by a fast chopper and a standing-wave-type pre-buncher. The DC gun has already demonstrated 1-μm emittance [5] at sufficiently high charge. The success of this scheme seems largely depend on the transverse and longitudinal optics design in the low-energy part from the gun exit to the beginning part of the first accelerating structure.

As the injector for the PAL XFEL, we are going to adopt the RF photo-cathode gun with the IE emittance compensation scheme. The SCSS-style injector will be chosen as a backup option. This is because it does not rely on the laser for generating electrons, and this would make the system inherently stable and reliable.

In order to deduce the basic requirements for the realization of the reliable RF photo-injector system, we briefly mention on the IE emittance compensation.[6] The transverse dynamics of charged-particle beams, with the perveance, κ_s, propagating through the linear focusing channel, K_r, and accelerated at the rate of γ' is described by the following equation,

$$\sigma'' + \sigma'\left(\frac{\gamma'}{\beta^2\gamma}\right) + K_r\sigma - \frac{\kappa_s}{\sigma\beta^3\gamma^3} - \frac{\varepsilon_n^2}{\sigma^3\beta^2\gamma^2} = 0 \quad (1)$$

The rms beam size, σ and derived qualities (e.g., emittance) are damped as the beam is accelerated because of the non-vanishing σ'. This implies that the so-called emittance oscillation is damped and the emittance can be made frozen to a very low value under a certain condition.

*Work supported by the MOST and the POSCO, Korea
#smartguy@postech.ac.kr

This is achieved by providing proper matching conditions at the accelerator entrance, in both the transverse and the longitudinal planes, given by two equations below,

$$\sigma' = 0 \qquad (2)$$

$$\gamma' = \frac{2}{\sigma}\sqrt{\frac{\hat{I}}{2I_0\gamma}} \qquad (3)$$

(2) is to require the beam waist be formed at the accelerator entrance, which is commonly done in linear electron beam devices, e.g., klystrons. (3) is a new requirement determining the accelerating gradient of the structure with given beam size, σ and peak current, $\hat{I}$. The constant I_0 in (3) is called the Alfvén current with the numerical value of 17 kA.

Fig. 1 shows normalized emittance evolutions after the RF gun and the emittance-compensating solenoid with and without the downstream acceleration. It is clearly seen that the emittance and the beam size are frozen to a certain value with acceleration (thick lines), which otherwise diverge (thin lines) due to the space-charge repulsion force.

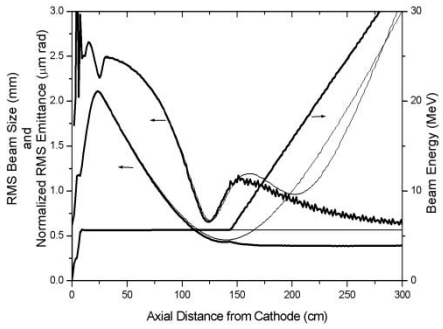

Figure 1: Comparison of beam rms sizes and normalized emittance evolutions with (thick lines) and without (thin lines) acceleration. Accelerator entrance is located at z = 1.5 m. Also shown are beam energy profiles (right scale).

Based on the principle of the IE emittance compensation, we list up practical requirements for the realization of reliable XFEL injectors,

- Low-emittance electron gun (such as the RF gun + high-power laser with profile control capabilities)
- High gradient booster accelerator with good alignment
- Solenoids with low field errors and good alignments
- Low-jitter RF system

Without describing the above requirements in detail, the author presents in Fig. 2 - 5 some results from the PARMELA simulations that have been done for evaluating impacts of operation parameters on the performance of the LCLS-type injector.

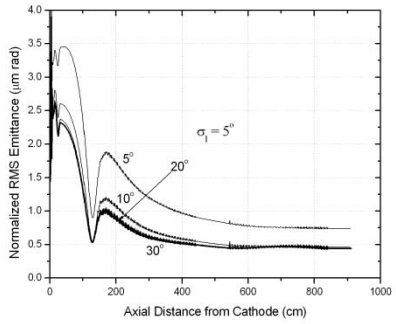

Figure 2: Variation of normalized emittance profiles (along z) with different rms bunch lengths. Bunch shape is Gaussian with cut at +/- 5°. Shown are emittance profiles for different rms bunch lengths. Notice better performance with larger rms length, i.e., more flat bunch shape.

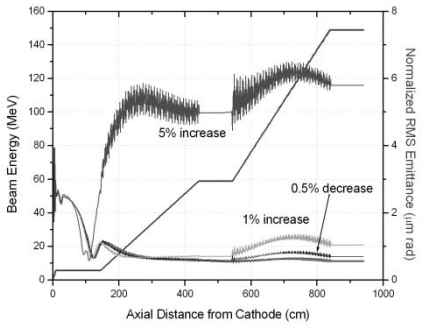

Figure 3: Variation of normalized emittance profiles and beam energies (along z) with different percent deviations of gun solenoid current from the optimum value.

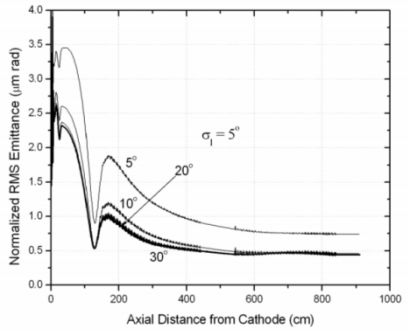

Figure 4: Variation of normalized emittance profiles and beam energies (along z) with different initial phases (w.r.t. rf zero phase)

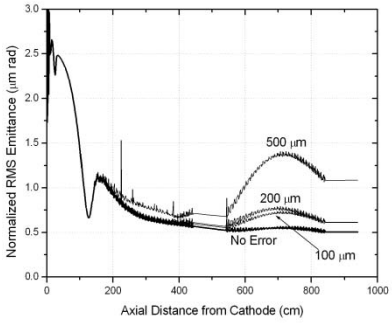

Figure 5: Variation of normalized emittance profiles with different alignment errors in the 1st accelerating column. Errors are input in a cell-by-cell manner and are assumed to be random with peak values as indicated.

FABRICATION OF RF GUN

We are fabricating the 1.6-cell RF photocathode gun (BNL Gun-IV type) for use in the injector test-stand that will be described in the next section. Another gun with similar design will be also fabricated for the femto-second electron diffraction facility [7] that is being established with the collaboration with the Chemistry department in the KAIST (Korea Advanced Institute of Scientist and Technology, Korea) and Dr. Xijie Wang at the BNL. At the PAL, there has been active work on developing high-power klystrons for use in the PLS linac. Recently, we have succeeded to fabricate an 80-MW pulsed klystron and all relevant facilities have been in-house established. [8] This capability would play a vital role in developing high-performance RF photo-injector at the PAL.

Before embarking in the fabrication of the RF gun, we have prepared a cold model to check the tuning property of the gun cavities. See Fig. 6 for its appearance.

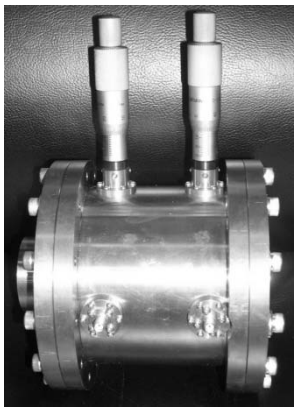

Figure 6: Appearance of cold model of RF gun cavity.

It has two tuners and loop couplers installed at each cell, which allow easy checks of cavity tuning properties. Tuning of each cell for resonating the gun cavity at the π mode with the required frequency (e.g., 2856 MHz) can be done referring to the following equations [9],

$$f_1 = f_\pi(1-\frac{k\sqrt{r}}{2}), \qquad f_2 = f_\pi(1-\frac{k}{2\sqrt{r}}) \tag{2}$$

where, f_1 & f_2 are resonant frequencies of half and full cells,
f_π is the (required) π-mode frequency,
k is the coupling factor between the two cells = mode separation / f_π,
and r is the volume ratio between the two cells (= 1/0.6 = 1.67).

Using k = 1.16 x 10^{-3}, r = 1.67, and f_π=2856 MHz, f_1 = 2853.861 MHz, f_2 = 2854.717 MHz. Dimensions of each cell can be determined from numerical calculation using computer codes such as the SUPERFISH. Specific parameters of each cell are obtained by completely detuning the other cells. Fig. 7 illustrates these procedures. The upper two figures are SUPERFISH calculation for the half (left) and the full (right) cells. After determining independent cell dimensions, those two cells are combined to yield the π-mode resonance at the required frequency, f_π as shown in the lower figure in Fig. 7.

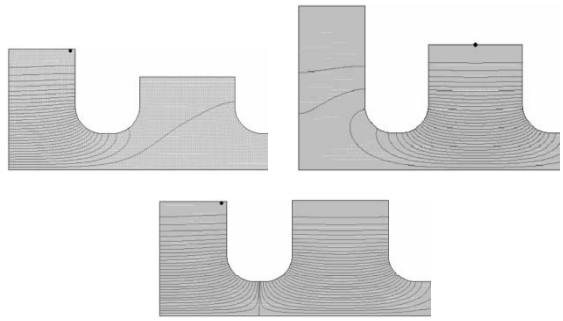

Figure 7: Scheme of determining cell dimensions. Dimensions of each cell are determined by completely detuning the other cells. (Upper figures) When both cells are combined, π-mode resonance occurs at the required frequency, f_π = 2856 MHz. (Lower figure)

Network-analyzer measurement of the two resonant modes in the gun cavity is shown in Fig. 8. With π-mode resonance at the 2856 MHz, the mode separation between the 0- and π-mode was 3.4 MHz. The suppression of the 0-mode is not done because the loop coupler used in this cold model is wide-band.

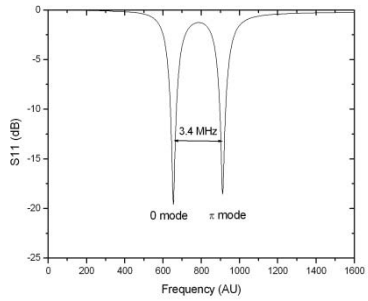

Figure 8: Network-analyzer measurement of the gun cavity cold-model.

Transient response of the gun cavity to pulsed rf power is important because of the mode beating phenomenon. By applying pulsed rf to the full-cell coupler, time-evolution of cavity field was observed at the other coupler in the half cell. In Fig. 9 we show the time-profile of the cavity field together with the input rf waveform. The rippling in the rising part of the cavity-field waveform is believed to be caused by the mode beating. Note the period of the rippling corresponds to the inverse of the mode separation. Since the characteristic time of the standing-wave cavity is proportional to the Q-factor of the cavity, measured transient period shown in Fig. 9 will be different from the real gun that is made of brazed copper. Also notice that the falling part of the cavity-field waveform is a simple exponential decay, which would be the indication of the enough decay of the 0-mode during the rf pulse. The relevance of these observations to the practical aspect of gun operation is that the pulse duration of the rf power input should be long enough to allow the 0-mode to decay sufficiently. Otherwise, the condition of the cell balance will not be met and the beam quality is deteriorated.

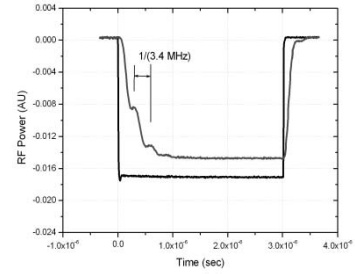

Figure 9: Transient response (upper trace) of gun cavity to pulsed rf input (lower trace).

We will proceed to machine the gun cavity by the use of ultra-precision turning lathe. After brazing, the assembly will be baked with procedures similar to the klystron fabrication. Whole fabrication will be controlled by well-arranged quality-control procedures in order to achieve high performance and reliability.

INJECTOR TEST-STAND

For the early development of the injector for the PAL XFEL, we are going to setup a test-stand that is equipped with a photo-cathode RF gun, an accelerating structure, diagnostic devices, and a rf source system. See Fig. 10 for the layout of the test-stand.

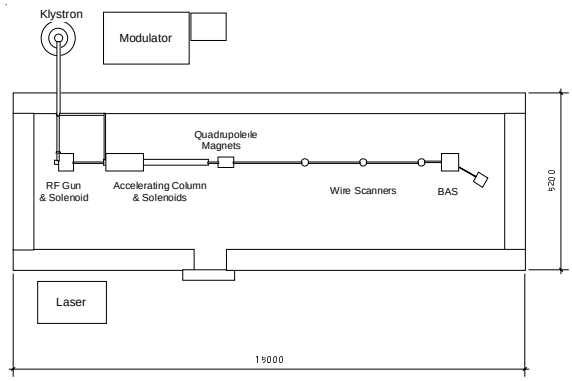

Figure 10: Layout of planned injector test-stand for the PAL XFEL.

We will employ standard diagnostics for measuring the emittance and the energy spread. Devices for measuring slice parameters will be also installed. Compact and movable emittance analyzer would be very useful for optimizing the delicate IE (Invariant-Envelope) emittance compensation.

REFERENCES

[1] J. S. Oh et al., NIM-A528, pp. 582-585.
[2] J. Yang et al., Proc. of the EPAC2002, pp. 1828-1830.
[3] V. Miltchev et al., these Proceeding.
[4] X.J. Wang et al., Proc. of the EPAC2002, pp. 1822-1824.
[5] K. Togawa et al., these Proceedings.
[6] R. Serafini et al., PRE-55, pp. 7565-7590.
[7] X.J. Wang et al., Proc. of the PAC03, pp. 420-422.
[8] S. J. Park et al., to be appear in Proc. of the APAC04.
[9] R. Bossart et al., Proc. of the EPAC92, pp. 1026-1028.

OPTIMIZATION OF A SOFT X-RAY SASE-FEL PARAMETERS AT POHANG ACCELERATOR LABORATORY

M. Yoon*, J. E. Han, E.-S. Kim, PAL, POSTECH, Korea

Abstract

A free-electron laser (FEL) based on self-amplified spontaneous emission has been designed. This FEL is utilizing the existing 2.5 GeV electron linear accelerator at Pohang Accelerator Laboratory (PAL). The radiation wavelength was chosen to be in the water-window region 3-4 nm which can be used for biological imaging. In this paper, it is shown that the PAL is particularly suited for this wavelength if the existing linear accelerator is employed without having major modification. For 4 nm wavelength, the saturated power is shown to be approximately 5 GW with a saturation length of about 30 m.

INTRODUCTION

Several free-electron lasers (FELs) based on self-amplified spontaneous emission (SASE) are under study, construction or operation around the world including LCLS, TTF, SCSS, LEUTL, VISA, etc. Among these, the Linac Coherent Light Source (LCLS) at Stanford Linear Accelerator Center (SLAC) in USA and the TTF project at DESY in Germany are under construction and aiming at producing hard x-rays with 1.5 Å and 1.0 Å wavelength, respectively. Recently, there is an increasing demand in these facilities to have a capability of producing soft x-ray radiation as well, 20-50 Å wavelength region. One of the promising applications in this wavelength is x-ray microscopic imaging in the water-window region (23-44 Å), especially the imaging of biological specimens in their natural state. Due to large absorption differences between carbon and oxygen in the water-window region, the natural contrast between protein and water can be attained. In addition, due to short pulse nature of the radiation of the order of 100 femto second, a single-pulse exposure measurements can be carried out to obtain images of living cells before the specimen changes in its structure caused by radiation damage.

The SASE principle is based on the FEL amplifier where the initial spontaneous radiation near the undulator entrance is used as input electromagnetic (EM) wave. This co-propagating EM wave combined with the undulator field generates a beat (i.e. ponderomotive) wave whose phase velocity is slower than the speed of light and can be synchronized with electrons. Depending on the relative phase with respect to the beat wave electrons can lose or gain energy, causing micro-bunching of the electron beam of the order of the wavelength of the EM wave. The electrons in the micro-bunch then acts coherently to produce an exponential growth of the radiation intensity which is proportional to the square of the number of electrons at saturation. This SASE principle has been successfully demonstrated recently at UCSB, LEUTL at Argonne National Laboratory (ANL) [1] and at DESY [2].

The wavelength of the output radiation through an undulator is given by

$$\lambda = \frac{\lambda_U}{2\gamma^2}\left(1 + a_U^2 + \gamma^2\theta^2\right), \qquad (1)$$

where λ_U is the undulator period, γ is the ratio between the electron energy and the electron rest energy 0.511 MeV, $a_U = K$ for helical and $a_U = \frac{K}{\sqrt{2}}$ for planar undulator. Here, K is the undulator parameter given by $K = \frac{eB_U\lambda_U}{2\pi m_0 c}$ with B_U the peak magnetic field on the mid-plane of the undulator, m_0 the electron rest mass, e and c the electron charge and speed of light respectively. In Eq. (1), θ is the angle between the undulator mid-plane and the observation position. The equation shows that the radiation wavelength is inversely proportional to the beam energy squared. Eq. (1) also shows that higher magnetic field (i.e., smaller undulator gap) gives longer wavelength and this is due to the fact that higher magnetic field reduces the magnitude of the longitudinal velocity of an electron beam.

Currently at the PAL, a 2.5 GeV electron linear accelerator (or linac) is used to inject electrons into the 2.5 GeV storage ring. The circulating electron beam in the storage ring then emits synchrotron radiation during the curved motion through bending magnets and insertion devices with a lifetime of 20 hours at maximum beam current 170 mA. Normally beam is injected two times per day and time required for injection is less than 10 minutes. Thus the linac is in stand-by mode for most of the time.

The electron energy of 2.5 GeV is particularly suited for soft x-ray generation with a FEL. This paper concerns a soft x-ray FEL using the PAL injector linac. First, we introduce the parameter optimization of the soft x-ray. For comparison purpose we consider two different energies of an electron beam, 2.5 GeV and 3 GeV respectively. We then show some characteristic feature of the FEL. Time-independent and -dependent numerical simulation results are depicted.

SOFT X-RAY FEL PARAMETERS

The amplification of the EM wave is due to the collective instability of an electron beam. The instability produces an exponential growth of the EM field intensity and of the bunching given by the bunching parameter:

$$B = \frac{1}{N_e}\sum_{k=1}^{N_e}\exp\left(\frac{2\pi i z_k}{\lambda}\right) \qquad (2)$$

* moohyun@postech.ac.kr

where z_k is the longitudinal position of the k^{th} electron with respect to the bunch center, N_e is the total number of electrons and $i = \sqrt{-1}$. The growth saturates when the bunching parameter is of the order of one. In one-dimensional approximation the power growth before saturation is given by

$$P \approx \frac{1}{9} P_n \exp\left(\frac{z}{L_{g,1d}}\right) < P_{sat}, \tag{3}$$

where $L_{g,1d} \approx \frac{\lambda_U}{4\sqrt{3}\pi\rho}$ is the one-dimensional gain length and P_n is the effective input-noise power proportional to the square of the initial bunching parameter $|B_0|^2$ and it is the power for spontaneous coherent undulator radiation of length L_g. P_n is proportional to the inverse of the number of electrons in a coherence length (i.e. $P_n \sim \frac{\rho^2 c E_e}{\lambda}$). In the case of SASE FEL, the saturation occurs approximately after 20 gain lengths. The FEL performance is mainly described by the FEL parameter ρ which is given by

$$\rho = \frac{1}{\gamma}\left(JJ(\chi)\frac{a_U}{4}\frac{\omega_p}{\omega_U}\right)^{2/3}, \tag{4}$$

where $\omega_U = \frac{2\pi c}{\lambda_U}$ and ω_p is the plasma frequency given by $\sqrt{\frac{n_e e^2}{\epsilon_0 m_0}}$. Here n_e is the electron density and ϵ_0 is the free-space permeability. Note that the FEL parameter ρ is proportional to $n_e^{1/3}$. The function $JJ(\chi)$ is given by

$$JJ(\chi) = \begin{cases} 1 & : \text{ helical undulator} \\ J_0(\chi) - J_1(\chi) & : \text{ planar undulator,} \end{cases}$$

where $\chi = \frac{K^2}{4(1+K^2/2)}$ and J_n is the n^{th}-order Bessel function. The radiated energy at saturation is roughly $\rho N_e E_e$, where N_e is the total number of electrons. The number of emitted photons per electron at saturation is then given by $N_\gamma = \rho\frac{E_e}{E_\gamma}$, where E_γ is the photon energy. The significance of the FEL parameter ρ can be summarized as

- Saturation length $L_{sat} \sim \frac{\lambda_U}{\rho}$
- Radiation power at saturation $P_{sat} \sim \rho P_{beam}$
- Frequency bandwidth $\frac{\Delta\omega}{\omega} \sim \rho$,

where P_{beam} is the peak power of the electron beam, $P_{beam} = E_e I_p$ with I_p the peak current. Therefore high peak current is desired to obtain high power at saturation. In Figs. 2 and 3 we have not taken into account the undulator segments which will increase the saturation length as in the case of Fig. 1.

In order for the collective instability to be developed the following three conditions should be met:

- Electron beam emittance must match the diffraction-limited emittance: $\epsilon < \frac{\lambda}{4\pi}$
- Beam energy spread must be smaller than the FEL parameter: $\frac{\sigma_\gamma}{\gamma} < \rho$
- Gain length must be shorter than the Rayleigh length: $L_g < Z_R = \frac{2\pi\sigma_x^2}{\lambda}$, where σ_x is the rms size of the radiation.

When three-dimensional effect is considered, the FEL-gain length can be expressed by introducing a universal scaling function [3]

$$L_g = L_{g,1d}\left(1 + \eta(\eta_d, \eta_\epsilon, \eta_\gamma)\right), \tag{5}$$

where

$$\begin{aligned} \eta_d &= \frac{L_{g,1d}}{2k\sigma_x^2} = \frac{L_{g,1d}}{Z_R} \\ \eta_\epsilon &= \left(\frac{L_{g,1d}}{\beta}\right)\left(\frac{4\pi\epsilon}{\lambda}\right) \\ \eta_\gamma &= 4\pi\left(\frac{L_{g,1d}}{\lambda_u}\right)\left(\frac{\sigma_\gamma}{\gamma}\right). \end{aligned} \tag{6}$$

In the above equations, η_d is the diffraction parameter, η_ϵ is the angular spread parameter, and η_γ is the energy spread parameter. These scaling parameters measure the deviation of the beam from ideal case. M. Xie fitted η numerically with 19 fitting parameters and listed the fitting coefficients which will be omitted here [3]. The saturated power obtained empirically by fitting results is given by

$$P_{sat} \approx 1.6\rho\left(\frac{L_{g,1d}}{L_g}\right)^2 P_{beam}. \tag{7}$$

Table I shows the major beam and FEL parameters for 4 nm at PAL. It is seen that the undulator-gap height is 0.85 cm and the period is 3.3 cm. A moderate gap height was chosen to prevent possible deterioration of the beam quality from wake field and surface roughness. For planar undulator with Nd-Fe-B hybrid permanent magnet, the peak magnetic field in the mid-plane is given by [4]

$$\begin{aligned} B_U[T] &= 0.95 \times 3.44 \exp\left[-5.08\frac{g}{\lambda_U} + 1.54\left(\frac{g}{\lambda_U}\right)^2\right] \\ & 0.1 < \frac{g}{\lambda_U} < 1.0 \end{aligned}$$

where g is the full gap of the undulator. This gives the peak magnetic field on the mid-plane of 1.03 T and as a result the undulator parameter K is 3.173 as Table I shows.

RESULTS

In order to obtain saturation power as a function of the length, the GENESIS program was invoked, which is a three-dimensional simulation code for a SASE FEL. This program has a capability of numerically integrating the equations of motion in time-independent or time-dependent mode. Fig. 1 shows the power as a function of the undulator length. It is seen that the saturated power is approximately 5 GW and the saturation occurs at around 30

Table 1: Parameters of the 4 nm FEL.

Parameter	
Radiation wavelength, λ (nm)	4
Electron beam energy, E_e (GeV)	2.5
Undulator period, λ_U (cm)	3.3
Undulator full gap, g (mm)	8.5
Undulator peak field	
in the mid-plane, B_U (T)	1.03
Undulator parameter, K	3.173
Normalized rms beam emittance,	
ϵ_n (μrad)	2.0
Peak electron beam current, I_p (kA)	3.0
Rms energy spread, σ_γ/γ	
	6.01×10^{-4}
Gain length (3-D), L_g (m)	1.146
FEL parameter (3-D), ρ	1.32×10^{-3}
FWHM bunch length, τ_B (fs)	231
Gain correction factor, η	$\sim$0.11
Saturation length, L_{sat} (m)	~ 30
Saturation power, P_{sat} (GW)	~ 5

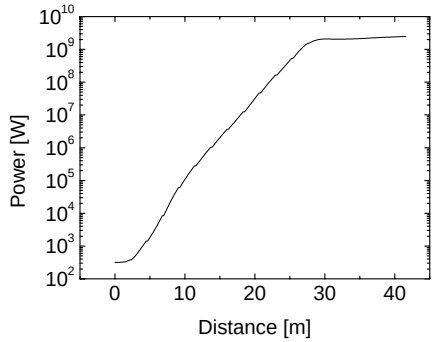

Figure 1: Power as a function of the undulator length for 4 nm FEL. Undulators are assumed to be segmented.

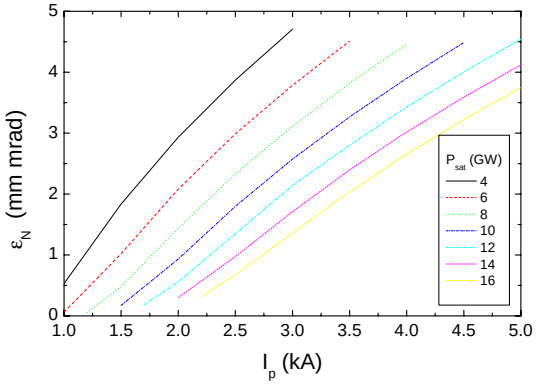

Figure 2: Saturation power as functions of the normalized emittance and peak beam current.

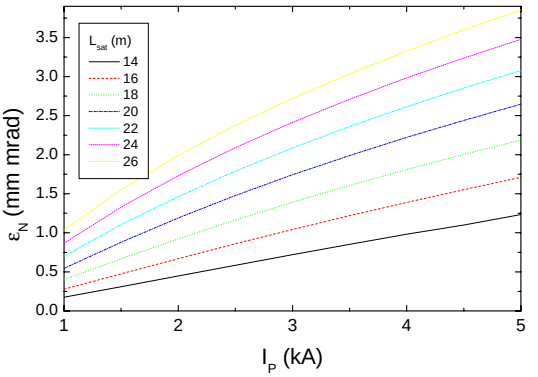

Figure 3: Saturation length as functions of the normalized emittance and peak beam current.

m. Figs. 2 and 3 show the saturation power and the saturation length as functions of the normalized emittance and the peak electron beam current. These figures were obtained assuming undulators were not segmented so that power and saturation length were slightly different from the segmented case. The saturation power increases as the normalized emittance decreases and the peak beam current increases. On the other hand the saturation length decreases as the normalized emittance decreases and the peak beam current increases. The natural emittance of 2 mm mrad and the peak beam current of 3 kA have been chosen in view of the reasonable performance of a rf photocathode electron gun.

To find the focusing requirement and therefore the optimal β functions, both the natural undulator focusing and quadrupole focusing by FODO structure were considered. It is well know that the planar undulator gives a vertical focusing due to edge effect of the magnet blocks and the equation of motion is given by

$$\frac{d^2y}{dz^2} + \frac{1}{2\rho^2}y = 0,$$

where z runs along the longitudinal axis of the undulator. The vertical transfer matrix due to a planar undulator is therefore

$$M_y = \begin{pmatrix} \cos(\frac{L}{\sqrt{2}\rho}) & \sqrt{2}\rho\sin(\frac{L}{\sqrt{2}\rho}) \\ -\frac{1}{\sqrt{2}\rho}\sin(\frac{L}{\sqrt{2}\rho}) & \cos(\frac{L}{\sqrt{2}\rho}) \end{pmatrix}, \quad (8)$$

where L is the straight length of the undulator and ρ is the radius of curvature on the axis where the magnetic field is peak.

To allow the space for quadrupole magnets and diagnostic instruments such as beam position monitors undulators are split. The space requirement between undulator sections is such that the phase slip of the electron bunch behind the electromagnetic wave is integer multiple of the radiation wavelength: $(c-v)t = n\lambda$ where v is the electron

speed n is an integer, and t is the gap-traversal time of the electron. Therefore, for n = 1,

$$L \approx \lambda_u \left(1 + \frac{K^2}{2}\right). \quad (9)$$

This yields L = 19.916 cm.

Fig. 4 shows the horizontal and vertical β functions as a function of the straight length. It is seen that average β function is about 4 m. Fig. 5 shows the saturation power

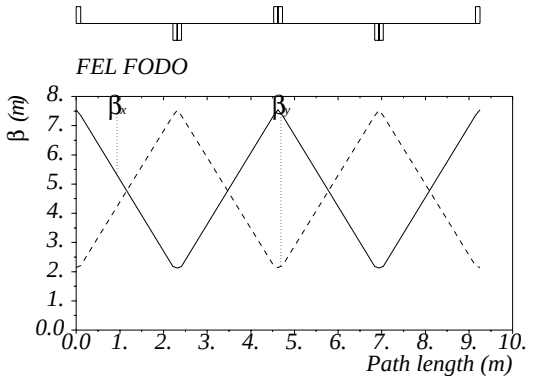

Figure 4: β function along the undulator and FODO focusing structure.

and the saturation length as a function of the average β function. This figure indicates that the chosen 4 m average β value is reasonably optimized to yield high saturation power and low saturation length.

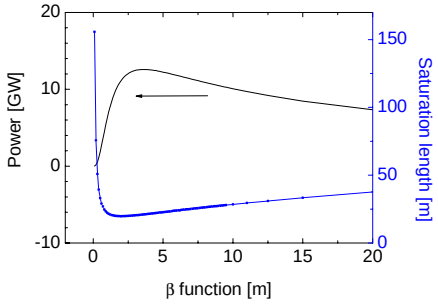

Figure 5: Saturation power and saturation length as a function of the average β function along the undulator.

Finally, effect of the wakefield due to the undulator vacuum chamber has been considered. In highly relativistic approximation, the longitudinal wakefield due to a resistive wall effect from a single electron is given by

$$W_z(s) = -\frac{4cZ_0}{\pi a^2}\left(\frac{1}{3}e^{-s/s_0}\cos\frac{\sqrt{3}s}{s_0} - \frac{\sqrt{2}}{\pi}\int_0^\infty \frac{x^2 e^{-x^2 s/s_0}}{x^6+8}dx\right), \quad (10)$$

for $s > 0$ and $W_z(s) = 0$ for $s < 0$, where s is along the longitudinal position of the test particle with respect to the particle generating field, Z_0 = 120π Ω, $s_0 = (2a^2/Z_0\sigma)^{1/3}$, σ is the conductivity of the chamber material, and a is the pipe radius. Table 1 shows that the full gap height of the undulator was chosen to be 8.5 mm. Assuming 0.5 mm thickness of the vacuum chamber, Fig. 6 shows that the saturation power decreases about a factor of 2 when copper chamber was assumed.

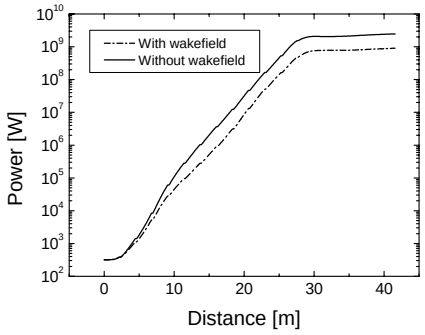

Figure 6: Power as a function of the undulator length with (dashed) and without (solid) wakefield in the undulator. Copper chamber with radius 3.75 mm was assumed.

CONCLUSION

In the paper we have described the SASE FEL to produce the soft x-ray. It is seen that with the present 2.5 GeV rf linear accelerator at the Pohang Accelerator Laboratory, the radiation of 4 nm wavelength can be produced with reasonable saturation power and the saturation length. The wavelength are decreased to 3 nm if the electron energy is increased to 3 GeV. Currently a design study is in progress which includes the start to end simulation. More details of this work is reported in these proceedings [5].

Acknowledgements

One of the authors (M. Yoon) would like to thank Dr. Heinz-Dieter Nuhn at SLAC for his help and a number of suggestions while carrying out this work. This work was supported by Ministry of Science and Technology (MOST).

REFERENCES

[1] S. Milton et. al. Science 292, 2037 (2001).

[2] R. Treusch and J. Feldhaus, Eur. Phys. J. D 26, 119 (2003).

[3] M. Xie, Proc. of the 1995 Particle Acc. Conf. (IEEE, Piscataway, NJ, 1995) p. 183.

[4] K. Halbach, J. Phys. (Paris) Collq, 44, C1-211 (1983).

[5] E.-S. Kim et. al., in these proceedigns.

SIMULATING FEM AMPLIFIERS: FEATURES IN VARIOUS REGIMES*

A.V. Elzhov+, A.K. Kaminsky, E.A. Perelstein, S.N. Sedykh, A.P. Sergeev
Joint Institute of Nuclear Research, Dubna, Russia

Abstract

Results of previous experimental investigations of Compton/Raman millimeter-wavelength FEL amplifiers are analyzed in numerical simulations. Compact quasi-one-dimensional models under helical-trajectory approach are employed. A tare on the stationary trajectories due to radiation is inserted. Reasonable agreement between simulation and experimental results is got in the regimes with reversed guide magnetic field.

1 INTRODUCTION

A full-scale three-dimensional simulation of an FEL amplifier allows one to get the best agreement between the simulation and experimental data. However the corresponding software possesses limited accessibility and requires considerable computing resource. Moreover not always one can distinguish principal physical factors defining features of particular FEL amplification regime. So use of compact approximate models seems to be attractive if they take account of dominating physical processes and allow one to determine parameters of amplifier operating with an acceptable accuracy.

In this paper quasi-one-dimensional models under helical-trajectory approach for various regimes of millimeter FEL (FEM) amplifier are considered, their applicability taking into account the experimental data [1–4] and problems of numerical simulation [5] are analyzed.

2 FEL REGIMES AND MODELS

A Raman regime of an FEL amplifier in which collective effects dominate is valid under 3 conditions [6]:

1°. The system is lengthy enough while the beam is high-dense so that several plasma oscillations get into the system length: $\lambda_p/L \le 1$. (1)

Here $\lambda_p = 2\pi/\omega_p$, ω_p is the relativistic plasma frequency: $\omega_p^2 = 4\pi n_e e^2/m_0\gamma_z^2\gamma_0$ where n_e is the electron beam density, m_0 is the electron rest mass and γ_0, γ_z are the total and longitudinal relativistic factors.

2°. Transverse velocities are much less than critical value [7] $\beta_w << \beta_{crit} \equiv F^{-1/2}(2\omega_p c^2 / v_{z0}^3\gamma_z^2 k_w)^{1/2}$. (2)

Here $k_w = 2\pi/\lambda_w$ is the wiggler wavenumber (λ_w is the wiggler period), v_{z0} is the initial longitudinal electron velocity, F is the beam-waveguide fill factor.

This criterion is based on comparison of contribution of ponderomotive and Coulomb potentials and obtained in helical-trajectory approach. Analyzing real experiments one should use it with caution [6] for the complications such as reduction of the effective plasma frequency in a waveguide, wiggler inhomogeneities, beam thermal effects and guide magnetic field. So the model may be insufficient for description of space-charge effects.

3°. Landau damping of the space-charge waves is not significant (the space-charge wavelength is greater than the Debye length) [6]. This restriction is imposed by the beam energy spread. For Gaussian distribution of electron velocities this requirement [8] transforms to

$(\delta\gamma/\gamma)_z < (L/2\gamma)(\omega_p/2c) \equiv \pi L/2\gamma\lambda_p$. (3)

Let us study a self-consistent spatial problem of relativistic electron beam moving in the microwave field provided the regime is stationary, the wave is a single-mode one and its amplitude is slowly varied with length.

Assuming the electrons obeying helical trajectories with longitudinal velocity $\beta_\perp$, we can write down a set of equations for a Raman FEL accounting [9,10,11]:

$$\frac{d\gamma_j}{dZ} = \frac{i\beta_{\perp j}}{2\sqrt{2}\beta_{zj}} a_s e^{i\psi_j} + \frac{c}{4\omega_0}\frac{\omega_{p0}^2\gamma_{z0}^2\Phi_0\beta_{zj}F_{s.c.}}{c^2(k_z+k_w)} ie^{i\psi_j}\left\langle e^{-i\psi_i}\right\rangle + c.c. \quad (4)$$

$$\frac{d\theta_j}{dZ} = \frac{1}{\beta_{zj}} - \frac{1}{\beta_{ph}} \quad (5), \quad \frac{d\hat{a}}{dZ} = \eta_0\gamma_0\left\langle\frac{e^{-i\theta_j}}{\gamma_j}\right\rangle \quad (6)$$

Here γ_j is the j-th electron's relativistic factor; $Z = z\omega_0/c$ is the dimensionless longitudinal coordinate, ω_0 is the amplifier operating frequency, k_z is the longitudinal wavenumber. The phase variables are: θ_j is the electron-to-wave one; φ is that of the complex RF amplitude ($\hat{a} = a_s e^{i\varphi}$), $\psi_j = \varphi + \theta_j$ is the total ponderomotive phase. The variable $a_s = eE_s/m_0\omega_0 c$ is the dimensionless amplitude of RF electric field. The gain factor is $\eta_0 = (I_b/I_A)(2\kappa_0/N)$, $\kappa_0 = a_w/2\gamma_0$ [11], $a_w = eB_w/(k_w mc^2)$ is the dimensionless amplitude of the wiggler magnetic field, Alfven constant is $I_A = m_0c^3/e \approx 17$ kA; N is the wave norm; β_{zj} and β_{ph} are longitudinal electron velocity and phase velocity of the microwave respectively. $F_{s.c.}$ is the attenuation factor of the space-charge wave, which is close to unity when the requirement (3) is satisfied. The constant in Eq.(4) is

$$\Phi_0 = 1 - \frac{\tilde{\beta}_w^2\gamma_z^2\Omega_0}{(1+\tilde{\beta}_w^2)\Omega_0 - k_w c\beta_{z0}} \equiv 1 - \frac{\tilde{\beta}_w^2\gamma_z^2}{1+\tilde{\beta}_w^2 - \gamma_0\beta_{z0}/a_g}$$

where $a_g = eB_g/m_0c^2k_w = \Omega_0\gamma_0/ck_w$ is the dimensionless amplitude of guide magnetic field with induction value of B_g, and $\tilde{\beta}_w = \beta_\perp/\beta_{z0}$ is the extended wiggling parameter.

The same system is suitable for simulation of high-gain Compton FEL if the $F_{s.c.}$ term in (4) is removed.

A uniform longitudinal guide magnetic field allows one to rise the electron beam stability relatively to

* This work is supported by grant №03-02-16530 of Russian Foundation for Basic Research.
+ Corresponding author: A. Elzhov, E-mail: artel@sunse.jinr.ru

transverse perturbations. But the trajectories became more complicated. Particularly for the wiggler field of helically symmetric distribution generated by a sinusoidal surface current in a bifilar helix [12], one can get a transcendental equation for stationary trajectories for a narrow beam.

The electron trajectories are stable with respect to the excitation of betatron oscillations, in two areas of beam parameters and external fields. These areas are separated by the vicinity of the cyclotron resonance where a perturbation of transversal oscillations results to their exponential growth, so the helical trajectory approach assuming $\beta_\perp/\beta_z << 1$ becomes non-applicable.

The stationary trajectories were derived from external magnetic fields (wiggler and guide ones) only. In a real FEL an RF wave appears that the relations for the velocity components should be derived more accurately. Assuming $a_s << a_w$, a_g we consider the effect of the RF wave as a tare for the motion over non-perturbed stationary trajectories. The velocity vector of each particle is resolved to "wiggler" and "radiation" parts: $\mathbf{v} = \mathbf{v}^w + \mathbf{v}^R$. The former is $\mathbf{v}^w = (c\beta^w \cos k_w z,\ c\beta^w \sin k_w z,\ c\beta_z^w)$, the latter is $\mathbf{v}^R = (c\beta_\perp{}^R \cos\theta,\ c\beta_\perp{}^R \sin\theta,\ c\beta_z^R)$. The equation for longitudinal momentum of the particle results in

$$\gamma \frac{d\beta_z^R}{dZ} = \frac{\beta_w}{\beta_{z0}}\left(\frac{ck_s}{\omega_0} + \frac{d\varphi}{dZ}\right) a_s \sin\psi - \frac{\beta_w}{\beta_{z0}} \frac{da_s}{dZ} \cos\psi + \\ + \frac{1}{\beta_{z0}}\left(\frac{d\gamma}{dZ}\right)_p - \beta_z^R \frac{d\gamma}{dZ} \qquad (7)$$

where $(d\gamma/dZ)_p$ is the potential term of Eq.(4) (i.e. the second one on the right side).

3 FEL AMPLIFIER EXPERIMENTS AND SIMULATION RESULTS

Basic parameters of FELs and electron beams in experiments [1–4] are presented in Table 1.

Table 1. Parameters of millimeter-wave FEL amplifiers [1–4].

	CESTA	JINR	MIT		
			I	II	III
Electron beam energy E_b, MeV	2.2	1.5	0.75	0.75	0.75
Electron current in wiggler I_b, A	500	50–70	90–119	300	300
Electron beam radius r_b, cm	0.5	0.3–0.5	0.25	0.25	0.25
Initial energy spread of the electron beam, %	< 1.5	1–2			
Wiggler period λ_w, cm	12	7.2	3.18	3.18	3.18
Wiggler magnetic field amplitude B_w, kGs	1.1	2.1	0.63	1.47	0.63
Guide magnetic field amplitude B_g, kGs	no	–1.4	4.06	10.92	–10.92
RF wave frequency $f_0 = \omega_0/2\pi$, GHz	35	35	33.9	33.9	33.9
Radiation spectral band (FWHM), GHz	0.16	0.2–0.3	<0.16	<0.16	<0.16
Operating mode (cylindrical waveguide)	H_{11}	H_{11}	H_{11}	H_{11}	H_{11}
RF power at the wiggler entrance, kW	8–10	6–20	8.5	8.5	8.5
RF power at the wiggler exit, MW	15	2–3	5.8	4.2	61
FEL amplifier efficiency, %	1.5	2–3	9	2	27
Spatial increment, dB/m	33	23	44	38	41
Saturation length, cm	~ 150	~ 120	~ 120	~ 150	~ 170

Numerical simulation of microwave amplification and electron beam bunching [9] for CESTA experiments [1,2] under Compton high-gain regime model agrees with the experiment well. It is in conformity with the above criteria for space-charge effects. The plasma wavelength ~ 11 m much exceeds the interaction length. The relation (2) is not satisfied at least by an order of magnitude.

For the JINR FEL amplifier with reversed guide magnetic field [3] the parameters are in the intermediate range where no any interaction type dominates. (Parts of the inequalities (1), (2) are comparable in pairs.) From (3), the Landau damping is negligible in this case.

The dispersion relation at non-zero guide magnetic field stated in [7] at $\beta_\perp/\beta_z << 1$, $a_s << a_w$, a_g allows one to transform Eq. (5) to

$$\frac{d\theta_j}{dZ} = -\frac{c(k_s + k_w)}{\omega_0} + \frac{1}{\beta_{zj}} + \frac{\omega_p \sqrt{\Phi_0}}{\omega_0 \beta_{z0}} \qquad (8)$$

The previous simulation [13] for the parameters of experiment [3] had been performed under Compton model with phase equation as (8). In this paper we allow space charge using Eqs. (4), (8), (6) for the simulation.

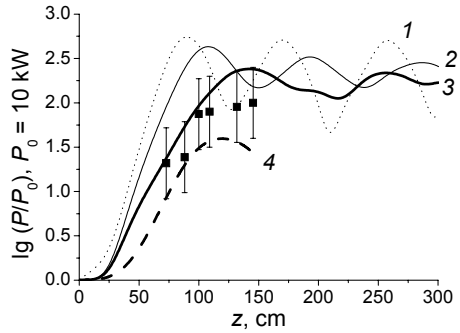

Figure 1: RF power of FEL amplifier [3] versus length. The experimental data are shown with dots. Curves 1,2,3 – Compton model simulation [13] at the energy spread of: 1) 0; 2) 3%; 3) 5%; curve 4 – Raman model simulation for cold beam.

Fig. 1 presents the results of RF power calculations [13] for different values of the initial energy spread of the beam, and the spatial distribution of RF power obtained in Raman model for cold beam (zero energy spread). The experimental results [3] are depicted by dots. They took an intermediate position between simulation results from extreme models. This fact is in agreement with the idea of continuity in the parameter space.

A detailed investigation of FEL amplifier with guide magnetic field was carried out at MIT [4]. Three basic regimes were studied: 1) positive (conventional-direction) guide magnetic field with Larmor frequency less than the cyclotron resonance frequency; 2) positive guide field at the other side from the cyclotron resonance; 3) negative (reversed) field (see Table 1). The experimental results indicated that the reversed field regime turned out to be most preferable by the beam current, spatial increment of RF power, saturation level and energetic efficiency.

According to the estimation over all criteria (1), (2), (3), the space charge effect is sufficient for each regime. The plasma wavelength (~ 20–30 cm) gets into the interaction length several times. The inequality (2) is satisfied by over than one order of magnitude. The limitation over thermal spread is practically absent: the right side of (3) amounts to several units.

So we have a definite Raman FEL amplifier. We simulated it over Eqs. (4), (5), (6), (7).

At the small positive guide field (I) the operating point is relatively near the cyclotron resonance. Transversal oscillations of the particles grow much so that helical-trajectory approach is not applicable, the solutions become nonconvergent. In the regime of large guide field (II) the simulation yields an excessive level of the output power. Though this discrepancy persists in the three-dimensional simulation [5] also. According to the paper [14], an amplification depression in the regimes with positive guide field may be caused by the competition between the operating wave and high-frequency modes excited from the noise level.

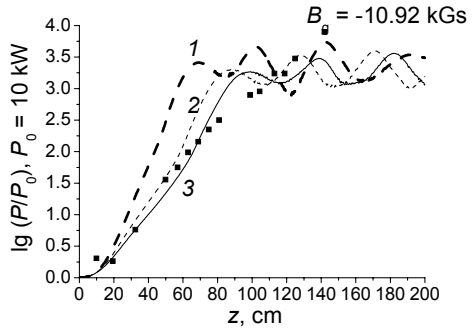

Figure 2: RF power of FEL amplifier [4] versus length: experimental data (dots) and simulation results for different values of the energy spread: 1) 2%; 2) 8%; 3) 10%.

For the reversed field case an acceptable agreement with the experiment has been obtained in the distribution of the radiation power over the length (Fig. 2).

The difficulties in the simulation of the positive-field regimes, especially approaching the cyclotron resonance, confirm the limited possibilities of quasi-one-dimensional helical-trajectory models for description of the particle motion. For more adequate simulation of the FEL amplification it is expedient to employ full-scale three-dimensional models. One should foresee a possibility of excitation of RF parasite modes, take into the account the features of beam delivery to the interaction region and wiggler&solenoid inhomogeneties.

4 CONCLUSIONS

Series of numerical simulation of experiments [1–4] in helical-trajectory approach in various FEL regimes have been carried out. The used models are compact and don't demand much computing resource. Simultaneously they are suitable for simulation of regimes with reversed guide field in order to define basic amplification parameters. This may be employed during preparation of an experiment for selection of amplifier operating parameters.

5 REFERENCES

[1] J. Gardelle, J. Labrouche, G. Marchese et al., Preprint CESTA/5, 1996.

[2] J. Gardelle, J. Labrouche and J.L. Rullier, Proc. of EPAC'1996, v. 1, p. 298.

[3] Yu.B. Viktorov, A.K. Kaminsky, S.B. Rubin at al., Proc. of XI All-Union Seminar on Charged Particle Accelerators, Dubna, 1989, v. II, p. 95 (in Russian).

[4] M.E. Conde and G. Bekefi, Nucl. Instrum. Meth., 1992, v. A318, p. 109.

[5] A.K Ganguly and H.P. Freund, Nucl. Instr. and Meth., 1993, v. A331, p. 501.

[6] H.P. Freund, Nucl. Instr. and Meth., 1993, v. A331, p. 496.

[7] C.W. Roberson and P. Sprangle, Phys. Fluids B, 1989, v. 1, N 1, p. 3.

[8] T.C. Marshall, "Free electron lasers", New York – London, McMillan Publ. Co., 1985.

[9] E.A. Perelstein, L.V. Bobyleva, A.V. Elzhov, V.I. Kazacha, Proc. of PAC'1997, p. 488.

[10] J.S. Wurtele, G. Bekefi, R. Chu and K. Xu, Phys. Fluids B, 1990, v. 2, N 2, p. 401.

[11] N.S. Ginzburg and A.S. Sergeev, J. of Tech. Phys., 1991, v. 61, p. 133 (in Russian).

[12] H.P. Freund and A.K. Ganguly, IEEE Trans. On Plasma Sci., 1992, v. 20, N 3, p. 245.

[13] E.A. Perelstein, L.V. Bobyleva, A.V. Elzhov, V.I. Kazacha, Problems of Atomic Science and Technology, Series "Nuclear physics investigations", 1997. N 2,3 (29,30), p. 78.

[14] A.T. Lin, C.C. Lin and K.R. Chu, Appl. Phys. Lett., 1992, v. 60, N 3, p. 292.

DESIGN CONSIDERATIONS FOR THE COHERENT RADIATOR, FEL, IN THE MAX IV PROPOSAL

Åke Andersson, Mathias Brandin, Mikael Eriksson, Tue Hansen, Jörgen Larsson, Lars-Johan Lindgren, Hamed Tarawneh, Sverker Werin, MAX-lab, Lund University, Box 118, S-221 00 Lund, Sweden

Abstract

The MAX IV proposal is a project for the next Swedish synchrotron radiation source. Currently a design study is produced with funding from the Swedish research council (VR). The first half of the project will be a double storage ring (at 3 and 1.5 GeV respectively) but the second half will be a coherent radiator, FEL, based on the 3 GeV linac injector.

INTRODUCTION

After spending effort on a number of different solutions (such as [1]) a basic design is now being elaborated. This consists of linac system providing a <1 nmRad sliced emittance, <1e-4 sliced energy spread, 2 KA peak current beam at 3 GeV which feeds three cascaded optical klystrons and a radiator undulator to produce radiation down to 1.5-3 nm at GW powers. The system will be seeded by a tunable laser system.

The linac system is foreseen to be normal conducting operating up to 100 Hz.

To assure synchronisation the gun laser and the seed laser share initial laser and amplifier.

BASIC LAYOUT INJECTOR AND LINAC SYSTEM

The basic layout now being sketched consists of a couple of building blocks which mainly show the ability of the system. This system will be adapted and optimised in the current environment as part of the continuing design work.

An injector system, which provides a suitable beam, has already been designed for the LCLS. As this is very much in line with the needs of the MAX IV injector we initially assume a similar system. [2] (table 1)

The linacs will be based on the same linac technology as already present in the new MAX-lab injector [3]. These are 5.2 m long normal conducting 3 GHz structures from ACCEL equipped with SLED cavities. They will be combined into 15 building blocks of one 35 MW klystron, one SLED system and two linac sections, thus providing 100 MeV per linac (20 MV/m). An additional 2 blocks will be used as back-up.

Two bunch compressors are foreseen to reach the necessary peak current. These will be placed at 150 and 500 MeV or slightly higher energy. The compression stages, strength and position, will be designed together with a wakefield and CSR analysis of the accelerator system.

NC v SC system

A normal conducting system is foreseen. A true CW system (SC-system) will be limited by the drive lasers for the PC-gun and the seeding to around 1 KHz. In this mode a linac such as the BESSY soft X-FEL will need a wall power in the order of 5 MW (3 KW @ 2K [4]). By going to semi CW operation the power will be reduced, and so the repetition rate. A NC system as the MAX IV system will be able to operate at 100 Hz needing a wall power of 1.5 MW. The gain by a factor of 10 in repetition rate is difficult to defend while regarding the increase in power demand and the complexity of a SC-system.

An increase of the repetition rate can be achieved by splitting the main laser pulse and generating several synchronised gun (and seed) pulses with 30 ns separation. These FEL pulses can also be chopped to different experimental stations.

Table 1. The parameters of the LCLS injector

Charge	1 nC
Bunch length	2.9 ps
Energy	150 MeV
Energy spread (integrated)	$1*10^{-3}$ RMS
Energy spread (slice)	$5*10^{-5}$ RMS
Emittance (slice)	<= 0.8 umRad

COHERENT RADIATION AND OPTICAL KLYSTRONS

The coherent radiation will be produced in a three stage optical klystron (figure 1). In each step the fifth harmonic will be extracted. The final stage will be an amplifier ("after burner") to provide the necessary power.

By using an electron beam with a small sliced natural energy spread lower modulating electric fields are required. Each stage will be supplied by electric fields strengths in the GV/m range to achieve adequate bunching.

It is important to match the electron beam optics to the divergence of the radiation. A compact system is thus a necessity especially at the longer wavelengths (the 53 nm stage) as the divergence otherwise kills the field strengths in the following modulator. Long undulators will of the same reason not pay off.

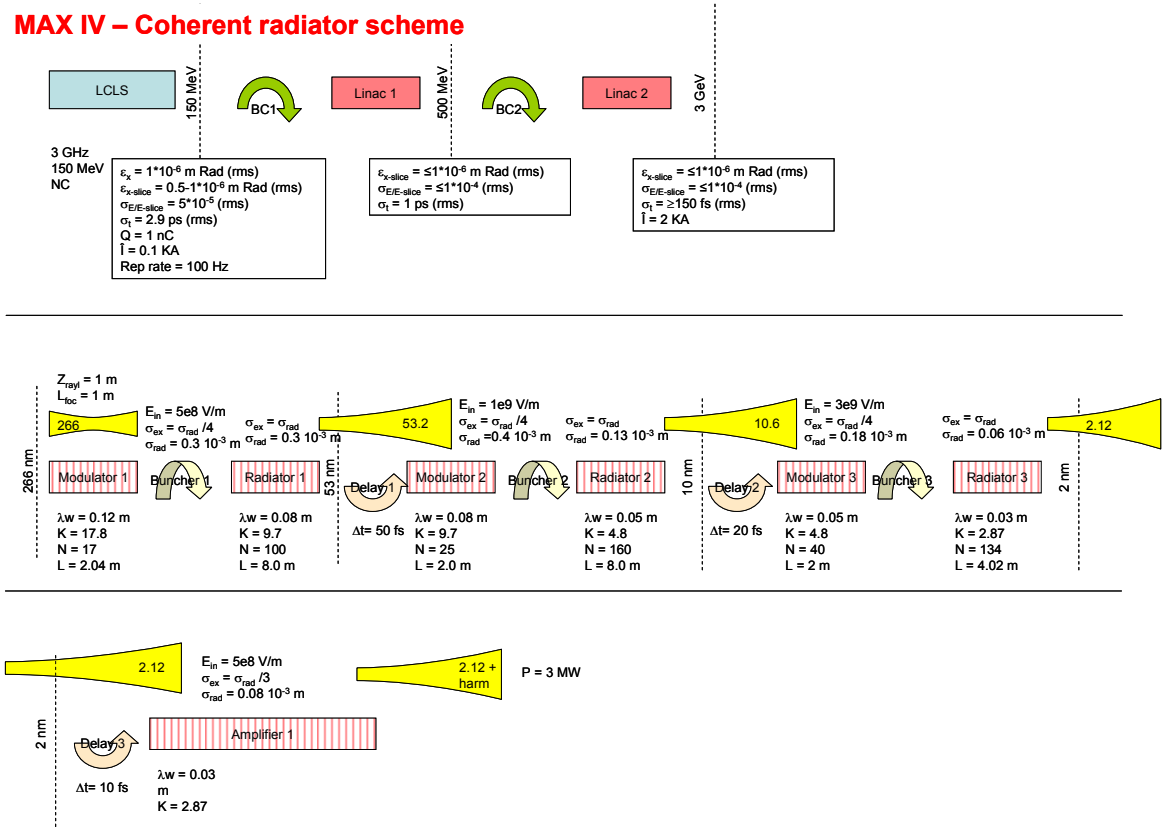

Figure 1. Schematics of the linacs and optical klystrons

The first HG stage can possibly use a bunch of lower energy generated in a second electron gun to allow for less powerful seed lasers, but the basic design only uses the fresh bunch technique.

GUN AND SEED LASER SYSTEM

A main Ti:Sa oscillator, synchronised to the RF-clock, will provide the source both for the gun laser pulse and the seed pulse. The gun pulse will be treated in a ps-laser (10ps), made top-hat and amplified thus controlling the charge and spatial distribution of the electron pulse. Another branch will be the FEL seed pulse which will be directed to a Ti:Sa laser to provide the power for HHG in a gas cell where a harmonic of the around the 25th order will be generated. The tunability in the Ti:Sa laser is enough to cover the distance between the harmonics in the HHG process. Thus full tunability in the 30-50 nm range can be achieved. It might turn out to be advantageous to introduce an OPA before the HHG cell to provide easier tuning over a larger range.

PERFORMANCE, CALCULATIONS AND MODELS

The radiation propagation in the cascades has been calculated by using an analytical approach focusing on the retarded potentials of the fields. Thus the full information on source point, divergence and relevant field strengths is achieved. The preliminary results are shown in figure 1.

The amplifier in the system has been simulated in Genesis [5]. The necessary undulator length at 2 nm is around 13 m with powers around 3 GW. (figure 2.)

TEST FACILITY

A test facility is currently being planned at the MAX-laboratory together with BESSY to be utlised within the EUROFEL co-operation (figure 3). It will make use of the 500 MeV linac injector recently put into operation. A first stage of a harmonic generation cascade will be installed and the electron source will be upgraded to a photo cathode RF-gun. Already available in the lab are a Ti:SA laser, space for undulator installations and the electron transport line. The same laser oscillator will feed both the gun and be used as a seed pulse in a similar fashion as depicted for the MAX IV. Initially seed pulses at 260 nm

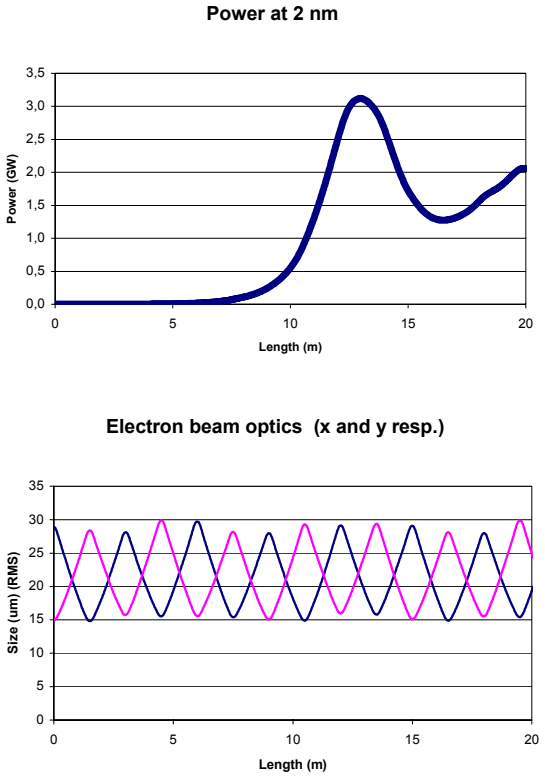

Figure 2. Amplification (top) and electron beam optics (below) in the amplifier.

will be utilised and coherent radiation at the third (90 nm) and fifth (53 nm) harmonic will be extracted.
In the test facility question like: benchmarking, electron beam control and transport, laser synchronisation, laser seeding, cascading etc. will be addressed.

SUMMARY

The design of the MAX IV coherent radiation source is taking form. The source will adopt the techniques of "second generation short wavelength FELs": Seeding, cascading and harmonic generation. A 3 GeV NC electron linac will provide a 100 Hz source which will generate tunable GW power pulses in the range of 2 nm. Basic simulations have been run using Parmela, Genesis and models using true field models.

REFERENCES

[1] M. Eriksson, L.-J. Lindgren, E. Wallen and S. Werin, A cascaded optical klystron on an energy recovery linac – race track microtron ,NIM A 507 (2003) 470
[2] LCLS design report (http://www-ssrl.slac.stanford.edu/lcls/cdr/)
[3] S. Werin et. al. Commissioning of the 500 MeV Injector for MAX-lab, EPAC04, Lucerne 2004
[4] BESSY soft X-FEL design report (http://www.bessy.de/publicRelations/publications/files/TDR_WEB.pdf)
[5] Genesis by Sven Reiche (http://corona.physics.ucla.edu/~reiche/)

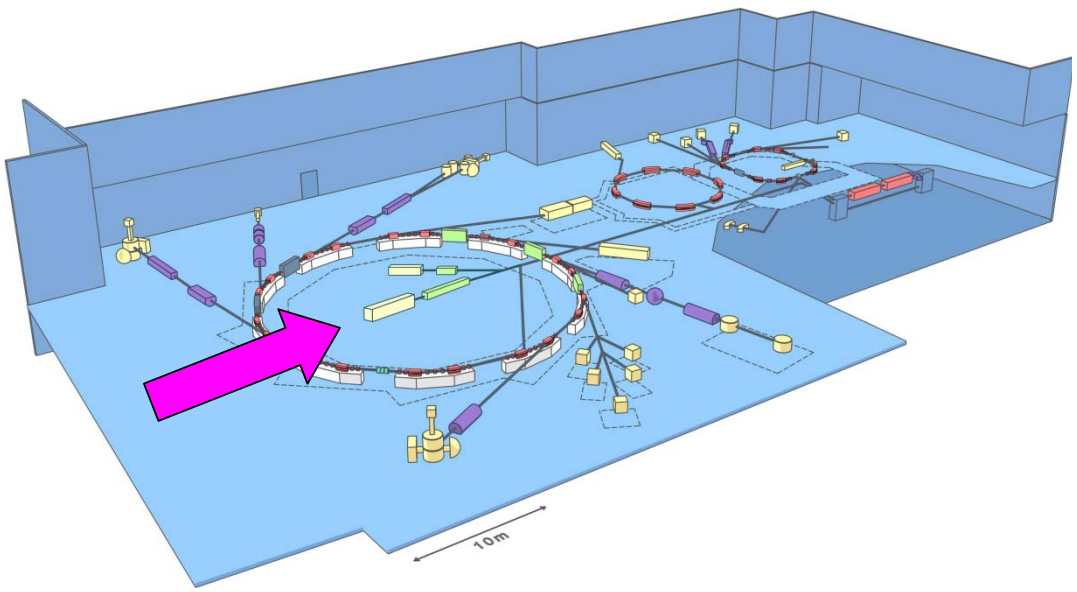

Figure 3. Placement of the test facility inside the MAX II storage ring.

COHERENT RADIATION EFFECTS IN THE LCLS UNDULATOR*

S. Reiche†, UCLA, Los Angeles, CA 90095, USA
Z. Huang, SLAC, Stanford, CA 94309, USA

Abstract

For X-ray Free-Electron Lasers such as LCLS and TESLA FEL, a change in the electron energy while amplifying the FEL radiation can shift the resonance condition out of the bandwidth of the FEL. The largest sources of energy loss is the emission of incoherent undulator radiation.

Because the loss per electron depends only on the undulator parameters and the beam energy, which are fixed for a given resonant wavelength, the average energy loss can be compensated for by a fixed taper of the undulator. Coherent radiation has a strong enhancement proportional to the number of electrons in the bunch for frequencies comparable to or longer than the bunch dimension. If the emitted coherent energy becomes comparable to that of the incoherent emission, it has to be included in the taper as well. However, the coherent loss depends on the bunch charge and the applied compression scheme and a change of these parameters would require a change of the taper. This imposes a limitation on the practical operation of Free-Electron Lasers, where the taper can only be adjusted manually.

In this presentation we analyze the coherent emission of undulator radiation and transition undulator radiation for LCLS, and estimate whether the resulting energy losses are significant for the operation of LCLS.

INTRODUCTION

Recent experiments [1, 2, 3] have shown successfully the operation of free-electron lasers (FEL) in the mode of self-amplified spontaneous emission (SASE), starting from the spontaneous undulator radiation. This supports the construction of SASE FELs in the X-ray regime [4, 5]. These 4th generation light sources allows for unprecedented brightness with Ångstrom spatial and femtosecond time resolution for all branches of science [6].

For a successful operation of an X-ray FEL it is essential to keep the electron beam synchronize with the radiation field. Any externally induced loss in the electron energy will degrade the performance. However if the energy change is known it can be compensated by an adjustment in the undulator field. The dominant contribution is the emission of incoherent undulator radiation [7], which is in the case for X-ray lasers even larger than the maximum FEL signal. Other sources are undulator wakefields, which have been already presented elsewhere (e.g. [8]).

In this presentation we calculate the contribution of coherent emission of radiation, which is enhanced by the number of electron per bunch ($\approx 5 \cdot 10^9$). In particular for X-ray FELs the bandwidth of coherent emission is large because the electron bunch is strongly compressed to reduce the FEL saturation length, and thus it excites higher frequency components. In addition the particular compression scheme at LCLS [4] generates a current profile which is rather flat with spikes at the edges than Gaussian (see Fig. 1). This increases the bandwidth of the excited frequencies. The two radiation processes, which can emit coherently in an undulator, are the undulator radiation and the transition undulator radiation at the entrance and exit of the undulator.

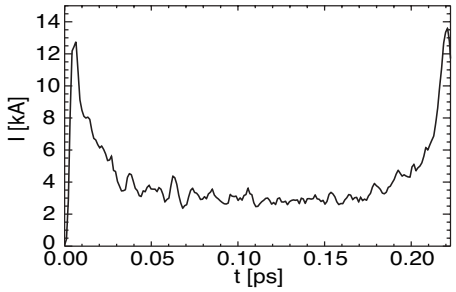

Figure 1: Current profile of the electron bunch in the LCLS undulator, calculated by start-to-end simulations.

COHERENT UNDULATOR RADIATION

Undulator radiation is the dominant radiation source and is emitted mainly in the forward direction due to the strong Doppler shift from the electron motion. The on-axis radiation can interact back on the electron beam, driving the free-electron laser mechanism. For larger emission angle with respect to the forward direction, the intensity drops quickly and the emitted wavelength is red-shifted. However beyond a threshold angle the radiation wavelength is comparable to the bunch length and the radiation adds up coherently. In the following we estimate the emitted energy due to the coherent enhancement by the particle distribution. Because we are integrating over a wide frequency range and including all directions of observation, any approximation in our calculation is excluded.

The energy emitted per solid angle and frequency interval is given by

$$\frac{d^2E}{d\omega d\Omega} = \frac{Q^2\omega^2}{16\pi^3\epsilon_0 c}|\tilde{I}(\omega)|^2 \left| \int \vec{n} \times [\vec{n} \times \vec{\beta}] e^{i\omega(t-\vec{r}\vec{n}/c)} dt \right|^2 , \quad (1)$$

with $\tilde{I}(\omega)$ the Fourier-transformed current profile, $\vec{n}$ the vector of observation, $\vec{\beta}$ the electron velocity in units of

*Work supported by the U.S. Department of Energy contract DE-AC02-76F00515

† reiche@physics.ucla.edu

the speed of light c, $\vec{r}$ the trajectory of the electron, and Q the bunch charge. For evaluation the transverse oscillation $\beta_x = K/\gamma \sin(\omega_u t)$ is in the xz-plane, where γ is the electron energy, K is the unitless undulator parameter, and $\omega_u = c\beta_0 k_u$ is the undulator wavenumber with $k_u = 2\pi/\lambda_u$ and λ_u as the undulator period. Although the longitudinal velocity β_z is modulated within a undulator period, the average velocity is given by $\beta_0 = 1-(1+K^2/2)/2\gamma^2$.

The dominant contributions in the integrations over t arise from the transverse oscillation β_x in the cross product and the transverse position r_x in the argument of the exponential function. The latter has the maximum amplitude $(\omega K/\gamma\omega_u)\sin(\theta) \ll 1$ and can be expanded in Taylor series. Both terms add up coherently as $(K/\gamma)\exp(i\omega_u t)$ with the cross product $\vec{n}\times[\vec{n}\times(\vec{e}_x + n_x(\omega/\omega_u)\vec{e}_z)]$.

The integral yield a sinc-function around the central frequency $\omega = \omega_u/(1-\beta_0\cos\theta)$, which is the resonant undulator wavelength, including the red shifting Doppler effect, when observed under an angle θ. Because the width of the sinc-function is the inverse of the number of undulator periods N_u, it selects only a narrow frequency window in the remaining integration over ω. We approximate the sinc-function by a Dirac-function $\delta(\omega_u - \omega(1-\beta_0\cos\theta))$. The integration over the frequency and the angle ϕ of the solid angle $d\Omega = \sin(\theta)d\theta d\phi$ yields

$$\begin{aligned}\frac{dE}{d\theta} &= \frac{Q^2 L_u K^2 k_u^2}{32\pi\epsilon_0\gamma^2}\frac{\left(1+\left[\cos\theta - \frac{\sin^2\theta}{1-\beta_0\cos\theta}\right]^2\right)}{(1-\beta_0\cos\theta)^3} \\ &\times \sin\theta\left|\tilde{I}\left(\frac{\omega_u}{1-\beta_0\cos\theta}\right)\right|^2 . \qquad (2)\end{aligned}$$

For our calculation we consider the cases of a Gaussian and rectangular profile with the rms bunch length σ_z and form factors

$$|\tilde{I}_G(\omega)|^= e^{-\omega^2\sigma_z^2} \quad \text{and} \quad |\tilde{I}_R(\omega)| = \frac{\sin^2\left(\omega\frac{\sqrt{3}\sigma_z}{c}\right)}{\omega^2\frac{3\sigma_z^2}{c^2}}.$$

Under the condition $k_u\sigma_z \ll 1$ the total emitted power is

$$E_G = \frac{Q^2 L_u K^2}{32\pi\epsilon_0\sigma_z^2\gamma^2} \quad \text{and} \qquad (3)$$

$$E_R = \frac{Q^2 L_u K^2}{96\pi\epsilon_0\sigma_z^2\gamma^2}\ln\left[\frac{2\gamma^2}{1+K^2/2}\right] \qquad (4)$$

for a Gaussian and rectangular current profile, respectively. For LCLS parameters ($K = 3.63$, $\gamma = 27500$ and $\sigma_z = 20$ μm) the energy losses are $E_G = 6.4$ μJ and $E_R = 40.5$ μJ, both three orders of magnitude smaller than the losses due to the incoherent undulator radiation of 17 mJ [4].

The transverse extension of the electron bunch σ_t can suppress the emission for very short bunches. Assuming a Gaussian distribution in the transverse direction the form factor of the current profile $|\tilde{I}(\omega)|^2$ has then the additional factor $\exp(-\omega^2\sigma_t^2\sin^2\theta/c^2)$. The applied correction function $S(\sigma_t/\sigma_z)$ is then

$$\begin{aligned}S(x) &= 1 - x^2\sqrt{\pi}k_u\sigma_t e^{x^2k_u^2\sigma_t^2(1+x^2)} \\ &\times\left[1-\Phi\left(\frac{k_u\sigma_t}{2}(1+2x^2)\right)\right], \qquad (5)\end{aligned}$$

where Φ is the Error function. The function $S(x)$ is shown in Fig. 2. For LCLS the ratio is about 1 and the reduction in the emitted energy is negligible.

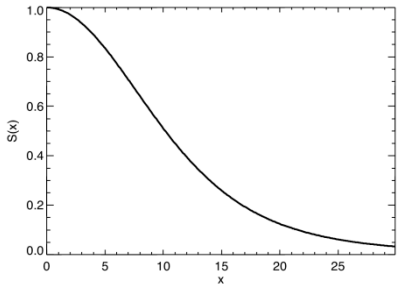

Figure 2: Suppression of the emitted energy due to the transverse size σ_t of the electron bunch. The function $S(x)$ depends on the ratio $x = \sigma_t/\sigma_z$.

COHERENT TRANSITION UNDULATOR RADIATION

Due to the transverse oscillation the average longitudinal velocity of the electron bunch is slower within the undulator than outside. The induced longitudinal acceleration of the short end pieces of the undulator, which match the straight trajectory outside of the undulator with the sinusoidal trajectory within, causes the emission of transition undulator radiation [9, 10]. The radiation footprint is similar to transition radiation [11], but there the emission is produced by the boundary condition of the electric field at the surface. A similar radiation source is edge radiation [12, 13], when an electron enters or exits the field of a bending magnet. However in transition and edge radiation the electron is modelled to come to a complete halt, while for transition undulator radiation the electron is only slowed down by $\Delta\beta = (K/2\gamma)^2$.

Low Frequency Approximation

In the low frequency model we assume that the change in the velocity is instantaneously. The emission of a single electron entering a undulator module is therefore

$$\frac{d^2E}{d\omega d\Omega} = \frac{Q^2}{16\pi^3\epsilon_0 c}\left(\frac{\beta_u\sin\theta}{1-\beta_u\cos\theta} - \frac{\beta_d\sin\theta}{1-\beta_d\cos\theta}\right)^2, \qquad (6)$$

where $\beta_u = 1-(1+K^2/2)/2\gamma^2$ is the velocity within the undulator and $\beta_d = 1-1/2\gamma^2$ the velocity in the free space

outside the undulator. If the electron would be stopped completely ($\beta_u \to 0$) then the emission (Eq. 6) is identical with that of transition and edge radiation. Due to the interference of the two terms in Eq. 6 the radiation is more confined in the forward direction. Emission under large angles $\theta \gg 1/\gamma$ is suppressed by a factor γ^{-2} in comparison to transition and edge radiation.

The radiation patterns from the undulator entrance and exit interfere with each other with opposite signs and an additional phase factor $\exp(i\omega\Delta\tau)$, where $\Delta\tau = (L_m/c\beta_u)(1-\beta_u\cos(\theta))$ is the retarded time-interval when the electron enters and exits the undulator module, and L_m is the undulator module length. If the undulator consists out of N modules additional terms arising with

$$\left|\sum_{n=0}^{N-1} e^{in\omega\tau}(1-e^{i\omega\Delta\tau})\right|^2 = 4\frac{\sin^2(\omega\Delta\tau/2)\sin^2(\omega N\tau/2)}{\sin^2(\omega\tau/2)},$$

$\tau = \Delta\tau + (L_d/c\beta_d)(1-\beta_d\cos(\theta))$, and L_d the drift length, separating two adjacent undulator modules. Including also the excitation by the current profile, expressed by the form factor $\tilde{I}(\omega)$ the angular distribution per frequency interval becomes

$$\frac{d^2E}{d\omega d\Omega} = \frac{Q^2}{16\pi^3\epsilon_0 c}\left(\frac{\beta_u\sin\theta}{1-\beta_u\cos\theta}-\frac{\beta_d\sin\theta}{1-\beta_d\cos\theta}\right)^2 \times 4\frac{\sin^2(\omega\Delta\tau/2)\sin^2(\omega N\tau/2)}{\sin^2(\omega\tau/2)}|\tilde{I}(\omega)|^2. \quad (7)$$

For a typical undulator the drift between two modules corresponds to the slippage of a few resonant wavelength, which is much shorter than the bunch length. As a result the phase difference $\omega(\tau-\Delta\tau) << 2\pi$ is negligible for frequencies excited by the bunch profile. Therefore the two sine-functions $\sin(\omega\Delta\tau/2)$ and $\sin(\omega\tau/2)$ cancel each other in good approximation in Eq. 7. Effectively the undulator modules are joined together into one single long undulator module.

For very long undulator ($N\tau \gg \sigma_z/c$) the sine-function $\sin^2(\omega N\tau)$ is fast oscillating and can be approximated by its average value 1/2. In this case the integration over the frequency is decoupled from the angle of observation θ, yielding $c\sqrt{\pi/4}/\sigma_z$ and $c\sqrt{\pi^2/12}/\sigma_z$ for Gaussian and rectangular profile, respectively. The resulting emitted energy is

$$E_0 = \frac{Q^2}{2\sqrt{\pi^3}\epsilon_0\sigma_z}\left[\frac{4+K^2}{2K^2}\ln\left(1+\frac{K^2}{2}\right)-1\right] \quad (8)$$

for the Gaussian profile and is higher by the factor $\sqrt{\pi/3}\approx 1.02$ for the rectangular profile.

It is useful to point out that $N\tau$ is proportional to the slippage length of the radiation field within the undulator. The limit, discussed above, is equivalent to the condition that the bunch length is shorter than the slippage length $L_s = (\lambda/\lambda_u)z$. Otherwise the radiation is suppressed due to $\sin^2(\omega N\tau) \ll 1$ for $\omega < 2\pi c/\sigma_z$. We solve Eq. 7 numerically and express the suppression by the additional factor

$$E = E_0 \cdot F(L_s/\sigma_z) \quad . \quad (9)$$

The function F is shown in Fig.3 and is quadratic/linear for Gaussian/rectangular profile and small arguments. For LCLS the suppression is 0.01, yielding a total emitted energy of 1.3 μJ, which is comparable in its magnitude to the coherently emitted undulator radiation. It would require an undulator of about 15 km for LCLS-like parameter in order to see no suppression by the destructive interference between undulator entrance and exit.

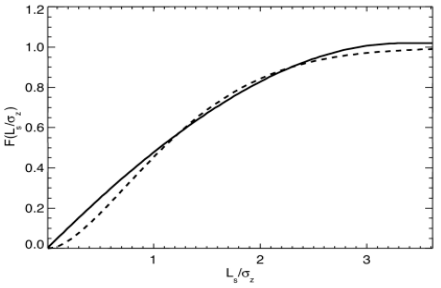

Figure 3: Function F for the suppression of the CTUR signal due to finite bunch length of a rectangular and Gaussian profile (solid and dashed line, respectively).

It seems to be counter-intuitive that the energy loss occurs over the entire undulator length, while the emission processes are spatially and temporarily localized at the entrance and exit of the undulator. But emission becomes only distinguishable in the far field zone, which lies outside the undulator. At the location of the electron the velocity field is the dominant field. In this model of undulator transition radiation the electrons are slower within the undulator and therefore the electrostatic field is less Lorentz contracted. However it is not seen be all electrons instantaneously. The change in the field is seen immediately only by the trailing electrons, while it requires some distance to catch-up with electrons ahead. This distance is the slippage length. As seen in Fig.3 the electron bunch has reached almost electrostatic equilibrium after $L_s > 3\sigma_z$ and only a negligible energy loss occurs further. At this point any retarded field information has propagated through the entire bunch.

High Frequency Limit

In the low frequency limit we assumed that the change in the velocity is instantaneously, but in reality each undulator module has a short tapering section to match the straight trajectory of the drift with the sinusoidal within. Typically the tapering section is one or two undulator periods long. Note that the characteristic frequency, which can 'probe' the explicit tapering is of the order of the res-

onant wavelength of the FEL. Thus, the low frequency approximation is valid for all current profiles, except for the micro-bunching, induced by the FEL process.

To estimate the high frequency dependence we refine our model by assuming a linear change in the velocity over the time interval δT. The acceleration is $\dot{\beta} = (\beta_u - \beta_d)/\delta T$ for entering the undulator module, yielding the profile of the electric field

$$E(\tau) = \frac{e \sin\theta}{4\pi\epsilon_0 c R} \frac{\dot{\beta}}{[(1-\beta_d \cos\theta)^2 - 2\dot{\beta}\tau\cos\theta]^{\frac{3}{2}}}, \quad (10)$$

where τ is the retarded time. The observed pulse length is $\delta\tau = (1 - \cos\theta(\beta_d + \beta_u)/2)\delta T$. The spectrum for small angle ($\theta \ll \pi/2$) is

$$\begin{aligned} \tilde{E}(\omega &= \frac{e\tan\theta}{4\pi\epsilon_0 c R}\left(\frac{e^{i\omega\delta\tau}}{1-\beta_u\cos\theta} - \frac{1}{1-\beta_d\cos\theta}\right. \\ &+ \sqrt{\pi}\varphi e^{(1-\beta_d\cos\theta)^2\varphi^2} \quad (11) \\ &\times \left.(\Phi((1-\beta_u\cos\theta)\varphi) - \Phi((1-\beta_d\cos\theta)\varphi))\right) \end{aligned}$$

with

$$\varphi = \sqrt{i\frac{\omega\delta T}{2(\beta_u - \beta_d)\cos\theta}} \quad . \quad (12)$$

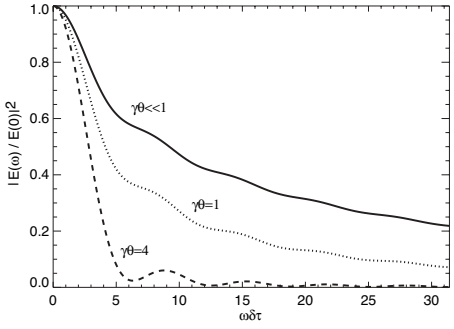

Figure 4: Power spectrum of the radiation pulse from a single electron at a single undulator entrance or exit.

Fig. 4 shows the spectra for different angle of observation. For larger value of $\theta > K/\gamma$ the pulse duration $\delta\tau$ becomes larger, resulting in a stronger suppression of emission at a given frequency. As an example a LCLS like undulator is tapered over two undulator periods. The time of observation $\delta\tau$ is about 1.7 Å$/c$ and even at the resonant wavelength at 1.5 Å the spectral power is only dropped by about 50% ($\omega\delta\tau \approx 7$) for $\theta \leq 1/\gamma$.

Because the spectrum is not suppressed significantly at the resonant wavelength, it might be considered to use CTUR as a parasitic emission signal to measure the degree of current modulation (micro bunching). With the assumption $|\tilde{I}(\omega)|^2 = |b|^2\delta(\omega - \omega_r)$ the resulting emitted energy per solid angle becomes

$$\begin{aligned} \frac{dE}{d\Omega} &= \frac{4|b|^2}{Z_0}|\tilde{E}(\omega_r,\theta)|^2 e^{-\omega_r^2\sigma_t^2\sin^2\theta/c^2} \\ &\times \frac{\sin^2(\omega_r\Delta\tau/2)\sin^2(\omega_r N\tau/2)}{\sin^2(\omega_r\tau/2)}. \quad (13) \end{aligned}$$

The radiation is strongly suppressed by two factors. First, the decoherence effect due to the finite transverse beam size confines the coherent radiation toward the forward direction $\theta \ll 1/\gamma$, where the sine-term in $\tilde{E}$ suppresses the radiation. Second, the interference of undulator entrance and exit is destructive because $\omega_r\Delta\tau$ and $\omega_r\tau$ are a integer number of π for any well tuned FEL, despite the enhancement N^2 from multiple undulator modules. However within a single undulator FEL, like the VISA FEL, the bunching occurs only within the undulator and there is no interference with the undulator entrance.

CONCLUSION

For X-ray Free-electron Laser the contributions of the coherent undulator radiation and transition undulator radiation to the overall energy loss of the electron bunch is negligible in comparison to the incoherent emission of undulator radiation. For CUR the emission is suppressed despite its enhancement by coherence because it requires the emission under an large angle so that the red shifted wavelength becomes comparable to the electron beam size. In contrast the transition undulator radiation is broadband but sees strong interference between the emission from the entrance and the exit of the undulator, which shifts the emission towards higher frequency and out of the bandwidth excited by the electron bunch. The possibility to measure the bunching factor in the FEL process is only given for long-wavelength FELs, where other methods exist to accomplish the measurement.

REFERENCES

[1] A. Tremaine *et al.*, Phys. Rev. Lett. **88** (2002) 204801

[2] S.V. Milton *et al.*, Science **292** (2001) 2037

[3] V. Ayvazyan *et al.*, Phys. Ref. Lett. **88** (2002) 104802

[4] *Linac Coherent Light Source (LCLS)*, SLAC-R-521, UC-414 (1998)

[5] TESLA-FEL 2001-05, Deutsches Elektronen Synchrotron, Hamburg, Germany (2001)

[6] C. Pellegrini and J. Stöhr, Nucl. Inst. & Meth. **A500** (2003) 33

[7] K.J. Kim, in AIP Conference Proceedings **184**, M. Month and M. Dienes, eds., (1989) 585

[8] S. Reiche and H. Schlarb, Nucl. Inst. & Meth. **A445** (2000) 155

[9] K.-J. Kim, Phys. Rev. Lett. **76** (1996) 1244

[10] B.M. Kincaid, Il Nuovo Cimento **20 D** (1998) 495

[11] V.L. Ginzburg and I.M. Frank, Zh. Eksp. Teor. Fix. **16** (1946) 15

[12] O.V. Chubar and N.V. Smolyakov, J. Optics**24** (1993) 117

[13] R.A. Bosch, Proc. of the 1999 Particle Accelerator Conference, New York (1993) 2397

SPONTANEOUS RADIATION BACKGROUND CALCULATION FOR LCLS*

S. Reiche†, UCLA, Los Angeles, CA 90095-1547, USA

Abstract

The intensity of undulator radiation, not amplified by the FEL interaction, can be larger than the maximum FEL signal in the case of an X-ray FEL. In the commissioning of a SASE FEL it is essential to extract an amplified signal early to diagnose eventual misalignment of undulator modules or errors in the undulator field strength.

We developed a numerical code to calculate the radiation pattern at any position behind a multi-segmented undulator with arbitrary spacing and field profiles. The output can be run through numerical spatial and frequency filters to model the radiation beam transport and diagnostic.

In this presentation we estimate the expected background signal for the FEL diagnostic and at what point along the undulator the FEL signal can be separated from the background. We also discusses how much information on the undulator field and alignment can be obtained from the incoherent radiation signal itself.

INTRODUCTION

Based on the successful demonstration of the Self-Amplified Spontaneous Radiation (SASE) Free-Electron Lasers (FEL) principle at longer wavelength [1, 2, 3], several X-ray FELs have been proposed and are currently under construction [4, 5]. The unique properties of the high-brightness radiation source allows to study femto-second processes with an Ångstrom spatial resolution, beneficial for all branches of sciences [6].

For SASE FELs the seeding field is the spontaneous radiation, although only a small bandwidth is amplified by the FEL process. The remaining part is emitted as a background signal, illuminating any detector to measure the FEL radiation. Because the total emitted power scales with the square of the energy of the driving electron beam [7], X-ray Free-electron lasers are more affected by the spontaneous radiation than FELs operating at longer wavelength. It is essential to estimate the spontaneous radiation due to three reason. First, the radiation power can be larger than the maximum FEL signal, yielding a large heat load on all X-ray optics elements. Second, the energy loss is strong enough to shift the electrons out of the FEL bandwidth, unless it is compensated by a taper of the undulator field. Third, spontaneous radiation overlaps with the FEL signal and defines the background signal for the FEL measurements.

* Work supported by the U.S. Department of Energy contract DE-AC02-76F00515

† reiche@physics.ucla.edu

From the FEL point of view it is essential to know the spectral and angular distribution of the spontaneous distribution to optimize the experimental set-up for the highest signal-noise ratio. Because the LCLS undulator lattice consists out of undulator modules and quadrupoles which are arrange with two short and one long drift sections between modules and because the closest detector is not place in the far field zone of the undulator, simple analytical calculations of the spontaneous radiation are not sufficient. For that reason we developed a numerical code to calculate the explicit background signal at the detector location. the algorithm is from first principle, based on the Lienard-Wichert potential [8]. The initial results for the LCLS undulator are presented here.

ANALYTICAL MODEL

The total radiated power from the incoherent part of the undulator radiation is given by [7]

$$P = \frac{N_u}{6} Z_0 I e k_u \gamma^2 K^2 \quad , \tag{1}$$

where N_u is the number of undulator periods, $Z_0 \approx 377\ \Omega$ is the vacuum impedance, I the beam current, e the electron charge, $k_u = 2\pi/\lambda_u$ the undulator wavenumber with λ_u as the undulator period, γ the electron energy in units of its rest mass energy, and K the undulator parameter. For LCLS parameters the emitted power is 75 GW [5], about 10 times larger than the maximum FEL signal. Enhancement due to the coherent emission at longer wavelengths are negligible.

Eq. 1 allows to calculate the total energy loss, which is sufficient to derive the required taper of the undulator field in order to preserve the resonance condition. However it lacks any angular or spectral information. To calculate the radiation seen by a detector behind the undulator, the electric field is

$$\vec{E} = \frac{e}{4\pi\epsilon_0 c} \frac{\vec{n} \times [(\vec{n} - \vec{\beta}) \times \dot{\vec{\beta}}]}{(1 - \vec{n}\vec{\beta})^3 R} \quad , \tag{2}$$

evaluated at the retarded time. Neither the direction of observation $\vec{n}$ nor the distance R between source and target is constant for LCLS FEL , where the closest detector is located 113 m behind the exit of the 130 m long, multi-segment undulator.

The emission is the strongest due to the maximum Doppler shift, where the electron moves parallel to the direction of observation, fulfilling the condition

$$\frac{K}{\gamma} \sin(k_u z) = \frac{n_x}{n_z} \quad . \tag{3}$$

Eq. 3 is only valid for observation angles θ between 0 and K/γ in the xz-plane. Beyond that as well as in the yz-plane the radiation intensity drops like the normal synchrotron radiation with a characteristic fall-off of $1/\gamma$. Note that the signal from a single period is antisymmetric in the retarded time frame with respect to the emission time at $z = \lambda/2$. The forward direction shows alternating, equally spaced unipolar pulses. The pulses are narrow due to the Doppler effect and excite a rich harmonic content of odd harmonics. To estimate the number of harmonics, we calculate the pulse length in the retarded time frame. The pulse shape is dominated by the denominator in Eq. 2 and scales as $E \propto (1-\beta_z)^{-2}$. With $\beta_z = 1-(1+K^2/2)/2\gamma^2 + (K^2/4\gamma^2)\cos(2ck_ut)$ the full-width half maximum is given by

$$\Delta T = \frac{1}{ck_u}\cos^{-1}\left[\frac{2(1-\sqrt{2})+K^2}{K^2}\right] \quad .$$

In the retarded time frame it becomes

$$\Delta\tau = \frac{1+K^2/2}{2\gamma^2}\Delta T - \frac{K^2}{4ck_u\gamma^2}\sin(ck_u\Delta T) \quad .$$

The ratio between resonant wavelength and FWHM of the observed pulse length ($c\Delta\tau$) defines the harmonic content. For LCLS parameters the value is 120.

For larger observation angles in the xz-plane pairs of adjacent unipolar pulses are shifted closer to each other till they merge to a single bipolar pulse at an angle of $\theta = K/\gamma$ and beyond. The emission of each nth harmonic has $n-1$ knots in the xy-plane and is slightly more confined in the forward direction than the fundamental, because the observed pulses are wider due to the reduced curvature in the electron trajectory, where Eq. 3 is fulfilled.

NUMERICAL MODEL

The program SPUR (SPontaneous Undulator Radiation) has been written to calculated the radiation pattern from an arbitrary undulator lattice at any point behind the undulator. It supports parallel architecture with a master-slave configuration using the Massage Passing Interface (MPI) method [9], where a master node assigns the work to slave nodes and thus optimizes the CPU usage for asymmetric nodes or unbalanced load upon a symmetric cluster.

Either the radiation pattern from a single electron onto a two dimensional grid or from multiple electrons onto a single point in space can be calculated, including single electron to single point configuration. The program is based on Eq. 2, calculating the time-domain signal in the retarded time frame. Fourier transformation methods of uneven sampled data [10] have shown an unacceptable level of noise, compared to standard Fast Fourier Transformation (FFT) of the signal, after it has been interpolated to an equidistant grid.

The undulator lattice can be defined down to each individual pole, including arbitrarily long drift sections between undulator modules. The electron trajectory is analytical calculated for each undulator period with a step width, sufficiently small enough to resolve all harmonics. In the case for LCLS with more than 100 harmonics, at least 256 steps per period are required and then interpolated to a 4 times finer grid in the retarded time frame to achieve convergence in the spectrum. For LCLS with a total of about 3700 periods it yields record sizes for the FFT of about 7 million sample points. Thus the memory demand is limited to 100 MByte. To reduce the output for runs with a large number of grid points, the spectrum can be downsampled to a frequency resolution, lower than the maximum resolution $\Delta f/(\lambda/c) \approx 1/N_u$.

RADIATION PROPERTIES

At LCLS the first detector station is located 113 m behind the end of the undulator [4]. It is exposed to the highest intensity of both FEL and spontaneous radiation compared to the second diagnostic station, which is further downstream of the X-ray beam transport line. Due to the close proximity of the first detector to the undulator, the calculation of the radiation cannot be simplified by assuming the far field zone. First, the R^{-2}-dependence of the emission sources along the undulator with respect to the fixed detector location is noticible. Second, the angle of observation is not constant for off-axis position, but shifts towards larger values. As a consequence a systematic redshift dominates the width of the harmonics, which minimal value of $1/N_u$ can only be observed on-axis. While the intrinsic energy spread is smaller than $1/N_u$, the finite beam size and divergence has a non-negligible effect on the bandwidth as well.

At the detector location the peak intensity is 20 GW/cm^2, illuminating an area of 6×2 cm^2 (full width in the x- and y-direction). The observed total power is 75 GW, which has a contribution of 0.6 GW due to the coherent emission of the bunch profile [11]. Fig. 1 shows the intensity distribution at the first detector location.

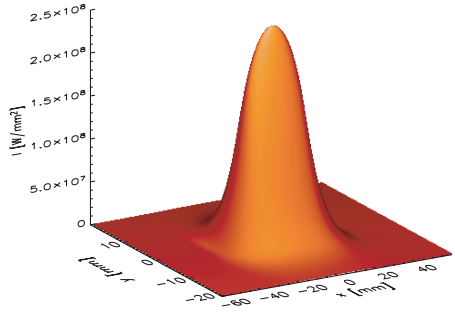

Figure 1: Intensity distribution of the spontaneous radiation at the detector location, 113 m behind the LCLS undulator.

It is essential for the FEL amplification that all undulator modules are well tuned and aligned to the undulator

axis. The on-axis field requirement is $\Delta K/K \approx 10^{-4}$ [5], which would be desirable to measure it for each undulator module individually. However this information cannot be extracted from the radiation distribution and intensity, which are insensitive to such small variation. The most promising measurement is the width of the harmonics of the on-axis radiation. While the fundamental harmonic has an intrinsic width of about 1% – corresponding to 112 undulator periods per module – a change in the width on a percent level is difficult to measure, but the effect of a detuned module becomes enhanced with higher harmonics. E.g. at the 100th harmonics the shift in the wavelength due to a detuning of $\Delta K/K \approx 10^{-4}$ is 1% and thus comparable to the intrinsic bandwidth. However the width can be broaden by beam trajectory alignment and the beam emittance and thus obscure the measurement. It seems more beneficial to derive the undulator field quality from the power versus undulator position measurement of the FEL signal.

BACKGROUND SIGNAL FOR THE FEL RADIATION

The radiation power of the incoherent emission is about 75 GW and therefore 10 times larger than the expected saturation power level of the FEL at 1.5 Ångstroem. To improve the signal to noise ratio the incoherent background signal can be either cut by spatial aperture limitation or by bandpass filters. In this section we estimate the efficiency of both methods. It excludes the frequency dependent sensitivity of the X-ray detector, which are typically less efficient at higher frequencies than at the FEL frequency [12]. The estimate, given below, is an upper limit for the detected signal.

Time-dependent FEL codes, such as Ginger or Genesis 1.3, cannot predict the total background signal, because they model only a narrow bandwidth around the resonant wavelength for an optimized calculation of the FEL process [13]. The typical full bandwidth in the FEL simulation of X-ray lasers such as LCLS and TESLA is between 5% and 10%. In addition the code discretize the radiation field to a finite set of radiation modes, imposing a limit on the maximum angle of emission. These cuts do not affect the result of the FEL simulation because strongly diffracting modes as well frequency deviation larger than the FEL bandwidth are amplified by the FEL process. To add the correct background signal, the spontaneous signal from the FEL simulation is removed first by subtracting the linear trend in the start-up process of the FEL signal. Then the background signal, calculate by SPUR, is added.

The FEL signal is much more confined in the spatial direction than the spontaneous radiation. With an rms diffraction angle of about 1 μrad the FEL signal covers an area of about 3 mm^2 at the detector position 113 m behind the end of the LCLS undulator. A smaller aperture would cut the FEL signal, which is not in the interest of the measurement. In the contrary the aperture has to be larger to allow for jitter in the FEL beam centroid. The dependence of the spontaneous radiation background signal and the FEL signal on the aperture is shown in Fig. 2. With an aperture of 1 mm^2 0.9 GW of the spontaneous radiation is detected, resulting in a signal-to-noise ratio of only 10:1. If the detector is array-based like a CCD camera, the measurement is rather intensity than power based. In case for LCLS the ratio between the intensities is 100 to 1, an improvement of one order of magnitude compared to a collecting detector with the aperture of 1 mm^2, mentioned above.

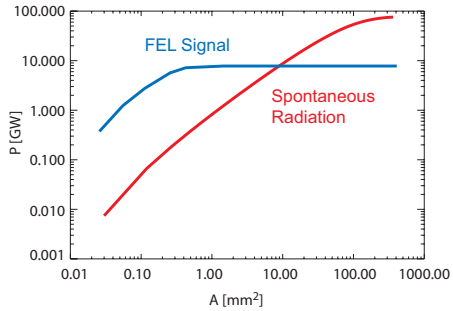

Figure 2: Detected power of the FEL signal and the spontaneous radiation for an aperture limit at the detector location, 113 m behind the undulator exit.

Spatial cuts are inferior to spectral cuts because even under the best circumstances a spatial aperture cannot filter out higher harmonics. For high K undulator such as LCLS a large number of odd harmonics are emitted on-axis, some of them with higher power than the fundamental. A significant reduction can be achieved when only the emission at the resonant wavelength is collected. Although higher harmonics can contribute to the resonant wavelength due to the red shift for larger emission angles θ, they can be filtered out by a loose spatial cut. For the second harmonic the angle to shift the wavelength to the fundamental wavelength is 100 μrad and can be easily collimated by a 1 cm^2 aperture in front of the LCLS detector.

Due to the intrinsic width of $\delta f/f_0 = 1/N_u$ of the spontaneous signal the radiation at the resonant wavelength is confined in the opening angle of

$$\Delta\theta = \frac{K}{2\gamma}\sqrt{\frac{1}{N_u}},$$

with $\Delta\theta = 1.5$ μrad for LCLS parameters. This correspond to an emission of 1 MW per 0.1% bandwidth. The full FEL signal falls within this bandwidth, yielding a signal-to-noise ratio of about 10^4:1. Even wider bandwidth cuts are still superior to the spatial collimation. The detectable FEL signal for LCLS and various methods of reducing the spontaneous background is shown in Fig. 3

From the point of view of detecting the FEL signal the situation is improved when the FEL is operated at lower energy, because the saturation power has a weak dependence on the energy while the incoherent radiation is 10 times smaller for a FEL wavelength of 1.5 nm. In addition the

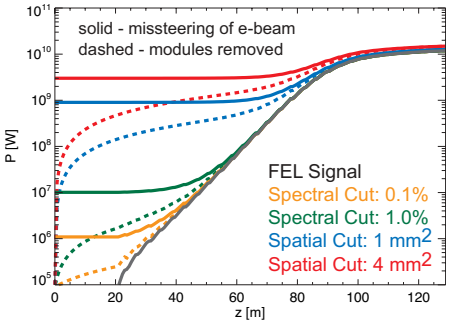

Figure 3: Detectable FEL signal for various method to reduce the background signal of the spontaneous radiation.

Table 1: Power level of the LCLS FEL and background signal for various spatial and spectral cuts at the near hall detector.

Signal	1.5 Å	1.5 nm
FEL	8 GW	4 GW
Spontaneous Radiation	75 GW	7.5 GW
Spectral Cut: 0.1%	1 MW	100 kW
Spectral Cut: 1.0%	10 MW	1 MW
Spatial Cut: 1 mm^2	0.9 GW	9 MW
Spatial Cut: 4 mm^2	3 GW	30 MW

opening angle is increased by $\sqrt{10}$, so that the on-axis intensity drops by two orders of magnitude for spatial cuts. Because the coherence angle is also increased the spectral power in a narrow bandwidth is improved only by a factor of 10. Tab. 1 summarize the different power levels of the FEL and background signal for the two limits in the FEL wavelength of LCLS.

CONCLUSION

We have written a numerical code to calculated the background signal from the spontaneous radiation at a given location to detect the X-ray FEL signal. Due to the complex lattice of the undulator and the close proximity of the detector the spontaneous radiation can be estimated analytically only in crude approximation and detailed numerical calculations are required. With a given intensity distribution and the associated spectrum of the background signal the X-ray optics and detector can be optimized to maximize the signal to noise ratio of the FEL signal.

Because the on-axis spectrum is rich in harmonics, spatial collimation are less efficient than spectral filters (monochromators or dispersive optical elements). In the ideal case, when only 0.1% of the spontaneous radiation illuminates the detector the background signal is dropped to 1 MW, while the FEL signal is not affected. Detection of the FEL signal after 20 m of undulator becomes possible. All modules after that point can be examine by the exponential growth for optimum alignment and tuning.

REFERENCES

[1] A. Tremaine *et al.*, Phys. Rev. Lett. **88** (2002) 204801

[2] S.V. Milton *et al.*, Science **292** (2001) 2037

[3] V. Ayvazyan *et al.*, Phys. Ref. Lett. **88** (2002) 104802

[4] *Linac Coherent Light Source (LCLS)*, SLAC-R-521, UC-414 (1998)

[5] TESLA-FEL 2001-05, Deutsches Elektronen Synchrotron, Hamburg, Germany (2001)

[6] C. Pellegrini and J. Stöhr, Nucl. Inst. & Meth. **A500** (2003) 33

[7] K.J. Kim, in AIP Conference Proceedings **184**, M. Month and M. Dienes, eds., (1989) 585

[8] J.D. Jackson, *Classical Electrodynamics*, (John Wiley and SOns, New York, 1975)

[9] Message Passing Interface Forum, Computer Science Dept. Techincal Report CS-94-230, University of Tennessee, Knoxville (1994)

[10] N.R. Lomb, Astrophysics and Space Science **39** (1976) 447

[11] S. Reiche and Z. Huang,*Coherent Radiation Effects in the LCLS Undulator*, presented at this conference.

[12] R. Bionta, *private communication*

[13] Z. Huang and K.-J. Kim, Nucl. Inst. & Meth. **A507** (2003) 65

Generation of GW-level, sub-Angstrom Radiation in the LCLS using a Second-Harmonic Radiator *

Z. Huang†, SLAC, Stanford, CA 94309, USA
S. Reiche, UCLA, Los Angeles, CA 90095, USA

Abstract

Electron beams are strongly microbunched near the high-gain free-electron laser (FEL) saturation with a rich harmonic content in the beam current. While the coherent harmonic emission is possible in a planar undulator, the third-harmonic radiation typically dominates with about 1% of the fundamental power at saturation. In this paper, we discuss the second-harmonic radiation in the Linac Coherent Light Source. We show that by a suitable design of an second-stage undulator with its fundamental frequency tuned to the second harmonic of the first undulator, coherent second-harmonic radiation much more intense than the third-harmonic is emitted. Numerical simulations predict that GW-level, sub-Angstrom x-ray pulses can be generated in a relatively short second-harmonic radiator.

INTRODUCTION

In a single-pass, high-gain free-electron laser (FEL) strong bunching at the fundamental wavelength can drive substantial nonlinear harmonic bunching [1]. For a planar undulator, third-harmonic radiation can typically reach 1% of the fundamental power level at saturation [2, 3]. While comparable second-harmonic power has been observed at the VISA [4] and the LEUTL [5] FELs and is in agreement with the theoretical expectations [6], the second-harmonic content is in general much smaller than 1% of the fundamental at very high-energy FELs such as the Linac Coherent Light Source (LCLS) [7]. To further increase the harmonic emission, a second undulator with its fundamental frequency tuned to a harmonic number of the first undulator may be used [8, 9, 10]. A major concern of this method is the effectiveness of the second undulator due to the increased beam energy spread induced by the nonlinear FEL interaction in the first undulator. Another harmonic generation method for a self-amplified spontaneous emission (SASE) FEL [11], similar to the high-gain harmonic generation (HGHG) scheme for seeded FELs [12], proposes to operate the first undulator in the linear regime for energy modulation and to use a dispersion section for nonlinear harmonic bunching. The relatively cold beam can then be sent into a second undulator for effective harmonic generation.

The shortest-wavelength x-ray for the LCLS fundamental radiation is 1.5 Å. While there is a great interest in reaching shorter x-ray wavelengths such as the 0.86-Å ^{57}Fe Mössbauer spectroscopy, generation and saturation of the FEL fundamental radiation at 1 Å or below is extremely difficult with the present state of the art electron beams (see, e.g., Ref. [13]). In this paper, we show that the second-harmonic radiation in the main LCLS undulator is very small and can be significantly enhanced by a second-harmonic radiator in order to expand the wavelength range and scientific capabilities of the facility. Since the electron beam quality at x-ray wavelengths is usually limited by the beam emittance rather than by the energy spread, operating the first undulator at saturation does not severely affect the performance of the second harmonic radiator. Instead, we find that by optimizing the focusing strength in the second-harmonic radiator and by applying the appropriate undulator taper, we can effectively extract more than 10% of the fundamental power in a relatively short undulator, which can then operate parasitically to the first undulator. Fully three-dimensional, time-dependent FEL simulation code GENESIS [14] is used to predict the performance of the second-harmonic radiator.

SECOND-HARMONIC CONTENT IN THE MAIN LCLS UNDULATOR

The LCLS uses the last one-third of the SLAC linac (about $\gamma mc^2 \approx 14$ GeV) to drive an x-ray SASE FEL at the fundamental wavelength $\lambda_1 = 1.5$ Å to reach a saturation power $P_1 \approx 10$ GW in a 100-m undulator. It is expected that the third-harmonic power can reach 100 MW near saturation. Although the second-harmonic bunching is higher than the third-harmonic bunching due to the nonlinear harmonic interaction, only odd harmonics are emitted in the forward direction. Even harmonics radiation can be emitted off-axis for a single electron and hence are present for a beam with a finite transverse extension [15]. In addition, even-harmonic emissions may be enhanced for a misaligned beam trajectory [16]. Before investigating the performance of the second-harmonic radiator, we estimate in this section the second-harmonic content in the main LCLS undulator due to both of these two effects.

The electron motion in the undulator consists of a fast wiggling oscillation and a slow betatron trajectory. Let us write the transverse velocities as $v_x = c[K/\gamma \cos(k_u z) + x']$ and $v_y = cy'$, where K is the undulator parameter, $\lambda_u = 2\pi/k_u$ is the undulator period, x' and y' are the transverse angles of the slow trajectory, and z is the undulator

* Work supported by the U.S. Department of Energy contract DE-AC02-76SF00515.

† zrh@slac.stanford.edu

distance. The longitudinal velocity is

$$\frac{dz}{dt} = v_z = \sqrt{v^2 - v_x^2 - v_y^2} = c\left[1 - \frac{1}{2\gamma^2} - \frac{K^2}{4\gamma^2} - \frac{K^2}{4\gamma^2}\cos(2k_u z) - \frac{Kx'}{\gamma}\cos(k_u z) - \frac{x'^2 + y'^2}{2}\right]. \quad (1)$$

It is convenient to treat z as the independent variable, and regard t as the electron arrival time at the undulator distance z. Integrating Eq. (1) yields

$$ct = ct^* + \frac{K^2}{8k_u\gamma^2}\sin(2k_u z) + \frac{Kx'}{k_u\gamma}\sin(k_u z),$$
$$ct^* = \left(1 + \frac{1 + K^2/2}{2\gamma^2} + \frac{x'^2 + y'^2}{2}\right) z, \quad (2)$$

where $(x'^2 + y'^2)$ is taken to be approximately constant after averaging over one FODO cell [17]. Thus, the average longitudinal motion ct^* is accompanied by a longitudinal oscillation at twice of the transverse wiggling frequency ck_u, as well as another longitudinal oscillation at the wiggling frequency due to the coupling to the horizontal orbit. We can change the time variable t to the ponderomotive phase θ:

$$\theta(z) = (k_u + k_1)z - ck_1 t^* \quad (3)$$
$$= (k_u + k_1)z - ck_1 t + \xi\sin(2k_u z) + \frac{8x'\xi}{K/\gamma}\sin(k_u z),$$

where $k_1 = 2\pi/\lambda_1 = 2\gamma^2 k_u/(1 + K^2/2)$ is the fundamental wavenumber and $\xi = K^2/(4+2K^2)$. Inserting this expression into the paraxial wave equation (e.g., Eq. (2) of Ref. [6]) and expanding the exponent for $8\gamma x'\xi/K \ll 1$, the n^{th} harmonic field E_n ($n = 1, 2, ...$) is given by

$$\left(\frac{\partial}{\partial z} + \frac{\nabla_\perp^2}{2ink_1}\right)E_n \approx -\frac{ecKZ_0}{\gamma\lambda_1}\int_{-\infty}^{\infty} d\theta e^{-in\theta} \times e^{ink_u z + in\xi\sin(2k_u z)}\cos(k_u z)\sum_{j=1}^{N_e}\delta(y - y_j)\,\delta(\theta - \theta_j) \times \left[\delta(x - x_j) + in\xi\frac{8x'_j}{K/\gamma}\sin(k_u z)\delta(x - x_j) - \frac{K}{\gamma k_u}\sin(k_u z)\delta'(x - x_j)\right], \quad (4)$$

where $\nabla_\perp^2$ is the transverse Laplace, $Z_0 = 377\ \Omega$ is the vacuum impedance, $\delta'(x) = d\delta(x)/dx$, and the sum is over N_e electrons.

Since both the FEL interaction and the betatron motion occur on a length scale much longer than the fast wiggling motion, we can average the current source (the right hand side) of Eq. (4) over the wiggling motion. The first term in the square bracket contributes to odd-harmonic radiation in the forward direction. After summing over all electrons for the second term in the square bracket, we obtain even-harmonic radiation due to trajectory errors with the coupling strength $8n\gamma x'_c\xi/K$, where x'_c is the trajectory angle of the beam centroid motion. Summing over all electrons for the last term of the square bracket yields even-harmonic emissions due to a finite beam size with the coupling strength $K/(\gamma k_u\sigma_x)$) [6], where σ_x is the rms transverse size of the electron beam. Using a bunching parameter $b_n = |\sum_{j=1}^{N_e} e^{-in\theta_j}|/N_e$ to characterize the current source at the n^{th} harmonic, we can estimate the second-harmonic power P_2 due to a finite beam size as

$$P_2 \approx P_1\left(\frac{K}{\gamma k_u\sigma_x}\right)^2\left(\frac{[\text{JJ}]_2}{[\text{JJ}]}\right)^2\frac{b_2^2}{b_1^2}, \quad (5)$$

where the Bessel function factors are [JJ]$= [J_0(\xi) - J_1(\xi)]$ and $[\text{JJ}]_2 = [J_0(2\xi) - J_2(2\xi)]/2 = J_1'(2\xi)$. Similarly, we can estimate the second-harmonic emission due to trajectory errors as

$$P_2 \approx P_1\left(\frac{8\gamma K\langle(x'_c)^2\rangle^{1/2}}{2 + K^2}\right)^2\left(\frac{[\text{JJ}]_2}{[\text{JJ}]}\right)^2\frac{b_2^2}{b_1^2}, \quad (6)$$

where $\langle(x'_c)^2\rangle^{1/2}$ is the rms angle of the beam trajectory.

The evolution of the fundamental and the harmonic bunching is determined by the nonlinear interaction of the fundamental radiation field with the electron beam. Figure 1 shows GENESIS simulation of the fundamental and the second-harmonic bunching for an average beta function $\langle\beta\rangle = 30$ m in the LCLS undulator. The electron beam is assumed to have a normalized transverse emittance $\gamma\epsilon = 1.2\ \mu$m, a peak current $I_0 = 3.4$ kA, and an initial rms relative energy spread $\sigma_{\delta 0} = 1 \times 10^{-4}$. For simplicity, no drift spaces between undulator sections are included in our simulations. At the FEL saturation (around $z = 86$ m), we have $|b_1| \approx 0.30$ and $|b_2| \approx 0.075$. Taking $K = 3.7$ and $\lambda_u = 3$ cm, we obtain from Eq. (5) that $P_2 \approx 50$ kW for a perfect trajectory. For BPMs that have a resolution of about 2-μm and are separated by about 4 m, the tolerable rms trajectory misalignment angle is $\langle(x'_0)^2\rangle^{1/2} \approx 2/4 = 0.5\ \mu$rad [18]. Assuming the FEL still

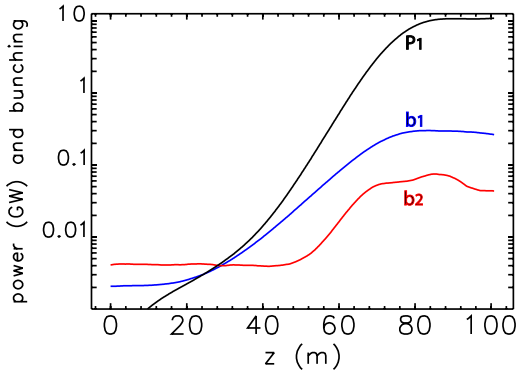

Figure 1: Fundamental radiation power (black) and bunching (blue), second-harmonic bunching (red) along the main LCLS undulator.

reaches saturation in the 100-m undulator, Eq. (6) yields 110 kW additional second-harmonic power due to the imperfect trajectory, still three orders of magnitude smaller than the expected third-harmonic power.

COHERENT HARMONIC GENERATION IN THE SECOND-HARMONIC RADIATOR

Since there is substantial second-harmonic bunching at the FEL saturation, it should be possible to significantly increase the second-harmonic radiation by using a second-stage undulator with its resonant wavelength tuned to the second-harmonic wavelength (i.e., $\lambda_2 = 0.75$ Å) of the LCLS. In this section, we study and optimize the performance of such a second-harmonic radiator. Table 1 lists the parameters for a planar Nd-Fe-B undulator that is resonant at 0.75 Å. The undulator gap $g = 5$ mm and the peak magnetic field B_0 are determined by Halbach's formula [19]. Since the field quality tolerance of the second-harmonic radiator is expected to be more relaxed than the first undulator, a helical undulator (with a wider gap) may be used to generate circularly-polarized second-harmonic radiation.

Table 1: Parameters for the LCLS second-harmonic radiator.

Parameter	symbol	value	unit
undulator period	λ_{u2}	2.38	cm
undulator gap	g	5	mm
peak magnetic field	B_0	1.26	Tesla
undulator parameter	K_2	2.81	
resonant wavelength	λ_2	0.75	Å
undulator length	L_{u2}	43	m
total linear taper	$\Delta K_2/K_2$	0.25	%
average beta function	$\langle\beta_2\rangle$	15	m

For a pre-bunched beam entering the second-harmonic radiator, the coherent radiation power is given by [20]

$$P_2 = \frac{I_0^2 Z_0}{8\gamma^2}\frac{K_2^2[\mathrm{JJ}]^2}{4\pi\sigma_x^2}\left(\int_0^{L_{u2}} b_2(z)dz\right)^2, \qquad (7)$$

where the Bessel function factor [JJ] is now evaluated for the new undulator parameter K_2. We see that a smaller transverse beam size can generate more coherent radiation, but the increased angular spread also leads to a larger spread in ponderomotive phase that degrades the bunching. The phase spread due to the emittance can be estimated from Eqs. (2) and (3) for the second-harmonic phase θ_2:

$$\left\langle\frac{d\theta_2}{dz}\right\rangle = \frac{2\pi}{\lambda_2}\sigma_{x'}^2 = \frac{2\pi}{\lambda_2}\frac{\epsilon}{\langle\beta_2\rangle}. \qquad (8)$$

For the FEL that reaches saturation in the first undulator, the micro-bunched beam has a rms relative energy spread $\sigma_{\delta f} \approx \rho \approx 4.5\times10^{-4}$, where ρ is the FEL parameter [21].

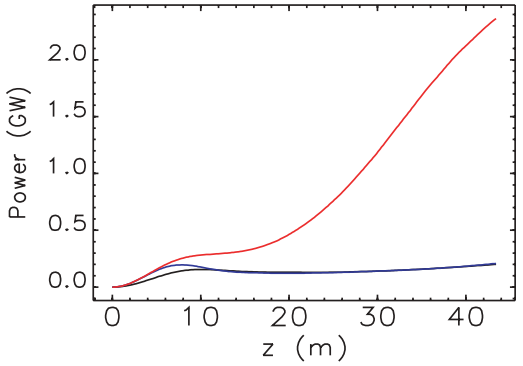

Figure 2: Radiation power in the second-harmonic radiator for (a) 15-m average beta, 0.25% linearly tapered undulator (red), (b) 15-m average beta, uniform undulator (blue) and (c) 30-m average beta, uniform undulator (black).

The resulting second-harmonic phase spread is

$$\left\langle\frac{d\theta_2}{dz}\right\rangle = \frac{4\pi}{\lambda_{u2}}\sigma_{\delta f} \approx \frac{4\pi}{\lambda_{u2}}\rho. \qquad (9)$$

The optimal focusing strength is obtained when the right hand side of both Eqs. (8) and (9) are equal. Thus, an average beta function $\langle\beta_2\rangle \approx \epsilon\lambda_{u2}/(2\rho\lambda_2) \approx 15$ m would generate the most coherent harmonic power without degrading the bunching beyond the level caused by the energy spread. Note that this value of the average beta function is about a factor of 2 smaller than the average beta function in the LCLS main undulator.

To simulate harmonic generation, GENESIS has been upgraded to allow for up-conversion of its internal particle distribution to higher harmonics. The particle phases are converted by $\theta_n = n\theta$, filling n successive slices to keep the spectral resolution of the simulation constant. It also requires a change in the shot noise algorithm to provide the correct bunching statistics on all harmonics supported by the simulation, and follows closely the method of harmonic decomposition of the fluctuation in the particle phase [22]. For the second-harmonic generation, the electron distribution is extracted at a post-saturation distance $z \approx 90$ m of the first undulator (with $b_2 \approx 0.06$ instead of the maximum value 0.075). As seen in Fig. 1, the second-harmonic bunching is somewhat reduced from the maximum value after saturation. If necessary, this reduction may be minimized by a slight increase of the initial energy spread with a designated energy-spread heater in the LCLS [23] to allow the FEL saturation at the end of the first undulator. The electron transverse phase space is assumed to be properly matched into the second undulator.

At this optimal focusing strength, the rapid build-up of coherent power in the second-harmonic radiator enables tapering the undulator parameter K_2 in order to trap sufficient electrons for effective harmonic generation. For simplicity, we consider here only a linear taper that starts at the beginning of the undulator. The taper strength is

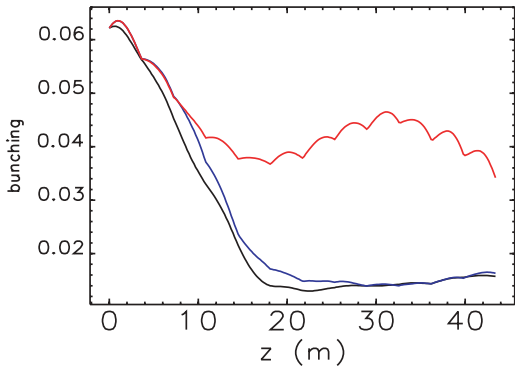

Figure 3: Bunching parameter in the second-harmonic radiator for (a) 15-m average beta, 0.25% linearly tapered undulator (red), (b) 15-m average beta, uniform undulator (blue) and (c) 30-m average beta, uniform undulator (black).

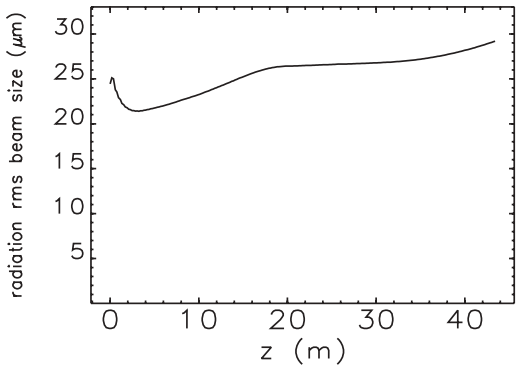

Figure 4: RMS beam size of the 0.75-Å radiation along the second-harmonic radiator.

then varied to maximize the output power. Figure 2 shows SASE simulations of both tapered and uniform undulators at $\langle\beta_2\rangle = 15$ m. An 43-m tapered undulator with a taper strength $\Delta K_2/K_2 = 0.25$ % generates more than 2 GW output power at 0.75 Å, which is about one order of magnitude larger than that from the uniform undulator. Examination of Fig. 3 indicates the effectiveness of the undulator taper in maintaining the second-harmonic bunching against the phase spread from both the emittance and the energy spread, while the bunching parameter drops almost independent of the focusing strength for a uniform undulator. Figure 2 also shows that a larger beam size in the undulator (with $\langle\beta_2\rangle = 30$ m) generates less coherent radiation initially. Hence the undulator taper may not be as effective.

Finally, Fig. 4 shows that the radiation rms beam size along the second-harmonic radiator follows closely to the rms electron beam size ($\sigma_x = 26$ μm), indicating a nearly diffraction-limited radiation at 0.75 Å. The relative rms spectrum bandwidth of the 0.75-Å radiation is about 0.05%, similar to the bandwidth of the saturated fundamental radiation at 1.5 Å in the first undulator. These x-ray pulses from both undulators are naturally synchronized as they are generated by the same electron beam.

CONCLUSIONS

Given that the LCLS reaches saturation in the planned 100-m undulator, the significant second-harmonic bunching can still be very useful in generating high-power, shorter-wavelength coherent radiation which is otherwise difficult to obtain with the current electron beam technology. The analysis and simulations presented in this paper show that an second-harmonic radiator operating parasitically to the main LCLS undulator can effectively produce GW-level, sub-Angstrom x-rays for scientific applications.

We thank P. Emma, J. Hastings, and K.-J. Kim for useful discussions.

REFERENCES

[1] R. Bonifacio, L. De Salvo, and P. Pierini, Nucl. Instr. Meth. A **293**, 627 (1990).

[2] H.P. Freund, S.G. Biedron, and S.V. Milton, IEEE J. Quantum Electron. **QE-36**, 275 (2000); Nucl. Instr. Meth. A **445**, 53 (2000).

[3] Z. Huang and K.-J. Kim, Phys. Rev. E, **62**, 7259 (2000).

[4] A. Tremaine *et al.*, Phys. Rev. Lett. **88**, 204801 (2002).

[5] S. Biedron *et al.*, Nucl. Instr. Meth. A **483**, 94 (2002).

[6] Z. Huang and K.-J. Kim, Nucl. Instr. Meth. A **475**, 112 (2001).

[7] Linac Coherent Light Source Conceptual Design Report, SLAC-R-593, 2002.

[8] R. Bonifacio *et al.*, Nucl. Instr. Meth. A **296**, 787 (1990).

[9] W. Fawley *et al.*, in *Proceedings of the 1995 Particle Accelerator Conference*, 219 (IEEE, Piscataway, NJ,1995).

[10] F. Ciocci *et al.*, IEEE J. Quantum Electron. **QE-31**, 1242 (1995);.

[11] J. Feldhaus *et al.*, Nucl. Instr. Meth. A **528**, 471 (2004).

[12] L.H. Yu, Phys. Rev. A **44**, 5178 (1991).

[13] M. Cornacchia, J. Synchrotron Rad. **11**, 227 (2004).

[14] S. Reiche, Nucl. Instrum. Methods Phys. Res. A **429**, 243 (1999).

[15] M.J. Schmitt and C.J. Elliott, Phys. Rev. A **34**, 4843 (1986).

[16] W.B. Colson, G. Dattoli, and F. Ciocci, Phys. Rev. A **31**, 828 (1985).

[17] S. Reiche, Nucl. Instrum. Methods Phys. Res. A **445**, 90 (2000).

[18] P. Emma, private communication.

[19] K. Halbach, J. Phys. (Paris) Colloq. **44**, C1-211 (1983).

[20] L.H. Yu and J. Wu, Nucl. Instrum. Methods Phys. Res. A **483**, 493 (2002).

[21] R. Bonifacio, C. Pellegrini, and L.M. Narducci, Opt. Comm. **50**, 373 (1984).

[22] W. Fawley, Phys. Rev. ST Accel. Beams 5, 070701 (2002).

[23] Z. Huang *et al.*, Phys. Rev. ST Accel. Beams **7**, 074401 (2004).

EMITTANCE AND QUANTUM EFFICIENCY MEASUREMENTS FROM A 1.6 CELL S-BAND PHOTOCATHODE RF GUN WITH MG CATHODE

J.F. Schmerge*, J.M. Castro, J.E. Clendenin, D.H. Dowell, S.M. Gierman, and R.O. Hettel, SLAC, Menlo Park, CA 94025, USA

Abstract

A comparison of electron beam parameters from a 1.6 cell S-band rf gun with Cu and Mg cathode at the SLAC Gun Test Facility are reported. The lower work function of Mg compared to Cu theoretically increases the quantum efficiency for a fixed laser wavelength and also increases the thermal emittance. Slice emittance measurements at low charge (15 pC) set an upper limit on the thermal emittance of 0.6 and 1.2 microns per mm radius for the Cu and Mg cathodes respectively. The longitudinal emittance measurements with both cathodes exhibit large energy spreads emitted from the gun. The measured quantum efficiency with no laser cleaning is approximately 3 10^{-5} at 110 MV/m and 30° laser phase for the Cu and 8 10^{-5} at 90 MV/m and 30° laser phase for the Mg cathode.

INTRODUCTION

The cathode is one of the most important components of a photocathode rf gun as it defines the quantum efficiency (QE) and the minimum achievable emittance or so called thermal emittance. In addition the cathode also affects the maximum attainable field in the gun due to rf breakdown at the cathode to back plate joint. The ideal cathode would exhibit high QE, low thermal emittance and would not limit the maximum attainable field. A peak on axis field of 120 MV/m is required in order to achieve an emittance of 1 μm with 1 nC of charge as desired for the Linac Coherent Light Source (LCLS) [1]. The maximum required field limits the choice of cathode materials to metals.

This paper reports the results of measurements made at the SLAC Gun Test Facility with a Mg cathode. The results are also compared with theoretical values and previously reported Cu cathode results [2]. The Cu cathode used in the study is a 1 cm diameter, single crystal (100 orientation) brazed into the polycrystalline Cu back plate. After brazing, the cathode was polished with 0.25 μm diamond paste and installed on the gun in a N_2 environment. The 2 cm diameter Mg insert was friction welded into the Cu back plate. After welding, the Mg cathode and back plate surface were machined using single point diamond tools. The cathode was offset from the lathe center to eliminate a machining defect at the center of the cathode. The Mg cathode was installed on the gun in air so that the electric field on axis could be measured with a bead drop measurement.

The maximum field attained with the Cu cathode was 127 MV/m with reliable operation at 110 MV/m and typically 2 10^{-9} Torr vacuum pressure during electron beam operation. The Mg cathode was limited to lower fields due to rf breakdown. The maximum field achieved was 107 MV/m with reliable operation at 95 MV/m and 5 10^{-10} Torr vacuum pressure with electron beam. For comparison, a polycrystalline Cu cathode with no braze or weld joint was operated up to 140 MV/m with reliable operation at 125 MV/m.

*schmerge@slac.stanford.edu

THEORY

The definition of thermal emittance is shown in equation 1 where x is the beam position and p_x is the transverse momentum [3]. Assuming a flat transverse laser pulse shape and averaging over the electron energy distribution leads to equation 2 where $r_{cathode}$ is the laser beam radius, E_k is the electron kinetic energy in the metal given by the sum of the Fermi energy and photon energy and E_b is the metal barrier energy which is the sum of the Fermi energy and work function less the Schottky barrier reduction. Using the definition of QE as the number of emitted electrons per incident photons, the QE can be computed as shown in equation 3 where R is the optical reflectivity. After integration the QE simplifies to equation 4 where E_F is the Fermi energy.

$$\varepsilon_{n-thermal} \equiv \frac{1}{mc}\sqrt{\langle x^2\rangle\langle p_x^2\rangle} \qquad 1$$

$$\varepsilon_{nthermal} = \frac{r_{cathode}}{2}\sqrt{\frac{2E_k}{mc^2}}\sqrt{\frac{\left(1-\left(E_b/E_k\right)^2+2\left(E_b/E_k\right)^{3/2}-2\left(E_b/E_k\right)^{1/2}\right)}{6\left(1+\left(E_b/E_k\right)-2\left(E_b/E_k\right)^{1/2}\right)}} \qquad 2$$

$$QE \equiv (1-R)\frac{\int_{E_{min}}^{E_b}\int_{0}^{\cos^{-1}\sqrt{\frac{E_b}{E+E_{photon}}}}\int_{0}^{2\pi} N_{electron}\sin\Phi\, d\theta\, d\Phi\, dE}{\int_{0}^{E_b}\int_{0}^{\pi}\int_{0}^{2\pi} N_{electron}\sin\Phi\, d\theta\, d\Phi\, dE} \qquad 3$$

$$QE = (1-R)\frac{\left(1+\left(E_b/E_k\right)-2\left(E_b/E_k\right)^{1/2}\right)}{2\left(E_F/E_k\right)} \qquad 4$$

Thermal emittance is primarily a function of the Fermi energy, work function and photon energy. The quantum efficiency depends on the same parameters and is also dependent on the optical reflectivity. The Cu and Mg cathode parameters are listed in Table 1 along with the calculated skin depth, QE and thermal emittance for 263 nm (4.71 eV) normal incidence photons. For the calculation it is assumed the Cu cathode has a 110 MV/m

rf field with 30° laser phase and 90 MV/m, 30° is assumed for the Mg cathode.

Table 1: Cathode parameters assuming 4.71 eV photons at normal incidence.

Parameter	Cu	Mg	Units
Work Function	4.59 [4]	3.66 [4]	eV
Fermi Energy	8.7 [5]	7.1 [5]	eV
Power Reflectivity	34 [6]	92 [7]	%
Skin depth	25	19	nm
QE	11	21	10^{-5}
$\varepsilon_{n\text{-thermal}}$	0.25	0.46	μm

The equations have been derived assuming a flat cathode surface at absolute zero and electron-electron scattering is ignored. Operation at room temperature increases the reported thermal emittance and QE for the Cu cathode by less than 2%. Temperature effects become significant above about 300 C for Cu and approximately 2000 C for Mg. The inelastic mean free path (IMFP) for electrons in Cu and Mg at 4.7 eV above the Fermi energy is not well documented. From the literature the IMFP is estimated to be on the order of 5 nm [5,8]. Since the mean free path is less than the skin depth it must be included for good agreement between theory and experiment. Including scattering will reduce the calculated QE and thermal emittance as it will decrease the average energy of photo-emitted electrons. Surface roughness has two effects. First, sharp surface features cause field enhancement that increase the Schottky effect and thus the QE and thermal emittance. Second, since electrons are emitted from a narrow cone with respect to the surface normal [3], roughness also affects the angular distribution. This effect increases the thermal emittance but has no effect on the QE. Both effects are localized and must be averaged over the entire cathode.

MEASUREMENTS

The measurements reported here are performed with a nearly Gaussian temporal pulse shape with approximately 2 ps FWHM duration. The transverse laser shape is flat and unless otherwise noted the radius is 1 mm. The laser is incident on the cathode at near normal incidence. The Cu cathode was operated at 110 MV/m and 30° laser phase resulting in 5.7 MeV beam exiting the gun. The Mg cathode was operated at 95 MV/m with 30° laser phase resulting in 5.0 MeV beam unless otherwise noted. All measurements are made with 15 pC of charge corresponding to about 12 A of peak current unless otherwise noted.

Quantum Efficiency

The QE is determined by measuring the laser energy incident on the cathode with a Joule meter and the charge exiting the gun on an insertable Faraday cup immediately downstream of the gun. The measured QE versus the laser phase for both cathodes is shown in figure 1. The QE from the Mg cathode exhibits less phase dependence than the Cu cathode because the Schottky effect is less significant due to the lower work function.

In an attempt to increase the QE from the Mg cathode, a high intensity laser pulse was scanned across the cathode with the rf off. A lens was inserted in the drive laser beam path which reduced the 2 mm diameter beam to a 68 μm rms spot size. The maximum energy available at the cathode was 22 μJ resulting in a maximum fluence at the cathode of 800 $\mu J/mm^2$. With the maximum fluence incident on the cathode there was no observable change in the vacuum pressure. Likewise there was no measurable increase in QE after the laser cleaning attempt. No attempt was made to laser clean the Cu cathode.

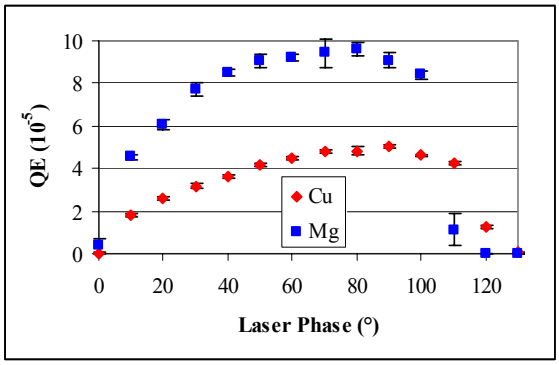

Figure 1: The QE versus laser phase. The peak field at the cathode is 110 MV/m for Cu and 90 MV/m for Mg.

The variation of QE across the cathode was also measured by scanning a 130 μm rms laser beam over a 1.5 X 1.5 mm area on the Mg cathode. The rms QE variation was 83% of the average and the minimum and maximum QE were 44% and 660% of the average respectively. The variation is probably due to localized surface contaminants either lowering the work function or altering the optical reflectivity. Since the Schottky effect is less significant for the Mg cathode it is unlikely the variation is caused by rf field enhancement due to localized sharp features on the cathode. The QE uniformity was significantly improved approximately 0.7 mm off center. Thus the laser was intentionally steered off axis away from several hot spots to improve electron beam uniformity for the emittance measurements reported below.

Significantly less variation was observed on the Cu cathode. The rms QE variation for the Cu cathode was only 11% of the average QE. The minimum and maximum were 76% and 125% respectively of the average QE.

Longitudinal Emittance

Emittance measurements were made downstream of a 3 m SLAC linac structure located approximately 90 cm downstream of the cathode. The longitudinal emittance was determined by measuring the energy spread downstream of a spectrometer magnet as a function of

linac phase [2]. The technique is analogous to a quad scan for the transverse emittance measurements. A relatively large energy spread exiting the gun was observed for both cathodes. As expected there is not a significant difference in the longitudinal phase space with the Cu and Mg cathodes.

Table 2 lists the electron beam longitudinal parameters. All parameters were determined from a standard linear least square error fitting routine. The emittance and uncorrelated energy spread listed in Table 2 are overestimated due to non-linear energy-time correlation terms. Better estimates of the uncorrelated energy spread can be determined using tomographic phase space reconstruction [9]. With the actual beam phase space distribution the true slice energy spread can be calculated as opposed to the beam envelope which includes non-linear correlated terms.

Table 2: Longitudinal Beam Parameters at Linac Entrance.

Parameter	Cu	Mg	Units
Emittance	2.5	2.8	keVps
Normalized Emittance	1.5	1.7	μm
Bunch Length	0.44	0.41	ps
Energy Spread	36	48	keV
Uncorrelated Energy Spread	5.7	6.9	keV
Linear Correlation	-81	-120	keV/ps

Slice Emittance

The transverse slice emittance is measured using a quadrupole scan technique on the identical screen used in the longitudinal emittance measurements. Since the screen is in a dispersive section, the linac phase can be varied until the beam is sufficiently chirped at the screen that the beam can be temporally sliced into 10 beamlets. The energy-time calibration can be calculated since the longitudinal beam parameters are known at the linac entrance. The known beam matrix is propagated through the linac with the amplitude and phase settings used in the transverse emittance measurement and the resulting linear energy-time correlation is the calibration used to determine the time axis for the slice emittance measurements shown later.

For the transverse measurements a total of five beam parameters are fit in a least square fitting routine. In addition to the three Twiss parameters, the phase space offset with respect to the projection in both position and angle are also included. Thus a total of five parameters for each slice are measured which determine both the position and ellipse orientation in phase space. Previously we reported the slice emittance for the Cu cathode [10] and it is repeated here after correcting the beam propagation through the spectrometer. Also included are the slice emittance results from a Mg cathode for comparison. The phase space for all ten slices and the total projected emittance is shown in figure 2 for both cathodes.

The projected emittance is larger than the slice emittance largely due to the phase space offsets in both angle and position. The offsets are measured with respect to the projected centroid and thus are not due to steering errors but rather time dependent kicks. The kicks appear independent of charge so they are not due to wakefields. This suggests they originate at the gun or linac rf couplers [11]. The reversal of the head and tail with respect to the x axis between the two cathodes may be due to the different gradients used on the cathode, the different linac phase (Mg +19° and Cu +29°) or the fact that the beam was steered slightly off center for the Mg case due to the non-uniform electron emission. This will be investigated in more detail in later experiments.

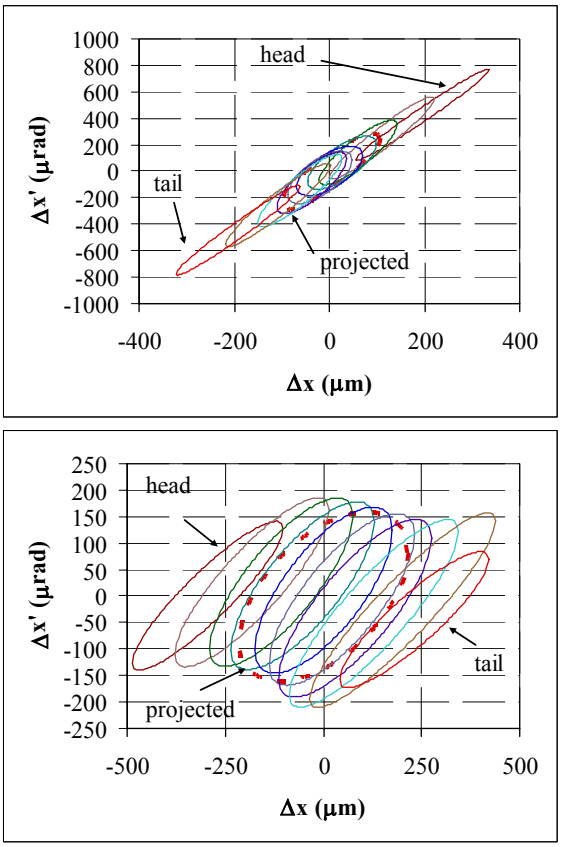

Figure 2: The upper plot shows the transverse phase space for the Cu cathode and the lower plot for the Mg cathode. The projected emittance is plotted as a red dashed line.

The minimum obtainable slice emittance is shown in figure 3 for both cathodes. The minimum emittance was obtained by measuring the emittance as a function of the emittance compensating solenoid field. It was determined empirically that the minimum emittance occurs when the solenoid focal length is adjusted to produce a waist near the linac exit.

The minimum slice emittance for the Cu cathode is approximately 0.6 μm while the Mg cathode is higher with 1.1 μm. The Cu results are in agreement with two other Cu cathode measurements at different laboratories using different techniques [12-13]. The measured values represent an upper limit for the thermal emittance from each cathode. The Mg cathode produces a higher emittance than the Cu cathode as expected although both values are approximately a factor of 2.5 times higher than the theoretical values listed in Table 1.

The emittance with the Mg cathode using a 0.5 mm radius cathode was also measured with approximately 20 pC charge and 11 A of peak current. The minimum emittance in this case was approximately 0.6 μm which is nearly half the value when the 1 mm radius laser was used. While this is consistent with the expected behavior due to thermal emittance (see equation 2) it is not conclusive that the measured emittance is equal to the thermal emittance. Experiments are underway to measure the projected emittance directly exiting the gun to better characterize the thermal emittance.

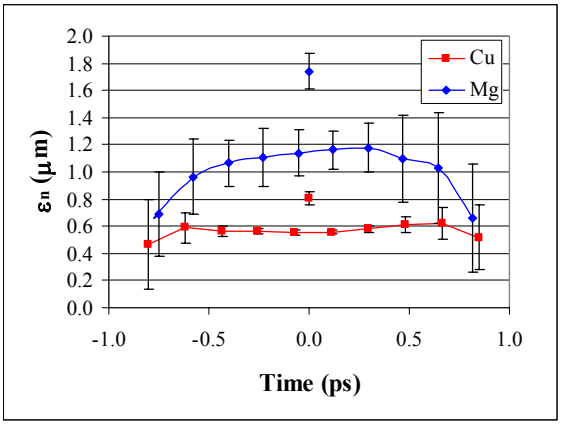

Figure 3: Emittance versus time for both the Cu and Mg cathodes. The projected emittance is plotted at t=0.

SUMMARY AND CONCLUSIONS

The transverse and longitudinal emittance in an S-band photocathode gun with a Cu and Mg cathode have been measured. No significant differences are observed in the longitudinal phase space. The minimum transverse emittance with a Cu cathode with 1 mm laser radius was 0.6 μm and 1.1 μm with the Mg cathode. The emittance from the Mg cathode decreased to 0.6 μm with a 0.5 mm radius laser spot size. These measured values set upper limits to the thermal emittance from Cu and Mg cathodes. The measurements are a factor 2.5 times larger than predicted by a theory that does not include temperature effects, surface roughness or electron-electron scattering. Only surface roughness can increase the theoretical emittance to the level of the measurements but it requires significantly roughened surfaces. It is more likely that a source of emittance growth in the gun or linac is contributing to the measured emittance. The time dependent position and angle offsets observed in the beam indicate the presence of a time dependent kick.

The QE was also measured from both cathodes. The Schottky effect is less pronounced with the Mg cathode due to the lower work function. The measured quantum efficiency with no laser cleaning is approximately 3 10^{-5} at 110 MV/m and 30° laser phase for the Cu cathode and 8 10^{-5} at 90 MV/m and 30° laser phase for the Mg cathode. No increase in QE for the Mg cathode was observed after scanning the cathode with an 800 μJ/mm^2 UV laser pulse.

ACKNOWLEDGEMENTS

The authors would like to acknowledge P. Pianetta for helpful discussions and the entire SSRL staff for helping to make this research possible. This work was supported by Department of Energy contract DE-AC02-76SF00515.

REFERENCES

[1] C. Limborg et al, NIM A528, (2004) 350-354.
[2] D. H. Dowell et al, NIM A507, (2003) 327-330.
[3] J.E. Clendenin et al, NIM A455, (2000) 198-201.
[4] R.C. Weast Editor, "CRC Handbook of Chemistry and Physics 1st Student Edition", (1988) E-78.
[5] S. Tanuma, C.J. Powell and D.R. Penn, Surface and Interface Analysis, Vol. 17, (1991) 911-926.
[6] M.J. Weber editor, "Handbook of Optical Materials", (2002) 317.
[7] E.D Palik editor, "Handbook of Optical Constants of Solids III", (1998) 239.
[8] D.R. Penn, Physical Review B, Vol. 35, No. 2, (1987) 482-486.
[9] H. Loos et al, NIM A528, (2004) 189-193.
[10] D.H. Dowell et al, Proceedings of the 2003 Particle Accelerator Conference, (2003) 2104-2106.
[11] D.H. Dowell et al, This conference, TUPOS56.
[12] W.S. Graves et al, Proceedings of the 2001 Particle Accelerator Conference, (2001) 2227-2229.
[13] J. Yang et al, Proceedings of the 2002 European Particle Accelerator Conference, (2002) 1828-1830.

THE UPGRADE OF THE DUV-FEL FACILITY AT THE BNL

X.J. Wang*, H. Loos, J.B. Murphy, G. Rakowsky, J. Rose, B. Sheehy, Y. Shen, J. Skaritka, Z. Wu, L.H. Yu, NSLS, BNL, Upton, NY 11973, USA

Abstract

The DUV-FEL linac is upgraded from 200 to 300 MeV to enable the HGHG FEL to produce 100 μJ pulses of 100 nm light. This will establish the DUV FEL as a premier user facility for ultraviolet radiation, and will enable state-of-the-art gas phase photochemistry research. Further more, the upgraded facility will also enable several critical R&Ds for future X-ray FELs, such as cascaded and higher harmonic HGHG (n>5), and experimental demonstration of the emittance spoiler for the LCLS .

The upgraded HGHG will operate at the 4th harmonic with the seed laser at 400nm. The increase of the electron beam energy will be accomplished by installing a 5th linac cavity and two 45 MW klystrons. New HGHG modulator and dispersion sections vacuum chambers will be manufactured to accommodate new matching optics and 8th harmonic HGHG. The status of the DUV-FEL upgrade and other beam physics R&D opportunities are presented..

INTRODUCTION

The Deep Ultra Violet Free Electron Laser (DUV-FEL), a laser linac facility at Brookhaven National Laboratory (BNL), is the world's only facility dedicated to laser-seeded FEL R&D and its applications. The high-gain harmonic generation (HGHG) FEL at the DUV-FEL reached saturation at 266 nm with 800 nm seeding [1] in 2002. Experiments were carried out at the DUV-FEL to further characterize the properties of the HGHG FEL and to demonstrate its fully coherence, stability and controllability. The narrower spectrum and better stability of the HGHG, compared to a self amplified spontaneous emission (SASE) FEL, were observed. Both the second and third harmonic HGHG FEL outputs were experimentally characterized using a vacuum monochromator. The pulse energies for both harmonics (133 and 89 nm, respectively) were measured to be about 1 μJ, which is about one percent of the fundamental value at 266 nm. A two-photon absorption auto-correlator with 100 fs resolution was developed to characterize the HGHG output pulse length. It was experimentally demonstrated that, the HGHG can produce output pulses with lengths from 1 ps down to 250 fs by varying the seed laser pulse length.

The first chemical science experiment – ion pair imaging, was successfully completed [2] at the DUV-FEL. The ion pair imaging experiment used the HGHG's third harmonic output (89 nm) to study the super excited states of methyl fluoride, a highly flammable gas. Velocity-mapped ion images of the fluoride ion, obtained using intense, coherent, sub-picosecond pulses of 86-89 nm light, revealed a low translational energy, implying a very high internal excitation in the molecule's methyl cation cofragment.

A series of workshops [3] was held at the NSLS to further explore the potential of the DUV-FEL facility, and to identify the future opportunities for chemical science, beam physics and FEL. The participants of the July 2003 NSLS Chemical Dynamics Workshop identified that, a VUV source with following properties will be a truly unique source for chemical science and other applications:

- Photon energy > 10 eV as a universal probe.
- Peak power > 10^{12} W/cm^2 for nonlinear process.
- $5x10^{13}$ ph/pulse for high sensitivity and single molecule detection.
- Pulse duration ~100 fs for time-resolved dynamics studies.
- Fully coherence for quantum physics and coherent control.

The workshop participants enthusiastic recommended that, the DUV-FEL facility be upgraded to make the FEL fundamental ~100 nm with the properties listed above.

Further more, the upgraded DUV-FEL should be able to enable several critical R&Ds for future X-ray FELs, such as cascaded and higher harmonic HGHG (n>5), and experimental demonstration of the emittance spoiler for LCLS [4].

In the rest of this report, the DUV-FEL upgrade options , status, and beam physics R&D opportunities with the upgraded facility will be discussed.

THE DUV-FEL UPGRADE

The DUV-FEL accelerator system consists of a 1.6-cell photo injector driven by a Ti:Sapphire laser system, and a four-section 2856 MHz SLAC-type traveling wave linac that is capable of producing a 200 MeV electron beam. The facility's magnetic chicane bunch compressor produces sub-picosecond-long electron bunches with a peak current of a few hundred amperes. The high-brightness electron beam travels down the 10 meter-long undulator to generate UV light with a fundamental wavelength of 266 nm. There are two options for the DUV-FEL to reach 100 nm fundamental. One is to replace the NISUS undulator with a shorter period one, such as VISA undulator; the other is to increase the electron beam energy (Fig.1).

After carefully considering cost, shutdown time and future experimental capabilities, the electron beam energy upgrade to 300 MeV was chosen. The longer period

* Corresponding author: xwang@bnl.gov

NISUS undulator will make the cascaded HGHG easier to realize in the future.

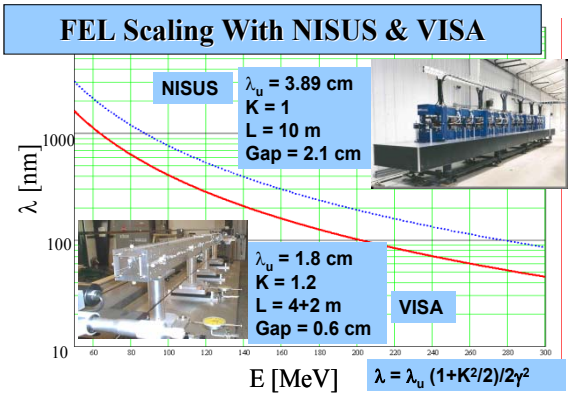

Fig. 1: The DUV-FEL output wavelength vs. beam energy for the two undulators.

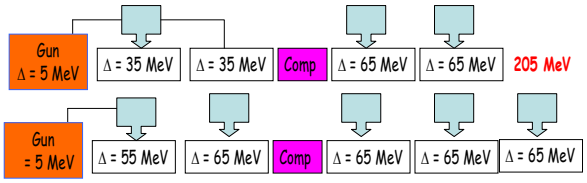

Fig. 2: The old (top) and upgraded (bottom) DUV-FEL linac configurations.

The old and upgraded DUV-FEL linac configurations are plotted in fig.2. The upgraded HGHG will operate at the 4th harmonic with the seed laser at 400nm. The increase of the electron beam energy will be accomplished by installing a 5th linac cavity and two 45 MW klystrons. New modulator and dispersion sections vacuum chambers will be manufactured to accommodate new matching optics and 8th harmonic HGHG. To make space for the new linac, two quadrupole doublets were removed. A new quadrupole triplet was installed immediately after the HGHG seeding station to achieve the beam matching for the FEL (fig.3). Fig.4 plots the electron beam envelops from the bunch compressor to the end of HGHG amplifier.

Various options for the HGHG seed laser injection were also investigated. A four-steering-magnet chicane was used for HGHG seed injection before the upgrade. The electron beam was displaced about 8 mm at the HGHG seeding station. The two steering magnets for the seed chicane before the seeding station were removed because of the space limitation. The on-line laser seed injection using a mirror with a center hole was simulated. For the hole size of 3 mm diameter, about 80% of the seed laser energy will be lost. A chicane is adopted for the upgrade with a new beam steering scheme. A special steering magnet was designed so it can be install on top of the exit cell of the newly installed linac. The diagnostic dipole magnet will be used for the seed chicane with a opposite polarity power supply.

For the upgraded DUV-FEL to be able to reach the 8th harmonic, significant modifications of the HGHG modulator were made. The minimum gap for the modulator before the upgrade is about 1.6 inch, and the gap for the 8th harmonic will be 0.93 inch. A new motor drive mechanism was installed to achieve such small gap. Fig.5 plots the pulse wire measurements for the electron beam trajectories inside the modulator. The trim magnets at both ends of the modulator will be adjusted to correct the trajectory error for the higher harmonic operation.

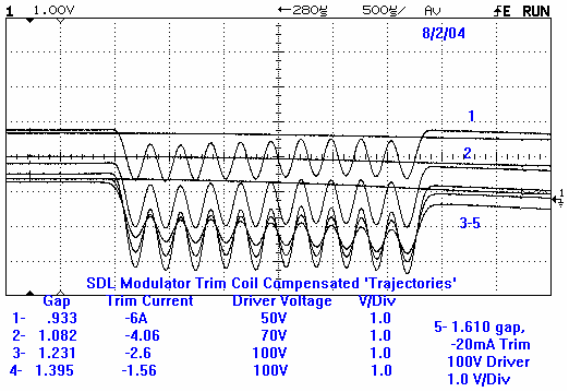

Fig. 5: The pulse wire measurements for the electron beam trajectories inside the HGHG modulator with trim magnets. 1 – 8th harmonic, 2 – 7th, 3 – 6th, 4 – 5th.

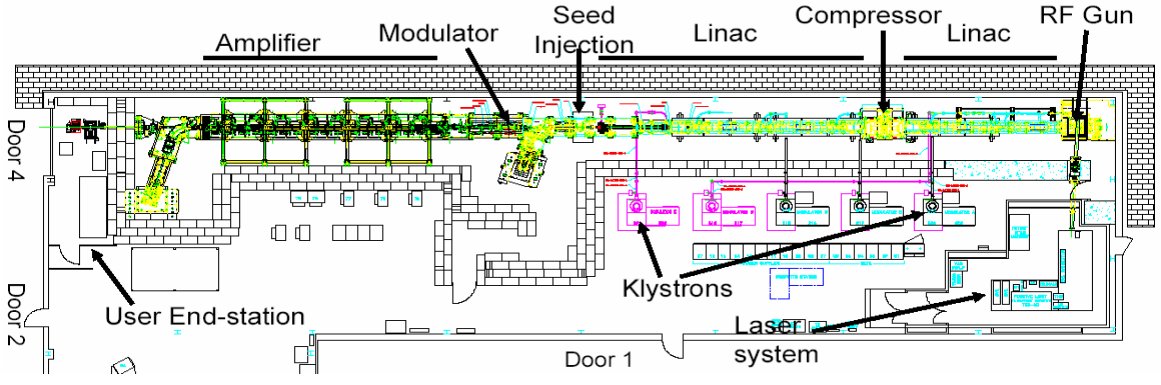

Fig. 3: The DUV-FEL layout after the upgrade.

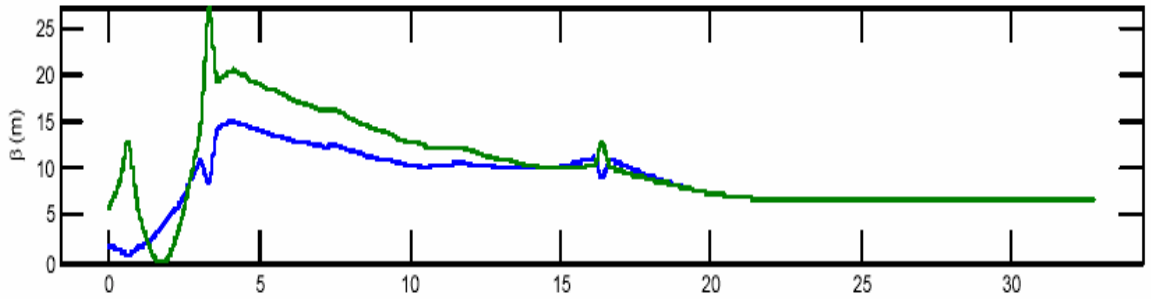

Fig. 4: The transverse electron beam envelops along the beam line, the HGHG amplifier (NISUS undulator) entrance is downstream 21 m from the starting point.

In order to accommodate the tunable HGHG [5] and laser heater [6] experiments, a much stronger HGHG dispersion magnet is needed. The OK-4 dispersion magnet on-loan from Duke was installed at the DUV-FEL. The maximum R_{56} will increase from 0.35 mm to 4.2 mm after the upgrade.

The all hardware for the upgrade is installed; the initial energy of the electron beam after the upgrade will be limited to about 250 MeV. The reason for that is, one of the klystron tubes was damaged in May 2004. The RF conditioning will start in early September of 2004. Electron beam commissioning is expected shortly after. The 4th harmonic HGHG with 800 nm seed laser will be commissioned in early December of 2004. 130 nm HGHG will be commissioned in early 2005.

BEAM PHYSICS AND FEL R&D

The future R&D opportunities in FEL and beam physics are discussed briefly in this section.

1. Seeded FEL R&D: though the basic properties and advantages of the HGHG have been experimentally demonstrated, there are still many significant challenges to realize a X-ray FEL based on the HGHG. The large gap of the longer wavelength of the HGHG seed laser and the X-ray users desired requires staging several HGHGs, i.e., cascaded HGHG. We are exploring the possibility of two-staged cascaded HGHG experiment in collaboration with other groups. The proposed experiment will demonstrate the staging and fresh bunch techniques.

To reduce the complexity of the cascaded HGHG, a higher harmonic HGHG is desired. The higher electron beam energy after the upgrade will make it possible to study the 8th harmonic. Higher harmonic HGHG will also make it possible to investigate the degradation of HGHG output, which scales as the square of the harmonic number.

2. Other FEL R&D: The upgraded DUV-FEL offers other unique opportunities for the FEL R&D. Two experiments now under consideration are emittance spoiler [4] and FEL gain enhancement by the inverse Free Electron Laser (IFEL) micro-bunching [7]. Preliminary estimation shows that, the FEL output pulse length will be reduced from 1 ps to about 200 fs using emittance spoiler.

The HGHG modulator introduces electron beam energy modulation via IFEL interaction. The large dispersion magnet installed will allow us to optimize the electron beam micro-bunching. A factor of 3 to 6 in peak current enhancement is expected by the IFEL micr-bunching.

3**. High-brightness electron beam R&D**: The importance of electron beam quality becomes increasing critical as the FEL going shorter wavelength. The gain length measurement is one of the most powerful tools to determine the 6-D quality of the electron beam. The upgraded DUV-FEL facility will continue the BNL tradition in high-brightness electron beam R&D. The proposed experimental program will cover from electron beam generation, compression to the preservation. An BNL/LCLS/SPAC collaboration is established to study the longitudinal laser pulse shaping on the transverse emittance. The experiment will take advantage of the broad bandwidth of the DUV-FEL laser system. We will also to carry out the feasibility studies of generating the femto-second kilo-Ampere electron beam using the longitudinal emittance compensation technique[8].

ACKNOWLEDGEMENTS

The supports of BNL director office and NSLS are gratefully acknowledged. We appreciate the assistance of Prof. Y. Wu of Duke University for lending the OK-4 dispersion magnet. The work was performed under DOE contract DE-AC02-98CH10886.

REFERENCES

[1] L. H. Yu *et al*, Phy. Rev. Lett. **91**, 074801-1 (2003).
[2] W. Li *et al*, Phy. Rev. Lett. **92,** 083002-1(2004).
[3]http://www.nsls.bnl.gov/organization/Accelerator/highlights.htm.
[4]P. Emma *et al*, Phys. Rev. Lett. **92**, 074801-1 (2004).
[5]. T. Shaftan et al, WEAISo1, this proceeding.
[6]Z. Huang *et al*, Phys. Rev. STAB. 7, 074401 (2004).
[7]Y. Liu, X.J. Wang *et al*, Phys. Rev. Lett. **80**, 4418-4421(1997).
[8] X.J. Wang and X.Y. Chang, NIM A **507**, 310–313 (2003).

EXPECTED PROPERTIES OF RADIATION FROM VUV-FEL AT DESY (FEMTOSECOND MODE OF OPERATION)

E.L. Saldin, E.A. Schneidmiller, and M.V. Yurkov
Deutsches Elektronen-Synchrotron (DESY), Hamburg, Germany

Abstract

For the next three years the nominal "long pulse" (200 fs) mode of FEL operation at VUV-FEL, based on a linearized bunch compression, is not available due to the lack of a key element – a 3rd harmonic RF cavity. Essentially nonlinear compression leads naturally to a formation of a short high-current leading peak (spike) in the density distribution that produces FEL radiation. Such a mode of operation was successfully tested at VUV-FEL, Phase I. In this paper we present optimized parameters of the beam formation system that allow us to get a current spike which is bright enough to get SASE saturation for the VUV-FEL, Phase 2 at shortest design wavelength down to 6 nm. The main feature of the considered mode of operation is the production of short (15-50 fs FWHM) radiation pulses with GW-level peak power that are attractive for many users. Main parameters of the SASE FEL radiation (temporal and spectral characteristics, intensity distributions, etc.) are presented, too.

INTRODUCTION

The vacuum ultra-violet (VUV) free-electron laser (FEL) at the TESLA Test Facility (TTF), Phase I has demonstrated saturation in the wavelength range 80-120 nm based on the self-amplified spontaneous emission (SASE) principle [1, 2, 3]. It was not simply a proof-of-principle experiment as it was planned at an early stage of the project. TTF FEL at DESY demonstrated an ultimate performance for this class of coherent radiation sources in the VUV wavelength range. It has been realized experimentally a unique mode of operation of SASE FEL producing radiation pulses of ultimately short duration, i.e. about coherence time. Each radiation pulse of about 40 fs duration consisted of one-two wave packets. In other words, TTF FEL produced radiation pulses close to Fourier limit. The degree of transverse coherence was pretty high, too. Peak power (averaged over ensemble) exceeded 1.5 GW. Thus, TTF FEL produced nearly completely coherent (longitudinally and transversely) VUV radiation pulses with ultimate peak power. Number of photons in one mode exceeded the value of 10^{13}. Excellent properties of FEL radiation were used in the pioneering user experiments [4, 5].

The beam dynamics in TTF1 linac was nontrivial [3]. Due to nonlinear compression and small local energy spread the short high-current (3 kA) leading peak (spike) in density distribution was obtained. Despite strong collective effects (of which the most critical was the longitudinal space charge (LSC) after compression) this spike was bright enough to drive FEL process up to the saturation for the wavelengths around 100 nm.

For the next few years the nominal "long pulse" (200 fs) mode of operation of the VUV-FEL at DESY (TTF2), based on a linearized bunch compression, is not available due to the lack of a key element – a 3rd harmonic RF cavity. Essentially nonlinear compression leads naturally to a formation of a short high-current leading peak (spike) in the density distribution that produces FEL radiation. A short current spike regime is the natural solution for producing short SASE pulses (that are requested by many users), provided that collective effects are tolerated.

In this paper we present the results of TTF2 linac optimization (with the codes Astra [7] and `elegant` [8]) for the short spike regime. Choosing appropriate injector settings and using two bunch compressors, one can tolerate collective effects on beam dynamics without 3rd harmonic cavity. SASE FEL process is simulated with the code FAST [9]. It is shown that the FEL can safely saturate even at the shortest design wavelength, 6 nm. SASE FEL output parameters (peak power, pulse duration, spectra, angular distributions etc.) are calculated for 30 nm and 6 nm. With a GW level of the peak power one obtains short pulses in the range 15-50 fs FWHM.

OPTIMIZATION OF TTF2 LINAC

The nominal design of TTF2 [6] (see Fig. 1) assumes the optimized injector and a linearized compression in two bunch compressors, BC2 and BC3, with the help of the 3rd harmonic superconducting RF cavity being developed. For the next few years this cavity will not be available, so that this regime cannot be realized. The main potential advantages of such a regime (as compared to a short spike regime) from the point of view of accelerator physicists

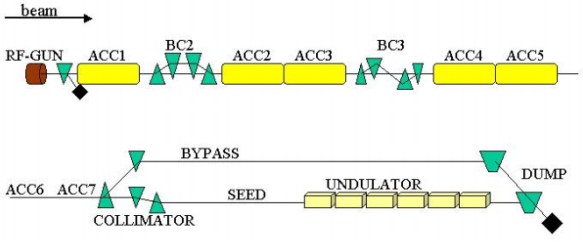

Figure 1: Schematic layout of the TESLA Test Facility, Phase 2.

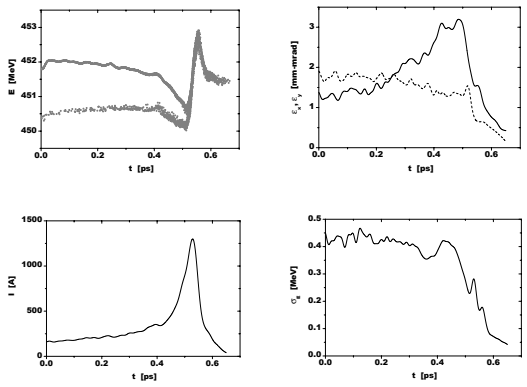

Figure 2: Phase space distribution, current, slice emittance and slice energy spread along the bunch at the undulator entrance. Bunch charge is 0.5 nC. Bunch head is on the right. Only small part of the bunch is shown.

are: longer high-current (lasing) part of the bunch (with rms length σ_z) is less sensitive to coherent synchrotron radiation (CSR) and LSC (for a given current these effects scale as $\sigma_z^{-1/3}$ and σ_z^{-1}, respectively); standard diagnostics (BPMs, screens) is better suited for such a regime since a larger fraction of total charge contributes to the lasing and one can hope that slice parameters do not differ strongly from projected ones. On the other hand, the short spike regime does not require very fine RF phase tuning and is, therefore, less sensitive to RF jitters (typical requirement for phase stability is $\delta\phi \ll 2\pi\sigma_{z0}/\lambda_{RF}$, where σ_{z0} is bunch length before compression and λ_{RF} is the wavelength of the accelerating RF field). From users' point of view, the short spike regime is advantageous for many experiments.

Two regimes of the spike formation were studied experimentally already at TTF1: the nominal one with only one bunch compressor (BC2) [3] and the alternative one with two bunch compressors (BC1 and BC2). The latter regime allowed one to get a longer spike after BC2 due to a mild preliminary compression in BC1. The collective effects could be efficiently tolerated this way. The question arises: can the TTF1 experience be extrapolated to a different layout of TTF2 and much shorter wavelengths? In this paper we give a positive answer: by using the optimized injector and two bunch compressors (BC2 and BC3) one can obtain a short current spike and preserve its quality at the level sufficient for lasing at short wavelengths (down to 6 nm, the shortest design wavelength of TTF2).

The optimization of the beam dynamics in TTF2 linac was done for the 30 nm case (beam energy 450 MeV). The following simulation scheme was used in order to include the most important effects. Simulation of the initial part of the machine (up to the first quadrupole) was performed with Astra. The injector settings and beam parameters can be found in [10]. Then the tracking was done with `elegant` up to the end of the 4th accelerating module, including CSR effects in both bunch compressors. The last part of the machine, up to the undulator entrance, was simulated with Astra using a simplified lattice (excluding dogleg) in order to take into account space charge effects. The low-current long tail of the bunch was cut out in this last part of the simulation.

For the nominal operation point the following main parameters were chosen. A Gaussian laser pulse with the 4 ps rms duration was used to extract 0.5 nC from the gun (the other injector settings and beam parameters at the exit of ACC1 can be found in [10]). Accelerating gradient is about 15 MV/m in the first three accelerating modules (ACC1-3) and 8 MV/m in ACC4. The phase of ACC1 is 8 degrees off-crest, in ACC2-4 beam is accelerated on-crest. The beam energy is about 125 MeV, 380 MeV and 450 MeV after ACC1, ACC3 and ACC4, respectively. The R_{56} are about 18 cm and 10 cm for BC2 and BC3, respectively[1]. For these settings we have a mild compression in BC2, and then a high-current spike (containing about 10 % of the total charge) in BC3. Combination of two phases, ACC1 and ACC2-3, defines a slice (in the initial distribution) of which the spike is made.

Slice parameters in the front part of the bunch at the undulator entrance are shown in Fig. 2. For the slice with a maximal current (1.3 kA) the mean geometric of x- and y-normalized emittances is about 1.5 mm-mrad, and the local energy spread is about 300 keV. One may notice unusual drop of slice emittances (well below the value of emittance in the best slice before compression) in the bunch head. This behavior does not violate Liouville's theorem (stating that phase space density is conserved, not the slice parameters) and is explained by specific correlations between longitudinal and transverse phase spaces in the injector (see [3] for the detailed explanation). Longitudinal phase space in Fig. 2 looks similar to that simulated in [3] for TTF1 case. However, the influence of energy chirp on the FEL saturation length for 30 nm case is a small correction, i.e. it is not that dramatic as it was in TTF1 case. It may become a dominating effect (for 30 nm case) if one does not tune the machine properly, i.e. if the spike becomes too sharp.

Although we did the simulations for 30 nm case (450 MeV), we can do a simple generalization towards higher energies. We assume that machine settings are the same up to the end of BC3. Then we accelerate the beam up to the required energy (say 1 GeV). Since space charge effect cannot be worse for higher energies, we can use the results of Fig. 2, and simply move the energy up. Although this is a pessimistic estimate, in the following section we show that even in this case one can safely reach saturation at 6 nm.

To illustrate the sensitivity of the FEL operation to the non-optimal settings of the accelerator, we simply changed the charge extracted from the cathode, keeping other ma-

[1] In [10] the R_{56} of the BC3 is 4.9 cm. In order to get the same current one should then accelerate beam off-crest in ACC2-3.

chine parameters untouched (see [11]) for more details). One can see from the next section that the FEL saturation at 30 nm should be relatively safely achieved, while a 6 nm case must be carefully optimized.

RADIATION PROPERTIES

Simulations of the FEL have been performed with three-dimensional, time-dependent simulation code FAST [9] using bunch parameters shown in Fig 2 for 0.5 nC case. In addition, a (non-optimized) 1 nC case was simulated in order to show the total sensitivity of the machine to non-optimal conditions [11]. Summary of the calculated FEL properties is shown in Table 1. More detailed information about the radiation properties is presented in graphical form in Figs. 3-5.

Figure 3 shows mean energy in the radiation pulse and rms fluctuations as functions of position along the undulator. One can see that for both charges saturation is reached in the middle of the undulator for the wavelength of 30 nm. For the wavelength of 6 nm the (optimized) 0.5 nC beam has a visible advantage, saturation is reached at the end of the 5th undulator module. The plots in Fig. 3 present numerical experiment of a specific measurement being planned for TTF2 (similar procedure has been used at TTF1). The interaction length is to be changed by means of switching on electromagnetic correctors installed inside the undulator. The value of the orbit kick provided by a corrector is sufficient to stop FEL amplification process downstream the corrector. The radiation energy is measured by means of a radiation detector installed 18.5 m downstream the undulator. When the FEL interaction is suppressed along the whole undulator length, the detector shows the level of spontaneous emission collected from the full undulator length into the detector aperture. Then FEL interaction is to be switched on gradually along the undulator and the energy in the radiation pulse is recorded. Contribution of spontaneous emission depends on the angular acceptance of the detector. In our simulations we used 10 and 5 mm diameter aperture for 30 and 6 nm wavelength, respectively.

The energy in the radiation pulse fluctuates from shot to shot. The plots for standard deviation σ, are presented in Fig. 3. At the initial stage fluctuations are defined mainly by the fluctuations of the undulator radiation in the central cone. When the FEL amplification process takes place, fluctuations of the radiation energy are mainly given by the fundamental statistical fluctuations of the SASE FEL radiation [12]. A sharp drop of the fluctuations in the last part of the undulator is a clear physical confirmation of the saturation process. When the FEL amplifier operates in the high-gain linear regime, the value of parameter $M = 1/\sigma^2$ gives the number of spikes (wave packets) in the radiation pulse. This allows one to estimate the radiation pulse length as $\tau_{\rm rad} \simeq ML_{\rm c}/c$. The cooperation length is about $L_{\rm c} \simeq 2\lambda L_{\rm g}/\lambda_{\rm u}$. The value of the power gain length $L_{\rm g}$ can be measured experimentally from the gain curve (see Fig. 3). Such an experimental technique has been proven to be very useful during operation of TTF FEL, Phase I [1, 2, 3].

Table 1: Expected parameters of the TTF FEL, Phase 2 (femtosecond mode of operation)

	Units	30 nm option	6 nm option
beam energy	MeV	450	1000
bunch charge	nC	0.5-1	
peak current	kA	1.3-2.2	
normalized emittance	μm	1.5-3.5	
bunch spacing	μs	1.6-3.5	
# of bunches in a train	#	up to 1800	
repetition rate	#	up to 10 Hz	
undulator period	cm	2.73	
undulator peak field	T	0.47 T	
averaged beta-function	m	4.5	
undulator length	m	27	
radiation wavelength	nm	30	6
power gain length	m	0.7-0.9	1.1-1.6
saturation length	m	18-22	22-32
radiation pulse energy	μJ	50-150	
radiation pulse duration	fs	15-50	
radiation peak power	GW	2-4	
radiation average power	W	up to 2 W	
spectrum width	%	0.8	0.4-0.6
radiation spot size	μm	180-270	120-180
angular divergence	μrad	70-80	25-35

Properties of the radiation at 30 nm wavelength are expected to be similar to those obtained at TTF1 [1, 2, 3]. Number of modes in the radiation pulse is expected to be $M = 3 \ldots 6$ depending on the tuning of the driving beam. As it was demonstrated at TTF FEL Phase I, we predict some suppression (down to 40%) of the fluctuations of the radiation energy after a narrow band monochromator [13]. Radiation properties are expected to be distorted by the energy chirp along the lasing part of the electron bunch. First, this is widening of the radiation spectrum. Second, spatial distortion of the beam radiation mode takes place. This is reflected by the angular distribution of the radiation intensity in the far zone – appearance of the tails at large angles.

SUMMARY

Conclusion of our study is optimistic: femtosecond mode of operation will allow overlapping complete operating wavelength range of the TTF FEL. Minimum wavelength will be mainly limited by the available energy of the electron beam. Starting of operation at 30 nm wavelength seems to be a reliable way to get success for the first lasing. The next milestone for the TTF FEL would be the operation at the wavelength around 12 nm (linac energy about 700 MeV) that can be done without installation of additional hardware. With the third harmonic of the radiation

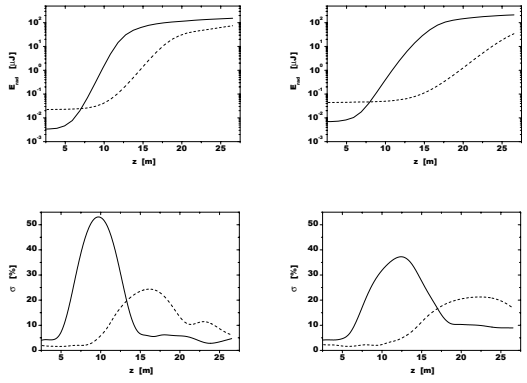

Figure 3: Top: energy in the radiation pulse versus undulator length. Bottom: fluctuations of the energy in the radiation pulse versus undulator length. Left column corresponds to the case of bunch charge 0.5 nC (see Fig. 2). Right column corresponds to the case of bunch charge 1 nC. Solid and dashed lines refer to the radiation wavelength 30 nm and 6 nm, respectively.

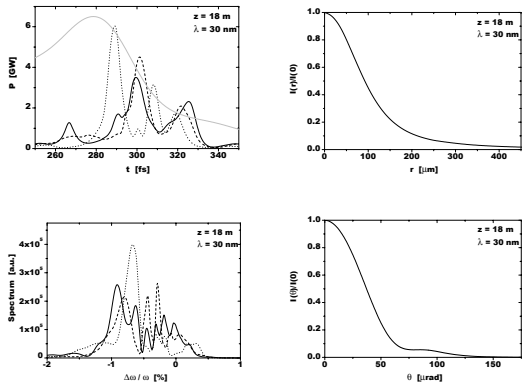

Figure 4: Summary of the radiation properties of TTF FEL operating in the nonlinear regime at the undulator length of 18 m. Bunch charge is 0.5 nC (see Fig. 2). Radiation wavelength is 30 nm. Left column: temporal and spectral structure of the radiation pulse. Three single shots are shown with different line shapes (solid, dashed, and dotted). Grey line shows profile of the bunch current. Right column: averaged distribution of the radiation intensity in the near and far zone.

it would be possible to reach the "water window" with the pulse duration on a 10 fs scale. This will greatly extend possibilities for user experiments. In principle, saturation at 6 nm can be achieved with five undulator segments. Replacement of the last segment with frequency doubler [14] will allow reaching 3 nm wavelength with GW level of output power.

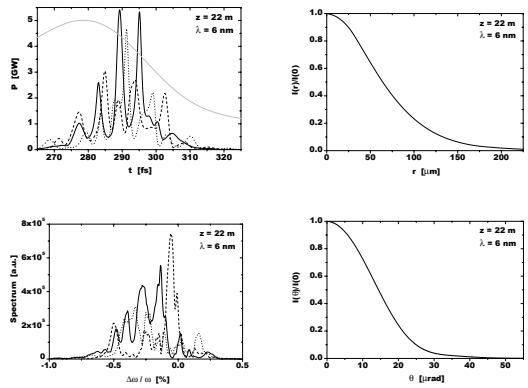

Figure 5: Summary of the radiation properties of TTF FEL operating in the nonlinear regime at the undulator length of 22 m. Bunch charge is 0.5 nC (see Fig. 2). Radiation wavelength is 6 nm. Left column: temporal and spectral structure of the radiation pulse. Three single shots are shown with different line shapes (solid, dashed, and dotted). Grey line shows profile of the bunch current. Right column: averaged distribution of the radiation intensity in the near and far zone.

REFERENCES

[1] V. Ayvazyan et al., Phys. Rev. Lett. **88**(2002)104802.

[2] V. Ayvazyan et al., Eur. Phys. J. **D20**(2002)149.

[3] M. Dohlus et al., Nucl. Instrum. and Methods A530(2004)217.

[4] H. Wabnitz et al., Nature 420(2002)482.

[5] L. Juha et al., Nucl. Instrum. and Methods **A507**(2003)577.

[6] The TTF FEL team, "SASE FEL at the TESLA Test Facility, Phase 2", TESLA-FEL-2002-01, June 2002.

[7] K. Flöttmann, Astra User Manual, http://www.desy.de/~mpyflo/Astra_dokumentation/.

[8] M. Borland, "`elegant`: A flexible SDDS-Compilant Code for Accelerator Simulation", APS LS-287, September 2000.

[9] E.L. Saldin, E.A. Schneidmiller and M.V. Yurkov, Nucl. Instrum. and Methods **A429**(1999)233.

[10] TTF2. Operation without 3.9 GHz cavity: Case 0.5 nC, 4 ps sigma, magnetic compression, http://www.desy.de/s2e-simu.

[11] E.L. Saldin, E.A. Schneidmiller and M.V. Yurkov, "Expected properties of the radiation from VUV-FEL at DESY (femtosecond mode of operation)", DESY report TESLA-FEL-2004-06, July 2004.

[12] E.L. Saldin, E.A. Schneidmiller and M.V. Yurkov, *The Physics of Free Electron Lasers*, Springer-Verlag, Berlin, 1999.

[13] E.L. Saldin, E.A. Schneidmiller and M.V. Yurkov, Nucl. Instrum. and Methods **A507**(2003)101.

[14] J. Feldhaus et al., Nucl. Instrum. and Methods A528(2004)471.

OVERVIEW OF TERAHERTZ RADIATION SOURCES

G.P. Gallerano, ENEA, UTS Advanced Physics Technologies, P.O. Box 65, 00044 Frascati – Italy
S. Biedron, Argonne National Laboratory, Energy Systems Division, 9700 South Cass Avenue, Argonne, Illinois 60439 USA

Abstract

Although terahertz (THz) radiation was first observed about hundred years ago, the corresponding portion of the electromagnetic spectrum has been for long time considered a rather poorly explored region at the boundary between the microwaves and the infrared. This situation has changed during the past ten years with the rapid development of coherent THz sources, such as solid state oscillators, quantum cascade lasers, optically pumped solid state devices and novel free electron devices, which have in turn stimulated a wide variety of applications from material science to telecommunications, from biology to biomedicine. For a comprehensive review of THz technology the reader is addressed to a recent paper by P. Siegel [1]. In this paper we focus on the development and perspectives of THz radiation sources.

INTRODUCTION

Throughout this paper we will use a definition of the THz region that extends over two decades in frequency, covering the spectral range from 100 GHz to 10 THz. This should allow a better understanding of the effort in the extension of microwave electronics towards high frequencies on one side and the development of photonic devices from the optical region towards low frequencies. According to this scheme, we will first cover the state of the art of solid state oscillators and then move to gas and Quantum Cascade Lasers (QCL), which lie at the low and high frequency boundary of the THz region respectively. A brief review of laser driven THz emitters will be presented, which are the most widely used sources of THz radiation. We will also briefly discuss the physical principles of the generation of THz radiation from free electrons, describing the mechanism of Coherent Spontaneous Emission and the development of table-top Free Electron Laser (FEL) sources.

SOLID STATE OSCILLATORS

Electronic solid state sources, like oscillators and amplifiers, are generally limited in frequency due to the transit time of carriers through semiconductor junctions, which causes high frequency roll-off. High frequency Gunn, IMPATT and TUNNET diodes are being developed by several research groups [2]. They are rugged and compact devices and can operate CW at room temperature with a relatively narrow linewidth (10^{-6}). A CW power of about 100 mW can be obtained around 100 GHz. The output power falls off as $1/f^2$ and then as $1/f^3$ as the frequency increases (see Fig. 1). Frequency multipliers with two or more diodes are generally employed to reach frequencies above 200 GHz, up to about 1 THz. The average power level achievable in the region around 400 GHz is typically in the range 0.1 to 1 mW. Due to their compactness, the range of application of these sources is rapidly growing. A 200 GHz Gunn diode is being used as a source in a low cost imaging system under development at RPI-Troy for security applications [3].

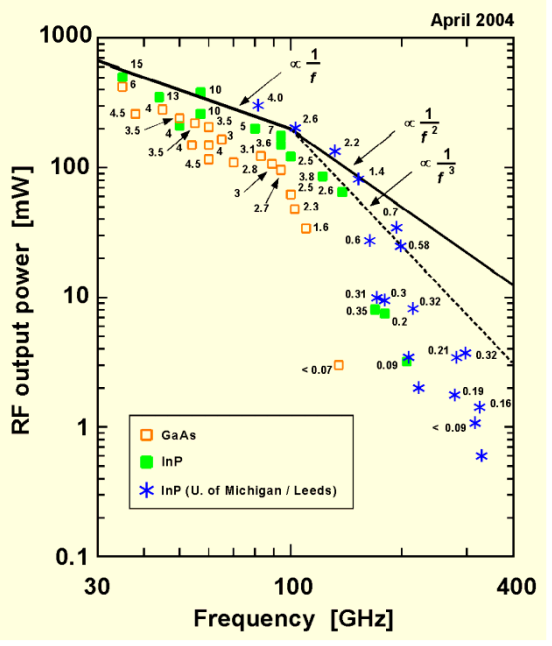

Fig. 1: State of the art results from GaAs and InP Gunn devices. Numbers next to the symbols denote dc to RF conversion efficiencies in percent (courtesy of H. Eisele, University of Leeds, UK).

GAS AND QUANTUM CASCADE LASERS

The Far Infrared (FIR) gas laser and the quantum cascade laser (QCL) are respectively the oldest and the newest coherent source developed in the THz region. Gas lasers date back to the sixties [4]. They are optically pumped lasers, which use a CO_2 laser to excite the roto-vibrational levels of gas molecules at pressures in the mbar range. The most widely used gas is methanol, which provides a powerful (typically 100 mW) emission line at 118 μm. Gas lasers are line-tunable in the range 0.3 to 5 THz (1000 to 60 μm) although with limited power and are commercially available by several companies, among which Coherent Inc. and Edinburgh Inst. The technology of FIR lasers has seen modest development in recent years, as it has been the case of most gas lasers. However they still are ideal sources for specific applications in

which continuous tunability is not a must, like for instance heterodyne spectroscopy and plasma diagnostics.

QCLs, the most recently invented optical lasers [5], have seen an impressive development in the THz region during the past two years. In a Quantum Cascade Laser, electrons are injected into the periodic structure of a superlattice under electrical bias. They undergo intersubband transitions with THz photon emission excited by resonant tunneling through the multiple wells. As a result a cascade process occurs, which gives name to the source.

The first QCL to operate in the THz region was developed by a joint collaboration between NEST-Pisa and the Cavendish Laboratory, Cambridge. It emitted at 4.4 THz providing about 2 mW of average power with 10% duty cycle at an operating temperature of 50 K [6]. Starting from this result, a great effort has been undertaken by several research groups worldwide (NEST-Pisa, Cavendish-Cambridge, MIT, Sandia, Neuchatel University), which has led to the record operating temperature of 137 K pulsed and 93 K CW achieved at MIT [7]. The group at MIT also holds the record of the longest wavelength (~141 μm, 2.1 THz) QCL to date without using magnetic fields [8], while the group at Neuchatel has recently reported an average output power approaching 50 mW [9]. 2.5 THz low threshold CW operation has been obtained at NEST-Pisa [9]. Recent progress in the QCL field also includes the development of THz QCLs using metal-semiconductor-metal waveguides for mode confinement. This method will be advantageous or even crucial as longer wavelengths are approached.

Among the solid state lasers, we also recall the p-type Ge laser [10], which can be tuned between 1 and 4 THz, but requires low temperature operation (20 K) and a large (1 T) applied magnetic field.

LASER DRIVEN THz EMITTERS

Today's most widely used sources of pulsed THz radiation are laser driven THz emitters based on frequency down-conversion from the optical region. Two main techniques have been developed to produce THz radiation. The first one is based on a short pulse (femtosecond) Ti:Sapphire laser [11, 12], which illuminates the gap between closely spaced electrodes on a photoconductor (e.g., silicon-on-sapphire or GaAs) generating carriers, which are then accelerated by an applied bias field (100 V). The resulting current transient, which is generally coupled to an RF antenna through a stripline, radiates in a wide band at THz frequencies corresponding to the Fourier transform of the laser pulse time profile. The upper limit in frequency for these devices is given by the carrier recombination time in the semiconductor and by the bandwidth of the stripline.

A similar terahertz spectrum can be obtained by applying a sub-picosecond laser pulse to a crystal with a large second-order susceptibility like ZnTe [13]. Due to the nonlinear response of the crystal, photomixing occurs, producing a time-varying polarization which in turn gives rise to THz emission. In this case higher frequencies can be reached due to the fast response of the crystal and to the absence of any stripline or conductor. Both techniques and the related electro-optical detection are at the basis of most THz imaging systems [13, 14].

Laser driven solid state emitters also include CW photomixers, in which offset-frequency locked CW lasers are focused onto a photoconductor under bias. The laser induced photocurrent is modulated at the laser difference frequency and is coupled to an antenna, which emits THz radiation [15]. In this case a narrow band continuous wave emission is obtained, which can be tuned over a fairly wide range by shifting the optical frequency of one of the two drive lasers.

The typical frequency range covered by laser driven solid state emitters is 0.2 to 2 THz or higher depending on the laser pulse parameters. Average power levels range from nanowatts to hundred microwatts and pulse energies are typically in the femtojoule to nanojoule range.

FREE ELECTRON BASED SOURCES

Free electron based sources like Klystrons, Travelling Wave Tubes (TWT), Backward Wave Oscillators (BWO) and Gyrotrons have been extensively studied since the mid of the past century to approach the high frequency part of the microwave region. With the exception of Gyrotrons, which are generally designed to reach high average power and deserve a review on their own [16], the above free electron sources suffer from simple physical scaling problems, metallic wall losses and the need for high magnetic and electric fields, as well as high electron current densities as the frequency is increased. For this reason, TWTs have received little attention as candidate sources of radiation above 100 GHz.

The BWO [17] is a slow wave device where the electrons spiralize through a corrugated structure in an axial magnetic field interacting with the first spatial harmonic of the backward wave. Indeed, in this region of the dispersion relation, the phase velocity of the wave is positive and the group velocity is negative. BWOs are table top devices that can operate in the THz region at moderate power levels (1 – 100 mW). The technology of BWOs has been mostly developed in Russia and they are now commercially available through companies in the US and Europe. BWOs operate with an accelerating potential in the range 1 to 10 kV and axial magnetic field of about 1 T. They can be tuned over tens of GHz by varying the accelerating potential. A number of different BWOs can be implemented in an integrated system to cover altogether a wide frequency range extending from 30 GHz to 1.2 THz (see Fig. 2).

To overcome the necessity of reducing the physical size of the source components as the frequency is increased, different schemes have been developed to let the electrons exchange momentum and allow photon emission. The most frequently used one is the magnetic undulator originally proposed by Motz [18], which was employed by Phillips in the Ubitron [19] back in 1960 to generate mm-wave radiation and which led to the realization of the

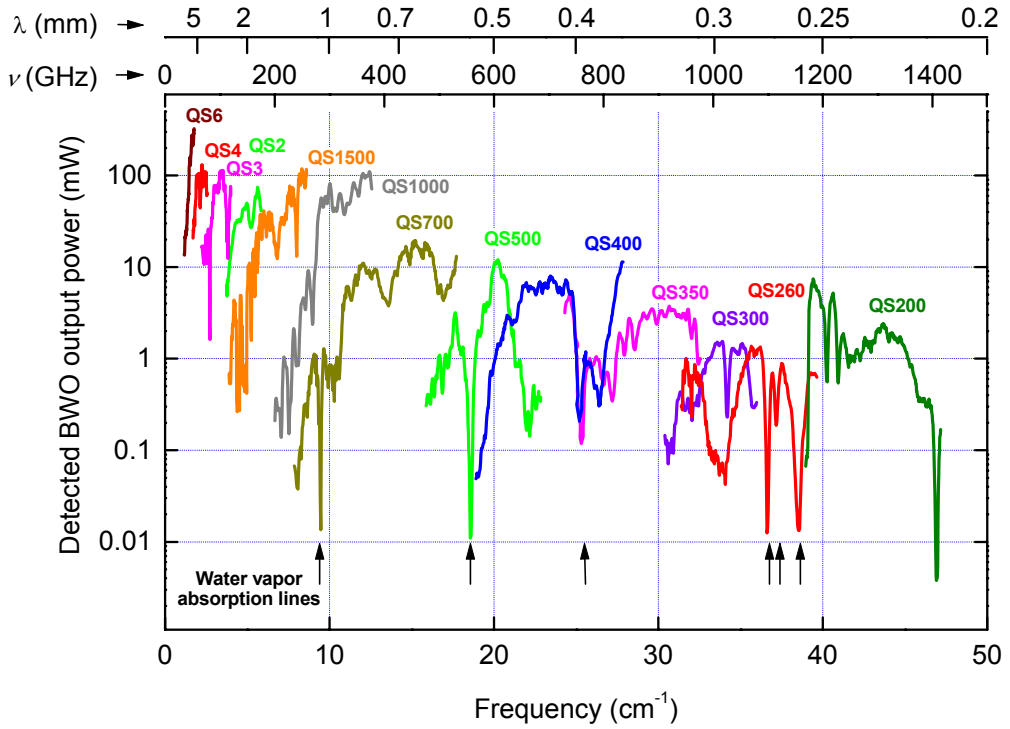

Fig. 2: Output power and spectral distribution of BWO devices employed in a CW spectroscopic system at the 1st Physics Institute of the University of Stuttgart. (Courtesy of M. Dressel, University of Stuttgart)

first Free Electron Laser (FEL) in 1977 [20]. Other free electron devices are the Cerenkov FEL, based on the interaction with a dielectric loaded waveguide [21], and the Metal Grating FEL, based on the Smith-Purcell effect [22].

Coherent spontaneous emission

In his pioneering work on the undulator radiation [18], Motz pointed out that in a uniform electron beam the contributions of individual electrons to the radiation field are random in phase, and therefore the square of the total field equals the sum of the squares of the individual fields. If the electrons were bunched within a distance comparable to the wavelength of the radiation, their fields would add up in phase, resulting in the emission of coherent radiation with a power level several orders of magnitude higher than the non-coherent radiation generated by a uniform beam. The idea of generating coherent radiation in the THz region utilizing bunched electron beams, such as those produced by radio-frequency (RF) accelerators, was indicated in [18], and different coupling structures, designed to extract energy at a harmonic of the bunch repetition rate, were investigated [23]. More recently the coherent spontaneous emission from an RF-modulated electron beam at wavelengths comparable to the electron bunch length has been the object of renewed interest because of its relevance in the generation of short pulses of coherent THz radiation [24, 25, 26]. Issues like the dependence of the emitted radiation on the bunch shape [27] and the observation of emission at discrete frequencies, which are harmonics of the fundamental RF [28], have also been addressed both theoretically and experimentally and have led to the realization of compact FELs in the THz region [29, 30].

FEL Facilities and THz Synchrotron Sources

Historically, the first Free Electron Laser facility to provide THz radiation to users has been the UCSB-FEL, which is driven by an electrostatic accelerator and operates in a quasi-CW mode. It provides tunable terahertz radiation in the region from 120 GHz to 4.8 THz (2.5 mm - 60 μm) with an output power in the range from 500 W to 5 kW and a pulse duration of 1 – 20 μs at 1 Hz repetition rate [31]. Several facilities have been built to operate in the infrared region and most of them can reach or plan to extend into the THz region. Besides the UCSB FEL, we recall here the Israeli EAFEL (100 GHz), based on a 6MeV EN-Tandem Van der Graaff accelerator [32], the Stanford FEL (15 – 80 μm) [33], FELIX (3 – 250 μm) with its planned FELICE extension for intracavity experiments at FOM-Nieuwegein [34], CLIO at LURE-Orsay, which has plans for a new hybrid resonator to reach wavelengths in the range 100 – 300μm [35], ELBE, which has recently lased at 20 μm and has plans to extend its operation to 150 μm [36], and the THz-FEL at Novosibirsk, based on a CW energy recirculated linac

(ERL) and providing about 100 W in the spectral range 120 – 180 μm [37].

The principle of coherent spontaneous emission is also exploited to generate THz radiation from bending magnets at FEL facilities and Synchrotron facilities. About 100 W of CW radiation have been produced from bending magnets in the band from 0.1 to 3 THz at JLAB [38]. The JLAB ERL accelerator overcomes some of the limitations of conventional linacs and storage rings. It produces 500 fs, 135 pC electron bunches at a very high repetition rate (75 MHz) by using superconducting RF cavities and recovering the energy of the spent electron beam. Coherent THz emission from a linac driven beam has been demonstrated at Brookhaven National Lab (see below). Coherent synchrotron radiation has also been observed in storage rings [39, 40, 41, 42]. A coherent THz beam line is operating at BESSY-Berlin and several others are planned at Lawrence Berkeley National Lab (CIRCE), Cornell University, and Daresbury (4GLS).

Compact FELs and Table Top Free Electron radiators

There also exist accelerator-based THz sources, which can fit on or scale to the size of a table-top. They are proof-of-principle experiments and should be looked upon as ideas that can be specified and tailored for particular types of experiments. Development work on electron beam based sources is under way at several sites. The RF-gun derived sources described below will benefit from ongoing design work, especially if electron guns can be made superconducting. Laser wake-field accelerators are actively being researched as possible alternative solutions for high energy systems and are still in the early stages of development. Some of these sources could be designed to produce half-cycle pulses of THz radiation.

In a table-top free electron radiator based on an RF modulated electron beam with short bunches, the modulator, klystron, waveguide, cooling, magnets, electron gun, accelerating structure, and all other peripheral accelerator components could easily be fitted into the space of 3 cubic meters. The FEL-CATS source at ENEA-Frascati [43] and the source under development at ANL [44] are examples of this compactness. Further engineering work and improved design in the X-ray shielding of the accelerator will also increase the compactness of these systems.

The coherent prototype radiator at Argonne National Laboratory (ANL) employs three different cathode types – thermoionic, photo-gated thermoionic, or photocathode. Even at a low RF repetition rate, as well as normal conducting, relatively high average powers are achievable if a laser gates the thermoionic cathode. The electron beam pulse length changes depending upon the cathode mode of operation and the degree of compression. Although this source is a prototype, it can be easily adapted to a specific experiment and packaged into a small space. The repetition rate, pulse width, average and peak power can be improved significantly.

At ENEA-Frascati the recently built source FEL-CATS utilizes a high-efficiency generation scheme based on the mechanism of coherent spontaneous emission, which allows operation in the frequency range between 70 GHz and 0.7 THz. Tunable operation has been obtained in the spectral region between 0.4 and 0.7 THz with a relative linewidth of about 10% FWHM [45]. The radiation has a pulsed structure composed of wave-packets in the 3 to 10 ps range, spaced at a repetition frequency of 3 GHz. A 5 microsecond long train of such pulses (macropulse) is generated and repeated at a rate of few Hz. The measured power in the macropulse is 1.5 kW at 0.4 THz.

The principle of operation of the source is based on the coherent spontaneous emission from short bunches of relativistic electrons. The FEL source utilizes a 2.5 MeV RF linac to generate the electron beam, which is injected into a linearly polarized magnetic undulator composed of 16 periods, each 2.5 cm long with a peak magnetic field of 6000 Gauss. A second RF structure, called Phase Matching Device (PMD), is inserted between the linac and the undulator and is controlled in phase and amplitude to correlate the electron distribution in energy as a function of time in the bunch [46]. In this way the contributions to the total radiated field by individual electrons in the bunch are added in phase, leading to a manifold enhancement of the coherent emission.

In the frame of a collaboration between University of Maryland and the Brookhaven National Laboratory (Source Development Laboratory) a proof of principle experiment based on the modulation induced on an electron bunch has been recently carried out [47]. This device uses a laser to generate a bunch train of electrons through photoemission. Each bunch is about a picosecond long, and they are separated by about a picosecond. An electron accelerator takes these short bunches and accelerates them up to 70 – 72 MeV. At this point the beam is intercepted by a mirror. When the environment around the beam changes from vacuum to metal, transition radiation is emitted. Because of the way the electrons are bunched, there is strong emission in the terahertz frequency range. The frequency spectrum can be controlled by controlling the way the electrons are initially bunched. The result is a tunable terahertz source that could be used for a wide variety of additional experiments.

At the Source Development Laboratory, Brookhaven National Laboratory, a linac-based source of coherent THz pulses has been developed. In this device electron bunches are compressed to ~300 fs rms. The degree of compression can be varied with the perspective of reaching 100 fs and possibly shorter pulse duration. Electron bunches produce single-cycle coherent THz as transition radiation or dipole radiation. An energy per pulse of ~100 μJ and peak electric field up to > 1 MV/cm has been demonstrated [48]. The method could be improved to produce shorter electron bunches and a broader spectral range. A pulsed laser driving the linac photocathode provides synchronized IR pulses for electro-optic coherent detection of THz pulses.

Advanced Energy Systems (AES) has plans to develop a multi-watt (50 – 100 W eventual goal; 5 W in this initial prototype), tunable, compact THz source.

Intense THz radiation from ultra-short electron bunches has been generated by a laser wakefield-based linac at Lawrence Berkeley Laboratory. This source is based on the production of ultra-short (< 50 fs rms), high charge (0.3 – 5 nC) relativistic electron bunches by using a laser excited plasma wave with large enough amplitude to trap background electrons and accelerate them in mm distance to 10's of MeV. As the electrons exit the plasma, a burst of transition radiation is produced. The source performance is controlled by the electron bunch properties and the density and transverse size of the plasma at the exit boundary. The THz radiation is intrinsically synchronized with an external laser and experiments are underway to measure the THz pulse structure with electro-optic sampling. Time averaged spectra have been measured and show that the spectrum with the present configuration is centered around 2 THz. Whereas presently energy levels on the order of 0.1 μJ/pulse have been collected, modeling indicates that significantly higher power can be achieved by optimizing the plasma properties (transverse size and longitudinal profile) and could be as high as 100 μJ/pulse [49]. Further progress on the laser driven accelerator performance is underway, including the production of quasi-monochromatic (few % energy spread) relativistic electron bunches (100 MeV), which will lead to intense radiation emission from conventional transition radiation foils.

MICROFABRICATED SOURCES

A challenge for the future is the further reduction in size of compact FELs. A Smith-Purcell emitter using a CW electron microscope gun as electron source has been developed at Vermont Photonics [50], providing CW power levels up to 10 microwatts at wavelengths in the range from 200 to 900 μm with an output bandwidth of about 1 to 2 cm^{-1}. This source is devoted to research applications like THz absorption spectroscopy, THz pump/probe experiments in biology and nanotechnology, test of bolometric arrays for THz astronomy, test of THz imaging concepts. New developments are in progress with corporate partners to provide output power in the mW range and to extend the tuning range from 100 to 1500 μm. Experiments and proposals are also in progress at Chicago University [51] and Vanderbilt University, where a 45 – 65 kV gun equipped with a laser driven needle cathode is being assembled to drive a miniaturized Smith-Purcell emitter with a 200 μm period grating [52]. The device is designed to operate in the range 0.3 – 0.7 THz.

The possibility of using "Computer Controlled 3-D Electron-beam Induced Deposition and Etching" to realize microfabricated Smith-Purcell emitters has been investigated at NawoTech (Germany) [53].

CalCreek Research (CCR) is developing miniaturized, efficient traveling wave tube (TWT) amplifiers incorporating micro-electro-mechanical systems (MEMS) fabrication techniques [54]. The MEMS based TWT is designed to provide 10 W of RF power at 83.5 GHz with 5 GHz bandwidth for communication applications in micro-satellites.

CONCLUSIONS

The development of a variety of THz sources has been gradually filling the THz gap in recent years, providing complementary characteristics in terms of frequency of operation, average and peak power.

Large scale FEL facilities are capable of providing high power CW THz radiation while low-cost solid state oscillators and QCLs are expected to drive the realization of THz systems for a variety of applications in the near future.

It has been shown that low-cost small size FELs can also be built in the THz region. Their peculiar feature is the capability of providing high peak power in the kW range with peak electric field in the range 10^4 – 10^6 V/cm, which is crucial for the investigation of non-linear phenomena. The generation of ultra-short electron pulses (50 – 100 fs) will significantly increase the available bandwidth of free electron THz radiators, and improvements in RF-gun technology will make a table-top high power CW source a possibility in the near future.

ACKNOWLEDGEMENTS

We gratefully acknowledge the contribution of all colleagues at our home institutions and from various laboratories worldwide, who have provided precious information on the different THz sources.

REFERENCES

[1] P. Siegel, "Terahertz Technology", IEEE Trans. on Microwave Theory and Techniques 50 (2002) 910.
[2] H. Eisele, "Recent advances in the performance of InP Gunn devices and GaAs TUNNETT diodes for the 100-300 GHz frequency range and above", IEEE Trans. on Microwave Theory and Techniques 48 (2000) 626.
[3] X.C. Zhang, private communication (2004).
[4] A. Crocker, H.A. Gebbie, M.F. Kimmitt, I.E.S. Mathias, Nature 201 (1964) 250..
[5] J. Faist et al., "Quantum cascade laser" Science 264 (1994) 553.
[6] R. Köhler et al., "Terahertz semiconductor heterostructure laser" Nature 417, (2002) 156.
[7] B.S. Williams et al., "Terahertz quantum cascade laser operating up to 137 K" Appl. Phys. Lett 83 (2003) 5142.
[8] B.S. Williams et al., Electron. Letter 40 (2004) 431.
[9] A. Tredicucci, private communication.
[10] E. Brundermann, D.R. Chamberin, E.E. Haller, Infr. Phys. Tech. 40 (1999) 141.

[11] D.H. Auston, K.P. Cheung, J.A. Valdmanis, D.A Kleinman, Phys. Rev. Lett. 53 (1984) 1555.
[12] C. Fattinger, D. Grischkowsky, "Terahertz beams," Appl. Phys. Lett. 54 (1989) 490.
[13] Z. Jiang and X.-C. Zhang, "Terahertz imaging via electrooptic effect" IEEE Trans. Microwave Theory Tech. 47 (1999) 2644.
[14] Q. Wu, T.D. Hewitt, and X.-C. Zhang, "Two-dimensional electro-optic imaging of THz beams," Appl. Phys. Lett. 69, (1996) 1026.
[15] E.R. Brown, K.A. McIntosh, K.B. Nichols, and C.L. Dennis, "Photomixing up to 3.8 THz in low-temperature-grown GaAs," Appl. Phys. Lett. 66 (1995) 285.
[16] S.H. Gold, G.S. Nusinovich, "Review of high power microwave source research" Rev. Sci Instrum. 68, 3945 (1997).
[17] A. Staprans, E. McCune, and J. Ruetz, "High-power linear-beam tubes", Proc. IEEE, 61 (1973) 299.
[18] H. Motz, J. Appl. Phys. 22 (1951) 527.
[19] R.M. Phillips, Nucl. Instr. Meth. Phys Res. A272 (1988) 1.
[20] D.A.G. Deacon et al., Phys. Rev. Lett. 38 (1977) 892.
[21] F. Ciocci, A. Doria, G.P. Gallerano, I. Giabbai, M.F. Kimmitt, G. Messina, A. Renieri, J.E. Walsh, Phys. Rev. Lett. 66 (1991) 699, and refs. therein.
[22] G. Doucas, M.F. Kimmitt, A. Doria, G.P. Gallerano, E. Giovenale, G. Messina, H.L. Andrews, J.H. Brownell, Phys.Rev. ST Acc. and Beams 5 (2002) 072802, and refs. therein.
[23] M.D. Sirkis, D. Coleman, J. Appl. Phys. 28 (1957) 944.
[24] A. Doria, R. Bartolini, J. Feinstein, G.P. Gallerano, R.H. Pantell, IEEE J. Quant. Elec., 29, 1428 (1993).
[25] A. Gover et al., Phys. Rev. Lett., 72, 1192-1195 (1994).
[26] P. Kung, H. Lihn, H. Wiedemann, D. Bocek, Phys. Rev. Lett. 73(1994) 967.
[27] D.A. Jaroszynski, R.J. Bakker, C.A.J. van der Geer, D. Oepts and P.W. van Amersfoort, Phys. Rev. Lett. 71(1993) 3798.
[28] G.P. Gallerano, A. Doria, E. Giovenale, G. Messina Nucl. Instr. Meth. Phys. Res., A358 (1995), 78.
[29] J. Schmerge, J. Lewellen, Y.C. Huang, J. Feinstein, R.H. Pantell, IEEE J. Quantum Elec. 31(1995) 1166.
[30] G.P. Gallerano, A. Doria, E. Giovenale, A. Renieri, "Compact free electron lasers: from Cerenkov to waveguide FELs" Infr. Phys. Tech. 40 (1999) 16.
[31] G. Ramian, Nucl. Instr. Meth. A318 (1992) 225.
[32] A. Gover et al., Nucl. Instr. Meth. A 528 (2004) 23.
[33] K.W. Berryman, E.R. Crosson, K.N. Ricci, T.I. Smith, Nucl. Instr. Meth., A375 (1996) 526.
[34] A.F.G. van der Meer, "FELs, nice toys or efficient tools?", Nucl. Instr. Meth. A 528 (2004) 8.
[35] R. Prazeres, F. Glotin, J.M. Ortega, "Newresults of the 'CLIO' infrared FEL", Nucl. Instr. Meth. A528 (2004) 83.
[36] P. Michel et al., "First lasing of the ELBE mid-IR FEL", these proceedings.
[37] N. Vinokurov et al., "Status of the Novosibirsk THz FEL", these proceedings.
[38] G.L. Carr, M.C. Martin, W.R. McKinney, K. Jordan, G. Neil, G.P. Williams, Nature 420 (2002) 153.
[39] H. Tamada et al., Nucl. Instr. Meth. Phys. Res. A331 (1993) 566.
[40] M. Abo-Bakr et al., Phys. Rev. Lett. 88 (2002) 254801.
[41] G.L. Carr et al., Nucl. Instr. Meth. Phys. Res. A463 (2001) 387.
[42] J.M. Byrd et al., Phys. Rev. Lett. 89 (2002) 224801.
[43] A. Doria, V.B. Asgekar, D. Esposito, G.P. Gallerano, E. Giovenale, G. Messina, Nucl. Instr. Meth. A475 (2001) 296.
[44] S. Biedron et al., work supported by Contract No. W-31-109-ENG-38 between the United States Government and Argonne National Laboratory.
[45] A. Doria, G.P. Gallerano, E. Giovenale, G. Messina, I. Spassovsky, "Enhanced coherent emission of THz radiation by energy-phase correlation in a bunched electron beam", submitted to Phys. Rev. Lett. (2004).
[46] A. Doria, G.P. Gallerano, E. Giovenale, S. Letardi, G. Messina, C. Ronsivalle, Phys. Rev. Lett. 80 (1998) 2841.
[47] J.G. Neumann et al., Nucl. Instr. Meth. Phys. Res. A507 (2003) 498.
[48] G.L. Carr, private communication (2004)
[49] W.P. Leemans et al., Phys. Rev. Lett. 91 (2003) 074802.
[50] M. Mross, T.H. Lowell, R. Durant, M.F.Kimmitt, J. Biol. Phys. 29 (2003) 295.
[51] K.J. Kim, private communication (2004)
[52] H.L. Andrews, C.H. Boulware, C. Brau, J.D. Jarvis, "Gain and coherent radiation from a Smith-Purcell Free Electron Laser" these proceedings.
[53] H. Koops, Nucl. Instr. Meth. Phys. Res. A483 (2002) 488.
[54] S. Bhattacharjee et al., IEEE Trans.Plasma Science 32 (2004) 1002.

HIGH AVERAGE POWER OPERATION OF A SCRAPER-OUTCOUPLED FREE- ELECTRON LASER

M. Shinn*, C. Behre, S. Benson, M. Bevins, D. Bullard, J. Coleman, L. Dillon-Townes, T. Elliott, J. Gubeli, D. Hardy, K. Jordan, R. Lassiter, G. Neil, S. Zhang

TJNAF, Newport News, VA 23606

Abstract

We describe the design, construction, and operation of a high average power free-electron laser using scraper outcoupling. Using the FEL in this all-reflective configuration, we achieved approximately 2 kW of stable output at 10 um. Measurements of gain, loss, and output mode will be compared with our models.

INTRODUCTION

Compared to other high average power laser systems, an advantage of a free-electron laser (FEL) is there are no heat dissipation issues within the gain medium. However, when operated in an oscillator configuration, one must mitigate and manage the effects of absorbed photons and the resultant thermally induced distortion of the otherwise spherical mirror surface. Previous analysis [1] and experiment [2] have shown that this distortion, when sufficiently large, causes the output to saturate. The obvious solution, to obtain low loss coatings and substrates, isn't always possible at certain wavelength ranges. For example, at 10.6 μm, the best outcoupler (OC) designs still have absorption levels in excess of 0.1% [3], which limits the extracted power to less than 10 kW [4]. In other wavelength regions such as the deep UV (< 150 nm) suitable substrates for outcoupling the output don't exist.

In these cases, some other scheme for outcoupling the laser radiation from the resonator must be used. In FELs, hole outcoupling is traditional [5], but is not particularly efficient. For many high average power lasers it is customary to use a scraper mirror intracavity, *i.e.*, an annular mirror were some fraction of the center of the laser mode is transmitted, and the wings of the mode are reflected out of the cavity. [6] Usually scraper outcoupling is used in positive branch unstable resonators, where the gain is very high and the outcoupling fraction may be large, *e.g.*, > 30%. The gain in the majority of FELs is not so high, and the wiggler in the FEL requires a negative branch unstable resonator, which adds its own complications. We chose to use our existing near-concentric resonator and place the scraper mirror close to one of the end mirrors. Only one theoretical paper [7] has been published on the use of an annular scraper, but to our knowledge there are no experimental results. Therefore, we analyzed this cavity configuration to confirm that we would get efficient and stable output. Finding that it was stable, we then proceeded to build and test it.

*shinn@jlab.org

DESIGN AND IMPLEMENTATION

The optical cavity configuration we modeled is shown in Fig, 1, and the resonator parameters are shown in Table 1. We chose to operate at ~ 10 μm, as we had been commissioning the IR Upgrade FEL at this wavelength using a conventional, transmissive outcoupling optical cavity, and had mirrors readily available.

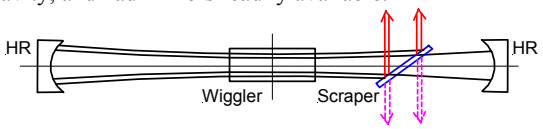

Figure 1 Schematic layout of the FEL optical cavity with an annular scraper. The solid arrows denote the outcoupled beam, the dashed arrows denote the diffracted beam that strikes the rear of the scraper.

Table 1 FEL resonator parameters

Parameter	Value
Cavity length	32.042 m
Rayleigh range	3 m
Mirror radius of curvature	16.6 m
Scraper position	15.4 m
Scraper outcoupling	10%

Given the single pass gain of our optical klystron was ~ 30%, and the extraction efficiency is highest when the outcoupling fraction is ~ 1/3 the gain [8], we designed the scraper to intercept 10% of the optical mode. This was done using the following analytical expressions [6]:

The power transmitted for a gaussian beam of $1/e^2$ radius ω through a circular aperture of radius a is given by:

$$P_{trans} = 1 - \exp\left(\frac{-2a^2}{\omega^2}\right) \quad (1)$$

In our case, we want $P_{trans} = 0.9$, so $a = 1.07\omega$.
At the position of the scraper (z=15.4m), the mode size is given by:

$$\omega(z) = \omega_0 \left[1 + \left(\frac{\lambda z}{\pi \omega_0^2} \right)^2 \right]^{\frac{1}{2}} \quad (2)$$

For our resonator configuration, ω_0 = 0.003 m, and with λ = 10 μm, $\omega(z)$ = 1.66 cm. From the relationship between a and ω, the radius of the hole in the scraper is. 1.78 cm. This was the starting point for our simulations. Simulations were carried out in both ZEMAX [9] and GLAD [10], with similar results. Given our interest in determining the losses due to diffraction, we primarily used GLAD. Since we were most interested in determining if the configuration was stable, we did the calculations in a cold cavity, *i.e.,* no gain. Rather than let the power in the cavity decrease on each pass, we simply reinitialized the power after each pass and let the mode develop until the losses (and power) converged to a steady state. These diffractive losses occur at two points, first when the mode traverses the scraper, and then as it approaches the wiggler vacuum chamber.

As the intracavity average power may be as high as 100 kW, the scraper should be thermally conductive and water cooled. We chose copper for the substrate, with a simple loop of copper tube brazed to its periphery for cooling. (Fig. 2). To have high reflectivity, the scraper was gold coated, using a RF magnetron deposition process. As the wavelength is long, the surfaces did not have to be polished to a high degree of flatness or smoothness. Specifications are given in Table 2. The polishing and coating were done in-house, and the optical specifications checked using a Wyko RTI4100 laser interferometer and NT1100 noncontact profilometer. We met or exceeded specifications; the mirror figure was 3 waves at 633 nm, and the roughness was 1 μm rms.

Table 2 Scraper specifications

Item	Parameter
Material:	Cu
Diameter:	3.500 in (+ 0 in, - 0.005 in)
Edge thickness:	0.500 in (+0 in, - 0.005 in)
Mirror figure:	10λ @ 632.8 nm
Surface roughness:	≤ 1 μm rms

Actuation of the scraper was on a modified "ultraviewer"; a linear insertion device that repeatedly maintains alignment of the pitch and yaw axes to better than 50 μrad. The outcoupled beam was in the horizontal plane, and intercepted into a diagnostic beam dump (a power meter with position sensing). Readout of the input and output temperatures is in our EPICS control system.

As mentioned earlier, as the mode traverses the scraper there will be diffraction, which after reflection from the end mirror does not pass through the scraper aperture but instead falls on the back of the scraper. Based on simulations, this amounts to ~ 10% of the intracavity power outcoupled by the scraper. This reflected laser light passed through an AR-coated viewport and was absorbed by a Molectron PM5K power probe. This system had a faster response time than the diagnostic beam dump.

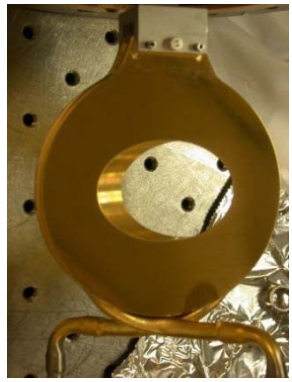

Figure 2 The scraper mirror. The mirror is moved in the vertical direction. At the bottom of the scraper is the cooling loop.

An IR camera imaged the surface. We could also use this radiation to study the laser dynamics. When operating in a macropulsed mode we could insert a mirror before the power probe and focus the light onto a Judson J15D12 cryogenically-cooled MCT detector.

RESULTS

Gain and loss measurements

Getting this system to lase was quite easy. In macropulsed mode, the output from the MCT detector (Fig. 3) was used to optimize the system.

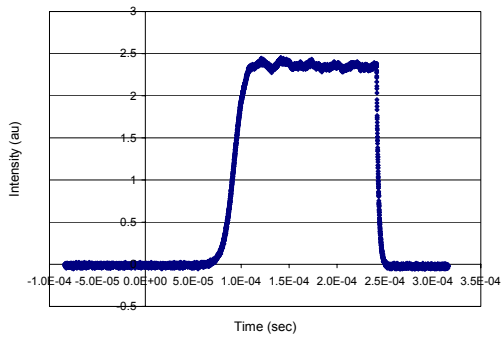

Figure 3 FEL output during a 250 μs macropulse.

We recorded the rise and decay of the macropulsed output at higher resolution to determine the gain and loss. This is shown in Figs 4 and 5, respectively.

Analysis of the FEL output's rise and fall allowed us to determine the gain and loss/pass. These values are 16% and 8%, respectively. The error bar on the measurements is +/- 1%. The lower than calculated gain was unanticipated, since we had measured higher gain at this

wavelength when operating the resonator with a transmissive outcoupler. We believe this was due to the accelerator setup.

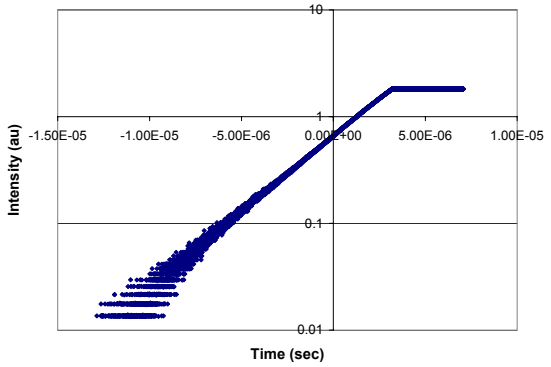

Figure 4 FEL start up

High average power operation

When operating at high average power, we found the power probe and IR camera was beneficial in optimizing the total output. Fig. 6 shows an image from the IR camera viewing the power probe.

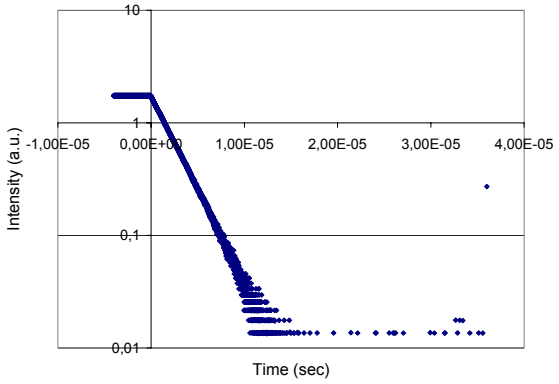

Figure 5 FEL decay

When operating at high average power, we found the power probe and IR camera was beneficial in optimizing the total output. Fig. 6 shows an image from the IR camera viewing the power probe.
So long as the image remained circular, the mirrors were well aligned and we had the highest output power - as measured on both the diagnostic dump and the diffracted light power probe. The highest power measured was ~1750 W, as inferred by measuring 139 W with the fast power probe, and using an experimentally determined ratio between the diffracted to outcoupled light of 1:12.5. A typical power trend is shown in Fig. 7. Once we were above 1 kW average power, note that each push up in power was rather short, only a few minutes in length. What was occurring was that both cavity mirrors would

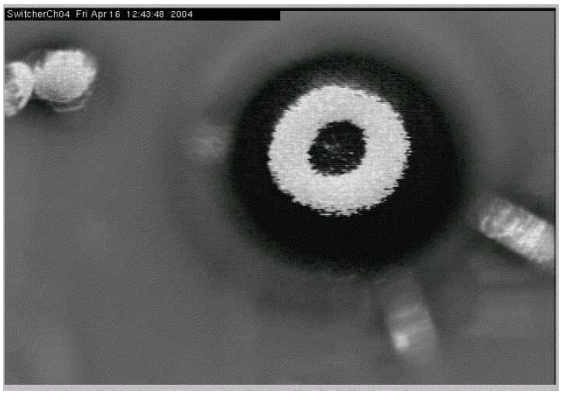

Figure 6 IR image of light reflecting from the rear of the scraper onto a power probe.

pitch as the mirrors absorbed power, and the cavity length would drift, first shorter, then longer. This made optimization problematic, and usually the cause of the laser shutting off was the cavity length. Once the laser was off, the mirrors would cool off and drift in the opposite direction. Fortunately, we were able to track this drift and could get the cavity realigned quickly.

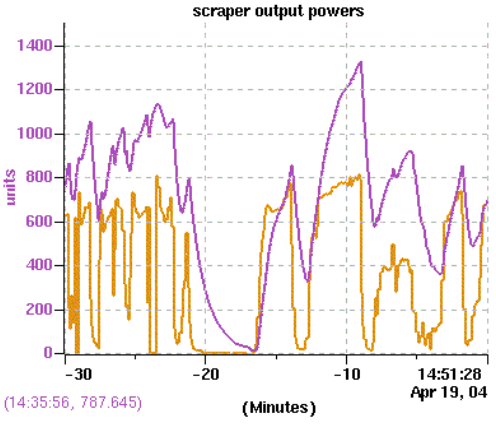

Figure 7 Power trends. The purple trace is the outcoupled light from the scraper. The yellow trace is the power from the diffracted light off the rear of the scraper (0-200W scale).

Why was this occurring? Subsequent to testing the scraper outcoupler, we added IR viewports and cameras that enabled us to image the interior of the optical cavity mirror vacuum vessels. What we found was that scattered light was scattered into a wide enough cone that it fell on the poorly cooled mirror fixturing hardware. These components warmed up and as they expanded, they caused the cavity length to grow longer. The more rapid shortening of the cavity length was the result of absorption of laser light (and in the case of the downstream mirror and its deforming assembly, THz and second harmonic light as well), that causes a thermal bump in the center of each mirror. The magnitude of this bump (for each mirror) is of order 1 um, and develops in

the course of a few seconds, forcing us to initially lengthen the cavity. There were other signs that the scattered (and absorbed) light was excessive. We saw pressure transients (as measured by the ion pumps) that correlated with strong lasing. In addition, enough scattered light was absorbed in a calcium fluoride vacuum viewport situated just upstream of the wiggler (part of the OCMMS hardware [11]) that it shattered. Clearly, better control of scattered light needs to be in place. We are designing water-cooled absorbing shields that will be placed before the mirror plane to minimize the heating effects we saw. Treating the beam tube in the vicinity of the scraper, so it absorbs scattered light, is being contemplated as well.

We can determine the amount of power absorbed by measuring the flow rate and temperature rise in the water that cools each cavity mirror. When lasing with a power of 1500 W, the mirror upstream of the wiggler absorbed ~ 120 W, while the downstream mirror absorbed 310 W, the highest value we have ever measured. We were able to partially compensate for the thermal bump by actively deforming each mirror. Due to the high absorption (~ 1.7% of the intracavity power for the downstream mirror) the uncompensated aberration lowered the lasing efficiency to the point that we decided to pursue lasing at a shorter wavelength, where we had better mirrors. Much lower loss 10 μm HR mirrors (absorption < 300 ppm) are available, and we are procuring them.

Table 3 Comparison between optical modeling and experimental results

	Model	**Experiment**
Loss/pass	11%	8%
Outcoupled/diffracted power	10	12.5

CONCLUSIONS

We found that operation of a FEL in a scraper-outcoupled near-concentric cavity configuration lased easily, and produced stable output. Experimentally derived values for the loss and ratio of outcoupled to diffracted light were in good agreement (Table 3) with the values from our simulations. The outcoupling efficiency of 92% is much higher than obtainable with a hole-outcoupler mirror. We found that this cavity configuration, using two high reflectors with backplane cooling and active ROC control allowed us to outcouple ~ 1.75 kW. With a more conventional, edge-cooled transmissive outcoupler with 0.4% loss, we could only achieve 0.7 kW. If we had better mitigated the effects of scattered light, and had lower loss coatings, we would have easily achieved higher output powers. Clearly, this demonstration proves that the annular scraper outcoupler can be used to produce high average power in wavelength regions where substrate and/or coating absorption precludes the use of a transmissive outcoupler.

ACKNOWLEDGEMENT

We thank the members of our review committee for suggesting that we explore this cavity configuration option. This work supported by the Office of Naval Research, NAVSEA PMS-405, the Joint Technology Office, the U.S. Night Vision Laboratory, the Commonwealth of Virginia, the Air Force Research Laboratory, and by DOE Contract DE-AC05-84ER40150.

REFERENCES

[1] S.V. Benson et al. "Optical modeling of the Jefferson Laboratory IR Demo FEL", *Nucl. Inst. and Meth*., **A407** 401 (1998)

[2] Stephen V. Benson, Joe Gubeli, and Michelle Shinn, "Mode Distortion Measurements on the Jefferson Lab IR FEL" *Nucl. Inst. and Meth*. **A483**, 434 2002.

[3] D. Ristau et al, "Round-robin test on optical absorption at 10.6 μm" SPIE **2714** 120 (1996).

[4] S.V. Benson, "What have we learned from the kilowatt IR-FEL at Jefferson Lab?" *Nucl. Inst. and Meth.* **A483** 1 (2002).

[5] "Performance of Hole Coupling Resonator in the Presence of Asymmetric Modes and FEL Gain", M. Xie and K.-J. Kim, *Nucl. Inst. and Meth.,* **A318** (1992) 877-884.

[6] A.E. Siegman, Lasers, University Science Books, Mill Valley CA, 1986.

[7] R. Nagai, et al, "An optical resonator with insertable scraper output coupler for the JAERI far-infrared free-electron laser", *Nucl. Inst. and Meth.* **A475** 519 (2001).

[8] G. Dattoli, L. Giannessi, and S. Cabrini, "Intensity Saturation Mechanism in Free-Electron Lasers", *IEEE J. Quantum Electron*, 28(4) 770 (1992).

[9] Information on ZEMAX is available at http://www.zemax.com/

[10] In formation on GLAD is available at http://www.aor.com/

[11] M.D. Shinn, et al, "Design of the Jefferson Lab IR Upgrade FEL optical cavity", *Nucl. Inst. And Meth*. **A507** pp196-199 (2003).

STATUS OF THE NOVOSIBIRSK TERAHERTZ FEL*

V.P. Bolotin, N.A. Vinokurov#, D.A. Kayran, B.A. Knyazev, E.I. Kolobanov, V. V. Kotenkov, V.V. Kubarev, G.N. Kulipanov, A.N. Matveenko, L.E. Medvedev, S.V. Miginsky, L.A. Mironenko, A.D. Oreshkov, V.K. Ovchar, V.M. Popik, T.V. Salikova, S.S. Serednyakov, A.N. Skrinsky, O.A. Shevchenko, M.A. Scheglov, Budker INP, Novosibirsk, Russia

Abstract

The first stage of Novosibirsk high power free electron laser (FEL) was commissioned in 2003. It is based on the normal conducting CW energy recovery linac. Now the FEL provides electromagnetic radiation in the wavelength range 120 - 180 micron. The average power is 200 W. The minimum measured linewidth is 0.3%, which is close to the Fourier-transform limit. The assembly of user beamline is in progress. Plans of future developments are discussed.

INTRODUCTION

A new source of terahertz radiation was commissioned recently in Novosibirsk. [1]. It is CW FEL based on an accelerator–recuperator, or an energy recovery linac (ERL). It differs from the earlier ERL-based FELs [2, 3] in the low frequency non-superconducting RF cavities and longer wavelength operation range. Full-scale Novosibirsk free electron laser is to be based on the four-orbit 50 MeV electron accelerator-recuperator (see Fig. 1). It is to generate radiation in the range from 3 micrometer to 0.2 mm [4, 5].

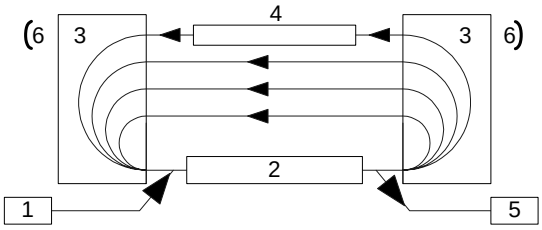

Figure 1: Scheme of the accelerator-recuperator based FEL. 1 - injector, 2 - accelerating RF structure, 3 - 180-degree bends, 4 – undulator, 5 – beam dump, 6 – mirrors of the optical resonator.

ACCELERATOR-RECUPERATOR

The first stage of the machine contains a full-scale RF system, but has only one orbit. Layout of the accelerator–recuperator is shown in Fig. 2. The 2 MeV electron beam from an injector passes through the accelerating structure, acquiring the 12 MeV energy, and comes to the FEL, installed in the straight section. After interaction with radiation in the FEL the beam passes once more through the accelerating structure, returning the power, and comes to the beam dump at the injection energy. Main parameters of the accelerator are listed in Table 1.

Table 1: Accelerator parameters (first stage)

RF frequency, MHz	180
Number of RF cavities	16
Amplitude of accelerating voltage at one cavity, MV	0.7
Injection energy, MeV	2
Final electron energy, MeV	12
Maximum bunch repetition rate, MHz	22.5
Maximum average current, mA	20
Beam emitance, mm·mrad	2
Final electron energy spread, FWHM, %	0.2
Final electron bunch length, ns	0.1
Final peak electron current, A	10

The electron source is the 300 keV DC gun with gridded cathode. Recently we changed the cathode-grid unit to the new one, and the charge per bunch increased to 1.5 nC.

FEL

The FEL is installed in a long straight section of a single-orbit accelerator-recuperator. It consists of two undulators, a magnetic buncher, two mirrors of the optical resonator, and an outcoupling system. Both electromagnetic planar undulators are identical. The length of an undulator is 4 m, period is 120 mm, the gap is 80 mm, and deflection parameter K is up to 1.2. One can use one or both undulators with or without a magnetic buncher. The buncher is simply a three-pole electromagnetic wiggler. It is necessary to optimize the relative phasing of undulators and is used now at low longitudinal dispersion $N_d < 1$.

Both laser resonator mirrors are identical, spherical, 15 m curvature radius, made of the gold-plated copper, and water-cooled. In the center of each mirror there is a hole. It serves for mirror alignment (using the He-Ne laser beam) and output of small amount of radiation. The distance between mirrors is 26.6 m. The forward mirror

* Work supported by the Siberian Branch of Russian Academy of Science under the integration grant #174.
#vinokurov@inp.nsk.su

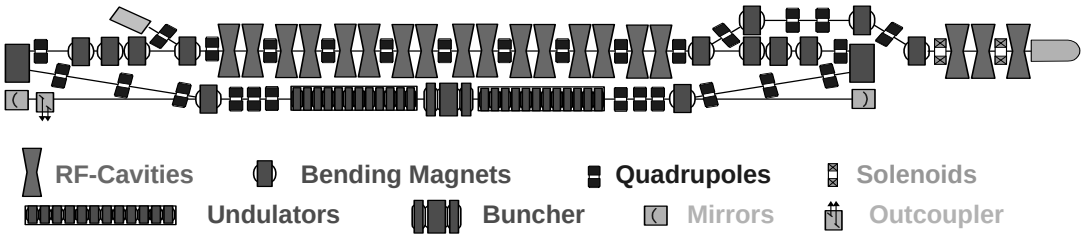

Figure 2: Scheme of the first stage of the Novosibirsk high power FEL.

has the hole with the diameter 3.5 mm, and the rear one - with the diameter 8 mm. The calculated transparency of the mirror with the 8-mm hole, at the wavelength 150 micron, is 1.5%. At this wavelength the measured round-trip loss are near 7%. The output radiation pass through two windows, which separated the FEL and accelerator vacuum from the atmosphere. After the forward mirror the additional iris and the normal-incidence quartz mirror are installed. After the rear one there is a diamond window, tilted at the Brewster angle.

For FEL operation we used both undulators. Beam average current was typically 8 mA at the repetition rate 5.6 MHz, which is the round-trip frequency of the optical resonator and 32-th subharmonics of the RF frequency $f_0 \approx 180$ MHz.

RADIATION STUDY

The first measurements of radiation parameters were reported before [1].

Instead of the fine tuning of the optical resonator length we tuned the RF frequency. The tuning curve is shown in Fig. 3. The preliminary simulation results [6] demonstrate a reasonable agreement with measured data.

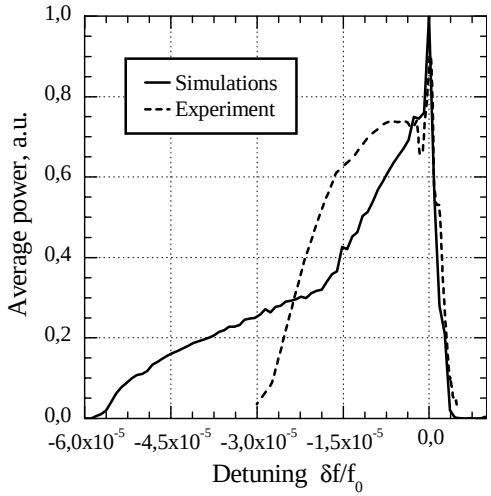

Figure 3: Dependence of the average power on the RF frequency detuning.

The average radiation power, passed through the hole at the rear mirror, was about 200 W. Taking into account the 7% loss, one get approximately 1 kW of power, extracted from the electron beam. The electron beam power was 100 kW. Therefore an electron efficiency is about 1%. The typical radiation parameters are listed in Table 2.

Table 2: The radiation parameters

Wavelength, mm	0.12...0.18
Minimum relative linewidth, FWHM	0.003
Pulse length, FWHM, ns	0.05
Peak power, MW	0.6
Repetition rate, MHz	5.6
Average power, kW	0.2

To demonstrate the capabilities of our terahertz radiation source we made a hole in a plexiglas (PMMA) cube (see Fig. 4). Using the short-focusing mirror the CW breakdown in air was achieved (see Fig. 5).

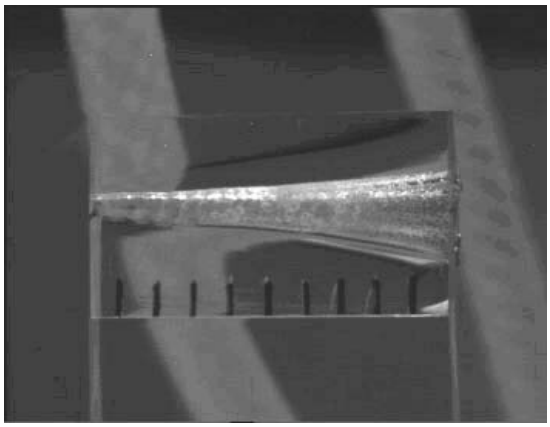

Figure 4: The conic hole in the PMMA cube, done with the terahertz radiation ablation. One division is 5 mm.

To transmit the radiation from the rear mirror hole to user stations, the beamline from the accelerator hall to the user hall was built. It comprises of one spherical mirror and 5 flat mirrors inside the stainless steel tubes. Now the beamline is filled by nitrogen. It is separated from the accelerator vacuum by the diamond window, and from the air by the polyethylene window. The beamline was commissioned successfully, and some preliminary optical measurements and experiments were done.

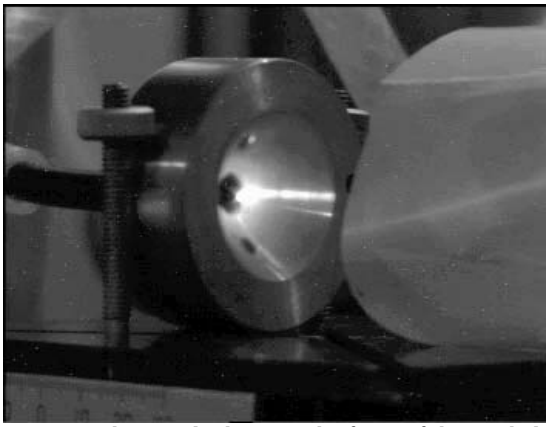

Figure 5: The CW discharge in the focus of the parabolic mirror.

FURTHER DEVELOPMENTS

We plan to increase further the output power. Factor two may be obtained by the increase of the diameter of the hole in the rear mirror. The electron gun upgrade for the increase of the average current up to 0.1 A is under consideration. As we have the two-section undulator, further attempts to increase the FEL efficiency by the proper tapering looks promising.

The mechanical design of the second stage of the FEL is in progress.

REFERENCES

[1] E. A. Antokhin et al. NIM A528 (2004) p.15-18.
[2] G.R. Neil et al. Phys. Rev. Lett. 84 (2000), p. 662.
[3] E.J. Minehara. Nucl. Instr. and Meth. A, V. 483, p. 8, 2002.
[4] N.G. Gavrilov et al. IEEE J. Quantum Electron., QE-27, p. 2626, 1991.
[5] V.P.Bolotin et al. Proc. of FEL-2000, Durham, USA, p. II-37 (2000).
[6] O.A. Shevchenko, A.V. Kuzmin, N.A. Vinokurov. Numerical modeling of the Novosibirsk Terahertz FEL and comparison with experimental results. These proceedings.

HIGH POWER LASING IN THE IR UPGRADE FEL AT JEFFERSON LAB

S. Benson*, D. Douglas, M. Shinn, K. Beard, C. Behre, G. Biallas, J. Boyce, H. F. Dylla, R. Evans, A. Grippo, J. Gubeli, D. Hardy, C. Hernandez-Garcia, K. Jordan, L. Merminga, G. R. Neil, J. Preble, T. Siggins, R. Walker, G. P. Williams, B. Yunn, S. Zhang, H. Toyokawa†
TJNAF, Newport News, VA 23606, USA
† Photonics Research Institute AIST-Tsukuba Japan

Abstract

We report on progress in commissioning the IR Upgrade facility at Jefferson Lab. Operation at high power has been demonstrated at 5.7 microns with over 8.5 kW of continuous power output, 10 kW for 1 second long pulses, and CW recirculated electron beam power of over 1.1 MW. We report on the features and limitations of the present design and report on the path to getting even higher powers.

INTRODUCTION

At last years' FEL conference we reported on first lasing of the IR Upgrade FEL in the infrared region [1]. Turn-on and commissioning of that device went quite smoothly and CW power of 300 W at 10 μm and 3 mA of CW electron beam current at 80 MeV were demonstrated. Two problems were noted—the FEL gain and power were lower than expected, and the mirror losses at 10 μm were higher than expected. This paper will discuss how these problems were overcome and how we intend to extend the power even higher that we have to date. The paper will describe the challenges we faced in the accelerator and our understanding of how to set it up to produce an electron beam capable of high power. It will also describe the challenge of running with over 100 kW of CW circulating power in a free-electron laser.

ACCELERATOR CHALLENGES

The accelerator layout is shown in figure 1. By the FEL 2003 conference almost the entire machine had been installed and commissioned. The first arc still used a dipole from the IR Demo machine [2], limiting the beam energy to 80 MeV. We also used pairs of reworked IR Demo sextupoles that limited operation to around 90 MeV and were only in one of the two locations necessary for dispersion suppression. There were no octupoles installed in the second arc. Finally, only two of the three cryomodules had been installed, limiting the energy to less than 90 MeV. In the fall of 2003 we took advantage of a hurricane-induced downtime to install the final dipole in the first arc. In early spring we upgraded the sextupoles with bigger coils that allowed operation at up to 160 MeV and installed the octupoles in the second arc. In May of 2004 we installed the middle cryomodule, which has operated with an accelerating voltage of over 80 MV with beam, giving a total available accelerator energy of 170 MeV.

* email address felman@jlab.org

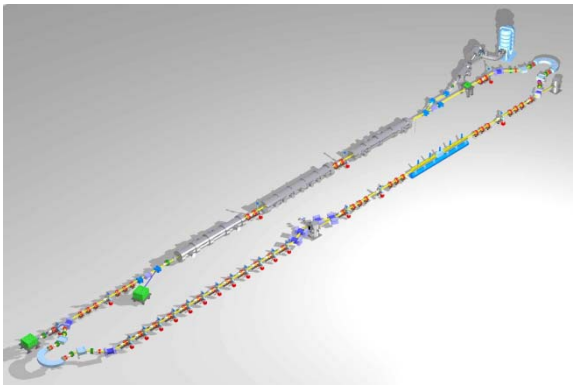

Figure 1. Layout of the IR Upgrade FEL in its final configuration. The beam starts at the injector at the upper right, is merged with the full energy beam in an injection chicane, accelerated up to as much as 160 MeV in three cryomodules, transported to the optical klystron, and from there back to the linac. At the exit of the linac the energy-recovered beam is separated from the accelerated beam and is dumped in a water-cooled copper dump.

The challenge of producing a high quality beam

The main reason for poor lasing performance last year was a large growth in the longitudinal emittance between the injector and the wiggler. To understand the tradeoffs involved with reducing this growth it is useful to describe the longitudinal matching around the accelerator.

The injector is designed to produce an upright longitudinal distribution at the entrance of the first accelerating module of the linac [3]. For our initial design the injected bunch length was 1.5 psec *rms* and the energy spread was 12 kV *rms*. The accelerator is designed to take that distribution and rotate it by 90 degrees in phase space. The bunch length and relative energy spread at the wiggler are then given by:

$$\sigma_{t,W} = \frac{\sigma_{E,I}}{E_L \omega \tan\phi} \text{ and } \frac{\sigma_{E,W}}{E_W} = \frac{\omega \tan\phi}{1 + E_I / E_L} \sigma_{t,I} \qquad (1)$$

where $\sigma_{E/t,W/I}$ are the rms bunch lengths and energy spreads at the injector and the wiggler, ω is the accelerator frequency, ϕ is the off-crest phase, E_L is the energy gain in the linac, and E_I and E_W are the beam energies at the injector exit and at the wiggler entrance. This equation assumes that the quadrupoles and sextupoles in the first arc are set to values that match the M_{56} and T_{566} of the arc to the slope and curvature imposed on the beam by the accelerator and thus perform a 90° rotation [4].

The bunch length calculated using equation (1) for the design injector and the accelerator operated at 80 MeV, 15 degrees off-crest, should have had an rms bunch length at the wiggler of 67 fsec and energy spread of 0.33%. In fact the energy spread was close to 0.3%, but the bunch length, measured using both a Martin-Puplett style interferometer looking at coherent OTR and a scanning Michelson interferometer looking at the coherent synchrotron radiation, was over 300 fsec rms and was sensitive to the transverse match in the machine. In addition, the first arc magnet strengths that produced the shortest measured bunch were not those noted above that rotated the phase space by 90 degrees. Finally, the rms energy spread at the end of the wiggler should not depend on the sign of the phase with respect to the peak of the linac's accelerating phase (see equation (1)). In fact, however, the energy spread was 50% larger on one side of crest than on the other side. All these discrepancies between the expected behavior and the accelerator performance are due to longitudinal space charge (LSC) in the linac and transport [5]. The LSC leads to longitudinal emittance growth and a tilt of the energy distribution that alters the longitudinal match to the wiggler. We reduced the effects of LSC by modifying the injector setup to increase the injected micropulse length to 2.5–3.0 psec. This reduced the longitudinal emittance growth, improved the FEL efficiency, and altered the longitudinal match so that the design magnet strengths were nearly optimal for the first arc. One cannot increase the injected bunch length by an arbitrary amount. Due to the energy acceptance of the FEL it is necessary to decrease the off-crest phase angle to offset the increase in bunch length. This leads to problems with energy recovery that will be discussed in the next section.

Using one family of sextupoles per arc it is possible to properly set the T_{566} for the longitudinal match and to cancel the dispersion to first order. It is not possible to correct the second order dispersion, which leads to a reduction in the efficiency of the FEL and to loss of halo at several points in the transport. This halo is produced in the gun at different launch phases than that of the accelerated bunches. The buncher cavity is set to bunch high charge bunches and strongly overbunches the halo. The halo then has a large energy spread at the end of the linac and, when the dispersion is corrected to only first order, grows dramatically in horizontal beam size at the wiggler entrance. With two families of sextupoles we were able to transport beam cleanly through the wiggler. The efficiency also more closely matched predictions.

Once the third cryomodule was installed we had a new challenge. The damping of the higher order modes (HOMs) in this cryomodule is not sufficient to raise the beam breakup (BBU) threshold above 10 mA. In fact one HOM was found to have a threshold of only 3 mA. We found that, since there was only one mode with a low threshold, we could alter the betatron phase advance to increase the threshold up to over 5 mA. As an experiment we also installed skew quads that changed a vertical kick into a horizontal motion at the offending cavity [7]. With these magnets set correctly we could run at least 8 mA at 145 MeV (1.16 MW of beam) with no evidence of beam breakup. In the future we will further characterize the BBU threshold dependence and study other ways to raise the threshold.

Challenges in energy recovery

The magnets after the FEL must transport a beam with very large energy spread to the dump with extremely low losses. To do this, the energy vs. time distribution must be properly matched to the decelerating gradient in the linac. When this is done correctly the longitudinal phase space is rotated 90 degrees by the time the electron beam reaches the beam dump. The matching is done to third order in the energy offset using quadrupoles, sextupoles, and octupoles. This system can, in principal, accept up to 15% energy spread [4]. Operating the accelerator close to crest leads to a problem with this scheme. The highest energy electrons in the distribution must be close to trough in order to decelerate all the electrons to the same final energy. If this is done, the mean phase ϕ_{dec} must be $\phi_{dec} = \sqrt{\Delta E / V_{linac}}$ or more where ΔE is the full energy spread and V_{linac} is the total linac voltage. If we have a distribution with 15% energy spread we must have a mean phase of at least 22.5 degrees. One would like to decelerate the beam 180° out of phase with the accelerating beam since no extra RF power is required as the current is increased. If one accelerates 10 degrees off crest this will not be possible due to the loss of the higher energy electrons at the dump. We have discovered that it is still possible to recover the electron beam with very low loss by decelerating less than 180° from the accelerated beam at the mean phase derived above. A minor drawback of this setup is that some RF is required to accelerate the beam since it ends up at a higher energy than at injection. The FEL power must come from somewhere. In the IR Demo it came from the injector. In the IR Upgrade it comes from the linac. When longer injector micropulses were used, the off crest phase was limited to 10° to keep the energy spread below the wiggler acceptance. We found that it was necessary to run about 4 degrees further from trough to energy recover during high power lasing. This configuration was stable and the electron losses were minimal.

A new challenge in the IR Upgrade was CSR-induced high-energy tails on the electron beam due to the shorter bunches and higher charge. If the bunches are fully bunched by the transport up to the wiggler, they will produce copious coherent synchrotron radiation. This leads to the growth of a high-energy tail on the beam in the energy recovery section of the beam. We have found that, by setting the transport to the wiggler to slightly underbunch the beam, the CSR can be greatly reduced and the bunch length is only slightly longer than the minimum. The FEL performance is actually better when this is done due to the smaller energy spread.

The final challenge is to correct for chromatic aberration. This can produce large growth in the beam size as the energy spread increases. This was found to be

a major cause of beam loss in the linac. We have found that having matched betatron phase advances in the lattices before and after the second arc can suppress the spot size growth due to chromatic aberration and lead to well-contained beams during energy recovery.

The machine is now essentially complete. Except for the average current and the longitudinal emittance the machine matches the design values. A current of 9 mA has been demonstrated at 88 MeV and we do not see any fundamental reason why we will not be able to run at 10 mA, 160 MeV this fall. With two families of sextupoles in the first arc we found that the FEL efficiency closely matched predictions made by pulse propagation codes. We are now working on stability and reproducibility in the lattice and are developing methods to ease setup of the transverse match around the machine.

OPTICAL CHALLENGES

Optical challenges fall into two categories: 1. Getting mirror losses down to acceptable levels, and 2. handling the circulating and outcoupled power. We gradually learned how to accomplish both of these.

Reducing mirror losses

Previous work has shown that there is a limit to how much power the mirrors can absorb before the power saturates [6]. For example a zinc selenide output coupler can absorb 5W/μm*λ of power before the FEL power will saturate. In practice one can slightly exceed this number but it is a good design point. With the first set of 10 μm mirrors we found a large amount of mirror heating for even low power. Mirror losses were found to be 0.74% and 0.3% for the output coupler (OC) and the high reflector (HR) respectively. We replaced the OC with a mirror with 0.4% loss. This allowed us to achieve up to 700 W of CW power but it was clear that 10 kW was out of reach unless the losses could be reduced to under 500 parts per million (PPM). Discussion with mirror vendors indicated that this was highly unlikely.

From our experience on the IR Demo we knew that lower loss coatings were available in the 6 micron range. We remounted our 97.3% reflectivity OC used for the first light operation in a water-cooled mount and found that we could produce up to 2.3 kW from the laser. This exceeded the IR Demo power record and produced a circulating power of 84 kW.

Using an OC with an even lower loss and a reflectivity of 92% we were able to push the power up to 4.1 kW. At this power level the FEL itself becomes a good diagnostic for measuring mirror absorption. This allowed us to tune the wavelength for minimum loss. We found that the loss for the output coupler at 5.75 microns was only 250 parts per million (PPM). The high reflector had a loss of 400 PPM including an estimated 100 PPM of transmission.

One hypothesis for the high losses in the downstream mirror was that THz edge emission from the dipole just upstream of the mirror might dominate the OC heating. Measurements with an electron-beam energy of 80 MeV indicated that this was not the case. At an electron beam energy of 145 MeV the absorbed THz power went up dramatically, ranging from 50–85 W at 5 mA. The maximum allowed power in the output coupler at 6 microns is 30 W. The absorbed THz power would not allow us to run at 10 kW CW, though we could run 10 kW with up to a 30% duty cycle and could run CW with over 6 kW of power output.

In order to avoid THz heating of the output coupler we reversed the optical cavity so that the backplane-cooled high reflector, which can absorb over 200 W of power before limiting laser power, was downstream. The power absorbed in the output coupler was now just the fundamental power. The power absorbed in the high reflector consisted of three sources: the absorbed fundamental power, coherent second harmonic power, and THz edge radiation. This configuration allowed us to run 10 kW with a duty cycle of over 50% and to run CW with up to 8.5 kW of laser output power.

Since the time constant for mirror distortion is quite long it proved possible to run for periods of up to 1 second with power exceeding 10 kW. The power during the laser pulse vs. time for a run on July 21, 2004 is shown in figure 2. The power during 1 second pulses was as large as 10.6 kW. When shorter pulses were run the power was as high as 11 kW during 0.25 second pulses. The macropulse power vs. pulse length is shown in figure 3.

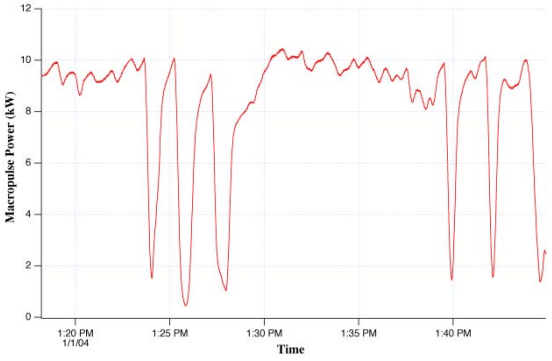

Figure 2. Power during 1 second pulses during time on July 21, 2004. The power could be repeatedly raised to higher than 10 kW. Dropouts are due to accelerator trips or mirror mis-steering.

Handling the power

When the power output of an FEL is several kilowatts in the mid-infrared even measuring the power is a challenge. We found that calcium fluoride windows could not handle transmitted power exceeding 1500 W at 6 microns. We therefore moved to an *in vacuo* power meter designed and built at Jefferson Lab capable of handling up to 50 kW of laser power. The power is absorbed in a black copper coating in a water-cooled cone. The rise in the water temperature of the cooling water and the flow are monitored and used to calculate the absorbed power. It is possible that power is also lost due to backscatter and conduction so the power numbers

quoted here are lower limits. Comparison at low power with a commercial power meter indicated that the power reading might be as much as 10% low, though the uncertainty was large in this calibration.

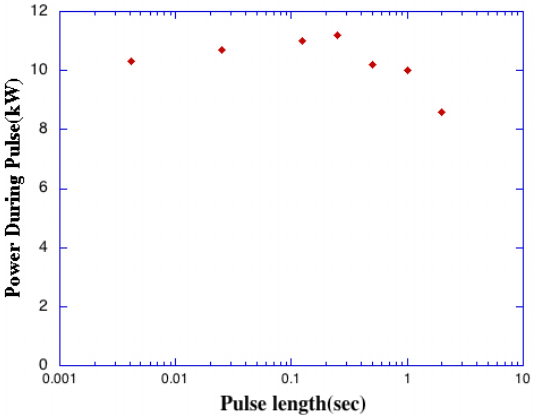

Figure 3. Macropulse averaged power as a function of pulse length. The point at 0.5 seconds was not fully optimized. The power was calculated assuming negligible turn-on time. The rise in power with pulse length is partly due to this and partly due to the fact that the high reflector radius of curvature was optimized for the longer pulses.

When lasing at 5.75 microns and 10 kW the output coupling was 8%. This means that the circulating power exceeded 125 kW. Even scatter of parts per thousand can lead to major problems in the cavity. We found that the rings holding the mirrors tended to heat after a time running at high power. This caused changes in the mirror alignment and cavity length. We had planned to use a helium-neon laser to track the mirror angle. Scattered light absorbed in the windows for this system distorted them sufficiently so that this was not possible. When we tried to shield the windows with metal screens we found that the scattered light melted holes in them. THz light also heated beamline elements and led to vacuum rises and optical distortion. Clearly, high power laser systems have to account for all power losses in the system and must be shielded from spurious light of all wavelengths. Our optical cavities are being modified to account for this reality.

CONCLUSIONS

The IR Upgrade has been a learning experience. Lessons learned from this machine can be used to both upgrade the present machine and better design the next generation machine. For example, in the future we plan to install a small chicane close to the wiggler that debunches the electron beam and reduces the THz edge emission to tolerable levels. We also plan to install a shorter period wiggler with a higher gain-efficiency product. This will allow us to increase the output coupling and reduce circulating power. It will also allow us to access shorter wavelengths where mirror losses are very low. We expect to be able to reach 10 kW CW with this setup. It should also allow operation at over 10 kW in the 6 micron range. Due to the lack of good mirrors we do not expect more than about 5 kW at 10 μm. We plan to explore broadband cavities to see what the average power limit is for a hole or scraper outcoupler system.

All these experiments dumped the laser power in the accelerator vault. We are in the process of installing an optical transport that will allow transport of the high power beam up to users. Note that we can produce over 300 μJ/micropulse with this laser in a subpicosecond pulse. It is not just a high average power laser but also a high peak power laser. This will be of great importance to users of the laser.

ACKNOWLEDGMENTS

This work supported by The Office of Naval Research the Joint Technology Office, NAVSEA PMS-405, the Air Force Research Laboratory, U.S. Army Night Vision Lab, the Commonwealth of Virginia, and by DOE Contract DE-AC05-84ER40150.

REFERENCES

[1] C. Behre et al., Nucl. Inst. And Meth. 528 (2004) 19–22.

[2] J. Karn, G. Biallas, A. Guerra, and L. Harwood, “Magnetic Measurements Of The Prototype Dipole For The IR-FEL At The Thomas Jefferson National Accelerator Facility”, Proceedings of the 1997 PAC conference (1997) 3334.

[3] C. Hernandez-Garcia et al., “Performance and Modeling of the JLab IR FEL Upgrade Injector”, these proceedings.

[4] “The Jefferson Lab 1 kW IRFEL”, Presented at the Linac 2000 conference, Aug. 2000, Monterey CA, http://www.slac.stanford.edu/econf/C000821/TH204.pdf

[5] C. Hernandez-Garcia et al., “Longitudinal Space Charge Effects in the JLAB IR FEL SRF Linac”, these proceedings.

[6] S. V. Benson, “Design details of the IR 10 kW Upgrade Free-electron Laser Resonator”, Jefferson Lab Technical note TN-02-014, http://tnweb.jlab.org/tn/2002/02-014.pdf.

[7] C. Tennant, D. Douglas, L. Merminga, E. Pozdeyev, and T. Smith, "Suppression of Multipass, Multibunch Beam Breakup in Two pass Recirculating Accelerators", these proceedings.

VUV OPTICS DEVELOPMENT FOR THE ELETTRA STORAGE RING FEL

St. Günster, D. Ristau, Laser Zentrum Hannover e.V., Hannover, Germany,
A. Gatto, N. Kaiser, Fraunhofer-Institut für Angewandte Optik und Feinmechanik, Jena, Germany,
M. Trovò, M.B.Danailov, Sincrotrone Trieste, Trieste, Italy
F. Sarto, ENEA-Casaccia, Italy

Abstract

Vacuum ultraviolet optical components for the storage ring FEL at Elettra are under continuous development in the European research consortium EUFELE. Target of the project is the progress to shorter lasing wavelengths in the VUV spectral range. The current status allows lasing with oxide mirror systems down to 190 nm. The main obstacles for the development of optical coatings for shorter wavelengths is the high energetic background of the synchrotron radiation impinging onto the front mirror in the laser cavity. Investigations in single layer systems and multilayer stacks of oxide or fluoride materials demonstrate that fluoride mirrors reach highest reflectivity values down to 140 nm, and oxide coatings possess a satisfactory resistance against the high energetic background irradiation. However, pure oxide multilayer stacks exhibit significant absorption below 190 nm, and pure fluoride stacks suffer from strong degradation effects under synchrotron radiation. Possible solutions could be based on hybrid systems, combining fluoride stacks with oxide protection layers to provide high reflectivity and a robust behaviour under synchrotron radiation load.

INTRODUCTION

Dielectric mirror coatings for the vacuum ultraviolet (VUV , 120 – 195 nm) spectral range are deposited with physical vapour deposition methods from oxide and fluoride compounds. Their optical properties in respect to reflectivity, losses and stability are acceptable for applications in metrology systems, material processing and lithography applications. [4] Mirror coatings for the Free Electron Laser (FEL) were produced from oxide compounds which allowed a FEL lasing at the shortest wavelength of 189,9 nm at Elettra. [2,3] However, the mirror coating deposition for FEL lasing in the spectral range between 150 and 190 nm has to overcome severe obstacles. In this contribution the mirror development for the FEL at Elettra is summarised from the viewpoint of optical coating production. The work was performed in the framework of the European research project "Development of the European Free-Electron Laser at ELETTRA as a VUV Research Facility" (EUFELE).

PROBLEM

Mirrors for the Elettra FEL running in the VUV range below 190 nm should be provided. The laser cavity is embedded in the Elettra storage ring. Enclosed in the cavity a wiggler accelerates the electron, which generates finally photons for the FEL (Fig.1). The lasing wavelength is determined by the electron energy and the wiggler parameters (period and gap). The front mirror suffers the load of spontaneous synchrotron radiation that, besides the laser wavelength, contains also photons with energy up to the MeV range. Therefore the front mirror must be able to reflect the fundamental wavelength and to tolerate these high energy background photons.

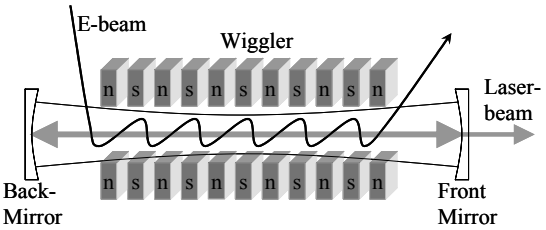

Fig. 1 : Configuration of a free electron laser resonator.

Laser action can be reached only if the amplification exceeds the optical losses, which in the case of FEL cavity are determined by the reflectivity of the two mirrors. While in the visible region losses due to absorption and scattering in the coating can be kept very low and are practically negligible, in the VUV range they have to be carefully considered and minimized. The tolerable minimum reflectivity for the SR-FEL at Elettra can be estimated to a value of 90 % for the front mirror, if the back mirror reflects above 95 %.

FEL systems are embedded in a vacuum environment (UHV). Residual molecules, especially hydrocarbon compounds, may lead to a surface contamination of optical components followed by a decrease of mirror reflectivity. In combination with VUV radiation and the chemical sensitivity of the coating material, this degradation effect can be amplified strongly.

DEVELOPMENT CONCEPT

Summarising the demands outlined before, suitable mirrors for the FEL laser system must provide a reflectivity above 95 %, they have to be able to withstand the high energetic background radiation, and they must be insensitive in respect to contamination effects. In the development phase suitable mirror materials were identified, different multilayer designs were developed, and complementary deposition methods were investigated. After coating deposition, the optical components were characterised in respect to their optical parameters. Then, the mirror coatings were irradiated at SR-FEL at Elettra. Finally, the components were inspected again and compared to the data gathered before

irradiation. Single layer coatings were investigated in a similar procedure. Results were reported elsewhere [4].

EXPERIMENTAL

Deposition of optical coatings

Coating properties are determined by material selection and the employed deposition technique. For mirror systems down to the wavelength 190 nm, pure oxide or fluoride systems can be used. However, the material selection for the VUV spectral range is restricted by the band gap of most common deposition materials. Among the oxide materials, only SiO_2 with its low refractive index exhibits a negligible absorption down to 160 nm. Al_2O_3 as the potential high index material can be employed down to 190 nm. For shorter wavelengths only fluoride compounds are applicable. In this study SiO_2 and Al_2O_3 as oxide materials and MgF_2 as low refractive index material in conjunction with LaF_3 as high refractive index compound from the fluoride class were investigated.

Deposition techniques strongly influence the physical properties of the thin film. The aggregation of thin films depends strongly on the kinetic energy of the particles impinging on the substrate surface or an additional ion assistance. In order to provide a broad spectrum of film properties, deposition techniques with low kinetic energy of the aggregating particles and with high kinetic energy of the aggregating particles were employed: Thermal evaporation methods (E-Beam and boat evaporation), ion assisted deposition (IAD), plasma ion assisted deposition (PIAD) and ion beam sputter deposition (IBS).

Mirror designs were developed for the central wavelength 180 nm with maximum reflectivity as main target parameter. (See table 1) A standard fluoride quarterwave stack was used as reference system. This system was deposited by thermal evaporation, ion assisted deposition (IAD) and ion beam sputtering (IBS) deposition for comparison purposes. From the single layer investigations it was concluded that LaF_3 exhibits the strongest degradation in the FEL environment. Thus, a so called bi-stack system, with reduced LaF_3 content was deposited as a pure fluoride system also. Protected mirrors were designed using a SiO_2 top layer on a fluoride stack. For the SiO_2 protection layer E-Beam films and IBS films were compared. In addition, protection systems using a combination of Al_2O_3 and SiO_2 were deposited. Besides the fluoride stacks, a pure bi-stack oxide system, which was designed for the central wavelengths 187 nm, was deposited by IBS. For this mirror the Al_2O_3 layer thickness was minimised to reduce the effect of absorption.

All coatings were deposited on CaF_2 substrates.

Characterisation

Optical characterisation was performed before and after the irradiation experiment. VUV, VIS, and IR optical spectra were recorded for all samples. A VUV-spectrometer developed at the Laser Zentrum Hannover has been employed for the measurement of the spectral behaviour in the VUV-range [5]. Spectra in the uv-visible range and the MIR range were measured employing commercial spectrophotometers (λ900 and F1600 [Perkin Elmer]). Also, spatially resolving techniques were adapted and applied [6] for all spectrophotometric methods. Microscopic surface inspection was performed for the untreated substrates as well as for the irradiated samples. The samples were tested in irradiation experiments at SR-FEL at Elettra.

Table 1 : Overview of the deposited optical coatings.

Multilayer model coatings HR@180 nm	**Multilayer design**	**Employed deposition technique**			
Oxide Compounds		Boat	IAD	PIAD	IBS
Al_2O_3 / SiO_2 HR@187 nm	$(0.65\ H\ 1.35\ L)^{20}\ 0.65\ H$				**x**
Fluoride Compounds					
MgF_2 / LaF_3 HR@180 nm	$(H\ L)^{20}\ H$	**x**	**x**		**x**
MgF_2 / LaF_3 Bi-Stack HR@180 nm	$(0.7\ H\ 1.3\ L)^{20}\ 0.7\ H$	**x**			
Hybrid mirrors: Oxide and Fluoride					
MgF_2 [L1]/ LaF_3 [H2] SiO_2 [L2-E-Beam]	$(H1\ L1)^{20}\ H1$ + 6 L2 (SiO_2 Protection)	**x**			
MgF_2 [L1]/ LaF_3 [H1] Al_2O_3 [H2-IBS] / SIO_2 [L2-IBS]	$(H1\ L1)^{20}$ + H2 L2 H2 (Oxide Protection)	**x**			**x**
MgF_2 [L1]/ LaF_3 [H1] SIO_2 [L2-E-Beam] / SIO_2 [L3-IBS]	$(H1\ L1)^{20}\ H1$ + 1 L2 + 5 L3 (SiO_2 Protection)	**x**			**x**

Synchrotron and FEL Radiation Characteristics

In the free electron laser mode, Elettra runs in 4-bunch filling mode at relatively low energies (0.75-1.5 GeV), however, these specific FEL conditions are restricted to a few shifts per year. The number of tests would be insignificant. To increase the number of irradiation experiments, a configuration routinely adopted for user operation (multi-bunch, 2 GeV) was used as standard test condition. To reduce the high energetic background radiation, the synchrotron radiation load was restricted to bending magnet contributions. For the evaluation of the experimental results it has to be considered, that the irradiation stress under standard conditions is more severe than in the FEL mode.

RESULTS

Pure Oxide Coatings

Measurements on bi-stacks of the material pair Al_2O_3 and SiO_2 show that, even with an extreme thin Al_2O_3 layer thickness, the absorption of aluminium oxides is dominating the mirror performance. An adequate reflectivity can not be reached below 190 nm due to the absorption of Al_2O_3. Figure 3 illustrates this with the reflectivity spectra of three different coating runs targeted to three different central wavelengths. The reflectivity of the produced HR@187 nm was below 90 % at 180 nm.

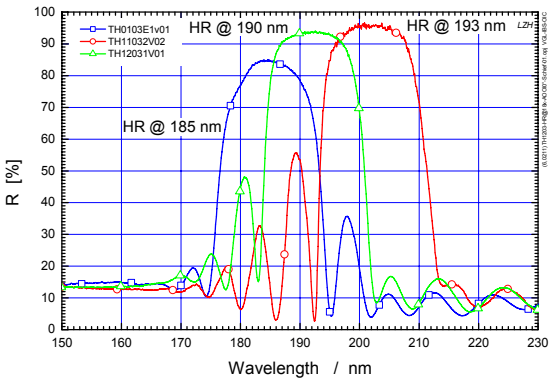

Fig. 2: Reflectivity of oxide Al_2O_3/SiO_2 deposited as bi-stack system [(0.65 H 1.35 L)20 0.65 H] for three different central wavelengths.

Pure Fluoride Coatings

Mirror system for the central wavelength 180 nm were deposited with different techniques. Multilayers produced by thermal evaporation and IAD deposition reach reflectivity values above 90 %. First results for IBS fluoride mirrors show, that a further process optimisation is essential. The results of the irradiation experiments on the conventional and the IAD mirror at Elettra display a strong degradation of reflectivity. Figure 3 and 4 present the behaviour for a bi-stack fluoride mirror deposited by thermal evaporation and for a standard mirror design produced by IAD, respectively. Both systems show strongest reflectivity degradation after irradiation. From additional measurements in the IR an intense hydro carbon contamination on the optics surface can be stated. The reflectance can be restored to approximately 90 % of the initial value of reflectivity with UV cleaning methods. A surface damage can not be observed by optical microscopy.

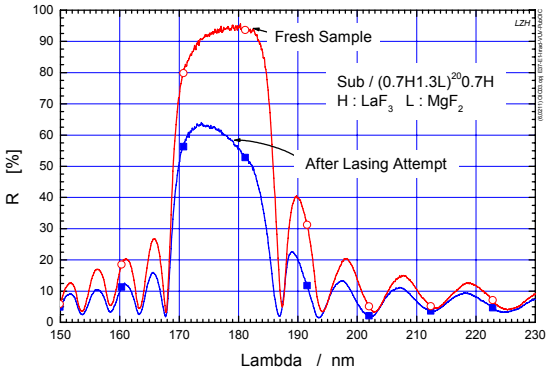

Fig. 3 : Reflectivity of fluoride bi-stack deposited by thermal evaporation before and after irradiation at SR-Elettra.

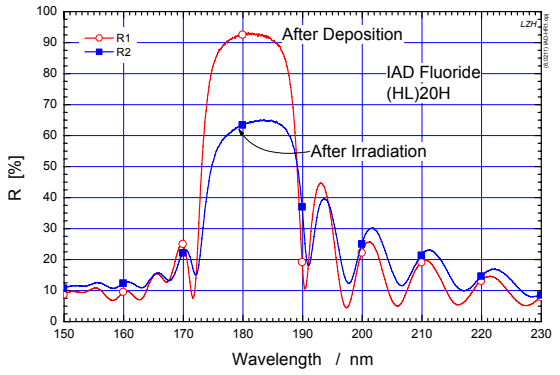

Fig. 4 : Reflectivity of a fluoride mirror deposited by ion assisted deposition (IAD) before and after irradiation at SR-Elettra.

Fluoride Coatings with Oxide Protection

Fluoride stacks, protected with SiO_2 single layers, could be produced with high reflectivity at 180 nm. However, the process concept has to be optimised to combine the fluoride and SiO_2 deposition. In particular, SiO_2 has to be deposited in a reactive O_2 atmosphere which may lead to an unwanted oxidation of the fluoride material. In addition, high energetic ions could create defects in the fluoride stack during the IBS process. After process optimisation, protected stacks with reflectivities above 95 % can now be realised.

The characterisation after SR-FEL irradiation reveals significant differences between the stacks protected with E-Beam SiO_2 and IBS SiO_2. Similar to the pure fluoride systems, the stack with E-Beam SiO_2 protection layer is

strongly degrading in respect to its reflectivity (Fig. 5). In contrast, the stack with the IBS SiO_2 protection layer shows only a small decrease of reflectivity of about 2 - 4 %. (Fig. 6). With a mirror of this type stored emission in the FEL cavity was observed.

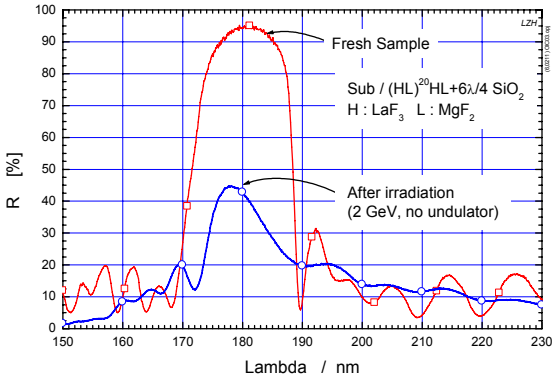

Fig. 5 : Reflectivity of a fluoride stack with E-Beam SiO_2 protection layer before and after irradiation at SR-Elettra.

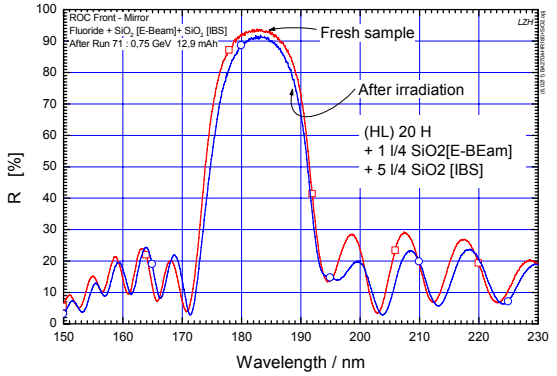

Fig. 6 : Reflectivity of a fluoride stack with IBS SiO_2 protection layer before and after irradiation at SR-Elettra.

Fluoride stacks protected with combinations of SiO_2 and Al_2O_3 did not achieve reflectivity values above 90 % at 180 nm. Further optimisation for this approach was terminated.

CONCLUSIONS

In the framework of this study optical materials for the production of VUV coatings were identified, adapted coating designs were developed and tested. Furthermore, the characteristics of selected deposition technique were studied. In the present stage, the protection of high reflecting fluoride stacks is considered as the major problem. Fluoride mirrors exhibit a high sensitivity for a hydro carbon contamination which causes a subsequent degradation of reflectivity in the FEL system. A clear improvement of robustness using ion assisted deposition technique, which produce film system with higher packing density, could not be observed until now. An adequate protection layer combination can be realised by an appropriate deposition of a dense SiO_2 layer on a fluoride stack. The structure of the sputtered SiO_2 layer seems to be much more effective for the protection of the fluoride surface, than the porous E-Beam SiO_2 layer. With optimised deposition cycle a reflectivity close to 99 % has been recently reached (Fig. 7). The FEL lasing test has to be performed.

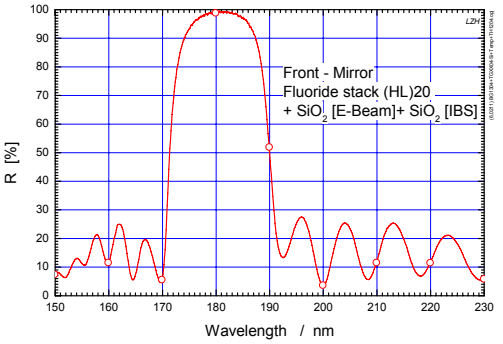

Fig. 7 : Reflectivity of an optimised fluoride stack with IBS SiO_2 protection layer after production.

The authors gratefully acknowledge the support of the European Commission (EUFELE-Project). "Development of the European Free-Electron Laser at ELETTRA as a VUV Research Facility", a Project funded by the European Commission under FP5 Contract No. HPRI-CT-2001-50025.

REFERENCES

[1] J. Ullmann et al "Substrates and optical coatings for 157 nm applications", Conference Inorganic Optical Materials II. Proceedings of SPIE Vol. 4102, 2000

[2] A. Gatto et al, "High-performance deep-ultraviolet optics for free electron lasers", Applied Optics, 41 (16), 3236-3241, (2002).

[3] M. Marsi, et al, "Operation and Performance of free electron laser oscillator down to 190 nm ", Appl. Phys. Lett. 80, 2852 (2002)

[4] St. Günster et al, "Radiation resistance of single and multilayer coatings against synchrotron radiation", Proc. SPIE 5250 , 146-157, (2004)

[5] P. Kadkhoda et al, " Investigations of transmission and reflectance in the DUV/VUV spectral range" , Proc. SPIE 4099, 311-318,(2001).

[6] H. Blaschke et al, "DUV/VUV spectrophotometry for high precision spectral characterization" , Boulder Damage Symposium XXXIV, (BD02) Proc. SPIE 4932, 536 , (2003)

COHERENT HARMONIC GENERATION USING THE ELETTRA STORAGE-RING OPTICAL KLYSTRON

G. De Ninno*, M. B. Danailov, B. Diviacco, M. Ferianis, M. Trovò, Sincrotrone Trieste, Italy
L. Giannessi, ENEA, Frascati, Italy

Abstract

Coherent harmonic generation using single-pass devices or oscillators is based on the frequency up-conversion of a high-power laser focused into the first undulator of an optical klystron. The seeding signal, which is necessary to produce the modulation of the electron density and hence to induce the coherent emission, may be provided by an external laser or, in the case of storage-ring oscillators, by the FEL itself. The latter possibility has been recently explored at Elettra allowing to generate radiation at 220 nm, i.e. the third harmonic of an intra-cavity signal at 660 nm. As for seeding using an external laser, a detailed campaign of simulations shows that the Elettra storage-ring optical klystron is also well suited for the realization of this configuration. These results make the Elettra FEL an attractive test-facility in view of coherent harmonic generation experiments planned on dedicated next-generation devices.

INTRODUCTION

The standard process leading to the generation of coherent harmonics (CHG) using single-pass devices or storage rings is based on the up-frequency conversion of a high-power seeding signal focused into an undulator, which can be the first one of an optical klystron, and synchronized with an upcoming electron bunch [1, 3]. In the optical klystron configuration (see Fig. 1), the seed-electron beam interaction leads to a modulation of the electrons energy inside the first undulator (Modulator). When the beam crosses the dispersive section, such a modulation is converted into a spatial partition of the electrons in micro-bunches separated by the seed wavelength. Therefore, a Fourier analysis of the bunch density shows, at the end of the dispersive section, a series of lines at the laser frequency and its harmonics. Finally, in the second undulator (Radiator), the light emission at the harmonics of the seed wavelength is enhanced by this coherent bunching and becomes proportional to the square of the number of electrons.

When installed on storage rings, an optical klystron generally serves as interaction region for oscillator free-electron lasers (FELs). In this case, electrons amplify the light stored in the optical cavity during successive interactions, till the achievement of the laser effect. The obtained intra-cavity signal, which is naturally synchronized at each pass with the electron bunch(es) at each pass, may provide the seeding power necessary to initiate CHG [4]. As an alternative, CHG can be obtained by removing the cavity mirrors and by coupling the electron bunch(es) with an external laser [5, 6]. It is worth stressing that in both cases a major difference with respect to the single-pass configuration is due to the fact the electrons are re-circulated and, therefore, they can keep track of previous interactions.

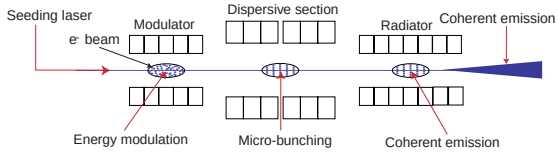

Figure 1: Schematic layout of CHG using an optical klystron.

FEL-induced CHG has been recently realized at Elettra, allowing to generate the third harmonic of an intra-cavity signal at 660 nm. In the first part of this paper, we report about the set of measurements that have been performed with the aim of characterizing the energy as well as the spectral and temporal features of the harmonic radiation. As for seeding using an external laser, a detailed campaign of simulations, partially reported in the second part of the paper, shows that the Elettra optical klystron is also well suited for the realization of this configuration.

THEORETICAL FRAMEWORK

The light-electron beam interaction inside each undulator can be studied by solving the coupled pendulum-maxwell equations (see, e.g., [7]):

$$\begin{cases} \dfrac{\mathrm{d}\zeta_j}{\mathrm{d}\tau} = \nu_j \\ \dfrac{\mathrm{d}\nu_j}{\mathrm{d}\tau} = |a_n| \cos\left(\zeta_j + \phi_n\right) \\ \dfrac{\mathrm{d}a_n}{\mathrm{d}\tau} = -2\pi g_{0,n} \left\langle \exp\left(-in\zeta\right) \right\rangle . \end{cases} \tag{1}$$

Here ζ_j is the phase of the jth electron in the combined "ponderomotive" (radiation + undulator) field; ν_j, the relative energy of the jth with respect to the resonance condition, is the variable conjugated to ζ_j; τ is the distance along the undulator (normalized to the undulator length); a_n and ϕ_n are, respectively, the nth harmonic component and the phase of the complex optical field; $g_{0,n}$ is the small signal gain and $\langle \exp\left(-in\zeta\right) \rangle$ stands for the bunching coefficient relative to the nth harmonic. The extracted power at a given

* giovanni.deninno@elettra.trieste.it

harmonic is maximized optimizing its bunching coefficient. This can be done by means of a proper adjustment of both the electron beam energy and dispersive section strength. When the case of CHG on a storage ring is considered, the system (1) has to be "closed" by two further equations. The first accounts for the laser evolution inside the optical cavity [8]:

$$(a_n)_{new} = (a_n)_{old}\sqrt{1-T_n} + (a_n)_0 \qquad (2)$$

where $(a_n)_{old}$ is optical field at the exit of the Radiator and $(a_n)_{new}$ its value at the beginning of the Modulator after a double reflection on the optical cavity mirrors. In practice, $(a_n)_{new}$ provides, turn after turn, the initial seeding value for Eqs. (1); T_n is the mirrors transmission (depending on the harmonic number) and $(a_n)_0$ stands for the spontaneous emission of the optical klystron.

The second equation, which is necessary for closing the loop, takes into account the damping of the electron-beam energy spread, σ_ν, when, along the ring, electrons do not interact with the seed [8]:

$$(\sigma_\nu)^2_{new} = (\sigma_\nu)^2_{old} - \frac{2T}{\tau_s}\left[(\sigma_\nu)^2_{old} - (\sigma_\nu)^2_0\right]. \qquad (3)$$

Here $(\sigma_\nu)_{old}$ is energy spread at the exit of the Radiator and $(\sigma_\nu)_{new}$ its value after one turn of the ring; $(\sigma_\nu)_{new}$ provides, turn by turn, the initial r.m.s. value of the v_j distribution (assumed, in first approximation, to be a Gaussian) in Eqs. (1). T and τ_s stand, respectively, for the bounching period of the laser in the optical cavity and the synchrotron damping time; $(\sigma_\nu)_0$ is the initial (laser-off) value of the energy spread. Note that Eq. (2) is no longer necessary when the optical cavity is removed and use is made of an external seed.

CHG INDUCED BY THE FEL INTRA-CAVITY SIGNAL

Let's start considering the case of CHG self-induced by the FEL light stored in the optical cavity.

Harmonic macro-pulse characterization

As demonstrated theoretically by Dattoli et al. [9] and experimentally on the Duke storage-ring FEL [4], the only way to generate enough intra-cavity power so to get a detectable harmonic signal is to run the FEL in giant-pulse regime. This can be done by means of different techniques. The one employed at Elettra [10] for Q-switching is based on a periodic variation of the radio-frequency so to induce a modulation of the temporal overlapping between the electron beam and the light stored in the optical cavity. When the system is completely detuned, the laser is switched off. If such a condition is kept for a time long enough (order of few synchrotron damping times), the electron beam cools down and the gain recovers its initial (laser-off) maximum value. The minimum duration of such a period of time fixes the maximum repetition rate at which the system can be operated. When the gain has recovered its maximum value, the perfect light-electron beam synchronism is re-established and maintained for the time (order of few hundreds of microseconds) necessary for a single giant pulse to be generated. Then, the system is detuned again and the entire cycle repeated. The obtained signal, which is found to be relatively stable and reproducible, is characterized by an increase of the peak intensity of about a factor 50 with respect to standard "cw" operation mode. In Table 1 are listed the experimental conditions for which results reported in the following have been obtained.

Table 1: Experimental conditions for CHG using the Elettra FEL as seed. The Elettra storage-ring optical klystron is made up of two identical undulators having 18 periods, 10 cm long. The mirrors of the optical cavity have total losses of about 0.2% at the fundamental wavelength.

Beam energy	900 MeV
Beam current (4 bunches)	25 mA (max)
Fundamental wavelength	660 nm
Intra-cavity peak power (fund)	$\simeq$ 100 MW
Third harmonic wavelength	220 nm
Repetition rate	2-10 Hz

The correlated temporal evolution of the fundamental and harmonic macro-pulses is shown in Fig. 2.

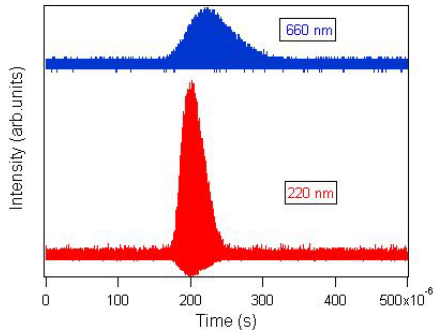

Figure 2: Correlated evolution of the fundamental (upper trace) and harmonic (lower trace) macro-pulses.

The harmonic pulse is characterized by a shorter rise-time than the fundamental one (about a factor 3 difference); moreover, it reaches the saturation and decays faster. Measuring the ratio between the maximum intensity of the harmonic signal and its background (corresponding to the spontaneous emission of the optical klystron at 220 nm) allows one to give an estimation of the energy carried by the most intense harmonic micro-pulse, i.e. about 0.2 nJ for the case of Fig. 2. The intensity of the fundamental and harmonic signals has been studied also as a function of the dispersive section strength. The obtained result, shown in Fig. 3, is a clear signature of the nonlinearity of the

process. Indeed, the dispersive section strength at which the harmonic intensity becomes maximum does not correspond to that maximizing the fundamental. The decrease of the harmonic signal above a given threshold is to be attributed to the concurrent decrease of the fundamental and not to an induced over-bunching (which never occurs in this regime).

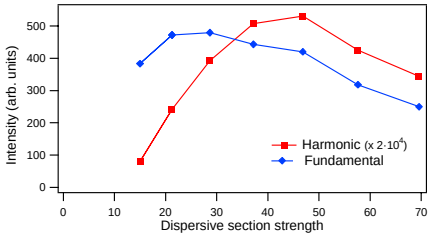

Figure 3: Evolution of the fundamental and harmonic intensities as a function of the dispersive section strength.

Temporal and spectral characterization of the harmonic micro-pulse

Measurements performed using a double-sweep streak camera (see Fig. 4) show that the duration of the harmonic micro-pulse is shorter than the fundamental one (about 6 ps r.m.s.). The measured value, i.e. 3 ps r.m.s, is at the limit of the instrument resolution [11]).

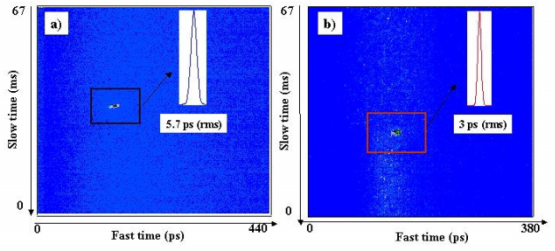

Figure 4: Streak camera images of the fundamental a) and harmonic b) macro-pulses. The insets represent the respective micro-pulse profiles.

As for the spectral domain, the pulse width has been found to be of the same order of the fundamental one (i.e. $\Delta\lambda/\lambda \simeq 10^{-3}$ and about a factor 20 narrower than the spontaneous emission of the optical klystron (see Fig. 5).

Comparison with theory

Eqs. (2) and (3) have been implemented into the numerical code PERSEO [12]. Simulations give results in good agreement with experiments. In particular, as reported in Table 2, the theoretical value of the micro-pulse peak power at the fundamental wavelength is close to the measured one. As for the harmonic, a good agreement is obtained assuming that the micro-pulse duration is 3 ps r.m.s, that is what has been measured using the streak camera (see Fig. 4).

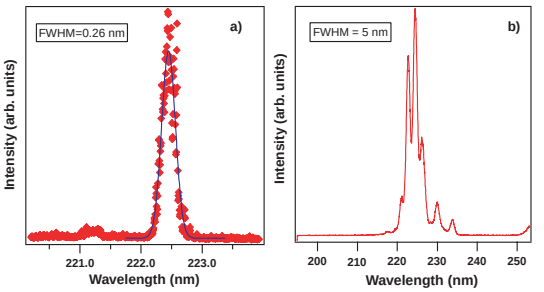

Figure 5: Specrum profiles at 220 nm of the coherent signal (Fig. a) and of the spontaneous emission of the optical klystron (Fig. b).

Table 2: Experimental and simulated micro-pulse peak power relative to the fundamental and harmonic signals.

	Fundamental (W)	**Harmonic (W)**
Experimental	$8.6 \cdot 10^5$	17.1
Simulated	$6.7 \cdot 10^5$	16.4

It is worth noting that the obtained value for the harmonic micro-pulse peak power (less than 20 W) is much weaker than the one reported by the Duke FEL group (i.e. tens of kW [4]).

CHG INDUCED BY AN EXTERNAL SEED

In the following are summarized the results of a campaign of time-dependent simulations performed, again using PERSEO, in order to investigate the possibility of CHG using the Elettra storage-ring optical klystron in combination with an external seed.

The seeding system that has been considered is a Ti:Sa delivering, after third harmonic generation, an optical pulse at 260 nm characterized by a duration of 100 fs and by a peak power of 2.5 GW. Figs. 6a and 6b show the seeding effect on the electron-beam phase space at the end of the modulator and of the dispersive section, respectively. The correspondent bunching coefficients for the third, fifth and seventh harmonics are reported in the Figure's caption. After the end of the dispersive section, the micro-bunched electron beam enters the radiator, which is tuned at the third harmonic of the seed wavelength. Fig. 7 shows the evolution of the harmonic signal along the undulator. The expected output power at 90 nm is about 1 MW. The power is reduced, respectively, by a factor 10 and a factor 100 (see Table 3) when the Radiator is tuned at the fifth ($\simeq$ 50 nm) and seventh ($\simeq$ 40 nm) harmonics of the seeding laser wavelength. Time-dependent simulations have been performed in order to get the output micro-pulse and spectrum profiles (see Fig. 8). As expected, the harmonic

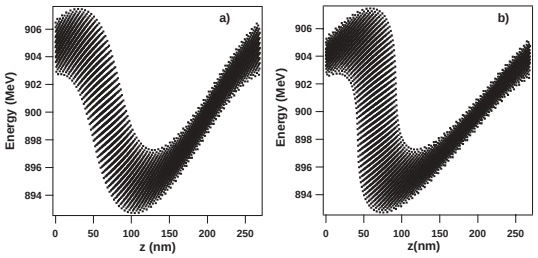

Figure 6: Effect of the seeding laser on the electron-beam phase space at the end of the Modulator, Fig. a), and at the end of the dispersive section, Fig. b). The bunching coefficients for the third, fifth and seventh harmonics (b_3, b_5, b_7) are in the two cases (0.15, 0.04, 0.01) and (0.34, 0.17, 0.07), respectively.

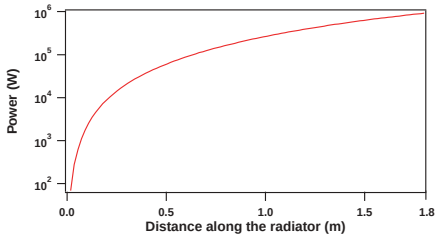

Figure 7: Evolution of the harmonic signal along the Modulator tuned at the third harmonic (about 90 nm) of the Ti:Sa seeding signal.

pulse duration is slightly shorter than the one of the seeding pulse (86 fs) and the spectrum profile is very clean ($\Delta\lambda/\lambda \simeq 1.2 \cdot 10^{-3}$).

CONCLUSIONS AND PERSPECTIVES

We have demonstrated the possibility of CHG using the Elettra storage-ring FEL as seeding signal. The temporal dynamics of the radiation at 220 nm has been studied and the harmonic micro-pulse characterized in terms of energy, duration and spectral width. Experiments are well reproduced by a simple 1D model developed exploiting the numerical code PERSEO. As a next step, we intend to extend the spectral range to the vacuum ultra-violet. As for CHG using an external Ti:Sa system, simulations performed using PERSEO in time-dependent mode (and partially benchmarked using GENESIS [13]) give the very promising results reported in Table 3.

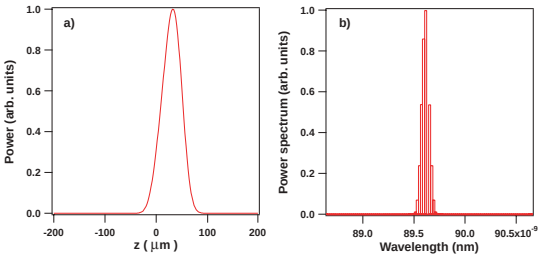

Figure 8: Simulated output micro-pulse and spectrum profiles (Figs a) and b), respectively).

Table 3: Expected performance of CHG using the Elettra storage-ring optical klystron in combination with an external Ti:Sa laser system delivering an optical pulse at 260 nm, characterized by a duration of 100 fs and a peak power of 2.5 GW.

Wavelength (nm)	90, 50, 40
Peak power (W)	10^6, 10^5, 10^4
Pulse duration (fs)	$\simeq 90$ fs
Repetition rate (Hz)	10-100
Spectral width	Same as seed pulse

Such a results indicate the Elettra storage-ring optical klystron as an attractive, ready-to-use, test facility in view of CHG experiments planned on dedicated next-generation devices.

ACKNOWLEDGMENTS

We are thankful to the Elettra accelerator group for technical support. We also acknowledge useful discussions with G. Dattoli that helped us in the development of the theoretical model. Thanks to M. Coreno, M.E. Couprie, G. Lambert and E. Longhi for participating to our shifts. This work has been partially supported by EUFELE, a Project funded by the European Commission under FP5 Contract No. HPRI-CT-2001-50025.

REFERENCES

[1] L. H. Yu, *Phys. Rev. A* **44**, 51178 (1991).

[2] L. H. Yu et al., *Phys. Rev. Lett.* **91**, 074801 (2003).

[3] B. Girard et al., *Phys. Rev. Lett.* **53**, 2405 (1984).

[4] V. Litvinenko, *Nucl. Instr. and Meth. A* **507**, 265 (2003).

[5] P.L. Csonka, *Part. Accele.* **8**, 225 (1978).

[6] R. Coisson and F. De Martini, *Phys. Quantum Electronics* **9**, 939 (1982).

[7] G. Dattoli et al., *Free Electron Laser theory and related topics* (World Scientific, Singapore, 1993).

[8] M. Billardon et al. *Phys. Rev. Lett.* **69**, 2368 (1992).

[9] G. Dattoli et al. *Journ. of Appl. Phys.* **83**, 5034 (1998).

[10] G. De Ninno et al., *Nucl. Instr. and Meth. A* **528**, 278 (2004).

[11] M. Ferianis and M. Danailov, *AIP Conference Proceedings/* **648** (2002), Gary A. Smith and Thomas Russo editors, BNL, Upton, NY, USA.

[12] L. Giannessi, *Perseo FEL-cad library*, http://www.afs.enea.it/gianness/perseo.

[13] S. Reiche, Nucl. Instr. and Meth. A **429**, 242 (1999).

SHORT RAYLEIGH LENGTH FREE ELECTRON LASERS

W. B. Colson, J. Blau, R. L. Armstead, and P. P. Crooker
Physics Department, Naval Postgraduate School
Monterey, CA 93943

Abstract

Conventional free electron laser (FEL) oscillators minimize the optical mode volume around the electron beam in the undulator by making the resonator Rayleigh length about one third of the undulator length. This maximizes gain and beam-mode coupling. In compact configurations of high-power infrared FELs or moderate power UV FELs, the resulting optical intensity can damage the resonator mirrors. To increase the spot size and thereby reduce the optical intensity at the mirrors below the damage threshold, a shorter Rayleigh length can be used, but the FEL interaction is significantly altered. A new FEL interaction is described and analyzed with a Rayleigh length that is only one tenth of the undulator length, or less.

INTRODUCTION

For several decades, it has been suggested that a free electron laser (FEL) oscillator can optimize the electron-optical coupling by minimizing the optical mode volume around the smaller relativistic electron beam. The origin of the idea was stated in Madey's initial paper inventing the FEL concept [1], and has lead to the common practice of designing the FEL's optical resonator so that its Rayleigh length Z_0 is about half of the undulator length L. That assumption is studied in this paper and it is found that there are several possible advantages to much shorter Rayleigh lengths including increased gain.

In Madey's original paper, the FEL gain was estimated using a "Filling factor" F in order to describe how the smaller electron beam exchanged energy with the slightly larger optical mode. The filling factor is defined as the ratio of the electron beam area to the optical mode area with both assumed to be constant along the interaction length L. FEL gain G is then estimated as proportional to the filling factor, and the usual practice was to minimize the optical mode volume around the smaller electron beam. Since that time, it has been common practice to design an FEL oscillator with minimum optical mode area along the undulator length L. A further refinement is to average the filling factor over L so that $G \propto (z_0 + 1/(12z_0))^{-1}$. The normalized Rayleigh length is defined as $z_0 = Z_0/L$ and the actual Rayleigh length is $Z_0 = \pi w_0^2/\lambda$, λ is the optical wavelength, and w_0 is the optical mode waist radius. The optimum weak field gain is then found by minimizing the mode volume over the undulator length L for $z_0 = 12^{-1/2} \approx 0.29$ [2]. Common practice uses values $z_0 \approx 0.3 \rightarrow 0.5$.

The short Rayleigh length FEL design is an alternative that makes use of a resonator cavity with a short Rayleigh length resulting in a larger laser spot at the mirrors [3]. Scientific, industrial, and military applications of FEL oscillators benefit from a more compact design. Laboratory space is always valuable. When the application also requires moderate to high power at infrared or shorter optical wavelengths, the conventional FEL oscillator design leads to high intensity at the mirrors and possible mirror damage.

A couple of examples illustrate how this common practice ($z_0 \approx 0.3 \rightarrow 0.5$) can limit an FEL performance. Take the mirror separation of the resonator to be $S = 12$ m with 10% output coupling. Typical mirrors can be damaged by a high laser intensity $\sim 10\,\mathrm{kW/cm^2}$ in the infrared and $\sim 1\,\mathrm{kW/cm^2}$ in the UV. Taking the electron beam and optical mode to be about 1mm in diameter in the undulator, the commonly used design criteria would lead to a limitation in output power of 150 W in the infrared and only 3 W in the UV. The UV FEL is a particular problem since the longer Rayleigh length Z_0 associated with the shorter UV wavelength λ increases mirror intensity further by decreasing the mirror spot size. Both FELs would benefit from a shorter Rayleigh length resonator in order to reduce the intensity on the mirrors and keep the system compact. The conventional estimate for gain would lead to $G \propto z_0$ for small Rayleigh length $z_0 \ll 1$. The research presented here shows that this is incorrect, and that there is little or no loss in gain for small $z_0 \ll 1$. The design option is illustrated in Figure 1 below.

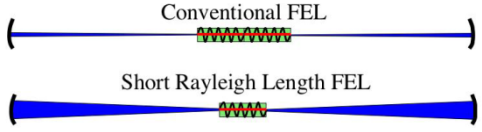

Figure 1: Schematic comparison of the conventional and short Rayleigh length FEL designs.

The FEL interaction is altered in the short Rayleigh length FEL because the optical field amplitude and phase change significantly along the undulator [4]. The field amplitude $a(\tau)$ and phase $\phi(\tau)$ at the mode center $r = 0$ are shown in Figure 2 and are given by

$$a(\tau) = a_0(1 + (\tau - \tau_w)^2/z_0^2)^{-1/2} \quad (1)$$

$$\phi(\tau) = -\arctan((\tau - \tau_w)/z_0) \quad (2)$$

where $\tau = ct/L$ is the dimensionless time of interaction along the undulator length L, c is the speed of light, a_0 is

the dimensionless optical field amplitude at the mode focus, and τ_w is the location of the mode focus along the undulator. When z_0 is small, the field amplitude and phase change rapidly along the undulator. While the rapidly changing field would appear to be detrimental to the bunching process, it may improve coupling by focusing laser light to a small waist to intensify the field strength.

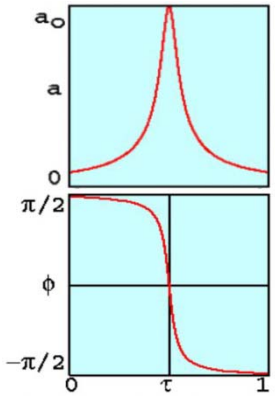

Figure 2: Optical field amplitude $a(\tau)$ and phase $\phi(\tau)$ as functions of dimensionless time $\tau = ct/L$.

SIMULATION RESULTS

As an example consider an FEL having an undulator of $N = 22$ periods with total length $L = 52$ cm, rms undulator parameter $K = 1$, and period $\lambda_0 = 2.36$ cm. The FEL with a shorter Rayleigh length requires a shorter undulator length so that the expanding mode does not scrape the undulator magnets. In this case the undulator gap is $g = 1$ cm and there is no significant scraping of the focused electron beam or optical mode. At the end of the undulator the optical mode radius is $w_u \approx (\lambda L/4\pi z_0)^{1/2} \approx 0.2 z_0^{-1/2}$mm in this case. In order to keep $w_u < 0.2g = 2$ mm to avoid even the slightest scraping, we keep $z_0 > 0.01$. An electron micropulse of $I = 400$ A peak current and energy of 80 MeV is focused to a small waist radius of $r_b = 0.06$ mm. The FEL resonance condition defines the optical wavelength as $\lambda \approx \lambda_0(1 + K^2)/2\gamma^2 = 1\,\mu$m in a resonator with mirror separation $S = 12$ m and 25% output coupling. FEL gain is evaluated from simulations following the electron beam dynamics and optical mode self-consistently [2].

Figure 3 is the result for this FEL, varying the dimensionless Rayleigh length over the range $z_0 = 0.1 \rightarrow 1$. The most dramatic result is that gain does not decrease like $G \propto z_0$ for small z_0, but remains roughly constant around $z_0 \approx 0.01$. This is due to optical mode distortion that is allowed to occur self-consistently in the simulations, but not in the simple estimate using the filling factor F. The single pass gain is large for this example (nearly 400%), but the trend shown here has been confirmed for much smaller gain as well. To the right are examples of the optical mode shape plotted in (x, y) as they are slightly distorted from their Gaussian fundamental shape. The distortion is not large, but sufficient to significantly increase the gain when the Rayleigh length is small. In these cases, the electron beam has been focused to a waist size of $r_b \approx 0.06$ mm so that it remains inside the focused optical mode waist. The normalized emittance required for this case is $\epsilon_n = 3$ mm-mrad, but larger emittances have been explored finding the same trend: there is no significant decrease in gain at small Rayleigh length when mode distortion is allowed. Also, the location of the optical mode focus is found to be optimum for $\tau_w = 0.5$, in the middle of the undulator.

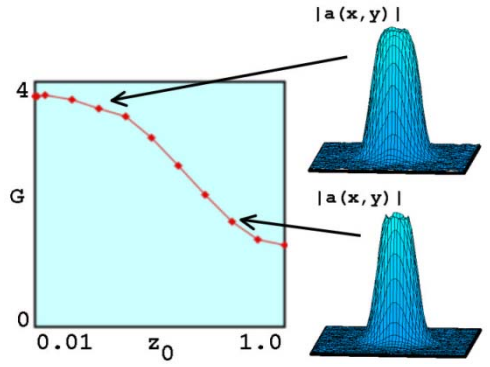

Figure 3: FEL gain as a function of Rayleigh length z_0.

If the electron beam focal radius r_b is made too large, some of the electron beam is outside of the optical mode waist, decreasing coupling and gain. If the electron beam focal radius is made too small, the larger angular spread resulting from fixed emittance ϵ_n results in some of the electron beam drifting outside of the optical mode at the ends of the undulator, so that again gain decreases. There is typically an optimum electron beam focal radius $r_b \sim 0.1$ mm for the short Rayleigh length designs examined.

The effects of mirror vibration and positioning are more critical in the short Rayleigh length design, but we find that they are still within normal design tolerances [5].

ACKNOWLEDGMENTS

The authors are grateful for the support from NAVSEA, ONR, and the JTO.

REFERENCES

[1] J. M. J. Madey, *J. Appl. Phys.*, 42, 1906 (1971).

[2] W. B. Colson, *Free Electron Laser Handbook*, North-Holland, 1990, Ch. 5, pp. 115-194.

[3] D. W. Small, R. K. Wong, W. B. Colson, R. L. Armstead, *Nucl. Instr. and Meth.* A393 (1997) 262.

[4] W. B. Colson, J. Blau, and R. L. Armstead, *Nucl. Instr. and Meth.* A507 (2003) 48.

[5] P. P. Crooker, T. Campbell, W. Ossenfort, S. Miller, J. Blau, and W. B. Colson, *Nucl. Instr. and Meth.* A507 (2003) 52.

ELECTRON-BEAM STABILIZATION FOR THE EUROPEAN STORAGE-RING FREE-ELECTRON LASER AT ELETTRA*

M. Trovò†, D. Bulfone, M. Danailov, G. De Ninno, B. Diviacco, V. Forchì, M. Lonza,
Sincrotrone Trieste, Trieste, Italy
L. Giannessi, ENEA, Frascati, Italy

Abstract

The temporal structure of the storage-ring free-electron laser at Elettra shows high sensitivity to electron-beam instabilities. In fact, even small beam perturbations may affect the FEL dynamics and periodically switch off the laser. In order to improve the FEL operation and performance, different and complementary feedback systems have been activated. This paper reports on their beneficial effect. Plans for future improvements are also briefly outlined.

INTRODUCTION

Instabilities of different nature may affect electron beams accumulated in a Storage Ring (SR) and degrade the performance of synchrotron light sources by leading to increased beam emittance, energy spread and transverse/longitudinal vibrations of the center of mass of the bunches. The origin of such instabilities can be traced back either to external perturbations (e.g. mains induced modulations, mechanical vibrations, etc.) or to the electromagnetic wake fields, which are generated by the interaction of the electron bunches with the surrounding vacuum chamber and other cavity-like structures. In general, such fields re-act on the bunches and perturb their motion.

Beam instabilities may affect the dynamics of a SR free-electron laser and, if strong enough, even prevent its onset. In this respect, beam perturbations which normally do not affect the performance of normal synchrotron radiation beamlines may instead have a strong effect on the FEL intensity. This is mainly due to the tight requirements on temporal synchronization and transverse overlap between electron bunches and light pulses stored in the optical cavity at each pass inside the interaction region [1].

We have observed that a longitudinal coupled-bunch instability (LCBI) of only few degrees in amplitude can spoil the laser synchronization and prevent it from starting. In order to damp LCBIs, a bunch-by-bunch digital feedback system [2] has been activated at Elettra during some FEL shifts.

A different effect is observed when a beam-orbit perturbation of only few microns in the FEL straight section imposes a temporal structure to the laser intensity, changing the natural behavior of the system. The use of a local orbit stabilization feedback (LOF) [3], recently installed in correspondence of the Elettra FEL section, has significantly reduced this low-frequency noise.

A further feedback system, complementary to the previous ones, has been developed in order to prevent the onset of a "naturally" pulsed FEL regime when the light-electron beam detuning is increased (e.g. by an external perturbation) above a given threshold.

In the following we summarize the results obtained so far using these different systems and we present a plan to develop a new feedback acting on the longitudinal bunch motion in the low frequency regime.

OPERATIVE FEEDBACKS

Without the use of any feedback system, the Elettra FEL is generally characterized by a macrotemporal structure showing a disturbed behavior and a high sensitivity to different kinds of electron beam instabilities. Figure 1 shows a measured FEL structure acquired with a photodiode together with its Fourier transform. The spectrum shows a strong 50 Hz component and harmonics.

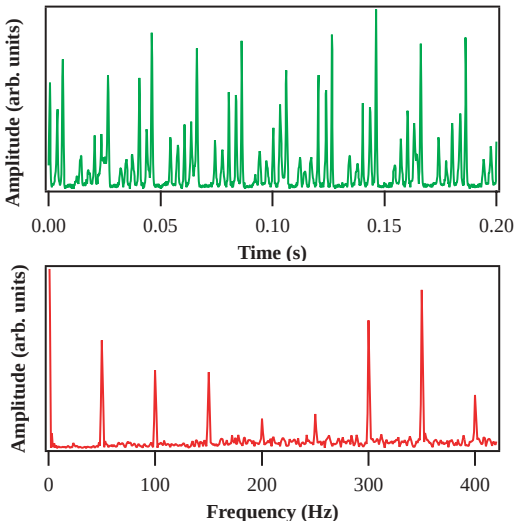

Figure 1: Typical temporal pulsed behavior of the FEL intensity (acquired with a photodiode) and its spectrum.

Since its first operation in February 2000 a lot of effort has been made in order to identify the major photon noise sources and to implement systems for their compensation.

* Partially funded by EC contract HPRI-CT-2001-50025
† mauro.trovo@elettra.trieste.it

Longitudinal Multi-Bunch Feedback

When there are many bunches in a storage ring and the electron-beam induced wake fields are strong and persistent enough to act back on successive ones, a coherent oscillation may grow up [4]. This oscillation can affect the bunch motion in the transverse plane and in the longitudinal direction. Both transverse and longitudinal instabilities are undesired for FEL operation, but the longitudinal one is the most dangerous for the laser onset.

During FEL operation, Elettra is run in 4-bunch filling mode at relatively low energies (0.75-1.5 GeV). This configuration is completely different from the one routinely adopted for user operation (96 % multi-bunch continuous filling, 2-2.4 GeV). In the 4-bunch mode, LCBIs can be damped by acting on the temperatures of the four radio-frequency cavities, finding a suitable higher-order mode combination [5]. However, the stability intervals are narrow and current dependent, so the operating temperatures have to be continuously adjusted following the natural current decay.

With the goal of improving the longitudinal beam stability and simplifying the operator task of keeping the beam stable, a longitudinal multi-bunch feedback has been recently activated. This feedback system acts on each individual bunch, which is considered an independent oscillator at the synchrotron frequency. A digital processing system is used to calculate the correction signal to be applied to the bunch through a dedicated kicker. Due to a limitation of the system bandwidth, the feedback is not effective in the low-frequency spectrum range.

This system has shown to be able to provide a perfect beam LCBI free, also without any specific adjustment of cavity temperatures. Moreover, its damping efficiency does not depend on the storage-ring filling pattern: we have already tested the case with eight bunches arranged in the ring in four pairs of two successive buckets and no LCBI was observed on the beam with the feedback on, whereas strong oscillations appeared without it.

This feature allows us to plan exotic fillings of the Elettra SR, e.g. four symmetric trains of bunches, which would increase the FEL average output power, being the latter proportional to the average beam current.

Local Orbit Feedback

SR-FEL theory predicts a pulsed time structure of the laser intensity on a millisecond temporal scale when the system is not close to synchronization, while a continuous wave (CW) mode of laser operation is expected around the perfect tuning condition. For Elettra, the CW region around the perfect synchronism is very narrow [7] and never experimentally observed. Due to that and to the 50 Hz (and harmonics) instability, the pulsed regime is the standard one for the Elettra SR-FEL. The natural frequency of the pulsed regime is given by the following relation [6]:

$$f_r = \frac{1}{\pi\sqrt{\tau_0 \tau_s}} \qquad (1)$$

where τ_s is the synchrotron oscillation damping time and $\tau_0 = T_0/(G-P)$ is the laser rise-time, with T_0 the optical cavity round-trip period, P the optical cavity losses and G the amplification gain at the laser start-up. Using the Elettra parameters, the expression above predicts a frequency of 180-340 Hz depending on the beam current and on the specific mirrors. The observed FEL behavior, see Figure 1, is not that of a free oscillator at its own frequency, but appears to be regularly perturbed at 50 Hz.

With the goal of understanding if and how much the FEL pulsed behavior is sensitive to transverse beam orbit instability, the synchrotron light emitted by the electron beam has been observed making use of a Position Sensitive Detector (PSD). As clearly shown in Figure 2 (continuous lines), a 50 Hz component and its harmonics are present in both planes.

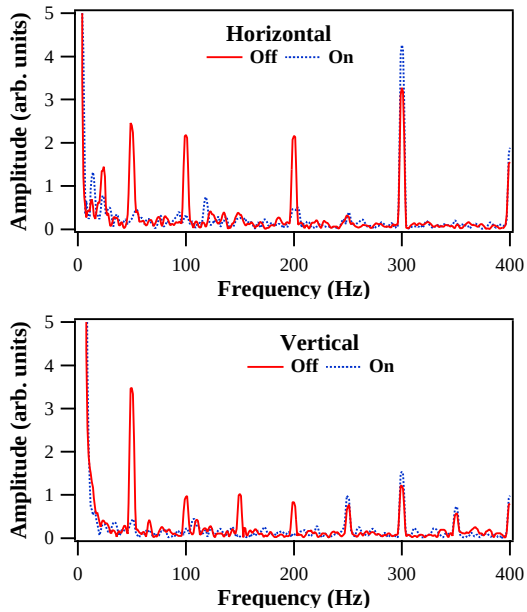

Figure 2: Photon beam transverse position spectra measured in the experimental area by a photon PSD with *(dotted line)* and without the orbit feedback. In this case, the operational bandwidth is limited up to 200 Hz.

Thanks to the recent implementation of a Local Orbit Feedback (LOF) on the SR section hosting the FEL, the transverse micron-range orbit instability has been measured and compensated up to frequencies of a few hundred Hz, see Figure 2 (dotted lines).

This feedback system detects the electron beam position and angle at the Insertion Device (ID) center and stabilizes it without affecting the rest of the orbit. Two Elettra Beam Position Monitors, located on both sides of the ID, are used to measure the beam position and angle, while four cor-

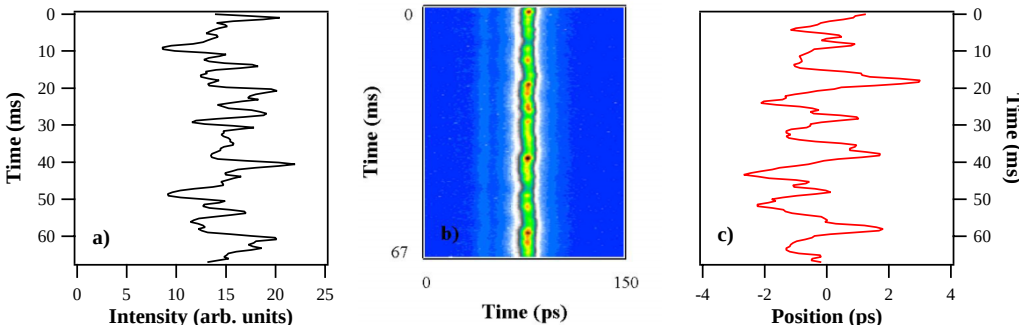

Figure 3: Streak camera image (b) of the FEL light without LOF. Along the vertical axis one can follow the time evolution of the laser on ms scale. Figure a) shows the intensity behavior along the slow time scale as obtained by an analysis of the images, while in Figure c) the phase stability with respect to RF is presented.

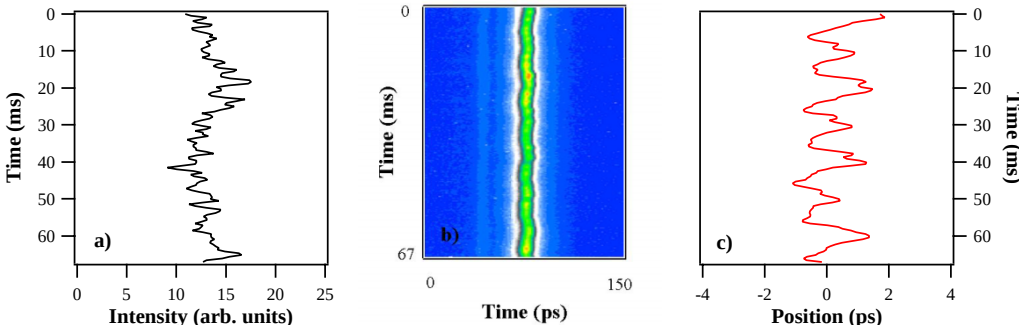

Figure 4: Streak camera image of the FEL light with LOF. Figures a) and c) as the previous figure.

rector magnets apply the closed local bump compensation. The feedback algorithm combines a PID (Proportional, Integral and Derivative) controller, which compensates the slow orbit drifts and lower frequency components of the beam noise spectrum, and a number of so called "Harmonic Suppressors" [3], which remove specific periodic components induced by the mains.

The LOF effect has been studied by means of a streak camera. Collected data (see Figures 3 and 4) show that the orbit stabilization due to the LOF reduces the fluctuations of the FEL intensity (a). Moreover, the FEL phase oscillation with respect to the radio-frequency (c) is halved when the feedback is on. Such oscillations, characterized by a frequency of 100 Hz, are probably induced by a low-frequency longitudinal noise source and, for this reason, they are not completely damped by the two feedback systems.

Derivative Feedback

A further feedback system has been developed as a result of a deeper theoretical understanding of the mechanism leading the system from the continuous to the pulsed behavior when the electron-photon synchronism is increased [8, 9]. When the system is active, the bunch revolution period is modulated making use of a signal proportional to the derivative of the laser intensity.

Preliminary results (see Figure 5) show a damping of the laser oscillations and the achievement of a quasi-continuous regime.

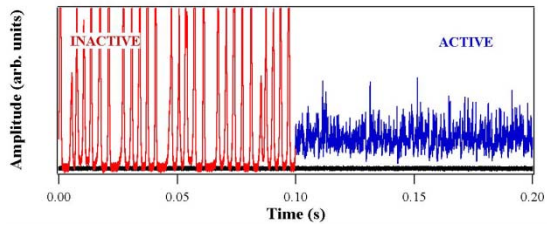

Figure 5: Stabilizing effect of the derivative feedback on the laser intensity.

PLANNED FEEDBACK

The combined action of the previous systems has been recently tested and it has shown to be beneficial for the laser performance. However, such a test has also pointed out that, in order to fully counteract the 50 Hz (+ harmon-

ics) instability affecting the bunch motion (see Figure 6) a further system is needed for the control of longitudinal, low-frequency, perturbations.

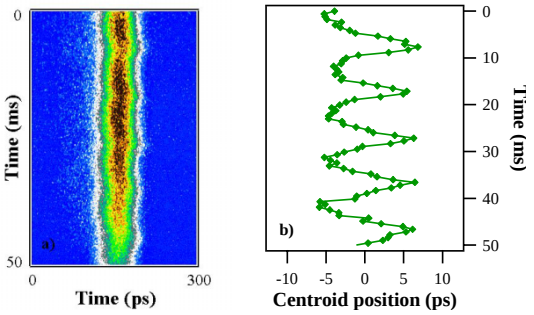

Figure 6: (a): streak camera image of the electron beam *(6 mA)*. A longitudinal instability of the bunch centroid is visible. (b): evolution of the beam center of mass obtained by the image analysis.

We plan to implement a new system to detect the longitudinal low-frequency bunch instability by exploiting the existing LOF Beam Position Monitors. Such devices are equipped with an analog front-end for the demodulation of the RF signal [3] plus a digital receiver. A suitable correction of the Elettra RF will be applied by means of a phase modulation.

CONCLUSION

The performance of a SR-FEL in terms of light stability and extracted power depends on the possibility of simultaneously controlling the electron-beam and laser dynamics. To this purpose, three feedback systems have been recently activated during FEL operation, one acting on longitudinal multibunch instabilities, another on transverse orbit vibrations and a third one directly on the pulsed regime of the FEL intensity. As we have shown, their action significantly improves the beam stability and thus laser performance. Efforts are, however, still required to reach a regular and reproducible CW regime. For that, we plan to design a low-frequency longitudinal feedback which should lead to a further, hopefully decisive improvement of the FEL temporal structure.

REFERENCES

[1] M. Billardon et al., “Saturation mechanism for a storage-ring free-electron laser”, Phys. Rev. Letters, **Vol. 69**, 2368 (1992).

[2] D. Bulfone et al., “Operation of the Digital Multi-Bunch Feedback Systems at ELETTRA”, PAC’03, Portland, May 2003.

[3] D. Bulfone et al., “Fast Orbit Feedback Developments at ELETTRA”, EPAC’04, Lucerne, July 2004.

[4] A. W. Chao, “Physics of collective Beam instabilities in High Energy Accelerators”, Wiley, New York (1993).

[5] M. Swandrlik et al., “The cure of Multibunch Instabilities in ELETTRA”, PAC’95, Dallas, May 1995.

[6] P. Elleaume, J. Phys., **Vol. 45**, 997 (1984).

[7] G. De Ninno and D. Fanelli, “Controlled Hopf Bifurcation of a Storage-Ring Free-Electron Laser”, Phys. Rev. Letters, **Vol. 92**, 094801 (2004).

[8] G. De Ninno and D. Fanelli, “Analytical theory and control of the longitudinal dynamics of a storage-ring free-electron laser”, Phys. Rev. E., **Vol. 70**, 016503 (2004).

[9] C. Bruni et al., “Stabilization of the Pulsed Regimes on a Storage Ring Free Electron Laser: The Case of Super-ACO and ELETTRA”, EPAC’04, Lucerne, July 2004.

TUNABILITY AND POWER CHARACTERISTICS OF THE LEBRA INFRARED FEL

T. Tanaka*, K. Hayakawa, Y. Hayakawa, A. Mori, K. Nogami, I. Sato, K. Yokoyama+, LEBRA, Institute of Quantum Science, Nihon University, 7-24-1 Narashinodai, Funabashi, 274-8501 Japan
K. Ishiwata, K. Kanno, K. Nakao, T. Sakai, Graduate School of Science and Technology, Nihon University, 7-24-1 Narashinodai, Funabashi, 274-8501 Japan

Abstract

The use of the infrared (IR) Free-Electron Laser (FEL) in medical science and material science started in October 2003 at the Laboratory for Electron Beam Research and Application (LEBRA) of Nihon University. The FEL resonator which consists of silver-coated copper mirrors has demonstrated a wavelength tunability ranging from 0.9 to 6.5 μm as a function of the electron energy and the undulator *K*-value. The wavelength dependence of the FEL output power has been measured in terms of different electron energies and different undulator *K*-values. At about 2 μm, an FEL energy of roughly 25 mJ/macropulse has been obtained at the FEL monitor port, which corresponds to the peak power of 1 to 2 MW, provided that the FEL pulse length is less than 0.5 ps that resulted from the measurement by the autocorrelation method. A power decrease observed in the long-wavelength range has resulted from the wavelength dependence of the coupling coefficient of the FEL resonator mirror and the transport efficiency of the FEL guiding optics.

INTRODUCTION

Since the first lasing at 1.5 μm by the LEBRA FEL system in 2001 [1], efforts have been made to achieve the saturation of the FEL power, and to stabilize the pulse-to-pulse power level.

In the early lasing experiment in the infrared region, the FEL resonator consisted of dielectric multilayer mirrors optimised for lasing at a narrow wavelength range of around 1.5 μm. The mirrors were easily damaged by a high optical power. However, this suggested that the property of the LEBRA FEL system including the electron beam is sufficient for intense lasing.

The resonator mirrors were changed to silver-coated copper mirrors in August 2003, which was intended to bring about an early beginning of user's experiments by a wide-range variability of the FEL wavelength and a high mirror tolerance for an intense FEL power. The FEL beam has been extracted from the mirror placed upstream from the undulator through a small coupling hole, and the FEL beam has been successfully transported to user's experimental rooms by the optical guiding system. The user's experiments in medical science and material science began in October 2003.

This paper reports on the improvement of the LEBRA FEL system, the result of the experiments on the wavelength variability and the power characteristics. The current specifications and arrangement of the FEL system are expressed elsewhere [2].

IMPROVEMENT OF THE FEL SYSTEM

Lasing by dielectric multilayer mirrors

Improvement of the FEL power stability has been an important problem for user's experiments. The uniformity of the electron beam energy and current in macropulse duration was improved by the reduction of the phase fluctuation of the accelerating rf in the linac [3]. Although it contributed to the increase of the FEL power, the improvement did not show a significant effect on the stability. Use of the dielectric multilayer mirrors with insufficient tolerance for high power FEL resulted in damage to the mirrors by the FEL before its saturation, which led to difficulty in the investigation of the stability.

In a series of lasing experiments using the dielectric mirrors, the 1.5 μm FEL was observed by detecting the light transmitted through one of the mirrors, where only a fraction of the light beam stored in the resonator was detected using the transmission property of the mirrors.

Vibration and drift of the mirrors

Besides the tolerance for the optical power, there were problems of the vibration of the mirrors and the drift of the mirror separation, which was found from the observation of the interference pattern by the alignment laser lights that reflected on the two mirrors in the resonator [4]. The drift of the mirror separation resulted from a change in room temperature. However, the behaviour of the temperature dependence has not yet been well understood. The slow drift of the mirror separation has been compensated for by adjusting a piezo device manually. The vibration of the mirrors resulted from the vibration of the mirror chambers, which was caused by the water flow for cooling of the bending magnets in the beam transport line, which suggested a lack of flexural rigidity of the mirror chamber's frame bases. The amplitude of the vibration in the bases, measured with a laser displacement gauge, was suppressed from several hundred nm to within 20 nm (limit of measurement) by the reinforcement of the frames, which was made with 6-mm thick steel plates attached to the side faces of the bases.

*E-mail address: tanaka@lebra.nihon-u.ac.jp
+Present address: KEK, 1-1 Oho, Tsukuba, 305-0801 Japan

Lasing by silver-coated copper mirrors

The FEL guiding optics system for user's experiments was constructed in June 2003. This system was designed to use an external-coupling mirror which has a small coupling hole. Since August 2003 the silver-coated copper mirrors have been used for the lasing experiments corresponding to the new optical guiding system. The nominal reflectance for the mirrors is greater than 99.3 % in the wavelength range longer than 0.9 μm. The FEL has been extracted from the mirror placed upstream from the undulator through a coupling hole of 0.15 mm in radius.

The silver-coated copper mirrors demonstrated a high performance. The saturation of the FEL power has been observed for the wavelength range from 0.9 to 6.5 μm. There has been no evidence of damage so far by the saturated FEL power.

Provided that the FEL in the resonator is a Gaussian beam, the coupling coefficient κ of the coupling hole is given by [5]

$$\kappa = 1 - \exp(-2a^2 / w^2), \quad (1)$$

where a is the radius of the coupling hole, w the FEL beam radius on the surface of the resonator mirror that is given as a function of the FEL wavelength λ_L, the Rayleigh length L_R in the resonator and the separation D between the two resonator mirrors by

$$w = \sqrt{\frac{\lambda_L L_R}{\pi}\{1 + (D/2L_R)^2\}}. \quad (2)$$

Using the parameters for the LEBRA FEL system, D = 6.718 m and L_R = 1.47 m, the wavelength dependence of the coupling coefficient is approximated as

$$\kappa = 0.687 \frac{a^2}{\lambda_L}, \quad (3)$$

where the units of a and λ_L are mm and μm, respectively. For instance the coupling coefficient of the 1.5 μm FEL is 0.0103.

The divergent FEL beam extracted from the resonator through the coupling hole has been converted to a parallel beam in the expander system which consists of an ellipsoidal mirror and the parabolic mirrors. Then, the optical size of the collimated beam is determined by the diffraction pattern on the surface of the ellipsoidal mirror.

EXPERIMENTAL SETUP

Fig. 1 shows a schematic layout of the FEL system and the guiding optics system from the accelerator room to the large experimental hall. Also, the experimental setup is shown in Fig. 1. All the measuring devices for monitoring of the FEL have been installed in the large experimental hall.

The macropulse waveform of the FEL and the spontaneous emission were observed with an LN_2-cooled InSb detector in combination with a focusing lens or neutral density filters depending on the intensity of the light. The light was picked up with a CaF_2 beam sampler or an aluminium total reflection mirror in the first FEL monitor chamber.

The light picked up from the second FEL monitor chamber can be divided into the infrared components and the visible components with a cold mirror as shown in Fig. 1. A simultaneous measurement is possible for the spectra of the higher harmonics in the near infrared to the visible region and the fundamental FEL power, if the FEL wavelength lies in the range where the absorption of the fundamental FEL in the cold mirror is negligibly small.

The optical power of the FEL in a wavelength range longer than 2 μm was measured by placing the power meter on the upstream side of the cold mirror. Then, the FEL power and the spectra of the higher harmonics were measured alternately. The FEL power was measured as an integrated energy over the macropulse duration of 20 μs by using a pyroelectric element.

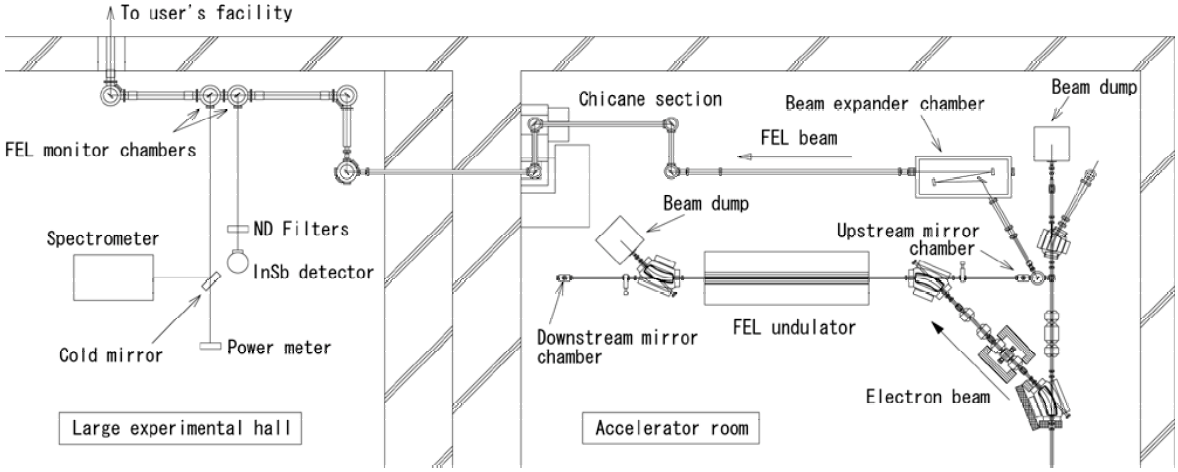

Fig. 1. Schematic layout of the FEL system, the FEL guiding optics system, and the experimental setup. The macropulse waveform, the power and the spectrum of the FEL have been measured in the large experimental hall in order to monitor the FEL during user's experiment. The intense FEL has been picked up with a CaF_2 beam sampler in each FEL monitor chamber.

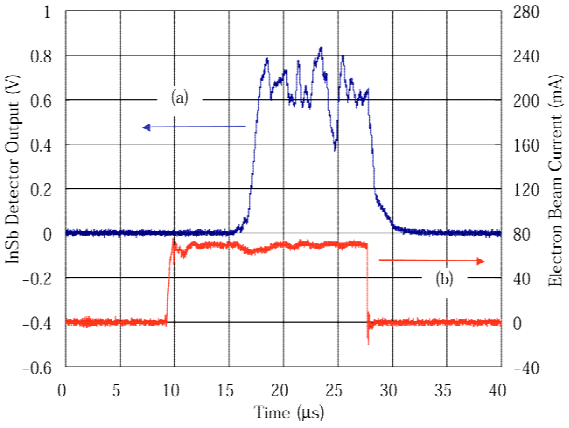

Fig. 2. An example of the macropulse waveform of the FEL lased at 5.75 μm (a). Also shown is the electron beam macropulse current (b).

Fig. 2 shows an example of the macropulse waveform of the FEL measured at a wavelength of 5.75 μm, where the FEL power was saturated in 8 μs from the beginning of the electron beam injection into the FEL system.

The macropulse energy of the FEL was measured using a pyroelectric element with an injection window of 24×24 mm^2, where no focusing device was placed in front of the element. In the experiment, the measured macropulse energy was calibrated only to the fraction contained in above square region in the FEL monitor chamber. It is assumed that the optical beam profile at the pyroelectric element has approximately the same size and shape as in the FEL monitor chamber. Then, the macropulse energy of 2 mJ for the case of Fig.2 was deduced from the measurement.

The electron beam from the linac has been bunched every period of the 2856 MHz RF. From the FWHM of the FEL macropulse in Fig.2, the average energy in each saturated FEL micropulse is estimated to be 0.064 μJ. An FEL micropulse length was deduced to be less than 0.5 ps for the wavelength of 1.5 μm from a measurement with the autocorrelation method [6]. As a result, the micropulse energy of 0.064 μJ corresponds to a peak power greater than 0.1 MW. The maximum FEL energy obtained in the lasing experiment was 25 mJ at a wavelength around 2 μm, which corresponds to the micropulse peak power of nearly 2 MW.

TUNABILITY OF THE WAVELENGTH

The result of the experiment on the FEL wavelength tunability is shown in Fig. 3, where the rhombus-shaped data points show the wavelengths measured in terms of the various undulator gap widths for the fixed electron energy E_e. The 2D analytical expression for the fundamental sinusoidal component of the undulator peak field B_0 is given as [7]

$$B_0 = 2B_r\{1-\exp(-2\pi h/\lambda_U)\} \times \exp(-2\pi g/\lambda_U)\frac{\sin(\pi/4)}{\pi/4}, \quad (4)$$

where B_r (= 1.2 T) is the remanent field of the permanent magnet, λ_U (= 48 mm) the undulator period, g the undulator half gap width, h (= 35 mm) the block height of the magnet [7]. The dependence of the wavelength on the undulator gap width was calculated from the magnetic field given by Eq. (4) as shown by the curves in Fig. 3. The electron energy has an ambiguity within ±1 % due to the momentum acceptance of the electron beam analysing system. Therefore, the curves were fitted to the experimental results by a small correction for the electron energy. The good agreement with the experimental result suggests that the undulator magnetic field is well described by Eq. (4).

The FEL lasing is possible over the range of g from 12 to 18 mm, which makes change of the K-value from 1.99 to 0.91. Thus, the FEL wavelength can be varied continuously to 1/2 of the wavelength at the minimum gap width for fixed electron energy.

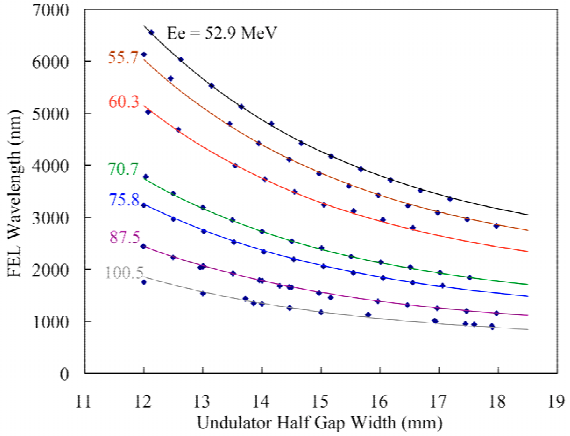

Fig. 3. The FEL wavelength measured as a function of the undulator half-gap width for fixed electron energies. The curved lines show predicted wavelength dependences on the gap width.

POWER AT THE FEL MONITOR PORT

Fig. 4 shows the dependence of relative FEL power on the electron energy and the FEL wavelength, which was measured as the macropulse energy using the pyroelectric element. The wavelength was changed by the adjustment of the undulator gap width with the electron energy fixed.

The experiment for the same electron energy was run in one machine shift, therefore the relative change of the power dependent on the wavelength was obtained with approximately the same electron beam condition. On the other hand, the relative power between the different electron energies involves the difference of the electron beam condition due to the difference of the beam emittance, the energy spread, and the beam focusing

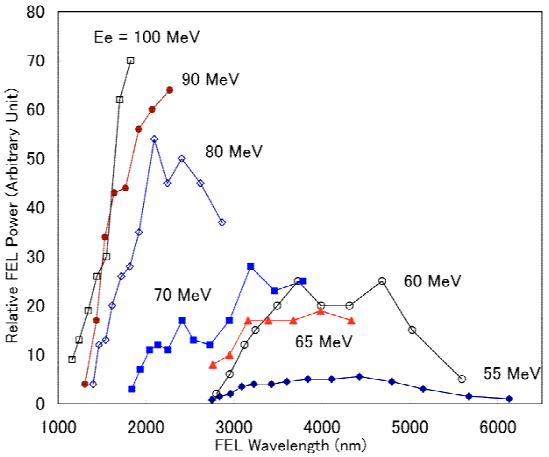

Fig. 4. Relative FEL power obtained with different electron beam energies.

parameters. Also, the absolute value and stability of the FEL macropulse energy has been strongly dependent on the beam handling and the alignment of the resonator mirror. However, the result shown in Fig. 4 gives a good indication of the power available at the user's port.

ESTIMATION OF THE POWER IN THE RESONATOR

The macropulse energy measured at the FEL monitor port represents the energy contained in the power meter injection window area of 24×24 mm^2. By a simple assumption that the profile of the parallel beam obtained at the output of the expander system is conserved at the FEL monitor chamber, the detection efficiency ε_d of the power meter for the total extracted energy is given by [8]

$$\varepsilon_d = 1 - J_0^2(2\pi aA/d\lambda_L) - J_1^2(2\pi aA/d\lambda_L), \quad (5)$$

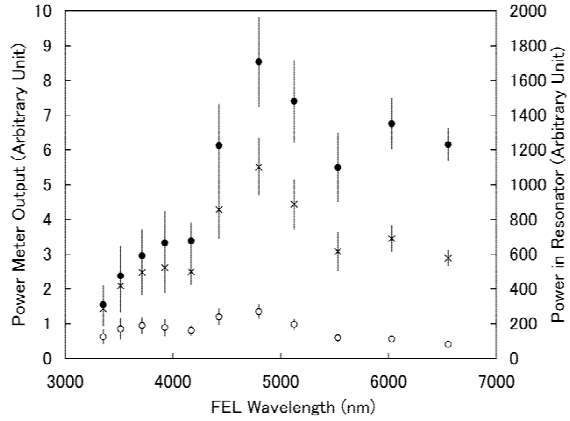

Fig. 5. The FEL power obtained at E_e = 52 MeV. Open circles: raw data divided by T_M, stars: corrected for ε_d, black circles: corrected for ε_d and κ. The error bars represent the fluctuation of the macropulse energy and the macropulse length in the experiment.

where d (= 2.5 m) is the distance between the coupling hole in the resonator mirror and the ellipsoidal mirror in the expander system, and the area of the power injection window was approximated by a circle with the radius A (= 13.5 mm).

From Eqs. (3) and (5), the micropulse peak FEL power in the resonator can be estimated by applying a factor

$$k = \frac{1}{\varepsilon_d \kappa \tau_L} \frac{T_{RF}}{T_M} \quad (6)$$

to the macropulse energy measured at the FEL monitor port, where τ_L is the FEL micropulse length, T_{RF} the period of the micropulse, T_M the FEL macropulse length.

The effect of corrections for ε_d and κ on the FEL power measured at E_e = 52 MeV is shown in Fig. 5, where the open circles are the raw data divided by T_M, the stars corrected for ε_d (the same vertical scale as raw data), the black circles corrected for ε_d and κ (corresponding to the power in the resonator). The FEL macropulse length was measured for each wavelength. Fig. 4 shows a decrease of the power in the wavelength region longer than 3 μm at the FEL monitor port. However, the result of corrections for ε_d and κ suggests that the power in the resonator was not necessarily decreased in this region.

SUMMARY

Saturation of the FEL power was achieved in the wavelength range from 1.0 to 6.5 μm by use of silver-coated copper mirrors in the FEL resonator. The property of the wavelength variability is in agreement with the theoretical prediction. The FEL power measured at the FEL monitor port has shown a decrease of saturated power in the wavelength region longer than 3 μm. However, the power in the FEL resonator has not been necessarily decreased, considering the detection efficiency and the coupling coefficient of the external-coupling mirror.

REFERENCES

[1] Y.Hayakawa et al., Nucl. Instr. and Meth. A 483 (2002) 29.
[2] T.Tanaka et al., "Guiding optics system for LEBRA FEL user facility", FEL2004, Trieste, Italy, Aug. 2004.
[3] K.Yokoyama et al., Nucl. Instr. and Meth. A 507 (2003) 357.
[4] K.Nakao et al., Proc. of the 28th Linear Accelerator Meeting in Japan, (2003) 396 (in Japanese).
[5] H.Kogelnik and T.Li, Applied Optics 5, No.10 (1966) 1550.
[6] K.Hayakawa et al., Proc. of LINAC2004, XXII International Linear Accelerator Conference, Lubeck, Germany, Aug. 2004 (to be published).
[7] K.Halbach, Nucl. Instr. and Meth. 187 (1981) 109.
[8] M.Born and E.wolf, Principles of Optics, Cambridge University Press (1999).

STATUS OF INSTITUTE OF FREE ELECTRON LASER, OSAKA UNIVERSITY

H. Horiike, N. Tsubouchi, K. Awazu, M. Asakawa, M. Heya, Y. Naito, H. Kondo and S. Suzuki

Institute of Free Electron Laser, 2-9-5 Tsudayamate, Hirakata, Osaka 573-0128 Japan

Abstract

Institute of Free Electron Laser at Osaka University is FEL research facility, where beam physics and light application studies are being carried out. Owing to huge research field and to scientists or students of the university, various scientific studies have been initiated under collaborations with schools and institutes in the university, national institutes and industrial companies. The main research field in the institute concerns beam physics towards high quality longer wave length, semiconductor application, environmental chemistry and bio-medical applications, which are supported by the beam quality assurance of the beam physics study.

INTRODUCTION

Since the establishment in April 2000, Institute of Free Electron Laser Osaka university (iFEL) [1] has supplied the laser beam for about 5000 hours as well as the beam study. While the first year was spent for the test run of the accelerator, beam operation time reaches 1500-2000 hours per year afterwards. The research field mainly lies in Bio-Medical application, semiconductor research and Photo-chemistry, where 60%, 24% and 8% of the total machine time were dedicated, respectively. These application studies were carried out within collaborations with research groups in universities, national laboratories and industries. Many users in the research programs used the far-infrared radiation in the wavelength range from 5 to 20 μm, and requested for the longer wavelength up to 100 μm. Therefore the physics research aims to stabilize the infrared FEL system and extend the wavelength region towards longer wavelengths.

In this paper, we will present the achievements and the future plan of our institute. The accelerators and FEL systems will be described in the next section, and then the status of the application programs will be reported in the following section. The future plan will be also presented.

FEL SYSTEMS

Two S-band (2.856GHz) linear-accelerators are housed at iFEL. One has a maximum energy of 180 MeV, and the other an energy of 20 MeV. With these accelerator, the FEL system covers the wavelength range from 0.28 to 60 μm. Details of the FEL systems are described in the followings.

Main Linac

The main linac consists of seven S-band standing-wave accelerating tubes and boosts the electron energy up to 180 MeV. The electron bunches are injected into the accelerator at a frequency of 22.3 MHz, 1/128 of the S-band frequency, from a thermionic electron gun driven by a grid pulser. A sub-harmonic buncher compresses the electron beam of 500 ps into a 10 ps bunch to increase the peak current before injection into the accelerating sections. The 24 μs-long macropulse contains 550 electron bunches. The charge of single bunch is 0.25 nC. This macropulse is produced at a repetition rate of 10 Hz, and the corresponding average current is 2 μA. A small fraction of the charge, 5%, is lost as the bunch passes through the sections. The peak current is about 80 A at the 180 MeV beam line.

Three wigglers are installed on this linac and cover the ultraviolet to mid-infrared part of the spectrum, 0.28 - 20 μm. The MIR wiggler is fed by 25 MeV electrons and lases in the range of 5 - 20 μm, the NIR wiggler 80 MeV and 1 - 6 μm, the UVV (ultraviolet-visible) wiggler 180 MeV and 0.28 - 1.3 μm. The wiggler periods of MIR, NIR and UVV are 3.4, 3.8 and 4.0 cm, respectively. Almost the same period, but they are driven by different energy electron. The FIR system is installed to cover the wavelength range from 20 – 60 μm and is now under development. The wiggler has a 9 cm period and is fed by 25 MeV electrons which have passed through the MIR wiggler. We are aiming for the simultaneous operation of MIR and FIR systems to deliver “two color FEL beams”.

All the resonators have a length of 6.72 m so that one radiation micropulse is restored in them. A coupling hole (1.5 mm in diameter) is bored on the center of the Au-coated metallic mirror installed on the upstream side. The FEL light passes through this hole and is then converted into the parallel beam with a diameter of 200 mm in order to reduce the diffraction loss in the 50 m long transport to the user's room. The transport tubes for MIR and NIR are evacuated to reduce the absorption loss by air.

Figure 1 shows the average power vs. wavelength on the MIR system. The MIR system covers the 5-20 μm range with an average power of 20-45 mW. The power falls off in the vicinity of 6.1 mm probably because of absorption by residual water in the transport tube. The decrease in power for the longer wavelength range is due to electron transport loss in the accelerator and magnetic chicane. In the case of 17 μm operation, the average current drops to 1.7 μA. The wavelength is changed in two ways: the strength of wiggler field and the electron beam energy. The wiggler parameter, or the K-parameter, ranges from 1.0 to 1.5 with a gap spacing from 25 to 17 mm, respectively. (Although the wiggler itself can vary the K-parameter from 0.5 to 1.5, the FEL power is too small with K less than unity.) The tuning range by

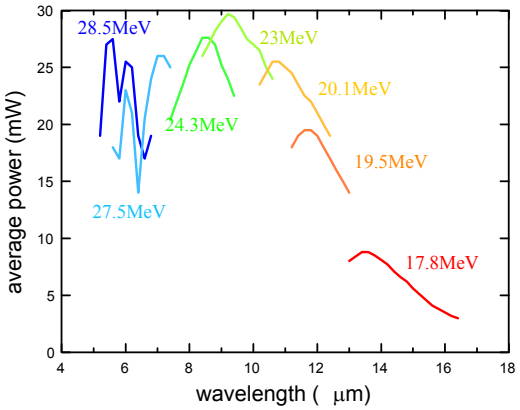

Figure 1. Tunabilty of the iFEL mid-infrared FEL system.

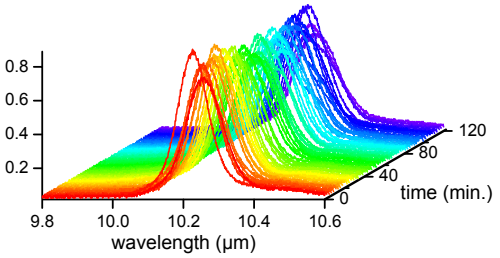

Figure 2. Spectral stability of the iFEL mid-infrared FEL system.

varying the K-parameter is then about 20%, for example, the wavelength can be varied from 8 to 10 mm with a fixed electron energy. In this way, the wavelength can be continuously varied in a minute.

For wider scanning, the electron energy is changed. The electron energy is varied by changing the rf-power to the accelerator. The energy is varied from 22 MeV to 26 MeV to cover the 5 - 20 μm range. Once the electron energy is changed, it takes about 10 minutes to adjust the accelerator components such as bending magnets, quadrupole lenses, phasing of the rf field, and so on.

The spectral width is varied by 0.8-1.6% according to the wavelength: for longer wavelength, the spectral purity tends to degrade. This ranges is limited by the device parameter (the number of wiggler periods is 58) and FEL physics (the spiking nature of the FEL micropulse).

For stable operation of the FEL, temperature control of the accelerator is the critical issue. The accelerator is cooled by water, which is controlled at a temperature of 40 degree centigrade with an accuracy of 0.1 degree. With this technique, we achieve long-period (-2-3 hours) stable operation. Figure 2 shows the spectral stability. The central wavelength fluctuates only 0.1 % during 2 hour long operation. This fluctuation is much smaller than the spectral width and does not make any practical problem so far. On the other hand, the average power stability is 1.9 %. Most of application programs call for better stability in the power. We are investigating the origin of the power fluctuation [2] and developing a more stable machine.

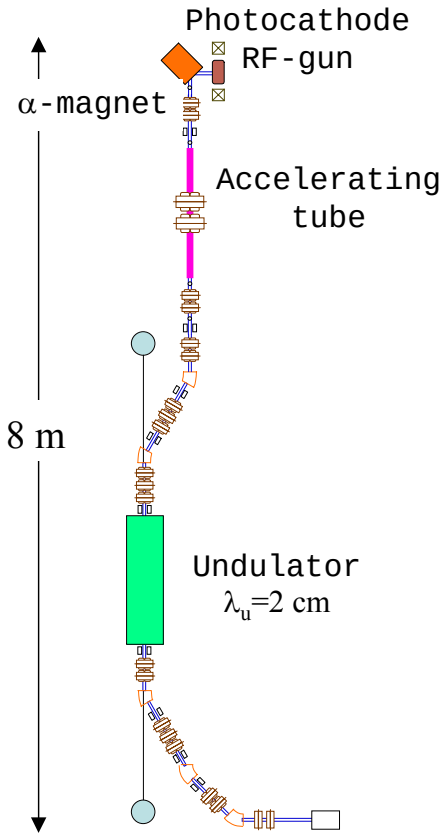

Figure 3. Compact FEL system for Bio-medical application programs

Compact FEL system for Bio research

In order to meet the growing request on the beam time, we are developing new far-infrared, 5-10 μm,FEL system fed by a compact 20 MeV accelerator. This system can be operated independently of the main accelerator and aims to drive the mass spectrometer for the Bio-Medical application programs. The accelerator consists of an RF-gun, the alpha-magnet and an accelerating tube. With a LaB6 thermionic cathode, the accelerator outputs an electron beam with a peak current of 10 A and pulse width of 3 ps during 5 μs macropulse-duration. This accelerator can also be operated as the photo-injector by irradiating the LaB6 cathode with a frequency-tripled mode-locked YLF laser running at 89.25 MHz which corresponds to 1/32 of the S-band RF frequency. In this case, the peak current reaches 60 A.

A hybrid planar undulator with a period of 2 cm and 50 total periods is installed in the magnetic chicane. With a gap spacing of 1 cm, the undulator achieves a K value of 0.5. The resonator consists of a pair of Au-coated mirrors with a spacing of 5.7 m. We expect 500kW peak power FEL output of and 20 mW average power.

For this FEL system, the pulse-picking system is developed to investigate the dynamics of photo-ionization and photo-dissociation. Also it is possible to use the mode-locked laser synchronized to the accelerator for the pump-probe experiments and MALDI experiment.

Research on the stability of FEL [2]

Figure 4 shows the detuning curve of the mid-infrared FEL system installed on the main linac and the time traces of the FEL macro pulse for various resonator lengths. It is seen that the stability of the FEL output is a function of the resonator. A detailed study has indicated that the power fluctuation was correlated with the fluctuation in the electron beam pulsewidth: the FEL power started to drop when the pulsewidth of the electron beam elongated while the power started to increase when the electron beam pulsewidth shortened. Numerical simulation reproduced these experimental result and revealed that the fluctuation in the FEL power arose from the non-linear evolution of the FEL micro pulse which was governed by the resonator length. The fluctuation in the electron beam pulse width has origin in the jitter between the grid pulse of the electron gun and rf of the sub-harmonic buncher. We are developing a feed back circuit to synchronize the grid pulse and the rf source of the sub-harmonic buncher.

Development of the light sources

In order to meet the resent growing interests of material science in the THz spectral range, we are developing a cyclotron laser [3]. This light source is installed on an 180 MeV beam-line of the main linac and produces radiation with a broadband continuous spectrum similar to the THz light source fed by femto-second laser. The peak power, however, is expected to be 1 MW, which is much more intense than the conventional light source in this spectral range. Also a millimeter range compact FEL using a micro-wiggler [4] and a tiny cherenkov FEL in the far-infrared range are under development. These small FEL systems are aiming at applications in practical situations.

Research in the photo-chemistry calls for a strong radiation source in the wavelength range from 2 μm to 4 μm. A near-infrared FEL system which can cover 1-5 μm is being developed using the 80 MeV beam-line of the main linac. For this wavelength range, we furnished a OPA light source fed by a femto-second Ti:Sapphire laser. This OPA system generates intense short-pulse light with a peak power of 1GW and a pulsewidth of 150 fs. Comparison of the response to FEL and OPA will be useful to study the nonlinear phenomena because of the large difference between the pulsewidth of these lasers.

APPLICATION PROGRAMS

So far, 40 application studies are performed within collaborations with research groups belonging to universities, national laboratories and private companies. The representative themes are listed in Table 1. Research

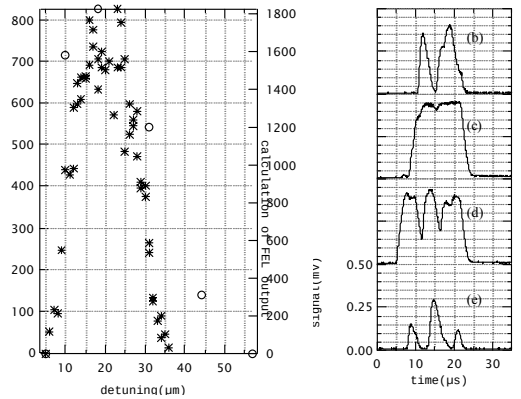

Figure 4. Detuning curve of the mid-infrared FEL system (a) and the time trace of the FEL macro pulse (b)-(e) φορ 9, 13, 26, ανδ 32 μm detuning, respectively.

Table 1. List of application programs

Theme	Collaborator
Semiconductor carrier dynamics under the mid-infrared radiation	Department of Electronics
Far-infrared absorption and photo-conduction of Semiconductors	Department of Physics
Ion-injection into the shallow junction formation using infrared FEL	Mitsubishi Electric Corporation, Ion Engineering Research Institute Corporation
Infrared sensor study	Mitsubishi Electric Corporation
THz semiconductor laser	Department of Physics
Thin-film deposition assisted by mid-infrared FEL	Osaka National Research Institute
Molecular ^{18}O concentration	Hitachi corporation
Domain Change of Columnar Liquid Crystal by FEL	National Institute of Advanced Industrial Science and Technology (AIST)
UV/FEL-MALDI mass spectroscopy for analysis of insoluble protein	the Intellectual Cluster Project
Photonic Intervention Processes for innovative Therapeutics	the Intellectual Cluster Project
Biomimetic lipped bilayers as matrix substances in MALDI-MS	National Institute of Advanced Industrial Science and Technology (AIST)
Infrared spectrographic distinguishing method for a phosphate group and the FEL irradiation effects against a phosphorylated peptide	Nara Institute of Science and Technology
Laser surgery in blood vessel for removal of cholesterol	School of Medicine
Modification of dental tissue by infrared lasers for caries therapy	Kinki university, Osaka dental university
Monitoring of soft tissue cutting using acoustic waves	Kansai university
Measurement of bio-regenerative material and modifications by FEL	Kyoto university

themes cover various fields: material science [5], chemistry [6], bio-medial research [7], and contain both fundamental and practical research.
Some of these programs of ^{18}O concentration, MALDI and semiconductor dynamics research, were proceeded with use of both the FEL and external lasers such as CO_2 laser, mode-locked YLF laser and N_2 laser. A synchronized OPA system which covers the 3-5 μm is operational.

FUTURE PLAN

The present operation project will be concluded at the end of March 2007. Beyond this period, a new project of application research that fully uses the present capability of the facility is being proposed. Development of medical applications is expected in the near future, including laser surgery and protein analysis with using the MALDI mass spectroscopy. Several years after 2007, it is hoped that advanced quantum semiconductors will be developed and widely used. These could not be performed or invented without using FEL grade lights, and such high quality light spectra can not be re-produced easily by conventional lasers.

The other application field of FELs would be in longer wave spectrum. So called radiation in terahertz region is difficult to be emitted by a conventional vacuum tube or by light crystals. Even though the accelerator based light source is large, it can generate much stronger radiation than existing sources. High quality light can be easily produced by FELs, and the present institute is strongly expected to supply light in this spectral range.

For the purpose of analysis, FEL stabilization is the key issue. Application projects that are based on steady physics research is the key issue of the institute, and our institute is expecting and welcomes innovative proposals of FEL itself and its application studies from all over the world.

CONCLUSION

Sine its establishment in 2000, iFEL Osaka university has supplied the FEL for 5000 hours during the operation period from 2001 to 2004. The users, belonging to the university, national laboratory and industrial company, utilized the facility for research in the various fields. Though the FEL system can potentially cover the spectral range from ultraviolet to fir-infrared, most of application programs were carried out with mid-infrared FEL system which can produce the mid-infrared from 5 to 18 μm. These programs call for the stability and the terahertz radiation. We are studying FEL physics and the accelerator physics for the stabilization. Proposals of the light source are also being developed to expand the wavelength range that our facility can deriver. The accelerator based radiation source is believed to be able to open a new scientific field in near future.

REFERENCES

[1] http://www.fel.eng.osaka-u.ac.jp/
[2] H. Nishiyama, M.Asakawa, et al, Nucl. Instr. and Meth. A507 (2003) 74.
[3] M. R. Asakawa, et. al., Nucl. Instr. and Meth. A 528 (2004) 152.
[4] N. Ohigashi, et al, Nucl. Instr. and Meth. A507 (2003) 250
[5] N. Mori, et al, Physica B **314** (2002) 431
[6] M. Yasumoto, et al, Nucl. Instr. and Meth. A475 (2001) 640
[7] K. Awazu, et al, Nucl. Instr. and Meth. A507 (2003) 547

MISALINGMENT TOLERANCE OF A HOLE-COUPLING OPTICAL RESONATOR FOR JAERI ERL-FEL

R. Nagai, R. Hajima, N. Kikuzawa, E. Minehara, N. Nishimori, M. Sawamura,
JAERI, Tokai, Ibaraki, Japan

Abstract

The misalignment tolerance of a hole-coupling optical resonator for the JAERI ERL-FEL is estimated with a wavelength of 22 μm by a Fox-Li procedure simulation code. To ensure the high-power and stable FEL operation, the misalignment tolerance has to be clear, because the FEL power depends on the misalignment of the optical resonator. It is found that the misalignment tolerance of the hole-coupling mirror is less than the non-coupling mirror and the offset effect of the non-coupling mirror is compensable the mirror tilting. The misalignment tolerance is sufficiently large for the FEL power fluctuation of 1%.

INTRODUCTION

An R&D program aimed at a 10-kW class free-electron laser based on a superconducting energy recovery linac (ERL-FEL) is in progress at the Japan Atomic Energy Research Institute (JAERI) [1]. To use the FEL light for various applications, the FEL power should be stable. The FEL power stability is depends on the electron beam stability and the misalignment tolerance of the optical resonator. To be stabilized the electron beam, the RF system and electron gun of the JAERI ERL was improved [2, 3]. In this paper, the misalignment tolerance of the optical resonator of the JAERI ERL-FEL is presented.

The optical resonator of the JAERI ERL-FEL consists of gold-coated end mirrors and a center-hole output coupler [4]. This allows wide broadband operation [5] and ultrashort optical pulse generation [6]. To ensure high-power and stable FEL operation, the misalignment tolerance should be larger than the setting error of the optical resonator and the vibration of the floor. The misalignment tolerance with a wavelength of 22 μm is estimated using a Fox-Li procedure simulation code [4].

MISALIGNEMT TOLERANCE

The FEL extraction efficiency is inversely proportional to the square root of round-trip loss and the square root of interaction mode volume of the optical resonator [7]. The output efficiency of the optical resonator is defined as $\eta_{out}=\alpha_{out}/\alpha_{loss}$, where α_{out} is the output ratio, α_{loss} is the round-trip loss. The FEL power is then represented by the following equation:

$$P_{fel} \propto \frac{\alpha_{out}}{\alpha_{loss}^{3/2} \cdot V^{1/2}}, \qquad (1)$$

where V is the interaction mode volume. The round-trip loss includes the output ratio, the reflective loss at the end mirrors, and the additional diffractive loss. Because the misalignment of the optical resonator introduces additional diffractive loss and expansion of the interaction mode volume, the FEL power is fluctuated by the misalignment. The FEL power is calculated by the Fox-Li simulation code. The FEL power is normalized by the FEL power of perfect aligned optical resonator. The misalignment tolerance for the FEL power fluctuation of 1% is estimated by calculation the normalized FEL power of the misaligned optical resonator.

Model of the Optical Resonator

The estimation model of the optical resonator consists of two end mirrors, four apertures, and a center-hole output coupler as shown in Fig. 1. The end mirror reflectivity is 99.4 %. The four apertures represent the undulator duct and bending magnet ducts. The optical guide and gain guide effect of the electron beam are not taken into account. The parameters of the estimation model are listed in Table 1.

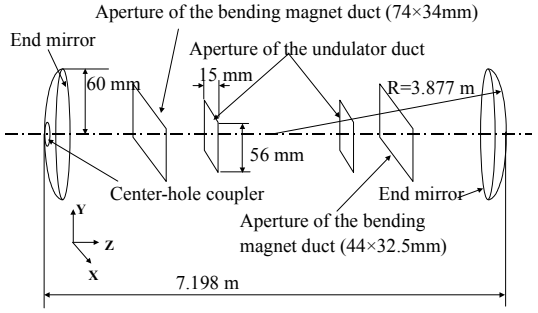

Fig. 1: Model of the optical resonator

Table 1: Parameters of the optical resonator

Length of the resonator	7.198 m
Length of the undulator duct	2 m
Rayleigh range	1 m
Radius of the end mirror	60 mm
Reflectivity of the end mirror	99.4 %
Radius of the center-hole coupler	1 mm

Tilt Tolerance of the Misalignment

To estimate tilt tolerance of the misalignment, the output ratio, the additional diffractive loss, and the interaction mode volume are calculated with the tilt misaligned optical resonator. The additional diffractive loss and the output ratio are shown in Fig. 2. The tilting directions are in yz and zx plane (see Fig. 1). M1 and M2 represent the hole-coupling mirror and the non-coupling mirror, respectively. The output ratio decreases with an increase of the tilt misalignment. In the tilt of less than 190 μrad, the additional diffractive loss decreases with an increase in the tilt misalignment due to the

decrease of the scattering at the edge of the center-hole coupler. In the tilt of larger than 190 μrad, the additional diffractive loss increases with an increase in the tilt misalignment due to the increase of the scattering at the aperture of the undulator duct. The interaction mode volume is approximately flat in this range of tilt misalignment. The mode degeneracy due to the tilt misalignment is therefore sufficiently small for the FEL interaction.

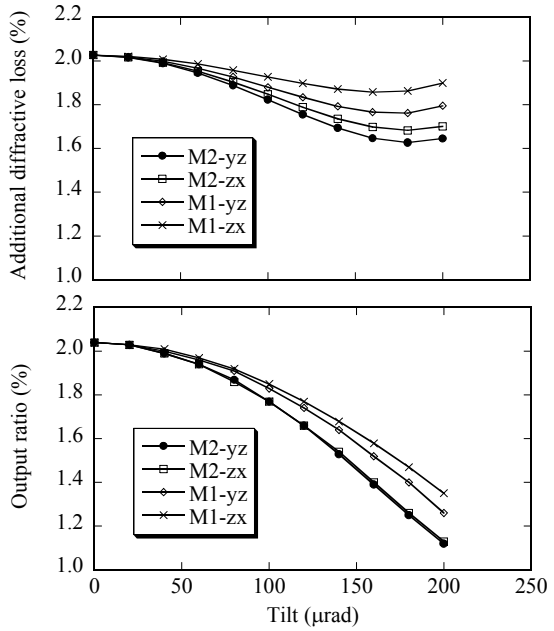

Fig. 2: Additional diffractive loss (upper) and output ratio (lower) for the tilt misaligned optical resonator

The normalized FEL power with the tilt misalignment is shown in Fig. 3. The tilt tolerance for the FEL power fluctuation of 1% is about 100 μrad for both end mirrors.

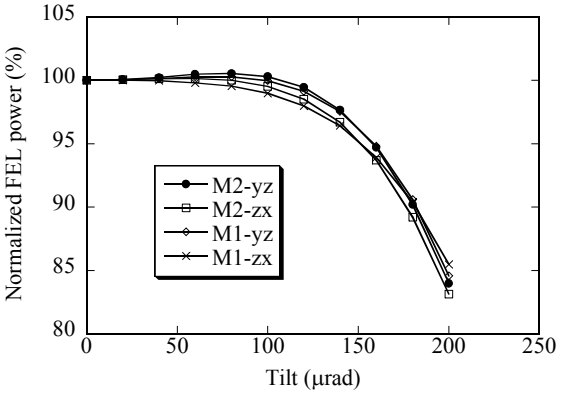

Fig.3: Normalized FEL power for the tilt misaligned optical resonator

The tilt tolerance of a symmetrical optical resonator is given by

$$\Delta\Theta_M << \left(\frac{2\lambda}{\pi d}\right)^{1/2} (1-g)^{1/4}(1+g)^{3/4}, \qquad (2)$$

where λ is the wavelength, d is the optical resonator length, and g=1-d/R (R is the curvature radius of the end mirror) is the stability parameter [8]. For JAERI ERL-FEL, the tilt tolerance is $\Delta\Theta_M$<<378μrad. This value is consistent with the estimation of the tilt tolerance.

Offset Tolerance of the Misalignment

To estimate offset tolerance of the misalignment, the output ratio, the additional diffractive loss, and the interaction mode volume are calculated with the offset misaligned optical resonator. The additional diffractive loss and the output ratio are shown in Fig. 4. The offset directions are in x and y direction (see Fig. 1). The output ratio decreases with an increase of the offset misalignment. In the offset of less than 0.8 mm, the additional diffractive loss decreases with an increase in the tilt misalignment due to the decrease of the scattering at the edge of the center-hole coupler. In the offset of larger than 0.8 mm, the additional diffractive loss increases with an increase in the tilt misalignment due to the increase of the scattering at the aperture of the undulator duct. The interaction mode volume is approximately flat in this range of tilt misalignment. The mode degeneracy due to the tilt misalignment is therefore sufficiently small for the FEL interaction.

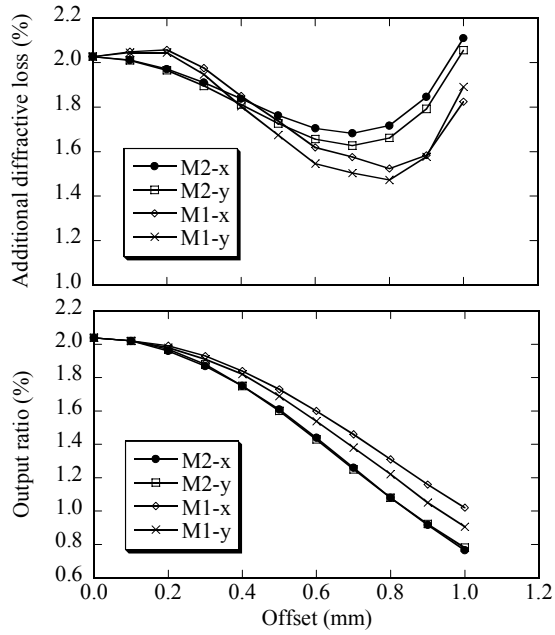

Fig. 4: Additional diffractive loss (upper) and output ratio (lower) for the offset misaligned optical resonator

The normalized FEL power with the offset misalignment is shown in Fig. 5. The offset tolerance for the FEL power fluctuation of 1% is about 0.1 mm and 0.4 mm for M1 and M2, respectively. In the tilt misalignment

and the offset misalignment of the M2, the center-hole coupler is aligned with the resonator axis. In the offset misalignment of M1, the center-hole is offset from the resonator axis. M1 is therefore more sensitive than M2 for the offset misalignment.

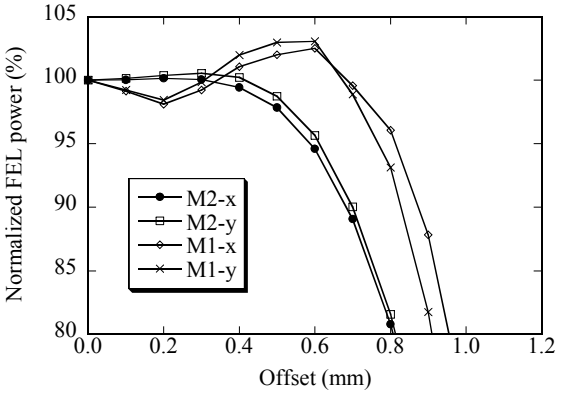

Fig. 5: Normalized FEL power for the offset misaligned optical resonator

Because the optical resonator of the JAERI ERL-FEL is near-concentric configuration, the relationship of the tilt tolerance and the offset tolerance is given by

$$\Delta_M \approx R \cdot \Delta\Theta_M . \quad (3)$$

In the case of M2, the offset tolerance of 0.4 mm corresponds to the tilt tolerance of 100 μrad.

Offset Effect Compensation by the Mirror Tilting

As mentioned above, the offset misalignment is similar to the tilt misalignment in the near-concentric optical resonator. Therefore, the offset effect compensation by the mirror tilting is possible. To estimate offset effect compensation of M2, the normalized FEL power is calculated with the offset and tile misaligned optical resonator. As shown in Fig. 6, the offset effect of M2 is compensable tilting the mirror with the offset of up to 1 mm.

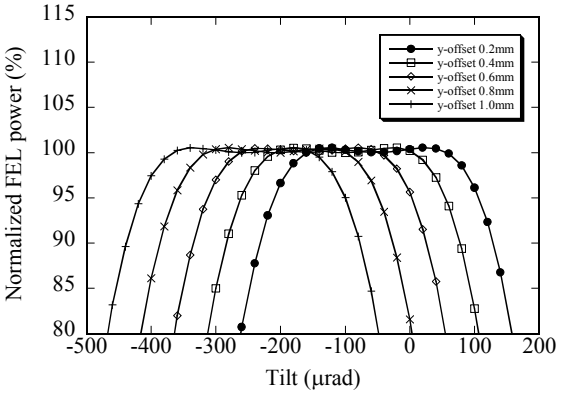

Fig. 6: Offset effect compensation by the mirror tilting for the non-coupling mirror

Because the offset effect of M1 is irregular due to the offset effect of the center-hole as shown in Fig. 5, the offset effect compensation is not expected. To investigate offset and tile misalignment effect of M1, the normalized FEL power is calculated with the offset and tilt misaligned optical resonator. The normalized FEL power is enhanced by the suitable offset and tilt misalignment as shown in Fig. 7. The flat top range of the normalized FEL power decreases with an increase of the offset misalignment. The offset and tile tolerance for the FEL power fluctuation of 1% are 0.1 mm and 40 μrad, respectively.

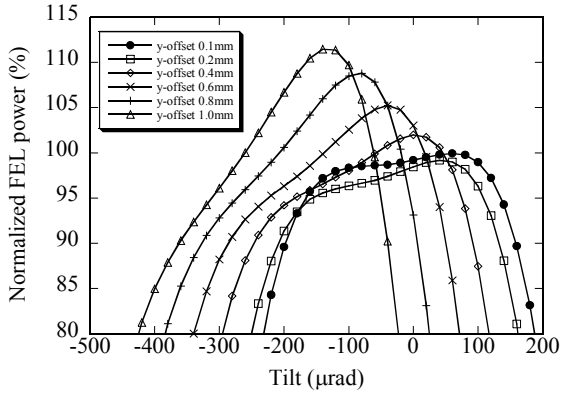

Fig. 7: Offset effect compensation by mirror tilting for the hole-coupling mirror

CONCLUSION

The misalignment tolerance of a hole-coupling optical resonator for the JAERI ERL-FEL is estimated with a wavelength of 22 μm by a Fox-Li procedure simulation code. The offset and tilt tolerance for the FEL power fluctuation of 1% are 0.1 mm and 40 μrad, respectively. The vibration of the floor is less than 1 μm. The accuracy of the He-Ne alignment system of the optical resonator is less than 20 μrad. The offset and tilt tolerance of the optical resonator is therefore sufficiently large for the FEL power fluctuation of less than 1%.

REFERENCES

[1] R. Hajima, et al., these proceedings.
[2] R. Nagai, et al., Proc. of the 1st Annual Meeting of Particle Accelerator Society of Japan, (2004) 293-295.
[3] N. Nishimori, et al., Nucl. Instr. and Meth. A445 (2000) 432-436.
[4] R. Nagai, et al., Nucl. Instr. and Meth. A528 (2004) 231-234.
[5] R. Nagai, et al., Proc. of the 13th Symposium on Accelerator Science and Technology (2001) 455-457.
[6] R. Hajima, R. Nagai, Phys. Rev. Lett. 91 (2003) 024801.
[7] N. Piovella, et al., Phys. Rev. Lett. E52 (1995) 5470-5486.
[8] C. A. Brau, "Free-Electron Laser", Academic Press Inc. (1990) pp.326

OPTIMIZATION OF THE NIJI-IV FEL SYSTEM FOR THE COHERENT HARMONIC GENERATION IN A Q-SWITCHED REGIME

H.Ogawa#, K. Yamada, N. Sei, M. Yasumoto

National Institute of Advanced Industrial Science and Technology, 1-1-1 Umezono, Tsukuba, Ibaraki 305-8568, Japan

Abstract

The Coherent Harmonic Generation (CHG) in the VUV region at the storage ring NIJI-IV has been numerically investigated. The harmonic radiation is produced in an FEL oscillator with a hole-coupled resonator including a 6.3-m optical klystron ETLOK-II. The evolution of light pulses through Q-switched FEL process is simulated using the code GENESIS1.3 and its extended version. The parameters of the NIJI-IV FEL system were optimized for electron-beam energy and optical cavity configurations.

INTORODUCTION

Several works on harmonic generation in storage ring FELs (SRFELs) have been experimentally and theoretically performed [1-9]. In the previous work [9], we have made simulation code for investigation the harmonic generation with a hole-coupled resonator combined with a 6.3-m optical klystron ETLOK-II [10]. In this paper the optimization of the NIJI-IV FEL system is studied by means of the code.

OUTLINE OF SIMULTAION

The detail of simulation procedure was described in Ref.[9] and this section presents the outline: The FEL process in an optical klystron ETLOK-II is simulated using the code GENESIS1.3 [11]. In SRFELs the electron energy spread induced by the FEL interaction accumulates from turn to turn. This code includes the energy spread growth which was calculated by GENESIS1.3. The optical field emitted from ETLOK-II is reflected by a hole-coupled resonator. The paraxial wave equation

$$\left(\Delta_{\perp} + 2ik_s \frac{\partial}{\partial z}\right) a_s e^{i\phi} = 0 \qquad (1)$$

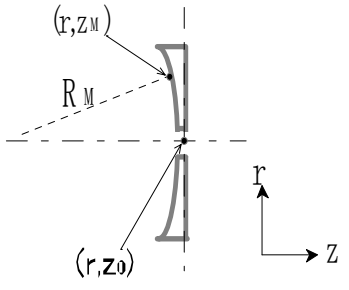

Figure1: Definition of mirror geometry

was used for the calculation. The reflected field $a_{ref}(r, z)$ $exp(-ik_s z)$ can be expressed in the incident field $a_{inc}(r, z)exp(ik_s z)$ in approximation of $k_s R \gg 1$ as

$$a_{ref}(r, z_0) = \left[a_{inc}(r, z_0) - \frac{ird_r rd_r}{2k_s R_M} a_{inc}(r, z_0) - \frac{r^2}{R_M^2} a_{inc}(r, z_0) - \frac{r^3 d_r}{R_M^2} a_{inc}(r, z_0) + \frac{ik_s r^4}{R_M^3} a_{inc}(r, z_0) \right] \exp(2ik_s z_M) \qquad (2)$$

Here the surface of a spherical mirror with radius of curvature R_M was parameterized as $z_M = z_0 - r^2/2R_M$, as shown in Fig. 1, and the last four terms in Eq.(2) can be neglected for NIJI-IV. In this simulation, the reflection of a hole on the mirror axis was assumed a smooth-edge function as $R(r)=2(r/R_a)^4-(r/R_a)^8$. The effective radius of the hole, $R_{eff} = 0.74R_a$, is defined as the radial position where the reflection R becomes 0.5 [12].

The coherent emission from the number of electron N_e in the straightforward direction at the harmonic n [7,8] was evaluated by

$$\frac{d^2 I_n}{d\omega d\Omega} = \frac{1}{2} N_e^2 a_n^2 \frac{d^2 I_0}{d\omega d\Omega} \qquad (3)$$

where

$$a_n = 2J_n\left(4\pi n N_d \frac{\Delta\gamma_m}{\gamma}\right) f_n$$

is the enhancement factor of nth coherent harmonic emission and $d^2I_0/d\omega d\Omega$ is the emission from a single electron and J_n is Bessel function of the order n and f_n the modulation factor. The energy modulation $\Delta\gamma_m$ was estimated by GENESIS1.3.

OPTIMIZATION OF THE NIJI-IV FEL SYSTEM

Electron beam energy

The NIJI-IV is a compact storage ring whose circumference is 29.6m and is usually operated at the beam energy of ~310MeV for UV/VUV FEL experiments.

There is a possibility to increase harmonic radiation power in the higher electron-beam energy operation, since the average power of an undulator FEL is proportional to γ^4. Therefore the beam energy dependence of third harmonic radiation power was investigated.

The electron-beam parameters for different energies were estimated as follows: The bunch length was calculated by $\sigma_l=(\sigma_{lp}^2+\sigma_{lM}^2)^{1/2}$. The bunch lengthening under the influence of the potential well distortion σ_{lp} was evaluated by

$$I=\frac{\sqrt{2\pi}E}{e\alpha R^3}\left(\frac{f_s}{f_{rev}}\right)^2\frac{\sigma_{lP}^3-\sigma_{l0}^2\sigma_{lP}}{(Z/n)_{eff}} \quad . \tag{4}$$

Here f_s and f_{rev} are synchrotron oscillation frequency and ring revolution frequency, α and R are momentum compaction factor and ring average radius, σ_{l0} and $(Z/n)_{eff}$ are natural bunch length and the effective longitudinal coupling impedance, η is the phase-slip factor defined as $\eta=\alpha-1/\gamma^2$. The bunch lengthening due to microwave instability occurs above the threshold current

$$I_{th}=\frac{(2\pi)^{3/2}\eta f_{rev}\sigma_l E}{ec|Z/n|_{bb}}\left(\frac{\sigma_\gamma}{\gamma}\right)^2 . \tag{5}$$

The bunch length σ_{lM} is described as

$$\sigma_{lM}=\left(\frac{\eta R^3 I|Z/n|_{bb}}{\sqrt{2\pi}(E/e)(f_s/f_{rev})^2}\right)^{1/3} \tag{6}$$

where $|Z/n|_{bb}$ and σ_γ/γ are longitudinal broad-band impedance and relative energy spread, respectively. The natural energy spread and emittance are proportional to E and E^2, respectively, which causes the decreases of FEL gain and power of harmonics at high energies. The emittance growth via intra-beam scattering (IBS) was estimated using the code ZAP of which the influence is remarkable at low energies.

The simulation has been performed at the energy of 310, 350, 380, 400 and 450MeV in a single-bunch operation at 30mA.The electron-beam parameters at 310MeV are listed in Table 1. In this study, the designed values of natural energy spread and emittance were used for simulation. The optical resonator parameters are listed in Table 2. The fundamental at 300nm was calculated at R_M=8m with an effective hole diameter of 0.2mm in a

Table 1: Parameters of NIJI-IV at the electron-beam energy of 310MeV

Natural relative energy spread	2.4×10^{-4}
Natural emittance	5.6×10^{-8}
Revolution frequency	10.1MHz
Momentum compaction factor	0.0884
Beam current	30 mA

Table 2: Parameters for ETLOK-II and optical resonator

Magnetic period	
Undulator section	72mm
Dispersive section	216mm
Total length	6.288m
Number of period	42×2
Cavity length	14.8m
Cavity loss	1.0%

Q-switched regime. In this condition, the intra-cavity peak power of third harmonic at 100nm was obtained as maximum intensity when the beam energy was 380MeV.

Asymmetric resonator

In the previous section, the calculation was performed with symmetric resonator, while there are some advantages of making use of asymmetric resonator: i) the spot size on the downstream mirror can be larger so that the cavity loss becomes smaller. ii) the beam waist position can be near the center of the upstream undulator so that the energy modulation $\Delta\gamma_m$ could be larger. Hence, in this section, asymmetric resonator is considered at the beam energy of 380MeV.

The intra-cavity power of third harmonic at 100nm was calculated by changing the radius of curvature of downstream mirror R_d with a 0.2mm effective hole diameter as shown in Fig.2. (The radius of curvature of upstream mirror R_u was fixed at 8m.) The third harmonic power of asymmetric resonator with R_d =9 and 10m is larger than that of symmetric resonator with R_d =8m. The value of R_d is optimized at 10m and the power decreases more than R_d =11m.

In order to understand the tendency in Fig.2, spot size on upstream w_u and downstream mirror w_d were calculated, as shown in Fig.3, by

$$w_d=\sqrt{\frac{\lambda_s R_d}{\pi}}\left(\frac{L_c(R_u-L_c)}{(R_d-L_c)(R_u+R_d-L_c)}\right)^{1/4} .$$

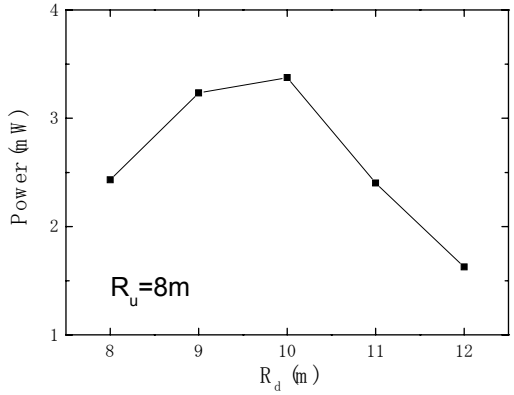

Figure2: Dependence of intra-cavity peak power for third harmonic on the radius of curvature of downstream mirror R_d with R_u=8m.

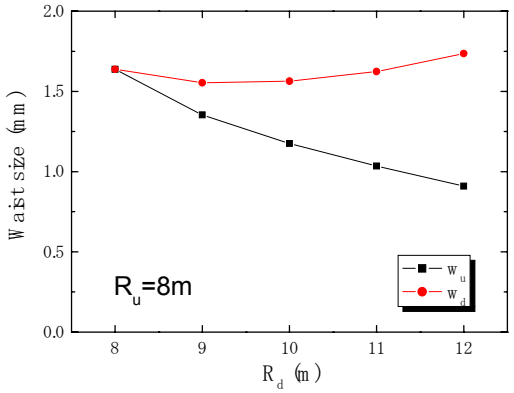

Figure3: Spot size on upstream w_u and downstream mirror w_d with R_u=8m.

$$w_u = \sqrt{\frac{\lambda_s R_u}{\pi}} \left(\frac{L_c(R_d - L_c)}{(R_u - L_c)(R_u + R_d - L_c)} \right)^{1/4}$$

where L_c is cavity length. The value of w_d is almost constant against R_d and that of w_u decreases with increasing R_d. The beam waist position was also calculated by

$$l_u = \frac{L_c(R_d - L_c)}{R_u + R_d - 2L_c}$$

The waist position for R_d =11 and 12m locates between the center and entrance of the upstream undulator. Therefore the filling factor for R_d =11 and 12m becomes small so that the power of third harmonic for R_d =11 and 12m is smaller than that for $R_d \leq 10$m. And the waist position for R_d =10m is found to be nearest the center of the upstream undulator. Hence the power of third harmonic for R_d =10m becomes maximum because the energy modulation $\Delta\gamma_m$ is largest.

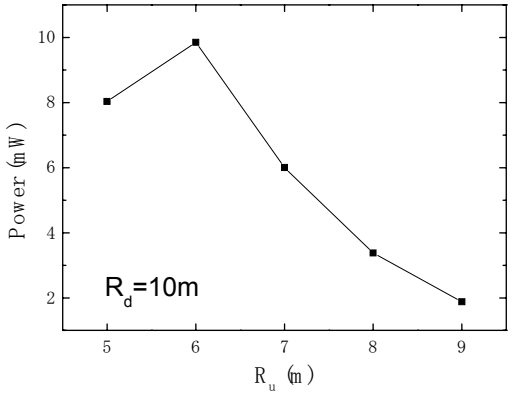

Figure4: Dependence of intra-cavity peak power for third harmonic on the radius of curvature of upstream mirror R_u with R_d=10m.

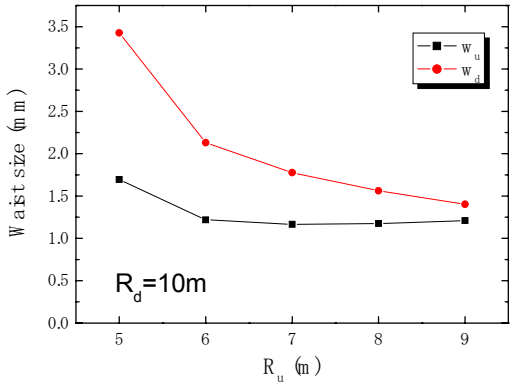

Figure5: Spot size on upstream w_u and downstream mirror w_d with R_d=10m.

The calculations have been also performed by changing R_u with R_d =10m. Figures 4 and 5 show dependence of power for third harmonic at 100nm and spot size on R_u, respectively. The optimized R_u was found to be 6m and the power of third harmonic was obtained as ~10mW which was much larger than the former one.

CONCLUSION

The generation of third harmonic in a Q-switched regime for the NIJI-IV FEL has been simulated using code GENESIS1.3 and its extended version. Optimization of asymmetric resonator has been performed by varying the radius of curvature for upstream and downstream mirror. The calculated intra-cavity peak power of third harmonic at 100nm was ~10mW with a hole-coupled resonator at the electron-beam energy of 380MeV.

ACKNOWLEDGEMENT

This study was financially supported by the Budget for Nuclear Research of the Ministry of Education, Culture, Sports, Science and Technology, based on the screening and counseling by the Atomic Energy Commission, Japan.

REFERENCES

[1] J.M. Ortega et al., IEEE J. Quantum Electron. QE-21 (1985) 909.
[2] R. Prazeres et al., Europhys. Lett. 4 (1987) 817.
[3] K. Yamada et al., Nucl. Instr. and Meth. A407 (1998) 193.
[4] V.N. Litvinenko, Nucl. Instr. and Meth. A507 (2003) 265.
[5] E.C. Longhi et al., Proceedings of the 25th Free Electron Laser Conference, Tsukuba, Japan, Sep. 8-12, 2003, to be published.
[6] R. Prazeres et al., Nucl. Instr. and Meth. A304 (1991) 72.
[7] P. Elleaume, Nucl. Instr. and Meth. A250 (1986) 220.
[8] J.M. Ortega, Nucl. Instr. and Meth. A250 (1986) 203.

[9] H. Ogawa et al., Nucl. Instr. and Meth. A528 (2004) 301.
[10] T. Yamazaki et al., Nucl. Instr. and Meth. A331 (1993) 27.
[11] S. Reiche, Nucl. Instr. and Meth. A429 (1999) 243
[12] B. Fattz et al., J. Phys. D: Appl. Phys. 26 (1993) 1023.

PRELIMINARY DESIGN OF A SYNCHRONIZED NARROW BANDWIDTH FEL FOR TAIWAN LIGHT SOURCE

W.K. Lau, J.R. Chen, T.C. Fan, F.Z. Hsiao, K.T. Hsu, C.S. Hwang, C.C. Kuo, G.H. Luo, D.J. Wang, J.P. Wang, M.H. Wang, NSRRC, Hsinchu, Taiwan
C.W. Chen, H.Y. Chen, NTHU, Hsinchu, Taiwan

Abstract

Design study for a narrow bandwidth, high power IR-FEL has been carried out at NSRRC. This device will be synchronized with the Taiwan Light Source (TLS) storage ring for two-colour experiments. Instead of using lower gradient super-conducting linacs at UHF frequency, it has been proposed to use a high gradient 1300 MHz TESLA super-conducting linac to accelerate a high average current electron beam up to 60 MeV to drive this FEL oscillator. To obtain narrow bandwidth, the beam is stretched in bunch length by using a chicane de-compressor before it passes through the U5 undulator of the FEL. Operating this linac in energy recovery mode is beneficial to improve system stability, wall-plug efficiency and to reduce neutron generation at beam dump. This device will be equipped with a low emittance injector for future upgrade towards shorter wavelengths. The ideas of the TESLA linac plus bunch stretcher scheme as well as a new type of low emittance high average current thermionic DC gun will be introduced in this report.

INTRODUCTION

Many high power THz and IR, FEL facilities that based on energy recovery linac (ERL) technology have been constructed [1-3]. Similar devices have been proposed and some are under construction [4-5]. Applications are mainly on photo-chemistry, isotope separation and material processing [6] etc.

TLS is a 1.5 GeV third generation storage ring synchrotron radiation source. It has been operating stably in the pass few years with high availability. The feasibility of building a high power IR FEL facility that will be synchronized with the synchrotron radiation from TLS beam-line is being discussed. It is believed that this facility will be a very valuable tool for local photo-chemistry and condensed matter research community. Some basic performance requirements as suggested by potential users are summarized as follows:

- Wavelength range: 2.5 ~ 10 μm
- Resolution: < 1 cm^{-1}
- Wavelength Stability: < 0.1 cm^{-1}
- High peak power
- Macro-pulse energy > 1 J/pulse
- Synchronize with TLS storage ring

Note that these requirements are actually quite similar to the FEL proposed for Chemical Dynamics Research Laboratory (CDRL) in 1992 at Berkeley [4]. However, as described in the later sections, we have a different approach. Figure 1 is a cartoon of the IR-FEL facility. Since the revolution frequency of the TLS storage ring is 2.4983 MHz, assuming that the storage ring is evenly filled with two electron bunches, the bunch crossing frequency is will be two times of the revolution frequency. Whereas the total number of rf buckets is 200. Continuous 4.9967 MHz IR pulses from the FEL oscillator will be synchronized with the synchrotron radiation from the U9 undulator in the TLS storage ring also at the same pulse repetition rate.

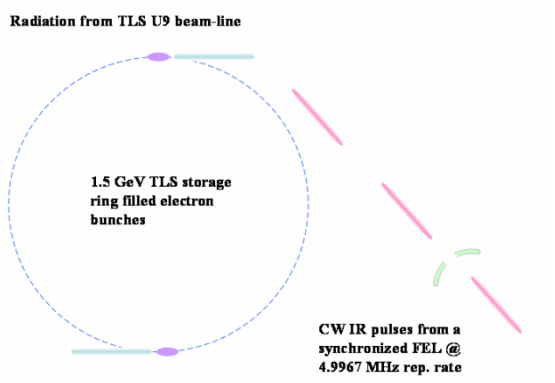

Figure 1: A cartoon showing the proposed IR-FEL in synchronization with the U9 radiation from the TLS storage ring

BASIC CONSIDERATIONS

Since the bandwidth of a linac-based FEL oscillator is just the Fourier transform of the electron bunch length [7], the choice of bunch length has to be consistent with the bandwidth requirement. To produce coherent infrared radiation at very narrow band-width, long bunch length is preferred. In our case, at 10 μm wavelength for example, the bandwidth according to users' wish list is better than 0.1%. Therefore, the required bunch length should be longer than 33 ps. Other means such as putting a grating in the optical cavity can be considered as further reduction in bandwidth. On the other hand, the injector should have significant peak beam current to get reasonable single pass gain to overcome total round trip loss in the optical cavity, but available bunch current is limited by total bunch charge provided the injector. For a fixed amount of bunch charge, as the bunch length become longer, the achievable peak current would be lowered. Therefore, an injector for high bunch charge is

necessary. Although the emittance requirement of an IR-FEL is not too stringent, we would also like to have a lower emittance injector so that upgrade for shorter wavelengths will be possible.

For high power operation, the choice of using super-conducting is natural. Furthermore, it also provides good stability because of its slow response time to external perturbations. To avoid the effect of Lorentz detuning, it is advantageous to employ the energy recovery concept and operate the super-conducting linac at CW mode (i.e. Energy Recovery Linac, ERL). ERL also helps to improve wall-plug efficiency and reduce neutron production at the beam dump. Since we are pursuing a relatively long bunch, it seems straight forward to use lower frequency linac (e.g. 500 MHz) to accelerate the beam to nominal beam energy without much degradation in energy spread. However, the gradient for such linacs are much lower than that for higher frequency linacs. For example, the TESLA linac has a record gradient of 35 MV/m [8] whereas a typical gradient of a few hundreds MHz linac is ~5 MV/m. But to accelerate such a long bunch with higher frequency linac, larger beam energy spread is expected due to the rf curvature. An alternative solution is to accelerate a short bunch electron beam to nominal energy with higher frequency linac and followed by a bunch de-compressor to elongate the bunch to specified beam length. Such scheme is in principle feasible except the beam current in the linac will be much higher. Longitudinal phase space manipulation and beam instability that may be excited in the ERL has to be treated carefully.

THE FEL OSCILLATOR

As an initial study, a single undulator FEL oscillator configuration is considered. And the parameters of the U5 undulator as described in the Berkeley CDRL IR-FEL design report [4]. It is a 40-period undulator with period length of 5 cm. The peak magnetic field is 0.45 T. The gap is adjustable from 23 mm to 36.5 mm. It provides a deflection parameter setting ranging from 0.9 to 2.1. The electron beam energy is set at 60 MeV based on the FEL resonant condition for planar undulator. An undulator with shorter period length helps to reduce beam energy. However, a narrow undulator gap (e.g. 12 mm) is required for operation in wavelength range from 2.5 to 10 μm. In the U3 case, operation at wavelength longer than 10 μm will be limited by the interception between the optical beam and narrow vacuum chamber. The optical cavity is a 30 m confocal configuration with a hole on one mirror for outcoupling of laser power. The choice of cavity length is determined by the micropulse repetition rate. The Rayleigh length of this optical cavity is chosen at half of the undulator length and a total round trip loss of 10% is assumed.

To meet those performance requirements as stated in the last section, some basic design parameters for the IR-FEL are listed in the following table and the electron beam parameters are listed in next section:

Table 1: Basic Design Parameters for the NSRRC IR-FEL

Wavelength [μm]	2.5~10
Bandwidth	0.1 % @ 10 μm (transform limited)
Micro-pulse peak power [MW]	16
Micro-pulse duration [ps]	33
Micro-pulse rep. rate [MHz]	4.996
Minimum Macro-pulse [ms]	> 10
CW mode operation	yes

Tuning of the laser wavelength is of critical importance to users. Interruptions to the users during tuning should be minimized. As depicted in Figure 2, wavelength tuning from 2.5 to 10 μm is unavoidably required a change in driver accelerator operation state. However, change of accelerator system energy and optimize all parameters for FEL lasing without much disturbance to the users is not an easy task. This is especially true for ERL.

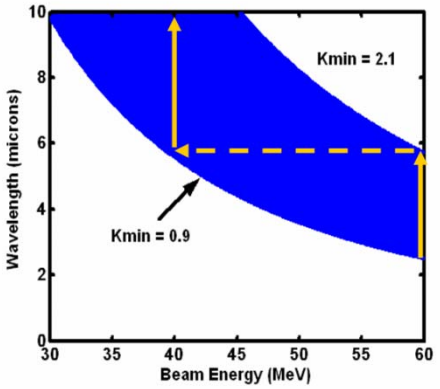

Figure 2: Wavelength tuning of the IR-FEL oscillator using U5 undulator

The use of a planar in-vacuo super-conducting elliptically polarized undulators with period length of 5 cm (SEPU5) is being study. At 100 MeV, the undulator is continuously tuneable from 1 to 10 μm without changing the electron beam energy. And the polarization of the laser field is also tuneable [9].

ACCELERATOR SYSTEM

In designing the accelerator system as a driver for the FEL, the 1300 MHz TTF SC linac is used as an example simply because it has a record high gradient of 35 MV/m. However, the linac is decided to operate at 15 MV/m for reasonably low cryo-load. Since the revolution frequency for TLS storage ring is 2.49833 MHz, the linac cavity frequency has to be multiples of the revolution frequency. The closest multiple to the TESLA linac cavity is 520. That is, the desired cavity frequency is 1299.13 MHz. The resonant frequencies of the cavities have to be adjusted to this value during fabrication [10]. The TESLA cryo-

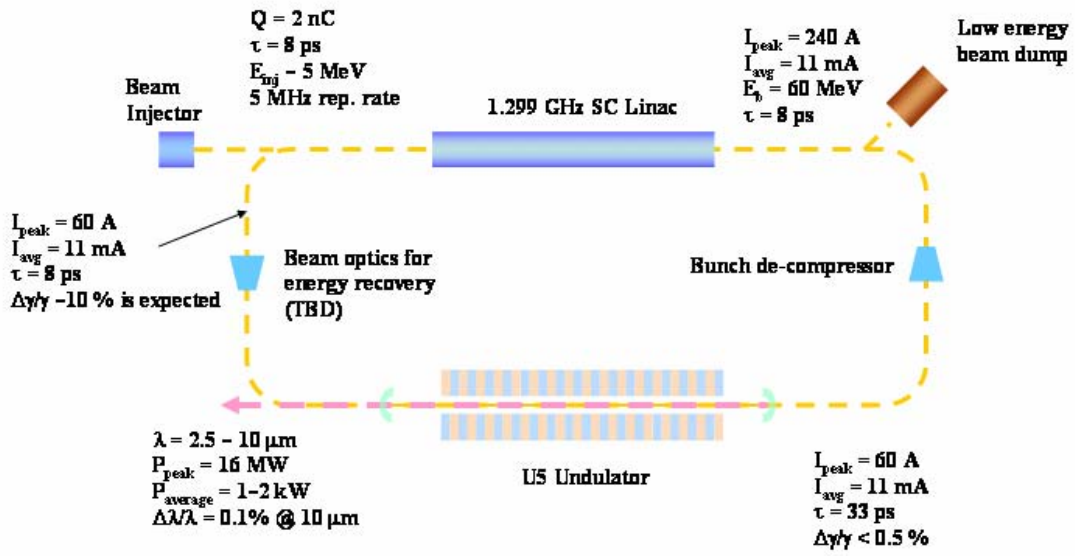

Figure 3: Layout of the ERL with bunch de-compressor before undulator

module consists of eight cavities and each cavity has 9 cells [11]. We hope we will have one such module in the system provide an energy gain of 120 MeV. The above FEL design parameters are based on a beam with following properties:

Table 2: Expected Electron Beam Parameters

Maximum beam energy [MeV]	60
Bunch current [A]	30-60
Beam average current [mA]	11
Bunch charge [nC]	> 2
Bunch length [ps]	> 33
Bunch rep. rate [MHz]	4.9967
FWHM energy spread	< 0.5%
RMS normalized emittance [mm-mrad]	< 25

A possible layout of the driver accelerator for the FEL oscillator is depicted in Figure 3. The beam injector provides a ~5 MeV beam with bunch charge of 2 nC. And bunch length is adjusted to about 8 ps before injection to the main linac. Since bunch repetition rate of the beam is about 5 MHz (two symmetrical filled bunches). Hence, the average current of the beam provided by the injector will be 11 mA. After the main linac, the beam is accelerated to 60 MeV. The expected energy spread induced by the linac is about 0.2 %. It is much lower than the allowable beam energy spread for the FEL interaction. The bunch de-compressor will be designed to expand the bunch by four times. In the first stage of the proposed project, the FEL will be operated at low macro-pulse repetition rate without energy recovery. Design of the return arc in the ERL that will remains as a challenge for future CW operation.

Two types of cathode technologies are being studied. That is, the photo-cathode DC gun and the CeB_6 cathode DC gun. For the photo-cathode dc gun which operates routinely at JLab's IR-FEL, the repetition rate is high but it provides only 135 pC bunch charge. Also, the GaAs cathode has to work in ultra-high vacuum environment of 10^{-12} torr. A high power mode-lock laser and special technique in treating the cathode are also required. The CeB_6 crystal cathode in the electron gun developed at Spring8 for the SCSS project is pulsed at -500 kV for 3 μs. And the repetition rate is at 60 Hz. In spite of its low duty factor, it has the advantages of low emittance, long lifetime and ultra-high vacuum is not essential. The measured normalized emittance of this gun is 1.1 π mm-mrad at 1 A beam current [12]. It has been discussed whether this type of electron gun can be built for high average current operation. Operation at lower cathode voltage for DC mode operation without causing breakdown is possible. For example, the cathode voltage can be set at -100 kV. A control grid can be added to pulse the beam at 5 MHz repetition rate (Figure 4). It allows an average beam current of 11 mA [13]. Preliminary EGUN simulation results showed that by changing the control grid voltage, emittance degradation due to space charge can be compensated by the focusing field near the grid.

It has been discussed in house that some users may find applications in the UV range with wavelength less than 200 nm. In such wavelength range, single pass high gain FEL can be used. The high gradient SC linac plus bunch de-compressor scheme allows easy beam energy upgrade just by adding more cryo-modules into the system. The de-compressor can be converted into compressor for

single pass high gain FEL operation. At such beam energy, ERL is of essential importance in relaxing rf power requirement.

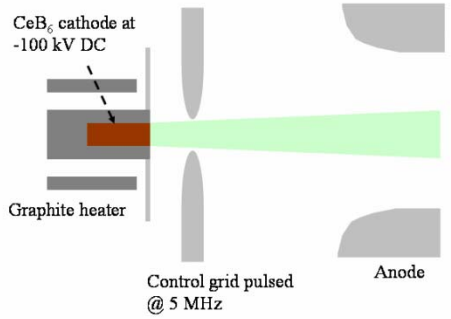

Figure 4: A CeB_6 cathode DC gun with control grid

SUMMARY

The feasibility of using the TESLA high gradient field super-conducting linac plus a bunch de-compressor to drive IR-FEL oscillator for a narrow bandwidth is being investigated. Further studies includes: the design of a low emittance high average current injector that based on CeB_6 cathode technology and beam transport system for energy recovery.

ACKNOWLEDGEMENT

The authors would like to thank Dr. George Neil, Dr. Tsumoru Shintake, Dr. Dieter Proch and Dr. Peter Michel for many stimulating discussions and provide very helpful information.

REFERENCES

[1] G.R. Neil *et al.*, Phys. Rev. Lett., **84**, p. 662-665 (2000).
[2] R. Hajima *et al*., Nucl. Instrum. Methods Phys. Res., **A507**, p. 115-119 (2003).
[3] E.A. Antokhin et al., Nucl. Instrum. Methods Phys. Res., **A528**, p. 15-16 (2004).
[4] Design Report of "An Infrared Free-Electron Laser for the Chemical Dynamics Research Laboratory", LBL PUB-5335 (1992).
[5] B.C. Lee *et al*., Nucl. Instrum. Methods Phys. Res., **A528**, p. 106-109 (2004).
[6] G.R. Neil, "Industrial Applications of Free Electron Lasers", in Workshop on Advanced Free Electron Lasers and Their Applications, Hsinchu (2004).
[7] K.J. Kim, Phys. Rev. Lett., **66**, p. 2746-2749 (1991).
[8] L. Lilje et al., TESLA report no. 2004-05 (2004).
[9] C.S. Hwang *et al*., in these proceedings.
[10] D. Proch, *private communication*.
[11] B. Aune *et al*., PRST-AB, **3**, 092001 (2000).
[12] K. Togawa *et al*., PAC2003 proceedings, p. 3332-3334 (2003); K. Togawa *et al*., in APAC2004 proceedings.
[13] T. Shintake, *private discussion*.

NUMERICAL MODELING OF THE NOVOSIBIRSK TERAHERTZ FEL AND COMPARISON WITH EXPERIMENTAL RESULTS

O.A. Shevchenko #, A.V. Kuzmin, N.A. Vinokurov,
Budker Institute of Nuclear Physics, 11 Acad. Lavrentyev Prosp., 630090, Novosibirsk, Russia

Abstract

Recently a new high-power terahertz FEL has been put in operation at the Siberian Center for Photochemical Research in Novosibirsk. The first lasing at the wavelength near 140 micrometer was achieved in April 2003. Since then some experimental data were obtained which required theoretical explanation. In this paper we use a simple 1-D model for numerical simulations of the FEL operation. The model is based on the excitation of multiple longitudinal radiation modes of the optical resonator by the charged discs. We restrict our consideration to the transverse fundamental mode only. This approximation is valid in the case of long-wave FELs. We compare the results of numerical simulations with some analytical estimates and experimental data.

INTRODUCTION

The Novosibirsk high power FEL started operation recently [1]. It operates in CW mode at terahertz band using simple two-mirror optical resonator. The computer code was created to provide simulations for all measured data. As the beam transverse sizes are significantly less than the radiation eigenmode size, it is enough to use a one-dimensional code.

MODEL DESCRIPTION AND BASIC EQUATIONS

Electron beam in our model is presented as a set of thin rigid disks with Gaussian transverse distribution of charge, which is supposed to be the same for each disk. The total charge of a disk is equal to the total charge of the bunch, divided by the number of disks and the charge-to-mass ratio is the same as for a single electron. We neglect the influence of the radiation field on the transverse motion of a disk. It means that transverse trajectory is definitely determined by the undulator field and the disk has only the longitudinal degree of freedom. We also neglect betatron oscillations and include their contribution to the longitudinal velocity as an additional energy spread. It is convenient to use the longitudinal spatial coordinate *z* as an independent variable. In this case the system of equations for the longitudinal motion can be written as

$$\frac{d\tau_n}{dz} = \frac{1}{V_z(\Delta_n)} - \frac{1}{V_z(0)}$$
$$\frac{d\Delta_n}{dz} = \frac{e}{\gamma_0 m_e c^2}\langle E_x\rangle x'(z) \qquad (1)$$

where *n* is the disk number, $V_z(\Delta)$ is the longitudinal velocity, τ_n is the time delay with respect to the reference particle with energy γ_0, Δ_n is the relative energy deviation, $\langle E_x\rangle$ is radiation electrical field, averaged over disk charge distribution. $x'(z)$ is the transverse trajectory angle in *x*-*z* plane, in our approximation it depends only on *z* coordinate, and in the case of planar undulator $x'(z) = -\frac{K}{\gamma_0}\sin(k_w z)$, where *K* is the undulator deflection parameter, k_w is the undulator wave number.

The radiation field inside the optical resonator may be represented as the linear combination of the resonator eigenmodes. Taking into account small transverse size of electron beam and relatively high damping rate for high-order transverse modes, one can restrict the consideration to the fundamental transverse mode only. Then the on-axis radiation electric field may be represented as

$$E_x(0,0,z,t) = 2\,\mathrm{Re}\left[\sum_k a_k(z)e^{ik(z-ct)}\right] \qquad (2)$$

For the numeric calculations it is convenient to consider the discrete spectrum wave packet with the carrier wave number k_0: $k_m = \frac{2\pi m}{cT_0} + k_0$, *m* is integer, and T_0 is the envelope period. T_0 have to be chosen much more, than the packet duration (typically, of the order of the electron bunch length). Using this field expansion, one can derive the FEL equations for a single pass of the wave packet and particles (charged disks) through the undulator

$$\frac{db_k}{d\theta} = \sum_n D e^{i[\theta\delta_k + \varphi_n(1+\delta_k)]}$$
$$\frac{d\Delta_n}{d\theta} = -\,\mathrm{Re}\sum_k b_k e^{-i[\theta\delta_k + \varphi_n(1+\delta_k)]} \qquad (3)$$
$$\frac{d\varphi_n}{d\theta} = -2\Delta_n$$

Here we introduced the following set of dimensionless variables and constants: $\varphi_n = k_0 c\tau_n$, $\theta = k_w z$, $\delta_k = \frac{k-k_0}{k_0}$, $b_k = -\frac{eK}{m_e c^2}\frac{(JJ)_0}{\gamma_0^2}\frac{i}{k_w}a_k$,

#O.A.Shevchenko@inp.nsk.su

$D = \pi \frac{Q}{T_0 S_0 I_0 \gamma_0^3} \left[\frac{K(JJ)_0}{k_w} \right]^2$, where $(JJ)_0$ is the standard combination of Bessel functions, $I_0 = \frac{m_e c^3}{e}$ - the Alfven current, S_0 is an effective area of radiation (the power over the on-axis intensity), and $k_0 = 2\gamma_0^2 k_w / (1 + K^2/2)$ is chosen.

One can easily check that the system Eq. (3) conserves the total energy

$$\frac{d}{dz}\left(\sum_k \frac{|b_k|^2}{2D} + \sum_n \Delta_n\right) = 0. \quad (4)$$

It also worth noting that this system can be derived from the Hamiltonian

$$H = -\sum_n \Delta_n^2 + \sum_n \sum_k \sqrt{\frac{2DI_k}{1+\delta_k}} \sin[\theta\delta_k + \varphi_n(1+\delta_k) - \Psi_k], \quad (5)$$

where $I_k = \frac{|b_k|^2}{2D(1+\delta_k)}, \Psi_k = \arg(b_k)$; Ψ_k, φ_n and I_k, Δ_n are canonical coordinates and momenta respectively. Then the existence of the integral Eq. (4) follows from the invariance of Eq. (5) with respect to the transformation $\varphi_n \to \varphi_n + \delta s$, $\Psi_k \to \Psi_k + (1+\delta_k)\delta s$.

NUMERIC APPROXIMATION AND COMPUTER CODE DESCRIPTION

To obtain the numeric solution of Eq.(3) we used the following difference scheme

$$b_k^{j+1} = b_k^j + hD\sum_n e^{i\left[\theta\delta_k + \varphi_n^j(1+\delta_k)\right]}$$

$$\Delta_n^{j+1} = \Delta_n^j - h\,\mathrm{Re}\sum_k \frac{b_k^{j+1} + b_k^j}{2} e^{-i\left[\theta\delta_k + \varphi_n^j(1+\delta_k)\right]}, \quad (6)$$

$$\varphi_n^{j+1} = \varphi_n^j - 2h\Delta_n^{j+1}$$

where j is the step number, h is the step size. This scheme implements a canonical transformation of the phase space. It also conserves the following value

$$\sum_k \frac{|b_k^j|^2}{2D} + \sum_n \Delta_n^j = const, \quad (7)$$

which corresponds to the energy integral (4).

The computational algorithm, which directly followed from Eq.(6), was realized in a simple computer code. The code simulates reiterated passes of the radiation wave packet and the electron beam through the undulator. At the beginning of each pass a new particle initial distribution is formed, and all amplitudes of the radiation field modes b_k are reduced with accordance to the losses of the optical resonator. The center of a new bunch is delayed by the optical resonator length L detuning $\delta T = 1/f_0 - 2L/c$ (f_0 is the bunch repetition rate). We used Gaussian distribution for energy Δ_n and uniform, parabolic or Gaussian distributions for coordinate φ_n. The typical number of radiation modes is 800 and the number of particles is 1000.

Accuracy of the code was checked for the small-signal low-gain calculations. The obtained dependences for the gain showed a very good agreement with the theoretical expressions. The results of simulation with the real FEL parameters are presented below.

SIMULATION RESULTS

Simulations were carried out with the Novosibirsk FEL parameters [1]. The dependence of the average radiation power inside the optical resonator on the pass number for different detunings is presented at Fig. 1. One can see that the radiation power reaches saturation after few hundreds of electron bunch passes through the undulator. For some detunings there was no constant saturation level and the power was non-stationary.

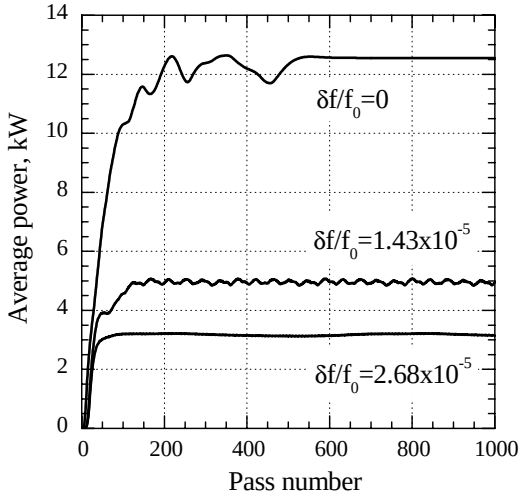

Figure 1: Dependence of average radiation power inside the optical resonator on pass number for different detunings $\delta f/f_0 = -c\,\delta T/(2L)$.

The maximum level of average power inside the optical resonator at zero detuning is about 12 kW, which is in a good agreement with the value obtained in the experiment.

Spectral density of radiation in the case of zero detuning is shown in Fig. 2. The presence of several bands in spectrum apparently indicates the development of side-band instability.

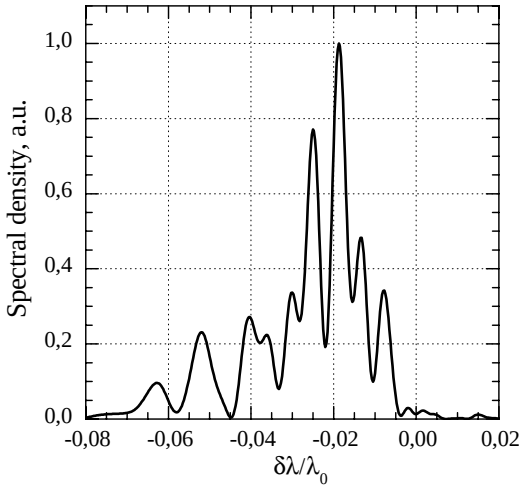

Figure 2: Spectral density distribution for zero detuning.

The corresponding power distribution in time domain is presented at Fig. 3. It can be seen, that the radiation wave packet in this case consists of three short pulses. The distance between adjacent pulses is slightly shorter then total slippage at the undulator length. The mechanism of such short pulse generation was described analytically in [2].

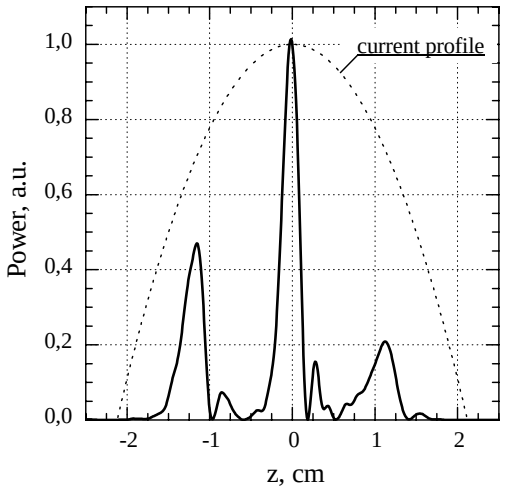

Figure 3: Power distribution over the wave packet length for zero detuning. The dot line corresponds to the beam current profile.

For large enough nonzero detuning the spectrum of radiation is narrow as it shown on Fig. 4. Similar spectrum with FWHM ~ 0.3% has also been observed in the experiment for some regimes.

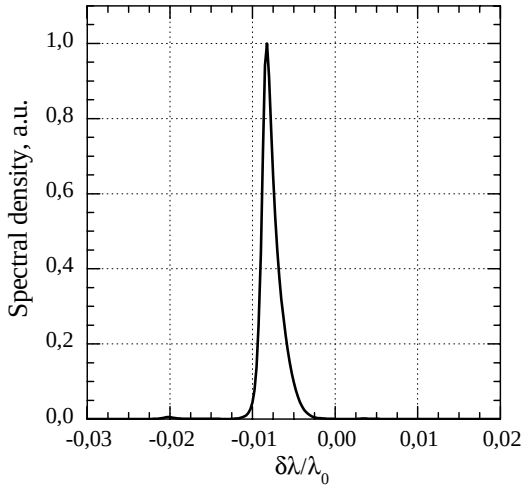

Figure 4: Spectral density distribution for the detuning $\delta f / f_0 = 2.65 \times 10^{-5}$.

Power distribution in time domain for nonzero detuning is presented at Fig. 5. The wave packet length in this case is much longer then in the previous one.

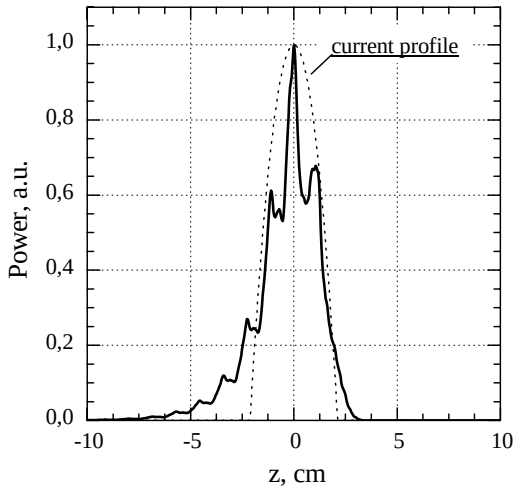

Figure 5: Power distribution for the detuning $\delta f / f_0 = 2.65 \times 10^{-5}$

In Fig. 6 one can see so-called detuning curve. Dependence, presented at this figure, shows, that there is a narrow peak near the zero detuning. The similar results were reported in [3].

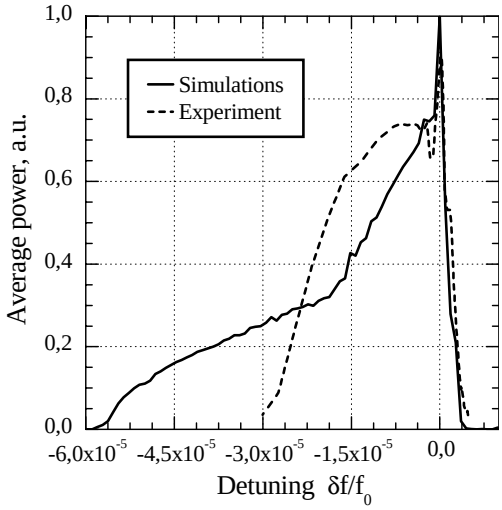

Figure 6: The average power vs. the detuning.

CONCLUSION

The results of calculations demonstrate a good agreement with the measured ones. The lack of information about the particle distribution in the real electron beam is, probably, the main limiting factor for the comparison of the experimental data and the simulation results. Calculations for more advanced FEL magnetic systems (multisection and tapered undulators, optical klystron, electron outcoupling, etc.) are planned.

REFERENCES

[1] E. A. Antokhin et al. NIM A528 (2004) p.15-18.
[2] N. Piovella, P. Chaix, G. Shvets and D.A. Jaroszynski, Phys. Rev. E 52, 5470 (1995)
[3] R. Hajima, N. Nishimory, R. Nagai, E.J. Minehara, NIM A483 (2002) p.113-118.

START-TO-END SIMULATIONS OF THE ENERGY RECOVERY LINAC PROTOTYPE FEL

C. Gerth*, M. Bowler, B. Muratori, H.L. Owen, N.R. Thompson,
ASTeC, Daresbury Laboratory, Warrington WA4 4AD, UK
B. Faatz, DESY, Notkestraße 85, D-22603 Hamburg, Germany
B.W.J. McNeil, University of Strathclyde, Glasgow, G2 0NG, Scotland

Abstract

Daresbury Laboratory is currently building an Energy Recovery Linac Prototype (ERLP) that serves as a testbed for the study of beam dynamics and accelerator technology important for the design and construction of the proposed 4th Generation Light Source project. Two major objectives of the ERLP are the demonstration of energy recovery and of energy recovery from a beam disrupted by an FEL interaction as supplied by an infrared oscillator system. In this paper we present start-to-end simulations of the ERLP including such an FEL interaction. The beam dynamics in the high-brightness injector, which consists of a DC photocathode gun and a super-conducting booster, have been modelled using the particle tracking code ASTRA. After the booster, particles have been tracked with the code elegant. The 3D code GENESIS 1.3 was used to model the FEL interaction with the electron beam.

INTRODUCTION

The performance of a free-electron laser (FEL) depends crucially on the electron beam parameters. While analytical calculations can give an estimate of the expected performance, numerical start-to-end (S2E) simulations are required to account for various aspects of beam dynamics during the generation, transport and compression of the beam [1, 2, 3]. FELs based on the Energy Recovery Linac (ERL) concept have a distinct advantage in terms of rf power and beam dump requirements. However, another aspect becomes important for S2E simulations: the electron beam, which may have a large energy spread induced by the FEL process, needs to be recirculated for deceleration and then transported into the beam dump [4].

Daresbury Laboratory are currently building an ERL Prototype [5] which will operate at a beam energy of 35 MeV and drive an infra-red oscillator FEL. In this paper we present the results of the first S2E simulations for the ERLP including the FEL. To account for space charge effects, ASTRA [6] was used for the modelling of the low energy part (350 keV) of the injector from the cathode to the booster. The beam was tracked with elegant [7] from the booster (8.35 MeV) to the main linac (35 MeV) and then to the FEL. The FEL interaction was modelled with GENESIS, and elegant was used to transport the beam back to the linac for energy recovery and then to the beam dump.

* c.gerth@dl.ac.uk

INJECTOR

The injector consists of a high-average current DC photocathode gun, a booster and a transfer line to the main linac. The DC photocathode gun is a replica of the 500 kV Jefferson Lab gun [8] and will operate at a nominal accelerating voltage of 350 kV and bunch charge of 80 pC. Electrons will be generated at a GaAs photocathode by the frequency-doubled light (532 nm) of a mode-locked Nd:YVO_4 laser with an oscillator frequency of 81.25 MHz. Two solenoids will be used for transverse focusing and emittance compensation, and a normal-conducting single-cell buncher cavity will be utilised to decrease the bunch length from the GaAs cathode. The buncher cavity will be operated at 1.3 GHz and is based on the buncher design employed at the ELBE facility [9]. Electrons are accelerated to an energy of 8.35 MeV in the booster, which consists of two super-conducting 9-cell TESLA-type cavities operated at 1.3 GHz. The cryo-module design is based on the design of the ELBE linac [10]. The layout of the ERLP injector is shown in Fig. 1 and a detailed description of the injector design can be found in Ref. [11].

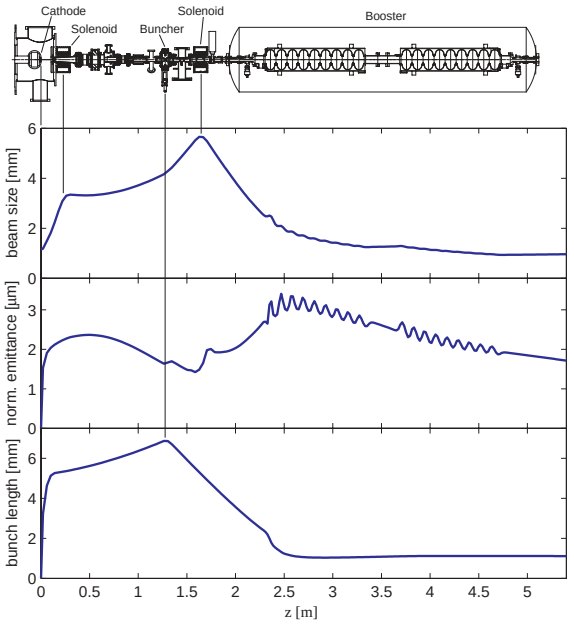

Figure 1: Layout of the ERLP injector and evolution of the beam size, norm. emittance and bunch length (all rms).

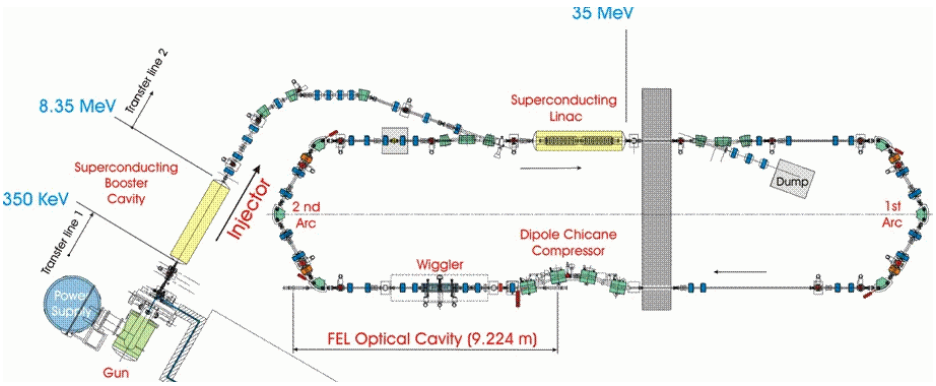

Figure 2: The layout of the ERL Prototype.

To account for space charge effects in the injector the particle tracking code ASTRA has been used for the modelling of the beam dynamics. The transverse properties of the electron bunch at the cathode are determined by the cathode laser parameters whereas the longitudinal profile is dominated by the GaAs cathode for short laser pulses due to the rather long response time of GaAs. For the modelling, a longitudinal Gaussian distribution with an rms length of 20 ps has been assumed. The transverse distribution was chosen to be Gaussian with an rms beam size σ_r = 1.25 mm truncated at $\pm 2\sigma_r$. Results for the evolution of the rms values of the beam size, normalised emittance and bunch length are shown in Fig. 1 for a simulation with 250k macro-particles.

The booster is followed by a transfer line which transports the beam to the straight of the main linac where it is merged with the full energy (35 MeV) single-pass recirculated beam. The transfer line employs four quadrupoles to match the beam into a double-bend achromat which is followed by a 2-dipole achromatic dog-leg. Tracking the beam from the booster to the main linac was carried out by the code elegant. This code does not include space charge effects and so the resulting emittance degradation, as studied in [12], have been simulated further upstream by using appropriate rf phase and sextupole settings.

BEAM TRANSPORT SYSTEM

The layout of the ERLP is shown in Fig. 2. Electrons from the injector are accelerated to 35 MeV in the superconducting main linac, which is identical to the booster and composed of two 9-cell TESLA-type cavities. Two 180° triple-bend achromat (TBA) arcs [13] are used to recirculate the beam to the main linac where the electrons are decelerated to their injection energy. The electrons are separated from the full energy beam (35 MeV) by an extraction chicane and then dumped in the beam dump. A 4-dipole chicane provides bunch compression upstream of the wiggler and bypasses one of the FEL mirrors.

The minimum bunch length is required within the wiggler. The compression chicane has a static R_{56}^C of 0.28 m (positive in our sign convention) [14]. For optimum bunch compression, the main linac needs to be operated at an off-crest phase of about $\varphi_{\rm rf} \simeq 9°$. The TBA arcs are able to provide a large negative R_{56}. In nominal setup, the first arc is set to $R_{56}^{A1} = 0$ whereas the second arc is tuned to $R_{56}^{A2} = -R_{56}^C$ in order to decompress the bunch. The sextupoles in the first arc can be used to linearise the lowest-order curvature induced by the sinusoidal rf during acceleration by varying T_{566}. The effect of the sextupoles on the longitudinal phase space is demonstrated in Figure 3. Two cases are compared: all sextupoles turned off and all sextupoles excited to 100 m^{-3}. The sextupoles in the second arc can be used to minimise the energy spread after deceleration for optimised energy recovery and extraction to the beam dump.

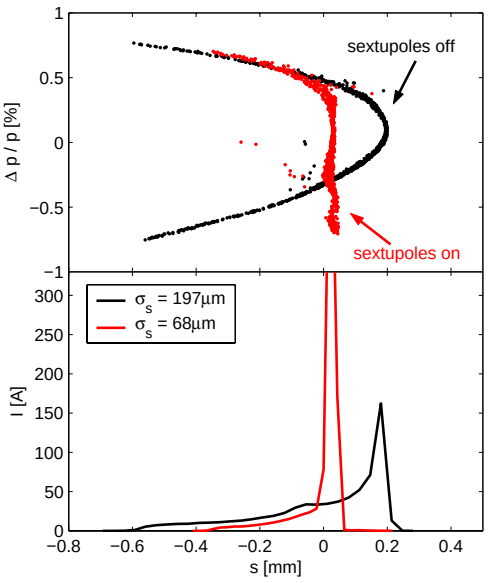

Figure 3: Comparison of longitudinal phase space after the compressor chicane with sextupoles turned on and off.

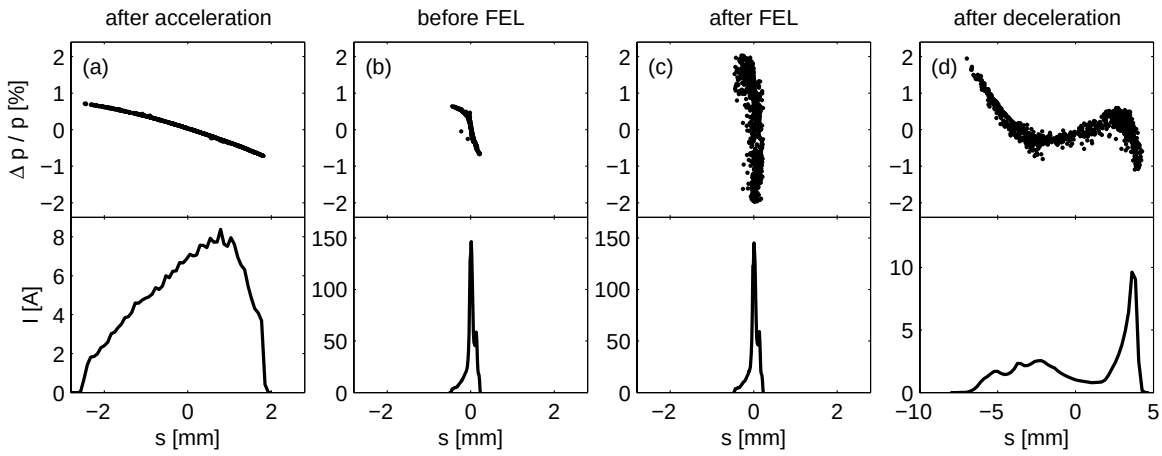

Figure 4: Longitudinal phase space and bunch profile at different locations in the ERLP: (a) after off-crest acceleration by $\varphi_{\rm rf} = 7.8^\circ$ in the main linac; (b) after the compressor chicane with the sextupoles set to 120 m^{-3}; (c) after FEL interaction; (d) after energy recovery in the main linac.

Results of the S2E simulations for the longitudinal phase space and bunch profile at 4 different locations in the ERLP are shown in Fig. 4: (a) after acceleration in the main linac, (b) after the compression chicane, (c) after the FEL, and (d) after deceleration. The ASTRA particle distribution from the injector modelling was used as an input for elegant, and the beam was tracked from the exit of the booster to the wiggler; the program MAD8 was used to match the lattice functions. The bunch was not fully compressed in the S2E simulation (Fig. 4(b)). The rf phase $\varphi_{\rm rf}$ and sextupole settings have been chosen to approximate the expected beam parameters at the wiggler enterance, thus simulating the effects of the neglected space charge in the injector to linac beamline. The FEL interaction, which induces a large energy spread as can be seen in Fig. 4(c), was modelled with GENESIS 1.3 and is described in more detail in the next section. The particle distribution was then converted back to elegant and tracked to the beam dump. When the second arc is set to $R_{56}^{A2} = -R_{56}^{C}$, the deceleration phase is given by $\varphi_{\rm rf} + \pi$. In order to achieve exactly the injection energy during deceleration, the deceleration phase needs to be reduced slightly to account for the mean energy loss of about 0.8% in the FEL process. Apertures were included in the elegant tracking, which were chosen to be 10% smaller than the envisaged vacuum chamber dimensions to approximately account for the effect of misalignment. No particles were lost during the recirculation even with the sextupoles turned off in the second arc.

FEL

The wiggler has been supplied on loan from Jefferson Laboratory, and is a planar device with 40 periods of length 27 mm. The magnet arrays are vertical giving focussing in the horizontal plane. The matched beam conditions in transverse phase space are therefore a waist in the horizontal plane at the entrance to the wiggler and a waist in the vertical plane at the centre of the wiggler. The desired β-function at the wiggler entrance in the horizontal plane is 0.5 m. In the vertical plane the α and β values are set to give a waist in the centre of the wiggler with the minimal vertical beam radius averaged along the wiggler. The optimum matched beam parameters at the wiggler entrance were found to be α_y = 1.75 and β_y = 1.25 m.

The shortest possible length of the optical cavity, defined by the bunch repetition frequency and layout constraints, is D = 9.22 m. The wiggler is positioned slightly off-centre within the cavity, and the mirror radii of curvature R_1 and R_2 are chosen to give a near-concentric cavity with an optical waist in the centre of the wiggler. The Rayleigh length is 0.75 m compared to a wiggler length of 1.08 m – the optimum Rayleigh length for FEL coupling would be less than this but would drive the cavity towards instability. The cavity stability is given by $g_1 \cdot g_2 = 0.9$, with $g_1 = 1 - D/R_1$ and $g_2 = 1 - D/R_2$.

The FEL process was modelled with GENESIS as follows: first, the projected rms values of the tracked particle distribution were calculated, and the predicted performance of the FEL was estimated with analytical formulae and GENESIS in steady-state mode (FEL wavelength, intracavity power, etc.). These results and the SDDS toolkit program elegant2genesis were then used to generate the input files for GENESIS, which was run in time-dependent mode with a seed power given by the analytic estimate of the intra-cavity peak power at saturation of ≈80 MW. This seed power is approximated by a uniform intensity over the entire electron bunch. Although this is not an exact representation of the pulse structure in a cavity it should approximate reasonably well the energy spread induced by the FEL interaction.

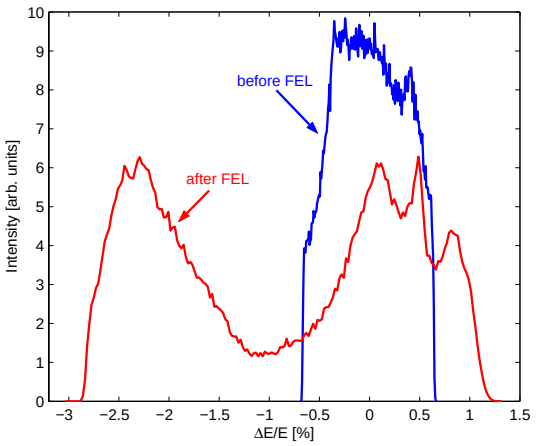

Figure 5: Results of GENESIS simulation: energy spread induced by the FEL interaction with 80 MW seed beam (data taken from Figs. 4(b) and (c)).

The utility code elegant2genesis discretises the elegant supplied macro-particle distribution into radiation wavelength slices (here 4.4 μm) and calculates the relevant GENESIS input parameters. The charge of each slice is proportional to the number of macro particles it contains. These parameters are then applied to form a GENESIS macro-particle distribution with a constant number of particles for each slice (typically 8192). To convert the GENESIS output file back to an elegant input file, the number of particles in each slice should again be made proportional to the slice charge. This is achieved by randomly sampling the GENESIS particles to give the required number of elegant macro particles.

Care should be taken when converting complex particle distributions using elegant2genesis. Inhomogeneous distributions may be inadvertently simplified as elegant2genesis only calculates the mean and rms values for each slice. For instance, in the 'sextupoles-off' particle distribution of Fig. 3, the tail of the distribution comprises two energy bands each of which has a relatively small energy spread. The calculation of the slice values by elegant2genesis results in a mean energy in the centre with a rather large energy spread. This situation does not arise for the 'sextupoles-on' particle distribution used here in the S2E simulation.

The energy profiles of the electron bunch before and after the FEL process are compared in Fig. 5 for a seed power of 80 MW. The mean energy loss in the simulation is 0.8% which is in good agreement with analytical predictions. The return arc must have an energy acceptance sufficient to transport all the electrons. Assuming a Gaussian distribution, a range of $\pm 3\sigma_E$ represents 99.7% of the electrons, so an estimate of the full FEL exhaust energy spread is given by $6\sigma_E$. A full energy spread of $\approx$ 4% is predicted by one-dimensional steady-state codes for the given parameters which is in good agreement with the GENESIS result shown in Fig. 5.

SUMMARY AND OUTLOOK

First S2E simulations of an ERL including both an FEL interaction and energy recovery have been performed. The particle tracking codes ASTRA and elegant were used for particle transport. The FEL oscillator was modelled as a seeded single pass amplifier configuration with a seed power equivalent to the estimated intra-cavity peak power at saturation.

There is ongoing work to improve the S2E simulations. Space charge effects will be included in the modelling of the transfer line from the booster to the main linac at 8.35 MeV. To improve the modelling of the FEL process, a Gaussian seed pulse of variable length will be implemented. The implementation of cavity feedback effects by feeding the output radiation back into the wiggler and including cavity parameters and slippage effects are also envisaged.

REFERENCES

[1] S. Reiche *et al.*, "Start-to-end Simulations for the LCLS Xray-FEL", PAC'01, Chicago, June 2001.

[2] M. Biagini *et al.*, "Start to End Simulations for the SPARX Proposal", PAC'03, Portland, May 2003.

[3] M. Dohlus *et al.*, "Start-To-End Simulations of SASE FEL at the TESLA Test Facility, Phase I: comparison with experimental results", Nucl. Instr. and Meth. A **528**, 448, 2004.

[4] P. Piot *et al.*, "Longitudinal phase space manipulation in energy recovering linac-driven free-electron lasers", Phys. Rev. ST-AB **6**, 030702, 2003.

[5] M.W. Poole, E.A. Seddon, "4GLS and the Prototype Energy Recovery Linac Project at Daresbury", EPAC'04, Lucerne, July 2004.

[6] K. Flöttmann, "ASTRA User Manual", September 18, 2000. `http//www.desy.de/~mpyflo.`

[7] M. Borland, "elegant: A Flexible SDDS-Compliant Code for Accelerator Simulation ", APS LS-287, September 2000.

[8] T. Siggins *et al.*, "Performance of a DC GaAs photocathode gun for the Jefferson lab FEL", Nucl. Instr. and Meth. A **475** (2001) 549.

[9] E. Wooldridge *et al.*, "Comparison of different Buncher Cavity Designs for the 4GLS ERLP", EPAC'04, Lucerne, July 2004.

[10] A. Büchner *et al.*, "The ELBE-Project at Dresden-Rossendorf", EPAC'00, Vienna, June 2000.

[11] C. Gerth, F.E. Hannon, "Injector Design for the 4GLS Energy Recovery Linac Prototype", EPAC'04, Lucerne, July 2004.

[12] B. Muratori *et al.*, "Space Charge effects for the ERL Prototype", EPAC'04, Lucerne, July 2004.

[13] H.L. Owen, B. Muratori, "Choice of Arc Design for the ERL Prototype at Daresbury Laboratory", EPAC'04, Lucerne, July 2004.

[14] B. Muratori *et al.*, "Optics Layout for the ERL Prototype at Daresbury Laboratory ", EPAC'04, Lucerne, July 2004.

STABILITY OF A SHORT RAYLEIGH RANGE LASER RESONATOR WITH MISALIGNED OR DISTORTED MIRRORS

P.P. Crooker *, J. Blau, and W.B. Colson
Naval Postgraduate School, Monterey, CA 93943 USA

Abstract

Motivated by the prospect of constructing an FEL with short Rayleigh length in a high-vibration environment, we have studied the effect of mirror vibration and distortion on the behavior of the fundamental optical mode of a cold-cavity resonator. A tilt or transverse shift of a mirror causes the optical mode to rock sinusoidally about the original resonator axis. A longitudinal mirror shift or a change in the mirror's radius of curvature causes the beam diameter at a mirror to dilate and contract with successive impacts. Results from both ray-tracing techniques and wavefront propagation simulations are in excellent agreement.

INTRODUCTION

Some designs for a high-power free electron laser (FEL) call for a short Rayleigh length optical resonator in order to reduce the system size while minimizing heat damage to the mirrors [1, 2]. An additional advantage of this design is improved optical beam quality, due to the small interaction region in the center of the resonator [3]. However, this design raises concerns about mode stability, in particular the sensitivity to motions of the mirrors. This paper presents a study of the effect on beam behavior of mirror motion and mirror radius change, particularly as they affect short Rayleigh length resonators.

We study the results of several cavity distortions: mirror tilt, transverse and longitudinal shifts in mirror position, and changes in mirror focal length. In order to isolate resonator effects, our results are for a resonator alone with no gain. Since mirror motions are relatively slow (∼ms) compared with the optical round trip time (∼ns), the motions are assumed to be fixed over many passes of the beam through the resonator.

In general, the optical beam in a laser resonator retraces itself — it is an eigenmode of the resonator. If a mirror is misaligned or distorted, however, the resonator eigenmode will be redefined and the existing optical beam will tend to walk around the mirrors [4]. For sufficiently large misalignment, the beam radius may increase indefinitely — i.e., the resonator may become unstable. These effects are most pronounced for short Rayleigh length resonators, which are already near the stability limit. In practical terms, the mirror misalignment and distortion will cause the beam displacement to exceed the size of the mirrors, thereby creating beam loss and lowering the resonator Q.

* ppcrooke@nps.edu

SIMULATION TECHNIQUES

We start by assuming a resonator with two identical mirrors of radius of curvature R (focal length $f = R/2$) separated by distance S and enclosing a Gaussian beam which is an eigenmode of the resonator with Rayleigh length z_0 (Fig. 1). If we normalize all longitudinal distances by S, all transverse distances by $(\lambda S/\pi)^{1/2}$ and all angles by $(\lambda/\pi S)^{1/2}$, then $f = z_0^2 + 1/4$, and the $1/e$ radius of the beam at any z is $w(z) = (z_0 + z^2/z_0)^{1/2}$. In particular, the waist radius is $w_0 = z_0^{1/2}$ [5]. For a 10 m long resonator with $\lambda = 1\mu$m, the transverse scaling length is 1.8 mm and the scaling angle is 0.18 mrad.

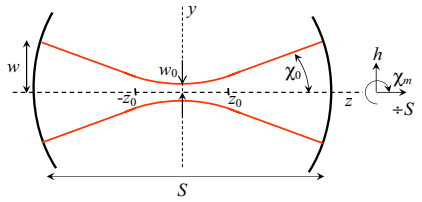

Figure 1: Resonator with Gaussian mode characterized by Rayleigh length z_0. Distortions of the right-hand mirror include tilt θ_m, transverse shift h, longitudinal shift ΔS, and focal length change Δf (not shown).

The beam is simulated using two techniques. In the *ray tracing* technique, a Gaussian beam is simulated by a random collection of rays, Gaussian distributed in both transverse position y and angle θ and set up at the beam waist [6]. For a beam whose amplitude in the y-plane is $A\exp(-y^2/w_0^2)$, the joint probability density is given by $f(y,\theta)$. Setting the distribution widths to $\delta y = w_0 = z_0^{1/2}$ and $\delta\theta = \theta_0 = z_0^{-1/2}$,

$$f(y,\theta) = \frac{1}{\pi}\, e^{-(y^2+z_0^2\theta^2)/z_0}. \qquad (1)$$

Here θ_0 is the angular spread of the beam at $z \gg z_0$ as shown in Fig. 1. Each ray is then propagated numerically with the usual ABCD ray matrices and the evolving ray density and direction is found to closely emulate the actual behavior of a Gaussian beam .

In the *wave propagation* technique [1], the spatial part of the Gaussian beam $a(x,y,z)$is set up at the beam waist and then propagated numerically by the paraxial wave equation $\partial_z a = (-i/4)\nabla_\perp^2 a$.

Both simulation methods can accommodate tilted,

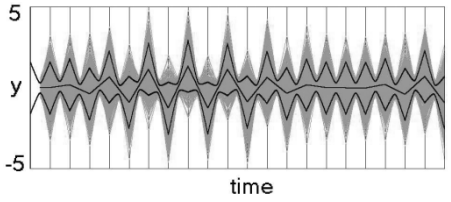

Figure 2: Evolution of an optical beam in a resonator with $z_0 = 0.1$ and $\theta_m = 0.05$. Each vertical line corresponds to a mirror, with the successive reflections unfolded to see the overall behavior. The shaded area shows the trajectories of 1000 random rays; the center line is the center of the optical beam; and the top and bottom lines, calculated from beam theory, correspond to the radius $w(z)$ for the Gaussian mode.

shifted, and distorted mirrors, while the latter method can also incorporate laser gain.

In a third analytical method [5], the Gaussian beam is represented by complex beam radius $q(z) = z + iz_0$. Propagation is then accomplished using the ABCD matrix elements in the form $q_2 = (Aq_1 + B)/(Cq_1 + D)$ and extracting the beam front curvature $R(z)$ and beam radius $w(z)$from $1/q = 1/R - i/w^2$. This method will accommodate longitudinal mirror shift and focal length change only. However, when coupled with ray tracing, can also describe the effects of tilt and transverse shift of the mirrors.

MIRROR TILT AND SHIFT

We now let the right-hand mirror undergo tilt θ_m and/or transverse shift h and investigate the subsequent behavior of the Gaussian beam. The immediate effect is that the reflection angle of any ray incident on the mirror will be increased by $2\theta_m + h/f$. The resonator *will* remain stable, but a new resonator axis will be defined which tilts with respect to the old axis by amount ϕ, where

$$\phi = -[(1 + 4z_0^2)\theta_m + 2h]/(8z_0^2). \qquad (2)$$

The optical beam, which initially was an eigenmode of the old resonator, now becomes tilted with respect to the new axis and is no longer an eigenmode of the realigned resonator. Consequently, with each reflection, its angle with respect to the old axis will change in a rocking fashion, depending on the value of z_0.

The effect of the rocking over many passes n is to make the beam position on the mirror walk sinusoidally up and down. If y_n is the beam position on the mirror after n reflections [5],

$$y_n = C_1[1 - \cos(\alpha n)] + C_2 \sin(\alpha n) \qquad (3)$$

where

$$\alpha = \cos^{-1}\left(\frac{2f^2 - 4f + 1}{2f^2}\right), \qquad (4)$$

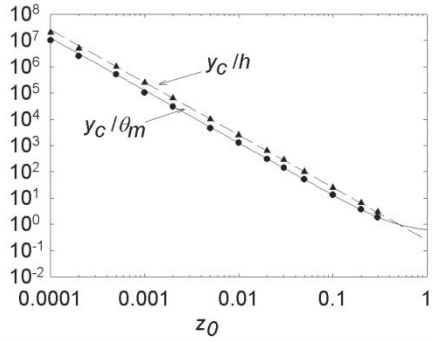

Figure 3: z_0 dependence of the maximum excursion y_c of the beam center from the original cavity axis when a mirror tilts by θ_m or undergoes transverse shift h. Tilt and shift are plotted separately. The lines are beam theory; the points are from wave simulations. For an FEL with S = 10 m and λ = 1 μm, $y_c = 10$ corresponds to 1.8 cm.

$$C_1 = \left(\frac{2f - 1}{4f - 1}\right)(h + 2f\theta_m), \qquad (5)$$

$$C_2 = \frac{-(h + 2f\theta_m)}{\sqrt{4f - 1}}. \qquad (6)$$

Figure 2 shows the result of mirror tilt. The beam is started on axis with the right mirror tilted. Successive reflections of the beam are unfolded, so that the horizontal axis is time. The beam angle changes continually, depending on z_0 and, for this figure, θ_m. In general, the maximum deflection of the beam center y_c is proportional to θ_m and h, as calculated from Eq.(3):

$$y_c = \frac{(4z_0^2 + 1)\theta_m + 2h}{8z_0^2}. \qquad (7)$$

The rocking period n_0 can also be calculated: $n_0 = 2\pi/\alpha$.

For the small z_0 case we are concerned with here, y_c is a strong function of z_0. We show this dependence in Fig. 3 where y_c/θ_m and y_c/h are plotted separately against z_0. As z_0 becomes smaller, the transverse excursions become comparable to the mirror diameter and the beam will walk off the mirrors.

LONGITUDINAL MIRROR SHIFT

Let the resonator contain a Gaussian beam which is a resonator eigenmode with Rayleigh length z_0. Since z_0 is small, the mirror focal lengths $f = z_0^2 + 1/4$ are already only slightly larger than the resonator stability limit $f_{min} = 1/4$. Let the right-hand mirror shift by (normalized) amount ΔS in the z-direction. Successive reflections of the beam will remain on axis, but the Rayleigh lengths of the beam and the resonator eigenmode will no longer be equal. If ΔS is positive (cavity length increases), the focal lengths decrease to $f' = f/(1 + \Delta S)$, and if $f' < 1/4$,

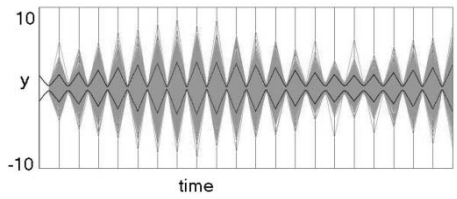

Figure 4: Evolution of an optical beam in a resonator with $z_0 = 0.1$ and right mirror shift $\Delta S/S = 0.031$. The vertical lines represent mirrors, with successive reflections unfolded to see the overall behavior. The gray areas are the trajectories of 1000 random rays; the dotted lines, calculated from beam theory, correspond to the radius $w(z)$ of the Gaussian mode. The beam remains on axis, but expands and contracts with successive reflections.

the resonator will become unstable and the beam will expand without limit. The maximum allowable value for ΔS is therefore $\Delta S_{max} = 4f - 1 = 4z_0^2$.

If $\Delta S < \Delta S_{max}$, the resonator remains stable but the beam will no longer retrace itself in succeeding passes, as shown in Fig. 4. With each pass, the beam width at the mirrors will expand and contract, depending on both ΔS and z_0. Figure 5 shows the effect of varying ΔS for several z_0. For $\Delta S < \Delta S_{max}$, the effect on y_{max} is small. However, as ΔS approaches ΔS_{max}, y_{max} increases and finally diverges at ΔS_{max}.

For $\Delta S < 0$ (resonator length decreases), the resonator remains stable but the beam width again expands dramatically as the difference between the Rayleigh lengths of the beam and the resonator eigenmode becomes large.

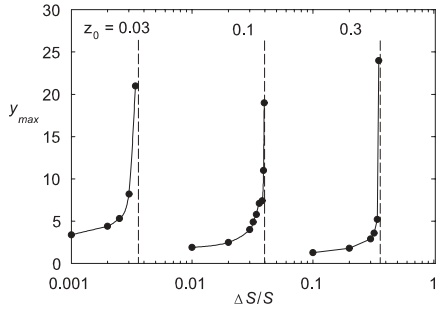

Figure 5: Maximum beam radius y_{max} for right-hand mirror shift ΔS at several values of z_0. The vertical dashed lines show the limits of resonator stability at $\Delta S_{max} = 4z_0^2$. The data points are taken from ray and beam simulations; the solid lines are guides to the eye. For an FEL with S = 10 m and λ = 1 μm, $y_{max} = 10$ corresponds to 1.8 cm.

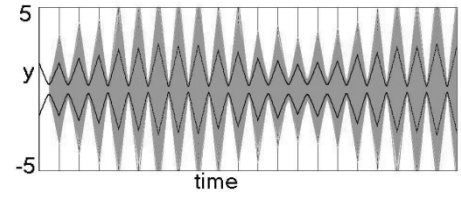

Figure 6: Evolution of an optical beam in a resonator with $z_0 = 0.1$ and right mirror shift $\Delta f/f = -0.05$.

MIRROR DISTORTION

Now let the focal length f of the right-hand mirror in the previously undistorted resonator change by amount $\Delta f/f$. Since the mirror focal lengths are unequal, the mode waist of the resonator eigenmode will move away from the resonator center. The effect is to change the resonator eigenmode so that it no longer corresponds to the original beam. Consequently the beam radius on the mirror will expand and contract with each subsequent reflection, as shown in Fig. 6. In addition, if $\Delta f/f$ is negative (a decrease in the mirror focal length) and made too large, the resonator will no longer be stable and the beam will diverge indefinitely. The stability criterion is $\Delta f > -8z_0^2/(1 + 4z_0^2)$.

Figure 7 shows the results from our simulations. The beam radius at the mirror is y_{max}, as before. As Δf is made increasingly negative, y_{max} increases slowly as the threshold for resonator instability (vertical dashed lines) is approached, and then diverges sharply at the threshold.

DISCUSSION

We have shown that for a short Rayleigh length resonator with no gain, the effects of mirror tilt, shift, and focal length

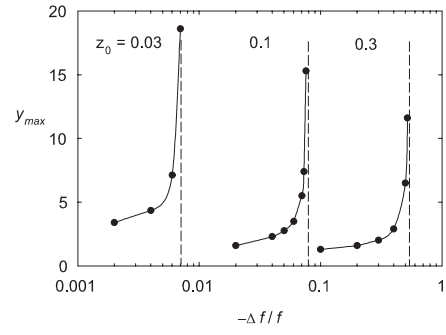

Figure 7: Maximum beam radius y_{max} for focal length change $\Delta f/f$ of the right-hand mirror at several values of z_0. The minus sign in front of Δf indicates the focal length is decreasing. The points are taken from ray simulations and beam calculations; the solid lines are guides to the eye; and the vertical dashed lines show the limits of resonator stability at $\Delta f = -8z_0^2/(1 + 4z_0^2)$.

change can produce dramatic changes in the beam direction and width. In the cases of mirror tilt and transverse shift, the effect is to cause the beam to rock up and down on the mirrors and, if the rocking amplitude is sufficiently large, to cause the beam position to exceed the mirror radius. In the cases of longitudinal mirror shift and focal length change, the beam will remain on axis but the beam radius at the mirror will expand and contract with successive reflections. If the beam radius becomes too large, portions of the beam may exceed the mirror radius. In either case beam power can be lost, or, equivalently, the cavity Q will be reduced. For comparison with actual mirrors, the y-axes in Fig. 3, 5, and 6 can be converted to real values by multiplying by the transverse scaling length $(\lambda S/\pi)^{1/2}$. For a laser with $S = 10$ m and $\lambda = 1$ μm, $y = 10$ corresponds to an actual y of 1.8 cm.

ACKNOWLEDGEMENT

The authors are grateful for support from NAVSEA, ONR, and the JTO.

REFERENCES

[1] W.B. Colson, J. Blau, and R.L. Armstead, "The Free Electron Laser Interaction with a Short-Rayleigh Length Optical Mode", Nucl. Instr. and Meth. A 507 (2003) 48.

[2] P.P. Crooker, et al., "A Study of a High-Power Free Electron Laser Utilizing a Short Rayleigh Length", Nucl. Instr. and Meth. A 507 (2003) 52.

[3] W. Colson, "Short Rayleigh Length Free Electron Lasers", Proc. FEL2004

[4] D. Herriott, H. Kogelnik, and R. Kompfner, "Off-Axis Paths in Spherical Mirror Interferometers", Appl. Opt. 3 (1964) 523.

[5] A. Siegman, "Lasers" (University Science Books, 1986).

[6] J.B. Rosenzweig, "Fundamentals of Beam Physics", (Oxford University Press, 2003).

GAIN AND COHERENT RADIATION FROM A SMITH-PURCELL FREE-ELECTRON LASER*

H. L. Andrews, C. H. Boulware, C. A. Brau, and J. D. Jarvis
Department of Physics, Vanderbilt University, Nashville, TN 37235, USA

Abstract

It has been shown recently that the electron beam in a Smith-Purcell free-electron laser interacts with an evanescent wave for which the phase velocity is synchronous with the electron velocity. However, the group velocity of this wave may be either positive or negative, and when the group velocity vanishes, the gain diverges. In addition, the bunching of the electrons by the interaction with the evanescent wave enhances the ordinary Smith-Purcell radiation due to coherent effects. In particular, the spacing of the bunches causes the Smith-Purcell radiation to peak at the harmonics (and corresponding Smith-Purcell angles) of the evanescent wave frequency. The high gain achievable near zero group velocity makes it possible to design high-power cw Smith-Purcell free-electron lasers. An experiment is being assembled to observe these effects.

INTRODUCTION

Smith-Purcell (SP) radiation is emitted when an electron passes close to the surface of a grating [1]. The virtual photons of the electron field are scattered by the grating, and the wavelength λ_{SP} of the radiation observed at the angle θ from the direction of the electron beam is

$$\frac{\lambda_{SP}}{L} = \frac{1}{\beta} - \cos\theta \tag{1}$$

where L is the grating period, βc the electron velocity, and c the speed of light. The angular and spectral intensity of SP radiation is described by the theory of van den Berg and Tan [2,3,4]. When the current in the electron beam is sufficiently high, the interaction between the electrons and the fields above the grating becomes nonlinear. This causes bunching of the electrons in the beam, which enhances the SP radiation. Recently, a tabletop SP-FEL has been demonstrated at Dartmouth [5]. This device operated near threshold in the spectral region from 300-900 μm. To improve on this performance, it is necessary to understand how these devices operate.

GAIN

A theoretical description of the small-signal gain in a Smith-Purcell free-electron laser (SP-FEL) is discussed in detail elsewhere [6]. The electron beam is represented by a uniform plasma traveling in the positive x direction with velocity βc that fills the region $y > 0$ above the grating. The electrons in the beam interact with an evanescent wave that travels along the surface of the grating in synchronism with the electron beam. To describe the evanescent wave, Floquet's theorem is used and the periodic function is expanded in a Fourier series. In the grooves of the grating the fields are expanded in a Fourier series, but numerical computations show that it is sufficient to keep just the zeroth term in this series. Across the interface between the grating and the electron beam, the tangential component of the electric field and the tangential component of the magnetic field must be continuous. When this expansion is substituted into the Maxwell equations, we get the dispersion relation

$$R_{00} - 1 + \chi_0 S_{00} = 0 \tag{2}$$

where

$$R_{00} = 2\tanh(\kappa_0 H)\sum_{p=-\infty}^{\infty}\frac{\kappa_0 A}{\alpha_p L}\frac{\cos[(k+pK)A]-1}{(k+pK)^2 A^2} \tag{3}$$

and

$$S_{00} = 2\tanh(\kappa_0 H)\frac{\kappa_0 A}{\alpha_0 L}\frac{\cos[kA]-1}{k^2 A^2} \tag{4}$$

in which A is the width of the grooves and H the depth, $K = 2\pi/L$ the grating wave number, k the x-component of the wave vector of the evanescent wave, and

$$\alpha_p^2 = (k+pK)^2 - \frac{\omega^2}{c^2} + \frac{\omega'^2_p}{c^2} \tag{5}$$

$$\kappa_0^2 = -\omega^2/c^2 \tag{6}$$

where ω is the frequency of the evanescent wave and ω'_p is the plasma frequency of the electron beam in the rest frame of the beam.

Table I. Parameters for the planned experiments.

Grating period	200 μm
Groove width	100 μm
Groove depth	175 μm
Grating length	12.7 mm
Electron energy	45-65 keV
Electron-beam current	1 mA
Electron-beam diameter	50 μm

In the absence of the electron beam, the last term in (2) vanishes, and we are left with the dispersion relation for the empty grating. Some simple computations carried out

*Supported by the Medical Free Electron Laser Program of the Department of Defense under grant number F49620-01-1-0429.

using MathCad are shown in Figure 1 for the grating parameters summarized in Table I. In Figure 1, the operating point of the laser is the point where the beam line, βk intersects the dispersion curve. As shown there, for 56-keV electrons the intersection occurs at a point $k/K \approx 0.5$, where $d\omega/dk \approx 0$. Below this point the group velocity is positive, and above this point the group velocity is negative, in the manner of a BWO.

When the effect of the electron beam is nonvanishing but small, the solution to (2) can be expanded about the no-beam case. Since the susceptibility diverges near the synchronous point, the gain is largest there and the amplitude growth rate is found to be

$$\mu = \frac{\sqrt{3}}{2}\left|\frac{\omega_p^2}{\gamma^3\beta^2 c^2}\frac{S_{00}(\omega_0,k_0)}{R'_{00}(\omega_0,k_0)}\right|^{1/3} \qquad (7)$$

where $\gamma = 1/\sqrt{1-\beta^2}$. The growth rate for the power is twice this. The total power gain per pass is then

$$g = e^{2\mu Z} \qquad (8)$$

where Z is the overall length of the grating.

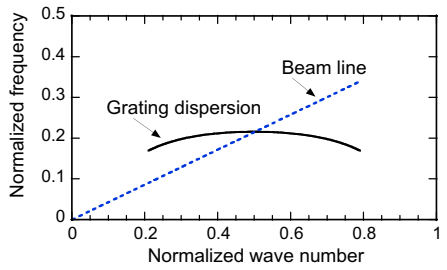

Figure 1. Dispersion diagram for a SP-FEL; beam line drawn for a 56-kV beam.

As shown in Figure 2, the gain has a strong peak near 56 kV, and actually diverges where the group velocity vanishes. In a fundamental sense, the net gain for the evanescent wave is a balance between the energy absorbed from the electron beam and that lost by energy flow along the grating. But the energy in the evanescent wave travels at the group velocity, $d\omega/dk$, and this depends on the wave number of the wave, as indicated in Figure 1.

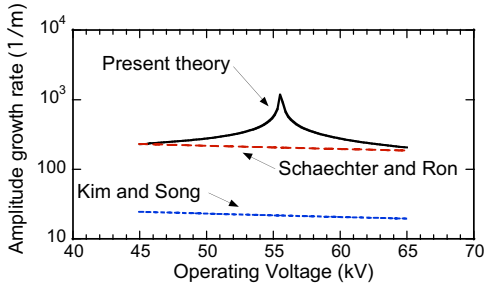

Figure 2. The gain of a SP-FEL.

Other theories have been proposed to describe the operation of a SP-FEL [7,8,9]. Schaechter and Ron analyze the interaction of an electron beam with a wave traveling along the grating, and include waves that are emitted by the beam and reflected off the grating [8]. Kim and Song consider an electron beam that interacts with a Floquet wave traveling along the surface of the grating, somewhat like the present theory [9]. However, they assume that at least one of the Fourier components of the Floquet wave is radiative, rather than evanescent. That is, at least one component of the wave is not exponentially decreasing away from the grating surface. The results of computations using these alternative theories are shown for comparison in Figure 2. In the present theory, the gain peaks near 56 kV due to the dispersion of the grating, which is not explicitly included in the other theories.

COHERENT RADIATION

The frequency of the synchronous evanescent wave is found from the dispersion relation (2). Some computations for the parameters of Table I are shown in Figure 3. As shown there, the free-space wavelength of the evanescent wave is always longer than that of the SP radiation. Since it does not radiate, the evanescent wave is coupled out from the SP FEL only at the ends of the grating. When the group velocity vanishes, this radiation disappears. The evanescent wave was not observed in the Dartmouth experiments.

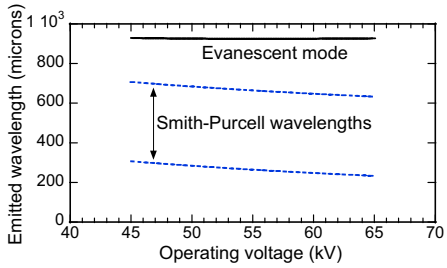

Figure 3. Wavelengths emitted from a SP-FEL.

For the grating parameters in Table I, the conventional SP radiation is emitted over a range of wavelengths from $\lambda/L = (1-\beta)/\beta$ to $\lambda/L = (1+\beta)/\beta$, as indicated by (1) and shown in Figure 3. When the electron beam interacts with the evanescent wave, it is bunched at the frequency of the evanescent wave. This bunching enhances the SP radiation at the harmonics of the evanescent wave. This can be seen in the following way. When a single electron passes over the grating, the angular spectral intensity S_{SP} of the SP radiation is proportional to q^2, where q is the electronic charge, and the total radiation from n_e electrons is proportional to $n_e q^2$. When the n_e electrons are formed into a bunch of charge $n_e q$ whose dimensions are small compared to a wavelength, the SP radiation is proportional to $(n_e q)^2$,

which represents a coherent enhancement of the radiation by the factor n_e over the entire band of SP radiation. However, when the electrons appear in periodically spaced bunches, there is yet another effect. As shown in Figure 4, the bunches interfere constructively at wavelengths that satisfy the relation

$$\lambda_b + \beta n_h L \cos\theta = n_h L \tag{9}$$

where $n_h > 0$ is an integer, $\lambda_b = \beta\lambda_\infty$ is the spacing between the bunches, and λ_∞ is the free-space wavelength of the evanescent wave. But if we use the SP relation (1) we find that

$$\lambda_\infty = n_h L\left(\frac{1}{\beta} - \cos\theta\right) = n_h \lambda_{SP} \tag{10}$$

so the coherent SP radiation is enhanced at the harmonics of the evanescent wave. Relative to the intensity from the same number of electrons in randomly spaced bunches, the angular intensity of the radiation at the harmonic n_h is enhanced by the number N_g / n_h of bunches that radiate in phase with the wave over the length of the grating, where N_g is the total number of grooves in the grating. However, the angular width of the harmonic is on the order of $1/N_g$, the angular resolution of a grating with N_g grooves, so the coherent radiation is compressed into a narrow angular width but the total power is conserved. These effects are indicated schematically in Figure 5.

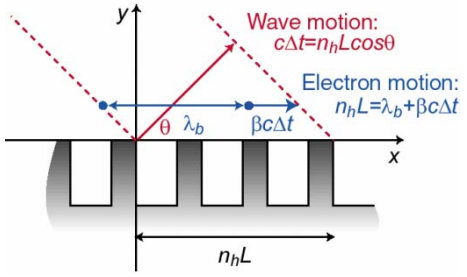

Figure 4. Coherent SP radiation is formed when successive bunches radiate in phase, where Δt is the time for a wave to catch up to the previous bunch.

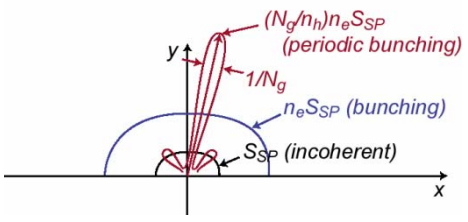

Figure 5. Incoherent and coherent SP radiation from a bunched electron beam.

For a numerical estimate of these effects we can use the parameters of Table I. The number of electrons in a bunch is on the order of

$$n_e = I_e \lambda_\infty / qc \tag{11}$$

where I_e is the total current in the electron-beam. For $\lambda_\infty = 920\ \mu$m this gives $n_e \approx 2\times10^4$, so if the electrons are perfectly bunched, the SP radiation is enhanced by this factor. Of course, even at saturation the bunching is less than perfect and the actual enhancement will be less than this. The number of periods in the grating is $N_g = 64$, so the angular spectral intensity at the peak of the second harmonic ($\lambda_{SP} \approx 460\ \mu$m) will be enhanced by the additional factor $N_g / n_h \approx 32$. But from the theory of van den Berg, the total power of the incoherent SP radiation emitted by this beam is on the order of a hundred nanowatts, so the coherent radiation should be on the order of a milliwatt at saturation. However, even with coherent enhancement, the SP radiation is still small compared with the power in the evanescent wave itself.

We can estimate the power in the evanescent wave at saturation by the following argument. The electrons continue to lose energy to the evanescent wave until they lose enough energy to drop out of synchronism. For small changes in energy, the change in the velocity of an electron is

$$\Delta\beta = \Delta\gamma / \beta\gamma^3 \tag{12}$$

and the phase shift in one gain length is

$$\Delta\phi = \frac{2\pi\Delta\beta}{\mu\beta\lambda_b} = \frac{2\pi\Delta\beta}{\mu\beta^2\lambda_\infty} \tag{13}$$

The total power lost by the beam is then

$$P = \frac{mc^2}{2\pi q} I_e \beta^3\gamma^3 \mu\lambda_\infty \Delta\phi \tag{14}$$

Saturation corresponds to $\Delta\phi = O(1)$. For the parameters in Table 1, the saturated power at 56 kV is on the order of a watt, which is much larger than the coherent SP radiation on the second harmonic of the evanescent wave.

When the group velocity is large, this power comes out from the evanescent wave at the ends of the grating. However, when the group velocity is sufficiently small, the power put into the evanescent wave by the electrons is lost by scattering from imperfections in the grating and by dissipation in the grating surface.

EXPERIMENT

At the present time, an experiment is being assembled to test these predictions. The parameters of the experiment are summarized in Table I, and a schematic diagram of the experiment is shown in Figure 6. The electron beam is emitted from the tip of a blunt needle illuminated by 3-ns pulses from the fifth harmonic of a Nd:YAG laser pulsed at 20 Hz [10,11]. The electron beam is focused by a solenoidal lens and aligned above the surface of the grating by two pairs of steering coils.

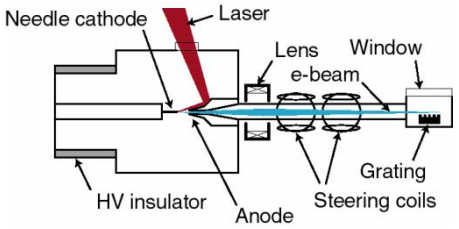

Figure 6. Schematic diagram of the experiment

The wavelength range of greatest interest is 400-1000 μm, as indicated in Figure 3, so a quartz window close to the surface of the grating can be used to provide a large collection solid angle. The radiation is detected using a liquid-He-cooled InSb bolometer, which is sensitive (above the noise level) to signals as small as nanowatts. Therefore, it should be possible to observe both the incoherent and coherent SP radiation. Measurements will be performed at voltages ranging from 45 to 65 kV, which spans the region of zero group velocity. It should be possible to observe the peak in the output power at the zero-group-velocity point, as well as the wavelength of the evanescent wave (about 930 μm) and the enhanced coherent emission at the second harmonic (around 420 μm).

CONCLUSIONS

The detailed theory of gain in a SP-FEL shows the importance of taking into account the dispersion relation for the evanescent wave. It has long been recognized that the electron velocity must be synchronous with the phase velocity in slow-wave devices, but in a SP-FEL the gain has a maximum near the condition where the group velocity vanishes. In a BWO, the output vanishes for this condition since the energy flows at the group velocity. However, in a SP-FEL an alternative source of output is provided by the coherent SP radiation at the harmonics of the evanescent frequency. Although this is radiated at lower power, the high gain makes it possible to envision low-current devices operating in cw mode with significant average power. In addition, if the group velocity is not too small, power from the evanescent wave can be directly coupled out from the ends of the grating. This would produce watts of average power from the device.

REFERENCES

1 S. J. Smith and E. M. Purcell, Phys. Rev. 92, 1069 (1953).
2 P. M. van den Berg, J. Opt. Soc. Am. **63**, 689 (1973).
3 P. M. van den Berg, J. Opt. Soc. Am. **63**, 1588 (1973).
4 P. M. van den Berg and T. H. Tan, J. Opt. Soc. Am. **64**, 325 (1974).
5 J. Urata, M. Goldstein, M. F. Kimmitt, A. Naumov, C. Platt, and J. E. Walsh, Phys. Rev. Lett. **80**, 516 (1998).
6 H. L. Andrews and C. A. Brau, Phys. Rev. ST-AB **7**, 070701 (2004).
7 A. Gover and P. Sprangle, IEEE J. Quantum Electron. **QE-17**, 1196 (1981).
8 L. Schaechter and A. Ron, Phys. Rev. **A 40**, 876 (1989).
9 K.-J. Kim and S.-B. Song, Nucl. Instr. Meth. **A 475**, 159 (2001).
10 C. Hernandez Garcia and C. A. Brau, Nucl. Instr. Meth. **A 475**, 559 (2001).
11 C. H. Boulware and C. A. Brau, "Photo-Field Emission from Needle Cathodes," proceedings of the 24th International Free-Electron Laser Conference, Argonne, Il, September 9-13, 2002.

EXPERIMENTAL DEMONSTRATION OF WAVELENGTH TUNING IN HIGH-GAIN HARMONIC GENERATION FREE ELECTRON LASER

T. Shaftan*, E. Johnson, S. Krinsky, H. Loos, J.B. Murphy, G. Rakowsky, J. Rose, B. Sheehy, J. Skaritka, X.J. Wang, Z.Wu, L.H. Yu, NSLS, BNL, Upton, NY 11973, USA

Abstract

Tunability is one of the key aspects of any laser system. In High-Gain Harmonic Generation Free Electron Laser (HGHG FEL) the seed laser determines the output wavelength. Conventional scheme of tunable HGHG FEL requires tunable seed laser. The alternative scheme [1] is based on compression of the electron bunch with energy-time correlation (chirped bunch) in the FEL dispersive section. The chirped energy modulation, induced by the seed laser with constant wavelength, is compressed as the whole bunch undergoes compression. In this paper we discuss experimental verification of the proposed approach at the DUV FEL [3,4] and compare experimental results with analytical estimates.

INTRODUCTION

High-gain FELs have been proposed as high peak power light sources for the short-wavelength range [5,6]. Ultrashort and powerful radiation pulses from VUV to X-ray provide a unique possibility for studying fast processes in a large variety of scientific applications. Output radiation coherence, stability and tunability are important measures of the FEL performance.

For an initially prebunched beam, i.e. when the beam density contains a coherent bunching at the FEL resonant frequency, the FEL radiation output preserves full longitudinal coherence. In this case FEL acts as an amplifier of the external seed. Due to the nonlinearity of the FEL process, not only the fundamental harmonic can be amplified, but the higher harmonics too. This allows for frequency multiplication and generation of radiation in VUV and X-ray wavelength regions [7,8].

Seeding by an external source offers an opportunity to control the output pulse properties by controlling the shape of the input seed pulse. State-of-the-art conventional lasers are capable of providing ultra-short pulses with high peak power. Using the Harmonic Generation (HG) approach, one can shift and amplify the seed laser pulse in the short-wavelength region, preserving the flexible temporal format of the seed and generating short radiation output. Important benefits of seeded HG scheme are high stability, control of the central wavelength and small energy fluctuations due to stable input from the seed laser.

In HGHG scheme (Fig. 1), a coherent seed at a subharmonic wavelength of the desired output radiation interacts with the electron beam in an energy-modulating section. The energy modulation is then converted into spatial bunching as it traverses a dispersive section. In the second undulator (the radiator), which is tuned to a higher harmonic of the seed radiation, the microbunched electron beam first emits coherent radiation and then amplifies it exponentially until reaching saturation.

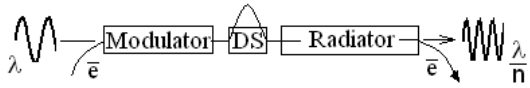

Fig.1: High Gain Harmonic Generation scheme

The seed laser determines the central wavelength of HGHG FEL. Therefore, as generally understood, to tune the wavelength of the seeded FEL, the seed laser should be tunable. An alternative technique for the tunable HGHG FEL [2,1] utilizes a seed with fixed wavelength. The essence of this technique is in the compression of the chirped electron bunch in the HGHG dispersive section. Since the whole beam undergoes compression, the laser-induced modulation along the bunch also must be compressed with the same compression factor. Therefore prebunched electron beam enters the radiator with a new bunching wavelength. Changing the value of the energy chirp allows for a smooth tuning of the FEL output wavelength.

In this paper we present and discuss the experimental verification of this technique. In the experiment at the Deep Ultra Violet Free Electron Laser (DUV FEL, BNL) we have demonstrated tuning of the HGHG output around wavelength of 265 nm.

EXPERIMENT

In order to test new approach we performed an experiment at the DUV FEL (Fig. 2). The DUV FEL parameters are listed in Table 1.

For a phase offset $\Delta\varphi_{ch}$ the energy chirp h is given by the following expression [5]:

$$h = \frac{1}{E}\frac{\partial E}{\partial z} = -\frac{2\pi}{\lambda_{RF}}\frac{E_{ch}\sin(\Delta\phi_{ch})}{E_0 + E_{ch}\cos(\Delta\phi_{ch})}, \quad (1)$$

where E is the energy, z is longitudinal coordinate, λ_{RF} is RF wavelength, E_{ch} is amplitude of the chirping tank and E_0 is energy of the beam entering chirping tank.

The compression ratio for a chirped beam is:

$$C = \frac{\sigma_{out}}{\sigma_{in}} \approx 1 - R_{56}h, \quad (2)$$

The wavelength detuning due to compression is given by (3) [1].

$$\frac{\Delta\lambda}{\lambda} = \frac{\lambda_C - \lambda_0}{\lambda_0} = R_{56}\cdot h, \quad (3)$$

* Corresponding author: shaftan@bnl.gov

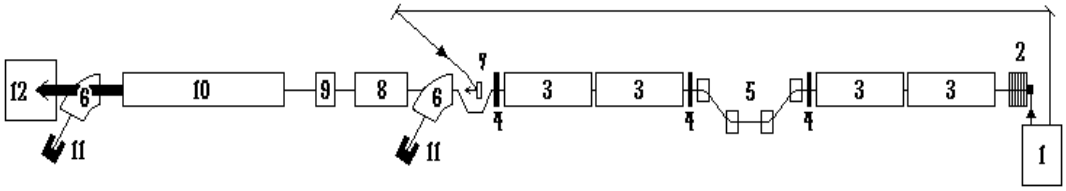

Fig. 2: The DUVFEL layout. 1 – gun and seed laser system, 2 – RF gun, 3 – linac tanks, 4 – focusing triplets, 5 – magnetic chicane, 6 – spectrometers dipoles, 7 – seed laser mirror, 8 – modulator, 9 – dispersive section, 10 – radiator, 11 – beam dumps, 12 – FEL radiation measurements area.

Beam energy, MeV	175
Seed laser wavelength, nm	800
Seed laser Raleigh range, m	2.4
Harmonic number	3
Radiator period, m	0.0389
Radiator length, m	10
Modulator length, m	0.8
Modulator period, m	0.08
Maximum R_{56} of DS, mm	-0.34
Bunch length (RMS), ps	0.5
HGHG pulse length (RMS), ps	0.5

Table 1: DUV FEL parameters

Using parameters from Table 1 together with expressions 1 and 3 we obtain the detuning of 0.37% for the phase offset of 33 degrees in the chirping tank. Changing sign of the chirp causes decompression of the energy modulation in the electron beam ($C>1$ in (2)) and, in turn, detuning towards longer wavelengths. Thus, for a symmetric chirp tuning range from +33° to -33° we calculate the DUV FEL tunability range of 0.74% or 2 nm around the nominal wavelength of 266 nm.

At the beginning of the experiment we minimized the projected energy spread in the beam canceling the energy chirp. The energy chirp has been measured by an energy spectrometer. The dispersion section current has been set to a maximum value, corresponding to the R_{56} value of -0.34 mm.

In the experiment we varied the phase of the last linac tank (tank 4 on Fig. 2), measuring HGHG spectrum for each value of the tank RF phase. The measured single-shot spectra are shown in Fig. 3. The nominal value of central wavelength for the beam without chirp has been measured as 265 nm. The overall wavelength tuning range is measured of about 1% (from 263.4 nm for -45° to 266.1 nm for 25° in RF phase).

Fig. 4 shows the dependence of the HGHG central wavelength versus energy chirp h. The first linear fit (solid line) is based on the expression 3, taking into account the R_{56} of the dispersion section. As it follows from the Figure, there is obvious disagreement between measured data and the fit. For a second linear fit (dashed line) we included dispersion in the radiator (R_{56}=-0.162 mm) into expression 3. In this case measurement is in a good agreement with calculation. This implies that the additional wavelength compression takes place in the radiator. The error bars in Fig. 4 correspond to the HGHG line width determined from the measured spectra.

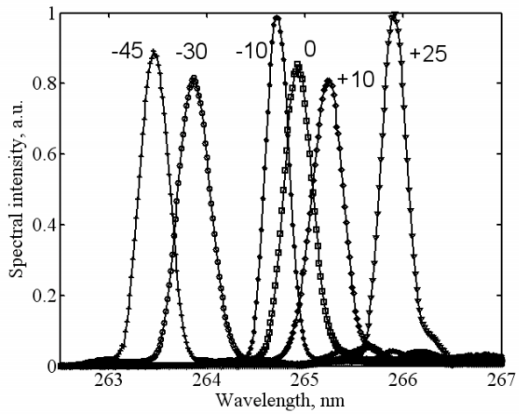

Fig. 3: Measured single-shot spectra for different values of energy chirp (phase offset from left to right: -45°, -30°, -10°, 0°, +10°, +25°).

At the DUV FEL the seed radiation is stretched out of approximately 100 fs long pulse with a bandwidth of 5.6 nm at 800 nm (Ti:Sapphire laser). The frequency-tripled seed pulse is 3 ps (RMS) long and contains wavelength chirp of 0.31 nm/ps at 266 nm. In Fig. 5 we compare the wavelength chirp in the DUV FEL seed laser with the energy chirp in the electron beam. For comparison we plot the chirped electron beam (bunch length of 1 ps, chirp is 11 m^{-1}) on the same figure, assuming that electron beam energy corresponds to the plot ordinate via expression for the FEL resonant wavelength. As follows from the plot, another way to achieve the wavelength detuning in our experiment would be by using the wavelength chirp in the seed laser pulse. In this case the electron bunch can be delayed (or expedited) in time and, therefore, would interact with a different local wavelength of the seed pulse. As the plot shows, measured tunability range of 1 % exceeds the seed laser bandwidth. Besides, in order to achieve the observed

maximum detuning range, electron beam must be shifted by more than 3 ps (Fig. 5). We note that laser-to-beam synchronization has been kept constant during our experiment. Thus, observed wavelength detuning is due to the compression of the chirped electron bunch in the FEL dispersive section.

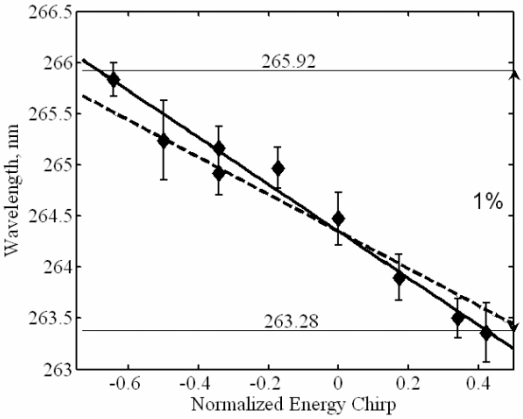

Fig. 4: Measured dependence of the HGHG central wavelength on the normalized energy chirp. Error bars represent measured single-shot HGHG linewidth. Tunability range of one percent lies between horizontal lines. First fit (dashed line) is calculated based on the DS calibration. Second fit (solid line) takes into account dispersion in the radiator.

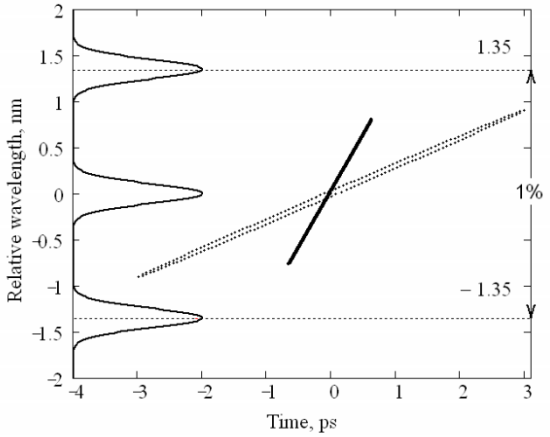

Fig. 5: Representation of the seed laser (dashed ellipse) and electron beam (solid) in wavelength (ordinate) – time (abscissa) coordinates. Tunability range of one percent lies between horizontal dotted lines. Measured tunability range exceeds the seed laser bandwidth.

CONCLUSION

In the experiment described in this paper we demonstrated control over HGHG FEL central wavelength. The precision of the positioning the central wavelength is, in general, a small fraction of the FEL bandwidth. This shows that we can tune the output photon energy with a high accuracy.

We performed wavelength tuning by changing only two parameters, linac section amplitude and phase. In contrast, when changing the seed laser wavelength, one has to change the seed laser set-up followed by optimization of the FEL set-up for new photon energy. The described method brings a simplification of the FEL tuning.

Demonstrated tuning range of one percent is below capabilities of modern lasers that can be used as a seed in HGHG FEL. In our experiment we were limited by the available dispersive section strength. Straightforward upgrade of the DUV FEL dispersive section is in progress. In this case we expect to increase the tuning range up to about 3 percent (it depends on the value of sliced energy spread that is not well known yet).

However, this is still not a limit. A special modification of the DUV FEL magnetic system [1] would increase the tunability range to ~20 %. The optimized HGHG scheme includes the secondary RF system located before and after FEL dispersive section. First RF section imparts a chirp in the beam, which, being compressed in DS, gets unchirped in the second RF section. Therefore chirp is provided only locally and, since it does not affect an FEL dynamics, can be made very large. In turn, this will provide a large wavelength tuning range.

Since the developed method can be used around any of HGHG harmonics (e.g. 4^{th}, 5^{th}, etc.), DUV FEL can be made tunable over a large wavelength range, having seed laser wavelength fixed.

ACKNOWLEDGEMENTS

We would like to thank M. Lehecka, V. Litvinenko, S. Mihailov, I.Pinayev and Y. Wu for their help with OK-4 dispersive section. The work was performed under DOE contract DE-AC02-98CH10886.

REFERENCES

[1] T. Shaftan and L.H. Yu, BNL-720-34-2004-JA, Feb. 2004 and submitted in Phys. Rev. E.
[2] S. Biedron, H. Freund and S. Milton, Nucl. Instrum. Methods Phys. Res. A **475**, p. 401
[3] L.H. Yu, A. Douyran, L. Di Mauro, *et al.*, Phys. Rev. Lett. **91**, No. 7, 074801-1, (2003).
[4] L. Di Mauro, A. Doyuran, E. Johnson, *et al.*, Nucl. Instrum. Methods Phys. Res. A **507**, 15 (2003).
[5] SLAC Report No. SLAC-R-593, edited by J, Galayda, 2002
[6] V. Ayvazyan et al., Phys. Rev. Lett. **88**, 104802 (2002).
[7] L.H. Yu *et al.*, Phys. Rev. A **44**, 8178 (1991)
[8] I. Ben-Zvi *et al.*, Nucl. Instrum. Methods Phys. Res., Sect. A **304**, 181 (1991).

SPECTRAL PHASE MODULATION AND CHIRPED PULSE AMPLIFICATION IN HIGH GAIN HARMONIC GENERATION

Z. Wu, H. Loos, Y. Shen, B. Sheehy, E. D. Johnson, S. Krinsky, J. B. Murphy, J. Rose, T. Shaftan, , X.-J. Wang, L. H. Yu, NSLS, Brookhaven National Laboratory, Upton NY, USA 11973

Abstract

Amplitude and phase measurements are conducted on the 266 nm output of the DUVFEL laser at the National Synchrotron Light Source (NSLS) at Brookhaven National Laboratory. With the FEL operating in High Gain Harmonic Generation (HGHG) mode, we have studied narrow-bandwidth HGHG output, and observe pulses near the transform limit. We have also chirped both the electron bunch energy and the seed pulse wavelength, and successfully imposed a linear chirp on the HGHG output. These results demonstrate the potential to generate short harmonic pulses through chirped pulse amplification [1] or coherently shape FEL output.

INTRODUCTION

In High Gain Harmonic Generation [2] operation of an FEL, a coherent optical seed pulse at a subharmonic of the resonant FEL output wavelength is used to impose a coherent microbunching of the electron bunch before it enters the radiator. This permits rapid saturation of the harmonic output over short distances, and the possibility of reaching X-ray wavelengths by cascading the process through a relatively small number of stages [3].

An important advantage of this scheme is the longitudinal coherence of the harmonic output. Longitudinal coherence in itself is important for many experimental applications of short pulse X-rays, but it also presents the possibility of achieving femtosecond pulses through chirped pulse amplification (CPA) [1], and shaping short-wavelength pulses on ultrafast time scales.

Pulse-shaping techniques developed for ultrafast laser systems allow complex modulations limited essentially only by the available bandwidth of the pulse. Manipulating optical interactions with such pulses yields unprecedented control over dynamics, and such 'quantum control' been demonstrated in a multitude of systems [4]. In principle, such techniques could be extended all the way down to X-ray wavelengths by seeding an HGHG cascade with a shaped seed pulse. The question then becomes what role noise or distortion introduced by HGHG will have on the shaping capabilities. For this reason, it is useful to consider the full "HGHG transfer function", and measure both the amplitude and phase of the output pulse as a function of the modulation of the seed pulse. This should also have an added benefit as an FEL diagnostic, since modulations introduced by HGHG are likely to be sensitive functions of electron bunch characteristics and radiator dynamics.

In this work, we study the simplest pulse shape: a linear frequency chirp. This is an important test of the feasibility of CPA. If a linear chirp can be imposed on the HGHG output, a dispersive line could compress it to pulse widths much shorter than the electron bunch length. A theoretical study of this process predicts achievable pulse widths of 4 fsec in X-ray FELs [1]. We demonstrate amplitude and phase measurements of HGHG, using spectral phase interferometry for direct electric field reconstruction (SPIDER) [5]. This is the first time that SPIDER has been reported for wavelengths this short. We examine first the narrow bandwidth emission produced by HGHG using an unchirped electron bunch, and a nearly-monochromatic seed. We then chirp both the frequency of the seed pulse and the energy of the electron bunch, and measure the chirp imposed on the HGHG output. Finally we discuss the implication for effective pulse compression.

EXPERIMENTAL SETUP

SPIDER

The SPIDER technique, developed by Walmsley and coworkers [5], is an interferometric technique for recovering the amplitude and phase of an ultrafast pulse. Its principal advantages in FEL applications are that a well-characterized reference pulse is not needed, and a rapid inversion algorithm that makes shot to shot measurements possible. We use a variant here known as down-conversion SPIDER [6]. A diagram of our implementation of the technique is shown in Fig. 1. Light from the seed pulse at 800 nm is separated from the 266 nm HGHG output and stretched in a grating compressor to a pulse width of 55 psec FWHM, to serve as the shearing pulse. The 266 nm pulse passes through a Michelson interferometer, which splits it into two

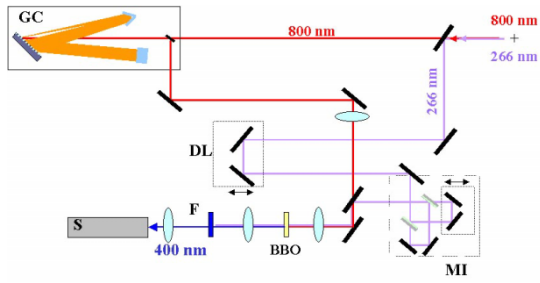

Fig 1. SPIDER implementation for measurement of 266 nm HGHG pulses. **GC**, grating compressor; **DL**, delay line; **MI**, Michelson interferometer, **BBO**, crystal for down-conversion; **F**, filter, **S**, spectrometer. For calibration, the 800 nm beam is blocked and filter **F** is removed.

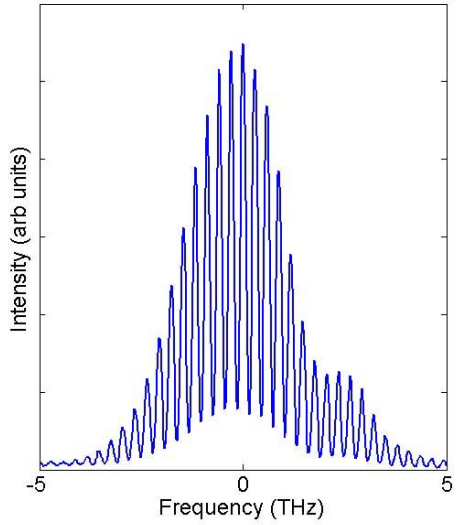

Fig. 2 SPIDER trace from a chirped HGHG pulse.

identical replicas with a delay of τ = 3.5 psec between them. Both 266 nm replicas are mixed with the chirped shearing pulse in a 250 μm thick BBO crystal, which is phase-matched for down-conversion to 400 nm (θ=44.7 deg. Type I). They each see a nearly monochromatic slice of the long shearing pulse, with a frequency difference $\Omega = \tau\beta_{ref} = 0.2$ THz, where β_{ref} = 0.06 THz/psec is the frequency chirp of the shearing pulse. The two 400 nm replicas produced in the down-conversion are thus shifted in frequency by Ω and, as phase is preserved in the down-conversion, a frequency component ω in one of the replicas carries the same phase information from the parent pulse as the $\omega+\Omega$ component in the other replica. Hence by interfering the two pulses, the phase difference between $(\omega,\omega+\Omega)$ frequency pairs may be measured and the spectral phase variation over the entire pulse determined.

Fig. 2 shows a SPIDER interferogram trace. In the absence of the spectral shear (Ω=0), the fringe spacing would be just $1/\tau$. The phase variation across the pulse spectrum is manifested in variations from this spacing. Abstracting this "carrier phase" from the measurement is a recurring problem in spectral interferometry, of which SPIDER is a special case. Dorrer [7] notes that such measurements are very sensitive to calibration errors in the spectrometer, and that this problem is often avoided in SPIDER by generating a calibration with Ω=0, while maintaining a spectrometer configuration identical to that used in the measurement. The effect of the spectrometer error is then largely canceled by subtraction of the calibration from the measurement. He also notes, and it has been experimentally demonstrated [6] that, if the ratio of parent and converted pulse wavelengths is an integer, then an identical spectrometer configuration can be maintained by using different grating orders for the calibration and the measurement. In fact, a slightly less restrictive condition holds: if these wavelengths are both harmonics of a third wavelength, the same can be done. Thus, here we set the spectrometer (a 320 mm focal length Jobin-Yvon TRIAX, using a 2400 line/mm grating) to a center wavelength of 800 nm, and measure the 400 nm SPIDER trace in second order. The calibration is made by interfering the 266 nm parent pulses directly, and measuring in third order.

For the inversion, we follow the procedure of Iaconis and Walmsley [8] to obtain the phase. The spider trace is fourier-transformed, filtered with a fourth-order supergaussian centered at $t = \tau$, with a 1/e half-width of 1.5 psec, and back-transformed to the frequency domain. This phase is unwrapped, the calibration phase subtracted, and the result concatenated to obtain the spectral phase of the test pulse. The amplitude is obtained from a similar procedure [9], using the $t = 0$ component of the transformed SPIDER trace. With the field fully specified in the frequency domain, the temporal profile, frequency chirp, etc, can be obtained after transforming into the time domain.

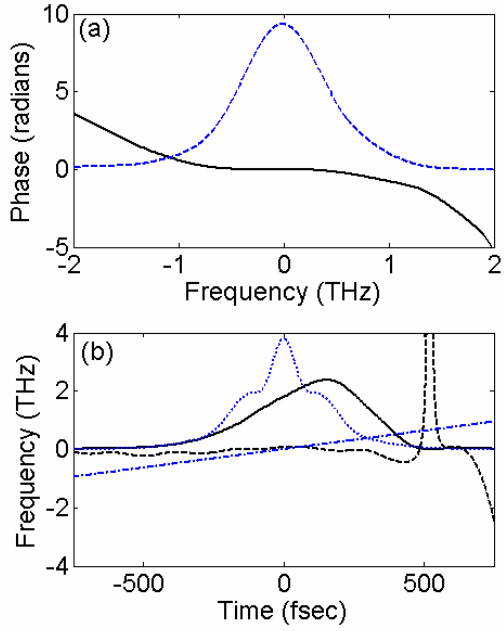

Fig. 3 Spectral and temporal characteristics of an unchirped HGHG pulse, retrieved from SPIDER. Intensity profiles are plotted in arbitrary units. (a) Spectral intensity (dashed), spectral phase (solid). (b) instantaneous frequency (dashed) , 3 times the residual frequency chirp of the 6 psec seed laser (dash-dot), intensity (solid), transform limited intensity (phases set to zero, dotted line)

HGHG

The Brookhaven DUVFEL operation in HGHG mode is fully described elsewhere [10]. A 170 MeV, 300 pC electron bunch is generated using a BNL GUN-IV

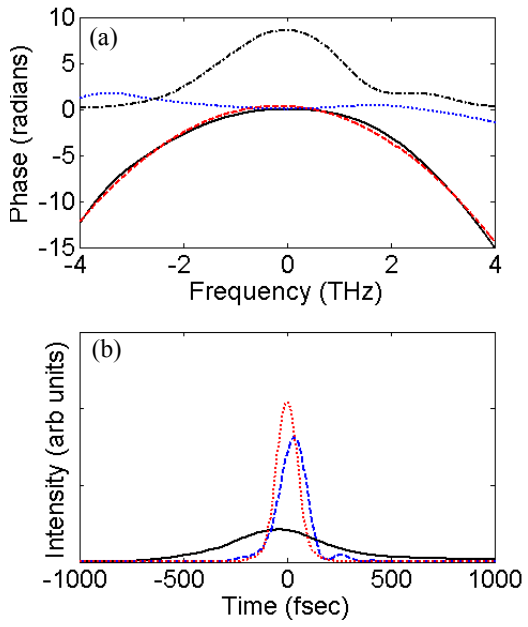

Fig. 4 Spectral and temporal characteristics of a chirped HGHG pulse, retrieved from SPIDER. (a) Spectral intensity (dash-dot), spectral phase (solid), 2nd order polynomial fit to spectral phase (dashed), spectral phase with quadratic component subtracted (dotted). (b) intensity profile (solid) , intensity with quadratic phase component subtracted (dashed), transform-limited intensity (dotted)

photoinjector followed by a 4-stage linear accelerator. A magnetic chicane compressor after the first two linac stages permits the compression of the electron bunch down to ~1 psec FWHM. Varying the phase of the third and fourth linac stages permits the imposition of an energy chirp on the bunch. Following the linac, the electron bunch energy is modulated using a synchronized optical seed pulse in a 1-meter undulator, which is resonant at the seed pulse wavelength of 800 nm. The seed pulse is derived from the same laser that drives the photoinjector, and its chirp is adjusted by varying its length in a grating compressor. Following a dispersive section, the coherently microbunched beam enters the 10-m NISUS wiggler, which is resonant at the third harmonic of the seed. Both the 266 nm third-harmonic HGHG output and the 800 nm seed propagate to the SPIDER set-up shown in Fig 1.

RESULTS AND DISCUSSION

We first examine narrow bandwidth HGHG (0.12% relative bandwidth rms), with no chirp. For this, the seed pulse was stretched to 6 psec in length (FWHM), and the electron beam parameters were optimized to minimize the HGHG bandwidth. Fig. 3 shows typical data, obtained from SPIDER from a single HGHG shot. In the first panel the spectrum and spectral phase variation are shown. The second panel shows the temporal profile of the pulse obtained by Fourier-transforming the data in the first panel, as well the instantaneous frequency of the pulse as a function of time. The center frequency is subtracted for clarity. The frequency is essentially flat over the length of the pulse, with some distortion towards the trailing end and in the wings. The chirp of the seed pulse, multiplied by the harmonic number n=3 of the HGHG process, is shown for reference. Because the electron beam is not chirped, we do not expect to see the chirp reflected in the HGHG output.

The flat phase profile indicates that the pulse is nearly transform-limited. The pulse shape does deviate significantly from a Gaussian though. The time bandwidth product is $\sigma_\omega\sigma_\tau = 0.9$, or 1.8 times the transform limit for a Gaussian pulse. However, if we set the spectral phase identically to zero, and take the calculated temporal profile as the transform limit, then the width (rms) of the measured profile is only 20 % larger than the transform-limited width, $\sigma_\tau/\sigma_{TL} = 1.2$. For a 50 shot sample, we obtain $\sigma_\omega\sigma_\tau = 1.15 \pm 0.15$ and $\sigma_\tau/\sigma_{TL} = 1.4 \pm 0.1$.

In order to obtain a chirped HGHG pulse, it is necessary to chirp the energy of the electron bunch so that the resonant frequency at each point along the bunch is equal to the third harmonic of the instantaneous seed frequency, i.e, the resonant frequency chirp must be 3 times that of the seed pulse. This is done by running the

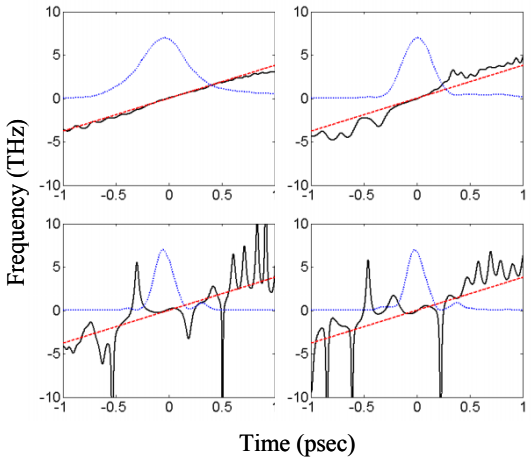

Fig. 5 Time-dependent frequency for several chirped HGHG pulses. The data in the first panel are for the shot represented in Fig 4. The curves are instantaneous frequency (solid), theoretical chirp (dashed, see text), and the intensity profile (dotted)

third and fourth linac tanks off-crest, and incompletely compensating the chirp imposed for bunch compression

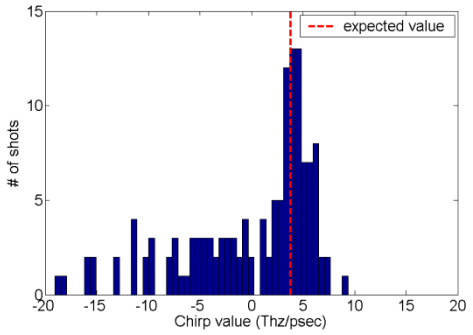

Fig. 6 Distribution of frequency chirp values measured in a 200 fsec window around the center of a set of 136 HGHG pulses. The dashed line indicates the chirp expected to be imposed by the chirped seed pulse

(using both tanks reduces the effect of rf curvature).

Due to technical problems during the experimental run, we were only able to match the electron and seed chirps to within 40%. The 800 nm seed pulse is 2 psec long FWHM, with a bandwidth of 5.4 nm FWHM, and a chirp of 1.27 THz/psec. The corresponding chirp to be imposed on the HGHG output is then β_{266}= 3.8 THz/psec, but the energy chirp imposed on the electron bunch corresponded to a resonant frequency chirp of only 2.7 THz/psec. We find however, that the seed chirp is still clearly observable in the HGHG output.

Fig. 4 shows the recovered spectrum, phase and temporal information for a single shot. A parabolic spectral phase indicates a linear frequency chirp. Panel (a) shows the spectrum, the spectral phase, a parabolic fit to the phase, and the resultant phase when the quadratic component of the phase is subtracted off. Panel (b) shows the temporal profile as measured, the transform-limited profile (obtained by setting the spectral phase identically to zero), and the temporal profile that would obtain if the quadratic part of the phase were removed. The latter is to simulate the temporal profile expected after putting the pulse through the appropriate compressor. We define the compression ratio as the ratio of the as-measured rms pulse width to the rms pulse width of this distribution.

The instantaneous frequency may be defined as the first derivative of the temporal phase, and the chirp is then the second derivative. Both may be obtained from the data, and the frequency vs time is displayed for several shots, along with their respective temporal profiles, in Fig. 5. The center frequency is subtracted for clarity, and the theoretical curve represents a constant chirp of 3 times the seed pulse chirp. The first shot displayed in Fig. 5 is for the same shot represented in Fig. 4., and shows a near-constant chirp over the length of the pulse. The compression ratio for this pulse is 3.2, and, as is clear from Fig. 4(b), the compressed pulse would be close to the transform limit. More typical shots are shown in the subsequent panels. The strong phase variation in the wings destroys the compressibility for most of the pulses, but a chirp near the expected value is usually observed near the peak of the pulse. If we simulate a single compressor for all pulses by extracting the same quadratic component from the phase as for the shot in Fig 4, we find that, for 136 pulses measured, 20, or 15%, would show some compression. However, if we fit the chirp in a 200 fsec window about the peak of the pulse we find that the distribution of chirp values (Fig. 6) is peaked about the expected value β_{266} .

The shot-to-shot fluctuations in compressibility probably arise from a combination of the mismatch of electron bunch and optical seed chirps, the 150 fsec (rms) synchronization jitter between the electron bunch and seed pulse, and fluctuations in the electron bunch compression that were due to technical problems during the experiment. The latter two, coupled with the nonlinearity of the electron bunch chirp due to rf curvature, can lead to emission effectively occurring over only a fraction of the electron bunch. Supporting this interpretation is a strong positive correlation observed between the pulse width of the HGHG pulse and the compression ratio.

While the control of these factors will be necessary for a practical implementation of chirped pulse amplification in high gain harmonic generation FEL systems, the observation of compressible pulses in the present work, does demonstrate the viability of the technique, and the potential for more complex shaping at short wavelengths.

ACKNOWLEDGEMENTS

The work was performed under DOE contract DE-AC02-98CH10886.

REFERENCES

[1] L. H. Yu, E. Johnson, D. Li, and D. Umstadter Phys. Rev. E **49**, 4480-4486 (1994)
[2] L. H. Yu Phys. Rev. **A 44,** 5178-5193 (1991); L. H. Yu et al. Phys. Rev. Lett. **91**, 074801 (2003);
[3] L. H. Yu, in Proceedings of the X-Ray FEL Theory and Simulation Codes Workshop *SLAC* Stanford University Sep 23-24, (1999)
[4] For a recent review, see D. Goswami, Phys. Rep. **374,** 385–481 (2003)
[5] C. Iaconis and I. A. Walmsley, Opt. Lett. **23**, 792–794 (1998).
[6] P. Londero *et al* J. Mod. Opt. **50**, 179 (2003)
[7] C. Dorrer. J. Opt. Soc. Am **B 16**, 1160–1168 (1999).
[8] C. Iaconis and I. A. Walmsley, IEEE J. Quant. Elect.. **35**, 501 (1999)
[9] A. Muller and M. Laubscher, Opt. Lett. **26**, 1915 (2001).
[10] A. Doyuran et al Phys Rev ST AB **7**, 050701, (2004)

STUDY OF COHERENCE LIMITS AND CHIRP CONTROL IN LONG PULSE FEL OSCILLATOR

Y. Socol, A. Gover, A. Eliran, M. Volshonok
Dept. of Physical Electronics – Faculty of Engineering, Tel Aviv University, Tel-Aviv, Israel
Y. Pinhasi, B. Kapilevich, A. Yahalom, Y. Lurie, M. Kanter, M. Einat, B. Litvak
Dept. of Electrical and Electronic Engineering – The College of Judea and Samaria, Ariel, Israel

Abstract

Electrostatic Accelerator FELs (EA-FELs) have the capacity to generate long pulses of tens microseconds and more, that in principle can be elongated indefinitely (CW operation). Since a cold beam FEL is by nature a "homogeneously broadened laser", EA-FEL can operate, unlike other kinds of FELs, at a single longitudinal mode (single frequency). This allows the generation of very coherent radiation. The current status of the Israeli Tandem Electrostatic Accelerator FEL (EA-FEL), which is based on an electrostatic Van de Graaff accelerator, allows the generation of pulses of tens microseconds duration. It has been operated recently past saturation, and produced single mode coherent radiation of record narrow inherent relative line width $\sim\Delta f/f = 10^{-6}$ at frequencies near 100 GHz. A clear frequency chirp is observed during pulses of tens of microseconds (0.3-0.5 MHz/μs). This is essentially a drifting frequency pulling effect associated with the accelerator voltage drop during the pulse. We report experimental studies of the spectral line width and chirp characteristics of the radiation, along with theory and numerical simulations, carried out using space-frequency model, matching the experimental data.

INTRODUCTION

The Israeli Electrostatic Accelerator FEL was relocated to Ariel and returned to operation a year ago. Peak power of 150W usable radiation was previously reported [1].

RADIATION MEASUREMENTS

The mm-wave radiation is transported to the user's rooms by means of a corrugated over-moded waveguide. The measurements were performed by two means: a) using W-band detector Millitech –DXP-10; b) using heterodyne mixer of Hughes-47496H-100 with local oscillator (LO) from a HP-8797D Network Analyzer. In both cases, Tektronix –TDS-784A oscilloscope was used to monitor the output. The input signal was attenuated in order to cope with the dynamic range of the detectors. The maximal peak power at the user location was measured to be 1200W.

SINGLE MODE OPERATION AND CHIRP

In most measurements single mode lasing was observed after a short mode competition period. This is expected because of the "homogeneous broadening" nature of FEL in the cold beam regime. The detector, operating at

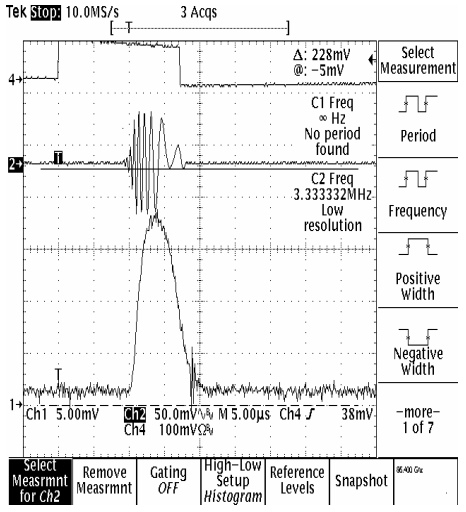

Figure 1(a)

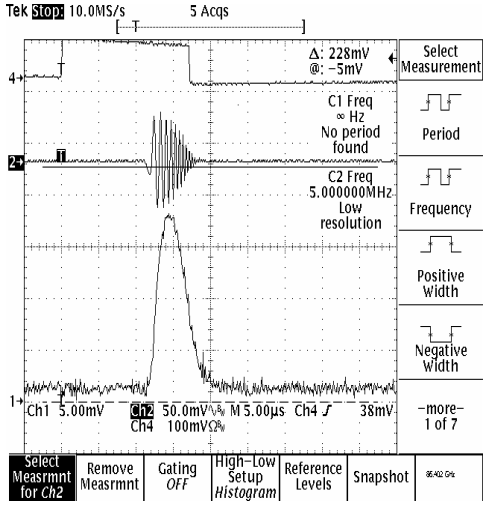

Figure 1 (b)

Figure 1: Typical oscillograms of the radiation. Middle line: heterodyne (IF) output. Lower line: W-band detector output. The local oscillator (LO) frequency f_{LO} is set very close to laser frequency: a) f_{LO}=86,400MHz – the IF frequency decreases with time; b) f_{LO}=86,402MHz – IF increases with time.

square-law detection scheme produces on the scope the difference (beat) intermediate frequency:

$$f_{IF} = f - f_{LO} \qquad (1)$$

there is no distinction in the measurement between negative and positive frequencies, and what is seen on the scope is a signal of frequency $|f_{IF}|$.

In all measurements the IF signal exhibited either negative or positive chirp (Fig. 1). To determine the chirp direction of the laser signal, one should notice that if the laser signal has negative chirp (f drops down with time) the IF signal would also exhibit negative chirp only when $f>f_{LO}$ and would exhibit positive chirp when $f<f_{LO}$.

Fig. 1 shows typical oscillograms of the radiation. The heterodyne mixer frequency was set at two close frequencies: (a) 86,400MHz and (b) 86,402MHz, enabling the accurate determination of the single mode radiation frequency ($f_m = 86.401 \pm 1 MHz$), and confirming negative direction of the laser chirp.

At heterodyne (local oscillator – LO) frequency 86,400MHz, the intermediate frequency (IF) decreases with time. At 86,402MHz – increases with time.

This behaviour of the IF signal indicates that the laser radiation exhibits a down shift frequency chirp. This effect is associated with the drift of the gain curve due to the beam energy drop during the pulse, and can be explained as time varying "frequency pulling" effect of the laser oscillator. A theoretical analysis of this effect was provided in on earlier publication [2].

CHIRP ANALYSIS

In order to analyze the chirp, we performed the so-called I/Q analysis (Fig. 3). The obtained oscilloscope signal (Fig 2.a) was multiplied by $sin(\omega_0 t)$ and $cos(\omega_0 t)$, with ω_0 corresponding to an arbitrary chosen frequency (169.0MHz at Fig. 2a). These multiplied signals I and Q were subjected to slow-pass filters (LPF) of 15MHz bandwidth. Then, amplitude $I^2 + Q^2$ (Fig 2,b) and phase deviation were extracted, and the frequency deviation $\Delta f(t) = f - f_0$ Eq. (2) was obtained as the deviation time derivative of the phase deviation:

$$\Delta f(t) = \frac{1}{2\pi}\frac{d}{dt} arctg\left[\frac{Q(t)}{I(t)}\right] \qquad (2)$$

To obtain the inherent spectrum width of the laser radiation (which we define as the linewidth of the wave when the spectral broadening due to the chirp is eliminated), we performed time-stretching. Namely, as the signal was approximated as $sin((\omega_o + \omega_1 t)t)$, the time was transformed as $t' = t(1 + t f_1 / f_0)$, with the chirp rate f_1=0.35MHz/μs as follows from the data (Fig 2.d). The Fourier spectrum of the transformed signal is shown in Fig 2.c, exhibiting inherent spectral linewidth (FWHM) of 0.2MHz (in comparison with 2.0MHz FWHM of the original chirped signal spectrum).

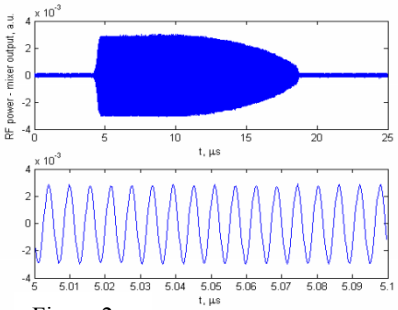

Figure 2a

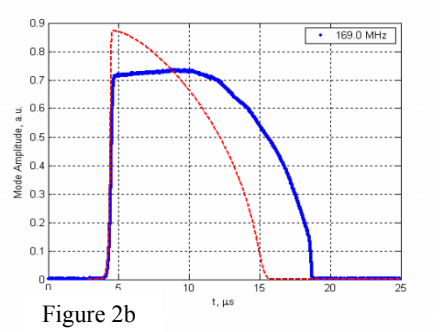

Figure 2b

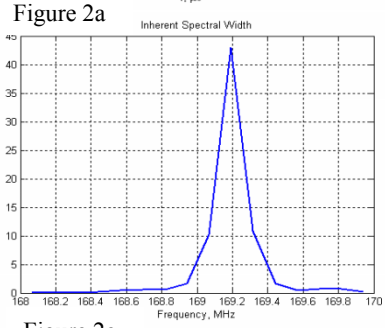

Figure 2c

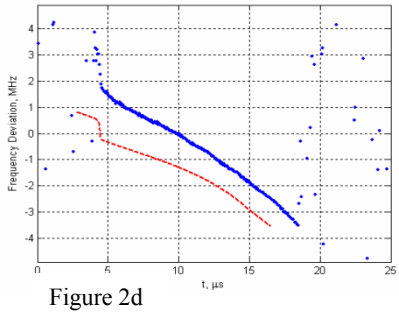

Figure 2d

Figure. 2: I/Q analysis of the oscilloscope signal – low-pass filter is set to 15 MHz band width. Fig. 2a: original oscillogram. Fig. 2b: mode amplitude (blue line-experimental data, red line FEL 3D calculations). The mode frequency is 83,669.0 MHz. Fig. 2c: inherent spectral width, nearly pulse-time-limited (the limit is 0.1 MHz). Since the actual chirp is non-linear in time, the spectrum is wider (0.2 MHz). Fig. 2d: frequency deviation obtained as phase deviation time derivative (blue line-experimental data, red line FEL 3D calculations). The chirp rate is approximately 0.35 MHz/μs

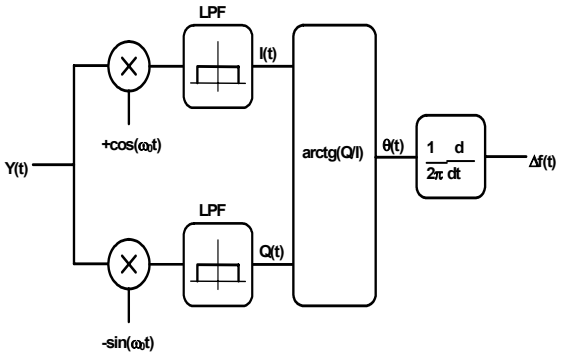

Figure. 3: I/Q analysis block-scheme of the intermediate frequency oscillograms.

Since the actual chirp is a little non-linear in time in the ends of the pulse, the spectrum width is somewhat higher than the pulse-duration-limited value (0.1MHz).

We analyze here the chirp effect in terms of the basic theory of frequency-pulling in laser oscillators [3]. In our case this frequency pulling shift varies with time (chirps) due to the drift of the gain curve associated with the accelerator voltage drop during the pulse. Namely, for resonator eigenmode frequency f_m, resonator mode linewidth (FWHM) $\Delta f_{1/2}$, maximum gain frequency f_{max} and gain bandwidth Δf the pulled oscillation frequency f is [3]:

$$f - f_m = (f_{\max} - f_m) \cdot \Delta f_{1/2} / \Delta f \qquad (3)$$

During the pulse, f_0 drifts towards lower frequencies (due to the accelerating voltage drop) with the rate

$$\frac{df_{\max}}{dt} = C\frac{dV}{dt} \qquad (4)$$

where:

$$C = \frac{e}{mc^2}\frac{df_{\max}}{d\gamma}\frac{\Delta f_{1/2}}{\Delta f} \qquad (5)$$

is the maximum gain frequency sensitivity to voltage drop (see e.g. [4]).

$$f_0 = \frac{\gamma_{z0}^2 \beta_{z0} c}{2\pi} \cdot \left(k_w + \frac{\bar{\theta}_{\max}}{L_w}\right) \cdot \left[1 + \sqrt{\beta_{z0}^2 - \frac{(2\pi f_{co})^2}{\left[\gamma_{z0}\left(k_w + \bar{\theta}_{\max}/L_w\right)c\right]^2}}\right] \qquad (6)$$

where:

$\bar{\theta}_{\max}$ - the maximal gain of detuning parameter

f_{co} - the cut off frequency of the resonator waveguide

For our operating regime we evaluated C=156MHz/kV. Synchronism width Δf (FWHM of the FEL gain) was calculated using FEL3D software [5] and yielded Δf= 6.0GHz. The resonator eigenmode linewidth $\Delta f_{1/2}$ was measured (in "cold" resonator) to be $\Delta f_{1/2}$=16MHz (Q-factor of $5 \cdot 10^3$ at 86GHz). The voltage drop rate was measured to be 0.7kV/μs. The chirp rate df/dt is therefore df/dt = 0.3MHz/μs.

This value is in excellent correspondence with the experimental data, taking into account accuracy of the parameters involved in the calculation.

The experimentally measured chirp behaviour (Fig. 2d) also agrees well with results of simulation of FEL3D.

The chirped instantaneous frequency is calculated by evaluating the rate of change of the computed phase accumulation in each round-trip traversal of the oscillation build-up[2].

We then eliminated the chirp mathematically and used a window of 10μs to obtain the Fig. 4b. In this case, bandwidth is window limited to 0.1MHz, enabling the determination of the inherent mode linewidth as 0.27 MHz.

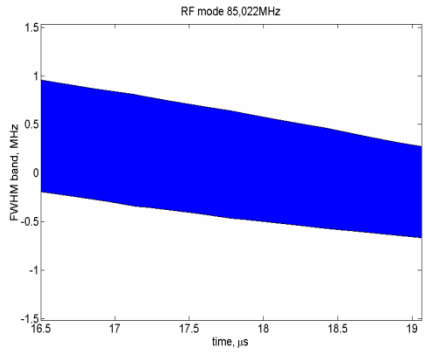

Figure 4(a)

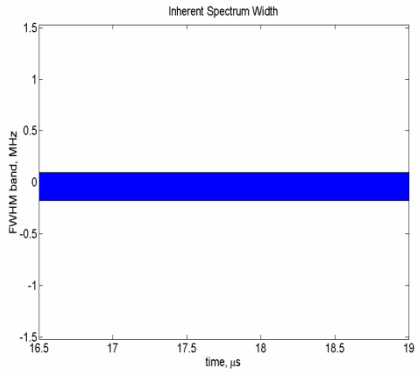

Figure 4(b)

Figure. 4: Spectrum (Fig.4a) and inherent spectral width (Fig.4b) of 85,022MHz RF mode. Time window is 1 μs (Fig.4a) and 10μs (Fig.4b).

In Fig. 4a we show different processing of the IF data. A spectrogram in ω-t phase space was computed by employing a running window Fourier-Transform [2] of 1μs width. This window makes it possible to observe the spectrum chirp, which agrees well with the 0.35MHz/μs estimate, but limits the measurable bandwidth to 1MHz=1μs^{-1}.

MODE HOPPING AND OSCILATOR RELAXATION OSCILATION

Mode hopping was observed in many cases, and is associated with accelerating voltage drop, which was measured to be in the range of 7 – 30kV (depending primarily on pulse duration) during the observed pulses. A typical case is shown in Fig. 5 (arranged like Fig. 2). The mode frequencies were uniquely identified by taking several oscillograms with different heterodyne frequencies (usually by steps of 100MHz). One can see that the first mode (85,021.5 MHz) decays when the second (83,676.5MHz) rises.

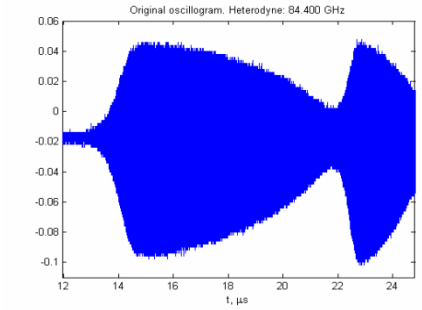

Figure 5(a)

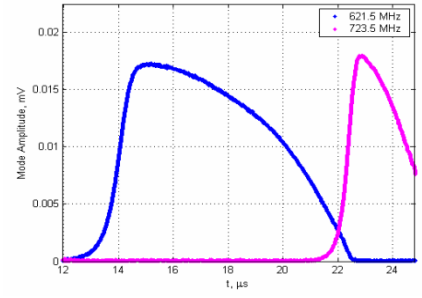

Figure 5(b)

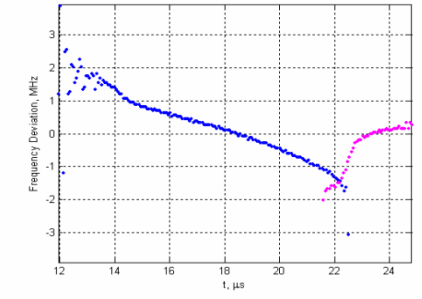

Figure 5(c)

Figure. 5: Demonstrating of mode hopping apposite with the accelerating voltage drop: (a) IF signal (b) signal growth and decay of the numerically filtered modes (c) isolated IF frequency chirp measurement of the two modes.

One can also see a clear trend (both modes at Fig. 5, also the mode at Fig. 1): chirp rate is significantly higher at the rising stage of each mode, and this rate is larger as the corresponding mode rise is steeper. This phenomenon is probably connected to damped relaxation oscillations and is well reproduced by the FEL3D [5].

The chirp direction in both modes is the same (frequency decreases with time). The opposite chirp sign of the IF signal of the 83,676.5MHz mode (Fig 5c) is because f_m, the mode frequency, is below that of the local oscillator f_{LO}, and therefore the IF frequency $f_{IF}=f_m-f_{LO}$ is negative (aliasing effect).

REFERENCES

[1] A. Gover et al. NIM A 528(2004) 23-27.
[2] A. Abramovich, et al, Phys. Rev. Lett. 82, (1999), 5257-5260
[3] A. Yariv. Optical Electronics, 3-rd ed. CBS College Publishing, 1985; see 6.2-5
[4] E. Jerby A. Gover IEEE QE-21 No.7 (1985) 1041-1057
[5] Y.Pinhasi et al. Int. J. of Elect. 78 (1995) 581.

CHARACTERIZATION OF LASER-ELECTRON INTERACTION AT THE BESSY FEMTOSLICING FACILITY *

K. Holldack, T. Kachel, S. Khan†, R. Mitzner, T. Quast, F. Senf
BESSY, 12489 Berlin, Germany

Abstract

A "femtoslicing" facility to generate ultrashort x-ray pulses by laser-electron interaction is being commissioned at the BESSY II storage ring. The energy modulation of electrons by femtosecond laser pulses is a good test case for FEL seeding schemes. The dependence of the interaction efficiency on various parameters is discussed.

INTRODUCTION

A laser pulse co-propagating with an electron bunch in an undulator modulates the electron energy if the resonance condition

$$\lambda_{\mathrm{L}} = \frac{\lambda_U}{2\gamma^2}\left(1+\frac{K^2}{2}\right) \qquad (1)$$

is fulfilled. Here, λ_L is the laser wavelength, λ_U is the undulator period, γ is the Lorentz factor of the electrons, and K is the undulator field parameter. The oscillatory energy modulation has a period length equal to λ_L and an envelope corresponding to the laser pulse shape enlarged by $\lambda_L\, N_U$, the slippage of the electrons relative to the laser field over N_U undulator periods.

Laser-induced energy modulation has a number of promising applications, among them seeding of a free-electron laser (FEL), either by high-gain harmonic generation (HGHG) [1] or by sideband seeding [2]. Energy modulation is the basic mechanism for "femtoslicing" [3, 4] and various proposals for sub-femtosecond pulse generation, e.g. [5]. Another idea is to generate coherent-light replica of electron bunches for diagnostics purposes [6]. Periodic energy modulation of electrons by a femtosecond laser pulse leads to:

– transverse displacement due to dispersion, which is the desired effect in the context of femtoslicing,

– the formation of microbunches for small differences (below $\lambda_L/2$) of the energy-dependent electron path length, emitting coherent radiation at a fraction of λ_L, particularly at higher harmonics of the laser, as in HGHG,

– a dip in the longitudinal electron distribution for path length differences exceeding the laser pulse length, giving rise to coherent radiation in the THz regime.

At the BESSY II storage ring, a femtoslicing source to generate x-ray pulses of 50 fs (fwhm) duration is currently being commissioned [7, 8]. Its purpose is to study ultrafast structural and magnetic changes in matter, and to gain experience in view of BESSY's soft-x-ray FEL project [9]. As a test case for FEL seeding schemes, femtoslicing allows to study the dependence of the energy modulation efficiency on various parameters. Relevant electron beam parameters are the electron energy (or Lorentz factor), the beam size given by emittance, beta functions and dispersion, and the energy spread. The laser properties of interest are the laser wavelength, bandwidth, chirp, polarisation, pulse energy and duration, as well as beam size and divergence, which in turn depend on λ_L and the quality parameter M^2. The undulator is specified by the period length, the number of periods, and to first order by the magnetic field parameter K, but higher harmonics of the field may also be relevant. The interaction efficiency depends critically on the overlap of laser and electrons in all phase space dimensions, i.e. horizontal and vertical position and angle, longitudinal coordinate (timing) and spectral overlap according to eq. 1.

The amplitude of the energy modulation ΔE is in principle given by [3]

$$(\Delta E)^2 = 4\pi\alpha A_L E_L \frac{K^2/2}{1+K^2/2}\frac{\Delta\omega_L}{\Delta\omega_U}\,, \qquad (2)$$

where α is the fine structure constant, A_L is the pulse energy, E_L is the photon energy, and K is the undulator parameter. The bandwidth ratio $\Delta\omega_L/\Delta\omega_U$ of laser and undulator radiation is roughly given by $N_U/N_L \leq 1$, the ratio of undulator periods and optical cycles in the laser pulse (if $N_U > N_L$, the electron slippage exceeds the laser pulse length and there is no further gain). There are corrections for matching laser and undulator spectra, and for the finite electron beam size [4], but the dependence on other parameters has to be studied by numerical simulation or experimentally, as discussed below.

FEMTOSLICING – PRINCIPLE AND IMPLEMENTATION AT BESSY II

The principle of femtoslicing involves energy modulation of electrons in an undulator ("modulator") by a short laser pulse, followed by transverse displacement in order to extract the short-pulse component of radiation emitted in a subsequent undulator. At BESSY II, the modulator U-139 (a planar wiggler with $\lambda_U = 139$ mm, $N_U = 10$) and radiator UE-56 (an elliptical undulator with $\lambda_U = 56$ mm, $N_U = 30$) are both placed in the same straight section to

* Funded by the Bundesministerium für Bildung und Forschung and by the Land Berlin.

† email: shaukat.khan@bessy.de

minimize pulse lengthening. The energy-modulated electrons are displaced by angles upto 1 mrad such that their radiation does not overlap with the radiation from the bunch core, which can be blocked by an aperture without using imaging elements, which would cause a large background due to non-specular scattering. A liquid-nitrogen cooled Ti:sapphire laser system [10] provides pulses at a wavelength of $\lambda_L = 800$ nm with a pulse energy up to 2.8 mJ at 1 kHz (alternatively 1.8 mJ at 2 kHz). Further details of the technical implementation at BESSY are given in the caption of fig. 1 and elsewhere [7].

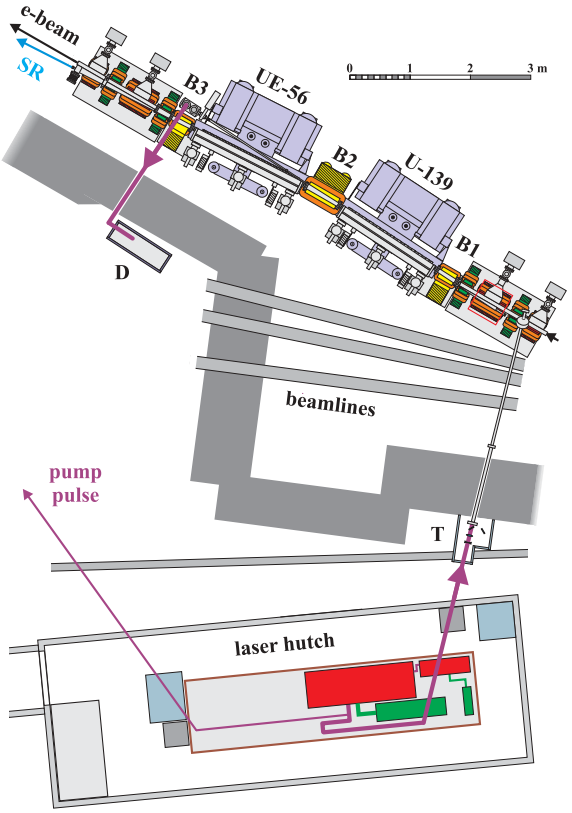

Figure 1: Overview of the femtoslicing facility. A laser hutch outside the storage ring tunnel houses a Ti:sapphire oscillator and amplifier (red) with respective pump lasers (green). The main pulse is focussed by a telescope (T) and enters the storage ring vacuum, while a small fraction will be sent as a pump pulse to the experiment. Modulator (U-139) and radiator (UE-56) are within a chicane formed by three bending magnets B1 (3.32°), B2 (6.40°) and B3 (3.08°). Laser and U-139 radiation are directed to a diagnostics station (D) above the storage ring tunnel.

NUMERICAL SIMULATIONS

Prior to the construction of the femtoslicing facility at BESSY II, numerical simulations were employed to determine the laser requirements (such as pulse energy, pulse duration and M^2), to study the effects of imperfect electron-laser overlap and other deviations from an ideal situation, and to devise a suitable separation scheme for the short-pulse x-ray component. The generation of a realistic distribution of energy-modulated electrons allows to predict the shape of the dip causing THz radiation emission as well as properties of the short x-ray pulses such as photon rate, background, spatial distribution and spectral characteristics.

The laser-induced energy deviation ΔE is modelled by integrating the product of the horizontally transverse electron velocity x' and the electric field $\mathcal{E}$ over the length $L = N_U \lambda_U$ of the modulator

$$\Delta E = -e \int_{-L/2}^{L/2} x'(s)\, \mathcal{E}(x,y,z)\, ds \qquad (3)$$

for an ensemble of randomly generated "macro-electrons". The electric field of the laser pulse is given by

$$\mathcal{E}(x,y,z) = \sqrt{2\rho(x,y,z)/\varepsilon_\circ}\, \sin\left[2\pi z/\lambda_L - \varphi_G(z)\right] . \qquad (4)$$

Here, $\varepsilon_\circ$ is the permittivity of free space, φ_G is the Guoy phase shift [11], and (x,y,z) is the electron position relative to the laser pulse, where z changes by one laser wavelength λ_L for each undulator period. The laser pulse is assumed to be Gaussian with an energy density ρ. While the pulse length is constant, the transverse rms size depends on the position s_L of the laser pulse relative to the waist position $s_\circ$ and on the beam quality factor M^2:

$$\sigma_{x,y}(s_L) = \sqrt{\sigma_{x,y}^2(s_\circ) + \left(\frac{M^2\lambda_L}{4\pi\sigma_{x,y}(s_\circ)}\right)^2 (s_L - s_\circ)^2} . \qquad (5)$$

Modifications of the laser field in this low-gain process are assumed to be small and are not included in the model.

The result of the simulation is the amount of energy acquired by each macro-electron in the interaction process and the energy-modulation "profile", i.e. the electron distribution along the ΔE-axis. The endpoint of that distribution is the modulation amplitude, which – for a realistic simulation – is systematically lower than given by eq. 1. Another useful quantity is the number of electrons exceeding a certain energy offset. For femtoslicing at BESSY II, for example, radiation from electrons with $\Delta E/E > 0.7\%$ is assumed to be separable.

EXPERIMENTAL METHODS

Successful electron energy modulation at a femtoslicing facility can be verified by various means, including

(1) cross-correlation of visible synchrotron radiation from transversely displaced electrons with laser pulses,

(2) measurement of the spectral dependence of the laser gain as a function of K, i.e. the single-pass FEL gain,

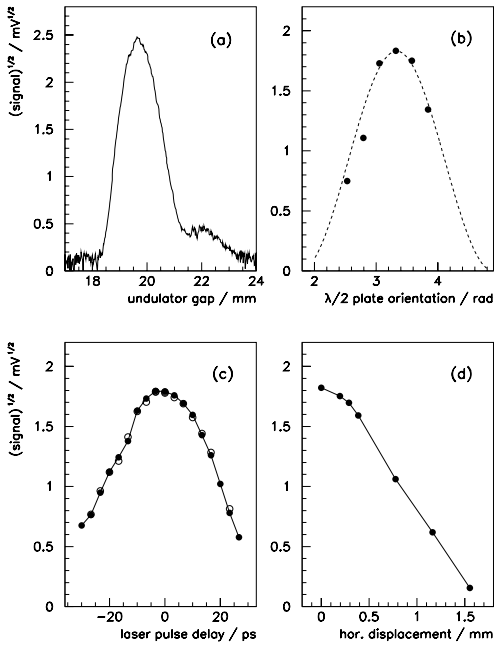

Figure 2: Square root of the THz signal, locked to the laser repetition frequency of 998 Hz, as function of (a) the undulator gap, (b) the orientation of a half-wave plate, where the dashed line indicates a $\sin^2$-dependence, (c) the longitudinal laser position and (d) horizontal misaligment with 0.33 mm corresponding to the rms electron beam size.

(3) detection of THz radiation from a dip in the longitudinal bunch profile,

(4) scraping transversely displaced electrons and measuring the electron loss rate,

(5) observation of synchrotron radiation from transversely displaced electrons,

(6) observation of enhanced radiation due to microbunching.

Methods (1) and (2), employed at the pioneering experiments described in [4], were not yet applied to the BESSY case, because method (3) offers very sensitive and simple on-line diagnostics, once THz detection is available. At BESSY II, a dedicated THz beamline with a fast infrared bolometer was constructed [12], and examples are presented below. THz diagnostics indicates the occurrence of energy modulation and allows to optimize its efficiency, but does not directly measure the modulation amplitude. The transverse displacement of electrons is proportional to their energy modulation and can be measured by methods (4) and (5), where (4) is very simple but destructive, whereas (5) involves the rather complex synchrotron radiation emission characteristics. Method (6), finally, is not easily realized in a storage ring and has not yet been attempted.

THz Diagnostics

The radiation power emitted by an electron distribution $\varrho(z)$ for a given photon wave number $1/\lambda$ is

$$P(1/\lambda) = N\, p_{1/\lambda} + f_{1/\lambda}\, N\,(N-1)\, p_{1/\lambda}\,, \qquad (6)$$

where $p_{1/\lambda}$ is the power emitted by a single electron, N is the number of electrons, and $f_{1/\lambda}$ is a form factor linked to the electron distribution via Fourier transform:

$$f_{1/\lambda} = \left| \int e^{i2\pi z/\lambda}\, \varrho(z)\, dz \right|^2 . \qquad (7)$$

When path length differences of energy-modulated electrons exceed the laser pulse length, a hole is created in the longitudinal electron distribution, giving rise to a large form factor around $1/\lambda \sim 100$ cm^{-1}, i.e. coherent radiation in the THz regime.

At BESSY II, THz radiation from a dipole magnet is routinely employed to detect laser-induced energy modulation and to optimize the spatial, temporal and spectral laser-electron overlap. The dependence of the THz signal, locked to the laser repetition rate of 998 Hz, on several critical parameters is shown in figure 2.

In part (c) of the figure, the square root of the signal is directly proportional to the electron density. Otherwise, quantitative conclusions regarding the energy modulation are not easily drawn from the THz spectrum. A model-dependent comparison would include the electron dynamics between modulator and the location of the THz beamline, application of eq. 7 to the resulting electron distribution, and consideration of the detector bandwidth.

Scraper Measurements

The energy modulation $\Delta E/E$ at a position with optical functions β_x, α_x, γ_x, dispersion D and $D' = dD/ds$ excites a horizontal betatron oscillation. With a scraper positioned at a distance Δx from the beam center, electrons contribute to the loss rate (i.e. the inverse beam lifetime) if

$$\Delta x \le \Delta E/E \sqrt{\beta_x^{\mathrm{S}}} \sqrt{\gamma_x D^2 + 2\alpha_x D D' + \beta_x D'^2}\,, \qquad (8)$$

where the horizontal beta function is β_x^{S} and the dispersion is zero at the location of the scraper. The top part of figure 3 shows the beam lifetime while the scraper is moved towards the beam and the laser is blocked periodically. The scraper position relative to the beam center is deduced from the position at which the quantum lifetime becomes dominant, as shown in the bottom part of figure 3. The solid line is derived from a simulated energy-modulation profile, where ideal overlap was assumed and the laser pulse energy was varied to match the data. The resulting pulse energy was about half the value measured at the laser exit, indicating power losses or insufficient overlap at the time of the experiment.

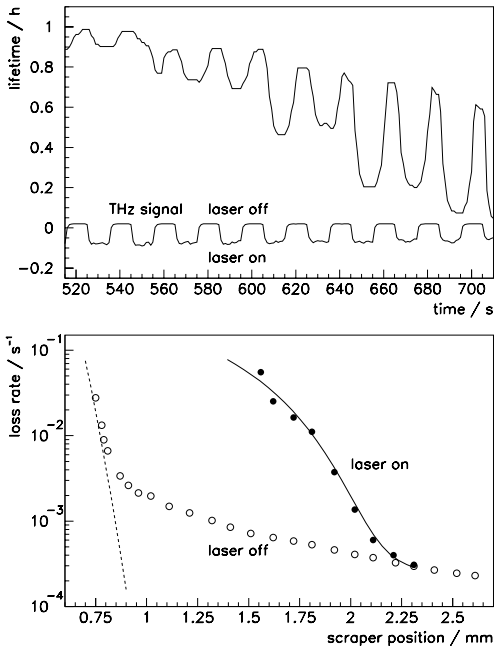

Figure 3: Top – beam lifetime versus time while a scraper is moved towards the beam and the laser is blocked periodically. Bottom – loss rate versus scraper position. The dashed line indicates the quantum lifetime limit, the solid line is a simulation result.

Synchrotron Radiation from Displaced Electrons

The purpose of femtoslicing is to generate short radiation pulses from electrons transversely displaced in the radiator. Figure 4 shows the photocurrent from a GaAs diode behind the exit slit of a monochromator, which was recorded while an aperture in the frontend was moved across the radiation distribution of the UE-56 radiator and the laser was blocked periodically. With laser-induced energy modulation, the average photocurrent is enhanced even though the single-bunch rate is 1250 times larger than the laser repetion rate. This is due to the fact, that the transverse displacement of an energy-modulated electron is maintained over many turns, given by the longitudinal and transverse damping time, and radiation from the same electron is detected many times, depending on the energy-modulation profile and the observation angle. The time-integrated measurement is a simple method to detect the presence of energy modulation, while a quantitative measurement requires:

– selection of a fast detector signal at the interaction time to exclude radiation from successive turns or from other electron bunches,

– pulse height analysis to detemine the number of simultaneously arriving photons,

– interaction with the same bunch only after one or two radiation damping times to exclude radiation from electrons excited at previous interactions.

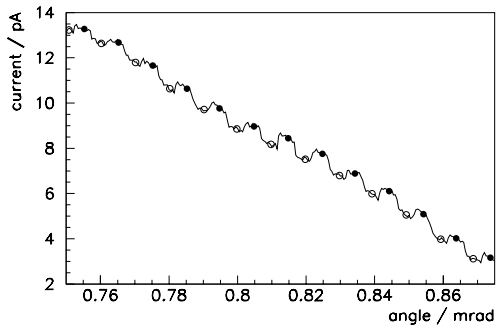

Figure 4: Angular distribution of undulator radiation at 707 eV recorded with a GaAs photodiode while the laser is blocked periodically. With laser (black symbols), the photocurrent is enhanced even though the laser repetition rate is only 1 kHz, while the electron bunch rate is 1.25 MHz.

Experiments to this end are in preparation. Until then, quantitative conclusions rely on scraper measurements during dedicated shifts, while THz diagnostics remains the best everyday tool for optimization.

ACKNOWLEDGEMENTS

We would like to express our gratitude to all BESSY colleagues contributing to the femtoslicing project. Helpful discussions with P. Heimann, R. Schoenlein, A. Zholents (LBNL, Berkeley), R. Abela, G. Ingold, A. Streun (SLS, Villigen) and hardware support by T. Lohse (HU, Berlin) are gratefully acknowledged.

REFERENCES

[1] L.-H. Yu, Phys.Rev. A44 (1991), 5178.

[2] W. Brefeld et al., NIM A 483 (2002), 62.

[3] A. A. Zholents, M. S. Zoloterev, PRL 76 (1996), 912.

[4] R. W. Schoenlein et al., Science 287 (2000), 2237.

[5] A. Zholents et al., EPAC'04, Lucerne (2004), MOPKF072.

[6] E. L. Saldin, et al., DESY 04-126 (2004).

[7] S. Khan et al., PAC'03, Portland (2003), 836.

[8] S. Khan et al., EPAC'04, Lucerne (2004), THPKF014.

[9] The BESSY Soft X-Ray Free Electron Laser, Technical Design Report, March 2004, `www.bessy.de`.

[10] Kapteyn-Murnane Laboratories Inc. MTS oscillator and HAP-AMP amplifier, Coherent Verdi V5, Quantronix 527DQE-S.

[11] A. E. Siegman, *Lasers*, University Science Books, Sausalito (1986).

[12] K. Holldack et al., EPAC'04, Lucerne (2004), THPKF013.

MEASUREMENT AND CALCULATION OF THE 'ELECTRON EFFICIENCY' ON THE 'CLIO' FREE-ELECTRON LASER

R. Prazeres, F. Glotin, J.M. Ortega : LURE, bat 209D, BP34, 91898 ORSAY CEDEX, FRANCE

Abstract

This paper describes the recent measurements of 'Electron efficiency' which has been done with the 'CLIO' Free-electron laser (FEL). The 'Electron efficiency' is the relative energy loss of the electron beam in the undulator during the FEL interaction. It gives an absolute measurement of the optical power produced by the FEL, which is then compared to the direct measurement using a power meter at the exit of the FEL. An analytical expression of the 'Electron efficiency' is given here, and it is compared to the measurements.

THE CLIO FREE ELECTRON LASER

The 'CLIO' Free Electron Laser (FEL) is an infrared tuneable laser source [1]. It uses a linear accelerator, which produces an electron beam of adjustable energy from 13MeV to 50MeV. The laser spectral range is tuneable from 5µm to about 120µm. Such a wide broadband is achieved by using, for $\lambda > 100\mu m$, a special set of toroidal mirrors. Also, in order to reduce the cavity losses at large wavelength, a waveguide is installed in place of the vacuum chamber in the undulator section. The laser extraction of the cavity is achieved by hole coupling in the front mirror.

The best configuration of radius of curvature for the cavity mirrors has been obtained with a numerical code [2] [3]. This code calculates the propagation of the laser wave front A(x,y) in the optical cavity. It uses an iterative process of wave propagation in the cavity, which converges to a steady state laser mode $A_s(x,y)$ corresponding to the FEL saturation regime. It takes into account the design of the cavity (mirrors, vacuum chamber,…) including the waveguide effect in the undulator section, and the hole coupling in the front mirror. This code gives the amplitude distribution $A_s(x,y)$ of the laser mode at saturation, in any point of the cavity, and it gives all related parameters : the cavity losses L, the 'extraction rate' Tx of hole coupling, the optical mode cross-section Σ_o,…

'ELECTRON EFFICIENCY', AND FEL POWER

In order to measure the energy distribution of the electrons after FEL interaction, an electron spectrometer [1] is installed at the exit of the undulator. It gives an experimental value of the 'Electron efficiency' η, which corresponds to the percentage of energy of the electron beam which is transferred to the laser optical mode, during the FEL interaction :

$$\eta = \Delta We / We \qquad (1)$$

where $We = Q.(\gamma mc^2/e)$ is the electron bunch energy, with Q the charge of each electron bunch, and ΔWe is the amount of energy produced in FEL interaction by each electron micro-bunch. The average extracted power (energy per second) of the FEL can be deduced from η by

$$\langle P_x \rangle \cong W_e \cdot \eta . \Delta T_{sat} \cdot \frac{T_x}{L} \cdot f_\mu \cdot f_M \qquad (2)$$

where f_M and f_μ are respectively the repetition rates of macro-pulses and micro-pulses, and ΔT_{sat} is the time duration of the FEL saturation in the macro-pulse. The ratio Tx/L is the 'extraction ratio' between the losses by hole coupling T_x and the total losses L of the laser cavity. It depends on the intracavity laser mode, and it is obtained here by numerical simulation. The power <Px>, deduced from expression (2), is compared here to the direct measurement using a detector at the exit of the FEL.

In order to fit the measurements of 'Electron efficiency' with the theory, we have written an analytical expression [4] for η, which is based on the analytical expression [5] [6] of the FEL intensity at saturation:

$$\eta \approx \frac{1}{4N_u} \cdot \left(\alpha + 0.22 \cdot g_o \alpha^2 + 4.85 \cdot 10^{-3} \cdot g_o^2 \alpha^3\right)\left(1 - e^{-h}\right) F_f\left(\frac{\Sigma_o \cdot \Delta t_o}{\Sigma_e \cdot \Delta t_e}\right) \qquad (3)$$

where g_o is the gain coefficient for linearly polarized undulators :

$$g_o = \frac{16\pi}{\gamma} \lambda_R L_u \frac{J_e N_u^2}{1.7 \cdot 10^4} \xi \left[J_0(\xi) - J_1(\xi)\right]^2 \qquad (4)$$

where $\xi = \frac{1}{4} \frac{K^2}{1 + K^2/2}$ and K is the undulator parameter, N_u and L_u are respectively the number of periods and length of the undulator, λ_R is the resonance wavelength and J_e is the density current of electrons. The coefficient $\alpha = F_{inh}.F_S$ in expression (3) is an attenuation factor for the gain coefficient g_o. It depends on the inhomogeneous broadening factor F_{inh} [5] :

$$F_{inh} = \frac{1}{1 + 1.7 \cdot \mu_e^2} \cdot \frac{1}{1 + \mu_y^2} \qquad (5)$$

with $\mu_e = 4N_u\left(\sigma_\gamma / \gamma\right)$ depending on the relative RMS energy spread (σ_γ/γ) of the electron beam, and $\mu_y = \frac{N_u \sqrt{2}}{\lambda_u} \frac{K}{1 + K^2/2} \cdot \varepsilon_{nor}$ corresponding [7] to the normalized emittance $\varepsilon_{nor} = 4\pi\gamma\sigma\sigma'$ along vertical axis (y). The longitudinal mode coupling factor F_S is [6] :

$$F_s = \frac{1}{1 + \mu_c / 3} \qquad (6)$$

where $\mu_c = N_u \lambda_R / c\sigma_e$ is the ratio between slippage length $N_u\lambda_R$ and electron bunch length $c\sigma_e$, with σ_e the RMS time duration of electron bunch. The last part of expression (3) involves the size of the laser pulse : $\Sigma_o = \pi\sigma_{ox}\sigma_{oy}$ and $\Delta t_o = \sqrt{\pi}\sigma_o$, which are respectively the cross-section and time duration of intensity, with σ_o the

RMS time duration of the laser mode amplitude. The size of the electron bunch is : $\Sigma_e=2\pi\sigma_{ex}\sigma_{ey}$ for the cross-section and $\Delta t_e=\sqrt{2\pi}\sigma_e$ for the time duration with σ_e the RMS time duration. The 'filling factor', used in expression (3), is depending on the transverse cross sections: $F_f \cong 1/(1+\Sigma_o/\Sigma_e)$. The coefficient $h=[1.8/(1+G^*_p)].[(1-L)G^*_p-L]/L$ in expression (3) depends on the 'Small Signal Gain' of power G^*_p, and on the optical losses L. The 'Small Signal Gain' of power is :

$$G^*_p = F_f \cdot \left[0.85\cdot(g_o\alpha)+0.19\cdot(g_o\alpha)^2+4.12\cdot10^{-3}\cdot(g_o\alpha)^3\right] \quad (7)$$

where $\alpha=F_{inh}.F_S$. Note that this expression includes the non linear components which are present for large values of the gain [5]. The expression (3) of 'Electron efficiency' also takes into account the non linear behaviour.

In first approximation, for small values of gain coefficient g_o, the expression (3) of η is close to $1/4N_u$ multiplied by the attenuation factor α which lies generally in the range 0.5 to 1. The factor [1-exp(-h)] becomes important when the 'small signal gain' G^*_p is close to the losses L. The last two terms of (3) are dependant on the volume of optical and electron bunches. Now, in high gain regime, i.e. for large values of gain coefficient g_o, the non linear behaviour of the gain G^*_p may increase strongly the 'Electron efficiency'. Note that, the third order correction in (7) works [5] in a large range of g_o values ($g_o \leq 20$) ; and this always keeps the 'Electron efficiency' $\eta<1$.

MEASUREMENTS

An example of electron spectra is shown in figure 1, with γmc^2=15.2MeV and laser wavelength λ=72µm. The horizontal axis of electron spectra is the time scale, and the vertical axis is the variation, in %, of the electron energy γmc^2 during the macro-pulse. Two spectra are displayed here: for 'laser OFF' and for laser 'ON'. The time evolution of electron energy centroid $\langle\gamma mc^2\rangle(t)$ is represented by a curve on each spectrum. The two curves on bottom of figure 1 represent a Y-cut of the energy distribution. The dashed vertical lines represent the centroid of electron energy $\langle\gamma mc^2\rangle$. The difference $(\langle\gamma mc^2\rangle_{OFF}-\langle\gamma mc^2\rangle_{ON})$, between the centroids, corresponds to the 'Electron efficiency' $\eta(t)=\Delta We/We$. At low electron beam energy (about 15MeV), the whole series of measured spectra show, as observed in figure 1, an important slope of electron energy versus time at macro-pulse time scale : about 1.5% of energy variation in 10µs. Indeed, the electron beam at low energy is much more sensitive to all perturbations than at high energy (> 40MeV). The slope of electron energy reduces the power at laser saturation, because the wavelength centroid is continuously shifted along the macro-pulse, by about $\Delta\lambda/\lambda$ =3% (twice of electron energy shift), whereas the FEL gain line width is only about $\delta\lambda/\lambda=1/2N_u$=1.3%. Therefore, the laser saturation is not fully obtained during the macro-pulse.

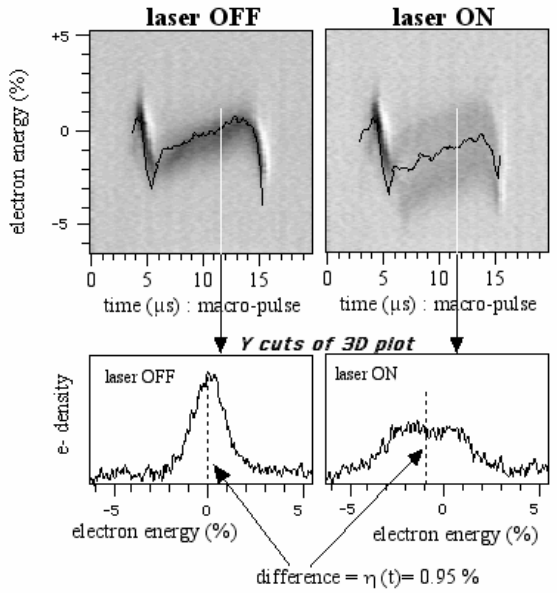

Figure 1: Electron energy spectrum at the undulator exit, with laser OFF and laser ON, at laser wavelength λ=72µm.

The loss of energy of the electrons during the FEL interaction is well represented by a subtraction between density spectra of figure 1 : 'laser ON'-'laser OFF'. This subtraction is represented in figure 2 by a series of Y-cut, performed in the middle of the electron macro-pulse. Each curve displays the subtraction of electron density (laser ON-laser OFF) as a function of the relative electron energy (in %). Each curve corresponds to a different undulator gap, from 18mm to 27mm, corresponding to laser wavelengths from λ=49µm to 92µm. The hollow which is observed here corresponds to a lack of electrons of nominal energy $\gamma_o mc^2$ (energy at undulator entrance). The bump corresponds to an accumulation of electrons which have lost energy during the FEL interaction. The whole set of curves in figure 2 exhibit a variation of amplitude, but they are keeping the same shape and same position of the peaks. This last feature means that the energy loss $\Delta\gamma mc^2/\gamma_o mc^2$ of the electrons, during the FEL interaction, is independent on wavelength: it is close to 2% in any case. Note that this parameter $\Delta\gamma mc^2/\gamma_o mc^2$ is not equivalent to the 'Electron efficiency' η, which values are always less than 2% (see figure 3). Indeed, η represents an average over the whole number of electrons, and it corresponds to the difference of centroid of the energy distributions.

At first sight, the similitude of the curves in figure 2 would lead to the conclusion that the 'Electron efficiency' η is also independent on wavelength. However, as it will be shown below (in figure 3), it is not the case. Indeed, the variations of η, according to wavelength, are well represented in figure 2 by a variation of amplitude of the curves of electron density. These amplitude variations correspond to a difference in the number of electrons

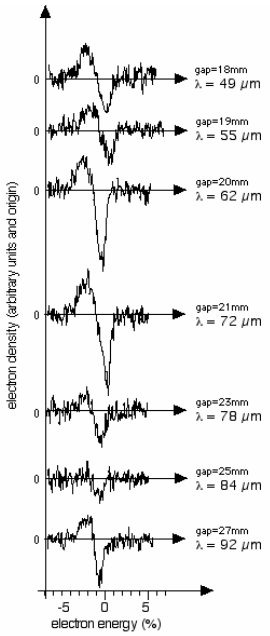

Figure 2 : Subtraction of electron density (laser ON-laser OFF) versus electron energy (in %). Each curve corresponds to a different undulator gap, and a different laser wavelength.

which are involved in the FEL interaction and which are losing energy. As a conclusion, a variation of η corresponds to a variation in the number of electrons involved in the FEL interaction, and not to a variation in the energy loss of the electrons. This conclusion is in good agreement with the fundamental theory [5] of the electron trapping in FEL interaction, which shows that the energy loss of the electrons is governed by the line width of the gain distribution, which only depends on $1/N_u$ and not on the laser wavelength.

The figure 3 represents the 'Electron efficiency' η as a function of the laser wavelength. The black dots represent an experimental estimation of the 'Electron efficiency' η which is deduced from the electron energy spectra (such as of figure 1). The estimation of the electron energy centroid $<\gamma mc^2>$, from the electron spectra, is rather sensitive to the noise background of these spectra. This represents the main source of error in the estimation of the 'Electron efficiency' η, because this parameter is obtained by a small difference between large and imprecise quantities $<\gamma mc^2>_{OFF}$-$<\gamma mc^2>_{ON}$. The experimental data in figure 3 are compared to a theoretical model, using the analytical expression (3). This expression is dependant on the electron beam cross-section Σ_e, which is not known with a good precision. Therefore, two theoretical curves are represented in figure 3. The line curve on the top of the grey area has been calculated with σ_{ex}=1.5mm and σ_{ey}=1mm ; and the line curve on the bottom of area has been calculated with σ_{ex}=2mm and σ_{ey}=1.5mm. The optical losses L, the

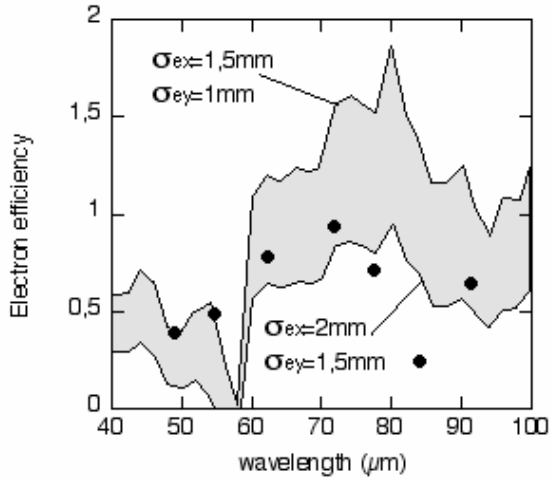

Figure 3: 'Electron efficiency' η versus laser wavelength. The dots are experimental data, and the gray area is theoretical from the analytical expression (3).

'Filling factor' F_f and the cross-section Σ_o of the optical mode are calculated by the numerical code [2] [3]. The optical pulse length Δt_o of the FEL is deduced from the spectrum line width $\Delta\lambda/\lambda$ of the laser. Taking into account the various sources of error for both theory and experiment, the figure 3 shows that the measurement of the 'Electron efficiency' is in rather good agreement with the analytical expression (3). In addition, this means that the numerical simulation, which gives L, F_f and Σ_o, is rather reliable.

The average extracted power <Px> of the FEL can be calculated from the value of 'Electron efficiency' η, using the expression (2). Three curves <Px>=f(λ) are displayed in figure 4 : (A) a purely experimental measurement of <Px>=f(λ) using a power meter at the exit of the FEL ; (B) a semi-experimental estimation of <Px> using the experimental values of η displayed in figure 3 ; (C) a theoretical estimation of <Px> using the theoretical values of η displayed in figure 3. The behaviour is similar for the three plots. The theoretical curve C fits rather well the curve B. Both of these curves are using the expression (2) for <Px>. The fit between these two curves B and C, in log scale here, corresponds to the fit of η (theoretical and experimental) in figure 3. The 'extraction ratio' Tx/L has no influence in the comparison between B and C because it is used in both curves. Now, a comparison between B or C, and A, shows a larger discrepancy: this means that the 'extraction ratio' Tx/L, obtained by numerical simulation, does not correspond to the experiment and is responsible of the rather bad fit of curve A. The figure 5 corresponds to the numerical simulation, and it shows L and Tx as a function of wavelength. Taking into account the above conclusion about the reliability of the numerical simulation for L, we can suppose that Tx is the parameter which gives the most important error. This conclusion is easy to understand, because Tx must be very sensitive to the alignment of the cavity mirrors and to the transverse

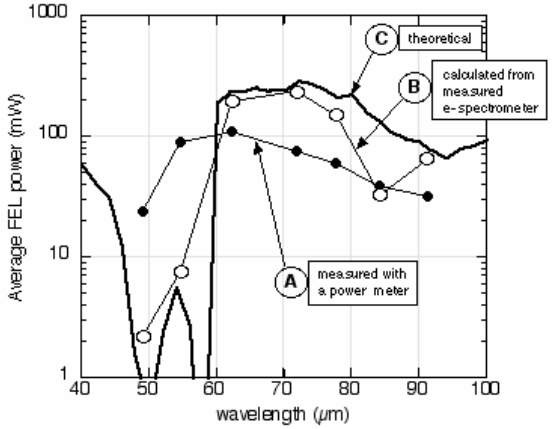

Figure 4: Average extracted laser power <Px> versus wavelength. The curve A is purely experimental: obtained with a power meter at exit of the FEL. The curve B is semi-experimental, using the measurement for η and the numerical simulation for Tx/L. The curve C is purely theoretical: η is obtained by analytical expression (3), and Tx/L is obtained by numerical simulation

profile of the laser mode. A small error of these parameters may change strongly the coefficient Tx. Note that the figure 5 exhibits, at λ=50μm, a strong decreasing of the laser extraction Tx and an increasing of the cavity losses L. This has already been commented in the past [8], and it is due to a special transverse distribution of the laser mode in the cavity, which has zero intensity on longitudinal axis. This effect can be observed in the experimental curve (A) in figure 4, which shows a decreasing of the power <Px> by a factor 5 between λ= 54μm and 50μm.

As a summary, the estimation of <Px> is less accurate than η because of the uncertainty on Tx. Nevertheless, the three curves of <Px> in figure 4 exhibit the same behaviour and they fit the same order of magnitude. Taking into account the various sources of error, both in measurements and simulation, we can consider that the estimation of laser power from the direct power measurement, from the analysis of electron beam spectra, and from the analytical expression, are in rather good agreement.

CONCLUSION

The electron energy spectra show the scattering due to the FEL interaction between the electron bunch and the laser pulse. This gives a measurement of the 'Electron efficiency' η of the FEL, corresponding to the ratio between the energy produced by the FEL and the input energy of the electron beam. The measurements of η are in rather good agreement with the analytical expression of 'Electron efficiency' which is written here. This expression involves the electron beam parameters, which some of them are only imprecisely estimated, and the optical cavity parameters, which are obtained by numerical simulation.

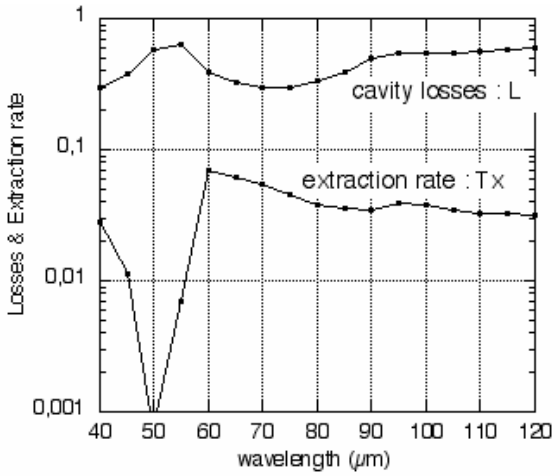

Figure 5: Numerical simulation : cavity losses L and 'extraction rate' Tx versus wavelength

The extracted laser power <Px> is deduced from the values obtained for η. We have made a comparison between the power <Px> and the direct measurement using a power meter at the exit of the FEL. These data are in rather good agreement, and the remaining error is mainly due to the error in the calculation of the 'extraction rate' Tx of hole coupling in the optical cavity. The calculation of the FEL power is less reliable than the calculation of the 'Electron efficiency', but both of them are still sufficiently reliable to give the right order of magnitude. The perfect knowledge of electron beam characteristics would give a much better result.

REFERENCES

[1] R. Prazeres, F. Glotin, JM. Ortega, C. Rippon, R. Andouart, JM. Berset, E. Arnaud, R. Chaput : Nucl.Instr.&Methods A445, n°1-3; (2000), p.204-207
[2] R. Prazeres, M. Billardon : Nucl. Istr. & Meth. A318 (1992) 889-894
[3] R. Prazeres : Eur. Phys. J AP **16**, 209-215 (2001).
[4] "Measurement and calculation of the 'Electron efficiency' of an F.E.L." : submitted to Eur. Phys. Jou. Appl. Phys.
[5] "Insertion devices for synchrotron radiation and free electron laser", by F. Ciocci, G. Dattoli, A. Torre & A. Renieri (ENEA INN-FIS, Frascati, Rome, Italy) ISBN 981-02-3832-0.
[6] G. Dattoli, Jou. of Appl. Physics, vol.84, (1998) p2393-2398
[7] G. Dattoli, T. Letardi, JMJ. Madey, A. Renieri, Nucl. Instr.& Methods A237 (1985) 326-334
[8] R. Prazeres, F. Glotin, JM. Ortega, Nucl. Instr. & Methods A528 (2004) 83-87

RECENT RESULTS OF THE JAERI ENERGY-RECOVERY LINAC FEL

R. Hajima*, M. Sawamura, R. Nagai, N. Kikuzawa, N. Nishimori,
H. Iijima, T. Nishitani, E.J. Minehara
JAERI, Tokai, Ibaraki 319-1195, Japan

Abstract

In Japan Atomic Energy Research Institute (JAERI), we are developing an energy-recovery linac (ERL) for a high-power free-electron laser (FEL). The ERL was completed in 2002 by remodeling the original superconducting accelerator. In this paper, we summerize recent research activities at JAERI-ERL.

INTRODUCTION

A research program towards a high-power free-electron laser (FEL) has been conducted at Japan Atomic Energy Research Institute (JAERI) since 1987. The initial target of the program, FEL lasing in kilowatt level, was achieved in 2000[1], and the research program is now stepping forward to the next stage, demonstration of a 5-10 kW FEL.

It is considered that same-cell energy-recovery in a superconducting linac is the only practical solution to put such a high-power FEL in work efficiently[2]. Hence, we decided to remodel the superconducting accelerator into an energy-recovery linac (ERL)[3]. The original linac was shut down in the spring of 2001, and the ERL was completed after a half-year construction period. We demonstrated first energy-recovery operation at 19 February, 2002, and first FEL lasing at 14 August, 2002 [4].

In this paper, we present recent research activities at JAERI-ERL FEL: upgrading major components of the superconducting accelerator, investigation of long-macropulse operation, beam dynamics studies and others.

COMPONENTS UPGRADE

Injector RF Sources

Increasing the injector beam current is a straightforward approach to enlarge the FEL power by taking full advantage of the energy-recovery. In the original JAERI-FEL without energy-recovery was operated at 5 mA injector beam current. Two single-cell cavities of the injector were driven by 6 kW solid state amplifier for each, enough capacity for 5 mA operation. The solid state amplifier has been replaced by an IOT-klystrode of 50 kW, which enables one to inject a 40 mA beam into the ERL. The IOT is designed for CW operation as well as pulsed operation, while the original amplifier allowed only pulsed operation with small duty-cycle such as 1 ms $\times$ 10Hz. We also plan to replace RF amplifiers for 5-cell main modules by the same IOT systems for future long-pulse operation.

* e-mail: hajima@popsvr.tokai.jaeri.go.jp

Gun Grid Pulser

The electron gun is equipped with a thermionic cathode and operated at 230 kV DC voltage. A train of electron bunch is generated by grid pulser. In the original configuration, the gun was designed to produce 0.5 nC electron bunches at 10.4 MHz repetition, that is 5 mA. We installed a new grid pulser working at 20.8 MHz, doubled repetition of the original one, and a 10 mA beam is now available [5]. The new grid pulser is designed at Budker Institute of Nuclear Physics and can be operated in CW-mode as well as pulse-mode.

We measured electron beam properties with the new grid pulser and confirmed that it keeps similar performance to the original one. The pulse width and the normalized rms emittance at the gun are 590 ps (FWHM) and 20 πmm-mrad, respectively.

As presented above, the injection cavities are ready for 40 mA beam, which requires 83 MHz operation of the grid pulser. Design of a grid pulser for the higher repetition rate, 41.5 MHz and 83 MHz, is under investigation.

RF low-level controllers

Stable operation of an FEL relies much on the stability of an accelerator. In a superconducting accelerator, an RF low-level controller is one of the key components for achieving good stability. The original JAERI-FEL was equipped with a low-level controller, which kept phase flatness at ± 1 degree within a 1 ms macropulse. This controller had been contributed to the 10-year operation of JAERI-FEL. After the remodeling into the ERL, however, we found that the stability of the low-level controller was insufficient to extract the full performance of the ERL. Since the controller had no special function to compensate temperature drift, we could hardly obtain long-time stability against the change of room temperature.

The low-level controller was replaced by new one. The new system is based on phase and amplitude control of the cavity RF field coupled with a tuner controller, which is same as the original system. In the design of the new low-level controller, we introduced the following functions for the better stability: the feedback gain and bandwidth can be varied during operation to obtain good flatness of RF phase and amplitude within a macropulse, all the circuits are contained in boxes with temperature stabilization.

The original controller was placed at the operation room, and the feedback loop involved 50-m cables to connect the controller and the RF cavity. We found that large temperature drift was caused by this long cables. The new con-

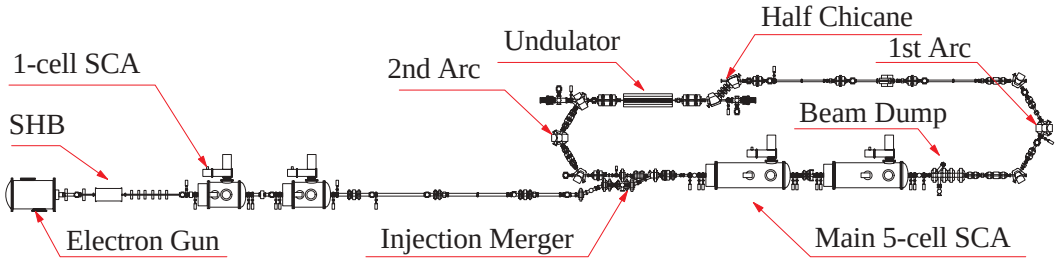

Figure 1: The layout of JAERI Energy-Recovery Linac. An electron bunch generated by 230 kV electron gun is accelerated to 2.5 MeV and injected into the energy-recovery loop. The electron bunch is accelerated to 17 MeV by main superconducting cavities and transported to the FEL undulator. The electron bunch is, then, reinjected to the main cavities and decelerated down to 2.5 MeV and collected by a beam dump. All the superconducting cavities are driven at 499.8 MHz.

troller is installed just beside the cavity to make the cable length as short as possible. Furthermore the cables between the controller and the cavities are contained in a temperature-controlled pipe to suppress the temperature drift.

After these upgrade, the accuracy and stability of accelerating RF has been greatly improved. The flatness of RF phase and amplitude within a 1 ms macropulse are 0.20 deg. and 0.013% for the old system, 0.06 deg. and 0.013% for the new system, where all the values are RMS. Phase and amplitude fluctuation for 5 minutes in the new system are measured as 0.15 deg. and 0.015%, respectively. In this measurement, mechanical vibration of the cavity due to the refrigerator is the dominant source of the fluctuation.

Operation Control System

The operation control system of JAERI-ERL has also been upgraded. The old system based on CAMAC and PC-9801 with Windows-95 became obsolete and difficult to maintain and make further extension. We have developed a new system consisting of CAMAC and local controllers working with μ-ITRON [6], which are robust hardware without mechanical component such as hard-disc drives. Console applications for the operation are written by JAVA and CORBA, modern software independent of platform. We have also prepared data-logging and database services using WEB and MySQL.

FEL Transport Line

A laser-beam transport line has been built to deliver FEL pulses to an experiment room. We have installed an optical-beam expander, which consists of two elliptic mirrors, at the end of FEL optical cavity to convert a diverging beam from a center-hole at a FEL cavity mirror into a parallel beam. The expanded beam is transported to the experimental room through a 24 m-long evacuated pipe.

LONG-MACROPULSE OPERATION

The superconducting accelerator of JAERI-ERL FEL has been operated in a pulse-mode, 1 ms (flat top) $\times$ 10 Hz, which is restricted by refrigerator capacity. For the demonstration of a high-power FEL in industrial applications, however, the longer macro pulses are preferable. In the upgrade of JAERI-ERL FEL, we designed all the new components to meet CW operation. The grid-pulser and the IOT's are CW-ready. Since the refrigerator has capacity for 3% duty cycle, long-pulse operation is only available with keeping this duty cycle such as a 1 second macro pulse every 30 seconds.

Several technical issues should be resolved for the long-pulse operation of the superconducting cavities, which were originally designed for 1 ms pulses. One is pressure rising of the cryostat during a macro pulse due to the heat unbalance between the dissipated RF power and the refrigerator power. This pressure rising causes detuning in the cavity resonance frequency. In the JAERI cryostat, a refrigerator is directly installed at the top of cryomodule. Mechanical vibration of the refrigerator is, therefore, another source of the cavity frequency detuning. We investigated the effect of pressure rising and mechanical vibration, and confirmed that long-pulse operation of 1-5 seconds is possible after minor modification of the existing piezo tuner[7].

BEAM DYNAMICS STUDIES

Injector Optimization by Simulated Annealing

It is known that spontaneous frequency-chirping is induced in a high-gain FEL oscillator. Such chirped pulses can be used to excite unharmonic potential ladder of molecular systems, one of coherent chemical processes. We demonstrated 14.3% frequency chirping in a FEL pulse at JAERI-FEL before the ERL modification[8].

To construct an ERL, the injector beam line was modified from a straight path into a 2-step staircase. This modification made it difficult to generate an electron bunch

as short as before, 5 ps (FWHM), which is important for the chirped-pulse generation. In the ERL design, we obtained the bunch length as 15 ps (FWHM) from particle simulations[9], and the measurement during the ERL operation almost agrees with this simulation result.

The bunch length is determined by electrons motion in the longitudinal phase space. In the JAERI-ERL injector, we have six parameters to manipulate electrons motion in the longitudinal phase space, which are amplitude and phase of the subharmonic buncher and two 1-cell cavities. We considered that these parameters can be further optimized to generate the shorter bunch, and applied simulated annealing algorithm[10] to the optimization. From the optimization using simulated annealing, we have found a parameter set of the injector, which gives 5.6 ps (FWHM) electron bunch[11]. The ERL operation with these new parameters will be tried soon.

Emittance Growth in the Merger

Energy redistribution in an electron bunch caused by longitudinal space charge force or coherent synchrotron radiation (CSR) along a dispersive path induces transverse emittance growth. The emittance growth by CSR in the constant wake regime, where the bunch keeps constant temporal profile, can be analyzed by linear matrix approach[12]. The linear analysis shows that the emittance growth can be minimized by matching the beam ellipse to the direction of displacement of bunch slices in the (x, x') phase space.

In the JAERI injection merger, longitudinal space charge force causes the emittance growth through the energy redistribution. We are studying the emittance growth during the merger by particle tracking simulations instead of the linear analysis, because the bunch length is not constant, 20 ps (FWHM) at the entrance and 10 ps at the exit of merger in typical operation. From PARMELA [13] simulation, it has been found that the emittance can be minimized by using appropriate beam envelope along the merger. As the best result, we obtain normalized RMS emittance and FWHM bunch length at the merger exit, $\varepsilon_x = 35\pi$mm-mrad, $\varepsilon_y = 26\pi$mm-mrad, and 9.4 ps.

OTHER R&D'S

An electron gun with low-emittance and high average-current is a key component for a high-power FEL and a future light sources based on the ERL technology. A DC photocathode gun with a NEA cathode is considered as the most promising device for high average-current ERLs, 10-100 mA [14]. We, therefore, started research activity on a DC photocathode gun. A test bench to study a DC photocathode gun is under development with components from a 200 kV gun [15] and an old MBE system. A mode-locked Ti:Sap. laser of 83.3 MHz is also prepared. Details are presented in an accompanying paper[16].

For FEL applications, we are proposing laser pealing of stainless steal surface to suppress stress-corrosion crack (SCC), which is a critical problem in nuclear reactors in Japan[17].

SUMMARY

An energy-recovery linac has been developed for a high-power free-electron laser at JAERI. An R&D program towards a 5-10kW FEL and future ERL light sources is in progress. We have upgraded major components of the ERL, RF low-level controller, injector RF sources, operation control system, a gun grid pulser, for stable operation of the ERL and high-power FEL demonstration. The upgrade has been almost completed, and we restart the ERL soon.

REFERENCES

[1] N. Nishimori et al., Nucl. Instr. Meth. **A475** (2001) 266–269.

[2] G.R. Neil and L. Merminga, Rev. Mod. Phys. **74**, 685 (2002).

[3] R. Hajima et al., Nucl. Instr. and Meth. **A445** (2000) 384–388; T. Shizuma et al., Nucl. Instr. and Meth. **A475** (2001) 569–573; R. Hajima et al., Proc. EPAC-2000, 1033–1035; T. Shizuma et al., Proc. EPAC-2000, 1074–1076.

[4] R. Hajima et al., Nucl. Instr. and Meth. **A507** (2003) 115–119.

[5] N. Nishimori et al., "20.8MHz Electron Gun System for an Energy Recovery Linac FEL at JAERI", Proc. APAC-2004.

[6] N. Kikuzawa, "Control system upgrade of JAERI ERL-FEL", Proc. FEL-2003.

[7] M. Sawamura et al., "RF Properties of the JAERI ERL-FEL for Long-Pulse Operation", Proc. 1st Annual Meeting of Particle Acc. Society of Japan, (2004) 305–307.

[8] R. Hajima and R. Nagai, Phys. Rev. Lett. **91** (2003) 024801.

[9] T. Shizuma et al., Proc. EPAC-2000, 1074–1076.

[10] W.H. Press et al., "Numerical Recipes in C, second ed.", Cambridge Univ. Press, (1992) p.444.

[11] R. Nagai et al., "Parameter Optimization of JAERI ERL Injector by Simulated Annealing", Proc. 1st Annual Meeting of Particle Acc. Society of Japan, (2004) 420–422 (in Japanese).

[12] R. Hajima, Jpn. J. Appl. Phys. **42** (2003) L974–L976.

[13] PARMELA ver. 3.34; L.M. Young, LA-UR-96-1835.

[14] C.K. Sinclair, Proc. PAC-2003 (2003) 76–80.

[15] E.J. Minehara and K. Whitham, Proc. EPAC-98 (1998) 1474–1476.

[16] T. Nishitani et al., "The Development of the JAERI 200keV Electron Gun with an NEA-GaAs Photocathode", Proc. FEL-2004.

[17] E.J. Minehara et al., "Femtosecond Laser Prevention for the Cold-Worked Stress Corrosion Crackings on Reactor Grade Low Carbon Stainless Steal", Proc. FEL-2004.

JAERI 200kV ELECTRON GUN WITH AN NEA-GaAs PHOTOCATHODE

T. Nishitani #, E. J. Minehara, R. Hajima, R. Nagai, M. Sawamura, N. Nishimori, N. Kikuzawa, T. Yamauchi
FEL Lab., Advanced Photon Research Center, Kansai Research Establishment, Japan Atomic Energy Research Institute, 2-4 Shirakata shirane, Tokai, Naka, Ibaraki 319-1195 JAPAN

Abstract

The photocathode DC-gun with high average current, low beam emittance and long operational lifetime is considered to be indispensable for ERL-FEL. We have started the developmental program of a 200keV electron gun with the NEA-GaAs photocathode for the first time in JAERI. In order to long an NEA surface lifetime, JAERI 200kV electron gun system consists of a 200kV DC-gun chamber on extreme high vacuum condition and an NEA activation chamber with load-lock system. We report the goal of photocathode DC-gun R&D and the schedule of a developmental program.

INTRODUCTION

ERL-FEL and 4th generation ERL-LS with higher output and higher luminosity than the existing technology can be realized by the extraordinary high injector performance. Especially, electron source with higher current and lower beam emittance than existing is indispensable in order to improve the injector performance.

As such an electron source, it is thought that the GaAs type semiconductor photocathode with negative electron affinity surface (NEA-GaAs) is a strong candidate.

It is because maximum quantum efficiency of NEA-GaAs photocathode is 10% or more of quantum efficiency and NEA-GaAs photocathode has the advantage that initial emittance can be made small by choosing the wavelength near a band gap for excitation laser [1].

We started development of the NEA-GaAs photocathode electron gun which generates the electron beam with the structure of 1.3GHz of repetitions and 77pC/bunch (the average current of 100mA).

NEA SURFACE

Since the surface of NEA-GaAs photocathode forms a NEA state by Cs and O2 of angstrom order of thickness (or NF3), the surface before NEA activation must be pure and NEA surface is also very weak.

Therefore, the countermeasure to clean-surface before NEA activation and long life time of NEA surface is indispensable to the design of an NEA photocathode electron gun.

The surface of the photocathode exposed into the atmosphere before the introduction to a vacuum chamber is being worn with impurities, such as an oxide and carbide.

#nisitani@popx.tokai.jaeri.go.jp

When the photocathode electron gun introduces photocathode out of the atmosphere, it needs surface cleaning such as annealing, atomic hydrogen cleaning [2] in order to remove impurities in the surface.

The following cause can be considered for degradation of NEA surface; the adsorption phenomenon to the surface of remains gas in vacuum chamber, and ion back bombardment due to field emission dark current between anode- and cathode-electrode.

The former degradation phenomenon can be suppressed by extra high vacuum chamber in order to suppression of the adsorption phenomenon.

It is thought that the field emission dark current is dependent not only on the fall of electrode work function due to the adsorption of caesium, but also the characteristic of the electrode material.

The following conditions are needed for good NEA surface.

- The photocathode surface before NEA surface activation is clean.
- The vacuum of chamber should be extra high vacuum in order to suppress the remains gas in chamber.
- In order to suppress of field dark current, it is choosing the electrode with the sufficient characteristic, and prevent caesium adsorption to the electrode.

DESIGN AND COMPONENTS OF JAERI PHOTOCATHODE GUN

As an electron gun which realizes the NEA surface of a long lifetime, development of the electron gun which combined MBE apparatus with NEA activation system and 200kV electron gun chamber under extreme high vacuum by the load-lock system was started.

JAERI photocathode gun has the performance of fabrication of photocathode in vacuum chamber by using MBE apparatus. That is, it means that surface cleaning process (such as anneal and atomic hydrogen cleaning) and the exchange of photocathode become unnecessary. It is the first photocathode gun which has the photocathode production system in the world.

Figure 1 show the design of JAERI photocathode gun which consists of three components (MBE chamber, gun chamber and mode-lock laser system).

The following describes a design and parts about each component.

MBE apparatus with NEA activation system

JAERI photocathode gun use MBE apparatus (EV-10: eiko-engineering co.) as an NEA activation chamber.

This main chamber can realize ultra high vacuum of a 10^{-8}Pa order by using an ion pump (500 l/s) and titanium sublimation pump (400 l/s) after 200 degree baking of 100 hours by a rotary pump and a turbo pump. This degree of vacuum fulfils the necessary condition for NEA surface formation. In the main chamber, it has the liquid nitrogen shroud, and a still better vacuum can be expected by introducing liquid nitrogen.

The semiconductor substrate on which is carried out photocathode growth is inserted from gate-bulb-A in Figure 1, and it introduces to a main chamber after a preliminary pump. In a main chamber, photocathode growth and NEA surface activation by vacuum evaporation of caesium and oxygen is carried out.

The photocathode with NEA-activated surface is transported to gun chamber with a transfer rod, and it equips with it from behind cathode electrode.

The design of gun chamber

In order to realize extreme high vacuum, it is necessary to make gun chamber capacity small. For this reason, cathode- and anode- electrode are designed small, a size of photocathode is made into the sufficiently larger diameter of 5mm than the excitation laser diameter of 2mm, and the gap between cathode- and anode- electrode is 30-50mm, and anode hole-size is 20mm.

About the vacuum of gun chamber, after baking of 200 degrees, the combination of an nonevaporating type getter pump and an ion pump aims at realization of a extra high vacuum (10^{-10}Pa order).

Anode- and cathode-electrode are under design using beam simulation codes, such as EGUN, PARMERA. As the material of electrode, Ti and Mo are used. It is thought that these materials have the advantage which suppresses the field emission dark current from SUS or Cu in recent years [3].

A high-voltage power supply uses 200kV power supply (PK200N18: GLASSMAN HIGH VOLTAGE INC.) with the maximum voltage of 200kV and the maximum current of 18mA.

Mode-lock laser

As excitation laser for photocathode, the mode lock Ti: Sapphire laser (TSUNAMI: Spectra Physics) of 83MHz of repetitions is used. Laser is irradiated from anode back to photocathode through an anode hole.

TSUNAMI has a maximum of 500mW output on the wavelength of 790nm. When it is 10% of quantum efficiency of photocathode, a maximum current of 16mA will be obtained by laser excitation with a wavelength of 790nm.

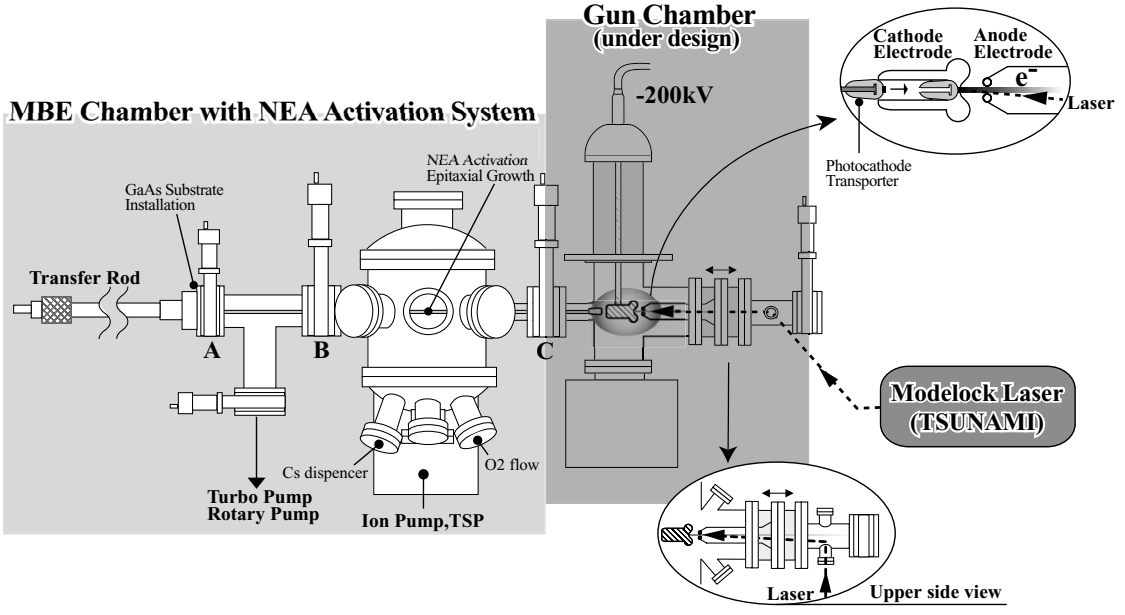

Figure 1: The design of JAERI photocathode gun.

The present condition and a work schedule

We consider the present target of JAERI photocathode gun as 200keV electron beam generation of 77 pC/bunch (average current of 6.2mA) and 83MHz repetition, and show the schedule of a developmental program in Table 1.

We are performing the design of photocathode holder, electrode (anode and cathode) and gun chamber, and the vacuum examination of MBE apparatus.

We are considering development of the beam evaluation system such as measurement of the bunch width and emittance as a next subject. Furthermore, by using MBE apparatus, development of the new type photocathode which has high quantum efficiency and the strong NEA surface compared with the conventional NEA photocathode is also planned.

REFERENCES

[1] S. M. Gruner and M. Tigner, eds., "Study for a proposed Phase I Energy Recovery Linac Synchrotron Light Source at Cornell University, CHESS Technical Memo 02-003, JLAB-ACT-01-04, 2001

[2] M. Yamamoto, et al., "Proceedings of the 28th Linear Accelerator Meeting in Japan, Tokai, July. 30-Aug. 3, 2003, P99-101

[3] F. Furuta, et al., "Proceedings of the 28th Linear Accelerator Meeting in Japan, Tokai, July. 30-Aug. 3, 2003, P111-113

Table 1: The schedule of a developmental program

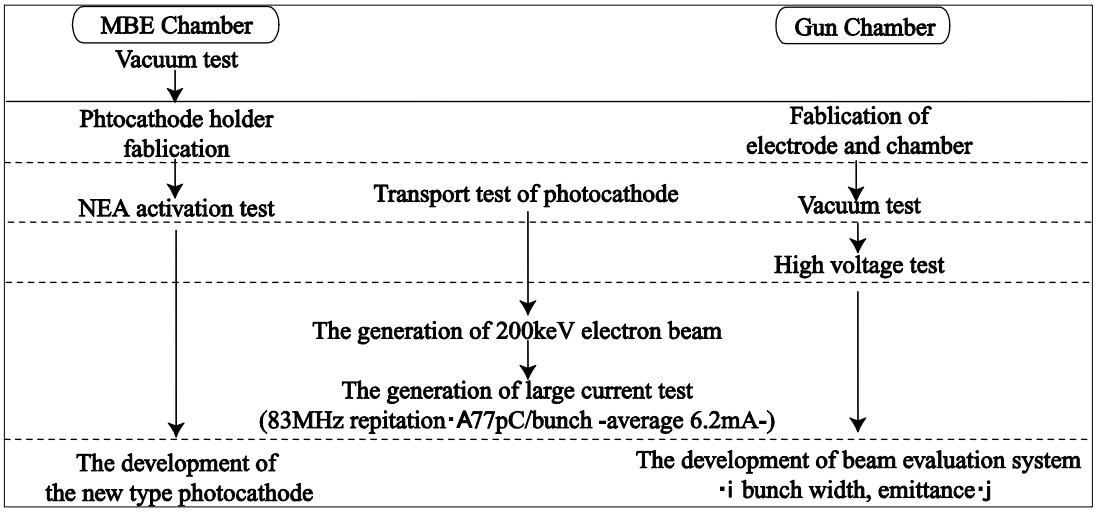

PERFORMANCE OF THE OPTICAL KLYSTRON ETLOK-III FOR DEVELOPING INFRARED STORAGE RING FREE ELECTRON LASERS*

N. Sei#, K. Yamada, H. Ogawa, M. Yasumoto, Research Institute of Instrumentation Frontier, National Institute of Advanced Industrial Science and Technology, 1-1-1 Umezono, Tsukuba, Ibaraki 305-8568, Japan

Abstract

Oscillations of free electron lasers (FELs) with the compact storage ring NIJI-IV in a wade wavelength region of 1-12 μm are planned in National Institute of Advanced Industrial Science and Technology (AIST). The optical klystron ETLOK-III for developing infrared FELs has been installed in a long straight section of the NIJI-IV. The ETLOK-III has two undulator sections of 7 periods and one 75 cm dispersive section. The maximum *K* value was estimated to be about 10.4 from a measurement of magnetic field. Fundamental and higher harmonics of spontaneous emission from the ETLOK-III were observed with large gaps. The modulation of the spectra of the spontaneous emission suggested that the maximum FEL gain would be about 2% in the visible and near-infrared regions.

INTRODUCTION

Oscillations of broad-band free electron lasers (FELs) have been studied with the storage ring NIJI-IV at National Institute of Advanced Industrial Science and Technology (AIST). Although the NIJI-IV is a compact storage ring with a 29.6 m circumference, it has two 7.25 m straight sections. The optical klystron ETLOK-II has been installed in one of the straight sections so as to realize FEL oscillations in a shorter wavelength region [1]. The NIJI-IV FEL system advanced the record of the shortest FEL wavelength down to 212 nm in 1998 [2]. It achieved the FEL oscillations at the wavelength of 198 nm in 2003, and became the third device which realized storage ring FELs in the VUV region [3]. Output power of an FEL at a wavelength around 200 nm was increased to 0.5 mW by using cavity-mirrors with higher transmission. Preliminary experiments of photoelectron emission microscopy were carried out, and the good spatial resolution was obtained with video-rate time resolution.

A new optical klystron ETLOK-III for FEL oscillations in the infrared region was installed in the other straight section in this February. Although many infrared FEL facilities based on linear accelerators are operating, no storage ring FEL has been achieved in the wide infrared region. However, the storage ring FEL has the advantage of a narrow line width and stability of the lasing wavelength compare with the linear accelerator FEL. It can be used as well as synchrotron radiation that passed a monochromator. Then, we have planed FEL oscillations with the ETLOK-III in a wavelength region of 1-12 μm [4]. The infrared storage ring FEL will be applied for not only a light source of photoelectron emission microscopy but also generation of a hard X-ray beam by the Compton backscattering process [5]. In this article, we explain the feature of the optical klystron ETLOK-III, and report results obtained from the spontaneous emissions of the ETLOK-III.

OPTICAL KLYSTRON ETLOK-III

Design

A planar undulator with bump magnets was remodelled into the ETLOK-III [4]. The 3 m undulator had magnets with 20 cm period. The magnet material was SEREM-N38H with a remanent field higher than 1.24 T. Magnets of undulator sections of the ETLOK-III reuse those of the old undulator. Then, number of the periods in one undulator section is 7. The gap of the undulator sections can be changed between 36 and 150 mm. The dispersive section of the ETLOK-III was designed so that N_d, which is a number of periods of the FEL wavelength passing over an electron in the dispersive section, became about 90 due to the then electron-beam qualities. In order to obtain the large N_d, the length of the dispersive section is set to be 72 cm and free spaces of 1.5 cm are installed between the dispersive section and the undulator sections. The gap of the dispersive sections can be changed between 36 and 188 mm. However, the magnets in the dispersive section are inserted between tables which fix the magnets of the undulator sections, so that the gap of the dispersive section must be smaller than addition of the gap of the undulator section and 38 mm.

. Figure 1 shows the outline of the ETLOK-III. The magnetic field on the center axis of the ETLOK-III under the some gap conditions was measured before the installation. The measured value of the magnetic field is about 4% larger than the designed one, and the maximum *K* value is 10.4.

Because the dispersive section is long, the NIJI-IV electron beam with comparatively low energy meanders greatly in it. When the uniformity of the magnetic field is insufficient horizontally in the dispersive section, the electron beam is kicked in it and comes off the center axis of the ETLOK-III. The calculated horizontal distribution of the magnetic field in the dispersive section under the minimum gap condition is shown in Fig. 2. Width of the magnet is small with 88 mm, so that the magnetic field weakens by 7.6 % at the point of 20 mm away from the center axis. Therefore, it is necessary to move an axis of the electron-beam orbit from the center axis of the ETLOK-III or to change the magnetic field in the dispersive section. Because the shift of the electron beam in the dispersive section is large, the latter idea would be

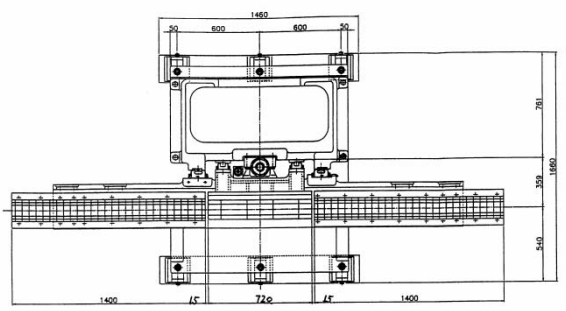

Fig. 1. Outline of the optical klystron ETLOK-III.

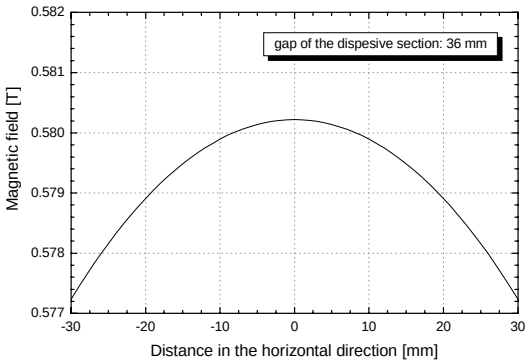

Fig. 2. Calculated magnetic field at the center of the dispersive section of the ETLOK-III. The gap is set to be the minimum of 36 mm.

more practicable. We plan an improvement that the magnetic field of the both end magnets of the dispersive section is shunted by iron plates and a steering coil is attached to a vacuum chamber in the dispersive section. At present, a small steering coil which can compensate for the magnetic field of ~2×10^{-3} T are attached, and the gap of the dispersive section can be set down to 120 mm.

Influence for the electron beam parameters

The ETLOK-III arranges the magnets horizontally, so that it has a vertical focusing effect. This effect causes vertical tune shift and distorts the vertical betatron function due to asymmetrical arrangement of the ETLOK-III in the straight section. Present betatron tunes of the NIJI-IV electron beam are 2.291 in the horizontal direction and 1.394 in the vertical direction, and the magnetic field of quadrupole magnets is adjusted with the gap of the ETLOK-III to keep the tunes. Figure 3 shows calculated betatron functions and dispersion functions with and without the ETLOK-III at the same betatron tunes. As this figure shows, vertical betatron function in the long straight sections decreases due to the strong vertical force with the ETLOK-III. Natural emittance also

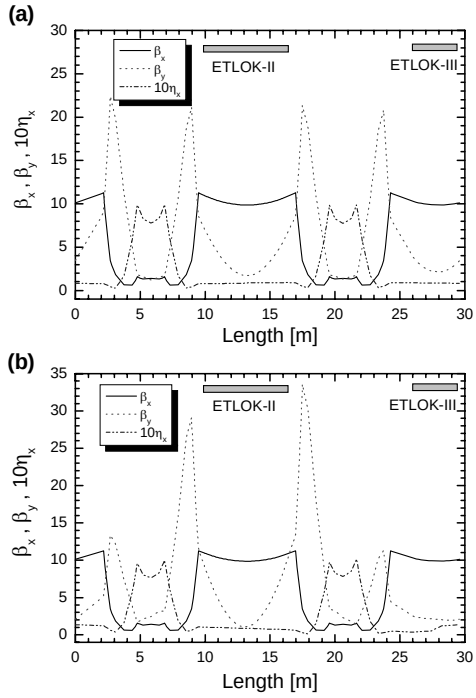

Fig. 3. Calculated betatron functions (horizontal β_x and vertical β_y) and dispersion function (η_x) without (a) and with (b) the ETLOK-III.

decreases by about 5%. Therefore the vertical beam size would become small about 10% at the center of the ETLOK-III. When the gaps are minimum, total radiation power from the NIJI-IV is about 6% stronger than that without the ETLOK-III. We can expect that the power of the short-wavelength FEL from the ETLOK-II enhances.

OBSERVATION OF THE SPONTANEOUS EMISSION

The optical klystron ETLOK-III has been installed in the NIJI-IV in this February, and the electron-beam current has been over 200 mA with the undulator gap of 125 mm. The electron-beam energy is set to be 340 MeV. Because the electron beam is kicked at the exit of the dispersive section, the undulator gap is set to be over 95 mm and the spontaneous emission is observed in the visible and near-infrared regions. Uniform area of the magnetic field in the ETLOK-III is narrow horizontally, so that the electron beam must be passed in parallel to central axis of the ETLOK-III in order to obtain symmetry spontaneous emission. A photograph of the spontaneous emission observed with the undulator gap of 140 mm is shown in Fig. 4.

Spectra of the spontaneous emission were measured by a photodiode array with a monochromator which had the resolution of 0.2 nm. Because the dispersive section has a parabolic distribution of magnetic field in the horizontal

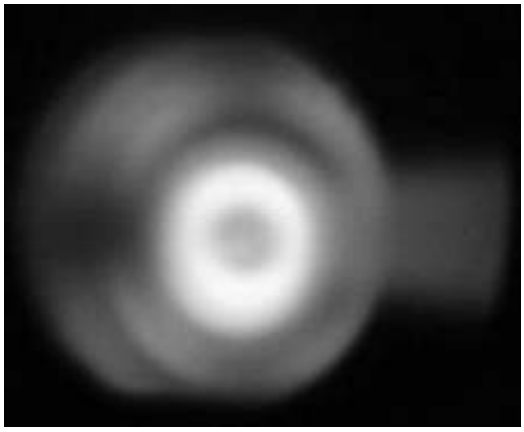

Fig. 4. Photograph of the spontaneous emission from the ETLOK-III. The gaps of the undulator section and the dispersive section are 140 and 150 mm, respectively.

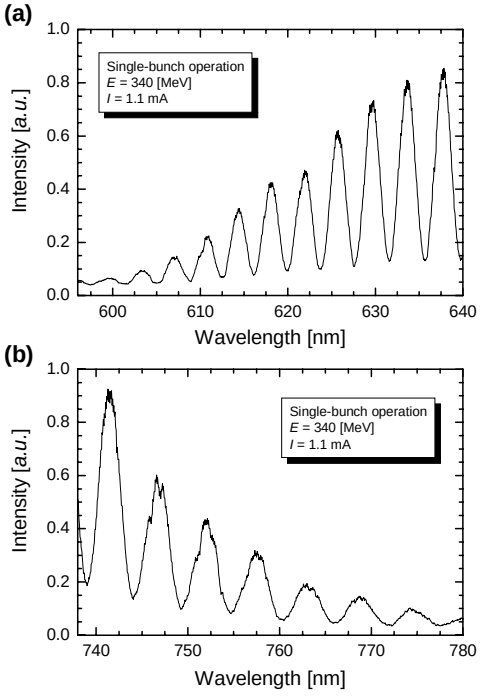

Fig. 5. Spectrum of the spontaneous emission from the ETLOK-III: (a) the end of the short wavelength and (b) the end of the long wavelength. The gaps of the undulator section and the dispersive section are 125 and 160 mm, respectively.

direction, precise adjustment of the electron-beam orbit is necessary so as to obtain a large modulation factor for the spontaneous emission. Figure 5 shows a spectrum of spontaneous emission with the undulator gap of 125 mm

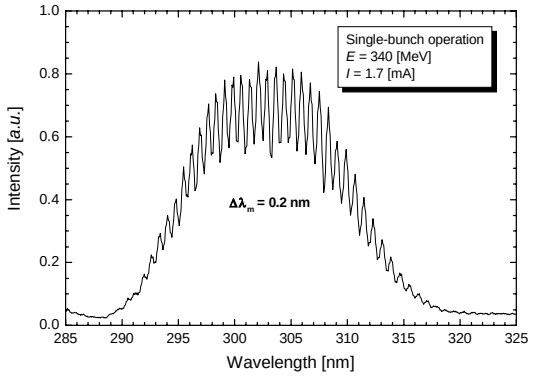

Fig. 6. Spectrum of the third harmonic emission from the ETLOK-III. The gaps of the undulator section and the dispersive section are 115 and 150 mm, respectively.

and the dispersive gap of 160 mm. The resonant wavelength measured in this condition was about 690 nm, and it was agreement with the wavelength estimated from the measurement of magnetic field in the ETLOK-III. The value of N_d estimated from intervals of the modulation of the fundamental was about 140. The value calculated from the magnetic field in the dispersive section was about 150. The difference between the measurement and the calculation would suggest that the adjustment of the electron-beam orbit was insufficient. Moreover, energy spread of an electron bunch can be estimated by using the modulation factor [6]. The energy spread measured with the undulator gap of 125 mm was $2.7\pm.0.2\times10^{-4}$, which was close to the natural energy spread of 2.6×10^{-4}.

The spectra of the higher harmonic emission were also investigated in the ultraviolet and the visible regions. Further precise adjustment of the electron-beam orbit is demanded for the higher harmonics. Figure 6 shows a spectrum of the third harmonic emission with the undulator gap of 115 mm and the dispersive gap of 150 mm. Relative width of the spectrum of the third harmonic emission was about 19 in Fig. 6. Because the theoretical one was 21, the spectrum was a little broader. The measured interval of the modulation of the third harmonic emission at the resonant wavelength was about 0.75 nm, and it was slightly narrower than the theoretical one of 0.72 nm. The modulation factor for the third harmonic emission which was removed an influence of the measurement system was smaller than that estimated from the modulation for the fundamental emission. We have not ascertained the whether these results were caused by misalignment of the electron-beam orbit or distortion of the magnetic field in the ETLOK-III yet. However, N_d can be decreased by closing the undulator gap. Because the modulation factor become over 0.6 with the narrow undulator gap, it will be possible to obtain FEL oscillations which amplify the third harmonic emission in the infrared region.

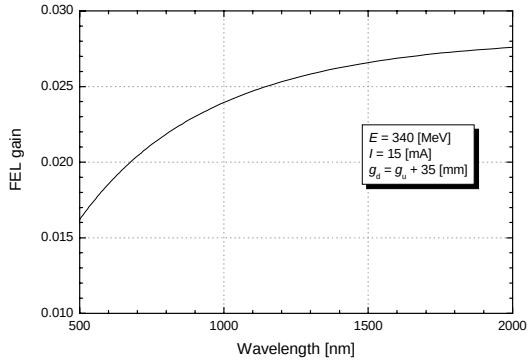

Fig. 7. Relationship between the wavelength and the estimated FEL gain at the electron-beam current of 15 mA. The gap of the dispersive section is set to be 35 mm wider than the gap of the undulator section.

We can estimate the maximum FEL gain from the observed spectra of the spontaneous emission. Figure 7 shows a relationship between the wavelength and the estimated FEL gain in the visible and the near-infrared regions. Though the *K* value is comparatively small (<3.5) in those regions, the maximum FEL gain is expected to be about 2% at the electron-beam current of 15 mA [3]. Because high-reflection mirrors of 99.8% or more are available in those regions, the FEL oscillations will be realized with the ETLOK-III. However, we have not operated the NIJI-IV with the undulator gap under 95 mm due to the bend of the electron-beam orbit in the dispersive section yet. It is impossible to evaluate the maximum FEL gain in the longer wavelength region for the present. We will improve the dispersive section to compensate non-uniformity of the magnetic field, so that it will allow us to observe the spontaneous emission with the narrower undulator gap.

CONCLUSIONS

We have installed the optical klystron ETLOK-III for developing infrared FEL oscillations in the long straight section of the storage ring NIJI-IV. The number of the 20 cm magnetic period in an undulator section of the ETLOK-III is 7, and the length of the dispersive section with two 1.5 cm free spaces is 75 cm. The maximum *K* value was designed to be about 10, and it was estimated to be 10.4 from the measurement of the magnetic field. We have also observed the spontaneous emission from the ETLOK-III in the visible and near-infrared regions. It was noted that the maximum *K* value which was estimated from the fundamental wavelength of the spontaneous emission on the axis of the electron-beam orbit was about 10.4. Value of N_d estimated from the measurements of the magnetic field in the dispersive section was also in accord with that obtained from the spectra of the spontaneous emission. The maximum FEL gain which was evaluated with the NIJI-IV electron-beam qualities and the performance of the ETLOK-III was about 2% in the visible and near-infrared regions. Then, it will be possible to realize FEL oscillations with the fundamental and higher harmonics in the regions.

Now an improvement of the dispersive section is planed in order to store the electron beam with the narrower gap of the ETLOK-III. In the mid-infrared region, the maximum FEL gain would be higher due to the higher *K* value. Because N_d becomes smaller, it would be easy to oscillate the FELs with higher harmonics. We will investigate the performance of the optical klystron ETLOK-III in the higher *K* value region.

ACKNOWLEDGEMENTS

This work was supported by the Budget for Nuclear Research of the Ministry of Education, Culture, Sports, Science and Technology of Japan.

REFERENCES

[1] T. Yamazaki *et al.*, Nucl. Inst. and Meth. **A331** (1993) 27.
[2] K. Yamada *et al.*, Nucl. Inst. and Meth. **A445** (2000) 173.
[3] K. Yamada *et al.*, Nucl. Inst. and Meth. **A528** (2004) 268.
[4] N. Sei *et al.*, Jpn. J. Appl. Phys. **41** (2002) 1595.
[5] N. Sei *et al.*, Nucl. Inst. and Meth. **A483** (2001) 429.
[6] D. A. G. Deacon *et al.*, App. Phys. **B34** (1984) 207.

IMPROVED PERFORMANCE OF THE NIJI-IV COMPACT VUV/IR FEL AND ITS APPLICATION TO THE SURFACE OBSERVATION*

K.Yamada, N.Sei, H.Ogawa, K.Watanabe, M.Yasumoto, Research Institute of Instrumentation Frontier, AIST, Central 2, 1-1-1 Umezono, Tsukuba, Ibaraki, 305-8568 Japan

Abstract

Increase of the transmittance of the out coupling mirror as well as e-beam energy brought a sufficient free-electron laser (FEL) power around 200 nm for a real-time surface observation. By irradiating surfaces of transition-metals, such as Chromium and Palladium, with deep-ultraviolet (DUV) FEL, fine structure and surface chemical reaction were successfully observed with spatial and temporal resolutions of ~ 300 nm and 33 ms, respectively. Every efforts to shorten the lasing wavelength below 190 nm are being made continuously by correcting magnetic-field errors in the optical klystron and developing cavity mirrors with a smaller optical loss. A new optical klystron for use in the infrared (IR) region was installed into the north straight section of the NIJI-IV to extend the lasing range up to ~ 10 μm.

INTRODUCTION

At AIST, an FEL with ultra-wide wavelength range from the vacuum ultraviolet (VUV) to the far infrared (FIR) is being developed based on a compact storage ring NIJI-IV. Though its shortest lasing wavelength is still limited to 198 nm because of an unexpected gain smaller than that estimated by the analytical calculation [1], a sufficient margin of the gain enabled us to obtain one-order larger FEL power than before, by adopting an output-coupler with a higher transmittance as well as increasing the stored beam energy in the ring.

Since the work function of transition-metals lies around 5 eV, DUV FELs with a wavelength of ~ 200 nm are suitable as a intense light source to observe surface fine structure or surface chemical reactions on such transition-metals with high spatial and temporal resolutions in combination with the photoelectron emission microscopy (PEEM). The intensity of NIJI-IV FEL recently obtained is large enough to extract sufficient amount of photoelectrons for sub-micron scale and video-rate real-time observation from transition-metal surfaces.

Unexpectedly small FEL gain is probably caused by some demagnetization of magnet blocks in the 6.3-m optical klystron, which may deflect the beam and reduce the overlapping between electron beam and optical mode. We are preparing high performance dielectric multilayer mirrors optimized around 190 nm to compensate such an insufficient gain. We also plan to replace or remagnetize such degraded magnet blocks.

A 3.6-m optical klystron for lasing in the IR was recently installed into the north straight section of the NIJI-IV to extend the lasing wavelength range up to ~ 10 microns. One of our interests in the IR-FEL application is the microscopic Raman spectroscopy which can examine adsorbed molecules and their bonding conditions on the metal surfaces. Establishment of a total surface analysis system using NIJI-IV compact VUV/IR FEL combined with characteristic surface analysis techniques is one of our goals in the near future.

*This work is supported by peaceful utilization technology of nuclear energy from the ministry of education, culture, sports, science and technology of Japan.

PERFORMANCE OF THE NIJI-IV FEL

We have been modifying the NIJI-IV FEL system to extend its lasing range. As shown in our previous paper [2,3], replacement of the NIJI-IV vacuum chambers to low-impedance-type ones as well as installation of thin sextupole magnets into the ring brought a higher peak current of the stored beam and a resultant higher FEL gain. This led to easy FEL lasing around 200 nm even with our compact system. To utilize such a DUV FEL, we tried to enhance the laser output power by increasing the transmittance of the output coupler of the optical cavity from 0.05 to 0.5 %. The beam energy was also increased by 10 % from 310 up to 340 MeV. As a result, the average output FEL power at 202 nm was successfully increased up to 0.5 mW per one laser port with a beam current of 15 mA, which is larger by an order of magnitude than before [2]. A higher power is expected through further increase of the beam energy as well as multi-bunch operation of the ring. Fig.1 shows the dependence of average output power on the beam energy.

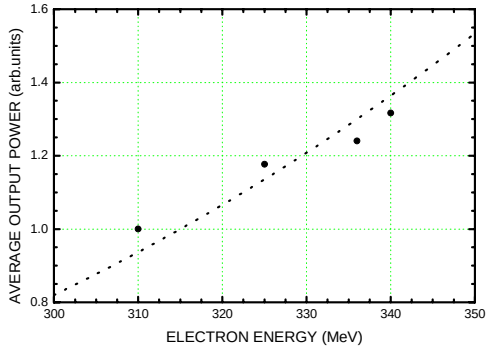

Fig.1. Dependence of average output power on the beam energy. Solid circles and solid curve indicate the observed power and an expected curve proportional to the 4th power of the beam energy.

Solid circles and curve respectively indicate the observed FEL power at 202 nm and an expected energy dependence of the laser power which can be proportional to the 4th power of the beam energy. In this figure, the observed average power was estimated from the peak height of the lasing line spectrum detected with a photodiode array attached to a 25-cm monochromator. Here, the peak height was corrected for the beam current. Absolute power was measured with a highly sensitive and stable CW power meter (Gentec TPM-310) with a wind block. It is found in Fig.1 that the observed output power was enhanced by at least 30 % during 10-% increase of the beam energy, which does not largely deviate from the expected curve. Now we plan to increase the beam energy from 0.31 up to at least 0.4 GeV which will bring three times power enhancement. A few-mW power in the DUV to the VUV range is in a sufficient level for PEEM measurement.

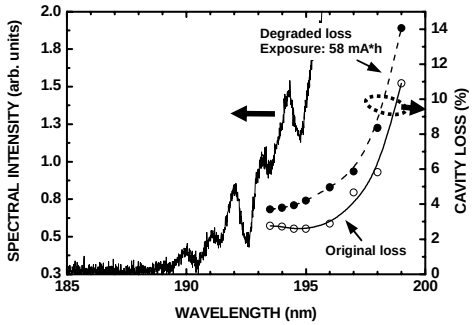

Fig. 2. Cavity-loss as a function of wavelength. A spectrum of the spontaneous emission resonating inside the optical cavity is also indicated.

Lasing around 190 nm and below is also being tried using a low-loss optical cavity composed of two Al_2O_3/SiO_2 mirrors. Though the original loss of this cavity was 2.8 % at 193 nm, it rapidly increased up to 3.7 % with 58 mA-h exposure to the undulator radiation. Due to an unexpectedly smaller FEL gain, probably caused by some demagnetization of the undulator magnets, we have not obtained lasing around 190 nm yet. Now we are preparing robust mirrors with an optical loss smaller than 1 % and also planning to replace the degraded magnet blocks in the optical klystron. Fig.2 shows the loss curve for the above mentioned cavity as a function of wavelength. A spectrum of the spontaneous emission resonating inside the optical cavity, observed at a beam current of ~ 7 mA, is also indicated in the figure. Though the spectrum is strongly distorted by intense long-wavelength off-axis components and light absorption by the Schumann-Runge system of Oxygen molecules around 193.8 nm, spectral modulation peculiar to an optical klystron is clearly seen. Since such a spectral modulation becomes much more obvious and even spiky for a beam current more than ~ 14 mA, the lasing seems to be achieved soon.

A new optical klystron for lasing in the IR was installed in the north straight section of the NIJI-IV. Its performance is being checked spectroscopically [4].

APPLICATION OF NIJI-IV DUVFEL TO SURFACE OBSERVATION

NIJI-IV DUVFEL was applied to surface observation, in combination with a PEEM system (STAIB Instrumente, type 350). This PEEM system has three sets of electrostatic electron lenses and a micro channel plate (MCP) equipped with a fluorescent screen. By viewing the focused images on the fluorescent screen with a CCD camera, transient phenomena, such as chemical reactions on transition-metal surfaces, can be monitored with video-rate time resolution. Since the spatial resolution of this system is 80 nm and our FEL intensity is large enough to extract sufficient amount of photoelectrons to recognize the surface contrasts within 33.3 msec, we can examine real-time physical and chemical information on transition-metal surfaces in a sub-micron scale. Fig.3 shows the experimental setup for FEL-PEEM measurement. The FEL with a wavelength of 202 nm comes from left-hand side through a long focus lens and is reflected by a flat aluminium mirror to focus onto the sample surface. The FEL intensity on the sample surface is roughly estimated to be 500 mW/cm^2.

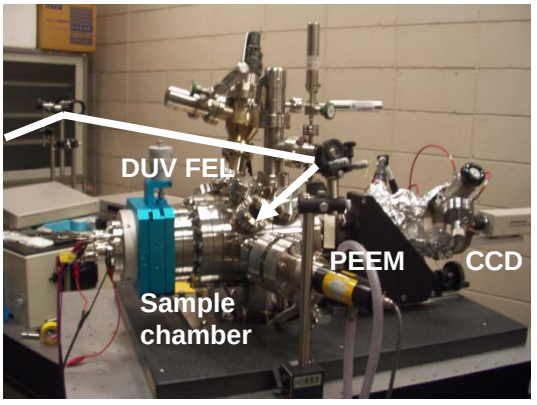

Fig.3 Experimental setup for FEL-PEEM measurement.

To examine the total resolution of our FEL-PEEM system, we observed a standard reference sample for scanning electron microscope (SEM) which has a fine structure formed with 70-nm thick CrO_2 on a Cr-overcoated SiO_2 substrate. A typical example of the video-rate real-time imaging of the standard SEM sample is shown in Fig.4 (a) and (b). It was found that the FEL was intense enough to obtain video-rate moving images on the Cr surface. From higher magnification image (Fig.4 (b)), the spatial resolution of our system is estimated to be ~ 300 nm at present. Suppression of mechanical vibration from a vacuum pump will be necessary to realize the specification of the PEEM system.

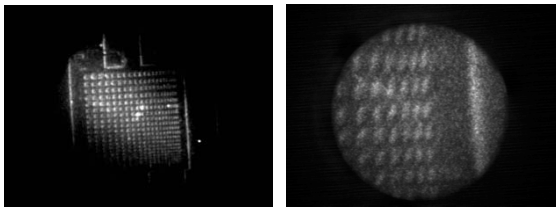

(a) (b)

Fig. 4. Typical example of the video-rate real-time imaging of the standard SEM sample for lower (a) and higher (b) magnifications. The narrowest feature width is 1 μm in both images.

As a preliminary experiment for the FEL-PEEM measurement, we observed a Palladium surface, introducing CO and O_2 gasses. In this case, CO_2 is created from adsorbed CO and O_2 molecules under the catalysis of Palladium and desorbed from the Palladium surface. Such a reaction process must be reflected in the contrast of the PEEM image [5]. Fig.5 (a) – (d) shows still shots for four deferent situations, sampled out from a real-time moving image. After cleaning with Argon sputtering and annealing at 1,100 K in a high vacuum below 5 x 10^{-7} Pa, pure surface of a Palladium standard sample (from Mateck) was exposed to the CO gas to be covered with CO molecules. Then, Oxygen gas was introduced to be reacted with adsorbed CO molecules to produce CO_2 which will desorb immediately. Fig.5 corresponds to the FEL-PEEM images for pure surface after cleaning (a), a CO-adsorbed surface (b), surface reaction of CO and O_2 (c), and the same surface reaction at a different moment (d). In these images the full width of the viewing field is 200 μm. During the measurement, the FEL was lasing at 202 nm with a beam current between 11 and 8.5 mA In Fig.5 (a), many crater-like structures are scratches which remains on the polished surface originally. One can see in Fig.5 (b) that the brightness of the image was reduced through the adsorption of CO molecules over the whole surface. On the other hand, the images indicated clearly different features after introducing Oxygen gases, Fig.5 (c) and (d), where a complicated black and white blindle appeared. The black small patches seen around upper right area of (d) imply Oxygen-adsorbed regions, while several bright islands seen from upper left to lower right of (c) seems to be the areas where the adsorbed CO molecules were desorbed to form CO_2 through chemical reaction with O_2. These patterns varied rapidly in a-few-second time scale and were observed only during FEL lasing. More detailed observation is being carried out under various conditions, such as different gas pressure and substrate temperature.

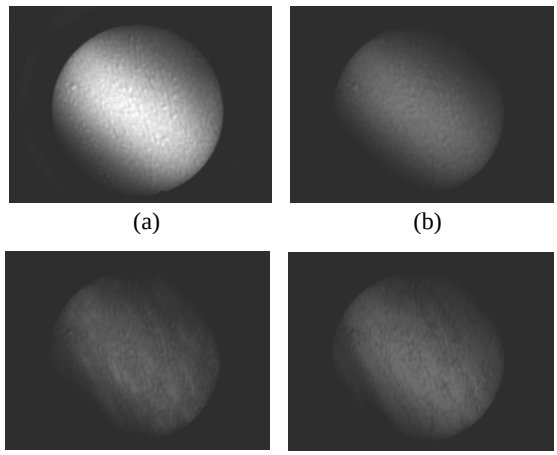

(a) (b)

(c) (d)

Fig. 5. Still shots, sampled from a real-time moving PEEM image, on a Palladium surface under deferent conditions; after surface cleaning by both Argon sputtering and annealing (a), with the surface covered by CO molecules (b), and during reaction of CO with O_2 (c)(d).

SUMMARY

Output power of the NIJI-IV FEL was enhanced by an order of magnitude in the DUV region around 200 nm. The DUV FEL was utilized to make real-time imaging of fine structures and chemical reactions on transition-metal surfaces in combination with a PEEM system. Moving images of reactions by CO and O_2 on a Palladium surface were visualized with video-rate time resolution. More detailed FEL-PEEM experiment is being carried out at present. Efforts to obtain FEL lasing at a wavelength shorter than 190 nm are being continued. Lasing in the IR using our compact ring is also expected to be realized. A total real-time analysis system based on the NIJI-IV compact VUV/IR FEL will be established in combination with characteristic surface analysis techniques in the near future.

REFERENCES

[1] K.Yamada, N.Sei, H.Ohgaki, T.Mikado, T.Yamazaki, Nucl. Instr. and Meth. A475 (2001) 205.
[2] K.Yamada, N.Sei, H.Ogawa, M.Yasumoto, T.Mikado, Nucl. Instr. and Meth. A528 (2004) 268.
[3] N.Sei, K.Yamada, H.Ohgaki, V.N.Litvinenko, T.Mikado, T.Yamazaki, Nucl. Instr. and Meth. A429 (1999) 185.
[4] N.Sei, K.Yamada, H.Ogawa, M.Yasumoto, in this proceedings.
[5] H.H.Rotermund, Surface Science 283 (1993) 87.

A MM-WAVE, TABLE-TOP CERENKOV FREE-ELECTRON LASER*

I. de la Fuente#, P.J.M. van der Slot, K.J.Boller
University of Twente, Laser Physics & Non-Linear Optics Group, PO Box 217, 7500 AE Enschede, The Netherlands

Abstract

A Cerenkov Free-Electron Laser (CFEL) has the advantage that the operating frequency increases with decreasing electron beam energy. The low beam energy allows for the construction of compact devices. We have designed and constructed such a device with a footprint of 0.5 m x 1.5 m, an operating frequency of 50 GHz and a design output power of 1 kW CW. We will present the overall design and experimental set-up, and first experimental results.

INTRODUCTION

High frequency microwave radiation has shown to be attractive for several applications such as wireless communication, material processing or microwave chemistry [1]. In some cases, also high output power is required, e.g., mm-wave radar applications that require increasingly higher output powers at higher frequencies [1,2]. However, industrial applications seem to be limited to the operating frequencies of the magnetron, though applications have been studied at higher frequencies.

The CFEL may be a welcome addition to the family of microwave sources as a cost-efficient, compact device capable of delivering kW-level output power at frequencies of up to 100 GHz. Compared to undulator based FELs, they have the advantage of generating higher frequencies at lower electron beam voltages and may be especially interesting for millimetre wavelength generation [3,4].

In order to test this potential of the CFEL and to research (industrial) applications as higher frequencies, a compact CFEL with a footprint of about 0.5 m by 1.5 m (excluding a 19 inch rack for power supplies and control electronics) producing an output power in access of 1 kW CW has been constructed and is currently being commissioned. In the remaining part of this paper we will report on the design and construction of this device and present some preliminary experimental results.

OVERVIEW OF THE SYSTEM

A general overview of the CFEL is presented in fig. 1. The main parts of the system are the electron gun, the interaction area, the outcoupler and the collector. Electrons are accelerated from the electron gun towards the lined cylindrical waveguide that forms the interaction area. The electrons are transported through this section up to the collector by means of an axial magnetic field. An outcoupler separates the generated radiation from the electron beam, while at the same time it acts as the down-stream mirror of the oscillator. Table 1 shows the general design values of the CFEL at the University of Twente.

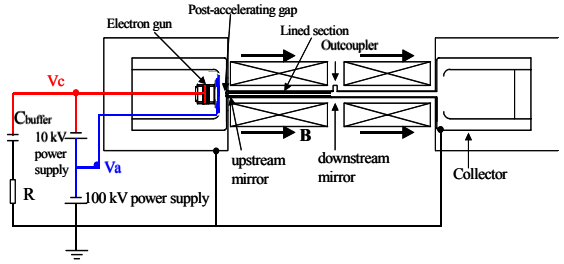

Figure 1. Overview of the CFEL. The depressed collector is initially not installed and instead a buffer capacitor is used to supply the beam current in pulsed operation.

Nominal operational frequency		50 GHz
Electronic tuning range		>10 %
Nominal peak output power		1 kW (10 μs-CW)
Nominal outcoupling		80-9 %
Accelerating voltage		From 65 to 100 kV
Liner	Material	fused GE quartz type 219
	Dielectric constant, ε_r	5.8
	Thickness, d_ε	1.3 mm
	Inner radius, R_d	1.5 mm
	Length, L	250 mm
Magnetic field on axis		0.15 T
Beam diameter		2 mm
Beam current		800 mA
Max HV Power Supply current		30 mA

Table 1: Design values of the tabletop Cerenkov FEL.

Electron gun and beam transport

In the CFEL, the electron beam is generated using a commercially available 10 kV, 800 mA, and gridded thermionic electron gun. The beam is further accelerated to a maximum of 100 kV using a post acceleration section. The grid allows for flexible temporal control of the electron beam and thus also for the generated radiation field. By keeping the acceleration and grid voltage of the (10 kV) electron gun constant, and by varying the post-acceleration voltage, an electron beam is produced with constant current and varying beam voltage.

* Research is funded by the EU, contract **G5RD-CT-2001-00546**
# i.delafuentevalentin@utwente.nl

A combination of commercial air insulated HV power supplies and home build supplies are used for the acceleration, respectively grid, and heater voltages of the electron gun. Short isolating distances are obtained by using SF_6 as an insulating gas and the overall footprint of the complete device could thus be limited to 0.5 by 1.5 m. The design value for the electron beam is 800 mA, whereas the HV power supplies are only able to supply 30 mA. In the final set-up a depressed collector will be installed for cw operation, however, initially the system will be operated in pulsed mode and a buffer capacitor is used to supply the beam current (see fig. 1). Using a buffer capacitor of 70 nF resulted in single pulses of up to 40 μs duration with a rise and fall time of about 0.1 μs, and a train of 10 μs pulses at a few Hz repetition rate. The capacitance, which essentially limits the pulse length, will be increased stepwise to 2 μF, thereby increasing the pulse duration to about one millisecond with a duty cycle of almost 4 %.

First measurements on performance of the electron gun show that the e-beam current varies linearly with the applied grid voltage between 0 and 725 mA and it is independent of the total accelerating voltage. Fig. 2 shows the peak current delivered by the cathode as a function of the grid voltage for a total acceleration of 69.45 kV and a pulse of 10 μs duration.

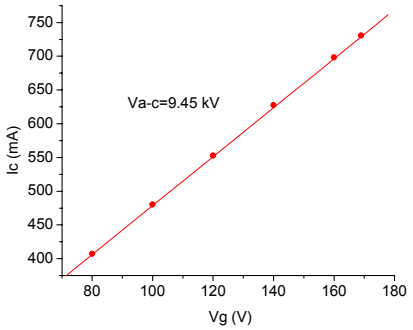

Figure 2: Beam current as a function of grid voltage for a first anode-cathode voltage $V_{a\text{-}c}$ of 9.45 kV.

Characterization of the electron beam transport up to the end of the interaction region, with no liner present, is done by measuring the collected current using a Faraday cup placed just after the first solenoid at the end of the waveguide. The Faraday cup consists of an OFHC copper plate. In addition, the Faraday cup contains a 50 μm-diameter tungsten wire, which can be swept vertically through the electron beam, in front of the plate. The latter gives information about the transverse spatial distribution of the electron beam.
So far, the collected current is 73 % of the current emitted by the cathode and the beam possesses a symmetric distribution in the scan direction. This measured value is consistent with the distance between the Faraday cup and the end of the first solenoid and indicates nearly complete beam transport from gun up to the end of the interaction region. This is concluded from simulations with the software package Trak 6.0 [5], which show that in absence of the second solenoid, Faraday cup collects only a fraction of the electrons within the beam.

Tuning and output characteristics

For sufficiently high frequency the electromagnetic wave propagating through the lined waveguide attains a phase velocity less than the speed of light in vacuum. Such a wave is mainly propagating through the liner and has an evanescent part extending into the vacuum. If the electron velocity is slightly higher than the phase velocity of the wave, the latter produces longitudinal bunches within the electron beam and consequently the beam will coherently amplify the wave, at least as long as it has a longitudinal electric field component. The resonant frequency is defined as the frequency for which the two velocities are equal. As the wave's phase velocity is not only determined by the value of the dielectric constant but also by the geometry, i.e., inner liner radius and waveguide radius, the tuning characteristics can be influenced by appropriate choices of these parameters. It should be pointed out here that variations in, e.g., the inner radius of the liner result in variations of the phase velocity of the wave along the liner and may thus degrade the gain of the device in a way similar to undulator errors in undulator based FELs [6]. This may be especially important for low-gain devices like the current CFEL.
The liner in the actual set-up is a tube made of fused quartz type GE 219 with a specified dielectric constant of 5.8 and dielectric loss less than tan $\delta = 10^{-4}$. As the exact value of the loss tangent is not known, a value of $1 \cdot 10^{-5}$ is used in the simulations. The liner tube has an inner diameter of 3 mm. At the outside of the tube a thin copper coating is applied, which acts as the waveguide wall, to ensure that no gap exists between the liner and the waveguide.

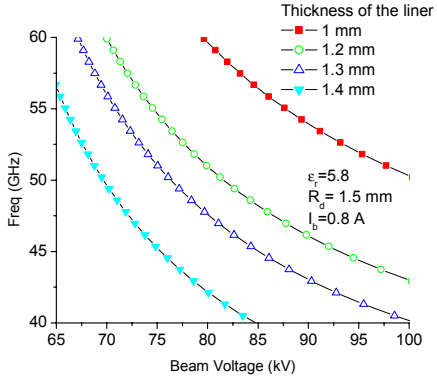

Figure 3: Resonant frequency as a function of electron beam accelerating voltage

Figure 3 shows the calculated output frequency of the CFEL as a function of the total electron accelerating voltage, for several thicknesses of the liner. It can be seen that the expected frequency range covers the interval from 40 GHz to 60 GHz by varying the voltage from 65 to 100 kV, for a 1.2 mm or 1.3 mm thickness of the liner. Larger and smaller values give a more limited tuning range. The thickness of the liner has not only an influence on the tuning characteristics, but it also influences the coupling strength between the electron beam and the co-propagating EM wave. A thickness of 1.3 mm will be chosen for the experiment as with this we expect a higher output power the CFEL (than with 1.2 mm).

The 800 mA current is not enough to provide saturation in a single pass within a reasonable distance, so that the system is configured as an oscillator. To determine the required total reflectivity for a particular length of the liner, fig. 4 shows an example of the calculated output and dissipated power due to dielectric losses as a function of the total reflection coefficient of the oscillator. The reflection coefficient includes all losses except dielectric losses in the liner.

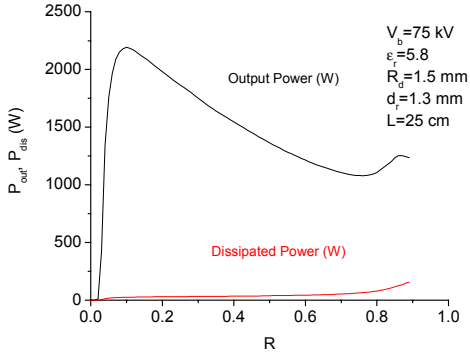

Figure 4: Calculated output and dissipated power due to dielectric losses for different reflection coefficients. The frequency is 50 GHz and a liner length of 25 cm is used.

Fig. 5 summarises the calculated maximum output power from the oscillator, the corresponding dissipated power due to dielectric losses, and the total reflection coefficient necessary to obtain that output power for different values of the liner length. The intra-cavity power should be small to keep the dissipation in the liner and waveguide as low as possible. Therefore, a relative small feedback with a large single pass gain is more desirable than a lower single pass gain and a higher feedback. However, fig. 5 shows that after an initial decrease in dissipated power with increasing interaction length (and thus with increasing single pass gain) it levels off. Apparently, the lower dielectric loss due to a lower intra-cavity power is compensated by the increase in liner length, which results in a higher loss. From fig. 5 it follows that a 20 cm interaction length would be sufficient, leading to a maximum output power of almost 2.3 kW and a required reflection coefficient of about 24 %. The design of the outcoupler indicates that a somewhat lower reflectivity was desirable, to keep mode conversion within the

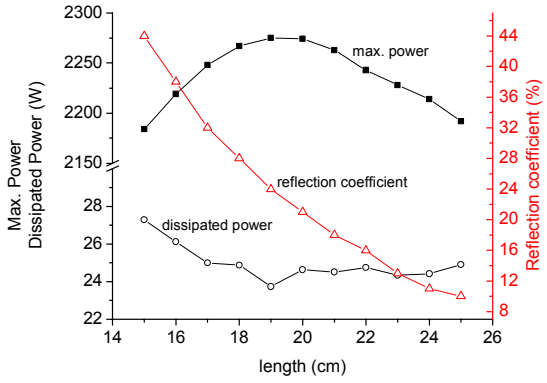

Figure 5: Calculated maximum output power and dissipated power due to dielectric losses with the corresponding reflection coefficient as a function of the length of the liner. The beam voltage is 75 kV and other parameters are as in Table 1.

outcoupler limited. Therefore the construction of the CFEL allows for a maximum liner length of 25 cm.

RF Outcoupler

To form an oscillator, the second anode (at ground potential) is used as the upstream mirror while the RF-outcoupler forms the downstream mirror. The upstream mirror contains a small aperture to pass the electron beam through. The aperture is below cut-off for the frequency range of interest. The RF outcoupler, which is shown in fig. 6, is designed to separate the electron beam from the generated radiation, to reflect part of that radiation and to convert the cylindrical geometry into the standard WR19 waveguide geometry for the output waveguide system. Both the radiation field and the electron beam reach the outcoupler at input port 1. The diameter of the cylindrical input waveguide is tapered down to a smaller value to

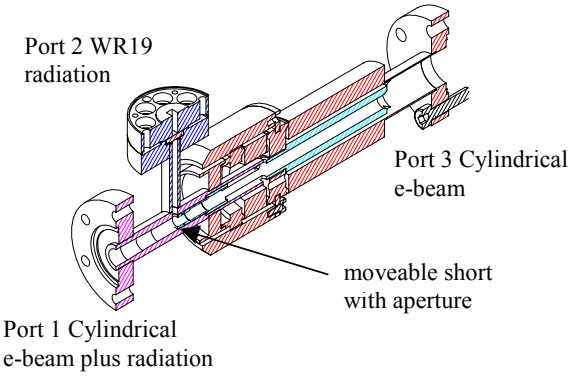

Figure 6: Outcoupler with the corresponding port denomination.

that all other higher order modes above the TM_{01} mode are below cut-off. The radiation is coupled into a standard rectangular WR19 waveguide mounted at a right angle with regard to the input cylindrical waveguide. The amount of coupling, and thus the amount of reflected radiation, can be controlled through the position of a movable short that is connected to port 3. This short contains an aperture that is below cut-off for the resonating frequencies and allows the e-beam to pass straight through to port 3 of the RF-outcoupler. Finally, a 1.85 mm thickness high-density polyethylene vacuum window is placed in the output port 2.

In order to characterize the reflection properties of the RF outcoupler we have measured the S_{11} parameter of port 2 as a function of the position of the short using a Network Analyser with a maximum frequency of 50 GHz. Measurements of the other S-parameters are currently not possible due to the non-standard geometries of port 1 and port 3. The results for a frequency of 50 GHz are shown avoid excessive mode conversion from the TM_{01} mode of the laser into the TE_{11} mode. The final diameter is such in Figure 7 for two cases, one with port 1 open and one when a short is applied to port 1. The measurement data do not change whether port 3 is opened or shorted. This indicates that no measurable radiation is coupled from port 1 or port 2 to port 3. When a short is applied to port 1 the measured S_{11} values indicate that the RF power is dissipated in the RF-outcoupler, which is mainly due to mode conversion. For the positional range of interest (3-6 mm), the dissipated power is less than 7 %, except near the 6 mm position where it increases to 26 %. For port 1 open, the S_{11} ranges from –2 dB to –8 dB when the short is moved from 3 mm to 6 mm, indicating that the desired reflection of 10-20 % is indeed obtained.

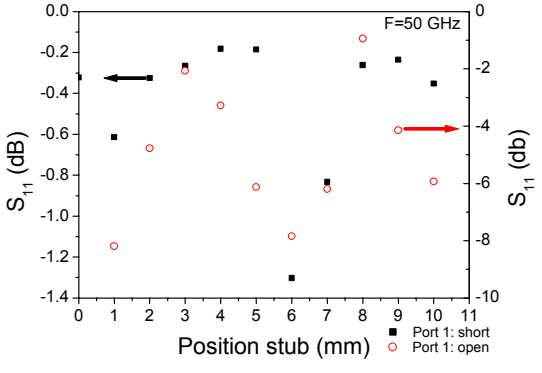

Figure 7: Measured S_{11} parameter at port 2 of the outcoupler for 50 GHz.

FUTURE PLANS

After the electron beam transport is optimised, the RF outcoupler will be installed. Initially, operation and characterization of the laser will be done in pulsed mode, with a progressive increment of the length of the pulses (via increasing the buffer capacitance). The results will provide the necessary data for designing the depressed collector, to be installed subsequently.

Once the source will be fully operational, it will be used to study several novel microwave applications.

REFERENCES

[1] M. Thumm, Free-electron masers vs. gyrotrons: prospects for high-power sources at millimetre and submillimetre wavelengths. *Nuclear Instruments and Methods in Physics Research A* 483 (2002) 186 –194.

[2] S. H. Gold *et. al*., Review of high-power microwave source research*, Rev. Sci. Instrum.* **68,** 11, November (1997).

[3] J.E.Walsh, T.C. Marshall and S.P. Schlesinger, Generation of coherent Cerenkov radiation with an intense relativistic electron beam, *The Physics of Fluids*, **20**, 4, (1977).

[4] E. Garate *et. al*., Cerenkov maser operation at lower-mm wavelengths*, J. Appl. Phys*. **58**, 2, (1985).

[5] Trak 6.0 from *Field Precision*, http://www.fieldp.com.

[6] I. de la Fuente, P.J.M. van der Slot K.-J. Boller, The effect of liner induced phase fluctuations on the gain of a Cerenkov FEL, *in these Proceedings.*

STATUS OF 30 GHZ FACILITY FOR EXPERIMENTAL INVESTIGATION OF THE COPPER CAVITY LIFETIME (CLIC COLLIDER PROJECT)*

A.V. Elzhov, E.V. Gorbachev, A.K. Kaminsky+, V.V. Kosukhin, E.A. Perelstein, N.V. Pilyar, T.V. Rukoyatkina, S.N. Sedykh, A.P. Sergeev, A.I. Sidorov, V.V. Tarasov
Joint Institute of Nuclear Research, Dubna, Russia
N.S. Ginzburg, S.V. Kuzikov, N.Yu. Peskov, M.I. Petelin, A.S. Sergeev, N.I. Zaitsev
RAS Institute of Applied Physics, Nizhny Novgorod, Russia

Abstract

The facility for experimental investigation of a copper cavity lifetime under multiple action of 30 GHz microwave power pulses is being created now by the collaboration of CLIC (CERN), JINR (Dubna) and IAP RAS (Nizhny Novgorod). A design of the test cavity, an estimation of the operating parameters of the FEM oscillator and the RF power transmission line was already discussed at FEL'03. Last year was devoted to the achievement of the design parameters of all of the elements of the facility. We have developed the equipment and the method of RF transmission line adjustment, improved the stability of the linac power supplies, created the new system of data acquisition. Effect of central mode splitting in Bragg resonators is one of the problems under study. Start of the full-scale experiments is planned to the end of 2004.

1 INTRODUCTION

One of the strict limits on the accelerating gradient in future linear colliders is the fatigue of the copper wall of high-gradient accelerating structure due to multiple action of powerful RF pulses [1]. Experimental investigation of this limitation at the frequency of 11.4 GHz has been carried out in SLAC for several recent years [2]. A similar research at the frequency of 30 GHz is prepared now by collaboration of CLIC team (CERN) [3], JINR (Dubna) and IAP RAS (Nizhny Novgorod) groups. The nearest our goal is a wall temperature rise about 200 K with the statistics of 10^6 pulses [4]. The source of RF power is JINR–IAP FEM oscillator with Bragg resonator which provides the 25 MW/150 ns pulses with spectrum width not greater than 30 MHz [5, 6] at the operating mode TE_{11}. The breakdown-safe mode TE_{01} has been chosen as the operating mode of the tunable copper test cavity which simulates the CLIC accelerating structure.

A key element of the experimental facility is the RF power transmission line. It should provide the high efficiency, elimination of the breakdown at the vacuum windows, possibility for diagnostics of the incident, reflected and transmitted RF power and radiation spectrum.

One of the effects under study is the mode splitting in FEM Bragg resonators observed both in cold and hot experiments. Possible reason of this undesirable effect is discussed.

* This work is supported by grants №№ 04-02-17118, 03-02-16530, 02-02-17438 of Russian Foundation for Basic Research and by INTAS grant №03-51-5319.

+ Corresponding author: Dr. A.Kaminsky, E-mail: alikk@sunse.jinr.ru

2 RF TRANSMISSION LINE

The scheme of the RF transmission line is presented in Fig. 1. It contains FEM output horn with cylindrical insertion, long oversized waveguide with vacuum window inside it, a diagnostic film with detectors of incident and reflected power, two quasi-optic focusing mirrors, a movable reflector, long input waveguide with vacuum window, accepting horn with cylindrical insertion, TE_{11} to TE_{01} mode converter, a test cavity, an output horn with vacuum window and a detector of the transmitted power.

It is well known that a Gaussian wavebeam is the most suitable one for quasi-optic focusing mirrors. In our line the Gaussian beam is formed at the FEM oscillator output by the special horn with cylindrical insertion (Fig. 2) which provides the optimal phase shift between the initial TE_{11} mode (87% of power) and TM_{11} mode (13%) formed in the horn. The long output waveguide employs the phenomenon of wave-front self-reproduction in oversized waveguide (Talbot effect) [7]. The wavebeam in an oversized waveguide may be considered as a superposition of partial eigenmodes with different phase velocities. So the phase relations between the partial modes evolve spatially and become similar to the initial one at a certain length (e.g. ~ 90 cm for the FEM output waveguide we had used). While the Gaussian wavebeam is reproduced at the end of the waveguide, it is possible to find the cross-section with almost uniform amplitude of the RF field to install the vacuum window and eliminate the breakdown. It is also possible to reduce the influence of the reflected wave on the FEM oscillator. Efficiency of the Gaussian wavebeam reproduction is about 90% due to mismatching phases of high-order modes.

The thin film is installed between the FEM output waveguide and the first mirror at the angle of 45° with respect to the wavebeam. Small reflection from both sides of the film provides possibility of non-destructive control of both incident and reflected power pulses.

The distant-controlled movable reflector can be lifted from its conventional horizontal position to direct the

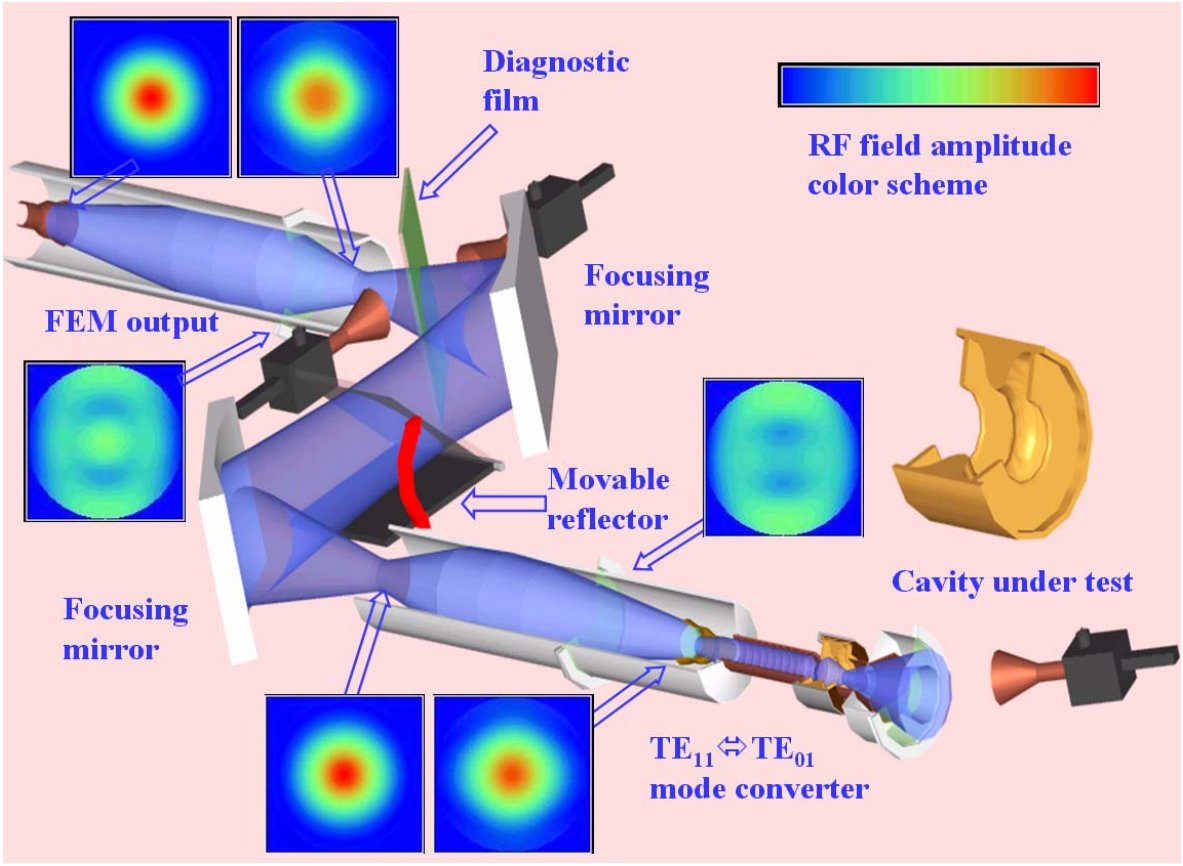

Figure 1: Overview of the quasi-optic RF transmission line.

radiation upward. It isolates the testing cavity from radiation when the radiation parameters don't match the requirements of the experiment.

The geometry of the transmission line is close to central-symmetrical one. The second oversized waveguide employing Talbot effect allows one to match the wave beam behind the second mirror and at the accepting horn as well as eliminate breakdown at the vacuum window of the test cavity. The position of the input vacuum window closer to the input horn allows us to reduce the volume of the vacuum chamber of the test cavity. The input horn with cylindrical insertion restores the pure TE_{11} mode at the input of the mode converter. The calculated transverse profiles of the RF field amplitude in several points of both waveguides are demonstrated in Fig. 1. General layout of the experimental facility is shown in Fig. 3.

A new system of optical laser alignment of the transmission line has been introduced. According to the results of cold measurements, we managed to reduce loss of the power delivered to the test cavity. The power transmission factor obtained in cold experiments was close to the designed level of 70% including all mode conversions and resistive losses.

An image of the wavebeam cross-section obtained behind the test cavity using the monitor of wavebeam position and size [4] is illustrated in Fig. 4. The intensity profile looks as well-expressed TE_{01}-like distribution.

Figure 2: Horn with cylindrical insertion.

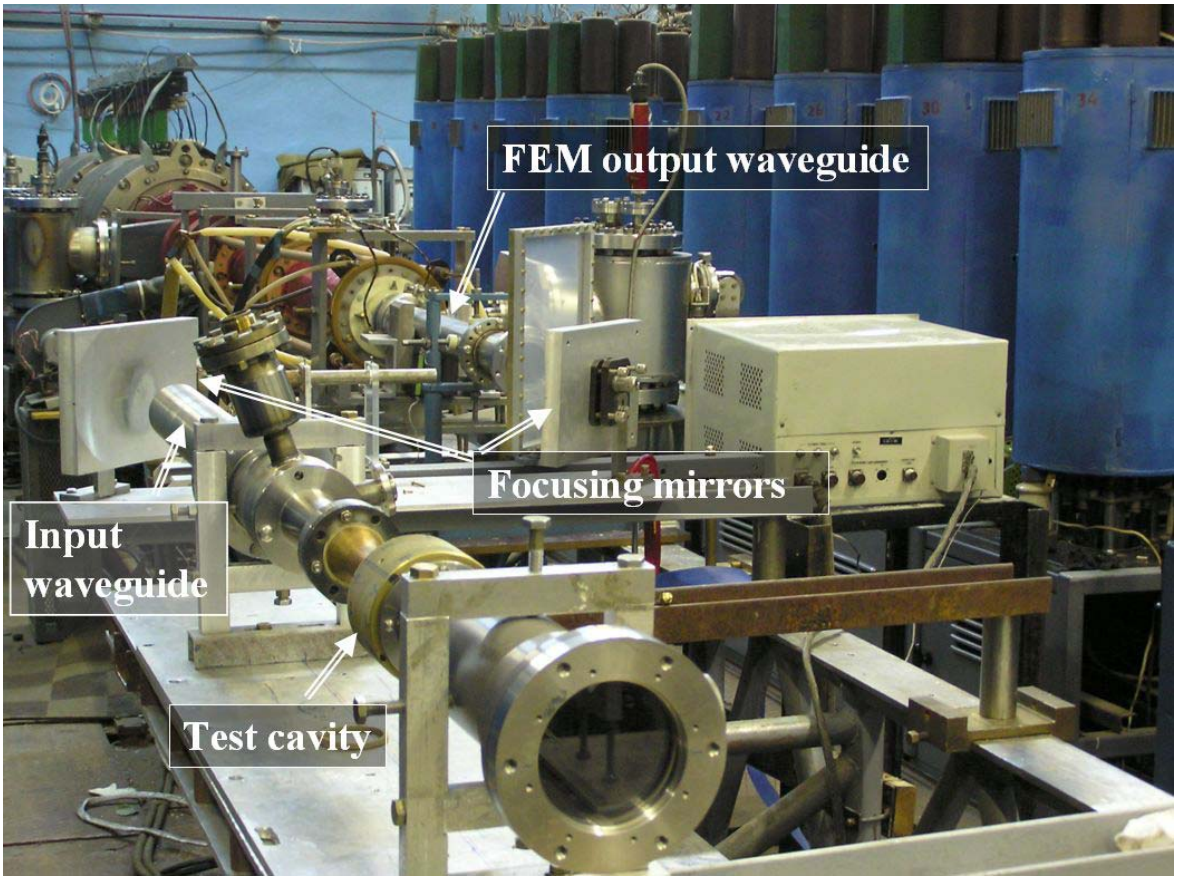

Figure 3: General view of the experimental facility.

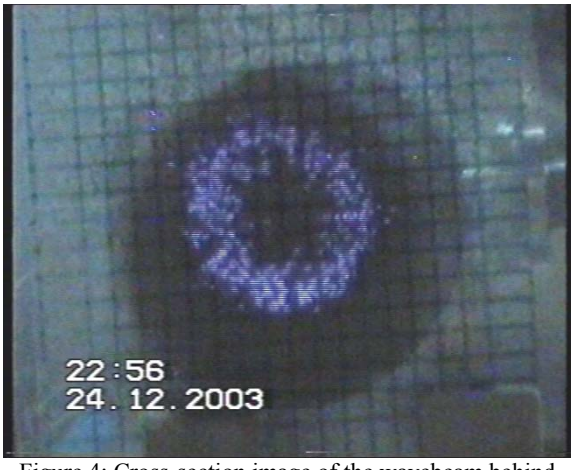

Figure 4: Cross-section image of the wavebeam behind the test cavity.

3 PROBLEM OF CENTRAL MODE SPLITTING IN BRAGG RESONATOR

According to the theory, Bragg resonators used in FEM oscillator have only one central mode with high Q-factor. But precise spectrum measurements both in cold and hot experiments show two modes with typical frequency difference of 50–100 MHz (Fig. 5). This effect is very undesirable for narrow-band loads such as RF pulse compressors or imitator of CLIC accelerating structure in our experiment.

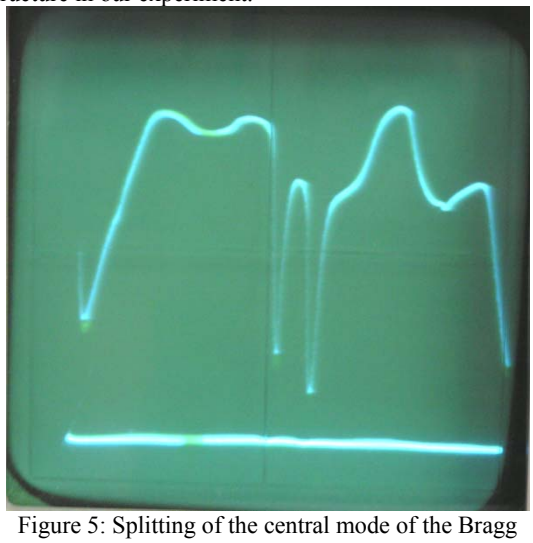

Figure 5: Splitting of the central mode of the Bragg resonator (cold measurements).

Reasons of this mode splitting are under study now. One of the possibilities is the influence of $TM_{11} \Leftrightarrow TM_{11}$ resonance not far from the operating $TE_{11} \Leftrightarrow TM_{11}$ resonance. Numerical simulation shows that this influence can be strong enough for our parameters of the resonator (Fig. 6).

Now we are developing a new type of Bragg resonator operating in $TE_{11} \Leftrightarrow TE_{11}$ reflection zone and much larger frequency distance from other possible resonances.

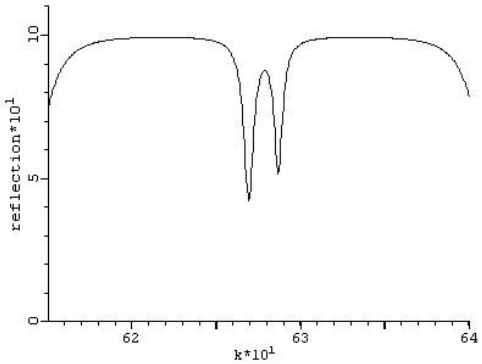

Figure 6: Splitting of the central mode of the Bragg resonator (numerical simulation).

4 DIAGNOSTIC EQUIPMENT AND DATA ACQUISITION SYSTEM

The experimental facility is equipped with 3 detectors of RF pulse which control the incident, reflected and transmitted power. The RF power and spectrum of each pulse from the required millions must be registered and stored in order to obtain correct value of the RF load at the cavity wall. We use a heterodyne spectrum meter with on-line fast Fourier transformation realized by the supplemental chip in the digital oscilloscope Tektronix TDS3032. Built-in procedure of the oscilloscope measures the spectrum width of the radiation. The oscilloscope also measures the pulse parameters of incident power. The oscilloscope sends the results to the computer via Ethernet switch using HTTP protocol. RF power of reflected and transmitted waves as well as electron beam currents and pulses of accelerating voltages are measured by the analog-to-digital converters with resolution time of 10 ns in CAMAC standard. We also have slow ADC to control the magnetic fields in the linear induction accelerator and FEM oscillator.

A distributed asynchronous object growing multi-channel system for data acquisition from the experimental facility has been built under client-server principle.

The system unites the servers of linac subsystems capable of maintaining autonomous operability of manifold equipment with different operating speed and master client computer collecting information on the whole system for subsequent processing and analysis. Such an organization allows one to reach stability relatively to faults of single servers, the flexibility, expanding capability due to the modularity principle and open system architecture.

The system of data acquisition has been built realized as several server programs and a single multi-client program employing API sockets in asynchronous regime.

Much attention is paid to modernization of power supplies both for accelerating voltages of the induction linac and focusing magnetic fields. They are very important elements of the facility in terms of providing stable parameters of the experiment during the whole statistics of 10^6 pulses.

5 CONCLUSIONS

A quasi-optic transmission line is designed for providing the high efficiency, elimination of the breakdown at the vacuum windows, possibility for full diagnostics of the incident, reflected and transmitted RF power and radiation spectrum. Multiple transformation of the transverse distribution of the wavebeam is used in the line.

A new technique of optical laser alignment of the transmission line has been introduced. According to the results of cold measurements, we managed to reduce loss of the power delivered to the test cavity. The power transmission factor obtained in cold experiments was close to the designed level of 70%.

An undesirable effect of central mode splitting in FEM Bragg resonator must be taken into account for providing the effective power transmission to narrow-band test cavity.

RF pulse diagnostic equipment and a distributed asynchronous system for data acquisition from the experimental facility built under client-server principle make it possible to register parameters of each pulse from required statistics of 10^6 pulses which is necessary to obtain correct value of the RF load at the cavity wall.

6 REFERENCES

[1] O.A. Nezhevenko, Proc. of PAC'97, Vancouver, Canada, May 1997, p. 3013.

[2] D.P. Pritzkau, Phys. Rev. Spec. Topics - Accel. & Beams, 2002, v. 5, 112002. 22 pp.

[3] J.-P. Delahaye et al., Proc. of EPAC'98, Stockholm, June 1998, p. 58.

[4] A.V. Elzhov, N.S. Ginzburg, A.K. Kaminsky et al., Nucl. Instr. and Methods, 2004, v. A528, p. 225.

[5] A.K.Kaminsky, N.S.Ginzburg, A.A.Kaminsky et al., Nucl. Instr. and Methods, 1998, v. A407, p. 167.

[6] V.L.Bratman, G.G.Denisov, N.S.Ginzburg, M.I. Petelin, IEEE J. of Quant. Electr., 1983, v. QE-19, № 3, p. 282.

[7] G.G. Denisov, S.V. Kuzikov, Strong Microwaves in Plasmas, Nizhny Novgorod, 2000, v. 2, p. 960.

CHARACTERIZATION OF STORAGE RING FEL OPERATING IN THE GIANT PULSE MODE

I. Pinayev, K. Chalut, Duke University, Durham, NC 27708, U.S.A., V.N. Litvinenko, BNL Upton, NY 11973, U.S.A.

Abstract

In this paper we present experimental results on the storage ring free electron laser operating in giant pulse mode with variable repetition rate. The experiments were conducted through a wide range of electron beam energies from 270 MeV to 600 MeV with the giant pulses generated using a gain modulator. Dependence of the peak and average power, and the other properties and parameters of giant pulses on the pulse repetition rate were studied. In particular, it was found that the average lasing power in the giant pulse mode can reach levels of 70-90% of that in the CW power mode. Applications of such mode of operation are discussed.

INTRODUCTION

The gain modulation technique [1] was initially designed for storage ring free electron lasers (SRFEL) to satisfy user experiments demanding high peak power. Later its application was extended for generation of harmonic of fundamental free electron laser wavelength. High peak intracavity power allowed expansion of the operational range of SRFEL into the vacuum ultraviolet range [2].

Somewhat unexpected use of the giant pulse mode of operation came when OK-4/Duke FEL was generating γ-rays for HIGS users [3]. The optical power was concentrated in a series of short macropulses and small filling factor (product of the macropulse length and repetition rate) made possible to reduce a background noise by using a time gate [4].

The electron beam excitations, caused by the noise of magnetic system power supplies or RF system, can strongly affect the stability of SRFEL output [5, 6]. In order to suppress variation of the optical power the Super-ACO group implemented a few feedback systems [7, 8]. Application of the giant pulse technique may be more attractive in this case as well.

THEORETICAL CONSIDERATION

Even a small modulation of the SRFEL gain can result in significant variations of the output power. Such phenomenon arises from the significant difference of two time constants: the synchrotron damping time and FEL optical power growth. It manifests itself usually in chaotic behavior of the output power [5].

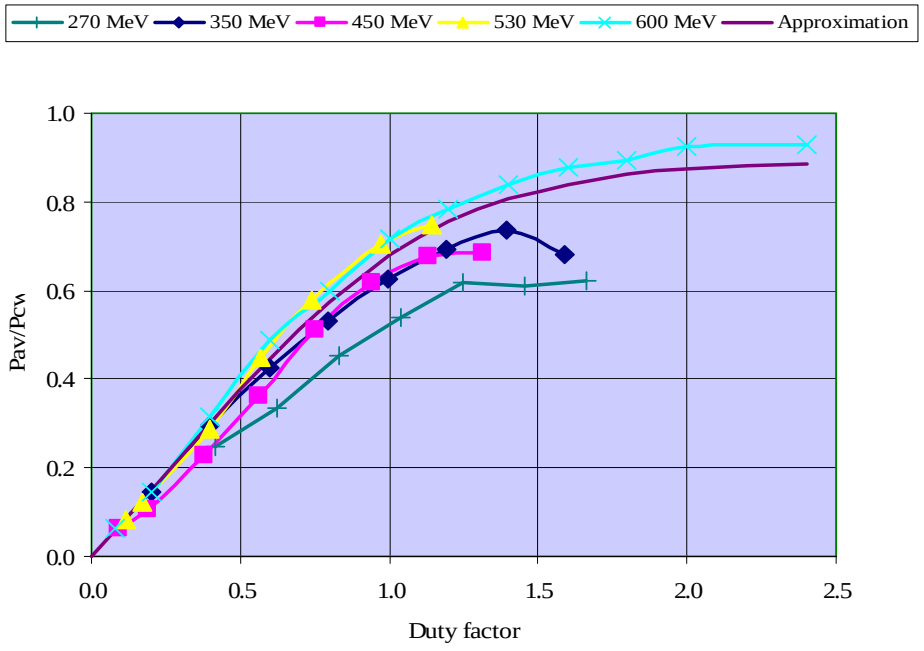

Figure 1. The dependence of the ratio of the average power in the giant pulse mode and CW power on the duty factor (product of the pulse repetition rate and synchrotron damping time). The pulse repetion frequency varies from 1 Hz at 270 MHz to 60 Hz at 600 MeV.

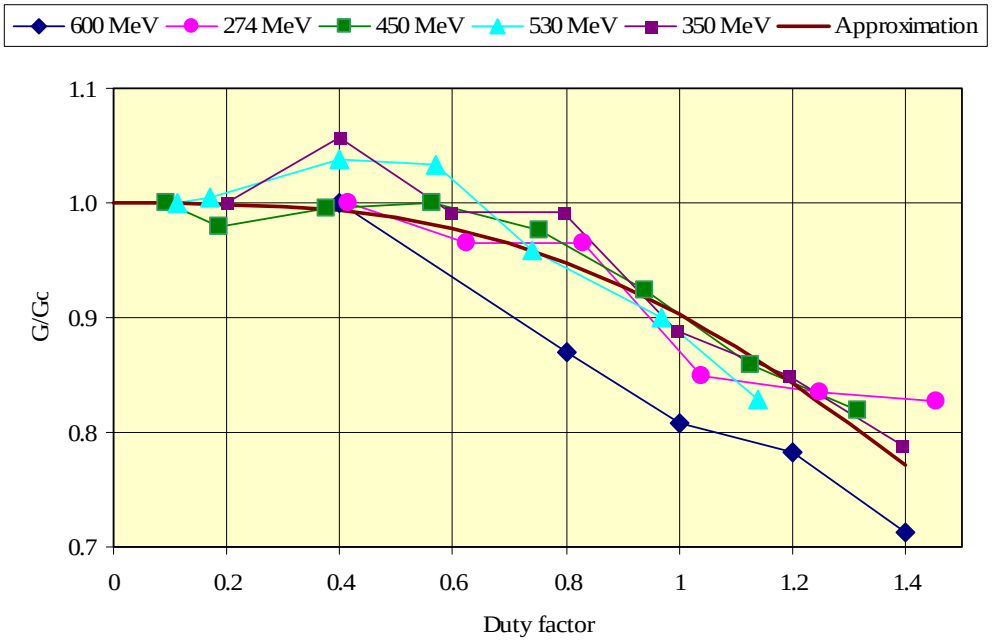

Figure 2. Dependence of the giant pulse' start-up gain on the duty factor. The gain is normalized with respect to the low repetition rate value.

Giant pulse mode of operation is an extreme case when the FEL gain is 100% modulated with relatively low frequency. However, it has the advantage of being fully controlled.

Duration of the giant pulse is much less than its repetition period. The longest duration of giant pulse during the experiments (at 10% level) was 300 microseconds, while the highest repetition frequency was 60 pulses per second. Therefore, it is possible to assume that energy spread of the electron beam instantly grows to the maximal value. The induced energy spread is directly proportional to the energy of the giant pulse [9, 10]. The synchrotron damping leads to the decay of the energy spread until the start of next giant pulse.

EXPERIMENTAL RESULTS

The experiments were conducted on the OK-4/Duke SRFEL for which the parameters were published elsewhere [11]. The operational wavelength was defined by the installed mirror set and was 450 nm. Electron beam energy varied from injection energy of 274 MeV to 600 MeV where the wiggler current reached its maximum. The synchrotron damping time changed from 416 milliseconds down to 40 milliseconds. The buncher was set at low level (N_D<7) providing maximal peak power. The RF voltage was in the 250–400 kV range well below the maximal value of 700 kV, due to the excitation of synchrobetatron oscillations. Optical losses of the cavity were 1% per roundtrip.

The radiant power meter manufactured by Oriel (model 70260) was placed downstream of the optical cavity to monitor FEL power. The silicon photodiode was used on the other side to observe envelope of the giant pulse. Malfunctioning streak-camera prevented us from measuring bunch length evolution.

All the dependencies were plotted versus duty factor *d* equal to the product of the repetition rate and synchrotron damping time. The ratio of average power in the giant pulse mode to the power in the CW mode is shown on Figure 1. At low values of duty factor, the average power

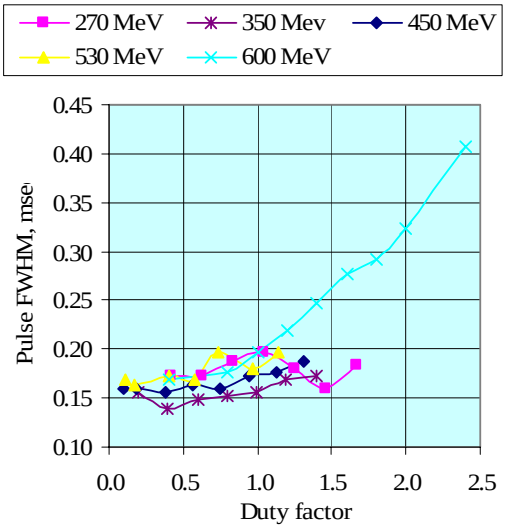

Figure 3. The dependence of the giant pulse width on the duty factor.

was proportional to the repetition rate and no changes in pulse shape were observed. With the increase of the repetition rates, the electron beam did not relax to the equilibrium energy spread and therefore the saturation was reached. This dependence has good fitting curve $P_{GP}/P_{CW}=0.75*d/(1+(d/1.2)^4)^{¼}$.

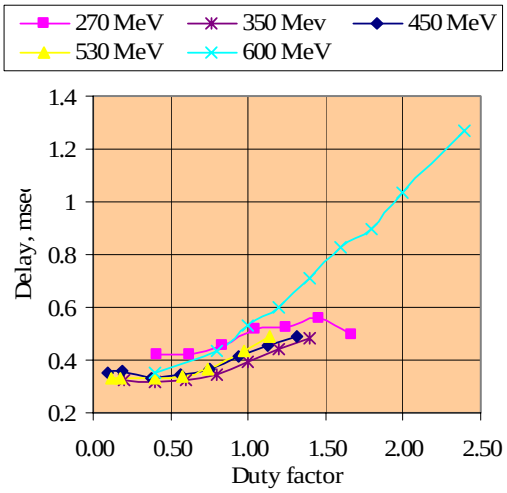

Figure 4. Dependence of the delay between giant pulse start and location of the maximal macropulse power.

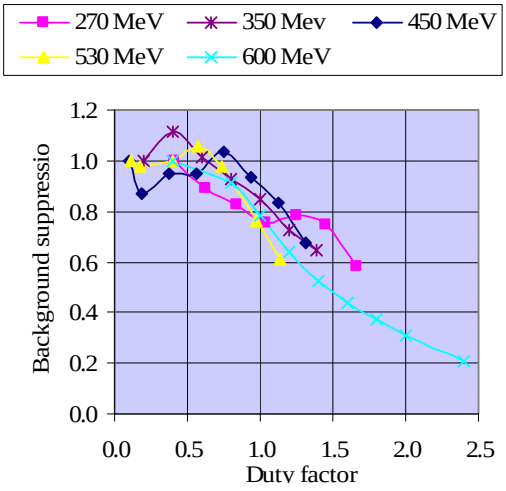

Figure 5. Dependence of the suppression of the uncorrelated background on the duty factor. The values are normalized to the level at low repetion rates. The absolute figures varies from 120 at 530 MeV to 1450 at 270 MeV.

The leading edge of the giant pulse shows exponential growth of the optical power [12]. From the time constant one can easily calculate the net gain of the FEL and knowing the optical cavity losses find its gain. Figure 2 shows changes in the start-up gain with duty factor. The FEL operation blows up energy spread to the level sufficient to suppress microwave instability especially for the giant pulse operation. This fact is very important because the major source, causing the increase of the electron bunch length, is eliminated and synchrotron damping occurs at faster rate. The evidence for this is that the initial gain G stays constant until duty factor reaches the value 0.8. With further rise of the duty factor the start up gain decreases for the same reason as mentioned earlier. This dependence can approximated with the following fit $G=G_0/(1+(d/2.1)^3)$, where G_0 is gain at low duty factor.

The reduction of the FEL gain leads to the lengthening of the giant pulse (Fig. 3) and to growth of the delay between trigger and location of the giant pulse maximum power (Fig. 4). Knowing the levels of the optical power in CW and giant pulse modes it is possible to estimate the suppression of the background noise for the HIGS experiments $S=P_{GP}/(P_{CW}*T*F_{rep})$, where T is giant pulse duration and F_{rep} is repetition rate. The normalized dependence is shown in Fig. 5. As well as the FEL gain the suppression does not change until duty factor d=0.8. Higher values of the duty factor can be used to reduce the data collection time due to growth of the average power.

CONCLUSION

Giant pulse technique can be used to obtain highly stable pulses of optical radiation from the SRFEL with average power constituting only 90% CW mode power. For the experiments requiring background reduction, the separation between giant pulses should be 0.8-1.2 of synchrotron damping time.

ACKNOWLEDGEMENT

This work is supported by DoD MFEL Program as administered by AFOSR, grant F49620-001-0370.

REFERENCES

[1] I.V. Pinayev, et al., Nucl. Instr. and Meth. A475 (2001), 222.
[2] V.N. Litvinenko, Nucl. Instr. and Meth. A507 (2003), 265.
[3] V.N. Litvinenko, Nucl. Instr. and Meth. A507 (203), 527.
[4] M.W. Ahmed, et al., Nucl. Instr. and Meth. A516 (2004), 440.
[5] M. Billardon, Phys. Rev. Lett., vol. 65, Number 6 (1990), 713.
[6] M.-E. Couprie, et al., Nucl. Instr. and Meth. A429 (1999), 165.
[7] R. Roux, et al., Phys. Rev. E58 (1998), 6584.
[8] M.E. Couprie, et al., Nucl. Instr. and Meth. A358 (1995), 374.
[9] N.A. Vinokurov, A.N. Skrinsky, Preprint 77-67 (1977), Budker INP, Novosibirsk, Russia.
[10] A. Renieri, Nuevo Cimento B53 (1979), 160.
[11] V.N. Litvinenko, et al., Nucl. Instr. and Meth. A475 (2001), 65.
[12] I.V. Pinayev et al., Nucl. Instr. and Meth. A528 (2004), 283.

VISA IB: ULTRA-HIGH BANDWIDTH, HIGH GAIN SASE FEL

G. Andonian, A. Murokh, R. Agustsson, C. Pellegrini, S. Reiche, J. B. Rosenzweig, and G. Travish
UCLA, Los Angeles, CA 90095, USA
M. Babzien, I. Ben-Zvi, J. Y. Huang, V. Litvinenko, and V. Yakimenko
Brookhaven National Laboratory, Upton, NY 11973, USA
M. Ferrario, L. Palumbo, and C. Vicario
Universita di Roma "La Sapienza", 185 Roma, Italy
I. Boscolo, S. Cialdi, and A. Flacco
INFN-Milano, 20133, Milano, Italy

Abstract

We report the results of a high energy spread SASE FEL experiment, the intermediary experiment linking the VISA I and VISA II projects. A highly chirped beam (1.7 %) was transported, without corrections of longitudinal aberrations in the ATF dogleg, and injected into the VISA undulator. The ouput radiation displayed an uncharacteristicly large bandwidth (12 %) with extremely stable lasing and measured energy of about 2 μJ. Start-to-end simulations reproduced key features of the experiment and provided an insight into the michanisms giving rise to such a high bandwidth. These analyses have important implications on the VISA II experiment.

INTRODUCTION

The advent of high-brightness, ultra-short duration X-ray radiation from self-amplified spontaneous emission free-election lasers (SASE FEL) promises to be an invaluable tool for the scientific community. There are current proposals [1, 2] to construct single-pass high gain free electron lasers that will generate angstrom wavelength radiation with femtosecond pulse lengths [3].

A possible scheme to obtain yet shorter pulses by creating and manipulating frequency chirped FEL output has been proposed [4]. In the first stage of the scheme, an energy chirped electron beam injected into the undulator would produce a frequency chirped output. This light is then monochromatized, and thus sliced, and injected into a second stage undulator, where only a short section of the electron beam is seeded by the shortened radiation pulse well above the shot-noise power level. This, and similar schemes, give motivation for VISA (Visible to Infrared SASE Amplifier) and VISA II, an extension of the VISA program. The ultimate goal of the VISA II experiment is to run a SASE FEL with the highest electron beam energy-time chirp allowable by the modified beam transport at the Accelerator Test Facility (ATF) in Brookhaven National Laboratory (BNL), enabling the production and measurement of strongly chirped SASE FEL radiation [5].

Summary of VISA I Results

A brief review of some results from the VISA (Visible-to-Infrared SASE Amplification) FEL experiment will place the recent measurements in context. In 2001, VISA successfully demonstrated saturation of a SASE FEL within a 4 meter undulator at 840 nm. [6]. An anomalous electron bunch compression mechanism created beam conditions allowing high-gain lasing. The large negative second order longitudinal time dispersion, T_{566} [7], yielded a longitudinal compression and an increase in peak current from 55 A to 240 A.

The nonlinear properties along the dispersive segment of the ATF transport line were studied using a start-to-end suite of simulation codes. The electron beam dynamics in the gun and linac sections were modeled with PARMELA [8], the electron beam transport matrix calculations were analyzed with ELEGANT[9], and the FEL studies were computed with GENESIS 1.3[10]. The reproduction of pulse energy, profile and angular distribution of the FEL radiation, as well as the measurements of the bunch compression process and other aspects of the beam phase space, were significant achievements of the start-to-end simulations. The benchmarking of the code suite against the experimental results at the ATF of the beam production and transport allowed reliance on the same modeling process to analyze microscopic aspects of the most recent measurements.

Motivation for VISA II

Although the original bunch compression mechanism facilitated high-gain lasing, it restricted the management and manipulation of the electron beam and its properties prior to injection. The ultimate goal of the VISA II program is to inject a linearly chirped beam into the undulator to produce frequency chirped output radiation. In the experiment, preservation of the electron beam chirp will be accomplished by elimination of the nonlinear longitudinal compression through the use of sextupole mangets at high horizontal dispersion points in the dogleg transport [11]. The sextupoles, installed along the dispersive line, mitigate second order effects, in particular diminishing T_{566} to a negligible value. The initial, nearly linear, electron beam

chirp applied at the linac, can then be preserved, and even enhanced by a modest amount of linear compression during transport, before injection into the undulator.

EXPERIMENT DESCRIPTION

Before the needed improvements in the linac to undulator transport were made, a set of measurements, performed without sextupole correction, took place at the existing facilities of the ATF. These measurements explored the use of a highly chirped pulse, with nonlinear longitudinal compression, and subsequent FEL amplification, as a stepping stone to VISA II. This transitional experiment demonstrated a previously unobserved large bandwidth of the FEL radiation of $\sim 12\%$, at high gain, accompanied by an anomalously wide far-field angular radiation pattern. We present these results below, as well as start-to-end simulations that reproduce some of the more striking aspects of the radiation measurements.

The VISA experimental schematic used in the present experiments is discussed in detail in Ref. [6]. The post-injector 20^{o} dogleg transport line that delivers beam to the VISA undulator contains an adjustable collimator located near the begining of the dispersive line, the high energy slit (HES). The measurements of beam size and transmitted fraction at the HES are used to determine the beam energy and energy spread at this point, which are important benchmarks for the simulations. The electron beam (500 pC) at the HES is observed to have a 2.8 % energy spread due to a correlation between energy and longitudinal position (chirp) after the linac exit. Approximately 330 pC propagates through the fully open HES, collimating the beam to a 1.7 % energy spread. Electron beam charge is measured by a Faraday cups located after the gun exit and after the undulator exit. The compression process in the dispersive section is monitored by a Golay cell, installed in front of the undulator, which measures the coherent transition radiation (CTR) intensity emitted from an insertable metallic foil. The CTR energy is peaked when the beam central momentum is chosen to optimize the compression in the dogleg.

The measured FEL radiation displayed an unusual spectrum. The spectrum contained a characteristic double peak structure with a full width bandwidth as high as 12 percent (Figure 1). An average SASE radiation energy of approximately 2 μJ was recorded; which is within an order of magnitude of the saturation energy of the initial VISA experiment. The dual spiked spectral structure indicates there are 2 distinct lasing modes. The lasing FEL output radiation was also unusually stable in energy, a result of the collimation at the HES, ensuring that the same energy portion of the beam was being transported on each shot. The FEL output was far less sensitive to rf fluctuations and laser and beam centroid jitter, as compared to earlier VISA runs.

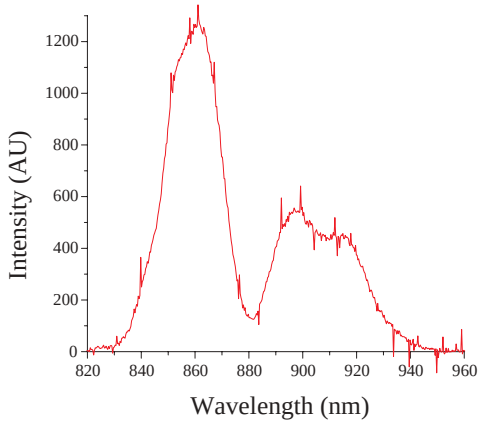

Figure 1: Sample shot of the ultra-wide bandwidth observed during the VISA IB runs (Ocean Optics USB2000 Spectrometer).

Simulations and Analysis

The PARMELA-ELEGANT components of the start-to-end simulations reproduced the compression process as observed by the combined slit and Golay cell measurements. The simulations show that the bunch peak current after nonlinear compression can reach up to 300 A. This peak is very short in duration (∼200 fs FWHM), containing only 25-30 pC of charge. Unlike the original VISA conditions, however, in the present experiment the compression was insensitive to injection phase fluctuations arising from either RF or photocathode laser timing errors. This is due to the large energy spread in the initially chirped beam (Figure

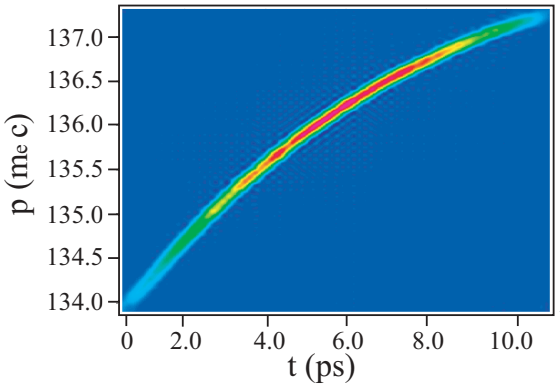

Figure 2: Longitudinal phase space of a linearly chirped electron beam at linac exit.

2), which guarantees that a component of the beam will be compressed, and thus have proper conditions for lasing, because the laser injection and rf phase errors are much smaller than the initial bunch length of 10 ps. The electron beam, prior to injection into the undulator, displays a highly nonlinear longitudinal phase space as a result of the second order dispersion effects of the transport line (Figure 3). Because of these effects, the beam distribution at the undulator entrance also has a highly distorted distribution in $x - t$ configuration space. As seen in Fig.4, the highly compressed lasing core of the beam lies off axis.

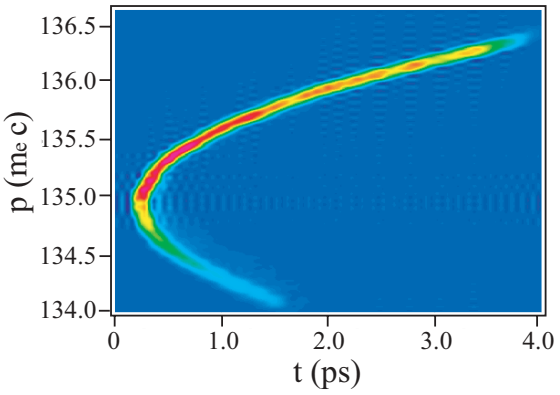

Figure 3: Longitudinal phase space of electron beam at undulator injection (Elegant Simulation).

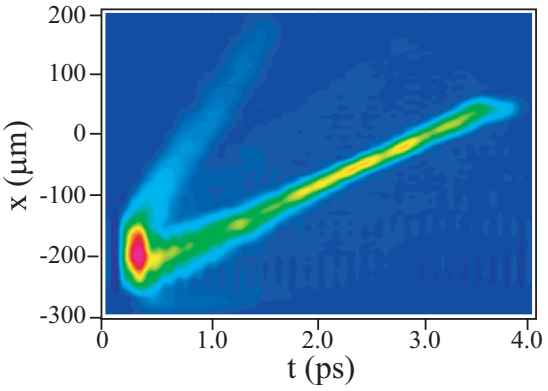

Figure 4: The time-position correlation of the electron beam prior to undulator injection (Elegant simulation).

The GENESIS module of the start-to-end simulation suite provided some insight into the basis of the observed FEL spectrum. In terms of general system performance, simulations showed that the FEL had reached near saturation, with gain comparable to that achieved in prior VISA runs. Simulations also reproduced some key facets of the observed spectrum, namely the large bandwidth and double spiked structure (Figure 5). Simulations also showed that the slice-emittance degradation, due to the large energy spread, compression, and residual dispersion, was not a crucial concern. The overall beam quality, in particular the high current, was sufficient for stable, sustained, high-gain lasing, close to saturation. The shorter wavelength spike in the spectrum of Fig. 1 is similar to that observed in VISA. The second, long wavelength spike is attributed to the amplification of a parasitic mode that is excited when the beam is off-axis in the undulator. Measurements indicate that the beam is slightly mismatched in centroid and envelope to the undulator quadrupole focusing lattice, which was incorporated into the simulations. This mismatch caused the lasing core of the beam to undergo betatron oscillations with as high as 300 μm secular amplitude. As seen in Figure 6, there is a strong correlation between the maxima in this core offset and the maxima of the observed spectral bandwidth. The relationship between the off-axis betatron motion and the spectrum has a number of components to it. The additional transverse undulation of the lasing electrons' trajectories due to the periodic application of alternating gradient quadrupoles (strong focusing) causes the FEL resonant condition to change when the beam core is off-axis. One may view this scenario as a bi-periodic undulator, with the long wavelength component of the trajectory due to the off-axis alternating, with no drift in between, quadrupole forces, which have a square-wave "FD" form, yielding an effective undulator parameter of $K_q = eB'\Delta x L_q/2\pi m_e c$, where Δx is the average offset, B' is the quadrupole gradient, and L_q is the period

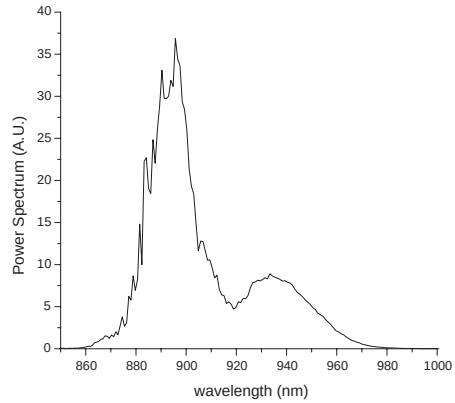

Figure 5: Wide FEL bandwidth (10%) and "double hump" structure are numerically reproduced (GENESIS Simulation).

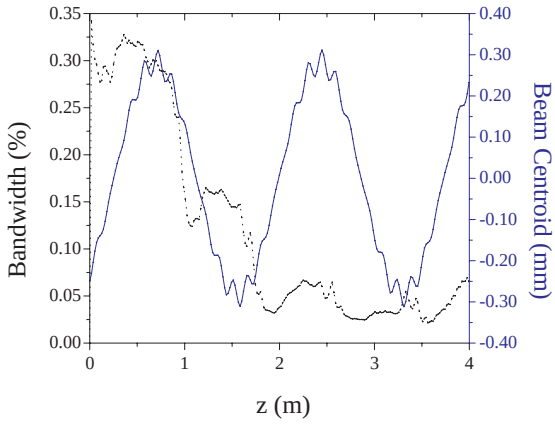

Figure 6: Simulations show a strong correlation between the beam centroid position and the FEL bandwidth (GENESIS Simulation).

of the quadrupole lattice. For the VISA parameters with $\Delta x = 300\mu$m, we have $K_q \simeq 0.23$. When one adds the effects of this additional oscillation in the central trajectory on the FEL resonance condition, the relation

$$\lambda_r = \frac{\lambda_u}{2\gamma^2}\left(1 + \frac{K^2 + K_q^2}{2} + (\gamma\theta)^2\right) \qquad (1)$$

is obtained, with the on-axis undulator parameter $K = 1.26$. The maximum redshifting of the resonant wavelength due to this effect in our experiment is predicted to be about 1.5 %. Another significant redshifting of the radiation is due to radiation into off-axis angles. As in VISA, the far-field angular spectrum is hollow, and has a maximum at an even larger angle of 2.1 mrad. For our present energies ($\gamma = 137$), the redshifting due to this effect is 4.1 %. This obviously important effect is also related to the off-axis motion, as when the beam moves off-axis, it more readily couples to higher order transverse modes having off-axis peaks. The gain in these higher order modes utilizes the bunching attained at by the gain at shorter wavelength in the near-axis lasing, and is therefore considered parasitic.

These two off-axis related effects produce nearly all of the observed redshifting in the long wavelength peak, which is about 5 % increased at its peak from the on-axis peak. One may have expected that the redshifting arises from the energy spread in the system. This is not so because the energy spread within the lasing core is quite small. In fact, when the energy spread of the beam is set to a near-zero value in the GENESIS simulations, leaving all other aspects of the phase space unchanged, the SASE output spectrum obtained is similar to that shown in Fig. 5.

CONCLUSION

The effects of bandwidth growth from off-axis radiation would be deleterious in the VISA II experiment, where the goal is to have the spread in measured frequencies be predominately due to time-correlated energy spread (chirp). In the case of VISA II, the total energy spread is expected to be 2 %, and thus the bandwidth due to this spread does not exceed 4 %. Thus the correction of second order distortions in the beam's transverse and longitudinal dynamics, through use of sextupoles, is mandatory, in order to avoid the effects observed in the present experiments.

It may also be of interest to purposefully use the mechanisms for exciting very large bandwidth radiation in a SASE FEL, for applications where spectral width is advantageous. This may be introduced at the end of a VISA-style undulator by simply introducing a mis-steering of the beam over the last few gain lengths. The coupling to large-angle radiation is limited, however, by the coherence angle of the system. In our case the lasing core of the beam was very narrow in the horizontal dimension, $\sigma_x \simeq 20\mu m$, as seen in Fig. 4, and the beam may radiate coherenty up to very large angles, $\theta \simeq 2\pi\sigma_x\lambda_r$. It is therefore easier to employ this mechanism for obtaining bandwidth increase with longer wavelength FELs.

REFERENCES

[1] M. Cornacchia *et al.*, Linac Coherent Light Source Design Study Report **SLAC-R-521** (1998)

[2] TESLA-FEL 2001-05, Deutsches Elektronen Synchrotron, Hamburg, Germany (2001)

[3] C. Pellegrini, J. Stohr, Nucl. Instrum. Methods Phys. Res. A **500** (2003) 33

[4] C. Schroeder *et al.*, J. Opt. Soc. Am. B **19** (2003) 1782

[5] J. B. Rosenzweig, presented at these proceedings

[6] A. Murokh *et al.*, Phys. Rev. E **67** (2003) 066501

[7] K. Brown, A First-and Second-Order Matrix Theory for the Design of Beam Transport Systems and Charged Particle Spectrometers **SLAC 75**, (1972)

[8] L. M. Young, J. H. Billen, **LA-UR-96-1835** (Rev. 2000)

[9] M. Borland, Advanced Photon Source **LS-287** (2000)

[10] S. Reiche, Nucl. Instrum. Methods Phys. Res. A **429** (1999) 243

[11] J. England *et al.*, Sextupoles Correction of the Longitudinal Transport of Relativistic Beams in Dispersionless Translating Sections, Submitted for publication (2004)

PRELIMINARY MEASUREMENTS OF THE HIGH-GAIN FEL RADIATION PROPERTIES ALONG THE RADIATOR

T. Shaftan*, H. Loos, B. Sheehy, L.H. Yu, NSLS, BNL, Upton, NY 11973, USA

Abstract

We present preliminary experimental results on evolution of properties of the DUV FEL [1,2] radiation along the radiator. Intercepting the electron beam at the different locations inside the undulator we recorded and analyzed transverse profiles, spectra and intensity of the FEL output. Shot-to-shot fluctuations of the FEL radiation may significantly affect the accuracy of measurement. In the paper we present and discuss a single-shot measurement technique, based on a special imaging system.

INTRODUCTION

Significant progress in understanding of high-gain FEL physics has been achieved during past decades. Both analytic and simulation tools are developed and being used for design of Self-Amplified Spontaneous Emission (SASE) [3,4] or High Gain Harmonic Generation (HGHG) [5,6] Free Electron Lasers. Start-to-end simulations [7,8] model the entire beam line from the generation of the photoelectrons at the gun to the transport of the FEL radiation light to the user station. Because the beam dynamics changes significantly along the beam line a series of "expert" codes are used. There are few of FEL simulation programs that calculate an FEL output for given initial shape and distribution of the electron bunch [9,10].

The code accuracy of prediction the FEL performance is being verified experimentally. FEL radiation transverse profile, spectrum, energy per pulse, etc. are important test points for any FEL code. Usually, all of the radiation parameters are measured and being compared with an FEL simulation at the end of the undulator. However, one of the key FEL parameters, gain length, is being measured by detecting the radiation intensity at the discrete points along the undulator.

There are several approaches for the gain length measurement. One of them [11] relies on the special optical system, transporting the FEL light from different cross-sections of the undulator to a single detector. Another approach [12] utilizes few detectors located along the undulator. In both cases, inserting a mirror deflects radiation to the detector and allows for measurements of the radiation intensity at the mirror location. Third approach is based on deflecting the electron beam by the trajectory corrector [13]. In this case the only portion of the undulator before the corrector contributes to the radiation intensity measured at the detector downstream of the undulator.

These measurements provide with a single parameter, that is, with radiation intensity distribution along the radiator. However, many more radiation parameters can be obtained using similar experimental set-up. Measuring transverse radiation distribution and spectrum along the radiator would present important data for comparison with a simulation. It is especially important for characterization of special FEL regimes like seeding with ultra-short laser pulse [17] or chirped bunch SASE or HGHG [18].

Spectral measurements of the SASE radiation evolution have been performed at LEUTL FEL (APS) [14,15]. During this experiment SASE radiation spectra were recorded at the different locations along the radiator. The analysis for the first and second harmonics has shown quantitative agreement with predictions of a simulation code.

Another application of such a "complete" characterization of the radiation properties along the radiator is in optimization of the FEL performance. Measured data may be directly compared with the electron beam parameters, such as emittance, trajectory or beam size. Necessary optimization of the electron beam parameters follows as a feedback.

In this paper we present initial results (a single data set) of the characterization of HGHG radiation evolution along the radiator.

The radiation spectrum, especially in SASE case is subject of fluctuation. Random set of SASE spikes from shot to shot makes comparison with simulation to be a difficult task. If measurement takes significant time, the beam parameters (for both SASE and HGHG) may drift resulting in incomprehensive set of data. In the closing we discuss a single-shot version of the spectral measurements device.

EXPERIMENT

The experiment has been performed at the DUV FEL at BNL [1,2]. The 800 nm laser radiation is used as a seed for HGHG FEL. The radiator is tuned to the third harmonic of the seed radiation (266 nm). In the experiment we measured properties of the output at 266 nm.

The experimental set-up is shown in Fig. 1. The 10 meter long NISUS undulator serves as a radiator in HGHG FEL magnetic system. The undulator is equipped with variety of diagnostics and correction, including 16 four-wire correctors equally distributed along the whole length. The diagnostics system at the experimental area consists of photodiode, CCD camera and spectrometer.

* Corresponding author: shaftan@bnl.gov

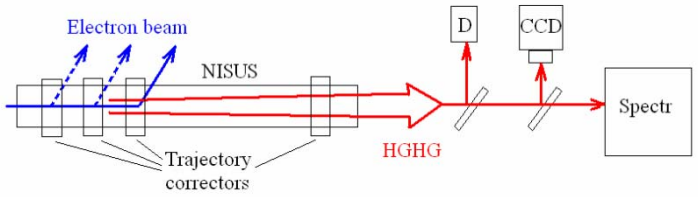

Fig. 1: Experimental set-up.

Using four-wire correctors we deflect the electron beam at consecutive locations along the undulator axis. We have chosen the kick strength to be sufficient for steering the beam onto the vacuum chamber wall at approximately 50 cm downstream of the corrector. Thus the only radiation from the portion of NISUS preceded the corrector has been recorded. In the following figures we plot the dependence of a parameter versus location of deflecting section along NISUS. The experimental set-up was installed 7 meters away from the undulator.

The radiation intensity as a function of the distance along the undulator (gain curve) is plotted in Fig. 2. The measured HGHG power at the end of NISUS was measured as 25 μJ.

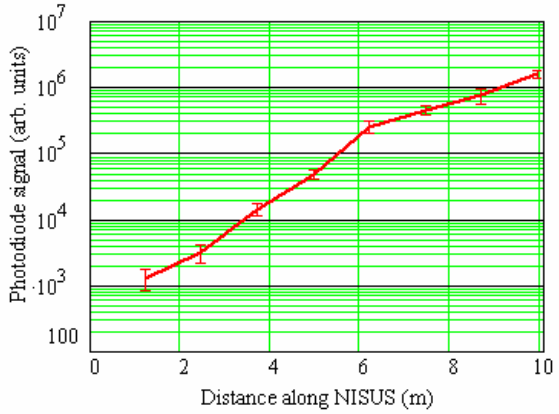

Fig. 2: HGHG gain curve.

Fig. 3 shows the images of the HGHG radiation observed at different locations along NISUS.

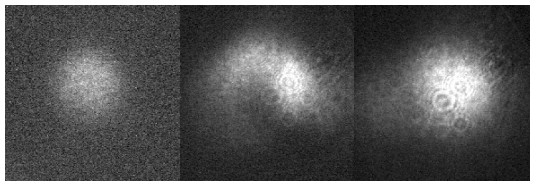

Fig. 3: Transverse images of HGHG radiation corresponding to beginning, middle and end of NISUS.

Dependence of the recorded transverse spot size on the distance along NISUS is plotted in Fig. 3.

The next plot (Fig. 5) presents evolution of the spot center versus distance along NISUS. This dependence will be compared with electron beam trajectories in the radiator.

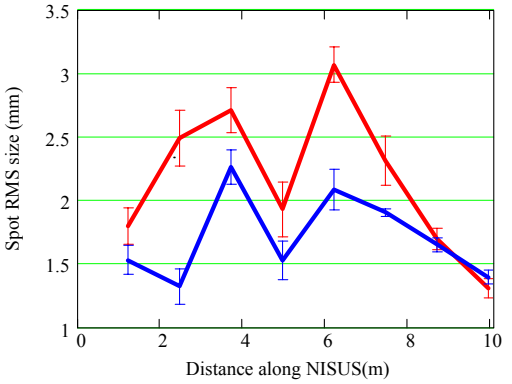

Fig. 4: Dependences of the HGHG spot size.

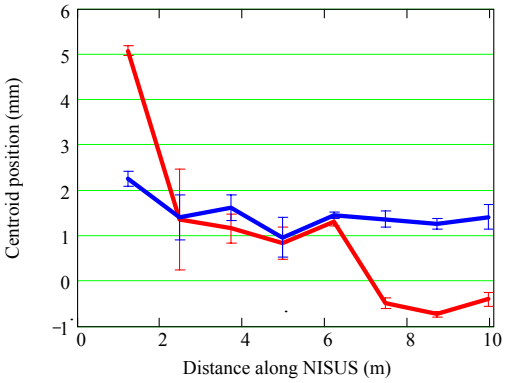

Fig. 5: Dependences of the center position of the HGHG spot.

Next we discuss the spectral measurements. The HGHG spectra are plotted in the next figure (Fig. 6). The black line corresponds to the central wavelength of the HGHG spectra. Average single-shot spectrum width is shown as blue error bars in red, averaged multi-shot width is plotted as blue error bars. From the figure we can observe that the central wavelength shifts by approximately 0.15 nm at the end of NISUS. Assuming these losses due to the radiated power we can estimate the peak power in the HGHG pulse. It can be shown that the peak power in MW is given by the following expression:

$$P_p = \frac{mc^2}{2e}\gamma I_p \frac{\Delta\lambda}{\lambda} = 0.256 \cdot \gamma I_p[A]\frac{\Delta\lambda}{\lambda}$$

Substituting experimental parameters in this expression (γ=350, λ=266 nm, $\Delta\lambda$=0.15 nm, I_p=400 A) we get about 20 MW. Assuming HGHG pulse length of 1 ps we calculate 20 μJ for the pulse energy, which is close to the measured value.

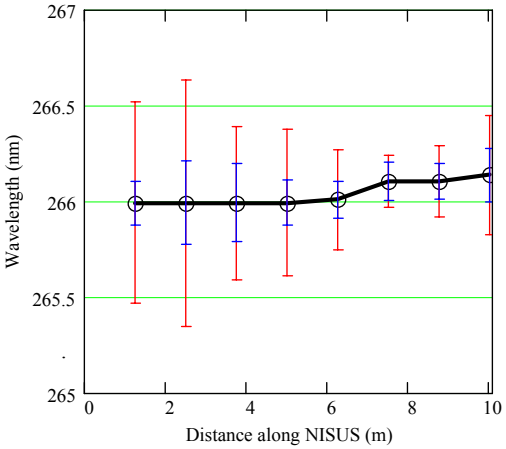

Fig. 6: Evolution of the HGHG spectrum.

On the next figure (Fig. 7) we present RMS fluctuation of the HGHG single-shot spectrum width along NISUS. As it follows from the plot, the RMS fluctuation of the spectrum width is generally decreasing towards the end of the undulator.

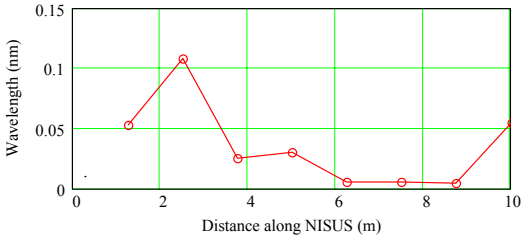

Fig.7: RMS fluctuation of the HGHG single-shot spectrum width.

SINGLE-SHOT METHOD OF SPECTRAL MEASUREMENTS

As we discussed in the Introduction, shot-to-shot fluctuation of radiation, as well as, accelerator performance stand technical problems for the accurate measurements of the radiation properties. In Fig. 8 we present a proposal for a single-shot spectral measurement device.

Special optical system (sketched as a green lens in Fig. 8) focuses the radiation downstream of the radiator. Due to the depth of image, the radiation from the beginning of undulator is focused later after the lens, vice versa for the end of the undulator. Using auxiliary optics (not shown in Fig. 8) and beam splitters one can split portions of radiations emitted along different regions of the radiator. Then these portions are recombined on the spectrometer slit.

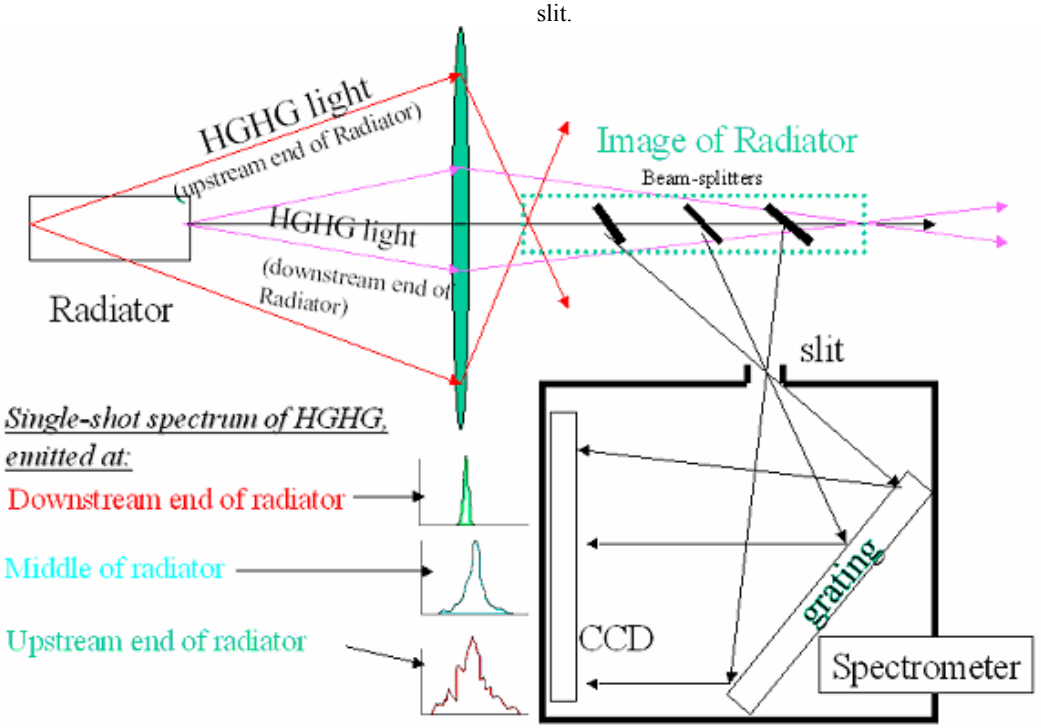

Fig. 8: Schematics of a single-shot measurements set-up.

Using non-dispersive axis of spectrometer we misalign different rays in order to see different spectral patterns recorded at the different locations on the spectrometer CCD. Thus, spectra of radiation from several locations along the radiator can be observed.

We note that the only diverging part of emitted radiation can be used in this set-up. The optical system must block the radiation coming at small angles as it is generated along the whole radiator. Another issue is the large range of the radiation intensity from different parts of the radiator (~7 orders of magnitude). This problem can be somewhat relieved by choosing an appropriate transmission of the beam splitters. However in experiment only last portion of the radiator might be effectively measured. Also, another problem is in the optical guiding effect [16] that will occur at the saturation. This will modify the angular divergence of the radiation, which has to be taken into account.

The study and optimization of the optical system for DUV FEL is in progress. Preliminary design is based on two-lens system with central and iris apertures.

ACKNOWLEDGEMENTS

We would like to thank S. Krinsky, J.B. Murphy and J.M. Wang for useful discussions. The work was performed under DOE contract DE-AC02-98CH10886.

REFERENCES

[1] L.H. Yu, A. Douyran, L. Di Mauro, *et al.*, Phys. Rev. Lett. **91**, No. 7, 074801-1, (2003).
[2] L. Di Mauro, A. Doyuran, E. Johnson, *et al.*, Nucl. Instrum. Methods Phys. Res. A **A507**, 15 (2003).
[3] SLAC Report No. SLAC-R-593, edited by J, Galayda, 2002
[4] V. Ayvazyan et al., Phys. Rev. Lett. **88**, 104802 (2002).
[5] L.H. Yu *et al*., Phys. Rev. A **44**, 8178 (1991)
[6] I. Ben-Zvi *et al*., Nucl. Instrum. Methods Phys. Res., Sect. A **304**, 181 (1991).
[7] M. Borland *et al*., Proc, of PAC 2001, p. 2707
[8] S. Reiche *et al*., Proc, of PAC 2001, p. 2751
[9] S.Biedron et al., Proc. of PAC 1999, p. 2486
[10] S.Reiche, Nucl. Instrum. Methods Phys. Res. A **A429**, 243 (1999).
[11] A. Murokh *et al.*, Proc. of PAC 1999, p. 2480
[12] A. Doyuran *et al*., Proc of EPAC 2002, p. 802
[13] S. Reiche, Nucl. Instrum. Methods **A445**, p. 139 (2000)
[14] V. Sajaev and Z. Huang, Nucl. Instrum. Methods **A507**, p. 154 (2003)
[15] V. Sajaev et al., Nucl. Instrum. Methods **A506**, p. 304 (2003)
[16] E. T. Scharlemann, A. M. Sessler and J. S. Wurtele, Phys. Rev. Lett. **54**, 1925 (1985)
[17] W. S. Graves, *et al.*, Proc. of PAC 2003, p. 959
[18] T. Shaftan *et al.*, these proceedings

ATTOSECOND X-RAY PULSES IN THE LCLS USING THE SLOTTED FOIL METHOD *

P. Emma†, Z. Huang, SLAC, Stanford, CA 94309, USA
M. Borland, ANL, Argonne, IL 60439, USA

Abstract

A proposal has been made to generate femtosecond and sub-femtosecond x-ray pulses in the Linac Coherent Light Source (LCLS) SASE FEL [1] by using a slotted spoiler foil located at the center of the second bunch compressor chicane [2]. This previous study highlighted a simple case, using the nominal LCLS parameters, to produce a 2-fsec FWHM, 8-keV x-ray pulse. The study also pointed out the possibility of attaining sub-femtosecond pulses by somewhat modifying the LCLS compression parameters, but did not undertake a full study for this more aggressive case. We take the opportunity here to study this 'attosecond' case in detail, including a full tracking simulation, exploring the limits of the technique.

INTRODUCTION

Within the community of synchrotron radiation users there is a rapidly growing interest in the availability of extremely short pulses as experimental probes in several fields of research, including structural studies of single biomolecules, x-ray diffraction from a single protein molecule, and femtosecond chemistry. The interest in sub-femtosecond (*i.e.*, attosecond [as] $= 10^{-18}$ sec) pulses lies in the fact that electron transfer reaction dynamics in atomic and molecular systems, providing information about the most basic reaction mechanisms in chemistry, biology, and soft/condensed matter physics, are on the femtosecond and sub-femtosecond time scales (see *e.g.*, [3]).

A previous study [2], based on the LCLS X-ray FEL, described the production of a 2-fs FWHM (full-width at half-maximum) long x-ray pulse generated by differentially spoiling the electron bunch by passing it through a thin slotted foil within the second magnetic bunch compressor chicane (see Fig. 1).

The method relies upon the fact that in a magnetic bunch-compressor chicane the beam is tilted at a large angle relative to the longitudinal axis t (or $z \approx ct$) as shown in Fig. 1. At the point of maximum tilt (center of the chicane) a thin foil is placed in the path of the beam. The foil has a vertically (y) oriented narrow slot at its center. The Coulomb scattering of the electrons passing through the foil increases the horizontal and vertical emittance of most of the beam, but leaves a very thin unspoiled slice where the beam passes through the slit. Spoiling the emittance of most of the beam by a factor of $\sim$5 will strongly suppress the FEL gain for these sections, while the very short unspoiled time-slice will produce an x-ray FEL pulse much shorter than the full 200-fs FWHM electron bunch length.

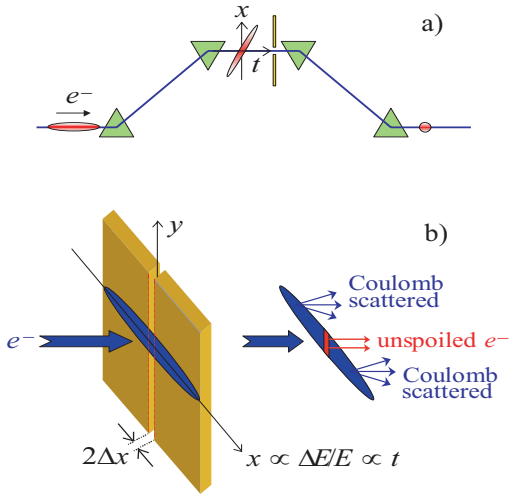

Figure 1: a) Sketch of electron bunch at center of magnetic bunch-compressor chicane with tilted beam in horizontal, x, and longitudinal coordinates, t. b) The slotted foil at chicane center generates a narrow, unspoiled beam center.

The previous study was based on the nominal LCLS machine parameters in order to highlight the compatibility of the technique with the baseline LCLS design. As briefly described therein, the pulse length can be further reduced by re-optimizing the operational machine parameters. We describe here the limiting pulse length of the unspoiled electrons and the necessary parameter adjustments to reach the limit, highlighting a detailed study which can produce a 400-as FWHM x-ray pulse duration using the LCLS design, but with a few changes to the operational configuration, such as an increased bunch compression factor and a reduced bunch charge, in order to avoid micro-bunching instabilities.

NOMINAL ACCELERATOR CONFIGURATION

Electron bunch length compression in the LCLS is accomplished in two stages. Each stage relies on an energy-chirped electron bunch passing through a magnetic chicane with energy-dependent path length. The chirp, h, is the slope of the relative energy variation along the bunch length coordinate, z_0, prior to the chicane, and is approximately

* This work is supported by the U.S. Department of Energy, contract DE-AC02-76SF00515.

† Emma@SLAC.Stanford.edu

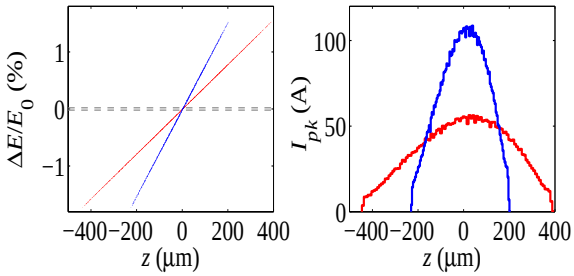

Figure 2: Chirped bunch (left) at start (red) and center (blue) of chicane with initial energy-chirp (red slope) of: $h \approx 39$ m^{-1}, and extremely narrow uncorrelated width. The foil slot is indicated as dashed lines and the current profiles are at right (100-pC case).

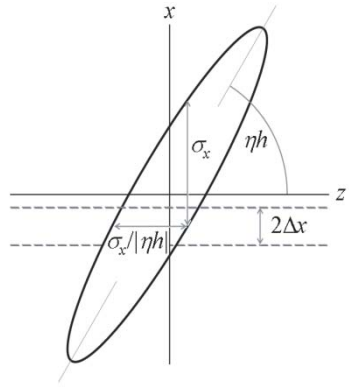

Figure 3: Energy-chirped (and therefore spatially-chirped) electron bunch at center of chicane.

equal to the total rms relative energy spread divided by the rms bunch length, as shown in Fig. 2 .

In the LCLS layout, the first bunch compressor chicane, BC1, is located at an energy of 250 MeV and nominally compresses the bunch length from 850 μm to 200 μm rms, while the second compressor is located at 4.5 GeV and compresses from 200 μm to 20 μm rms. The energy-dependent path length coefficient, or momentum compaction, of the BC2 is $R_{56} \approx -25$ mm, which describes the path length change for a particle with relative energy error: $\delta \equiv \Delta E/E_0$. The minus sign indicates that a high energy particle takes a shorter path, $\Delta z = R_{56}\delta$. The larger momentum dispersion, smaller uncorrelated energy spread, and smaller transverse beam size in the BC2 make this location the best choice for producing the shortest duration unspoiled electron pulse.

UNSPOILED ELECTRON PULSE LENGTH

The final unspoiled electron pulse duration is limited by several effects. The time-sliced rms horizontal betatron beam size at the foil (*i.e.*, $\sigma_{x_\beta} = \sqrt{\epsilon\beta}$, where ϵ is the horizontal beam emittance and β is the horizontal beta-function at the foil) limits the width of the slit (see σ_x in Fig. 3). The slit half-width, Δx, should be larger than, or similar to, approximately 3-times the betatron beam size (*i.e.*, $\Delta x \gtrsim 3\sqrt{\epsilon\beta}$), otherwise the peak current will be cut, and the FEL gain of the spike will be reduced. Similarly, the beam size in the slit has a contribution from the intrinsic (uncorrelated) rms relative energy spread (increased by ~ 2 due to half compression at the slit) times the chicane's dispersion at the foil (*i.e.*, $\Delta x \gtrsim 6|\eta|\sigma_{\delta_0}$), although this contribution to beam size is typically not significant. These contributions determine the minimum slit width that will not cut the peak current.

The minimum length of the unspoiled section of the electron bunch can be calculated in the following way, assuming ultra-relativistic electrons. The final bunch length coordinate (after the chicane), z, is expressed in terms of the initial bunch length coordinate (prior to the chicane), z_0, the chicane's momentum compaction, R_{56}, the bunch energy-chirp prior to the chicane, h, and the initial uncorrelated relative energy deviation of the particle, δ_0.

$$z = z_0 + R_{56}(hz_0 + \delta_0) = (1 + hR_{56})z_0 + R_{56}\delta_0 \quad (1)$$

Similarly, the transverse extent of the beam at the foil, x, can be written in terms of the momentum dispersion at the foil, η, the betatron component of the transverse coordinate, x_β, and the energy-chirp, h.

$$x = x_\beta + \eta(hz_0 + \delta_0) \quad (2)$$

Solving Eq. (1) for z_0 and inserting this into Eq. (2) gives

$$x = (1 + hR_{56})x_\beta + h\eta z + \eta\delta_0. \quad (3)$$

From Fig. 3 the length of the unspoiled section of electrons is a minimum when the slit width, Δx, approaches zero (temporarily ignoring the loss of peak current as described above). This is arranged by simply setting Eq. (3) to zero (with the slit at $x = 0$) and solving for z.

$$z = -\frac{\delta_0}{h} - \frac{(1 + hR_{56})x_\beta}{h\eta} \quad (4)$$

Since x_β and δ_0 are by definition uncorrelated, the rms length of the unspoiled bunch, $\langle z^2\rangle^{1/2} = \sigma_{z_u}$, for a zero slit width, is then

$$\sigma_{z_u} = \frac{1}{|\eta h|}\sqrt{\eta^2\sigma_{\delta_0}^2 + (1 + hR_{56})^2\sigma_{x_\beta}^2}, \quad (5)$$

where σ_{δ_0} is the initial rms uncorrelated relative energy spread at the start of the chicane and $\sigma_{x_\beta} = \sqrt{\epsilon\beta}$ is the rms betatron beam size at the foil.

From Fig. 3 the contribution to this length from a finite slit width is the rms of the nearly uniform x-distribution

in the slit, $\Delta x/\sqrt{3}$, converted to the z-direction by $1/|\eta h|$, and added in quadrature to the betatron beam size term in Eq. (5). Therefore, the FWHM duration of the unspoiled portion of the electron bunch is given by

$$\Delta\tau \approx \frac{2.35}{|\eta h|c}\sqrt{\eta^2\sigma_{\delta_0}^2 + (1+hR_{56})^2\,[\Delta x^2/3 + \epsilon\beta]}, \quad (6)$$

where c is the speed of light and $2.35 \approx 2\sqrt{2\ln(2)}$.

Equation (6) shows that an increased energy-chirp value, $|h|$, provides a shorter unspoiled pulse. It is also clear that the betatron beam size, $\sqrt{\epsilon\beta}$, and the slit half-width, Δx, are both effectively compressed by the inverse of the bunch compression factor: $1/C \equiv |1+hR_{56}| \ll 1$. The uncorrelated energy spread term, $\eta\sigma_{\delta_0}$, however, is not compressed and typically sets the minimum length limit. This small energy spread is established in the electron gun where it has been measured at about 3 keV rms [4], which agrees well with computer simulations. The 3-keV energy spread is amplified linearly by the bunch compression factor of the BC1. In the case of the LCLS, it is increased by a factor of 4.5, to 13.5 keV, which at 4.54 GeV, prior to the BC2, is an extremely small rms relative energy spread of $\sigma_{\delta_0} \approx 3\times10^{-6}$.

This very small local energy spread can allow various micro-bunching instabilities to develop in the linac [5] by providing no effective Landau damping in the chicanes. In fact, the LCLS design includes a beam heater system to increase the local energy spread to 40 keV (prior to BC1 compression) to Landau damp the micro-bunching instabilities. This increased energy spread, however, excludes the possibility to generate sub-femtosecond pulses using the slotted-spoiler foil, and leads to the 2-fs FWHM x-ray pulse discussed in reference [2]. For this reason, we propose a greatly reduced bunch charge of 100 pC for this sub-femtosecond application (rather than 1 nC in [2]). This reduced charge, and proportionally reduced peak current in the linac sections leading to BC2, moderates the instability and allows the preservation of this very small local energy spread from the RF photo-injector gun, thus enabling sub-femtosecond pulse generation with the foil.

ACCELERATOR PARAMETERS AND ISSUES

For this low charge (100 pC), we assume a transverse normalized emittance of $\gamma\epsilon_{x,y} \approx 0.5$ μm is possible (rather than the nominal level of 1 μm at 1 nC); a level which seems fairly conservative given the factor of ten charge reduction. In addition, the linac RF phases and voltage levels are necessarily adjusted to compensate for the reduced longitudinal wakefields in the accelerating structures, but in this example the initial bunch length is unchanged, the BC1 and BC2 chicane strengths are not altered, and the compression factor of 4.5 in the BC1 is maintained. Because of the factor of 10 charge (and current) reduction compared to the standard LCLS design, the microbunching instability driven by longitudinal space charge and coherent synchrotron radiation without the beam heater (assuming only 3 keV initial uncorrelated rms energy spread) is very mild. For example, for any initial beam modulation wavelength $\lambda > 50$ μm, we estimate that $\pm$ 1% density modulation at the end of the injector can cause no more than 0.7×10^{-6} rms energy modulation at the BC2 entrance, which adds insignificantly to the intrinsic beam energy spread $\sigma_{\delta_0} \approx 3\times10^{-6}$. Nevertheless, the temporal profile of the photocathode drive laser should be sufficiently smooth in order to not introduce any excessive beam density modulation. A Gaussian laser profile instead of a flattop profile might be preferable for this attosecond x-ray generation since only the emittance of the Gaussian core needs to be about 0.5 μm.

Table 1: LCLS BC2 chicane and beam parameters.

Parameter	**symbol**	**value**	**unit**
bunch charge	Q	100	pC
chicane energy	E_0	4.54	GeV
chicane dispersion	η	363	mm
momentum compaction	R_{56}	-24.7	mm
energy chirp	h	39.0	1/m
rms initial E-spread	σ_{δ_0}	3	10^{-6}
beta at foil	β	8.0	m
normalized emittance	$\gamma\epsilon$	0.5	μm
length of each bend	L_B	0.50	m
angle of each bend	$\lvert\theta_B\rvert$	1.98	deg

Table 1 lists the BC2 chicane and beam parameters used to generate a sub-femtosecond x-ray pulse. Using these parameter values, Fig. 4 shows Eq. (6) plotted (blue) versus the slit half-width, Δx, along with an almost identical (red) curve from particle tracking. The dash-dot curve (green) includes the local energy spread generated from incoherent synchrotron radiation in the chicane dipoles (3.6×10^{-6} rms per 0.5-m long, 2-degree bend at 4.54 GeV), which is not included in Eq. (6). The parameters in Table 1, and a 70-μm slit half-width ($=\Delta x$), chosen to preserve at least 1.3 kA of peak current, will produce a FWHM unspoiled electron pulse of 1.3 fs. This will be 'gain-narrowed' in the FEL producing a FWHM x-ray pulse as short as 400 as, while the spoiled beam has transverse emittance levels of $\gamma\epsilon_{x,y} \approx 6$ μm and does not produce FEL radiation.

TRACKING SIMULATIONS

To test these parameters and better estimate the final x-ray pulse length, the entire LCLS is simulated with three consecutive particle tracking computer codes: *Parmela* [6], *Elegant* [7], and *Genesis 1.3* [8]. The tracking includes space-charge forces in the RF photo-cathode gun and low-energy injector systems (*Parmela*), 2nd-order optics, wakefields, and coherent synchrotron radiation (CSR) in the dipole magnets (*Elegant*), and time-dependent FEL exponential gain and saturation in the undulator (*Genesis 1.3*).

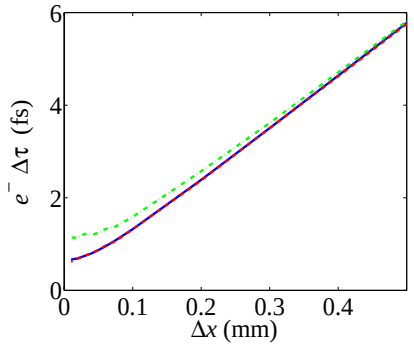

Figure 4: FWHM unspoiled e^- bunch duration as a function of slit half-width, Δx. The blue (solid) curve is Eq. (6), the red (dashed) is from particle tracking, and the green (dash-dot) is tracking which includes synchrotron radiation in the dipoles.

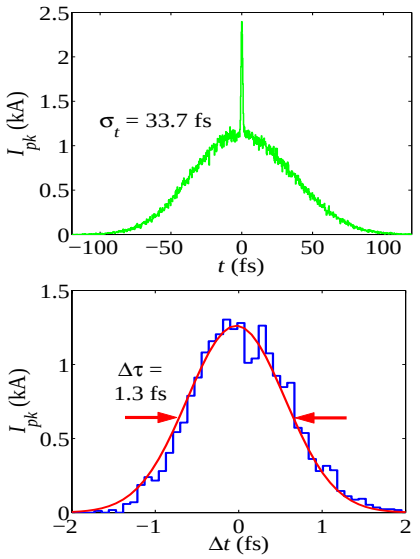

Figure 5: Current profile after BC2 (top) with spike created by e^- passing through the slit, and unspoiled e^- only (bottom) after BC2 with 1.3-fs FWHM and 1.3 kA.

Although the possibility of <0.5-μm emittance at 100 pC was verified [9] with *Parmela*, for convenience, a 1-nC run was used and each particle's action was scaled to produce a 0.5-μm core emittance.

As seen at the top plot in Fig. 5, the narrow section of electrons which pass through the slit produce a sharp spike on the current profile after the BC2 chicane. This spike is the result of electrons near the edge of the slit scattering in the foil. The scattering generates a slightly different path length for the electrons through the last half of the chicane and causes a small time-smearing inside the bunch according to

$$\Delta\sigma_t \approx |\eta|\sigma_\theta/c, \tag{7}$$

where σ_θ is the rms Coulomb scattering angle (22 μrad) through a 50-μm thick Be foil. Some of the scattered electrons then overlap in time with the unspoiled time-slice, raising the local peak current, and creating both an unspoiled core (the electrons that pass through the slit) and a spoiled halo (the time-smeared electrons from near the edge of the slit). The FEL process amplifies only the cold beam core and is unaffected by the halo. This sharp spike, however, can potentially damage the bend-plane emittance through CSR effects, which is a further reason to choose a very low bunch charge of 100 pC. Calculations with a line-charge (1D) CSR model (50-nm bin size) indicate very little emittance growth (<2%) in the unspoiled electrons through all LCLS bend magnets beyond the foil, partially due to the large tilted transverse beam size in the bends.

The Coulomb-scattered time smearing also keeps the peak current of the full bunch below 1.5 kA (not including the spike), limiting the possible CSR-induced beam brightness degradation from the full beam. Without this time-smearing, the peak current may approach 10 kA and the beam may break up in the chicanes.

The Coulomb scattering in the foil is simulated in *Elegant*, which includes a model for very thin foils with thickness $<10^{-3}$ of its radiation length [10]. The 50-μm thick Beryllium foil is $\sim 10^{-4}$ of its radiation length ($X_0 \approx 35$ cm), and the angular distribution produced by *Elegant* agrees well with theoretical calculations for very thin foils [11].

Finally, a model for the transition radiation wakefield [12] of the foil, but ignoring the slot, has been included in previous simulations [2] at 1-nC of charge and was found to have an insignificant effect on the unspoiled beam. In this case, at only 100-pC of total charge, the time-consuming simulation of the wakefield is not included here.

The bottom plot in Fig. 5 shows only the unspoiled electrons after the chicane with a FWHM duration of 1.3 fs and 1.3-kA of peak current with 1.8-pC of charge. The emittance of these unspoiled electrons is $\gamma\epsilon_{x,y} \approx 0.4$ μm (smaller than 0.5 μm because they are taken from the cold core of the *Parmela*-generated distributions). Their relative rms energy spread at 14.3 GeV is 6×10^{-5}, including the effects of CSR. It is also estimated, but not included in tracking, that the longitudinal space-charge forces in the 1100-m of linac and transport lines beyond the BC2 chicane will generate an additional rms energy spread of $<10^{-4}$ within this unspoiled electron section, which should increase the FEL gain length by <5%. Similarly, the resistive-wall longitudinal wakefield in a 100-m long undulator with radius 2.5 mm and copper surface, produces an insignificant rms energy spread of $< 2 \times 10^{-5}$. The tracked particles, both spoiled and unspoiled, are transferred to the FEL code *Genesis 1.3* for a time-dependent FEL simulation.

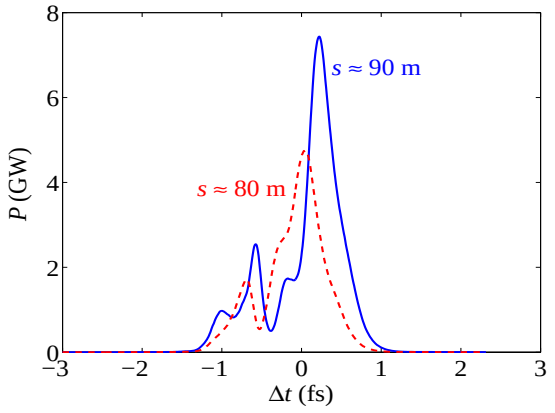

Figure 6: X-ray power profile at $s \approx 80$ m (red-dash) and $s \approx 90$ m (blue-solid) along the undulator, with 570-as (80 m) and 380-as (90 m) FWHM spike duration at 5-7 GW.

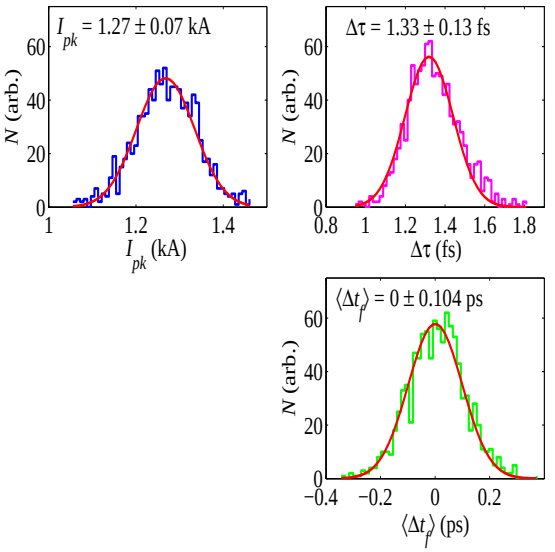

Figure 7: Peak current (top-left), FWHM unspoiled e^- pulse width (top-right), and bunch arrival time (bottom-right) variation over 8-sec of LCLS operation at 120 Hz, using rms machine jitter levels given in Table 3.

FEL SIMULATIONS

The FEL performance is simulated using *Genesis 1.3* [8] with parameters as listed in Table 2. Only a time window of about 6 fs containing the unspoiled 1.3-fs electrons is used in the simulation, since the spoiled electrons do not participate in the FEL interaction as shown in ref. [2]. The FEL interaction with the unspoiled electrons saturates around 80 m, with the radiation pulse further narrowed from the unspoiled electron pulse due to the nonlinear interaction. The x-ray power profile is shown in Fig. 6 at both 80 and 90 meters along the undulator. The pulse at 90 m has a 380-as FWHM duration with 7-GW of peak power and $\sim 2 \times 10^9$ 8-keV photons in this one spike.

Table 2: LCLS FEL Parameters.

Parameter	symbol	value	unit
electron energy	E_0	14.3	GeV
radiation wavelength	λ_r	1.5	Å
undulator parameter	K	3.71	
undulator period	λ_u	3	cm
mean beta function	$\langle\beta\rangle$	30	m

STABILITY AND SYNCHRONIZATION

In a real operating machine, the beam energy, timing, and charge will vary from shot to shot, as will RF phases and amplitudes of the various linac sections. If the beam energy centroid changes prior to the BC2 chicane, the mean horizontal beam position in the slot will also change. This may affect the peak current and pulse width of the unspoiled electron pulse, as well as the final bunch arrival time in the FEL undulator.

To estimate these levels, 1000 2D-tracking runs were performed (ignoring transverse variations) to simulate an 8-second span of LCLS operation at 120 Hz. Each beam or machine parameter in Table 3 is randomly varied in a Gaussian distribution with rms value as listed (1 deg-S ≈ 1 ps). The RF phase and amplitude errors are applied independently to each of the 5 main linac sections (see ref. [1], Ch. 7, pg. 7-28, Table 7.10). The tracking also includes the effects of charge-dependent longitudinal wakefields. The final unspoiled beam energy, arrival time, peak current, and pulse width, are then recorded to estimate the stability of the unspoiled beam.

Table 3: Expected short-term machine jitter levels (rms).

Parameter	symbol	value	unit
Relative bunch charge	$\Delta Q/Q$	2	%
Drive laser-gun timing	Δt_g	0.5	ps
RF phase of each linac	ϕ_{RF}	0.1	deg-S
RF amp. of each linac	$\Delta V/V$	0.1	%

The fixed slot position determines the energy of the unspoiled beam, after the chicane, to a very high degree, but the peak current, arrival time, and pulse width vary as shown in Fig. 7. Although the relative peak current and pulse width each vary by <10% rms, the final bunch arrival time varies by 100 fs rms, which is quite large in comparison to the 400-as pulse width. This is one clear limitation of this method, where pump-probe experiments may have to measure this timing variation in order to meaningfully 'time-bin' the data collection. Longer term machine variations will be stabilized by beam feedback systems.

REFERENCES

[1] LCLS Conceptual Design Report, SLAC-R-593 (2002), http://www-ssrl.slac.stanford.edu/lcls/cdr/.

[2] P. Emma et al., *Femtosecond and Sub-Femtosecond X-ray Pulses from a SASE-Based Free-Electron Laser*, Phys. Rev. Lett. 92:074801, (2004).

[3] R. Neutze et al., Nature **406** 752-757 (2000); M. Drescher et al., *ibid*. **419** 803-807 (2002).

[4] M. Hüning and H. Schlarb, *Measurement of the Beam Energy Spread in the TTF Photoinjector*, Proc. of the 2003 Particle Acc. Conf., Portland, OR (IEEE, Piscataway, NJ, 2003).

[5] Z. Huang et al., *Suppression of Microbunching Instability in the Linac Coherent Light Source*, Phys. Rev. ST Accel. Beams 7:074401 (2004).

[6] J. Billen, *PARMELA*, Los Alamos National Laboratory Report LA-UR-96-1835 (1996).

[7] M. Borland, APS LS-287, Sep. 2000.

[8] S. Reiche et al., Nucl. Instrum. & Methods, **A483** (2002) 70.

[9] C. Limborg, private communication, June 2004.

[10] M. Borland, ANL/APS, OAG-TN-2003-007, 2003.

[11] W.R. Leo, *Techniques for Nuclear and Particle Physics Experiments*, (Springer-Verlag, Berlin, 1994).

[12] K.L.F. Bane and G. Stupakov, *Transition Radiation Wakefields for a Beam Passing through a Metallic Foil*, SLAC-PUB-9726, June 2003.

LARGE-SCALE TIMING DISTRIBUTION AND RF-SYNCHRONIZATION FOR FEL FACILITIES

J. Kim*, F. Ö. Ilday, F. X. Kärtner, O. D. Mücke, M. H. Perrott, MIT, Cambridge, MA 02139, USA
W. S. Graves, D. E. Moncton, T. Zwart, MIT-Bates Linear Accelerator Center, Middleton, MA 01949, USA

Abstract

For future advances in accelerator physics in general and seeding of free electron lasers (FELs) in particular, precise synchronization between low-level RF-systems, photo-injector laser, seed radiation as well as potential probe lasers at the FEL output is required. In this paper, we propose a modular system that is capable of achieving synchronization of various RF- and optical sub-systems with femtosecond precision over distance of several hundreds meters. Typical synchronization methods based on direct photo-detection are limited by detector nonlinearities, which lead to amplitude-to-phase conversion and introduce excess timing jitter. A new synchronization scheme for extraction of low jitter RF-signals from optical pulse trains distributed by mode-locked lasers is demonstrated. It is robust against photo-detector nonlinearities. The scheme is based on a transfer of timing information into an intensity imbalance between the two output beams from a Sagnac-loop interferometer. As a first experimental demonstration, sub-100 fs timing jitter between the extracted 2-GHz RF-signal and the 100 MHz optical pulse train from a mode-locked Ti:sapphire laser is demonstrated. Numerical simulations show the scaling to sub-femtosecond precision is possible. Together with low-jitter mode-locked lasers and timing stabilized fiber links, this scheme can be applied for large-scale femtosecond timing distribution and synchronization of RF- and optical sub-systems in accelerator and free electron laser facilities.

INTRODUCTION AND MOTIVATION

Seeding of free electron lasers operating in the EUV and soft X-ray regime with radiation generated via high harmonics from noble gases may result in a fully coherent X-ray laser. For seeding of such large-scale facilities spanning over several hundreds meters, it is critical to synchronize lasers and RF-systems with low (preferably sub-femtosecond range) timing jitter in a long-term stable arrangement. Figure 1 shows the schematic outline of timing distribution and synchronization for such a facility. The pulse repetition rate of an optical master oscillator implemented as a mode-locked laser is stabilized to a frequency standard or a low noise microwave oscillator. The pulse train is distributed to all critical sub-systems by use of timing stabilized fiber links, i.e., the pulse trains leaving different fiber links are highly synchronous. The RF- or optical sub-systems are then synchronized to the pulse trains at the fiber outputs.

* jungwon@mit.edu

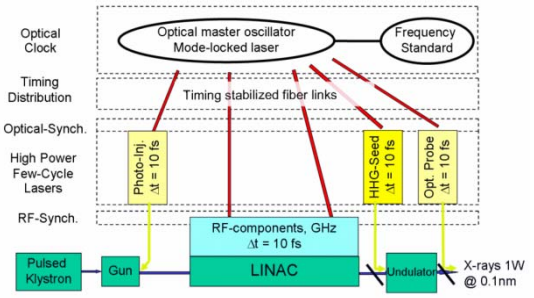

Figure 1: Schematic outline of timing distribution and synchronization for FEL facility.

It has been shown recently that the extraction of a microwave signal from an optical pulse train emitted by a mode-locked laser using direct photo-detection is limited in precision by excess phase noise [1]. The origin of this excess noise has been identified to be amplitude-to-phase conversion in the photo-detection process, beam-pointing variations, and pulse distortions by photo-detector nonlinearities [1]. In addition to this excess phase noise and timing jitter by photo-detector nonlinearities, the long-term synchronization stability is limited by the temperature dependence of semiconductor photodiodes. Thus, a new synchronization scheme to avoid these problems is highly desirable.

In the next section, a module for the synchronization between RF-signal and optical pulse train from a mode-locked laser is experimentally demonstrated and discussed in detail. The same module can also be used for the optical-to-optical synchronization between various lasers. The required technical criteria for timing stabilized fiber links and optical master oscillators are addressed in the last sections.

RF-SYNCHRONIZATION

Outline of the Scheme

The general idea for suppression of excess noise due to the photo-detection process is shown in Figure 2. While still in the optical domain, the timing information is transferred into an intensity imbalance between two beams by sending the pulse train through a pair of amplitude modulators. The modulators are driven by the output signal from a voltage-controlled oscillator (VCO) with 180° phase difference. The intensity difference is detected with a balanced detector and this signal controls the input to the VCO via a loop filter. With this step, we shift the problem of photo-detector nonlinearities on the electronics side to the realization of amplitude modulators with drift-free bias points on the optical side. The 180°

out-of-phase amplitude modulators can be realized by a Mach-Zehnder interferometer with a phase modulator in one arm. However, this scheme will suffer from the phase drifts in the interferometer arms due to temperature fluctuations, air currents, and mirror vibrations. To remove these problems, the interferometer is implemented in a Sagnac-loop configuration with a phase modulator inside the loop.

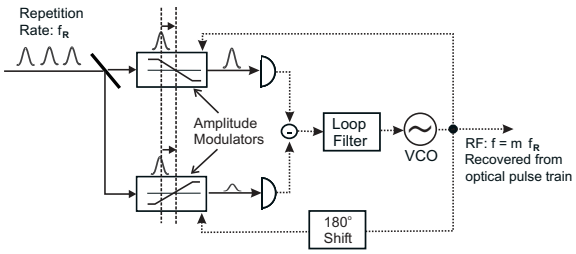

Figure 2: General idea of synchronization scheme based on a transfer of timing information into an intensity imbalance in the optical domain.

Experiments

Figure 3 shows the synchronization scheme.

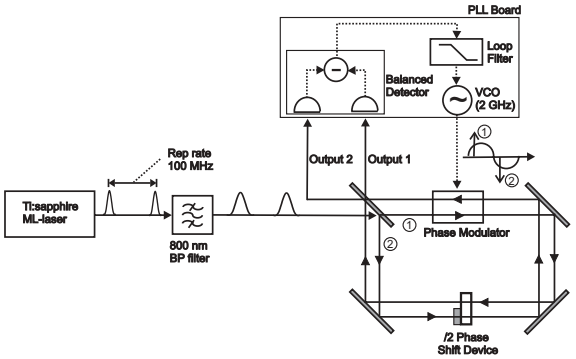

Figure 3: The synchronization scheme for extraction of a 2 GHz signal from a 100 MHz repetition rate Ti:sapphire laser.

A 100 MHz repetition rate mode-locked Ti:sapphire laser is used as the pulse source. After passing a bandpass filter at 800 nm to limit the pulsewidth to about 100 fs, the input optical pulse train is sent into the Sagnac-loop. A resonant phase modulator at 2 GHz is positioned in the Sagnac-loop in such a way that the optical delay between counter-propagating pulses at the phase modulator is set to half of the RF-signal period. This assures that the two pulses experience opposite phase modulation. The output beams are detected by a balanced detector that generates a difference signal between the two photocurrents from the two Si pin-photodiodes. The output current from the balanced detector is transferred to a passive loop filter (type II, order 2 topology [2]) for proper filtering. The passive loop filter structure is advantageous over an active counterpart since it allows a simple circuit and also ensures excellent noise performance. The loop filter output signal drives the VCO and changes the driving frequency of the phase modulator until it reaches a phase-locked state by balancing the two output powers from the interferometer. This closes the phase-locked loop operation. For a stable and drift-free biasing of the interferometer, an effective quarter-wave plate is inserted in one of the beams using a thin-film coating covering only half of the substrate. A very stable and drift-free phase-locked operation is achieved with this scheme.

Phase Noise Measurement Set-up

The phase noise of the RF-output signal from the VCO is characterized in two ways: (i) by the frequency discriminator technique using a commercial phase noise measurement setup PN9000 from Aeroflex; (ii) by mixing the output signal of the VCO in quadrature with the 2 GHz component of the directly detected pulse train in order to measure the relative phase noise between the optical pulse train and the extracted RF-signal. Figure 4 shows the measurement set-up. Using method (i), the input is delayed and mixed with itself in quadrature to extract the phase noise of the input [3]. Method (ii) is a standard technique to measure the residual phase noise between two locked RF-signals [4] where an oscilloscope is used to monitor that the two RF-signals are in quadrature, and a vector signal analyzer is used to measure the noise spectrum.

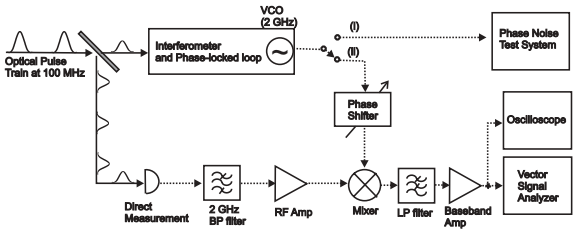

Figure 4: Phase noise measurement set-up: (i) frequency discriminator technique using a commercial phase noise instrument (PN9000, Aeroflex) and (ii) mixing the output signal of VCO in quadrature with the same frequency component of the directly detected pulse train.

Phase Noise Measurement Results

The measured single-sideband (SSB) phase noise spectra from 1 Hz to 10 MHz are shown in Figure 5. Curve (1) shows the phase noise spectrum of the free-running VCO measured with the Aeroflex phase noise measurement system. Curve (2) shows the phase noise measured by the same method when the system is locked. The locking is clearly visible in the spectrum covering the range of 100 kHz to 10 MHz. At lower frequencies, the phase noise of the free-running Ti:sapphire pulse train dominates.

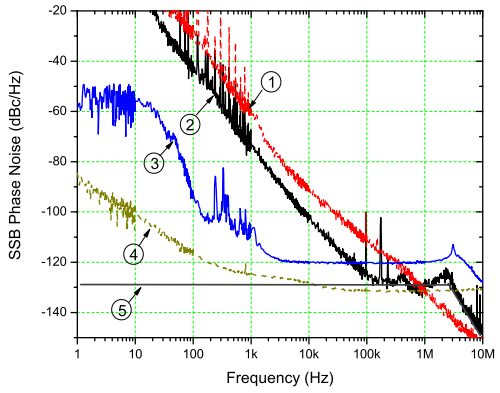

Figure 5: Single-sideband phase noise measurement result: (1) free-running VCO and (2) locked VCO using method (i); (3) measured phase noise between extracted RF-signal and the 20th harmonic of directly detected pulse train using method (ii); (4) noise floor of vector signal analyzer; (5) estimated phase noise level of extracted RF-signal from result of curve (2).

In order to verify the assumption that the phase noise of the laser dominates at low frequencies in the frequency discriminator measurement results, we measured the relative phase noise between the pulse train and the RF-signal by using the second phase noise characterization method. The result is shown in curve (3) of Fig. 5. Due to the noise floor of the vector signal analyzer (curve (4) in Fig. 5) and excess noise in the photo-detector that generates the reference signal, the high frequency noise floor is increased in comparison to method (i). But this measurement clearly shows that the noise increase at low frequencies in curve (2) is the phase noise of the free-running Ti:sapphire laser. This result suggests that better shielding of the laser against environmental perturbations, higher pulse repetition rate as well as the use of a VCO with lower phase noise, will lead to drastic improvements in the timing jitter of the microwave signal extracted from the laser source.

Note that the origin of the enhanced phase fluctuations below 1 kHz may be due to either mechanical vibrations in the Sagnac-loop or excess phase noise in the photo-detection process resulting from converted laser amplitude fluctuations. These hypotheses will be further investigated in the near future by building two RF-synchronization systems and beating the two outputs against each other. Based on the current system and measurements, the relative timing jitter between the RF-signal and the pulse train integrated from 100 Hz to 10 MHz can be estimated by the area underneath curve (5), which lines up with the high frequency noise of the Aeroflex measurement (curve (2) in Fig. 5) and results in about 60 fs timing jitter.

The demonstrated timing jitter is not as low as using pure microwave techniques based on high-speed photo-detection [5,6] or using purely optical means [7] yet. However, with improved system design, this method will be able to reduce the relative jitter to the sub-femtosecond range over the full Nyquist bandwidth in the near future. For long-term stability, a fiber implementation of the Sagnac loop is preferable. This will eliminate a large part of the drift problems in the low frequency range. In addition, a lower-noise VCO combined with a higher phase detector gain of phase-locked loop will dramatically reduce the phase noise of high frequency range. Numerical simulations also show that scaling down to sub-femtosecond timing jitter is possible with the improved design.

OPTICAL-TO-OPTICAL SYNCHRONIZATION

Synchronization is necessary not only between optical and RF-subsystems but also between different optical systems, for example, the photo-injector laser and the master oscillator as shown in Fig. 1. Figure 6 shows how the optical-to-RF synchronization technique can be used to synchronize two pulsed lasers with each other. By use of the RF-synchronization module described in the previous section, we first lock the RF signal to the pulse train from one laser (ML-laser 1 in Fig. 6). This locked RF-signal drives the phase modulator of another RF-synchronization module. However, instead of driving VCO, the error signal from balanced detector drives the piezoelectric transducer (PZT) to control the repetition rate of the second laser (ML-laser 2 in Fig. 6). In this way, an effective synchronization of multiple lasers is also possible by locking lasers to the same RF signal synchronized to one laser.

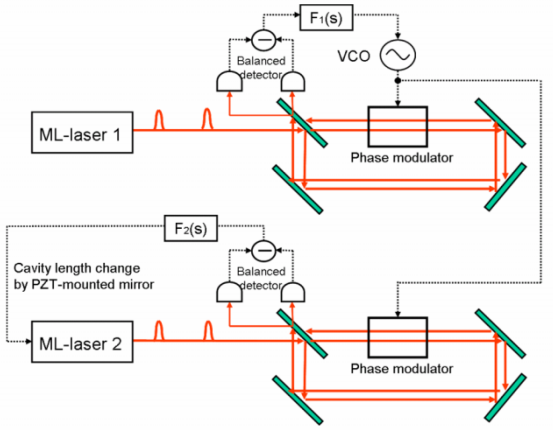

Figure 6: Possible optical-to-optical synchronization scheme with the proposed RF-synchronization technique.

TIMING DISTRIBUTION

Precise transfer of RF-signals through fiber links has been demonstrated recently [8,9]. For timing distribution over a large-scale free electron laser facility, timing stabilized fiber links will be used. If the fiber length is L,

we assume that no length fluctuations are faster than (2nL)/c, where n is the refractive index of the fiber and c is the vacuum velocity of light. Relative fiber expansion by temperature change is typically on the order of 10^{-7}/K, which can be compensated for by a fiber length control loop as shown in Figure 7 by referencing the back reflected pulse from the fiber end with a later pulse from the mode-locked laser. This approach is applicable up to a precision fundamentally limited by the high frequency jitter of the laser from frequency of c/(2nL) up to the Nyquist frequency, i.e., half of the repetition rate. Therefore this jitter should be on the order of a few femtoseconds or below if 10-fs overall jitter needs to be achieved. This puts a serious constraint on the high frequency timing jitter of the optical master oscillator.

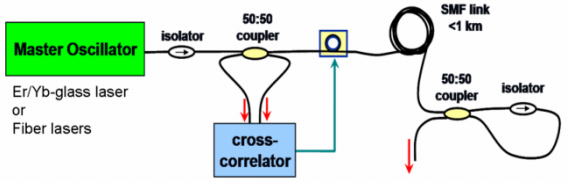

Figure 7: Timing stabilized fiber link.

OPTICAL MASTER OSCILLATOR – LOW-JITTER MODE-LOCKED LASER

Currently the most promising candidates for ultra-low jitter optical master oscillators are Er/Yb-glass lasers [10], passively mode-locked Er-doped fiber lasers [11] and Yb-doped fiber lasers [12]. Particularly, Er/Yb-glass lasers with sub-20 fs timing jitter have been demonstrated recently [10]. The crucial performance indicator for such a source is the phase noise or timing jitter integrated from c/(2nL) to the Nyquist frequency. This jitter will set an inherent limitation to the precision in timing achievable with a given distribution system. Construction and evaluation of several of these lasers with respect to timing jitter requirements are currently in progress.

CONCLUSION AND OUTLOOK

In summary, we introduce a scalable timing distribution and synchronization scheme for future accelerator and seeded free electron laser facilities. We demonstrate a modular RF-synchronization scheme between laser and RF-subsystem which is robust against photodiode nonlinearities. This technique can also be used for optical-to-optical synchronization. Together with timing stabilized fiber links driven by an ultra-low jitter mode-locked laser, we anticipate large-scale timing distribution and synchronization techniques with femtosecond precision in the near future.

REFERENCES

[1] E. N. Ivanov, S. A. Diddams and L. Hollberg, IEEE J. Sel. Top. Quant. Elec. **9**, 1059 (2003).

[2] M. H. Perrott, "PLL Design using the PLL Design Assistant Program" (MIT High Speed Circuits and Systems Group, Cambridge, MA, 2002), http://www-mtl.mit.edu/research/perrottgroup/tools.html.

[3] Aeroflex, "PN9000 Automated Phase Noise Measurement System", Application Note #2 (Aeroflex, Plainview, NY, 2003).

[4] R. P. Scott, C. Langrock, B. H. Kolner, IEEE J. Sel. Top. Quant. Elec. **7**, 641 (2001).

[5] R. K. Shelton, S. M. Foreman, L.-S. Ma, J. L. Hall, H. C. Kapteyn, M. M. Murnane, M. Notcutt, J. Ye, Opt. Lett. **27**, 312 (2002).

[6] A. Bartels, S. A. Diddams, T. M. Ramond, L. Hollberg, Opt. Lett. **28**, 663 (2003).

[7] T. R. Schibli, J. Kim, O. Kuzucu, J. T. Gopinath, S. N. Tandon, G. S. Petrich, L. A. Kolodziejski, J. G. Fujimoto, E. P. Ippen, F. X. Kaertner, Opt. Lett. **28**, 947 (2003).

[8] J. Ye, J.-L. Peng, R. J. Jones, K. W. Holman, J. L. Hall, D. J. Jones, S. A. Diddams, J. Kitching, S. Bize, J. C. Bergquist, L. W. Hollberg, L. Robertsson, L.-S. Ma, J. Opt. Soc. Am. B **20**, 1459 (2003).

[9] K. W. Holman, D. J. Jones, D. D. Hudson, J. Ye, Opt. Lett. **29**, 1554 (2004).

[10] J. B. Schlager, B. E. Callicoatt, R. P. Mirin, N. A. Sanford, D. J. Jones, J. Ye, Opt. Lett. **28**, 2411 (2003).

[11] G. Lenz, K. Tamura, H. A. Haus, E. P. Ippen, Opt. Lett. **20**, 1289 (1995).

[12] F. Ö. Ilday, J. R. Buckley, H. Lim, F. W. Wise, W. G. Clark, Opt. Lett. **28**, 1365 (2003).

HIGH TEMPORAL RESOLUTION, SINGLE-SHOT ELECTRON BUNCH-LENGTH MEASUREMENTS

G. Berden*, B. Redlich, A.F.G. van der Meer,
FOM Institute Rijnhuizen / FELIX, Nieuwegein, The Netherlands

S.P. Jamison†, A.M. MacLeod, W.A. Gillespie,
School of Computing and Advanced Technologies, University of Abertay Dundee, Dundee, UK

Abstract

A combination of electro-optic detection of the Coulomb field of an electron bunch and single-shot cross-correlation of optical pulses, is used to provide single-shot measurements of the shape and length of sub-picosecond electron bunches. This so-called temporal decoding technique has been applied to the measurement of electron bunches at the Free Electron Laser for Infrared eXperiments (FELIX), where electric field profiles with a FWHM of 650 fs have been recorded. The measurement temporal resolution is limited primarily by the electro-optic crystal thickness and the relatively low energy of the electrons (50 MeV), and the bunch length is estimated to be around 635 fs. The single-shot electron bunch longitudinal profile measurement is real-time and non-destructive, and can therefore be used as an online diagnostic tool. The temporal decoding technique has also been used to measure the electric field profiles of single far-infrared laser pulses from the FELIX free electron laser.

INTRODUCTION

X-ray free electron lasers (FELs) require dense, relativistic electron bunches with bunch lengths significantly shorter than a picosecond. For operating and tuning these lasers, advanced electron bunch length monitors with sub-picosecond temporal resolution are essential. Ideally, non-destructive and non-intrusive monitoring of a *single* electron bunch should be available in real-time. A promising candidate for such monitors is the determination of the electron bunch longitudinal-profile via electro-optic (EO) detection of the co-propagating Coulomb field, an area subject to on-going research and development at the Free Electron Laser for Infrared eXperiments (FELIX) [1-7] and at other laboratories [8-12].

With the EO detection technique, the Coulomb electric field of the bunch induces birefringence in an EO crystal placed adjacent to the beam. The birefringence is determined through ellipsometry using a synchronized ultrafast Ti:sapphire (Ti:S) laser probe pulse. To enable a single-shot measurement, the Ti:S pulse is chirped to a duration exceeding the measurement window, and the induced birefringence is determined as a function of time within the probe pulse. In previously reported experiments, the timing was inferred from the wavelength-time relationship of the chirped probe pulse [2]. However, this spectral decoding method is intrinsically subject to limitations on the time resolution, and can introduce significant measurement artifacts [3, 13, 14, 15].

A recently demonstrated technique [5, 6, 13], which we refer to as temporal decoding, overcomes these limitations. The envelope of the probe pulse is measured directly in the time-domain, using single-shot second harmonic cross-correlation. In this contribution we report temporal decoding measurements of the longitudinal electric field of single electron bunches and of far-infrared FEL pulses.

ELECTRON BUNCH MEASUREMENTS

Measurements were performed on relativistic electron bunches (250 pC, 50 MeV) that are produced in the linear accelerator at the FELIX facility [16]. The electron bunch profile is measured inside the accelerator beam pipe at the exit of the undulator of the short wavelength IR FEL.

The setup is depicted schematically in Fig. 1. A near infrared laser pulse is obtained from a femtosecond Ti:Sapphire amplifier (wavelength 800 nm, pulse energy 1 mJ, repetition rate 1 kHz, pulse length 30 fs) which is actively synchronized to the accelerator rf clock [17]. This pulse is split into a probe pulse and a reference pulse. The probe pulse is stretched to a length that is longer than the length of the electron bunch. Subsequently, the probe pulse is passed through an electro-optic crystal (ZnTe) that is placed between two crossed polarizers. In this way, the birefringence induced by the Coulomb field of a single co-propagating electron bunch is translated into an intensity modulation of the probe pulse. The temporal profile of this intensity modulation, and thus the temporal profile of the electric field of the electron bunch, is measured with a sub-50 fs resolution in a single-shot cross-correlator [13, 7] where the intensity modulated probe pulse is cross-correlated with the 30 fs reference pulse. The position dependent emission of the second harmonic light from the BBO crystal is imaged onto an intensified CCD camera.

Binning of the pixels of single-shot images along the direction perpendicular to the plane containing the probe and reference beams provides single-shot electron bunch mea-

* berden@rijnh.nl
† also at: University of Strathclyde, Glasgow, UK

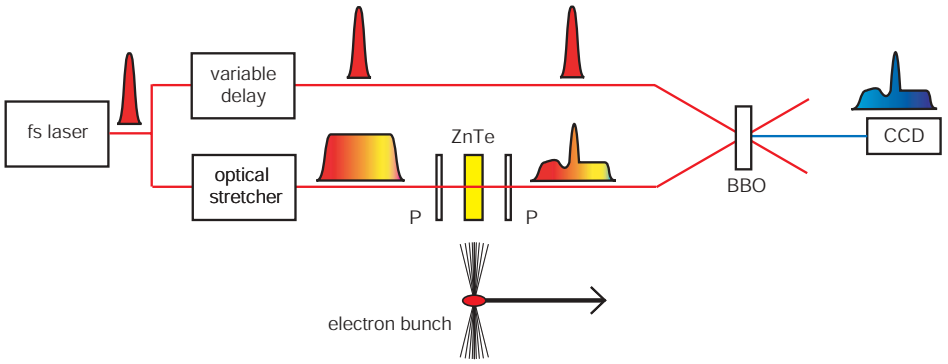

Figure 1: Scheme for single-shot measurements of the electric field profile of individual electron bunches. The electric field profile induces an intensity modulation onto a stretched optical pulse via the electro-optic effect. The electric field profile of the electron bunch is obtained with the temporal decoding method where the intensity modulated probe pulse is measured by a single-shot cross-correlation with an ultra-short optical pulse. For the experiments discussed here, the pair of polarizers P are crossed, with minimum transmission in the absence of the electron bunch.

surements. The position of the pixels in the parallel direction is proportional to time.

Examples of single-shot measurements are shown in the left hand panel of Fig. 2. As a result of the polarizer geometry used, the electro-optic signal scales quadratically with the electric field strength as has been experimentally verified (see Ref. [7] for more details). The traces shown in Fig. 2 correspond to electric field profiles with a FWHM of 650 to 700 fs, and have been recorded at the same settings of the accelerator. From the figure it is clear that the time jitter between the probe laser pulse and the electron bunch is of the order of the width of the electron bunch.

The right hand panel of Fig. 2 shows the temporal jitter of 108 electron bunches; the rms value is 390 fs. At FELIX, the timing jitter originates from the synchronisation of the probe laser pulses and the electron bunches to the rf clock. The former is determined by the quality of the active locking of the probe laser cavity round trip time to the rf clock. The latter is mainly determined by phase fluctuations of the klystron feeding the accelerator. Previous optical cross correlation measurements between 9 μm FEL radiation and the Ti:Sapphire laser at 800 nm in a 100 μm thick $AgGaS_2$ crystal showed a jitter of 400 fs rms [17], a value similar to that presently obtained with the electron bunch measurements.

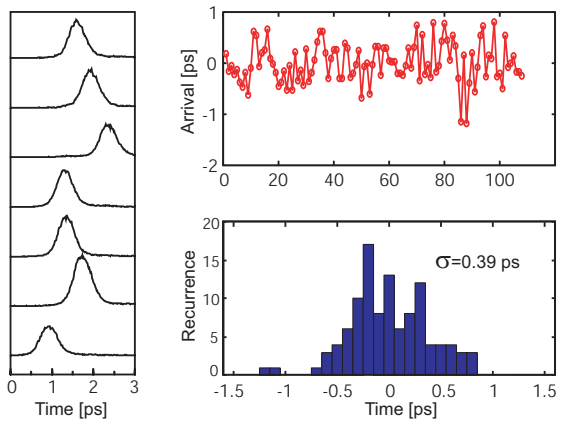

Figure 2: Left panel: a sequence of single shot electron bunch measurements. Right panel: a graph (top) and a histogram of the relative arrival time of 108 electron bunches. See text for further details.

For accelerators with a photo-injector, the laser which triggers the photo-cathode can be used for electro-optic detection of the electron bunches as well, which gives a method to directly monitor the time jitter introduced by bunchers and accelerators. The electro-optic detection method can also be used to produce accurate timing information (triggers) for user experiments.

The temporal resolution is determined by several factors. The increased duration of the Coulomb field at the probe position, when compared to the electron bunch duration, leads to a temporal resolution of $2R/(\gamma c)$ where R is the radial distance between the electron beam and the optical probe in the electro-optical crystal [1]. For a 50 MeV beam and a distance of 1.5 mm this temporal resolution is 100 fs. The thickness and the material of the crystal contribute to the temporal resolution as well [3, 4, 18]. For a 0.5 mm ZnTe crystal, electric field Fourier components with a frequency lower than 2.8 THz will be detected with minimal distortions. These contributions to the temporal resolution are present for all current electro-optic detection schemes. However, alternative EO materials, or deconvolution of material response in data analysis, both have potential for surpassing the material dependent limitations. An analogous single-shot auto-correlation technique routinely

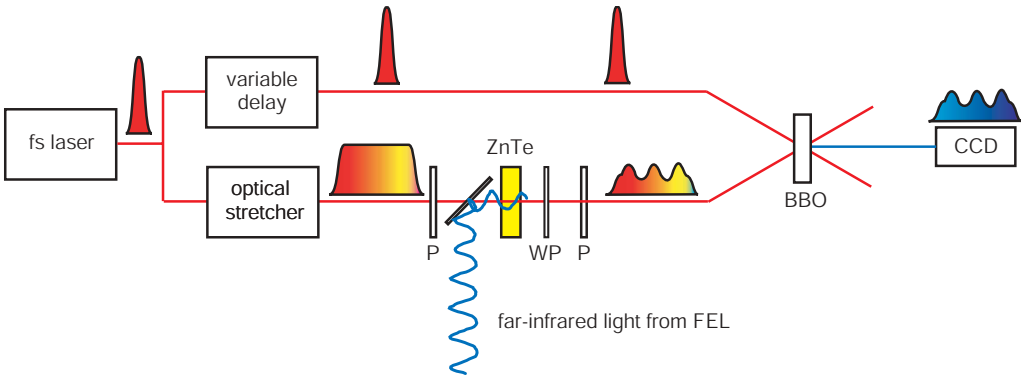

Figure 3: Scheme for single-shot measurements of the electric field profile of individual FEL optical pulses. The electric field profile induces an intensity modulation onto a stretched optical pulse via the electro-optic effect. The electric field profile of the FEL pulse is obtained with the temporal decoding method where where the intensity modulated probe pulse is measured by a single-shot cross-correlation with an ultra-short optical pulse. The polarizer (P) and quarter waveplate (WP) angles were varied according to specific experimental requirements.

characterises sub-50 fs optical pulses [19]. Ultimately, the time resolution is determined by the length of the reference optical pulse (30 fs).

FEL PULSE MEASUREMENTS

The output from a far-infrared FEL can be characterized with the electro-optic technique as well [20]. At a wavelength of 150 μm, a 20 ps long optical pulse consists of 40 optical cycles and is quasi-monochromatic. Since the timing jitter of the electron bunches ($\sim$400 fs, see Fig. 2) is of the same order of magnitude as the duration of one cycle of the far-infrared light, it is evident that one needs a single-shot detection technique to resolve the oscillating electric field.

Figure 3 shows the scheme for single-shot electro-optic detection with temporal decoding of the electric field of the FEL pulse. The laser system, the optical stretcher, and the cross-correlator are identical to those used in the electron bunch measurements. For the experiments described in this section, FELIX produces light at a wavelength of 130 μm at a macropulse repetition rate of 5 Hz. The micropulse repetition rate is 25 MHz, and the micropulse energy is about 1 μJ. The far-infrared laser beam and the 800 nm probe pulse are overlapped in space with an ITO coated glass plate acting as a far IR - optical dichroic mirror. Alternatively a gold coated mirror with a small hole for the probe pulse may be used to combine the two beams. A parabolic mirror with a focal length of 100 mm, not shown in the schematic diagram of Fig. 3, is used to focus the FEL pulse and the probe pulse onto the ZnTe electro-optical crystal.

The second harmonic light (400 nm) emerging from the BBO crystal is imaged onto an intensified CCD camera. The upper panel of Fig. 4 shows an image obtained by subtracting an image without the presence of an FEL pulse (background) from an image where an FEL pulse was present. The image shows a horizontal line because a cylindrical lens had been positioned in the probe pulse path, just before the BBO crystal. In the horizontal direction, the position in the image is proportional to time. The time axis can easily be calibrated since the duration of one cycle (one

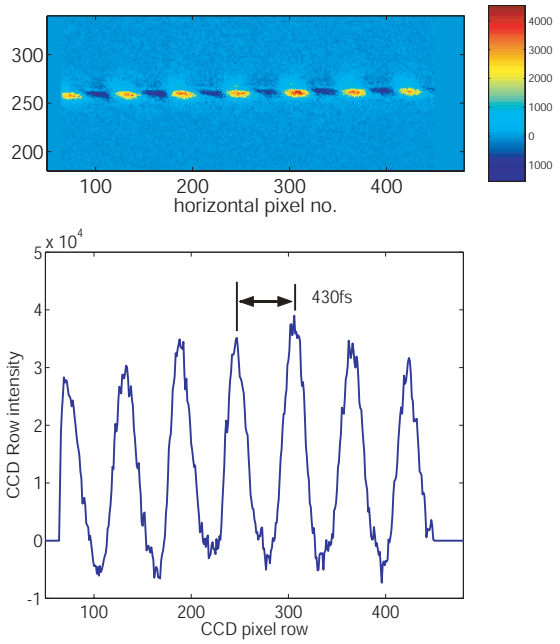

Figure 4: Electro-optic temporal decoding measurement of a quasi-monochromatic FEL pulse. The wavelength is 130 μm, and one cycle therefore corresponds to 430 fs. The image has been obtained by subtracting an image without the presence of an FEL pulse (background) from an image where an FEL pulse was present. The graph has been obtained by vertically binning the image.

oscillation of the electric field) is λ/c and the wavelength is known from the online spectrometer. By binning the image along the vertical direction, the electric field profile is obtained and is shown in the lower panel of Fig. 4.

The independently determined oscillating time structure of the FEL pulse measurements makes it attractive to use such FEL pulse measurements for the quantitative study of the capabilities of EO detection. At FELIX, we have used this approach to undertake initial experiments into alternative EO materials that may have the potential for improved time-resolution measurements. Furthermore, FEL measurements have been performed, outside the accelerator vault and with free access, to pre-align the cross-correlator and imaging setup before undertaking electron bunch measurements.

CONCLUSIONS

Electro-optic sampling of the Coulomb field of the electron bunch is a promising method for real-time monitoring of the electron bunches. The method is non-intercepting and non-destructive. It is largely non-intrusive, although it is expected that the modification of the beamline and induced wakefields will slightly influence beam properties. At FELIX we have measured femtosecond longitudinal electron bunch profiles using the new temporal decoding technique. The method has also been used to measure the electric field profile of the optical far-infrared FEL pulse, which is a convenient way to calibrate and test the experimental capabilities of the technique.

REFERENCES

[1] X. Yan, A.M. MacLeod, W.A. Gillespie, G.M.H. Knippels, D. Oepts, A.F.G. van der Meer, and W. Seidel, Phys. Rev. Lett. **85**, 3404 (2000).

[2] I. Wilke, A.M. MacLeod, W.A. Gillespie, G. Berden, G.M.H. Knippels, and A.F.G. van der Meer, Phys. Rev. Lett. **88**, 124801 (2002).

[3] G. Berden, G.M.H. Knippels, D. Oepts, A.F.G. van der Meer, S.P. Jamison, A.M. MacLeod, W.A. Gillespie, J.L. Shen, and I. Wilke, *Proceedings of the 6th European workshop on beam diagnostics and instrumentation for particle accelerators (DIPAC2003)*, Mainz, Germany, 2003, p. 20.

[4] G. Berden, G.M.H. Knippels, D. Oepts, A.F.G. van der Meer, S.P. Jamison, A.M. MacLeod, W.A. Gillespie, J.L. Shen, and I. Wilke, *Proceedings of the 2003 Particle Accelerator Conference (PAC2003)*, Portland (OR), 2003, p. 519.

[5] G. Berden, B. Redlich, A.F.G. van der Meer, S.P. Jamison, A.M. MacLeod, and W.A. Gillespie, *Proceedings of the 25th International Free Electron Laser Conference, and the 10th FEL Users Workshop (FEL2003)*, Tsukuba, Japan, 2003, p. II-49.

[6] G. Berden, B. Redlich, A.F.G. van der Meer, S.P. Jamison, A.M. MacLeod, and W.A. Gillespie, *Proceedings of the ninth European Particle Accelerator Conference (EPAC2004)*, Lucerne, Switzerland, 2004.

[7] G. Berden, S.P. Jamison, A.M. MacLeod, W.A. Gillespie, B. Redlich, and A.F.G. van der Meer, Phys. Rev. Lett. (2004), in press.

[8] T. Tsang, V. Castillo, R. Larsen, D.M. Lazarus, D. Nikas, C. Ozben, Y.K. Semertzidis, and T. Srinivasan-Rao, J. Appl. Phys. **89**, 4921 (2001).

[9] M.J. Fitch, A.C. Melissinos, P.L. Colestock, J.-P. Carneiro, H.T. Edwards, and W.H. Hartung, Phys. Rev. Lett. **87**, 034801 (2001).

[10] T. Srinivasan-Rao, M. Amin, V. Castillo, D.M. Lazarus, D. Nikas, C. Ozben, Y.K. Semertzidis, A. Stillman, T. Tsang, and L. Kowalski, Phys. Rev. ST Accel. Beams **5**, 042801 (2002).

[11] L. Bentson, P. Bolton, E. Bong, P. Emma, J. Galayda, J. Hastings, P. Krejcik, C. Rago, J. Rifkin, and C.M. Spencer, Nucl. Instrum. Methods Phys. Res., Sect. A **507**, 205 (2003).

[12] H. Loos, A. Doyuran, J.B. Murphy, J. Rose, T. Shaftan, B. Sheehy, Y. Shen, J. Skaritka, X.J. Wang, Z. Wu, and L.H. Yu, *Proceedings of the 2003 Particle Accelerator Conference (PAC2003)*, Portland (OR), 2003, p. 2455.

[13] S.P. Jamison, J. Shen, A.M. MacLeod, W.A. Gillespie, D.A. Jaroszynski, Opt. Lett. **28**, 1710 (2003).

[14] J.R. Fletcher, Opt. Express, **10**, 1425 (2002).

[15] S.P. Jamison, et al. (to be published).

[16] http://www.rijnh.nl/felix

[17] G.M.H. Knippels, M.J. van de Pol, H.P.M. Pellemans, P.C.M. Planken, and A.F.G. van der Meer, Opt. Lett. **23**, 1754 (1998).

[18] G. Gallot, J. Zhang, R.W. McGowan, T.I. Jeon, D. Grischkowsky, Appl. Phys. Lett. **74**, 3450 (1999).

[19] F. Salin, P. Georges, G. Roger, and A. Brun, Appl. Opt. **26**, 4528 (1987).

[20] G.M.H. Knippels, X. Yan, A.M. MacLeod, W.A. Gillespie, M. Yasumoto, D. Oepts, and A.F.G. van der Meer, Phys. Rev. Lett. **83**, 1578 (1999).

RECENT RESULTS AND PERSPECTIVES OF THE LOW EMITTANCE PHOTO INJECTOR AT PITZ

F. Stephan[#], K. Abrahamyan[&], G. Asova[§], J. Bähr, G. Dimitrov[§], U. Gensch, H.-J. Grabosch, J.H. Han, M. Krasilnikov, D. Lipka, V. Miltchev, A. Oppelt, B. Petrossyan, D. Pose, S. Riemann, L. Staykov, DESY, 15738 Zeuthen, Germany
M.v. Hartrott, E. Jaeschke, D. Krämer, D. Richter, BESSY, 12489 Berlin, Germany
I. Bohnet, J.P. Carneiro, K. Flöttmann, S. Schreiber, DESY, 22603 Hamburg, Germany
J. Roßbach, Hamburg University, 22761 Hamburg, Germany
P. Michelato, L. Monaco, C. Pagani, D. Sertore, INFN Milano, 20090 Segrate, Italy
I. Tsakov, INRNE, 1784 Sofia, Bulgaria
W. Sandner, I. Will, Max-Born-Institute, 12489 Berlin, Germany
W. Ackermann, W.F.O. Müller, S. Schnepp, S. Setzer, T. Weiland, TU Darmstadt, 64289 Darmstadt, Germany

Abstract

The Photo Injector Test Facility at Zeuthen (PITZ) was built to study the production of minimum transverse emittance electron beams for Free Electron Lasers and future Linear Colliders. Until November 2003, the electron beam from the rf gun has been fully characterized at PITZ. For a bunch charge of 1 nC a minimum normalized projected beam emittance of 1.5 π mm mrad in the vertical plane and a minimum geometrical average of both transverse planes of 1.7 π mm mrad have been achieved. This fulfills the requirements of the VUV-FEL at DESY. In this contribution, an overview of the measured electron beam and high duty cycle rf parameters including transverse emittance, thermal emittance, bunch length, momentum, and momentum spread will be given. In addition, planned major upgrades and first results towards fulfilling the even more challenging requirements for the European XFEL will be discussed. This includes measurements with increased average and peak rf power and the improvement of the transverse laser beam profile.

INTRODUCTION AND LAYOUT

The successful operation of short wavelength SASE FELs requires electron sources providing high phase space densities. For the case of the VUV-FEL at TTF2 in Hamburg, a normalized transverse projected emittance at the undulator entrance of about 3 π mm mrad at 1.5 kA peak current is needed for saturation at about 30 nm and 2 π mm mrad at 2.5 kA peak current is needed for saturation at 6 nm, in both cases assuming a rms energy spread of 1 MeV [1]. For the XFEL, even more demanding parameters are requested: for a charge of 1 nC a projected normalized emittance of 1.4 π mm mrad is needed at the undulator entrance which corresponds to an emittance of about 0.9 π mm mrad at the injector exit [2, 3]. For the development of such electron sources the PITZ facility was built. After the decision to build the facility at Zeuthen was taken in September 1999, the civil construction happened in 2000 and in 2001 the necessary hardware components were installed. In January 2002, the first photoelectrons were produced and the facility was continuously upgraded. In November 2003, the first cavity installed at PITZ was fully characterized, fulfilling the VUV-FEL parameter requirements. The experimental results obtained with this cavity (called prototype #2 because it was the second rf gun cavity produced at DESY) will be summarized in the first half of this paper. Since January 2004 this cavity has been installed at the VUV-FEL at TTF2 in Hamburg and went smoothly into operation [4].

After moving the prototype #2 to Hamburg, the older gun cavity prototype #1 was installed at PITZ. Although we knew several shortcomings of this cavity beforehand (limited surface quality, problems with bulk copper material, for more details see [5]), it is suited to study the high average power behavior of the rf gun. Those measurements together with electron beam dynamics studies will be summarized in the second half of this paper. Beyond this, the R&D program necessary to reach the XFEL requirements will be shortly described.

The experimental set-up used for the measurements with gun prototypes #2 and #1 has essentially been identical and is shown in Figure 1. It consists of a 1.5 cell L-band rf gun with a Cs_2Te photo-cathode, a solenoid system for compensating space charge induced emittance growth, a photo-cathode laser system capable of generating long pulse trains with variable temporal and spatial micro pulse shape, and an extensive diagnostics section.

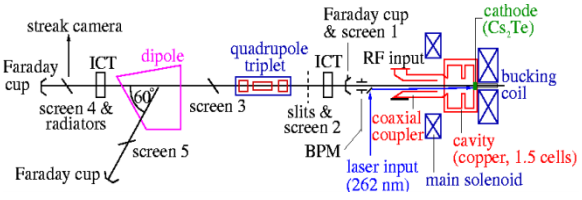

Figure 1: Layout of PITZ.

[#] frank.stephan@desy.de
[&] on leave from YERPHI, 375036 Yerevan, Armenia.
[§] on leave from INRNE, 1784 Sofia, Bulgaria.

LASER PARAMETERS

The laser system operated at PITZ was developed at the Max-Born-Institute (MBI) in Berlin. Its schematic layout is shown in Figure 2. The system produces laser pulse trains up to 800 µs length with a repetition rate of up to 5 Hz and a single pulse repetition rate of 1 MHz.

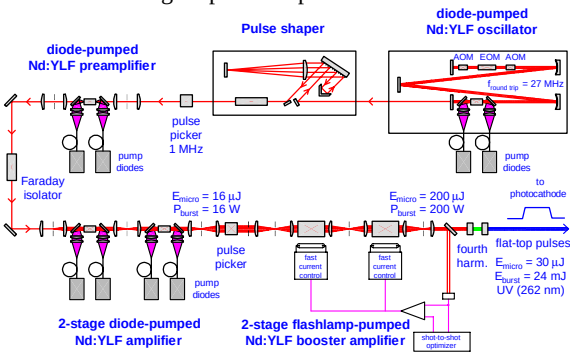

Figure 2: Layout of the PITZ laser system.

The temporal and transverse properties of the individual laser pulses on the photo-cathode play a major role in obtaining a good electron beam quality. Therefore, those parameters are regularly monitored using a streak camera for the temporal laser profile and a CCD camera at a position equivalent to the photo-cathode location (virtual cathode) for the transverse laser shape. Typical distributions for the optimized laser settings obtained during the operation of gun cavity prototype #2 at PITZ are shown in Figure 3. It is obvious that the transverse profile is not the desired flat-top distribution but more close to a truncated Gaussian with some modulations.

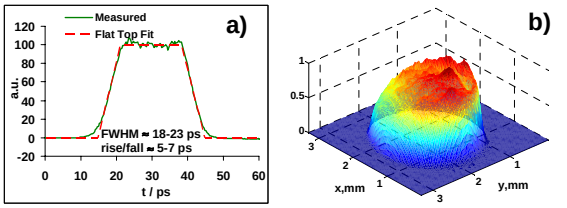

Figure 3: Typical a) temporal and b) transverse laser profile used for the operation of gun cavity prototype #2. The temporal profile was measured at a wavelength of 524 nm. The transverse rms beam size on the cathode was 0.51 mm for x and 0.63 mm for y.

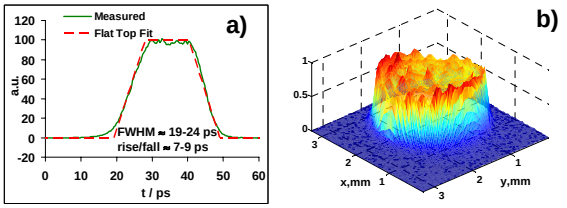

Figure 4: Typical a) temporal and b) transverse laser profile used for the operation of gun cavity prototype #1. The temporal profile was measured at a wavelength of 262 nm. The transverse rms beam size on the cathode was about 0.58 mm in x and in y.

To improve the transverse laser profile on the photo-cathode the laser beam transport line was re-designed and put into operation in June 2004. The laser parameters for the beam dynamics measurements with the gun cavity prototype #1 are shown in Figure 4. Now, the transverse shape is close to a flat-top profile, but modulations are still visible.

CHARACTERISATION OF THE RF GUN FOR THE VUV-FEL AT TTF2

Achieved RF Parameters

A smooth conditioning procedure of the gun cavity prototype #2 yielded an operation with rf pulses of up to 900 µs length, a repetition rate of 10 Hz, and a peak rf power of about 3 MW. This corresponds to a duty cycle of 0.9 % and about 27 kW average power in the cavity. Since the field strength on the cathode is 11% higher than in the full cell for gun prototype #2, an accelerating gradient of about 42 MV/m was obtained on the cathode.

Normalized Transverse Emittance

After the entire beam diagnostics had been put into reliable operation an experimental optimization procedure was started [6]. During the parameter scans it turned out that the mirror in the vacuum system, which deflects the laser beam onto the photo-cathode, was affecting the beam quality [6, 7]. After the beam was steered horizontally around the vacuum mirror and a fine adjustment of the laser parameters was done (result is shown in Figure 3), a minimum normalized projected emittance of 1.5 π mm mrad was obtained in the vertical plane and a minimum geometrical average of both transverse planes of 1.7 π mm mrad was achieved, see Figure 5. Details of the emittance measurement procedure are described in reference [8]. These results agree with simulations, fulfill the requirements of the VUV-FEL, and were confirmed several times in different weeks and by different shift crews.

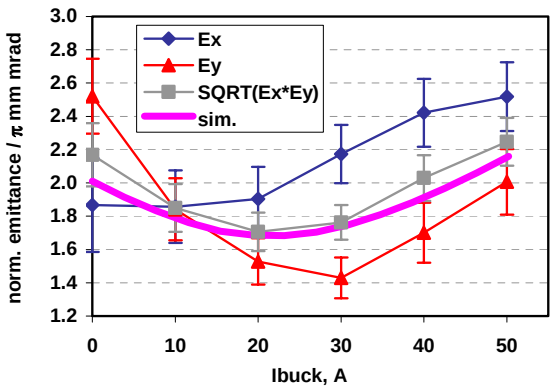

Figure 5: Projected normalized transverse emittance for gun cavity prototype #2 as a function of bucking solenoid current which is used to compensate the magnetic field on the photo-cathode. The rf phase is 5 degrees lower than the phase with maximum mean energy gain, the main

solenoid current is 305 A, and the charge is 1 nC. The fat line shows an ASTRA simulation [9] of the geometrical average using input parameters as described in the previous sections.

Momentum and Momentum Spread

Using the dipole and screen 5 the momentum distribution was measured [10]. The mean momentum and the momentum spread are shown in Figure 6. The error bars come from the uncertainties in the dipole field and the mechanical alignment as well as from the non-zero beam size and divergence at the dipole entrance. Good agreement between measurement and simulation is obtained.

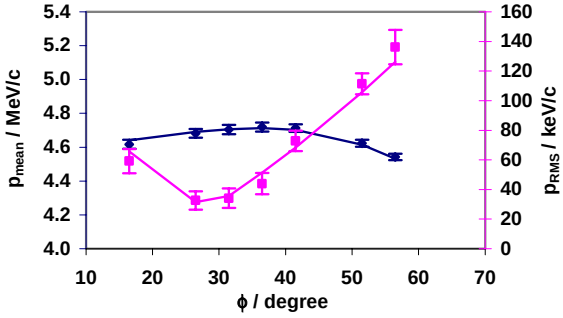

Figure 6: Mean momentum (blue) and momentum spread (magenta) as a function of rf phase for gun cavity prototype #2. The points are the measurements and the line represents the corresponding ASTRA simulation. The emitted charge was tuned to be 1 nC for each of the measurement points. The laser settings used correspond to Figure 3.

Bunch Length

The electron bunch length was measured using silica aerogel as Cherenkov radiator, an optical transmission line, and a streak camera [10]. A minimum bunch length of 21ps FWHM was measured at the same phase where the momentum spread is minimum. The minimum bunch length is about 3 ps shorter than the emitting laser pulse used at that time.

MEASUREMENTS WITH THE NEXT RF GUN AT ZEUTHEN

Achieved RF Parameters

When the older cavity prototype #1 was installed at PITZ in the beginning of 2004, the main goal was to condition it up to the maximum rf power available from the 5 MW klystron installed [11]. The maximum peak power was reached with about 4 MW in the gun cavity. A maximum average power of 30 kW was obtained on July 8th (1000 µs, 10 Hz, 3 MW), limited by the available water-cooling system. Its upgrade was already scheduled for Dec. '04 to Feb. '05. Nevertheless, the cavity has been operated stable with rf pulse lengths of up to 1300 µs and full peak power at 5 Hz repetition rate, see Figure 7.

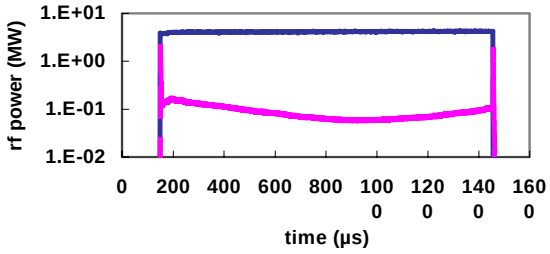

Figure 7: Forward power and reflected power from the gun cavity prototype #1 operated at 5 Hz.

Normalized Transverse Emittance

With the increased rf input power and the improved transverse laser profile the emittance has been re-measured [8]. The current status of optimization is shown in Figure 8. The main error contribution comes from the background subtraction. Although the optimization is still in progress, the minimum emittance in one plane and the minimum geometrical average are about the same or slightly better than the year before. One obvious difference is that the emittances in x and y do not cross over for different bucking coil currents anymore. This can be explained by the difference in the transverse laser beam profile (compare Fig. 3 and Fig. 4 and the laser beam sizes on the cathode). Further optimization will include measurements at different transverse laser spot sizes.

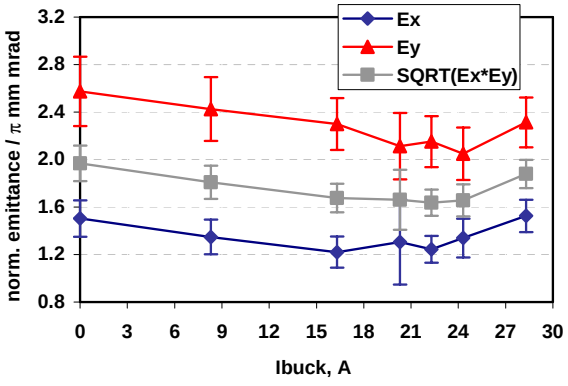

Figure 8: Preliminary measurement of the projected normalized transverse emittance for gun cavity prototype #1 as a function of bucking solenoid current. The rf phase is 5 degrees lower than the phase with maximum mean energy gain, the main solenoid current is 326 A, and the charge is 1 nC.

Thermal Emittance

Measurements for estimating the thermal emittance from Cs_2Te cathodes have been done with gun cavity prototypes #2 and #1. Details are described in reference [8]. Average kinetic energies between 0.7 eV and 0.9 eV have been obtained with different cathodes and different measurement procedures. For a rms laser spot size on the cathode of 0.55 mm this corresponds to a thermal emittance of about 0.6 π mm mrad.

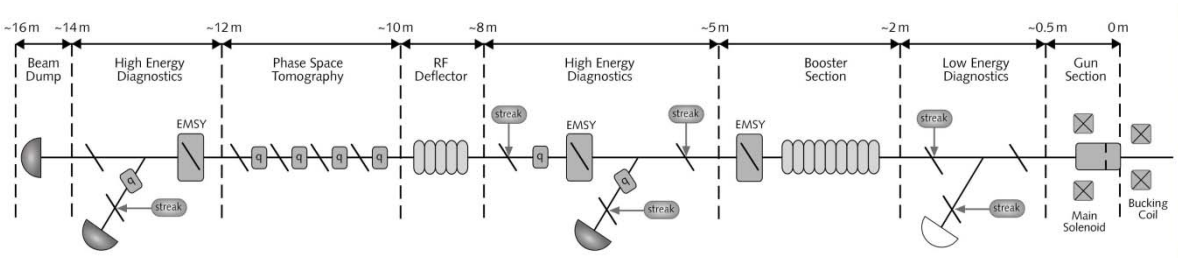

Figure 10: Simplified schematic layout of the PITZ2 set-up. The beam goes from right to left.

Momentum and Momentum Spread

With the increased rf power in gun cavity prototype #1, the momentum distribution was re-measured. The mean momentum and the momentum spread are shown in Figure 9. The error sources are the same as mentioned before. Compared to the operation with lower rf input power, the minimum momentum spread is now reduced by about a factor 2 and the phase difference between minimum momentum spread and maximum mean momentum is reduced to about 5 degrees.

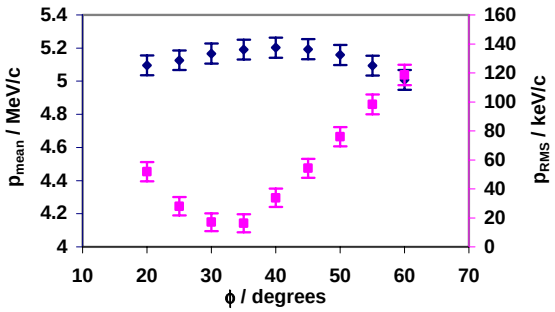

Figure 9: Measured mean momentum (blue) and momentum spread (magenta) as a function of rf phase for gun cavity prototype #1. The emitted charge was tuned to be 1 nC for each of the measurement points. The used laser settings correspond to Figure 4.

R&D PROGRAM TOWARDS THE XFEL REQUIREMENTS

To reach the very demanding requirements for the XFEL mentioned in the introduction, a second phase of PITZ was started (called PITZ2), which is a large extension of the facility and its research program. The work will go into two directions: a) further improve the emittance from the rf gun and b) study the principle for conserving small emittance up to higher beam energy. To reach the required emittance from the rf gun the accelerating gradient at the cathode needs to be increased to ~ 60 MV/m, the rise and decay time in the temporal laser intensity profile of individual pulses has to be reduced to ~ 2 ps, and the transverse laser profile must be further improved. For studying the emittance conservation principle, a booster cavity will be installed and the beam diagnostics section will be upgraded (for details see [12]). A schematic layout of PITZ2 is shown in Figure 10.

SUMMARY

The rf gun for the VUV-FEL at TTF2 was optimized at PITZ. An overview on the results was presented, yielding a minimum projected emittance in the vertical plane of 1.5 π mm mrad. Experimental results of the next rf gun cavity installed at PITZ were summarized as well, demonstrating a reliable operation at increased peak and average rf power. Although the optimization procedure for this cavity is not yet finished, very promising results are already obtained. The future plans at PITZ were briefly described.

REFERENCES

[1] K. Flöttmann and Ph. Piot, "An Upgraded Injector for the TTF FEL - User Facility", EPAC'02, Paris, June 2002.
[2] For a list of beam parameters of the XFEL linac see http://xfel.desy.de/content/e159/e160/index_eng.html
[3] Ph. Piot et. al., "Conceptual Design of the XFEL Photoinjector", TESLA FEL report 2001-03, February 2001.
[4] S. Schreiber for the VUV-FEL group, "Commissioning of the VUV-FEL Injector at TTF", EPAC'04, Lucerne, July 2004.
[5] J.H. Han et. al., "Conditioning and High Power Test of the RF Guns at PITZ", EPAC'04, Lucerne, July 2004.
[6] M. Krasilnikov et. al., "Optimizing the PITZ Electron Source for the VUV-FEL", EPAC'04, Lucerne, July 2004.
[7] S. Setzer et. al., "Influence of Beam Tube Obstacles on the Emittance of the PITZ Photoinjector", EPAC'04, Lucerne, July 2004.
[8] V. Miltchev et. al., "Transverse Emittance Measurements at the Photo Injector Test Facility at DESY Zeuthen", (TUPOS09, these proceedings).
[9] ASTRA manual, http://www.desy.de/~mpyflo/
[10] D. Lipka, PhD thesis, Humboldt University Berlin, May 2004.
[11] J. Bähr et. al., „High Power Conditioning and Measurements of the Longitudinal Emittance at PITZ", (TUPOS03, these proceedings).
[12] A. Oppelt et. al., „The Photo Injector Test Facility at DESY Zeuthen: Results of the First Phase", Linac'04, Lübeck, August 2004.

EMITTANCE MEASUREMENT ON THE CEB6 ELECTRON GUN FOR THE SPRING-8 COMPACT SASE SOURCE

K. Togawa*, T. Shintake, H. Baba, T. Inagaki, K. Onoe, T. Tanaka, SPring-8 / RIKEN Harima Institute, Hyogo 679-5148, Japan
H. Matsumoto, High Energy Accelerator Research Organization (KEK), Ibaraki 305-5148, Japan

Abstract

A 500 kV pulsed electron gun has been developed for the injector system of the X-ray FEL project at SPring-8. A single-crystal CeB_6 cathode is chosen as a thermionic emitter, because of its excellent emission properties, i.e., high resistance against contamination, uniform emission density, and smooth surface. A gun voltage of -500 kV was chosen as a compromise between the need for suppressing emittance growth and reducing the risks of high voltage arcing. We have succeeded in producing a 500 keV beam with 1 A peak current and 3 μsec width. A normalized rms emittance of 1.1π mm.mrad has been measured by means of double-slit method. In this paper, we report on the result of the emittance measurement and discuss improvements for X-ray FEL.

INTRODUCTION

In X-ray FEL theory, it is well known that the fine structure of the beam dominates the FEL gain. To achieve the SASE-FEL in Angstrom wavelength region, the sliced emittance of the beam should be very low and the peak current should be of the order of kA. Moreover from the application point of view, the FEL machine should be stable for long periods of operation.

In the SASE-FEL, the electron beam generated by the gun is accelerated in the main linac, then it is directly injected into the long undulator and generates the X-ray beam there. Therefore, any electron bunch fluctuation in transverse position, timing, size, charge, etc., will directly affect the X-ray lasing. This is markedly different from the storage ring type machine situation. As a result, the stability of the electron gun is essential for producing stable X-ray FEL light.

We decided to use a pulsed high-voltage gun with a single-crystal CeB_6 thermionic cathode followed by a buncher system [1]. A side view of the CeB_6 gun with an emittance monitor bench is shown in Fig. 1, and the beam design parameters at the gun exit are summarized in Table 1 [2].

Table1 : The beam design parameters at the gun exit.

Beam energy	500 keV
Peak current	3 A
Pulse width (FWHM)	1.6 μsec
Repetition rate	60 Hz
Normalized emittance (rms)	0.4π mm.mrad

* togawa@spring8.or.jp

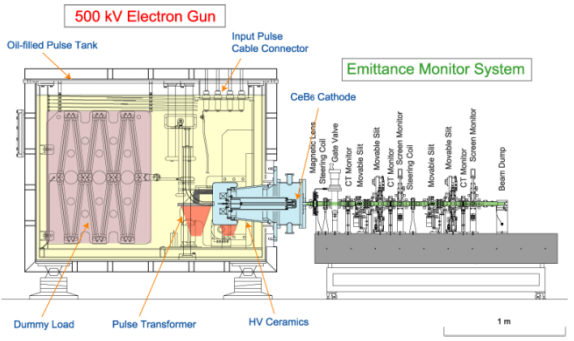

Fig. 1 : A side view of the CeB_6 electron gun with an emittance monitor bench.

THE CEB6 GUN

CeB_6 Cathode

The normalized rms thermal emittance of electrons emitted from a hot cathode is described by

$$\varepsilon_{n,rms} = \frac{r_c}{2}\sqrt{\frac{k_B T}{m_e c^2}},$$

where r_c is the cathode radius, k_B is Boltzman's constant, and T is the cathode temperature. From the above relation, in order to obtain the small emittance less than 1π mm.mrad required for the X-ray FEL, the diameter of the cathode must be in the range of a few mm at the temperature of 1000-1500°C. On the other hand, very high emission density (~50 A/cm^2) is required to produce a several ampere peak current from the small surface. Only the rare-earth hexaborides, such as LaB_6 or CeB_6 can emit such an intense current over long lifetimes. A single crystal is preferable for obtaining low emittance because of its extremely flat surface (roughness ≤1 μm) with low porosity after surface material evaporation [3]. The emission density is more uniform because the crystal orientation is the same over the whole surface. In recent years, single crystal CeB_6 cathodes are widely used for electron microscope and superior stability has been demonstrated [4]. We decided to use a single-crystal CeB_6 cathode with a [100] crystal face. The diameter of our CeB_6 cathode is 3 mm. 3 A peak current will be produced when heated to ~1400°C. The theoretical thermal emittance is 0.4π mm mrad.

Fig. 2 shows the CeB_6 crystal, the cathode assembly and the cathode being heated in the test chamber. The CeB_6 crystal is mounted in a graphite sleeve. This produces a uniform electric field over the entire cathode

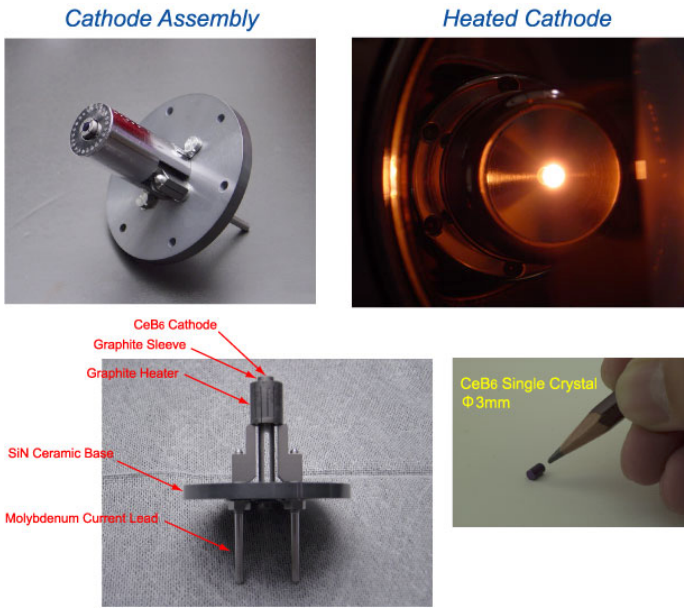

Fig. 2 : CeB_6 cathode assembly.

surface. This is quite important for elimination of any beam emission halo coming from the cathode edge, which could cause damage to the undulator magnets.

We use a graphite heater rather than the conventional metallic filament made of tungsten or the like. Graphite is mechanically and chemically stable even at very high temperatures and does not evaporate like other metals. Since its electrical resistance does not change much as a function of temperature, it is easy to control the heater power. The heater resistance is 0.18 Ω.

A tantalum cylinder covers the graphite heater to shield the thermal radiation from its surface. A base plate for the cathode assembly is made of silicon nitride, which is mechanically strong even when thermal stresses are applied.

The cathode was heated up to ~1400°C in the test chamber by applying 210 W of heater power (see the upper right side of Fig. 2). A reference temperature was measured from the graphite sleeve surrounding the cathode by means of a radiation monitor. We still need more study in order to determine the cathode temperature distribution precisely. Up to now, the cathode has been operated for 4000 hours without failure.

High-voltage Gun

Basically, the gun high-voltage tank follows the design conventional for a klystron tank. We use the same model C-band klystron modulator [5] to feed a -24 kV pulsed voltage to the gun high-voltage tank. The primary pulse is stepped-up to a -500 kV by a pulse transformer, with a turn's ratio of 1:21. In order to match the impedance of the gun to the modulator PFN output circuit, a 1.9 kΩ dummy load is connected in parallel with the cathode. Since we need to apply a -500 kV pulse voltage to the cathode, all the high-voltage components, namely, the ceramic insulator, pulse transformer, dummy load, etc., are immersed in insulating oil to eliminate discharge problems.

Fig. 3 shows the waveform of the gun voltage and beam current. The beam current was measured by a current transformer (CT) located in the beam line right after the gun. The beam energy is 500 keV, and the peak current is 1 A. The flat-top portion of the pulse is about 0.8 μsec, which is sufficient to generate a nsec bunch.

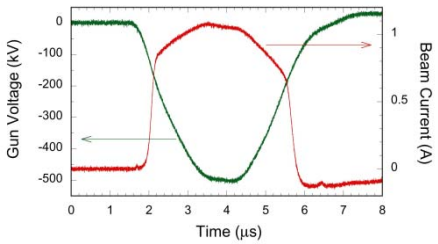

Fig. 3 : Waveform of the gun voltage and beam current.

The current-voltage characteristic of the CeB_6 gun has been measured for various cathode temperature (Fig. 4). The gun is operated in temperature limited region. In this region, the beam current is dominated by Schottky effect ($I \propto exp(\sqrt{V})$) rather than Child's law ($I \propto V^{3/2}$), that is, the slope of the current-voltage curve becomes gentle. Therefore, it is expected that the beam intensity jitter caused by the gun voltage jitter is suppressed.

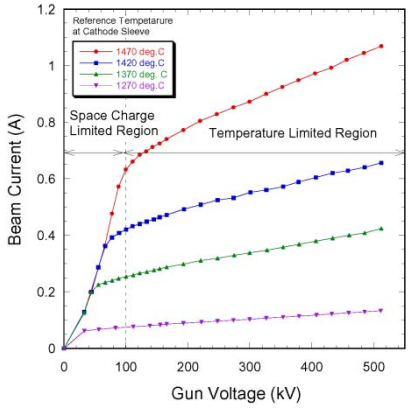

Fig. 4 : Current-voltage characteristic of the CeB_6 gun.

EMITTANCE MEASUREMENT

Double-slits Method

We measured the beam emittance by the so-called double-slits method (Fig. 5) [6]. The upstream slit cut out a sheet shaped beamlet from the round beam, which

spreads after passing through the drift space due to transverse thermal motion and space charge. The downstream slit measures the beamlet profile. By scanning the both slits throughout the whole beam area, the intensity profile in the phase space can be obtained.

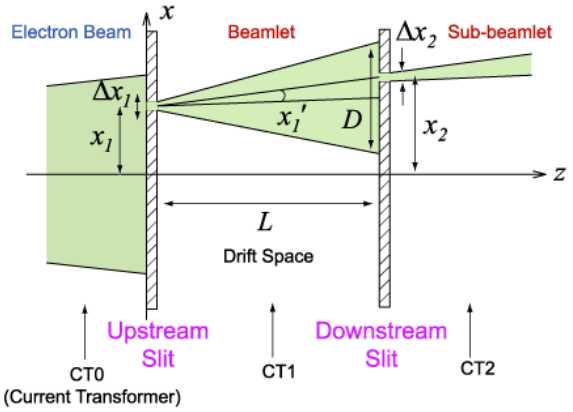

Fig. 5 : Principle of emittance measurement.

We prepared four slits, two for horizontal (x-direction) scan and two for vertical (y-direction) scan. The upstream x-slit are located at 50 cm downstream from the cathode, followed by a 60 cm drift space and the downstream slit. The opening width must be narrow enough to ignore the beamlet broadening due to space charge. Fig. 6 shows the beamlet intensity profiles for several upstream slit width (25, 50, 100, 200 μm). The original beam energy and current was 400 keV and 0.9 A, respectively. The downstream slit width was set to 25 μm. Accuracy of the width and position is better than 10 μm. The profile became Gaussian for the narrow width less than 100 μm, as expected from the thermal spread. The beamlet broadening due to space charge is ~15% of the thermal spread at 50 μm width in the experimental condition.

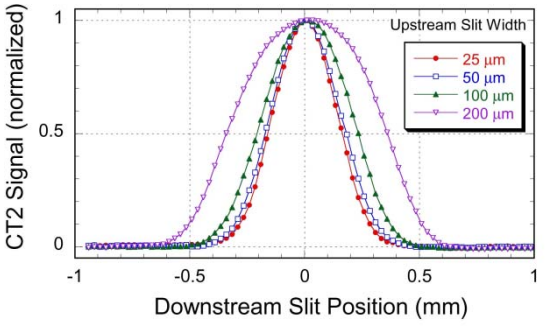

Fig. 6 : Beamlet profiles for different upstream slit width.

We found that the combination of a slit and a CT monitor with a digital scope is a very powerful tool to analyse the beam dynamics in time domain. The sub-beamlet current waveform provides the information about the time evolution of the phase space intensity at a certain point. From about 1500 waveforms stored by the slit scan, the time evolution of the phase space profile can be reconstructed. Fig. 7 shows an example of the animation screens of the phase space profile evolution.

Using a pair of vertical and horizontal slits, a time-resolved beam profile can be also measured by the same method.

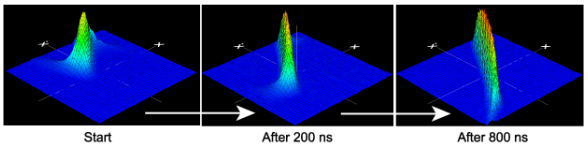

Fig. 7 : Time evolution of the phase space profile.

Experimental Result

We have measured the current density profile for the 500 keV beam with 1.0 A peak current. Fig. 8 shows the 3-dimensional plot of the current density profile. The width for both the x- and y-slits was set to 0.5 mm × 0.5 mm and the scan step was 0.5 mm. It shows fairly flat top shape as we expected from the cathode geometry.

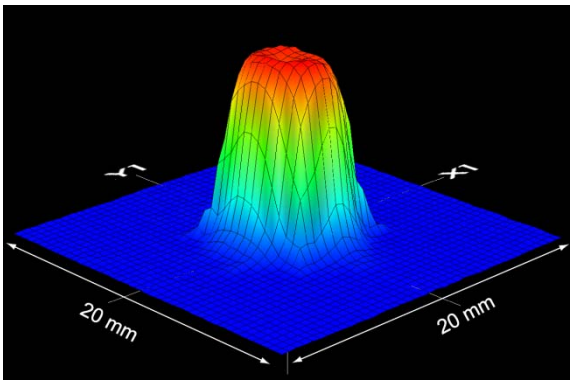

Fig. 8 : Current density profile of the 500 keV, 1.0 A beam.

Fig. 9 shows the 2-dimensional plot of the phase space profile (x-direction) measured for the same beam parameters. The width for both the upstream and downstream slits was set to 50 μm and the scan step was 0.25 mm for the upstream slit and 0.1 mm for the downstream slit. From the phase space profile, we analysed the normalized rms emittance, defined as

$$\varepsilon_{n,rms} = \beta\gamma\sqrt{< x^2 >< x'^2 > - < xx' >^2} ,$$

where $<x^2>$, $<x'^2>$ and $<xx'^2>$ denote mean square values weighted by current. The result was 1.1π mm mrad. The demonstrated beam parameters at gun exit are summarized in Table 2

The measurement of the rms emittance was very sensitive to the background noise. The noise signal of the CT monitor became a source of false emittance increase. The noise level (3σ) was ~1% of the peak intensity. To reduce the noise influence, we analysed the emittance using the signal, which was larger than that of the noise level, then corrected it to the expected value without noise. In order to overcome this ambiguity, we will improve the

noise reduction and study the method of emittance analysis.

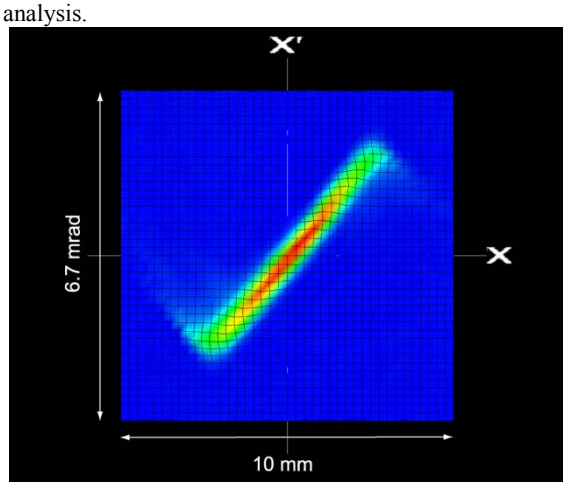

Fig. 9 : Phase space profile of the 500 keV, 1.0 A beam.

Table 2: Demonstrated beam parameters at gun exit.

Beam energy	500 keV
Peak current	1 A
Pulse width (FWHM)	3 μsec
Repetition rate	10 Hz
Normalized emittance (rms)	1.1π mm.mrad

IMPROVEMENTS FOR X-RAY FEL

Based on the experimental results, the following improvements will be done for the real injector system:

1) Beam current: we need to increase the beam current by a factor of 3 for operation. The current cathode emission may not be activated well as possible. The increase in cathode temperature to obtain a 3 A peak current is estimated to be ~120°C.

2) Pulse width: the high-voltage pulse width turned out to be two times longer than the design value. The fairly big stray capacitance of the dummy load resistors no doubt causes the pulse to be stretched out to this long duration. As a result, the heat load that must be removed from the high-voltage tank was higher than the design expectation. The large size of the high-voltage tank is also determined by the resistors. In order to shorten the pulse width and to make the tank more compact, we are now developing an electron tube dummy load, which will replace the load resistors.

3) Emittance: we successfully achieved a very small emittance, but even so, it was somewhat larger than the theoretical predicted value. A small tail at the profile edge is a source of the emittance increase. It may be generated in the following mechanism. The electrons around the beam edge diffuse to the outside of the beam by the transverse thermal motion. In this region, radial electric field generated by the space charge is not linear, that is, it decreases in inverse proportion to radius. Therefore, the diverging angles of the diffusing electrons become smaller than that of the electrons in the beam edge. As a result, the phase space profile becomes S-shape after travelling in the drift space. The concept of the mechanism is shown in Fig. 10.

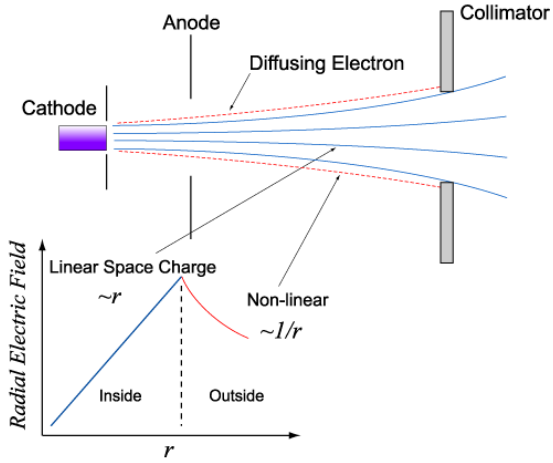

Fig. 10 : Mechanism of the emittance increase by thermal diffusion and space charge force.

The emittance without this tail can be roughly estimated by making the product of the rms diverging angle at the beam centre ($\sigma_{x'}$) and the rms beam radius ($\sim r/2$). The 0.6π mm.mrad value obtained is near the theoretical thermal emittance. Since the nonlinear tail comes from the edge region of the round beam, it could be removed by using a beam collimator. We expect that doing that we should realize the required small emittance of less than 1π mm.mrad.

REFERENCES

[1] T. Shintake et al., "SPring-8 Compact SASE Source, SPIE2001, San Diego, USA, June 2001

[2] K. Togawa et al., "CeB_6 Electron Gun for the Soft X-ray FEL Project at SPring-8", FEL2003, Tsukuba, Japan, Sept. 2003, Nucl. Instr. Meth. A 528 (2004) 312

[3] H. Kobayashi et al., Emittance Measurement for High-Brightness Electron Guns, 1992 Linear Accelerator Conference, Ottawa, Canada, August 1992

[4] http://www.feibeamtech.com/

[5] H. Matsumoto et al., "A Closed Compact Modulator for 50 MW C-band (5712 MHz) Klystron" 25th International Power Modulator Symposium and 2002 High Voltage Workshop, Hollywood, USA, 2002, ISBN 0-7803-7540-8

[6] K. Togawa et al., "Emittance Measurement on the CeB_6 Electron Gun for the SPring-8 Compact SASE Source FEL Project", APAC2004, Gyeongju, Korea, March 2004

AMPERE AVERAGE CURRENT PHOTOINJECTOR AND ENERGY RECOVERY LINAC*

I. Ben-Zvi#, A. Burrill, R. Calaga, P. Cameron, X. Chang, D. Gassner, H. Hahn, A. Hershcovitch, H.C. Hseuh, P. Johnson, D. Kayran, J. Kewisch, R. Lambiase, V. Litvinenko, G. McIntyre, A. Nicoletti, J. Rank, T. Roser, J. Scaduto, K. Smith, T. Srinivasan-Rao, K.-C. Wu, A. Zaltsman, Y. Zhao, BNL, Upton, NY, USA
H. Bluem, A. Burger, M. Cole, A. Favale, D. Holmes, J. Rathke, T. Schultheiss, A. Todd, Advanced Energy Systems, Medford, NY USA,
J. Delayen, W. Funk, L. Phillips, J. Preble, Thomas Jefferson National Accelerator Facility, Newport News, VA USA

Abstract

High-power Free-Electron Lasers were made possible by advances in superconducting linacs operated in energy-recovery mode. In order to get to very high power levels, say a fraction of a megawatt average power, many technological barriers are yet to be broken. We describe work on CW, high-current and high-brightness electron beams. This will include descriptions of a superconductinglaser-photocathode RF gun employing a new secondary-emission multiplying cathode and a superconducting accelerator cavity, both capable of producing of the order of one ampere average current, as well asand plans for an ERL based on these units.

INTRODUCTION

A frontier of very high power Free-Electron Lasers (FEL) is opening up. The Energy Recovery Linac (ERL) based FEL at Jefferson Laboratory [1,2] demonstrated the potential of ERL- based FELs to obtain kilowatts of average power, with a record of 10 kW recently achieved in the JLAB ERL upgrade, operating with an average current of the order of 10 mA and energy of the order of 100 MeV, or a beam power of the order of one megawatt. However, much higher FEL powers are possible with the right technology; hundreds of kilowatts should be possible. An ERL current of the order of one ampere is desirable with reasonably good emittance, of the order of a few microns normalized RMS. This level of high-brightness, high-power beam performance does not yet exist. The purpose of this paper is to describe work carried out at Brookhaven National Laboratory in collaboration with industry (Advanced Energy Systems, Inc.) and Jefferson Laboratory to push the frontier of high-brightness ERLs. There are three main elements in this effort:

1. Development of an electron source providing CW, ampere-class electron beams with low emittance.
2. Development of an ampere-class linac structure
3. Demonstration of an ampere-class ERL.

We define ampere-class current refers to currents of between a few hundred mA to one ampere micron-class emittance refers to normalized RMS emittances of one to a few microns.

While beam optics and dynamics also play an important role in the systems under discussion, this paper will not cover these subjects for reasons of compactness.

AMPERE-CLASS CURRENT, MICRON-CLASS EMITTANCE ELECTRON GUN

There are two aspects that must be considered in order to obtain ampere-class currents and micron-class emittance in CW gun operation. First is the attainable RF field needed for accelerating high-charge low–emittance electron bunches. Second is a cathode capable of generating high charge electron bunches at the right repetition rate. As we will se later, these aspects are closely related.

The RF gun

A simple argument can be made to narrow down the range of technological possibilities for ampere-class, micron-class electron sources. Since the accelerator is necessarily an RF linac at the frequency range of the order of one giga-Hertz, (say from 0.7 GHz to 1.5 GHz), and the electron bunches must occupy no more than a few degrees of RF phase, the bunch-length in the linac must be of the order of 10 picoseconds. A much longer bunch would lead to distortions of the longitudinal phase-space that would be difficult to correct even with cavity harmonics. The transverse emittance is also increased due to time dependent RF forces. A much shorter bunch would lead to increased wake fields and High-Order Mode (HOM) power, as well as other potential problems such as coherent synchrotron radiation (CSR). It is well known from the experience of developing and operating electron guns with space-charge related emittance growth, that high electric fields are essential for obtaining a good emittance at a reasonable bunch charge. High bunch charge of the order of one or more nano-Coulomb with short bunches of the order of a few pico-seconds to a few tens of pico-second have been demonstrated only with photocathode RF guns. At low duty factors it is possible to achieve accelerating fields of a few tens to slightly over 100 megavolts per meter. Using these accelerating gradients laser-photocathode RF guns achieved

*Work supported by the US Department of Energy and Office of Naval Research.
#ilan@bnl.gov

spectacular successes with sub-micron emittance at a bunch charge of about half a nano-Coulomb [3], and a few microns for bunch charges of one to a few nano-Coulomb. The problem is to combine high fields with CW operation. The best performance to-date of nearly CW RF gun (to be precise, 25% duty factor) has been demonstrated with the Boeing photoinjector [4]. Los Alamos and AES are developing a CW photoinjector [5]. It is clear that even with a large fraction of a megawatt spent on maintaining the field in a copper cavity, the field is limited to under 10 MV/m.

Since it is clear that the ERL will be based on Superconducting Radio Frequency (SRF) technology based on considerations of efficiency and sheer size, it is natural also to seek an SRF photoinjector. A SRF photoinjector will convert all the input RF power (which is to be on the order of one or two mega-Watts) into beam power and permit an accelerating field significantly larger than 10 MV/m. Why has this obvious solution been playing catch-up to other gun technologies? To understand this we have to look into the cathode issue.

The Collider-Accelerator Department at Brookhaven National Laboratory, in collaboration with Advanced Energy Systems and Jefferson Laboratory, is developing a superconducting gun that will accept a high-quantum efficiency photocathode. As a first step we are testing a 1.3 GHz superconducting photoinjector that is used for photocathode development. The initial development has been done by using the niobium as the photocathode. Following that we plan to install a high quantum-efficiency cathode package and test it in the gun. Following that, we are working on the development of a 703.75 MHz half-cell gun with a demountable cathode and couplers for megawatt power. The megawatt CW RF power system, shielding and cryogenics are being installed at BNL.

The performance requirements of this gun are:

1. A frequency of 703.75 MHz to match a RHIC revolution harmonic and the ERL cryomodule frequency (see below)
2. Achieve coupling of 1 MW into the half-cell (with possible upgrade to twice this power) using two opposed input couplers
3. Deliver a current of 0.5 ampere (example: 1.42 nC at 351.87 MHz), requiring a high quantum efficiency cathode insertion
4. Provide a high average accelerating field of about 20 MV/m.

Figure 1 shows the electric field lines of a half-cell gun cavity with a cathode insertion using a double choke-joint. This design allows the cathode itself to be at liquid nitrogen temperature while the gun cavity is at liquid helium temperature. The cathode stalk is slightly recessed to provide RF focusing for the emerging electrons. The beam port is large to allow High-Order Modes (HOM) to escape the cavity to be dumped by a ferrite beam-pipe HOM absorber. Not shown are the input coupling ports, which are a non-trivial part of the gun package, since the amount of CW power required to accelerate the beam is extremely high.

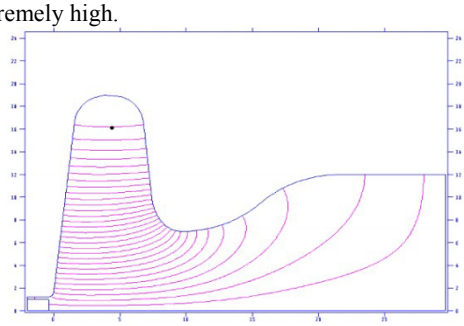

Figure 1. Superfish simulation of a half-cell gun cavity showing part of a choke-joint for the photocathode. The cathode surface is slightly recessed to provide focusing of the electrons.

The photocathode and laser

The photocathode is an enabling technology for the high-current accelerator system. The list of photocathodes that can produce ampere-class average current is short to begin with, and has much to do with laser technology. Without going into details, one must understand that mode-locked lasers operating in CW mode are limited to a few tens of watts in the near IR or visible range of the spectrum, and take a huge penalty (in terms of the number of photons per pulse) when converted to UV. Even a 30 watt average power visible laser is a complicated and expensive device, costing over $0.5M. The higher quantum efficiency photocathodes such as multi-alkaline and cesiated gallium arsenide are short lived unless provided with an ultra-high vacuum, and have volatile materials that are not compatible with superconducting RF technology, since even minute quantities of a material like cesium would lead to field emission and multipactoring in a superconducting cavity by lowering the work function of the niobium. An additional problem with gallium arsenide is non-prompt emission of the photoelectrons. There is a critical requirement for a photocathode that will have the following properties:

1. It should be compatible with a superconducting gun, the only gun that can provide the high accelerating fields to preserve emittance.
2. It should have high quantum efficiency to make the drive laser reasonably feasible.
3. It should have long life, to provide a usable MTBF (mean time between failures).
4. It should have prompt emission, to avoid blowup of longitudinal and transverse phase-space.
5. It would be advantageous to have a sealed cathode capsule that can be exposed to air yet not lose its other properties, to simplify servicing the photoinjector.
6. It would be also advantageous in some cases to have a low thermal emittance.

The last requirement, low thermal emittance, is important only for very low bunch charge, much lower than a nano-Coulomb, since at higher charge the

emittance is dominated by collective effects and non-linearities.

Single stage photocathodes simply do not possess these properties. A solution to this problem was recently proposed [6] and R&D on the system is in progress. The basic concept is shown in Figure 2. The idea is to use secondary emission to amplify by a large factor (between one and two orders of magnitude) the emission from a photocathode. A thin (of the order of 20 micrometers) diamond window is positioned between a photocathode (taken to be cesium potassium antimonite in the figure) and the gun (not shown, above the capsule). The primary electrons are generated in the photocathode by the laser (shown coming in on the left), accelerated in the gap between the photocathode and the diamond and strike the diamond with 5 to 10 KeV. The accelerating field is provided by the gun cavity field that penetrates the diamond window. The primary electrons produce a large shower of secondary electrons (up to 100 secondaries per primary, depending on the primary energy). The secondary electrons drift through the diamond, thermalizing to a small fraction of an electron volt in the process and exit the diamond to the gun. A critical element here is endowing the diamond side facing the gun with a negative electron affinity, by bonding hydrogen to the diamond's dangling bonds.

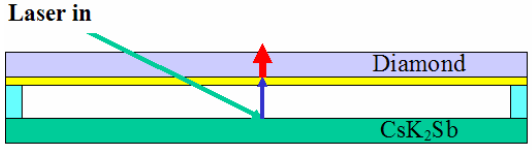

Figure 2. A schematic diagram of an encapsulated diamond amplified photocathode. The diamond is coated with a very thin gold layer on the primary injection side, the one facing the CsK_2Sb photocathode.

Starting with the quantum efficiency of cesium potassium antimonite, which is typically 5 to 10 percent for visible photons, the effective quantum efficiency of the amplified cathode is a few hundred percent. The diamond window protects the superconductor from the cathode materials and the cathode from poisoning by back-streaming contaminants. The emission is prompt and has very low thermal energy. The diamond properties are such that the heat generated by the various processes (mainly the primary energy deposition, RF heating of the gold and the heat generated by the transport of the secondaries through the diamond) is conducted efficiently to the walls with an insignificant temperature gradient. In addition, the mechanical strength of the diamond promises that the capsule may hold atmospheric pressure for transporting the evacuated photocathode.

AMPERE-CLASS ERL SUPERCONDUCTING CAVITY

ERLs need a specially designed cavity for best performance. Until now, cavities used in ERLs have been developed as a non-energy-recovering linac structures. To achieve ampere-class currents it is clear that a dedicated design must be done.

Higher order modes are one of the dominating factors influencing the design of high current cavities. These modes give rise to two limits on the performance and operation of a cavity:

• Multi-pass, multi-bunch instabilities driven by high impedance dipole modes resulting in beam-breakup.

• Power loss into the HOMs which must be removed safely from the cavity and the cryogenic system.

We designed a 5-cell linac cavity optimized for most efficient removal of HOM power. The cavity has been described in detail in various conferences [7,8]. The shape of the cavity is shown in Figure 3.

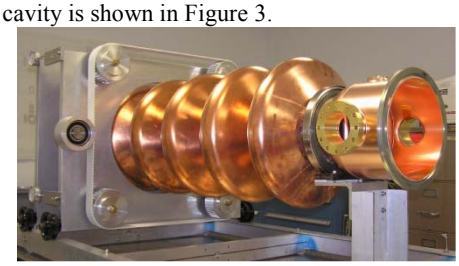

Figure 3. The 5-cell ERL cavity copper model in its tuner. Note the large iris and beam pipe diameters, designed for removal of HOM power to ferrite absorbers.

The main performance measures of the cavity are given in Table 1.

Table 1: Electric properties of the ERL 5-cell cavity

Property	**Units**	**Value**
Frequency	MHz	703.75
E_p/E_a	-	2.0
H_p/E_a	mT/(MV/m)	5.8
R/Q	Ω	807
Geometrical factor	Ω	225
Cell-to-cell coupling	%	3
Expected unloaded Q	-	$2x10^{10}$
Dynamic power loss	Watt	22
External Q	-	$2x10^{7}$
Max. amplifier power	kW	50
1st Mechanical resonance	Hz	96
Lorentz detuning	$Hz/(MV/m)^2$	1.5
Loss factor	V/pC	1.2

Ep/a is the peak surface electric field to accelerating field ratio; Hp/Ea is the peak surface magnetic field to accelerating field ratio; R/Q is the shunt impedance normalized to the Q. The number given for the expected

Q is assuming a total surface resistance of 10 nΩ. The dynamic power loss assumes this surface resistance and a field of 20 MV/m (or 20 MV acceleration, given that the length is 1 meter). Non-linear Q droop at this field may make this figure worse, however the Tesla experience shows that at this field the droop may be negligible.

The assembled cryomodule is shown in Figure 4.

The cavity has been extensively simulated using the MAFIA FEA code and the results were reported elsewhere [7,8]. The simulations show that the HOMs are very effectively damped, leading to loaded Q of the HOMs that range from 10^2 to a few times 10^3 in the worst case. No trapped modes were found. Using the calculated values of the Q and R/Q of the HOMs, we used the TDBBU code to estimate the beam breakup (BBU) threshold current for a 4 cavity ERL and found a BBU threshold of about 1.5 (+/-0.2) amperes based on a Gaussian distribution of 3 (+/- 2) MHz of the HOMs.

Using the ABCI code we find that the longitudinal loss factor of the cavity is 1.2 volts per pico-Coulomb (just the bare cavity, not including other beam line elements such as ferrites, valves etc.). This is an excellent value, about a factor of 6 or more lower than the TESLA cavity. We can conclude that we have designed a cavity that has a very high BBU threshold current and which generated significantly less HOM power than previous linac cavities, making it ideal for ampere-class ERL service.

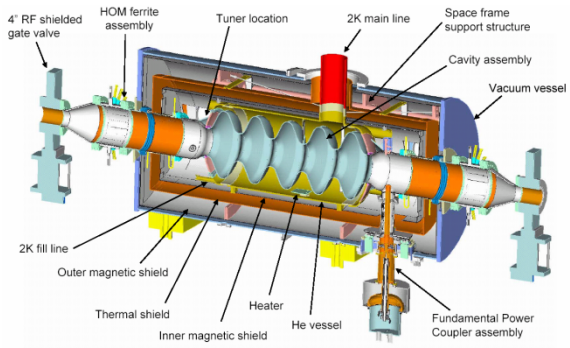

Figure 4. The cryomodule assembly configuration.

AMPERE-CLASS ERL

The only way to prove the performance of the photoinjector and linac cavity as a platform to produce high-brightness, ampere-class CW current is to use them in an energy recovery linac. For this purpose we are moving forward with the construction of such an accelerator. The superconducting gun described in section 2 will be combined with the accelerating structure described in section 3 to form an energy recovery linac. A schematic layout of this ERL is shown in Figure 5.

The return loop of the prototype ERL includes all necessary controls for studying the electron beam dynamics in ERLs: the arcs are achromatic with tunable longitudinal dispersion (R_{56}) and the lattice provides for full control of the phase advances and the optics in both x and y directions.

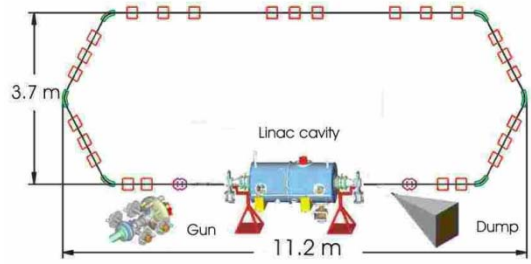

Figure 5. Schematic layout of the ERL-prototype based on 5-cell SRF linac. Details of the gun and dump beam optics and high-energy beam separation are left out.

The circumference of the entire ERL loop will be about 20 meters and will be determined after the final lattice design is frozen. It is important that the time of flight of electron from the exit of the SRF cavity till its entrance must be equal to an exact integer number and a half of RF cycles – this insures that after passing through the re-circulating loop the accelerated beam returns in the decelerating field with exactly same amplitude (but with opposite sign).

Each arc has an achromatic lattice, which comprises of three bending magnets and up to six quadrupoles (the number of quadrupoles is to be finalized later). This structure provides adjustable longitudinal dispersion (so-called R_{56}, where R is the transport matrix of the system) while remaining achromatic. A preliminary simulation shows that β and D functions can be kept under 5 and 0.6 m, respectively.

The straight section will have from six to twelve quadrupoles, which will provide for complete control of the elements of the one turn matrix, including the elements R_{12} and R_{34}, which will determine threshold of the transverse beam break-up instability.

REFERENCES

[1] G. R. Neil et al., Phys. Rev. Lett., 84 (4), 662 (2000)
[2] G. R. Neil, Proceeding of this conference.
[3] V. Yakimenko, et al., Nucl. Instr. and Meth. **A483**, 277 (2002)
[4] D. H. Dowell et al., Appl. Phys. Lett. 63 (15), 2035 (1993)
[5] H. P Bluem, et al., MOPLT156, Proc. EPAC'04, 5-9 July 2004, Lucerne, Switzerland.
[6] I. Ben-Zvi et al., Accelerator Physics Note C-A/AP/149, BNL April 2004.
[7] R. Calaga et al., Proc. 11th Workshop on RF Superconductivity, 8-12 September 2003 Lubek, Germany.
[8] R. Calaga et al., Proc. EPAC'04, 5-9 July 2004, Lucerne, Switzerland.

STATUS OF THE 3 ½ CELL ROSSENDORF SUPERCONDUCTING RF GUN

D. Janssen#, H. Büttig, P. Evtushenko, U. Lehnert, P. Michel, Ch. Schneider, J. Stephan, J. Teichert,
Forschungszentrum Rossendorf, Dresden, Germany
V. Volkov, S. Kruchkov, O. Myskin, BINP SB RAS, Novosibirsk, Russia

Abstract

The status of the Rossendorf superconducting RF gun is discussed. This gun allows continuous wave operation with an energy of 9.5 MeV and an average current of 1mA. The 3½ cell niobium cavity contains a normal conducting photocathode. A special choke flange filter at the cathode side prevent the RF leakage of the cavity. The design of the cavity, the tuner, the RF coupler the LHe-vessel together with the cryostat is finished and now in manufacturing. In the paper three features are discussed, which follows from the special demands of the 3½ cell superconducting RF gun. The first feature is the tuning system. For the cavity two different tuners are necessary, one for the half cell (gun cell) and one for the accelerating cells. The second feature is the tuning of the cathode. The beam properties depend very sensitive on the cathode position. Therefore a special cathode tuner has been developed, which allows to move and to adjust the cathode position inside the cavity. The third no conventional feature is the excitation of a second RF mode inside the cavity. This is a magnetic mode (TE mode) which replaces the static magnetic field in normal conducting RF guns and decreases the transverse emittance of the beam by more than a factor of two.

INTRODUCTION

The success of many evolving future accelerator applications is contingent upon the development of an appropriate source to generate the electrons.

Today photo cathode RF guns are the most advanced type of electron injectors. They are able to produce high peak currents and low emittances, which is necessary for FEL application. However their low duty factor can limit the performance of superconducting accelerators. Efforts are under way to increase the duty factor of RF guns for the price of cooling problems, high demands on klystron power and low power conversion efficiency. The more elegant way is to combine the high brightness of RF guns with the low RF losses of superconducting technology.

Superconducting RF (SRF) photo injectors offer great promise for cw mode operation with high average current. At present four groups are working on SRF photo injector projects. There are the Peking University [1], Advanced Energy Systems (AES) [2], Brookhaven National Laboratory (BNL) [3] and Forschungszentrum Rossendorf (FZR) [4]. In 2002, the successful operation of a SRF injector with a half cell cavity was demonstrated at FZR for the first time [4].

The design and treatment of superconducting cavities with there specific geometry, the much more complex tuning system and the RF choke flange filter causes additional difficulties and requires new technical solution.

#janssen@fz-rossendorf.de

These new technical solutions enter in the design of a new injector in Rossendorf, working with a 3 ½ cell superconducting cavity. The first overview about the design of this injector has been represented in [5]. In the sec. 2 and 3 we will discuss some new developments.

A disadvantage of the superconducting technology is its sensitivity to external magnetic fields. It is not possible to apply a static magnetic field of the required strength for emittance compensation as described in the case of normal conducting RF guns. In [6] it has been shown, that the focussing by the static field can be replaced by RF focussing, which is applicable also in the case of superconducting RF guns. The RF focusing is achieved by pulling the cathode backward, somewhat behind the back plane of the cavity. After extensive beam dynamic calculations for different bunch charges this concept is integrated into the gun design of the new 3 ½ cell Rossendorf injector.

A new idea to compensate the emittance growth in the RF gun is to apply a magnetic RF field, which is an eigenmode of the cavity. This mode can be excited together with the accelerating RF field in the superconducting cavity. First results concerning magnetic modes in superconducting cavities are published in [7]. The excitation of magnetic modes in the Rossendorf 3 ½ cell gun cavity and the influence of these modes on the beam dynamics is described in sec. 3 together with first experimental results.

DESIGN, FIELD AND BEAM PARAMETERS OF THE NEW ROSSENDORF GUN

The superconducting cavity inside the He vessel is shown in Fig. 1. A choke filter, which prevent the leakage of RF power is connected with the gun cell by a small superconducting tube. This tube contains the cathode, which is isolated by a vacuum gap of 1mm from the surrounding cavity. The cathode is cooled down to LN_2 temperature and exchangeable. The length of the gun cell is small in comparison to the following TESLA like cells. This has the advantage, that the optimal phase angle for the start of the electron bunch is near 90° where the electric RF field has its maximum. In contrast to the TESLA cavities the two HOM coupler the main coupler and the pic-up probe are arranged in a single plane outside the He vessel. Possible "cross over talking" of this arrangement has been discussed in [8]. A second pic-up allocated on the cathode side of the cavity allows the measurement of the field amplitude in the gun cell.

Fig.2 shows some details of the cryostat. It contains a magnetic and only one LN_2 shield to protect the cavity from the magnetic earth field and from heat transfer. The LHe and the LN_2 supply have a common port and the cavity support system contains special damping elements

against microphonics. The drivers for the tuning system are arranged outside of the cryostat.

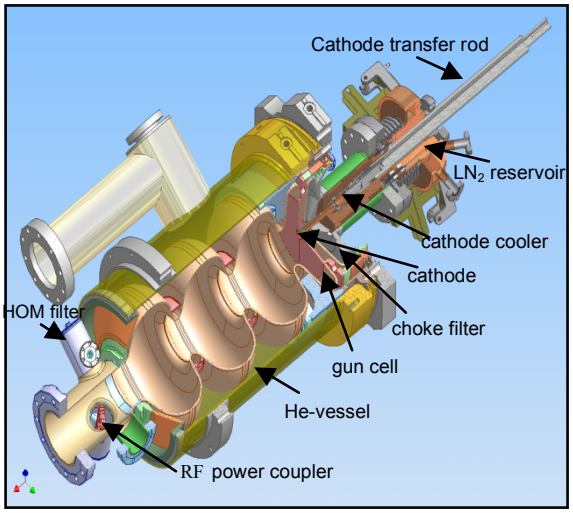

Figure 1: 3 ½ cell cavity of the Rossendorf superconducting RF gun

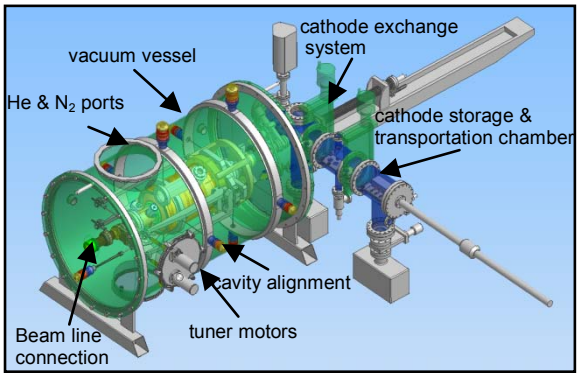

Figure 2: Cryostat of the Rossendorf superconducting RF gun

In the following we will discuss two features of the design, which are not standard. The first feature results from the circumstance, that the cavity of the RF gun contains two different type of cells, the gun cell and the TESLA cells with two different stiffness. Therefore it is not possible, to get the same frequency and approximately the same field amplitude in all cells of the cavity, using one tuner only. To avoid this difficult, our design of the gun contains two tuner and two pic-up probes for field measuring, one for the gun cell and one for the TESLA cells respectively. The tuners are able to change the thickness of the gun cell by ± 0.25 mm and that of the TESLA cells together by ± 0.3 mm, which corresponds to a frequency shift of ± 137 kHz for the gun cell ± 286 kHz for the TESLA cells. Furthermore we are able to adjust the choke flange cell at LHe temperature inside the cryostat.

In Fig.3 and Fig.4 the principle of the tuning system is shown, which is adapted from the cryostat of the Rossendorf ELBE project [10].

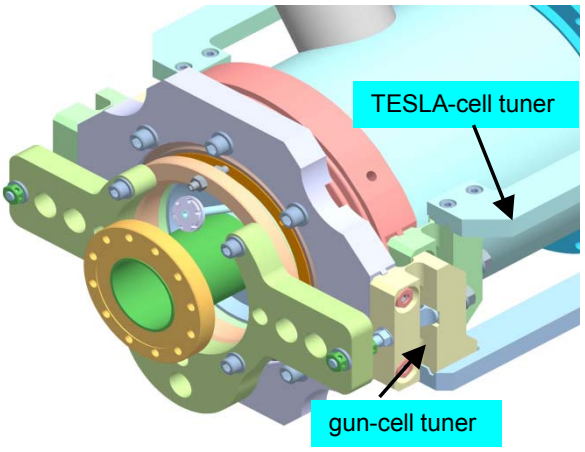

Figure 3: Tuner system of the cavity

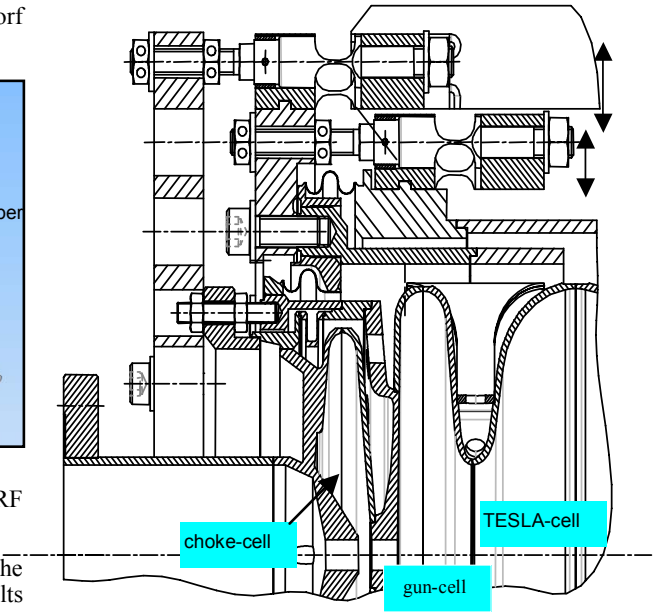

Figure 4: Sectional view of the tuning system

Now we will discuss the second feature, which is not standard.

For this gun the results of beam dynamic calculation are published in [5]. Accelerating a bunch with a charge of 1nC to an energy of 9.5 MeV, a transverse emittance of 2.5 mm mrad has been obtained. The axis RF field, used in this calculation is given in Fig.5. Immediately after the cathode the radial component of the electric field is negative and has a minimum. This behaviour results from the position of the cathode, which is located 2 mm behind the back wall of the gun cell. The negative value of the radial field focus the beam after the cathode, where the energy is small. This effect of "RF focusing" has been

described in [6]. The RF focusing replaces in the superconducting cavity the static magnetic field, which is used inside the cavity of normal conducting RF guns for beam focusing and emittance reduction.

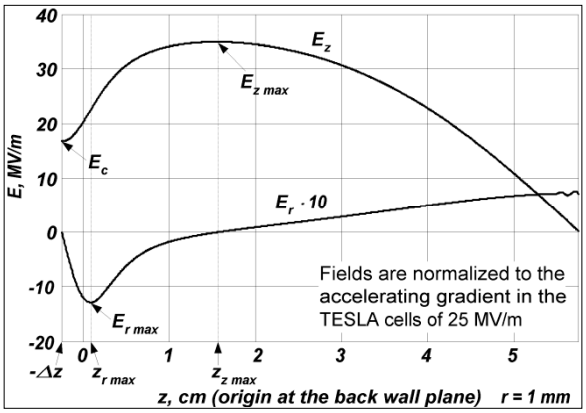

Figure 5: RF field near the axis of the gun cell

The focusing by the RF field and also the axial alignment of this field are very sensitive with respect to the cathode position. So the second special feature of our design work is a cathode tuner. This tuner allows to adjust the cathode with respect to the cavity axis and to move it ±1mm in axial direction. The scheme of this tuner is given in Fig. 6.

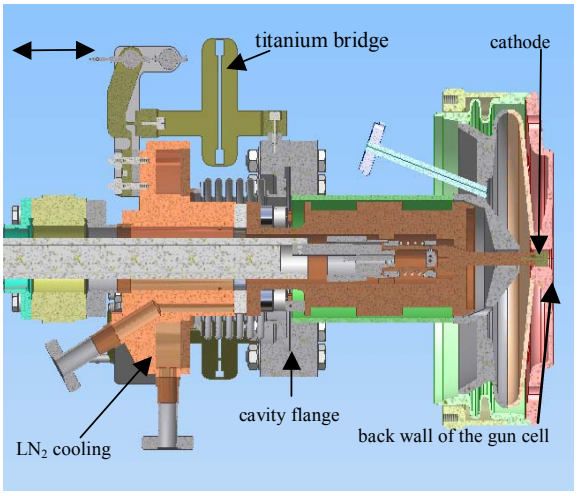

Figure 6: Cathode tuner of the Rossendorf superconducting RF gun

Three movable titanium bridges connect the flange of the cavity with the LN_2 cooling system. This cooling system has a ridged connection with the cathode and the steering of the bridges follows outside of the cryostat.

EMITTANCE COMPENSATION WITH A MAGNETIC MODE

In the proceeding section we discussed the compesation of transverse emittance of the superconducting gun by the RF focusing of the beam. Another possibility to prevent the growth of transverse emittance is to excite together with the accelerating TM mode a magnetic RF mode (TE mode) inside the superconducting cavity. This possibility has been extensively discussed in [7]. In the case of the Rossendorf gun cavity we use the TE_{021} mode. The corresponding RF field, which has been calculated by the code SUPERLANS is shown in Fig. 7. The field of the TE mode is concentrated in the last TESLA cell and can easy excited by a coupling loop in the beam pipe. At the cathode surface the magnetic field is equal to zero.

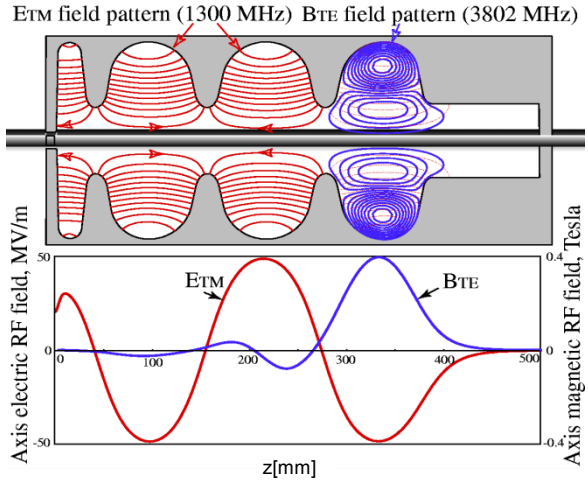

Figure 7: Field pattern and axis fields of the electric and magnetic mode inside the Rossendorf gun cavity

In superconducting cavities the quench limit for the surface magnetic field is 0.18 T [9]. Fig.8 shows the surface magnetic fields of the Rossendorf gun cavity.

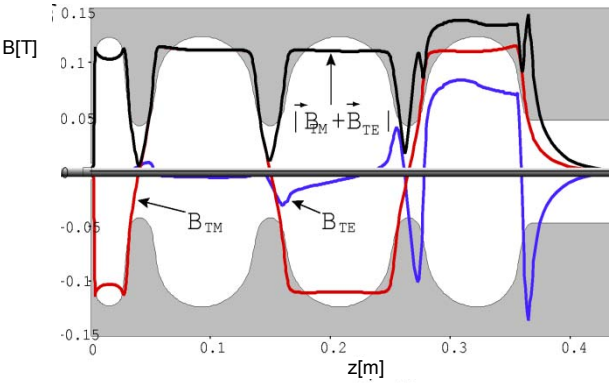

Figure 8: Surface magnetic field of the TE mode, the TM mode and the vector sum of both fields for the Rossendorf gun cavity

The peaks of the magnetic TE mode are disposed between the peaks of the accelerating TM mode. The resulting field, which is the vector sum of both modes has an maximum amplitude comparable with that of the separate modes.

Table 1: Parameter and results of the tracking calculation

Beam parameter		Field parameter		Laser parameter	
ε_x[mm mrad]	0.78 – 0.98	B_{TMsurf}[mT]	115	Puls length [ps]	20
σ_x [mm]	3.06	B_{TEsurf}[mT]	136	Raise time [ps]	1
ε_z[keV mm]	72.4	$\lvert B_{TM} + B_{TE} \rvert_{surf}$[mT]	144	Spot size [mm]	2.6
Δz [mm]	2.79	$E_{TM,axis}$ [MV/m]	50	Bunch charge[nC]	1
E_{av} [MeV]	8.82	φ_{TM}[grad]	75		
ΔE_{rms} [keV]	53.9	φ_{TE}[grad]	0 - 180		

After the calculation of the RF fields we did tracking calculation using the ASTRA code. The parameters and results of this calculation are given in Table 1. An electron bunch of 1 nC starts with a length of 20 ps at the cathode. At a distance of 4.44 m it has a length of 9.3 ps and its transverse emittance changes between 0.78 and 0.98 mm mrad in dependence on the phase of the TE mode. This dependence is explicitly shown in Fig.9.

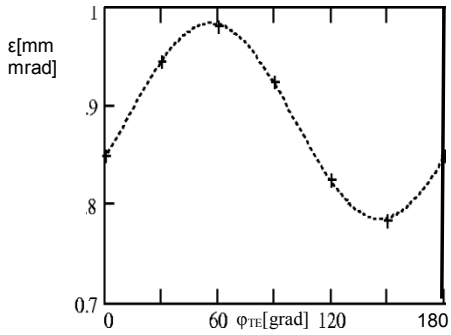

Figure 9: Dependence of the transverse emittance from the start phase with respect to the magnetic mode.

The results of this calculation are the following:

- By exciting an magnetic mode in the last cell of the gun cavity the transverse emittance decreases by more than a factor of two.
- The frequency of the magnetic mode is not necessary a harmonic of 1.3GHz. The transverse emittance depends only weak on the phase of the magnetic mode.
- The sum of the surface magnetic fields of the TM mode and the TE mode is clearly below the quench limit.

The last statement is confirmed by Fig.10. Here the first measurement of the peak magnetic surface field for a TE and a TM mode in a single cell cavity is represented

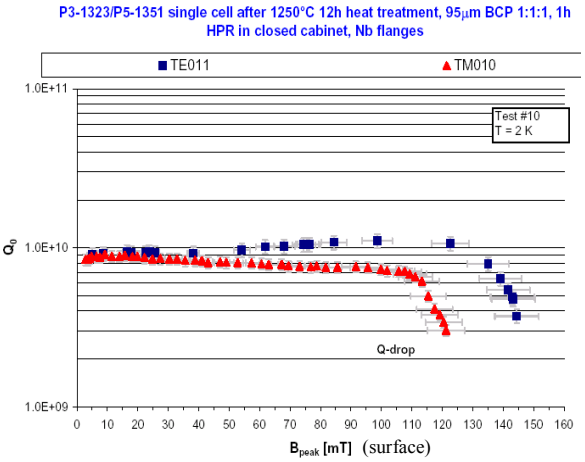

Figure 10: Quench limit and Q values for the TM and the TE mode in a single cell cavity.

SUMMARY

- The cathode and the cavity tuner are new elements in the design of superconducting RF guns.
- The magnetic RF mode replaces the static magnetic field and decreases the emittance by a factor of more than two.
- The new Rossendorf superconducting RF gun is in manufacturing, first components are finished.

REFERENCES

[1] K. Zhao, et al., NIM A475 (2001) 564.
[2] H.Bluem, et al, EPAC'04, Lucern, Swiss, July 5-9, 2004
[3] T. Srinivasan-Rao, et al., PAC'03, Portland, USA, May 12-16, 2003.
[4] D. Janssen, et al., NIM A507 (2002) 314
[5] D. Janssen, et al., FEL'03, Tsukuba, Japan, Sept. 8-12, 2003, NIM A(2004) in print.
[6] D. Janssen, V. Volkov, NIM A452 (2000) 34-43.
[7] D. Janssen, V. Volkov, EPAC'04, Luzern, Swiss, July 5-9,2004
K. Flöttman, D. Janssen, V. Volkov, Phys. Rev. ST accepted
[8] Yongxiang Zhao, Michael Cole, PAC'03, Portland, USA, May12-16, 2003
[9] K. Saito, Proc. of the PAC'03, p.462, Portland, Oregon, USA, May12-16, 2003
[10]F. Gabriel, et al., NIM B 161-163 (2000) 1143.
[11]G.Ciovati, P.Kneisel, privat communication

LONGITUDINAL SPACE CHARGE EFFECTS IN THE JLAB IR FEL SRF LINAC

C. Hernandez-Garcia*, K. Beard, C. Behre, S. Benson, G. Biallas, J. Boyce, D. Douglas, H. F. Dylla, R. Evans, A. Grippo, J. Gubeli, D. Hardy, K. Jordan, L. Merminga, G. Neil, J. Preble, M. Shinn, T. Siggins, R. Walker, G. P. Williams, B. Yunn, S. Zhang, TJNAF, Newport News, VA 23606, USA

Abstract

Observations of energy spread asymmetry when operating the Linac on either side of crest and longitudinal emittance growth have been confirmed by extending PARMELA simulations from the injector to the end of the first SRF Linac module. The asymmetry can be explained by the interaction of the accelerating electric field with that from longitudinal space charge effects within the electron bunch. This can be a major limitation to performance in FEL accelerators.

INTRODUCTION

During the commissioning of the Jefferson Lab 10 kW Upgrade IR FEL several intriguing questions regarding the performance of the injector and the longitudinal phase space management were encountered. The full-energy momentum spread of the beam showed an asymmetry as a function of linac gang phase. Furthermore, the compressed bunch length at the wiggler and therefore the longitudinal emittance showed a clear dependence on transverse match into and through the linac and was as much as a factor of 4 larger than the emittance predicted at the end of the injector. Operational and performance issues in the linac such as cavities being out of phase and/or wake fields were ruled out as the source of the problem after careful investigation. Then, PARMELA modeling was extended from injection to the end of the first cryo-module to study the longitudinal beam dynamics as a function of linac gang phase [1].

The machine design for the Jefferson Lab 10 kW Upgrade IR FEL has been described in detail elsewhere [2]. It consists of a 10 MeV injector, a linac comprised of three Jefferson Lab cryo-modules, and a recirculation lattice. The machine layout is shown in Figure 1.

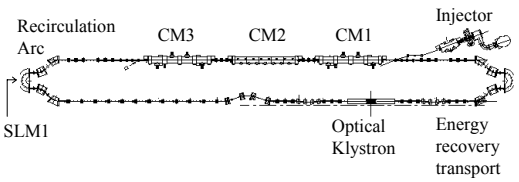

Figure 1: Jefferson Lab 10 kW Upgrade IR FEL. CM1, CM2, and CM3 are CEBAF-type cryo-modules. SLM1 is a synchrotron light monitor.

* Corresponding author: Tel: 1-757-269-6862; fax:1-757-269-5519; E-mail address: chgarcia@jlab.org

The injector consists of a high-voltage-DC GaAs photocathode gun driven by a frequency-doubled Nd:YLF laser, a 10 MeV quarter cryo-unit with two 5-cell CEBAF cavities, a transverse match section and a bunch compressor [3]. The photocathode gun delivers 135 pC, 23 ps rms-long electron bunches operating at 350 kV in pulse (demonstrated up to 8 mA) and CW (demonstrated up to 9.1 mA) modes [4]. The photocathode gun performance has been studied earlier [5]. After initial acceleration at 10 MeV, the electron beam is transversely matched to the linac by means of a quadrupole telescope, longitudinal match is provided by an achromatic compressor chicane [6].

The linac further accelerates the electron beam at energies between 80 and 200 MeV. The first (CM1, see Figure 1) and third (CM3) cryo-modules are conventional 5-cell CEBAF cavities, while the middle module (CM2) is based on a new 7-cell JLab design [7]. The beam is accelerated off-crest to impose a phase correlation on the longitudinal phase space.

The first part of the recirculator transports the beam after acceleration to the FEL. A six quad telescope transversely matches the high-energy beam to a 180°-recirculator arc, which is based on a Bates geometry [8]. At the middle of the arc, a synchrotron light monitor (SLM1, see Figure 1) is employed to measure the energy spread after acceleration. The beta function is always very small at this location so the spot size is dominated by the energy spread. After interaction with the FEL, the beam is re-circulated for energy recovery by a second Bates-style arc.

MEASUREMENTS AND MODELING

With only the first and third cryo-modules installed in the machine at the time (CM1 and CM3), an asymmetry in the beam momentum spread as a function of linac gang phase was observed during the FEL commissioning activities. The injector had been setup accordingly to PARMELA to produce an upright longitudinal phase space distribution at the entrance of the linac [4], as shown in Figure 2.

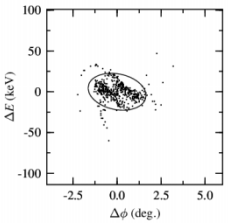

Figure 2: PARMELA longitudinal distribution at the entrance of the first cryo-module. The predicted full energy spread is 44.3 keV, the full bunch length is 6 ps (or 11.1°), and the longitudinal emittance is 16.8 ps-keV

If the distribution is upright at injection, then the beam momentum spread after acceleration (measured at SLM1 in Figure 1) should be symmetric around crest. This was not the case. With the injector se up to produce the phase space in figure 2, the beam full momentum spread when accelerating 15° ahead of crest (nominal operating conditions for a longitudinal match to the wiggler) was 1%, and 1.5% when accelerating 15° behind crest, was 1.5%. The full-energy momentum spread is established from a spot size measurement at a point of high dispersion by

$$\frac{\Delta E_W}{E_W} = \frac{\Delta x}{\eta_x}, \qquad (1)$$

where ΔE_W is the beam full-energy spread, E_W is the beam energy at the high dispersion point (SLM1 at the middle of the first recirculator arc, see Figure 1), Δx is the spot size and η_x is the dispersion function of the arc dipole (70 cm). The calibration was performed by measuring the displacement of the centroid of the spot in the SLM1 video screen when the beam energy was changed by 1%. Figure 3a shows a snapshot of the synchrotron light at SLM1. The spot size is measured by means of a frame grabber software that gives the spot size profile in pixels for both x and y-axis [9]. Figure 3b shows the frame grabber output generated from the spot shown in Figure 3a.

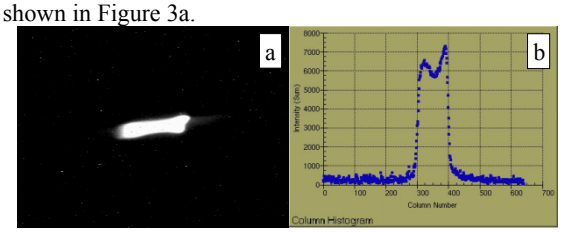

Figure 3: (a) Snapshot of the synchrotron light monitor in the middle of the first recirculation arc. (b) Output generated by the frame grabber to measure the spot size of the synchrotron light shown in (a).

Assuming that the asymmetry in the energy spread is a linear effect (this assumption was later confirmed by PARMELA simulations), the injected bunch full length (in ps) can be established by back-propagating the average of energy spreads at either side of crest via the following

$$\Delta t = \frac{\Delta E_W}{E_W} \frac{\left(1 + E_I / E_L\right)}{\omega \tan\phi}, \qquad (2)$$

where $\Delta E_W / E_W$ is the full energy spread at the wiggler, E_I is the injector energy, E_L is the energy gain in the linac, ω is the accelerator frequency, and ϕ is off-crest phase. With the downstream cavity in the injector operating at 20° off crest and the linac at 15° off crest, the measured average of the energy spread is 0.0125. For E_W = 80 MeV, and E_{inj} =9.2 MeV, equation 2 yields Δt = 5.6 ps. This result agrees quite well with PARMELA (see Figure 2).

The performance of the injector regarding longitudinal phase space management was questioned after eliminating operational and performance issues in the linac as a source of the problem (i.e. one or more cavities being out of phase, wake fields, etc.). PARMELA modeling was then extended from the injector to the end of the first cryo-module. The electron beam energy at injection is 9.2 MeV, therefore no transverse space charge effects are expected from PARMELA through the cryo-module.

However, PARMELA indicates that longitudinal space charge will induce what appears to be a phase-dependent asymmetry in the beam momentum spread during and after acceleration. When accelerating 15° ahead of crest the model predicts an increase in the rms energy spread from 45.3 keV at the entrance of the first cryo-module to 520 keV at the exit. For acceleration behind crest the predicted full energy spread is 659 keV at the exit of the cryo-module. These results are shown in figure 4.

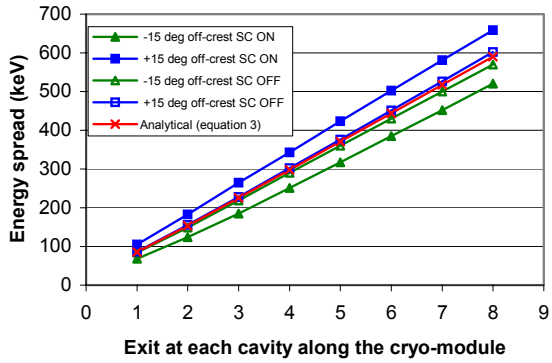

Figure 4: PARMELA calculations at either side of crest show the growth in the imposed correlated energy spread (Space Charge ON). The correlated energy spread (SC OFF) grows as well and is in close agreement with equation 3 (which has been multiplied by 4).

The predicted asymmetry is on the order of 27% after the first cryo-module alone (which is as far as the

simulation has progressed so far). This result is quite consistent with observed momentum spread asymmetry (50%) at the end of the two cryo-modules (exit of CM3, see Figure 1).

The imposed energy spread (by the RF system during acceleration, without space charge) should be symmetric around crest after acceleration, as expressed by

$$\sigma_E = \sqrt{\sigma_{Einj}^2 + \left(V_{linac}\sin(\phi)\sigma_t\right)^2}\ , \qquad (3)$$

where σ_{Einj} is the injected rms energy spread, V_{linac} is the total accelerating voltage in the linac to that point, ϕ is the off-crest phase, and σ_t is the injected rms bunch length in radians. PARMELA is in good agreement with the Equation 3 when the simulation is carried out with the space charge option turned off, as shown in Figure 4.

ANALYSIS

The longitudinal space charge force within the electron bunch accelerates the head and decelerates the tail, creating a tilt in the longitudinal phase space: the head goes to higher energy, and the tail to lower as the beam travels down the linac. This is the correlated energy spread of the beam due to space charge. When accelerating *ahead* of crest (nominal operating conditions for longitudinal phase space management), the head of the bunch is driven to lower, and the tail to higher energy by the RF field. This imposed phase/energy correlation adds to the correlated energy spread, and the observed momentum spread is *reduced*. On the other hand, acceleration *behind* crest drives the head of the bunch to higher energy, and the tail to lower. The imposed phase/energy then adds to the correlated energy spread and the final energy spread is *increased*. Figure 5 illustrates this mechanism.

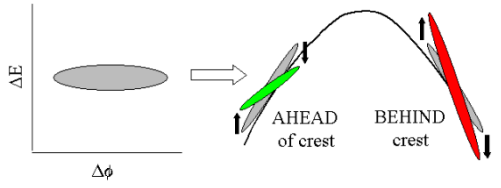

Figure 5: In acceleration ahead of crest, the final momentum spread is reduced. In acceleration behind crest, the final momentum spread is increased.

PARMELA also shows that the longitudinal emittance grows by 57% at the end of the first cryo-module alone. Since the length of the cryo-module is 1/6 of the distance to the wiggler, the longitudinal emittance at the wiggler is around 3 times larger that the longitudinal emittance at injection.

If the injected bunch length is increased, the longitudinal space charge forces are reduced, the energy spread asymmetry alleviated and the longitudinal emittance growth less severe. For a fixed bunch charge, the imposed correlated energy spread depends on the inverse square of the bunch length [10], while the imposed energy spread from the RF system depends linearly on the bunch length (see Equation 3). The optimum bunch length to minimize the correlated energy spread while maintaining the imposed energy spread acceptable for the FEL is about 1.5 times the bunch length with the original injector configuration (1.5 ps rms) [10].

PARMELA predicts that the injected rms bunch length increases from 1.5 ps to 2.37 ps if the downstream cavity in the injector is operated closer to crest (10°, instead of the design value at 20° ahead of crest). The predicted full energy spread at injection decreases from 44.3 keV to 40.5 keV, but the longitudinal emittance increases from 16.8 ps-keV to 19.6 ps-keV. Also, the longitudinal phase space distribution is no longer upright at the entrance to the linac.

The phase/energy slew imposed to the longitudinal distribution by the RF system and space charge effects can be cancelled out with proper longitudinal phase space management elements in the transport system, but the compressed bunch length at the wiggler is limited by the intrinsic longitudinal emittance of the beam due to thermal effects during its creation. The intrinsic longitudinal emittance growth along the cryo-module can be calculated by removing from the bunch particle distribution the quadratic term and the phase/energy slew imposed by the RF. The bunch particle distribution is written by PARMELA at specified intervals along the cryo-module to a separate log file. In another program, each bunch is read back in from the log file, has its longitudinal momentum vs. position fit to a in 2nd order polynomial, then that dependence removed from the distribution and the energy spread recalculated based on the corrected distribution.

Figure 5 shows that the intrinsic energy spread through the cryo-module grows by 76% with for a 1.5 ps rms injected bunch, while for a 2.5 ps rms bunch the intrinsic energy spread increases by 64% at the exit of the cryo-module.

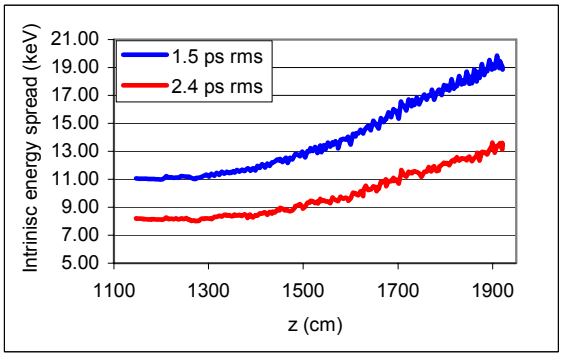

Figure 5: PARMELA-based calculations of the intrinsic energy spread growth along the first cryo-module operating at 15° ahead of crest for two different injected bunch lengths.

The calculations confirm that with a longer injected bunch the longitudinal space charge forces are less severe and the intrinsic energy spread is not only smaller, but it grows slower. Figure 5 also shows that the longitudinal emittance is slightly larger for the longer injected bunch, but grows slower.

When this was implemented, it was quickly confirmed that the asymmetry in the energy spread after acceleration was reduced from 50% to less than 20%. PARMELA shows a reduction in the energy spread asymmetry from 30% to 17%. In fact, with the longitudinal space charge effects less severe with longer bunch at injection, the compressed bunch length at the wiggler was reduced from about 0.8 ps FWHM (injector at 20°, linac at 15° off crest) to less than 0.5 ps FWHM. Laser gain with this configuration was about as strong as the previous configuration but peak efficiency in the detuning curve was much higher (1.25%) efficiency.

The FEL lased better with a non-design buncher gradient, about 10% higher than the one that produces the smallest energy spread at injection. PARMELA shows that the injected bunch is around 20% longer (which is good for alleviating longitudinal space charge forces), but the energy spread is about 30% larger. The optimal injector configuration for the FEL seems to be a compromise between the bunch length and energy spread at injection.

CONCLUSIONS

Extending the injector PARMELA model through the first cryo-module confirmed observations of an asymmetry in the final energy spread of the electron beam after acceleration and a significant growth in the longitudinal emittance. The asymmetry can be explained by the interaction between the electric field within the electron bunch created by space charge forces, and the electric field from the RF system during acceleration. Injecting a long bunch alleviates the longitudinal space charge force. PARMELA modeling provided guidance towards achieving a longer bunch at injection, simply operate the downstream cavity of the injector closer to crest. Once this was implemented in the machine, the asymmetry in the final beam energy spread was reduced, the longitudinal match throughout the accelerator became very close to lattice design, and the growth in the longitudinal emittance was decreased.

The interaction of the longitudinal space force with the RF system will be an important factor to consider in the design of high charge accelerators for FELs. Since the FEL gain depends on peak charge, it is desirable to have a short bunch with high charge at the wiggler. The present study reveals that bunch length at the wiggler is limited by the intrinsic longitudinal emittance of the beam generated during its creation, since the imposed phase/energy correlation in the energy spread by the RF system is removed by proper longitudinal phase space management, and the correlated (space charge) energy spread can be reduced by means of a long injected bunch.

ACKNOWLEDGMENTS

This work supported by The Office of Naval Research, the Joint Technology Office, NAVSEA PMS-405, the Air Force Research Laboratory, U.S. Army Night Vision Lab, the Commonwealth of Virginia, and by DOE Contract DE- AC05-84ER40150.

REFERENCES

1 Parmela_fel0.2: FEL Injector Simulation, JLAB-TN-03-028, K. B. Beard, B. Yunn, C. Hernandez-Garcia
2 D. Douglas et al., “Driver accelerator design for the 10 kW Upgrade for the Jefferson Lab IR FEL”, LINAC2001, pp. 867-9, Monterey, CA 2001.
3 D. Engwall, et al., PAC’97, pp. 2693-5, Vancouver, May 1997.
4 C. Hernandez-Garcia, these proceedings.
5 T. Siggins et al., “Performance of a GaAs DC photocathode gun for the Jefferson Lab FEL”, *Nucl. Inst. Meth*. A 475 (2001) 549-553.
6 B. C. Yunn, “Physics of the JLab FEL injector”, PAC’99, pp. 2453-5, New York, April 1999.
7 J. R. Delayen et al., PAC’99, pp. 934-6, New York, 29 March-2 August 1999.
8 J. Flanz et al., *Nucl. Inst. Meth*. A421:325 –33 (1985).
9 WesCam©, developed by W. Moore, JLab FEL.
10 D. Douglas, private communication.

LCLS UNDULATOR DESIGN DEVELOPMENT

Isaac Vasserman, Roger Dejus, Patric Den Hartog, Elizabeth Moog, Shigemi Sasaki,
Emil Trakhtenberg, Marion White, ANL/APS, Argonne, Illinois 60439, USA

Abstract

The undulator segments of the 130.4-m-long undulator line for the Linac Coherent Light Source project (LCLS) [1] must have a deflection parameter K_{eff} that matches the nominal value for that segment to within $\Delta K_{eff}/K_{eff} < 1.5 \times 10^{-4}$. Mechanical shims were used to set the undulator gap to control K in the prototype, but this is too tedious a procedure to be used for all 33 undulator segments. Although the prototype undulator [2-4] met all of the LCLS specifications, development continued in order to simplify the system. Various other alternatives for adjusting the field were considered. A canted-pole geometry was chosen, allowing the *K* value to be changed by lateral translation of the entire undulator segment. This scheme also facilitates tapering the undulator line to accommodate electron beam energy loss. The prototype undulator was subsequently modified to test the canted-pole concept. Magnetic measurements demonstrated that the undulator with canted poles meets all LCLS specifications, and is more cost effective to implement.

INTRODUCTION

The LCLS prototype undulator cross section is shown in Fig. 1. Wedged spacers are located between the titanium core and the aluminum bases. Translation of a canted undulator segment in the transverse horizontal direction *(X)* allows the desired K_{eff} to be achieved with the required accuracy during initial tuning.

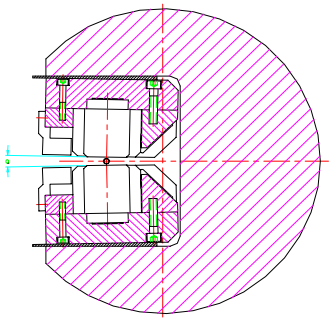

Figure 1: LCLS prototype cross section for the modified design with canted pole-gap.

Remote control of the device's *X* position can serve to keep the field stable despite temperature changes. It can also be used to tune the phase between devices when particle energy loss has disrupted the phasing. The range of *X* motion could be as large as ±5 mm to compensate for the beam energy loss at saturation. It is important to keep the performance (phase errors, trajectory straightness, etc.) of the undulator segments within the required tolerances [1] in this wide transverse position range. To confirm that this can be done, the LCLS prototype undulator was modified to introduce a 3-mrad cant. Measurements of the rms phase errors, K_{eff} and the *X*-dependence of the field integrals are described below. Alignment of the magnetic elements is critical for this project. The option of using magnetic needles to locate the magnetic center of the undulator segment is discussed. Additional design changes that were implemented recently are described elsewhere [5].

MAGNETIC MEASUREMENT OF THE PROTOTYPE UNDULATOR

Phase Errors

The LCLS undulator will use the first harmonic of the radiation so its output is not very sensitive to phase errors between the particle beam and radiation [6-8]. The allowable upper limit of rms phase errors is 6.5º. The *X* dependence of the rms phase error was measured in the range of ±3 mm and was found to be negligible.

Effective Field

Figure 2 shows the X dependence of the effective field (B_{eff}) and the effective deflection parameter (K_{eff}). This dependence is linear in *X*, and close to the 1.9 G/μm previously measured for the gap dependence. The difference can be attributed to the initial wedging in the pole gap created by pole sorting to allow for easy gap measurement [3].

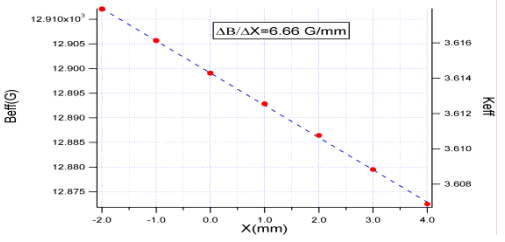

Figure 2: B_{eff} and K_{eff} dependence on *X*. $\Delta X = 0.3$ mm corresponds to the alignment accuracy needed for the tolerance $\Delta B_{eff}/B_{eff} = 1.5 \times 10^{-4} \sim 2$ Gauss.

The 3-mrad cant is small so that the alignment accuracy required in the *X* direction, 0.3 mm, is not difficult to achieve. With this cant angle, the change in field strength

due to a temperature change of 1°C can be compensated by a lateral shift of the undulator segment by 1.2 mm, which can be done remotely.

Horizontal and Vertical Trajectories

The horizontal trajectories for different *X* positions in the range of ±3 mm are shown in Fig. 3.

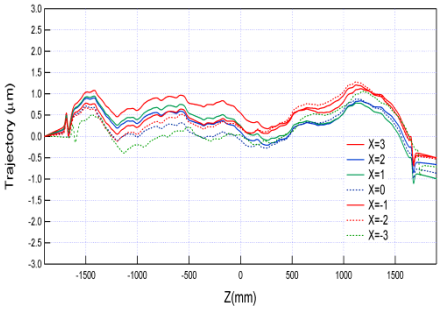

Figure 3: Horizontal trajectories at different *X* positions for a beam energy of 14.1 GeV.

The trajectories are well behaved and well within the tolerance requirement of 2 μm maximum walk-off from a straight line for a particle energy of E=14.1 GeV. The change in the vertical field integrals can be calculated from Maxwell's equation $\partial B_y/\partial x=\partial B_x/\partial y$, using the horizontal trajectory measurements. Final tuning of the undulator segments may require tuning of the vertical trajectories as well.

Magnetic Field Fine Tuning

The method for adjusting K_{eff} is: a) Select among spacers with thickness step ~ 15 μm to set the effective field within ±30 G (1 μm in gap corresponds to ~ 2 Gauss in field); b) Set the horizontal position of the spacers to adjust the effective field to ~ ±6 Gauss (for a 3-mrad cant, 6 G corresponds to a 1-mm shift in horizontal position); c) Set the horizontal position of the undulator segment as a whole so that the effective field is in the range of ±2 G ($\Delta B_{eff}/B_{eff}$ ~ $\pm 1.5 \times 10^{-4}$). The last step saves shimming time and provides better accuracy.

PHASE TUNING

The phase slippage along the undulator can be calculated using [9]:

$$\varphi(z)=\frac{k}{2\gamma^2}\left[z+\int_0^z I_{1x}^2(z')\,dz'+\int_0^z I_{1y}^2(z')\,dz'\right],$$ where

k is the fundamental harmonic wave-vector of the radiation, γ is the relativistic factor, and I_{1x} and I_{1y} are the normalized particle angles in the vertical and horizontal directions, respectively. In free space, with zero field and zero angle we have:

$$\varphi(z)=\frac{k}{2\gamma^2}z, \quad L_{free}=n\lambda_u(1+K_{eff}{}^2/2),$$ where

L_{free} is the required distance in free space for n periods of phase slippage. An initial magnetic tuning will be required for each undulator segment to match its phasing to the standard mechanical break length. Full-width magnet shims (phase shims) will be applied to correct the field, if needed. Such shims were successfully used in the APS FEL project. The result of the phase shim test is shown in Fig. 4. The physical break length will be chosen to match what is typical for an undulator with six phase shims. This will allow adjustment in either direction. Other ways of tuning break length, such as K_{eff} tuning and trajectory shims, will be used if necessary.

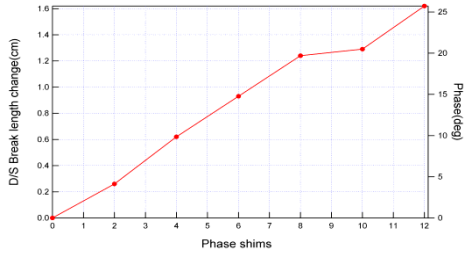

Figure 4: Break length and phase change from 0.2-mm-thick phase shims applied at one end of the undulator. The first two shims were applied to magnet #7, one each on the top and bottom jaws, the next two to magnet #6, etc.

Particle energy loss results in a change of phase in and between the undulator segments that must be corrected. The estimated energy loss in the first 100 m of undulator is 0.26%; 0.4% is estimated for the last 30 m with saturation [1]. The resulting phase slippage in the undulator segment can be corrected by remotely changing the K_{eff} of the undulator segment. The phase change in the drift space must also be corrected. The previous prototype undulator design had active end-gap corrections to correct the phasing, but modifying K_{eff} instead is simpler. Tests were conducted to demonstrate the feasibility.

Polar plots based on the complex radiation amplitude are powerful tools in understanding phasing issues. The complex radiation amplitude A is defined as [9]:

$$A(z)=\int_0^z I_{1y}(z')e^{-i\varphi(z')}dz'.$$

The magnitude of A is plotted as the radius, and the complex phase angle of A is plotted as the angle. These values, calculated for a sequence of points along the undulator, are plotted. A properly phased undulator will be represented as a straight line, radially outward from the center of the graph. Phasing errors appear as curved lines or kinks. The absolute value of the complex radiation amplitude at the undulator segment end $A(L)$ is represented in the polar plot as the distance between the initial and final points of the vector. The radiation intensity is proportional to $|A|^2$.

Consider the case with a long line of ideal undulators and ideal particle beam energy, followed by two undulators separated by a long break section with three periods of phase slippage in the drift space. Also, assume that the particle beam energy is 0.4% too low through those two undulators, due to a beam energy loss. Figure 5 is a polar plot through those two undulators and the drift

space between them. The line curvature is so extreme that the radiation intensity from the two undulators is sharply reduced. The performance of the undulator is seen to be very sensitive to the particle energy.

The curvature in Fig. 5 can be understood because spontaneous radiation from the undulators and the reduced particle beam energy would not be at the nominal wavelength. Figure 6 shows what happens when the magnetic field strength of the two undulators is adjusted so the spontaneous radiation is at the nominal wavelength, despite the reduced beam energy. The traces through the two undulators are straight, as they should be, but now there is a kink between the two undulators, showing that the drift space is not the right length for the reduced beam energy. This type of plot can clearly show and help diagnose the origin of an effect that only impacts the final radiation amplitude by 2% of the ideal value.

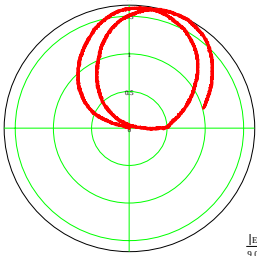

Figure 5: After passing through a line of undulator segments where the undulators are perfect and the beam energy is ideal, the beam loses 0.4% of its energy prior to passage through two undulators that are separated by a drift space with three periods of phase slippage. The magnitude and complex phase angle of A are plotted in polar coordinates at points along the two undulators. The radiation amplitude from those two undulators, represented by the length of a vector from the beginning to the end of the trace, is very small.

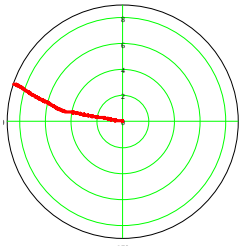

Figure 6: Same type of plot as in Fig. 5. The K_{eff} of the two undulators has been adjusted so that the spontaneous radiation is at the nominal wavelength, despite the beam energy loss. The lines through the undulators are straight, and the kink between them indicates a phasing error in the drift space. The radiation amplitude from these undulators is now 98.2% of ideal.

An additional improvement can be obtained if, instead of adjusting K_{eff} to match the spontaneous radiation to the nominal wavelength, K_{eff} is adjusted to maximize the overall |A|. The polar plot resulting from such a change is shown in Fig. 7. As can be seen by the curvature in the traces through the undulators, there is a small phase slippage in the undulator segments, but the net effect is that the radiation amplitude is 99.1% of ideal.

It may at some time be desirable to remove an undulator segment from the undulator line. An issue that must be considered before doing so, however, is what becomes of the phasing between the undulator segments immediately upstream and downstream of the removed one. If the new undulator-long drift space is the same length as an integer number of free-space slippage lengths, then the phasing between the adjacent undulator segments will be good. (Some steering correction may be needed, however, to compensate for the environmental magnetic field.) If, as is more likely, the drift length isn't right, resulting in a phase error, then an adjustment of the K_{eff} of the undulators may be able to compensate.

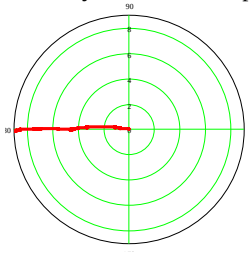

Figure 7: Same as Fig. 6, but with K_{eff} of the two undulators adjusted to maximize the overall |A|. The K_{eff} through the undulators is not perfect, as can be seen by the slight curvature, but the overall |A| is 99.1% of ideal.

An example of such an adjustment is shown in Fig. 8. When K_{eff} = 3.62, the drift-space length is nearly an integer number of slippage lengths so the required K_{eff} adjustment is small. Another example is shown in Fig. 9 for nominal K_{eff} = 3.44. (The electron beam energy is also changed, to keep the wavelength of the radiation at 1.5 Å.) At this new nominal K_{eff}, the drift space length is nearly perfectly wrong, so even tuning K_{eff} is not enough. The phasing correction would be easier in this case if two undulators were removed.

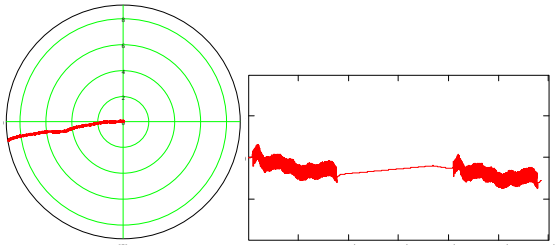

Figure 8: Polar plot (left) and trajectory (right) with one device removed. K_{eff} was changed by 0.03% (0.6-mm shift in X) to compensate for the phase distortion in the drift space. Nominal K_{eff} =3.62. |A| is 99.3% of ideal for two undulators.

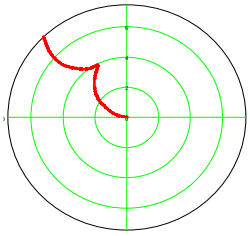

Figure 9: Same as Fig. 8 but with nominal K_{eff} = 3.44. The drift space length is 17.54 slippage lengths, making the second undulator almost exactly out of phase. |A| was optimized by a 0.16% change in K_{eff} (3.2-mm shift in X), but still only 81.6% of ideal was reached.

MAGNETIC NEEDLES

With a canted gap undulator, accurate alignment in both the horizontal and vertical directions is critical, and a method to accomplish this has been studied. The magnetic center of the undulator can be determined using a Hall probe. The position of the Hall probe's sensitive area is difficult to determine, therefore the probe will be used to relate the undulator magnet centerline to positions of magnetic needles attached to the undulator.

A Sentron Hall probe was used to scan past a magnetic needle and the results are shown in Figs. 10 and 11.

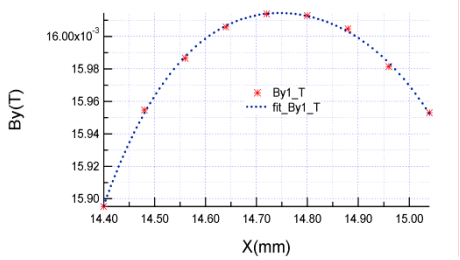

Figure 10: Horizontal scan past the tip of a vertical-pointing magnetic needle.

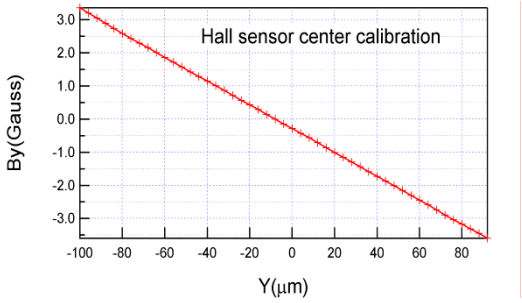

Figure 11: Vertical scan past the tip of a horizontal-pointing magnetic needle. The magnetic center of the undulator is at y = 0. By = 0 is the center of the needle. The distance between them can be determined from the plot to within 5 μm.

The vertical field distribution along the X-axis is shown in Figure 10. The spacing between data points was determined by the 50-μm encoder resolution. An encoder with finer resolution will be used in the final system. Alignment in the Y direction is shown in Fig. 11. The needle points horizontally in this case, and the Hall probe scan direction is vertical. The magnetic center of the undulator is at y = 0. By = 0 is the center of the needle. The distance between them can be determined from the plot to within 5 μm.

SUMMARY

Wedged spacers were inserted between the aluminum base plates and the titanium strongback of the existing LCLS prototype undulator, to give a 3-mrad cant to the pole gap. (A 4.5-mrad cant has since been determined to be preferred for the final LCLS undulator.) The measured variation of the magnetic field with horizontal position was as expected, making it possible to move the undulator laterally to adjust the on-axis field strength. The rms phase error did not change significantly with X, so the undulator can be used at different lateral positions. Coarse adjustment of the field strength can be done by the choice of spacer thickness, and by sliding the chosen spacer horizontally. The fine adjustment will be accomplished by lateral translation of the undulator. Horizontal translation of the undulator can also be used to correct the temperature dependence of the field strength. Magnetic needles were found to be effective alignment tools.

ACKNOWLEDGMENTS

The authors would like to thank Dr. J. Pflueger for his suggestion to cant the undulators. This work is supported by the U.S. Department of Energy, Office of Basic Energy Sciences, under Contract No. W-31-109-ENG-38.

REFERENCES

[1] Coherent Light Source Project, SLAC-R-593, April 2002, http://www-ssrl.slac.stanford.edu/lcls/cdr/.
[2] E.R. Moog et al, "Design and Manufacture of a Prototype Undulator for the LCLS Project," Proc. of PAC 2001, Chicago, June, 2001.
[3] I.B. Vasserman et al., "Magnetic measurements and tuning of the LCLS prototype undulator," Nucl. Instrum. Methods A, 507 (2003) 191-195.
[4] LCLS Prototype Undulator Report, R.J. Dejus, editor, ANL/APS/TB-48 (2004).
[5] E. Trakhtenberg et al., "Undulators for the LCLS Project – from the prototype to full-scale manufacturing," XV Int'l. Synchrotron Radiation Conf., July 19-23, Novosibirsk, Russia (2004).
[6] B.M. Kincaid, J. Opt. Soc. Am. B, 2 (1985) 1294.
[7] B. Diviacco, R.P. Walker, Nucl. Instrum. Methods A, 368 (1996) 522.
[8] L.H. Yu et al., Phys. Rev. A, 45 (1992) 1163.
[9] E. Gluskin et al., Nucl. Instrum. Methods A, 475 (2001) 323.

COMMISSIONING OF THE TTF LINAC INJECTOR AT THE DESY VUV-FEL

K. Honkavaara*, DESY, 22603 Hamburg, Germany
for the VUV-FEL Injector group

Abstract

The upgrade of the TESLA Test Facility (TTF) at DESY is almost completed. With electron beam energies up to 1 GeV, it serves the new SASE FEL user facility (VUV-FEL) in the wavelength range from VUV to soft X-rays. The first installation phase of the redesigned photoinjector is finished. We report on its commissioning during spring 2004, including the first measurements of electron beam parameters. Since this injector is also a prototype for the XFEL injector, the results obtained are important for future SASE XFEL drive linacs.

INTRODUCTION

The TESLA Test Facility Linac, phase 1 (TTF1) [1] has been operated at DESY until November 2002. Besides performing various tests and experiments related to the TESLA linear collider project [2], the TTF linac was used to drive a SASE free electron laser at wavelengths in the range of 120 nm to 80 nm [3, 4]. Presently the TTF linac is upgraded to drive a new SASE FEL user facility (VUV-FEL) [5]. The VUV-FEL is also a piloting project for the XFEL project [6, 7].

In present stage of the upgrade, five accelerating modules with eight 9-cell superconducting TESLA cavities in each are installed providing electron beam energies up to 800 MeV. Later, one or two more modules can be added to increase the beam energy to 1 GeV, or even beyond. Beginning of the year 2004 the installations in the accelerator tunnel have been almost completed, and from March to June 2004 the redesigned photoinjector has been successfully commissioned, which has already been briefly reported in [8].

THE VUV-FEL

With the electron beam energies available at TTF1 it was possible to produce SASE radiation down to the wavelength of 80 nm. To reach shorter wavelengths, the energy of the linac has to be increased. Also several other upgrades are needed to meet the more demanding beam parameter requirements in terms of transverse emittance, peak current, and energy spread. Taking these requirements and our experience at TTF1 into account, both the linac and the injector have now been redesigned to extend the wavelength range down to 6 nm. For a detailed discussion on the linac and the parameter choices refer to [5].

* katja.honkavaara@desy.de

For the start-up and commissioning phase this year, emphasis is put on achieving lasing and saturation at a wavelength of 30 nm, which requires an electron beam energy of 450 MeV. For the longer wavelength the requirements on the beam parameters are relaxed, which eases the commissioning. Later, lasing at longer and shorter wavelengths will follow.

THE INJECTOR CONCEPT

The upgrade of the VUV-FEL photoinjector [9] implements the main ideas of the XFEL injector proposal [10]. The optimization of the XFEL injector concept is going on, and the experience and results achieved by the VUV-FEL injector are important for its final layout.

Figure 1 shows a schematic overview of the VUV-FEL injector. Electron bunch trains with a nominal bunch charge of 1 nC are generated by a laser-driven RF gun. The design normalized emittance is 2 mm mrad. In order to reduce space charge effects, the design shape of the laser pulse is flat, both transversally and longitudinally, having a length of 20 ps (FWHM). The design rms bunch length at the gun exit is 2.2 mm.

A complete TESLA module with 8 accelerating cavities is used to boost the beam energy to 130 - 150 MeV. To avoid strong focusing, the first four cavities are operated with a moderate gradient (12 MV/m). In the last four cavities full acceleration ($>$ 20 MV/m) is used. The first magnetic chicane bunch compressor is placed downstream of the first accelerating module. A second compression stage follows after two additional accelerating modules at a higher energy. With the two compression stages the bunch can be compressed down to 50 μm (design).

Off-crest acceleration is required for magnetic bunch compression. The sinusoidal accelerating field induces a curvature in the longitudinal phase space. The compression of the off-crest accelerated bunch leads to a longitudinal bunch structure with a high peak current spike and a long tail. This irregular bunch structure complicates the use of the second bunch compressor. The energy-phase plane curvature can be removed by using a superconducting third harmonic cavity (3.9 GHz) [11] before the bunch compressor. This cavity is under construction, and thus not yet available. Therefore the start-up lasing strategy is similar than at TTF1: The leading spike after the first compression stage is used to produce the required peak current [12].

During the injector commissioning reported here, the first accelerating module has been operated with a constant gradient of 12 MV/m in all the cavities yielding to beam en-

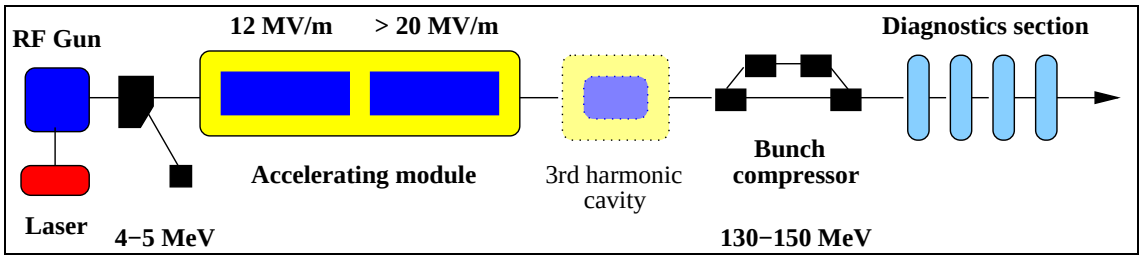

Figure 1: Schematic overview of the TTF VUV-FEL injector (not to scale). Beam direction is from left to right, and the total length is about 37 m. During the commissioning the beam was dumped into a small temporary beam dump before the second accelerator module. The 3rd harmonic cavity is not installed yet.

ergy around 100 MeV. The beam was dumped into a temporary beam dump before the second accelerator module.

THE RF GUN

The new RF gun has been successfully commissioned and characterized at PITZ (DESY Zeuthen) [13]. It is a 1.5 cell L-band cavity (1.3 GHz) powered by a 5 MW klystron.

The design of the photocathode system is the same as at TTF1. The Cs_2Te photocathode is inserted via a load-lock system to the back of the half cell of the RF gun. The new cathodes have higher quantum efficiency than the ones used at TTF1 [14].

The maximum accelerating field on the cathode is determined by the available klystron power, and it is currently limited to 42 MV/m. In order to reduce space charge induced emittance growth, the electron beam is focused by a solenoid magnet. A bucking solenoid is used to compensate the magnetic field on the cathode surface to zero. The RF power and the RF phase in the gun are regulated by a low level RF system based on digital signal processors.

The RF gun was transported from Zeuthen (PITZ) to Hamburg and installed at the TTF tunnel in January 2004. At PITZ, the gun has been operated at 10 Hz with an RF peak power of 3 MW and an RF pulse length of up to 0.9 ms [15]. After a short commissioning period a similar performance was achieved also at TTF. However, for convenience, during most of the commissioning time 5 Hz repetition rate, and shorter RF pulse length was used.

THE LASER SYSTEM

The TTF1 laser system [16] has been upgraded. A similar system is tested and operated at PITZ. The laser system is based on a mode-locked pulse train oscillator synchronized to the 1.3 GHz RF of the accelerator. In contrast to the old system, two of the four laser amplifiers use laser diodes instead of flashlamps for pumping. The remaining flashlamp pumped amplifiers will be replaced later. One advantage of using diode pumping is the increased laser pulse energy stability: before the upgrade the measured fluctuation in the electron bunch charge from shot to shot was 3 to 6 % rms, now it is only about 1 % rms.

After the conversion of the initial wavelength of 1047 nm to UV (262 nm), the laser beam is transported to the RF gun cathode by an optical beam line consisting of lenses and mirrors. The laser spot position on the cathode is controlled by a set of remote movable mirrors. A remotely controlled iris allows controlling the laser beam size on the cathode. The nominal laser spot size at the cathode is 3 mm diameter.

The laser system is designed to produce pulse trains with up to 800 μs length with pulse spacing of 1 μs (1 MHz). A 9 MHz operation mode is in preparation. The laser pulse length and shape has been measured in the UV wavelength with a streak camera. The shape is near gaussian and has a length of $\sigma = 4.4 \pm 0.1$ ps, which is shorter than before the laser upgrade. However, in order to obtain a small transverse emittance, a flat laser pulse profile, both in transverse and longitudinal, is preferred. At PITZ, a laser pulse shaper producing longitudinal flat-hat profile laser pulses of $\sim$ 20 ps has been tested. The measured transverse emittance has been reduced by a factor of two compared to a gaussian laser pulse [17]. However, since for the start-up of the VUV-FEL the gaussian laser profile is sufficient, this pulse shaper will be installed at TTF only later, when the development at PITZ is completed.

MEASUREMENTS OF BEAM PARAMETERS

The first electron beam was produced by the new RF gun at TTF in the middle of March 2004. The first month of beam operation was dedicated to the commissioning of the hardware and software components of different measurement and control devices as well as to study the basic beam parameters in the RF gun section.

In the gun section the charge can be measured by two devices: a toroid and a Faraday cup located close to each other at the gun exit. During the commissioning we operated with a charge of 1 nC per bunch. The number of bunches in a bunch train was 1 to 10.

The energy of the beam produced by the RF gun has been measured by means of a spectrometer dipole installed before the first accelerating module. The beam energy corresponding to the nominal 3 MW RF input power is 4.6

MeV. The measured data agree well with the expectation from the simulation [8].

Typically, in order to have the smallest transverse emittance, the RF phase of the gun with respect to the laser phase is tuned to a phase between 30 to 40° from zero crossing. The rms phase stability of the laser is estimated to better than 0.2° (0.5 ps) from shot to shot and within the pulses of the pulse train.

The commissioning of the injector including the first accelerating module, the first bunch compressor, and the diagnostics section started in April 2004. The accelerating module has been operated with a gradient of 12 MV/m yielding a beam energy around 100 MeV. An energy stability of $8.5 \cdot 10^{-4}$ rms has been achieved by using a feedback system regulating the phase and amplitude of the accelerating structures.

The uncorrelated energy spread has been estimated from the beam image on the dispersive section of the bunch compressor. The energy spread has a leading peak with an rms width of about 30 keV and a tail of about 200 keV.

One of the eight accelerating cavities in the first accelerating module has been prepared by using a surface treatment technique based on electropolishing. The performance of this cavity was tested with the electron beam. An accelerating gradient of 35 MV/m was achieved.[18]

The transverse beam shape and size after the acceleration is measured using optical transition radiation (OTR). The OTR system is designed and constructed by INFN-LNF and INFN-Roma2 in collaboration with DESY. The measured resolution (rms) of the system is 11 μm (magnification 1:1). More details of the system are in [19, 20].

For the measurements of the transverse emittance and Twiss parameters, 4 OTR monitors combined with wire scanners are embedded in a FODO lattice of 6 quadrupoles with a periodic beta function. During the commissioning only the OTR monitors were available. The emittance and Twiss parameters are obtained by fitting the measured beam sizes to the expectation from the lattice. The projected rms beam sizes are estimated from the beam images with different methods. In the first method, the sigma of a gaussian fit on the projected profiles is used to estimate the rms beam size. In the second, the true rms is calculated from the data within 90 % of the intensity of the beam. In the latter case, two different image analysis codes are used to determine the rms size. Especially when the beam shape is irregular and far from a gaussian shape, the different methods and codes yield different results.

Figure 2 shows the normalized horizontal and vertical emittance as a function of the solenoid current. The RF gun and the module have been operated with nominal parameters. The bunch compressor was by-passed to avoid dispersive effects. The data are partly taken at different days and with different optics to match into the FODO lattice. The emittance values using different analysis methods on the same data set are indicated. The expected emittance from simulation is shown as well.

For accurate emittance measurements it is important to have the FODO lattice well matched such that the beam image on each of the four monitors is regular and has similar dimensions. During this first commissioning phase, this was only sometimes the case. Therefore further measurements with better measurement conditions are needed to confirm the results. The study of measurement errors and systematic effects of different analysis methods is not yet finalized, and the data is still subject to a further analysis. Therefore, the emittance results shown here have to be treated preliminary.

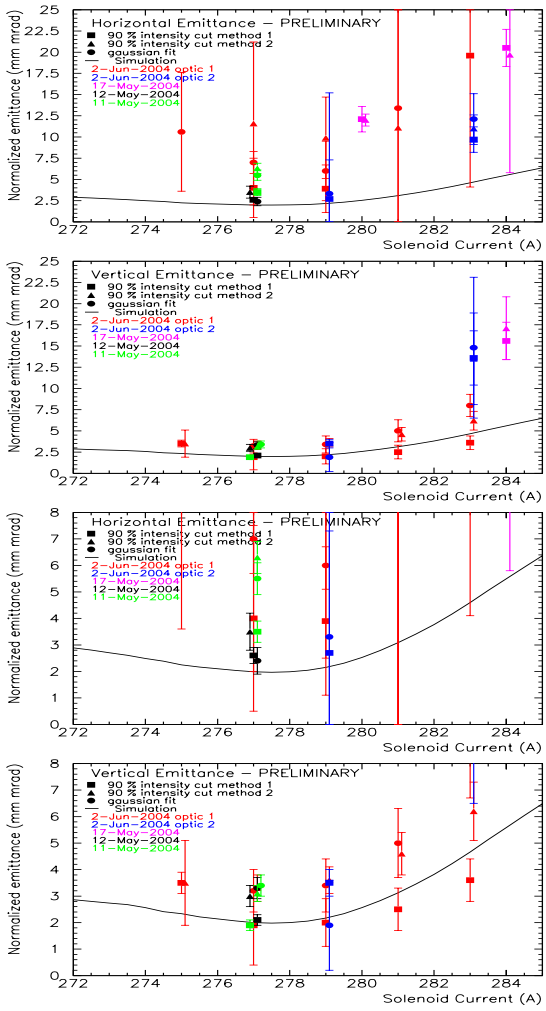

Figure 2: Normalized emittance measured at 100 MeV for a bunch charge of 1 nC as a function of the solenoid current. Horizontal and vertical projected emittances are shown for different beam conditions and matching optics. In addition, three different ways to obtain the rms beam size are shown: the rms size from a 90 % intensity cut with 2 different image analysis methods and an estimate from a gauss fit. Error in beam size is assumed to be 10 %. The two lower plots are zooms of the upper ones. The data are still object to further analysis and have to be treated preliminary.

Nevertheless, the emittance results obtained are already now useful to determine a tentative working point in terms of a preferred solenoid current. We can also see that in the horizontal case, the data scatter largely. Typically the beam quality in the horizontal plane is worse than vertical. The reason is not yet understood, but possible candidates are non-optimized injection into the first module, a non-uniform laser beam, and a beam passing too close to the laser mirror, which is inside the beam pipe. The latter has been observed at PITZ as well.

The rms bunch length has been measured using synchrotron radiation (SR) from the last dipole of the bunch compressor. This radiation is guided out of the accelerator tunnel and used in bunch length measurements by an interferometer and a streak camera [21]. The analysis of the interferometer data is on going.

The uncompressed bunch length measured by the streak camera is $\sigma = 1.7 \pm 0.2$ mm as expected. In the compressed case, we expect to have a bunch structure consisting of a 100 μm leading peak (FWHM), and a tail (rms size of 0.5 mm). We observed that the bunch shortens as expected when the phase of the accelerating module is changed. However, accurate measurements of the shape and size of short bunches have not yet been possible due to too low number of SR photons on the streak camera, which prevents us from using a wavelength filter. The filter is essential to avoid smearing the data due to dispersion effects in the streak camera optics [22]. Since the number of SR photons increases with the electron beam energy, the situation should be improved when the full acceleration in the last four cavities of the first accelerating module is used.

SUMMARY AND OUTLOOK

The new photoinjector of the TTF linac driving the VUV-FEL has been successfully commissioned. Beam parameters are mostly understood, although fine tuning and more accurate measurements are still needed. Improvements in the reliability and beam stability are also necessary. After the short shutdown from June to August 2004, the beam operation of the whole linac will start in the beginning of September. The goal is to obtain first lasing at 30 nm by the end of this year.

ACKNOWLEDGMENT

I would like to thank all colleagues participating in the realization of the new injector, as well as the PITZ and TTF staff and operators for its successful commissioning. Special thanks are due to S. Schreiber for help on preparation of this paper.

REFERENCES

[1] "TESLA Test Facility Linac: Design Report", ed. D. A. Edwards, DESY-TESLA-95-01

[2] "TESLA: The superconducting electron positron linear collider with an integrated X-ray laser laboratory. Technical design report. Part 2: The accelerator", ed. R. Brinkmann *et al.*, DESY-01-011

[3] V. Ayvazian *et al.*, Phys. Rev. Lett. **88** (2002) 104802.

[4] V. Ayvazian *et al.*, Eur. Phys. J. D **20** (2002) 149.

[5] "SASE FEL at the TESLA Facility, Phase 2," DESY-TESLA-FEL-2002-01

[6] "TESLA XFEL: First stage of the X-ray laser laboratory. Technical design report, supplement", ed. R. Brinkmann *et al.*, DESY-02-167

[7] H. Weise, "The TESLA X-FEL Project", EPAC 2004, Luzern, Switzerland, July 5-9, 2004

[8] S. Schreiber, "Commissioning of the VUV-FEL injector at TTF", EPAC 2004, Luzern, Switzerland, July 5-9, 2004

[9] K. Flöttmann and P. Piot, "An upgraded injector for the TTF FEL-user facility", EPAC 2002, Paris, France, June 3-7, 2002

[10] K. Flöttmann *et al.*, "The TESLA X-FEL injector," PAC 2001, Chicago, Illinois, June 18-22, 2001

[11] J. Sekutowicz *et al.*, "A design of a 3rd harmonic cavity for the TTF2 photoinjector," DESY-TESLA-FEL-2002-05

[12] S. Schreiber *et al.*, "Performance of the TTF Photoinjector for FEL Operation", Workshop "The physics and applications of high brightness electron beams", Chia Laguna, Sardinia, July 1-6, 2002, ed. J. Rosenzweig, G. Travish, L. Serafini, World Scientific, Singapore, ISBN 981-238-726-9

[13] M. Krasilnikov *et al.*, "Optimizing the PITZ electron source for the VUV-FEL", EPAC 2004, Luzern, Switzerland, July 5-9, 2004

[14] S. Schreiber *et al.*, "Properties of cathodes used in the photoinjector RF gun at the DESY VUV-FEL", EPAC 2004, Luzern, Switzerland, July 5-9, 2004

[15] J.P. Carneiro *et al.*, "Behavior of the TTF2 RF gun with long pulses and high repetition rates", DESY-TESLA-2003-33

[16] S. Schreiber *et al.*, Nucl. Instrum. Meth. A **445** (2000) 427.

[17] V. Miltchev *et al.*, "Transverse Emittance Measurements at the Photo Injector Test Facility at DESY Zeuthen", these proceedings

[18] L. Lilje, "Achievement of 35 MV/m in the TESLA Superconducting Cavities Using Electropolishing as a Surface Treatment", EPAC 2004, Luzern, Switzerland, July 5-9, 2004

[19] K. Honkavaara *et al.*, "Design of OTR Beam Profile Monitors for the TESLA Test Facility, Phase 2 (TTF2)", PAC 2003, Portland, Oregon, May 12-16, 2003

[20] A. Cianchi *et al.*, "Commissioning of the OTR Beam Profile Monitor System at TTF/VUV-FEL Injector", EPAC 2004, Luzern, Switzerland, July 5-9, 2004

[21] O. Grimm *et al.*, "Synchrotron Light Beam Line for TTF2", EPAC 2004, Luzern, Switzerland, July 5-9, 2004

[22] Ch. Gerth *et al.*, Nucl. Instrum. Meth. A **507** (2003) 335

A NOVEL DIAGNOSTICS OF ULTRASHORT ELECTRON BUNCHES BASED ON DETECTION OF COHERENT RADIATION FROM BUNCHED ELECTRON BEAM IN AN UNDULATOR

E.L. Saldin, E.A. Schneidmiller, and M.V. Yurkov
Deutsches Elektronen-Synchrotron (DESY), Hamburg, Germany

Abstract

We propose a new method for measurements of the longitudinal profile of 100 femtosecond electron bunches for X-ray Free Electron Lasers (XFELs). The method is based on detection of coherent undulator radiation produced by modulated electron beam. Seed optical quantum laser is used to produce exact optical replica of ultrashort electron bunches. The replica is generated in apparatus which consists of an input undulator (energy modulator), and output undulator (radiator) separated by a dispersion section. The radiation in the output undulator is excited by the electron bunch modulated at the optical wavelength and rapidly reaches a hundred-MW-level power. We then use the now-standard method of ultrashort laser pulse-shape measurement, a tandem combination of autocorrelator and spectrum (FROG – frequency resolved optical gating) providing real-time single-shot measurements of the electron bunch structure. The big advantage of proposed technique is that it can be used to determine the slice energy spread and emittance in multishot measurements. We illustrate with numerical examples the potential of the proposed method for electron beam diagnostics at the European X-ray FEL.

INTRODUCTION

The past decade has been tremendous progress in the development of electron accelerators that produce ultrashort bunches approaching sub-100 femtosecond durations [1]. The use of ultrashort electron bunches for both fundamental studies and applications is increasing rapidly, too [2]. As electron bunches shrink in length and grow in utility, the ability to measure them becomes increasingly important. There are several reasons for this. First, precise knowledge of the bunch properties is necessary for verifying theoretical models of bunch creation [3]. Second, in order to make even shorter bunches, it is necessary to understand the distortions that limit the length of currently available pulses. Third, in experiments using these bunches, it is always important to know at least the pulse length in order to determine the temporal resolution of a given experiment. Moreover, in many experiments – studies of X-ray SASE FELs, for example - additional details of the bunch structure play an important role in determination of the outcome of the experiment. Of particular importance is the variation of peak current, emittance and energy spread along the bunch. Finally, numerous applications have emerged for emittance-shaped ultrashort electron bunches and, of course, it is necessary to be able to measure the emittance, or energy spread shape of the electron bunch used in these experiments [4].

The new principle of diagnostic techniques described bellow offers a way for full characterization of ultrashort electron bunches [5]. It is based on a construction of an exact optical replica of an electron bunch.

OPTICAL REPLICA SYNTHESIS

A basic scheme of the optical replica synthesizer and optical replica of a complex test electron bunch is shown in Fig. 1 [5]. A relatively long laser pulse is used to modulate the energy of electrons within the electron pulse at the seed laser frequency. The electron pulse will be timed to overlap with the central area of the laser pulse. The duration of the laser pulse is much larger than the electron pulse time jitter of a fraction of ps, so it can be easily synchronized with the electron pulse. The laser pulse serves as a seed for modulator which consists of a short undulator and dispersion section. Parameters of the seed laser are: wavelength 1047 nm, energy in the laser pulse 1 mJ, and FWHW pulse duration 10 ps. The laser beam is focused onto electron beam in a short (number of periods is equal to $N_{\rm w} = 5$) modulator undulator resonant at the optical wavelength of 1047 nm. Optimal conditions of focusing correspond to the positioning of the laser beam waist in the center of the modulator undulator. The size of the laser beam waist is 10 times larger than the electron beam size. The seed laser pulse interacts with the electron beam in the modulator undulator and produces an amplitude of the energy modulation in the electron bunch of about 250 keV. Then the electron bunch passes through the dispersion section (momentum compaction factor is about of $R_{56} \simeq 50\mu$m) where the energy modulation is converted to the density modulation at the laser wavelength. The density modulation reaches an amplitude of about 10%. Following the modulator the beam enters the short (number of periods is equal to $N_{\rm w} = 5$) radiator undulator which is resonant at laser (or double) frequency. Because the beam has a large component of bunching, coherent emission is copiously produces by the electron bunch. The bandwidth-limited output radiation pulse (see Fig. 2) has 10 μJ-level pulse energy and is delivered in a diffraction-limited beam.

The optical replica synthesizer is expected to satisfy certain requirements which can be achieved by suitable design

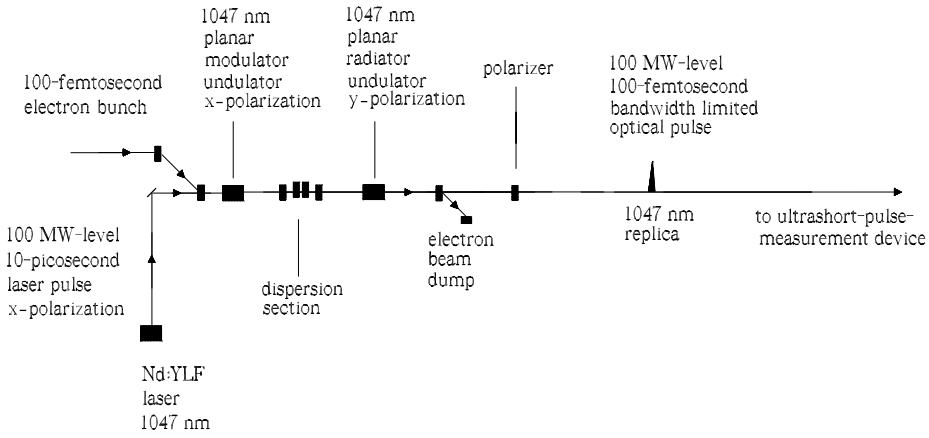

Figure 1: Schematic diagram of the optical replica synthesis through optical modulation of electron bunch and coherent radiation in the output undulator. Signal beam filter based on polarizer: y-polarized light is transmitted, while x-polarized light is reflected

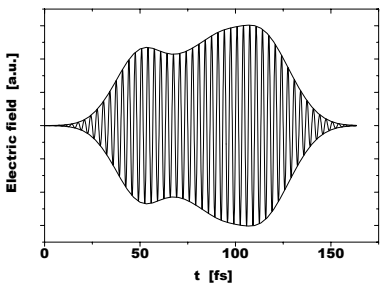

Figure 2: Optical replica (rapidly oscillating curve) of a test electron bunch. Radiator operates at the wavelength of 1047 nm

and choice of the components. A complete optimization of the proposed diagnostic device can be performed only with three-dimensional time-dependent numerical simulation code. Numerical results presented in this paper are obtained with version of code FAST [6] modified for simulation of optical replica synthesis. This code allows one to perform simulations of coherent undulator radiation taking into account all physical effects influencing the synthesizer operation.

One important point in the construction of replica synthesizer is separation of the optical replica from the seed laser pulse. Numerous designs are possible – for example, the combination of two planar undulators placed in crossed positions, as it is illustrated schematically in Fig. 1. In another scheme a frequency doubler can used to distinguish the optical replica from the intense seed laser pulse. when input undulator operates at a seed frequency, and an output undulator operating at a multiple of this frequency.

When propagating in vacuum, the radiation field is faster than the electron beam, and it moves forward (slips) by one wavelength, λ, per one undulator period, $\lambda_{\rm w}$. It is clear that the resolution of the electron pulse shape is determined by the slippage of the radiation with respect to electrons in the output undulator. If the slippage time is much less than the electron pulse duration, $N_{\rm w}\lambda/c \ll \tau_{\rm e}$, then one can neglect the slippage effect.

MEASUREMENT OF ELECTRON CURRENT PROFILE

The study and detailed understanding of the cause and nature of collective effects is important for successful design of replica synthesizer. Proposed design is conducted to eliminate collective effects as much as possible through installation of short input and output undulators. The signal produced by replica synthesizer is thus a pulse of electric field amplitude:

$$E(t) = F(I(t), \epsilon_{\rm n}(t), \Delta\mathcal{E}(t)) = I(t) f(\epsilon_{\rm n}(t), \Delta\mathcal{E}(t)) \ ,$$

where $\epsilon_{\rm n}(t)$ is the normalized slice emittance and $\Delta\mathcal{E}(t)$ is the slice energy spread in the electron bunch. If longitudinal beam dynamics in the synthesizer is governed by purely single-particle effects then this field directly proportional to the peak current $I(t)$.

Within the scope of the electrodynamic theory the output characteristics of the replica synthesizer are controlled by three dimensional parameters: $\lambda, \quad L_{\rm w}, \quad \sigma$, where λ is the radiation wavelength, $L_{\rm w} = N_{\rm w}\lambda_{\rm w}$ is the radiator undulator length, and σ is the electron beam transverse size.

At an appropriate normalization of electrodynamic equations, the coherent undulator radiation is described by only one dimensionless parameter [5]:

$$N = 2\pi\sigma^2/(\lambda L_{\rm w}) \, .$$

The parameter N can be referred to as the electron beam Fresnel number, or as diffraction parameter. In general case the electric field of the wave radiated in the undulator depends on the transverse size of the electron beam. For a proposed diagnostic technique it is of great interest to minimize the influence of the transverse emittance on the radiation field amplitude. In the case of a wide electron beam

$$\lambda L_{\rm w} \ll 2\pi\sigma^2 \, , \qquad \text{or} \quad N \gg 1 \, , \tag{1}$$

the most of the radiation overlaps with electron beam and field of the wave is inversely proportional to the square of electron beam [5]:

$$E(t) \propto I(t)/\sigma^2(t) \, .$$

Reducing the particle beam cross-section by diminishing the betatron function reduces also the size of the radiation beam and increases the total power of output radiation. This process of reducing the beam cross-section is, however, effective only up to some point. Further reduction of the particle beam size would practically no effect on the radiation beam size and total radiation power because of diffraction effects (see Section 4). In the limit of a thin electron beam the transverse radiation beam size tends to the constant value and the dependence of the output radiation on the transverse size of the electron beam is rather weak. The boundary between these two asymptotes is about $\sigma^2 \simeq \lambda L_{\rm w}$.

From the preceding discussion we may want to optimize the beam geometry as follows. The transverse size of the electron beam has to be much smaller then the diffraction limited radiation beam size

$$\sigma^2 \ll \lambda L_{\rm w}/(2\pi) \, , \qquad \text{or} \quad N \ll 1 \, , \tag{2}$$

The radiation wavelength and the undulator length dictate the choice of the optimum transverse size of the electron beam. Let us present a specific numerical example. Suppose $\gamma = 10^3$, $\epsilon_{\rm n} = 2\pi\mu$m, $\lambda_{\rm w} = 6.5$ cm, $N_{\rm w} = 5$, $\lambda = 1\mu$m. If the focusing beta function is equal to 1 m the diffraction parameter is $N = 2\pi\sigma^2/(\lambda L_{\rm w}) \simeq 0.04$. We come to the conclusion that we can treat this situation as a coherent undulator radiation generated by a thin electron beam. This condition may be easily satisfied in practice.

Proposed design is conducted to eliminate emittance effects as much as possible through installation of a special electron beam focusing system. In the radiator undulator the betatron function should reach small values (of about 1 m) forming a narrow beam waist. The signal generated by a replics synthesizer is thus a pulse of electric field with amplitude:

$$E(t) = F(I(t), \epsilon_{\rm n}(t), \Delta\mathcal{E}(t)) = I(t) f(\Delta\mathcal{E}(t)) \, .$$

Optimum parameters of the dispersion section can be estimated in the following way. The expression for the fundamental component of the bunched beam current is $i_1(t) = 2I(t)J_1(X)$, where $X = 2\pi R_{56}\delta\mathcal{E}/(\lambda\mathcal{E}_0)$ is dimensionless quantity known as the bunching parameter, $\delta\mathcal{E}$ is the amplitude of energy modulation induced in the modulator undulator. The function $J_1(X)$ approaches $X/2$ for small X; thus the microbunching approaches $i_1(t) \simeq XI(t)$. We see that microbunching depends on the choice of the dispersion section strength. One might think that all we have to do is to get microbunching amplitude to maximum – we can always increase R_{56} of the dispersion section and we can always increase output power. It is not impossible to build dispersion section that has large R_{56} function. In fact, one of the main problems in the modulator operation is preventing the spread of microbunching due to local energy spread in the electron beam. For effective operation of replica synthesizer the value of suppression factor should be close to unity. To get a rough idea of the spread of electron density modulation, the position of the particles within the electron beam at the dispersion section exit has a spread which is equal to $\Delta z' \simeq R_{56}\Delta\mathcal{E}/\mathcal{E}_0$, where $\Delta\mathcal{E}$ is the local energy spread in the electron bunch. We know that uncertainty in the phase of the particles is about $\Delta\psi \simeq 2\pi\Delta z'/\lambda$. Therefore, a rough estimate for the microbunching spread to be small is

$$2\pi R_{56}\Delta\mathcal{E}/\mathcal{E}_0 \ll 1 \, . \tag{3}$$

The result of more careful analysis (see Section 3) shows that in our case the optimal condition can be written as $X \simeq 0.1$, $\delta\mathcal{E} \simeq \max(\Delta\mathcal{E})/3 \simeq 250$ keV. The amplitude of energy modulation dictates the choice of the seed laser parameters. In our case the optimal peak power of the seed laser is about of 100 MW.

In general, radiation field depends on the peak current, $I(t)$, local energy spread, $\Delta\mathcal{E}(t)$, and local emittance, $\epsilon_{\rm n}(t)$. However, under conditions of a thin electron beam (2) and of a microbunching spread to be small (3), the electric field of the wave radiated in the replica synthesizer is directly proportional to the peak current of the electron beam:

$$E(t) = F(I(t), \epsilon_{\rm n}(t), \Delta\mathcal{E}(t)) = \text{const.} \times I(t) \, .$$

Thus, conditions (2) and (3) should be treated as optimal tuning of undulator length, strength of the dispersion section and focusing beta function for measurement of the electron bunch profile.

MEASUREMENT OF SLICE EMITTANCE AND ENERGY SPREAD

We found that longitudinal profile of the electron bunch $I(t)$ can be reconstructed on the basis of a single-shot measurements. The next problem is determination of slice

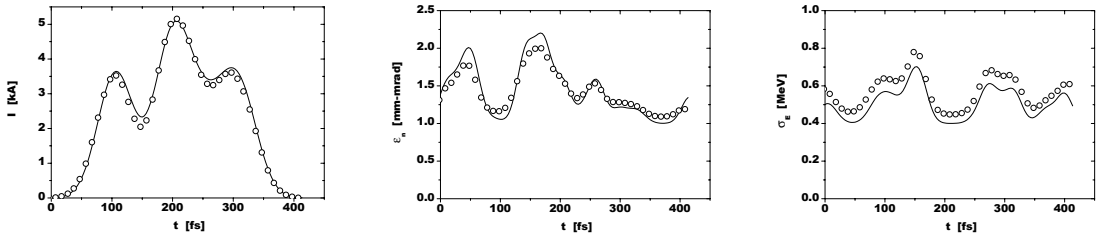

Figure 3: Target (solid curve) and retrieved (circles) electron beam peak current, slice emittance and slice energy spread. The nominal energy of electrons is equal to $\mathcal{E}_0 = 500$ MeV. Number of undulator periods is equal to $N_{\rm w} = 5$. The optical replica is generated at the radiation wavelength 1047 nm. Calculations were performed with code FAST.

energy spread ($\Delta\mathcal{E}(t)$) and slice emittance ($\epsilon_{\rm n}(t)$). This can be done on the basis of multishot measurements. If the electron pulse shape, $I(t)$, is known, the local energy spread $\Delta\mathcal{E}(t)$ can be determined from the dispersion section strength scan. In this way, the problem of slice energy spread measurement is transformed into a relatively simple task of measuring the radiation field amplitude maximum ($\max E(t) \propto \max i_1(t)$). An attempt to increase of the amplitude of the fundamental harmonic, by increasing the strength of dispersion section, is countered by decrease the energy spread suppression factor. In Section 3 we demonstrate that the microbunching $i_1(t)$ has clearly a maximum

$$\max i_1(t) = \text{const.} \times \delta\mathcal{E}[I(t)/\Delta\mathcal{E}(t)] \,,$$

and the optimum strength of the dispersion section is

$$R_{56} = \frac{\lambda\mathcal{E}_0}{2\pi\Delta\mathcal{E}(t)} \,.$$

Thus, measuring the $\max E(t)$ is strictly equivalent to measuring the local energy spread variations along the electron bunch: $I(t)/[\max E(t)] = \text{const.} \times \Delta\mathcal{E}(t)$. Since the optimal strength of the dispersion section is known, that of the unknown absolute value of slice energy spread, $\Delta\mathcal{E}(t)$, is easily found too.

Slice emittance can be measured in the following way. Let us consider for illustration of the method a simple model of the electron bunch, assuming that slice emittances are different, but Twiss parameters are the same in all slices (more general model is discussed in section 5). The solution in our case is to realize that in a wide electron beam asymptote (1) the most of the radiation overlaps with the electron beam and the field of the wave is inversely proportional to the square of the electron bunch, $E(t) \propto I(t)/\sigma^2(t)$. If the electron pulse shape, $I(t)$, is known, the problem of the slice emittance measurement is transformed into a simple task of measuring the radiation field amplitude in the case of a wide electron beam

$$I(t)/E(t) = \text{const.} \times \sigma^2(t) \quad \text{as} \quad \min(\sigma^2) \gg \lambda L_{\rm w}/(2\pi) \,.$$

Since the value of beta function and projected emittance are known (from a standard method using a screen and quadrupole scan), then the unknown absolute value of slice emittance $\epsilon_{\rm n}(t)$ is easily determined, too.

In Fig. 3 we illustrate retrieval of the slice bunch properties from the optical replica of the electron bunch. Numerical calculations were performed using code FAST. The nominal energy of electrons is equal to $\mathcal{E}_0 = 500$ MeV. Number of undulator periods in the modulator and radiator undulator is equal to $N_{\rm w} = 5$. Period length is 6.5 cm. The optical replica is generated at the radiation wavelength 1047 nm. The seed laser power is 100 MW, FWHM pulse duration is 10 ps. Upper plots in Fig. 3 show comparison of target and reconstructed values for the beam current. When taking these data, parameters for the numerical experiment were set according to conditions (2) and (3): focusing beta function in the radiator is 1 meter, and net compaction factor of the dispersion section is 50 μm. Calculations show that pulse energy in the optical replica exceeds 30 μJ. Slice energy spread was determined by means of the scan of dispersion section strength at the value of beta-function of 1 meter (lower plots in Fig. 3). The values of slice emittance were extracted with the help of additional set of calculations with large value of beat function of 50 m which corresponds to the limit of a wide electron beam. We see that slice bunch properties can be retrieved with high accuracy if optical replica can be characterized with high accuracy.

REFERENCES

[1] V. Ayvazyan et al., Phys. Rev. Lett. 88(2002)104802.

[2] P. Audebert et al., "TESLA XFEL: First stage of the X-ray laser laboratory – Technical design report (R. Brinkmann et al., Eds.)", Preprint DESY 02-167, DESY, Humburg, 2002.

[3] M. Dohlus et al., Preprint DESY 03-197, DESY, Humburg, 2003.

[4] P. Emma et al., Phys. Rev. Lett. 92(2004)074801.

[5] E.L. Saldin, E.A. Schneidmiller and M.V. Yurkov, Preprint DESY 04-126, DESY, Humburg, 2004.

[6] E.L. Saldin, E.A. Schneidmiller and M.V. Yurkov, Nucl. Instrum. and Methods A429(1999)233.

INDUSTRIAL PRODUCTION OF SUPERCONDUCTING 1.3 GHZ ACCELERATOR MODULES AND COMPONENTS FOR FEL APPLICATION

Michael Pekeler, Hanspeter Vogel, Peter vom Stein,
ACCEL Instruments GmbH, Bergisch Gladbach, Germany

Abstract

Daresbury Laboratory contracted ACCEL in April for the delivery of two superconducting 1.3 GHz modules for the R&D phase of their 4GLS [1] project. The modules are delivered with guaranteed performance on cavity voltage and cryogenic losses. The modules contain 2 TESLA [2] type cavities each and are of the design developed at Forschungszentrum Rossendorf [3]. To investigate the capabilities of our cavity treatment and preparation techniques, our infrastructure was further upgraded to allow chemical treatment and high pressure rinsing of TESLA cavities. First test results on TESLA cavities produced for BESSY are very encouraging. 23 MV/m accelerating gradient were achieved in the cold vertical test. In addition 12 power couplers of the TTF III type were produced for DESY and BESSY. The conditioning of those couplers was performed at DESY in a very short time of approximately 50 hours demonstrating our high quality surface treatment capabilities.

SRF BI-CAVITY MODULES

The superconducting bi-cavity modules (s. fig.1) are optimized for operation in cw mode with moderate beam currents. The module design has been developed at Forschungszentrum Rossendorf and is used under a license agreement. ACCEL performs beside the module integration the whole cavity manufacturing and preparation including guaranteed performance values (s. tab.1). Each module is equipped with two TESLA type cavities, which run at 2 K in superfluid helium. Both cavities are mechanical coupled to a rigid string, which improves the stiffness against microphonic oscillations. The diameter of the two phase helium line connection to the helium tank is increased compared to the TESLA design to improve the performance with high dynamic rf losses.

RF frequency	1300 MHz
Operating temperature	2 K
Accelerating gradient	15 MV/m guaranteed 20 MV/m goal
Q_0 @ 15 MV/m	$5x10^9$
Rf power per coupler	8 kW cw
Stand by losses	<15 W
Length (flange to flange)	3.26 m

Table 1: Basic parameters srf bi-cavity module

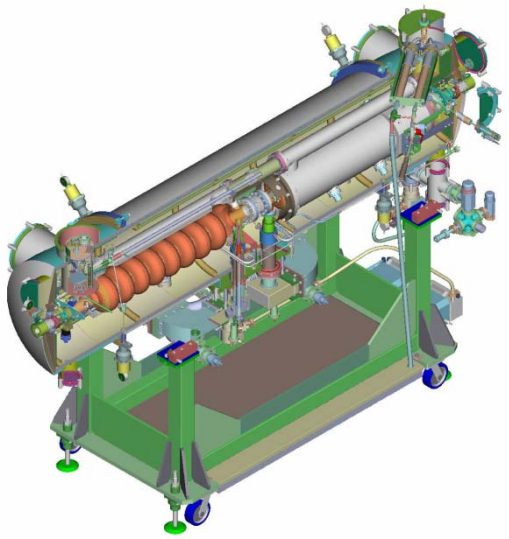

Figure 1: SRF bi-cavity module (courtesy FZ-Rossendorf)

The power capability of the rf input coupler is approx. 10 kW cw per cavity. The thermal shield of the module is cooled by liquid nitrogen at atmospheric pressure. The magnetic shielding is provided by a mu-metal shield housed at the inner side of the vacuum tank.

TESLA TYPE CAVITIES AND COUPLERS

Two 1.3 GHz TESLA cavities have been prepared at ACCEL for vertical test so far. The preparation including tuning to field flatness was done this spring. Figure 2 shows one of the cavities during the high pressure rinsing procedure.

Figure 3 and 4 show the results of cavities BE1 and BE2. The RF test was performed at DESY. The two cavities were produced for BESSY for FEL studies. During preparation of the first cavity (BE2) a leak occurred and the cavity needed to be vented and sealed again. In addition, this cavity was shipped under N2 atmosphere whereas the second cavity (BE1) was shipped under vacuum. Shipping under vacuum has the advantage that one only needs to open the all metal valve located at the cavity after pumpout of the insert pump line. Thus there is no risk of contaminating the cavity by dust accumulated in the pumping line.

Figure 2: High pressure rinsing of a nine cell 1300 MHz TESLA cavity at ACCEL.

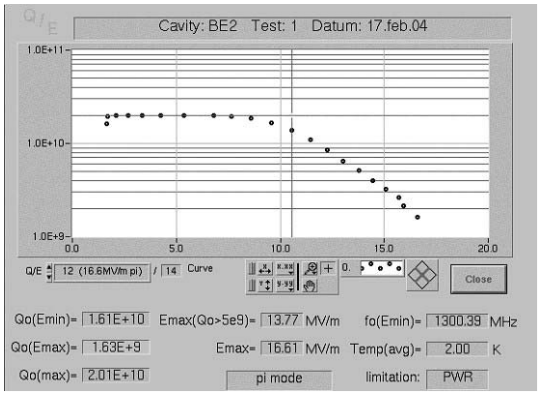

Figure 3: Test result of first prepared TESLA cavity BE1. Field emission was observed above 10 MV/m.

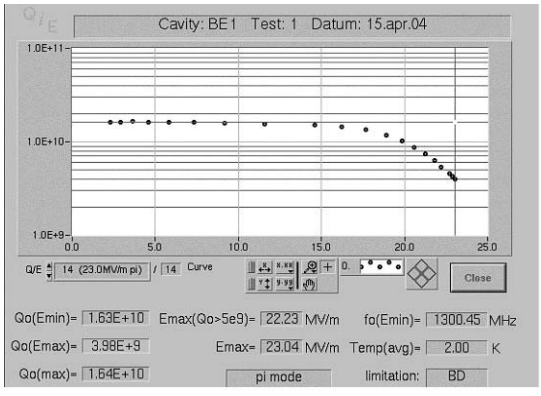

Figure 4: Test result of second prepared TESLA cavity BE2. No field emission was observed. The Q drop at highest fields is without indication of x-rays. The cavity was limited at 23 MV/m by a quench.

Cavity BE1 is now at ACCEL for the helium vessel welding. After that they will be prepared at ACCEL for horizontal test. The needed input power couplers of the TTF III style were produced also at ACCEL and have been conditioned on a test stand at DESY already. After approx. 50 h of conditioning the power couplers reached the design values [4]. The horizontal test of the cavities will be done at BESSY.

Figure 5: TTF III style power coupler

REFERENCES

[1] M.W.Poole et al.,"4GLS: A New Prototype of Fourth Generation Light Source Facility", PAC 2003, Portland, May 2003, p.189

[2] F. Richard ed.,"TESLA TDR", ECFA 2001-209, March 2001

[3] A. Büchner et al.,"The ELBE-Project at Dresden-Rossendorf", EPAC 2000, Vienna, June 2003, p. 732

[4] W. D. Möller, private communication

COLLIMATION SYSTEM FOR THE BESSY FEL*

T. Kamps
Berliner Elektronenspeicherring-Gesellschaft für Synchrotronstrahlung
BESSY, D-12489 Berlin, Germany

Abstract

Beam collimation is an essential element for the successful running of a linear accelerator based free electron laser. The task of the collimation system is to protect the undulator modules against mis-steered beam and dark-current. This is achieved by a set of apertures limiting the succeeding transverse phase space volume and magnetic dogleg structure for the longitudinal phase space. In the following the design of the BESSY FEL collimation system is described together with detailed simulation studies.

MOTIVATION

Experiences from linac driven FEL operation (for example at TTF1 [1]) indicate that beam collimation is essential in order to provide protection of the undulator modules ensuring safe FEL operation.

The collimator section serves as transverse and longitudinal phase space filter which lets particles within a certain energy bandwidth and transverse phase space volume pass. Particles outside this region are blocked and cannot be lost in the undulator modules. In the transverse plane this is achieved by a set of apertures limiting the succeeding transverse phase space volume. In addition the collimator is designed to remove halo and dark-current created and transported through the linac upstream. The various halo sources include the bunch compressor, wakefield generated tails in the linac, mis-matched and mis-steered beam, and particles produced by Coulomb Scattering. In the longitudinal plane off-energy particles are dark current electrons and energy tails produced in the bunch compressors. Dark current is mainly created in the gun and through field emission in the super-conducting cavities [2]. Another important role for the collimator is set during the commissioning of the machine as linac and collimator tune-up dumps are part of the system.

Undulator Protection

The BESSY FEL facility [3] will provide light from three different lines running at different energies. Each FEL line will have its own collimator section directly in front of the undulator modules. The collimator is designed with the high energy beamline running at 2.3 GeV electron beam energy in mind but is without any modifications adaptable for all other FEL lines. The modulators and radiators of the FEL are realized as planar pure permanent magnet undulators. Each undulator is composed of modules with length ranging from 1.6 m to 3.9 m, the total length of the high energy FEL line is 70 m. A FODO lattice is superimposed onto the undulator structure with the quadrupole magnets located at the intersections between the undulator modules. For the present analysis in total 14 undulator modules are taken into account for the simulation studies. The gap between the undulator poles is 10 mm, the beampipe radius is 4 mm. The undulator magnets are made of NdFeB in order to obtain large undulator K parameters. This material is very sensitive to irradiation, especially to the reduced dose deposited by high-energy electrons ($>$ 20 MeV). From studies with NdFeB under electron irradiation [4] the limit for acceptable beam loss in the undulator chamber has been derived. It can be shown that for 1% demagnetization the acceptable beam loss in the vacuum chamber is 300 nC [3]. It is evident that a collimator system together with a fast-acting machine protection system must be included in the FEL design.

Machine Protection System

The three FEL lines will initially operate at a bunch repetition frequency of 1 kHz each. With a bunch charge of 2.5 nC and a beam energy of $\leq$ 2.3 GeV the beam power is 3×6 kW. At no location in the accelerator the structures can withstand the power load for 6 successive incidents, the vacuum chamber wall will be destroyed within 2 ms. The goal of the machine protection system will be to limit the relative beam loss to 10^{-5} of the maximum beam current. This can be achieved by comparing the signals of a series of fast current monitors that allow one to measure the bunch charge at a precision of better than 0.2 pC. Together with two other systems based on NaI beam loss monitors and optical fibers this safety chain of triple redundancy will be able to enable machine operation in case of sudden beam losses.

SYSTEM OVERVIEW

In Fig. 1 the general layout of the collimator section is depicted. After the last accelerating module the beam enters first the transverse collimation section containing a matching quadrupole triplet and the two transverse collimator apertures. From there the beam passes another matching section before going through a dogleg structure made up with two dipole magnets separated by a drift region with a quadrupole triplet. The two energy collimators are located before the first and after the third quadrupole.

* Funded by the Bundesministerium für Bildung und Forschung, the state of Berlin and the Zukunftsfonds Berlin

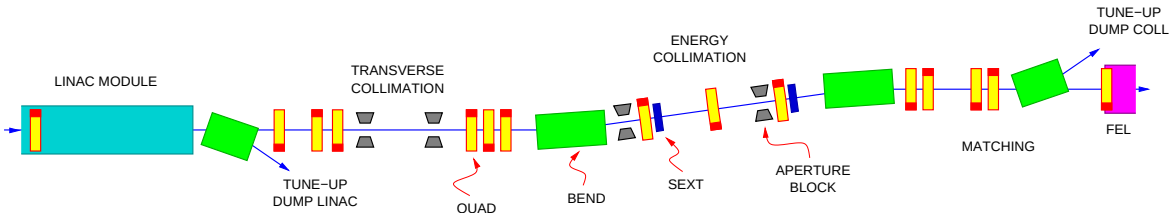

Figure 1: Collimator beamline including the last accelerating module and the beginning of the FEL undulator section.

An additional set of sextupoles is placed close to these quadrupoles. In order to minimize the flux of photons escaping the transverse collimation section the dogleg is placed between undulator and transverse collimation section. The collimator beamline ends with the last matching section preparing the twiss parameters according the specification of the undulator lattice. The section contains two tune-up dump beam exits. One directly after the linac, the other just before the entrance of the undulator. The whole section is less than 43 m long.

Transverse Collimation

For transverse collimation many configurations with aperture slots or holes are possible [5]. The most common solution is to place a thin ($\sim$ 1/2 radiation length) spoiler with a small aperture in front of a long ($\sim$ 20 radiation length) absorber block with a slightly larger aperture. The spoiler produces a large transverse momentum spread in the intercepted particles. The increased transverse momentum spread is converted into a large radial spread which is completely attenuated by the following absorber block. Two or more pairs are located in an optics channel with adequate twiss functions, which could be a FODO lattice with $\pi/2$ phase advance between two pairs.

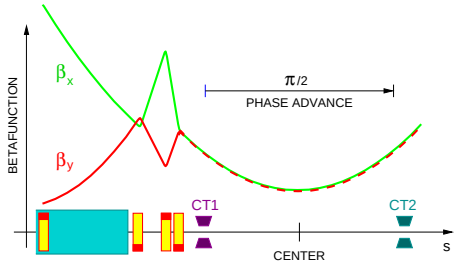

Figure 2: Transverse collimation scheme with two apertures CT1 and CT2.

In order to keep the BESSY FEL collimator system as compact as possible and the total length under 50 m the scheme with two spoiler-absorber pairs was dropped in favor of a setup with two single absorbers. Recent studies for the TTF2 collimator [6] show that with this scheme a high collimation efficiency can be achieved with just two apertures working in parallel for both transverse dimensions. The transverse collimation section contains two absorber blocks separated by $\pi/2$ phase advance. Each block is fitted with a small round aperture limiting the passage for the horizontal and vertical direction at the same position. This scheme requires that the twiss parameters for both dimensions are the same as well as the phase advance. This is achieved by producing a waist with the beam coming from the linac by means of a quadrupole triplet as shown in Fig. 2. The beam enters the transverse collimator from left coming out of the last accelerating section. The quadrupole triplet focuses the beam in both dimension to waist, which is located at the center between the two apertures CT1 and CT2. The horizontal phase space portrait at the center between CT1 and CT2 is illustrated in Fig. 3. The inner

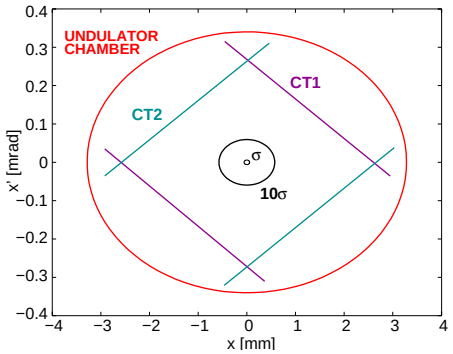

Figure 3: Phase space portrait at the center between CT1 and CT2. Also shown is the inner boundary of the back-transformed undulator vacuum chamber.

boundary of the undulator vacuum chamber is completely shaded by the two apertures. The area inside the parallelogram is the upper limit for the collimator acceptance and is given by the beam stay clear distance Δx_{clear} and the maximum beta function in the undulator β_{max} according to

$$a_{coll} \leq \frac{(r_{pipe} - \Delta x_{clear})^2}{2\beta_{max}} \qquad (1)$$

and for the given case the collimator acceptance is $a_{coll} = 0.3575\ \mu$m. From this the aperture radius can be calculated with $g_{coll} = \sqrt{a_{coll} \cdot L_{coll}}$ where the transverse collimator length L_{coll} is the distance between the two apertures CT1 and CT2 which is equal to the value for the betafunction at these location. The collimator aperture radius is then 2.6 mm. In the following copper is assumed for the absorber material. More studies are underway to compare the

performance for copper and titanium. The length of the absorber is around 10 radiation length and thus 140 mm. In order to minimize wakefield effects and to keep the total block length within limits a step-in plus taper combination was chosen for the transition between gap radius to beampipe radius. At the step-in the aperture changes from 20 mm beam pipe radius to 5 mm at the taper start. The taper length is 200 mm bringing the radius down to the value of 2.6 mm as required at the aperture. The exit face of the collimator block is of the same design. Taper radius and length have been chosen to minimize the transverse wakefield kick on the beam. The same type of absorber blocks are also used in the energy collimation section.

Energy Collimation

Energy collimation is achieved with apertures in a closed dispersion bump created by a magnetic dogleg structure. The scheme is depicted in Fig. 4. The optics consists of

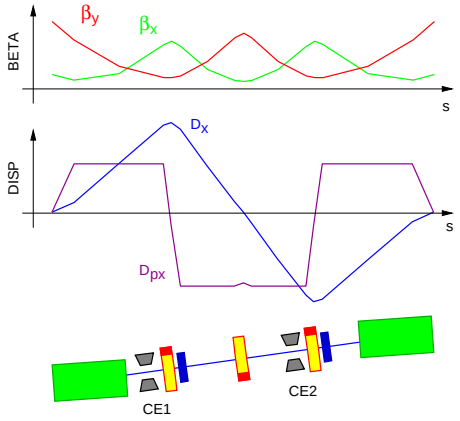

Figure 4: Energy collimation scheme with dogleg bend and two apertures CE1 and CE2.

two bending magnets with 2.5^o bending angle separated by 2π phase advance. The phase advance is realized over the short length of the dogleg of roughly 9 m by a three quadrupoles. Sextupoles are added at locations of high dispersion to reduce orbit deviations at the undulator entrance for off-energy particles. The apertures are also located at points where the electrons are mainly sorted according to their energy deviation close to the outer two quadrupoles. The first aperture CE1 has a slightly larger radius of 3.75 mm providing an energy cut at $\pm$10% for dark-current rejection. The second aperture is of the same kind as the apertures in the transverse collimation part. With a local dispersion function of around 0.1 m the acceptance bandwidth is around 5% energy spread. The total length of the dogleg is 8.8 m producing an orbit offset of 0.36 m.

SIMULATION STUDIES

The twiss parameters in the collimator beamline are plotted in Fig. 5 together with the locations of the various apertures.

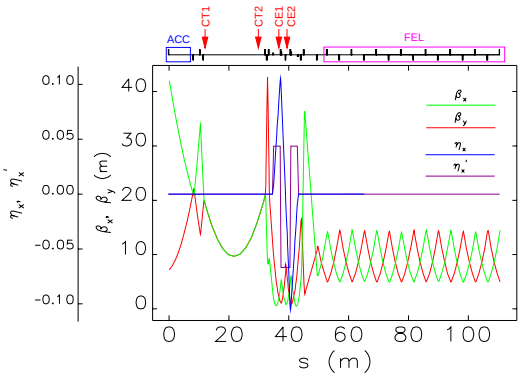

Figure 5: Twiss parameters in the collimator and undulator sections.

Particle losses and and the energy bandwidth of the collimator system have been simulated using the elegant simulation package [7]. In Fig. 6 results for a seed with $5 * 10^5$ particles filling the whole beam pipe with an emittance of 5250 mm mrad with an energy spread of dp/p $= 0.10$. The plots in Fig. 6 show the loss distribution along the beamline and phase space portraits at the end of the undulator beamline. The energy bandwidth of the system is $\pm$4.7%. From these simulations it can be concluded that no primary particle can hit the inner vacuum chamber of the undulator beampipe. The sextupole magnets inside the dogleg keep the orbit deviation for off-energy particles down. Switching these magnets off results in orbit deviation of up to 1 mm for electrons with 5% energy deviation.

Back-reaction on the electron beam in terms of wakefields and coherent synchrotron radiation (CSR) effects have been estimated. The emittance growth due CSR effects in the bending magnets leads to an emittance growth of 0.1% for the vertical and 2% for the horizontal emittance for an input emittance of 1.5 mm mrad and energy spread of 0.01%. The taper angle was chosen such that the resistive and geometric wakefield kicks are equal [8]. This results with a bunch length of $\sigma_t = 1$ ps and gap radius of 2.6 mm to a taper angle of roughly 75 mrad. After the local radius has reached 5 mm a step-in realizes the transition to the nominal beam pipe radius.

Diagnostics

The collimator section is a key component in the linac beamline as it is positioned directly in front of the FEL undulator. All phase space parameters like emittance, bunch length and energy spread can be measured here. For orbit steering some quadrupoles in the beamline will be equipped with stripline BPMs. For tuning of the transverse collimator an OTR station is planned for the location of the beam waist between CT1 and CT2. The energy spread can be measured with another OTR station in the dispersive arm. To study the efficiency of the dark cur-

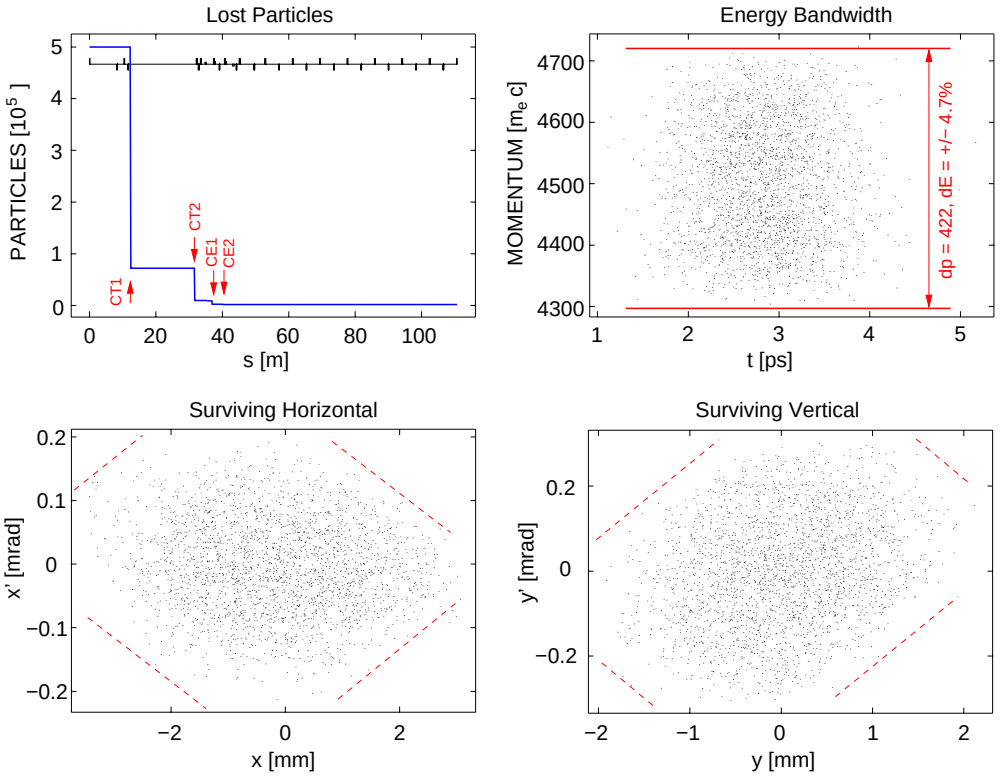

Figure 6: Performance studies for particle losses. Top left: Particle losses along the beamline. Top right: Final energy bandwidth of the particle distribution. Bottom left and right: Horizontal and vertical phase space at the undulator exit.

rent suppression current transformers are located in front of and after the dogleg. Besides that more current transformers will be put at the beginning and the end of the collimator section to monitor overall transmission through the system. The dipole chambers will all have exit windows to enable detection of the synchrotron radiation for beam profile measurements. For commissioning the collimator section is equipped with two tune-up dumps, one straight after the linac enabling commissioning of the linac without the need to bring the beam through the collimator. The other tune-up dump is located just in front of the first FEL undulator module.

CONCLUSION AND OUTLOOK

A collimator system for the BESSY FEL has been discussed. The system is compact and protects the undulator against impact by off-momentum and mis-steered particles. With the next steps damage limits for the collimator material have to be derived. Furthermore the performance for secondary particles will be studied.

ACKNOWLEDGMENTS

The author would like to thank M. Abo-Bakr, N. Golubeva and M. Körfer for their interest and many useful discussions.

REFERENCES

[1] H. Schlarb, “Design and performance of the TESLA Test Facility collimation system,” AIP Conf. Proc. **693** (2004) 209, EPAC’02, Paris, June 2002.

[2] H. Schlarb, “Simulation of dark current transport through the TESLA Test Facility linac,” DESY-M-02-01ZG, EPAC’02, Paris, June 2002.

[3] The BESSY Soft X-ray Free Electron Laser, TDR BESSY March 2004, eds.: D. Krämer, E. Jaeschke, W. Eberhardt, ISBN 3-9809534-0-8, BESSY, Berlin (2004).

[4] T. Bizen, T. Tanaka, Y. Asano, D. E. Kim, J. S. Bak, H. S. Lee and H. Kitamura, “Demagnetization of undulator magnets irradiated high energy electrons,” Nucl. Instrum. Meth. A **467** (2001) 185.

[5] D. R. Walz, A. McFarlane, E. Lewandowski and J. Zabdyr, “Momentum slits, collimators and masks in the SLC,” PAC 1989, Chicago, Ill., March 1989.

[6] V. Balandin, K. Flottmann, N. Golubeva and M. Korfer, “Studies of the collimator system for the TTF phase 2,” DESY-TESLA-2003-17.

[7] M. Borland, “elegant: a flexible SDDS-compliant code for accelerator simulations,” Advanced Photon Source LS-287.

[8] NLC Zeroth Order Design Report, 1996.

HIGH POWER RF CONDITIONING AND MEASUREMENT OF LONGITUDINAL EMITTANCE AT PITZ

J. Bähr*, K. Abrahamyan[&], G. Asova[§], G. Dimitrov[§], H. Grabosch, J. H. Han, M. Krasilnikov, D. Lipka, V. Miltchev, A. Oppelt, D. Pose, B. Petrosyan, S. Riemann, L. Staykov, F. Stephan, DESY, D-15738 Zeuthen, Germany

M. v. Hartrott, D. Richter, BESSY, D-12489 Berlin, Germany

I. Bohnet, J. P. Carneiro, K. Flöttmann, S. Schreiber, DESY, D-22603 Hamburg, Germany

P. Michelato, L. Monaco, D. Sertore, INFN Milano, 20090 Segrate, Italy,

Abstract

In 2003 the PITZ rf gun at Zeuthen has been completely characterized. After the rf conditioning, 3.0 MW peak input power at 10 Hz and a rf pulse length of 0.9 ms have been reached. This corresponds to a gradient of 42 MV/m at the cathode. The goal is to increase the accelerating gradient of the gun and the duty cycle significantly. The motivation is based on the expectation of a remarkably increase in beam quality at higher gradients. A high duty cycle is of advantage for FEL users. The conditioning procedure of a new gun cavity was started in spring 2004. The paper will report about procedure and results of the conditioning. The preparation of an experimental setup for the measurement of the complete longitudinal phase space at about 5 MeV using a streak camera will be finished in summer 2004. Cherenkov light created by Silica aerogel radiators in the dispersive arm of PITZ is transmitted to a streak camera by an optical transmission line. The light distribution of the momentum spectrum is projected onto the entrance slit of the streak camera. The setup will be presented.

INTRODUCTION

The photo injector PITZ at Zeuthen [1] is a dedicated facility for the investigation of rf guns for FELs, i.e. the VUV-FEL and the European XFEL and future linear colliders. The experimental setup consists of a 1.5 cell L-band rf gun with a Cesium-Telluride photo-cathode. A solenoid system is used for space charge compensation. The photocathode laser is capable to generate pulse trains up to 0.8 ms length with a pulse to pulse separation of 1 µs. An extended diagnostics section is used for the experimental investigation of the produced electron beam. The first stage of the PITZ project (PITZ1) was successfully finished in fall 2003 with the complete characterization of the rf gun [2] which was then transferred to the VUV-FEL project of DESY in Hamburg. A schematic of the PITZ1 setup is shown in Fig.1.

In spring 2004 another rf gun was installed at PITZ and a dedicated program of rf conditioning was started. The goals of this high power conditioning are essentially the following:

- maximize the gradient at the cathode
- increase the duty cycle

The maximization of the gradient is aimed to optimize the beam quality, especially for minimization of the transverse emittance. The increase of the duty cycle is useful for the user community of the future FELs. The results of the conditioning program are outlined in the next chapter.

The preparation of the longitudinal emittance measurement is described in the third chapter. The aim is the measurement of momentum spread and bunch length as well as the correlation between them. The principle of the measurement will be outlined with emphasis on optical problems of light collection and imaging.

HIGH POWER RF CONDITIONING OF THE PITZ GUN

Status reached in 2003

The results of the rf conditioning of the rf gun in 2003 are shown in Table 1.

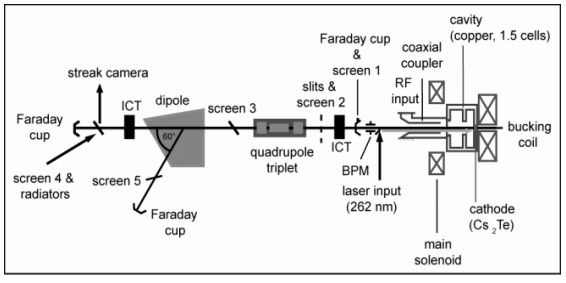

Figure 1: Scheme of the PITZ setup

* juergen.baehr@desy.de
[&] on leave from YERPHI, 375036 Yerevan, Armenia
[§] on leave from INRNE, 1784 Sofia, Bulgaria

Table 1: Results of rf conditioning of the gun achieved in 2003

repetition rate	10 Hz
rf pulse length	0.9 ms
peak power at gun	3 MW
gradient at cathode	42 MV/m
mean power	27 kW
duty cycle	0.9%
maximum momentum	4.7 MeV/c

Program for gun conditioning

A longer term program for the conditioning of rf guns at PITZ was set up, which considers also the availability of a high power klystron and further hardware conditions.

This program consists of four steps:

1) Conditioning up to the status reached for the gun operated in 2003
2) Conditioning to the maximum reachable peak power, rf pulse length, mean power and duty cycle using the currently available 5 MW klystron
3) Replace the 5 MW klystron by a 10 MW klystron, perform conditioning to the maximum reachable parameters of peak power, mean power and duty cycle
4) After performing R&D on the rf system increase the repetition rate (and such the duty cycle and mean power) in a first step to 50 Hz repetition rate for a future RF gun

Status of conditioning using a 5 MW klystron

Concerning most of the essential parameters of last year [3] the status of conditioning was again reached in spring 2004. After that, a dedicated conditioning with three parameter sets was performed. The goals were the maximization of the rf peak power using the 5 MW klystron, the maximization of the rf pulse length, the maximization of the mean rf power and of the duty cycle for the given hardware conditions. The three parameters sets are characterized by a repetition rate of 10 Hz and a length of the rf pulse of 0.5 ms for the first set, by 5 Hz repetition rate and 1.3 ms pulse length for the second set and 10 Hz and 1.0 ms for the third set. The results are shown in Table 2. The high energy edge of the dark current spectrum for a 0.5 ms rf pulse is shown in Fig.2.

Table 2: Results of rf conditioning in 2004

Repetition rate	**10 Hz**	**5Hz**	**10 Hz**
rf pulse length	0.5 ms	1.3 ms	1.0 ms
peak power at gun	4 MW	4 MW	3 MW
mean power	20 kW	26 kW	30 kW
duty cycle	0.5%	0.65 %	1%
maximum momentum	5.17 MeV/c	5.17 MeV/c	–

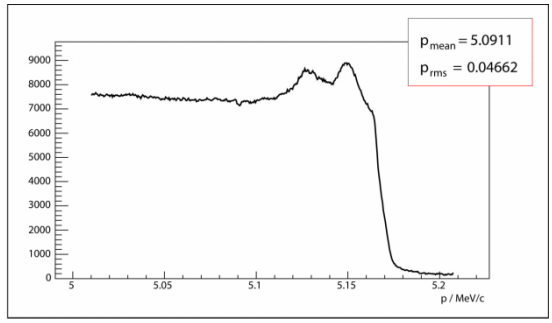

Figure 2: High energy part of dark current spectrum for the parameter set with 0.5 ms rf pulse

The maximum rf peak power, the mean power, the duty cycle and the beam momentum could already be increased compared to 2003. At present, the current water cooling system is a limitation for reaching higher mean power. At the end of 2004 the cooling system will be upgraded to higher cooling power. The program will be continued afterwards.

Dark current

The measured dark currents are about a factor 10 higher for this gun than for the former one. It is assumed that the reason for the higher dark currents is based on a limited copper surface quality of the present gun [4]. The dark current depending on the solenoid current is shown in Fig. 3 for an input power of 4 MW.

Outlook

The conditioning program will be continued. The next essential milestone will be the replacing of the 5-MW-klystron by a 10-MW-klystron in 2005. This will allow an essential increase of the peak power and mean power.

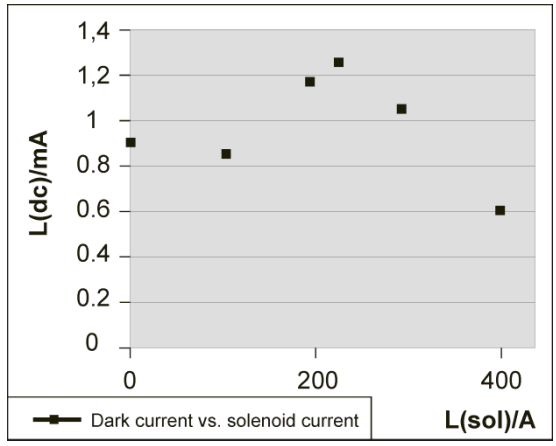

Figure 3: Dark current vs. current of main solenoid for 4 MW input power for the current PITZ gun (prototype #1)

MEASUREMENT OF THE LONGITUDINAL EMITTANCE AT PITZ

The goal is the quasi-simultaneous measurement of momentum, momentum spread and bunch length as well as the correlation between the last two items.

The measurement of momentum and momentum spread will be performed in the usual way [5] in the magnetic spectrometer of PITZ. The measurement of the bunch length will be realized using a streak camera. The length of the electron bunches is measured by transforming the electron bunch in light pulses of same length. This is mainly done using Cherenkov effect, but Optical Transition Radiation (OTR) is also used for cross-check. At a beam energy of less than 5 MeV OTR is less suitable because of the low light output and the spatial emission characteristics which make it difficult to collect the light.

The streak camera to be used for the measurement is a synchroscan camera type C5680 from Hamamatsu [6] with a time resolution of about 2 ps.

The light created by the radiators (Cherenkov, OTR) [5] is transmitted by an Optical Transmission Line (OTL) to the streak camera. For PITZ the length of the OTL is 27 m which is a challenge for the design of the optical system.

Optical transmission line

A simplified schematic of the OTL is shown in Fig. 4:

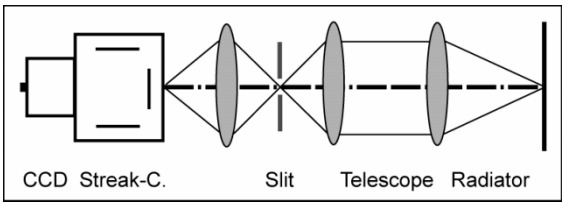

Figure 4: Schematic of an optical transmission line

The light is emitted by the radiator. It is collected by the first lens of the optical chain mainly consisting of several telescopes. The object light distribution is imaged onto the entrance slit of the streak camera. The light distribution in the slit plane is projected onto the photocathode of the streak camera by an internal optical system.

Most of the time during data taking, the streak camera at PITZ is also used for the measurement of the length of the photocathode laser pulse and the corresponding optimization of the temporal profile. The laser emits light in the UV region, therefore the internal optics should have transmission for 262 nm. System 1 in Table 3 is suitable for these conditions but has a small aperture. For measurements of light from radiators a high aperture of the internal lens is needed in some cases. This is realized with system 2 which has the largest aperture, but is not suitable for the measurement of the laser pulse length in the UV region. Furthermore the internal lens should not contribute to the time dispersion. System 3 in Table 3 fulfills these demands but has a rather small aperture. Therefore three different internal optical systems are available at PITZ to match the different demands of the experiment properly.

Table 3: Properties of the internal optical systems of the streak camera

	Name	Spectr. Trans-mission/nm	Eff. F_{no}	Magnification
1	A 1976-01	200..1600	5.0	1
2	A 1974	400...900	1.2	1
3	A 6856 (mirror lens)	200...1600	4	1

There are several demands to the optical transmission line:

- project the image of the light distribution of the radiators onto the entrance slit of the streak camera
- assure, that the readout for the streak camera measurement is possible for screen 5 in the dispersive arm and for screen 4 in the straight section behind the dipole
- match the optical system of the OTL to different input optical systems

Two principle solutions of the optical input system directly behind the radiators are foreseen. The reason is the condition, that one cannot simultaneously image an extended object, for example the object light distribution of the beam momentum spectrum with a width of about 40mm, with a high aperture by a chain of lenses. Therefore we have foreseen two input optical systems, one for high aperture and small object extension using the full Cherenkov cone ("full cone"), the second for imaging the full momentum spectrum with small aperture, i.e. with a small angular section of the Cherenkov cone. Basing on these design considerations and further design principles [7] the OTL was designed. The schematic of the full OTL is shown in Fig. 5.

It includes two branches for the dispersive arm (measurement of the longitudinal emittance) and two branches for measurements at screen 4.

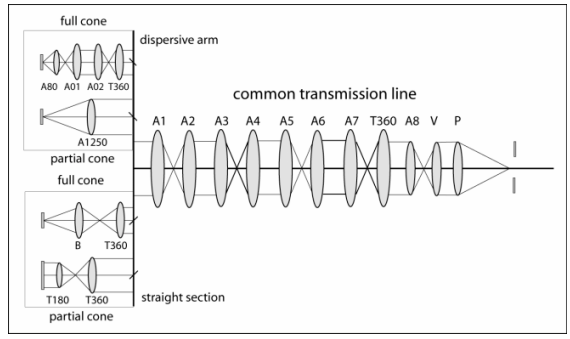

Figure 5: Schematic of the optical transmission line, the abbreviations are presented in Table 4

Table 4: Explanation of abbreviations in Figure 5

Achromats		Photo lenses	
name	focal length/mm	name	data
A80	80	B	Biotar 1.5/75mm
A01, A02	500	V	Visionar 1.6/71mm
A1, A2, A3, A6	2250	P	Pancolar 1.8/50m
A4, A5, A1250	1250	T180	Tessar 4.5/180mm
A7	800	T360	Tessar 4.5/380mm
A8	160	–	———

Special subsystems

Two special subsystems are included in the OTL:

- the Image Rotating System (IRS)
- the Image Turning Box (ITB)

The Image Rotating System is used to rotate the image such that the azimutal direction of the image light distribution of the momentum spectrum matches to the horizontal orientation of the entrance slit of the streak camera. This is needed because the axis of the dispersive arm has an inclination of 60 degrees and consequently the orientation of the light distribution of the momentum spectrum too. The Image Turning Box is used to check whether the Image Rotating System introduces unwanted contributions to fractions of the image distribution in the light propagation direction. The Image Turning Box turns the image by 180 degrees. Measurements with and without the Image Turning Box allow to correct on such unwanted contributions. Besides these two systems, several diagnostics tools are foreseen, for example several illuminated objects which can be moved in a plane corresponding to the object plane. These objects can be used to adjust the OTL and find the low level light image distribution in front of the streak camera slit. The use of an illuminated slit object helps to prove the azimutal orientation of the image of the momentum spectrum light distribution. The elements are mounted in a box containing switchable optical components near to the optical port.

Time dispersion

The optical transmission line mainly consisting of large achromats causes a non-negligible time dispersion [8]. The main sources of the time dispersion are chromatic aberrations of the diffractive systems as could be demonstrated by the use of optical bandpass filters [5], see Fig. 6. For a small bandwidth the time dispersion is negligible. The use of the internal optical system of the streak camera consisting of reflective optics results in a decrease of the measured bunch length by 3 ps. A R&D project which aims in replacing refractive optics by reflective optics is ongoing.

Status of the project

The optical transmission line will be mounted and adjusted in September 2004. The first measurements with electron beam will start end of September 2004.

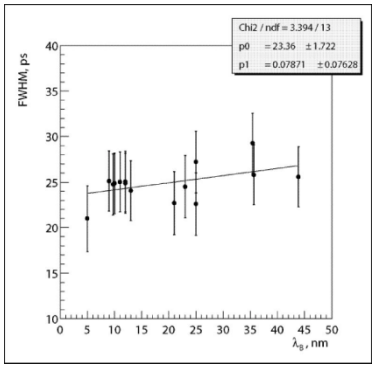

Fig. 6: Optical pulse length vs. filter bandwidth

OUTLOOK

Besides the conditioning program, the preparation of the longitudinal emittance measurement, and a complex measurement program for the characterization of the rf gun currently in use [9], an essential upgrade of PITZ, the PITZ2 project [10], is in preparation. The main goal is studying the principle of conserving small emittance to higher beam energy and further improving the emittance generated in the gun. A minimal version of PITZ2 will be commissioned in the beginning of 2005. The measurement of the longitudinal emittance is foreseen at PITZ2 in the low energy and high energy section at several ports basing on the principles explained in this paper.

REFERENCES

[1] F. Stephan et al., Photo injector test facility under construction at DESY Zeuthen, FEL'00, Durham, September 2000.

[2] M.Krasilnikov et al., Optimizing the electron source for the VUV-FEL, EPAC'04, Lucerne, July 2004.

[3] J. Bähr et al., Behavior of the TTF2 RF gun with long pulses and high repetition rates, TESLA 203-33

[4] J. H. Han et al., Conditioning and high power tests of the RF guns at PITZ, EPAC'04, Lucerne,July 2004.

[5] D. Lipka, Untersuchungen zum longitudinalen Phasenraum an einem Photodetektor für minimale Strahlemittanz, PhD thesis, Humboldt University Berlin, May 2004

[6] Hamamatsu Photonics K.K., Systems Division, 812 Joko-cho, Hamamatsu city, 431-9196 Japan

[7] J. Bähr et al., Optical transmission system for streak camera measurements, DIPAC'03, Mainz, May2003.

[8] J. Bähr et al., Measurement of the longitudinal phase space at the Photo Injector Test Facility at DESY Zeuthen, FEL'03, Tsukuba, September 2003.

[9] F. Stephan et al., Recent results and perspectives of the low emittance photo injector at PITZ, FEL'04, Trieste, September 2004.

[10] A. Oppelt et al., Future plans at the Photo Injector Test Facility at DESY Zeuthen, FEL'03, Tsukuba, September 2003.

AN ELECTROMAGNETIC UNDULATOR FOR THE FAR INFRARED AT ELBE

Th. Dekorsy, K. Fahmy, E. Grosse, P. Michel, W. Seidel, A.Wolf, R. Wünsch
FZ-Rossendorf, Dresden, Germany

Abstract

The first lasing in the mid infrared (IR) at the ELBE FEL [1, 2] allows us to specify the parameters of an additional undulator for longer wavelengths to complement the U27 undulator which is useful up to about 25 microns at most. In the longer wavelength range FELs constitute a unique radiation source with appealing properties. Radiation quanta in this range are appropriate for the low-energy spectroscopy of various interesting modes in solid-state quantum-structures as well as in complex biological systems (e. g. DNA molecules).

We envisage an electromagnetic undulator with a period of roughly 12 cm. Using the electron beam of ELBE, IR light from 15 to 150 microns and beyond can be produced. To keep the transverse beam extension small, the IR beam is to be guided by a partial waveguide. An appropriate bifocal resonator mirror minimizes the mode coupling losses at the exit of the waveguide. Detailed calculations and computer simulations predict an outcoupled laser power of roughly 15 W at 150 microns which will be transported to experimental stations. The maximum power is expected to be 35 W at wavelengths between 40 and 90 μm.

WHY ANOTHER UNDULATOR?

At present the U27 undulator at the radiation source ELBE is producing IR light between 16 and 22 μm at electron energies around 16 MeV. Soon a second cryostat with 18 more accelerator cells will be installed. The higher electron energy (up to 40 MeV) extends the range down to 3 μm. To extend the range to the far infrared ($\lambda \leq 150\,\mu$m) another undulator with a larger period is envisaged.

In the far infrared a FEL constitutes a unique radiation source. Radiation quanta with this energy (10 - 100 meV, 2 - 20 THz) are appropriate for the spectroscopy of low-energy elementary and collective excitations. Such excitations are observed in solid-state quantum-structures and in complex biomolecules as well. Their study establishes the basis for understanding complex phenomena in solids and liquids and for elucidating processes in biological material. Technological and medical innovations are the long-term output of such investigation.

ITS PARAMETERS

To produce radiation in the THz region by means of the ELBE beam an undulator with a period λ_u of several centimeters is needed. To avoid the use of electron energies below 20 MeV, where the energy spread is larger than 0.3%, we propose an undulator period of λ_u= 12 cm which should preferably be made of electromagnets with an undulator gap of 18 mm. To get a sufficiently high single-pass gain 30-40 undulator periods are necessary resulting in a total undulator length of 4-5 m. The design of the electron beam line requires an asymmetric installation of this long undulator. Its middle is located roughly 1 m downstream from the resonator center. The maximum undulator parameter of $K_{\rm rms} \approx 2.5$ corresponds to a field amplitude of 0.3 T on the undulator axis.

Fig. 1 shows the wavelength range covered by such an FEL. It slightly overlaps the range of the U27 undulator [2] and allows to produce light up to 200 μm. Above 150 μm the diffraction losses in the presently designed IR beam line diminishes the power available in the user laboratories considerably.

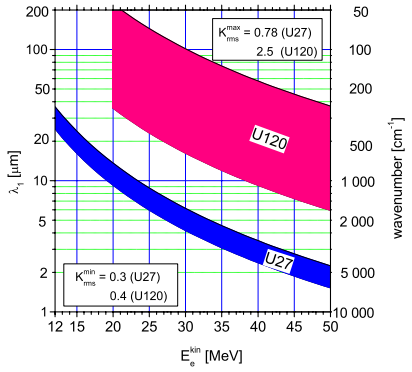

Figure 1: Wavelength ranges of the existing U27 and the planned U120 undulator of ELBE as a function of the kinetic electron energy E_e^{kin}. The colored areas indicate the wavelength λ_1 of the first (fundamental) harmonic.

Above roughly 50 μm the diffraction of the IR beam has seriously to be taken into account. It increases the beam radius in the resonator and the beam line and reduces the coupling with the electron beam in the undulator (filling factor). Big resonator mirrors, large diffraction losses and a small laser gain are the result. The long resonator (11.53 m) and the long undulator (4-5 m) make it even more difficult. That is why we propose a vertical beam compression by means of a rectangular waveguide spanning from the undulator entrance to the downstream resonator mirror (see Fig. 2). It should be 10 mm high. To avoid ohmic losses in the side walls the waveguide has to be broad enough to al-

low a free beam propagation in the horizontal direction [4]. The free propagation on the upstream side of the resonator simplifies the passage through the dipole and quadrupole magnets and provides an approximately round beam profile at the outcoupling mirror (M1). The downstream mirror (M2) has to be cylindrical. The proposed setup is similar to that used at the FELIX facility [5]. Alternatively a complete waveguide without mode-coupling losses but with a rather asymmetric outcoupled beam profile can be used.

To minimize the optical beam cross section in the undulator we propose an asymmetric resonator with the horizontal beam waist located in the undulator center and a Rayleigh length of half the undulator length (≈ 2.5 m). The proposed height of the waveguide and the resulting pole gap are large enough for the electron beam and allows a sufficiently large magnetic field on the axis (0.3 T) at a reasonable current in the undulator coils.

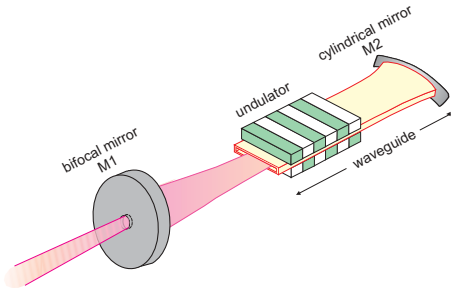

Figure 2: Optical mode compression by means of a resonator with partial waveguide.

While the horizontal radii of curvature are solely determined by the Rayleigh length and the waist position the vertical curvature of M1 can be used to minimize the mode conversion losses at the waveguide entrance. In general the optimum curvature depends on the wavelength (black line in Fig. 3).

Calculations using the code GLAD [6] have shown that a radius of curvature which is equal to the distance between resonator mirror and waveguide entrance (407 cm, far-field limit, red curve in Fig. 3) minimizes the mode conversion losses at $\lambda > 30\,\mu m$. Here, the losses per resonator pass do not exceed 7%. At shorter wavelengths the losses grow up to 12% per pass at 20 μm. For short electron pulses the gain exceeds this value. Using a larger radius of curvature (500 cm, blue curve) the losses can be reduced to 7%. But this mirror has an advantage only between 15 and 25 μm.

The parameters of electron beam, undulator and resonator are summarized in Table 1. The beam parameters are close to the actual beam parameters of ELBE. Putting into operation the superconducting RF-gun [3] the energy range can be extended to roughly 50 MeV.

EXPECTED GAIN AND POWER

Using the parameters of Table 1 we have calculated the single-pass gain (Fig. 4) and the outcoupled average laser

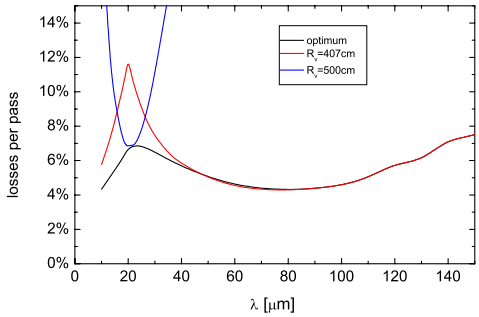

Figure 3: Resonator round-trip losses as a function of the wavelength λ calculated for various vertical radii of curvature R_v. The black line indicates the minimum losses while the red and blue lines stand for definite radii of curvature. Additionally to the mode conversion the absorption (2 x 0.7%) on the mirror surfaces has been taken into account.

Electron beam	
Kinetic energy	(10) 20-45 (50) MeV
Pulse charge	70 pC
Energy spread	60 keV
Norm. transv. emittance	15 mm mrad
Undulator	
Undulator period	12 cm
Number of periods	40
Magnetic field amplitude on axis	≤ 0.3 T
Undulator parameter (K_{rms})	≤ 2.5
Pole gap	18 mm
Resonator	
Length	1153 cm
Horizontal Rayleigh length	2.5 m
Horizontal radii of curvature	M1: 768.9 cm, M2: 607.7 cm
Vertical radii of curvature	M1: 407 cm M2: ∞
Waveguide height (internal)	10 mm
Waveguide length	746 cm

Table 1: Parameters of electron beam, undulator and resonator

power [7] (Fig. 5). Changing the rms pulse length from 1 to 4 ps the λ of maximum gain is shifted from 40 μm (45%) to 150 μm (30%). Notice that Fig. 4 displays the gain maximum with respect to resonator desynchronization. Maximum power is obtained at a smaller desynchronization where the gain is considerably smaller. That is why the maximum gain should clearly exceed the losses in the resonator. The maximum average outcoupled power is predicted to be approximately 35 W independently of the

electron pulse length. The wavelength with the highest power varies from 12 μm at 1 ps to 70 μm at 4 ps. The pronounced drop of average power around 20 μm is caused by the large mode-coupling losses in this region (see Fig. 3).

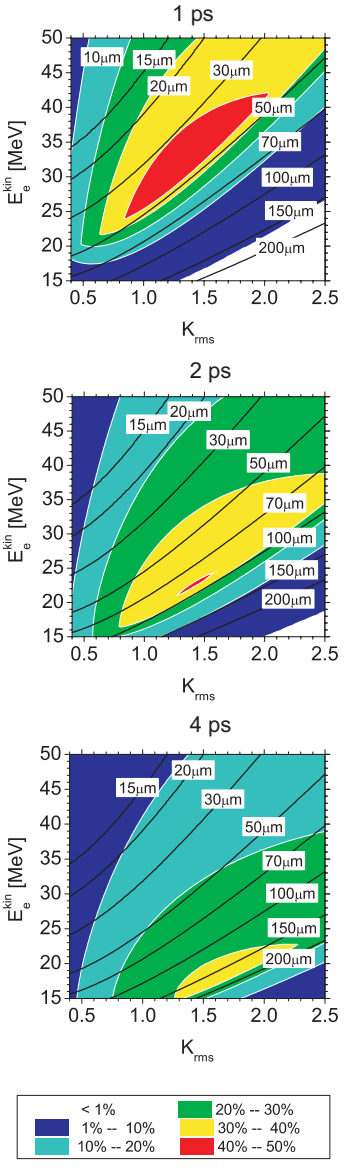

Figure 4: Laser gain predicted for 1, 2 and 4 ps (rms) electron pulses of ELBE as a function of undulator parameter $K_{\rm rms}$ and kinetic electron energy $E_{\rm e}^{\rm kin}$. Calculation for the parameters of Table 1 and optimum cavity desynchronization.

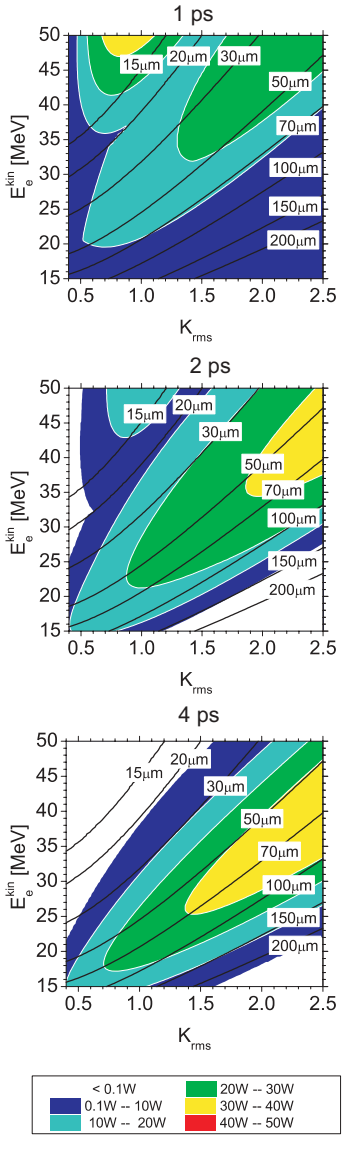

Figure 5: Maximum outcoupled average laser power predicted for 1, 2 and 4 ps (rms) electron pulses of ELBE as a function of undulator parameter $K_{\rm rms}$ and kinetic electron energy $E_{\rm e}^{\rm kin}$. Calculation for the parameters of Table 1.

REFERENCES

[1] F. Gabriel et al., Nucl. Instr. Meth. B161-163 (2000) 1143; http://www.fz-rossendorf.de/ELBE.

[2] P. Michel et al., these proceedings; http://www.fz-rossendorf.de/FELBE.

[3] D. Janssen et al., Nucl. Instr. Meth. A507 (2003) 314.

[4] L.R. Elias and J. Gallardo, Appl. Phys. B31 (1983) 229.

[5] http://www.rijnh.nl.

[6] GLAD, Applied Optics Research, Woodland, WA 98674, USA.

[7] S.V. Benson, CEBAF TN#94-065.

BUNCH LENGTH MEASUREMENTS AT THE SLS LINAC USING ELECTRO OPTICAL SAMPLING

Bernd Steffen, Sara Casalbuoni, Peter Schmüser, Stefan Simrock (DESY, Hamburg)
Manfred Tonutti, Axel Winter (RWTH Aachen)
Timo Korhonen, Thomas Schilcher, Volker Schlott, Hans Sigg, Daniel Suetterlin (PSI, Villigen)

Abstract

An electro optical sampling experiment has been carried out at the 100 MeV electron linac of the Swiss Light Source (SLS). Coherent transition radiation produced by the relativistic electron bunches was focused by parabolic mirrors onto an optically active ZnTe crystal. The induced birefringence was sampled with ultrashort titanium sapphire laser pulses. The laser repetition frequency of 81 MHz was phase-locked to the 500 MHz radio frequency of the linac with a relative timing jitter of less than 40 fs. The minimum measured bunch length amounts to 3.0 ps (FWHM) with an estimated resolution of 300 fs (rms).

INTRODUCTION

Bunch length measurements in the 100 femtosecond regime are of high interest for VUV and X ray free electron lasers and for the planned femto-slicing experiments at the Swiss Light Source and BESSY. The technique of electro-optical sampling (EOS) provides the possibility to measure the longitudinal charge distribution with very high resolution, determined by the width of the optical laser pulse, the relative time jitter between electron bunch and laser pulse and the dispersion of the electric field pulse in the nonlinear optical crystal. A 15 fs titanium-sapphire (Ti:Sa) laser is used to sample the birefringence which is induced in a nonlinear optical crystal by the co-moving electric field of a relativistic electron bunch or, alternatively, by the coherent transition radiation (CTR) generated by the bunch. The initial linear polarization of the laser pulse is converted into a slightly elliptical polarization which is then converted into an intensity modulation. By shifting the timing of the laser pulse relative to the bunch in sub-picosecond steps the time profile is obtained by sampling over many bunches. Previous accelerator-related EOS experiments have been carried out at the infrared free electron laser FELIX [1], Fermilab, the TESLA Test Facility TTF [2] and SLAC. Here we report on the successful continuation of our TTF experiments at the 100 MeV injection linac of the SLS.

EXPERIMENTAL SETUP

A schematic drawing of the experimental setup inside the tunnel of the SLS linac is shown in figure 1. Transition radiation is produced at a screen made from a 380 μm thick silicon wafer with a 1 μm thick aluminum coating. Both optical and coherent transition radiation are coupled out of the beam pipe through a 60 mm diameter quartz window. The coherent transition radiation (CTR) is focused onto the

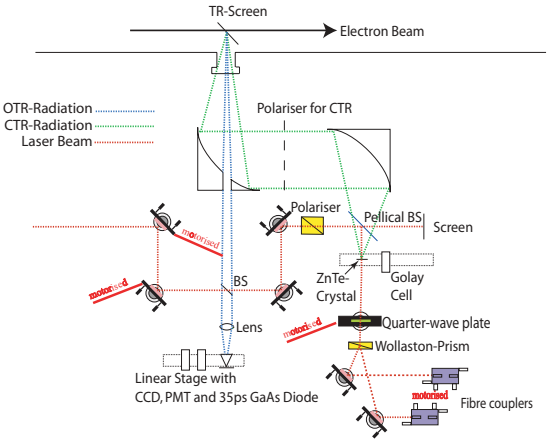

Figure 1: Scheme of the setup inside the linac area.

ZnTe crystal by two parabolic copper mirrors with focal lengths of 200 mm. The optical transition radiation (OTR), having only a small divergence of $\approx \pm\frac{1}{\gamma} = \pm 10\,\mathrm{mrad}$, passes a 12 mm hole in the first mirror and is focused onto a photomultiplier which registers also the laser pulses and allows to adjust the temporal overlap of the Ti:Sa pulses and the electron bunches with sub-nanosecond precision.

The Ti:Sa laser has a pulse width of 15 fs, a central wavelength of 800 nm and a bandwidth of 65 nm. It is mounted on a vibration-damped optical table in the technical gallery of the SLS. The laser beam is guided into the linac bunker by a 15 m long optical transfer line equipped with five mirrors and two lenses ($f = 4$ m) which image the Ti:Sa laser onto the ZnTe crystal. The dispersion in the lenses stretches the laser pulses to about 120 fs FWHM. Since the expected length of the linac bunches is far longer, no attempt was made to compensate for the pulse lengthening. The beam transfer line has proven very stable, neither short-term nor long-term motions of the laser spot position inside the linac tunnel were observed.

A simplified view of the signal detection scheme is shown in figure 2. ZnTe is optically isotropic at vanishing field but acquires a birefringence in the presence of a strong electric field. The crystal is cut in the (110) plane with the the crystallographic (-1,1,0) axis oriented horizontally. Both the CTR and the Ti:Sa pulse are polarized horizontally. The induced birefringence can be described by a refractive index ellipse whose large axis is rotated by 45° with respect to the horizontal axis. The laser polarisation

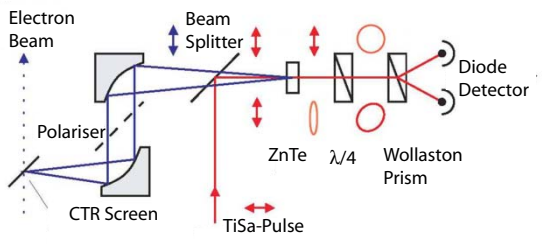

Figure 2: Simplified view of the signal detection using a quarter-wave plate, Wollaston prism and a balanced diode detector. The laser and CTR radiation are polarized horizontally, parallel to the (-1,1,0) axis of the ZnTe crystal.

components along the two main axes of the index ellipse acquire a phase shift difference when passing the crystal of $\Gamma \propto r_{41} E_{CTR}$ where r_{41} is the electro optical coefficient of ZnTe and E_{CTR} the electric field of the CTR pulse. Behind the ZnTe crystal the laser pulse will then be elliptically polarized. The most sensitive method to measure this ellipticity is to pass the beam through a quarter wave plate, transforming the slight elliptic polarisation into a slightly perturbed circular polarisation, and then through a Wollaston prism, which serves for a spatial separation of the two orthogonal polarisation components. These are then coupled into optical multimode fibers and guided to a balanced diode detector located outside the linac tunnel. In the case of coincidence between CTR pulse and laser pulse the balanced detector signal is proportional to $\sin\Gamma$ and thereby roughly proportional to the electric field of the CTR pulse while without CTR the balanced detector signal will vanish.

The EOS technique as a tool for ultra precise longitudinal bunch diagnostics depends critically on the synchronisation between the femtosecond laser pulses and the radio frequency (RF) of the linac. This proved to be a considerable challenge since the linac RF of 500 MHz has no subharmonics close to the 81 MHz repetition frequency of the Ti:Sa laser. The synchronisation scheme is described in [3, 4].

An rms time jitter of $\sigma_t = 35$ fs was reached in the synchronisation. However, this does not include the relative jitter between the electron bunches and the linac RF.

DATA ANALYSIS AND RESULTS

Transfer function for coherent transition radiation

The CTR produced by the SLS linac bunches ranges up to 500 GHz. Diffraction has strongly limiting effects on the transfer of this radiation to the ZnTe crystal. The optics code ZEMAX was used to compute the frequency-dependent transmission of the radiation from the CTR screen to the ZnTe crystal. The finite radius of the CTR screen ($r = 23$ mm) and the aperture limitations provided

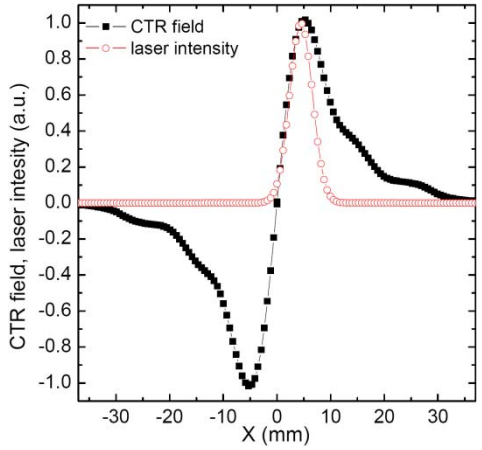

Figure 3: CTR electric field distribution at the crystal for 100 GHz. The center of the crystal, and so the laser spot, has been shifted to the position where a movable Golay cell has registered the maximum signal.

by the vacuum window ($r = 30$ mm) and the parabolic mirrors ($r \approx 130$ mm) were taken into account. The finite laser spot size ($\sigma = 2$ mm) is responsible for the strong suppression of frequencies below 50 GHz. The spatial intensity distribution of the laser pulse and the CTR electric field ($f = 100$ GHz) on the ZnTe crystal is shown in figure 3. The center of the ZnTe has been moved to a position where a movable Golay cell has registered the maximum signal.

Data acquisition

The linac was operated with 3.125 Hz bunch repetition frequency. After having established the coarse time overlap between the bunch arrival at the CTR screen and the Ti:Sa laser by means of the photomultiplier, a time interval of ± 500 ps was scanned in ps steps to find a coincidence signal in the balanced detector. This turned out to be straightforward. Once this signal was found, a narrow interval was scanned in 200 fs steps. At each time step the photomultiplier signal as well as the balanced detector signal for 10 consecutive bunches were recorded by a 7 GHz digital oscilloscope and stored in the internal memory of the scope. The first EO-signal seen is shown in figure 4. The signal of the balanced detector is plotted in figure 5 (top) as a function of the time delay. One observes a peak of several ps width with undershoots at the front and rear end due to the suppression of the low frequency components of the CTR signal.

Determination of the longitudinal bunch profile

Starting from an assumed shape of the bunch a Fourier transformation was made and the CTR transfer function applied. The resulting frequency spectrum was Fourier back-transformed and compared to the measured signal. A sin-

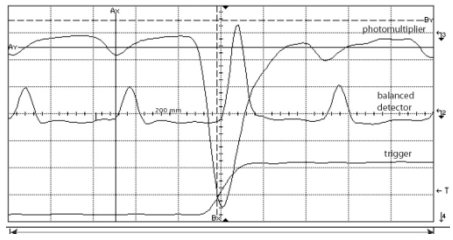

Figure 4: Oscilloscope screenshot with electro-optic signal. Top trace: Signal of the timing photomultiplier with laser pulses; Center trace: Signal of the balanced diode detector; Bottom trace: Linac trigger

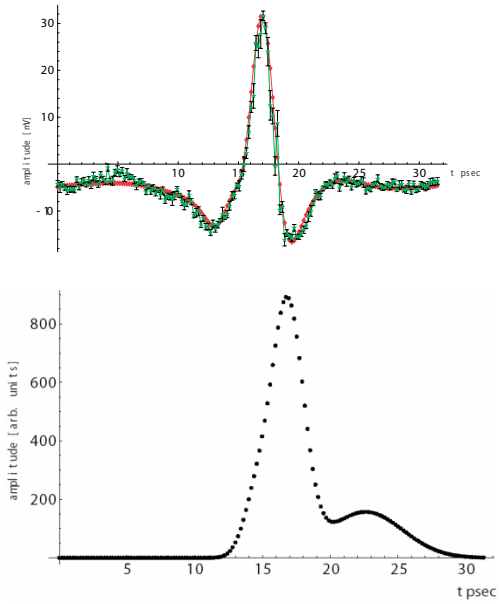

Figure 5: Top: The measured time profile of the CTR pulse (green with error bars) and the fit obtained with bunch profile composed of three Gaussians (see below). Bottom: Assumed bunch profile composed of three Gaussians whose parameters are optimized to obtain the best fit of the measured profile (red curve in the upper plot).

gle Gaussian for the bunch shape turned out to be inadequate. The best fit was found for an assumed bunch profile composed of three Gaussians of different amplitude, position and width, see figure 5 (bottom). At optimum bunch compression the FWHM of the electron bunch is 3.0 ps. The overall time resolution of this experiment can be estimated by measuring the amplitude fluctuation of the balanced detector signal when the laser pulse is put on the rising edge of the CTR pulse. The amplitude jitter is then dominated by the arrival time jitter of the electron bunches. Assuming a linear dependence between time and amplitude on the flank of the signal, we derive an overall timing jitter of $\sigma_t = 300$ fs over a time span of 5 minutes. Here all sources of time jitter are included. The reproducibility was tested by two consecutive measurements with positive and negative time steps but otherwise identical parameters (figure 6). No significant difference between the measurements was seen, suggesting a high reproducibility over the time of 9 minutes needed to take the two measurements.

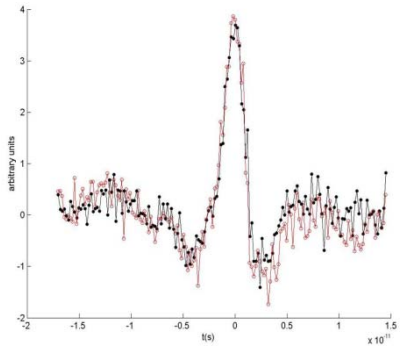

Figure 6: Two measurements taken directly after one another with positive and negative phase steps respectively.

CONCLUSION AND OUTLOOK

The electro-optic technique has been successfully applied for bunch length measurements at the SLS linac. The synchronisation accuracy of the 81 MHz laser repetition frequency to the 500 MHz linac RF was better than 40 fs. Further improvements appear possible by employing a digital control scheme. This is planned for the electro optical sampling experiment at the DESY VUV FEL. Here the ZnTe crystal will be mounted inside the beam pipe of the linac to permit a direct measurement of the bunch field. This has the further advantage that the EOS measurements no longer need a transition radiation screen intercepting the electron beam. Hence longitudinal bunch diagnostics will be possible in parallel to FEL operation.

REFERENCES

[1] D. Oepts et. al. Picosecond electronbunch length measurement using an electro-optic sensor. In *Proceedings of the 21st International FEL Conference*, Hamburg, 1999.

[2] M. Brunken et. al. *Electro-Optic Sampling at the TESLA Test Accelerator: Experimental Setup and First Results*. DESY, 2003. TESLA Report 2003-11.

[3] A. Winter et al. Bunch length measurements at the SLS linac using electro optical techniques. In *Proceedings of the EPAC'04*, Lucerne, 2004.

[4] A. Winter. Bunch length measurements using electro-optical sampling at the SLS linac. Master's thesis, DESY, 2004. DESY-THESIS-2004-027.

LONGITUDINAL BUNCH SHAPE DIAGNOSTICS WITH COHERENT RADIATION AND A TRANSVERSE DEFLECTING CAVITY AT TTF2

L. Fröhlich, O. Grimm*, K. Klose, M. Nagl, O. Peters, J. Rossbach, H. Schlarb
DESY, Hamburg, Germany
M. Ross, T.J. Smith, D. McCormick, P.J. Emma
SLAC, Menlo Park, USA

Abstract

At the DESY TTF2 linear accelerator three special techniques to characterize the longitudinal charge distribution of the electron bunches that drive the free-electron laser are currently under study: electro-optical sampling, far-infrared spectral analysis of coherent radiation and the use of a transverse deflecting cavity to streak the bunch. The principles and implementations of the latter two are described in this paper. Details on electro-optical sampling can be found in [1].

INTRODUCTION

The VUV-FEL at DESY, Hamburg, will require novel techniques to characterize the longitudinal charge distribution of the electron bunches that drive the free-electron laser. Conventional methods, e.g. streak cameras, are inadequate due to both the short bunch lengths of the linac and the high sensitivity of the lasing process to spikes in the charge distribution which therefore need to be known with high resolution. Three techniques are currently investigated at TTF2:

- Analysis of the far-infrared spectrum of synchrotron, transition, diffraction and undulator radiation. At wavelengths comparable to or longer than the bunch length or a particular longitudinal feature of the bunch, the spectrum will be modified by coherent effects.
- Streaking the bunch with a transverse deflecting RF structure. The longitudinal profile is converted into transverse space and thus becomes observable with a camera on, e.g., an optical transition radiation screen.
- Measuring the electric field strength through electro-optical sampling. The interaction of a laser pulse much shorter than the electron bunch with the bunch electric field in a nonlinear crystal gives rise to a detectable effect on the laser polarization (see [1] for details).

The first technique, working in the frequency domain, has no requirements on timing or triggering precision, but the bunch shape is accessible only through an ambiguous inversion process, whereas the latter two techniques are directly sensitive to the longitudinal charge distribution and need precise timing.

* Corresponding author. E-Mail: oliver.grimm@desy.de

A new method, consisting essentially of the generation of an optical replica of the longitudinal bunch shape and then a two-dimensional measurement of this replica in frequency and time domain simultaneously, has recently been proposed in [2].

FAR-INFRARED ANALYSIS OF COHERENT RADIATION

Analysis principle

The bunch shape is imprinted on the radiation spectrum $\mathrm{d}U/\mathrm{d}\lambda$ through the form factor $F(\lambda)$,

$$\frac{\mathrm{d}U}{\mathrm{d}\lambda} = \left(\frac{\mathrm{d}U}{\mathrm{d}\lambda}\right)_0 \left(N + N(N-1)\left|F(\lambda)\right|^2\right), \qquad (1)$$

where $(\mathrm{d}U/\mathrm{d}\lambda)_0$ is the emission spectrum of one single electron, N is the total number of electrons and the form factor is the Fourier transform of the normalized longitudinal charge distribution $S(z)$ ($\int_{-\infty}^{\infty} S(z)\,\mathrm{d}z = 1$),

$$F(\lambda) = \int_{-\infty}^{\infty} S(z) \exp\left(\frac{-2\pi\mathrm{i}}{\lambda} z\right) \mathrm{d}z. \qquad (2)$$

The basic assumption in the derivation of these equations is that each electron generates a time-dependent electric field at a given position that is the same for all electrons except a time delay (corresponding to a spacial distance), i.e. $\vec{E}_i(t) = \vec{E}_0(t + \Delta t_i)$.[1]

Measurement of the total spectrum and knowledge of the number of electrons and the single-electron spectrum then gives access to the modulus of the form factor. The final step of inverse Fourier transforming this to arrive at the bunch shape requires knowledge of the phase of the Fourier transform. The phase is not completely arbitrary but also not unambiguously determined by the modulus [3], therefore a full bunch shape reconstruction is impossible. The technique of Kramers-Kronig analysis, however, allows to retrieve some of the missing phase information. If one writes for the complex form factor $F(\omega) = |F(\omega)| \exp(\mathrm{i}\psi(\omega))$, with ω the angular frequency, then

$$\psi(\omega) = -\frac{2\omega}{\pi} \int_0^{\infty} \frac{\ln(|F(x)|/|F(\omega)|)}{x^2 - \omega^2} \mathrm{d}x \qquad (3)$$

[1] This limits the allowable transverse size: particles offset from the centre will contribute with a time delay just as particles further behind, thus washing out spacial structures. Additionally, the emission spectrum generally changes with angle, also limiting the tolerable transverse size.

is the minimum phase value consistent with the measured modulus [4]. Application of the Kramers-Kronig analysis requires knowledge of the form factor modulus from zero to infinite frequency, thus an extrapolation of measured data. Some extrapolation has been suggested in [4], but experiences from the first run of TTF show that the results are quite sensitive to these extrapolations and detailed studies of their effects are necessary [5].

Currently, the opposite way is pursued: simulations are performed to calculate the spectrum for some expected bunch shapes and then compared to the measurements. An example, referring to the synchrotron radiation beamline described in the next section, where the actual magnetic field of the fourth BC2 magnet, the vacuum chamber cut-off (see [6]) and the form factor for three bunch shapes have been taken into account is shown in Fig. 1. The spectrum is averaged over the clear aperture of the window. A parametrization for the two sharply peaked shapes is given in [7]. Not yet included is the transmission characteristic of the beamline and the frequency response of the pyroelectric detectors. Interference with radiation from the third magnet will modify the spectrum, but also requires further understanding of the beamline optics and has been neglected here.

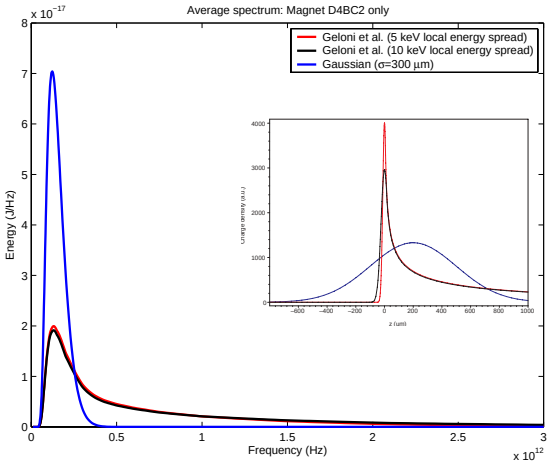

Figure 1: Simulated spectrum after (1). Included are the form factor for the bunch shapes shown in the inset, the chamber cut-off and the window transmission.

Precise knowledge of all spectral modifications by the vacuum chamber, beamline mirrors and apertures, interferometer and detectors is required to extract the form factor. One experimental approach to determine these factors is to use a blackbody source (having a known emission spectrum) at the beginning of the beamline and then to measure the spectrum with the interferometer as used for bunch length determination. This way, all effects are taken into account correctly except the coupling between source and beamline. The intensity in the far-infrared of such a source is very low, but might be sufficient if a sensitive liquid Helium cooled bolometer is used. The other, calculational approach is to use optical simulation software to assess the transmission characteristics of the beamline and the interferometer and to calculate vacuum chamber cut-off and detector response from detailed considerations of their geometries and configurations. A combination of all techniques appears to be necessary to get to a sufficiently precise answer.

An interesting alternative would be a synchrotron radiation source that is guaranteed to emit only incoherent radiation at the frequencies of interest. This requirement would be fulfilled by long, smooth bunches, but it is currently not clear how this could be assured at TTF2. Even small bunch structures would easily dominate due to coherent emission.

Synchrotron radiation beamline at TTF2

A beamline to guide both far-infrared (50–3000 µm) and visible synchrotron radiation from the first bunch compressor (BC2) of the TTF2 linear accelerator to a diagnostic station outside of the controlled area at some 10 m distance has recently been constructed [8]. It will allow a direct comparison between streak camera and far-infrared measurements for features on length scales above some 100 µm (the streak camera resolution). Later, infrared techniques extending to shorter wavelengths, i.e. to shorter bunch lengths, will also be used further downstream the accelerator, employing synchrotron, transition and undulator radiation.

The principle design of the beamline relies on simple optics: a paraboloid mirror close to the synchrotron radiation viewport transforms radiation originating from an arc of about 7 cm length in the source region at some 81 cm distance into a nearly parallel beam which is then transported by large flat mirrors through Aluminium pipes to the experimental station. The beamline including the interferometer is flushed with dry Nitrogen to reduce the strong absorption of water vapour in the far-infrared. It is already partly prepared for later evacuation to fore-vacuum in case the absorption needs to be reduced further. A crystalline Quartz window (z-cut, clear aperture ⌀60 mm, 4.8 mm thick) is used as viewport.

Outcoupling port The synchrotron port at the fourth BC2 magnet (D4BC2) is at 18° relative to the beam axis, seeing approximately the first 2.5° of the beam trajectory arc. With a nominal bending radius of about 1.6 m at 130 MeV, this corresponds to an arc length of 7 cm. A photo of the port is shown in Fig. 2, a sketch of the geometry in Fig. 3.

The radiation is emitted along the arc into a cone of typical half-opening angle of 2.4° (42 mrad) at 250 µm and of 0.2° (3.5 mrad) at 500 nm. In the vertical the radiation beam is restricted by the vacuum chamber height of 16 mm, in the horizontal by the 60 mm diameter window. To transport this beam over some 10 m distance requires focusing of the infrared radiation soon after the chamber window

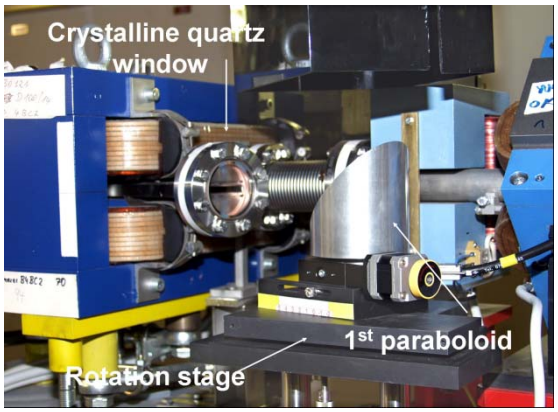

Figure 2: Outcoupling port of the beamline.

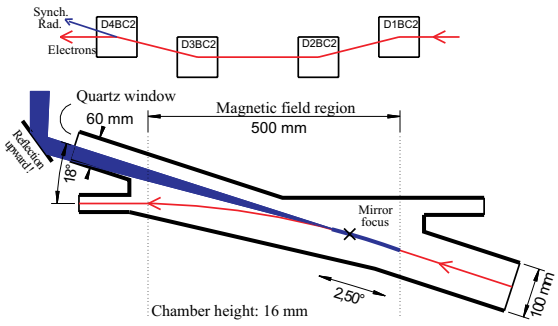

Figure 3: BC2 layout and D4BC2 vacuum chamber.

to limit the necessary mirror sizes. To this end, a 90° off-axis paraboloid mirror is installed after the window, reflecting the parallelized beam upwards to the tunnel roof. The paraboloid is machined from Aluminium, has a projected diameter of 100 mm and 810 mm focal length.

Depending on the bunch compressor settings, the electron beam can enter the dipole chamber at any position allowed by its 100 mm width. The mirror can be rotated around its vertical axis, such that the focal point follows the emission region of the synchrotron radiation. The rotation plane is aligned with the nominal electron beam plane. The focusing is not very sensitive to the exact longitudinal position, so that no translation of the mirror in this axis is necessary.

Transport line The approximately parallel beam from the paraboloid is reflected by a flat mirror under the tunnel roof straight out to further flat mirrors in the diagnostic container that feed the radiation into the interferometer or the streak camera. For the latter, narrow wavelength filters are used to avoid resolution loss due to dispersion in the window. The beam travels within large Aluminium pipes of 250 mm diameter (200 mm over a short section through the radiation protection wall) to avoid additional diffraction losses. Nitrogen is flushed from the diagnostic station into the tunnel at flow rates below 1 l/s, so that effluence into the tunnel is of no security concern.

Interferometer A polarizing Martin-Puplett interferometer[2] is used to analyze the spectrum of the far-infrared radiation. The wire grids are wound from 10 µm gold-plated Tungsten wire with 30 µm spacing, so that the interferometer works at wavelengths longer than about 60 µm. The clear aperture of the device is about 10 cm diameter. Currently, DTGS pyroelectric detectors are used, a liquid Helium cooled bolometer will also be available for the next TTF2 run. Details of the device can be found in [9, Chapter 7].

Compared to a Michelson interferometer, this type has the advantage of an almost perfect beam splitter characteristic for wavelengths longer than about twice the wire spacing and full transmission of the incoming radiation to the detectors (whereas on average half is reflected back to the source with a Michelson device).

First results

During the first run of TTF2 in May/June 2004, the infrared beamline was commissioned and first interferograms were taken. Fig. 4 shows one example. Clearly visible is one advantage of the Martin-Puplett interferometer: it allows suppression of radiation intensity fluctuations by normalizing the detector signals to the total intensity, i.e. their sum. Such fluctuations were strong during this startup phase.

The interferogram shows a small secondary signal at about 67 ps delay, coming from reflections within the 4.8 mm thick Quartz window, also reflected in the spectrum by the interference structure. The spectral shape shows agreement on a broad scale with the first simulations (see Fig. 1), but more detailed understanding of transmission and detector effects is necessary to extract quantitative information.

TRANSVERSE DEFLECTING CAVITY

LOLA[3] is a disk-loaded waveguide structure with constant impedance, using the TM 11 hybrid mode. It was originally build as a separator for secondary particles with the same momentum but different mass, and is used now as a transverse deflector to streak electron bunches.

The main parameters of the structure are: length 3.66 m, iris aperture 44.88 mm, peak deflecting voltage 26 MV (at 20 MW), frequency 2856 MHz, filling time 645 ns (quality factor 12100). The latter characteristic allows to streak only a few bunches from the TTF2 bunch train, working in quasi parasitic-mode. Because of the constant impedance, the transverse deflecting electric field is decreasing along the structure. The phase shift per cell (35 mm length) is 120°. A photograph of the structure installed in the TTF2 tunnel is shown in Fig. 5.

[2] Build by RWTH Aachen.

[3] The name comes from its designers: Greg **LO**ew, Rudy **L**arsen and Otto **A**ltenmueller. It was built at SLAC 1968.

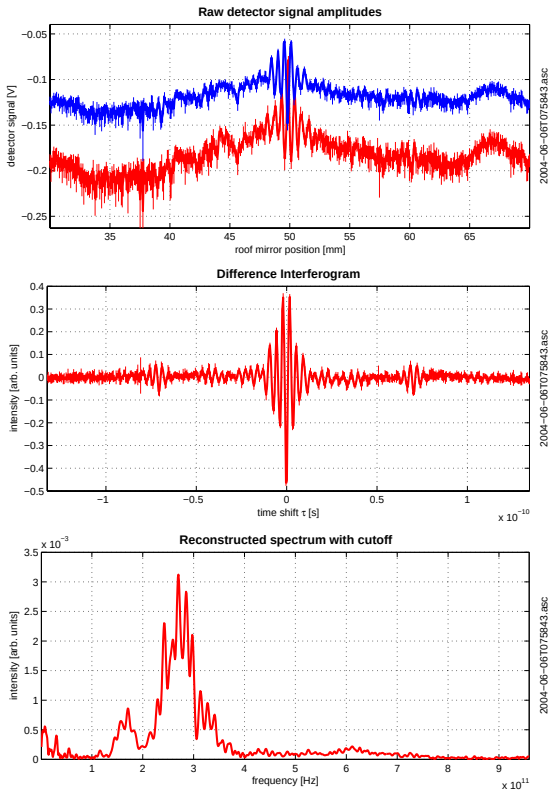

Figure 4: Measured raw (top) and normalized difference (middle) interferogram and the reconstructed spectrum (bottom) from the first run of TTF2 in May/June 2004.

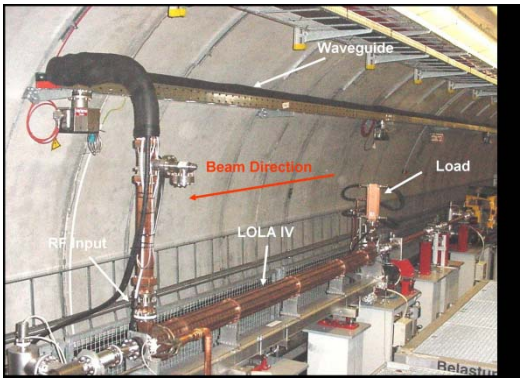

Figure 5: Photograph showing LOLA in the TTF2 tunnel.

Analysis

A particle within a bunch with position z relative to some origin will, after traversing the deflecting structure, have an offset $\Delta y(z)$ on a screen given by

$$\Delta y(z) = \frac{eV_0}{E_0}\sqrt{\beta_c\beta_p}\sin\Delta\psi_y\left(\frac{2\pi z}{\lambda}\cos\varphi + \sin\varphi\right). \quad (4)$$

Here, β_c and β_p are the beta function values at the cavity and at the screen, respectively, $\Delta\psi_y$ the beta function phase advance between them, V_0 the peak deflecting voltage and λ the wavelength of the structure, E_0 the electron energy and φ the phase angle between RF zero crossing and the bunch origin [10]. The observed spot size on the screen σ_y is related to the bunch length σ_z through (see Fig. 6)

$$\sigma_y = \sqrt{\sigma_{y,0}^2 + \sigma_z^2\beta_c\beta_p\left(\frac{2\pi eV_0}{\lambda E_0}\sin\Delta\psi_y\cos\varphi\right)^2}, \quad (5)$$

where $\sigma_{y,0}$ is the bunch transverse size along the streak direction on the screen.

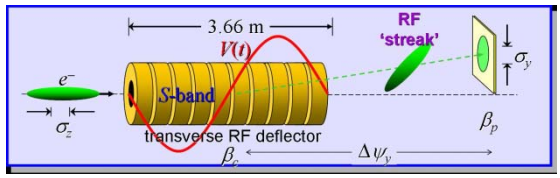

Figure 6: LOLA operation principle.

From (5) it is obvious that σ_y is not very sensitive to φ for small φ, but (4) shows that the centroid offset is then proportional to φ. For high resolution, the bunch should be streaked over a large fraction of the screen. The phase stability is then required to be significantly better than the phase length of the bunch: ≈0.1° for a bunch length of 25 µm and the 105 mm wavelength of the structure. Otherwise, the spot on the screen will jitter by more than the screen size.

Energy change due to beam loading from the LOLA structure within a bunch train is confined to approximately the first 80 bunches and amounts to no more than 0.03% [11].

REFERENCES

[1] B. Steffen, this conference (Paper ID TUPOS06)

[2] E.L. Saldin et al., DESY 04-126 (July 2004), also this conference (Paper ID THPOS65)

[3] J.S. Toll, Phys. Rev. **104**,1760 (1956)

[4] R. Lai, A.J. Sievers, Nucl. Instr. Meth. A397(1997) 221

[5] J. Menzel, private communication

[6] M. Dohlus, T. Limberg, Nucl. Instr. Meth. A407(1998) 278

[7] G. Geloni et al., DESY 03-031 (March 2003)

[8] S. Casalbuoni et al., EPAC '04, 5–9 July 2004, Lucerne, Switzerland (Paper ID THPLT046)

[9] M.A. Geitz, DESY-THESIS-1999-033 (November 1999)

[10] M. Nagel, FEL Report 2004 (to be published)

[11] K.L.F. Bane et al., SLAC-PUB-10160/TESLA Report 2003-24 (September 2003)

TRANSVERSE EMITTANCE MEASUREMENTS AT THE PHOTO INJECTOR TEST FACILITY AT DESY ZEUTHEN

V. Miltchev*, K. Abrahamyan†, G. Asova‡, J. Bähr, G. Dimitrov§, H.-J. Grabosch, J.H. Han, M. Krasilnikov, D. Lipka, A. Oppelt, B. Petrosyan, D. Pose, S. Riemann, L. Staykov, F. Stephan
DESY, Zeuthen, Germany
M.v. Hartrott, D. Richter, BESSY GmbH, Berlin, Germany
J.P. Carneiro, K. Flöttmann, S. Schreiber, DESY, Hamburg, Germany
P. Michelato, L. Monaco, D. Sertore, INFN Milano-LASA, Segrate (MI), Italy
I. Tsakov, INRNE Sofia, Sofia, Bulgaria
I. Will, Max-Born-Institute, Berlin, Germany
W. Ackermann, S. Schnepp, S. Setzer, TU Darmstadt, Darmstadt, Germany

Abstract

This contribution summarizes the transverse emittance studies done at the Photo Injector Test Facility at Zeuthen (PITZ) for producing an electron beam that meets the requirements of the VUV-FEL. Systematic measurements of the beam emittance in a wide range of parameters (e.g. bunch charge, rf phase, solenoid fields) will be presented and compared with simulations.

INTRODUCTION

The main goal of PITZ is the development of electron sources for Free Electron Lasers. Since the first production of photoelectrons in January 2002 several upgrades have been realized. An important step was the transition from temporal gaussian laser profile to flat top distribution in the spring of 2003. This change was motivated by the resulting significant emittance reduction, which will be demonstrated in the first part of this paper. In the second part of the paper the optimization of the rf gun toward the VUV-FEL requirements is summarized. In the third part the measurements of thermal emittance are discussed and finally some of the latest emittance measurements are presented.

MEASUREMENTS WITH VARIOUS TEMPORAL PROFILES OF THE UV LASER PULSE

The emittance was measured as a function of the main solenoid current using gaussian temporal profile of the laser pulse of 6.0±1.0 ps FWHM. The bunch charge was set to 0.49 ±0.02 nC. The radial laser beam profile was about flat top, but with a modulation depth of ∼20 % , σ_x = 0.53 ±0.02 mm, σ_y = 0.65 ±0.02 mm. The rf phase ϕ was set to the phase with maximum mean energy gain ϕ_m. This phase ϕ_m will be used as a reference phase throughout this paper. The electric field gradient on the cathode surface was about 41 MV/m. A single slit scanning technique was used for the emittance measurements [1, 3]. Results of the measurements compared with ASTRA [4] simulation are presented in Fig. 1(a). The minimal emittance is about 4 mm mrad. Since the emittance scales with the charge, we expect the emittance for the gaussian

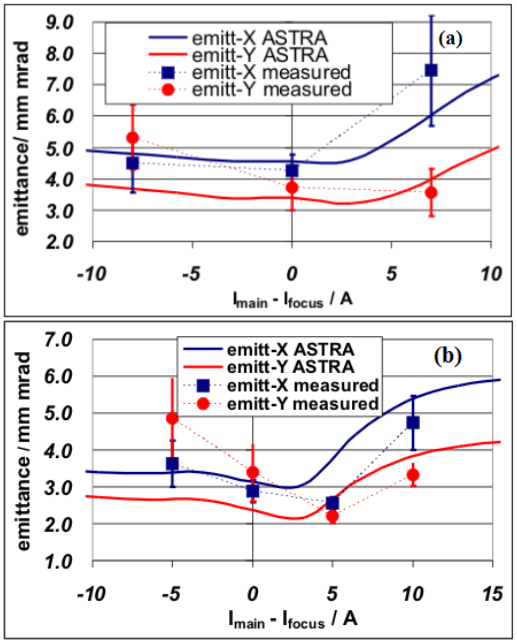

Figure 1: Projected normalized emittance as a function of the main solenoid current I_{main}: (a) for a bunch charge of 0.5 nC and a gaussian laser pulse with a length of 6.3 ps FWHM, and (b) for a bunch charge of 1.0 nC and a flat top laser pulse with a length of 23 ps FWHM. I_{focus} denotes the solenoid current to focus the beam on the position of the slit mask.

* velizar.miltchev@desy.de
† on leave from YERPHI, Yerevan, Armenia
‡ on leave from INRNE Sofia, Sofia, Bulgaria
§ on leave from INRNE Sofia, Sofia, Bulgaria

case at 1 nC to be even larger. The same set of measurements has been repeated with a flat top longitudinal laser pulse profile of 23.0±1.0 ps FWHM. The bunch charge was set to 1.00±0.02 nC. The laser beam transverse sizes are: σ_x=0.52±0.02 mm, σ_y=0.63±0.02 mm. The rf phase was set to ϕ_m; the electric field gradient on the cathode was about 42 MV/m. The parameters have not yet been optimized for minimum emittance, these measurements are to compare flat hat with gaussian laser pulses. The measurements compared with an ASTRA simulation are presented in Fig. 1(b). The minimal emittance is about 2.3 mm mrad. Since the measurement conditions for both solenoid scans are about the same, a flat hat laser profile yields a more than two times smaller emittance than the gaussian profile.

EMITTANCE OPTIMIZATION TOWARD VUV-FEL REQUIREMENTS

After the upgrade of the laser system an extended measurement program was carried out at PITZ in order to characterize and optimize the VUV-FEL rf gun (cavity prototype #2) for TTF [2, 5].

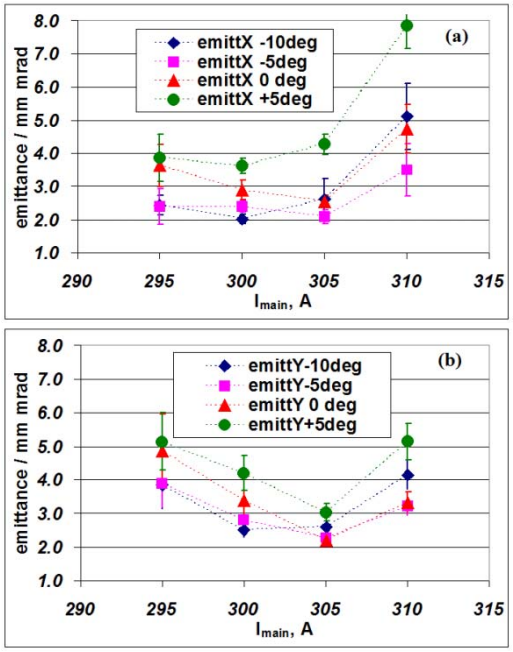

Figure 2: Projected normalized horizontal (a) and vertical (b) emittance for different main solenoid currents and gun phases $\phi - \phi_m = -10°$, $-5°$, $0°$, $+5°$. The bunch charge is 1.0 nC.

Optimization strategy

As a first optimization step, the emittance for a bunch charge of 1 nC is measured as a function of the main solenoid current $I_{\rm main}$ for the rf phases $\phi - \phi_m = -10°$, $-5°$, $0°$, $+5°$ at a maximum accelerating gradient on the cathode of 42 MV/m. During this first optimization step the magnetic field at the photo-cathode was not compensated by the bucking solenoid. Later on, for the settings $\{I_{\rm main}, \phi\}$ with the smallest emittance, the bucking solenoid current has been fine tuned. During the measurements, the laser temporal and transverse properties were frequently monitored and adjusted. The laser pulse temporal profile was a flat top of 18 to 23 ps FWHM with a rise and fall time of 5 to 7 ps. The transverse shape was slightly asymmetric: σ_x = 0.50 to 0.52 mm, σ_y = 0.61 to 0.63 mm.

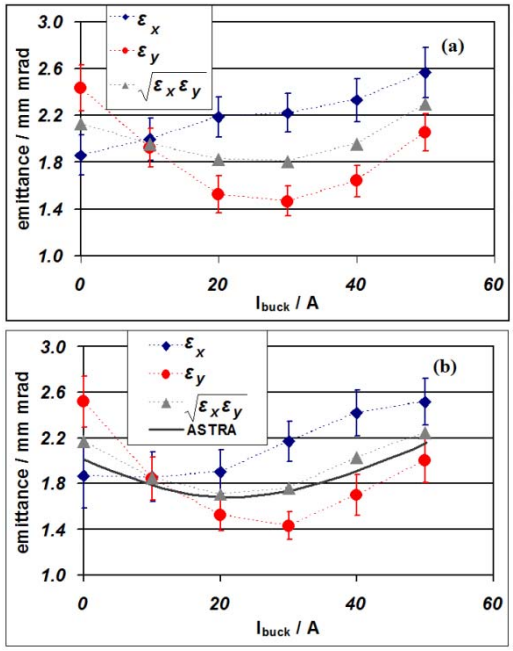

Figure 3: Projected normalized emittance for different bucking solenoid currents. The bunch charge is 1.0 nC, the main solenoid was set to 305 A. The the gun phase is: (a) $\phi - \phi_m = 0°$, and (b) $\phi - \phi_m = -5°$. The horizontal and vertical emittance as well as their geometrical average are shown. The solid line in the lower graph represents a corresponding ASTRA simulation at the geometrical average.

Results of the solenoid and phase scans

According to the strategy described above, the emittance was measured as a function of the main solenoid current for various rf phases. Results of these scans are presented in Fig. 2. The smallest emittance is about 2 to 2.5 mm mrad measured in both transverse planes for a main solenoid current of 305 A and for rf phases $\phi - \phi_m = 0°$, $-5°$.

Further optimization by scanning the bucking solenoid

As pointed out, for the measurements plotted in Figure 2 the residual magnetic field on the photo cathode has not

been compensated. Therefore, additional scans with the compensating bucking solenoid were performed for the settings with the smallest emittance: $\{305\,\mathrm{A},\ \phi-\phi_m=0^\circ\}$ and $\{305\,\mathrm{A},\ \phi-\phi_m=-5^\circ\}$. The results are shown in Fig. 3. Error contributions of the background noise [3], finite optical resolution and statistical fluctuations are all taken into account and propagated to the final measurement errors represented with the error bars. As shown in [5] and in Fig. 3(b) the experimental data agree well with simulations. The smallest vertical emittance is 1.5 mm mrad, a minimum geometrical average $\sqrt{\epsilon_x\epsilon_y}$ of 1.7 mm mrad is obtained.

Impact of vacuum components

The PITZ experience shows that the impact of the vacuum components on the beam emittance should be studied and must be in the list with optimization items. For the first of the two sets of measurements shown in Fig. 4, the electron beam has been horizontally shifted with respect to its design orbit. The beam is steered 6 mm closer to the laser vacuum mirror then the nominal distance of 12 mm. This metallized glass mirror is being charged up by the beam and dark current and the resulting electrostatic field affects

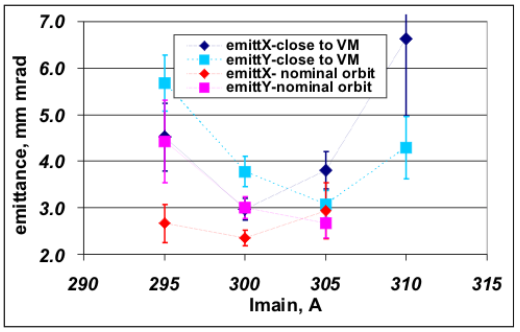

Figure 4: Impact of the laser vacuum mirror (VM) on the emittance. The bunch charge is 1.0 nC, the gun phase $\phi-\phi_m=-5^\circ$.

the beam quality. As it is demonstrated in the second measurements set in Fig. 4 an emittance reduction of 0.5 to 1.0 mm mrad is achieved by steering the beam away from the vacuum mirror. A detailed simulation study of this phenomena [6] agrees well with the presented measurements.

THERMAL EMITTANCE MEASUREMENTS

The thermal emittance is limiting the emittance reach in photo-cathode rf guns. Therefore, its measurement is of high importance to understand the ultimate performance limit of rf gun based electron sources. The thermal emittance measurements use a laser pulse with a gaussian temporal profile of 6 to 8 ps FWHM. Simulations with ASTRA show that for these short pulses the emittance growth due to the rf field should be negligible ($\leq 2\,\%$) compared to the expected thermal emittance ϵ_{th}. The final goal of the measurements is to estimate the average kinetic energy E_k of the electrons emitted from the Cs_2Te photo-cathode. An emission model introduced in [7] is assumed, such that:

$$\epsilon_{th}=\sigma\sqrt{\frac{2E_k}{3m_0c^2}} \tag{1}$$

Hence,

$$E_k=1.5m_0c^2\left(\frac{d\epsilon_{th}}{d\sigma}\right)^2 \tag{2}$$

where σ denotes the r.m.s. laser spot size.

Emittance scaling with the laser spot size

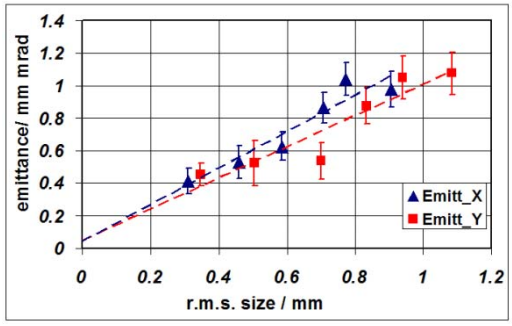

Figure 5: Transverse emittance vs. laser spot r.m.s. size measured with the slit scanning technique at 3 pC.

Figure 5 shows the normalized emittance for different r.m.s. laser spot sizes measured with the single slit scanning method at a charge of about 3 pC and an accelerating gradient at the cathode of 32 MV/m. For these conditions (tiny charge, low gradient) simulations predicts an emittance growth of less than 5 % due to space charge effects. From a straight line fit one obtains $\frac{d\epsilon}{d\sigma}$ =1.0 to 1.1 mrad. Inserting the fit values into Eq. 2 yields:

$$E_k=1.5m_0c^2\left(\frac{d\epsilon}{d\sigma}\right)^2=0.8\pm0.1\,eV \tag{3}$$

For comparison a second set of measurements similar to the set presented in Fig. 5 has been done using the solenoid scan method to determine the emittance. The analysis of the solenoid scan data takes into account the evolution of beam energy along the magnetic axis as well as space charge effects and yields about the same kinetic energy as the slit technique.

Dependence of the emittance on the accelerating gradient

The emittance was measured at a charge of 2 to 3 pC as a function of the accelerating field E at the cathode. The single slit scanning technique was used for these measurements. The electric field amplitude E_0 was varied in the

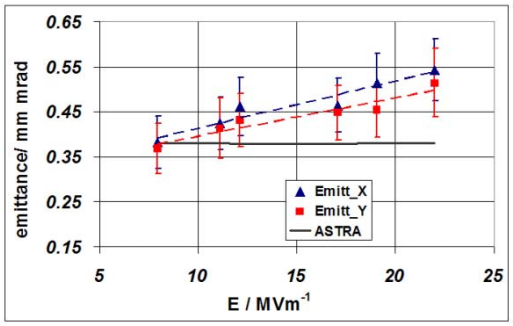

Figure 6: Emittance as a function of the accelerating field on the cathode surface E for a charge of 2 to 3 pC.

range from 24 to 37 MV/m. The laser spot size of σ_x= 0.46 mm, σ_y= 0.51 mm was kept fixed. The solenoid current was adjusted such that the beam was focused on the position of the slit mask. The rf phase ϕ was set to ϕ_m for each measurement. In addition, before each measurement the charge was measured as a function of the rf phase. From the rising edge of the phase scan the zero crossing phase ϕ_0 was determined. Finally the applied field at the cathode is calculated as $E = E_0 sin(\phi_m - \phi_0)$. The results presented in Fig. 6 show an increasing emittance with the accelerating field. The simulation predicts a constant emittance. It includes the beam dynamics in the rf gun, but does not scale the kinetic energy of the emitted electrons with the applied field at the cathode. The increasing thermal emittance corresponds to a rising kinetic energy of the emitted electrons. This phenomena can be explained by assuming a modified Schottky effect [8].

RECENT MEASUREMENTS WITH CAVITY PROTOTYPE #1

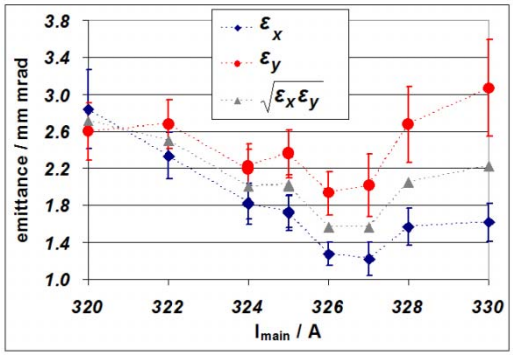

Figure 7: Measurements with cavity prototype #1.

After cavity prototype #2 was fully characterized at PITZ and installed at TTF, cavity prototype #1 was put into operation at PITZ in the beginning of 2004 [2] followed by the rf conditioning [9]. The beam dynamics optimization is ongoing. Figure 7 shows emittance measurements done for a bunch charge of 1 nC at the current stage of optimization.

SUMMARY

The impact of the temporal laser pulse profile on the emittance has been demonstrated. A longitudinal flat top laser pulse yields a significantly better emittance than a gaussian shape. The characterization of the rf gun cavity for the VUV-FEL was presented. The smallest normalized projected emittance is measured with 1.5 mm mrad in the vertical plane. The smallest geometrical average emittance of both transverse planes is 1.7 mm mrad. Measurements to estimate the thermal emittance have been done using a very small bunch charge and moderate accelerating gradients. The average kinetic energy of the emitted photo electrons is estimated to be 0.8±0.1 eV. An increasing of the thermal emittance with the accelerating field on the cathode has been observed. The characterization of the next cavity at PITZ is ongoing and shows promising results.

REFERENCES

[1] M. Krasilnikov *et al.*, "Characterization of the Electron Source at the Photo Injector Test Facility at DESY Zeuthen", FEL 2003, Tsukuba, Sept. 2003.

[2] F. Stephan *et al.*, "Recent results and perspectives of the low emittance photo injector at PITZ", these proceedings.

[3] V. Miltchev *et al.*, "Transverse Emittance Measurements at the Photo Injector Test Facility at DESY Zeuthen (PITZ)", DIPAC2003, Mainz, May 2003.

[4] ASTRA manual, http://www.desy.de/∼mpyflo/

[5] M. Krasilnikov *et al.*, "Optimizing the PITZ electron source for the VUV-FEL",EPAC 2004, Luzern, July 5-9, 2004.

[6] S. Setzer *et al.*, "Influence of Beam Tube Obstacles on the Emittance of the PITZ Photoinjector", EPAC 2004, Luzern, July 5-9, 2004.

[7] K. Flöttmann, "Note on the Thermal Emittance of Electrons Emitted by Cesium Telluride Photo Cathodes ",TESLA-FEL 97-01 (1997).

[8] G. Suberlucq, "Development and Production of Photo Cathodes for the CLIC Test Facility", FEL 1996, Rome, August 1996.

[9] J. Bähr *et al.*, "High power rf conditioning and measurement of longitudinal emittance at PITZ", these proceedings.

THE SHORT-RANGE WAKEFIELDS IN THE BTW ACCELERATING STRUCTURE OF THE ELETTRA LINAC

P. Craievich*, G. D'Auria, Sincrotrone Trieste, Trieste, Italy
T. Weiland, I. Zagorodnov†, Technische Universitaet Darmstadt, Darmstadt, Germany

Abstract

Future FEL operations in the ELETTRA LINAC require a high quality beam with an ultra short bunch. The knowledge of the short-range wakefields in the backward traveling wave (BTW) accelerating structure is needed to predict the beam quality in term of the single bunch energy spread and emittance. To calculate the effect of the longitudinal and transverse wakefields we have used the time domain numerical approach with a new implicit scheme for calculation of wake potential of short bunches in long structure [1, 2]. First the wake potentials of the BTW structure are numerically calculated for very short bunches, than an analytical approximations for wake functions in short range are obtained by fitting procedures based on analytical estimations. Finally the single bunch energy spread induced by short-range longitudinal wakefields is analyzed for the first phase of the project FEL-I (up to 40 nm).

INTRODUCTION

The FERMI@ELETTRA project aims to construct a single-pass FEL user-facility in the spectral range 100-10 nm using the exiting normal conducting 1.0 GeV linac. Figure 1 shows the proposed machine layout for the two phase of the project: FEL-I (100-40 nm) and FEL-II (40-10 nm) [3].

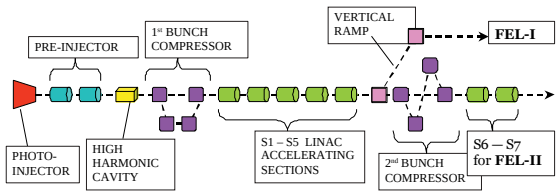

Figure 1: Schematic layout of the configuration for the FEL-I and FEL-II stages.

The new scheme foresees the installation of an RF photocathode gun [4], providing a high quality electron beam, with parameters directly related to those required at the entrance of the undulator lines [3]. At the photoinjector exit the beam is further accelerated with a 100 MeV preinjector, composed by two 3 m accelerating sections with focusing solenoids, that get the beam out of the space-charge energy domain and creates an energy-position correlation for bunch compression. After the first magnetic chicane, five accelerating structures of the exiting linac, each equipped with an RF pulse compression system (SLED), allow the beam to reach the energy required by FEL-I, 700 MeV. In total the present linac includes seven 6 m accelerating sections, the remaining two accelerating sections will be located after the second bunch compression and will be used for the FEL-II to rise the beam energy up to 1 GeV. Each accelerating section is a backward traveling wave (BTW) structure composed by 162 nose cone cavities magnetically coupled and operated in the $3/4\pi$ mode. In this scenario, to avoid undesirable beam degradations, in term of energy spread and emittance, the wakefileds effects have to be carefully considered. We have studied the longitudinal and transverse cases using the time domain code ECHO with a new implicit scheme for the calculation of the wake potentials of short bunches in long structures [1, 2]. We have considered the wakefields evolution for bunches of different lengths passing through a single cell, a multi-cell and a complete accelerating structure [5]. This paper reports the longitudinal and transverse wakefields calculations for a complete BTW accelerating structure and the single bunch energy spread induced by short-range longitudinal wakefields for the FEL-I. A preliminary optimization of the energy spread has been carried out by varying the energy gain and RF phase of the accelerating structure.

LONGITUDINAL WAKE FUNCTION OF THE BTW STRUCTURE

The wake potentials of Gaussian bunches with length ranging from $1000\mu m$ to $50\mu m$ are calculated for a whole BTW accelerating structure. In figure 2 the calculated longitudinal wake potentials (solid lines) are reported. To find an analytical approximation of the wake function we have chosen a combination of periodic [7] and one cell [6] dependence since the BTW structure can be treated as a periodic structure of finite length. From the fit of the numerical wake potentials we have obtained an analytical expression approximating the wake function (in V/pC):

$$w1_{\parallel}^{0}(s) = A_{01}e^{-\sqrt{s/s_0}} + \frac{A_{02}}{\sqrt{s}} \qquad (1)$$

where $A_{01} = 7300$, $s_0 = 3.2 \cdot 10^{-4}$ and $A_{02} = 3.4$.

Figure 2 shows the longitudinal wake function (1) (black dotted line), which tends for small s to be an envelope function to the wakes and fits the numerical results up to $1.5mm$. To find an analytical approximation up to $5mm$, we have added to expression (1) an additional term with

* paolo.craievich@elettra.trieste.it
† This work was supported in part by the Deutsche Forschungsgemeinschaft under contract WE1239/22

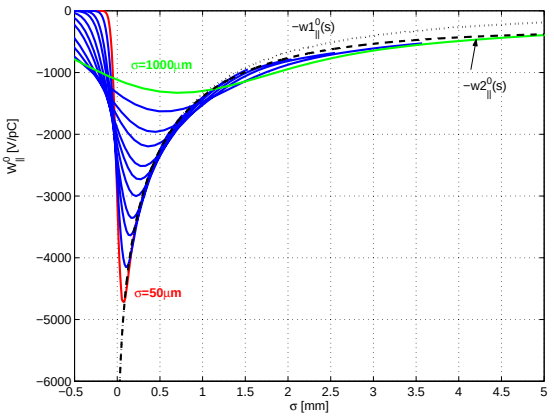

Figure 2: Longitudinal wake potentials (solid lines) and longitudinal wake functions (1)(black dotted line) and (2) (black dashed line) of the BTW structure.

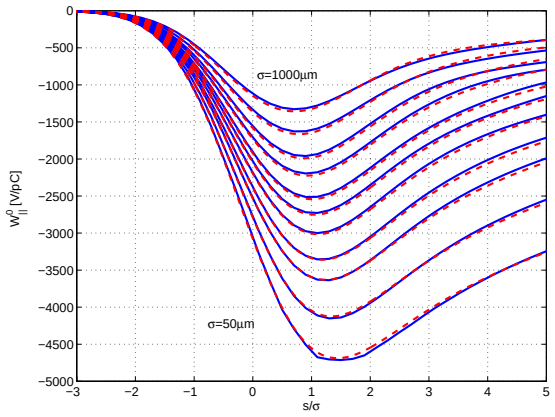

Figure 3: Longitudinal numerical (blue solid lines)and analytical (red dashed lines) wake potentials of the BTW structure.

$\sqrt{s}$ dependence. Taking into accoutn the last correction term the fit gives the following analytical expression for the wake function:

$$w2_{\parallel}^{0}(s) = A_{01}e^{-\sqrt{s/s_0}} + \frac{A_{02}}{\sqrt{s}} + A_{03}\sqrt{s} \qquad (2)$$

where $A_{01} = 7450$, $s_0 = 3.1 \cdot 10^{-4}$, $A_{02} = 3$ and $A_{03} = 3000$.

The previous relation approximates the longitudinal wake function on a wider range compared to expression (1). Figure 2 shows the longitudinal wake function (2) (black dashed line) that tends to be an envelope function to the wakes up to $5mm$. Figure 3 presents the calculated longitudinal wake potentials (blue solid lines) together with analytical approximation (2) (red dashed lines). A more detailed analysis of figures 2 and 3 shows that the analytical expression 2 approximates very well the longitudinal wake function up to $5mm$.

TRANSVERSE WAKE FUNCTION OF THE BTW STRUCTURE

Figure 4 shows the calculated transverse wake potentials (solid lines) for different bunch length σ. As in the previous case, the BTW structure is treated as a periodic structure of finite length and to find an analytical approximation for the transverse wake function, a combination of periodic [7] and one cell [6] dependence was chosen. The expression for the wake function is obtained with a fit of the numerical wake potentials (in $V/pC/m$):

$$w_{\perp}^{1}(s) = A_{11}\left[1 - \left(1 + \sqrt{\frac{s}{s_1}}\right)e^{-\sqrt{s/s_1}}\right] + A_{12}\sqrt{s} \quad (3)$$

where $A_{11} = 1.7 \cdot 10^5$, $s_1 = 1.2 \cdot 10^{-4}$ and $A_{12} = 8.5 \cdot 10^4$.

Figure 4 shows the transverse wake function (3) (black dashed line), which tends to be envelope function for the

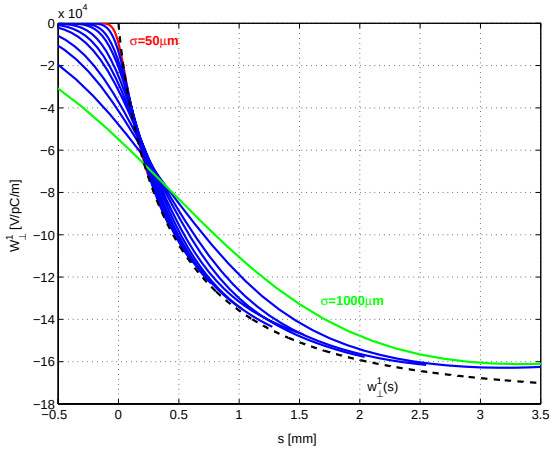

Figure 4: Transverse wake potentials (solid lines) and transverse wake functions (black dashed line) of the BTW structure.

wakes up to distance $s = 2mm$ after the bunch center. Figure 5 plots the calculated transverse wake potentials (blue solid lines) together with their analytical approximations (3) (red dashed lines). For transverse case no additional term is introduced and the wake function fits the results up to $2mm$.

SINGLE BUNCH ENERGY SPREAD IN BTW STRUCTURE

The first phase of FERMI foresees a bunch acceleration up to 700 MeV with bunch length $\sigma = 120\mu m$ and total charge Q=1nC. At the exit of each accelerating module, the single bunch energy spread is determined by the RF accelerating fields produced by the external generator and the wakefields excited by the beam in the accelerating structure. As already shown in [8], for Gaussian bunch the

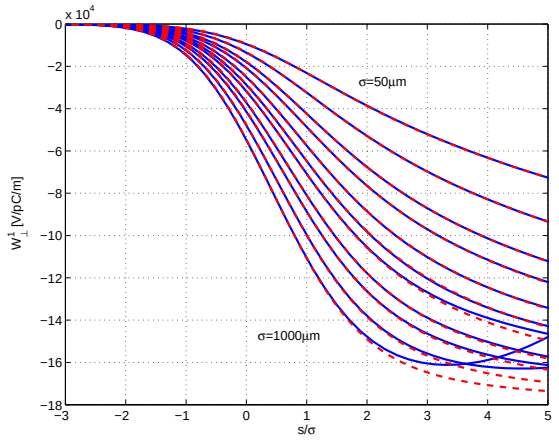

Figure 5: Transverse numerical (blue solid lines)and analytical (red dashed lines) wake potentials of the BTW structure.

RMS energy spread can be evaluated by knowing four integral parameters of the wakefields: the loss factor $K_{||}$, the average wake energy spread $\sqrt{\Delta W^2}$, the cosine-Fourier part I_{cos} and the sine-Fourier part I_{sin}. The last two parameters are needed to take into account the correlation between the wake potentials and the accelerating voltage [8]. Table 1 summarizes the four integral parameters for bunches of different length obtained with numerical time domain simulation (a), and analytical calculations (b) using (1): an excellent agreement between the two sets of data is shown. Figures 6 and 7 show the relative energy spread $\Delta U/\langle U\rangle$ and relative average energy gain $\langle U\rangle/U_0$ as a function of the RF phase ϕ, for different energy gain per section U_0. The calculations have been made under the assumption that the energy spread is negligible with respect to the total energy gain for acceleration section and considering a maximum energy gain for section up to 170 MeV. We can see that the average energy gain at optimum phase ϕ_{opt} is approximately 27% lower than the corresponding value on crest, $\phi = 0^o$, for each value of the peak of the acceleration voltage (figure 7). Table 2 contains the relative energy spread when the beam is accelerated on crest, RF phase $\phi = 0^o$, and the minimum relative energy spread at the optimum phase ϕ_{opt}. These parameters are given for different peak of the accelerating voltage. The relative energy spread decrease with the increase of the accelerating voltage. With an maximum energy gain of 170 MeV the minimum relative energy spread is about 2 times lower than the corresponding at $\phi = 0^o$.

To obtain the required 700 MeV of FEL-I, the BTW strucutres have to be operated with a gradient of 21 MV/m [9]. Figure 8 shows different behaviors of the relative energy spread as a function of the electric filed gradient (changing the RF phase from -50^o to 10^o) for different peak accelerating voltage U_0, for a bunch with length $\sigma = 120\mu m$ with a charge $Q = 1nC$. Considering the

Table 1: Numerical and analytical integral parameters of the wake potentials of Gaussian bunches in the BTW structure.

σ $[\mu m]$	$K_{\|\|}$ $[V/pC]$	I_{cos} $[V/pC]$	I_{sin} $[V/pC]$	$\sqrt{\Delta W^2}$ $[V/pC]$
Numerical integral parameters (a)				
50	-2861.7	-0.001477	-4.368020	1459.8
120	-2298.3	-0.009598	-7.860948	1118.4
150	-2145.5	-0.015227	-8.964911	1029.0
Analytical integral parameters (b)				
50	-2861.2	-0.001546	-4.307913	1441.2
120	-2295.4	-0.009476	-7.831107	1112.5
150	-2145.8	-0.014982	-8.961020	1026.3

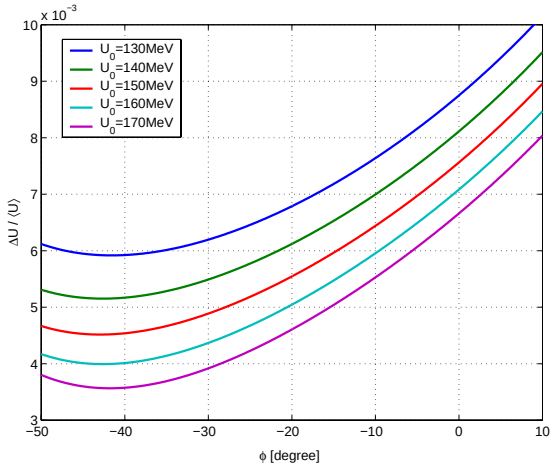

Figure 6: Relative energy spread as a function of the RF phase in the BTW structure (bunch length $\sigma = 120\mu m$ and $Q = 1nC$).

$21MV/m$ required, we can see that the relative energy spread is near its minimum value only for $U_0 = 170MeV$. With lower values of U_0 the relative energy spread don't get its minimum value through the tuning of RF phase.

CONCLUSION

Calculations of the wakefields for short bunches passing through a complete BTW accelerating structure have been presented. The short-range longitudinal and transverse wake potentials are been calculated in time domain with the code ECHO. From the numerical results analytical approximations of the point-charge wake functions were found. For the analytical model we have chosen as a combination of periodic and one-cell dependences. In the longitudinal case the term that describes the finite structure (one cell behavior) is very small compared to the periodic structure term. Hence in range of σ we have considered, the longitudinal wakes shows mainly a periodic structure behavior. In addition, for better fitting of the data up to 5

Table 2: Energy gain and energy spread in the BTW structure (bunch length $\sigma = 120\mu m$ and $Q = 1nC$).

U_0 $[MeV]$	RF phase	$\langle U \rangle$ $[MeV]$	$\Delta U/\langle U \rangle$ %
130.0	$\phi = 0.0^o$	127.70	0.87
	$\phi_{opt} = -41.6^o$	94.96	0.59
140.0	$\phi = 0.0^o$	137.70	0.81
	$\phi_{opt} = -42.6^o$	100.69	0.51
150.0	$\phi = 0.0^o$	147.70	0.76
	$\phi_{opt} = -43.0^o$	107.48	0.45
160.0	$\phi = 0.0^o$	157.70	0.71
	$\phi_{opt} = -42.6^o$	115.44	0.40
170.0	$\phi = 0.0^o$	167.70	0.67
	$\phi_{opt} = -41.8^o$	124.47	0.36

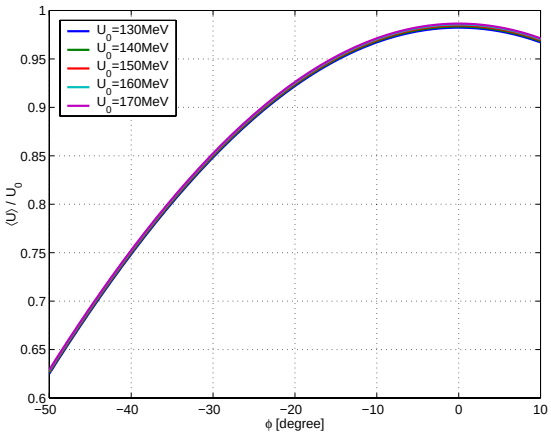

Figure 7: Relative energy gain as a function of RF phase in the BTW structure (bunch length $\sigma = 120\mu m$ and $Q = 1nC$).

mm, we have used an additional term in the model. Furthermore, the single bunch energy spread induced by longitudinal wakefields has been analyzed for the first phase of the project FEL-I. We have seen that the wakefield effects can be compensated by shifting the bunch injection phase to optimum values, decreasing the energy gain of about 27%. For the 700 MeV energy design of FEL-I and a peak gradient of 27.8 MV/m (170 Mev energy gain for section) this means to operate at $\phi = -41.8^o$ and a gradient of 21 Mv/m.

REFERENCES

[1] A. Novokhatski, M. Timm, T. Weiland, "Transition Dynamics of the Wake Fields of Ultra Short Bunches", Proceeding of the ICAP 1998, California, USA.

[2] I. Zagorodnov, T. Weiland, "Calculation of Transverse Wake Potential for Short Bunches", ICAP 2002.

[3] "FERMI@ELETTRA machine project update", Sincrotrone Trieste, 2003.

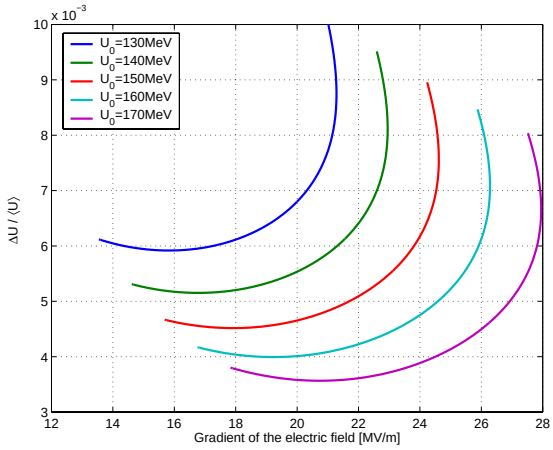

Figure 8: Relative energy spread as a function of the gradient of the electric field in the BTW structure (bunch length $\sigma = 120\mu m$ and $Q = 1nC$).

[4] V.A. Verzilov et al., "Photo-injector study for the ELETTRA linac FEL", FEL-2003, Tsukuba, Japan.

[5] P. Craievich, T. Weiland, I. Zagorodnov, Report ST/M-04/02, Sincrotrone Trieste, 2004.

[6] K. Bane, M. Sands, "Wakefields of very short bunches in an accelerating cavity", SLAC-PUB-4441, 1987.

[7] K. Bane, "Shortrange dipole wakefields in accelerating structures for the NLC", SLAC-PUB-9663, LCC-0116, 2003.

[8] A. Novokhatski, M. Timm and T. Weiland, "Single Bunch Energy Spread in the TESLA Cryomodule", TESLA Report 99-16, 1999.

[9] S. Di Mitri et al., "Start-to-end simulation for the FERMI project at ELETTRA", this conference.

THE SPARX PROJECT: R&D ACTIVITY TOWARDS X-RAYS FEL SOURCES

D.Alesini, S.Bertolucci, M. Bellaveglia, M.E.Biagini, R.Boni, M.Boscolo, M.Castellano, A.Clozza, G.Di Pirro, A.Drago, A.Esposito, M.Ferrario, D. Filippetto, V.Fusco, A.Gallo, A.Ghigo, S.Guiducci, M.Incurvati, C.Ligi, F.Marcellini, M.Migliorati, A.Mostacci, L.Palumbo, L.Pellegrino, M.Preger, P. Raimondi, R.Ricci, C.Sanelli, M.Serio, F.Sgamma, B.Spataro, A.Stecchi, A.Stella, F.Tazzioli, C.Vaccarezza, M.Vescovi, C.Vicario, INFN-Frascati

F.Alessandria, A.Bacci, I.Boscolo, F.Broggi, S.Cialdi, C.De Martinis, D.Giove, C.Maroli, M. Mauri, V.Petrillo, M.Rome`, L.Serafini, INFN-Milano

M.Mattioli, P. Musumeci, INFN-Roma1

L.Catani, E.Chiadroni, A. Cianchi, C. Schaerf, INFN-Roma2

F.Ciocci, G.Dattoli, A. Di Pace, A.Doria, F.Flora, G.P.Gallerano, L.Giannessi, E.Giovenale, G.Messina, L.Mezi, P.L.Ottaviani, S. Pagnutti G. Parisi, L.Picardi, M.Quattromini, A.Renieri, C.Ronsivalle, A. Torre, A. Zucchini, ENEA-Frascati

S. De Silvestri, M. Nisoli, S. Stagira, Politecnico/Milano

J.B. Rosenzweig, S. Reiche, UCLA - Dept. of Physics and Astronomy

P.Emma, SLAC

Abstract

SPARX is an evolutionary project proposed by a collaboration among ENEA-INFN-CNR-Universita` di Roma Tor Vergata aiming at the construction of a FEL-SASE X-ray source in the Tor Vergata Campus. The first phase of the SPARX project, funded by Government Agencies, will be focused on R&D activity on critical components and techniques for future X-ray facilities as described in this paper.

INTRODUCTION

SPARX is an evolutionary project proposed by a collaboration among ENEA-INFN-CNR-Universita` di Roma Tor Vergata aiming at the construction of a FEL-SASE X-ray source in the Tor Vergata Campus. The first phase of the SPARX project, funded by Government Agencies with 10 Million Euro plus a preliminary contribution of 2.35 Million Euro by INFN, will be focused on R&D activity on critical components and techniques for future X-ray facilities. A R&D program towards a high brightness photoinjector (SPARC project [1]) is already under way at LNF-INFN. Its aim is the generation of electron beams with ultra-high peak brightness to drive a SASE-FEL experiment at 500 nm, performed with a 14 m long undulator [2]. The R&D plans for the X-ray FEL source will be developed along two lines: (a) use of the SPARC high brightness photo-injector to develop experimental test on RF compression techniques and other beam physics issues, like emittance degradation in magnetic compressors due to CSR, (b) explore production of soft and hard X-rays in a SASE-FEL with harmonic generation, in the so called SPARXINO test facility, upgrading in energy and brightness the existing Frascati 800 MeV Linac at present working as injector for the DAΦNE ϕ-factory (Fig. 1).

Figure 1: View of the Frascati linac

A parallel program will be aimed at the development of other critical component for X-rays FEL sources like high repetition rate S-band gun, high Quantum Efficiency cathodes, high gradient X-band RF accelerating structures

and harmonic generation in gas. In the next sections we describe preliminary start to end simulations for the SPARXINO test facility, the required R&D efforts and a possible solution for the DAΦNE linac upgrade.

THE SPARXINO TEST FACILITY

The spectral range from 10 nm to 1 nm, has been considered for the radiation source. In order to generate the SASE-FEL in this wavelength range, it is necessary to produce a high brightness beam to inject inside the undulators. A preliminary analysis of the beam parameters required for such a source leads to the values reported in Tab. 1.

Table 1: Electron beam parameter

Beam Energy	1	GeV
Peak current	2	kA
Emittance (average)	2	mm-mrad
Emittance (slice)	1	mm-mrad
Energy spread (correlated)	0.1	%

The basic scheme is shown in Fig. 2 and consits of an advanced high brightness photoinjector followed by a first linac driving the beam up to 350 MeV with the correlated energy spread required to compress it in a following magnetic chicane. The second linac drives the beam up to 1 GeV while damping the correlated energy spread taking profit of the effective contribution of the longitudinal wake fields provided by the S-band accelerating structures.

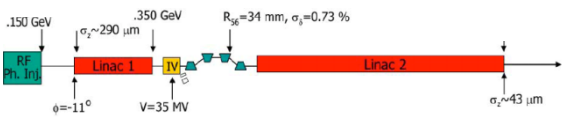

Figure 2: Scheme of the SPARXINO test facility.

A peculiarity of this linac design is the choice to integrate a rectilinear RF compressor in a high brightness photoinjector, as proposed in [3], thus producing a 300-500 A beam in the early stage of the acceleration. The SPARXINO linac will be the first SASE FEL experiment operating with RF and magnetic compressors in the same linac. The potentially dangerous choice to compress the beam at low energy (<150 MeV) when it is still in the space charge dominated regime, results from simulations not too difficult provided a proper emittance compensation technique is adopted [4], a possibility that is not viable in a magnetic chicane. In addition the propagation of a shorter bunch in the first linac reduces the potential emittance degradation caused by transverse wake fields and longitudinal wake fields result to be under control by a proper phasing of the linac. A comparison between the two compression techniques is scheduled during the SPARC phase II operation.

The preliminary design of the injector for the SPARXINO test facility is a copy of the SPARC high brightness photoinjector [1]. It considers a 1 nC bunch 10 ps long (flat top) with 1 mm radius, generated inside a 1.6-cell S-band RF gun of the same type of the BNL-SLAC-UCLA one [5] operating at 120 MV/m peak field equipped with an emittance compensating solenoid. Three standard SLAC 3-m TW structures each one embedded in a solenoid boost the beam up to 150 MeV.

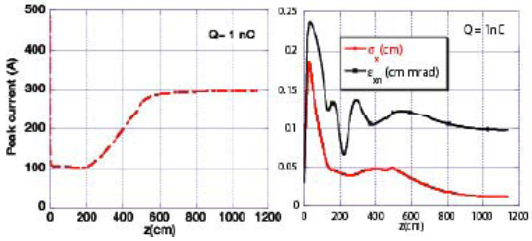

Figure 3: rms current (left), rms norm. emittance and rms beam envelope (right) along the injector, up to 150 MeV.

With a proper setting of the accelerating section phase and solenoids strength it is possible to increase the peak current preserving the beam transverse emittance. In the present case we have got with PARMELA simulation a bunch average current of 300 A with a normalized rms emittance below 1 mm-mrad.

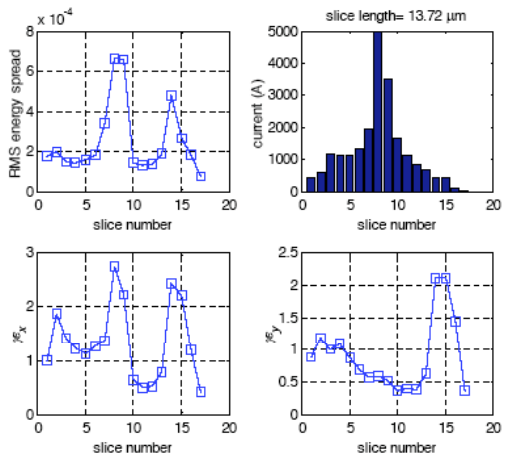

Figure 4: Energy spread, peak current and transverse emittances along the bunch, at the linac exit.

The low compression ratio (a factor 3) has been choosen to keep the longitudinal and transverse emittances as low as possible in order to simplify the second compression stage. We used the first two TW sections as compressor stages in order to achieve a gradual and controlled bunching, the current has to grow at about the same rate of the energy, and we increased the focusing magnetic field during the compression process. Fig. 3 (left) shows the current growth during bunch compression until 150 MeV, envelope and emittance evolution are also reported

(right), showing the emittance compensation process driven by the solenoids around the accelerating section that keep the bunch envelope close to an equilibrium size during compression.
The 10k macro-particles beam generated by PARMELA [6] has been propagated through Linac1, Magnetic Compressor and Linac2 with the code ELEGANT [7]. The correlated energy spread induced by Linac1 is 0.7% in order to compress the beam by a factor 6 in the 10 m long magnetic chicane with R_{56} = 34 mm. At the exit of Linac2 the required parameters for FEL operation have been achieved over more than 30% of the bunch length, as shown in Fig. 4. A further improvement is expected by fully optimizing the compression scheme and by using a 4th harmonic cavity [8] for the linearization of the longitudinal phase space distribution

THE SASE FEL SOURCE

Time dependent FEL simulations, performed with the code GENESIS [9] using the particle distributions produced by the Linac simulations presented in the previous section are in progress showing saturation for 30% of bunch slices after 16 m of active undulator length. We assume to use the same undulator of the SPARC project [2] with two additional 2.13 m long modules required to saturate at 10 nm, see Fig. 5. These first preliminary results are encouraging and will be the starting point for further optimizations

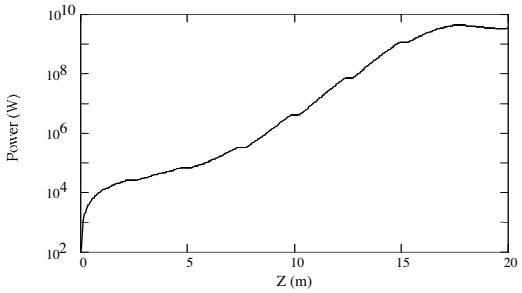

Figure 5: Power vs. z for the 10 nm SPARXINO SASE-FEL source, GENESIS simulation (slice energy spread 8*10^{-4}, slice norm. emittance 1 mm mrad, slice peak current 2 kA , undulator parameter K=2.2)

DAΦNE LINAC UPGRADE

The DAΦNE injection system is a 60 m long. LINAC equipped with 15 S-band (2.865 GHz) SLAC-type 3 m long accelerating structures driven by four 45 MW klystrons each followed by a SLED peak power doubling system. At present it delivers 0.8 μs RF pulses at a repetition rate of 50 Hz as required for DAΦNE operation. A quadrupole FODO focusing system is distributed along the entire linac. It accelerates the positron bunches emerging by the Positron Converter, up to the maximum energy of 550 MeV and the electron bunches up to 800 MeV. A drift space of about 15 m is available at the linac output for the installation of the undulator.
The Linac energy upgrade to 1 GeV can be achieved, as shown in figure 6, by pushing the accelerating field of the existing units up to 26 MV/m, which is today easily attainable and by adding 2 new SLAC-type sections to reach 1.1 GeV. The Linac waveguide network must also be modified in order to supply two accelerating units per RF station. This system configuration requires two new 45 MW klystrons.
High beam brightness can be achieved by installing a copy of the 12 m long SPARC photoinjector upstream the DAFNE linac with a minor modification of the existing building and a magnetic compressor at 350 MeV in the area of the Positron Converter, thus keeping the possibility to operate the linac as DAΦNE injector. A detailed analysis of the SPARXINO test facility compatibility with the proposed DAΦNE energy upgrade operation is under way [10].

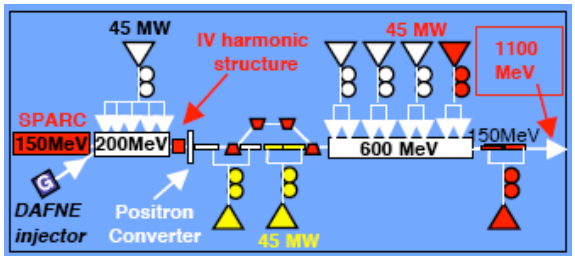

Figure 6:Scheme of the Frascati linac upgrade for SPARXINO and DAΦNE operation. Existing elements (white). Additional SPARXINO elements (red). Additional elements for positron acceleration (yellow).

CONCLUSIONS

The SPARX R&D project has been approved by the Italian Government and funded in June 2004 with a schedule of three years. The critical components for an X-ray FEL source will be tested during phase II of the SPARC project and assembled in a high energy and high brightness linac, the SPARXINO test facility, by upgrading the existing Frascati linac.

REFERENCES

[1] SPARC Project Team, Sparc Injector TDR www.lnf.infn.it/acceleratori/sparc/
[2] A. Renieri et al., “Status Report on SPARC Project”, this conference.
[3] L. Serafini and M. Ferrario, Velocity Bunching in PhotoInjectors , AIP CP 581, 2001, pag.87
[4] M. Boscolo et al., Beam Dynamics Study of RF Bunch Compressors for High Brightness Beam Injectors, Proc. of EPAC 2002, Paris.
[5] D.T. Palmer, The next generation photoinjector , PhD. Thesis, Stanford University
[6] J. Billen, “PARMELA”, LA-|UR-96-1835, 1996.

[7] M. Borland, “elegant: A Flexible SDDS-Compliant Code for Accelerator Simulation” LS-287, ANL, Argonne, IL 60439, USA.
[8] A. Bacci, M. Migliorati, L. Palumbo, B. Spataro, “An X-Band structure for a longitudinal emittance correction at Sparc”, LNF - 03/008 (R), and D. Alesini, A. Bacci, M. Migliorati, A. Mostacci, L. Palumbo, B. Spataro: "Studies on a Bi-Periodic X-Band Structure for SPARC", LNF-03-013(R).
[9] S. Reiche, Nucl. Instrum. & Meth. A429,243 (1999).
[10] R. Boni, “Feasibility of the DAFNE-Linac energy doubling”, Proc. of the Workshop on e+e- in the 1-2 GeV range, Alghero, Italy, September 2003

SPECTRAL ANALYSIS OF CHARGE EMISSION SPATIAL INHOMOGENEITIES AND EMITTANCE DILUTION IN RF GUNS

M. Quattromini, L. Giannessi, C. Ronsivalle,
ENEA, C.R. Frascati, Via E. Fermi, 45
I - 00044 Frascati (Rome), Italy.

Abstract

The effects of fluctuations in cathode's quantum efficiency and other sources of dis-homogeneities in the performances of a typical RF photo-injector have been investigated with PARMELA and TREDI numerical codes. The RF gun layout includes a focusing solenoid in a configuration aimed at minimizing the emittance growth due to space charge effects.

INTRODUCTION

Many applications from X-ray Free electron lasers to high energy colliders require high brightness beams produced by photo-injectors. The final performances of these devices are strictly linked to the beam quality produced by the electron source. In the case of FELs the role played by emittance becomes crucial at sub-nm wavelengths where the emittance is related to the transverse coherence of the output radiation. Most of the emittance budget that characterizes the beam at the undulator is produced at the injector in the first stages of the beam acceleration. The emittance optimization procedure rely on the linear theory[1] which has been verified both experimentally and numerically. In this paper we extend the analysis presented in Ref.[2] where the role played by a non uniform electron emissivity was examined. This study has been performed by using two different codes based on different algorithms: the Los Alamos version of PARMELA (PARMELA-LANL)[3] and TREDI[4]. TREDI has been used in "static" mode, i.e. ignoring effects associated to the finite velocity propagation of signals within the bunch.

PROBLEM DESCRIPTION

The aim of this work is to study the effect of charge in-homogeneities at the cathode surface, by decoupling in a transverse Fourier space, the in-homogeneities occurring at a specific wave-number , on a scale of the beam spot radius R, and higher. We have considered a standard S-Band (2856 MHz). 1.6 cells, BNL type photo-injector configuration[5], in a set-up optimized at minimizing the emittance in terms of accelerating gradient, extraction phase, beam spot size, focusing solenoid strength. Space charge effects compensation is achieved assuming both transverse and longitudinal flat charge distribution at extraction. The gun starts at z=0 and the drifts ends at z=2 m. The peak electric field in the gun and the solenoid peak magnetic field have been set respectively to 120 MV/m and 2.73 kG. The longitudinal shape of the pulse is square with a length of 10 ps and the charge is 1 nC. The phase of the centre of the bunch is 35°. No thermal emittance is included. The beam spot radius R is 1 mm. In Ref.[2] the charge distribution extracted from the cathode was modelled as a perturbation with respect to the ideal case with the following cosine function showing a maximum on the centre of the spot:

$$\rho_p(x,y) = \rho_0 \left[1 + \delta \cdot \cos(k_n x)\right] \left[1 + \delta \cdot \cos(k_n y)\right] \quad (1)$$

for

$$x^2 + y^2 \leq R^2 \qquad \text{and} \qquad k_n = n\frac{2\pi}{R}$$

In this contribution we analyze the effect of a sin-like (odd) perturbation of the type

$$\rho_p(x,y) = \rho_0 \left[1 + \delta \cdot \sin(k_n x)\right] \left[1 + \delta \cdot \sin(k_n y)\right] \quad (2)$$

Assuming that the values of δ and k_n are small, we may write in first approximation

$$\epsilon(k_n, \delta) = \epsilon_0 + \sum_n a_{n,j} \delta^j \quad (3)$$

where ϵ_0 is the value of the unperturbed emittance and the coefficients $a_{n,j}$ show the sensitivity of the emittance in this injector configuration to the charge in-homogeneities at the frequency .

The study has been performed by varying the two parameters δ and n and estimating the effect on the normalized rms emittance at the location of the first minimum (fig.1). The parameter δ has been varied between 0 and 40% and n has been given the values $n = 1/2, 1, 2, 4$.

A previous comparison between codes in the ideal configuration, i.e. at $\delta = 0$, has shown a good agreement[6].

RESULTS

The behaviour of the transverse emittance as a function of the longitudinal coordinate at $\delta = 20\%$, for different values of k_n is shown in figs. 1 and 2 for perturbed charge densities as of eqs. (1) and (2), respectively, as computed by TREDI. The emittance undergoes a typical series of oscillations due to the changes in correlation between longitudinal slices along the bunch which are subject to different focusing as a function of the extraction phase. These oscillations exhibit the well known structure with a double minimum located at the places where the correlation is maximized. In this analysis the second minimum does not appear since it falls behind the final longitudinal coordinate.

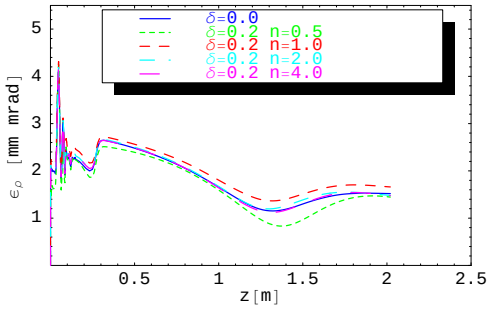

Figure 1: RMS transverse normalized emittance vs z for $\delta = 20\%$ and $n = 1/2, 1, 2, 4$ and perturbed density ρ as in eq. (1).

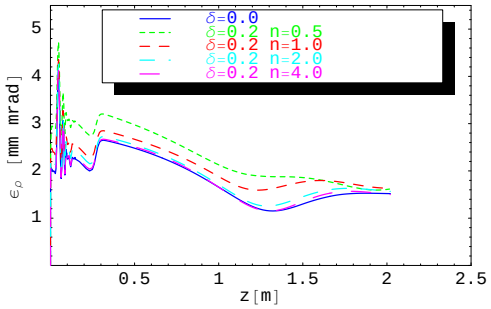

Figure 2: RMS transverse normalized emittance vs z for $\delta = 20\%$ and $n = 1/2, 1, 2, 4$ and perturbed density ρ as in eq. (2).

As an indication of the emittance of the beam we have considered the first minimum, whose position may depend on the in-homogeneity parameter δ especially at the lower perturbation frequencies k_n. The effect of the asymmetry in perturbed density (2) induces clearly a much larger emittance dilution at lower values of the transverse "frequency" k_n. As expected, at higher frequencies, for the same value of δ, the effect of different parity in charge distribution is negligible. In figure 3 the value computed by TREDI of the horizontal normalized rms emittance divided by the value obtained with a completely uniform distribution is plotted as a function of n. The data at $n = 4$ may be affected by some aliasing. The transverse mesh size used to describe the space-charge fields is 20×20 and could not be sufficient to resolve the fluctuations at $n = 4$. This may explain the slight emittance diminution observed in fig. 3. A more visible effect is predicted by TREDI for $n = 0.5$ and $\delta = 10\%$ (see fig. 4) for the charge distribution described by eq. (1). While this result is not evidenced by PARMELA, and require a further investigation, for $n \geq 1$ the two codes are in fairly good agreement and both give the maximum emittance increase for $n = 1$. A possible explanation could be related to the reduced transverse coupling of the beam with the RF photo-injector at the early stage of extraction[7].

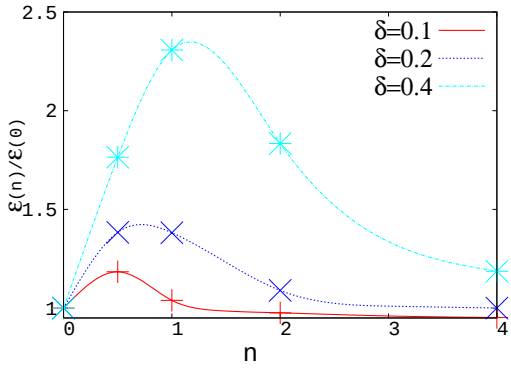

Figure 3: Emittance growth vs n in the position of the first minimum of the emittance as computed by TREDI for ρ as in eq. (2).

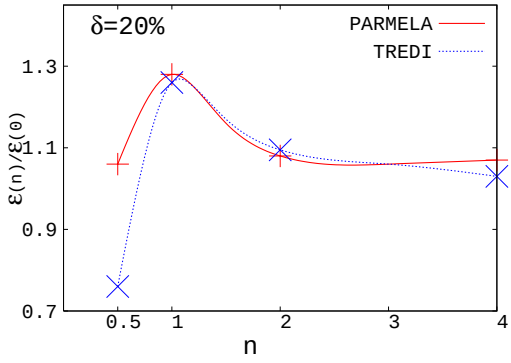

Figure 4: Emittance growth vs n in the first emittance minimum for $\delta = 20\%$ as computed by PARMELA and TREDI for ρ as in eq. (1).

This behaviour may be understood by looking at the x-y space shown in fig.5 in three longitudinal positions: at the cathode ($z = 0$), near the minimum of emittance ($z \approx 1.30\mathrm{m}$) and the local maximum of emittance ($z \approx 1.5\mathrm{m}$). The non-linear space charge forces induced by the non uniform transverse distribution at the cathode give a deformation of the beam shape. The distortion is stronger when the non-uniformities are more localized respect to the cases in which they are more diffused and tend to a partial recompensation along the drift.

In fig 5 the action of the solenoid focusing is also visible as a rotation of the distribution around the axis.

The emittance degradation increases with the modulation depth δ, as expected. An analysis of the data similar to that performed in [2] yielded the same scaling law at high values of k_n . In fig 6 the result of a fit of $\epsilon(\delta)/\epsilon_0$ for $n = 2$ is shown. Clearly the function $a_0 + a_3\delta^3$ fits the

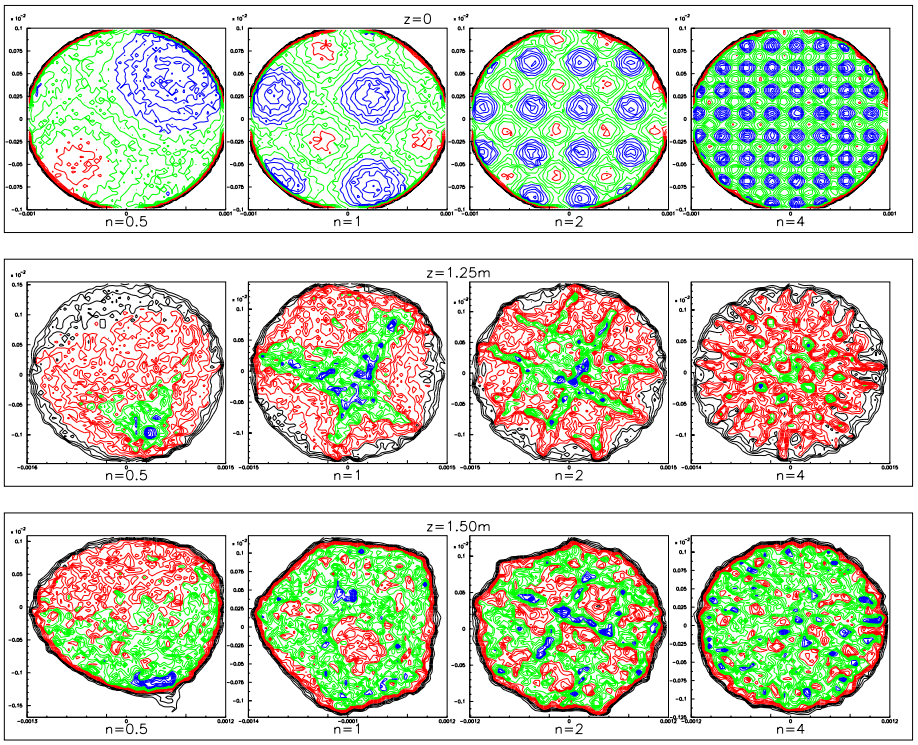

Figure 5: X-Y plots derived from TREDI computations for $\delta = 20\%$ in different longitudinal positions for ρ as in eq. (2).

data better than $a_0 + a_2\delta^2$. By converse for $n = 1$ (see fig 7) the quadratic law fits the data better than the cubic. This result is probably related to the asymmetry induced by the charge distribution (2) and is in agreement with the analysis developed in Ref. [8] where a quadratic scaling law was shown to reproduce well the emittance behaviour due to beam misalignments.

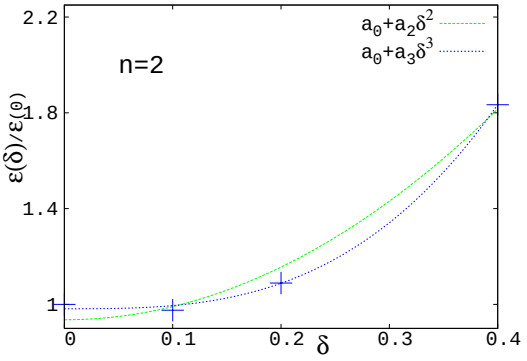

Figure 6: Emittance growth vs δ for $n = 2$ in the position of the first minimum of the emittance as computed by TREDI for ρ as in eq. (2).

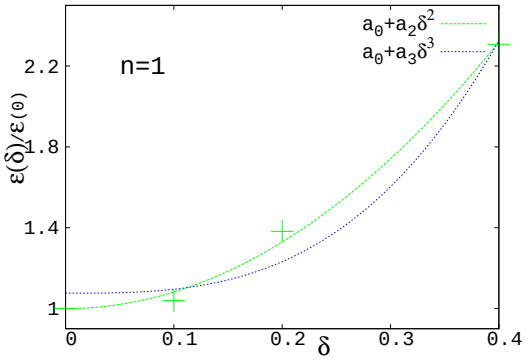

Figure 7: Emittance growth vs δ for $n = 1$ in the position of the first minimum of the emittance as computed by TREDI for ρ as in eq. (2).

CONCLUSIONS

In this contribution we have extended the analysis of the emittance dilution as a function of the frequencies associated to a non axi-symmetric perturbation of the ideal transverse density extracted from the photocathode. A scaling law of this effect in function of the perturbation amplitude has been derived and some indications of the dependence of the effect with the transverse frequency have been ob-

tained. In the future we plan to further refine this analysis and check the scaling laws derived here against the predictions from other numerical codes. At high k_n the results observed for a sine-like (odd) perturbation of the type (2) are similar to the predictions for a cos-like (even) perturbation like (1). At low n the results are substantially different since the parity of the initial charge distribution plays a significant role. We plan to continue this study to the beam slice emittance, which is not affected by correlations between slices and is probably a better indicator of the influence of cathode inhomogeneities on the beam quality. This work will require a significant computational effort since the number of macroparticles and the transverse mesh fineness for the evaluation of the fields grow non-linearly with the frequency associated to the transverse mode.

REFERENCES

[1] L. Serafini, J.B. Rosenzweig, "Envelope analysis of intense relativistic quasilaminar beams in RF photoinjectors: a theory of emittance compensation" Phys. Rev. E55 (1997) p.7565.

[2] L. Giannessi, M. Quattromini and C. Ronsivalle, “Emittance dilution due to 3D perturbations in RF-photoinjectors”, Proceedings of 9^{th} European Particle Accelerator Conference, 5 to 9 July, 2004, Lucerne, to be published.

[3] L. Young, J. Billen "PARMELA" *LA-UR-96-1835*.

[4] L. Giannessi, M. Quattromini, “TREDI simulations for high-brilliance photoinjectors and magnetic chicanes”, PRST-AB 6 120101 (2003), Web site: http://www.tredi.enea.it.

[5] AA.VV., LCLS Design Report, SLAC-R-593, April 2002.

[6] C. Limborg et al. "Code comparison for simulations of photoinjectors ", Proceedings PAC2003.

[7] M. Ferrario, private communication.

[8] F. Ciocci et al., Nucl. Instr. and Meth. A393, (1997), 434.

ON-LINE SPECTRAL MONITORING OF THE VUV FEL BEAM AT DESY

P. Nicolosi, L. Poletto[#], M.G. Pelizzo, INFM & Dep. of Information Engineering, Padova (Italy)
J. Feldhaus, U. Jastrow, U. Hahn, E. Ploenjes, K. Tiedtke, HASYLAB-DESY, Hamburg (Germany)

Abstract

A stigmatic spectrometer for the 2.5-40 nm EUV region has been realized. The design consists of a grazing-incidence spherical variable-line-spaced grating with flat-field properties and of a spherical mirror mounted in the Kirkpatrick-Baez configuration that compensates for the astigmatism. The spectrum is acquired on a fluorescent screen optically coupled to an intensified CCD detector, that can be moved along the spectral focal curve to select the spectral region to be acquired. The spectral and spatial resolution of the system have been characterized by using the emission from an hollow-cathode lamp or a laser-produced plasma. At present, the instrument is installed at the VUV-FEL at DESY for the spectral monitoring of the FEL beam in the 20-45 nm region.

INTRODUCTION

The FEL at the TESLA Test Facility (TTF) at DESY achieved first self amplified spontaneous emission (SASE) in the vacuum-ultraviolet in early 2000 [1] and it reached gain up to saturation between 80–120 nm in 2001 [2]. During an on-going upgrade which will be completed at the end of 2004, the VUV-FEL at DESY is being transformed into the worldwide first FEL user facility for vacuum-ultraviolet (VUV) and soft X-ray radiation from 100 to 6 nm wavelength.

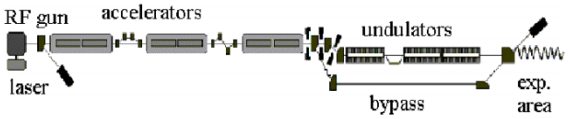

Fig. 1. Layout of the VUV-FEL at DESY

Fig. 1 shows the layout of the linear accelerator. The complete accelerator is currently newly constructed to finally reach energies of up to 1 GeV [3]. A new photoinjector/bunch compression concept is used, and the gun has reached a minimum normalised emittance of 1.5 and 1.7 π mm mrad in the vertical and horizontal plane respectively. In addition, a special collimator system has been designed to protect the undulators, the electron beam focusing along the undulator has been changed, and improved diagnostics have been developed both for the electron and the photon beam. A short accelerator section with third-harmonic cavities to linearize the energy chirp along the electron bunch, which is required for optimum bunch compression, as well as the 6th accelerator module will not be installed into the injector until 2006. Consequently, the wavelength range of the FEL will initially be limited to approximately 20 - 60 nm.

FELs based on self-amplified spontaneous emission produce highly intense, transversely coherent radiation within a single pass of a relativistic electron bunch through a long undulator. The exponential amplification process of a SASE FEL starts from spontaneous emission of the electron beam. Hence, individual radiation pulses differ in intensity, temporal structure, and spectral distribution. Extensive characterization of the FEL beam [4] as well as a first set of experiments on the interaction of such VUV radiation with cluster beams [5] and surfaces [6] was carried out during TTF Phase 1. For commissioning of the VUV-FEL various photon diagnostic units used for beam intensity and profile measurements during the proof-of-principle experiments on TTF1 have been modified and will be installed at the end of the accelerator tunnel, above the electron beam dump. Initial start-up of the FEL is planned in the 30-40 nm spectral region. A grazing incidence grating spectrometer will replace the normal incidence spectrometer used for TTF1 in this area to measure the spectral structure of the FEL pulses on a single shot basis.

An important feature of the SASE FEL pulses is their short duration of 40-200 femtoseconds. An estimate of the pulse duration can be derived from the spectra of the spectrometer already during the commissioning phase, since the spectral width of each peak shown in a single shot-spectrum is related to the radiation pulse length [1].

Tab. 1. Expected parameters of the FEL beam.

Wavelength	100 – 6 nm
Pulse energy	0.1 – 1mJ
Pulse duration (FWHM)	30 – 400 fs
Peak power	0.3 - 2.8 GW
Spectral width (FWHM)	~0.5 %
Spot size at undulator exit (FWHM)	1.4 – 0.14 mm
Angular divergence (FWHM)	170 – 24 μrad
Peak brillance	$1\cdot10^{28}$–$3\cdot10^{30}$ ph/s/mrad^2/mm^2/0.1 %bw

The expected parameters of the VUV-FEL are summarized in Tab. 1 [7]. It is developed into a full user facility with five experimental stations using the FEL beam alternately [3]. Three experimental stations use the direct SASE FEL beam and are equipped with focusing mirrors providing spot sizes of approximately 100 or 10 μm. Two experimental stations for experiments requiring a spectral bandwidth narrower than the natural FEL bandwidth are served by a high resolution plane grating

[#] Contact person: poletto@dei.unipd.it

monochromator, that has a resolution of 80000-10000 while providing a wide tuning range from 10 eV to 1 keV. Alternatively to the monochromator beamlines, the spectral distribution of individual FEL pulses will be determined online by a variable-line-spacing (VLS) grating spectrometer serving the three "SASE beamlines" [8]. One of the plane mirrors in the FEL beam distribution system will be replaced by the VLS grating which reflects most of the radiation in zeroth order to the experiment and disperses only a small fraction in first order for spectral analysis.

The grazing-incidence stigmatic spectrometer that will be used to measure the single-shot spectral structure of the FEL pulses in the 20-46 nm spectral region is presented here. The instrument was designed and realized by the INFM-LUXOR laboratory (Padova, Italy) for absorption spectroscopy on laser-produced plasmas in the 5-45 nm spectral region [9]. The main system requirements are high spatial and spectral resolution and a plane focal curve with the detector used at almost normal incidence, such as in the case of using grazing-incidence spherical variable-line-spaced (SVLS) gratings [10]. The design consists of a SVLS grating with flat-field properties and of a spherical mirror mounted in the Kirkpatrick-Baez configuration that compensates for the astigmatism. The spectrum is acquired on a fluorescent screen coupled to an intensified CCD detector, that can be moved along the spectral focal curve to select the spectral region to be acquired. The spectral and spatial resolution of the system have been characterized by using the emission from an hollow-cathode lamp.

SPECTROMETER DESIGN AND REALIZATION

The design principle of the SVLS grating for flat-field spectrographs is already well established [10] and will be here briefly resumed. The groove density along the grating surface is expressed as

$$\sigma(y) = \sigma_0\left(1 + 2\frac{b_2}{R}y + 3\frac{b_3}{R^2}y^2 + 4\frac{b_4}{R^3}y^3\right) \quad (1)$$

where σ_0 is the central groove density, R is the grating radius and b_2, b_3, b_4 are the ruling parameters for space variation.

The main aberration to be corrected is the spectral defocusing, which increases linearly with the width of the illuminated area. The spectral focal curve, that is the curve where the spectral defocusing zeroes, is given by

$$\frac{\cos^2\alpha}{r} + \frac{\cos^2\beta}{r'} - \frac{\cos\alpha + \cos\beta}{R} + 2(\sin\alpha + \sin\beta)\frac{b_2}{R} = 0 \quad (2)$$

where r, r' are respectively the grating entrance and exit arms, and α and β are the incidence and diffraction angles, which are related to the grating equation

$$\sin\alpha - \sin\beta = m\lambda\sigma_0 . \quad (3)$$

To minimize the defocusing on the detector, it is necessary to make the focal curve given by Eq. (2) as close as possible to the detector surface in the spectral range of interest, by acting on the parameters R and b_2. Similarly it can be shown that the parameters b_3 and b_4 can be chosen to minimize coma and spherical aberration.

The main difference between the grazing-incidence SVLS design and the classical grazing-incidence Rowland configuration with uniform-line-spaced gratings is that the focal surface as given by Eq. (2) is almost flat with the detector operated at near normal incidence.

The astigmatism in the plane perpendicular to the plane of spectral dispersion is corrected by a spherical mirror mounted with its tangential plane coincident with the equatorial plane of the grating, i.e. a Kirkpatrick-Baez configuration in which one of the two elements is a grating [11]. The mirror does not provide any focusing in the plane of spectral dispersion, leaving unchanged the grating focal properties given by Eq. (2) that determine the spectral resolution. On the other side, the grating does not provide any spatial focusing, that is in a plane perpendicular to the plane of dispersion, so the spatial performances are determined only by the characteristics of the mirror. The radius of the mirror R_m is determined as

$$R_m = \frac{2}{\cos\theta_m}\left(\frac{1}{p_m} + \frac{1}{q_m}\right)^{-1} \quad (4)$$

where p_m and q_m are respectively the mirror entrance and exit arms and θ_m is the incidence angle.

It can be shown [9] that such a configuration has also spectral and spatial resolution capability for extended sources (e.g. a laser-produced plasma), due to the Kirkpatrick-Baez configuration that maintains separated the spectral and spatial focal properties on two different optical components. The spectral resolution is constant also for off-axis points, while the spatial resolution decreases with the off-axis distance. In case of a 2 mm source size, the spatial resolution with 5 mrad acceptance angle and a mirror operated at 87° is 25 μm on-axis and 130 μm at the extremes of the field-of-view (i.e. ±1 mm off-axis distance). In other stigmatic designs with spherical or plane VLS gratings, the astigmatism is corrected by an additional mirror mounted on the same plane as the grating [12, 13]: in this case, the spectral and spatial focusing properties are coupled on the mirror and both spectral and spatial resolutions decrease for extended sources far from the optical axis.

The layout of the configuration is shown in Fig. 2. The central groove density of the SVLS grating is 1200 lines/mm; the parameters for groove space variation have been optimized to have an almost flat focal surface in the 10-40 nm spectral region. The calculated focal curve is shown in Fig. 3: it is almost perpendicular to the tangent to the grating on its vertex. Given the low accepted angular aperture of the grazing-incidence system (5 mrad in the spectral plane) and the detector pixel size (20-25 μm), the depth of focus for this system is considered about 5 mm.

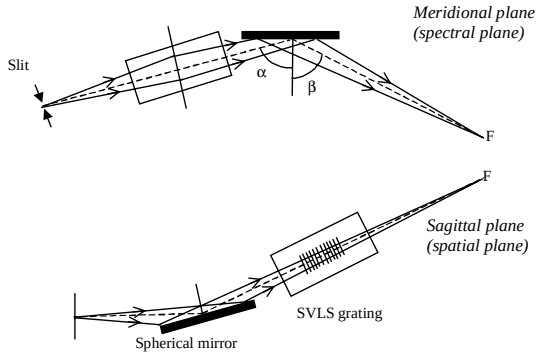

Fig. 2. Layout of the grazing-incidence spectrometer.

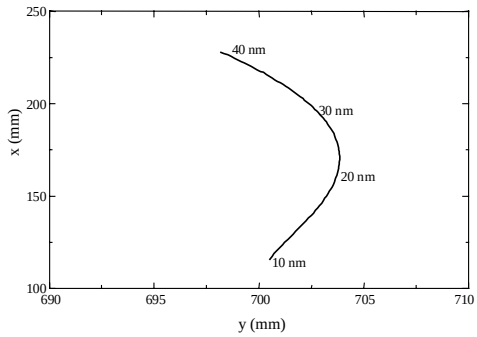

Fig. 3. Spectral focal curve of the SVLS grating. The *x* and *y* axes are defined respectively parallel to the grating normal and parallel to the tangent to the grating on its vertex. The origin of the reference system is the grating vertex.

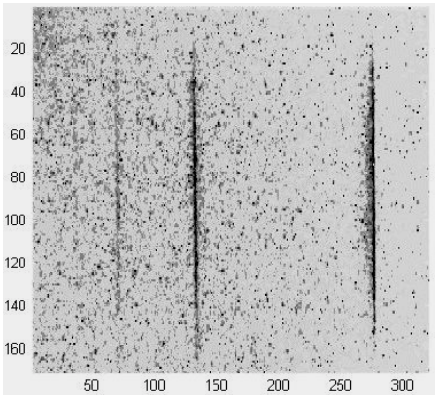

Fig. 4. He spectrum. The wavelength is increasing from left to right. The two most intense lines are HeII 25.6 nm (pixel 130) and 24.3 nm (pixel 275).

The spectrum is acquired on a fluorescent screen optically coupled to an intensified CCD detector. Since the length of the spectrum is larger than the detector size, the latter must be translated along a straight line fitting at the best the focal curve in the region of interest. In order to do this, the detector is mounted on a linear drive and connected to the spectrometer with a system with three laminar bellows. An acquired spectrum is shown in Fig. 4. Additional details of the optical design are presented elsewhere [9].

The parameters of the spectrometer are resumed in Tab. 2.

Tab. 2. Parameters of the spectrometer.

Accepted aperture	5 mrad (spectral plane) 10 mrad (spatial plane)
Spherical mirror	
Entrance/exit arms	400 mm / 1000 mm
Incidence angle	87.5°
Coating	Gold
SVLS gratings	
Central groove density	1200 gr/mm
Spectral range	5-50 nm
Entrance/exit arms	650 mm / 750 mm
Incidence angle	87°
Coating	Platinum
Detector	
Phosphor screen diameter	25 mm
Objectives	50 mm f/1.0 105 mm f/1.8
Intensified CCD camera	MCP and cooled CCD
Detector format	1280 pixel × 1024 pixel

INSTRUMENT PERFORMANCE

The spectrometer was aligned and calibrated in the 24-46 nm spectral region using as source an hollow-cathode lamp. The measured performance are very close to the theoretical predictions: the spectral lines have FWHM of about two pixels. Being the optics aligned at the best, the detector was positioned on the straight line fitting at the best the spectral focal curve. The spectral region of operation is selected by moving the detector along this straight line. An absolute encoder gives the relative translation of the detector with respect to a reference point.

The system calibration is divided in two steps: 1) the measurement of the detector scale factor and 2) the wavelength calibration.

The scale factor (μm/pixel) expresses the size of the phosphor screen imaged in one CCD pixel: it has been measured as 8.0 μm/pixel.

The wavelength calibration is performed by measuring the position of the focal plane with respect to the grating vertex. The parameters that allow to identify the detector plane (i.e. the straight line where the detector is moved) are calculated by acquiring some known spectra from the hollow-cathode source together with the encoder measurements on the detector position, and then applying a fitting procedure. The residual calibration errors are less than 0.03 nm and are mainly due to the intrinsical precision of the encoder.

The actual spectral dispersion is shown in Fig. 5 assuming 32 μm pixel size (i.e. a binning factor of 4 on the CCD). The resolution, calculated as the ratio $\lambda/\Delta\lambda_{2px}$ with $\Delta\lambda_{2px}$ evaluated within two pixels, is 1500@30 nm and 1900@45nm, definitely higher than the expected FWHM of the FEL emission.

Some calibrated spectra are finally shown in Fig. 6.

At present, the instrument is installed at the VUV-FEL at DESY for the spectral monitoring of the FEL beam in the 20-45 nm region.

REFERENCES

[1] J. Andruszkow et al, Phys. Rev. Lett. 85 (2000), 3825
[2] V. Ayvazyan et al, Phys. Rev. Lett. 88 (2002), 104802
[3] http://www-hasylab.desy.de
[4] R. Ischebeck et al, Nucl. Instr. and Meth. A 507 (2003), 175
[5] H. Wabnitz et al, Nature 420 (2002), 482
[6] A. Andrejczuk et al, HASYLAB An. Rep. 1 (2001), 117
[7] K. Tiedtke et al, to be published in AIP Conf. Proc. 2004 (SRI 2003, San Francisco, CA, U.S.A.)
[8] R. Reininger et al, to be published in AIP Conf. Proc. 2004 (SRI 2003, San Francisco, CA, U.S.A.)
[9] L. Poletto et al, Appl. Opt. 41 (2002), 172
[10] T. Harada and T. Kita, Appl. Opt. 19 (1980), 3987
[11] L. Poletto and G. Tondello, Appl. Opt. 39 (2000), 4000
[12] P. Fan et al, Appl. Opt. 31 (1992), 6720
[13] M. Hettrick and S. Bowyer, Appl. Opt. 22 (1983), 3921

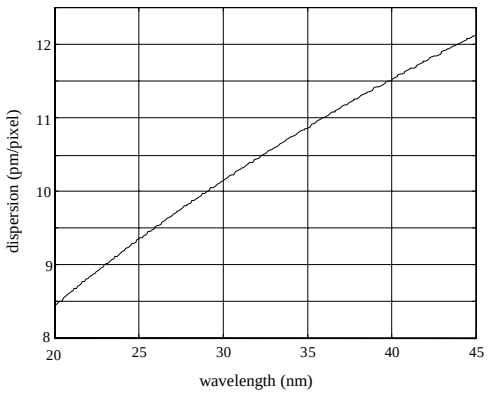

Fig. 5. Actual spectral dispersion. The pixel size is assumed 32 μm.

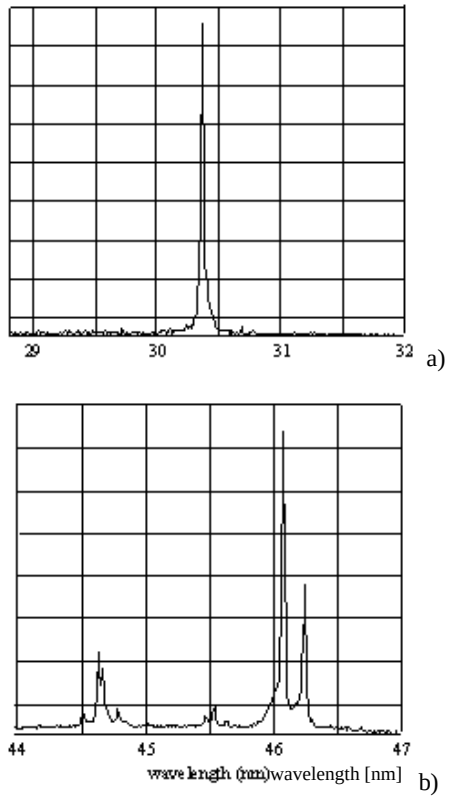

Fig. 6. Spectra acquired with the hollow-cathode lamp. The plots are horizontal cross-sections across the CCD image. a) He spectrum (HeII 30.4 nm line); b) Ne spectrum (NeII 44.62, 44.66, 46.07 and 46.24 nm lines).

ABCD MATRIX METHOD: A CASE STUDY

Z. Seidov*, Y. Pinhasi, A. Yahalom,
The College of Judea and Samaria, P.O. Box 3, Ariel 44837, IL

Abstract

In the Israeli Electrostatic Accelerator FEL (EAFEL), the distance between the accelerator end and the wiggler entrance is about 2.1 m. A 1.4 MeV, 2 Amp electron beam is transported through this space using four similar quadrupoles. The transfer matrix method (ABCD matrix method) was used for simulating the beam transport. We found a reasonable agreement between experimental results and simulations. The inverse problem of finding the electron beam emittance at S1 screen position (before quads) by using the spot dimensions at S2 screen (after quads) as function of quad currents is considered. Spot and beam are described as ellipses by using STB (Spot-to-Beam) procedure [1], and the trace-ellipse transformation is used to find the emittance.

EXPERIMENTAL LAYOUT

The scheme of quadrupoles *Q1-Q4* and diagnostic screens S1 and S2 between the end of accelerator and the wiggler entrance at the Israeli EAFEL [2] is shown in Fig. 1. We use the following numerical values of parameters: $E = 1.4$ MeV, electron beam energy; $d = 0.205$ m, drift space between quadrupoles; $d_q = 0.140$ m, effective length of quadrupoles; $d_1 = 0.207$ m, drift space between S1 screen and first quadrupole; $d_2 = 0.308$ m, drift space between last quadrupole and S2 screen; however all formulas are quite general and valid for any value of the parameters involved.

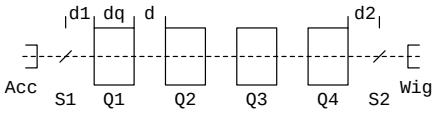

Figure 1: Experimental layout (not in scale).

TRANSFER MATRICES

We need transfer matrices of two kinds: for drift space and for quads (see, e.g., [3], [4]).
Drift space matrices are

$$D = \begin{pmatrix} 1 & d \\ 0 & 1 \end{pmatrix},\ D_i = \begin{pmatrix} 1 & d_i \\ 0 & 1 \end{pmatrix},\ i = 1, 2. \quad (1)$$

Converging and diverging quadrupole matrices are

$$M_c(I) = \begin{pmatrix} c & s/t \\ -s\,t & c \end{pmatrix}, \quad \begin{array}{l} c = \cos(t\,d_q), \\ s = \sin(t\,d_q), \end{array} \quad (2)$$

$$M_d(I) = \begin{pmatrix} ch & sh/t \\ sh\,t & ch \end{pmatrix}, \quad \begin{array}{l} ch = \cosh(t\,d_q), \\ sh = \sinh(t\,d_q), \end{array} \quad (3)$$

$$t \equiv \sqrt{\alpha\,I}, \quad \alpha = \frac{e\,\eta}{\gamma\,m\,v} = 24.78\,\mathrm{A^{-1}m^{-2}}, \quad (4)$$

where I is quad's current, e, m, v, γ are electron's charge, mass, velocity, and relativistic parameter, η is quad's magnetic field gradient, $\eta = 0.1522$ T/m for quads used in EAFEL, and value of α is given for E=1.4 MeV beam energy.

It is of interest to mention, comparing (2) and (3), that $M_d(I) = M_c(-I)$.

The combined transfer matrix from S1 to S2 for X-coordinate is a *scalar* product of all relevant matrices

$$\begin{aligned} M_x \;=\; & D_2 \cdot M_d(I_4) \cdot D \cdot M_c(I_3) \\ & \cdot D \cdot M_d(I_2) \cdot D \cdot M_c(I_1) \cdot D_1. \end{aligned} \quad (5)$$

Without loss of generality we consider in (5) the case when the first quadrupole is *converging* in X (and *diverging* in Y, but we consider here only X-coordinate of the beam). To simplify notations, we write down the matrix M_x as

$$M_x = \begin{pmatrix} A_x & B_x \\ C_x & D_x \end{pmatrix}, \quad (6)$$

with $\det(M_x) = 1$, that is:

$$A_x\,D_x - B_x\,C_x = 1. \quad (7)$$

Relation between initial, at screen S1, beam parameters (x_1, x_1'), and final, at screen S2, beam parameters (x_2, x_2') is

$$\begin{pmatrix} x_2 \\ x_2' \end{pmatrix} = M_x \cdot \begin{pmatrix} x_1 \\ x_1' \end{pmatrix}. \quad (8)$$

BEAM WAIST AT S1

Of particular interest is the case where initially, at screen S1, there is a *waist* of *circular* beam with emittance $\varepsilon_x = \varepsilon_y = \varepsilon \cdot \pi$ and radius $R_x = R_y = r_1$; then the equation of the trace-ellipse is (without loss of generality, hereafter we consider only X-coordinate)

$$\left(\frac{x_1}{r_1}\right)^2 + \left(\frac{x_1'}{\varepsilon/r_1}\right)^2 = 1. \quad (9)$$

We note that "area" of the ellipse (9) is $S = \pi\,\varepsilon$, that is the area of trace-ellipse is a measure of beam emittance. The maximal values of x_1 and x_1' are r_1 and ε/r_1, respectively. Expressing (x_1, x_1') in terms of (x_2, x_2') from Eq. (8),

$$\begin{pmatrix} x_1 \\ x_1' \end{pmatrix} = M_x^{-1} \cdot \begin{pmatrix} x_2 \\ x_2' \end{pmatrix}, \quad (10)$$

* seidov@bgumail.bgu.ac.il

and inserting (x_1, x_1') from Eq. (10) into Eq. (9), we obtain the equation for the final trace-ellipse at screen S2

$$a_x\, x_2^2 + 2\, b_x\, x_2\, x_2' + c_x\, {x_2'}^2 = 1, \tag{11}$$

$$\begin{aligned} a_x &= \left(\frac{D_x}{r_1}\right)^2 + \left(\frac{C_x}{\varepsilon/r_1}\right)^2, \\ b_x &= -\frac{B_x\, D_x}{r_1^2} - \frac{A_x\, C_x}{(\varepsilon/r_1)^2}, \\ c_x &= \left(\frac{B_x}{r_1}\right)^2 + \left(\frac{A_x}{\varepsilon/r_1}\right)^2. \end{aligned} \tag{12}$$

Here coefficients a_x, b_x, and c_x are functions of all twelve input parameters: d_1, d, d_2, d_q, η, r_1, ε, I_1, I_2, I_3, I_4, E. Note that due to the *paraxial* approximation, determinants of all used transfer matrices are equal to 1, hence the area of final trace-ellipse (11) is equal to the area of initial trace-ellipse (9), that is *emittance* of the beam is preserved (in both X- and Y-coordinates).
We notice that

$$a_x\, c_x - b_x^2 = 1/\varepsilon^2, \tag{13}$$

analog of Courant-Snyder invariant. Thus coefficients a_x, b_x, c_x are analogs of the transport parameters or Twiss parameters.

Beam envelope at S2

From Eq. (11) we may find parameters of the beam at S2 screen position. The envelope of beam in X is

$$r_2 = x_{2,max} = \sqrt{\frac{c_x}{a_x\, c_x - b_x^2}} = \varepsilon\, \sqrt{c_x}. \tag{14}$$

The slope of the beam envelope is

$$r_2' = (x_{2,max})' = -\frac{\varepsilon\, b_x}{\sqrt{c_x}}. \tag{15}$$

The area of the final trace-ellipse is equal to area of the initial trace-ellipse that is the *emittance is preserved*. Maximal value of x_2' is

$$(x_2')_{max} = \sqrt{a_x}/\varepsilon. \tag{16}$$

Notice the difference between $(x_{2,max})'$ and $(x_2')_{max}$: the first is x_2' at point $x_2 = x_{2,max}$, while the second is x_2' at the point where x_2' is maximal. From (14) and (12) the radius of beam in X-coordinate is

$$r_2 = r_1 \sqrt{\left(\frac{\varepsilon\, B_x}{r_1^2}\right)^2 + A_x^2}. \tag{17}$$

Also from (15) and (12) the condition $r_2' = 0$ for the *beam waist* at S2 is

$$B_x\, D_x\, \varepsilon^2 = -A_x\, C_x\, r_1^4. \tag{18}$$

If we require that beam has a waist also in Y-direction then we have similar equation

$$B_y\, D_y\, \varepsilon^2 = -A_y\, C_y\, r_1^4. \tag{19}$$

Equations (18, 19) are *two* equations for *four* free parameters, quad currents, so we have in principle a 2D set of possible solutions (not all of them having physical meaning). Equation (17) allows a fully *analytical* study of beam radius r_2 at S2 as function of any variable parameter (mainly quad currents) *assuming* that beam at S1 is at its waist and has emittance ε, while we can measure radius r_1 from spot at S1. As an example, for beam waist at S1 with $r_1 = 14$ mm and $\varepsilon = 6$ mm mrad, expansion of transfer matrix elements up to terms linear in quad currents gives

$$\begin{aligned} A_x &= 1 - 4.90\, I_1 + 3.71\, I_2 - 2.51\, I_3 + 1.31\, I_4, \\ B_x &= 1.69 - 1.35\, I_1 + 2.30\, I_2 - 2.42\, I_3 + 1.72\, I_4, \\ C_x &= 3.47\, (-I_1 + I_2 - I_3 + I_4), \\ D_x &= 1 - 0.961\, I_1 + 2.16\, I_2 - 3.35\, I_3 + 4.55\, I_4, \\ r_2 &= 14.02 - 68.6\, I_1 + 51.8\, I_2 - 35.1\, I_3 + 18.4\, I_4. \end{aligned} \tag{20}$$

In another case with $I_1 = I_2 = I_3 = I_4 = I$, expansion can be easily made up to I^4:

$$\begin{aligned} A_x &= 1 - 2.39\, I - 3.57\, I^2 + 1.26\, I^3 + 1.32\, I^4, \\ B_x &= 1.69 + 0.242\, I - 1.68\, I^2 - 0.128\, I^3 + 0.336\, I^4, \\ C_x &= -7.18\, I^2 + 3.77\, I^4, \\ D_x &= 1 + 2.39\, I - 2.84\, I^2 - 1.26\, I^3 + 0.944\, I^4, \\ r_2 &= 14.02 - 33.46\, I - 49.77\, I^2 + 18.21\, I^3 + 20.21\, I^4. \end{aligned} \tag{21}$$

Note that in practice approximations (20) can be used for values of currents lower less than $\approx$ .1 A, while (21) are good up to $I \approx .25$ A, see Fig. 2.

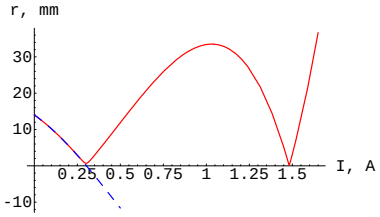

Figure 2: Radius r_2 of beam at S2 vs. current $I = I_1 = \ldots = I_4$; beam has waist at S1, with emittance $\varepsilon = 6$ mm mrad, and radius $r_1 = 14$ mm. Blue dashed line is approximation for r_2 in Eq. (21). Note that, at minima, the radius of beam is very small, yet non-zero.

Beam emittance at S1

We can reverse Eq. (17) to find emittance from experimentally measurable radii of beam, r_1 and r_2, at S1 and S2 (and known quad currents)

$$\varepsilon_1 = \frac{r_1}{B_x} \sqrt{r_2^2 - (r_1\, A_x)^2}. \tag{22}$$

Though in paraxial approximation the beam emittance is preserved, that is $\varepsilon_1 = \varepsilon_2$, still we keep index 1 at ε_1 taking into account that real experimental errors (and nonlinearities in electron-optic elements) will give a set of values of emittance (for various quad currents) and all these refer to *beam emittance at S1* (and should be properly averaged). Also we note that the procedure of emittance finding by Eq. (22) is applicable for any electron-optic element (e.g. solenoid) which can be described in terms of transfer matrix. The only (but *very* essential) assumption is that beam has a waist at S1. The other (not so essential for the real parameters used in EAFEL) assumption is neglecting space-charge effects, which is admissible in our first approximation. Also of interest is to mention that for *switched off quads* (all quad currents are zero) we have $A_x = 1$, and $B_x = 1.69$ m (full distance from S1 to S2), and we recover from (22) the well-known envelope equation for free-space expansion of beam with non-zero expansion. In this relation we note that distance $B_x = 1.69$ m is *too* small to deduce the emittance by usually used formula $\varepsilon \approx r_2\, r_1/B_x$, which gives a *much smaller* value of emittance. The exact formula is

$$\varepsilon = \frac{r_1}{B_x}\sqrt{r_2^2 - r_1^2}. \qquad (23)$$

EXPERIMENT AND SIMULATIONS

Experimental data

In Fig. 3 some pictures are presented of spot at S2 for various currents of Q3 and Q4, while I_1=1.26 A and I_2=1.14 A are kept constant. The quality of pictures does not allow to measure accurately the dimensions of spot (and beam), though general feature (strong dependence on I_3 and very weak dependence on I_4) is evident. Spot at S1 (not depending on quad currents) was treated by STB procedure [1] and found to have radii $r_x = 15$ mm and $r_y = 9$ mm.

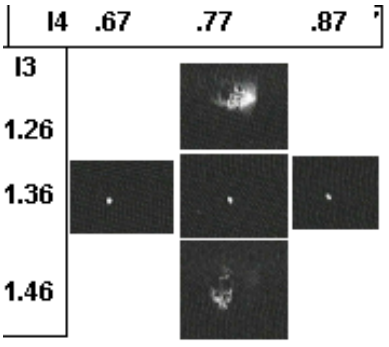

Figure 3: Spot at S2 for various currents I_3 and I_4, for I_1=1.26 A and I_2=1.14 A.

Simulations

In Table 1 the radii in X- and Y-coordinates are shown according to Eq. (17), for two emittances, 6 and 18 mm mrad.

Table 1: Radii of beam at S2, in mm, for various I_3 and I_4, for fixed currents I_1=1.26 A and I_2=1.14 A

	I4=.67		I4=.77		I4=.87	
I3 / ε	r_x	r_y	r_x	r_y	r_x	r_y
1.26 / 6	11.8	2.4	14.3	1.2	16.7	0.23
1.26 / 18	11.8	2.6	14.3	1.5	16.7	0.69
1.36 / 6	1.8	4.1	3.7	2.8	5.7	2.8
1.36 / 18	4.3	6.8	3.0	4.6	5.7	1.7
1.46 / 6	8.1	5.9	6.7	4.4	20.1	5.0
1.46 / 18	8.2	6.1	6.7	4.5	20.1	5.1

The values of radii of beam at S1 $r_x = 15$ mm and $r_y = 9$ mm are used. The general tendency is in agreement with experimental data. The very small dependence of spot dimensions on beam emittance is good from one point of view (the simulation results are safe), and not so good from the other point of view (defining the beam emittance is very difficult, practically impossible for given quad currents). We note, that though not so critical in defining the beam dimensions at S2, the value of the emittance is critical for the beam quality and for getting lasing in the wiggler.

DISCUSSION

We reported here briefly on the procedure used for simulation of electron beam transport between accelerator section and the wiggler of the Israeli EA FEL. The formulas for envelope Eq. (17) and for emittance Eq. (22) of the beam at S2 are valid under the assumption that at S1 there is the beam's *waist* (in the relevant coordinate). Another assumption is neglecting the (small) space-charge effects. We note also that Eq. (17) and Eq. (22) are valid for *any* current distribution (without "holes") across the beam cross-section. The case of converging/diverging beam at S1 screen can be treated by introducing a *virtual* focusing/defocusing coil at the S1 position. It changes the resultant transfer matrix while Eq. (17) and Eq. (22) are not changed. Also included in the program (mainly in MATEMATICA) are cases of arbitrary trace-ellipse and non-circular non-centered beam at S1, and due to space reasons we only mention them here.

The problem with finding beam emittance at S1 from spot at S2 (spot's variation with quad currents) is that, for most quad currents practically used in the EAFEL, the spot at S2 depends on emittance very weakly. We attempted to find the situation when the influence of emittance on spot is essential. Note that transfer matrix elements A_x and B_x in Eq. (17) and Eq. (22) do not depend on beam emittance or radius at S1 but only on quad parameters (and beam en-

ergy). For example, the situation $A_x = 0$ is the most favorite for defining emittance. In this case the beam radius at S2 is proportional to the beam emittance at S1 and inversely proportional to the beam radius at S1. However, in all considered cases when $A_x = 0$ the resulting spot/beam radius at S2 screen is *very* small (due to small value of B_x) and the exact measurements are impossible (also due to a rather poor quality of pictures obtained by the frame grabber hardware and software available to us at present). Still we believe that the "quad scanning method" (which is not claimed to be quite novel, see, e.g., [5]) can be successfully applied in the future experiments in EAFEL. What we reported here are only the preliminary results.

ACKNOWLEDGEMENTS

The idea of the *virtual coil* should be credited to A. Gover. The work was supported by Israeli Ministries of Immigrant Absorption, Science, and Environment.

REFERENCES

[1] Z. Seidov, Y. Pinhasi, A. Yahalom, Spot-to-beam procedure, these Proceedings, TUPOS15.

[2] A. Gover et al, Nucl. Instr. and Meth. A 528 (2004) 23; arXiv.org/physics/0408054.

[3] M. Reiser, *Theory and Design of Charged Particle Beams*, (John Wiley & Sons, Inc., New York, 1994).

[4] S. Humphries, Jr., *Charged Particle Beams*, (Wiley, New York, 1990).

[5] R. Chaput et al, Nucl. Instr. and Meth. A 393 (1997) 474.

SPOT-TO-BEAM PROCEDURE

Z. Seidov*, Y. Pinhasi, A. Yahalom,
The College of Judea and Samaria, P.O. Box 3, Ariel 44837, IL

Abstract

We describe the interactive spot-to-beam MATHEMATICA procedure for a) approximating the spot image at the screen (and beam at screen position) as an ellipse, b) getting five parameters of the elliptic beam (two diameters, center coordinates, and orientation angle). The basic idea is to "map" the *reference* holes at the diagnostic screen onto the XY plane normal to the beam propagation direction (Z-axis). All distortions of the image, e.g., due to camera-screen disposition can be, in principle, taken into account. With the non-linear LSM fitting, the "curved" coordinate system of the holes at image is transferred to the Cartesian "Laboratory" coordinate system (C.S.) at XY plane. Then the fitting ellipse is found in the C.S., by solving the system of N linear equations for 5 unknown parameters of beam ellipse, where N>5 is a number of the sample points on edge (boundary) of the spot image. Examples of the real measurements in the Israeli Electrostatic Accelerator FEL (EAFEL) are demonstrated. The accuracy of the beam diameter values is ≈.5 mm depending on picture quality and the operator's experience (and patience!). The procedure is to be used in routine measurements of EAFEL to improve the electron beam transport.

INTRODUCTION

In the EAFEL [1], the distance between the electron gun cathode and the accelerator's entrance is about 1.9 m and 45 keV, 2 Amp electron beam is transported through this space by using (among other electron-optics elements) four focusing coils C1-C4 and two diagnostic screens SP and S0. Unfortunately the hardware and software used by us at present do not provide a brightness distribution in a spot image and even the spot boundary is not always well defined. Hence we had to try to measure the spot (and beam) geometric parameters to the best of our ability.

EXPERIMENTAL LAYOUT

The scheme of the focusing coils *C1-C4* and the diagnostic screens SP and S0 is shown in Fig. 1.

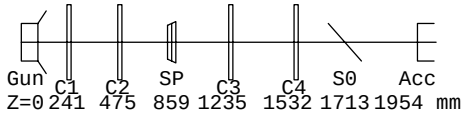

Figure 1: Experimental layout (not in scale).

* seidov@bgumail.bgu.ac.il

We use the following numerical values of parameters: $E = 45$ keV, electron beam energy; Z-coordinates of screens and coils (assuming that electron gun is at Z=0): $z_{sp} = 859$ mm, position of pepperpot screen SP (Ti-Al_2O_3), $z_{s0} = 1713$ mm, position of S0 screen (ceramic); $z_1 = 241$ mm, $z_2 = 475$ mm, $z_3 = 1235$ mm, and $z_4 = 1532$ mm, positions of focusing coils C1, C2, C3 and C4, respectively.

Note that SP screen is rotated by 45 deg around vertical (Y) axis, while S0 screen is rotated by 45 deg around horizontal (X) axis, both X and Y axes being normal to Z axis, direction of beam propagation. For the spot measurement purposes, there are made *reference holes* at all diagnostic screens of EAFEL. Due to the various optical distortions (mainly caused by too close and not proper camera-screen disposition), the problems with the frame grabber hardware and software etc., there is no direct way to measure the spot (and beam) parameters from the raw images. That is why the special interactive Spot-to-Beam (STB) procedure (written in MATHEMATICA [2]) was developed in the EAFEL group.

STB PROCEDURE

Basic assumptions of STB

The basic assumptions of the STB procedure are:

a) the *reference hole* positions at the diagnostic screen are well known and their centers are perfectly aligned along straight lines (that is we ignore manufacture errors if any)

b) the screen position is known (the screen center is on Z-axis which is *not* necessarily position of the spot and beam centers), the screen rotation angle is 45 deg, and only around one of axes, X or Y

c) we neglect the difference in the ray paths to the nearest and farthest sides of screen (this difference is $D/\sqrt{2} \approx 0.71\,D \approx 3.6$ cm for the screen diameter $D = 5$ cm); we do such not because we think that this difference is negligible but rather because right now we do not know how properly to take it into account in the STB procedure

d) the other essential assumption is that the beam (necessarily) and the spot (optionally) can be described as the elliptical figures

e) it is assumed that the beam propagates (at least near the screens) along the Z-axis; otherwise the procedure gives the parameters of the cross-section of the elliptic beam normal to Z-axis (that is the real dimension of the elliptic beam is *smaller* than that given by the procedure).

The "flow-chart" of STB

The STB procedure of the spot/beam treatment is highly interactive: it requires the experimentalist/operator's active involvement. If the specialized hard/sofware is available the whole procedure can be fully automated.

At present, the STB procedure comprise of the following stages.

Reference picture of the screen First we need the reference picture of the diagnostic screen with the best seen reference holes. By using any graphical software we save the reference file in any suitable format.

Spot image at diagnostic screen We need the picture of spot image at diagnostic screen with all necessary data, focusing/steering coil currents, quad currents etc. If (which is most preferable) the image of spot with clearly seen reference holes is available, the "reference picture" is not necessary. Also we note that the reference picture and the spot picture should be got for the same camera-screen disposition etc. Again we save the spot image file in any suitable format.

Import the image file STB procedure itself starts with using MATHEMATICA's "Import" command to input the reference and spot image files (in any format) into MATHEMATICA notebook.

Getting coordinates of reference holes Then by using "Get Graphic Coordinates" command we obtain coordinates of the reference holes (in the coordinate system of the imported image), and save them as the **"holes"** variable with 2 x N_x x N_y elements (each of them being 2-vector, $\{x_i,\, y_i\}$ of i-th hole), where N_x is the number of holes in each x-row, and N_y is the number of holes in each y-column (for rectangular array of reference holes, otherwise the procedure is slightly more complex). For example, at SP screen, $N_x = N_y = 5$, while at S0 screen, $N_x = 3$ and $N_y = 5$.

Getting coordinates of spot boundary Similarly, the coordinates of the N (N should preferably be $\gg$5) "sample" points at the spot image boundary are got and saved in the **"spot"** variable with 2xN elements (each of them being 2-vector, $\{x_i,\, y_i\}$ of i-th spot boundary point).

This finishes the "data extracting" procedure and the further treatment operations are simply done by "clicking" the relevant cells in MATHEMATICA notebook with right sequence. Still some knowledge of "what is going on" is useful.

Mapping reference holes to the Laboratory C.S. The "holes" variable is used to "map" the holes (their coordinates, $(x_i,\, y_i)$), to the "Laboratory" Coordinate System (C.S.), (X,Y),: e.g. x[central hole]$\rightarrow$X = 0, y[central hole]$\rightarrow$Y = 0; x[next-to-central right hole]$\rightarrow$ X (= 10 mm for S0 screen, and = $5/\sqrt{2}$ mm for SP screen), y[next-to-central upper hole]$\rightarrow$ Y (= 5 mm for SP screen, and = $10/\sqrt{2}$ mm for S0 screen).

Very important is the scaling by $1/\sqrt{2}$ for x-coordinates at SP screen and y-coordinates at all other screens of EAFEL. At this stage it is assumed that the diagnostic screen is perfectly aligned with its central hole's center at Z-axis and the angle of the screen rotation is exactly 45 deg. Otherwise instead of $1/\sqrt{2}$ we should use $1/\cos\varphi$ where φ is an inclination angle. We mention that $\varphi = 45 \pm 1$ deg gives 2% relative deviation from $1/\sqrt{2}$. In contrary, if rotation (around second axis) is (erroneously) non-zero, the effect is much less: for $\varphi < 12$ deg the deviation from 1 is less than 2%.

Transition from image c.s. to Lab. C.S. Now using the fact that reference holes "are connected" to the laboratory coordinate system, we find the *transition rule* from the whole {x,y} c.s. of the given image to the laboratory {X,Y} C.S. To this end we solve by LSM (actually we use "Fit" command of MATHEMATICA), $N_y \cdot N_x$ non-linear equations, separately for X(x,y) and Y(x,y). In the simplest case we use only the linear and cross-terms in (x,y), that is e.g $X(x,y) = c_0 + c_1\,x + c_2\,y + c_3\,x\,y$ and the similar "rule" (with other coefficients of course) is for Y(x,y).

Transformation of reference holes and spot to Lab. C.S. Using the *transition rules* X(x,y) and Y(x,y) we transform the reference holes positions at image to points in Lab. C.S., and also do the same for sample points of spot boundary. We present, in Fig. 2, left panel , the example for the case of I4 = .8 A. In getting beam in Fig. 2, we used

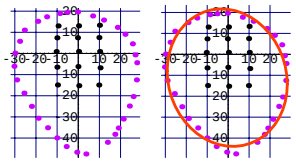

Figure 2: (Color) Left panel: the "true beam" and reference holes as obtained by STB for the case of I4 = .8 A. Right panel: additionally fitting ellipse found by STB is shown.

32 reference points. We may note that reference points are nicely aligning in the ellipse-like order. By checking such a figure one may notice the *outlying points* (which are most probably due to non-accurate clicking when getting coordinates of spot boundary). Then you may simply remove them from the **"spot"** variable, or try to obtain more accurate sample points.

This finishes the important part of the STB procedure: we obtained the "true beam"; and now we deal with another particular problem: how to draw ellipse through the given set of points and find the parameters of the ellipse.

FITTING ELLIPSE

This section describes another essential part of STB. We note that the problem of fitting the given set of point by any given curve is quite general and solved in many fields of science and technics. We only briefly outline the procedure used in STB.

Let us have N (in our particular case N=32) points with coordinates $\{x_i,\, y_i\},\, i = 1, \ldots, N$. To fit elliptic curve through this set of points, we first write the general equation of the ellipse in the form

$$a\,x^2 + 2\,b\,x\,y + c\,y^2 + 2\,d\,x + 2\,e\,y + 1 = 0. \quad (1)$$

If i-th point lies exactly on the ellipse (1) then we may put $x \to x_i$ and $y \to y_i$ and Eq. (1) will be exactly valid. In general this equation will be valid only approximately, and we may ask which ellipse (that is which set of coefficients $a,\, b,\, c,\, d,\, e$) fits the given set of N points best. To find these coefficients we write the system of N equations

$$a\,x_i^2 + 2\,b\,x_i\,y_i + c\,y_i^2 + 2\,d\,x_i + 2\,e\,y_i + 1 = 0, \quad (2)$$

and the solve the system (2) by one of LSM methods. In MATHEMATICA the relevant command is

$$\{a, b, c, d, e\} = \text{PseudoInverse}\,[mat]\,.B, \quad (3)$$

where mat is the 5xN matrix of coefficients in system (2), and B is N-vector with all elements equal to -1.

Parameters of fitting ellipse

Now when we have coefficients of the ellipse equation, we can define parameters of ellipse.

First we write three so-called invariants of the ellipse

$$\triangle = \det\begin{pmatrix} a & b & d \\ b & c & e \\ d & e & 1 \end{pmatrix},\ \delta = a\,c - b^2,\ S = a + c. \quad (4)$$

Now, ellipse's center coordinates are

$$x_c = (b\,e - c\,d)/\delta,\ y_c = (b\,d - a\,e)/\delta; \quad (5)$$

diameters of the ellipse are

$$D_{1,2} = 2\ \left[-\triangle/(\delta\,u_{1,2})\right]^{1/2}, \quad (6)$$

where $u_{1,2}$ are solutions of the quadratic $u^2 - S\,u + \delta = 0$.

Finally, the angular coefficient of the X-diameter of the ellipse is

$$k = \left[c - a + \sqrt{(c-a)^2 + 4\,b^2}\right]/(2\,b). \quad (7)$$

Example of resulting fitting ellipse is shown at the right panel of Fig. 2, see also Fig. 4.

With this we finish the description of the STB procedure and pass to describe EAFEL experiments, STB treatment, EGUN simulation and comparison of the results.

EXPERIMENT AND SIMULATIONS

We consider the case when the first focusing coil current is of the *negative* sign (according to agreement in EAFEL group), that is C1 coil rotates the image counter-clockwise. Other coil current signs are positive or negative with respect to C1 current. In the case considered here (and usually used in EAFEL), the current signature is -/+/+/+ that is only I1 is negative.

Experimental data

In Fig. 3, four spots at S0 screen are shown for values of C4 coil $I4 = .8,\ 2.5,\ 3,$ and 4 Amp with three other focusing coil currents fixed as $I1 = -7.25$ A, $I2 = 3.75$ A, and $I3 = 3.6$ A. Also shown are the elliptical approximations of spots found by STB procedure.

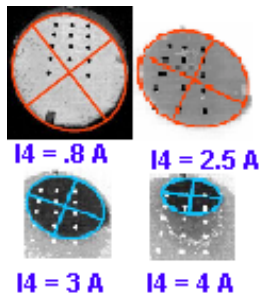

Figure 3: (Color) Spots at S0 vs. current of C4. Note that at the screen surface, the distance between neighbor holes are 10 mm in both x- and y-directions. Screen S0 is rotated around horizontal (X) axis by 45 deg, so that at images, the vertical distances between holes are (or rather should be) $1/\sqrt{2} \approx 7.1$ mm. Note also a rather strong distortion of images apparent from the holes misalignment. First, in general, the camera is too close to the screen, then it seems that the camera is closer to the upper side of the screen than to the lower side of the screen, and again it seems that the orientation angle is not exactly 45 deg. Also shown are the elliptical *spot* approximations (and reference holes!) as defined by using STB. The *beam* ellipses are shown in Fig. 4

.

STB treatment results

The most important is of course to present the *beam* near the given diagnostic screen as ellipse, and this is exactly what was done by STB procedure. Results of the STB procedure treatment are presented in Fig. 4, where four beams at S0 screen are shown for the values of C4 coil current $I4 = .8,\ 2.5,\ 3,$ and 4 Amp with three other coil currents fixed as $I1 = -7.25$ A, $I2 = 3.75$ A, and $I3 = 3.6$ A. With an increasing current, the elliptical beam at S0 rotates counter-clockwise, its center moving almost vertically upward, and both diameters decreasing.

Also we mention that all beams are (curiously enough) touching each other in one point.

The analysis of such a behavior of the beam with changing coil currents will be the subject of another paper.

Here we present only numerical results. For C4 coil currents $I4 = .8, 2.5, 3,$ and 4 Amp, the coordinates of beam centers, in mm, are $\{X_c, Y_c\} = \{-0.4, -11.1\}, \{5.1, 0.3\}, \{4.6, 4.9\},$ and $\{2.6, 13.2\}$, respectively.

Apparently the beam, at least near the S0 screen position, is off-axis, non-circular and moves at some angles (in XZ- and YZ-planes) in respect to Z-axis.

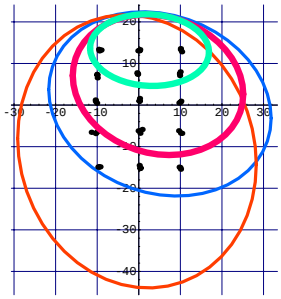

Figure 4: (Color) Beams at S0 screen position (as found by using STB procedure) for four values of current of C4 coil: .8 A (the light-red largest ellipse), 2.5 A (the dark-blue second-largest ellipse), 3 A (the dark-red second-smallest ellipse), and 4 A (the light-green smallest ellipse). With increasing current, the elliptical beam at S0 rotates counterclockwise, its center moving almost vertically upward, and both diameters decreasing.

EGUN simulations

We used the EGUN code [3] to calculate the beam projectiles from the electron gun (of Pierce type) up to S0 screen. We present here only the current density distribution across the (circular) beam cross-section, which allow to estimate the beam dimension.

In Fig. 5, four beams at S0 screen position (found by using EGUN code) are shown for values of C4 coil $I1 = .8, 2.5, 3,$ and 4 Amp with three other coil currents fixed as $I1 = -7.25$ A, $I2 = 3.75$ A, and $I3 = 3.6$ A.

Experiment/simulation comparison

In Fig. 6, the red lines show the upper and lower diameters (obtained by using STB) of beams at S0 screen position, for values of C4 coil $I1 = .8, 2.5, 3,$ and 4 Amp, with three other coil currents fixed as $I1 = -7.25$ A, $I2 = 3.75$ A, and $I3 = 3.6$ A. The "simulated" (by EGUN) values (blue dash line) are close to the lower diameters of "experimental" beam ellipses (obtained by STB) for smaller I4 and to the upper "experimental" diameters for larger I4. Note that EGUN code (at least in its standard operational mode) can treat only axially symmetric circular

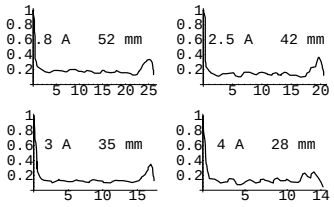

Figure 5: Current density distribution (in arbitrary units) in the cross-section of the axially-symmetric circular beam at S0 screen position, as calculated by using EGUN, for various values of C4 coil current. Value of C4 current, in Amp, and assumed beam diameter, in mm, are shown at each panel. Note a *spurious* increase of current density at the edge of beam. This "hump" in the beam edge current distribution is (unwilling) characteristic of EGUN code.

beams (with a due account of space-charge effects), while in reality, beam at SP and S0 positions are off-axis, non-circular and even not-parallel to Z-axis. This precludes the rigorous comparison of simulations and experiments. Still we mention a very good agreement between the "simulated" circular-beam diameters and the lower/upper diameters of the "experimental" beam ellipses. The relative variance in the beam diameter is about 10% for I4 = .8 Amp and is much less for the larger currents of C4 coil.

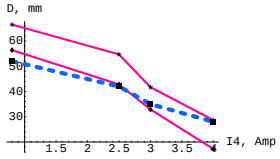

Figure 6: (Color) Beam dimensions at S0 position vs C4 coil current. Red curves: "experimental" (as obtained by using STB) minor and major diameters of elliptic beam. Blue dash line: diameter of the circular beam simulated by EGUN. Ordinates: diameters in mm; abscissas: current of C4 coil in Amp.

ACKNOWLEDGEMENTS

The idea of "mapping" the reference holes to the "laboratory" coordinate system should be credited to Y. Lurie. The work was supported by Israeli Ministries of Absorption, Science and Environment.

REFERENCES

[1] A. Gover et al, Nucl. Instr. and Meth. A 528 (2004) 23; arXiv.org/physics/0408054

[2] http://www.wolfram.com

[3] W.B. Herrmannsfeldt, SLAC-Report-331, (Stanford Univ., 1988)

GUIDING OPTICS SYSTEM FOR LEBRA FEL USER FACILITY

T. Tanaka*, K. Hayakawa, Y. Hayakawa and I. Sato, LEBRA, Institute of Quantum Science, Nihon University, 7-24-1 Narashinodai, Funabashi, 274-8501 Japan

Abstract

The FEL guiding optics system for the LEBRA user's experimental facility was completed in 2003. The optical beam extracted from the Infrared FEL resonator has been guided through a long vacuum system to the user's experimental rooms, where a maximum of 17 aluminium-coated mirrors have been used in the guiding optics. The maximum length of the optical line is approximately 50 m. The divergent FEL beam extracted from the resonator through a coupling hole has been converted into a parallel beam. An approximately identical diffraction pattern of a guide laser was observed at the output ports of the experimental facility. The guiding optics has two FEL monitoring ports, each containing a CaF_2 beam sampler and a total reflection mirror, which has advantages for simultaneous measurement of the power and the spectrum of the FEL during user's experiments. The transport efficiency of the guiding system depends on the FEL wavelength and the radius of the coupling hole in the resonator mirror.

INTRODUCTION

Use of the infrared free-electron laser (FEL) for experiments in medical science and material science was started in 2003 at the Laboratory for Electron Beam Research and Application (LEBRA) of Nihon University. The FEL guiding optics completed prior to the beginning of user's experiments was designed to transport the FEL and its higher harmonic undulator radiations. The lights in the wavelength region of 0.2 to 6 μm are extracted from the FEL resonator through a coupling hole in one of the resonator mirrors. After converted to a parallel beam, the lights are transported to user's experimental rooms using aluminium-coated plane mirrors. The top view of the LEBRA accelerator facility and the user's experimental facility is shown in Fig. 1.

This paper reports on the present status of the LEBRA FEL system and the optical guiding system for the FEL user facility.

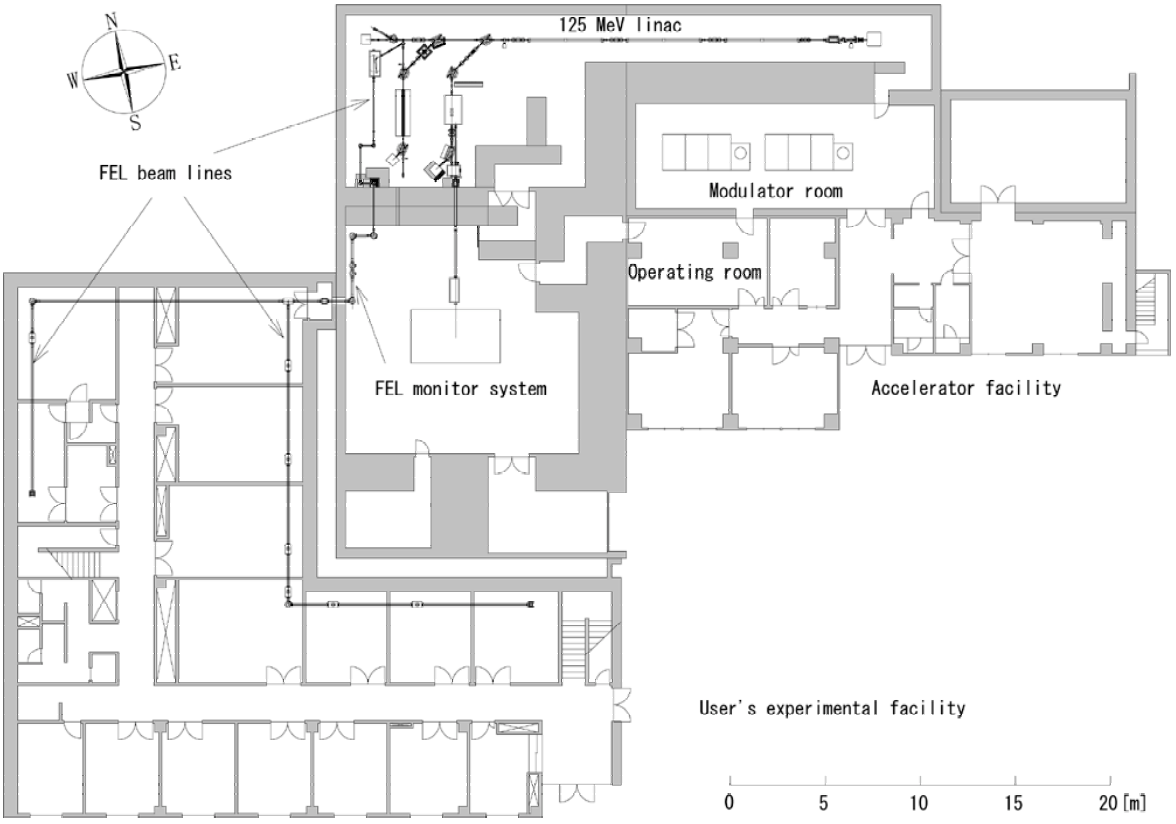

Fig. 1. Top view of the LEBRA accelerator facility and the user's experimental facility.

*E-mail address: tanaka@lebra.nihon-u.ac.jp

THE FEL SYSTEM OF LEBRA

Table 1 shows the specifications of the infrared FEL system installed in LEBRA. A schematic layout of the system is shown in Fig. 2. The FEL guiding optics system in the accelerator room is also shown in Fig. 2. The planar FEL undulator consists of Halbach-type NdFeB permanent magnets [1]. The electron beam wiggles in a vertical direction in the undulator so that the focusing field of the undulator binds the electron beam orbit in a horizontal direction.

The highest electron energy is currently restricted to 100 MeV due to the maximum klystron output rf power. The minimum undulator gap width was reduced by 5 mm compared with the earlier design specification by replacing with a thinner undulator vacuum duct, which increased the maximum undulator *K*-value from 1.5 to 2. The wavelength of the FEL is variable in the range from 0.9 to 6.5 μm, which is accomplished by adjusting the electron beam energy and the undulator gap width i.e. the undulator *K*-value [2].

The electron beam from the linac has a longitudinal bunch structure with a period of 105 mm corresponding to the accelerating rf of 2856 MHz. The separation D between the two resonator mirrors is 6.718 m, i.e. 64 times the free space wavelength of the microwave. The curvature radius R of the resonator mirrors was decided to be 4.0 m. Then the Rayleigh length L_R of the FEL in the resonator, given by the relation [3]

$$L_R = \sqrt{D(2R-D)}/2, \qquad (1)$$

Table 1. Specifications of the LEBRA infrared FEL system.

Maximum electron beam energy	125	MeV
Maximum undulator *K*-value	2	
Micropulse beam current	> 20	A
Period of undulator field	48	mm
Number of periods	50	
FEL wavelength range	0.6 - 6	μm

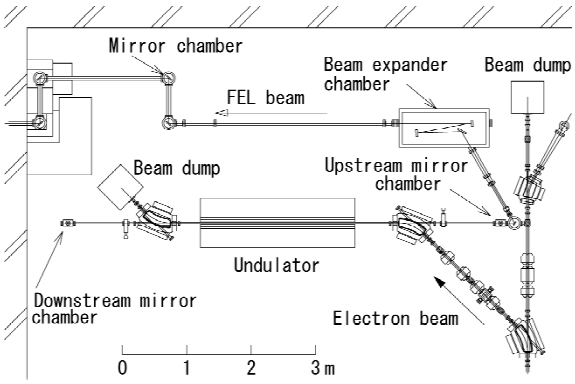

Fig. 2. Schematic layout of the LEBRA FEL system and the FEL guiding optics system in the accelerator room.

is 1.47 m, which is slightly longer than the half of the undulator length. For the resonator mirrors, silver-coated copper mirrors with a diameter of 25 mm were manufactured at Rocky Mountain Instrument Co. (RMI). The nominal reflectance of the mirrors is greater than 99.3 % for the wavelength range from 1 to 20 μm. The FEL power is extracted from the resonator through a small coupling hole on the center of the upstream mirror.

The radius a of the coupling hole at the mirror in current use is 0.15 mm. Provided that the FEL in the resonator is a Gaussian beam, the FEL beam radius w on the surface of the resonator mirror is given by

$$w = \sqrt{\frac{\lambda_L L_R}{\pi}\{1+(D/2L_R)^2\}}, \qquad (2)$$

where λ_L is the FEL wavelength. Then the coupling coefficient κ of the hole, defined as a ratio of the optical power contained in the cross section of the hole to the total power incident on the mirror, is given as

$$\kappa = 1-\exp(-2a^2/w^2). \qquad (3)$$

For the FEL wavelength of 0.9 μm, obtained with the electron beam of 100 MeV and the *K*-value of 0.93, the coupling coefficient deduced from Eq. (3) is 0.017. Therefore the sum of the mirror loss and the external coupling loss for each round-trip of lights in the resonator is approximately 3.1 % of the total power.

Lasing by this system has been experimentally confirmed over the *K*-value range from 1 to 2, which suggests a broad variability of FEL wavelength at fixed electron energy. Lasing at 0.6 μm is feasible with the present system by increasing the electron energy up to 125 MeV, though the estimated total loss in each round-trip increases to about 5 % due to a decrease of the mirror reflectance and an increase of the coupling loss.

THE BEAM EXPANDER SYSTEM

The FEL extracted from the resonator through the small coupling hole has a divergence angle due to a diffraction effect referred to as the Fraunhofer diffraction. For the first dark ring or the central core of the diffraction pattern that contains 84 % of the extracted optical power, the divergence angle θ of the radius is approximated as [4]

$$\theta = \frac{3.833\lambda_L}{2\pi a}. \qquad (4)$$

For the 5 μm fundamental FEL, the coupling-hole radius of 0.15 mm causes the divergence of the core radius with θ = 20 mrad. The maximum distance between the FEL output mirror and the user's port is approximately 50 m. Therefore, a conversion optics system is necessary for efficient guiding of the light beam to user's experimental rooms. In the optical guiding system of LEBRA, the divergent beam has been converted to a parallel beam by means of a beam expander system consisting of an ellipsoidal mirror and a parabolic mirror. The expander mirror system was manufactured and aligned by CANON Inc..

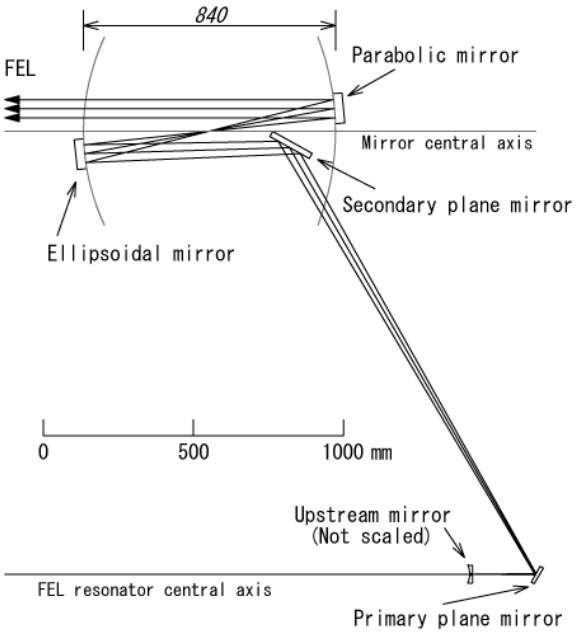

Fig. 3. Geometrical configuration and ray trace of the beam expander system. The rear surface of the upstream mirror lies at the position equivalent to one of the focal points of the ellipsoidal mirror.

The geometrical configuration of the mirrors in the expander system is shown in Fig.3. The basic idea of the optics system is the same as which was installed in FEL-SUT MIR FEL beam line [5]. The FEL extracted through the coupling hole in the upstream mirror is reflected with the primary and the secondary plane mirrors, and then directed toward the ellipsoidal mirror. The optical path length between the coupling hole and the ellipsoidal mirror decided to be approximately 2.5 m so that the rear surface of the upstream mirror or the exit of the coupling hole is placed at the position equivalent to one of the focal points of the ellipsoidal mirror. Therefore the divergent light beam which comes out of the coupling hole is focused at another focal point of the ellipsoid.

As seen in Fig. 3, the ellipsoidal mirror and the parabolic mirror have been aligned to form a confocal configuration so that the light beam, once focused at the common focal point, is converted to a parallel beam by the parabolic mirror, where the focal length is 420 mm for both mirrors. These mirrors have a common central axis parallel to the FEL resonator axis. Then, the collimated beam obtained at the exit of the beam expander has approximately the same profile as that on the surface of the ellipsoidal mirror.

PARALLEL BEAM TRANSPORT AND FEL MONITOR SYSTEM

As seen in Fig. 2 the output parallel beam from the expander chamber is sent to the next room through a rectangular chicane section. This section was installed to suppress the leakage of gamma rays and neutrons to the next room through the vacuum duct in the shielding wall. Concrete, lead and plastic blocks surrounding the fourth mirror chamber in the chicane section effectively shield the direct radiations from the electron beam dump.

The parallel beam is guided to nine separate experimental rooms by switching the beam line with retractable plane mirrors. The guiding system in the user's facility was installed in the pit under the floor. Every switching section is equipped with a total reflection mirror (aluminium coated) and a partial reflection mirror (CaF_2 plate), which allows for parallel experiments in the different rooms.

For the purpose of monitoring and control of the FEL lasing during user's experiments, two monitor chambers have been inserted in the midstream of the guiding system. Each chamber contains a CaF_2 beam sampler and a total reflection mirror for alternate monitoring of high intensity fundamental FEL and higher harmonics during user's experiments, or low intensity spontaneous emission during electron beam adjustments.

The FEL monitor chambers and associated optics placed in the large experimental hall are shown in Fig. 4. The output from the upstream side chamber has been used for the measurement of the FEL macropulse waveform by means of an InSb detector. The output from another chamber has been used for the measurement of the FEL macropulse energy and the spectra of higher harmonics. Use of separate beams in simultaneous measurement of different FEL properties requires no wide-band half mirror. Also, it allows easy alignment of the devices on the optical base.

The wavelength of the fundamental FEL has not been measured directly in the wavelength range longer than 1.6 μm due to the restricted range of the array detector and the spectrometer in LEBRA. Instead, the spectra of the higher harmonics in the visible region have been used to extrapolate the wavelength of the fundamental FEL.

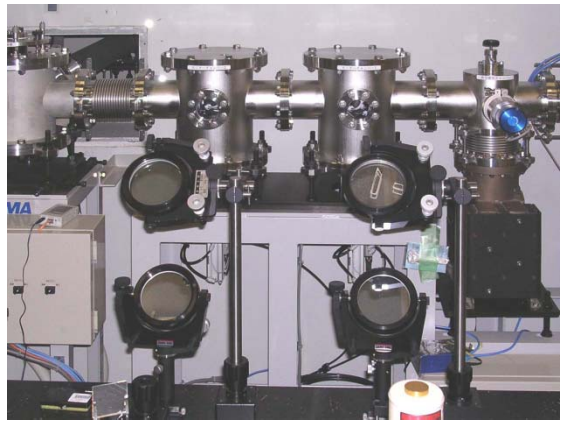

Fig. 4. The picture of the FEL monitor chambers and associated optics on the optical base. Each chamber contains a CaF_2 beam sampler and a total reflection mirror for an alternative use.

CONSIDERATIONS ON THE POWER LOSS IN THE GUIDING SYSTEM

The radius of the plane mirrors used in the guiding system downstream from the beam expander is 50 mm, which results in an effective radius of 35 mm due to the reflection angle set at 45 °. The minimum inner radius of the vacuum duct is about 25 mm. Therefore, the aperture of the vacuum duct is the main restriction for the transport efficiency of the FEL power except for the mirror reflectance.

The profile of the parallel light beam transported to the user's facility is primarily determined by the wavelength of the light, the radius of the coupling hole in the upstream mirror, and the distance between the coupling hole and the ellipsoidal mirror. From Eq. (4) the core radius a_A of the diffraction pattern at the ellipsoidal mirror is given by

$$a_A = \frac{3.833\lambda_L d}{2\pi a}, \qquad (5)$$

where d (= 2.5 m) is the distance between the coupling hole and the ellipsoidal mirror. The radius is assumed to be conserved in the travel to the experimental rooms.

The guiding system was originally designed to use a resonator mirror with a coupling hole of 0.5 mm radius for the lasing in the wavelength range of 5 μm or longer, where the core radius is greater than 15 mm but still less than the inner radius of the vacuum duct. On the other hand, the mirror with the coupling hole of 0.15 mm radius in current use was intended for use in lasing at the wavelengths shorter than 2 μm by taking into account the coupling coefficient. For this mirror, the core radii of the FELs with the wavelength of 2, 3, 4 and 5 μm are approximately 20, 30, 40 and 50 mm, respectively.

Thus, the use of the current mirror for lasing in the wavelength range longer than 3 μm results in a large power loss due to the eclipse caused by the aperture of the vacuum duct.

The current FEL system takes at least 1 day to replace the mirror. However, a more efficient optical beam transport and a relatively high coupling coefficient by an optimised mirror will allow for the use of considerably higher FEL power at the user's experimental rooms for longer wavelength FELs.

SUMMARY

The FEL in the wavelength range from 0.9 to 6.5 μm has been lased with the LEBRA infrared FEL system. The divergent beam extracted through a small coupling hole in the FEL resonator mirror has been converted into a parallel beam with the beam expander system consisting of an ellipsoidal mirror and a parabolic mirror. The transport efficiency for long-wavelength FELs is low due to the large radius of the parallel beam. However, the efficiency in the long wavelength region can be improved by replacing the current mirror with a resonator mirror which has a larger coupling hole.

REFERENCES

[1] K.Halbach, Nucl. Instr. and Meth. 187 (1981) 109.
[2] T.Tanaka et al., "Tunability and Power Characteristics of the LEBRA Infrared FEL", FEL2004, Trieste, Italy, Aug. 2004.
[3] H.Kogelnik and T.Li, Applied Optics 5, No.10 (1966) 1550.
[4] M.Born and E.Wolf, Principles of Optics, Cambridge University Press (1999).
[5] K.Nomaru et al., Nucl. Instr. and Meth. A445 (2000) 379.

UPGRADE OF A PHOTOCATHODE RF GUN AT SPRING-8

T. Taniuchi#, T. Asaka, H. Dewa, H. Hanaki, T. Kobayashi, A. Mizuno, S. Suzuki, H. Tomizawa, K. Yanagida, JASRI/SPring-8, Hyogo 679-5198, Japan
M. Uesaka, NERL, University of Tokyo, Tokai, Ibaraki 319-1188, Japan

Abstract

A new test bench for a photocathode RF gun has been built to verify the beam characteristics in higher energy regions up to 30 MeV and develop a sophisticated injector system for practical use. The accelerator room has been expanded, and two beam lines including a 3-m long accelerating structure, have been installed. A clean room for the driving laser system was also expanded in which the air temperature control was improved and higher humidity could be maintained to reduce the charge-up on the optical elements. RF conditioning has been completed and the electric field gradient on the cathode of the RF gun reached up to 183 MV/m. The first beam has been successfully commissioned and a new emittance monitor using the quadrupole scan has been tested. We have investigated a new gun cavity system to improve the emittance in higher charge regions exceeding 1 nC/bunch. Presently we are investigating a multi-cavity system, in which the current single-cell cavity is used as the first cavity. According to a simulation result, the normalized emittance of 2.4 πmm•mrad can be achieved in a two-cavity system at a charge of 1.4 nC/bunch. The second RF cavity and a high power distributor system have been also designed.

INTRODUCTION

A photocathode RF gun has been investigated at SPring-8 to develop a low-emittance and short-bunch injector for the linac. We commenced this R&D with a single-cell cavity in which the inner copper wall was used as a photocathode. This cavity has an output port for extracting a part of the RF power and the loaded Q is lowered. This enables to shorten the filling time and achieve a higher-gradient field.

Using this cavity, we have examined dependences of beam characteristics on RF, solenoid fields and laser parameter and phenomena in a high-gradient field situation such as RF breakdown, dark current and so on. In these experiments, the lowest emittance of 2π mm•mrad at a beam charge of 0.1 nC/bunch [1] and a maximum field gradient of 175 MV/m at the cathode surface has been achieved [2] and we understood how to control parameters to minimize the beam emittance.

The next step of this R&D project is to verify the beam performance, especially the emittance, in the higher beam energy region because the single-cell cavity can only accelerate beams up to 4.1 MeV and the emittance can easily grow in this energy region. There were some problems in the laser system. A fluctuation of the air temperature in the clean room made the laser unstable and a charge up on optical elements collected dust and cause damages. To improve these problems, a new test bench has been constructed that includes an expanded radiation shield and an air temperature- and humidity-controlled clean room for the driving laser system. The construction began in March 2003 and was completed in December of that year. In parallel with the experiments using this facility, a new gun system is under investigation to achieve a lower emittance in higher-charge regions.

NEW TEST BENCH

As shown in Fig. 1, the test bench is located in Machine Laboratory building, which can be connected with the linac building at the L1 beam transport line (250 MeV) by removing a concrete plug. Therefore, in the future it will be possible to inject the electron beam produced by the photocathode RF gun into the 1-GeV linac.

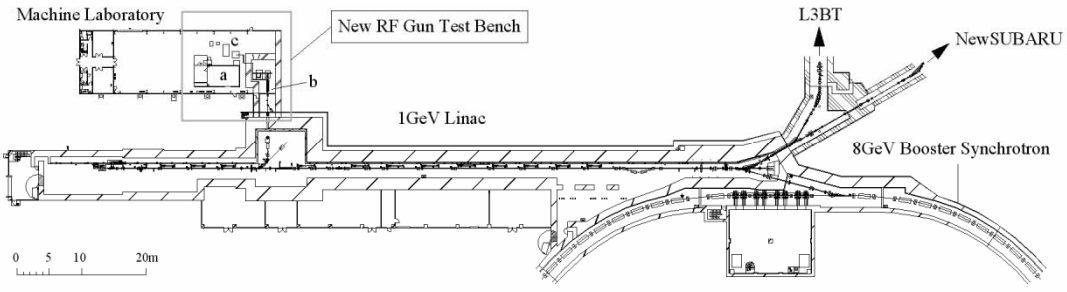

Figure 1: Location of new RF test bench. (a: Clean room for driving laser system, b: Radiation shielded accelerator room, c: Klystron and modulator)

#ihcuinat@spring8.or.jp

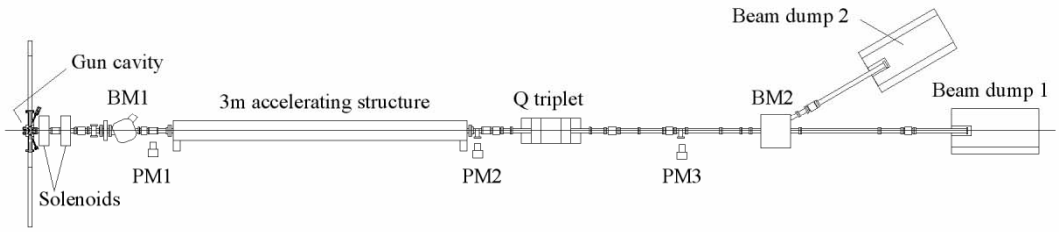

Figure 2: Layout of 30-MeV linac with photocathode RF gun.

A 3-m travelling wave structure has been added after the RF gun and the approved maximum beam energy has been increased from 4.5 MeV to 30 MeV. The thickness of the concrete shield has been increased from 0.5 m (partly 1.0 m) to 1.4 m, while the floor area of the accelerator room has been expanded to make it three times larger. This test bench will be used not only for the photocathode RF gun R&D but also for high-gradient tests in collaboration with other institutes and high-power tests of RF components before installation in the 1-GeV linac and so on.

There are two accelerators in the radiation shield. One is a 30-MeV linac with the photocathode RF gun and the other is a standalone RF gun for photocathode experiments. The latter includes experiments for cartridge-type electric tube with Cs2Te cathodes [3]. The layout of the 30-MeV linac is shown in Fig. 2.

The RF source is an 80 MW klystron (Toshiba E3712), and the RF power is distributed into two RF gun cavities and a 3-m long travelling wave accelerating structure, which is the same one as is used for the SPring-8 1-GeV linac.

As shown in Fig. 3, the high-power RF distributing system comprises magic-tees, 3-dB directional couplers, phase shifters, dummy loads, RF windows and so on. A combination of a magic-tee, a phase shifter and 3-dB directional coupler divides RF power into two waveguides in an arbitrary ratio. Therefore, the RF power and phase for the two RF gun cavities and the travelling wave structure are variable in this distributing system.

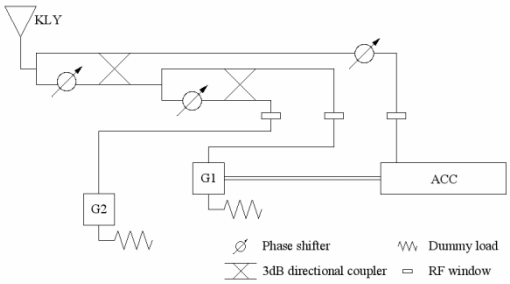

Figure 3: High-power RF distribution system. (G1: RF gun cavity #1, G2: RF gun cavity #2, KLY: 80 MW klystron, ACC: 3-m travelling wave structure)

A feature of this system is that there is no circulator to protect the klystron from the reflected RF power because the loaded Q value of the RF gun cavity is lowered to one fourth of that for typical standing wave cavities by extracting some of the power, and then the reflected power is much smaller -- like travelling wave structures.

Regarding the driving laser system, a highly stabilized and profile-controlled system has been under development in a new clean room with a cleanness of class 1000 [4]. The total floor area of the clean room becomes 2.7 times larger than the previous one. The air temperature near the laser table is stabilized within 0.6 degree and the humidity is kept at around 55% R.H. to minimize the charge-up and avoid damages on the optical elements. The down-flow of the air is dispersed to decrease the fluctuation of the laser path. To maintain the cleanness of the air, the previous clean room is used as an anterior chamber of the new one.

RECENT PROGRESS

Following the installation of the accelerator system, automated RF conditioning for waveguides and RF cavities was performed successfully.

We tested a chemical etching method for surface treatment of the RF gun cavity to improve the quantum efficiency (QE) and high-gradient performance qualities such as the RF breakdown rate and dark currents. As a result, the conditioning time was clearly shortened, achieving a maximum QE of 8.6×10^{-3} % for our cathode and a maximum field gradient on the cathode of 183 MV/m [5].

Beam acceleration was also successful, and an emittance measurement by using the quad-scan method was tested for a 24.5-MeV beam [6].

R&D concerning the driving laser system is focused on laser pulse shaping in both the spatial and temporal dimensions which is required for the emittance reduction. A deformable mirror system for spatial shaping and a spatial light modulator based on a fused-silica plate for temporal shaping, are under development [4].

MULTI-CAVITY RF GUN

We are currently investigating an RF gun system that can attain lower emittance in higher-charge regions. In

order to reduce space charge induced emittance growth at higher bunch charge while maintaining a high-gradient acceleration using our low-Q cavity, an addition of RF cavities after the current cavity has been investigated. The acceleration by single-cell cavities will also be effective for the emittance reduction because a field gradient can be higher than that of the disk-loaded accelerating structures. In the following subsections, the result from a computer simulation, a design of the RF cavity and a new configuration of the high power RF distributor are described.

Simulation

The beam dynamics in a two-cavity RF gun have been investigated by using a simulation code PARMELA. As a result of an optimization for the RF phase and field strength, it was found that the beam emittance could be lowered to 2.4 π mm•mrad at a charge of 1.4 nC/bunch, which is lower than that of current single-cell cavity system. Fig. 4 shows an example of the beam emittance along the beam line.

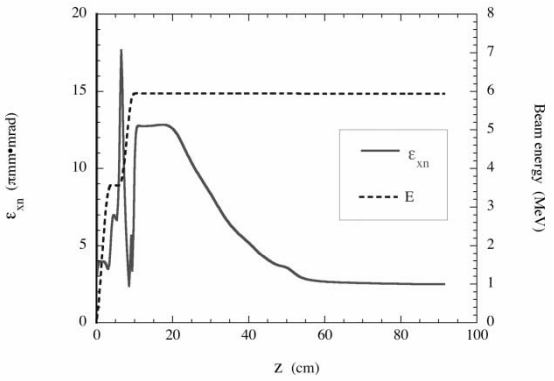

Figure 4: Simulated result for emittance in a two-cavity RF gun.

Design of RF cavity

In the simulation, optimum RF phase and field strength for the two cavities are obtained. Then a realistic RF cavity for the second one was designed using a 3D field solver code, MAFIA.

To maintain high-gradient performance and employ the present RF distribution system, a low-Q type cavity is adopted. The external Q value for the output port was determined considering the RF distribution system described in the next subsection. Relevant parameters for the second cavity are listed in Table 1.

Table 1: Design parameters for second and third cavities.

Radius of beam pipe	10 mm
Curvature radius of cavity nose	5 mm
Cavity length	38 mm
Q_0	15,800
Q_{ext} for input port	3,160
Q_{ext} for output port	3,950
Loaded Q	1,580
Shunt impedance for β=1	5.3 MΩ
Maximum accelerating field gradient	100 MV/m

High-power RF system

We are currently investigating the two-cavity system, but simulation results indicate an effectiveness of three-cavity system for the emittance reduction. Therefore, a high power RF distributor for the three-cavity RF gun has been designed. If we adopt the low-Q type cavity, the required total RF power will exceed the maximum power of the klystron, i.e., 80 MW. One option for solving this problem is to install an RF compression system such as SLED. However, we selected another system that utilize the output power from our low-Q type cavity and minimizes the cost. However, the filling time of the first cavity becomes longer. Fig. 5 illustrates the high-power RF distribution system for the three-cavity RF gun.

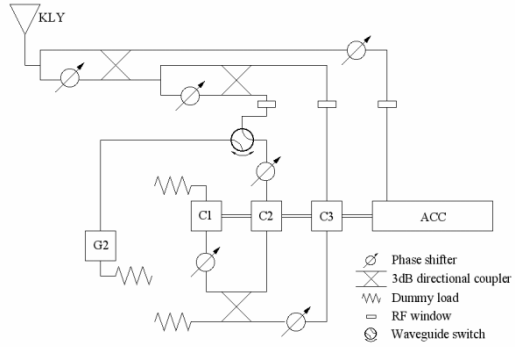

Figure 5: High-power RF distribution system for the three-cavity RF gun system. (C1~C3: Three-cavity RF gun, G2: RF gun cavity #2, KLY: 80 MW klystron, ACC: 3-m travelling wave structure)

This system can divide the RF power and feed it into the second and third cavities in any arbitrary ratio. The output power from the second and third cavities are subsequently recombined in a power distributor and fed into the first cavity, which requires the highest RF power of all three cavities. Use of this system enables the RF power and phase for the three cavities being tuneable.

For a fast switching between the experiments using the 30-MeV linac and that using RF gun #2, we will install a vacuum-type waveguide switch in the waveguide before the second cavity.

CONCLUSION

The construction of the new test bench for the photocathode RF gun R&D has been completed, and the 30-MeV linac and the standalone RF gun for the cathode development are now ready for further experiments.

We are planning to measure and optimize the emittance of the beam that is produced from the RF gun and accelerated up to 30 MeV. The optimization includes a shaping of laser pulses in both the spatial and temporal dimensions, RF phase and field strength of each cavities, solenoid fields and so on.

To attain practical use of a photocathode RF gun, a new cavity system is under development that is designed to lower the beam emittance in higher-charge regions exceeding 1 nC. Presently a multi-cavity RF gun is a promising candidate for the above requirement with simulation work and RF design continuing.

REFERENCES

[1] H. Dewa et al., Proc. of ICFA Workshop, "The Physics and Applications of High Brightness Electron Beams", Chia Laguna, July 2002, p. 28.

[2] T. Taniuchi et al., "Characteristics of a Photocathode RF Gun in Higher Field Gradient", LINAC'02, Gyongju, August 2002, p. 683.

[3] J. Sasabe et al., "Photocathode RF gun using cartridge-type electric tubes", FEL'03, Tsukuba, September 2003, Nucl. Instr. and Meth. A 528 (2004) 382.

[4] H. Tomizawa et al., "Development of Adaptive Feedback Control System of Both Spatial and Temporal Beam Shaping for UV-Laser Light Source for RF Gun", LINAC'04, Lübeck, August 2004, (to be published).

[5] H. Tomizawa et al., "Effects of Chemical Etching as a Surface Treatment for Accelerating Structures Made of Copper", Proc. of the 29th Linear Accelerator Meeting in Japan, Funabashi, Japan, August 2004, p. 147.

[6] H. Dewa et al., "Photocathode RF Gun Designed as a Single Cell Cavity", EPAC'04, Lucerne, July 2004, (to be published).

FEL SIMULATION CODE FOR UNDULATOR PERFORMANCE ESTIMATION

Takashi Tanaka
RIKEN/SPring-8, Koto 1-1-1, Mikazuki, Sayo, Hyogo 679-5148, Japan

Abstract

An FEL simulation code called SIMPLEX is introduced, which has been developed to investigate the effects of the undulator field error on the FEL gain. It can perform FEL simulations with the magnetic field distribution actually measured along the undulator axis so as to check the performance of the undulator as an FEL driver. Basic equations are derived that enable the numerical implementation of the FEL equations with the error fields taken into account. Practical examples for investigation of the undulator field error are also presented.

INTRODUCTION

The undulator is one of the most important components of an FEL. In particular, a quite large number of periods is required to achieve saturation in SASE-based x-ray FELs. Because the permanent magnets in the undulator are not perfect, the undulator field has necessarily error components. Needless to say, the tolerance on the undulator field error is more severe for larger number of periods. It is thus important to check the performances after construction of an undulator by measuring the magnetic field and calculating optical properties with it.

As a spontaneous-emission synchrotron radiation (SR) source, the performances of an undulator are in general specified by a quantity called the phase error. It is also possible to compute the intensity of SR by Fourier transforming the electric field generated by an electron moving in the undulator field. On the other hand, it is not easy to check the performances of the undulator as an FEL driver. The most promising way is to perform simulations of the FEL processes driven by the undulator with error fields. We have recently developed an FEL simulation code called SIMPLEX that can perform FEL simulations with the magnetic field distribution actually measured along the undulator axis. The details of which are described in the following sections.

FEL EQUATIONS

The amplification process in the FEL is represented by three equations, i.e., the wave, energy and phase equations.

The wave equation of the radiation field under the paraxial approximation is written as

$$\mathrm{e}^{i\omega(z/c-t)}\left[\nabla^2+2i\frac{\omega}{c}\left(\frac{\partial}{\partial z}+\frac{1}{c}\frac{\partial}{\partial t}\right)\right]\tilde{E}+\text{c.c.}=\mu_0\frac{\partial j_x}{\partial t},$$

where $\tilde{E}$ is the complex amplitude of the radiation field, j_x is the horizontal component of the beam current density, μ_0 the permeability of vacuum. Averaging over the period of radiation, $T=2\pi/\omega$, and integrating by part, we have

$$\left[\nabla^2+2i\frac{\omega}{c}\left(\frac{\partial}{\partial z}+\frac{1}{c}\frac{\partial}{\partial t}\right)\right]\tilde{E} = \frac{i\mu_0\omega e}{T}\sum_{j=1}^{N}\beta_{jx}\mathrm{e}^{ik_uz}\mathrm{e}^{-i\psi_j}\delta(\boldsymbol{r}-\boldsymbol{r}_j), \quad (1)$$

with

$$\psi_j(z)=k_uz+\frac{\omega}{c}\left(z-\int^z\frac{dz'}{\beta_{\perp j}(z')}\right),$$

where $\lambda_u=2\pi/k_u$ is the periodic length of the undulator, N is the number of electrons existing in the averaging area, and $\boldsymbol{\beta}_j$, $\boldsymbol{r}_j$, and ψ_j are the velocity, position and phase of the j-th electron, respectively. The phase equation can be modified as

$$\frac{d\psi_j}{dz}=k_u\left(\frac{2\Delta\gamma_j}{\gamma_0}-\frac{\Delta\omega}{\omega_0}-\frac{\gamma_j^2\beta_{\perp j}^2-K^2/2}{1+K^2/2}\right), \quad (2)$$

with

$$\Delta\gamma_j=\gamma_j-\gamma_0,\quad \Delta\omega=\omega-\omega_0,$$

where γ_j is the energy of the j-th electron, γ_0 is the average energy of the electron beam at the undulator entrance, ω_0 is the fundamental energy of the undulator radiation, and K is the deflection parameter of the undulator.

The energy of each electron changes by interaction with the radiation field, which is described by the equation

$$\frac{d\gamma_j}{dz}=\frac{e}{mc^2}(\beta_{jx}\mathrm{e}^{-ik_uz}\mathrm{e}^{i\psi_j}+\text{c.c.}). \quad (3)$$

The differential equations (1) $\sim$ (3) can be solved numerically with a certain longitudinal step Δz. In most FEL simulations, a multiple length of the undulator period λ_u is chosen for Δz. This is because the electric field $\tilde{E}$ and electron energy γ_j do not change drastically over such a length, and the equations can be averaged over Δz with the periodic condition of the magnetic field for ideal undulators. For real undulators, however, the periodic condition cannot be applied to modify the FEL equations because of the field error intrinsic to the real undulators.

NUMERICAL IMPLEMENTATION

The most straightforward way to solve precisely the FEL equations with the field-error effects taken into account is

to adopt a fine integration step, i.e., $\Delta z \ll \lambda_u$. Needless to say, it takes a lot of computation time. Because $\tilde{E}$ and γ_j are slowly varying functions compared to λ_u even in the case with the real undulator, averaging is again a promising way for practical simulation. It should be noted, however, that the averaging should be performed at every integration step, i.e., $z = \Delta z, 2\Delta z, \ldots, n\Delta z, \ldots$. In the following sections, the FEL equations are modified to the forms that are convenient for averaging.

Magnetic Field Model

In order to specify the electron trajectory in arbitrary magnetic fields $\boldsymbol{B}$, the equation of motion should be solved with the Lorentz force taken into account, which needs 3-dimensional field mapping. In the undulator line, however, the electron trajectory can be decomposed into two components, which considerably simplifies the problem.

One is the the sinusoidal (or more generally, quasi-periodic) orbit that cause the interaction between the electrons and radiation field. For real undulators, it also contains random walks both in the horizontal (x) and vertical (y) directions due to error fields. In general, it hardly depends on the transverse coordinate of the injected electron at the entrance of the undulator and is thus determined by the magnetic field distribution $\boldsymbol{B}_u$ measured along the undulator axis.

The other is the betatron oscillation induced by the focusing force on the electron beam generated by quadrupole magnets and (natural) focusing in the undulator. It is reasonable to assume that the focusing field $\boldsymbol{B}_f$ is uniform over the distance occupied by each magnetic device as shown in Fig. 1.

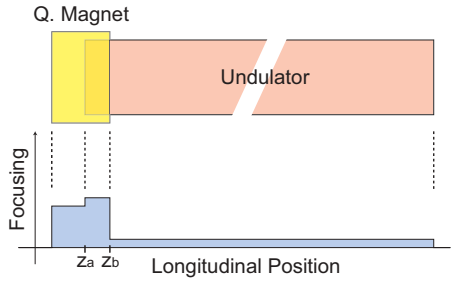

Figure 1: Example of a magnetic device configuration and focusing force distribution in the undulator line.

The above discussion arrows us to introduce an effective magnetic field $\boldsymbol{B}_{\rm eff}$ that has no longitudinal components and the form

$$\boldsymbol{B}_{\rm eff}(\boldsymbol{r}) = \boldsymbol{B_u}(z) + \boldsymbol{B_f}(x, y, z),$$

which can be used to calculate the electron trajectory instead of the real field $\boldsymbol{B}$. The field $\boldsymbol{B_f}(x, y, z)$ can be regarded to be uniform with respect to z within a limited range, e.g., $z_a < z < z_b$ as shown in Fig. 1.

Electron Motion

Now let us consider an electron travelling from z_0 to z with an initial condition $\boldsymbol{\beta} = \boldsymbol{\beta}_0$ and $\boldsymbol{r} = (x_0, y_0, z_0)$ at the longitudinal position of z_0. Assuming that the travelling distance $\Delta z = z - z_0$ is much shorter than the period of the betatron oscillation, the transverse position of the electron, x and y, does not change significantly. Thus, the focusing field $\boldsymbol{B_f}$ can be regarded to be constant. Then, the velocity and position of the electron are obtained just by integrating the field distribution along z axis

$$\begin{aligned} \beta_x(z) &= \beta_{0x} + \gamma^{-1}[I_{uy}(z_0, z) + I_{fy}(z_0, z)], \\ x(z) &= \beta_{0x}\Delta z + \gamma^{-1}[J_{uy}(z_0, z) + I_{fy}(z_0, z)\Delta z/2], \end{aligned} \tag{4}$$

with

$$\begin{aligned} I_{uy}(z_0, z) &= \frac{e}{mc}\int_{z_0}^{z} B_{uy}(z')dz', \\ I_{fy}(z_0, z) &= \frac{e}{mc}(z - z_0)B_{fy}, \\ J_{uy}(z_0, z) &= \int_{z_0}^{z} I_{uy}(z_0, z')dz', \end{aligned}$$

and similar expressions for the vertical components β_y and y.

Interaction Factor

In the differential equations (1) and (3), there exists an identical factor $\beta_x \mathrm{e}^{ik_u z}\mathrm{e}^{-i\psi}$ (and its complex conjugate), which is regarded to be an efficiency of interaction between the electrons and radiation field. It is easy to show that this factor is almost periodic with a period of $\lambda_u/2$. It is therefore necessary to average it over the distance of the integration step Δz, which, in most cases, longer than $\lambda_u/2$. In averaging, we can omit the trajectory components related to the betatron oscillation because the period of the betatron oscillation is much longer than λ_u, In other words, we replace as follows

$$\beta_x \to I_{uy}/\gamma, \;\; (\gamma\beta_\perp)^2 \to I_{uy}^2 + I_{ux}^2.$$

In addition, we can neglect the terms $\Delta\gamma$ and $\Delta\omega$ in the phase equation because they are nearly constant over Δz. Then, we have

$$\langle \beta_x \mathrm{e}^{ik_u z}\mathrm{e}^{-i\psi}\rangle = i\frac{J_a(z_0)}{\gamma}\mathrm{e}^{-i\psi_j(z_0)},$$

with

$$J_a(z_0) = \frac{1}{i\Delta z}\int_{z_0}^{z} I_{uy}(z')\exp\left[\frac{ik_u\rho(z_0, z')}{1 + K^2/2}\right], \tag{5}$$

and

$$\rho(z_0, z) = \int_{z_0}^{z}[I_{uy}^2(z_0, z') + I_{ux}^2(z_0, z') - K^2/2]dz'$$

For ideal undulators without any field errors, $I_{ux} = 0$ and $I_{uy}(z_0, z) = K \sin k_u z$, thus we have

$$J_a(z) = \frac{K}{2}\left[J_0\left(\frac{K^2/4}{1+K^2/2}\right) - J_1\left(\frac{K^2/4}{1+K^2/2}\right)\right].$$

Substituting this formula into (1) gives an ordinary wave equation to describe the amplification process in the FEL driven by an ideal undulator.

Electron Phase

Because the electron energy does not change significantly over Δz, the electron phase can be calculated by integrating equation (2) directly. Substituting (4) into (2) and integrating between z_0 and z, we have

$$\begin{aligned}\psi(z) &= \psi(z_0) + k_u \Delta z\left(\frac{2\Delta\gamma}{\gamma_0} - \frac{\Delta\omega}{\omega_0}\right) \\ &\quad + \frac{k_u(R_x + R_y - K^2\Delta z/2)}{1+K^2/2}, \qquad (6)\end{aligned}$$

with

$$\begin{aligned}R_x = &\int_{z_0}^{z} I_{uy}^2(z')dz' - \frac{2I_{fy}(z_0,z)}{\Delta z}\int_{z_0}^{z} J_{uy}(z_0,z')dz' \\ &+\Delta z[(\gamma\beta_{0x})^2 + \gamma\beta_{0x}I_{fy}(z_0,z) + I_{fy}^2(z_0,z)/3] \\ &+2J_{uy}(z_0,z)[\gamma\beta_{0x} + I_{fy}(z_0,z)], \qquad (7)\end{aligned}$$

and similar expression for R_y. Note that the subscript j has been omitted in the above equation for simplicity.

Processing of the Undulator Field Data

The above modifications on the FEL equations arrow us to process the undulator field data convenient for numerical implementation, i.e., the entire undulator line is divided into adequate integration steps and the quantities such as I_{uy}, J_{uy} and J_a are calculated in each step before starting the simulation. In most x-ray FELs, the gain length is much longer than the undulator period, which requires a great number of periods to achieve saturation. Thus, longer integration step is necessary to save the computation time. The data processing scheme described here ensures a good reproducibility of the electron motion and interaction efficiency regardless of the length of the interaction step, as far as the electron energy and radiation field does not change drastically within the step.

After the data processing, the FEL equations can be solved easily. The electron energy and phase can be calculated by substituting (5) and (7) into (2) and (3). The wave equation (1) that describes the growth of the radiation field can be modified to a more convenient form for numerical computation, by means of spatial and temporal Fourier transforms [1].

EXAMPLES

An FEL simulation code, SIMPLEX, has been developed at SPring-8 using the numerical schemes described above. Let us now show several examples of results to investigate the effects due to the undulator field error using SIMPLEX. Accelerator and undulator parameters used in the simulations are summarized in Table 1.

Electron Energy	250 MeV
Normalized Emittance	1πmm. mrad
Energy Spread	2×10^{-4}
Peak Current	2 kA
Average betatron function	7 m
Undulator Period	15 mm
Undulator Length	4.5 m
Undulator K Value	1.3
Wavelength	60 nm
Gain Length	0.16 m

Table 1: Example of a magnetic device configuration and focusing force distribution in the undulator line.

Performance of SCSS Prototype Undulator

SCSS stands for "SPring-8 Compact SASE Source" and aims at an X-ray FEL in the Angstrom wavelength region [2]. A prototype undulator for the SCSS project has been constructed in 2003, the details of which are described in [3]. Here we check the magnetic performance of the prototype. Figure 2(a) shows the phase errors as functions of the longitudinal position calculated with the magnetic field measured before and after the undulator field correction. We can see a drastic improvement between the two. In order to check the actual performance as an FEL driver, we performed FEL simulations, the results of which are shown in Fig. 2(b) as the radiation power growth along the undulator. As in the phase error, the FEL gain curve is improved significantly by the field correction, and we can expect the radiation power close to the ideal value with the constructed undulator.

Effects due to the Ambient Field

The ambient field means weak and uniform magnetic fields that cause a parabolic electron orbit. The main source for this is the geomagnetic field and/or an offset voltage of the Hall probe that is usually used in the undulator field measurement. In addition, the electron beam injected into the undulator with a vertical position offset with respect to the undulator axis experiences a parabolic-like orbit due to the natural focusing, which brings undesirable effects similar to those by the ambient field. The examples of the effects due to the ambient field ΔB_y in the vertical direction are shown in Fig. 3 in terms of the electron trajectory and power-growth curve. It is found that ΔB_y of 0.5 Gauss has little effects on the FEL gain, while those of 1.0 Gauss are not negligible.

Effects due to Inhomogeneous Demagnetization

It is well known that permanent magnets can be damaged by irradiation of the electron beam, which cause an

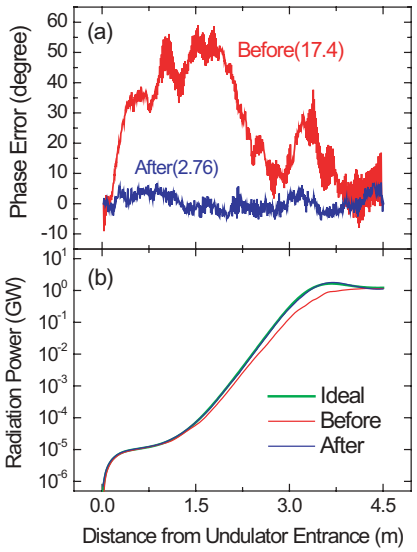

Figure 2: Magnetic performances of the prototype undulator for the SCSS in terms of the (a) phase error and (b) power-growth curve.

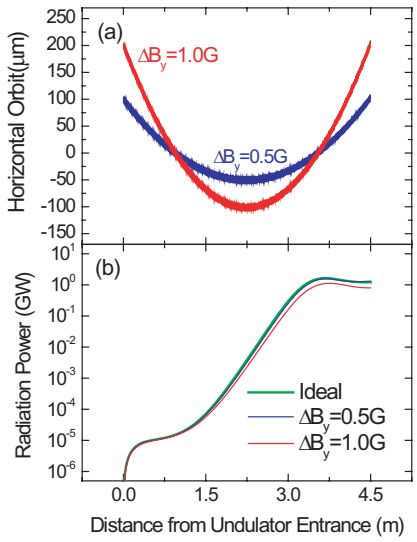

Figure 3: Effects due to the ambient fields of 0.5 and 1.0 Gauss on the (a) electron trajectory and (b) FEL gain.

inhomogeneous field variation along the undulator. As an example, let us consider the case when the magnetic field distribution is given as

$$B_y(z) = B_0 \sin(k_u z) F(z),$$

with

$$F(z) = 1 - A\mathrm{e}^{-z/D},$$

being an field envelope function to describe the radiation-induced demagnetization, where A and D denote the maximal fraction and typical depth of demagnetization, respectively. The examples are shown in Fig. 3 for two values of A. The depth D is fixed at 1.0 m in each simulation. We find a significant gain degradation even for the 0.5 % demagnetization.

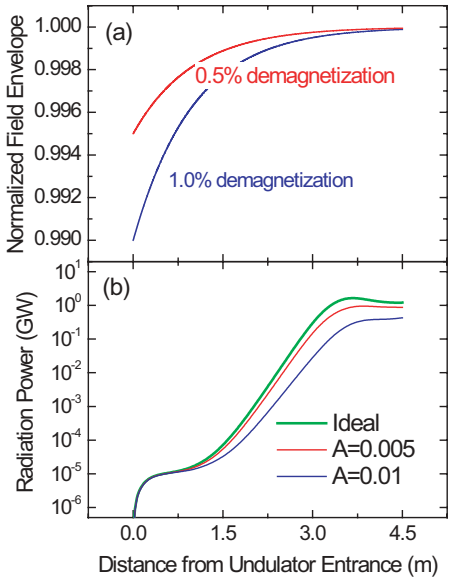

Figure 4: Effects of radiation-induced demagnetization on the (a) field envelope and (b) FEL gain for two values of the maximal demagnetization fraction A.

SUMMARY

The FEL simulation code, SIMPLEX, has been introduced. SIMPLEX has functions for FEL simulations as follows: steady-state simulation with seeding; time-dependent simulation with shot noise implementation for SASE regime; wakefield implementation; error sources related to phase slippage between undulator segments, field discrepancy, and trajectory straightness; graphical output. SIMPLEX is freely available from the web site [4]. It is equipped with a full graphical user interface for pre- and post-processing and does not need any other commercial softwares or libraries. Because of the portability of the graphical library used in SIMPLEX, it works on many platforms such as Microsoft Windows, Mac OS X, and unix-based OS such as Linux.

REFERENCES

[1] T. Tanaka, H. Kitamura and T. Shintake, Nucl. Instrum. Meth. A528 (2004) 172

[2] T. Shintake, these proceedings

[3] T. Tanaka, K. Shirasawa, T. Seike and H. Kitamura, Proc. 8th Int. Conf. Synch. Rad. Instrum., 227 (2004)

[4] http://radiant.harima.riken.go.jp/simplex

ELECTRON BEAM SIMULATIONS ON THE SCSS ACCELERATOR

T. Hara*, T. Shintake, H. Kitamura,
RIKEN/SPring-8, 1-1 Koto, Mikazuki, Sayo, Hyogo, 679-5148, JAPAN

Abstract

The SCSS (SPring-8 Compact SASE Source) is an X-ray SASE-FEL project with a 6 GeV electron beam accelerator. In the year of 2005, the construction of a 250 MeV facility will be started as a preliminary step towards the X-ray radiation. One of the unique features of the SCSS is the use of a pulsed high-voltage electron gun with a thermionic cathode. Meanwhile, the electron bunch should be compressed properly at the injector in order to obtain sufficiently high peak currents. In this paper, a layout of the 250 MeV accelerator is presented with the expected parameters of the electron beam.

INTRODUCTION

The SCSS (SPring-8 Compact SASE Source) is an X-ray SASE-FEL project based on a linear accelerator [1]. The full facility is planned to be constructed next to the 1 km beamline of SPring-8. In order to obtain 0.1 nm radiation, a low emittance electron beam with 6 GeV energy is necessary in combination with 15 mm period in-vacuum undulators [2]. As a preliminary step, we are planning to construct a 250 MeV facility to demonstrate SASE radiation in a VUV region and test the accelerator components in the year of 2005.

One of the unique features of the SCSS accelerator is the use of a pulsed high-voltage electron gun with a thermionic cathode [3, 4]. Main reason for this choice is its high stability and well developed technology relating to the gun. However, the emission current of a theomionic DC gun is small, typically a few amperes, comparing with the RF photo-cathode guns employed in most of the X-ray FEL projects such as LCLS or TESLA. Therefore the electron beam should be properly compressed in the injector to obtain sufficiently high peak currents at the undulator section [1]. Figure 1 is the layout of the SCSS at the 250 MeV stage. In the following sections, the electron beam parameters are estimated using the beam simulation code "PARMELA".

INJECTOR

The injector predominantly determines the quality of the electron beam in linear accelerators. In order to make operate the SASE process, the electron beam with high brightness is required, meaning that low emittance, a high peak current and a small energy spread. When the electrons pass through the undulators, only the electrons in a slice of the bunch can contribute to the amplification process of the SASE. The size of this slice is transversely determined by a diffraction limit of emitted light and longitudinally by a slippage length at a maximum. Therefore the beam parameters of the sliced electron bunch are important rather than total integrated or projected parameters of the whole bunch.

The initial condition of the simulation is given based on the results of the emittance measurements carried out on the electron gun. The measured profile in the phase space is shown in fig. 2 (a) and its normalized emittance was 1.1 π mm-mrad with a emission current of 1 A [3, 4]. The ends of the measured profile have slightly curved tails due to the space charge effect at the edge region of the round beam, and these tails increase the emittance in fig. 2 (a). When the electron gun is installed in the injector, these tails will be eliminated using a slit without loosing a major part of the charge. After eliminating the tails, the emittance of the core beam can be estimated from the beam size and the divergence at the beam center and it is about 0.6 π mm-mrad in fig. 2 (a).

Since "PARMELA" can not treat a DC electron gun, the simulation can not fully reproduce the conditions of the emittance measurement. In the simulation, 500 keV energy is immediately given to the electrons at the start and no DC acceleration process is considered. Therefore, the initial condition of the electron beam is determined so that the electron beam reproduces the core emittance of 0.6 π mm-mrad and the same divergence at the beam center under the identical layout of the beam optics. The obtained phase space profile by "PARMELA" is shown in fig. 2 (b), in which the effect of the space charge is different from the measured one (fig. 2 (a)) due to lack of DC acceleration in the simulation. The measured and simulated divergences at the beam center (x=0) are compared in fig. 2 (c).

A schematic layout of the SCSS injector is shown in fig. 1. The emission current of the cathode is assumed to be 3A in the simulation. The μsec cathode emission is immediately accelerated by a 500 keV pulsed DC voltage. At the chopper, an electron pulse with 1$\sim$2 ns duration is sliced out from the μsec emission as shown in fig. 3 (a). Then in the 238 MHz SHB (Sub Harmonic Buncher), the energy of the electrons is modulated as a function of their longitudinal position in the bunch (fig. 3 (b)). Since this energy modulation causes the velocity difference between the electrons, it turns into a density modulation as they fly through a drift space. The bunched electrons are accelerated to 1 MeV in a 476 MHz booster cavity and the length of the bunch is further compressed before arriving at the first S-band LINAC (fig. 3 (c)). In the first S-band LINAC, the electrons are again compressed by placing the bunch at off crest of the RF field. Finally at the exit of the injector,

* toru@spring8.or.jp

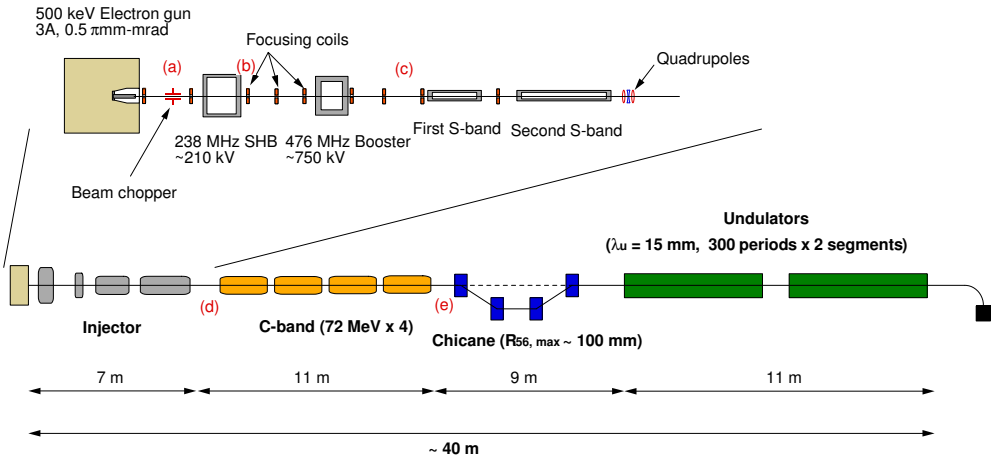

Figure 1: Layout of the SCSS at the stage of 250 MeV beam energy. (a)∼(e) corresponds to the locations used in figs. 3 and 4

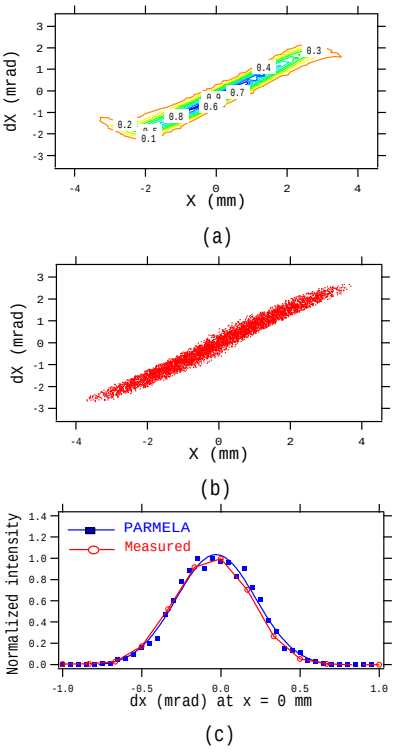

Figure 2: Phase space profiles of the electron bunch, (a) measured [3] and (b) calculated by ”PARMELA”. The measured and simulated divergences at the electron beam center (x = 0 mm) is plotted in (c).

the peak current close to 100 A can be obtained with the beam energy of 23 MeV (fig. 3 (d)).

In the simulation, APS (alternating periodic structure) standing wave cavities are used for the S-band LINACs and traveling wave disk loaded structure is assumed for the C-band LINACs. The RF fields of the cavities are calculated by ”SUPERFISH” and 2-D axisymmetric fields are given to ”PARMELA”.

Figures. 4 (a)∼(d) are the slice RMS emittance at the locations same as fig. 3. The length of the slice is 1 ps for fig. 4 (a)∼(d), which is larger than the slippage length by rougly one order. The electron beam is focused by using solenoid lenses in the injector and quadrupole magnets after the injector. The parameters of the focusing elements are determined so as to minimize the slice emittance. With the current injector parameters used in figs. 3 and 4, the bunch compression is stopped at each components so that the electrons are not over bunched to keep the emittance small. With the same configuration of the components as in fig. 1, higher compression ratio can be obtained by slightly changing the parameters of the SHB. However, the increase of the peak current at low energy results in the degradation of the emittance due to the space charge effect.

EXPECTED PARAMETERS OF THE ELECTRON BEAM

After the injector, the electron beam is accelerated to 250 MeV by four 1.8 m long C-band accelerator tubes. The expected acceleration gradient is 35∼40 MV/m. Figures 3 (e) and 4 (e) show the profile and slice emittance of the electron bunch at 250 MeV. Expected paremeters of the 250 MeV electron beam are summarized in table 1.

In order to cut out a dark current from the accelerator tubes, a chicane is installed between the C-band LINACs and the undulators. The chicane is composed of four bending magnets and X-Y collimators will be installed between the second and third magnets in the chicane. This chicane is also necessary to inject laser light for the purpose of the undulator alignment [1] and FEL operation with seeding light [6, 7].

A saturation length corresponding to the parameters in table 1 is about 18 m. In order to obtain a shorter saturation length, the peak current should be increased in the injector at the expense of the emittance, or in the chicane. The current design of the chicane has the maximum $R_{56} \approx 100$ mm and it can be used as a bunch compressor. The emittance growth due to the CSR effect (Coherent Synchrotron Radiation) is discussed in ref. [5] in case of a similar bunch compressor design.

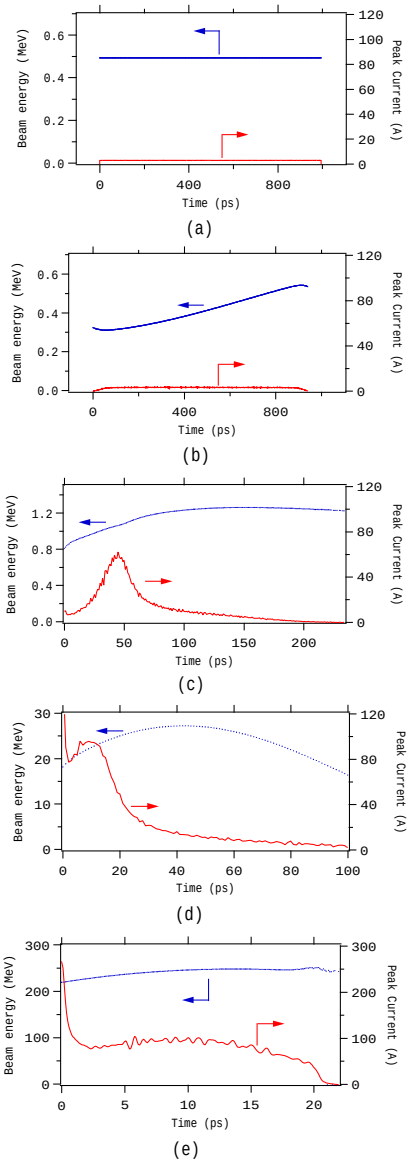

Figure 3: Electron beam energy (blue lines) and peak current (red lines) as a function of longitudinal position (time) in the bunch. (a)∼(e) corresponds to the location marked in fig. 1, at (a) chopper, (b) after SHB, (c) before first S-band LINAC, (d) injector end (before first C-band LINAC) and (e) accelerator end (before chicane). The emission current of the gun is set at 3A and the head of the electron bunch corresponds to the time zero.

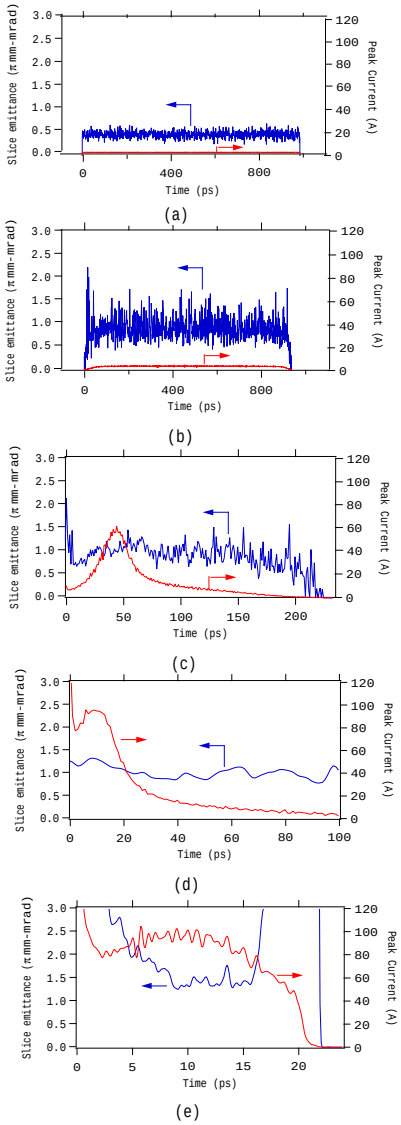

Figure 4: RMS normalized slice emittance (blue lines) and peak current (red line) as a function of longitudinal position (time) in the bunch. (a)∼(e) corresponds to the location marked in fig. 1, at (a) chopper, (b) after SHB, (c) before first S-band LINAC, (d) injector end (before first C-band LINAC) and (e) accelerator end (before chicane). The length of the slice is 1 ps for (a)∼(d) and 0.1 ps for (e). The emission current of the gun is set at 3A and the head of the electron bunch corresponds to the time zero.

Table 1: Expected parameters of the electron bunch at the undulator of SCSS.

Electron Energy	250 MeV
Normalized Slice Emittance	$\sim 1.5\pi$ mm-mrad
Peak Current	100 A (before chicane)
Slice energy spread	$\sim 2 \times 10^{-4}$
Undulator period	15 mm
Nominal operation gap	3.5 mm
K parameter	1.3
Radiation wavelength	60 nm

SUMMARY

As a preliminary step to the X-ray SASE-FEL, a 250 MeV facility is planned to be constructed in the SCSS project. The purpose of the 250 MeV facility is to demonstrate the SASE-FEL and test the accelerator components, since the SCSS has unique features in its design, such as the thermal DC electron gun and in-vacuum undulators. The electron beam parameters of the 250 MeV facility are estimated using the code "PARMELA". The design performance of the accelerator will be compared with measurements after the completion of the facility including a bunch compressor.

Regarding the SASE operation at 60 nm with 250 MeV electrons, we need to obtain a shorter saturation length than the expected one in this paper. After further optimization of the beam parameters, particularly with the higher peak current, the saturation length of ≈ 10 m is expected.

REFERENCES

[1] T. Shintake, H. Matsumoto, T. Ishikawa and H. Kitamura, "The SPring-8 Compact SASE Source", Proc. of the SPIE's 46th Annual Meeting, San Diego, USA, June 2001.

[2] T. Tanaka, K. Shirasawa, T. Seike and H. Kitamura, "Development of the short-period undulator for the X-ray FEL project at SPring-8", Proc. of 8th International Conference on Synchrotron Radiation Instrumentation, San Francisco, USA, August 2003, p. 227.

[3] K. Togawa, H. Baba, T. Inagaki, K. Onoe, T. Shintake, T. Tanaka and H. Matsumoto, "Low Emittance 500 kV Thermionic Electron Gun", Proc. of 12th International Linear Accelerator Conference, Lübeck, Germany, August 2004, p. 318.

[4] K. Togawa, H. Baba, T. Inagaki, K. Onoe, T. Shintake, T. Tanaka and H. Matsumoto, "Emittance Measurement on the CeB_6 Electron Gun for the SPring-8 Compact SASE Source", in these proceedings.

[5] Y. Kim, T. Shintake, H. Matsumoto, H. Kitamura and K. Sawada, "Beam Parameter Optimization for the Phase-I Stage of the SPring-8 Compact SASE Source (SCSS) Project", Proc. of EPAC 2002, p. 808.

[6] D. Garzella, T. Hara, B. Carré, P. Salières, T. Shintake, H. Kitamura and M.E. Couprie, Nucl. Inst. Meth., A528 (2004), p. 502.

[7] G. Lambert, B. Carré, M.E. Couprie, D. Garzella, Y. Mairesse, P. Salières, A. Doria, L. Giannessi, T. Hara, H. Kitamura and T. Shintake, "Seeding High Gain Harmonic Generation with Laser Harmonics Produced in Gases", in these proceedings.

REDUCING BACK-BOMBARDMENT EFFECT USING THERMIONIC CATHODE IN IAE RF GUN

#T. Kii, K. Hayakawa, K. Masuda, S. Murakami, H. Ohgaki, T. Yamazaki, K. Yoshikawa, H. Zen

Institute of Advanced Energy, Kyoto University, Uji, Japan

Abstract

We have studied the improvement in electron beam macropulse properties from a 4.5 cell thermionic RF gun. Energy spectrum, macropulse duration and emittance, were measured with a 2 mm diameter slim thermionic dispenser cathode. The effect of a transverse magnetic field reducing back-streaming electrons was studied experimentally. The effect of non-flat RF power to compensate decreasing beam energy during macropulse due to a back-streaming electrons has also been studied.

INTRODUCTION

Compact and simple FEL machines will be important for various applications such as material processing, medical, bio science, and so on. A thermionic RF gun seems to be a good choice for such compact machines, because it is compact, easy to operate, and can produce high brightness electron beams. However, back-bombardment problem is limiting the macropulse duration.

We evaluated the effect of back-streaming electrons quantitatively, using an IR thermometer and numerical simulations[1,2], and the effect of transverse magnetic field on cathode surface quantitatively[3],[4]. Furthermore, we have estimated the effect of a combination of slim cathode and transverse magnetic field[5], and concluded that the combination is effective to suppress a temperature rise during macro pulse.

In this study, the effect of slim cathode and transverse magnetic field is studied experimentally. Effect of a non-flat RF input to compensate for decreasing beam energy during macropulse due to a back-bombardment effect is studied.

EXPERIMENTAL SETUP

Fig. 1 shows the experimental setup. A dispenser cathode of disk like shape with 2 mm diameter is mounted in the first half cell of our 4.5 cell RF gun. Initially the surface temperature of the cathode is kept at around 1020 °C. To reduce back-streaming electrons, transverse magnetic field is applied by a dipole magnet, which is located just behind the RF gun. The amplitude of the magnetic field on the cathode surface is 29 gauss.

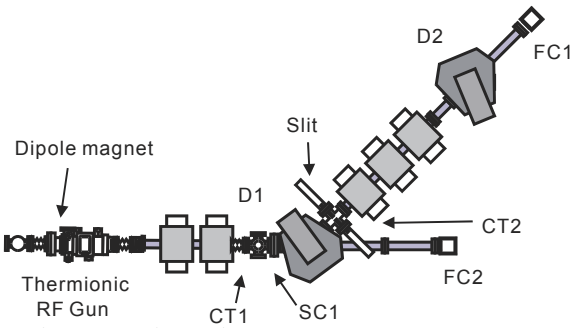

Fig. 1 Experimental setup

RF power fed to the RF gun is controlled by changing reactance in a pulse forming network (PFN) of modulator during operation by controlling remotely the reactors with stepping motors. By using the variable reactor system, we can modulate the RF amplitude up to about 20%.

The performance of the modulator is shown in table 1.

Table 1 Performance of the modulator NKLY-170-10u (manufactured by Nissin High Voltage)

Pulse voltage	170 kV
Pulse current	140 A
Pulse duration	10 μs
Maximum repetition	10 pps

Extracted beam properties are measured using current transformers (CT1 and CT2), Faraday cups (FC1 and FC2) and a fluorescent screen (SC1).

RESULTS

Beam properties

Effect of the slim cathode and the transverse magnetic field on the cathode surface was checked by measuring maximum electron macro pulse width after the bending magnet (D1). Results on a previous cathode with 6 mm diameter and on the slim cathode are shown in table 2.

#kii@iae.kyoto-u.ac.jp

Table 2 Maximum macro pulse width

Condition	Pulse width
6 mmϕ without magnetic field $T_{cathode}$ = 1000 °C Pin=7.4 MW	<500 nsec
6 mmϕ with magnetic field $T_{cathode}$ = 1000 °C Pin=7.4 MW	500 nsec
2 mmϕ with magnetic field $T_{cathode}$ = 1020 °C Pin=5.0 MW	3.0 μsec

As shown in table 2, pulse width has been improved by using the slim cathode and the transverse magnetic field, but this is still not sufficient for the FEL experiment[6].

Emittance with / without the transverse magnetic field were also measured using the fluorescent screen (SC1) and quadrupole magnet (Q1). Projected images on the screen are analyzed with tomographic method using algebraic reconstruction technique[7,8]. The measured geometric emittance are shown in table 3.

Table 3 Beam emittance

Condition	Emittance
2 mmϕ without magnetic field	1.96 πmm-mrad
2 mmϕ with magnetic field	1.79 πmm-mrad

As shown in tables 2 and 3, the transverse magnetic field can reduce back-streaming electrons without changing beam emittance.

Energy spectra were also measured with / without the magnetic field. As shown in fig. 2, the energy spectrum is not changed by the transverse magnetic field.

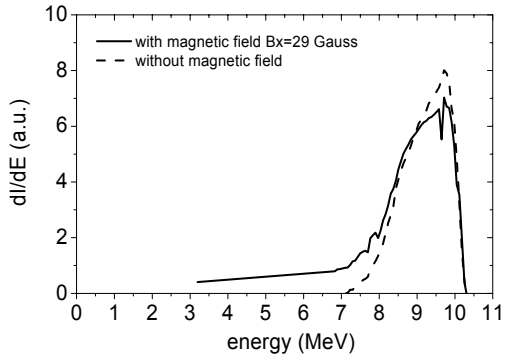

Fig. 2 Energy spectra

Energy compensation

For the FEL experiment, a macro pulse longer than 3 μsec will be required. For this purpose, we tried to compensate for the decrease of the beam energy during macro pulse by controlling input RF waveform.

When flat RF power was fed to the RF gun as shown in fig. 3 by open circles, peak energy decreases rapidly as shown in fig. 4 by dotted line. Thus, pulse width after the bending magnet (D1) is limited to about 3.0 μsec as shown in fig. 5 by open circles. To compensate the energy decrease, amplitude of the input RF power was modified as shown in fig. 3 by solid line. As shown in fig. 4, the peak energy was successfully kept constant up to 3.5 μsec. Pulse width is improved and peak current increases as shown in fig. 5 by solid line and total charge in a macropulse increases up to about twice that with the flat input. The effect of the amplitude modulation method is summarised in table 4.

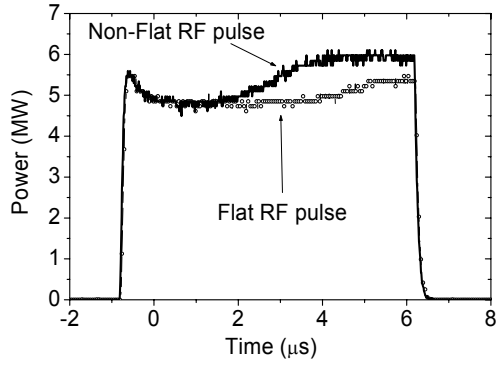

Fig. 3 Flat/non-flat RF power fed to the RF gun

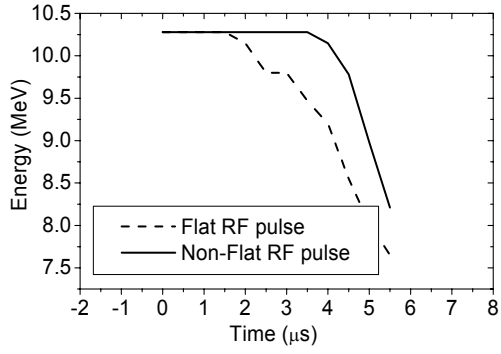

Fig.4 Time evolution of the peak energy during macro pulse

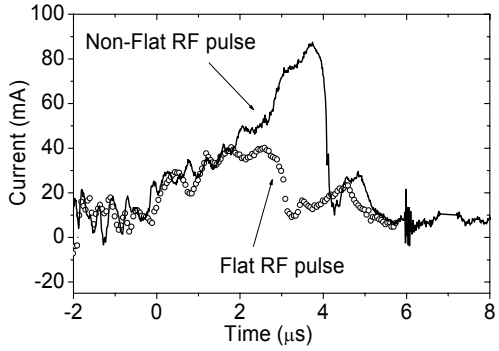

Fig. 5 Wave form of the beam current, measured using CT2

Table 4 Effect of non-flat RF input

	Flat RF pulse	Non-Flat RF pulse
Pulse width	3.0 μs	4.2 μs
Peak current	40 mA	90 mA
Total charge	97.7 nC	205.8 nC

ANALYSIS

To establish the energy compensation method using amplitude modulation, we have estimated the effect of this method with a particle simulation code PARMELA (version 3.30)[9]. As a first step, current density during macro pulse on the cathode surface was evaluated. Time evolution of the current density on the cathode is shown in fig. 6

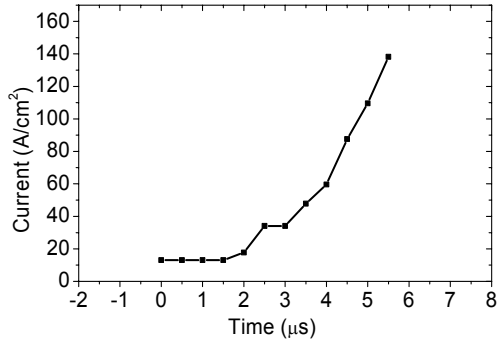

Fig. 6 Time evolution of current density during macropulse

Next, we evaluated the RF power required to accelerate up to the same energy as that for the initial current density. The required power is shown in table 5. Thus, the ideal RF wave form is derived as shown in fig. 7.

Table 5 Required RF power to keep beam energy constant

Current density [A/cm^2]	Required power [MW]
15.9	8.88
31.8	8.99
47.8	9.13
63.7	9.24
79.6	9.42
95.5	9.60
111.4	9.81
127.3	9.90
143.2	10.03

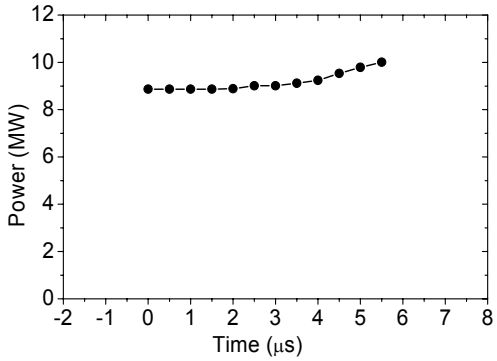

Fig. 7 Ideal RF wave form to extract electron beams with constant energy.

According to the results, in case for the maximum modulation of 19% of our power modulator, more than 1000% change of the current density is acceptable to keep the peak energy constant. In this case, estimated width of the macro pulse is longer than 5.5 μsec, but it is not consistent with the experimental results.

The reason of the inconsistency may be due to a transient phenomenon of the RF cavity and difference between matched loading and real beam loading.

SUMMARY

To improve electron beam properties, a slim cathode and transverse magnetic field are used. We could produce longer macro pulse, but it was not enough for FEL experiment, because beam energy is decreasing in the macro pulse due to the back-streaming electrons.

Thus, we fed non-flat RF to the 4.5 cell thermionic RF gun to compensate for the decrease of the beam energy by adjusting the reactance of the PFN. As a result, we

succeeded in producing high-brightness electron beam with 4 μsec macropulse duration.

The effect of the energy compensation using this technique was numerically studied also. In the case of our 4.5cell thermionic RF gun, it was found that the amplitude modulation of 19% could keep the peak energy constant even when the current on the cathode surface changed by more than 1000%. To understand the discrepancy, transient analysis in the RF gun seems to be necessary.

For the future application of the FEL experiment, phase stability of electron micro bunches and beam emittance are also very important. These parameter will be measured and checked to see whether the extracted beam is acceptable for the FEL experiment.

REFERENCES

[1] T. Kii, et al., Nucl. Instr. And Meth. A 475 (2001) 588
[2] T. Kii, et al., Nucl. Instr. And Meth. A 483 (2002) 310
[3] C.B. McKee and John M.J Maday, Nucl. Instr. And Meth. A296 (1990), 716
[4] T. Kii, et al., Nucl. Instr. And Meth. A 507 (2003) 340
[5] T. Kii, et al., Nucl. Instr. And Meth. A 528 (2004) 408
[6] H. Ohgaki et al., Nucl. Instr. And Meth. A 507 (2003) 150
[7] C. B. McKee et al., Nucl. Instr. and Meth., A358 (1995) 264; X. Qiu et al., Phys. Rev. Let. 76 No.20 (1996) 3723
[8] H. Ohgaki et al., Nucl. Instr. And Meth. A 528 (2004) 366
[9] L.M. Young, J.H. Billen, PARMELA, LA-UR-96-1835, 2001

RENEWAL OF KU-FEL FACILITY

#T. Kii, K. Hayakawa, S. Murakami, H. Zen, K. Masuda, H. Ohgaki, K. Yoshikawa, T. Yamazaki,

Institute of Advanced Energy, Kyoto University, Gokasho, Uji, Kyoto 611-0011, Japan

Abstract

We have started construction of new FEL facility (Kyoto University FEL: KU-FEL) which will be used for research on energy science. In the past, we have developed the KU-FEL parasitically at a shared experimental facility. Thus construction time was quite limited, and we had no space for future applications of the IR-FEL. Therefore we decided to renew an old experimental hall. In this paper, status of construction and future plans are described.

INTRODUCTION

Users demands in the area of energy-related science to a high-power tunable IR lasers are increasing in Japan, such as basic study of high-efficiency solar cells, generation of sustainable energy source of alcohol and/or H_2 from polluted gas, and separation of DNA and/or RNA. To satisfy these demands, we decided to renew our FEL facility to be more user friendly and to operate more flexibly.

DESIGN

Experimental hall

Construction and fundamental studies on the KU-FEL have been carried out parasitically at a building belonging to the Institute of Chemical Research where a few other accelerators were operating. Therefore, available machine time for our experiments was quite limited. We decided recently to move the KU-FEL to our own building and reconstruct the machine. The building used to be for plasma experiments and there was no provision for radiation shielding. We modified the room by adding concrete walls of 2-m thickness and some space for users.

A Schematic drawing of the experimental hall is shown in fig.1. The room with the shielding was completed in June, 2004. We decided not to use a costly shielding door by use of stairs to step up to the top of the shielding wall and down to the accelerator room. Concrete blocks can be removed temporarily when large equipment is to be carried in.

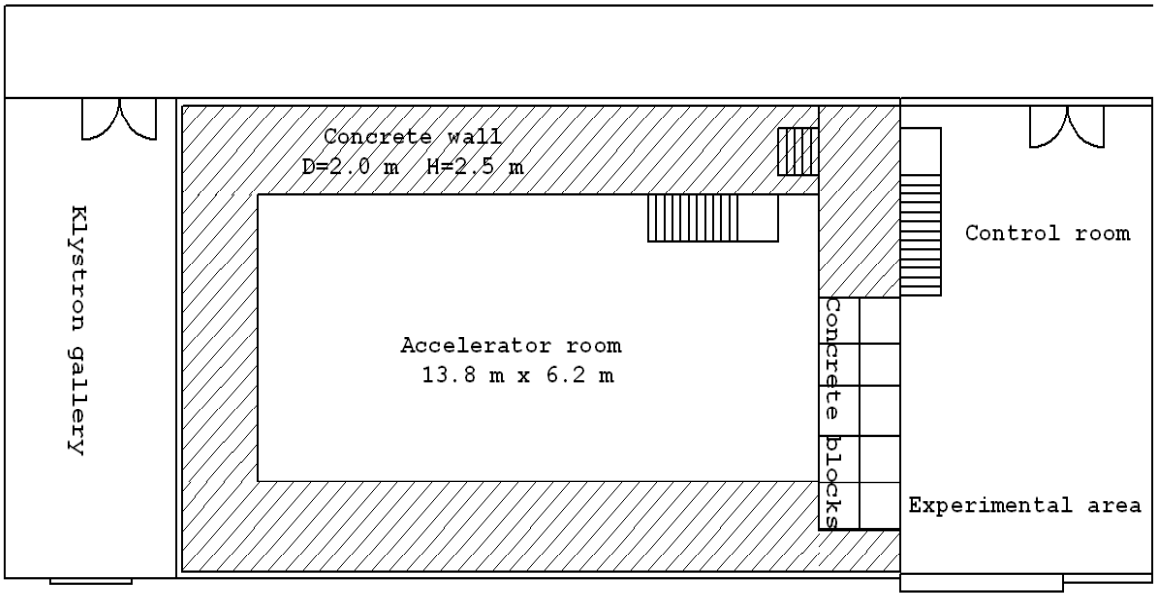

Fig. 1 Experimental hall

#kii@iae.kyoto-u.ac.jp

Initial plan

As a first step, we are planning to construct a compact IR-FEL system, which consists of a 4.5 cell thermionic RF-gun, a 3 m accelerator tube and 1.6 m Halbach type undulator. Schematic view of the system is shown in fig. 2.

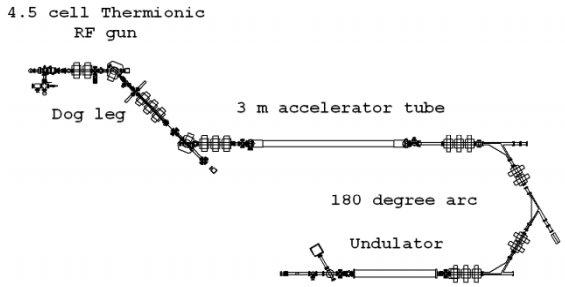

Fig.2 4.5 cell gun and linac

The electron beam of about 30 MeV will be provided by the thermionic RF gun and the linac. The configuration has been already designed to achieve a FEL lasing from 4 to 13 μm [1,2], and acceleration test has been carried out at the previous experimental hall.[3, 4]

All devices were moved to the new hall in July, 2004. We hope to resume the operation of the linac in fall of 2004. The FEL is expected to lase next year. However, the lasing wavelength will be limited to around 13 μm because the undulator is an old one which used to be used for a different system and not adequate to the present system.

Future plans

A 1.6 cell photocathode RF-gun system will be added to the system in the near future and it will be used alternately with the present thermionic RF-gun according to the demands of users. The photocathode material will be Cs_2Te.[5]

Fig. 3 shows a schematic view of the photocathode upgrade.

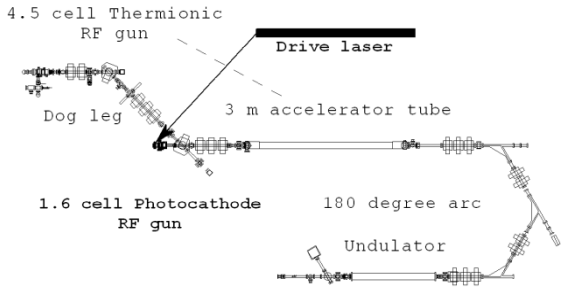

Fig.3 Photocathode upgrade

After the photocathode upgrade, we will install an energy recovery system using a normal conducting accelerator tube.[6] This upgrade is mainly to reduce shielding duty to the radiations from used electrons.

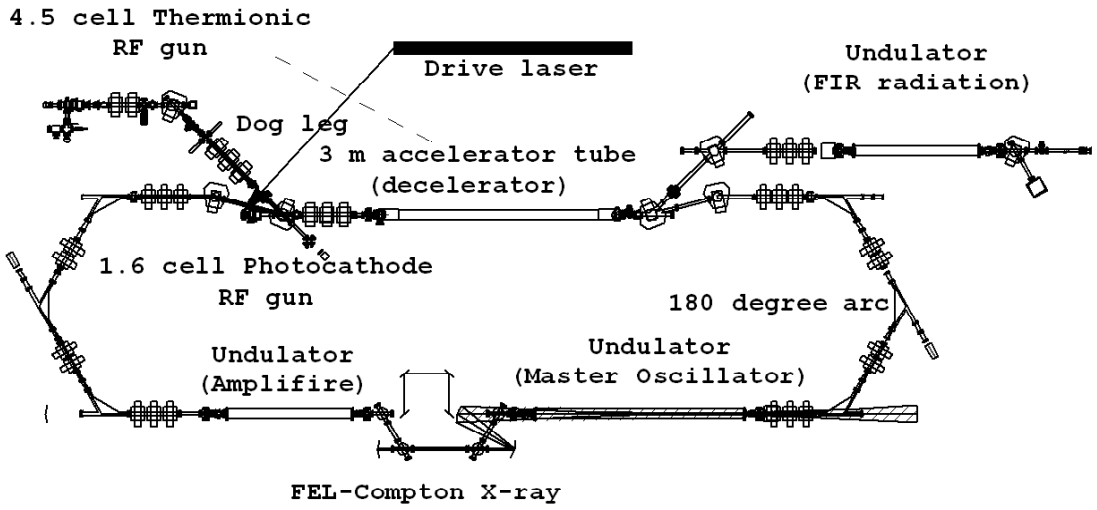

Fig. 4 Future upgrades

Some experiments on material science and bio science will need polarized laser light, and a helical undulator will be needed to satisfy some users' demands. APPLE-II type undulator[7] or Onuki type undulator[8] is considered at present. Two-stage FEL system to increase the FEL power[9] is also planned for the future. Generation of FEL-Compton backscattering x-rays is also planned. In order to compensate for the low yield of this method, the IR FEL in a cavity will be directly used. The expected x-ray energy is from 2 keV to 20 keV by using 32-MeV electron beam and 10-100 μm FEL. FIR radiation is also planned using thermionic RF gun.

These upgrades are shown in fig. 4.

SUMMARY

We have renewed an experimental hall for FEL experiments. The accelerator and the IR-FEL system will be installed shortly. The building is completed, and beam commissioning will be started in this year.

After lasing in the 10 μm wavelength region, we are planning to upgrade our facility to satisfy users' demands. By using various types of radiations (e. g. FIR radiation, IR FELs, Compton X-ray), material and bio/chemical science will be studied.

REFERENCES

[1] T. Yamazaki, et al., Nucl. Instr. And Meth. A 483 II (2002) 13.
[2] H. Ohgaki, et al., Nucl. Instr. And Meth. A 507 (2003) 150.
[3] S. Murakami, et al., Proceedings of the 1st Annual Meeting of Particle Accelerator Society of Japan and the 29th Linear Accelerator Meetings in Japan, (2004) 599
[4] K. Masuda, et al., in these proceedings
[5] H. Ohgaki, et al., in these proceedings
[6] K. Masuda, et al., Nucl. Instr. And Meth. A 507 (2003) 133.
[7] A. Bhowmik et al., Nucl. Instr. And Meth. A272 (1988) 183.
[8] H. Onuki et al., Appl. Phys. Lett. 52 (1988) 173.
[9] O. Chubar et al., J. Synchrotron Rad. (1998) 5, 481.

BEAM PROPERTY MEASUREMENTS ON THE KU-FEL LINAC

K. Masuda*, K. Hayakawa, T. Kii, S. Murakami, H. Ohgaki, T. Yamazaki, K. Yoshikawa, H. Zen,
Inst. of Advanced Energy, Kyoto Univ., Gokasho, Uji, Kyoto 611-0011, Japan

Abstract

An infrared FEL facility, KU-FEL, is under construction for advanced energy researches. An S-band rf gun and an accelerating tube has been installed. Measurements of beam properties have been carried out. An energy spread below 1 % at 50 mA current has been obtained. The normalized emittances were measured to be 78 π mm mrad in horizontal and 70 π mm mrad in vertical directions by the tomographic technique. A dipole sweep magnet was set for sweeping the back-streaming electrons vertically out of the cathode in the rf gun. It is found that the magnet does not affect the beam emittance, but results in poor current transmittance through the linac. PARMELA simulation suggests the use of a horizontal Sweep magnet instead of the vertical one.

INTRODUCTION

An infrared FEL facility, KU-FEL[1,2], is under construction for researches on advanced sustainable energies, such as bio-energy, solar energy. An electron beam of 30 MeV has been obtained by an S-band rf gun with a thermionic cathode and a recently installed accelerating tube. In this paper, we will describe measurements of the beam properties on the KU-FEL linac, such as transverse emittance, energy spread, and beam current. Comparison with PARMELA[3] simulations will be also presented.

One of the critical R&D issues on our KU-FEL linac is that of reducing and/or compensating the adverse effect due to back-streaming electrons onto the cathode, and time-varying beam-loading and accordingly time-varying output beam energy during a macropulse [4], inherent in thermionic rf guns. The introduction of transverse dipole magnetic fields along the cathode surface [5] has been found effective against this back-bombardment effect in our rf gun [6], while effects of the induced transverse beam deflection on the output beam transport through the linac as well as the beam emittance have not been evaluated. In this paper, we will discuss comparisons of the beam properties with and without the transverse B-field in the vicinity of the cathode.

EXPERIMENTAL SETUP

The KU-FEL linac consists of an S-band 4.5-cell rf gun with a thermionic cathode, a 3-m accelerating tube, and a beam transport system, shown schematically in Fig. 1. The typical output energy by the gun is 9 MeV. An energy analyzer consisting of a 45-degree bending magnet and a horizontal slit is located between the gun and the accelerating tube. The energy analyzer is followed by 3

* E-mail: masuda@iae.kyoto-u.ac.jp

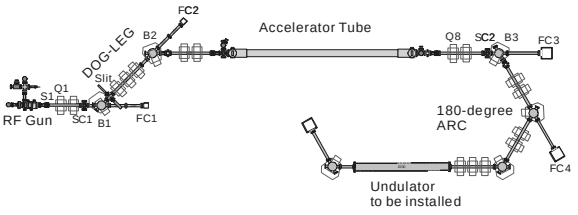

Figure 1: Schematic view of the KU-FEL linac.

quadrupole magnets and another dipole which comprise an achromatic transport system (Dog-Leg section in Fig. 1) to the accelerating tube. The designed maximum beam energy is 40 MeV, which will be led through the 180-degree arc section into the undulator to be installed to produce 4-13 μm IR-FEL [7].

On one hand a thermionic rf gun has advantageous features over a photocathode one, such as low cost, easy operation, and high average current. On the other hand it inherently has some disadvantages such as current and energy fluctuations during a macropulse due to beam-loading and back-streaming electrons hitting the cathode. To cope with the last problem, we have set a dipole magnet (called 'Sweep magnet' hereafter) to sweep out the back-streaming electrons by providing horizontal transverse B-field along the cathode surface [5]. In order to compensate the resultant vertical beam deflection with respect to the gun axis, a steering dipole magnet set at the gun exit (S1 in Fig. 1) was used.

Also, aiming at a further reduction of back-streaming electrons, use of a cathode with smaller diameter in combination with the Sweep magnet is being studied [8]. In the present measurements, a tungsten dispenser cathode of 2 mm diameter was used instead of the cathode of 6 mm diameter previously used [9]. The cathode surface temperature was measured by an IR pyrometer and was fixed to 1473 K. The corresponding current density on the cathode surface is 38.1 A/cm^2.

Throughout the measurements, the macropulse duration of rf input to the gun was fixed to 2 μsec in order to minimize the degradation in the projected beam's properties owing to the time-variation during the macropulse. The rf input powers to the gun and the accelerating tube were 7 and 10 MW respectively. In this paper, the magnetic flux density by the Sweep magnet in the vicinity of the cathode was fixed to 29 gauss.

RESULTS AND DISCUSSIONS

Beam properties at the gun exit

Measurements of beam currents, transverse emittances, and energy spectra at the gun exit were carried out with

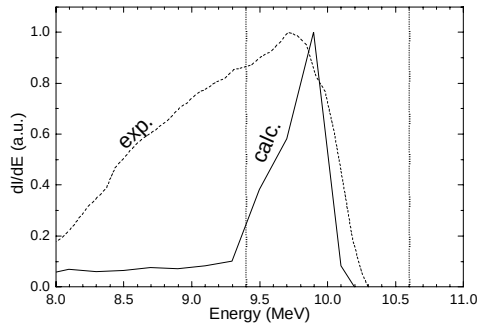

Figure 2: Energy spectra at the gun exit by the measurement (dashed line) and by the simulation (solid line). The dotted lines indicate the energy acceptance of the following energy slit (B1 and Slit in Fig. 1).

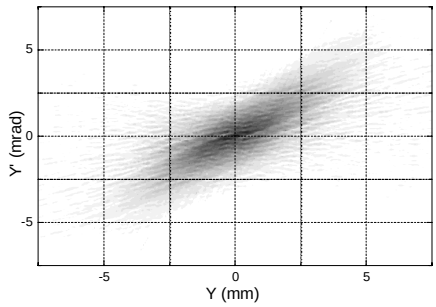

(a)

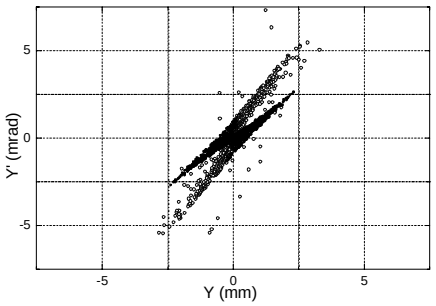

(b)

Figure 3: Vertical phase space distribution in the vertical direction, (a) reconstructed by the tomographic technique from the observed images in SC1 in Fig. 1, and (b) by the simuration. The black circles in (b) show particles within the major high energy component indicated in Fig. 2.

and without the Sweep magnetic field. The tomographic method described in [9] was applied for the measurements of the transverse phase space distributions and corresponding emittances, with a quadrupole magnet (Q1 in Fig. 1) and a phosphor screen (SC1). The energy spectra were taken with a bending magnet (B1) and a Faraday cup (FC2). The energy resolution was found to be $\Delta E/E$ = 13 % by a PARMELA run.

Introducing the Sweep magnet, the beam current, measured with a Faraday cup (FC1 in Fig. 1), was seen to decrease from 460 mA to 400 mA. No degradation in the transverse emittances in both horizontal and vertical directions was observed, while a slight improvement in the energy spread was seen, as stated in [8]. The experimental results in the case without the Sweep magnet are shown in Figs. 2 and 3, together with PARMELA results for comparisons.

Table 1: Unnormalized emittances at Q1 downstream the gun exit (see Fig. 1). The emittances by the simulation take only the high energy component indicated in Fig. 2 into account, while those in the parentheses include all particles. [π mm mrad]

		measurement	simulation
with Sweep magnet	horizontal	1.9	0.23 (0.18)
	vertical	1.8	0.23 (1.25)
w/o Sweep magnet	horizontal	1.8	0.21 (0.22)
	vertical	2.0	0.14 (0.23)

The energy spectra are shown in Fig. 2. The difference between the measured and the calculated energy spreads in the figure, may be due the time-dependent beam-loading effects during the macropulse which are ignored in the simulation. In the measurements downstream the Dog-Leg section, the energy acceptance of the energy slit was fixed to 10.0 ± 0.6 MeV, which is indicated in Fig. 2 by the dotted lines.

Figures 3 (a) and (b) show the phase space images in the vertical direction, and the corresponding emittances. Both the beam emittances with and without the Sweep magnet are listed in Table 1. The rotational angle in the phase space shown in fig.3, is reproduced well by the simulation, although appreciable differences in the corresponding emittances can be observed. As before this difference can be due to time dependent effects along the macropulse, and also to the broad energy spread in the reconstruction process in the tomographic measurement, which are neglected in the simulation, though extremely low energy component must be swept out of the phosphor screen (SC1) in the measurement also.

Beam properties at the accelerating tube exit

The beam without the Sweep magnetic field applied in the vicinity of the gun cathode was transported through the Dog-Leg section to the accelerating tube. The beam properties were measured at the accelerating tube exit, with a quadrupole magnet (Q8 in Fig. 1) and a screen monitor (SC2) for transverse emittances, and with a bending magnet (B2) and a Faraday cup (FC4) for the energy spectra.

For the SC2, either a 1-mm thick phosphor (chromium-doped alumina) or an aluminium plate can be used at exactly the same position. As it is seen in Fig. 4, the fluorescence profile from the phosphor screen is found broader than the transition radiation profile from the aluminium plate. The broadening was around 35 % in both horizontal and vertical directions, depending neither

Table 2: Beam currents [mA], from the gun down to the accelerating tube exit.

		gun exit	accelerating tube entrance	accelerating tube exit
experiments	w/o Sweep magnet	460	60	48
	with Sweep magnet	400	46	<5*
simulation	w/o Sweep magnet	633	197	65
	with Sweep magnet	520	105	20

*average over macropulse duration

on the incident beam angle of 0 and 45 degrees nor on the beam size of 2.2 and 1.6 mm in FWHM. Although this broadening with phosphor screen would result in an overestimate in the emittances, we used the phosphor screen, characterized by a much higher signal to noise ratio.

Reconstructed images by the tomographic technique in the transverse phase spaces are shown in Figs. 5(a) and (b). The resultant geometric emittances were 1.3 π mm mrad in horizontal and 1.2 π mm mrad in vertical, corresponding to normalized emittances of 78 and 70 π mm mrad.

Then we tried to transport the beam with the Sweep magnetic field applied, by changing the strength of the quadrupole magnets and of the steering magnet at the gun exit (S1 in Fig. 1). In contrast with the case without the Sweep magnet, the beam could hardly be transported through the accelerating tube, although, as presented in the previous section, almost no degradation in the beam properties were seen at the gun exit either in the measurement or the PARMELA simulation. So far, we have obtained beam currents listed in Table 2 from the gun exit to the accelerating tube exit. The tendency of a poor transmittance in the case with the Sweep magnet can be also seen in PARMELA results as summarized in the table.

Figure 6 shows the measured energy spectra with and without the Sweep magnet, both normalized as their peaks are unity. Although the energy resolution and signal to noise ratio were poor for the case without the Sweep magnet, the energy spread with the Sweep magnet was found 1.5 % (FWHM), and was found to be broader than the one obtained without the Sweep magnet (less than 0.7%). We can see this tendency more clearly in the PARMELA results in Fig. 7, showing that the energy spreads (FWHM) with and without the Sweep magnet were 2.4% and 0.49% respectively, which seem to agree with the experimental ones. From the simulations in Fig. 7 we can see that the sharp peak in the energy spectrum without the Sweep magnet was almost lost with respect to the case with the Sweep magnet.

As shown in the evolution of the beam envelope by the PARMELA simulations in Figs. 8 (a) and (b), we could hardly compensate the effects due to the vertical deflection induced by the Sweep magnet in the gun, even with an additional steering magnet between the gun and

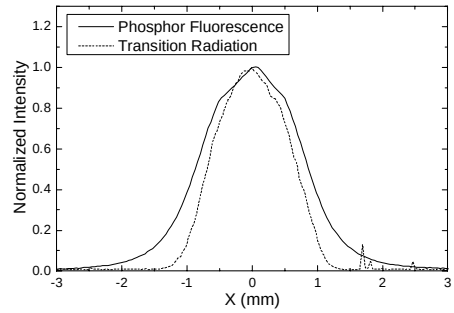

Figure 4: Comparison between the horizontal profiles of the fluorescence from the phosphor plate, and the transition radiation from the aluminium plate.

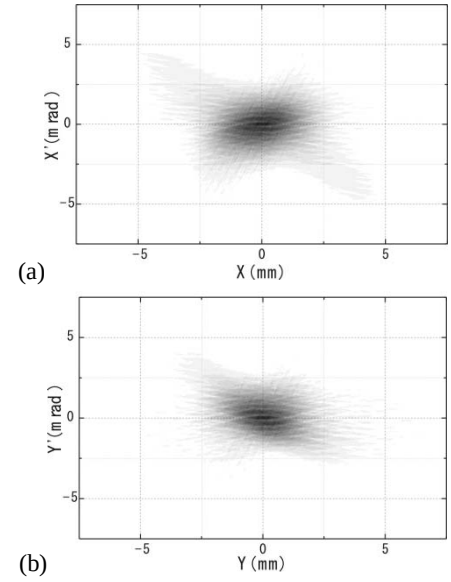

Figure 5: Transverse phase space distributions at the accelerating tube exit obtained with Q8 and SC2 in Fig. 1 in (a) horizontal and (b) vertical directions.

the following quadupole magnet (Q1). Then we performed PARMELA runs with a horizontal Sweep magnet instead of the vertical Sweep. In this case, because horizontal dispersion can be controlled in the quadrupole magnets in the Dog-Leg section, we could

find a set of the magnet parameters showing a better transmittace to the end as shown in Fig. 9. As a result, the calculated current at the accelerating tube exit was 181 mA.

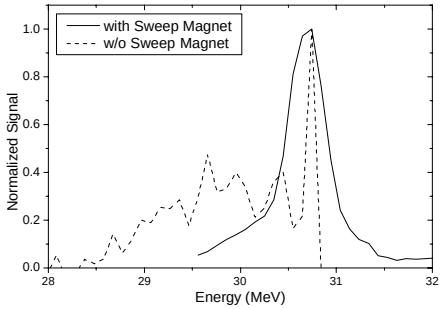

Figure 6: Measured energy spectra with and without the Sweep magnet, both of which are normalized to their peaks.

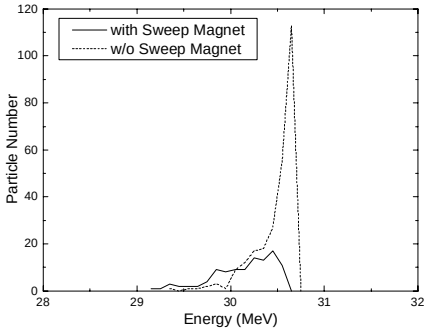

Figure 7: Energy spectra by the simulations with and without the Sweep magnet.

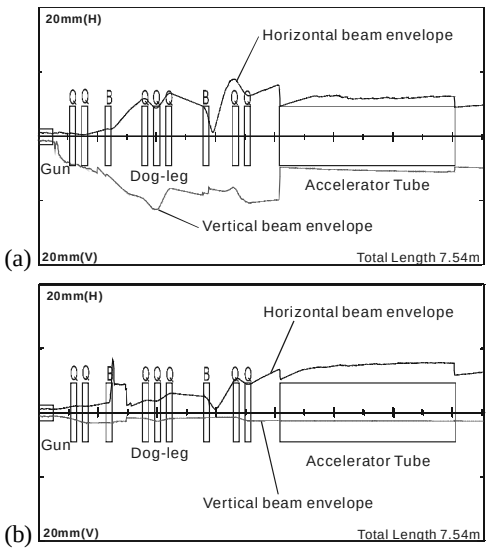

Figure 8: Calculated evolution of the horizontal and vertical beam envelopes, for the case (a) with and (b) without the Sweep magnet.

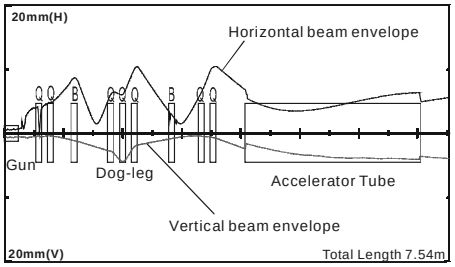

Figure 9: Calculated evolution of the horizontal and vertical beam envelopes with a horizontal Sweep magnet instead of the vertical one.

CONCLUSION

We have measured the electron beam properties, namely energy spread, and transverse emittances at the rf gun exit, and at the exit of the accelerating tube where the energy was measured to be 30.7 MeV. A beam with energy spread of less than 1 % and 48 mA current was obtained. The normalized emittances were measured to be 78 π mm mrad in horizontal and 70 π mm mrad in vertical directions by the tomographic technique with a phosphor screen.

A dipole (Sweep) magnet was set for sweeping the back-streaming electrons vertically out of the cathode in the rf gun. The induced beam deflection in the vicinity of the cathode was found not to degrade the output beam emittances in the present case. However, the vertical deflection by the Sweep magnet resulted in poor transmittance down to the accelerating tube exit. The simulation predicts that much better transmittance can be achieved by use of a horizontal Sweep magnet instead of the vertical one in our layout.

REFERENCES

[1] T. Yamazaki, et al., Proc. of 23rd Int'l FEL Conf. (2002) II13.
[2] T. Kii, et al., "Renewal of KU-FEL facility" in these proceedings.
[3] L. M. Young, J. H. Billen, PARMELA, LA-UR-96-1835.2001.
[4] K. Masuda, et al., Nucl. Instr. and Meth. A 483 (2002) 315.
[5] C.B. McKee and J.M. Maday, *Nucl. Instr. Meth.* A 296 (1990) 716.
[6] T. Kii, et al., Nucl. Instr. And Meth. A 507 (2003) 340.
[7] H. Ohgaki, et al., Nucl. Instr. And Meth. A 507 (2003) 150.
[8] T. Kii, et al., "Reducing back-bomdardment effect using thermionic cathode in IAE rf gun" in these proceedings.
[9] H. Ohgaki, et al., Nucl. Instr. and Meth. A 528 (2004) 366.

UPGRADE DESIGN OF KU-FEL DRIVER LINAC USING PHOTO-CATHODE RF-GUN

H. Ohgaki#, K. Hayakawa, S. Murakami, H. Zen, T. Kii, K. Masuda, K. Yoshikawa, T. Yamazaki

Institute of Advanced Energy, Kyoto University
Gokasho, Uji, Kyoto 6110011, JAPAN

Abstract

Upgrade design of KU-FEL driver linac has been carried out to obtain a stable oscillation in the infrared FEL. The existing 4.5-cell thermionic RF gun will be operated with a photocathode to enhance the FEL gain. The numerical evaluation of beam properties is carried out from gun to FEL by using PARMELA and TDA3D. The evaluated peak current is 4 times and the expected FEL gain is 10 times as high as those with the thermionic cathode. A 1.6-cell photocathode RF gun dedicated to photocathode operation is also examined to obtain an excellent electron beam. Expected FEL gain is more than 2 times as high as the gain with the 4.5-cell photocathode RF gun.

INTRODUCTION

An infrared FEL (4-13 μm) facility for energy science is under construction at the Institute of Advanced Energy, Kyoto University[1]. The electron beam of 30 MeV has been successfully accelerated by a linac system which consists of a 4.5-cell thermionic RF gun, a 'dog-leg' transport system, a 3m s-band linac, and a 180-degree arc for bunch compression[2]. Figure 1 shows the schematic view of the linac system which includes the upgrade plan view. To reduce the back-bombardment effect in the 4.5-cell RF gun, several attempts have been made, and the macro pulse duration of 3 μs has been achieved[3]. However, there still needs several efforts are needed to extend the macro pulse duration to reach the FEL saturation[4]. Upgrade from the present thermionic RF gun to a photocathode RF gun is one of promising ways, because a photocathode RF gun is free from back-bombardment. Thus, a design work for the system upgrade of the linac system from gun to FEL has been performed. At first, we evaluate the beam parameters of the existing 4.5-cell RF gun which is operated as a photocathode. Then the FEL gain is compared with the original design. Next, the beam parameter and the FEL gain with a 1.6-cell photocathode RF gun are also evaluated.

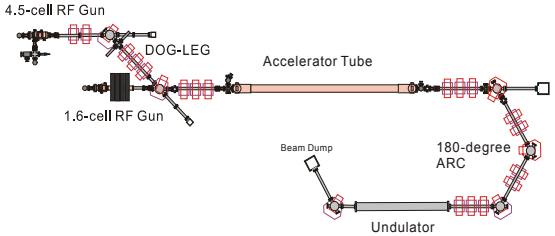

Fig. 1 Schematic view of the KU-FEL driver linac.

#ohgaki@iae.kyoto-u.ac.jp

4.5-CELL RF GUN

The 4.5-cell RF gun has been used for a thermionic cathode in the original system[4] and successfully generated several hundred mA, 10 MeV electron beam[5]. The maximum electric field at the cathode surface is 32 MV which is limited by 7 MW output power of the RF source. We fixed the maximum electric field to be 32 MV during the calculation. The driver laser assumed here is a picosecond UV laser, i.e. the SHI type one[6,7], whose beam profile is 0.7 mm at the cathode surface and the pulse duration is 6.0 ps. The Gaussian shapes are also assumed both for the transverse(1mm cut-off) and for the longitudinal(12 ps cut-off) distribution to simplify the

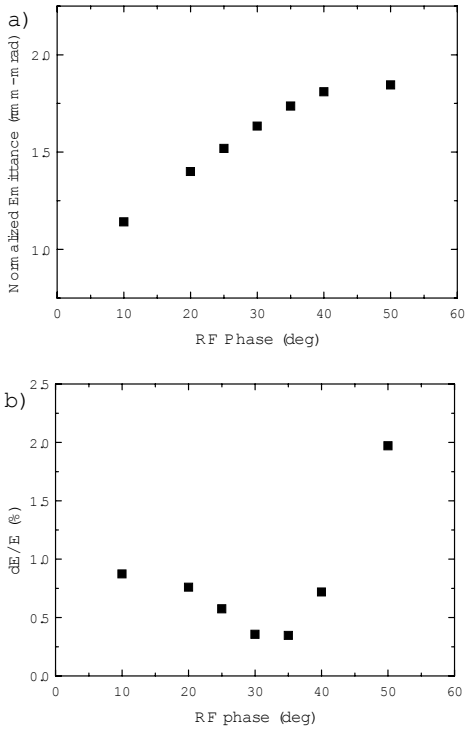

Fig.2 Transverse RMS emittance(a) and energy spread(b) of the electron beam from the gun as a function of the laser injection timing.

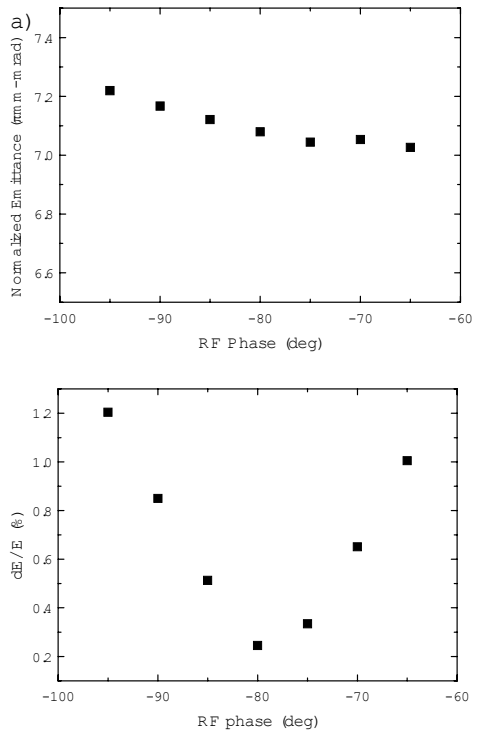

Fig.3 Transverse RMS emittance(a) and energy spread(b) of the electron beam from accelerator tube.

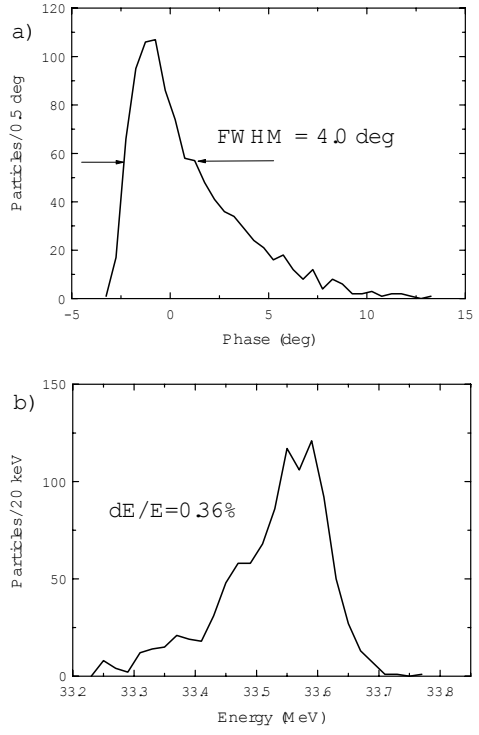

Fig.4 Phase(a) and energy(b) spectrum at the entrance of the undulator.

calculation. Figure 2 shows the transverse RMS emittance(a) and energy spread(b) of the electron beam from the gun as a function of the laser injection timing. PARMELA is used for calculations. It is clear that the electron beam with the transverse RMS emittance below 2 πmm-mrad and the energy spread below 1% can be expected with the 4.5-cell photocathode RF gun. On the other hand, the transverse RMS emittance of 4 πmm-mrad and the energy spread of 22% have been calculated with the thermionic RF gun[4]. The beam charge of 250 pC, which is obtained with normal operation in the existing gun, is assumed. The laser timing of 30 degree, where the best energy spread is obtained in fig.1, is used for the following calculations.

It should be noted that the thermionic RF-gun needs an energy compressor and/or an energy filter for its' broad energy distribution. Therefore, the original design of the linac system employs a 'dog-leg' transport system for the energy filter[4]. Although, we can omit this section for the photocathode RF gun for its' narrow energy spread, we will keep the 'dog-leg' section for the thermionic operation of the RF-gun which is preferable for experiments which need high total power beam. We may omit the 180-degree arc section because of a short bunch beam from the photocathode RF-gun. However, since we are planning to extend our system to the energy recovery one for the future[8], we will keep the 180-degree arc in this calculation, too. The beam transport system is designed by TRACE3D to satisfy the achromatic condition in 'dog-leg'. Figure 3 shows the transverse RMS emittance(a) and energy spread(b) from the accelerator tube as a function of the RF-phase of the accelerator tube. It is clear that the transverse emittance is almost constant (-7 πmm-mrad), although the energy spread varies with the RF-phase. The smallest energy spread, 0.2%, is obtained with -80 degree which is used in the following calculations. We found that the transverse emittance is mainly enlarged by the 'dog-leg' section.

The achromatic 180-degree arc section is set both for the matching condition of the undulator parameter and for the bunch compression condition with matrix element, R56, by using TRACE3D. The phase spectrum and the energy spectrum at the entrance of the undulator are shown in figure 4. Consequently, a beam with peak current of 150 A and an energy spread of 0.36% beam can be generated by using the 4.5 cell photocathode RF gun. The normalized emittance is calculated to be 7.0 πmm-mrad in horizontal and 11 πmm-mrad in vertical. On the other hand, a beam with 40 A peak current and 0.4 % energy spread beam with a normalized emittance of 11 πmm-mrad in horizontal and 10 πmm-mrad in vertical has been obtained with the thermionic RF gun[4]. As a result, almost 4 times large peak current can be expected with the photocathode RF-gun. However, the beam emittance and the energy spread are not so improved from those of thermionic system. The main reason of this emittance

Table 1 Main parameter of the undulator

Period	40 mm
Number of period	40
Total length	1600 mm
Gap	26-56 mm
K value	0.95-0.17

growth is a slight difference between PARMELA and TRACE3D.

The expected FEL gain is calculated with the evaluated electron beam parameters by using TDA3D. The undulator parameter used is shown in table 1. We assumed that the Rayleigh length and the position of the beam waist are fixed at centre of the undulator, 0.8 m. K parameter, 0.95, is also fixed. The calculated FEL gain in wavelength of 6.86 μm is 310% with the electron beam generated with the 4.5-cell photocathode RF gun. On the other hand, the FEL gain with the 4.5-cell thermionic RF gun is 32% at the same conditions as in the photocathode. Consequently, the expected FEL gain with the 4.5-cell photocathode RF gun is almost 10 times as high as that with the original design. This enhancement in FEL gain is mainly due to the enhancement of the peak current. The round-trip development of the FEL gain is also calculated by using modified TDA3D code assuming 10% loss per round-trip. The result shows that the gain saturation can be observed from about 35 round-trips, 0.4 μs. Here we assume the optical cavity length of 3.78 m which is adjusted to the mode-lock frequency of the laser, 79.34 MHz. On the other hand, 175 round-trips is required for the thermionic RF gun. As a result, the FEL saturation will be easily achieved and stable FEL will be expected by the 4.5-cell photocathode.

1.6-CELL RF GUN

Although the existing 4.5-cell RF gun can be operated both as a photocathode and as a thermionic one, as shown in previous section, the estimated emittance is enlarged by the 'dog-leg' beam transport system. However, the thermionic operation is still preferable for a high total charge operation. Thus we plan to introduce a new RF gun dedicated to the photocathode operation into our system to obtain an excellent electron beam. The BNL type 1.6-cell photocathode RF gun, which is widely used for generation of a high brightness electron beam[9] and 1 πmm-mrad with 1 nC electron beam has been generated, is presently considered as a photocathode RF gun. As is shown in figure 1, the 1.6-cell photo-cathode RF gun will be placed just upstream of the accelerator tube. The RF system will be shared with the existing RF gun.

The beam evaluation for the 1.6-cell RF gun is also carried out with the maximum electric field of 100 MV at the cathode surface. Figure 5 shows the transverse RMS emittance(a) and energy spread(b) of the electron beam from the RF gun as a function of the laser injection timing. It is clear that the transverse RMS emittance of 1.5 πmm-mrad and energy spread of 0.25% can be generated at the 30 degree. These values are almost same

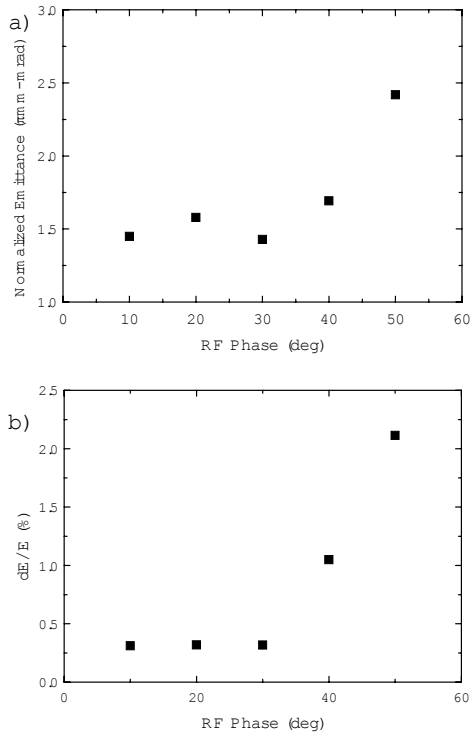

Fig.5 Transverse RMS emittance(a) and energy spread(b) of the electron beam from the gun as a function of the laser injection timing.

as the 4.5-cell photocathode RF gun. The solenoid field for the emittance compensation[10] is also taken into account. The solenoid field used is the same geometric configuration of reference[11]. The field distribution is calculated by using POISSON. We choose the maximum field of 1800 Gauss, where the smallest transverse emittance, 2.4 πmm-mrad, is obtained from the accelerator tube. Figure 6 shows the transverse RMS emittance(a) and energy spread(b) of the electron beam from the accelerator tube as a function of RF phase of the accelerator tube. RF-phase of 65 degree, where the smallest energy spread is obtained in figure 6, is used in the successive calculations. It should be noted that the transverse emittance slightly growths in the solenoid field and further optimization of the solenoid field will be required for our configuration. Figure 7 shows the phase spectrum and the energy spectrum at the entrance of the undulator with a matched 180-degree arc which also works as a bunch compressor. Finally, a peak current of 180 A and an energy spread of 0.31% electron beam can be generated by the 1.6-cell photocathode RF gun. The normalized emittance is calculated to be 10 πmm-mrad in horizontal and 1.7 πmm-mrad in vertical. Consequently, by using 1.6-cell photocathode RF gun, we can expect an improved transverse emittance and a higher peak current electron beam.than that from 4.5-cell photocathode RF gun.

The expected FEL gain can be calculated with the numerical evaluation. The undulator parameter used is the same as 4.5-cell RF gun (table 1) except for the FEL wavelength, because the electron energy(28 MeV) is different from that of 4.5-cell photocathode system(34 MeV). The calculated FEL gain in wavelength of 9.8 μm is 810%. On the other hand, the FEL gain with the 4.5-cell photocathode RF gun is calculated to be 320%. It should be noted that the same electron beam parameter as in the previous section is used for the 4.5-cell photocathode RF gun except for the beam energy. More than 2 times larger FEL gain will be obtained with the 1.6-cell photocathode RF gun. This enhancement in FEL gain is both due to the enhancement of the peak current and improvement in the transverse emittance. The round-trip development of the FEL gain is also calculated as the same manner as the previous section. The result shows that the gain saturation can be observed from about 10 round-trips. As a result, the FEL gain will be further enhanced by using the 1.6-cell photocathode RF gun.

CONCLUSION

Upgrade design of KU-FEL driver linac has been carried out to obtain a saturated FEL in the infrared region. The existing 4.5-cell thermionic RF gun will be operated with a photocathode. The numerical evaluation is carried out from gun to FEL by using PARMELA and TDA3D codes. The expected FEL gain is 10 times larger than that of original system. A 1.6-cell photocathode RF gun dedicated to photocathode operation is also considered to obtain an excellent electron beam. The FEL gain with the 1.6-cell photocathode RF gun is more than 2 times as high as that with the 4.5-cell photocathode RF gun. Further studies are needed to optimize the final upgrade design both for the photocathode operation and for the thermionic cathode operation which is still attractive for high average current.

The authors would like to thank F. Sakai (SHI) for his help for this work

REFERENCES

[1] T. Yamazaki, et al., Free Electron Laser2001 (2002),II-13.
[2] K. Masuda, et al., to be presented in FEL2004.
[3] T. Kii, et al., to be presented in FEL2004.
[4] H. Ohgaki, et al., NIM A507 (2003) 150.
[5] H. Ohgaki, et al., NIM A528 (2004) 366.
[6] F. Sakai, et al., Proceedings of the PAC1999 (1999) 2036.
[7] J. Yang, et al., NIM A491 (2002) 15.
[8] K. Masuda, et al., NIM A528 (2004) 134.
[9] e.g. D. Palmer, et al., Proceeding of the PAC1995 (1995) 2432; R. Alley, et al., NIM A429 (1999) 324; Y. Aoki, et al., Proceedings of the PAC1999 (1999) 2018.
[10] R.E. Carlsten, NIM A285 (1989) 313.
[11] F. Sakai, et al., Jpn. J. Appl. Phys., Vol.41 (2002) 1589.

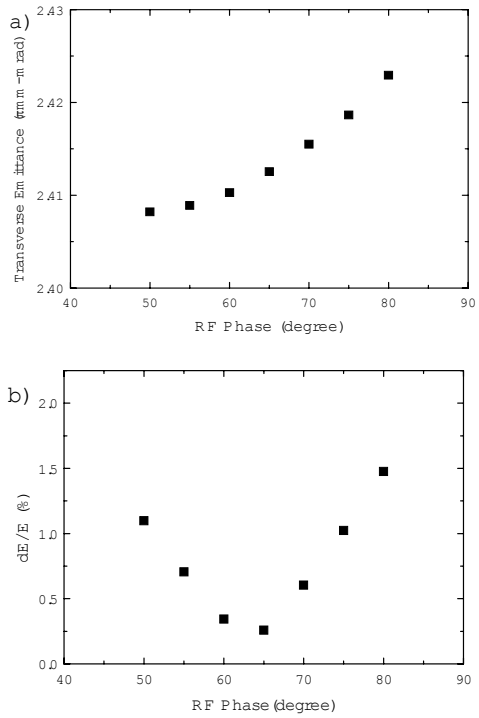

Fig.6 Transverse RMS emittance(a) and energy spread(b) of the electron beam from the accelerator tube.

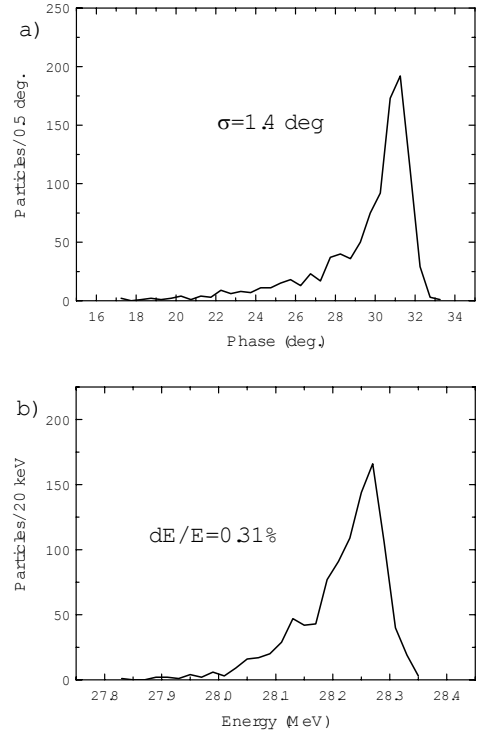

Fig.7 Phase(a) and energy(b) spectrum at the entrance of the undulator.

FIRST MODEL OF THE EDGE-FOCUSING WIGGLER FOR SASE

S. Kashiwagi#, K. Kobayashi, T. Noda, R. Kato, G. Isoyama,
ISIR, Osaka University, 8-1 Mihogaoka, Ibaraki, Osaka, Japan
S. Yamamoto and K. Tsuchiya
Institute of Materials Structure Science, KEK, 1-1 Oho, Tsukuba, Ibaraki, Japan

Abstract

The first model of the edge-focusing (EF) wiggler, which produces the strong transverse focusing field incorporated with the normal wiggler field, has been fabricated to evaluate its performance. It is a five-period planar wiggler with an edge angle of 2 degrees and a period length of 60 mm. The magnetic field in the wiggler is measured using Hole probes at four different wiggler gaps. It is experimentally confirmed that a high field gradient of 1.0 T/m is realized along the beam axis in the EF wiggler.

INTRODUCTION

A conventional planar wiggler of the horizontal oscillation type focuses the electron beam in the vertical direction, but does not focus in the horizontal direction. If the beam is injected to the wiggler with the matching condition in the vertical direction, the vertical beam size will remain constant as it moves along the wiggler. In the horizontal direction, however, no focusing force exists and the beam size will increase and diverge if the external focusing force is not provided. Various schemes have been proposed or investigated to provide the focusing force in the both directions in the wiggler for Self-Amplified Spontaneous Emission (SASE) in the short wavelength region so that the beam size is kept small over the whole length of the very long wiggler [3-9]. In these schemes, either pole faces are shaped or permanent magnet blocks are added in the wiggler gap, in order to produce the field gradient for focusing the beam. The magnet gap of the wiggler is sacrificed in some of these methods or the good field region is limited in the other methods.

As a new method for the integrated-focusing, we proposed the Edge-Focus (EF) wiggler, which can produce the high magnetic field gradient superimposed on the normal wiggler field [1,2]. The EF wiggler has an advantage that the strong field gradient can be produced with no obstacles in the wiggler gap and the good field region is as large as that of the normal wiggler field. It can be used not only for SASE experiments but also for FEL in order to enhance the gain. As a next step of our proposal, we have fabricated the first experimental model of the EF wiggler. In the fabrication process of this model wiggler, we developed a new method to make a low-error wiggler without adjustment of the magnetic field by trial and error, and reported at the preceding FEL conference [2]. The wiggler parameters of the first model have been chosen to meet requirements from our SASE experiment in the far-infrared region being conducted at the Institute of Scientific and Industrial Research (ISIR), Osaka University [10,11]. In this paper, we will describe the first model of the EF wiggler and report results of the magnetic field measurement for the EF wiggler.

E-mail: shigeruk@sanken.osaka-u.ac.jp

FIRST MODEL OF THE EDGE-FOCUSING WIGGLER

The EF wiggler is basically a Halbach type wiggler made only of permanent magnet blocks, but their shapes are not rectangular parallelepipeds. The magnet blocks of the EF wiggler with vertical magnetization have a trapezoidal shape with an edge angle ϕ, while those with longitudinal magnetization have a parallelogram shape with the same angle (shown in Figure 1). The average focusing force of the EF wiggler can be calculated using the simple model with the edge angle for the bending magnets. In the simple model based on transfer matrices, the focusing force in the EF wiggler (horizontal oscillation type) is approximately given by

$$k_x = \frac{1}{B\rho}\left(\frac{\mathrm{d}B_y}{\mathrm{d}x}\right) = \frac{4e}{m_0 c}\frac{B_0}{\gamma}\times\frac{\phi}{\lambda_w} \tag{1}$$

$$k_y = k_0 - k_x = \frac{8-\pi}{3\pi}\left(\frac{e}{m_0 c}\right)^2\left(\frac{B_0}{\gamma}\right)^2 - k_x \tag{2}$$

where k_0 is the natural focusing force of the wiggler for the vertical direction and $k_0 = k_x + k_y$. From Eq. (1), the field gradient is given by

$$\frac{\mathrm{d}B_y}{\mathrm{d}x} = 4\frac{B_0}{\lambda_w}\phi\,. \tag{3}$$

The field gradient is approximately proportional to the edge angle and hence the focusing force along the wiggler can be easily adjusted with the edge angle ϕ.

The first model of the EF wiggler consists of five-periods with the period length λ_W = 60 mm and the edge angle ϕ = 2 degrees. The main parameters of the model wiggler are listed in Table 1. The magnetic gap is mechanically fixed, but it can be easily changed by changing columns supporting the upper magnet array. The permanent magnet is Nd-Fe-B with the residual induction of 1.32 T, and the standard dimensions of the magnet blocks are 2a × 2b × 2c = 100 × 20 × 15 mm^3. The peak magnetic field of the wiggler at g = 30 mm is

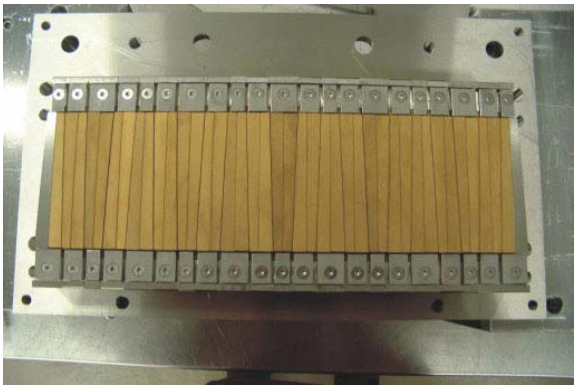

Figure 1: Magnet array of the first model of the EF wiggler. The vertical magnetization magnet blocks have a trapezoidal shape, while those with longitudinal magnetization have a parallelogram shape.

Table 1: Main parameters of the model EF wiggler

Block size (2a×2b×2c)	100×20×7.5 mm^3
Gap	30 mm
Number of periods	5 periods
Residual induction of magnet	B_r = 1.32 T
Peak magnetic field (analytical)	B_0 = 0.43 T
Edge angle	ϕ = 2.0 °
Averaged field gradient (ϕ= 2°)	dB_y/dx = 1.0 T/m

calculated using a 3D program to be 0.43 T [12]. The field gradient of the model wiggler averaged over a wiggler period is about 1 T/m at 30 mm gap and the edge angle of 2 degrees. This edge angle is chosen so that the double focusing is realized in both the vertical and the horizontal directions for the 11.5 MeV electron beam.

FIELD MEASUREMENT OF THE WIGGLER

In order to evaluate performance of the EF wiggler, the magnetic field has been measured at the High Energy Accelerator Research Organization (KEK), using a magnetic sensor with two Hole probes for simultaneous measurement of the vertical and the horizontal field components, which is mounted in a small oven to control the temperature of the sensor. Owing to the temperature control, an accuracy of the magnetic field measurement is achieved to be about 0.1 Gauss. The Hole probes were calibrated using NMR. The magnetic sensor is mounted on a 3-axis linear stage, with which it is scanned along the wiggler axis and its transverse position (x-y position) is adjusted. Figure 2 shows the experimental setup for the magnetic field measurement of the EF wiggler. We measure the magnetic field simultaneously in the horizontal and the vertical directions using this measurement system and make the field mapping in the wiggler.

Figure 3 shows the vertical magnetic field $B_y(z)$ measured at the 30 mm gap along the wiggler axis from –300 mm to +300 mm . We calculate the three-dimensional magnetic field in the EF wiggler numerically with the magnetic charge method [12] and compare the calculated values with the measured ones. The calculated values agree quite well with the measured values except for the absolute value. The measured magnetic field at the middle of the wiggler axis (the peak magnetic field) is approximately 4200 Gauss. This value is about 2% smaller than a calculated value. This small difference seems to come from short and shallow steps at the both ends of the magnet blocks for mechanical clamping to folders, which are not taken into account in the calculation.

To obtain the field gradient (dBy/dx) of the model wiggler, we measure the magnetic field along the

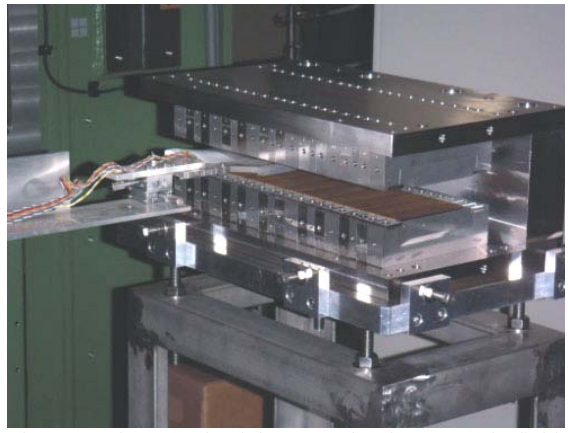

Figure 2: Photograph of the setup for the magnetic field measurement of the EF wiggler at KEK.

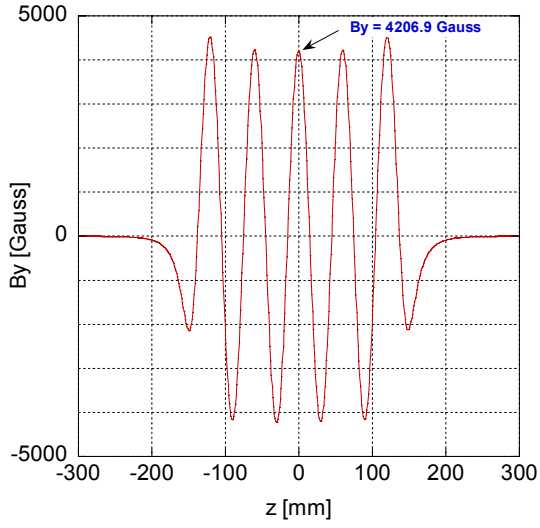

Figure 3: Measured vertical magnetic field $B_y(z)$ along the central wiggler axis.

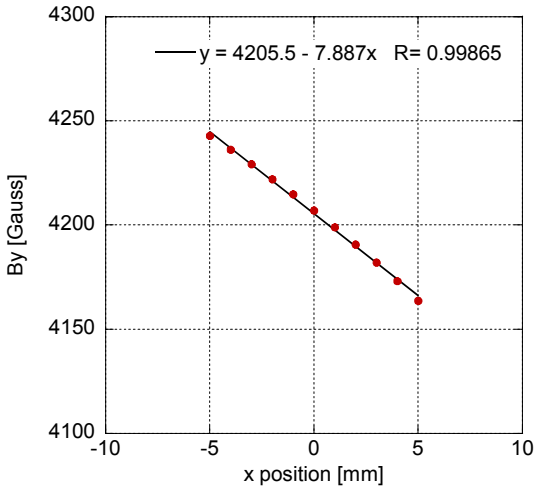

Figure 4: Measured magnetic field *By*(x, y=0) as a function of the horizontal position at the middle of the wiggler.

longitudinal axis at several transverse positions. Figure 4 shows the measured vertical magnetic field along the x-axis (horizontal) at the middle of the model wiggler, where the vertical magnetization block is located. The vertical magnetic field changes linearly with the horizontal position over the width of the wiggler and the slope is steep. The field gradient is derived with linear fitting of the data points as shown in Figure 4. The electron beam receives the focusing force produced by this large field gradient.

We measure the magnetic field at wiggler gaps g = 30, 40, 50, and 60 mm by changing columns supporting the upper magnet array and derive the transverse field gradient as a function of the wiggler gap. The field gradient averaged over the wiggler periods is shown in Figure 5, together with the peak magnetic field. The solid circles and open circles show the measured peak magnetic field and the averaged field gradient of the EF wiggler, respectively. The solid line and the dashed line show the peak magnetic field and the averaged field gradient calculated with the 3D program, respectively. The measured values are in good agreement with the numerical calculation as shown in Figure 5. The peak magnetic field of the wiggler decreases exponentially with increasing the wiggler gap and the averaged field gradient also decreases exponentially as shown in Figure 5, but the slope for the field gradient is gentler than that for the peak magnetic field. The peak field at the gap 60 mm decreases to one fifth of the value at 30 mm, whereas the field gradient at 60 mm decreases to only a half of the value at 30 mm. This behaviour is favourable in the view of the beam dynamics in the wiggler.

The simple model based on transfer matrices fails to explain this behaviour, because the field gradient of the EF wiggler given by Eq. (3) is proportional to the peak magnetic field. We think that this is because the variation of the fringe field with the wiggler gap is not taken into account in the simple model calculation for the field gradient of the EF wiggler. This indicates that the field measurement and the 3D magnetic field calculation of the wiggler are important to understand the field distribution in the wiggler.

The EF wiggler can produce the high field gradient in the wiggler and the sum of the vertical focusing force and the horizontal one is constant and equal to the natural focusing force, as shown by Eq. (2). The electron beam is simultaneously focused in the both directions with the weak focusing scheme if the horizontal focusing force generated by the edge angle is smaller than the natural focusing of the wiggler, which is realized when the electron beam energy is low and the peak magnetic field of the wiggler is high as well as the edge angle is not very large. If the horizontal focusing force of the EF wiggler is larger than the natural focusing, the defocusing force is provided in the vertical direction. In this case, the strong focusing scheme can be applied to focus the electron beam in the both directions, using two kinds of EF wigglers with positive and negative edge angles. The peak field decreases exponentially with increasing the magnetic gap and accordingly the natural focusing force also decreases exponentially. When the wiggler field becomes weak, the double focusing condition may not be fulfilled at larger gaps. It is, therefore, important to carefully choose the focusing scheme, either the weak focusing or the strong focusing. As an example of the double focusing, the square roots of the betatron functions in the 2m-long conventional planar wiggler with the edge angle = 0 deg. and in the EF wiggler with the edge angle of 1 degree are shown in Figure 6. The EF wiggler can produce focusing forces in the both directions and the

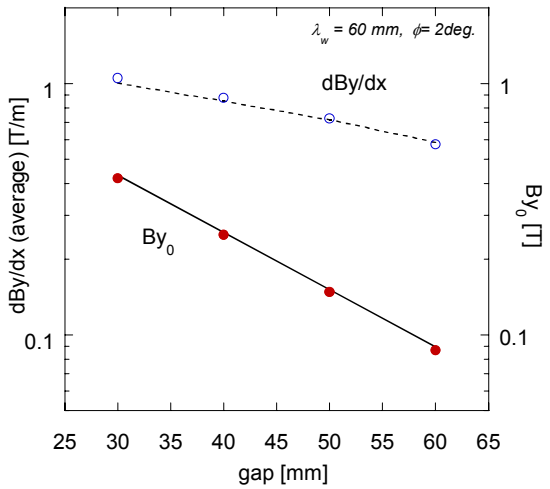

Figure 5: Peak magnetic field and the field gradient of the EF wiggler as a function of the wiggler gap. The solid circles and the open circles show the measured peak magnetic field and the average field gradient over the wiggler period, respectively. The solid and the dashed lines show calculation using the 3D program.

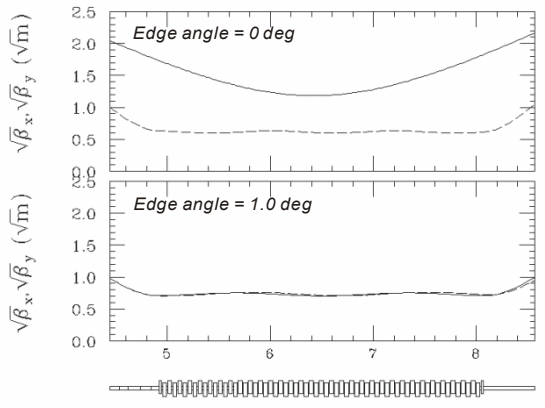

Figure 6: Square root of the betatron function for the conventional planar wiggler with no edge and the EF wiggler with the edge angle of one degree. The solid and the dashed lines show the horizontal and vertical betatron functions, respectively.

betatron functions can be made small and almost constant through the wiggler, using the matching conditions. For the conventional planar wiggler, the horizontal focusing force has to be provided with external quadrupole magnets and hence the beam cannot be focused as small as it is in the double focusing scheme. The EF wiggler can be used to enhance the gain of SASE and FEL.

CONCLUSION

In order to advance the development of the EF wiggler, which we had proposed, we fabricated the first model of the EF wiggler. The magnetic field in the wiggler was measured using Hole probes at four wiggler gaps. It was experimentally confirmed that a high field gradient of about 1.0 T/m was realized along the beam axis in the EF wiggler, which was superimposed on the normal wiggler field. We obtained the relation between the magnetic field gradient and the magnetic gap of the EF wiggler. The field gradient decreases with increasing the magnet gap more slowly than the peak magnetic field does, which is favourable in view of the beam focusing in the wiggler. We experimentally evaluated the performance of the EF wiggler with the magnetic field measurement. We plan to further study characteristics of the EF wiggler.

ACKNOWLEDGEMENT

The authors would like to thank Mrs. T. Koda and K. Okihira of NEOMAX Co., Ltd. for their help on the fabrication and the magnetic field measurement of the EF wiggler. This research was partly supported by the Joint Development Research at the High Energy Accelerator Research Organization (KEK), 2003-17, 2003 and the Ministry of Education, Science, Sports and Culture, Grant-in-Aid for Exploratory Research, 15654036, 2003&2004.

REFERENCES

[1] G. Isoyama et al., Nucl. Instr. and Meth. A 507 (2003) 234
[2] S. Kashiwagi et al., Nucl. Instr. and Meth. A 528 (2004) 203
[3] J. Pfluger and Yu. M. Nikitina, Nucl. Instr. and Meth. A 381 (1996) 554
[4] M. Takabe et al., Nucl. Instr. and Meth. A 331 (1993) 736
[5] Y. Tsunawaki et al., Nucl. Instr. and Meth. A 304 (1991) 753
[6] M. Shiho et al., Nucl. Instr. and Meth. A 304 (1991) 141
[7] A. A. Varfolomeev and A. H. Hairetdinov, Nucl. Instr. and Meth. A 341 (1994) 462
[8] A. A. Varfolomeev, et al., Nucl. Instr. and Meth. A 358 (1995) 70
[9] Ross D. Schlueter, Nucl. Instr. and Meth. A 358 (1995) 44
[10] R. Kato, et al., Nucl. Instr. and Meth. A 407 (1998) 157
[11] R. Kato, et al., Nucl. Instr. and Meth. A 445 (2003) 164
[12] G. Isoyama, Rev. Sci. Instrum., Vol. 60, No. 7 (1989) 1826

UPGRADE OF THE L-BAND LINAC AT ISIR, OSAKA UNIVERSITY FOR A FAR-INFRARED FEL

R. Kato#, S. Kashiwagi, T. Yamamoto, S. Suemine, G. Isoyama,
ISIR, Osaka University, Mihogaoka, Ibaraki, Osaka 567-0047, Japan

Abstract

The L-band linac at the Institute of Scientific and Industrial Research, Osaka University, has been renewed in order to realize high stability of the electron beam and easy changes of operation modes for various kinds of experiments. In the modification, it was included the replacements of the klystron and the pulse modulator for it to provide the rf power with the pulse duration up to 8 μs to realize power saturation of the FEL. The modification of the linac has been completed and commissioning is now in progress. The intensity fluctuations of the beam intensity in the transient and the single-bunch modes were decreased to one-tenth compared with previously measured values before the remodelling. The fluctuation of the beam energy in the single-bunch mode was less than 0.1% in standard deviation.

INTRODUCTION

We are developing the far-infrared free-electron laser (FEL) using the L-band electron linac at the Institute of Scientific and Industrial Research (ISIR), Osaka University. The first lasing of the FEL was obtained at wavelengths from 32 to 40 μm in 1994 [1], and the wavelength region has been extended up to 150 μm [2]. The linac was designed and constructed for producing the high-intensity single-bunch beam for pulse radiolysis, but not optimized for development of FEL. Though the duration of the rf pulse could be extended to 4 μs, the maximum macro-pulse length of the electron beam is limited to 2 μs, since the filling time of the accelerating structure is 1.8 μs. As a result, the FEL could not reach power saturation because the number of amplification times was limited.

Recently, the linac has been extensively remodelled to realize high operational stability and reproducibility for advanced studies in beam science and technology. Almost all the power supplies, including the main rf power source, are replaced with new ones. At this opportunity, the linac is also made suitable for FEL. The electron beam with a macro-pulse up to 6 μs can be accelerated, so that the FEL will reach power saturation. The modification of the linac has been completed and commissioning is now in progress. In this paper, we will report performance and characteristics of the linac after the modification.

NEW LINAC SYSTEM

The schematic layout of the L-band linac is shown in Figure 1.The linac consists of a thermionic gun, three-stage sub-harmonic buncher (SHB) system, a pre-buncher, a buncher, and a 3 m long accelerating tube. The thermionic gun (Eimac, YU-156) is a dispenser type with

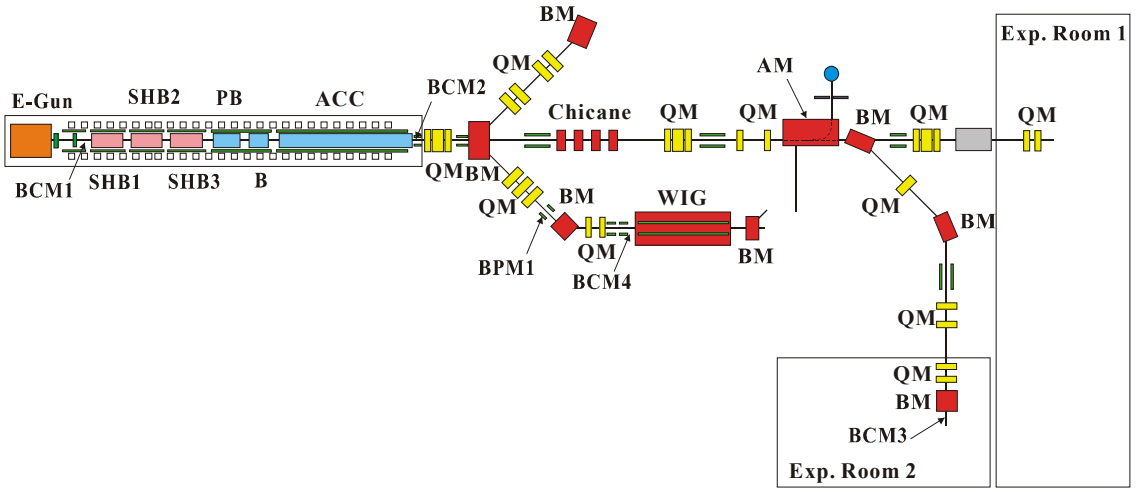

Figure 1: The schematic layout of the L-band linac. E-GUN: Electron gun, SHB1: 108MHz SHB cavity #1, SHB2: 108MHz SHB cavity #2, SHB3: 216MHz SHB cavity, PB: Prebuncher, B: Buncher, ACC: 1.3 GHz accelerating tube, BM: Bending magnet, QM: Q-magnet, AM: Analyser magnet, WIG: Wiggler, BCM1-4: beam current monitors, BPM1: beam position monitor.

#kato@sanken.osaka-u.ac.jp

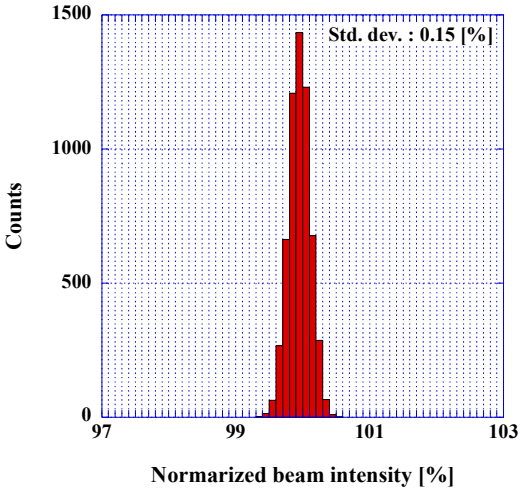

Figure 2: Histogram of the electron beam intensity extracted from the cathode. The intensity was measured with BCM1 at the entrance of the first SHB cavity.

the cathode diameter of 3.0 cm^2 and the operating voltage is 100 kV. The cathode voltage and the cathode heater are stabilized with regulated AC power sources (Behlman, BL1350; Takasago, ARH500). The SHB system is composed of two 108 MHz and one 216 MHz standing wave cavities, and each cavity is independently driven with a 20 kW rf amplifier. The pre-buncher, the buncher, and the accelerating tube have travelling wave type structures with the accelerating frequency of 1.3 GHz driven with one 30 MW klystron (Thales, TV-2022E) and a new pulse modulator, while they were driven with two klystrons before the remodelling. The new klystron system has two operation modes with different pulse durations. One is called the normal mode, in which the flat top is 4 μs long and the peak power is 30 MW. The other is the long pulse mode for FEL experiments, in which the pulse duration is 8 μs but has the peak power is 25 MW. The maximum reputation rate is 60 Hz in the normal mode, while it is reduced to 30 Hz in the long pulse mode. The pulse height fluctuation of the output voltage of the modulator is measured to be less than 0.1 % (peak-to-peak) and the undulation of the flat top to be below 0.2 % (peak-to-peak). In a test experiments, the flatness of 0.1 % was realized over a 5.5 μs time region on the flat top.

BEAM STABILITY

Stability of the beam current from injector

A histogram of the electron beam intensity extracted from the cathode is shown in Figure 2. The beam intensity was measured with a current transformer, BCM1 at the entrance of the first SHB cavity. A sampling period is 0.5 seconds and the measurement time is 1,500 seconds. The intensity is normalized with the average. The standard deviation is 0.15 %.

Stability of the beam current in the transient mode

The transient mode is most frequently used in the L band linac. In this operation mode, the SHB system is switched off. Since the single rf power source is used for the three rf structures, the beam stability deteriorated mainly by the fluctuation of the rf amplitude in the short period. In the long period, it becomes worse due to the temperature drift of the electron gun cathode, as well as the periodical temperature change of the cooling water system and the air-conditioner.

The beam intensities measured with time in this mode are shown in Figure 3. They were measured with BCM2 at the exit of the accelerating tube and with BCM3 at the beam port in the 2nd experimental room. The sampling period is 0.5 seconds and the measurement time is 4,500 seconds. The intensities are normalized with their respective average values. Figures 4 and 5 show respective histograms of the beam intensities derived from the data shown in Figure 3. In addition to fluctuations of the beam intensities in short periods, it can be seen that the intensities slightly decrease with time. The long-term drift per ten minutes is 0.04 % for the beam intensity at the exit of the accelerating tube and it is 0.08 % for that at the beam port of the 2nd experimental room. These long-term drifts were subtracted from the data and then the intensity distributions were calculated. The standard deviation is 0.25 % for the beam intensity at the exit of the accelerating tube as shown in Figure 4 and it is 0.34 % for the beam intensity at the beam port of the 2nd experimental room. These values are as small as one-tenth of previously measured values before the

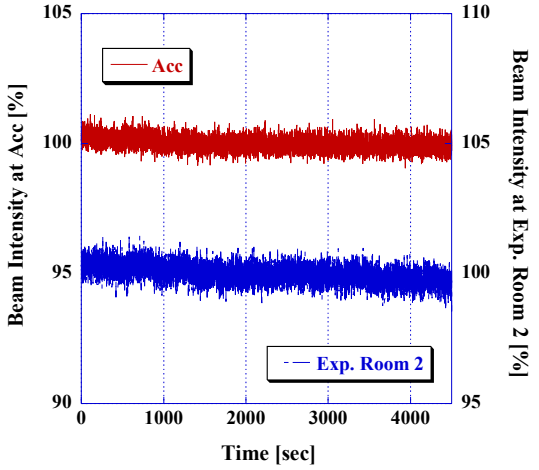

Figure 3: The beam intensities measured with BCM2 at the exit of the accelerating tube (red lines) and with BCM3 at the beam port in the 2nd experimental room (blue lines).

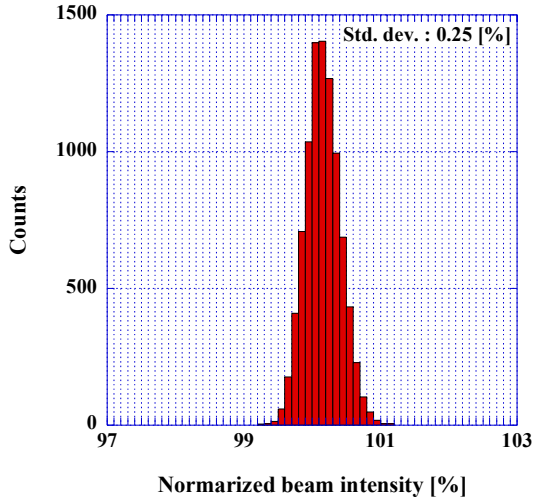

Figure 4: Histogram of the beam intensity measured with BCM2 at the exit of the accelerating tube in the transient mode.

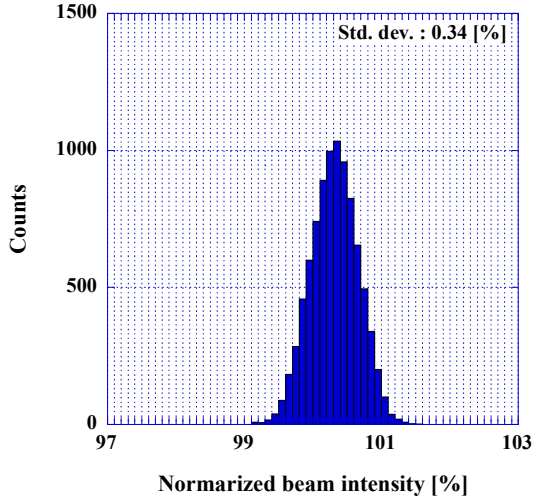

Figure 5: Histogram of the beam intensity measured with BCM3 at the beam port in the 2nd experimental room in the transient mode.

remodelling. The fluctuation of the beam intensity is larger at the beam port in the 2nd experimental room, 0.34%, than at the exit of the accelerating tube, 0.25 %.

The transverse position of the electron beam is determined by the energy of the electron beam, which is a characteristic of the electron beam, and by the dispersion function, which is a characteristic of the beam transport line. At the exit of the accelerating tube, the dispersion function is zero, so that the beam does not move even when the energy changes. For the beam port in the 2nd experimental room, on the other hand, the beam line is long and there are some regions where the dispersion function is not zero. If the electron energy fluctuates, the horizontal position changes there and portion of the electron beam scraped out, so that the beam intensity changes. This is the reason why the standard deviation of the beam intensity measured with BCM3 is larger than that measured with BCM2. Similarly, the standard deviation of the beam intensity measured with BCM2, 0.25 %, is larger than that measured with BCM1, 0.15 %, because a part of the beam is lost in the bunching process due to the fluctuation of the rf power.

Stability of the rf power

As mentioned previously, the variation of the rf phase does not significantly affect the beam intensity in the transient mode. We, therefore, simultaneously measured the beam intensity and the rf power with time. Figure 6 shows the rf power measured at dummy loads for the buncher and the accelerating tube. They are normalized with respective average values. The fluctuation of the rf power is 0.14 % (standard deviation) for the buncher and 0.11 % (standard deviation) for the accelerating tube. Since the single rf power source is used for buncher and the accelerating tube, both of the rf power shows similar fluctuation pattern.

Stability of the single-bunch beam

The single-bunch mode is used in the SASE-FEL experiments. In this mode, the SHB cavities are driven with the independent rf sources. Since the number of the rf sources is four in the single-bunch mode, which should be compared with one in the transient mode, influences of phase jitters of the sources are added to the beam. Figure 7 shows the beam intensities measured with BCM2 at the exit of the accelerating tube and with BCM4 at the entrance of the wiggler with time. The measurement time is 730 seconds and the sampling period is 0.73 seconds. The intensities are normalized with respective average values. The long-term drift per ten minutes is 0.76 % for

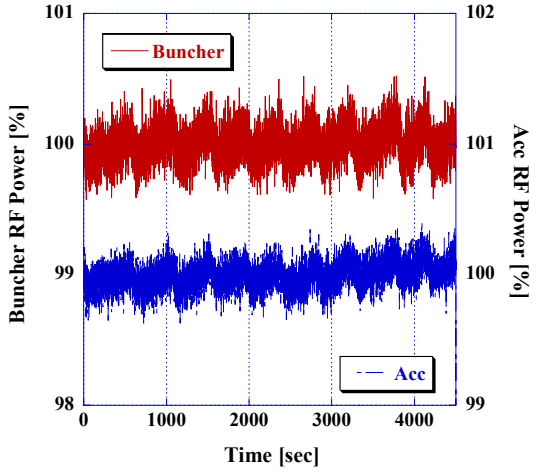

Figure 6: The rf power measured with time at dummy loads for the buncher and the accelerating tube.

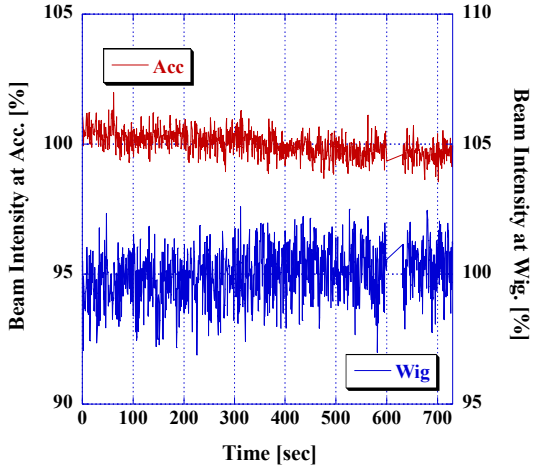

Figure 7: The beam intensities measured with BCM2 at the exit of the accelerating tube (red lines) and with BCM4 at the entrance of the wiggler (blue lines) in the single-bunch mode.

the beam intensity at the exit of the accelerating tube and it is 0.77 % for that at the entrance of the wiggler. The standard deviation of the beam intensity without the long-term drift is 0.40 % at the exit of the accelerating tube, while it is 1.00 % at the entrance of the wiggler. These values decreased one-tenth in comparison with previously measured values before the remodelling, too. However, since the stability of the SHB system is not enough, it is thought that there is still room for improvement in the system.

Figure 8 shows the beam energy measured with BPM1 on the beam transport line to the FEL system in the single-bunch mode. The sampling period is 0.73 seconds and the measurement time is 730 seconds. The standard deviation of the beam energy was 0.08 % as shown in Figure 9. Since almost energy fluctuation is included within the limit of ±0.15 % from the centre energy, wavelength shift caused by the energy fluctuation is estimated to be less than ±0.3 %.

SUMMARY

We evaluated the beam stability of the transient and the single-bunch modes after the remodelling. In the both modes, the current stability was improved drastically, the fluctuation of the beam intensity decreased to one-tenth compared with measured values before the remodelling. Since the fluctuation of the beam energy for the single-bunch mode was less than 0.1% in the standard deviation, the FEL oscillation can be expected to be more stable. Next we will evaluate the beam stability of the long pulse mode for the FEL oscillation experiment.

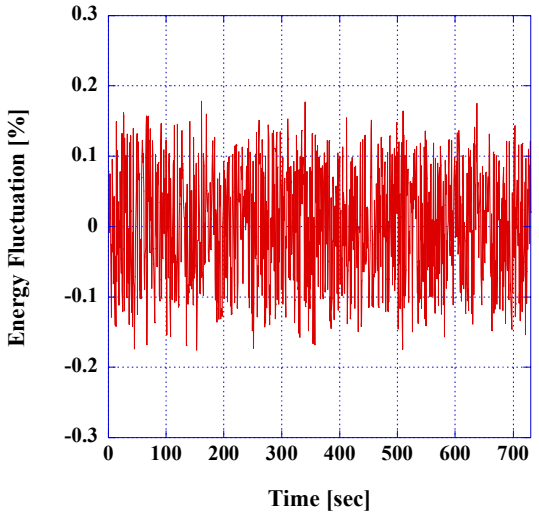

Figure 8: Temporal fluctuation of the beam energy measured with BPM1 on the beam transport line to the FEL system.

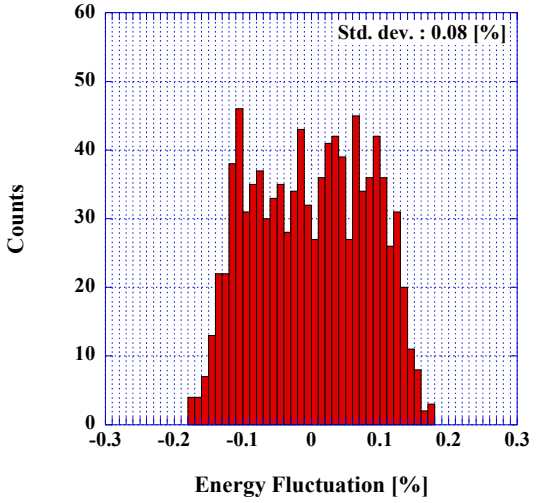

Figure 9: Histogram of the beam energy fluctuation measured with BPM1 on the beam transport line to the FEL system.

REFERENCES

[1] S. Okuda, et al., Nucl. Instr. and Meth. A 358 (1995) 244.
[2] R. Kato, et al., Nucl. Instr. and Meth. A445 (2000) 169.

DEVELOPMENT OF COMPACT SOFT X-RAY SOURCE BASED ON LASER UNDULATOR *

R. Kuroda#, D. Ueyama, T. Saito, S. Minamiguchi, K. Hidume, M. Washio,
Waseda University, Tokyo, Japan
S. Kashiwagi, Osaka University, Osaka, Japan,
J.Urakawa, H.Hayano, KEK, Ibaraki, Japan

Abstract

A compact soft X-ray source is required in various research fields such as material and biological science. The laser undulator based on Compton backward scattering has been developed as a compact soft X-ray source for the biological observation at Waseda University. It is performed in a water window region (250eV - 500 eV) using the interaction between 1047 nm Nd:YLF laser and 4.6 MeV high quality electron beam generated from rf gun system. The range of energy in the water window region has K-shell absorption edges of Oxygen, Carbon and Nitrogen, which mainly constitute of living body. Since the absorption coefficient of water is much smaller than the protein's coefficient in this range, a dehydration of the specimens is not necessary. As a preliminary experiment, about 370 eV X-ray generation was carried out. In this conference, we will report results of experiments and our future plan.

INTRODUCTION

Short-pulse X-ray source is required in various research fields, such as material and medical science. To meet these demands, R&D on the next-generation light source has been initiated at several laboratories in the world. One of the most promising approaches to short-pulse X-ray sources is the laser undulator, which is based on Compton or Thomson backward scattering [1, 2].

The Compton backward scattering, in which a photon reverses its on colliding head-on with an electron, has been proposed as a way to generate X-rays with optical laser beam and low energy electron beam either through the spontaneous emission or the free-electron laser (FEL) mechanism[3]. The mechanism is closely related to undulator radiation so that the laser field acts as an electromagnetic undulator generating up-shifted radiation in the X-ray regime. In this case, it is easily to generate picosecond X-ray using the recent developments of the laser and the accelerator technologies because the pulse length of the generated X-ray is roughly obtained from the electron and the laser pulse lengths.

On the other hand, Soft X-ray with the energy in "water window" region, which is 250 eV – 500 eV (2.5 nm – 5 nm), can be extensively applied to biological studies, because the absorption coefficients of proteins in this region are larger than that of water. Dehydration of biological specimens can be avoided in both studies *in vivo* and *in vitro*. K-shell absorption edges of O (532 eV), C (284 eV) and N (400 eV), which are main elements of living bodies, exist in "water window" region [4]. The monochrome X-ray with energy between these edges can be employed for the intrinsic contrast imaging in hydrated samples. The compounds containing these elements in the sample can be highlighted. The laser undulator possesses so many features including its wide energy tunability and its compactness of instruments X-ray with narrow energy bandwidth and good directivity can be selected by cutting out with the scattered angle.

*707 HRC: High Tech Research Project, MECSST
#rkuroda@waseda.jp

HIGH QUALITY ELECTRON BEAM GENERATION SYSTEM

RF gun system

The rf gun system is composed of the BNL type 1.6 cell S-band rf cavity with Cu photocathode, a set of solenoid magnets for emittance compensation [5, 6, 7], a stabilized laser and rf power source. Figure 1 shows the total beam line which is within 2×2 m^2 as a table-top size. The photocathode surface of the rf gun cavity was polished using diamond powders. Present quantum efficiency of Cu cathode has been achieved about 5×10^{-5} without laser cleaning. High accelerating field is effective to reduce an emittance growth due to space charge effect for a high current beam. However, we will suffer the increase of dark current due to field emission in the high gradient operation. Therefore, in order to reduce the dark current, a diamond turning method has been applied for a fine manufacturing of the rf gun cavities.

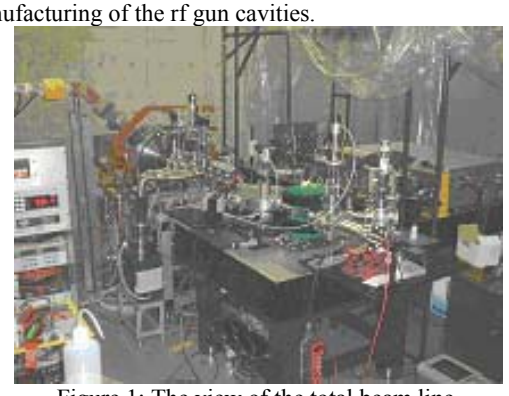

Figure 1: The view of the total beam line

Main parts of rf source consists of 10 MW S-band klystron (Tomson: TV2019B6) and a small pulse modulator (Nissin Electric Co., Ltd.). The pulse

modulator has good stability and flatness of the output pulse.

Laser system

All solid state picosecond Nd:YLF laser system (PULRISE-V), which was developed by SHI (Sumitomo Heavy Industries, ltd.), is used not only for the irradiation onto potocathode to generate the electron beam, but also for the soft X-ray generation using the laser undulator. The laser system has an active timing and intensity stabilization systems against a temperature change and timing jitter from a reference rf signal. Fluctuation of air and vibrations of mirrors on the laser optical path affect the laser intensity and pointing stability on the photocathode. The laser system is put inside the accelerator room to achieve short optical path length to the photocathode. The timing and amplitude fluctuation due to an electro-magnetic noise and radiation had been investigated using time domain demodulation technique between a seed laser and the reference rf signal [8,9]. As a previous result, the timing jitter was measured less than 0.5 ps and the effects of the electromagnetic noise and radiation were negligible for the laser stability. It is sufficiently small timing fluctuation for the soft X-ray generation.

Additional laser amplification

Our all solid state Nd:YLF laser system (PULRISE-V) can provide about 1 mJ/pulse at fundamental wavelength. However, our requirement for the soft X-ray generation experiment and the pulse radiolysis experiment is larger than 10 mJ/pulse. Therefore, a flush lamp pumped 2-pass laser amplification using Nd:YLF crystal (65 mmϕ × 90mm) has been installed. The maximum gain of the amplifier is about 10^2 at 900 V flushing voltage. The optimum laser energy can be arbitrary obtained by changing the flushing voltage. High power laser beam was obtained by amplifying the residual fundamental laser beam (IR: 1047 nm) to collide with the electron beam for the laser undulator.

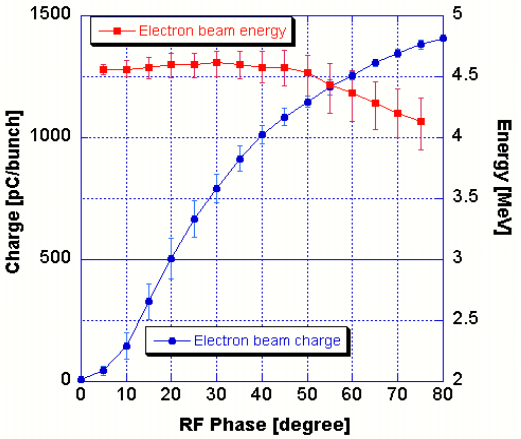

Figure 2: The charge and energy of the electron beam as a function of the rf phase.

Electron beam status

High quality electron beam is produced by a photocathode rf gun system. The 4th harmonic laser (UV: 262 nm) which is irradiated onto the photocathode of the rf gun is obtained from a Nd:YLF fundamental laser (IR: 1047 nm) by passing through two beta barium borate (BBO) crystals in the PULRISE-V laser system. The electron bunch charge and beam energy was measured as a function of rf phase. The typical results are shown in Fig. 2. The bunch charge of 1 nC is achieved at the beam energy of 4.6 ± 0.1 MeV. UV laser to drive the rf gun and IR laser for the applications were generated from a same seed oscillator, so that it was easily to make synchronization between them. Figure 3 shows the block diagram of the synchronization system.

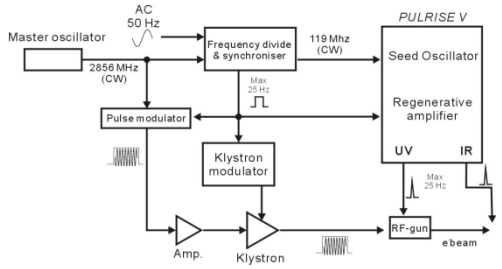

Figure 3: Block diagram of the synchronization system

The beam emittance and the bunch length measurements were carried out using slit scan method and two-frequency analysis technique, respectively [10]. Comparing between results of experiments and simulations, these were agreed well [11].

SOFT X-RAY GENERATION

Analysis

A simple approach to analyze the Compton scattering in a general configuration is to notice the similarity between the role of a laser beam and a static magnetic undulator in inducing a sinusoidal motion of the electrons[1, 12]. The wavelength of the up-shifted radiation as the X-ray can easily be calculated from energy and momentum conservation as

$$\lambda \cong \frac{\lambda_0(1+K^2/2+\gamma^2\theta^2)}{2\gamma^2(1-\cos\phi)}, \qquad (1)$$

where the Compton shift has been neglected. Here, γ is the Lorentz factor, K the wiggler strength, θ the angle of observation, ϕ the angle of the laser propagation toward the electron beam and λ_0 the incident laser wavelength. The wiggler strength is expressed by

$$K = eA_0/m_e c^2 \approx 0.85\times10^{-9}\lambda_0\sqrt{I}, \qquad (2)$$

where I [W/cm^2] and λ_0 [μm] are the intensity and the wavelength of the incident laser, respectively. Here, c is the light velocity, e the elementary electric charge, m_e the electron rest mass, A_0 the vector potential of the incident laser.

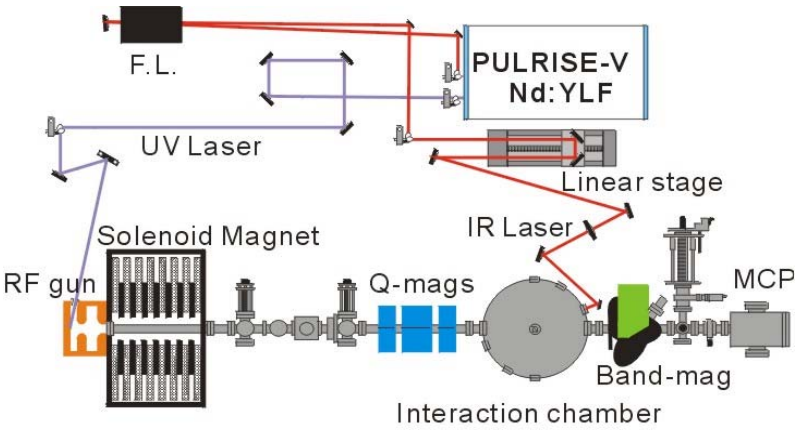

Figure 4: Experimental layout including the rf gun system and the laser system

Soft X-ray generation experiment

Figure 4 shows the experimental layout for the laser undulator. Our system is a table-top size within 2 × 2 m^2 including the rf gun system and Nd:YLF laser system. The electron beam parameters and the laser beam parameters in this experiment are given in Table 1 and 2, respectively.

Table 1: Electron beam parameters

Electron beam	
Ave. beam energy	4.6 MeV
Beam charge	0.60 nC/bunch
Bunch length	10 ps (FWHM)
Beam size σ_x	280 μm
Beam size σ_y	250 μm
Repetition rate	5 Hz

Table 2: Laser beam parameters

Laser beam	
Wavelength	1047 nm
Energy / pulse	10 mJ
Pulse length	10 ps (FWHM)
Beam size σ_x	80 μm
Beam size σ_y	80 μm
Repetition rate	5 Hz

In this experiment, Short-pulse soft X-ray generation using the laser undulator based on the Compton backward scattering between a 4.6 MeV electron beam and a 1047 nm laser beam at 160 deg of the laser propagation angle ϕ toward the electron beam has been successfully performed. A spatial overlap between the electron beam and the laser beam is confirmed by observing both beam images on the identical phosphor screen located at the collision point using a CCD camera. Cherenkov light is emitted by electron beam passing through a 5 mm-thickness glass plate and reflected by an Al mirror with a small pinhole at the collision point, so that the Cherenkov light can be guided toward the same direction of the laser beam to make time and spatial coincidence between them. The laser beam passes through the pinhole and both the laser beam and the Cherenkov light are guided to a streak camera. The generated X-ray is separated from the electron beam using the analyzer magnet and guided to an X-ray detector. The detector is a circular microchannel plate (MCP) (F4655-10: HAMAMATSU PHOTONICS K. K.) with high speeded response that has about a gain of 5 × 10^6 and the quantum detection efficiency of the MCP is about 10 % at 370 eV X-ray [13]. The distance between the collision point and the detection point is about 840 mm and the effective diameter is 15mm. The X-ray scattered within about 8.9 mrad was detected.

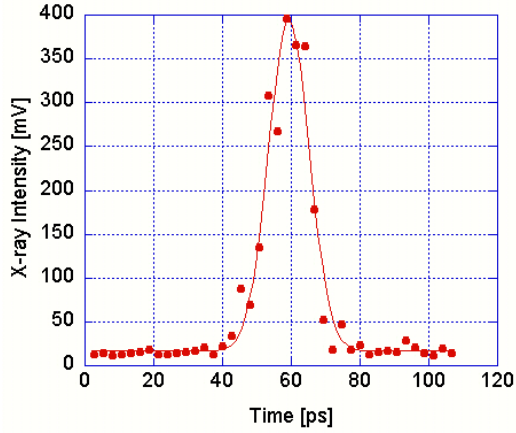

Figure 5: The typical X-ray signals

Figure 5 shows the typical X-ray signals detected by the Microchannel plate (MCP) by changing the timing between the electron beam and the laser beam. The total number of the detected photons is obtained from the

amplitude of the maximum X-ray signal using its gain and the quantum detection efficiency. The amplitude of X-ray signal that is about 380 mV corresponds to the number of detected photons about 1.9×10^2 /pulse. In this case, the total number of generated photons is analytically estimated to be approximately 1.9×10^4 /pulse This X-ray has maximum energy of about 370 eV with 0.2 % energy bandwidth that is between the K-shell absorption edges of N and C. It is expected that this soft X-ray will have many application to the biological observation.

SUMMARY

Soft X-ray generation in "water window" region based on the laser undulator have been successfully performed using the rf gun system with Nd:YLF laser system which is a table-top size within 2×2 m^2. This X-ray has maximum energy of about 370 eV and the total number of generated photons is analytically 1.9×10^4 photons/pulse. Out of total generated X-ray, the useful soft X-ray that has energy between the K-shell absorption edges of N and C is analytically about 4.0×10^3 photons/pulse within about 50 mrad scattered angle that correspond to about 5.2 % energy bandwidth and we can select such useful soft X-ray by cutting out within the scattered angle. It is expected that this X-ray will have many application to many wide research fields such as biological observation. As next step, soft X-ray optics with zone plates or an X-ray CCD camera was proposed for the soft X-ray microscopy to apply to the biological observation.

ACKNOWLEDGEMENT

Authors would like to express sincere thanks to Mrs. T. Takatomi and Y. Watanabe of KEK for their deep help on manufacturing the rf gun cavity. We would like to express our gratitude to Dr. K. Ushida of RIKEN for many technical supports and insightful discussion for its application. We would like to express great thank Drs. A. Endo and Y. Aoki of SHI and FESTA group for their expert technical support about laser system.

REFERENCES

[1] W. Leemans et al., Proc. PAC '95, p. 174 (1995).
[2] S. Kashiwagi et al., NIM A455, 36 (2000).
[3] A. Ting et al., NRL preprint NR/MR14790-92-6973 (1992).
[4] B. L. Henke et al., Atomic Data and Nuclear Data Table 27 (1982).
[5] X. J. Wang et al., Phys. Rev. E 54-4, 3121 (1996).
[6] X. Qiu et al., Phys. Rev. Lett. 76 **20**, 3723 (1996).
[7] D. T. Palmer et al., Proc. PAC '97, p. 2843 (1997).
[8] T. Oshima et al., Proc. PAC 2001, p. 2400 (2001).
[9] H. Tsuchida, Optical Lett., 23, 286 (1998).
[10] R. Kuroda et al., Jpn. J. Appl. Phys. (2004) in press.
[11] K. Sakaue et al., Proc. EPAC 2004 (2004).
[12] K.-J. Kim et al., NIM A341, 351 (1994).
[13] G. W. Fraser et al., NIM A195, 523 (1982).

REPETITIVE BUNCHES FROM RF-PHOTO GUN RADIATE COHERENTLY

C.A.J. van der Geer, S.B. van der Geer, M.J. de Loos,Pulsar Physics*, Soest, The Netherlands
D.A. Jaroszynski, University of Strathclyde†, Glasgow G4 0NG, Scotland, UK

Abstract

We consider injecting the plasma wake field accelerator of the Alpha-X project [1] by a sequence of low charge pancake shaped electron bunches. This solves the problem of undesired expansion due to space-charge forces of a single high charge bunch. To this end the photo-excitation laser pulse of the RF-photo-injector is split into a sequence of sub-pulses. The inter-bunch distance can be chosen such that the sub-bunches fall into successive ponderomotive wells of the plasma accelerator. In this way the total radiated output is kept as high as possible. The repetitive photo gun can be tested, at low energy, by injecting its output into an undulator and monitor the radiation. This programme is informed by results of new GPT simulations [2].

INTRODUCTION

In the ALPHA-X-project an ultra-short electron bunch, of the order of 30 μm (100 fs) will be accelerated in a laser driven plasma wake-field accelerator and then subsequently sent through an undulator [3] to produce useful radiation. The main purpose of the experiment is to demonstrate the possibility of constructing a table top FEL.

As with conventional accelerators, the first problem to attack is the production of electron bunches which are sufficiently short to inject into the accelerating potential. The ponderomotive wavelength of the wake-field accelerator is of the order of 40 μm for a plasma density, $n_e = 7 \cdot 10^{17}$ cm^{-3}. The RF-photo-injector used will deliver 5 MeV, 30 μm, bunches of several hundreds pC, but due to the space-charge forces, such bunches can not be transported over the inevitable space required for other beam line components between the gun and the accelerator. Even pancake-shaped bunches of this size with only 100 pC total charge will expand considerably.

In order to keep the total accelerated charge to an acceptable level while maintaining the bunches short we propose to split the bunch into a number, say ten, sub-bunches and to fill not one, but 10 successive buckets of the ponderomotive wave in the plasma wave accelerator. This bunch splitting is obtainable via Fourier plane filtering of the laser pulse illuminating the photocathode. The generated sequence of sub-bunches will have a total length of ≈ 1 mm, still corresponding to a small fraction in the RF-cycle of the gun (3 GHz) and thus the resulting sub-bunches can be considered almost identical. In this paper we fill every other bucket of the PMW, to ease interpretation. This results in a total length of ≈ 2 mm, still short with respect to the 3 GHz cycle.

As the plasma wave accelerator is already a quite complicated device on its own, it is useful to test the generation of sub-bunches separately. At 5 MeV, the midrange of the RF-photo gun, the ponderomotive wavelength of the generated light in the undulator is quite close to that of the wake-field accelerator. If successive PMW-well's in the undulator are filled with sub-bunches, the output radiation is in phase and adds coherently. This can be monitored with a spectrometer or THz-detector [5], and so, the repetitive photo gun can be tested with the undulator alone.

In this paper we calculate the output of the undulator for a single bunch when the bunch length is varied, and for a sequence of sub-bunches when the inter sub-bunch distance is varied.

The simulations are carried out with GPT. The electron bunch and undulator parameters used in this paper are compiled in tables 1 and 2.

Table 1: Electron bunch parameters

Energy	$E_0 = 5$ MeV
Emittance	$\epsilon_n = 3$ μm
Sub bunch Charge	$q_b = 10$ pC
Total bunch Charge	$Q_b = 100$ pC
Sub bunch length	$\sigma_z = 30$ μm (Gaussian)
Total bunch length	$L_b \approx 2$ mm
Tranverse size	$\sigma_r \approx 1$ mm

Table 2: FEL parameters

Undulator per.	$N_u = 96$	$\lambda_u = 15$ mm
Magnet strength	$B_u = 0.72$ T	$K_{rms} = 0.71$
Gap width	$G = 3.5$ mm	
Slot dim.	$w = 5$ mm	$d = 1$ mm
waveguide dim.	$a = 4$ mm	$b = 4$ mm
rad. wavelength	$\lambda_s = 98.5$ μm	$\lambda_{pmw} = 97.9$ μm

EXPANSION OF THE ELECTRON BUNCH

The longitudinal expansion of a 30 μm bunch, in the beam line between the gun and the accelerator, is shown in fig. 1 for two values of the bunch charge, 100 pC and 10 pC respectively. The transverse dimensions of the bunch

* http://www.pulsar.nl
† http://tops.phys.strath.ac.uk

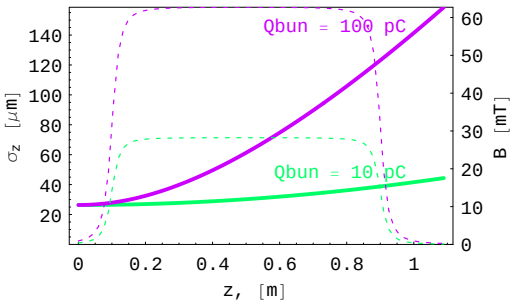

Figure 1: Longitudinal expansion of a short bunch due to the space-charge forces in one meter drift space. The bunch energy is 5 MeV, the bunch length is initially 30 μm. The bunch charge is indicated. Its transverse size in both cases, is kept at $\approx$ 1 mm with a solenoid, the field of which is shown as dotted lines.

are kept at $\sigma_r = 1$ mm using a solenoid lens, the B_z component of which is shown as a dotted line in the figure. The one meter drift space is necessary for beam line components between the gun and the plasma wake-field accelerator. It is also the approximate length of the undulator. A 100 pC bunch becomes more than 5 times longer, while the expansions of a 10 pC bunch is acceptable. Hence, in order to fill one bucket of the plasma wake field accelerator the bunch charge should be maintained at or below 10 pC.

COMPUTER MODEL

Codes	RADIA, GPT, MATHEMATICA
RADIA subdivisions	3,3,3
GPT field map divisions	0.5, 0.5, 0.375 mm
Number of modes	$100 < N_m < 1000$
No of particles	$1000 < N_p < 10\,000$

Table 3: *Simulation parameters*

3D particle tracking simulations have been carried out with the General Particle Tracer Code (GPT), in the combined field of radiation, undulator and space charge. The radiation is self consistently calculated with a custom model, similar to the one presented at EPAC[4]. The mode frequencies used in the model were chosen to be multiples of an imaginary gun repetition frequency, such that the radiation pattern repeats itself after a distance which is much longer than the electron bunch or sequence of bunches. This way the set remains complete with a reasonable number of modes.

The modes used are the HE_{nm} modes with $n = m = 1$ of a corrugated waveguide without losses.

$$E_x = sin(k_x x)sin(k_y y)sin(\omega t - k_z z)$$

$$E_y = 0$$

$$E_z = -\frac{k_x}{k_z}cos(k_x x)sin(k_y y)cos(\omega t - k_z z)$$

with $k_x = n\,\pi/a$, $k_y = m\,\pi/b$, $k^2 = k_x^2 + k_y^2 + k_z^2$.

The interaction is calculated via the innerproduct $\vec{v} \cdot \vec{E}$ for each particle at each time step for each mode without any averaging. This model is very general, includes spontaneous and stimulated emission and covers FEL-interaction from start-up to the saturated regime. The undulator field is calculated with RADIA and introduced into GPT via a field map.

RADIATION FROM ONE (SUB)-BUNCH

The shorter the bunch the stronger the spontaneous radiation from that bunch. The total radiated power decreases rapidly when the bunch length increases.[5] Fig. 2 gives the total radiated power as a function of the (initial) bunch length expressed in Joule per Coulomb *squared* for a bunch charge of 10 fC and for a bunch charge of 10 pC. We see that the radiation is proportional to the square of the bunch charge, which is typical for spontaneous emission of extremely short bunches.

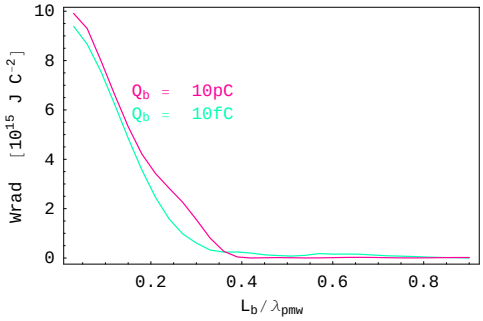

Figure 2: Radiated Energy per square Coulomb versus bunch length for a single sub-bunch. For bunch length smaller than half the PMW-length, the total radiated power is proportional to the square of the bunch charge.

The spectral evolution from "high" and low bunch charge has the same profile and is shown in fig. 3 for a bunch length of 30 μm ($0.3\lambda_{pmw}$). The 3D representation eases interpretation, while below the calibrated contour plots give contours of constant power per mode. The bunch position in the undulator (and in time) increases from bottom to top. For the low bunch charges, the final level (green) is reached at the end of the undulator, while this level is already reached only after a few cm for a high bunch charge.

RADIATION FROM SEQUENCE OF BUNCHES

The total energy radiated by a sequence of sub bunches depends on the inter sub-bunch spacing. It is maximum

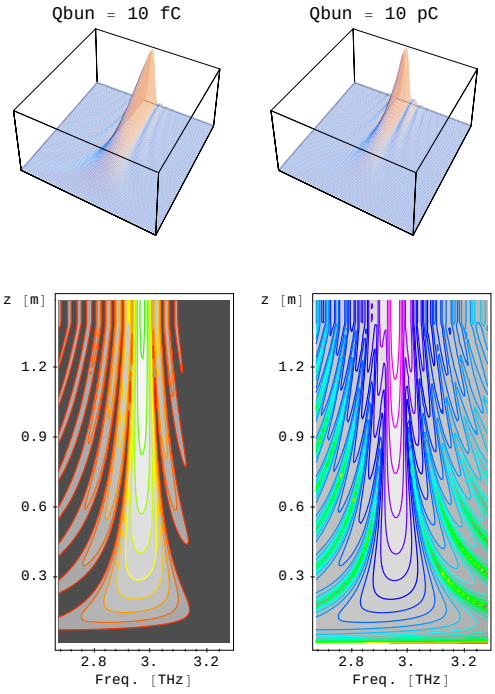

Figure 3: Spectral evolution for a single bunch of 30 μm for the indicated bunch charge. The upper plots are on a linear scale to help interpretation of the contours of constant intensity on a logarithmic scale. The contour distance is 3 dB.

when the individual bunches radiate in phase, which is when $D_{bb} = n\,\lambda_{pmw}$ with an integer value for n. This is shown in fig. 4, which shows the total radiated energy at the end of the undulator as a function of the ratio D_{bb}/λ_{pmw}. This dependence can be used to measure the inter bunch distance. At a higher bunch charge, however, the pronounced peak at $D_{bb} = \lambda_{pmw}$ disappears, because of stimulated emission.

The evolution of the spectrum radiated by a sequence of 10 sub-bunches is given in fig. 5 for the case that the inter bunch distance $D_{bb} = 2\,\lambda_{pmw}$. The bunch charge Q_{sb} is 10 fC in the plots at left and 10 pC in the plots at right. The plots are similar to those in fig. 3, however, in this case we see that at higher bunch charge the generated spectrum broadens and the power level flattens in the second half of the undulator.

HIGHER HARMONICS

The short bunches not only radiate at the first harmonic but also produce significant radiation at higher harmonics. Fig. 6 shows the spectra generated by the sequence of 30 μm sub bunches with $D_{bb} = 2.05\,\lambda_s$ for 0.1 pC and for the nominal 10 pC charge per sub-bunch. In both cases we

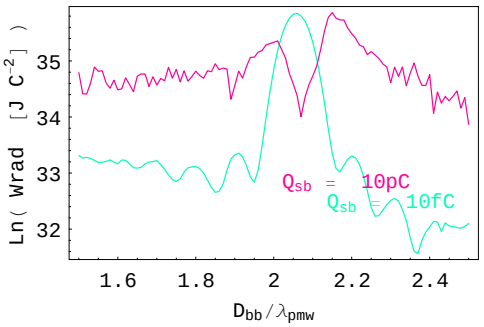

Figure 4: Total power radiated by a sequence of ten sub-bunches as a function of the distance between them. When the charge per sub-bunch is low, the maximum radiation occurs when D_{bb} is around a multiple of the PMW. However, at the nominal bunch charge of 10 pC per sub-bunch this dependence almost disappears due to stimulated emission.

see peaks at both the second and third harmonic of 3 THz but at low bunch charge these peaks are much narrower and more distinct.

CONCLUSION

The plasma wake field accelerator of the Alpha-X project requires extremely short injected bunches in order to deliver a reasonable low energy spread at its output. These bunches are produced by a RF-photoinjector but expand rapidly due to their space-charge, in the space between the gun and the wakefield accelerator. If, however, this bunch is split into a sufficiently large number of equidistant sub bunches, fitting into the buckets of the accelerating field, this problem can be solved. It is shown that, for a typical sub bunch of 5 MeV, 10 pC, 30 μm (100 fs) the parameters of the bunch sequence can be tested without the plasma wave accelerator by monitoring the radiation that it produces in the undulator.

REFERENCES

[1] D.A. Jaroszynski and G. Vieux, *Lasers and Particle Beams*, (2003) Coherent spontaneous emission.

[2] S. B. van der Geer, M. J. de Loos, The General Particle Tracer Code, Thesis TU Eindhoven 2002, ISBN 90-386-1739-9;
Pulsar Physics, General Particle Tracer, http://*www.pulsar.nl*

[3] B.J.A Shepherd and J.A. Clark, "Magnetic Design of a focusing undulator for Alpha-X", proceedings EPAC 2004.

[4] M. J. de Loos, C. A. J. van der Geer, S. B. van der Geer, 3D Multi-Frequency FEL Simulations with the General Particle Tracer Code, EPAC 2002, Paris, France, pp.849;

[5] D.A. Jaroszynski et al. PRL 71, (23), 3798-3801 (1993)

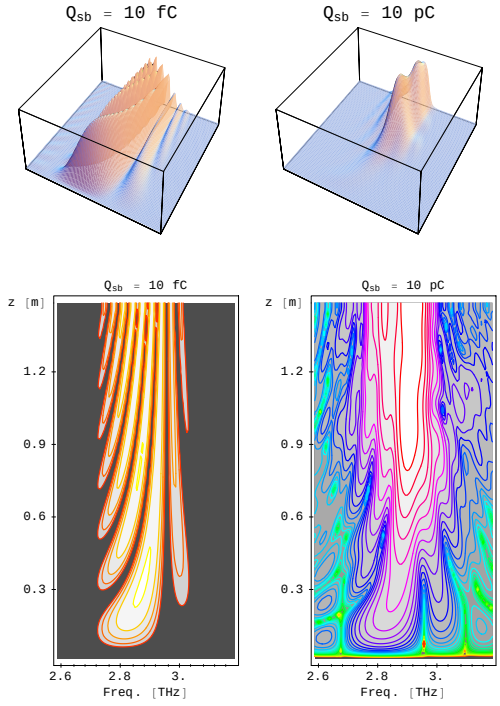

Figure 5: Spectral evolution from a sequence of ten sub-bunches separated by $2.05\,\lambda_{pwm}$, the position of the peak in fig. 4. On the left are the results for Q_{sb} = 10 fC, while on the right Q_{sb} = 10 pC. The 3D plot aids interpretation. The contour distance is 3 dB.

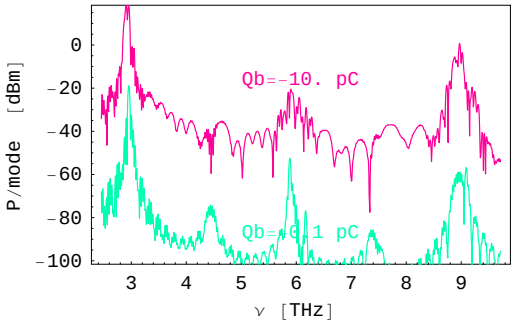

Figure 6: Spectra generated by a sequence of 10 sub-bunches, each with the indicated charge.

RESEARCH ON THE UNDULATOR USED FOR PKU-FEL

H.H. Lu *, J.P. Dai, Y. F. Yang, C.T. Shi, W. Chen, Y.N. Li, J.J. Zhuang
BFEL Laboratory, IHEP CAS, P.O.Box 2732, Beijing, 100080, China

Abstract

A 5m-long combined function undulator used for the Peking University Infrared SASE FEL facility (PKU-FEL) is currently under construction at IHEP, and a 10 period prototype has already been developed. This paper describes the design study of the undulator, which is a hybrid planar magnet structure with extra focusing. The results of magnetic measurements performed on the prototype are also reported and discussed, and it demonstrates that the proposed combined function magnet structure is very promising for the use in the SASE FEL at Peking University.

1. INTRODUCTION

Supported by Major State Basic Research Development Program, a FEL facility to study the physical and technical issues of single pass SASE FEL at IR wave band and high average power FEL is being constructed at Peking University. This facility mainly consists of a superconducting RF photoinjector and superconducting main linac, a bunch compressor and an undulator. The main parameters of the SASE FEL platform are given in Tab.1 [1].

In this paper, we emphasize on the design of undulator, which is a key component of SASE-FEL experiment. The theoretical and numerical simulation of the undulator prototype is described, and the first results of magnetic measurements on the prototype are given.

*Corresponding author. Tel.:+8610 62563452; Fax:+8610 62563454; e-mail:luhh@ihepa.ac.cn

Table1: Parameters of PKU SASE FEL

Electron Beam	
Energy	~40 MeV
Peak Current	>200 A
RMS Emittance	5 mm.mrad
RMS Energy Spread	80 keV
Bunch Duration	~ 5 ps
Undulator	
Period Length	27mm
K Parameter	1.5
Average β Function	25cm
Undulator Length	5 m
FEL	
Wavelength	4μm
Saturation length	~4 m
Saturation power	~50MW

2. THEORETICAL AND NUMERICAL SIMULATION OF THE PROTOTYPE

From the overall concept of PKU SASE FEL program, we got the main parameters of the undulator such as period length, K value, and average β function. We used the experiential formula [2] as follows to compute the peak field of the structure. We got the value of 0.56T when the gap between the two jaws is 11mm. And the corresponding K value is 1.41. These parameters are fit for the PKU SASE-FEL program.

$$B_0 = 3.44\exp[-5.08\frac{g}{\lambda_w} + 1.54(\frac{g}{\lambda_w})^2] \quad (1)$$

Where $0.07 < \frac{g}{\lambda_w} < 0.7$

$$K = 0.934\lambda_w[cm]B_0[T] \quad (2)$$

2.1 The Magnetic Structure Design

A variety of different technologies have been proposed in the past to build insertion devices. We select the planar hybrid magnets structure because it can achieve higher peak fields. The magnet design has been carried out using RADIA code, which is made by ESRF [3]. This code uses the method called Boundary Integral Method with the characteristics of high calculating speed, high accuracy, and perfect field integral function. Fig.1 shows part of the structure used for the simulation.

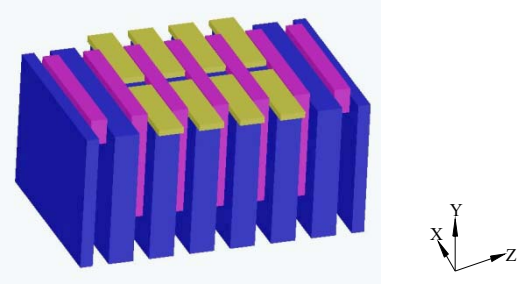

The magnet structure consists of a conventional hybrid structure using NdFeB magnets with a remanent magnetization Mr =1.2T. Poles are made of Vanadium Permendur which has high permeability. With respect to the magnets, the pole tips have an overhang of 2.5mm into the gap region. There is 0.5mm for lowering saturation effects in the poles, and the rest 2mm is the space for the quadrupoles.

The optimization is an iterative process. Our goal is to get the parameters to match the criteria, such as: the magnets and poles should be of reasonable dimensions to achieve peak field we need, the field roll-off should be less than the Pierce parameter ρ, the electron trajectory less than one fifth of electron bunch radius which is 40 microns in this program, and the field integrals have to be trimmed to zero by means of a special end pole configuration.

The curves in Fig.2 show the final calculation results of determining the geometrical dimensions of magnets and poles.

After the calculation, we got the final dimensions: 60mm × 45mm × 8.2mm (width × height × length) for magnets and 43mm×36mm×5.3mm for poles.

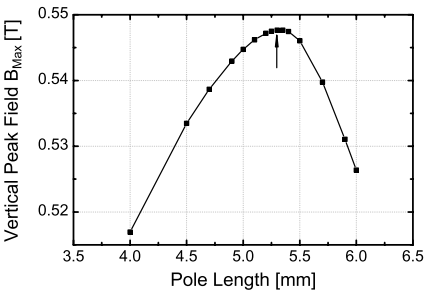

(a) Dependence of the vertical peak field on the pole length for constant period length (27mm) and constant gap (11mm); the arrow marks the design value.

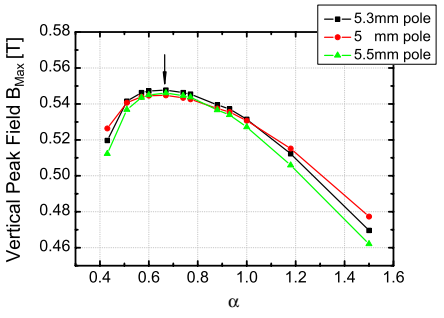

(b) Peak field as function of the ratio of magnet height to magnet width with constant period length and magnet volume corresponding to different pole length; the arrow marks the design value.

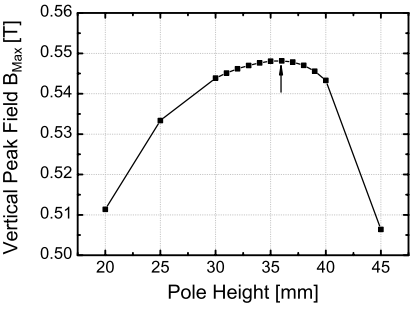

(c) Peak field as function of pole height for constant period length, gap and magnet volume; the arrow marks the design value.

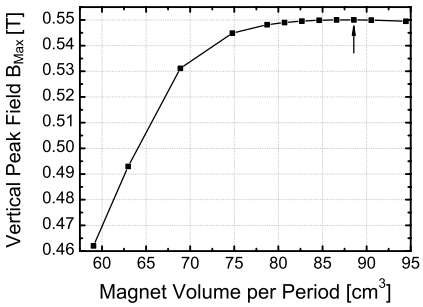

(d) Peak field growth as function of the applied magnet volume for constant period length ,gap and constant transverse magnet proportions; the arrow marks the design value.

Figure 2: Optimization results of hybrid structure.

2.2 FODO Lattice Design

Normally, there are two ways to focus the electron beam, one is called superimposed FODO lattice, the other is called separated FODO lattice. For PKU-SASE-FEL program, the optimized average beta function is only 25cm, and the energy of electron beam is 35-40MeV, which is not very high. So, we select superimposed FODO structure to realize the focusing function.

We made a series of calculations using RADIA code and determined the FODO parameters at last. Some simulation results are shown in Fig.3. The whole parameters of 10 periods prototype are shown in Tab.2.

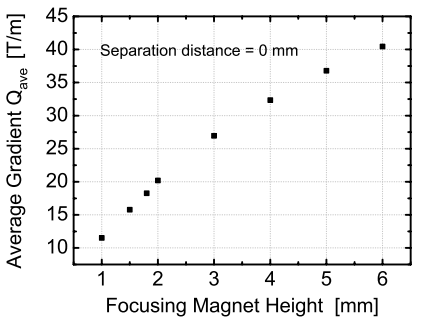

(a) Dependence of the gradient on the height of focusing magnets

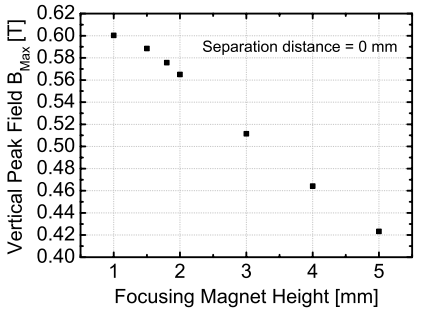

(b) Dependence of the peak field in the gap on the height of the focusing magnets

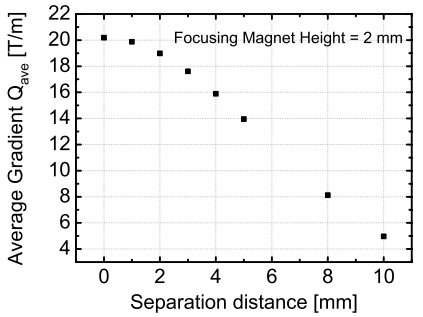

(c) Dependence of the gradient on the separation distance between the focusing magnets

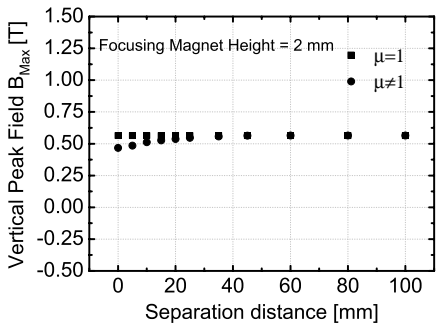

(d) Dependence of the peak field in the gap on the separation distance between the focusing magnets

Figure 3: Optimization results of FODO structure.

2.3 The Prototype with 10 Periods

A 0.283m long prototype structure has been developed, which includes 10 periods and two end-pole structures, shown in Fig.4.

Table 2: Parameters of the undulator prototype

Parameters	Value
Period Length	27mm
Peak Field	0.56T
Average β Function	25cm
Magnetic Gap	11mm
Magnets Dimensions	60mm×45mm×8.2mm
Poles Dimensions	43mm×36mm×5.3mm
Focusing Magnets	30mm×2mm×8.2mm
Gradient	~17T/ m
Quadrupole Length	54mm

Figure 4: The photo of the prototype with 10 periods.

3. THE FIRST RESULTS OF MAGNETIC MEASUREMENTS

We did the primary test. A 3m long measuring bench is used to characterize the magnetic performance of the prototype structure. And we use the Hall probe with 1× 0.5mm sensitive area to do the measurement. The whole system provides sufficient mechanical accuracy. The measuring results comparing to the designed parameters are shown in Tab.3. From the table, we can see we got the identical parameters of prototype according to the simulation. At the same time, we showed some graphs of the measurements in Fig.5, so the magnetic performance is clearer.

Table 3: Comparison of parameters between design and measurement (Electron Beam Energy 40MeV)

	Design	Measurement
Peak Field	0.56 T	0.5619 T
Second Integral	5 Tmm^2	4.6 Tmm^2
Beam Offset	36 μm	31.7 μm
Spontaneous Radiation Wavelength	4.39 μm	4.4 μm

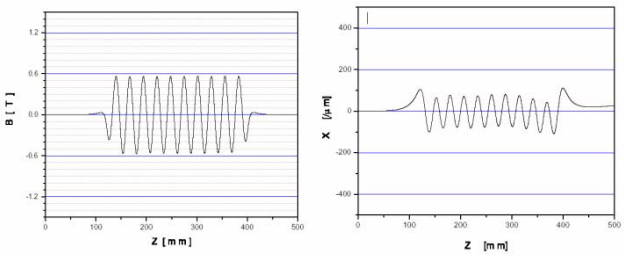

Figure 5: The measurements of prototype. (a) Peak field distribution on axis (b) Beam offset

4. CONCLUSIONS

The results demonstrate that the proposed combined function magnet structure is very promising for the use in the SASE FEL at Peking University. Future work will include physical and mechanical design with length of 5 meters, the end-pole design to realize the phase matching of different segments, and so on.

5. ACKNOWLEDGEMENTS

The authors thank Prof. Y.G. Wang for suggestions and discussions. The work was supported by Major State Basic Research Development Program (2002CB713600).

6. REFERENCES

[1] Yuantao Ding, et.al., Design and Optimization of IR SASE FEL at Peking University, NIM A, in press.

[2] Pflueger J., Nikitina Y. M. Undulator Schemes with the Focusing Properties for the VUV-FEL at the TESLA Test Facility. DESY Print TESLA-FEL 96-02(1996)

[3] Chubar O., Elleaume P., Chavanne J.. A 3D Magnetostatics Computer Code for Insertion Devices.1997

STUDY ON THE PLANAR UNDULATOR SCHEME WITH FOCUSING PROPERTIES FOR PKU-FEL*

Yuantao Ding#, Jia'er Chen, Senlin Huang, Yuangang Wang, Kui Zhao, Jiejia Zhuang
IHIP, Peking University, Bejing, 100871, China

Abstract

An IR range SASE FEL test facility will be built at Peking University. The project is designed to get the SASE FEL at 7 micron driven by a superconducting accelerator. A hybrid planar Nd-Fe-B undulator is employed and the optimization of the external focus system for the undulator is studied. In the PKU-FEL facility, the electron energy is about 30-40 MeV. The combined function undulator with FODO lattice imposes quite stringent tolerances on the strength of the quads. To solve this problem, the weak natural focusing of the undulator in the vertical plane together with horizontally focusing quads, is proposed to supply the focusing in the facility. The combined function undulator of FOFO lattice and FF lattice in the horizontal plane are studied. Compared with the FODO lattice, the FOFO and FF lattice make the saturation a bit longer and the requirements of the field accuracy for the focusing system are much reduced.

INTRODUCTION

Short-wavelength FELs are primarily directed toward x-ray regime at wavelength down to 1 Å. Such a source of coherent laser-like x-rays would have many applications [1]. SASE mode is one of the best methods to get short wavelength FEL.

Table 1 The main parameters of PKU-FEL

Electron beam	
Energy	20-40MeV
Peak current	200A
RMS emittance	5mm.mrad
RMS energy spread	80keV
Bunch duration	~ 1ps
Undulator	
Period length	27mm
K parameter	1.5
Undulator length	5 m
FEL	
Wavelength	7 μ m
Saturation length	~4.5m
Saturation power	~80MW

PKU-FEL facility is an ideal platform to study the physical and technical issues of single pass SASE FEL and high average power FEL. Peking University Superconducting Accelerator Facility (PKU-SCAF) [2], which comprises a superconducting RF photoinjector and superconducting main linac, will be used to drive FELs. The main coupler and cryostats are designed to work at CW mode. At the first stage, SASE FEL experiment at wavelength of 7 μm will be studied [3]. In this paper, the undulator focusing structure is studied.

* Work supported by Chinese department of Science and Technology under the National Basic Research Projects No. 2002CB713600.
#dingyt@pku.edu.cn

THE COMBINED FUNCTION UNDULATOR

Undulator is the most prominent FEL specific component. Given electron beam and undulator parameters, the radiation wavelength is determined by a resonance condition

$$\lambda = \lambda_w(1+a_w^2)/2\gamma_0^2$$

where $a_w = K/\sqrt{2}$ for planar undulator, γ_0 is related to the average beam energy. The undulator has to provide a sinusoidal magnetic field so that FEL process can take place, and it also has to keep the beam size small over the whole undulator length. A planar hybrid permanent magnet undulator combined with a superimposed periodic quadrupole lattice structure (Four Magnet Focusing Undulator, 4MFU[4]) is adopted at PKU SASE FEL[5].

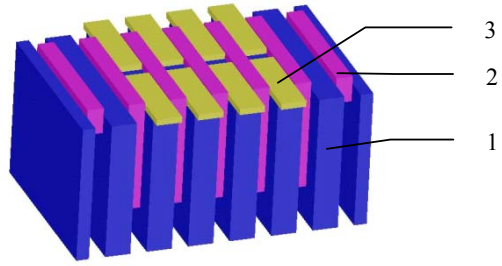

Figure 1: The scheme of combined function undulator, 1: magnets for undulator field; 2: poles; 3: focusing magnet arrays

We optimized the undulator parameters according to the fitting numerical solutions of the coupled Maxwell-Vlasov equations [6]. The electron beam parameters I, ε_n, σ_e are fixed at nominal values given in table 1. The beta function is used the optimized value.

For this undulator used in the IR range FEL, the weak natural focusing in the vertical plane can be used. For example, while the energy of the electron beam is 35MeV, the average beta function in the vertical plane is about

30cm. In the design of the external focusing structure, the natural focusing in the vertical plane will be included. The FODO, FOFO and FF structure is calculated with GENESIS1.3 in steady state mode in this paper.

FODO scheme

First the focusing magnet arrays were calculated as FODO structure. According to the optimization, the FODO period length is $8\lambda_w$ with focusing field gradient of 17T/m and dispersing field gradient of 14T/m at x direction. With this FODO lattice and natural focusing of the planar undulator, average beta functions of 26cm at both x and y direction are obtained. Figure 2 shows the electron beam rms size along undulator in x and y direction. The average beam sizes are almost equal in the two directions [7]. Figure 3 gives the FEL power along undulator. The undulator field is assumed to be ideal, and the influences of different rms quadrupole offsets to the FEL saturation are also shown in Figure 3.

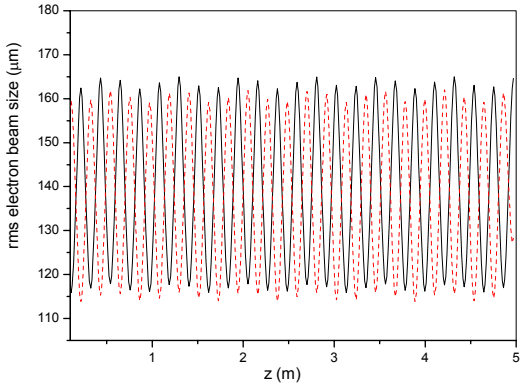

Figure 2: The transverse rms electron beam size with FODO focusing scheme, the solid black line shows the beam size at x direction, the dashed red line shows that at y direction.

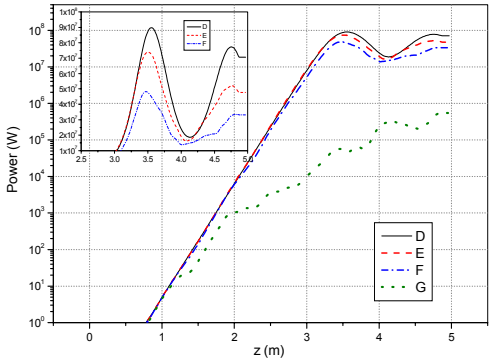

Figure 3: The influences of the rms quadrupole offsets to FEL gain with FODO scheme. The undulator field is assumed to be ideal. The lines marked by D, E, F, G mean that the quadrupole offsets are 0, 30μm, 50μm and 80μm respectively.

FOFO scheme

The FODO lattice in the undulator keeps the transverse beam dimensions within a well specified variation. But the alignment precision of quadrupole is high. Since the natural focusing keeps the beam dimension small in the vertical plane, we put the external focusing quadrupole only in x direction. So the external focusing system is a FOFO structure. The optimized parameters are that the field gradient is 2T/m. The length of the focusing quadrupole is $2\lambda_w$ and the the drift length is $10\lambda_w$. With this structure, the average transverse beam size at x direction is bigger than that of at y direction, as showed in Figure 4. From Figure 5, we can see that the influences of the quadrupole offsets to the FEL saturation power are much decreased, and the saturation length is about 4.2m.

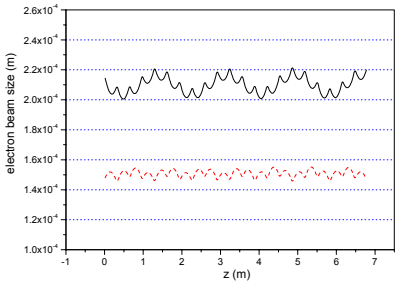

Figure 4: The transverse rms electron beam size with FOFO focusing scheme. The solid black line shows the beam size at x direction, the dashed red line shows that at y direction.

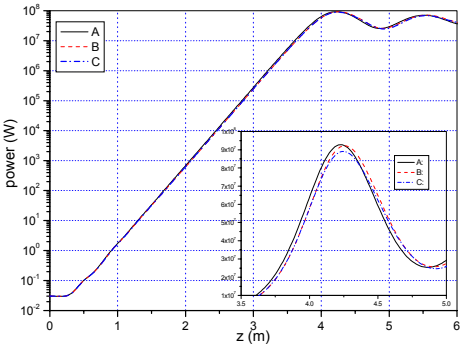

Figure 5: The influences of the rms quadrupole offsets to FEL gain with FOFO focusing scheme. The undulator field is assumed to be ideal. The lines marked with A, B, C mean that the quadrupole offsets are 0, 100μm, 200μm respectively.

To get a round beam size in the transverse section, we can increase the strength of the field gradient of the FOFO structure. When the field gradient is increased to 4.5T/m, the average beam size is nearly round. In this case, the alignment precision of quadrupole is much stricter than that in Figure 5. To make the gain reduction

less than 10%, the quadrupole offsets have to be smaller than 70μm.

FF scheme

In fact, the FOFO scheme can be transferred to FF scheme. That is, the focusing magnet arrays are put in the full length of x direction. There is no drift length in external focusing period. According to the optimization, the focusing field gradient is 0.8T/m. The rms transverse beam size is shown in Figure 6. It is nearly round in the transverse section. The FEL power along the undulator is shown in Figure 7, with different quadrupole offsets. To get the gain reduction of FEL power less than 10%, the quadrupole offsets have to be smaller than 150μm.

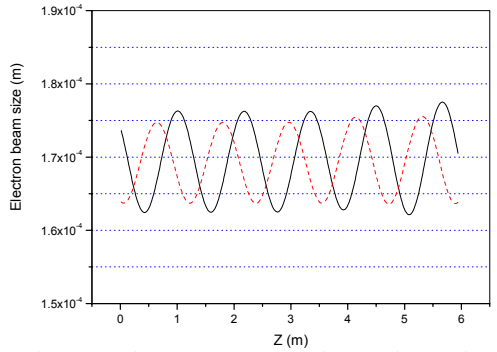

Figure 6: The transverse rms electron beam size with FF focusing scheme, the solid black line shows the beam size at x direction, the dashed red line shows that at y direction.

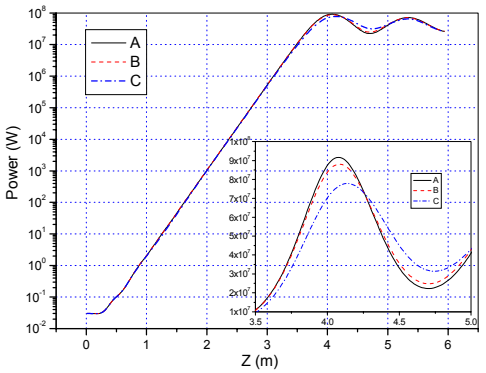

Figure 7: The influences of the rms quadrupole offsets to FEL gain with FF focusing scheme, the undulator field is assumed to be ideal, the lines marked with A, B, C mean that the quadrupole offsets are 0, 100μm, 200μm respectively.

SHORT BUNCH EFFECT

For the IR range FEL, the short bunch effect has much influence at this facility. With the electron beam rms bunch duration of 1ps, the SASE FEL process was simulated in the time-dependent mode using GENESIS 1.3 code. There is only a single temporal spike in the FEL radiation pulse. The radiation FEL pulse has full transverse and longitudinal coherence. The fluctuation of the FEL power and saturation length is large. With the time-dependent mode simulation, the average saturation length of the SASE FEL is about 30cm longer than the result from steady state mode.

SUMMARY

In this paper, the focusing properties of the 4MFU used for IR SASE FEL were investigated. For IR range FEL, the natural focusing in vertical plane and the external focusing quadrupoles in horizontal plane control the electron beam transverse dimensions along the undulator. With the FF focusing scheme, the average beta function is about 38cm. The design and measurement of an undulator model with 10 periods have been finished at BFEL lab. The measurement results agree well with the design values.

.

REFERENCES

[1] Patrick G. O'Shea and Henry P. Freund, Science,2001, **292**:1853-1858.

[2] Zhao Kui, Quan Shengwen,Hao Jiankui et al, Nucl. Instr. & Meth. In Phys. Res. ,2002, **A483**:125-128

[3] Ding yuantao, Huang Senlin, Zhuang Jiejia, Wang Yugang, Zhao Kui, Chen jiaer, Nucl. Instr.& Meth. In Phys. Res. 2004, A528, 416-420;

[4] Plufger J., Nucl. Instr. & Meth. In Phys. Res. , 1996, **A381**:554-559.

[5] Lu Huihua et al, HEP & NP, 2004, **28**:902-907

[6] Xie Ming, Nucl. Instr. & Meth. In Phys. Res. ,2000, **A445**:59-66.

[7] Yuantao Ding, Senlin Huang, Jiejia Zhuang et al, Nucl. Instr. & Meth. In Phys. Res. ,2004, **A528**:416-420.

BEAM LOADING TESTS ON DC-SC PHOTOINJECTOR AT PEKING UNIVERSITY*

Senlin Huang, Jia'er Chen, Xiangqiang Chu, Yuantao Ding, Jiankui Hao, Fei Jiao, Lin Lin, Xiangyang Lu, Shengwen Quan, Guimei Wang, Lifang Wang, Rong Xiang, Binping Xiao, Datao Xie, Limin Yang, Baocheng Zhang, Kui Zhao# , Feng Zhu, SRF Laboratory, Institute of Heavy Ion Physics, Peking University, Beijing 100871, China

Abstract

Since the beginning of commissioning in February 2003, lots of tests on the DC-SC photoinjector test facility have been performed. At present, Q_0 of the 1+1/2-cell superconducting cavity has reached 2×10^8 (at 4.2 K) and the average gradient was about 3.5 MV/m in operation. The DC gun can provide stable electron beams. When the power of output laser went up to 100mW (266 nm), the average beam current reached 500 μA. Beam tests at 4.2 K have been carried out, and superconducting acceleration was achieved. Average current of electron beams was about 100 μA after acceleration.

Beam loading tests at 2 K will be carried out soon. At the same time, further investigations are in progress to improve diagnostics system and to measure the emittance, energy spread and pulse length of electron beams.

INTRODUCTION

A FEL facility (PKU-FEL [1]) is under construction at Peking University. Based on PKU-SCAF [2], a superconducting accelerator facility, PKU-FEL has the characteristics of high stability and high average power. PKU-FEL will run in IR (5~10 μm) and THz (100~3000 μm) region. The facility can also provide high-quality electron beams for experimental studies in some relative fields such as nuclear physics experiments and so on. Figure 1 gives a schematic layout of PKU-FEL facility. One of the most important features is that a superconducting photoinjector - DC-SC photoinjector [3] is selected to supply electron beams with high average current and outstanding beam quality.

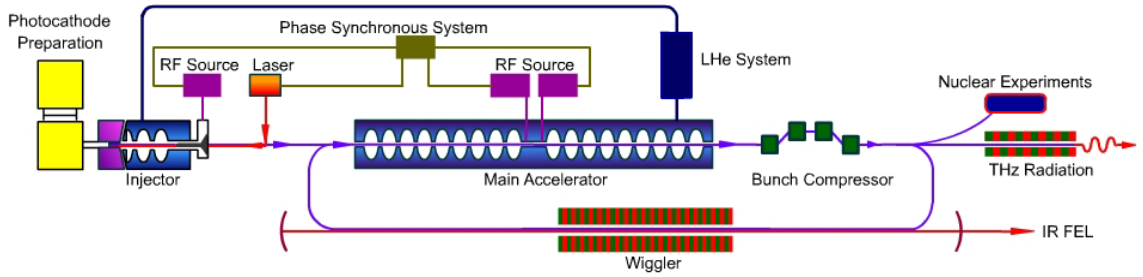

Figure 1: Schematic Layout of PKU-FEL facility.

As has been reported before, in January 2003, the DC-SC photoinjector test facility was constructed. After a year of commissioning and testing, we have accomplished the first successful step. The DC gun can provide stable electron beams and when the power of output laser went up to 100 mW (266 nm), the average beam current reached 500 μA. However we found that the 1+1/2-cell cavity had a relatively low Q_0 value and multipacting was encountered frequently which could not be easily eliminated. For some time low Q_0 and multipacting troubled us so much that we almost could not go on. To improve the quality of the 1+1/2-cell cavity, sputtering technology was employed. Experiments show that Q_0 of the 1+1/2-cell cavity has reached 2×10^8 (at 4.2 K). Moreover, multipacting could be easily eliminated, and when eliminated at low input power (~ mW), multipacting would not appear at higher input power any more.

QUALITY IMPROVEMENT OF SUPERCONDUCTING CAVITY

Earlier experiments indicated that the Q_0 of the 1+1/2-cell cavity was about 10^7. Furthermore multipacting was encountered from time to time during experiments. It seemed that the inner surface of the cavity was not good enough and earlier mechnical polishing and BCP did not work well. To improve the quality of the cavity, a dry-processing method - DC sputtering - was employed. (Figure 2). DC sputtering has several effects. Fisrt, local annealing. Through controlling the working pressure, sputtering could take place in different areas. The second effect is surface polishing. (Figure 3) Sputting could eliminate small emitters and contaminants. The improvement of inner surface leads to the improvement

* Supported in part by Chinese Ministry of Science and Technology under the National basic Research Projects (No.2002CB713602)
# kzhao@pku.edu.cn

of superconducting performance and also increases the multipacting threshold.

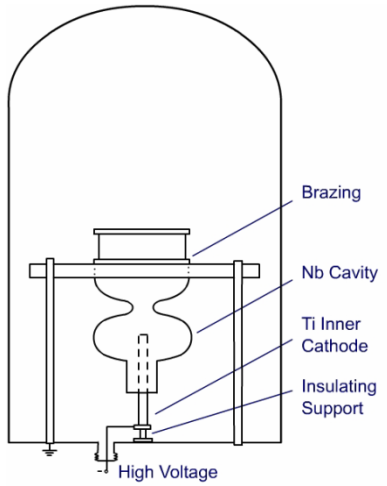

Figure 2: DC sputtering device for post-treatment of 1+1/2-cell cavity.

Figure 3: 1+1/2-cell cavity after DC sputtering.

The post-treatment of the 1+1/2 cavity was carried out step by step, including mechanical polishing, cleaning, DC sputtering, BCP, HP rinsing with ultrapure water and cleanroom assembly. Main parameters of DC sputtering were as following: background pressure was 10^{-6} Pa; sputtering current was about 2 A. High-purity Ar served as sputtering gas and working pressure was 17~20 Pa. Time for DC sputtering was 2 hours.

Experiments after post-treatment validated that DC sputtering worked remarkably. Q_0 of the 1+1/2-cell cavity reached 2×10^8. Moreover, multipacting could be easily eliminated, and when eliminated at low input power (~ mW), it would not appear at higher input power any more.

BEAM TESTS

Beam loading tests have been carried out at 4.2 K, and we have succeeded in superconducting acceleration. In experiments E_{acc} of the cavity was about 3.5 MV/m (at 4.2 K), and energy of electron beams after acceleration was about 300 keV (after the B-Magnet). Evident superconducting acceleration was observed through RF phase shift. A curve of electron beam current vs. phase difference between RF and laser is shown in figure 4. Acceleration effect could also be observed obviously from the difference between beam spots at fluorescence before and after acceleration. (Figure 5 and Figure 6)

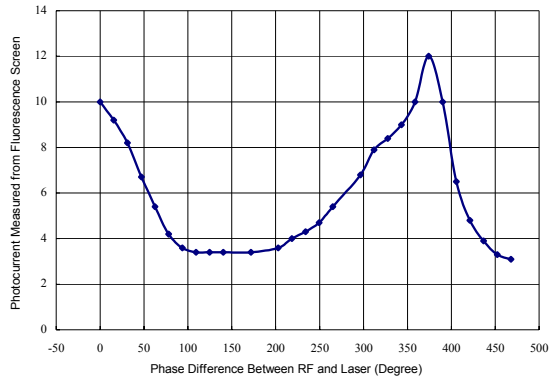

Figure 4: Electron beam current vs. phase difference between RF and laser.

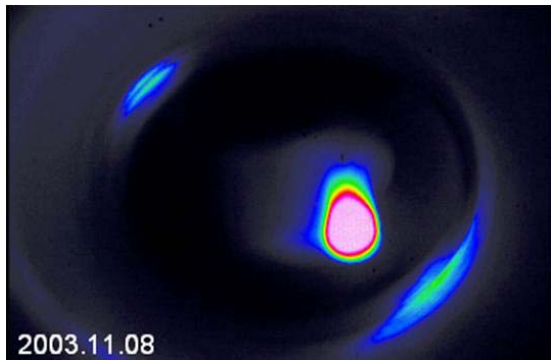

Figure 5: Beam spot at fluorescence target, about 2 m apart from photocathode (before acceleration by superconducting cavity).

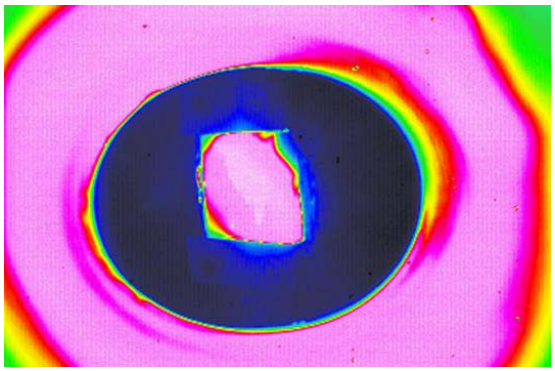

Figure 6: Beam spot at fluorescence target, about 2 m apart from photocathode (after acceleration by superconducting cavity).

Energy gain of the electron beams through the superconducting cavity is about 270 keV, which is quite lower than expected. The reason lies in the relative lower

E_{acc} of superconducting cavity. In the operation E_{acc} of this cavity was 3~4 MV/m, and it was hard to enhance E_{acc} at 4.2 K. Therefore 2 K beam loading tests is underway to improve Eacc and thus to reduce phase slippage in multi-cell cavities.

UPGRADE OF DC-SC PHOTOINJECTOR

DC-SC photoinjector was designed for PKU-FEL, which aims at high average power FEL. Through experiments on the DC-SC photoinjector test facility, we have validated that the DC-SC photoinjector is a good choice to provide moderate average current electron beams with low bunch charge and very high repetition rate.

Table 1: Parameters of the new photoinjector

2+1/2-cell cavity	
E_{acc}	15 MV/m
Drive laser	
Pulse length	10 ps
Spot radius	2 mm
Repetition rate	81.25 MHz
Electron bunch	
Charge/bunch	<60 pC
Energy	3.72 MeV
Energy spread (rms)	1.68%
Emittance (rms)	2.0 mm-mrad

Experiments on the test facility also indicate that to fulfil the requirements of PKU-FEL to the injector, it is necessary to upgrade the core elements of photoinjector-- DC gun and superconducting cavity. Voltage of the DC gun will rise to 150 keV, and accordingly, the structure of high voltage terminal will be improved which will lead to some changes in the structure of cryostat. A 2+1/2-cell cavity will be employed for the new injector. Design and optimization have been accomplished. Stamping technology and electron beam welding technology will be used to fabricate the new cavity. High-purity Nb plates from Ningxia of China will be chosen for the 2+1/2-cell cavity. Parameters of the new photoinjector are list in Table 1.

SUMMARY

We have found a new and simple method to process superconducting cavities. Through this method, DC sputtering, the quality of cavity improves remarkably in a dry way.

Beam tests (at 4.2 K) on DC-SC photoinjector test facility have been carried out. The results of beam tests agree with those of simulations. At present 2 K beam tests are in progress.

REFERENCES

[1] Kui Zhao, et al., Proceedings of APAC 2004, Gyeongju, Korea.
[2] Zhao Kui, et al., Nucl. Instr. and Meth. A 483 (2002) 125.
[3] Zhao Kui, et al., Nucl. Instr. and Meth. A 475 (2001) 564.

THE DRIVE LASER SYSTEM FOR DC-SC INJECTOR*

Xiangyang Lu#, Lin Lin, Fang Wang, Shengwen Quan, Kui Zhao
Institute of Heavy Ion Physics, Peking University, Beijing 100871

Abstract

PKU-SCAF has developed a photoinjector which adopt a 1+1/2 cell super conducting cavity and DC electron gun. We also developed a low cost drive laser system for the photocathode DC gun to provide high average beam current. This laser system include a commercial high repetition rate, ps, all solid-state laser, the home made SHG and FHG, Fourier relay optics and the uniform illumination optics. The test results shows the output power at 266 nm of the laser system is more than 1.2W and got more than 500 μA beam current from CsTe cathode from the DC gun.

INTRODUCTION

FEL needs high quality electron beam. For the advantages of laser driven photo-electron gun, many laboratories choose this approach. In general, the beam design requires the drive laser should be operated with high pulse energy stability, short pulse duration and high timing precise for a long term. Some of the applications need high peak power and for high average current needs the high average power. The drive laser system became complex under those requirements. That means both the laser cost is high and it needs experts to keep the daily maintenance.

A photo-injector which adopts a 1+1/2 cell super conducting cavity and DC electron gun has been developed at Peking University for years [1], [2]. This design is very good for average current acceleration. Peking University RF superconducting acceleration study group is a relative small team. For this reason, we need a good drive laser system to operate, develop this injector, which should be low cost, low maintenance. To study the characters of the injector and exam the physic conceptions, the drive laser also have to fit some special requirements, such as to provide the uniform beam profile.

After investigating the laser market, we choose GE-100-XHP, TBWP, Switzerland, laser as the main part of our drive laser system. According to the requirement of cathode material, CsTe, we develop the second and fourth harmonic generator, beam transport system and designed the beam shaping device. Now, this system is daily operated in the laboratory and the output of the photo-electron gun reaches more than 500 μA with the home made CsTe cathode. In this paper, authors describe the drive laser system and its specifications.

* supported by NSFC (Grand No: 10299021&50132010) and National Basic Research Program (973) (Grand No: 2002CB713602).
#xylu@pku.edu.cn

LASER AND SHG/FHG

The Series GE-100-XHP are passively mode-locked diode-pumped solid-state laser systems using semiconductor saturable absorber mirrors (SESAMs). The GE-100-XHP is combined of a semiconductor pump laser and saturable absorber and yields very clean picosecond pulses with exceptional amplitude and phase noise performance. The detail descriptions refer to TBWP documents [3].

There is a built-in nanosecond-response photodiode at the laser head back panel which not only allows the user to confirm pulsed operation but also provides the signal for feedback control. In our system, the CLX-1100 timing synchronization with the phase-locked-loop feedback is used.

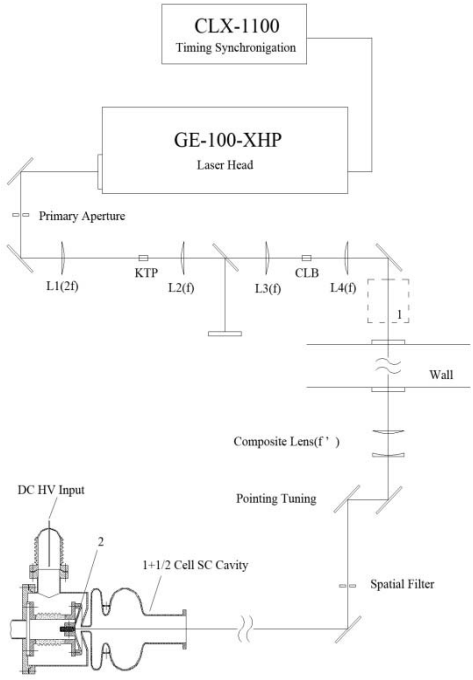

Fig. 1 The drive laser system for DC-SC injector. In the fig, f = 100 mm f ' = 3400 mm, "1" is the special flattener, "2" is the cathode

The working function of CsTe requests light wavelength should be shorter than 270 nm. For this reason, we developed SHG and FHG system. Second harmonic generation (SHG) is realized with a critically phase-matched Potassium Titanyl Phosphate harmonic

(KTiOPO4 or KTP) crystal. The fundamental laser (1064 nm) is focused by a lens (focus length is 200 mm) then pass into a 7×7×10 mm KTP crystal cut in the x-y plane for type II. A second lens (focus length is 100 mm) is positioned after the KTP crystal to realize a 6f system to collimate the 532 nm, second-harmonic beam. The fundamental and second harmonic beam are separated by a 45° harmonic separator which reflecting more than 98% 1064 nm light and transmitting more than 95% 532 nm light.

Table 1: The parameters of the laser system

Wave length (nm)	1064	532	266
Power (W)	10	> 4	> 1.2
Pulse Width (ps)	9.9		
Repetition rate (MHz)	81.25		
Power Stability	~ 1%		
Timing jitter (ps)	< 0.5		
Spot size on Target (mm)			~ 3

The resulting second-harmonic beam passes through a lens (100 mm) that focuses it into a 6×5×15 mm CLBO crystal ($\theta = 62.5°$, $\varphi = 90°$, type I). A Pellin Broca prism separates the unconverted 532 nm light from the UV beam. To avoid the CLBO crystal damaged by water vapor, it is installed in a home made heating oven. The oven temperature is keen in 105°C.

The maximum 1064-532 nm conversion efficiency is about 50%. After adjusting the tilt of KTP crystal, the maximum UV power has been reached 1042 mW and the 532 nm beam was at 4.35 W. It should be noted that the UV transmission of the AR coating at each surface of the lens is 90% and the UV losses of the Pellin Broca prism are about 10%, a total UV power of more than 1.4 W should be generated . If there is an AR coating of 266 nm on the CLBO crystal surface, the measured power also should be higher.

LASER BEAM TRANSPORTATION AND BEAM SHAPING

The distance from our laser room to the cathode position is about 8 m. The fundamental laser beam divergence is about 1 mrad. After SHG and SHG, the beam divergence is even more, e.g., the walk-off of CLBO is about 1.2°. So, when the drive laser reaches the cathode, the beam spot size will be larger than 100 mm.

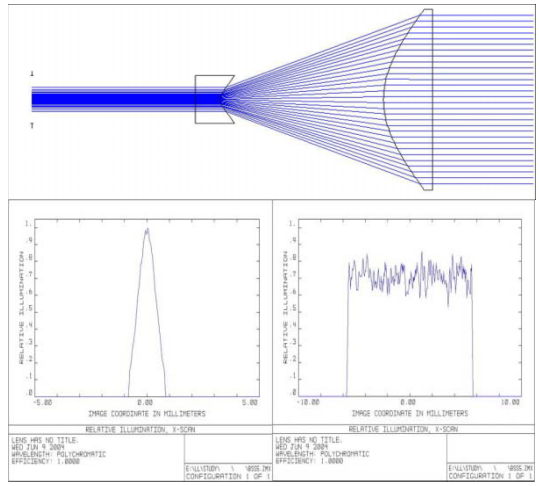

Fig. 2 The two elements beam shaping system

The beam spot size on the cathode surface is required from 2 to 5 mm. If the beam spot is too small, the high power density will damage the cathode. If beam spot is too large, the electron beam profile will be also too larger. To solve this problem, the Fourier relay technique is used. This approach could also maintain a clean transverse mode and improve the beam spot pointing stability.

The primary aperture position is chosen at the beam waist of the fundamental beam, before the SHG crystal. The first lens of focal length 200 mm is placed the distance 200 mm after the primary aperture and 200 mm before the KTP crystal. As the description above, lens L_1 and L_2 are in 6f relation. Then the other lenses are placed in 4f relation. The final is a composite lens of focal length of 3400 mm. By tuning the gap between the convex and concave lens, the beam spot size could be adjusted. The typical UV beam spot size is about 3 mm.

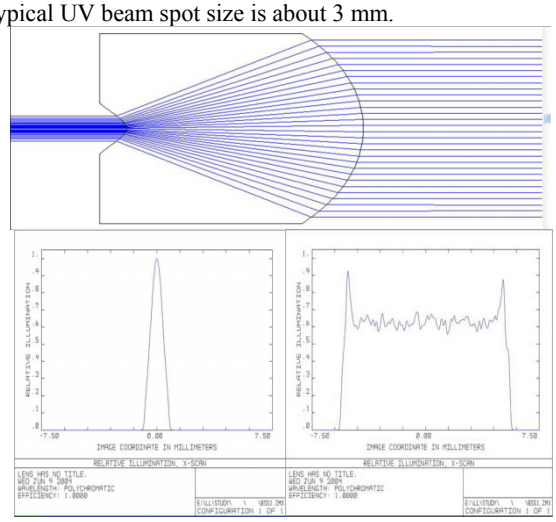

Fig. 3 The single element beam shaping and the simulation result

Beam dynamic simulation result shows that if laser beam spatial profile were uniform, the accelerated beam emittance would be smaller. To prove this achievement, we like to add a spatial flattener in our system. There are numbers approach could produce the uniform beam profile [4], [5]. We have designed both two elements and single element beam shaping system. The simulation results are shown in Fig.2 and Fig.3. From the simulation, there is not much different between two approaches. After further study, we will decide to adopt which one.

CONCLUSIONS

We use a commercials laser, GE-100-XHP, as the main parts to set-up our drive laser. The home made SHG and FHG performed high efficiency. This is a compact and low maintenance system. By use of the Fourier relay technique, the laser transportation is well and the typical beam spot on target is about 3mm. With this system, we have got electron beam current more than 500 μA from the home made TeCs cathode.

We also designed beam shaping system to get the uniform beam profile. The simulation shows both single and two elements system can generate good beam profile. If the spatial flattener is adopted, the Fourier relay system should be redesigned.

REFERENCES

[1]. Kui Zhao, Jiankui Hao, Yanle Hu, et al., Research on DC-RF superconducting photocathode injector for high average power FELs, Nucl. Instr. Meth. A475 (2001) 564-568.

[2] http://apac04.postech.ac.kr/

[3] http://www.tbwp.com/Time_Bandwidth/

[4] David L.Shealy , "Theory of Geometrical Methods for Design of Laser Beam Shaping System," San Diego, 2 August 2000 SPIE's 45 th Annual Meeting, Laser Beam Shaping Conf., 4095-011

[5] J.A.Hoffnagle and C.M.Johnson, "Design and performance of a refractive optical system that converts a Gaussian to a flattop beam," Appl.Opt.39,5488-5499(2000)

[6] S. Zhang, G. Neil and M. Shinn, "Single-element laser beam shaper for uniform flat-top profiles" Optical Society of America

SIMPLIFIED METHOD FOR EXPERIMENTAL SPECTRAL RATIO CALCULATION OF CHG-FEL*

Nian Chen#, Pengfei Zhang, Duohui He, Ge Li, Shancai Zhang, Yuhui Li
National Synchrotron Radiation Laboratory, University of Science and Technology of China, Hefei, Anhui 230029, China

Abstract

Coherent harmonic generation free-electron laser (CHG-FEL) acts as a harmonic amplifier of the seed laser. The spectral ratio, which is defined as the ratio of coherent radiation intensity and incoherent radiation intensity in infinitesimal bandwidth and solid angle aperture, can evaluate the performance of CHG-FEL. In the experiment, we can only get the experimental integral ratio integrated over the actual bandwidth and solid angle aperture of the radiation measurement system. Because the coherent radiation and incoherent radiation are very different in the spatial and spectral structure, the experimental integral ratio is greatly influenced by the measurement system and can not be directly used to evaluate the performance of CHG-FEL. So we must calculate the experimental spectral ratio according to the experimental integral ratio, the bandwidth and solid angle aperture of the measurement system and the parameters of CHG-FEL. And our work is to give a simplified method for the calculation of experimental spectral ratio.

INTRODUCTION

Coherent harmonic generation free-electron laser (CHG-FEL) is one way of storage ring FEL [1-3]. The main component of CHG-FEL is optical klystron (OK), which consists of three sections - two undulators separated by a dispersive section. In the first undulator (modulator), an energy modulation is imposed on the electron beam by interaction with a seed laser. The energy modulation is converted to a coherent spatial density modulation as the electron beam traverses the dispersion section which is a single-period wiggler with strong magnetic field. The second undulator (radiator), tuned to a higher harmonic n_0 (n_0=1, 2, 3…) of the seed laser wavelength λ_s, causes the micro-bunched electron beam to emit coherent radiation whose fundamental wavelength is λ_s/n_0. CHG-FEL acts as a harmonic amplifier of the seed laser. It becomes high-gain harmonic generation free-electron laser (HGHG-FEL) if the radiator is long enough for amplification until saturation is achieved [4].

In CHG-FEL experiment, we can obtain, on axis, the coherent (with seed laser) and incoherent (without seed laser) radiation at the wavelength λ_s/n_0n_r (n_r=1, 3, 5…) from radiator and the incoherent radiation at the wavelength λ_s/n_m (n_m=1, 3, 5…) from modulator. The aim of CHG-FEL is to gain the coherent radiation at the wavelength λ_s/n_0n_r. For example, in the experiment of CHG-FEL on the ACO storage ring at Orsay of France, they have obtained the 3rd and 5th harmonic coherent radiation of the seed laser wavelength 1064nm using a symmetrical OK (n_0=1, n_r=3, 5) [3]. And for our experiment, the OK is unsymmetrical, which benefits the HGHG study. It has two working modes: first, to obtain the 2nd harmonic coherent radiation of the seed laser wavelength 532nm (n_0=2, n_r=1); second, to obtain the 3rd harmonic coherent radiation of the seed laser wavelength 1064nm (n_0=1, n_r=3) [5].

The performances of different CHG-FELs can be effectively evaluated by the experimental spectral ratio R'_{spe} which can be approximately calculated by experimental integral ratio R'_{int} and the ratio of theoretical spectral ratio R_{spe} and theoretical integral ratio R_{int}:

$$R'_{spe} = R'_{int} \times R_{spe} \big/ R_{int} \ . \qquad (1)$$

R'_{int} can be directly measured in experiment, and R_{spe}/R_{int} can be calculated according to the bandwidth and solid angle aperture of the measurement system and the parameters of CHG-FEL.

We give a simple method to calculate the R_{spe}/R_{int} in this paper. In the following discussion, the variables with subscript u, m, d and r represent parameters of any undulator, modulator, dispersive section and radiator respectively.

UNDULATOR RADIATION

When an electron beam traverses the periodic magnetic field provided by an undulator, it emits radiation at the well-known resonant wavelength λ and its nth odd harmonics λ/n. λ is defined as

$$\lambda = \frac{\lambda_u}{2n\gamma^2}\left(1+K_u^2/2\right). \qquad (2)$$

Here, λ_u is the undulator period, γmc^2 is the electron beam energy, m is the electron mass, c is the light speed, $K_u=eB_0\lambda_u/(2\pi mc)=93.37B_0\lambda_u$ is the undulator parameter, e is the charge on the electron, and B_0 is the maximum on-axis magnetic field strength of the undulator.

The radiation energy by a single electron per unit solid angle ($d\Omega$) and per uint wavelength ($d\lambda$) is given by [6]:

$$\left.\frac{d^2I}{d\lambda d\Omega}\right|_{1e^{-1}} = \frac{e^2}{4\pi\varepsilon_0 c\lambda^2}\left|\int_{-\infty}^{+\infty} \boldsymbol{n}\times\left(\boldsymbol{n}\times\boldsymbol{v}(\tau)\right)e^{i\frac{2\pi}{\lambda}\left(c\tau-\boldsymbol{n}\cdot\boldsymbol{x}(\tau)\right)}d\tau\right|^2 , \qquad (3)$$

where ε_0 is permittivity of vacuum, $\boldsymbol{n}$=(sinθcosφ, sinθsinφ, cosθ) is the unit vector from the point of emission to the observer, $\boldsymbol{v}$=(v_x, v_y, v_z) is the electron velocity, and $\boldsymbol{x}$=(x, y, z) is the electron trajectory. The magnetic field in an ideal planar undulator isgiven by $B_y(z)=B_0\cos(2\pi z/\lambda_u)$, for $0\le z\le N_u\lambda_u$, with $B_x(z)=B_z(z)=0$, N_u is the period number. The electron velocity and trajectory can be calculated according to B(z), and then with equation (3), the

*This work is supported by Foundation of National Key Program for Basic Research of China (2001CCB01000), National Natural Science Foundation of China (20173055), Natural Science Foundation of Anhui Province (01046202).
#chnian@mail.ustc.edu.cn

radiation energy can be calculated at any solid angle and wavelength. Here, we only give the single-electron radiation intensity on axis at the resonant wavelength:

$$\left.\frac{\mathrm{d}^2 I}{\mathrm{d}\lambda \mathrm{d}\Omega}\right|_{1\mathrm{e}^{-1}}^{\theta=0,\,\lambda=\lambda} = \frac{e^2 n^2 N_\mathrm{u}^2 \gamma^2 K_\mathrm{u}^2}{4\pi\varepsilon_0 c\left(1+K_\mathrm{u}^2/2\right)^2}\mathrm{F}_n^2\left(K_\mathrm{u}\right), \qquad (4)$$

with

$$\mathrm{F}_n\left(K_\mathrm{u}\right) = \mathrm{J}_{\frac{k-1}{2}}\left(\frac{kK_\mathrm{u}^2}{4\left(1+K_\mathrm{u}^2/2\right)}\right) - \mathrm{J}_{\frac{k+1}{2}}\left(\frac{kK_\mathrm{u}^2}{4\left(1+K_\mathrm{u}^2/2\right)}\right), \qquad (5)$$

here $\mathrm{J_n(x)}$ is the Bessel function of nth order.

For a bunch with N_e electrons whose distribution is $\rho(x, y, z)$, according to equation (3), the radiation intensity of the electrons is given as follows:

$$\left.\frac{\mathrm{d}^2 I}{\mathrm{d}\lambda \mathrm{d}\Omega}\right|_{N_\mathrm{e}\mathrm{e}^{-1}} = \left.\frac{\mathrm{d}^2 I}{\mathrm{d}\lambda \mathrm{d}\Omega}\right|_{1\mathrm{e}^{-1}} \times \left|\iiint \rho(x,y,z)\,\mathrm{e}^{-\mathrm{i}\frac{2\pi}{\lambda}(\theta\cos\varphi\cdot x+\theta\sin\varphi\cdot y+z)}\,\mathrm{d}x\mathrm{d}y\mathrm{d}z\right|^2 . \qquad (6)$$

INCOHERENT RADIATION OF CHG-FEL

The incoherent radiation at measured wavelength $\lambda_s/n_0 n_\mathrm{r}$, not only comes from radiator but also from modulator when n_0 is an odd number. From the principle of CHG-FEL and resonant relation (1), we obtain $\lambda_\mathrm{r}(1+K_\mathrm{r}^2/2)=\lambda_\mathrm{m}(1+K_\mathrm{m}^2/2)/n_0$. And combining this equation with equation (4), the relation between the single-electron radiation intensity on axis at the wavelength $\lambda_s/n_0 n_\mathrm{r}$ from modulator $\mathrm{d}^2 I_\mathrm{m}/\mathrm{d}\lambda\mathrm{d}\Omega$ and that from radiator $\mathrm{d}^2 I_\mathrm{r}/\mathrm{d}\lambda\mathrm{d}\Omega$ can be calculated as follows:

$$\left.\frac{\mathrm{d}^2 I_\mathrm{m}}{\mathrm{d}\lambda \mathrm{d}\Omega}\right|_{1\mathrm{e}^{-1}}^{\theta=0,\lambda=\frac{\lambda_\mathrm{s}}{n_0 n_\mathrm{r}}} = P\times\left.\frac{\mathrm{d}^2 I_\mathrm{r}}{\mathrm{d}\lambda \mathrm{d}\Omega}\right|_{1\mathrm{e}^{-1}}^{\theta=0,\lambda=\frac{\lambda_\mathrm{s}}{n_0 n_\mathrm{r}}}, \qquad (7)$$

with

$$P = \begin{cases} \dfrac{\lambda_\mathrm{m}^2 N_\mathrm{m}^2 K_\mathrm{m}^2 \mathrm{F}_{n_0 n_\mathrm{r}}^2\left(K_\mathrm{m}\right)}{\lambda_\mathrm{r}^2 N_\mathrm{r}^2 K_\mathrm{r}^2 \mathrm{F}_{n_\mathrm{r}}^2\left(K_\mathrm{r}\right)} & n_0 = 1,3,5,7\mathrm{L} \\ 0 & n_0 = 2,4,6,8\mathrm{L} \end{cases} . \qquad (8)$$

Without seed laser, the energy and spatial density of electrons are not modulated. Thus, electrons can be regarded as uniformly distributed over the radiation wavelength and the radiation fields of two individual electrons are incoherent. The incoherent radiation intensity is proportional to the number of electrons in the bunch, we get

$$\left.\frac{\mathrm{d}^2 I_\mathrm{inc}}{\mathrm{d}\lambda \mathrm{d}\Omega}\right|_{N_\mathrm{e}\mathrm{e}^{-1}}^{\theta=0,\lambda=\frac{\lambda_\mathrm{s}}{n_0 n_\mathrm{r}}} = N_e\left(1+P\right)^2\left.\frac{\mathrm{d}^2 I_\mathrm{r}}{\mathrm{d}\lambda \mathrm{d}\Omega}\right|_{1\mathrm{e}^{-1}}^{\theta=0,\lambda=\frac{\lambda_\mathrm{s}}{n_0 n_\mathrm{r}}} . \qquad (9)$$

The bandwidth and solid angle aperture of incoherent radiation are far larger than those of the measurement system. So, within bandwidth and solid angle aperture of the measurement system, the incoherent radiation intensity can be regarded as invariable which is equal to the value on axis at the wavelength $\lambda_s/n_0 n_\mathrm{r}$.

COHERENT RADIATION OF CHG-FEL

With seed laser, the distribution of electrons is no longer uniform after the energy and spatial density modulation. The initial distribution of electrons can be approximately expressed as Gaussian distribution:

$$\rho_0(x,y,z) = \frac{N_\mathrm{e}}{(2\pi)^{3/2}\sigma_x\sigma_y\sigma_z}\mathrm{e}^{-\frac{x^2}{2\sigma_x^2}-\frac{y^2}{2\sigma_y^2}-\frac{z^2}{2\sigma_z^2}}, \qquad (10)$$

where σ_x and σ_y are transverse sizes of bunch, σ_z is the longitudinal size of bunch. The distribution of electrons at the exit of the dispersive section can be expressed as

$$\rho(x,y,z) = \rho_0\left\{1+\sum_{n=1}^{\infty}2\mathrm{J}_n(n\eta)\mathrm{f}_n\cos\left(\frac{2n\pi}{\lambda_\mathrm{s}}z\right)\right\}, \qquad (11)$$

with $\eta=4\pi(N_\mathrm{m}+N_\mathrm{d})\Delta\gamma_\mathrm{m}/\gamma$ and $\mathrm{f_n}=\exp\{-8[n\pi(N_\mathrm{m}+N_\mathrm{d})\sigma_\gamma/\gamma]^2\}$, where N_d is the parameter of dispersive section, $2\pi N_\mathrm{d}$ represents the dephasing created by the dispersive section between an electron and the seed laser wave, $\Delta\gamma_\mathrm{m}/\gamma=eN_\mathrm{m}\lambda_\mathrm{m}K_\mathrm{m}E_\mathrm{s}\mathrm{F}_1(K_\mathrm{m})/(2\gamma^2 mc^2)$ is the maximum relative shift of the electron induced by the seed laser, E_s is the electromagnetic wave amplitude of seed laser, σ_γ/γ is the energy spread of the electron beam [1]. As a consequence of Equations (6) and (11), we get the following expression for the coherent radiation intensity of CHG-FEL:

$$\left.\frac{\mathrm{d}^2 I_\mathrm{coh}}{\mathrm{d}\lambda \mathrm{d}\Omega}\right|_{N_\mathrm{e}\mathrm{e}^{-1}} = N_\mathrm{e}^2\,\mathrm{J}_{n_0 n_\mathrm{r}}^2\left(n_0 n_\mathrm{r}\eta\right)\mathrm{f}_{n_0 n_\mathrm{r}}^2 \times \mathrm{e}^{-\frac{4\pi^2}{\lambda^2}\left(\theta^2\cos^2\varphi\sigma_x^2+\theta^2\sin^2\varphi\sigma_y^2\right)} \times \mathrm{e}^{-4\pi^2\sigma_z^2\left(\frac{1}{\lambda}-\frac{n_0 n_\mathrm{r}}{\lambda_\mathrm{s}}\right)^2}\left.\frac{\mathrm{d}^2 I_\mathrm{r}}{\mathrm{d}\lambda \mathrm{d}\Omega}\right|_{1\mathrm{e}^{-1}} . \qquad (12)$$

According to the above equation, we give the bandwidth $\Delta\lambda_\mathrm{coh}$ and solid angle aperture $\Delta\Omega_\mathrm{coh}$ of coherent radiation:

$$\Delta\lambda_\mathrm{coh} = \frac{\sqrt{\ln 2}}{\pi\sigma_z}\lambda^2, \quad \Delta\Omega_\mathrm{coh} = \frac{\lambda^2}{2\pi\sigma_x\sigma_y} . \qquad (13)$$

Within bandwidth and solid angle aperture of the measurement system, the coherent radiation intensity can not be regarded as invariable because $\Delta\lambda_\mathrm{coh}$ and $\Delta\Omega_\mathrm{coh}$ are very small.

EXPERIMENTAL SPECTRAL RATIO CALCULATION

According to equations (9) and (12), we can get the theoretical spectral ratio as follows:

$$R_\mathrm{spe} = \left.\frac{\mathrm{d}^2 I_\mathrm{coh}}{\mathrm{d}\lambda \mathrm{d}\Omega}\right|_{N_\mathrm{e}\mathrm{e}^{-1}}^{\theta=0,\lambda=\frac{\lambda_\mathrm{s}}{n_0 n_\mathrm{r}}} : \left.\frac{\mathrm{d}^2 I_\mathrm{inc}}{\mathrm{d}\lambda \mathrm{d}\Omega}\right|_{N_\mathrm{e}\mathrm{e}^{-1}}^{\theta=0,\lambda=\frac{\lambda_\mathrm{s}}{n_0 n_\mathrm{r}}} = \frac{1}{\left(1+P\right)^2}N_\mathrm{e}\,\mathrm{J}_{n_0 n_\mathrm{r}}^2\left(n_0 n_\mathrm{r}\eta\right)\mathrm{f}_{n_0 n_\mathrm{r}}^2 . \qquad (14)$$

From equations (9) and (12), we can also get the theoretical integral ratio in bandwidth $\Delta\lambda$ and the solid angle $\Delta\Omega$ of the measurement system. Here, we skipped

the rather tedious details of the integral and reported the final result only as equations (15)-(17):

$$R_{\mathrm{int}}=\frac{\int_{\Delta\lambda}\int_{\Delta\Omega}\left(\left.\frac{\mathrm{d}^2 I_{\mathrm{coh}}}{\mathrm{d}\lambda\mathrm{d}\Omega}\right|_{N_e\mathrm{e}^{-1}}\right)\mathrm{d}\Omega\mathrm{d}\lambda}{\int_{\Delta\lambda}\int_{\Delta\Omega}\left(\left.\frac{\mathrm{d}^2 I_{\mathrm{inc}}}{\mathrm{d}\lambda\mathrm{d}\Omega}\right|_{N_e\mathrm{e}^{-1}}\right)\mathrm{d}\Omega\mathrm{d}\lambda}=R_{\mathrm{spe}}I_{\Delta\Omega}I_{\Delta\lambda}\,, \quad (15)$$

where

$$I_{\Delta\Omega}=\frac{\left(\lambda_{\mathrm{s}}/n_0 n_{\mathrm{r}}\right)^2}{4\pi\sigma_x\sigma_y\Delta\Omega}\times\left[1-\frac{\sigma_x\sigma_y}{2\pi}\int_0^{2\pi}\frac{\mathrm{e}^{-\frac{4\pi\Delta\Omega}{\left(\lambda_{\mathrm{s}}/n_0 n_{\mathrm{r}}\right)^2}\left(\cos^2\varphi\sigma_x^2+\sin^2\varphi\sigma_y^2\right)}}{\cos^2\varphi\sigma_x^2+\sin^2\varphi\sigma_y^2}\mathrm{d}\varphi\right] \quad (16)$$

and

$$I_{\Delta\lambda}=\frac{\left(\lambda_{\mathrm{s}}/n_0 n_{\mathrm{r}}\right)^2}{2\sqrt{\pi}\sigma_z\Delta\lambda}\int_{-\frac{\sqrt{2\pi}\sigma_z\Delta\lambda}{\left(\lambda_{\mathrm{s}}/n_0 n_{\mathrm{r}}\right)^2}}^{\frac{\sqrt{2\pi}\sigma_z\Delta\lambda}{\left(\lambda_{\mathrm{s}}/n_0 n_{\mathrm{r}}\right)^2}}\frac{\mathrm{e}^{-\frac{\tau^2}{2}}}{\sqrt{2\pi}}\mathrm{d}\tau\,. \quad (17)$$

Here, we list four particular cases and give their approximate expressions.

If $\Delta\lambda>\Delta\lambda_{\mathrm{coh}}$ and $\Delta\Omega>\Delta\Omega_{\mathrm{coh}}$, then:

$$R_{\mathrm{int}}=R_{\mathrm{spe}}\frac{\left(\lambda_{\mathrm{s}}/n_0 n_{\mathrm{r}}\right)^4}{8\pi^{3/2}\sigma_x\sigma_y\sigma_z\Delta\lambda\Delta\Omega}\,; \quad (18)$$

If $\Delta\lambda>\Delta\lambda_{\mathrm{coh}}$ and $\Delta\Omega<<\Delta\Omega_{\mathrm{coh}}$, then:

$$R_{\mathrm{int}}=R_{\mathrm{spe}}\frac{\left(\lambda_{\mathrm{s}}/n_0 n_{\mathrm{r}}\right)^2}{2\sqrt{\pi}\sigma_z\Delta\lambda}\,; \quad (19)$$

If $\Delta\lambda<<\Delta\lambda_{\mathrm{coh}}$ and $\Delta\Omega>\Delta\Omega_{\mathrm{coh}}$, then:

$$R_{\mathrm{int}}=R_{\mathrm{spe}}\frac{\left(\lambda_{\mathrm{s}}/n_0 n_{\mathrm{r}}\right)^2}{4\pi\sigma_x\sigma_y\Delta\Omega}\,; \quad (20)$$

If $\Delta\lambda<<\Delta\lambda_{\mathrm{coh}}$ and $\Delta\Omega<<\Delta\Omega_{\mathrm{coh}}$, then: $R_{\mathrm{int}}=R_{\mathrm{spe}}$.

For our experiment, the reference [7] gives a set of its parameters: σ_x=0.518mm, σ_y=0.051mm, σ_z=11.3mm, n_0=2, n_r=1, λ_s=532nm and λ=266nm. According to equation (13), $\Delta\lambda_{\mathrm{coh}}$=0.0017nm, $\Delta\Omega_{\mathrm{coh}}=0.43\times10^{-6}\mathrm{rad}^2$. For the actual measurement system, $\Delta\lambda$=0.15nm, $\Delta\Omega=0.12\times10^{-6}\mathrm{rad}^2$, we can get $R_{\mathrm{spe}}/R_{\mathrm{int}}$=192 using equation (15)-(17). If $\Delta\lambda$=0.15nm, $\Delta\Omega=1.2\times10^{-6}\mathrm{rad}^2$, $R_{\mathrm{spe}}/R_{\mathrm{int}}$=478 using equation (18) and $R_{\mathrm{spe}}/R_{\mathrm{int}}$=678 using equation (15)-(17). If we have measured the experimental integral ratio R'_{int}, then, using equation (1), we can calculate the experimental spectral ratio R'_{spe}.

REFERENCES

[1] J.M. Ortega, Y. Lapierre, B. Girard, et al. IEEE Journal of Quantum Electronics. QE-21 (1985) 909.

[2] R. Prazeres, J.M. Ortega, C. Bazin, et al. Nucl Instr and Meth. A 272 (1988) 68.

[3] R. Prazeres, P. Guyot-Sionnest, J.M. Ortega, et al. Nucl Instr and Meth. A 304 (1991) 72.

[4] L.H. Yu, M. Babzien, I. Ben-Zvi, et al. Science. 289 (2000) 932.

[5] Chen Nian, Xu Hong-liang, Liu Jin-ying, et al. High Power Laser and Particle Beams. 15 (2003) 524.

[6] J.D. Jackson. Classical Electrodynamics (wiley, New York, 1965) p.480.

[7] J.Y. Liu, C.Z. Diao, D.H. He, et al. Proceedings of the 2003 Particle Accelerator Conference. Portland: 2003.968.

MULTI-OBJECTIVE OPTIMIZATION FOR PURE PERMANENT-MAGNET UNDULATOR MAGNETS ORDERING USING MODIFIED SIMULATED ANNEALING *

Nian Chen#, Duohui He, Ge Li
National Synchrotron Radiation Laboratory, University of Science and Technology of China, Hefei, Anhui 230029, China

Abstract

Undulator filed errors influence the electron beam trajectories and lower the radiation quality. Angular deflection of electron beam is determined by first field integral, orbital displacement of electron beam is determined by second field integral and radiation quality can be evaluated by rms field error or phase error. Appropriate ordering of magnets can greatly reduce the errors. We apply a modified simulated annealing algorithm to this multi-objective optimization problem, taking first field integral, second field integral and rms field error as objective functions. Undulator with small field errors can be designed by this method within a reasonable calculation time even for the case of hundreds of magnets (first field integral reduced to 10^{-6}T·m, second integral to 10^{-6}T·m^2 and rms field error to 0.01%). Thus, the field correction after assembling of undulator will be greatly simplified. This paper gives the optimizing process in detail and puts forward a new method to quickly calculate the rms field error and field integrals.

INTRODUCTION

Undulators and wigglers are the main components of third-generation synchrotron radiation sources and free-electron lasers [1]. Undulators are mostly built of permanent magnets with iron poles (hybrid undulators) or without iron poles (Pure Permanent-Magnet undulators or PPM undulators). The unavoidable remanence inhomogeneities of these magnets and construction errors cause the undulator magnetic field errors [2], which affect the trajectories of the electron beam and lower the radiation quality of undulator or FEL [3]. Angular deflection of electron beam is determined by first field integral along the beam axis, orbital displacement of electron beam is determined by second field integral along the beam axis, and radiation quality can be evaluated by rms field error or phase error [4]. To reduce the undulator magnetic field errors, we need a sufficiently precise mechanical construction and a certain method to overcome the influence of remanence inhomogeneities. That is, we should not only provide a precise method to measure the individual permanent magnets and assemble them to form undulator [5], but also provide an appropriate ordering of undulator magnets before assembly. And the sorting procedure of ordering is mainly based on "Simulated Annealing" [6] although "genetic algorithms" have also been used [7] and it is widely applied to the PPM undulator where linear superposition can be used.

We apply a modified simulated annealing algorithm to this multi-objective optimization problem, taking first field integral, second field integral and rms field error as objective functions. And we put forward a new quick method to directly calculate the rms field error and field integrals according to remanence and positions of individual magnets. Illustrations are drawn from the reconstruction of the first undulator (modulator of optical klystron) of CHG-FEL for National Synchrotron Radiation Laboratory.

OBJECTIVE FUNCTIONS

Figure 1 shows the structure of undulator. The undulator consists of three configuration magnets, which are horizontal ("H") magnets with the main remanence in the horizontal direction, vertical ("V") and terminal ("T") magnets with the main remanence in the vertical direction. "T" magnets differ from "V" magnets only in width and their width is half those of "V" magnets. *X*, *Y*, *Z* are length, height, width of the magnet. And *g* is the gap of undulator magnetic field.

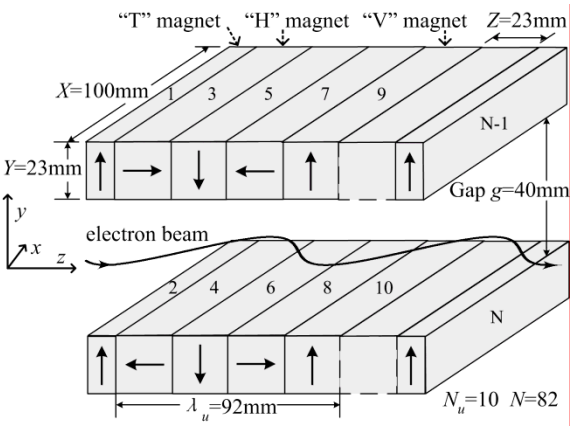

Figure 1: Structure of undulator.

For purposes of discussion, we assume a rectangular coordinate system with the electron propagation axis in the *z* direction, the principal component of the magnetic field B_y in the vertical *y* direction, and the *x*-*z* plane being thus the plane of the electron sinusoidal motion.

Measurement and Calculation of Magnets

To measure all the magnets equivalently, we define a reference position with the main component in the upward vertical *y* direction. Therefore, for a magnet, the

*This paper is supported by Foundation of National Key Program for Basic Research of China (2001CCB01000), National Natural Science Foundation of China (20173055).
#chnian@mail.ustc.edu.cn

remanence components B_{r1}, B_{r2}, B_{r3} are in the x, y, z direction respectively. For ideal magnets, B_{r1}=B_{r3}=0. For real magnets, in general, $|B_{r1}|:|B_{r2}|:|B_{r3}|$ approximately equals 1:1000:10.

After measurement of individual magnets, we can obtain the values of $B_{r1,n}$, $B_{r2,n}$, $B_{r3,n}$, and here n is the serial number of magnets from 1 to N_{total} (the total number of all the magnets). We choose N magnets among the N_{total} according to $B_{r2,n}$ and arrange them to assemble the undulator.

If the magnet is used in the "V" or "T" configuration, B_{r1} corresponds to B_{rx}, B_{r2} to B_{ry} and B_{r3} to B_{rz}. If the magnet is placed in the "H" position, B_{r1} corresponds to B_{rx}, B_{r2} to B_{rz} and B_{r3} to B_{ry}.

Take the centre of the magnet as the origin of the coordinate, and the magnetic field in y direction $B_y(x,y,z)$, generated by this system outside the magnet, is given by the following expression:

$$\begin{aligned} B_y(x,y,z) = {} & b(X,Y,Z) - b(-X,Y,Z) - b(X,-Y,Z) \\ & + b(-X,-Y,Z) - b(X,Y,-Z) + b(-X,Y,-Z) \\ & + b(X,-Y,-Z) - b(-X,-Y,-Z) \end{aligned} \quad (1)$$

For ideal "V" and "T" magnets,

$$b(X,Y,Z) = \frac{B_r}{4\pi} \mathrm{tg}^{-1} \left[\frac{\left(x-\frac{X}{2}\right)\left(z-\frac{Z}{2}\right) \Big/ \left(y-\frac{Y}{2}\right)}{\sqrt{\left(x-\frac{X}{2}\right)^2 + \left(y-\frac{Y}{2}\right)^2 + \left(z-\frac{Z}{2}\right)^2}} \right] \quad (2)$$

For ideal "H" magnets,

$$b(X,Y,Z) = \frac{-B_r}{4\pi} \ln \left[\frac{X}{2} - x + \sqrt{\left(x-\frac{X}{2}\right)^2 + \left(y-\frac{Y}{2}\right)^2 + \left(z-\frac{Z}{2}\right)^2} \right] \quad (3)$$

B_y of individual magnets can be calculated using Equations (1), (2) and (3). For calculating rms field error of undulator, we should record the values in the positions whose distances from the centre of the magnet are integer times of Z. "V" magnets are recorded as B_{V0}, B_{V1}, B_{V2}, B_{V3}…. And for "H" magnets, they are B_{H0}, B_{H1}, B_{H2}, B_{H3}....

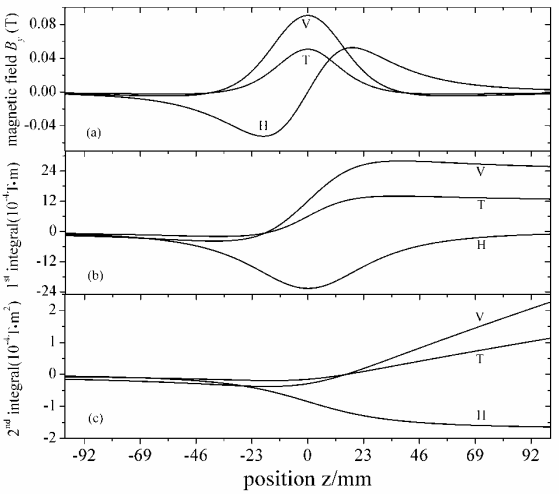

Figure 2: Distribution of magnetic field B_y, 1st integral and 2nd integral of individual magnet (remanence B_r=1T).

Figure 2 shows the distribution of magnetic field B_y (a), first integral (b) and second integral (c) of individual magnets (remanence B_r=1T).

To get the first integral of individual magnet I_1, we integrate B_y along the z-axis from $-\Delta z$ to Δz, where Δz is the distance between the centre of the magnet and the measured position. Integrating B_y twice, we can get the second integral I_2. For magnets with unit remanence (1T), "V" magnets: I_1= K_1, I_2= $K_1\Delta z$; "T" magnets: I_1= K_1/2 and I_2= $K_1\Delta z$/2; "H" magnets: I_1= 0 and I_2= K_2. When Δz is big enough, K_1 and K_2 are constants, decided by X, Y, Z, x, y. In our illustration, X=100mm, Y=23mm, Z=23mm, x=0, y=Y/2+g/2, Δz=600mm, K_1=2.4143mm, K_2=170.78mm^2, B_{v0}=0.0904T, B_{v1}=0.0246T, B_{v2}=-0.0034T, B_{v3}=-0.0043T; B_{H0}=0T, B_{H1}=0.0505T, B_{H2}=0.0106T, B_{H3}=-0.0012T.

Field Integrals Calculation of Undulator

For nth real magnets, field integral is given as:

If it is "H" magnet (n=3, 4, 4i-1, 4i...),

$$\begin{cases} I_{1,n} = (-1)^{\mathrm{INT}\left(\frac{n-1}{4}\right)} (-1)^n K_1 B_{r3,n} \\ I_{2,n} = (-1)^{\mathrm{INT}\left(\frac{n-1}{4}\right)} \left[(-1)^n K_1 B_{r3,n} \Delta z_n + K_2 B_{r2,n} \right] \end{cases} \quad (4)$$

If it is "V" magnet (n=5, 6, 4i+1, 4i+2…),

$$\begin{cases} I_{1,n} = (-1)^{\mathrm{INT}\left(\frac{n-1}{4}\right)} K_1 B_{r1,n} \\ I_{2,n} = (-1)^{\mathrm{INT}\left(\frac{n-1}{4}\right)} \left[K_1 B_{r1,n} \Delta z_n + (-1)^{n-1} K_1 B_{r1,n} \right] \end{cases} \quad (5)$$

If it is "T" magnet (n=1, 2, N-1 and N),

$$\begin{cases} I_{1,n} = (-1)^{\mathrm{INT}\left(\frac{n-1}{4}\right)} (-1)^n K_1 B_{r3,n} \\ I_{2,n} = (-1)^{\mathrm{INT}\left(\frac{n-1}{4}\right)} \left[(-1)^n \frac{K_1}{2} B_{r3,n} \Delta z_n + \frac{K_2}{2} B_{r2,n} \right] \end{cases} \quad (6)$$

For undulator, the first field integral I_1 and second field integral I_2 are given as:

$$I_1 = \sum_{n=1}^{N} I_{1,n} \qquad I_2 = \sum_{n=2}^{N} I_{2,n} \quad (7)$$

Rms Field Error Calculation of Undulator

The peak values of magnetic field appear at the centre of "V" magnets. So the total number of peak values in the undulator is INT(N/4)-1. The peak value is given as:

$$\begin{aligned} |B_i| = {} & B_{V0} \left[B_{r2,(4i+1)} + B_{r2,(4i+2)} \right] \\ & + B_{V1} \left[B_{r3,(4i-1)} - B_{r3,4i} - B_{r3,(4i+3)} + B_{r3,(4i+4)} \right] \\ & + B_{V2} \left[-B_{r3,(4i-3)} - B_{r2,(4i-2)} - B_{r2,(4i+5)} - B_{r2,(4i+6)} \right] \\ & + B_{V3} \left[-B_{r3,(4i-5)} + B_{r3,(4i-4)} + B_{r3,(4i+7)} - B_{r3,(4i+8)} \right] \\ & + B_{H1} \left[B_{r2,(4i-1)} + B_{r2,4i} + B_{r2,(4i+3)} + B_{r2,(4i+4)} \right] \\ & + B_{H2} \left[B_{r3,(4i-3)} - B_{r3,(4i-2)} - B_{r3,(4i+5)} + B_{r3,(4i+6)} \right] \\ & + B_{H3} \left[-B_{r2,(4i-5)} - B_{r2,(4i-4)} - B_{r2,(4i+7)} - B_{r2,(4i+8)} \right] \end{aligned} \quad (8)$$

Here, i=1,2,…, INT(N/4)-1, is the serial number.

For undulator, the rms field error is given as:

$$\sigma_B / |\overline{B}| = \frac{1}{|\overline{B}|} \sqrt{\frac{1}{\mathrm{INT}(N/4)-4} \sum_{i=2}^{\mathrm{INT}(N/4)-2} \left(|B_i| - |\overline{B}| \right)^2} \qquad (9)$$

MULTI-OPTIMIZATION MODIFIED SA

Simulated annealing (SA) is a technique used to find good approximate solutions for combination optimization problem. We apply a multi-optimization modified SA algorithm (with heating procedure and the best move strategy based on standard SA) to optimize the problem of PPM undulator magnets ordering [8]-[9].

The multi-objective functions are (s is a solution):

f_1(s): the rms field error of undulator;

f_2(s): the absolute value of first field integral;

f_3(s): the absolute value of second field integral.

Preliminaries

- A weighting function $S(s)$ is chosen:

$$S(s) = w_1 \frac{f_1(s)}{f_1(s_0)} + w_2 \frac{f_2(s)}{f_2(s_0)} + w_3 \frac{f_3(s)}{f_3(s_0)} \qquad (10)$$

  Here, w_1, w_2 and w_3 are weighting factors, and $w_1+w_2+w_3=1$.
- Parameters of the heating procedure are initialized as: h (the heating factor) and H_{step} (the heating length).
- Parameters of the cooling procedure are initialized as: T_0 (initial temperature, calculated in modified SA, but given in standard SA), α (the cooling factor <1) and N_{step} (the cooling length of temperature step).
- Two stopping criteria are fixed: T_{stop} (the final temperature) and N_{stop} (the maximum number of iterations without improvement).
- A neighborhood $N(s)$ of feasible solution in the vicinity of s is defined.

Procedures

- Initialization. Initialize w_1, w_2, w_3, h, H_{step}, α, N_{step}, T_{stop} and N_{stop}, set $m=n=H_{count}=N_{count}=0$; Draw at random an initial solution s_0, and evaluate $f_1(s_0)$, $f_2(s_0)$, $f_3(s_0)$ and $S(s_0)$; Set a list of potentially efficient solutions PE.
- Heating procedure. Draw at random a solution $s' \in N(s_n)$, and evaluate $f_1(s')$, $f_2(s')$ and $f_3(s')$ and $S(s')$; If $S(s')>S(s_n)$, we accept the new solution: $s' \rightarrow s_{n+1}$, $H_{count}= H_{count}+1$, else, $s_n \rightarrow s_{n+1}$. Update the list PE with the solution s', and set $n=n+1$. If $n=H_{step}$, then break and set $T_0=h \times H_{count}$, else, iterate.
- Cooling procedure. Randomly draw K solutions from the $N(s_n)$, and evaluate f_1, f_2, f_3 and S of them. Let the best solution among the generated K solutions be s'; Replace s_n by s' with probability:

$$p = \min\left[1, \exp\left(\frac{S(s_n) - S(s')}{T_m}\right)\right] \qquad (11)$$

  If s' is accepted $s' \rightarrow s_{n+k}$, $N_{count}=0$, else, $s_n \rightarrow s_{n+k}$, $N_{count}= N_{count}+K$. Update the list PE with the solution s'; Set $n=n+K$. $m=m+K$. If m/N_{step} is an integer, then $T_m=\alpha T_{m-k}$, else $T_m= T_{m-k}$; If $T_m< T_{stop}$ or $N_{count}=N_{stop}$, then stop, else, iterate.

OPTIMIZATION RESULTS

We use the following parameters: w_1=0.6, w_2=0.2, w_3=0.2, h=1.0, H_{step}=100, α=0.9, N_{step}=200, T_{stop}=0.0001, N_{stop}=500, K=10.

We initialize 10 orderings of magnets, and optimize each ordering by five methods, including modified SA, modified SA only with heating procedure (K=1), standard SA, Local Search ($T \rightarrow 0$) and Exhaustion approach. It takes approximately 100 seconds for each process (CUP 2.0G).

Table 1 shows the optimization results of modified SA and some other methods after 10 calculations of each. We can see that the ordering of magnets provided by SA can reduce the undulator field errors much more greatly compared with the results of other methods listed in the table. And modified SA is better than other SA Algorithms with smaller mean value and rms divergence.

Table 1: Optimization results of Modified SA and other methods

Algorithm	Rms field error (10^{-4})	1st integral (10^{-6}T·m)	2nd integral (10^{-6}T·m^2)
Initial solution	58.6±9.7	295±239	312±251
Modified SA	1.71±1.12	1.18±1.91	0.71±0.87
Modified SA (only with heating procedure)	1.82±1.14	1.55±1.40	3.22±4.67
Standard SA	2.13±1.28	1.13±1.59	0.42±0.47
Local Search	3.15±1.87	3.89±7.09	0.64±1.54
Exhaustion approach	31.9±3.8	26.1±23.5	17.4±17.9

In order to demonstrate the precision of the quick method in calculation of undulator field errors, we design a very precise three-dimensional program in which we first calculate undulator field according to remanence and positions of individual magnets, and then analyze the undulator. From Table 2, we can see the two results are very close (can be ignored considering the construction errors), but actually the time used by our quick method is over 1000 times less than the latter.

Table 2: Calculation results of objective functions by quick method and three-dimensional program (in parentheses)

	Before optimization	After optimization
Rms field error σ_B/B	0.653%(0.634%)	0.103‰(0.099‰)
1st integral (10^{-6}T·m)	-463.4 (-464.9)	-1.33 (-2.01)
2nd integral (10^{-6}T·m^2)	-566.5 (-568.3)	-0.79 (0.23)
Rms phase error σ_φ	/ (13.11)	/ (0.78)

Figure 3 shows the trajectory of electron beam before and after optimization. Angular deflection $\Delta x'$and orbital displacement Δx of electron beam are given as:

$$\Delta x' = \frac{300 I_1}{E[MeV]} \qquad \Delta x = \frac{300 I_2}{E[MeV]} \qquad (12)$$

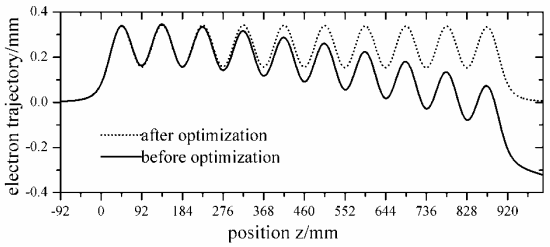

Figure 3: Electron trajectory before and after optimization

Figure 4 shows the spectrum of spontaneous emission before and after optimization.

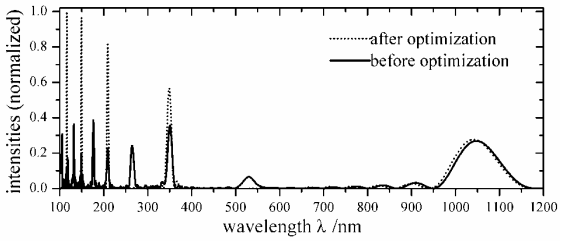

Figure 4: Spontaneous emission spectrum before and optimization

CONCLUSION

The optimization results exposed in this paper show that the undulator field errors can be greatly reduced (rms field error reduced to 0.01%, first field integral to 10^{-6}T·m, second integral to 10^{-6}T·m^2 and rms phase error to 1 degree). The field after assembly will inevitably differ from predictions from the optimization results due to the construction errors, and because of this reason, we don't consider the multipole field errors and set the weighting factors 0.6 for rms field error, 0.2 for first integral, 0.2 for second integral [5].

Once the magnets have been constructed and measured, the remaining errors can be overcome by swapping magnets, or more commonly by "shimming" [10]. Optimization of the magnets ordering can also save the time for field measurement and correction after assembling.

REFERENCES

[1] P.G. O'Shea, H.P. Freund. Free-electron lasers: status and applications. Science. 292 (2001) 1853.

[2] B.M. Kincaid. Analysis of field error in existing undulators. Nucl Instr and Meth. A 291 (1990) 363.

[3] E. Esarey, C.M. Tang, W.P. Marable. The effects of field errors on low-gain free-electron lasers. IEEE Journal of Quantum Electronics, 27 (1991) 2682.

[4] B.L. Bobbs, G Rakowsky, P. Kennedy, et al. In search of a meaningful field-error specification for wigglers. Nucl Instr and Meth. A 296 (1990) 574.

[5] R.A. Cover, G Rakowsky, B.L. Bobbs, et al. Undulator design for synchrotron radiation source using simulated annealing. IEEE Journal of Quantum Electronics. 31 (1995) 664.

[6] M.E. Couprie, C. Bazin, M. Billaron. Oprimization of the permanent magnet optical klystron for the super-ACO storage ring free electron laser. Nucl Instr and Meth. A 278 (1989) 788.

[7] R Hajima, F Matsuura. Advanced optimization of permanent magnet wigglers using genetic algorithm. Nucl Instr and Meth. A 375 (1996) 19.

[8] H Ishibuchi, S Misaki, H Tanaka. Simulated annealing with modified generation mechanism for flow shop scheduling problems. European Journal of Operational Research. 81 (1995) 388.

[9] J. Teghem, D. Tuyttens, E.L. Ulungu. An interactive heuristic method for multi-objective combinatorial optimization. Computers & Operations Research. 27 (2000) 621.

[10] J Chavanne, P Elleaume. Undulator and wiggler shimming. Synchrotron Radiation News. 8 (1995) 18.

DESIGN OF UNDULATOR FOR THE SHANGHAI DUV-FEL

Jia Qi-ka, Zhang Shancai, Lu Shengkuan, He Duohui
NSRL,University of Science and Technology of China, Hefei,China
Zhou Qiaogen, Cao Yun, Dai Zhimin, Zhao Zhentang
SSRF, Shanghai Institute of Nuclear Research, Shanghai, China

Abstract

The design study of the undu1ator for Shanghai deep ultra violate free electron laser source (SDUV-FEL) is presented. The optimum undulator parameters for the FEL performance have been studied. The scheme of focusing and segmentation is discussed. The requirements of undulator magnet field and main technical demand are given.

INTRODUCTION

The project SDUV-FEL [1] was proposed by Shanghai Institute of Applied Physics (SINAP), National Synchrotron Radiation Laboratory (NSRL), and Institute of High Energy Physics (IHEP) in 1998. The design and the relevant R&D of the SDUV-FEL facility have been under way since 2000. The aim of the project is to provide a high-brightness stable narrow-bandwidth coherent deep ultra-violet (DUV) source, and promote an R&D activity oriented to the development of a coherent X-ray source in China.

The SDUV-FEL project plan implement HGHG research in DUV wavelength， for the first step the SASE experiment study will be carried out in the spectral region about 260*nm*. The undulator system includes a modulator section, a dispersive section and a multi-segmented radiator. In this paper, the design study of the radiator undu1ator is presented. The optimisation of modulator and dispersive sections with the HGHG experiment will be given in a separate paper.

.

PARAMETER OPTIMIZED

The long undulator with high precision, small gap and transverse focusing is key technology for high gain short wave length FEL. Design and optimization of the undulator is impartible with design and optimisation of whole FEL experiment. The main design parameters of SDUV FEL are listed in the Table 1.

The design target of high gain FEL is to reach the maximum saturation power by the minimum saturation length. In principle the period of undulator should be as short as possible. But owning to wakefield effect, radiation damage and the practical condition limit, the undulator gap cannot be decreased along with the decreasing of undulator period. Therefore when the undulator period is decreased too much, the undulator parameter K will be too small and radiation power will be too weak. For our case, given radiation wavelength (88nm) and electron energy (~300MeV)，the selection range of λ_u and K are not large. Overall consideration gives the undulator parameters as Table 2

Table 1 Main parameters of the SDUV-FEL

FEL Wavelength (*nm*)	88
Electron beam Energy (*MeV*)	269
Bunch charge (*nC*)	1
Peak Current (*A*)	400
ε_N(*mm-mrad*)	4
Local energy spread (%)	0.1

. Table 2 Main parameters of the Undulator

type	hybrid
Gap(*mm*)	10
Period (*mm*)	25
Peak magnetic field (*T*)	0.6
Section number	6
Section length (*mm*)	1512.5
Drift between sections (*m*)	0.1
Average beta function (m)	~3.0
K	1.4

FOCUSING AND SEGMENTATION

The radiator undulator is about 10 meter long. In order to reach the best couple of electron beam and radiation the electron beam must be properly focused.

There are several schemes of focusing. For natural focusing the beta function β_{y0} (*cm*)=0.241γ/B_u(T) (with parabolic pole face: $\beta_n=\sqrt{2}\beta_{y0}$) is constant, the segment length can be chosen arbitrary. Natural focusing is weak and suitable for longer wavelength FEL. For integrate focusing which combine the focusing quadrupole magnet into the undulator, the technology is complex. The cost for long undulator is too much.

Separate focusing is a relatively simple scheme, which was adopted on the storage rings widely. But the segments length can't be chosen arbitrary. The break length restricted by the quadrupole magnet (and beam monitor) can't be too short. The FEL performance is affected by the "filling factor" of undulator.

The selection of focusing scheme is connected with the average beta function. For a given emittance, a smaller average beta function means a smaller beam size, a larger pierce parameter ρ, i.e. a shorter gain length. But a smaller average beta function also means larger angular spread at the same time. That makes the gain length longer. Therefore an optimal average beta function exists. The optimal beta function tie up with ε、σ_γ、and I_p, the choice shouldn't be too sensitive to the electron beam parameters.

To accumulate experience for future development of shorter wavelength FEL and considering complexity of technica, separate focusing scheme with FODO lattice is adopted.

For the FODO focusing, in the thin lens approximation, average beta function can be given as [2]:

$$\overline{\beta} = \frac{2f}{\sqrt{1-(\lambda_{FD}/4f)^2}} \geq \lambda_{FD} \qquad (1)$$

$$\lambda_{FD} = 2(L_i + l_d) \leq \overline{\beta} \leq \beta_n \qquad (2)$$

λ_{FD} is FODO period length, L_i and l_d is the undulator segment length and break length respectively. f is quadrupole focusing length. From expression (2) it can see that with shorter segment length a larger range of the average beta function can be available.

To make variation of e-beam envelope small, the variation of β should be small, namely

$$\frac{\beta_M}{\beta_m} = \frac{1+\lambda_{FD}/(4f)}{1-\lambda_{FD}/(4f)} \qquad (3)$$

should be small. It requires $\lambda_{FD}/(4f) \ll 1$, this also means prefer shorter segment length.

But the shorter segment length, the less "filling factor" of undulator is. That will cause the FEL saturation power to decrease greatly.

Average beta function, quadrupole focusing length, FODO period length and undulator segment length and break length satisfy the relation:

$$\overline{\beta} > 2f >> \frac{\lambda_{FD}}{2} \geq L_i >> l_d \qquad (4)$$

According the fitting formula of Xie Ming [3], the optimized average beta function is β^{opt} =1.26*m* (Fig.1), and ρ=2.87*10^{-3}, L_g=76*cm*, Z_R=1.37*m*, $\sigma_\perp$=0.098*mm* for the parameters of Table 1. The gain length dependence on emittance, energy spead and beam peak current are also given in Fig.1. The result demand $L_i + l_d < \beta/2$=0.6*m*, that is too short. In the formula of Xie Ming, the undulator "filling factor" is not considered.

To get more accurate result, the 3D simulation code GENESIS is used. The break length is included in the simulation, which is kept as 20*cm* long. The electron beam is matched into the undulator. The average beta function is varied by varying the quadrupole magnet field strength. The natural focusing effect is also included. From the simulation results (Fig.2 and Fig.3) 1.2*m* to 1.5*m* long segmentation is good choice for shorter gain length, higher saturation power and good control of beam size. So the segment is chosen as 1.5*m* long with a symmetric configuration and the optimal beta function is about 2.8*m*.

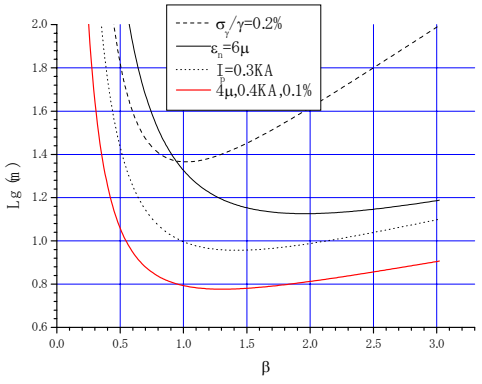

Fig.1 optimized β function by Xie Ming's formula

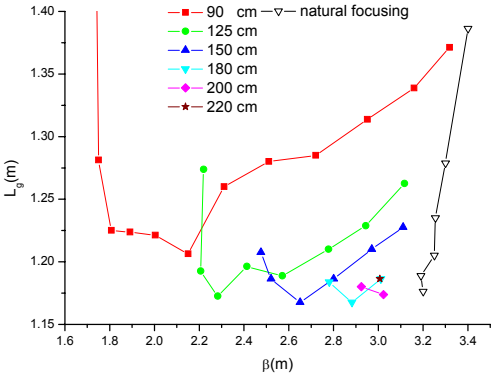

Fig.2 Gain length versus β
for different segment length

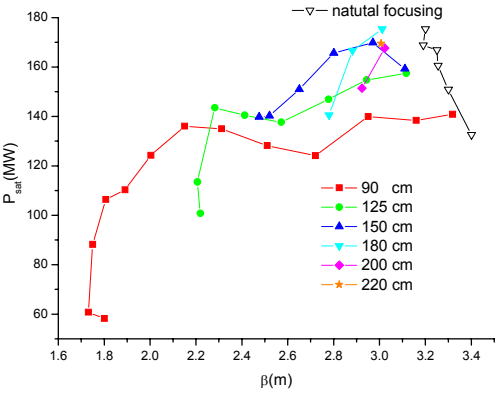

Fig.3 Saturation power versus β
for different segment length

All undulator segments should be in good consistency. The segments in succession must be well matched. The

phase matching and break length have the relation as follow

$$l_d = M\lambda_u\left(1+\frac{K^2}{2}\right)-\left[z_u+\left(L_i-z_d\right)\right]- \left(\frac{e}{mc^2}\right)^2\left[\int_{z_d}^{\infty}\left(\int_z^{\infty}B_u dz'\right)^2 dz+\int_{-\infty}^{z_u}\left(\int_{-\infty}^{z}B_u dz'\right)^2 dz\right] \quad (5)$$

where the M is an integer. The arrangement of undulators is shown as Fig.4. Where the quadrupole magnet is placed in the break length.

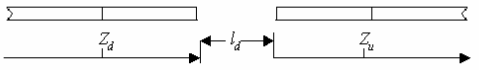

Fig.4 arrangement of undulator

The correctors will be used to correct trajectory, quadrupole offset and match phase. The end pole configuration is being carefully optimized to erase edge field's effect.

MAGNETIC FIELD REQUIREMENT

Field integral

We demand the gain bandwidth due to angular spread to be smaller than natural bandwidth, i.e. $\Delta x' < \sqrt{2\lambda_s \rho/\lambda_u}$. This gives the requirement for the field first integral

$$I(G.m) < 17\sqrt{\rho(1+K^2/2)} \quad (6)$$

For K=1.38, ρ=2*10^{-3}, it has I≤1G*m, it's not too difficult to achieve.

For the field 2nd integral we demand the transverse offset of electrons in the undulator to be smaller than the undulating amplitude of undulator. It gives:

$$\sigma_{II}(G.m^2) < \frac{\lambda_u(cm)K}{12\pi} \quad (7)$$

For K=1.38, ρ=2*10^{-3}, we have σ_{II}<9T*mm^2, corresponding σ_x<10μm, it is not easy to achieve.

Peak field error

Also from gain bandwidth requirements, it gives

$$\frac{\Delta B}{B} < \left(\frac{1}{2}+\frac{1}{K^2}\right)\frac{\Delta\lambda_s}{\lambda_s} \approx \rho \quad (8)$$

For our condition, it is about 0.002 and is rather difficult.

Phase error

Phase error will increase FEL gain length. [4,5].

$$L_g \rightarrow L_g e^{\frac{\sigma_\varphi^2}{3}} \quad (9)$$

$$\Delta L_g/L_g \cong \sigma_\varphi^2/3 \quad (10)$$

For σ_φ=10°, the gain length variation is $\Delta L_g/L_g \cong 1\%$, it is easy to realize.

Effects of quadrupole offsets

The misalignment of quadrupole will cause the FEL saturation length growth and power degradation. From the simulation result (Fig.5 and Fig.6), the tolerance on quadrupole offsets is Δx<20μm, $\Delta x'$<13μrad, the corresponding field integral is 2nd <18T*mm^2, 1st <120 G*cm.

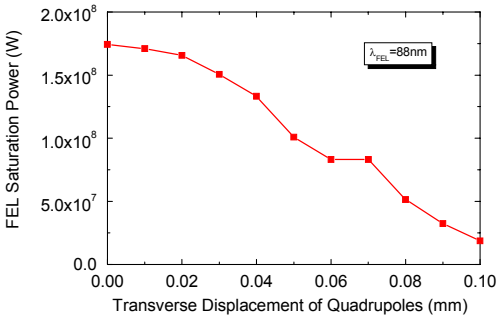

Fig.5 Effects of quadrupole offsets on the saturation power

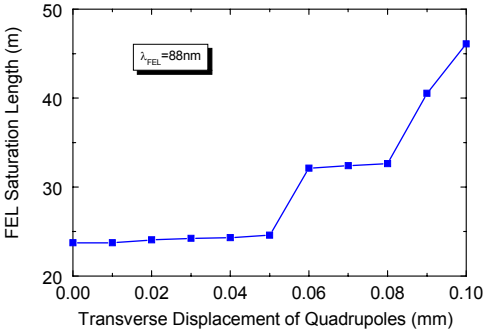

Fig.6 Effects of quadrupole offsets on the saturation length

TECHNICAL DESIGN

Considerations of Hybrid vs. PPM

For the pure permanent magnet (PPM) undulator the design and analysis is convenient, but the magnet block requirement is stringent, it needs more workload. For hybrid undulator the design and analysis is rather complicate. It can give higher peak field than PPM ones when g/λ_u < 0.4 (Fig.7), but the harmonic component may be larger, the field is highly affected by the pole shape. The segments matching problem is more serious for hybrid structure. The radiation damage problem is more serious for PPM structure. For our case (g/λ_u~0.4), either one can be used. The hybrid structure is chosen.

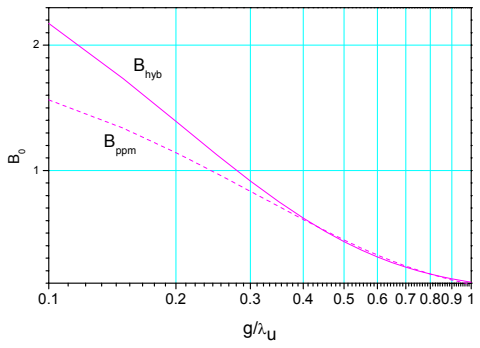

Fig. 7，Peak field versus gap/period

The peak field of hybrid undulator can be calculated by the following empirical formula

$$B_0 = 0.95ae^{-\frac{g}{\lambda_u}(b-c\frac{g}{\lambda_u})} \qquad 0.07\leq g/\lambda_u \leq 0.7 \quad (11)$$

$$\begin{cases} a = 0.55B_r + 2.835 \\ b = -1.95B_r + 7.225 \\ c = -1.3B_r + 2.97 \end{cases}$$

where B_r is the remanent field strength of permanent magnet. The permanent magnet material we choose NdFeB N38SH for it has enough high coercivity. The magnet pole, we choose vanadium permendur for its higher saturation field.

Pole geometry optimization

The goal of pole dimension optimization is that with sufficient field strength on the axis insured the field in the pole is far from saturation, the demagnetizing field in magnet block is not large, and magnet material is minimized [6].

Thickness (electron moving direction)： with the thicker permanent magnet the larger field can be achieved, but the harmonic field may be larger too. The thickness rate of pole and magnet block usually is z_p/z_m~1/2.

The height (gap direction) of magnet and pole is chosen as y_m/y_p~1.2. [7]

The width (undulating direction) of magnet and pole are determined by good-field-region requirement ($\Delta B/B$<ρ in sufficient wide range). Usually y_m/x_m~0.9 is chosen. The final geometry dimension is as follow:

For the magnet: z_m=8±0.011*mm*, y_m=45±0.05*mm*, x_m=60-0.10*mm*, perpendicular of magnet：±0.02 *mm*

For the pole: z_p=4.5+0.012*mm*, y_p=38±0.012*mm*, x_p=40-0.050, -0.089*mm*.

To avoid saturation of the pole, the all edges of pole and magnet facing toward gap are chamfered.

The numerical simulation by OPERA-3D show that the maximum field is 0.64*T*, the good field for $\Delta B/B_0$=0.1% is about ±8.5*mm*. And good field for $\Delta B/B_0$=0.2% is about ±9.9*mm*. The worst demagnetizing field is adjacent to the end corner of pole and just above the chamfer.

Mechanical design

A C type girder support structure is chosen. A fixed gap is adopted to simplify the fabrication. The magnetic force between poles is 710*Kg*. The main mechanical requirements and specifications are:

1) The beam parallelism：0.02*mm*
2) Pole gap tolerance ±0.05*mm*.
3) Neighbour pole gap difference tolerance ±0.03*mm*
4) Pole displacement in "z" direction (top and bottom) ±0.10*mm*

Minor adjustment can be done individually for each pole to tune the field. The base of undulator can be vertically and horizontally adjusted. The alignment precision for horizontal direction is about 5μm, and for vertical direction is given by:

$$\Delta y = \frac{\lambda_u}{\pi}\sqrt{\frac{\Delta B}{2B}} < 0.25mm \qquad (12)$$

Now a two periods prototype of undulator is under construction. The optimal design of undulator end part is under way. The much more detail work will be continued.

REFERENCE

[1] Z.T.Zhao et al., Nucl.Instr. & Meth. A**528**,pp591-594,2004
[2] TESLA Technical Report Part V, Eds.:G.Materlik, T.Tschentscher, DESY Report 2001-XX, Chapter 4(2001)
[3] M.Xie, Proc. PAC95, 183(1995)
[4] Kwang-Je Kim, Nucl.Instr. & Meth.A445 (2000) 24
[5] Jia Qi-ka, High Power Laser and Particle Beams, Vol.14, No.2, (2002) pp165-168
[6] LCLS Conceptual Design Report Chapter 8 (2002)
[7] R.D.Schlueter, China Accelerator Physics School(1998)

STUDY OF CONTROL GRID THERMIONIC CATHODE RF GUN

Xiao Jin#, Xinfan Yang, Ming Li, Yanan Chen, Xumin Shen, Jie Liu, Zhou Xu,
Applied Electronics Institute, CAEP, China

Abstract

In this paper, the beam loading effect in the thermionic cathode RF Gun was studyed. To minimize the energy spread in macropulse of RF Gun, a design of Control Grid Thermionic Cathode RF Gun was given. In numerical simulation, the result of this kind RF Gun is: electron beam energy is 2MeV, transverse emittance is 23πmm.mrad, micropulse width is 25ps, micropulse beam current is 12A. The primary experiments has been done. For 1% electron beam energy spread selected by α magnet, the beam current can get 400mA.

1 INTRODUCTION

The thermionic RF-gun has been widely used in FEL experiment. The main problem of thermionic RF-gun is electrons back bombardment.

At CAEP, a L-band thermionic RF-gun was used for the 100um FEL device. To produce 4us macropulse electron beam, the micropulse current in 2% energy spread is limited by effect of back bombardment to 5A. The electron back bombardment change the beam load of thermionic RF-gun, and increase the electron energy spread in beam macropulse. To increase the beam current, the effect of back bombardment must be controlled.

2 EFFECT OF BACK BOMBARDMENT

The standing wave accelerator includes RF generator, circulator, coupler, and cavity (Fig. 1). And its equivalent circuit can be drawn as figure 2.

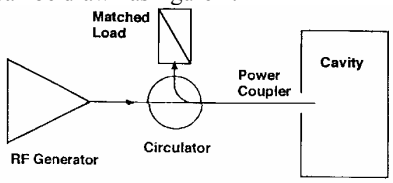

Figure 1: RF system of the standing wave accelerator[1].

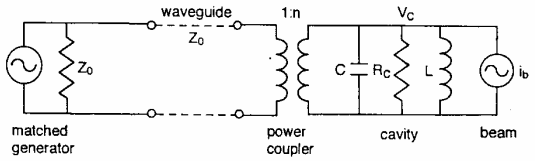

Figure 2: The equivalent circuit of the standing wave accelerator[1].

By the equivalent circuit of accelerator, the stored energy of cavity is

$$\Delta U = CV_c\left(V_{\max} - V_c\right)\frac{\Delta t}{\tau} \tag{1}$$

Where $V_{\max}$ is the maximum voltage of cavity without electron beam, V_c is the voltage of cavity, $U = (1/2)CV_c^2$ is the stored energy, and τ is the resonance time constant.

For the steady-state of cavity, the average electron beam power P_b equals to the increasing of stored energy of cavity.

$$P_b = CV_c\left(V_{\max} - V_c\right)\frac{1}{\tau} \tag{2}$$

We express $\tau = 2Q/\omega$ and $Q = \omega U/(P_{ex} + P_c)$, where P_{ex} is the external power dissipated, P_c is the power dissipated in cavity wall. Substituting these expressions into Eq. 2, we can get

$$V_c = V_{\max}\frac{P_{ex} + P_c}{P_{ex} + P_c + P_b} \tag{3}$$

So, the change of cavity voltage can be written as

$$\frac{dV_c}{V_c} = -\frac{1}{1 + \dfrac{P_{ex} + P_c}{P_b}}\frac{dP_b}{P_b} \tag{4}$$

For the accelerator design, the waveguide-to-cavity coupler is always set to critically coupled with the designed beam current. So Eq. 4 can be written as

$$\frac{dV_c}{V_c} = -\frac{1}{2 + 2\dfrac{P_c}{P_b}}\frac{dP_b}{P_b} \tag{5}$$

When the beam power is larger compared with the average power dissipated in cavity wall, the change of electron beam load will remarkably influence the beam energy. Figure 3 shows the electron beam waveform of thermionic RF-gun in CAEP.

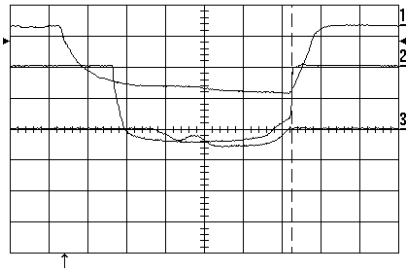

Figure 3: Electron beam waveform of thermionic RF-gun(<ch1>).

#xiao_jin@hotmail.com

3 CONTROL GRID THERMIONIC RF-GUN DESIGN IDEA

In FEL experiment, the electron beam energy spread must be controlled strictly (always less than 1%). So the main problem of thermionic RF-gun is the effect of back bombardment. The process of the back bombardment is:

- Electrons back bombardment
- The temperature of cathode increasing
- The electron beam current increasing
- The electric field of cavity reducing
- Electron beam energy reducing

So there are many methods to minimize the effect of back bombardment.

- To control the electrons back bombardment, we can carefully design the cavity, use the cathode with a hole in center, use the magnetic field, et al.
- To control the temperature of cathode, a laser can be used to heat the cathode.
- To control the electron beam current, we can use the control grid electron gun.
- To control the electric field of cavity, the power of microwave is needed to be controlled.
- To control electron beam energy, a external electrical source can be used to change the electrical potential of cathode.

In our design of the new RF-gun, the control grid electron gun was used. To minimize the emittence of the electron beam, the grid was put into the first cell. Figure 4 shows the position of the grid and the cathode. The space between grid and cathode is about 0.9mm, the voltage of cathode is 600-1000V. Figure 5 shows the structure of the new RF-gun cavity. .

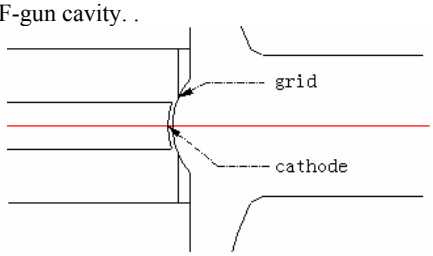

Figure 4: Structure of the RF-gun near the cathode.

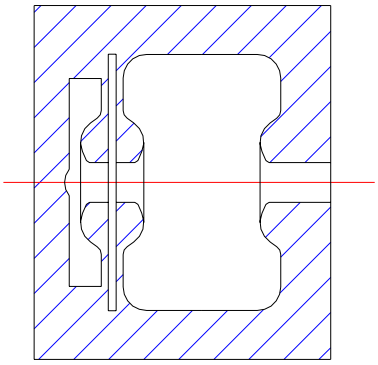

Figure 5: Structure of the RF-gun cavity.

4 SIMULATION RESULT

The first cells of the RF-gun act as a bunching segment too. The bunching segment makes the electron and the microwave synchronize better and more electron will be captured. The SUPERFISH CODE and the GPT CODE has been used to calculate the electron beam. The current of the cathode is 2A. The field ratio of the second cell to the first cell is about 4, the electrons get energy mainly from the second cells.

The simulation result (energy spread 1%) is: beam energy is 2MeV, emittence is 23pi mm*mrad, micropulse width is 25ps, micropulse current is 12A. Some simulation results show in figure 6 and figure 7.

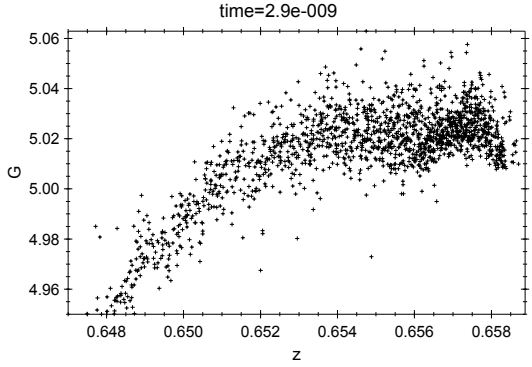

Figure 6: Electron beam energy distribution at the exit.

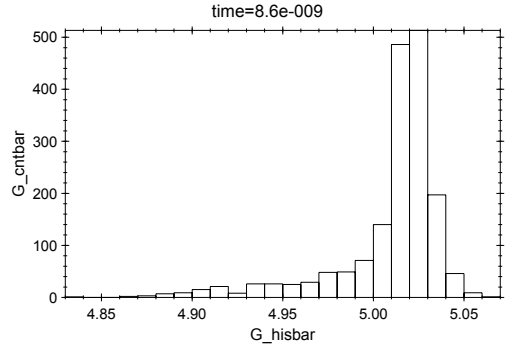

Figure 7: Electron beam energy spectrum.

5 EXPERIMENT RESULT

The characteristic parameters of the control grid RF-gun are measured by net work analyzer: The resonant frequency of the π/2 mode is 1300.16MHz, the coupling coefficient of the wave guide to the cavity is 5.2. The klystron microwave source is 3.5MW. The voltage between grid and cathode is 400V. The macropulse width is 4μs, the beam current at the a magnet exit during the macropulse up to 400mA. Fig.8, Fig.9, and Fig.10 show some pictures of the new RF-gun and some experiment results.

Figure 8: Picture of control grid electron gun.

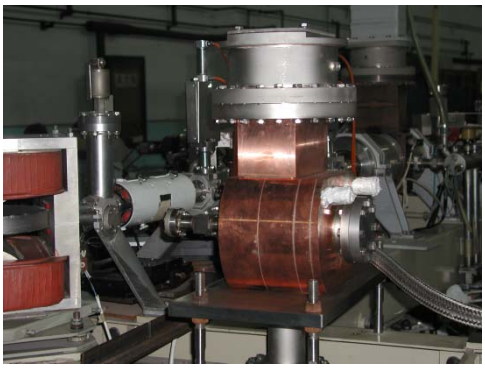

Figure 9: Picture of the new RF-gun.

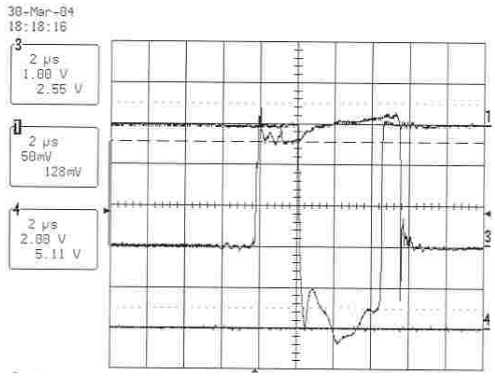

Figure 10: Electron beam waveform of the new RF-gun(<ch1>).

6 CONCLUSIONS

The thermionic cathode RF gun is a kind of excellent electron source. In this work, the control grid electron gun has been used to reduce the effect of back bombardment. The experiment results show that these methods work efficiently. But we also found that the beam emittence is larger than simulation result.

REFERENCES

[1] Wangler T P, Principles of RF Linear Accelerators, New York, J. Wiley & Sons Inc., 1998

SUPERCONDUCTING UNDULATOR WITH VARIABLY POLARIZED LIGHT

C. S. Hwang*, P. H. Lin, W. P. Li, C. H. Chang, T. C. Fan
NSRRC, 101 Hsin-Ann Road, Hsinchu Scien Park, Hsinchu 30077, Taiwan

Abstract

This study investigates planar in-vacuo superconducting elliptically polarized undulators with periodic length of 5 cm (SEPU5) producing linearly and circularly polarized infrared rays or x-rays source. The vertically wound racetrack coil is chosen for the coil and pole fabrication of the SEPU5. When the up and down magnetic pole arrays with alternative directions rotated wires in the horizontal plane, an elliptical field radiates elliptically polarized light in the electron storage ring, the free electron laser (FEL), and the energy recovery linac (ERL) facilities. Meanwhile, an un-rotated wire magnet array is constructed together with the rotated wire magnet array on the same undulator is used to switch the linear polarization in horizontal and vertical, as well as the right- and left-circular polarization radiation. This investigation describes the main factors of the planar and helical undulator design for FEL and the concepts concerning the magnet array structures of the superconducting undulators.

INTRODUCTION

The circular polarization mode of the elliptically polarized undulator provides the high gain and high flux in the FEL scheme. Several schemes [1-4] have been developed to generate the function of linear and helically distributed fields, using electromagnets with copper coils, and hybrid or pure structures with permanent magnets in various configurations. These schemes, either with helical geometry, which combines separate horizontal and vertical devices, or with planar geometry with a variable phase, yield variably polarized light. A planar superconducting elliptical polarization undulator [5] with 5 cm period length (SEPU5) produces a helical field in the storage ring, and in the FEL or ERL accelerator facilities are developed. This magnet provides more intense right- and left-circularly polarized light, and is linearly polarized in the horizontal and vertical direction. Combining two magnet arrays with (inner magnet array) and without (outer magnet array) pole rotation in the same structure creates various tunable polarizations. The vertical-winding racetrack coil structure for the in-vacuo superconducting undulator [6] is chosen for the requirements of the tunable polarizations function. Therefore, given a periodic length of 5 cm and a gap of 13 mm and 23 mm for the outer and inner magnet array, respectively, the maximum magnetic flux densities in the helical undulator are B_z = 2.7 T and B_x = 0.54 T when the wires are rotated by 35°[7]. When the SEPU5 operated with 100 MeV energy of the linac accelerator, the SEPU5 provides 1-10 μm circular polarization IR wavelength in the FEL facility for the user requirements in Taiwan. Additionally, the SEPU5 can also provide horizontal and vertical linear polarization in the energy ranges of 1-100 μm and 1-10 μm, respectively. This study describes concepts related to the elliptical, helical and linear polarization mode in the same undulator, and presents the design of the magnet array structures of the elliptical superconducting undulators. The use of two different excitation currents to generate the mechanism of the polarization switching in the right- and left-circular polarization radiation and linear polarization is discussed. Furthermore, the features of magnetic field and photon spectra on the in-vacuo superconducting elliptical polarization undulators are also elucidated. Finally, the photon flux in different polarization mode and the mechanism of the switching polarization radiation are discussed.

*cshwang@nsrrc.org.tw

DESIGN CONCEPT OF THE SWITCHING POLARIZATION MECHANISM

Two planar magnet arrays with period length of 5 cm comprise the superconducting elliptical polarization undulator (SEPU5) structure. The outer magnet array has a rotated pole [5,8] that the rotation angle is 35° and the inner magnet array does not have a rotated pole [9]. The two magnet arrays are combined as in Fig. 1. According to this SEPU5 structure, the maximum magnetic force between the two magnet arrays is about 4.5 kg. However, each coil in every pole was divided by four parts to analysis the force in the local coil between the two magnets arrays. The maximum force is 10 kg in the local coil parts. Hence, the force between the local parts is not an issue on the magnet operation. The total energy of this magnet is 56 kJ. Table I lists the main design parameters of the superconducting elliptical polarized undulator.

Depending on the IRFEL requirement in NSRRC, the Rayleigh range Z_R is 1 m and the maximum optical beam waist $w_0 = (Z_R\lambda/\pi)^{1/2}$= 1.75 mm in the photon wavelength between 1-10 μm. Therefore, the undulator minimum gap was estimated as g_{min}= 5 w_0 + 2t = 13 mm. Where t denotes the thermal shielding and redundancy factor for the superconducting magnet operation. The excitation current J_i and J_o on the superconducting coil of the inner array and outer array is independent. In this structure, the polarization can be switched via different combinations of the two-excitation currents. Table II lists the features in the six types of polarization mode by different combinations of the two-excitation currents in the superconducting elliptical polarized undulator. The polarization modes are changed by the different

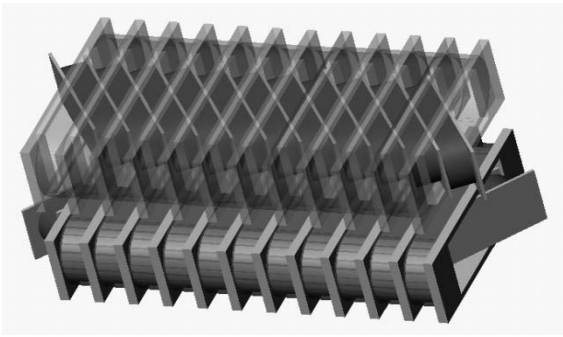

Figure 1: 3D schematic drawing of the superconducting elliptical undulator structure. The pole of the inner magnet array rotated 35° and the outer magnet array displays no pole rotation.

Table 1: Design parameters and features of the superconducting elliptical polarization undulator.

Number of poles	80
Periodic length λ_u (cm)	5
Magnet gap g of inner (outer) array (cm)	1.3 (2.42)
Physical length L (cm)	220
Inner pole rotation angle θ (deg)	35
Outer pole rotation angle θ (deg)	0
Field strength on coil B_s (T)	4.6
Maximum excitation current J_i (A/mm^2)	678
Maximum excitation current J_o (A/mm^2)	850
Total energy (kJ)	56.04
Force between magnet arrays {F_x,F_y,F_z}(Kg)	{1, 1, 4.5}

combination of the two-excitation currents. (1) When the inner and outer magnet array is excited by J_i =678 A/mm^2 and J_o =0, respectively, the SEPU5 produces an elliptical field with field strength of B_z = 1.34 T and B_x = -0.5 T. This operation mode is a right elliptical polarization mode. In this mode, high-energy photon is radiated by means of the higher harmonic spectra. (2) If the current J_o = -398 A/mm^2 was also excited on the outer magnet array, then the elliptical field becomes the helical field with the field strength of B_z = -B_x = 0.5 T. In this operation mode provide a right circular polarization. (3) If the current continuously increases to J_o = -620 A/mm^2, then the right circular polarization becomes the vertical linear polarization with the field strength of B_z = 0 T and B_x = -0.5 T. (4) If the current continuously increases to J_o = -750 A/mm^2, the vertical linear polarization becomes the left elliptical polarization with field strength of B_z = -0.3 T and B_x = -0.5 T. (5) If the current continuously increases to J_o = -850 A/mm^2, the left elliptical polarization becomes a left circular polarization with field strength of B_z = B_x = -0.5 T. (6) If the excitation current was set at J_i = 0, J_o = 678 A/mm^2, then the SEPU5 produces horizontal linear polarization with field strength of B_z = 1.8 T and B_x = 0. Table II lists the relationship between the polarization mode and the excitation current combination.

SPECTRA FEATURES OF THE SUPERCONDUCTING ELLIPTICAL UNDULATOR

The SEPU5 operates in a 100 MeV linac to provide the infrared source between 1-10 μm. Figure 2 shows the spectra features of the SEPU5 operated on a different polarization mode in the 100 MeV electron accelerator energy. The high radiation gain and flux occurs in the circular polarization mode that only exists in the first harmonic spectrum, Fig. 2 only showed the flux in the circular polarization mode and in the first harmonic spectra of the elliptical and linear polarization modes. However, in the storage ring or ERL accelerator facility, the higher harmonic spectra can be extended to higher energies. Figure 2 reveals a higher flux in the right- and left-circular polarization mode, and demonstrates that the energy spectrum range is between 1-8 μm. However, to extend the spectrum energy range, the elliptical polarization mode was selected to provide the energy range of 1-30 μm. However, the circular polarization rate is reduced in the elliptical polarization mode, and the photon flux is smaller than the circular polarization mode in the same energy range. Additionally, Fig. 2 shows that the SEPU5 also provides the horizontal and vertical linear polarization mode. If the SEPU5 was operated in the vertical (horizontal) polarization, the spectrum energy range will be located in the range 1-6 (1-60) μm. However, the photon flux is also slightly smaller than that in the elliptical polarization mode. If the higher harmonic spectra radiates from the SEPU5 in the 3 GeV storage ring or ERL, the energy can reach up to 4 keV. Figure 3 shows the higher energy photon in the soft x-ray region was radiated in the 3 GeV accelerator facilities.

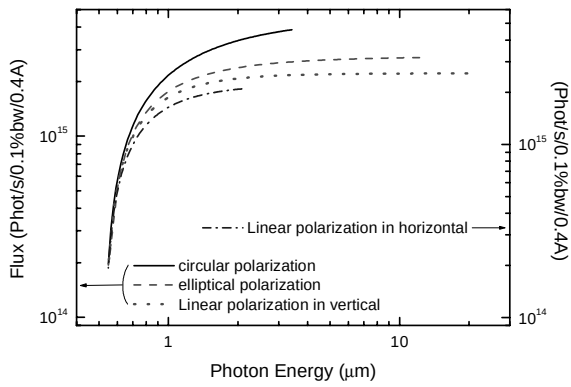

Figure 2: Spectra distribution of various polarization modes in the superconducting elliptical polarization undulator (SEPU5) was obtained in the 100 MeV electron linac.

Table 2: Combination of the excitation current for different polarization mode on the superconducting elliptical polarization undulator. Six polarization modes exist that are operated in the electron energy 100 MeV: Right Elliptical Polarization (REP), Left Elliptical Polarization (LEP), Right Circular Polarization (RCP), Left Circular Polarization (LCP), Vertical Polarization (VP) and Horizontal polarization (HP).

	REP	**LEP**	**RCP**	**LCP**	**VP**	**HP**
Excitation current J_i (J_o) (A/mm^2)	678 (0)	678 (-750)	678 (-398)	678 (-850)	678 (-620)	0 (678)
Magnetic flux density B_z (B_x) (T)	1.3 (-0.5)	-0.3 (-0.5)	0.5 (-0.5)	-0.5 (-0.5)	0 (-0.5)	1.8 (0)
Flux @ 1(6) μm (p/s/0.1%bwx10^{15})	1.7 (2.3)	1.9 (2.9)	2.2 (3.3)	2.2 (3.3)	1.7 (2.0)	1.7 (2.0)
Spectrum energy range (100 MeV) (μm)	30 – 1	7 – 1	8 – 0.96	8 – 0.96	6 – 0.99	60 – 1
Deflection parameter K_z (K_x)	6.3 (2.3)	1.3 (2.3)	2.3 (2.3)	2.3 (2.3)	0 (2.3)	8.4 (0)

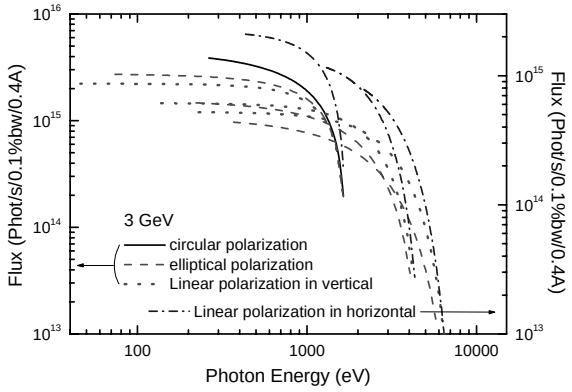

Figure 3: Spectra distribution obtained in the 3 GeV electron energy on various polarization modes.

CONCLUSION

It is possible and feasible to radiate the circular and linear in horizontal and vertical polarization light in an in-vacuo superconducting elliptical undulator. For the infrared ray FEL in a 100 MeV electron linac, the superconducting elliptical undulator with period length of 5 cm radiates the energy range between 1-30 μm in the elliptical polarization light or between 1-60 μm in the horizontal linear polarization light. The switch between all polarization modes does not involve mechanical movements and simply tunes the excitation current on the inner and outer magnet array. In addition, the in-vacuo superconducting elliptical undulator can also operate in the medium-accelerator storage ring or the ERL facility with shorter period length, and can use the higher harmonic spectrum to extend the energy range to the hard x-ray range.

ACKNOWLEDGEMENTS

The authors would like to thank the National Science Council of Taiwan for support of this research under Contract No. NSC93-2112-M-213-001. Mr. H. H. Chen and M. H. Huang are appreciated for discussing mechanical structure of the elliptical undulator.

REFERENCES

[1] K. Halback," Physical and optical properties of rare earth cobalt magnets", Nucl. Instrum. Methods Phys. Res., Sect. A 187, 109 (1981).

[2] H. Onuki," Elliptically polarized synchrotron radiation source with crossed and retarded magnetic fields", Nucl. Instrum. Methods Phys. Res., Sect. A 246, 94 (1986).

[3] S. Sasaki, " Analysis for a planar variable-polarizing undulator", Nucl. Instrum. Methods Phys. Res., Sect. A 347, 83 (1994).

[4] R. P.Walker and B. Diviacco, " Studies of insertion devices for producing circularly polarized radiation with variable helicity in ELETTRA", Rev. Sci. Instrum. 63, 332 (1992).

[5] A. Bernhard, B. Kostka, R. Rossmanith, et al., " Planar and planar helical superconducting undulators for storage rings: state of the art", 9th European particle accelerator conference (EPAC 2004), 5-9 July 2004, Lucerne, Switzerland.

[6] C. S. Hwang, W. P. Li, P. H. Lin, C. H. Chang, "Comparison of Predesign Parameters for Mini-Pole In-Vacuo Superconducting Undulators", IEEE Trans. On Appl. Supercon. (in press).

[7] C. S. Hwang, P. H. Lin, "Comparison of two superconducting elliptical undulators for generating circularly polarized light", Phys. Rev. ST Accel. Beams. (in press).

[8] S. Sasaki, " Concept design for a superconducting planar helical undulator", presented in the Workshop on Superconducting Undulators & Wigglers, Grenoble, June 30 – July 1, 2003.

[9] Andreas Geisler, Achim Hobl, Detlef Krischel, Robert Rossmanith, and Michael Schillo, "First field measurements and performance tests of a superconductive undulator for light source with a period length of 14 mm", IEEE Trans. On Appl. Supercon. 13, No. 2, 1217 (2003).

COMMISSIONING OF STRONG TAPERED UNDULATOR DEVELOPED FOR IFEL ACCELERATOR

S.V. Tolmachev[#], A.A. Varfolomeev, A. Varfolomeev Jr., T.V. Yarovoi,
RRC "Kurchatov Institute", Moscow 123182, Russia,
P. Musumeci, C. Pellegrini, J. Rosenzweig,
UCLA, Los Angeles, CA 90085, USA

Abstract

Here we describe the manufactured KIAE-2p planar undulator designed for the Inverse Free Electron Laser experiment at the University of California in Los Angeles. New technology enabled to fabricate the installation responding to the stringent requirements on mechanical construction accuracy and magnetic field strong tapering. Results of the magnetic field measurements by different methods are given. The obtained magnetic field maps were used for final simulations of the acceleration process. It is shown that for nominal electron beam and laser beam parameters up to 30% of electrons can be captured and accelerated from initial 14 MeV up to 52 MeV. Special analysis of the undulator acceptances for these parameters is made. It is shown that the acceleration is possible up to energies >30 MeV for rather wide ranges of laser pulse energy, Rayleigh length and e.b. emittance.

INTRODUCTION

The KIAE-2p undulator was designed and manufactured for the UCLA – Kurchatov Institute IFEL project [1,2]. Physical requirements for the undulator and simulations results of the design were given earlier [3]. The main particularity of the undulator is strong tapering of both magnetic field periods and strength of the fields as well. This tapering is required since the projected Inverse FEL should be driven by a high power CO2 laser beam focused inside the undulator by a lens with rather small focus distance. The nominal Rayleigh length (3.6 cm) is relatively small in comparison with the size of the IFEL installation so diffraction of the laser beam should be taken into account. This diffraction dominated regime was carefully investigated in a series of numerical simulations [4–7] results of which were used in the designing of the undulator.

UNDULATOR CONSTRUCTION

Technical problems followed from the undulator requirements could not be solved without new technologies unusual for routine undulator production. To make the problem of magnets and poles supports less complicated a new type of support construction was suggested and used (Fig. 1). The basic array of poles is made as a frame from titanic (non magnetic) side blocks (2) and profiled permendure (magnetic) central block melted in one block. Windows between poles were cut out by electroerrosion method, enabling to provide the required high accuracy of the shaped construction.

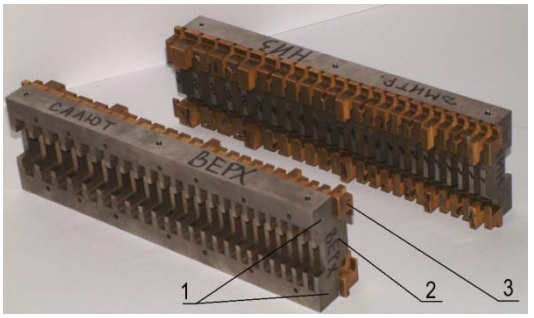

Figure 1: Photo of the melted block systems: 1 – non-magnetic side blocks; 2 – permendure central block; 3 – magnets fixation.

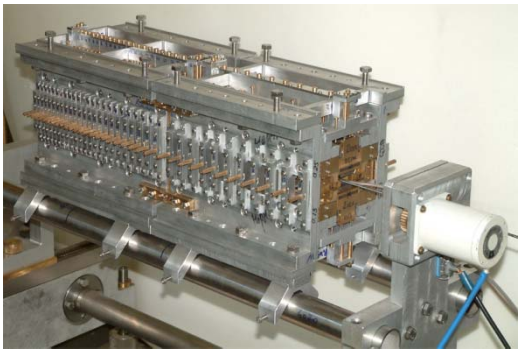

Figure 2: Common view of the KIAE-2p undulator with the Hall probe stepmotor driver.

Higher fields in comparison with routine hybrid undulators were needed. Enhancement over Halbah limits of the fields was required. For this purpose new cone shape of poles (2) were used. Not equal magnetic field fluxes of two neighbouring magnet cells required by strong tapering were achieved by using coneshaped side magnets with specific support systems. Common view of the assembled two section undulator is shown in Fig. 2.

Two sections of the undulator were mounted on tube rails as a support. Alignment of the two sections mounted on the rails was performed with using a granite table. Small slopes have been got. The first section axis gives deviation <0.012 mm on the total section length. The second section was aligned up to <0.003 mm and the slope between two undulator section axes gives <0.003 mm misalignment.

[#]tsv@kiae.ru

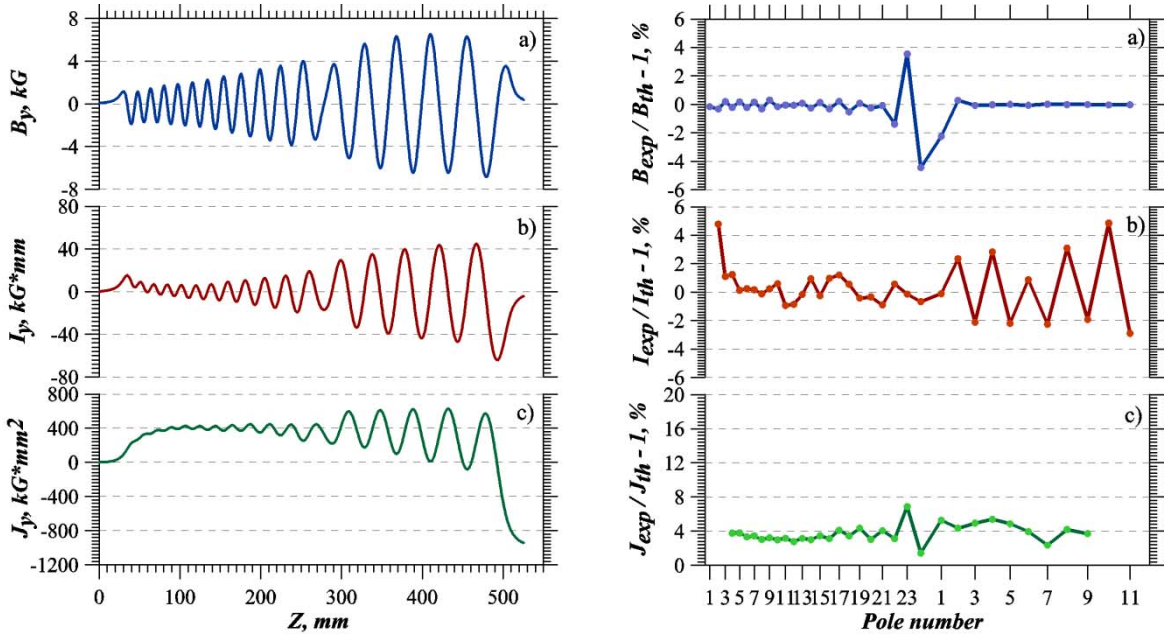

Figure 3: Magnetic fields directly measured by the Hall probe (a) and following from (a) the first (b) and the second (c) field integrals of KIAE-2p undulator (left graph). Deviations from projected ones respectively (right graph).

MAGNETIC FIELD TESTS

During tuning and commissioning the undulator magnetic fields were measured with high accuracy and by different methods. Some special measures were used to get high precision. A unit was manufactured for automatic scanning by the Hall probe. So it was possible to make measurements in many (from 60 to 200) points per one period length. For the same reason of getting high precision very small Hall probe crystal was used ($0.5\times1.0\times0.38$ mm^3) with very high (10^{-5}) stability of the current supply. Hall probe voltage was measured with accuracy ±0.1 μV. Calibration of the Hall probe was made with using a special reference magnet. As a result the Hall probe mean response ratio was found to be 7.9 μV/G. For more higher precisions corrections on nonlinearity of this response has been taken into account. The Hall probe was fixed on a special nonmagnetic carriage which could be moved by a stepmotor driver (Fig. 2) along the undulator axis in the gap keeping the Hall probe just on the undulator axis. Total accuracy of the magnetic field measurements ±0.1 G was achieved. Tuning of the undulator fields was made by moving side magnets or small moveable pieces of the poles. In extreme cases the basic magnets and (or) side magnets interchanged positions in the frames what gives some kind of sorting.

After the first stage of tuning magnetic field profiles became similar to that found in simulations [7] within ±0.08%. At the same time for the second integral of the field deviations were not so small. An additional tuning was needed to improve the field integrals. It was made by admitting some larger field deviations. The final results of the field tuning using Hall probe are given by Fig. 3. Deviations of the measured magnetic fields, first and second field integrals from the projected ones are also given. The field deviations here are ±0.4%, and grow up to 4% in the intersection gap caused probably by small geometrical changes in this gap. The second integrals coincide with the theoretical ones within 5%.

For the final testing of the second field integrals and focusing ability of the undulator the pulsed wire method was used. A BeCu wire of 50 μm diameter and 1.6 m long was used. Special optical detector provided sensitivity 247 μm/V at working range 60 μm. To get information about the focusing properties of the undulator the wire should be positioned parallel to the undulator axis in transverse (x or y) direction [8]. Fig. 4 shows measurement results for both the horizontal and vertical planes respectively. It is seen, that for the horizontal wire displacement curves remain parallel to the undulator axis showing absence of the defocusing in x-z plane. For the vertical wire displacement curves are inclined to the undulator axis showing that focusing in y-z plane takes place.

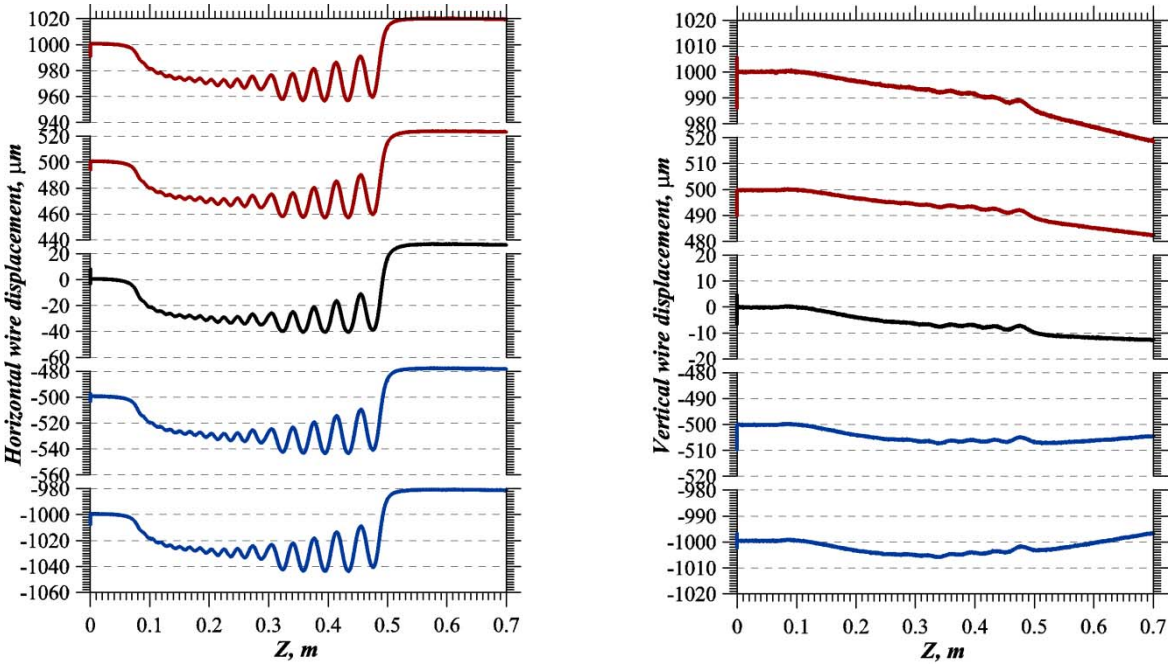

Figure 4: Illustration of the horizontal (left graphs) and vertical (right graphs) focusing properties of the KIAE-2p undulator measured by pulsed wire method.

ACCEPTANCE FOR THE LASER BEAM PARAMETERS PROVIDED BY THE UNDULATOR

As a final test of the tuned magnetic fields a new simulation of the acceleration process was made with using the measured magnetic field map (Fig. 3). Calculations of the maximum accelerated electrons energy γ_{max} and the capture ratio χ were made for different deviations from nominal ones in laser pulse energy, Rayleigh length z_r and laser focus position z_f. Results are summarized in Table 1.

Table 1. Simulation results

Laser and e-beam parameters	Laser power, GW		
	250	300	400
Nominal regime			
z_r = 3.6cm, z_f = 0 cm γ_o =28.5, ε =10 mm·mrad			γ_{max}=105, χ=34%
Not nominal regime			
z_r = 1.8cm, z_f = 0 cm γ_o =28.5, ε =10 mm·mrad	γ_{max}=42, χ=0%	γ_{max}=53, χ=1%	γ_{max}>95, χ=3%; γ_{max}>90, χ=4%; γ_{max}>85, χ=6%
z_r = 1.8cm, z_f = -2.0 cm γ_o =28.5, ε =10 mm·mrad	γ_{max}=50, χ=0%	γ_{max}>85, χ=2%; γ_{max}>80, χ=8%; γ_{max}>75, χ=9%	γ_{max}>85, χ=2%; γ_{max}>80, χ=8%; γ_{max}>75, χ=23%

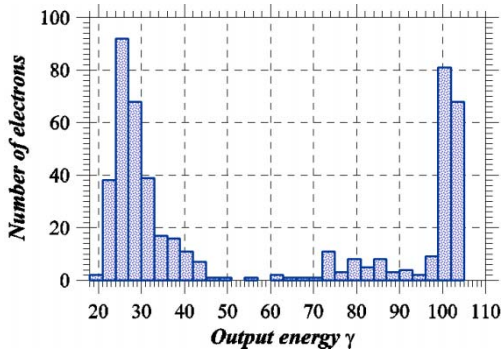

Figure 5: Energy distribution of the output electrons for the nominal regime.

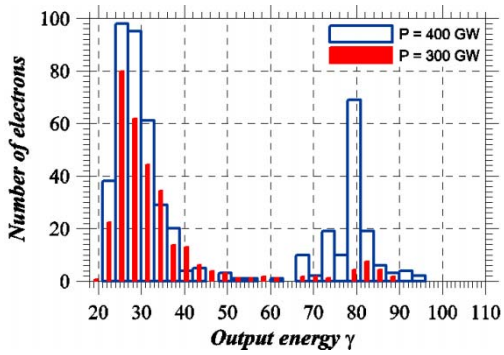

Figure 6: Energy distribution of the output electrons for the not nominal regime (z_r = 1.8 cm, zf = -2.0 cm).

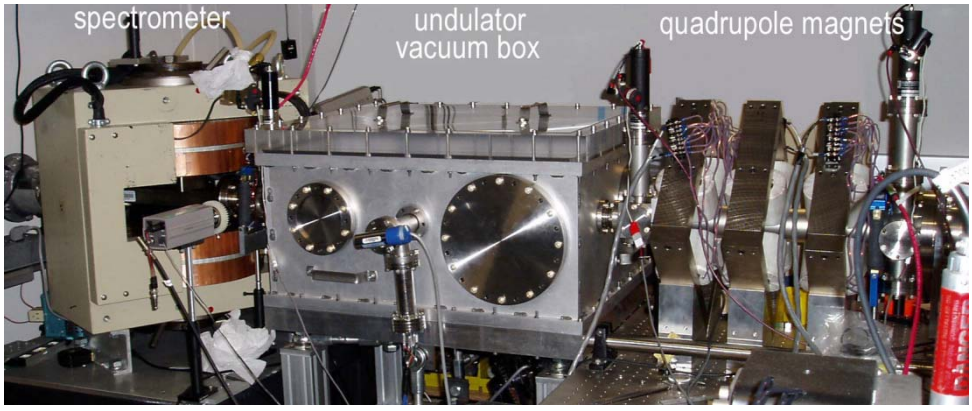

Figure 7: Photo of the IFEL beamline.

Maximum electron energy for nominal parameters is equal to 52 MeV (γ=105). Corresponding energy spectrum of the output electrons is shown in Fig. 5. Total capture ratio equals to 34±1%. All these data are adequate to the IFEL project requirements. The histogram of the output electrons energy for not nominal regime is shown in Fig. 6. Not nominal regime date given by Table 1 shows strong sensitivity of the whole acceleration process to the laser beam parameters (shape, power and focus position). On the other hand these data can be considered as rather wide acceptances for these parameters not stoping the acceleration process in the first undulator section.

* * *

After commissioning undulator was placed in the special vacuum box. The box was installed on the IFEL beamline (see Fig. 7). Alignment of all beam line elements was made with accuracy 0.1 mm by using a reference laser.

REFERENCES

[1] P. Musumeci, C. Pellegrini, J. Rosenzweig, A. Varfolomeev, S. Tolmachev, T. Yarovoi. “On the IFEL experiment at the UCLA Neptune Lab”. Proc. of the PAC2001, June 18-22, 2001, Chicago, IL, p.p. 4008-4010.

[2] P. Musumeci, C. Pellegrini, J.B. Rosenzweig, S. Tochitsky, G. Travish, R. Yoder, A. Varfolomeev, S. Tolmachev, A. Varfolomeev Jr., T. Yarovoi “Status of the Inverse Free Electron Laser Experiment at the Neptune Laboratory”. Proc. of the PAC2003 Conference, May 12-16, 2003, Portland, Oregon, USA, p.p. 1867-1869.

[3] A.A. Varfolomeev, S.V. Tolmachev, T.V. Yarovoi, P. Musumeci, C. Pellegrini, J. Rosenzweig. “Undulator with nonadiabatic tapering for IFEL project”. Nucl. Instr. and Meth. A483 (2002) 377.

[4] A.A. Varfolomeev, S.V. Tolmachev, T.V. Yarovoi. “First approach to simulations of the undulator for the IFEL project of UCLA”. Int. report CRL 01-01, 2001, Moscow.

[5] A.A. Varfolomeev, S.V. Tolmachev, T.V. Yarovoi. “Beam acceptances for UCLA IFEL project estimated along with special undulator design simulations.” Int. report CRL 02-01, 2001, Moscow.

[6] A.A. Varfolomeev, S.V. Tolmachev, T.V. Yarovoi. “Simulations with the purpose to optimize IFEL undulator design for UCLA-RRCKI project.” Int. report CRL 03-01, 2001, Moscow.

[7] S.V. Tolmachev. “Design of the undulator construction with taken into account technological capabilities of its fabrication”. Preprint IAE-6237/2, 2001, Kurchatov institute, Moscow (in russian).

[8]. N.S. Osmanov, S.V. Tolmachev, A.A. Varfolomeev. “Further development of the pulsed wire technique for magnetic field and focusing strength measurements in long undulators”. Nucl. Instr. and Meth. A407 (1998) 443.

FEL AND LIBERA BOTH PUSH PERFORMANCE INTO NEW FRONTIERS

R. Ursic, B. Solar, Instrumentation Technologies, Slovenia

Abstract

Free Electron Lasers and Libera electron beam position processor share a common vocation – they both push performance into new frontiers. Advances in electron accelerator technology that enabled FELs to fulfill their earliest days promises have also been due to the recent developments in the beam instrumentation. Libera that has till now been successfully employed in the light sources projects promises to become an indispensable tool also in the FEL field. The three main advantages of Libera are: all-in-one, customization and connectivity. All-in-one is the concept of unification of various building blocks and thus various functionalities in one product. The customization is enabled by the product's reconfigurability that allows it to grow and support new requirements and application without changing hardware. The consequence of the two is the capacity of the single instrument to perform a variety of tasks that before were split among different devices. Connectivity improves the communication between controls and beam diagnostics, brings out-of-the-crate-freedom and opens unforeseen possibilities for feedback building, inter-accelerator cooperation and remote technical support.

INTRODUCTION

FELs are often called the fourth generation light sources. Even if they are quite different from storage rings there is one goal they certainly have in common: a high quality beam. For FELs the quality of the electron beam is measured by the brightness, where is it not only necessary to create a bright electron beam but it is also necessary to preserve the brightness as the electron is accelerated and transported to the laser. From the earliest days of FELs, it was clear that they were capable to overcome the limitations of the previous generations light sources in the field of very high average power and very short wavelengths. But it is only the recent developments in electron accelerator technology that enabled FELs to start to fulfill their earliest day promises.

With a practical example of Libera we would like to show that the revolutionary design of this beam position processor could with success be employed to improve the quality of beam. We start with the description of the first member of the Libera product family, the electron beam position processor, which is an all-in-one, customizable product with rich connectivity options. It is intended for demanding beam position monitoring and local and global feedback applications on the light sources.

However, a Libera common, reconfigurable hardware platform allows expanding the number of family members. Developing a new Libera member, which would cover the specific needs of pulsed machines like free electron lasers is certainly an option, which we demonstrate with some preliminary measurements in the final paragraph. Each user can customize various attributes of the system to its needs, yet at the same time benefit from the portability of the core all-in-one encapsulated software. Flexible software architecture allows rapid adaptation to multiple applications. By leveraging "commodity" technologies, this flexibility is actually achieved at reduced cost. The use of "open standards" for intra- and inter-system communication simplifies integration within the lab, feedback building, and enables a broader view of integration between research facilities

LIBERA ADVANTAGES

Libera electron beam position processor is the first member of the Libera family. Its advantages are as follows:

All-in-One

All-in-one is the concept of unification of various building blocks and thus various functionalities in one product. Libera is an all-in-one solution that enables accurate beam position monitoring, trouble-free commissioning, and local and global feedback building. The timing and housekeeping functions do not span across multiple boards in different racks, but are all contained in a single module.

Customization

Customization is a capability that allows adaptation of functionality of the device to specific requirements without changing hardware. For the purpose of this paper we identify three types of customization:

The parametric customization allows adjustment of performance by simply changing parameters, without affecting architecture of the programmable hardware. Examples are analog board gain control and FIR filter bandwidth by changing tap settings.

The architectural customization involves changes of logic configuration (FPGA firmware, DSP code and other software) to optimize performance for a particular purpose. It allows building specific logical and signal processing blocks, data-flow paths and algorithm implementations.

The customization of communication interfaces involves communication interfaces that can facilitate implementation of different communication standards without changing hardware.

Connectivity

Fast serial interconnect technologies provide a brand new perspective on the process of developing high-availability and next-generation accelerator control and feedback systems.

In general, individual modules may have their own processors, operating systems and memory and can communicate independently with other modules. Because nodes are operating-system agnostic, integration is no longer required at the driver/backplane level but ascends to the network and transport layers, using standard protocols, which means significant time savings and simpler design models.

LIBERA BUILDING BLOCKS

In the following part of the paper we discuss details about the Libera electron beam position processor. A 1U 19" enclosure with a power supply accommodates analog and digital boards, which are supported by software that is easily adjustable to customer needs.

Analog Board

The analog board consists of a quasi-crossbar switch, four identical RF channels, four analog-to-digital converters, and an interface to the digital board.

The innovative patent-pending quasi-crossbar switch matrix unites the benefits of both the multi-channel and the multiplexed system, and at the same time compensates for the disadvantages of the two. We achieve reproducibility and good "beam vs. current" dependence, which are multiplexed system characteristics and – using a multi-channel approach – we ensure a broader band of operation facilitating position measurements on a turn-by-turn basis. Specifically, the switch facilitates redirection of any of the four input signals to any of the four RF channels.

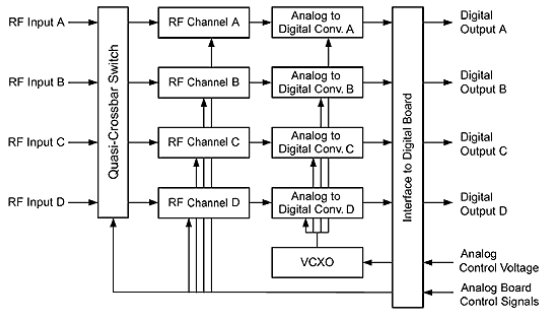

Figure 1: Analog board block diagram.

Digital Board

Core building blocks of the Digital Board are the FPGA (Free Programmable Gate Array), SBC (Single Board Computer) and Memory. The board has also a very rich set of interfaces.

The Virtex II Pro **FPGA** with two IBM PowerPC™ 405 processors from Xilinx is the core of the digital board. It is a system-on-chip (SoC) solution, which facilitates the following functionalities: digital signal processing, communication, formatting, timing, and housekeeping. This architecture allows replacement of some hard-wired DSP functionality with more flexible procedural description of algorithms. Another powerful feature of the Virtex-II Pro FPGA is integrated up to 3.125 Gbps Rocket IO transceivers. The transceivers address all existing connectivity requirements as well as emerging high-speed interface standards.

The **SBC** (Single Board Computer) built around a StrongArm-based Intel Xscale PXA255A processor, is a mezzanine board. It provides application software, bootstrap for the configurable FPGA logic, configuration, diagnostics and maintenance of Libera. Programming of the FPGA via SBC is extremely efficient and it takes approximately 1 second. The SBC downloads the FPGA code via LAN, facilitating easy configuration of a BPM system consisting of many Liberas. The embedded Linux operating system with networking capabilities simplifies integration into an accelerator control system. Fast Ethernet is a native networking solution.

High capacity **Memory** enables the storage of a large amount of data. The basic Libera electron beam position processor configuration allows storing 32 Mbytes of data or 1 million turn-by-turn samples.

The **SFP** (Small Form Pluggable) widely supported open standard enables hot swap of various types of fiber optic and copper-based transceivers into host equipment. This provides the user with the flexibility to choose between different protocols. Applications include: Gigabit Ethernet, Fibre Channel, and Infiniband.

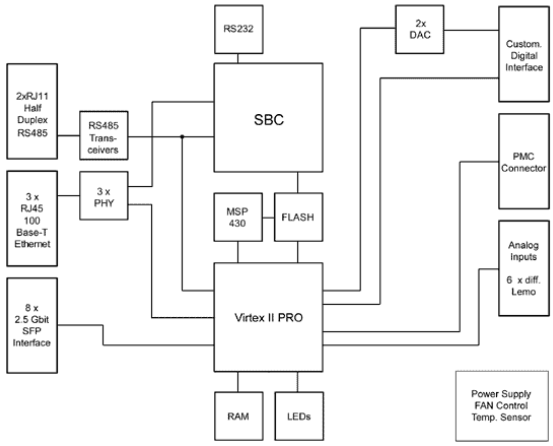

Figure 2: Digital board block diagram.

Software

The software is composed of system software and application software. The application software is limited to the SBC. System software, on the other hand, spans FPGA with embedded PowerPC processors, in addition to the SBC

The **System Software** can be roughly divided into the operating system component, covering GNU/Linux and the embedded, digital signal processing (DSP) component on the FPGA. The key elements of the latter are various filtering and decimation algorithms. These can be tuned to the end-user's requirements so that BPM data is available on a precise time scale, with desired bandwidth and

accuracy. Additionally, fast feedback can be implemented upon the end user's request. The GNU/Linux operating system on the SBC provides a flexible and capable platform for such tasks as networking, maintenance and customization.

The **Application Software** enables seamless integration of Libera into various accelerator control systems. It allows users to interface Libera across a network, deploy custom applications on Libera and use Libera in fields or for tasks previously not envisioned, yet in a way that is consistent and well defined. The Control System Programming Interface (CSPI) is a high-level programming interface that allows separating control system-dependent knowledge from logic and details related to Libera. The CSPI is effectively shielding applications from intricacies and changes in the underlying system software and hardware. Implemented as a library, the CSPI facilitates accessing full Libera functionality in a consistent and documented way.

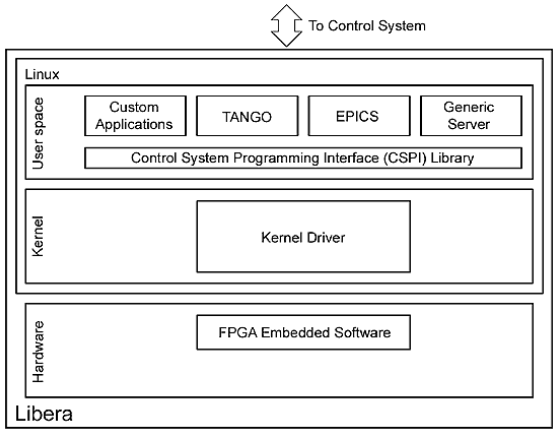

Figure 3: Software block diagram.

COVERING THE NEEDS OF THE PULSED MACHINES

The performance of the first Libera family member was optimized for the 3rd generation light sources, which are based on storage rings and where signals originating from the pickups are periodic in nature. However, we also encouraged our users to put Liberas in their Linacs and transfer lines. The motivation for that is very practical: to have a uniform BPM system installed on the whole accelerator facility. This approach simplifies system integration, commissioning and maintenance, which in turn significantly lowers system life-cycle cost.

One of the most challenging aspects of measuring beam position on FELs is pulse to pulse position measurement fluctuation, which limits measurement resolution. In order to evaluate how well Libera covers the needs of FELs, we performed laboratory measurements of Libera electron beam position processor. Individual pulses were generated using a step recovery diode. Figure 4 shows measurement resolution as a function of bunch charge. To estimate bunch charge we took sensitivity of a typical storage ring button pickup and assumed that current sensitivity of a typical stripline is ten times higher.

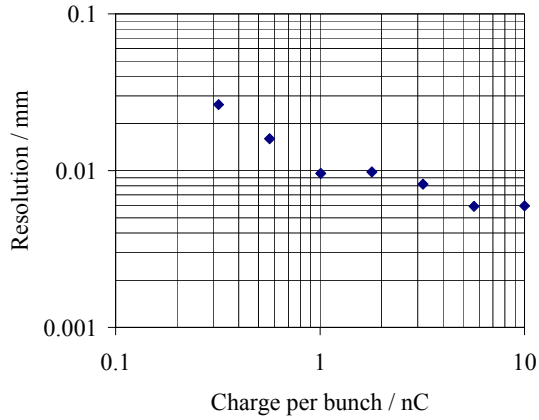

Figure 4: Laboratory measurement of pulsed to pulse position fluctuation for a typical stripline pickup with position sensitivity of 0.1 mm^{-1}.

CONCLUSIONS

Libera is a product family, which open architecture provides solid foundation for building different family members, each optimized to satisfy specific beam instrumentation needs. In this article we have explained all-in-one, customization and connectivity advantages of Libera family. We have also demonstrated that already the first member of the Libera family, the electron beam position processor, is showing excellent performance. Despite being optimized for storage rings, it may satisfy also the FEL beam position monitoring needs. Developing a new Libera member especially for the FEL machines, we are confident to be able to significantly improve the performances.

ACKNOWLEDGEMENTS

We would like to express our gratitude to the Instrumentation Technologies colleagues, who to a great extend contributed to the Libera design and development.

REFERENCES

[1] S.V. Benson, “Free –Electron Lasers Push into New Frontiers”, 2003, Optic&Photonic News
[2] http://www.i-tech.si
[3] R. Ursic, R. De Monte, “Digital Receivers Offer New Solutions to Beam Instrumentation”, 1999 Particle Accelerator Conference, New York, USA
[4] R. Ursic, “Reconfigurable Instrumentation Technologies, Architectures and Trends”, Beam Instrumentation Workshop, 2002, Upton, USA
[5] R. Ursic, B. Solar, “Holy trinity of Instrumentation Development”, Beam Instrumentation Workshop, 2004, Knoxville, USA

OPTICAL SYSTEMS FOR THE FOURTH GENERATION LIGHT SOURCE, 4GLS

F. M. Quinn, M. Bowler, M. D. Roper, M. MacDonald,
CCLRC Daresbury Laboratory, Synchrotron Radiation Department

Abstract

4GLS is a multi-user, multi-source facility proposed for construction at Daresbury Laboratory in the UK. By exploiting super-conducting linac technology with energy recovery, it will combine three free electron lasers and a range of conventional synchrotron radiation sources covering the THz to SXR region. The facility will provide femtosecond pulses at high repetition rate, with the FELs delivering GW peak power in the VUV and XUV region. This paper discusses the options and challenges for the optical systems associated with the suite of photon sources. The beamlines will need to operate both independently and in flexible, synchronised combinations. Together with the requirements for preserving the ultra-bright, fast pulse properties, this places unique demands on the design, layout and operational modes. The paper summarises current technical achievements and identifies the research and development necessary before detailed design of the 4GLS optical systems.

INTRODUCTION

The Fourth Generation Light Source, 4GLS, was conceived as an optimal solution to the needs of the low energy photon-based research community in the UK [1]. Funding for a research and development phase was awarded in 2003; this includes production of a conceptual design and the construction of an ERL-prototype.

The 4GLS suite of light sources

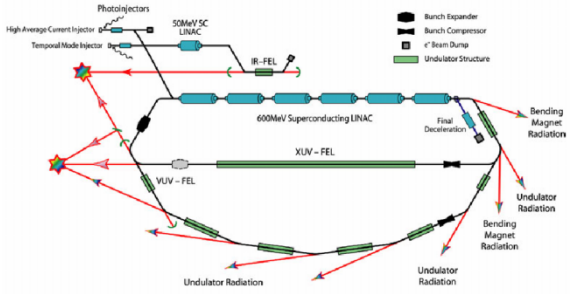

Figure 1. A scheme for the layout of 4GLS and its proposed FEL and spontaneous sources.

The uniqueness of 4GLS is due to combining superconducting energy recovery linac technology for production of high quality electron beams with a variety of free electron lasers, undulators and bending magnet sources.

Figure 1 shows a scheme for the layout of the suite of sources. A driver for this layout is the aim to direct multiple sources onto a user experiment; this is constrained to varying degrees by the usable optical deflection angle. Hence the XUV FEL is shown on a bypass arm of the electron beam transport system. This layout will evolve during the conceptual design process.

Table 1: 4GLS sources and existing relevant systems

4GLS source	**Examples of relevant existing systems**
XUV FEL 10-100eV	One user facility in second phase commissioning: Tesla Test Facility, 10-200eV[2] phase 2 due October '04
VUV FEL 3-10eV	Several experiment projects: EUFELE, 3.5-6.5eV [3] DUV-FEL BNL [4] NIJI IV [5]
IR FEL 0.02-0.4eV	Several user facilities: FELIX [6] 0.25-0.005 eV Jefferson Lab [7] CLIO 0.012 - 0.4[8]
CBS KeV-Mev	Purpose built facility for medical applications: Vanderbilt FEL Centre [9] Several FEL based experiments [10]
THz CSR <0.01eV	Demonstration experiments: For example, BESSY II [11], Jefferson lab [12], ALS [13]
Undulators 1-400eV	examples on 3rd generation storage rings with longer pulse lengths
Bending magnets <3000eV	examples on 2nd and 3rd generation storage rings with longer pulse lengths

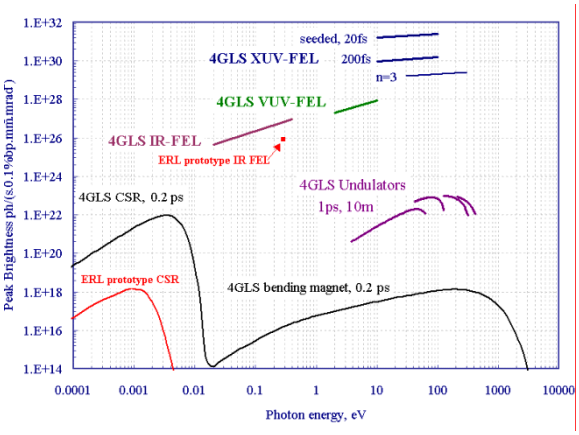

Figure 2. Estimated peak brightness for the 4GLS suite of photon sources. Also shown are the calculations for the ERL prototype currently under construction

Determination of required research and development during the design phase depends on the current operational experience with sources similar to those proposed for 4GLS. Table 1 lists the 4GLS suite of FELs and other sources and identifies the most comparable, existing facilities; the calculated peak brightness is shown in Figure 2. While the potential of FEL sources is being explored in several projects, only IR FELs have significant operational experience as user facilities.

ISSUES AND OPTIONS FOR THE PHOTON BEAMLINES

The optical systems for 4GLS need to match the proposed science programme and to preserve the unique properties of the source. As the conceptual design phase starts, it is important to understand the current state of the art and to highlight key technological challenges.

XUV FEL

The XUV FEL will operate in single pass mode with no constraints due to cavity optics. The design parameters are still to be determined, but pre-design goals are shown in Table 2.

Table 2. Goals for XUV FEL performance.

parameter	**Pre-design values**
range	10-100eV
energy/pulse	2mJ
Pulse length	20-100fs
Micro-pulse	Repetition rate 65Mhz, 650 pulses
Macro-pulse	Repetition rate 60Hz
Average power	80W
bandwidth	3-6 x 10^{-4}
divergence	30 – 150 μrad

The proposed experimental programme will require both monochromated and direct FEL beams with micro-focussing options, covering the first and higher harmonics of the radiating undulator.

The most challenging source parameters for the XUV FEL beamline design are the energy per pulse which is sufficient to cause component damage and the ultrashort pulse length goal which will place optical path difference and stability constraints on the mechanical design.

No operational experience is available for pulse energies at this photon energy or pulse length; the only similar source is the Tesla Test Facility VUV FEL, currently in phase 2 commissioning and due to take beam in October 2004. Significant research has been done on laser ablation and damage thresholds, mostly driven by micromachining requirements [14]. These show that several damage mechanisms exist such as ablation, lattice damage, and photoemissive stress [e.g. 15] which depend on the energy deposited per unit area, the surface condition, absorption efficiency in the material, the pulse length and the photon energy. Schemes to mitigate the effects are proposed in design studies for Tesla X-FEL [16], LCLS X-ray FEL [17] and TTF VUV FEL [18]. These are based on using grazing incidence geometries and low Z materials to reduce flux density and absorption. More exotic schemes such as multifaceted reflectors, gas optics, and renewable mirrors have also been proposed [15, 19].

The most relevant values for laser damage thresholds (LDT) come from research carried out at TTF phase 1 showing that LDT ranges from 0.03 J/cm^2 for bulk Si to 0.06 J/cm^2 for bulk carbon [20]. Using the LDT for carbon and the estimated energy density per pulse for the 4GLS XUV FEL, a grazing incidence optic would need to be at a minimum distance of 30m to give a safety margin of 1/10 of the LDT. While this has been accommodated easily in the layout of TTF phase 2 which is a single source entering an experiment building via a long tunnel, it could have a significant impact on the layout of 4GLS. The use of low Z materials will also affect the output spectrum of the optical system, giving undesirable absorption edges in the XUV and SXR range; for example, carbon mirrors would affect the exploitation of higher harmonics.

However, the available data are very limited as they only give values for ablation from a few bulk materials whereas SR optics traditionally exploit thin coatings on substrates (frequently dielectrics). Also, the accumulated effects during long term exposure at different repetition rates are not known. Gratings may have specific issues due to the surface profile. More measurements are required to ensure appropriate optical engineering designs.

It is expected that apart from the instantaneous heat load considerations, designs similar to existing 3rd generation SR beamlines can be adapted for use on 4GLS [21]. Ultrafast pulse length and stability preservation will demand isochronous photon beam design; optical path differences experienced by a 200 fs pulse as it transits a beamline will need to be less than 10 microns (compared to several mm for 3rd generation storage ring pulses of ~10 ps). Vibration and thermal drift also need to be considered at this level.

A schematic layout is shown in Figure 3 which incorporates an expansion space to reduce the power density on the beamline optics and a pair of deflection mirrors to select use of either the direct or monchromated beam. To cover the full harmonic photon energy range of 10 to 500 eV with a higher resolving power than the FEL bandwidth may need two optimised monochromator modules. The expansion space could usefully contain gas phase filtering, intensity attenuation and photon diagnostics similar to the systems developed for TTF phase 2 [22].

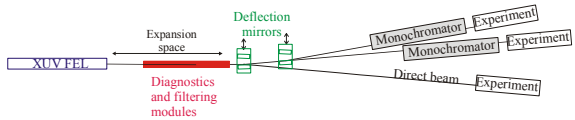

Figure 3. Schematic layout for XUV FEL beamline.

VUV FEL

The proposal for the VUV FEL is based on an optical klystron; the pre-design goals are shown in Table 3. Such systems have operated successfully on storage ring facilities [23] with the highest energy so far, 6.5 eV, 190 nm, demonstrated by EUFELE at Elettra [24].

Table 3. Goals for VUV FEL performance.

parameter	**Pre-design values**
range	2-10eV
energy/pulse	15 μJ
Pulse length	200-1000 fs
repetition	Repetition rate 6.25 MHz
Average power	100W
bandwidth	$<4 \times 10^{-4}$
divergence	150-400 μrad

Again, both monochromated and direct FEL beam will be required with a range of post focussing options. Designs evolved for 3rd generation storage ring sources utilising near normal incidence optics can be used. While the average power loading is non-trivial, it is within current experience. The instantaneous power loading is much reduced from the XUV FEL case but may yet restrict the acceptable mirror incidence angles.

The most critical issue is that of cavity optics receiving the full radiation load at normal incidence from the laser cavity while needing to maintain very high reflectivity to sustain lasing. Outcoupling this power also requires either significant transmission or a holed resonator. These technical issues are currently limiting the lasing and tuning range of cavity FELs to less than 6.5eV[25]. In order to reach the pre-design goal of 10 eV, 4GLS will exploit the enhanced gain due to higher bunch charge and shorter electron bunches. This reduces the requirement for cavity mirror reflectivity from the extremely high value of >95% required for storage ring FELs. Even with this relaxed criterion, cavity mirror technology working over long periods above 6.5 eV still needs to be proven. Recent experimental results for capped aluminium mirrors give a best reflectivity of 75% at 10eV [26]. Damage thresholds for these are now needed.

An alternative scheme would exploit high gain harmonic generation and remove the need for an optical cavity. Lasing has been achieved at 4.6 eV (266nm) at the Brookhaven DUV FEL with 80-100 μJ per pulse [27]. The third harmonic has been used for experiments at 13.9 eV (88 nm) with measured power of 0.3 μJ per pulse [28].

IR FEL

The IR FEL is based on an optical cavity design; the pre-design goals are given in Table 4. In the infra-red, a wide variety of optical systems is possible and a significant operational experience is available from IR FELs and dedicated laser facilities [29].

Table 4. Goals for IR FEL performance

parameter	**Pre-design values**
range	0.4 – 0. 017 eV
energy/pulse	75 μJ
Pulse length	100 fs – few ps
repetition	10 MHz
Average power	900 W
divergence	0.4 – 7 mrads

Compton Backscattering source

Recent assessment has shown the potential of using Compton backscattering on 4GLS to generate ultra-short X-ray pulses. Existing projects cover the use of CBS in medical imaging and extending the applications of IR FEL facilities [9, 10]. The average flux ranges from 10^9 to 10^{12} ph/sec thus the primary optical difference from 3rd generation storage ring sources is mainly in the pulse duration. Pulse lengths below 300fs become shorter in physical length than the extinction lengths of Bragg crystals affecting the diffraction process. This problem is being addressed by the research and development activities for LCLS and TESLA X-FEL[16, 17].

Coherent Synchrotron Emission (THz)

Coherent radiation is produced in accelerators when the electron bunch length is becomes less than the wavelength of the radiation [12], giving flux enhancements of the order of 10^9. Emitted power levels up to 1 Wcm^{-1} have been measured [30]. As with the IR FEL, there are no specific challenges for optics in this region.

Spontaneous sources

4GLS will also provide a suite of undulator and bending magnet sources; the primary operational mode may need to have pulse lengths of ~1 ps to reduce the likelihood of SASE and CSR emission. The proposed devices will be high flux and brightness sources covering IR to SXR with variable polarisation and the flexible pulse characteristics of the ERL. The absorbed heat load on the undulator beamlines will be substantially reduced from devices on existing 3rd generation machines, while providing a peak brightness two orders of magnitude higher. As with the FEL beamlines, existing optical concepts will be transferable to 4GLS, requiring only the additional consideration given to preserving the fast timing characteristics of the emitted photon pulses. The exploitation of IR and visible light will be simplified by the ease of extracting large apertures from the smaller, more flexible ERL ring architecture.

CONCLUSIONS

In summary, the progress from 3rd generation storage ring to 4th generation ERL and FEL photon sources both brings new optical challenges and removes others.

The greatest challenge will be finding suitable optical materials which can withstand the instantaneous heat load, particularly from the XUV FEL, reducing the constraints on the optical design to more optimal levels.

A further need is to find cavity mirror optics which deliver the desired tuning range for the VUV FEL.

General optical systems mechanical design has to preserve the fast pulse properties for all the 4GLS sources. This is likely to be most acute for large optical systems (high performance XUV monochromator and beamline can extend over 30m) or for optics requiring significant cooling.

The ease of extracting large apertures will remove difficulties experienced by IR and visible beamlines on storage ring sources. The low electron beam energy also removes the average power load issue for low energy undulators sources.

Research into optics resilient to high instantaneous and average heat load will be part of the next stage of the 4GLS project.

REFERENCES

[1] W. Flavell, E. A. Seddon, P. Weightman, M. A. Chesters, M. W. Poole, F. M. Quinn, D. T. Clarke, J. A. Clarke, M. J. Tobin, J. Phys.: Condens. Matter 16 (2004) s2405-12
[2] DESY report 'TESLA-FEL 2002-01'
[3] R. P. Walker et al, NIM A 467(2001) 34-37
[4] L. DiMauro et al, NIM A 507 (2003) 15-17
[5] K. Yamada et al, NIM A 475 (2001) 205-10
[6] A. F. G. van der Meer, NIM A 528 (2004) 8-13
[7] G. R. Neil et al, Phys. Rev. Lett. 84 (2000) 6622
[8] R. Prazeres, F. Glotin, J. M. Ortega, NIM A 528 (2003) 83-87
[9] F. E. Carroll, American J. of Roentgenology 179 (2002) 583; F. E. Carroll et al, SPIE 3614 (1999) 139-46
[10] J. R. Boyce et al, Proc. Of the 2003 Particle Accel. Conf. P938; F. Glotin et al, Phys. Rev. Lett. 77 (1996) 3130; I. V. Pogorelsky et al, Phys. Rev. Special Topics; Accel. and Beams 3 (2000) 090702
[11] E. J. Singley et al, Phys. Rev. B 69 (2004) 092512; M. Abo-Bakr et al, Phys. Rev. Lett. 90 (2003) 094801
[12] G. P. Williams, Phil. Trans. R. Soc. Lond. A, 362 (2004) 403-14
[13] J. M. Byrd et al, Euro. Part. Accel. Conf. 2004 LBNL-55688
[14] R. M. Wood, 'Power and Energy Handling Capability of Optical Materials' TT60, SPIE Press (2002); J. K. Chen et al, Int. J. Solids and Struct. 39 (2002) 3199; F. Stiez et al, App. Surf. Sci. 127-9 (1998) 64; B. C. Stuart et al, Phys. Rev. B 53 (1996) 1749; J. Holfield et al Chem. Phys. 251 (2000) 237; P. B. Corkum et al Phys. Rev. Lett. 61 (1988) 2886; J. Gudde et al App. Surf. Sci. 127-9 (1998) 40
[15] R. Tatchyn, SLAC publication SLAC-PUB 6064 (2001)
[16] Tesla Technical Design Report, Part V (2001)
[17] LCLS Conceptual Design Report, SLAC-R 593 (2002)
[18] 'Sase FEL at the Tesla Facility; Phase 2' TESLA-FEL 2002-01
[19] D. Ryutov and A. Toor, SPIE 4500 (2001) 140-55
[20] A. Andrejczuk et al, Hasylab Annual Report Part 1 (2001) 117
[21] H. Petersen et al, Rev. Sci. Instr. 66 (1995) 1; J. H. Underwood in 'Vacuum Ultraviolet Spectroscopy II', ed. J. A. Samson and D. L. Ederer, Academic Press (2000) Chapter 3
[22] K. Tiedtke et al, AIP Conference Proceedings 705 (2003) 588; M. Richter et al, App. Phys. Lett., 83 (2003) 2970
[23] M. E. Couprie, NIM A 393 (1997) 13; W. B. Colson NIM A 429 (1999) 37
[24] M. Trovo et al. NIM A 483 (2002) 157
[25] D. Garzella NIM A 507 (2003) 170-4; A. Gatto et al NIM A 483 (2002) 357-62
[26] F. Bridou et al, Proc. SPIE vol 5250 (2003) 627
[27] L. H. Yu et al, NIM A 528 (2004) 436-42
[28] W. Li et al, Phys. Rev. Lett. 92 (2003) 083002
[29] S. V. Benson, NIM A 483 (2002) 1-7; H. A. Schwettman, NIM A 528 (2004) 1-7; R. Prazeres et al, NIM A 528 (2004) 83-87
[30] G. L. Carr et al, Nature 420 (2002) 153

A CONCEPT FOR Z-DEPENDENT MICROBUNCHING MEASUREMENTS WITH COHERENT X-RAY TRANSITION RADIATION IN A SASE FEL*

A.H. Lumpkin#, W.M. Fawley†, and D.W. Rule‡
Advanced Photon Source, Argonne, Illinois 60439 USA
†Lawrence Berkeley National Laboratory, Berkeley, California 94720 USA
‡NSWC, Carderock Division, West Bethesda, Maryland 20817 USA

Abstract

We present an adaptation of the measurements performed in the visible-to-VUV regime of the z-dependent microbunching in a self-amplified spontaneous emission (SASE) free-electron laser (FEL). In these experiments a thin metal foil was used to block the more intense SASE radiation and to generate coherent optical transition radiation (COTR) as one source in a two-foil interferometer. However, for the proposed x-ray SASE FELs, the intense SASE emission is either too strongly transmitted at 1.5 Å or the needed foil thickness for blocking scatters the electron beam too much. Since x-ray transition radiation (XTR) is emitted in an annulus with opening angle $1/\gamma$ = 36 μrad for 14.09-GeV electrons, we propose using a thin foil or foil stack to generate the XTR and coherent XTR (CXTR) and an annular crystal to wavelength sort the radiation. The combined selectivity in angle and wavelength will favor the CXTR over SASE by about eight orders of magnitude. Time-dependent GINGER simulations support the z-dependent gain evaluation plan.

INTRODUCTION

Previously, measurements in the visible-to-VUV regime of z-dependent e-beam microbunching in a self-amplified spontaneous emission (SASE) free-electron laser (FEL) have provided important information about the fundamental mechanisms [1-3]. In those experiments a thin metal foil was used to block the more intense SASE radiation and to generate coherent optical transition radiation (COTR) as one source in a two-foil interferometer. However, for the proposed Linac Coherent Light Source (LCLS), the intense SASE emission is either too strongly transmitted at 1.5 Å or the needed foil thickness for blocking scatters the electron beam too much. On-axis crystals used in Bragg or Laue configurations are also subjected to the intense x-rays and 14.09-GeV electron beams. In order to extend the COTR techniques to the x-ray regime, we have evaluated a novel concept that takes advantage of the fact that x-ray transition radiation (XTR) is emitted naturally into an annulus with opening angle $1/\gamma$ = 36 μrad for 14.09-GeV electrons. This angle corresponds to a projected annular radius of 850/425 μm at a distance of 24/12 m (where 12 m is the LCLS diagnostics station interval). We propose using a thin foil or foil stack to generate the XTR and coherent XTR (CXTR). Additionally, if the foil stack is designed appropriately, resonant XTR (RXTR) would be emitted with enhanced angular brilliance. We would use an annular crystal to wavelength-sort the radiation. The high-power e-beam, incoherent spontaneous emission radiation (SER), and SASE would each go through the on-axis hole in the crystal. Importantly, at the CXTR angular location of 24 m, the SASE and SER are red shifted and would not be Bragg-reflected into the converter crystal and detector. The combined radial position and wavelength selectivity will favor CXTR over SASE by at least eight orders of magnitude. A mosaic crystal would be needed to cover the expected CXTR normalized bandwidth of 0.1%. For the LCLS, time-dependent GINGER simulations indicate that sufficient coherent microbunching and concomitant detectable CXTR occur by $z \sim 20$ m. This should allow an evaluation of the z-dependent gain and microbunching from this point onward. We believe this to be more viable than sorting the on-axis SER and SASE before the z =40-m point.

* Work supported by the U.S. Department of Energy, Office of Basic Energy Sciences, under Contract Nos. W-31-109-ENG-38 and DE-AC03-76SF0098.
#lumpkin@aps.anl.gov

BACKGROUND AND PHYSICS CONSIDERATIONS

One of the major issues is the survivability of foils or crystals put into the intense x-ray and electron beams. Based on assessments done previously [4], it is actually the absorption of a significant fraction of the x-ray power that is the larger challenge. The nominal particle beam parameters of a 1.5 π mm·mrad normalized emittance beam of 1-nC charge and 14.09-GeV energy are projected to result in x-ray power of 10 GW at 1.5 Å.

Issues related to performing a z-dependent gain measurement using intraundulator diagnostic stations are daunting. In particular:

1. The high absorption of x-ray power for the full operating conditions is projected to melt any material at 15 Å and all above carbon at 1.5 Å.
2. The beam energy jitter of 0.1%, or 0.2% in wavelength, compared to the natural bandwidth of 10^{-5} for a diamond crystal monochromator creates a mismatch.
3. The high level of SER for a 3% bandwidth (BW) was projected to mask the SASE radiation in the first 40 m of the undulator string. Of course, in 0.3% BW the SASE would be apparent sooner in z.

We propose that critical information on the FEL performance could be obtained by tracking XTR as it

evolves into significant intensities of CXTR. We take advantage of the fundamental angular distribution of XTR that is annular, in contrast to the on-axis SASE. This is schematically illustrated in Fig. 1.

The features of the diagnostic technique are summarized below. We assume that a low-z foil (carbon or Be) can survive in the 1.5-Å regime as reported, or a lower-power commissioning scheme might be used. In fact, this might be the selective emittance spoiler concept described by Emma et al. [5] to produce fs x-ray pulses with GW peak power, but much lower average power than the full LCLS mode.

Conversion Mechanism

The transition radiation generated at the boundary of a material and the vacuum as the e-beam transits the interface is the basis of this technique. Although the photon yield is lower in the x-ray regime than in the visible light regime, there are still detectable photons. For a single foil we have two interfaces producing x-rays in the forward direction. The signal scales as the square of the number of interfaces if the thickness is an integral phase step. The foil could be inserted at the intraundulator stations at 0 m, 12 m, 24 m, etc. We estimate there would be about 10^4 photons in a 1% BW at ~8 keV from a carbon foil and 1-nC beam.

Resonant X-ray Transition Radiation (RXTR)

To boost the XTR signal, we propose evaluating the RXTR technique developed by a number of laboratories a decade or more ago [6,7] to make an x-ray source based on relativistic e-beams transitioning a foil stack consisting of M foils. They demonstrated that by choosing the thickness and separations in integral phase steps, they could enhance the radiation angular density by a factor of M^2. We need to evaluate if one can scale the beam energies up by 50 and still make a realistic (compact) radiator at 8 keV. The sharpness of the annulus of RXTR depends partly on M, and intensity peak angle (θ_{opt}) depends on 1/γ and the material plasma frequencies. Even a simple nonresonant stack of five to ten foils would increase the XTR by five to ten over a single foil.

Coherent X-ray Transition Radiation (CXTR)

In addition, the microbunching of the e-beam in the SASE process would enhance the CXTR signal at 1.5 Å by a few orders of magnitude by the 100-m point. As shown in Fig. 2, the spectral content is already narrowed by the 18.5-m point as predicted by GINGER simulations. In Fig. 3, the z-dependent growth of the microbunched fraction of nearly 32% is shown. With high bunching fraction in mind, we now consider a calculation based on extending the model described in a companion paper on coherent optical transition radiation [8,9]. The CXTR spectral-angular distribution is given by a product of functions as shown in Eq. (1):

$$\frac{d^2N}{d\omega\, d\Omega} = \frac{d^2N_1}{d\omega\, d\Omega} \boldsymbol{F}(\boldsymbol{k}), \qquad (1)$$

where the single particle TR distribution is given by $\frac{d^2N_1}{d\omega d\Omega}$ in the case of a single foil, and the coherence function $\boldsymbol{F}(\boldsymbol{k})$ is given by

$$\mathrm{F}(\boldsymbol{k}) = N + N_B(N_B - 1)\left|H(\boldsymbol{k})\right|^2, \qquad (2)$$

where the bunching fraction $f_B = N_B/N$ and $H(\boldsymbol{k}) = \frac{\rho(\boldsymbol{k})}{Q} = g_x(k_x)g_y(k_y)F_z(k_z)$ is the Fourier transform of the charge form factors with Q = *Ne* = total charge of the micropulse. The transverse form factors are modeled as Gaussian $g_i(k_i) = \frac{1}{\sqrt{2\pi}} e^{-\sigma_i^2 k_i^2/2}$, i = x,y. In particular we consider $g_x(k_x)$ for the paraxial beam trajectories with $\theta_x << 1$, where $k_x \approx k\theta_x$ and $k = \frac{2\pi}{\lambda}$ with λ the radiation wavelength of 1.5 Å. In Fig. 4 we

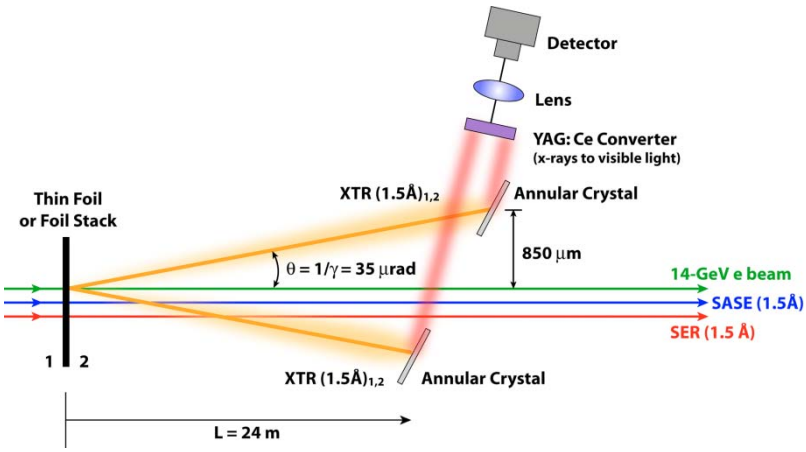

Figure 1: A schematic of the competing beams of SASE, SER, electrons, and XTR in the bore of the FEL vacuum chamber. The thin foil that generates XTR/CXTR and the annular crystal are shown as separated by 24 m in this example. The CXTR angle is expected to fall well inside of the XTR angle due to coherence function factors.

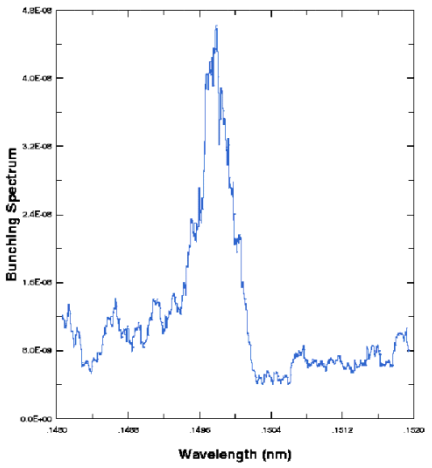

Figure 2: A GINGER simulation of the LCLS showing the microbunching spectral content at z =18.5 m.

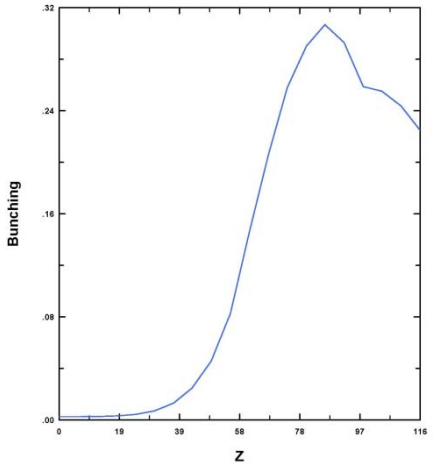

Figure 3: GINGER simulation predictions for the z-dependent microbunching fraction over the wavelength region shown in Fig. 1.

show that CXTR falls well within the 1/γ cone of XTR for an assumed projected radius σ_x = 5 μm. This assumes some substructure on this length scale in the electron-beam transverse phase space such as occurred in our visible-UV COTRI experiments. The vertical axis is photon intensity per steradian-μbunch-0.1% BW. Since we estimate that 500 microbunches are in a coherence length, the incoherent curve intensity would be multiplied by 500 while the CXTR part would be multiplied by 500^2. The lobes are peaked in the 5-μrad angular regime and would move out in angle for smaller effective beam sizes. We analytically show the effects of a bunching fraction of 0.1, 0.2, and 0.3 as well in Fig. 4. In concept we do have the annular cone versus the on-axis SASE, but we need sufficient CXTR at an angle where the SASE radiation is red shifted out of the crystal bandwidth.

Details of the coherence length and the effective number of electron/microbunches radiating coherently need to be addressed. For a 0.1% BW we estimate that 500 microbunches would be coherent at 1.5 Å. In this case we assumed that the foil-induced scattering or energy straggling will not drastically reduce the microbunching fraction. This aspect needs to be evaluated in more detail.

Detection Concept

At a downstream position (+24 m from the foil for 14.1-GeV energy), we would use an annular crystal to interact with the off-axis XTR concentrated in a ring of radius 850 μm (the CXTR, Fig. 4, will be at a smaller angle/radius due to the coherence function). This crystal would Bragg-select the 1.5 Å x-rays to be directed with high efficiency in its BW (~2×10^{-4} for Ge or Si) to the x-ray detector. A mosaic crystal might increase the BW to 0.1%. The on-axis SASE, SER, and e-beam would each go through the on-axis hole in the crystal. The off-axis SASE or SER would be red shifted ~1.3% by the $\gamma^2\theta^2$ term (at 10 μrad) of the FEL resonance condition given in Eq. 1 for the generated wavelength λ,

$$\lambda = \frac{\lambda_u}{2\gamma^2}\left(1 + \frac{K^2}{2} + \gamma^2\theta^2\right), \qquad (3)$$

where γ is the Lorentz factor, λ_u is the period of the undulator (3.0 cm), K=3.5 is the undulator parameter, and θ is the angle relative to the beam axis. Unlike CXTR, these red-shifted photons will not satisfy the Bragg's law condition at 1.5-Å wavelength. The x-rays would be directed to an area x-ray detector or possibly converted to visible light with a YAG:Ce converter screen. The visible light would be detected by an area detector or an intensified camera.

GINGER Simulations

Additional information on the source strengths competing in the off-axis location is provided by GINGER simulations of the predicted LCLS performance. Based on 1.2 mm mrad normalized

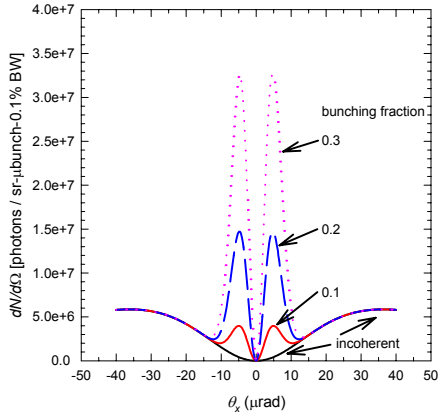

Figure 4: Calculated angular distribution for XTR and CXTR for an effective projected radius of σ_x = 5 μm and 14.1-GeV beam on a graphite foil. The incoherent intensity and those at bunching fractions of 0.1, 0.2, and 0.3 are shown.

emittance, the FEL power saturates at 85 m at a level of ~20 GW and has a power gain length of ~4.4 m as seen in Fig. 5. The peak of the time-averaged microbunching occurs at z = 85 m.

Using a GINGER diagnostic of microbunching phase and amplitude, one can calculate the instantaneous microbunching spectrum b(ω) at a given z. By z = 15.7 m, the coherent signal-to-noise ratio in 0.6% BW is better than 10:1. Another aspect is the strength of the SASE at the off-axis location. One analytically estimates that the intensity is down by a factor of 10^{-4} at a distance of 4σ for a Gaussian function, which is corroborated by the GINGER simulation at r = 200 μm for z = 42.81 m as seen in Fig. 6. This effect, combined with the Bragg angle selectivity, explains why we expect to see the CXTR detection favored by eight orders of magnitude over SASE.

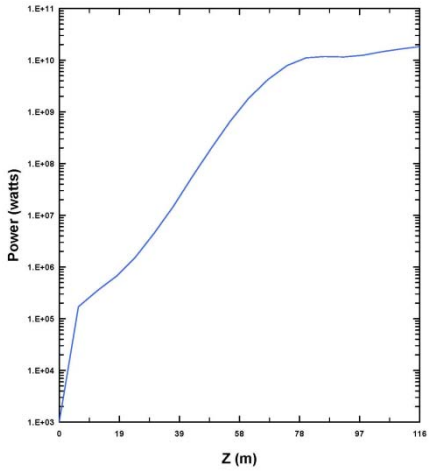

Figure 5: A GINGER prediction of the x-ray SASE power showing the z-dependent gain.

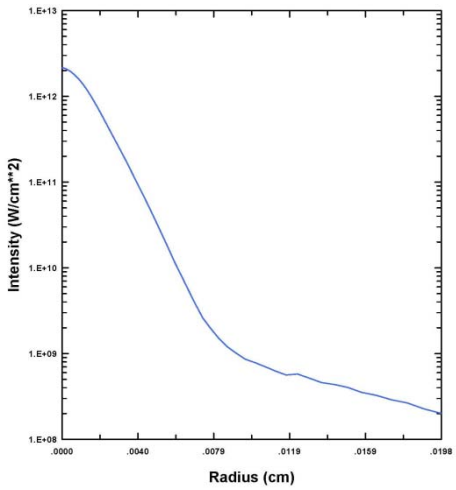

Figure 6: A GINGER simulation of the x-ray SASE FEL showing the SASE radiation intensity as a function of radial position. The intensity has already dropped by 10^{-4} at r = 200 μm for z = 42.8 m.

SUMMARY

In summary, we have described for the first time an experimental technique to measure the electron-beam z-dependent microbunching in an x-ray SASE FEL. We propose taking advantage of the fundamental annular angular distribution of CXTR as compared to the on-axis SASE radiation and the spectral red shift of the SASE to detect the CXTR at the fundamental x-ray wavelength. Initial experiments on XTR generation are being proposed on SLAC's Sub-Picosecond Pulse Source (SPPS) in the next year.

ACKNOWLEDGMENTS

We thank B.X. Yang for useful discussions on x-ray issues, and also M.J. Hogan and P. Krejcik of SLAC on FFTB and SPPS issues, respectively. We also acknowledge the support of H.-D. Nuhn (SLAC) and S.V. Milton (ANL).

REFERENCES

[1] A.H. Lumpkin et al., Phys. Rev. Lett., 86(1), 79, January 1, 2001.
[2] A.H. Lumpkin et al., Phys. Rev. Lett., 88(23), 234801, June 10, 2002.
[3] A.H. Lumpkin et al., "First Observations of COTR due to a Microbunched Beam in the VUV at 157 nm," Nucl. Instrum. Methods (in press 2004).
[4] R. Bionta et al., "Report of the LCLS Diagnostics and Commissioning Workshop," SLAC-R-715 and LCLS-TN-042, 2004.
[5] P. Emma et al., Phys. Rev. Lett., 92(10), 074801-1, 2004.
[6] M.L. Ter-Mikaelian, High Energy Electromagnetic Processes in Condensed Media (Wiley-Interscience, New York, 1972).
[7] M.A. Piestrup et al., Phys. Rev. A., 45(2), 1183, January 1992.
[8] D.W. Rule and A.H. Lumpkin, Proc. of the IEEE 2001 Particle Accel. Conf., Chicago, IL, pp. 1288-1290 (2001).
[9] A.H. Lumpkin, R.J. Dejus, and D.W. Rule, "First Direct Comparisons of a COTRI Analytical Model to Data from a SASE FEL at 540, 265, and 157 nm," these proceedings.

FIRST DIRECT COMPARISONS OF A COTRI ANALYTICAL MODEL TO DATA FROM A SASE FEL AT 540, 265, AND 157 nm*

A.H. Lumpkin#, R.J. Dejus, and D.W. Rule†
Advanced Photon Source, Argonne, Illinois 60439 U.S.A.
†NSWC Carderock Division, West Bethesda, Maryland 20817 U.S.A.

Abstract

We have been addressing fundamental aspects of the microbunching of electron beams that are induced by the self-amplified spontaneous emission (SASE) free-electron laser (FEL) process using coherent optical transition radiation interferometry (COTRI) techniques. Over the last several years we have extended operations from the visible to the VUV regime at the Advanced Photon Source (APS) low-energy undulator test line (LEUTL) project. We have now performed our first direct comparison of the results of an analytical model to COTRI experimental data at 540, 265, and 157 nm.

INTRODUCTION

The interest in using coherent optical transition radiation interferometry (COTRI) patterns to elucidate self-amplified spontaneous emission (SASE) free-electron laser (FEL) experiments has increased as we have explored the technique's sensitivities. In the past we had only reported qualitative agreement on reproducing the main features of the far-field interferometric images [1-3]. As an exercise to develop our understanding and to test our COTRI analytical model [4], test cases from the APS SASE FEL data at wavelengths of 540, 265, and 157 nm were evaluated. Although the beam energy is the main parameter change, the relative angular pattern at these three wavelengths compared to the transform of the particle distribution does help to probe the phenomena. The direct comparisons reveal a number of details in the images that are not matched by a simplifying assumption of a single Gaussian transverse beam profile of the size consistent with the incoherent OTR measurements. Instead typically we need to use a split Gaussian with a smaller rms size to reproduce the fringe peak intensities in the vertical plane and the asymmetry in the horizontal and vertical angles for the 540-nm and 265-nm cases. These results indicate that there are localized transverse portions of the beam distribution with a higher bunching fraction than the mean. The different beam energies used in operating at three wavelengths result in different overlaps of the Fourier-transformed bunch form factor and the single-electron OTR angular distribution for a two-foil geometry. This aspect probes the model's applicability and sensitivities. We also provide evidence of the changes in the effective microbunching transverse radius from the exponential gain regime into the saturation regime. Finally, we recognize that the experimental COTRI patterns are not ideal, and that e-beam distributions and trajectory/coalignment issues are also part of the phenomena.

*Work supported by U.S. Department of Energy, Office of Basic Energy Sciences, under Contract No. W-31-109-ENG-38.
#lumpkin@aps.anl.gov

EXPERIMENTAL BACKGROUND

The experiments were performed at the APS SASE FEL facility. This facility includes the drive laser, S-band linac, bunch compressor, matching station, and the undulator hall with the UV-visible and VUV-visible diagnostics stations. Details have been reported previously [5] and most recently in these proceedings [6]. The emphasis in this paper will be on the description of the analytical model in the next section and comparisons to data in the subsequent section.

COHERENT OPTICAL TRANSITION RADIATION MODEL

Optical transition radiation (OTR) is generated when a charged-particle beam transits the interface of two media with different dielectric constants (e.g., vacuum to metal). The techniques have been more widely employed with electron beams, but so far only a few labs have looked at coherent OTR (COTR) and used COTR interferometry. Overall, the techniques provide information on transverse position, transverse profile, divergence and beam trajectory angle, emittance, intensity, energy, and bunch length. There are coherence factors for wavelengths longer than the bunch length and for microbunched beams such as those induced by a SASE FEL process.

It is this latter process that we have explored with the concomitant intense images. We use the model developed previously [4] to show the first direct comparisons of our COTRI data and calculations. The model describes the phenomenon in the spectral-angular distribution as a product of several functions as shown in Equation (1):

$$\frac{d^2N}{d\omega\, d\Omega} = \left|r_{\perp,\parallel}\right|^2 \frac{d^2N_1}{d\omega\, d\Omega} I\left(\boldsymbol{k}\right)\boldsymbol{\mathcal{F}}\left(\boldsymbol{k}\right), \qquad (1)$$

where $r_{\perp,\parallel}$ are the reflection coefficients, $I(\boldsymbol{k})$ is the interference term, and $\boldsymbol{\mathcal{F}}(\boldsymbol{k})$ is the coherence function. The single particle OTR distribution is

$$\frac{d^2N_1}{d\omega d\Omega} = \frac{e^2}{\hbar c}\frac{1}{\pi^2\omega}\frac{\left(\theta_x^2+\theta_y^2\right)}{\left(\gamma^{-2}+\theta_x^2+\theta_y^2\right)^2}, \qquad (2)$$

where the angles θ_x and θ_y are measured with respect to the angle of specular reflection, and $\frac{e^2}{\hbar c} = \alpha$ is the fine structure constant.

$I(\boldsymbol{k})$ is given by

$$I(\boldsymbol{k}) = 4\sin^2\left[\frac{kL}{4}\left(\gamma^{-2} + \theta_x^2 + \theta_y^2\right)\right], \qquad (3)$$

where L = the foil separation and $\boldsymbol{k}$ is the wave vector. The coherence function is given by

$$\mathcal{F}(\boldsymbol{k}) = N + N_B(N_B - 1)\left|H(\boldsymbol{k})\right|^2, \qquad (4)$$

where the bunching fraction $f_B = N_B/N$ and $H(\boldsymbol{k}) = \frac{\rho(\boldsymbol{k})}{Q} = g_x(k_x)g_y(k_y)F_z(k_z)$ is the Fourier transform of the charge form factors with Q = total charge of the micropulse. The transverse form factors are $g_i(k_i) = \frac{1}{\sqrt{2\pi}}e^{-\sigma_i^2 k_i^2/2}$, i = x,y, and the longitudinal form factor for a microbunch is $f(k_Z) = \frac{1}{\sqrt{2\pi}}e^{-\sigma_Z^2 k_Z^2/2}$.

The coherence function reduces to just the number of particles N when the number of microbunched particles N_B is zero. For the 540-nm case, we have f_B at 10 to 20% so the coherence enhancement of OTR is several orders of magnitude!

Besides tracking the z-dependent growth of COTR, the 540-nm COTRI patterns have an unusual sensitivity to electron beam size compared to OTR as shown in Fig. 1 for 220-MeV beam and 0.2 mrad divergence. Here, the different bunch form factors for 100-, 50-, and 25-μm size and 0.2% bunching fraction explicitly enhance different peak fringes. The smallest beam size with largest form factor in θ-space enhances the first three fringes compared to only the inner lobes for the 50- and 100-μm sizes. The sensitivity is less in the 100-, 150-, 200-μm regime as shown in Fig. 2, but there are still detectable differences. Basically the OTRI fringe peaks act as a built-in metric.

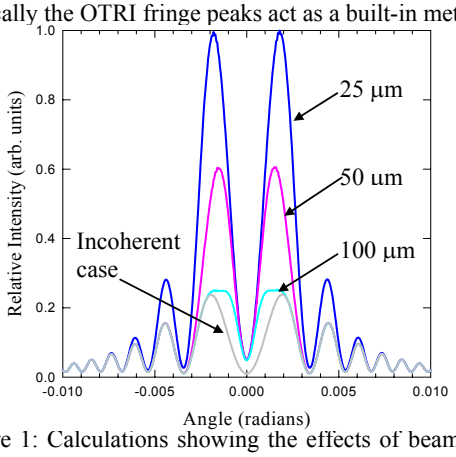

Figure 1: Calculations showing the effects of beam sizes of 100, 50, and 25 μm on the COTRI fringe peak relative intensities. A 220-MeV beam energy and 0.2 mrad divergence were used.

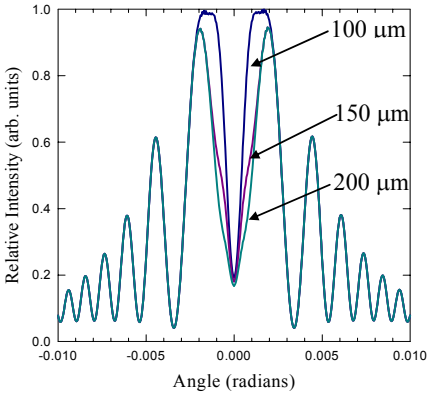

Figure 2: Calculations showing the effects of beam sizes 200, 150, and 100 μm on the COTRI fringe inner lobe relative intensities. The cofactors are narrow in angular space and only multiply the inner lobe distribution for this parameter set.

COMPARISONS OF DATA AND THE MODEL

540-nm Wavelength, Postsaturation Regime

The first case we wanted to study in more detail was the far-field image taken from the saturation regime in z after undulator 8 reported previously [2]. This particular image is very rich in features as we noted at that time. The most obvious effect after the reduced integrated intensity compared to data after undulator 5, is the difference in the θ_x and θ_y structure seen in Figs. 3 and 4, respectively. This is attributed to an elliptical e-beam and the corresponding asymmetric transform of the bunch form factor in θ-space. In the θ_y axis the presence of three fringe peaks versus the single inner lobe in θ_x is seen. The data in the exponential gain regime late in z do not exhibit three fringe peaks in any plane, so larger effective beam sizes are indicated.

The resulting calculations of the model using E = 220 MeV and $\sigma_{x',y'}$ = 0.2 mrad are directly compared in Fig. 3 for θ_x and Fig. 4 for θ_y. As the beam form factor is adjusted, it is clear that the shape of the first lobe is also sensitive to the effective beam size in the 50- to 100-μm σ_x size.

In the θ_x plane (Fig. 3), beam sizes of 75, 85, and 95 μm with a bunching fraction (BF) of 2% were evaluated. The first fringe peak at about ±1 mrad is narrower than that of the first θ_y peak. This is due to the larger effective σ_x, which transforms to a narrower bunch form factor in θ-space centered at θ = 0 so that only the inner side of the first lobe is involved in the products of Eq. (1).

When looked at closely, the vertical fringe pattern image has a slight tilt in the θ_x - θ_y plane so that our three-column-averaged profile does not hit the fringe peak at its maximum for both $+\theta_y$ and $-\theta_y$ values (Fig. 4). Attempts to match the asymmetry in peak intensities were made, but it appears that while σ_y = 20 μm works for fringe

peaks 1, 3, and 4 at negative θ_y, the second fringe peak is overestimated. A σ_y = 25 μm value seems to give the correct height for peak #2, but it then misses the intensities for peaks 3 and 4.

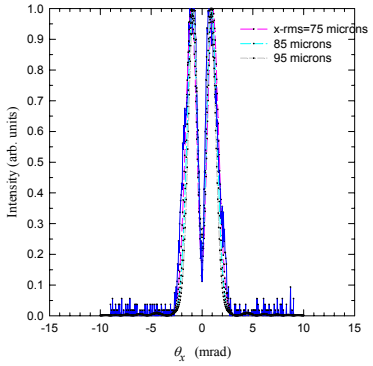

Figure 3: A direct comparison of model results with σ_x = 75, 85, and 95 μm and 2% bunching fraction and experimental θ_x data for the saturated regime case at 540 nm.

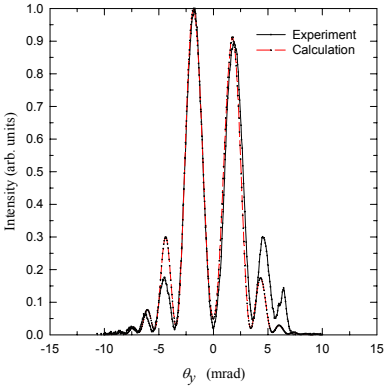

Figure 4: A direct comparison of model results and experimental θ_y data for the saturated regime case at 540 nm. A split Gaussian with 20-25 μm was used.

265-nm Case

The image to be examined was previously published as Fig. 3 of reference 7. The beam energy is now nominally 308 MeV.

The θ_x data are puzzling because although the two peaks fit in the envelope of the θ_y peaks, they do not match, as seen in Fig. 5. However, the peak locations match a calculation using the second harmonic wavelength at 132.5 nm as shown in Fig. 6. The $+\theta_x$ size is matched using σ_x = 20 μm, but the peak intensity symmetry is not matched. We suspect this is a beam coalignment or steering effect that is not in the model yet. We do not believe our 265-nm bandpass filters would pass the second harmonic, and furthermore, our camera is insensitive at 132 nm. There has been a report of second harmonic generation in a laser-field-accelerated electron beam [8], and there may be some related physics issues.

For this run, the effective beam size at this location seems to be elliptical with the major axis now on the y axis. This results in only seeing the two inner peaks with a valley depth between them consistent with $\sigma_{y'}$ = 0.1 mrad, BF = 2%, and σ_y = 35 μm as shown in Fig. 7.

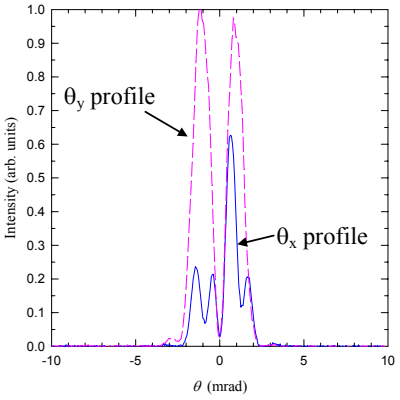

Figure 5: A comparison of the experimental θ_x and θ_y data for the 265-nm case.

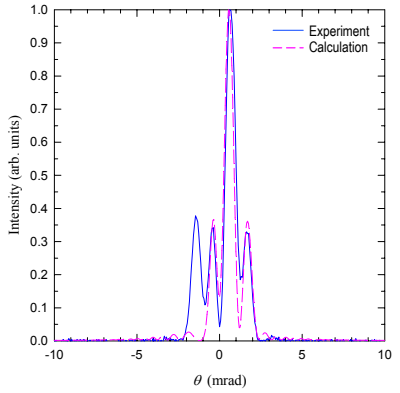

Figure 6: A direct comparison of model results and experimental θ_x data using the second harmonic wavelength of 132.5 nm.

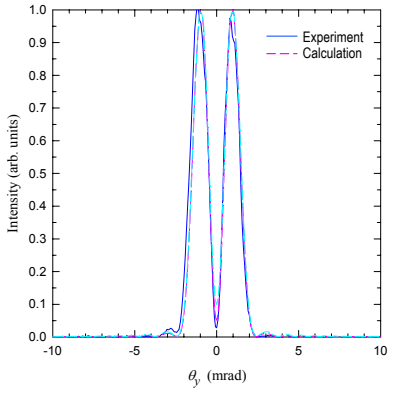

Figure 7: A direct comparison of model results at 265 nm for σ_y = 35 μm and two divergences (0.2 and 0.1 mrad). (The 0.1-mrad case has a deeper valley (red) like the data (blue)).

157-nm Case

The next wavelength regime used a new set of diagnostic stations to detect VUV radiation [5]. All optical transport is done with reflective optics. The beam energy is now 400 MeV, and the spherical mirrors are such that the camera only covers ± 2.5 mrad. At 400 MeV and L = 63 mm we calculate that the second fringe peak locations are at ± 2.0 mrad. This means that the majority of the detected information is in the first fringe peaks. We find that the bunch form factors and the narrower cone angle still result in sufficient sensitivity to beam size.

The image is somewhat like a four-leaf clover with four lobes of comparable intensity at 90° to each other. The fringe peak positions are different in θ_x and θ_y, and this we still attribute to the elliptical beam size. Only now the game is played on the first peak shape, not the visibility of the second or third fringe. The θ_x profile is matched with an asymmetric Gaussian of 43 μm and 25 μm for negative and positive angles, respectively, as shown in Fig. 8. The first peak location at 0.75 mrad is matched with the lobe width as well. There is a strong sensitivity of the lobe intensity to beam size in the $-\theta_x$ data where 43 μm matches better than 40 or 45 μm, but we probably also have an alignment effect as well.

The θ_y profiles and fringe peak positions at ± 0.5 mrad are matched with $\sigma_y \sim 50$ μm as seen in Fig. 9. The 40-μm calculation has too large of a lobe width and the 60-μm case mismatches the central minimum depth as well as the peak position.

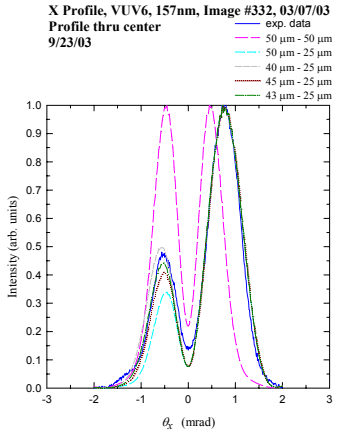

Figure 8: A direct comparison of the model results and experimental θ_x data at 157 nm. A split-Gaussian beam size is used to reproduce the asymmetry in the lobes and their peak positions.

SUMMARY

In summary, we have directly compared the results of a COTRI analytical model and data ranging from 540 nm to 157 nm corresponding to beam energies of 220 to 400 MeV. We have found that we can interpret fringe peak asymmetry in θ_x - θ_y in terms of beam size asymmetry in x and y. We also show that details involved in the ± θ_x or ± θ_y asymmetry can be reproduced with a split-Gaussian assumption for ± x or ± y beam profiles. COTRI has been shown to be a sensitive diagnostic of electron microbunch structure for the SASE process in the visible to VUV regimes. We expect that a similar formalism can be extended to the x-ray regime as discussed in another paper in these proceedings [9].

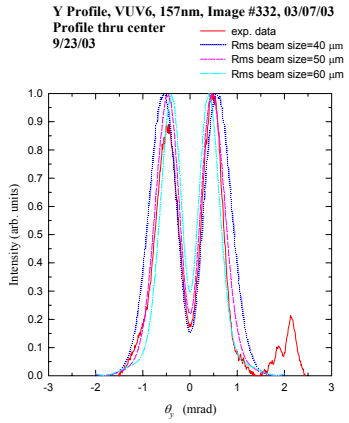

Figure 9: A direct comparison of model results for beam sizes of 40, 50, and 60 μm and the experimental θ_y data from VUV-6 at 157 nm. Best fit is for $\sigma_y = 50$ μm.

ACKNOWLEDGEMENTS

The authors acknowledge the support of Kwang-Je Kim and the Advanced Accelerator Research Initiative at Argonne National Laboratory.

REFERENCES

[1] A.H. Lumpkin et al., Phys. Rev. Lett. 86, 79 (2001).
[2] A.H. Lumpkin et al., Phys. Rev. Lett. 88, 234801 (2002).
[3] A.H. Lumpkin et al., "First Observations of COTR due to a Microbunched Beam in the VUV at 157 nm," Nucl. Instrum. Methods (in press 2004).
[4] D.W. Rule and A.H. Lumpkin, Proc. of the IEEE 2001 Particle Accelerator Conference, Chicago, IL, pp. 1288-1290 (2001).
[5] P. Den Hartog et al., Nucl. Instrum. Methods A483, 407 (2002).
[6] A.H. Lumpkin et al., "Use of VUV Imaging to Evaluate COTR and Beam-Steering Effects in a SASE FEL at 130 nm," these proceedings.
[7] A.H. Lumpkin et al., Nucl. Instrum. Methods A483, 402 (2002).
[8] S.D. Baton et al., Phys. Rev. Lett. 91(10), 105001-1 (2003).
[9] A.H. Lumpkin, William M. Fawley, and Donald W. Rule, "A Concept for z-dependent Microbunching Measurements with Coherent X-ray Transition Radiation in a SASE FEL," these proceedings.

USE OF VUV IMAGING TO EVALUATE COTR AND BEAM-STEERING EFFECTS IN A SASE FEL AT 130 NM*

A.H. Lumpkin**, Y.-C. Chae, R.J. Dejus, M. Erdmann, J.W. Lewellen, and Y. Li
Advanced Photon Source, Argonne National Laboratory, Argonne, Illinois 60439, USA

Abstract

We report the first experimental data on coherent optical transition radiation (COTR) at 130 nm as well as first tests of the analytical model for single-kick-error effects on gain in a SASE FEL. We use both near-field and far-field imaging of the SASE radiation. We also use the COTR near-field data to identify a calibration factor error in the rf BPM system so that the SKE analysis is based on the camera centroid positions and their relation to those of the alignment laser only.

INTRODUCTION

We have continued to explore VUV operations on the Advanced Photon Source (APS) self-amplified emission (SASE) free-electron laser (FEL) [1]. With installation of a fifth VUV imaging station located after undulator 7 of an eight-undulator series, we have performed our most complete SASE gain curve measurements at 130 nm as well as obtaining beam profile, position, and divergence information. This is the shortest wavelength to date for our complementary coherent optical transition radiation (COTR) measurements [2]. We have also done the first experimental test of Tanaka et al.'s analytical model for the effects of a single-kick error of the e-beam on gain and microbunching in a SASE FEL [3]. In the course of the experiments, we performed a direct comparison of the beam position as determined by the local rf BPMs and the VUV video cameras. An rf BPM calibration factor error was determined so all steering data were evaluated using the COTR near-field image centroids obtained from the cameras adjacent to and one undulator downstream of the selected horizontal corrector in the single-kick error tests. In addition, we compared the e-beam image centroid positions with those of the alignment laser at the available cameras to sort out the effective trajectory and its effect on overall gain. The FEL performance was consistent with GENESIS simulations of the experiment described in detail in a companion paper [4].

EXPERIMENTAL BACKGROUND

The APS injector system for the storage ring includes an S-band linac that can be configured with the photocathode (PC) rf gun to provide bright beams to the FEL. The drive laser is a Nd:YLF oscillator with an amplifier, and the fundamental frequency is quadrupled to attain laser light at 266 nm. The PC gun was operated with a Cu photocathode at the time of these experiments [5]. Typically, about 300 pC of charge were accelerated and then bunch compressed in a chicane where the beam energy is 150 MeV [6]. The normalized emittance $\varepsilon_{x,y}$ = 4.5/3.5 mm mrad was measured after the chicane, and the bunch length was measured with a zero-phasing rf technique to be about 200 fs (rms). The beam is further transported to the low-energy undulator test line (LEUTL) tunnel where eight, 2.4-m-long undulators are installed. The gun, linac, and undulator system are schematically shown in Fig. 1, and the e-beam parameters are summarized in Table 1.

Before and after each undulator station we have a quadrupole, steering correctors, rf BPMs, and visible light imaging station. The quadrupole and horizontal and vertical correctors are located first in the drift space followed by the rf BPM buttons. For the purpose of these experiments we used the five VUV imaging stations installed after undulator numbers 2, 4, 5, 6, and 7 and denoted as VUV-2, etc. As shown in Fig. 2, the station included a first actuator that has a YAG:Ce screen, a thin Al foil option, and pinhole reference target. At a

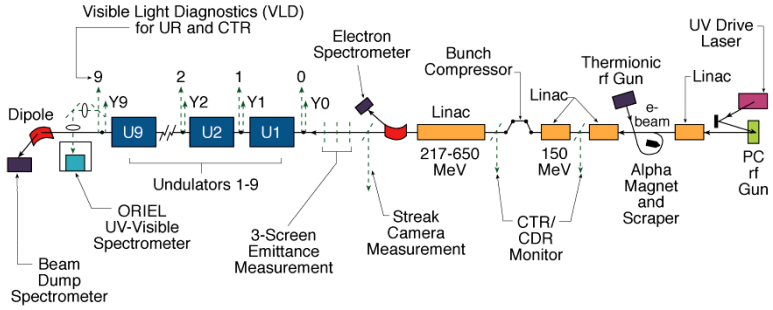

Figure 1: A schematic of the APS SASE FEL showing the PC gun, linac, bunch compression stage, three-screen emittance matching station, and the undulator series with diagnostics.

* Work supported by the U.S. Department of Energy, Office of Basic Energy Sciences, under Contract No. W-31-109-ENG-38.
**lumpkin@aps.anl.gov

Table 1: Nominal Electron Beam Parameters with the PC-gun Beam Injected into the Undulators during the Experiments

Parameter	Value
Beam Energy (MeV)	439
Emittance x,y (mm-mrad)	4-6
Peak Current (A)	300 to 500
Bunch Length (ps rms)	0.3
Charge (pC)	300-400
Energy Spread (%)	0.1-0.2

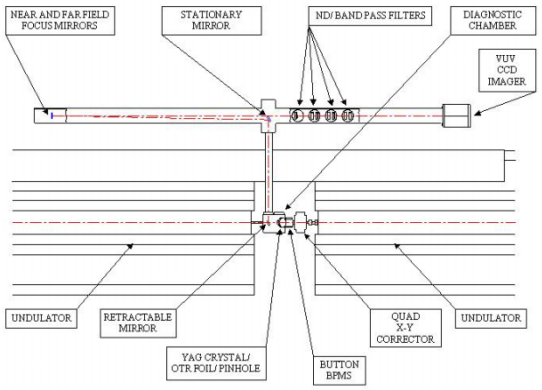

Figure 2: A schematic of the upgraded diagnostic stations for VUV imaging after undulators 2, 4, 5, 6, and 7. The quadrupole with H and V correctors, the rf BPM, the first actuator stage, the 45° retractable mirror, and reflective optics to the VUV camera are shown.

distance of 63 mm downstream a second pick-off mirror is located on a stepper motor. In one position the mirror surface is oriented to send optical radiation to the UV-visible cameras on the wall and the other position directs radiation upward into the VUV transport. A fixed mirror redirects the radiation to one of two selectable spherical mirrors of focal length 900 and 2000 mm that provide near-field and far-field imaging, respectively, for the VUV CCD camera. A series of stepper motors located between the spherical mirror and camera control the selectable filter assemblies, which include visible light bandpass filters, neutral density (ND) filters, VUV bandpass filters, and VUV regime attenuation. The CCD camera is a Roper Scientific model with a 512 × 512 pixel array sensor, which detects radiation from about 120 nm through the visible regime [7] with a well depth of 10^5. The camera is based on the Marconi VUV EEV57-10 back-thinned chip with no antireflection coating and can transfer the full image at a maximum rate of 3 Hz. The data are digitized by a 16-bit board and saved on a local PC disk. Usually, we acquire 100 images for each z-position or angular kick position. The images are subsequently transferred to the UNIX system and processed off-line with GIANT or J Data Miner [8], local programs with an IDL base. Background subtractions are performed and the integrated intensities in a prescribed region-of-interest are determined. We also obtain the projected profile centroids and sizes at FWHM.

The single-kick-error experiments were performed in the undulator 5 region by turning off the quadrupole (Q5) and corrector (H5) after the undulator and using the H4 corrector before the undulator. The first test was to establish the amount of steering strength by assessing the rf BPM readings and the VUV-4 and VUV-5 camera readings.

RESULTS AND DISCUSSION

The experiments were initiated with a z-dependent gain scan following the tune-up through each of the five VUV stations. The near-field gain curve is presented in Fig. 3 which was not available during the experiment. From the selected VUV attenuators as a function of z, we assessed that we were in the exponential gain regime at undulator 5 so we could test the model.

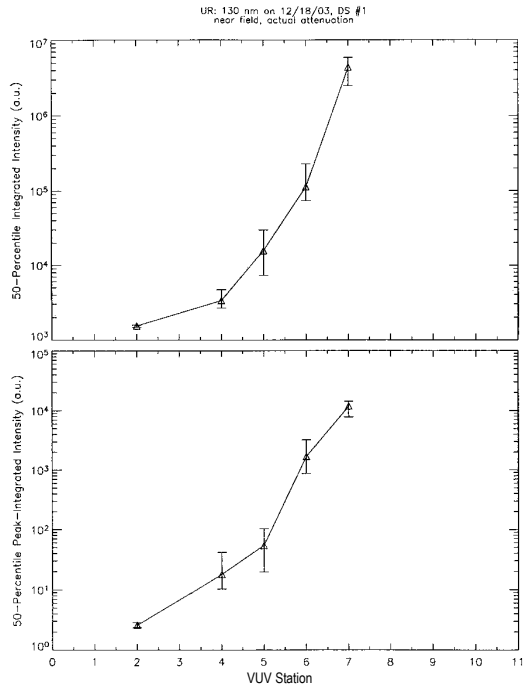

Figure 3: Results of the z-dependent gain measurement.

As part of the steering tests, the recorded rf BPM positions before and after undulator 5 were tracked with steering strength of H4. The results are shown in Fig. 4. However, when we compared the deflections to the VUV image centroids with H4 settings, we ascertained that the rf BPM calibration factor was too low by a factor of six. Since the VUV camera's images were clearly moving beam diameter distances and the calibration factor of the camera had been confirmed by using the stepper motor to move the pinhole target position a known amount, we decided to rely on the VUV camera images. Examples of the image position changes are given in Table 2, where the calibration factor is 11 μm/channel, and in Fig. 5. The

effective kick angle is shown in Fig. 5 (bottom) with an average of ~0.3 mrad per Amp of corrector strength. We also had recorded the alignment laser image positions in each camera so we could reference the e-beam position to the "straightline" of the alignment laser. The final results indicate that in the undulator 5 region the beam trajectory is actually fairly close to the alignment laser (within 50 μrad) so the analytical model should apply.

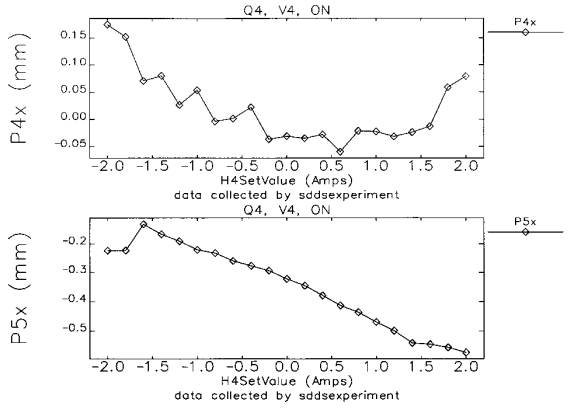

Figure 4: Results of the rf BPM readings versus H4 corrector strength. The reported deflections are found to be too small compared to VUV image centroids.

Table 2: Summary of Image Centroid Positions at VUV-5 versus Corrector Setting (12-18-03)

Note: Foil in, ND0.0, Q_5 off: H5 off

File #	Q4:V4	H4 (A)	X_c*	D_x*	Y_c*	D_y*
4228	On	-2	37	---	120	
4244	On	0	161	124	126	6
4249	On	2	290	129	117	-9
4259	Off	2	252		224	
4268	Off	0	115	-137	218	-6
4278	Off	-2	(4)		229	11

*Positions in channels (ch) at 11 μm per ch.

Note: When turn off Q4/V4 with H_4=0, the image moves -46 ch = -500 μm in x. V4 was at -1.7A in tuned state, and we have a vertical motion down of 109 ch = 1100 μm.

The SKE model of Tanaka et al., [3] defines the new SASE gain length L_g' in terms of a critical angle, $\theta_c = \sqrt{\lambda/Lg}$, where λ is the wavelength of the SASE and L_g is gain length at zero error. We can rewrite this as

$$L_g' = \frac{L_g}{1-x^2} \quad \text{where } x = \theta/\theta_c\,, \qquad (1)$$

and θ is the kick angle. The camera steering data are given in Figs. 5 and 6. In Fig. 6 the ratio of P5/P4 represents the ratio of the VUV-5/VUV-4 image intensities. By steering the beam close to one half the critical angle, the gain is reduced by a factor of two under these conditions. Any offset, x_0, is to be determined. In addition, this model addressed a smearing of the microbunching, which would cause a change in its gain length L_g to

$$L_g'' = \frac{L_g}{1-\pi x^2}\,, \quad \text{where } L_g \text{ is the SASE gain length.} \qquad (2)$$

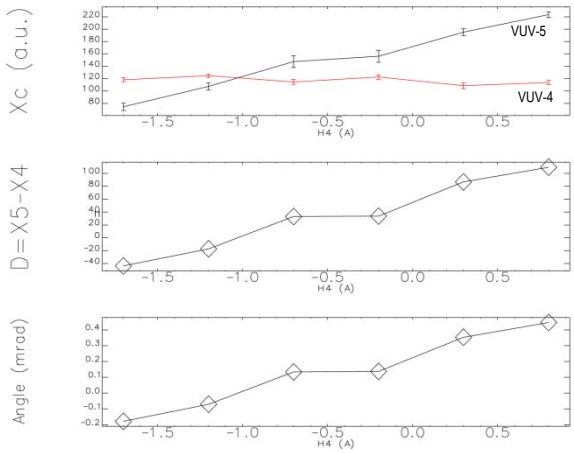

Figure 5: Results of the VUV-4 and VUV-5 camera image centroid shifts (top), the position difference in the two cameras (middle), and the effective kick angle (bottom) versus H4 corrector strength.

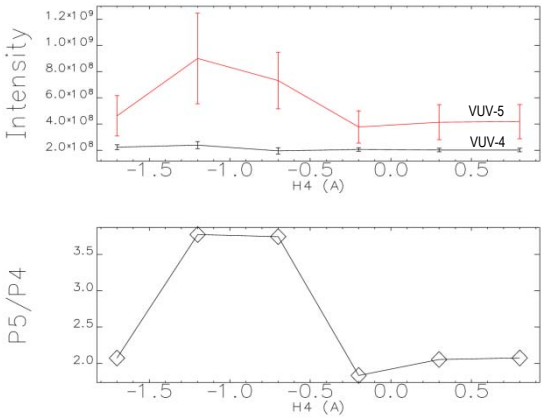

Figure 6: The measured image intensities for VUV-4 and VUV-5 versus H4 corrector strength (top) and the basic ratio P5/P4 of VUV-5/VUV-4 for the SASE undulator light with far-field imaging (bottom).

The multiplier of π in the denominator on x^2 causes a more rapid reduction in gain length versus θ, but the curve is also only a bound on the inner θ limit. However, at the low gains at the time of the experiment the far-field images were too weak and the near-field images may have a contribution from the broadband UV-visible OTR light. We have repeated the experiments with rf thermionic gun beam recently and will continue this evaluation of microbunch smearing as detected by COTR signals.

SUMMARY

In summary, we have extended our COTR experiments to 130 nm. The near-field images were used in the single-kick error tests to determine beam steering instead of the rf BPMs whose calibration was found to be incorrect. The comparisons of VUV SASE gain to steering error were found to be in agreement with the model and GENESIS simulations as described in more detail in a companion paper [4]. The test of the microbunching smearing effect in the model was experimentally less clear, and further experiments and analysis are warranted.

ACKNOWLEDGEMENTS

The authors acknowledge the support of Kwang-Je Kim and the Advanced Accelerator Research Initiative at Argonne National Laboratory.

REFERENCES

[1] S.V. Milton et al., Science 292 (2002) 2037.
[2] A.H. Lumpkin et al., "First Observations of COTR due to a Microbunched Beam in the VUV at 157 nm," Nucl. Instrum. Methods (in press 2004).
[3] T. Tanaka et al., "Consideration on an Alignment Tolerance of BPMs for SCSS Undulator Line," Nucl. Instrum. Methods (in press 2004).
[4] Y.-C. Chae et al., "An Experimental Study of the Beam-Steering Effect on FEL Gain at LEUTL's Segmented Undulator," (these proceedings).
[5] S. Biedron et al., Proc. of 1999 Particle Accelerator Conference, New York, NY, 2024-2026 (1999).
[6] M. Borland et al., A.W. Chao (Ed.), Proc. of the 2000 Linac Accelerator Conference, Monterey, CA, SLAC R561, 863 (2001).
[7] P. Den Hartog et al., Nucl. Instrum. Methods, A483, 407 (2002).
[8] B. Tiemann, J Data Miner analysis program, ANL, (2003).

TEST OF HORIZONTAL MAGNETIC FIELD MEASUREMENTS IN THE PRESENCE OF A STRONG VERTICAL FIELD

Isaac Vasserman, Experimental Facility Division, Argonne National Laboratory, Argonne, Illinois 60439, USA

Abstract

Trajectory straightness is an important parameter in defining the performance of free electron laser (FEL) devices. Horizontal field measurements using Hall probes were tested in 1997 in preparation for the tuning of the undulators for the FEL project at the Advanced Photon Source (APS) [1]. This work is a continuation of the 1997 work, now for the demanding LCLS project. Tolerances for the Linac Coherent Light Source (LCLS) FEL undulator [2] specify a trajectory of <2 μm excursion in both (horizontal and vertical) planes for a particle energy of 14.1 GeV, which means that measurements of a small horizontal field in presence of strong (up to 1.5 T) vertical field are required. Hall probe measurements under such conditions are complicated due to the planar Hall probe effect [3, 4]. The previous test done in 1997 showed that the 2-axis Sentron probe is a possible choice. High sensitivity of horizontal field integrals to the vertical position of the sensor was observed. By positioning the probe accurately in the Y direction, this probe could be used for fast measurements and tuning of devices for LCLS undulator with a much larger magnetic field, than for the APS FEL project. Good agreement with reference moving coil measurements was obtained. The Sentron probe was recently used for LCLS prototype measurements and tuning.

INTRODUCTION

The very tight schedule for the LCLS project assumes rather little time for tuning and measurements of the 33 devices comprising the undulator. So it is important to limit the measurement technique options while tuning the device. A Hall probe is an essential part of this technique, which allows measurements and tuning of the field to obtain the best possible radiation performance of the device, including phase errors and trajectory straightness. An important part of the tuning is reducing the first (J1) and second (J2) field integrals responsible for particle trajectory angles and displacement to provide an overlap of radiation and particle beam. Measurements of integrated over device field integrals with help of rotation coil and/or stretch wire is the most reliable way of obtaining such data. The LCLS undulator consists of 3.4-m-long sections with a 6.5 mm fixed gap, which makes problematic the possibility of using such a technique, especially for horizontal field integrals measurements. Improving the accuracy of the Hall probe measurements allowing the use of the Hall probe for all tuning purposes is a main goal of this work.

SUMMARY OF 1997 TEST

Test of horizontal field measurements, using different types of Hall probes, was done in 1997 with a regular undulator A device, which is the main undulator type at the APS storage ring [1]. Two Hall probes: the usual Bell-type probe and the Sentron probe were used in this test. The main challenge with horizontal field measurements is a planar Hall-probe effect, which is associated with the angle between the vertical field and the axial probe current flow direction. The main result from the 1997 test is that it is impossible to obtain the first and second field integrals corresponding to reference measurements done by moving coil. By adjusting the angle of the Bell Hall probe around the horizontal (X) axis, either the first or second field integrals could be made equal to the reference data but not both of them simultaneously. Such an effect for the Sentron probe is rather small, as can be seen from Fig. 1. The Sentron probe is a new type of Hall probe, a so-called vertical Hall device, which is sensitive to the magnetic field parallel to the chip plane [5]. A different effect contributes to the distortion of horizontal field measurements in presence of a strong vertical field for this probe: the field integrals dependence on vertical

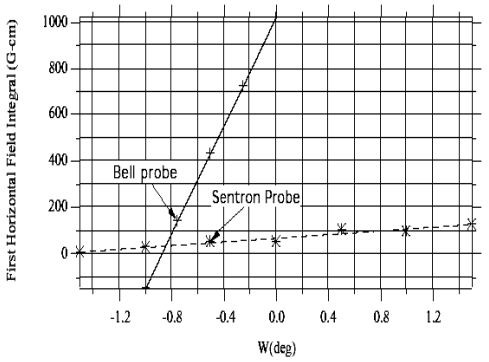

Fig. 1 Sensitivity of Bell and Sentron Hall probes to angular positioning: first horizontal field Integral vs. rotation angle around the X axis.

position (see Fig. 2). Results of the 1997 test showed a rather small dependence of the angle but strong dependence on vertical position. By choosing the proper vertical position of the Sentron probe, both first and second horizontal field integrals are found to be very close to the reference measurements done by moving coil, and such probe was used for tuning of the devices for the APS FEL project.

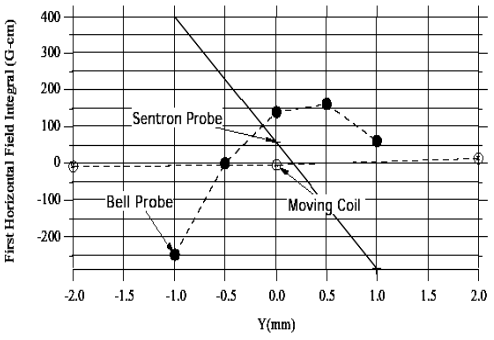

Fig. 2 Sensitivity of Bell and Sentron Hall probes to vertical position: ΔJ1/ΔY≈350 (G-cm)/mm.

NONLINEARITY OF SENTRON 2-AXIS HALL PROBE

The LCLS undulator has a much bigger vertical magnetic field (up to 1.5 T) than does undulator A. To check the possibility of using the Sentron probe in this case, a special test, using a LCLS prototype, was done. At first, the nonlinearity of the horizontal field sensor in the presence of strong longitudinal and vertical fields was investigated. The Hall probe was placed in the APS calibration magnet with a vertical field up to 1.5 T. To create a horizontal component of the magnetic field, the probe was inclined by a small (<1°) angle. The vertical field was measured by a separate probe. The vendor's calibration of the horizontal probe sensor shows a very small nonlinearity. The analog signal to the magnetic field ratio for this probe is constant with an accuracy of 0.1%. However, these measurements show that the presence of a vertical field makes a difference. Results of such measurements are shown in Fig. 3 (red crosses). The horizontal field was calculated from the measured vertical field:

$$B_x = B_y * \sin\varphi ,$$

where φ is the inclination angle of the probe.

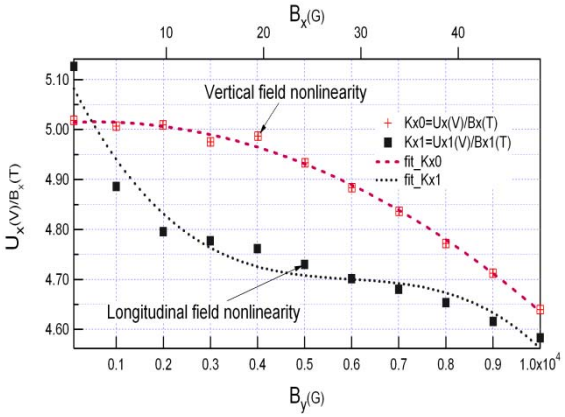

Fig. 3 Nonlinearity of a horizontal Sentron probe sensor vs. vertical and longitudinal fields.

The vendor's value for the analog-to-field ratio is 5 V/T. The nonlinearity of the Hall probe in the region of the vertical field up to 1.0 T is about 6%. The amplitude of the horizontal field for the LCLS prototype is < 10 Gauss, where the nonlinearity is small. Another, and much stronger, source of errors is the contribution of the longitudinal field. By rotating the probe around the axial axis at 90°, a longitudinal component of the field was created. The results of the test are shown in Fig. 3 (black squares). There is a clear contribution of the longitudinal component of the field, especially in the region of small (up to 300 Gauss) field, which is of most interest for us. Results of the test with the LCLS prototype are described below.

HORIZONTAL FIELD MEASUREMENTS

As was found in the test of 1997, there is a strong dependence of horizontal field integrals on the vertical position of the 2-axis Sentron probe. Sentron probe SN #367 was used for measurements of the LCLS prototype. Results of the test show the same behavior of the integral vs. vertical displacement dependence, as during 1997 test, with big quantitative difference: ΔJ1/ΔY ~1330 (G-cm)/mm. Fig. 4 shows different trajectories calculated for different vertical positions of the probe. As discussed earlier [1], these results are related to measurement errors associated with field vs. vertical displacement dependence. What is the reason for such dependence? From Maxwell's equations, we have $\partial B_y/\partial x - \partial B_x/\partial y = 0$. The results of measurements of the first vertical field integral dependence on X, $\partial J_y/\partial x$, made by moving coil and flipping coil, agree with Maxwell's equation, while the same measurements made by Sentron probe disagree. Measurements of $\partial B_y/\partial x$ are close to each other for different magnetic measurement techniques, including the Hall probe. It means that horizontal field measurements, made by an axial Hall probe, are not real and have some induced error. A possible explanation could be associated with the existence of both longitudinal and vertical magnetic fields. To find the correct vertical trajectory, a

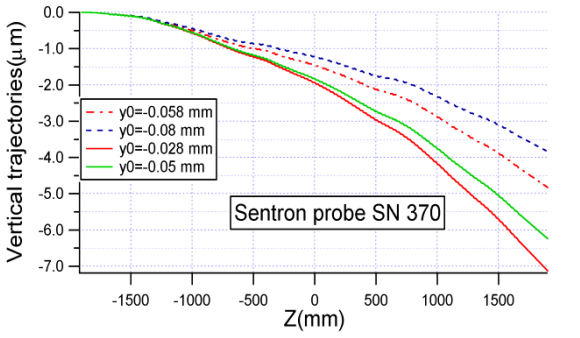

Fig. 4 Vertical trajectories calculated from Sentron Hall probe measurements at different vertical positions, E=14.1 GeV.

reference test was done using the 81-mm-long moving coil. A close match of the vertical trajectory was found for the Hall probe, using the proper vertical position of the

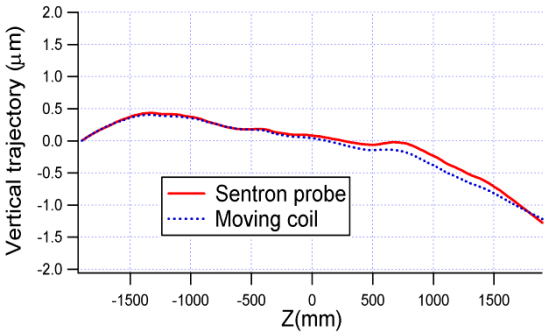

Fig. 5 Comparison of vertical trajectories measured by a Sentron probe and a moving coil.

probe. The result is shown in Fig. 5 for a particle energy of E=14.1 GeV. Comparison of moving coil measurements and Hall probe measurements of the vertical field was done as well and showed the same level of agreement as for the horizontal field. No additional adjustment was required in this case. Fig. 6 shows horizontal field data measured with probe

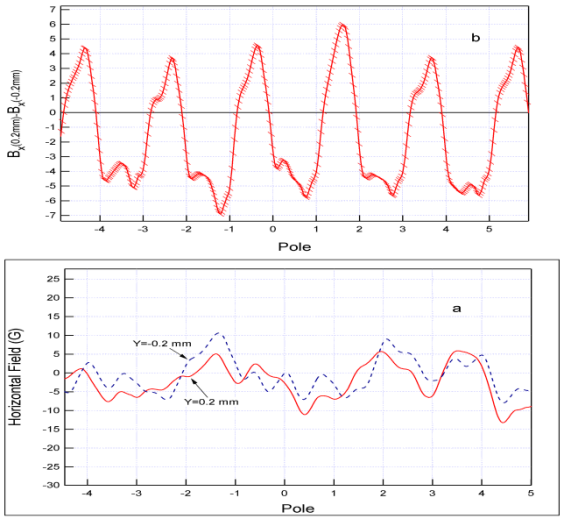

Fig. 6 a: Horizontal field for y=-0.2 mm and y=0.2 mm; b: difference of the fields B_x (0.2mm) –B_x (-0.2 mm).

vertical offsets of ±0.2 mm and the difference between these two measurements. From the data shown in Fig. 6b, we can see that two types of nonlinearity exist: one is due to the contribution of the longitudinal field, and another is due to the vertical field. The undulator magnetic field in the ideal case is determined by horizontal, vertical and longitudinal components [6]:

$B_x=0$

$B_y=B_0*\cosh(ky)*\cos(kz)$

$B_z=-B_0*\sinh(ky)\sin(kz)$, where $k=2\pi/\lambda$, λ is an undulator period.

We have two possible scenarios:

a) in the case, where errors are defined by the longitudinal field, we will have horizontal field distortion $\Delta B_x=B_x(0.2\text{mm})-B_x(-0.2\text{mm})=0$, when the longitudinal field $B_z=0$ (pole centers);

b) in the case, where only the vertical field is responsible for the distortion, we will have $\Delta B=0$, when the vertical field $B_y=0$ (in-between the poles).

Taking this into account, we can conclude: the main contribution to field errors is due to the B_z field ($\Delta B=0$ close to the pole centers). Two neighboring poles have the zero crossing point shifted in opposite directions, which could be explained by the fact that the longitudinal field has the same sign and vertical field has the opposite sign in this location. It creates a DC component of the horizontal the field and distortion of first and second field integrals. Fortunately the effect of the vertical field is rather small for this range of magnetic field, and it is possible to find the proper Y, where the results of measurements are close enough to reference measurements, and the Hall probe could be used for measurements and tuning of vertical trajectories.

CONCLUSION

Tests of horizontal field measurements done with the LCLS prototype provided reliable results such that the Sentron probe could be used for the LCLS project horizontal field measurements and tuning. A test using a calibration magnet examined the nonlinearity of horizontal field measurements in presence of strong vertical and longitudinal fields. The most probable reason for horizontal field errors is associated with a strong longitudinal B_z field for $y\neq0$, and has to be taken into account, especially in the case of devices with a strong magnetic field. Some contribution of a strong vertical field can be observed as well.

ACKNOWLEDGMENTS

This work is supported by the U.S. Department of Energy, Office of Basic Energy Sciences, under contract No. W-31-109-ENG-38.

REFERENCES

[1] I. Vasserman, "Test of Horizontal Field Measurements Using Two-Axis Hall Probes at the APS Magnetic Measurement Facility," Argonne National Laboratory report ANL/APS/TB-32 (1998).

[2] Conceptual Design Report (CDR) for the Linac Coherent Light Source Project, SLAC-R-593, April 2002, http://www-ssrl.slac.stanford.edu/lcls/cdr/

[3] D. Swoboda, IEEE Trans. Magn. MAG-17, 2125 (1981).

[4] W. Poole and R. P. Walker, IEEE Trans. Magn. MAG-17, 2129 (1981).

[5] B. Berkes, R.S. Popovich. "New type of a 3-axis Hall Probe," 9th International Magnet Measurement Workshop, CEA/Saclay, France, June, 1995.

[6] H. Wiedemann, *Particle Accelerator Physics II*, Springer, 1995.

DEVELOPMENT AND MEASUREMENT OF STRAIN FREE RF PHOTOINJECTOR VACUUM WINDOWS *

Sandra G. Biedron[1], Marcus Babzien[2], Lahsen Assoufid[3], Yuelin Li[3], Greg Gill[4], John W. Lewellen[1,3], Jun Qian[3]

[1]Energy Systems Division, Argonne National Laboratory, Argonne, IL 60439 USA, [2]Accelerator Test Facility, Brookhaven National Laboratory, Upton, NY 11973 USA, [3]Advanced Photon Source, Argonne National Laboratory, Argonne, IL 60439 USA, [4]Formerly of Insulator Seal, Division of MDC Vacuum Products Corporation, FL 34243 USA

Abstract

RF photoinjectors produce the highest brightness electron bunches only under nearly ideal illumination by a drive laser [1]. The vacuum window used to introduce the laser beam is an essential element that may potentially degrade the distribution, making it difficult or impossible to know the actual uniformity achieved at the cathode. Because of the necessity to obtain ultrahigh vacuum near the photoinjector, some restrictions are imposed on the fabrication technology available to manufacture distortion-free windows. At the UV wavelengths commonly used for photoinjectors, it is challenging to measure and eliminate degradation caused by vacuum windows. Here, we discuss the initial measurements of a strain-free, coated, UHV window manufactured by Insulator Seal in collaboration with members of Brookhaven and Argonne National Laboratories.

INTRODUCTION

The effectiveness of RF photoinjectors is dependent upon near ideal illumination of the cathode by a drive laser. Much progress has been made in developing laser systems that meet the requirements imposed by photoinjectors and high-brightness experiments. These requirements include precision control of intensity within the active region of the cathode, a necessity for minimizing space-charge-induced emittance growth. Most approaches involve producing a uniform, or other mathematically simple, laser intensity profile. However, laser diagnostics do not typically extend into the vacuum system of the photoinjector, and electron beam measurements to assess the uniformity of the laser intensity distribution provide very complex results. The vacuum window used to introduce the laser beam is an essential element that may potentially degrade any distribution, making it difficult or impossible to know the actual uniformity achieved at the cathode. Because of the necessity to obtain ultrahigh vacuum near the photoinjector, some restrictions are imposed on the fabrication technology available to manufacture distortion-free windows. At the UV wavelengths commonly used for photoinjectors, it is challenging to measure and eliminate degradation caused by vacuum windows. Here, we discuss the initial measurements of a strain-free, coated, UHV window manufactured by Insulator Seal (ISI) in collaboration with members of Brookhaven National Laboratory (BNL) and Argonne National Laboratory (ANL).

THE WINDOW

A class of laser input windows based on a new technological design has been fabricated for use with high-brightness, photocathode-rf gun systems. The ISI-designed window is a special fused silica deep ultra violet viewport with a dual-band or double "V" antireflection (AR coating) coating between 264 nm (<0.15% reflectance from 250-270 nm) and 529 nm (<0.15% reflectance from 515-535 nm for ease of alignment in the visible) mounted on a 2.75" rotatable flange. We chose this bandwidth of coating to accommodate both the ANL Low-Energy Undulator Test Line (LEUTL) photocathode-rf gun drive laser (fourth harmonic of Nd:Glass) [2] and the BNL Accelerator Test Facility (ATF) photocathode-rf gun drive laser (Nd:YAG). The window assembly was designed to be parallel to within 10 arcseconds with a surface quality of 10-5 scratch-dig, and has a flatness of 0.1 wave at 632 nm.

MEASUREMENTS

The first set of measurements was performed at the ATF at BNL using the frequency quadrupled Nd:YAG (266 nm) photocathode-rf gun drive laser operating at 30 microjoules. The laser spot size at the window was approximately 5 mm diameter. The laser profile was imaged at the cathode monument, a fluorescent target which is at the conjugate image plane of the RF photocathode surface, without and with the window in the path. The window, when inserted, was placed unmounted (no vacuum equipment/flanges) perpendicular to the laser at ~ 1 meter upstream of the cathode monument. As shown in Figure 1, there is only a slight change in the beam profile in the comparison of the two cases. Although the window could be installed as close as 0.2 meters from the cathode assembly, we believe this simple experiment and its positive result represents the behavior if this window is mounted in the photocathode-rf

*Corresponding author: biedron@anl.gov, Tel: 630 252 1162, Fax: 630 252 4886

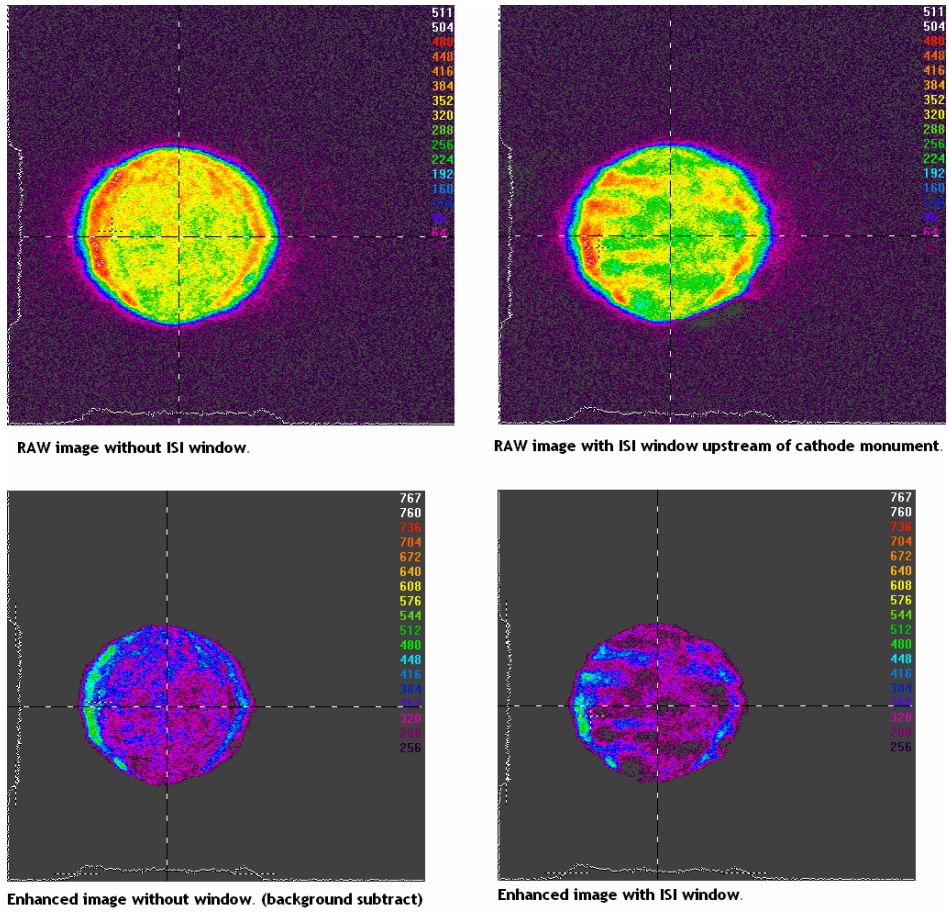

Figure 1: Raw and enhanced laser profile of 30 microjoules of frequency quadrupled Nd:YAG without (left column) and with (right column) the ISI window in its path.

gun assembly. In fact, since the window can be mounted as close to ~0.2 meters from the cathode, any induced phase distortion will not result in an intensity modulation.

The second set of measurements was performed at ANL at the metrology laboratory of the Advanced Photon Source. We measured both unmounted and mounted windows to emulate the effect of the window actually being attached to the photocathode-rf gun assembly. We also measured the flatness profiles and present the raw and best fit, with the spherical aberration removed. The flatness is presented. Note that we refer to Window 1 as that which is mounted on the vacuum cross and Window 2 as the unmounted window. In the case of the mounted window, the laser only passes the window from the most accessible surface. In the case of the unmounted surface, flatness measurements could be taken from laser introduction on either side. The instrument used was a WYKO-6000 interferometer (WYKO Corp., 2650 East Elvira Road, Tucson, AZ 85706, USA) that employs He-Ne (λ=632.8 nm) laser test beam with 150 mm diam aperture. The window measurements were done by zooming onto their surfaces for maximum lateral resolution.

Note that the optical AR coating is a three layer base of SiO_2 with a HfO_2 coating of a proprietary to ISI thickness. The index of refraction for $Si0_2$ is 1.47 and the index of refraction of HfO_2 is approximately 2.25.

In Figures 2 and 3, respectively, the best fit with spherical aberrations removed is presented for the mounted window. In Figures 4 and 5, respectively, the best fit with the spherical aberrations removed is presented for the case of the unmounted window from one side. In Figures 6 and 7, respectively, the best fit with the spherical aberrations removed is presented for the case of the unmounted window for the laser entering from the opposite side. Both windows present very good surface flatness with values below the specification requirement of 0.1 wv rms.

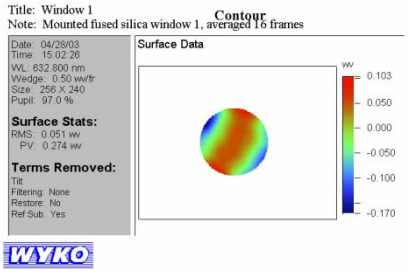

Figure 2: Measured surface profile of the mounted window #1. Here only tilt was removed. Unit: wv.

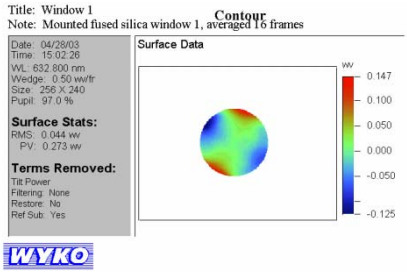

Figure 3. Measured surface profile of the mounted window #1, with both the tilt and power removed. Unit: wv.

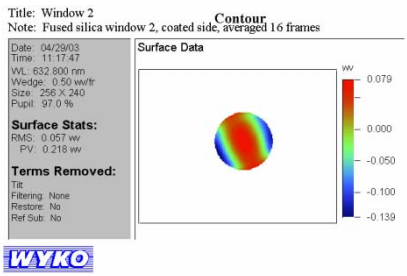

Figure 4. Measured profile of one surface of the unmounted window #2. Here only the tilt was removed. Unit: wv.

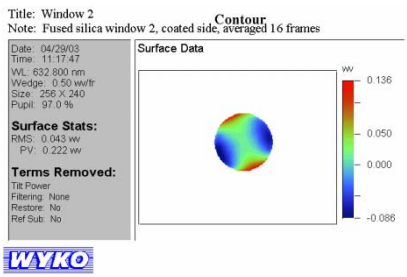

Figure 5. Measured profile of one surface of the unmounted window #2, with the tilt and power removed.: Unit: wv.

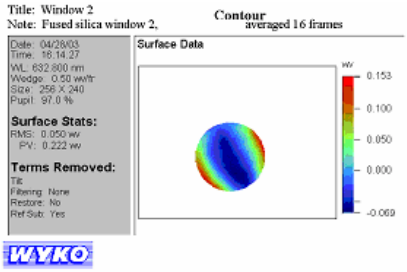

Figure 6. Measured profile of the opposite surface of window #2. Here only the tilt was removed. Unit: wv.

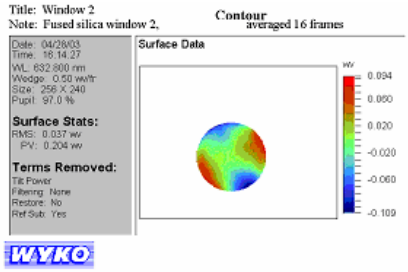

Figure 7. Measured profile of the opposite surface of the window #2, with the tilt and power removed. Unit: wv.

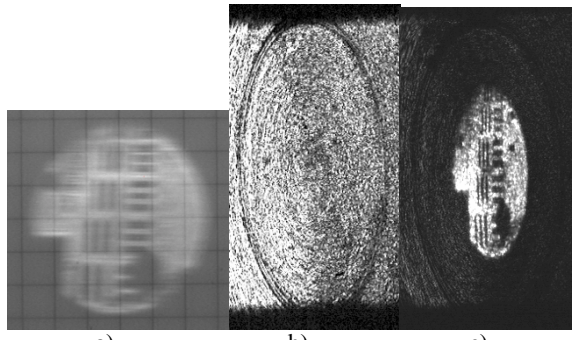

a) b) c)

Figure 8: a) Input laser beam distribution before window as imaged at cathode "monument", b) cathode image from exit port showing 5 mm diameter fiducial ring, c) cathode image with incident laser spot.

The third set of measurements was an experimental test conducted at the ATF at BNL. The new window was mounted on the entrance port of the gun, and the "old" standard style window without flatness consideration on the symmetric port – referred to as the "output" port - on the other side of the gun. There is a camera imaging the cathode on this output port that provides and excellent real-time view of the UV on the cathode that also reveals surface features. To assist with measurements, the ATF has machined a 5 mm diameter fiducial groove onto the surface of the cathode to assist in locating the precise geometric center and provide a scale factor for the beam image. The window appears to have added no distortion

to the beam, and with the larger clear aperture, it is expected that the cathode should be able to accept 4 mm uniform laser spots. The cathode image and the laser imaged on the cathode is shown in Figure 8. No downstream measurements have been performed as of yet, as there have been a number of challenges in this replacement gun's commissioning.

CONCLUSIONS

Future plans include testing and characterization of these new technology laser input windows downstream of the gun at the Accelerator Test Facility. Such work will be critical to future photoinjector-based light source projects such as the Linac Coherent Light Source (LCLS) [3] and the high-average power free-electron lasers [4].

ACKNOWLEDGEMENTS

This work is supported by the US Department of Energy, Office of Basic Energy Sciences under Contract No. W-31-109-ENG-38 and by the Air Force Research Laboratory and the Joint Technology Office of the High Energy Laser Program under funding source number JTO-04-602-23. The work of M. Babzien is supported by the United States Department of Energy under contract DE-AC-02-98CH10886. The work of G. Gill was supported by Insulator Seal, a Division of MDC Vacuum Products.

REFERENCES

[1] V. Yakimenko *et al*, NIM A, 483 (2002) 277-281

[2] S.V. Milton et al., "Measured Exponential Gain and Saturation of a Self-Amplified Spontaneous Emission Free-Electron Laser," originally published in Science Express as 10.1126/science.1059955 on May 17, 2001; Science, Vol. 292, Issue 5524 (2001) 2037.

[3] LCLS Design Group, LCLS Design Report, NTIS Doc. No. DE98059292, April 1998 (Copies may be ordered from the National Technical Information Service, Springfield, VA 22162).

[4] G.R. Neil *et al*., Phys. Rev. Lett. **84**, 662 (2000).

COMPARISON OF PARMELA AND MAFIA SIMULATIONS OF BEAM DYNAMICS IN HIGH CURRENT PHOTOINJECTOR

Sergey S. Kurennoy, LANL, Los Alamos, NM 87545, USA

Abstract

A high-current RF photoinjector producing low-emittance electron beam is an important technology for high power CW FEL. LANL-AES team designed a 2.5-cell π-mode 700-MHz normal-conducting RF photo-injector [1] with magnetic emittance compensation. Using the electric field gradients of 7, 7, and 5 MV/m in the three subsequent cells, the photoinjector will produce a 2.5-MeV electron beam with 3-nC charge per bunch and 7-mm-mrad transverse rms emittance. Beam dynamics in the photoinjector has been modeled in detail. In addition to the usual approach, with fields calculated by Superfish-Poisson and beam simulations performed by Parmela, we also used MAFIA group of codes, both to calculate cavity fields and to model beam dynamics with its particle-in-cell module TS. The second way naturally includes wake-field effects into consideration. Results of simulations and comparison between two approaches are presented.

INTRODUCTION

The normal-conducting RF cavity of the high-current CW photoinjector (PI) for high-power free-electron lasers consists of 2.5 cells plus a vacuum plenum [1]. The cells have an on-axis electric coupling through large beam apertures. The PI has an emittance-compensating solenoid with a bucking coil. After the first half-length cell, where a photocathode will be housed, there are two full-length cells, followed by a vacuum plenum with vacuum-pump ports. Two ridge-loaded tapered waveguides for RF input are connected to the third cell. The vacuum-plenum cell has its resonance at about 650 MHz, well below the frequency 700 MHz of the working π-mode in the cavity.

The photoinjector RF cavity is practically axisymmetric except for the RF couplers and vacuum pump ports. These discontinuities create only small perturbations of the cavity RF fields, even though the coupler irises are the locations of the highest power density of the wall ohmic losses, see [1, 2]. Therefore, field calculations and beam dynamics study in the cavity can be performed with good accuracy using 2-D codes. The 2-D design of the cavity and magnets was performed using the Poisson / Superfish (SF) codes [3] for field computations and Parmela [4] for beam dynamics simulations.

CAVITY FIELDS

The layout used for field computations in MAFIA [5] and the electric field of the working RF mode are shown in Fig. 1. Unlike the case of SF/Parmela, where the fields calculated by SF are interpolated for Parmela, here we want to use exactly the same mesh for both field computations and PIC simulations.

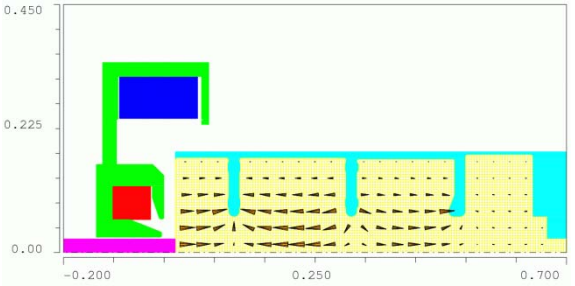

Figure 1: 2.5-cell PI RF cavity layout used in MAFIA. Dimensions are in m. The main solenoid (dark blue) and bucking coil (red) are surrounded by steel (green).

The emittance-compensating magnetic field in MAFIA is calculated by the static solver S. Near the photocathode this field vanishes due to properly adjusted currents in the main solenoid and the bucking coil. The comparison of the fields computed by Poisson/SF and MAFIA is presented in Fig. 2. The left graph shows the profile of the longitudinal electric field on the cavity axis. The electric field alternates its direction from one cell to the next, as it should be in a π-mode. The fields in the third cell are designed to be lower than in the first two cells to reduce the power density on the coupler irises in that cell. The fields in the vacuum plenum are low. The right picture shows the longitudinal component of the emittance-compensating magnetic field on the cavity axis. In addition to vanishing near the photocathode, the field decreases again far from it, where the beam is already relativistic and more rigid, so that the solenoidal focusing is no more needed. Both the electric and magnetic fields found by two different codes agree perfectly.

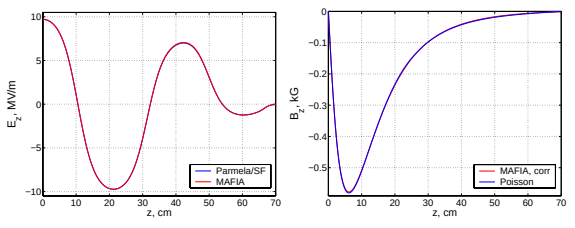

Figure 2: Longitudinal electric field (left) and longitudinal static magnetic field (right) on the cavity axis.

WAKE FIELDS

Wake field effects can be, in principle, included into Parmela beam dynamics simulations [4]. However, Parmela does not compute the wakes: they must be calculated externally, by another code. Here is the main difficulty of this particular problem: one has to calculate wake fields in the photoinjector cavity, where the beam is

accelerated from a non-relativistic, almost zero speed to the speed of light, becoming relativistic only by the second cell. A standard numerical approach with ABCI or MAFIA T-module, where a rigid bunch travels through the structure at the speed of light and the wakes behind it are calculated, does not work in this case. In fact, there is no other way to calculate wake fields in such a problem except using a self-consistent numerical solution of the Maxwell equations with account of particle motion, e.g., a particle-in-cell (PIC) simulation. This is exactly what TS-codes (TS2 for 2-D and TS3 for 3-D problems) in the MAFIA suite do. Unlike that approach, Parmela applies particle-push method using the RF and static fields extracted from SF and Poisson, respectively, in the region where the beam travels. It takes into account the beam space-charge, as well as the image currents in the photocathode plane, but does not calculate fields created due to the beam charge interaction with the cavity walls, i.e. the wake fields.

BEAM DYNAMICS SIMULATIONS

TS2 PIC Simulations

An example of beam dynamics modeling with the MAFIA TS2 PIC code is illustrated in Fig. 3. Snapshots of the electric field (arrows) and particles (red dots) show the bunch evolution during its acceleration in the cavity. The injected 3-nC bunch has a uniform charge density with a longitudinal flat-top pulse shape of the total length of 6° RF, and its center is injected at the RF phase equal to 15°. In TS2 the number of injected particles in the bunch is defined by the code, unlike the case of Parmela, and depends on the number of mesh points. The particles can have different charges. For a typical TS2 run with 1.45 M mesh points in the whole 2-D region of Fig. 1, including magnets and outside the cavity, the number of particles in the bunch of 1-cm radius is 6360 (only 10% of particles are plotted in Fig. 3). The mesh has the step sizes inside the cavity $\Delta z \approx \Delta r \approx 0.5$ mm (it should be homogeneous in z inside the cavity for TS). The TS2 run with this 1.45-M mesh takes 1.4 hours on a 3.2-GHz PC, with a significant fraction of this time spent preparing the output file. For a finer mesh of 4.41 M points, with $\Delta z \approx \Delta r \approx 0.3$ mm in the cavity, the same bunch consisted of 8040 particles, and the TS2 run took 3.6 hours.

For each frame in Fig. 3 (numbered in its lower left corner), Table 1 gives the physical time and the value for a maximal arrow of the electric field in that frame. The fields in the frames are scaled independently; enforcing one global scale would not be useful here since the field values differ by almost two orders of magnitude. A few frames in Fig. 3 show the RF field near its minima (RF phases are close to 0° or 180°), to emphasize the bunch self-fields (space charge) and wake fields. In particular, in the frames 3, 5, and 6, there are noticeable field arrows near the bunch, which deviate from the RF field pattern and correspond to the bunch self-fields. In the frame 8 one can clearly see the fields left after the bunch (wakes) near the cavity exit.

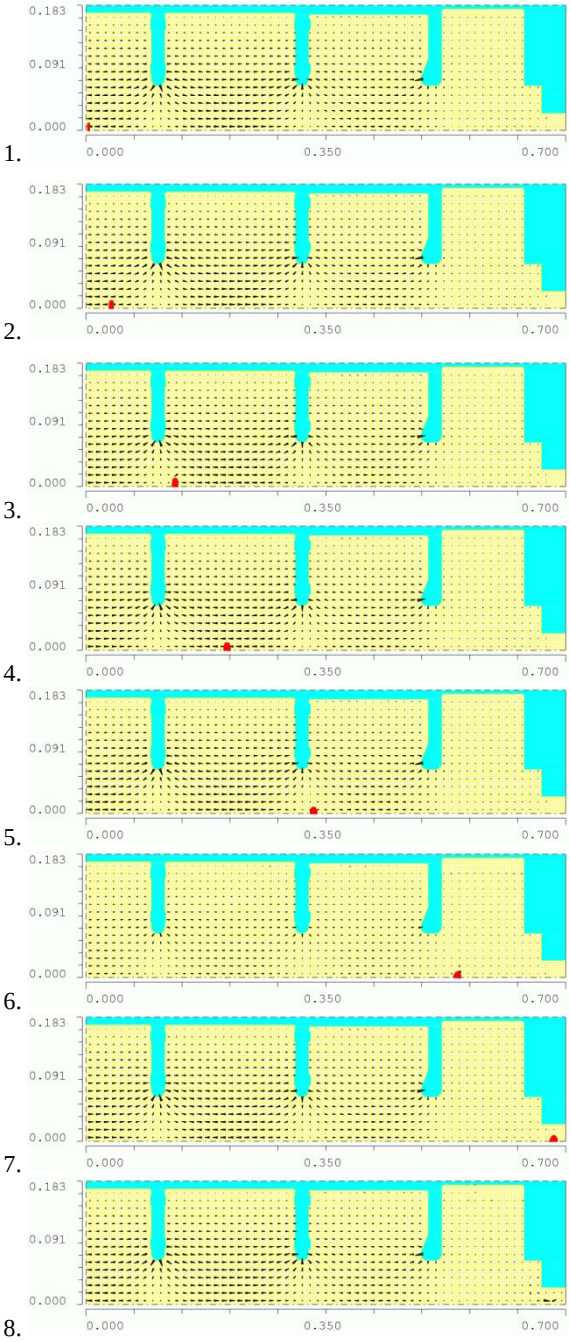

Figure 3: Electric field and bunch evolution in the cavity.

Table 1: Time (ns) and max arrows (MV/m) in Fig. 3

Frame	1	2	3	4	5	6	7	8
Time	.12	.32	.67	.95	1.4	2.1	2.6	2.8
E_{max}	10	15	.53	14	.53	.53	13	.52

Figure 4 shows two snapshots of the electron bunch shortly after injection. The bunch is very short and shaped like a pancake. Its size rapidly increases due to space-charge forces until it moves away from the photocathode

where the magnetic field is getting stronger to prevent the bunch radial expansion. The bunch shape near the cavity exit and the wakes are shown in Fig. 5 in detail, cf. Fig. 3 (note different scales in Figs. 4-5; dimensions are in m).

Figure 4: Electron bunch near the photocathode (*a*. t=0.08 ns, E_{max}=5.3 MV/m; *b*. t=0.24 ns, E_{max}=9.4 MV/m).

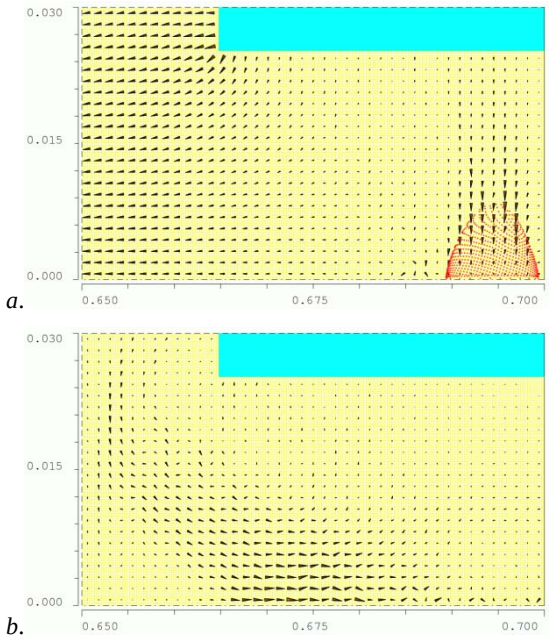

Figure 5: Bunch and fields near the cavity exit (*a*. t=2.62 ns, E_{max}=1.1 MV/m; *b*. t=2.82 ns, E_{max}=0.63 MV/m).

From Figs. 3-5 we see that the 3-nC bunch is focused well by the external magnetic field and remains compact. Its maximal transverse size at the cavity exit is below 7 mm, smaller than the initial size of 1 cm. The bunch length increases, of course, but remains below 1 cm.

Analyzing Figs. 3-5 and similar field snapshots, one can conclude that the beam space-charge electric fields are below 1 MV/m, while the wake fields do not exceed 0.7 MV/m. These values are small compared to the maximal RF field values of 10-15 MV/m.

We performed TS2 runs with a few (up to four) identical 3-nC bunches separated in time by two RF periods, which corresponds to 350-MHz bunch repetition rate. Simulations show identical bunch parameters during the passage and at the cavity exit. This confirms that even at a very high bunch repetition rate no noticeable wake influence is observed.

Comparison of TS2 and Parmela results

We now will compare results of TS2 and Parmela beam dynamics simulations of the photoinjector RF cavity. Figures 6 show the beam transverse rms size, the beam transverse rms emittance in the lab frame, and kinetic energy as the function of the beam position in the cavity for 3-nC charge per bunch.

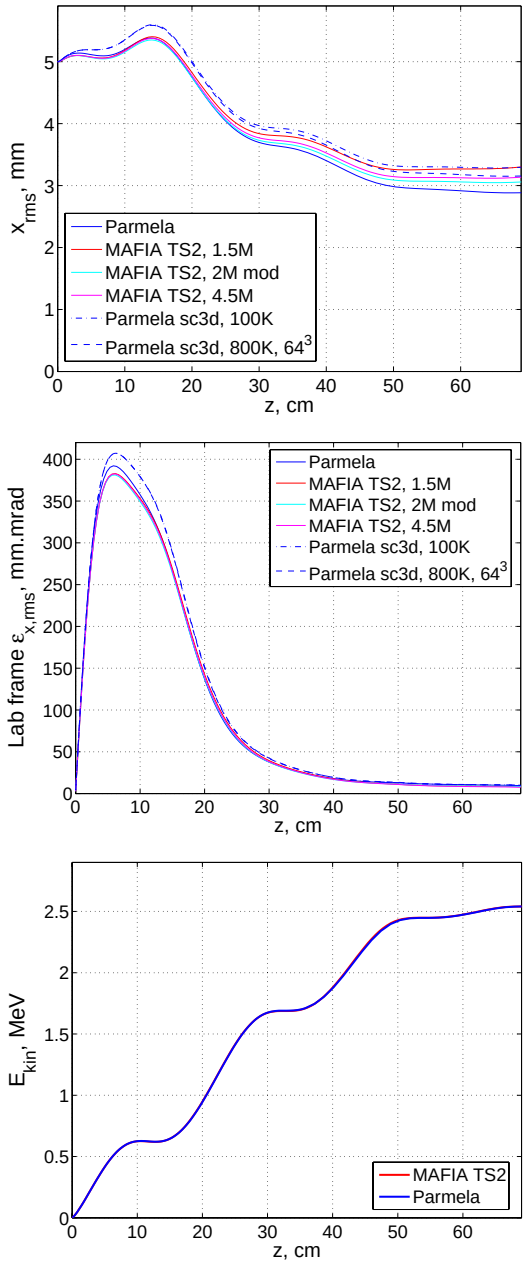

Figure 6: Beam transverse rms size (*a*), emittance (*b*), and kinetic energy (*c*) versus beam position for a 3-nC bunch.

According to Figs. 6, TS2 and Parmela results agree well. The kinetic energy curves from both codes just overlap. The rms beam size predictions agree in general, but there are some differences accumulated by the cavity end. The transverse emittance was calculated in the lab frame, so the apparent emittance blow-up in the first cell is simply due to the bunch rotation in the solenoidal field. In Fig. 6*b* we see differences between two codes near the point where the rotational part of the emittance reaches its maximum. Investigating the reasons, we performed a few code runs with modified parameters. In MAFIA, finer meshes were used. In Parmela, we used optional 3-D space-charge computations with *spch3d* instead of the standard axisymmetric 2-D space-charge routine *scheff* [4]. These results are also plotted in Figs. 6. One can say that the results obtained using 3-D and 2-D routines in Parmela differ more than those of Parmela and TS2.

It is interesting to see how the results depend on the bunch charge. For that purpose, a few runs with bunch charges of 10 nC and 1 nC have been performed, without changing other parameters. Obviously, when the bunch charge is varied without changing the magnetic field that was tuned for 3 nC, the bunch focusing is no longer optimal. As one can expect, the beam is under focused for 10-nC bunch (Fig. 7), and over focused for 1-nC one. For 1-nC, the bunch becomes so tiny near the cavity exit (below 2 mm transversely) that its self-field is getting high, about 2.3 MV/m. The wake fields remain rather weak. For the 10-nC case, the bunch is much larger both transversely (more than 1.5 cm) and longitudinally (about 2.5 cm) than for 3 nC. The self-field of 10-nC bunches is not large because the charge density is reduced due to the bunch blow-up. There was also no noticeable wake-field increase. More details can be found in [6].

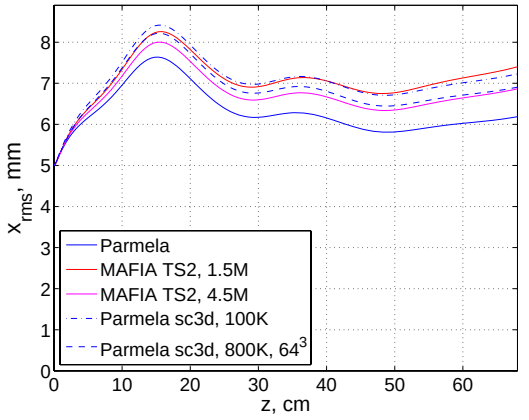

Figure 7: Transverse beam size versus beam position in the cavity for a 10-nC bunch.

For all bunch charges, the kinetic energy plots are very similar to that in Fig. 6*c*. As for other parameters, for 1-nC bunches the agreement between the codes is excellent, but for 10 nC the differences are more noticeable than in the 3-nC case. The reason is most likely in the strong effects of the space charge at the initial stage of simulations, where both Parmela and TS2 have difficulty computing space-charge fields of the thin pancake-like bunches accurately.

The transverse emittance values at the exit of the PI RF cavity are between 7 and 10 mm·mrad. The bunch slices in the phase space are not completely aligned yet after the PI cavity. The design goal was to provide the lowest beam emittance at the wiggler. If we allow a 3-nC bunch to drift after the PI cavity, its transverse emittance will reach about 6 mm·mrad that corresponds to the best possible alignment of the bunch slices. The design requirement for the photoinjector was to have the beam transverse rms emittance below 10 mm·mrad for 3-nC charge per bunch.

SUMMARY

The beam dynamics simulations of the high-current photoinjector for high-power FEL using the MAFIA PIC code TS2 are described. Results obtained from TS2 and Parmela simulations agree well. Since the wake fields are not taken into account in Parmela computations, this agreement confirms that the wake-field effects in the photoinjector RF cavity are negligible. The wakes are weak not only for the design bunch charge of 3 nC, but even for the higher bunch charge of 10 nC. The main reason for that is the large size of the beam apertures in the photoinjector RF cavity. The only noticeable wake fields are observed near the RF cavity exit, where the aperture radius is reduced to its smallest value of 2.5 cm. However, the wakes die out before the next bunch arrival, even at the very high bunch repetition rate, 350 MHz, as was confirmed by TS2 simulations with a few bunches. For the design beam current of 100 mA, the bunch repetition rate is 35 MHz.

The author would like to acknowledge useful discussions with L.M. Young, J.H. Billen, F.L. Krawczyk, and D.C. Nguyen.

REFERENCES

[1] S.S. Kurennoy, D.L. Schrage, R.L. Wood, et al. "Normal-conducting RF cavity of high current photoinjector for high power CW FEL", these proc.

[2] S.S. Kurennoy, D.L. Schrage, R.L. Wood, et al. "Development of photoinjector RF cavity for high-power CW FEL", NIM A528 (2004) 392.

[3] J.H. Billen and L.M. Young. "SUPERFISH/Poisson Group of Codes", report LA-UR-96-1834, Los Alamos, 1996 (rev. 2003).

[4] L.M. Young (documentation by J.H. Billen). "PARMELA", report LA-UR-96-1835, Los Alamos, 1996 (rev. 2004).

[5] MAFIA, v.4.107, CST GmbH (Darmstadt, Germany), 2002; www.cst.de

[6] S.S. Kurennoy. "Simulation of beam dynamics in high-power CW photoinjector cavity with MAFIA PIC code TS2", tech note LANSCE-1: 04-012 (TN), Los Alamos, 2004.

RF DESIGN FOR THE LINAC COHERENT LIGHT SOURCE (LCLS) INJECTOR*

D.H. Dowell#, L. Bentson, R.F. Boyce, S.M. Gierman, J. Hodgson, Z. Li, C. Limborg-Deprey, J. Schmerge, L. Xiao, N. Yu, SLAC, Menlo Park, CA 94025, USA

Abstract

The Linac Coherent Light Source (LCLS) will be the world's first x-ray free electron laser, and the successful operation of this very short-wavelength FEL will require excellent beam quality from its electron source. Therefore a critical component is the RF photocathode injector. This paper describes the design issues of the LCLS RF gun and accelerator structures. The injector consists of a 1.6 cell s-band gun followed by two 3-meter SLAC sections. The gun and the first RF section will have dual RF feeds both to eliminate transverse RF kicks and to reduce the pulsed heating of the coupling ports. In addition, the input coupler cavities will be specially shaped to greatly reduce the RF quadrupole fields. RF designs for the gun and the first accelerator section are now complete. The work includes the gun's new dual coupler and full cell shape as well as the dimensions of the L0-1 dual RF feed and coupling cell. Engineering has begun on the L0-1 structure. These and other aspects of the gun and RF structure design will be discussed.

GENERAL DESCRIPTION OF THE INJECTOR

The Linac Coherent Light Source (LCLS) is a SASE free electron laser using the last 1/3 of the SLAC two mile linac to produce 1.5 to 15 angstrom x-rays in a 120 meter long undulator for use in a variety of x-ray science experiments[1]. In order to satisfy the demanding electron beam requirements, a new 135MeV photo-injector shown in Figure 1 will be built in an existing, off-axis vault at the 2/3 point of the main linac. The injector accelerator consists of a modified BNL/SLAC/UCLA 1.6 cell S-band gun followed by two 3-meter long SLAC accelerator sections. The 6MeV beam from the gun is matched into the first accelerator section and accelerated to 135MeV before injection onto the main linac axis with a 35degree bend [2]. Several modifications to the rf gun, linac and beamline as well as the inclusion of several diagnostics have been incorporated into the injector design to achieve the required 1.2micron projected and less than 1micron slice emittance at a charge of 1nC.

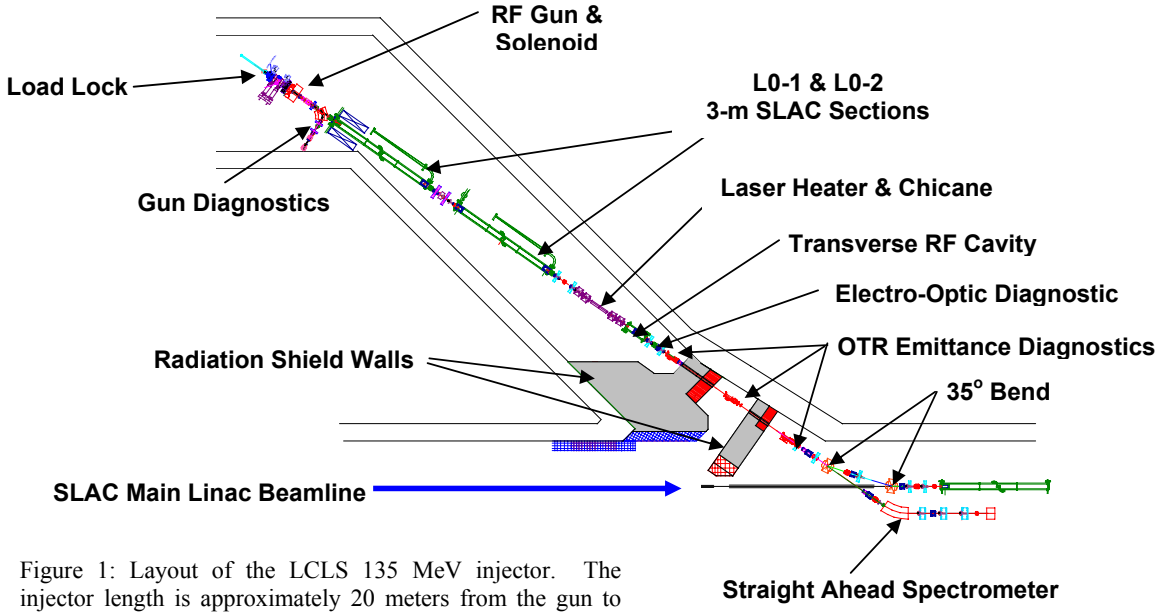

Figure 1: Layout of the LCLS 135 MeV injector. The injector length is approximately 20 meters from the gun to the straight ahead spectrometer.

*SLAC is operated by Stanford University for the Department of Energy under contract number DE-AC03-76SF00515.
#dowell@slac.stanford.edu

Recently an inverse free electron laser, e.g. laser heater [3], has been included in the injector to increase the uncorrelated energy spread which suppresses the coherent synchrotron radiation and longitudinal space charge instabilities in the main accelerator and bunch compressors [4].

This paper describes the RF design of the gun and accelerator structures.

RF GUN DESIGN ISSUES

The design of the BNL/SLAC/UCLA s-band gun is being studied to meet the demanding beam requirements for LCLS. In general, the issues can be divided into two types: thermal effects and RF field quality.

Gun Thermal Design

The need for 120 Hz operation of this gun necessitates a careful analysis of both the average and pulsed heating thermal effects. ANSYS modeling of the gun was done to obtain the average temperature and stress distributions at 120 Hz. The gun temperature distribution is shown in Figure 2 for the gun operating at 3.7kW of average power (120Hz, 3microsecond/pulse and 130MV/m peak cathode field).

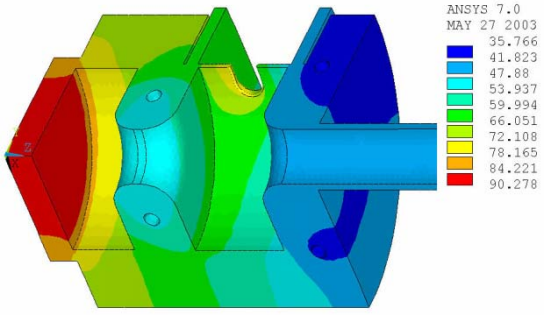

Figure 2: Equilibrium gun body temperature distribution of the BNL/SLAC/UCLS operating at 3.7kW of average power with an inlet water temperature of 20 degrees C and a flow velocity of 16 fps. The temperatures are given in degrees C.

The gun's bulk distortion between ambient and operating temperatures shown in Figure 2 shifts the pi-mode resonant frequency downward 1750 kHz. Additional cooling and adjusting the water temperature to keep the gun body temperature at 30 degrees C lowered the pi-mode shift to an acceptable 100 kHz. This was for 4 kW average RF power and 13.9 degrees C inlet water. [5] Therefore in the LCLS injector, the gun frequency will be kept constant by regulating the gun temperature via the cooling water.

The mechanical stress distribution due to the average thermal load is shown in Figure 3. The location of greatest stress is around the hole which couples the RF from the waveguide into the full cell. The maximum static stress here is 14 ksi, which far exceeds the accepted maximum of 3-5 ksi for brazed copper.[5] In addition, this is also the location of the largest dynamic stress due to pulsed heating. The temperature rise per pulse is computed to be 137 degrees C for the original BNL/SLAC/UCLA gun.

Both the static and dynamic stresses around the coupling apertures are too large and would drastically shorten the gun lifetime at continuous 120Hz operation. Therefore a new coupling-hole was designed with a pulse temperature rise of 41 degrees C, well below 50 degrees C which is considered acceptable for the NLC x-band structures [6]. Further analysis is required to confirm the bulk stress is similarly reduced.

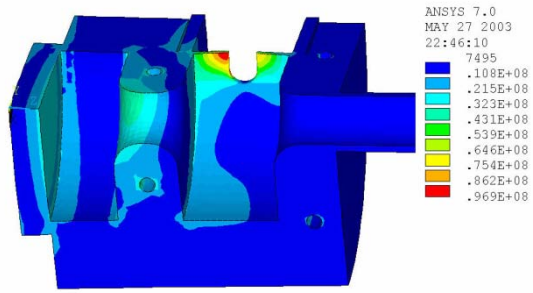

Figure 3: Mechanical stresses at 120 Hz operation. The von Mise stress is given in Pascals.

RF Gun Dual Feed and Racetrack Design

The electron source for the injector is the 1.6 cell, s-band gun which will be modified to have dual RF feeds and a racetrack shape for the full cell. The dual feed is motivated by the desire to reduce the time-dependent dipole field perturbation introduced by a single feed. In the conventional BNL/SLAC/UCLA gun, the dipole field from the single feed is compensated with another un-powered, symmetric port opposite the power feed. In addition, for the standard gun, the RF is coupled into the cell using θ-coupling which also reduces the dipole field [7]. However, even with the symmetric port and θ-coupling, there remains a dipole kick due to the power flowing into the cavity which dual feed eliminates.

Although the dual RF feed eliminates the dipole fields, it increases the full cell quadrupole field. To study this effect the 3-D fields where computed using the parallel code S3P developed by the Advanced Computation Department of SLAC. These fully 3-D fields were used to obtain the gun quadrupole strength as plotted in Figure 4. The original full cell cylindrical shape has a large quadrupole strength which for a normalized electron energy of 10 (5MeV) would have a quadrupole focal length of approximately 300 cm. Although this is 20-times weaker than the gun's strong focusing (focal length of approximately 15 cm) due to the rotationally symmetric radial fields at the ends of the cells, it generates an asymmetric beam and emittance growth.

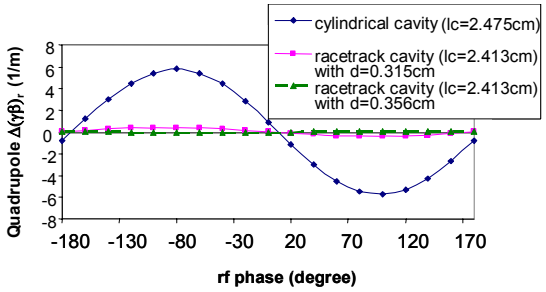

Figure 4: RF quadrupole kicks $(\gamma\beta)_r$ in the full cell with cylindrical and racetrack shapes.

In order to eliminate the quadrupole fields the full cell is made slightly elliptical with the long axis perpendicular to the dual feed axis. The ideal elliptical shape is well represented by offsetting two cylinders a distance d as shown in Figure 5. The cylinder offset distance d is adjusted to eliminate the quadrupole field.

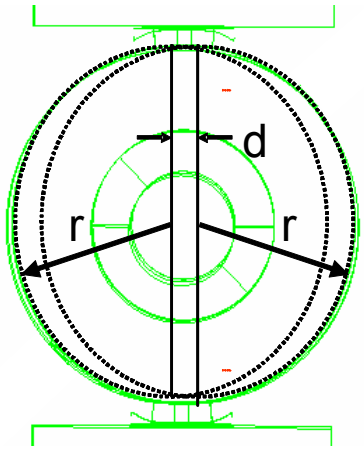

Figure 5: Racetrack shape of the full cell which cancels the quadrupole field of the dual RF coupling holes. The waveguide is above and below the cell. The optimal full cell dimensions are r = 4.061cm cylinders offset a distance d=0.340cm.

Other Gun Field Quality Issues

In addition to rotational field asymmetries, there are also fields which depend upon the radius that are both chromatic and geometric. One chromatic effect is shown in Figure 6, where the difference between the off-axis and on-axis longitudinal fields is plotted vs. z for radii of 1, 3 and 5mm. This radial field dependence is significant, for example, integrating an electron from rest along a trajectory at r=1mm has 2.7keV lower kinetic energy than the on axis electron. This energy spread contributes to the uncorrelated slice energy spread although initially it has a radius-energy correlation in the gun.

It is interesting to note that the measured uncorrelated energy spread is a few keV[8], suggesting that a significant portion of the uncorrelated energy spread is due to the radial-dependence of the RF field and not only to the space charge field.

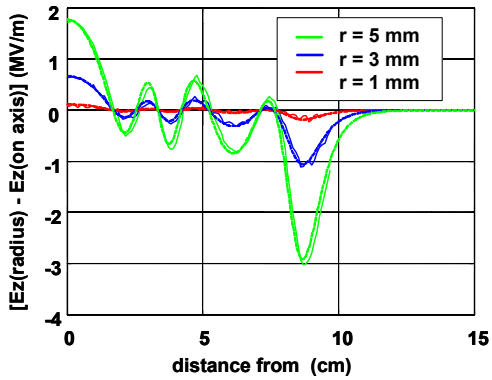

Figure 6: The difference of the off-axis and on-axis longitudinal electric field along lines of constant radii, $E_z(r,z)$-$E_z(r=0,z)$ for R=1,3 and 5 mm. Solid curves: S3P (3D), dashed curves: Superfish (2D).

The dependence of the radial electric field upon distance from the axis is shown in Figure 7. These radial fields have a linear dependence upon radius, indicating little spherical aberration.

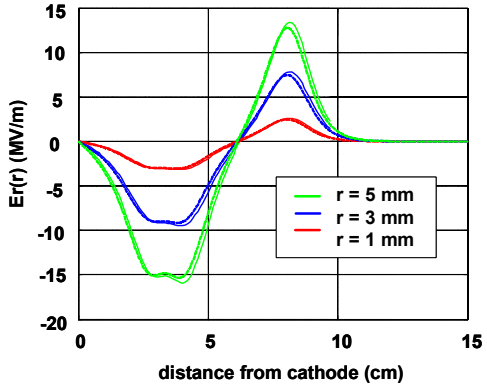

Figure 7: The radial electric field along lines of constant radii: 1, 3 and 5 mm. Solid curves: S3P (3D), dashed curves: Superfish (2D).

L0-1 STRUCTURE RF DESIGN

The 3-meter SLAC RF structures have known dipole fields in both the input and output coupler cells due to the single-side feeds. In the original design the coupler cells were offset transverse to the structure axis to compensate for the amplitude part of the field, however the phase or power flow term could not be canceled.[9] Our analysis for the LCLS injector shows the remaining dipole and quadrupole fields lead to unacceptable emittance growth. Therefore the coupler cell of L0-1 has been redesigned to have a dual feed and a racetrack shape as shown in Figure 8.[10]

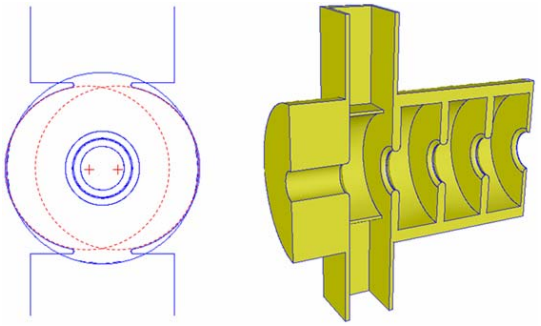

Figure 8: The L0-1 structure coupler cell with dual RF feed and racetrack shape. The optimal distance between the cylinder centers is 13 mm.

The integrated quadrupole kick as a function of RF phase (crest at 0 degrees) is given in Figure 9 for four coupler configurations. The original single feed and the cylindrical dual feeds both have approximately the same quadrupole kick. Both a cross dual feed and the racetrack shape are effective at canceling the quadrupole field. We have chosen the racetrack design for ease of fabrication and because it introduces no additional penetrations in the cell walls.

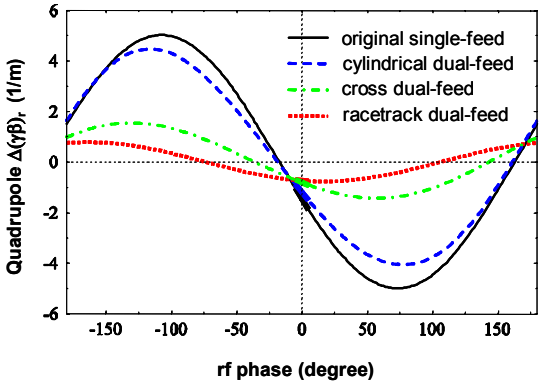

Figure 9: Change in transverse momentum as a function of RF phase for various coupler cell geometries.

It is useful to compare the angular kicks with the natural divergence of the beam. For an emittance of 1 micron, assume the beam is at a waist of radius 1 mm (rms). The beam divergence is then

$$\sigma_{x'} = \frac{\varepsilon_n}{\beta\gamma\sigma_x} = 100\ micro-radians$$

Table I gives the head-tail kick for a 10 degree (~10ps) long bunch traveling though the L0-1 input coupler cell. The head-tail angle for the original SLAC coupler is 78 micro-radians per mm. As this is nearly the same as the beam's natural divergence, the coupler field will increase the projected emittance. The racetrack dual feed quadrupole field is 20 times smaller, producing negligible emittance growth

Table I: Comparison of the original SLAC input coupler with three dual feed coupler designs. Quadrupole head-tail kick, $\Delta(\perp\beta\gamma)$/m, is given for a 10 degree bunch at 5MeV.

	$\Delta(\gamma\beta_\perp)$/m	Head-tail angle $\Delta\theta$ (rad/m)
SLAC Single feed	0.78	0.078
Symmetric dual	0.63	0.063
Race-track dual	0.04	0.004
Cross Dual	0.20	0.020

SUMMARY AND CONCLUSIONS

A thermal analysis for the 120 Hz gun was performed and the region of greatest heating and stress was determined to be the RF coupling apertures in the full cell. New apertures were designed with thicker copper and larger radii to reduce the pulse temperature rise to 41 degrees C/pulse. This is considered acceptable based upon NLC structure studies. The bulk thermal distortions will be controlled by regulating the gun coolant to keep the gun body at a constant temperature.

The designs of the RF gun and first accelerator section were studied and found to have larger RF kicks than acceptable for LCLS beam requirements. The RF coupling cells for the gun and the L0-1 structure were redesigned to have both dual feeds and racetrack shapes. The dual feed eliminates the dipole fields and the racetrack shape cancels the quadrupole fields.

The RF design of L0-1 is finished and the engineering of the dual feed accelerator structure has begun. The gun design is nearing completion.

REFERENCES

[1] Linac Coherent Light Source (LCLS) Design Study http://www-ssrl.slac.stanford.edu/lcls/cdr/.

[2] C. Limborg et al., "Sensitivity studies for the LCLS PhotoInjector Beamline", Proceedings of the 2003 International FEL Conference.

[3] R. Carr et al, "Inverse Free Electron Laser Heater for the LCLS," EPAC'04, Luzern, July 2004.

[4] Z. Huang, et. al. "Suppression of Microbunching Instability in the Linac Coherent Light Source," EPAC'04, Luzern, July 2004.

[5] R. Boyce et al., LCLS Tech Note LCLS-TN-04-4.

[6] D.P. Pritzkau and R.H. Seeman, Phy. Rev. ST Accel. Beams 5, 112002(2002)

[7] D.T Palmer et al., SLAC-PUB-95-6799.

[8] H. Loos et al., "Longitudinal Phase Space Tomography at SLAC GTF and BNL DUV-FEL," Proceedings of the 2003 International FEL Conference

[9] R.B. Neal ed., "The Stanford Two Mile Accelerator," W.A. Benjamin, 1968, pp. 144-148.

[10] Z. Li et al., "Coupler Design for the LCLS Injector L0-1 Structure." To be published as LCLS Technical Note

OPTIMAL RF SYSTEMS FOR LIGHTLY LOADED SUPERCONDUCTING STRUCTURES

T. Zwart[#], D. Cheever, W. S. Graves, D. Wang, A. Zolfaghari,
MIT Bates Accelerator Center, Middleton MA 01949
W. North, Consultant

Abstract

Recent developments in the field of RF accelerators have created a demand for power amplifiers that can support very high accelerating gradients, 15-25 MV/m, in superconducting structures with extremely low losses. Free electron lasers with modest beam current, I<10 uA, or those based on energy recovery linacs may have intrinsic power demands of less than 1 kW/m. We present a design concept for an amplifier and external tuner system that will efficiently meet this requirement. A likely amplifier for this application is the Inductive Output Tube (IOT) which offers high AC/RF efficiency, flexible power output and switching capability without the need for external modulation. The use of solid state amplifiers is also considered. The external tuner circuit makes use of low loss RF components, include waveguide, circulators and ferrite phase shifters to create a moderate quality standing wave between the amplifier and the superconducting cavity. The potential effective Q_{ext} exceeds 3×10^7. Plans for future work are presented.

INTRODUCTION

For emerging high gradient, low beam power superconducting (SC) accelerators, including energy recovery linacs (ERL's) and free electron lasers (FEL's), the bulk of the generated RF power is reflected from the SC structure and absorbed in an external load, connected to the reflected-power port of a ferrite circulator. MIT is pursuing the design of a system that would recycle this reflected RF power while maintaining adequate phase and amplitude control of the accelerating cavities. This will greatly reduce the power needed from the RF amplifier, thus substantially reducing the capital and operating costs associated with these devices.

The intrinsic RF power required by an ERL or an FEL can be quite low. For today's state-of-the-art superconducting structures with unloaded quality factors (Q_0) in excess of 10^{10} [1] the power to maintain the cavity field amplitude is less than 50 W/m at gradients of 25 MV/m. For average beam currents (or imbalanced currents in the case of an ERL) of less than 10 uA, the beam power is limited to 250 W/m at a gradient of 25 MV/m. An ideal RF source coupled to a one meter cavity would therefore need to supply only 300 W to meet these demands.

Despite these low intrinsic demands, present accelerator designs call for amplifiers with power capabilities in excess of 5 kW/m [2]. This additional power is necessary to compensate for small changes in the superconducting cavity geometry due to mechanical vibrations. This problem, known as microphonics, can be addressed by spoiling the cavity quality factor with a stronger coupling to the amplifier than would be necessary in the absence of the microphonic perturbation.

One strategy under development is to actively correct the cavity geometry by means of a piezo-restrictive tuner [3]. This tuner adjusts the length of the cavity to compensate for the mechanical vibrations and maintain the cavity center frequency. The device must be able to correct the micron scale deformations of the cavity at frequencies between DC and a few hundred Hz.

Another approach is to make use of an external tuner to apply a corrective phase shift to the reflected RF wave and reintroduce it to the cavity structure [4, 5]. In essence a second standing wave circuit of much lower quality factor has been introduced into the RF system between the amplifier and the superconducting structure. The necessary external control (phase shift) could be realized by means of low loss ferrite phase shifters similar to those presently in use at the Bates accelerator. Such phase shifters with very low insertion loss (<0.7 dB), adequate range ($d\varphi$ > ±90°), resolution ($d\varphi$ < 1°), and high power handling capability (P_{avg} > 5 kW), are now available commercially. Efforts are also underway at Fermilab National Accelerator Laboratory to construct a device with similar specifications for use in tuning individual cavities of the TESLA Test Facility II Accelerator [6].

INTRINSIC RF POWER DEMAND

The power demand for an RF cavity can be divided into two categories: power to maintain the cavity fields and power to accelerate the beam. Equation 1 shows the distribution of these power requirements:

$$P = \frac{V^2}{(r/Q)Q_{ext}} \cdot \frac{\beta+1}{4\beta} \cdot \left[(1+a+b)^2 + (2Q_{ext}\frac{\delta\omega}{\omega})^2 \right] \quad (1)$$

[#]zwart@rocko.mit.edu

Here P is the power required by the RF amplifier, V is the cavity peak voltage, r/Q is the cavity shunt impedance, β is the coupling factor, a and b are factors for the beam power at two distinct phases (these terms almost cancel in the case of the ERL) and $\delta\omega$ is a measure of the frequency variation of the cavity due to uncontrolled sources. For superconducting structures where β is much greater than unity and applications with negligible beam loading equation 1 becomes

$$P = \frac{V^2}{4(r/Q)Q_{ext}} \cdot \left[1 + (2Q_{ext}\frac{\delta\omega}{\omega})^2 \right] \qquad (2)$$

Note that the power requirement due to the last term in equation 2 pertaining to the frequency variation of the cavity would vanish if the RF source was able to vary its frequency to match the variation in the cavity center frequency. Clearly this is not acceptable for an accelerator where many 100's of individual cavities must be phase locked with respect to each other. In this case additional amplifier power is required to compensate for a lower gain as the cavity frequency fluctuates about the linac center frequency.

In the case where the beam power is small, the width of the frequency variation determines the optimum coupling and thus the power demand of the cavity. Figure 1 shows the power demand at a beam current of 10 uA as a function of coupling factor for several values of the frequency variation width.

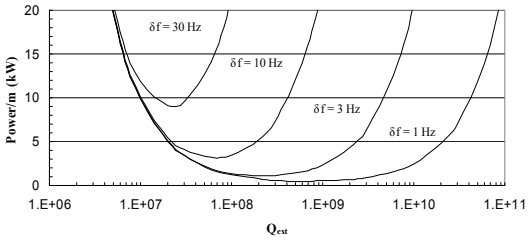

Figure 1: Amplifier power demand vs external coupling (Q_{ext}) for TESLA cavities at 1.3 GHz. All curves assume a cavity voltage of 25 MV and a beam current of 10 uA.

Notice that if the frequency variation could be controlled at the level of 1 Hz the required power would be reduced to less than one kW per RF amplifier. The use of solid-state amplifiers rather than vacuum tubes might then become possible.

Initial results using a piezo tuner indicate that in some environments microphonics can be controlled to values less than 50 Hz [Hof03]. The piezo tuner also has substantial advantages in that it is a very low power device and it has the potential to maintain the cavity center frequency by applying a correction directly to the source of the perturbing influence, ie variations in the cavity length. However the piezo also requires operation at cryogenic temperatures and will have limited access inside the cryomodule in the event of a failure. Further, the piezo device has its own mechanical resonances which may interfere with control system performance if the self-resonance frequency overlaps with the microphonic excitation to be controlled.

The approach considered here to reduce the frequency variation of the system is by the introduction of an additional external oscillator of much lower Q. Corrective phase shifts can be applied to the external system which will reduce the frequency variation of the coupled system.

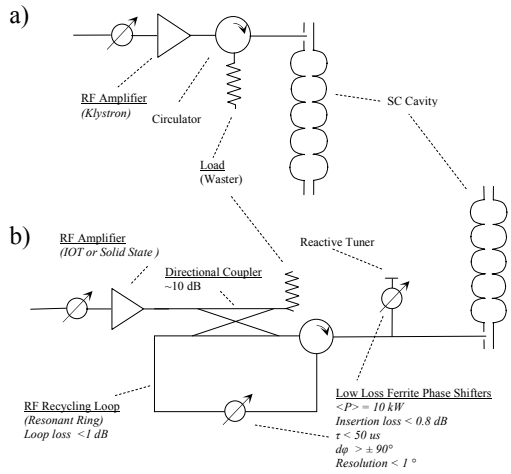

Figure 2: Standard Amplifier Configuration (a) and reactive tuner/RF recycler configuration (b).

Figure 2 shows conceptually how a higher value of Q_{ext} might be reached with the introduction of an external tuner and resonant ring into the amplifier cavity circuit. Figure 2a shows the standard configuration where the amplifier output is delivered to the cavity through a "protected" system, including circulator and load. All reflected power from the cavity is delivered to the load port of the circulator. In Figure 2b several new features have been introduced into the amplifier/tuner circuit. First, the klystron is replaced with either an Inductive Output Tube or Solid State power amplifier. Second, the amplifier is coupled into a resonant ring waveguide structure through a directional coupler of -10 dB. The optimum value of the coupling will depend on the losses in the resonant ring. The phase of the traveling wave in the ring is adjusted by means of a low loss phase shifter which does not

Beam & Cavity Power	Circulator Loss (dB)	Phase Shifter Loss (dB)	Other Loss (dB)	Total Loss (dB)	Dir. Coupler (dB)	Power Gain (G)	P_{ring} (kW)	P_{source} (kW)
240	0.00	0.00	0.00	0.16	14.4	27.3	10	<0.4
240	0.35	0.35	0.14	1.00	6.8	4.8	10	2.1
240	0.45	0.45	0.14	1.20	6.1	4.1	10	2.5
240	0.60	0.60	0.14	1.50	5.3	3.4	10	3.0
240	0.70	0.70	0.14	1.70	4.9	3.0	10	3.4
240	0.80	0.80	0.24	2.00	4.3	2.7	10	3.7

Table 1: Amplifier power requirements and resonant ring power gain for varying component insertion losses. The value of the directional coupler is optimized for each different total loss. 20 MV/m, 10 uA beam current and $Q_{ext} = 10^7$ are assumed

require fast response time for CW beams as it will respond to variations in the real component of the cavity power which should depend only on changes in the dissipated power. Third, a reactive tuner has been installed on the waveguide leg between the resonant ring and the superconducting cavity. This tuner makes use of a low loss ferrite phase shifter as it will require operation at bandwidths significantly greater than the frequency of the microphonic excitation. The enhancement in field strength in the resonant structure should exceed a factor of two and will depend critically on the losses in the phase shifter and circulator. Table 1 list the optimum coupling of the resonant ring as a function of ring losses and indicates that amplifier powers of only ~3 kW should be necessary to achieve stable operation at gradients of 20 MV/m.

RF AMPLIFIER SELECTION

At an operating frequency of 1.3 GHz three distinct amplifier types appear to have the potential to meet the power needs of these lightly loaded SRF cavities. They are the klystron, the inductive output tube (IOT) and the solid-state power amplifier (SSPA). As described above the power demand is likely to fall in the range of 2-15 kW per meter of accelerating structure. The exact power requirement will depend on the beam loading and the degree to which the cavity center frequency can be controlled. Both klystron and IOT offer power levels in excess of 10 kW. The klystron is the more established amplifier for accelerator applications, while the IOT technology is presently in the prototype stage at frequencies in the 1-2 GHz range. SSPA's have lower power capability but may offer many system advantages in simplicity, size, cost, flexibility, and reliability and maintenance.

Prototype IOTs have recently become available at frequencies of interest. The EIMAC Division (San Carlos, CA) of CPI has built four devices at 1300 MHz for accelerator applications, which have demonstrated 20 kW power output, 23 dB gain and over 50% efficiency (more is expected). In addition, THALES has also developed a 1.3 GHz IOT and L3 Corp. (formerly Litton Electron Dynamics) also produce IOTs for UHF TV service and will have a prototype IOT at 1300 MHz in few months.

IOTs are operated near Class B, approaching a conduction angle of 180 degrees, and a maximum theoretical efficiency of 78.5% ($\pi/4$). Practical UHF IOTs have demonstrated efficiency above 70%. Efficiency of an IOT operating at 1300 MHz is less than that of a lower-frequency device because of increased losses in the cavities and distortion of the cathode-current "discs" due to transit-time effects. Nevertheless, computer-simulated data shows conversion efficiency exceeding 68%, which has yet to be demonstrated in the prototypes.

In addition to the advantage of high efficiency the IOT offers a very flexible pulse structure and power output. Unlike the klystron the IOT's efficiency is maintained across a wide dynamic range in power. Further the IOT does not require external modulation. Removal of the low power RF from the IOT grid turns off the beam current in the tube. As the IOT is electrically "short" it has a low phase pushing factor of about one degree per percent relative voltage variation. One drawback of the IOT as compared to the klystron is lower gain. The IOT offers ~23 dB where in the case of the klystron gains in excess of 40 dB are readily achieved. This lower power gain of the IOT will place additional demands on the RF driveline distribution system.

Although no SSPA can compete with either a klystron or an IOT at the 15 kW output level, the successful realization of the tuning circuit described above would require amplifier power no greater than ~3 kW. A 1.3 GHz SSPA at 3 kW CW is quite practical and has certain advantages, including low-voltage operation and low phase and amplitude pushing factors. At every frequency there is a "cross-over" power level above which the relative advantages of Microwave Vacuum Electron Devices (MVEDs)

exceed those of SSPAs. A power level of 3 kW is probably below the "cross-over" point.

SUMMARY & RESEARCH PLAN

In the past year a team of MIT faculty and accelerator physicists at the Bates laboratory have proposed creating a Center for Accelerator Science and Technology (CAST)at MIT. The core missions of this center would be to educate students in the field of accelerator science and to promote the development of cutting edge accelerator technologies. Under the auspices of CAST MIT Bates has developed a three year plan to design, construct and qualify the highly efficient RF amplifier, RF recycler and reactive tuner system described above. The first phase will be devoted to an analysis of the amplifier performance, component requirements and engineering design. A preliminary model using the MATLAB Simulink platform will be refined. Further measurements of the open and closed loop characteristics of existing cavities at JLAB, TTF and other labs will be performed. These results will be evaluated to produce a set of specifications for the amplifier-tuner system which should yield an effective coupling of $Q_{ext} > 3\times10^7$ while still maintaining adequate phase and amplitude control of the cavity. In the final phase of this effort the system would be assembled at Bates and subsequently tested at one of the laboratories with the appropriate SRF cavity infrastructure

REFERENCES

[1] TESLA Collaboration, "*TESLA Technical Design Report*" DESY 2001-011, (2001) II 27
[2] M. Liepe et al, "*RF Parameter and Field Stability Requirments for the Cornell ERL Prototype*", Proceedings of PAC 2003 (2003) 1329
[3] S. Simrock *et al.*, "*First Demonstration of Microphonic Control of a Superconducting Cavity with a Fast Piezoelectric Tuner*", Proceedings of PAC 2003 (2003) 470
[4] Y. Kang *et al.*, "*Reactive RF Tuning for Compensation of a Detuned Accelerating Cavity*", Proceedings of Linac 2002 Gyeongju Korea (2002) 733
[5] D.Horan, E.Cherbak, "*Fast-Ferrite Tuner Operation on a 352 MHz Single Cell RF Cavity at the Advanced Photon Source*", Proceedings of PAC 2003 (2003) 1177
[6] S. Simrock, M. Huening Private Communication

ELECTRON BEAM DIAGNOSTICS USING DIFFRACTION RADIATION*

Bibo Feng†, William E. Gabella,
FEL Center, Vanderbilt University, Nashville, TN 37235, USA
Tamas R. Sashalmi, Steven E. Csorna,
Dept. of Physics, Vanderbilt University, Nashville, TN 37235, USA

Abstract

Diffraction radiation emitted from electron bunches has the potential application as a non-intercepting electron beam diagnostic. The electron longitudinal distribution in a bunch can be obtained from the coherent diffraction radiation spectrum; the transverse beam properties, such as beam size, divergence and emittance, can be measured through the analysis of the angular distribution of the coherent diffraction radiation. The design study and initial experimental results at the Vanderbilt FEL facility are presented.

INTRODUCTION

Diffraction radiation (DR) is a promising technique for electron beam diagnostic. DR technique can be developed as a low cost, compact, and non-intercepting monitor which can be very useful for free electron lasers and linear colliders. Electron bunch profile measurements have been conducted using coherent synchrotron radiation (CSR), coherent transition radiation (CTR), as well as coherent diffraction radiation (CDR)[1, 2, 3].

Diffraction Radiation is generated when a relativistic electron passes through an aperture in a metallic plate. DR intensity for N electrons can be described by

$$I_{total}(\omega) = I_1(\omega)[N + N(N-1)F(\omega)], \qquad (1)$$

where $I_1(\omega)$ is the DR intensity at frequency ω from a single electron, and $F(\omega)$ is the bunch form factor. DR, like transition radiation, is emitted in the forward direction along the electron path, and in the backward direction along the direction of specular reflection from the metal screen.

CDR has a fixed phase relative to the electron bunches, and the measurement of the coherent radiation gives the longitudinal bunch form factor $f(\omega)$, thus providing information about the longitudinal bunch distribution function $S(z)$. The electron distribution in a bunch can be obtained from the inverse Fourier transformation of the form factor. CDR is a better choice for monitoring the electron beam bunch shape as CDR perturbs the electron beam less than CTR and CSR.

The use of diffraction radiation for measuring the transverse beam dimension is a new non-invasive technique. There are a few experimental investigations at the present time [4, 5, 6] . DR intensity is proportional to the square of γ, and is distributed in angle as $1/\gamma$, where $\gamma = E_{beam}/m_e c^2$ is the normalized electron energy; thus, both the intensity and the angular distribution can be used to deduce the beam energy[7]. DR has the potential capability to diagnose multiple beam parameters such as longitudinal and transverse beam sizes, energy, position, divergence and emittance. DR technique can also be developed as a single shot measurement.

Using the DR technique, one measures the spectrum and angular distribution in the frequency domain. High spatial and time resolution are potentially possible, hence DR is able to satisfy the requirements of a linear collider facility. In addition, the angular distribution of the DR from an electron passing through a slit in a metal foil has polarization properties because of the interference effects between the two half-planes of the radiator. The polarization shows different properties with the electric field parallel and normal to the plane of the slit. The electron beam transverse dimension can be measured through the analysis of the angular distribution of the diffraction radiation.

In this paper, we present our initial results of bunch length measurements using coherent diffraction radiation from a slit. Following this introduction, we give a description of the diffraction radiation from a slit and we show the method of extracting the bunch length from the CDR interferogram in the time domain. We measured spectrum of CDR from the slit and extracted the bunch length. As an application, we investigated the effects of changing linear accelerator parameters such as phase and cathode heating on the electron bunch length.

EXPERIMENTAL SETUP AND RESULTS

DR experiments were carried out at the Vanderbilt FEL Center on a Mark III type linear accelerator. The electron beam energy is variable between 25 and 45 MeV. The electron beam macropulse duration is about 8μs, and the average beam current is about 150 mA. The pulse contains 23,000 bunches, each with approximately 50 pC and a bunch length of approximately 1 ps.

The CDR experimental setup is shown in Fig. 1. A diffraction radiator is mounted at an angle of 45° to the electron beam. The gap of the radiator is adjustable, when closed it operates as a transition radiator. DR or TR is emitted as the electron beam passes through the radiator. This radiation passes through a quartz window and is reflected by a parabolic mirror and a couple of flat mirrors into an

* Work is supported by the NSF and DOD through the MFEL program under award No. F49620-01-1-0429.

† Corresponding author. Tel.:+1-615-343-6446; fax: +1-615-343-1103. Email: bibo.feng@vanderbilt.edu

interferometer to measure the radiation spectrum. The experimental system was aligned using a HeNe laser injected upstream into the beam line.

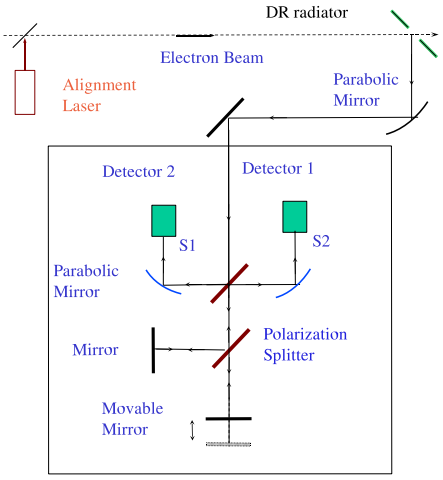

Figure 1: Schematic of the experimental setup.

The diffraction radiator consists of two separated screens and a stepping motor to adjust the width of slit. The resolution of the stepping motor is 5 μm per step. We select a polished silicon wafer as the screen because of its flatness. The thickness of screen is about 500 μm and its size is about $75 \times 50 mm^2$. One of the silicon screens is mounted on an adjustable frame, so the reflection angle can be changed in order to keep both screens coplanar.

The interferometer is a wire grid Martin-Puplett type as shown in Fig. 1. The incident light is split onto orthogonal polarization components by a 45° tilted polarizing grid splitter. One component is reflected and focused onto a reference detector; the other is incident onto another vertical polarizing grid where the light is split into two beams, reflected by the roof mirrors, and finally recombined and focused onto a pyroelectric detector(P4-45,Molectron Inc.). Only one detector was used in this experiment because of another Golay cell detector malfunctioning. The frequency limitation of the interferometer is determined by the diffraction losses, the finite aperture of the detector and the grating constant of the wire grid. The frequency range is estimated between 2 cm^{-1} and 50 cm^{-1} (wavelengths of 5 mm to 200 μm).

A typical CDR interferogram is shown in Fig. 2. The electron beam had an energy of 25 MeV and an average macropulse current of 135 mA. It was focused and centered between the edges of the two screens. The beam size was about 2.5 mm and the slit width was set to 5 mm. The CDR spectrum is obtained by Fourier transformation of the interferogram as shown in Fig. 3. We observed relative strong power peak at the frequency of 0.13 THz (wavelength of 2.3 mm). The low frequency part of the spectrum is suppressed by the detector and the interferometer.

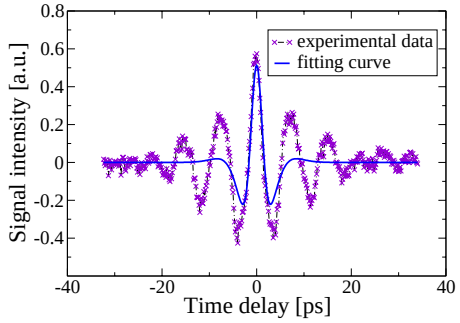

Figure 2: Typical CDR interferogram and time domain fit.

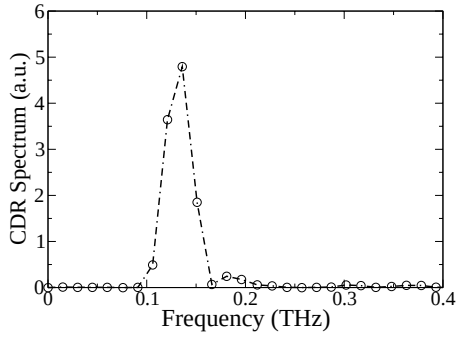

Figure 3: CDR spectrum corresponding to interferogram in Fig. 2.

A calculation of the coherent emission is shown in Eq. 1, giving the longitudinal bunch form factor $F(\omega)$ and hence providing information about the longitudinal bunch distribution function $S(z)$. Therefore, the electron distribution in a bunch can be obtained from the inverse Fourier transform of the form factor through the Kramers-Kronig relation [8].

A simpler technique to extract the electron beam bunch length from the CDR interference spectrum was introduced in reference [9]. Assuming a Gaussian longitudinal electron distribution of pulse length σ and the low frequency suppressed by the interferometer at cut-off frequency $1/\xi$, the time domain interferogram of the coherent radiation is described as

$$S(t) = e^{-\frac{t^2}{4\sigma^2}} - \frac{2\sigma e^{-\frac{t^2}{4(\sigma^2+\xi^2)}}}{\sqrt{\sigma^2+\xi^2}} + \frac{\sigma e^{-\frac{t^2}{4(\sigma^2+2\xi^2)}}}{\sqrt{\sigma^2+2\xi^2}}. \quad (2)$$

The bunch length σ can be obtained by fitting this two parameter formula to the time-domain interferogram. For example, a fit is shown in Fig. 2,which gives the electron bunch length $\sigma \simeq 0.87$ ps.

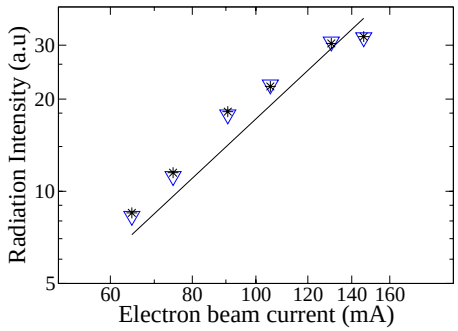

Figure 4: Dependence of CDR intensity on the electron beam current. Two measurement sets as symbols; solid line is $0.016I^2$, a fit to aI^2.

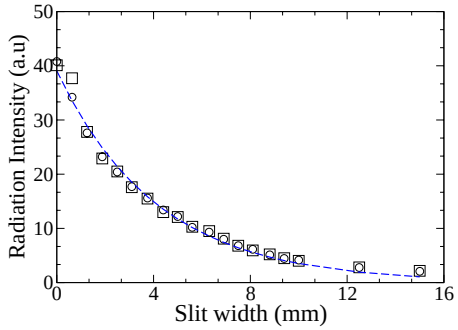

Figure 5: Dependence of CDR intensity on the slit width.

The experiment confirms that the CDR intensity is proportional to the square of the beam current (Fig.4). CDR is emitted from the slit with width of 5 mm, and using an electron beam size of 2.5 mm and energy of 39 MeV. As shown in the figure, the intensity is approximately proportional to the square of the beam current and therefore to the square of the electron number N in a bunch.

The dependence of the intensity on the slit width is shown in Fig.5. The electron beam has an energy of 29 MeV and a current of 154 mA. It has a diameter of 2.5 mm and it passes through the center of the slit. The CDR intensity decreases exponentially with increasing slit width.

The electron bunch length is affected by many parameters in the injection section and in the accelerator, including cathode heat, alpha magnet current, and accelerator phase. We observed the bunch length change while tuning these parameters. The accelerator was operating at 30 MeV, and the electron beam current was about 130 mA. The cathode needs to run within a certain temperature range to provide high current emission density and to keep the final electron beam current constant. Cathode heating in a RF gun affects the FEL efficiency. Fig. 6 shows the electron bunch length change while changing the cathode heat.

Alpha magnet strength is another important parameter for controlling the electron bunch length and optimizing a free electron laser. The alpha magnet acts both as both a momentum filter and a bunch compressor for the electron beam. Changing magnet strength selects a different energy partition of the electron beam. Fig.7 shows the dependence of electron bunch length on alpha magnet current. Electron beam bunch length decreases with respect to increasing alpha magnet current.

Changing the RF phase between the gun and the accelerator, we also observed the bunch length change. By increasing RF phase, the bunch length becomes longer as shown in Fig. 8.

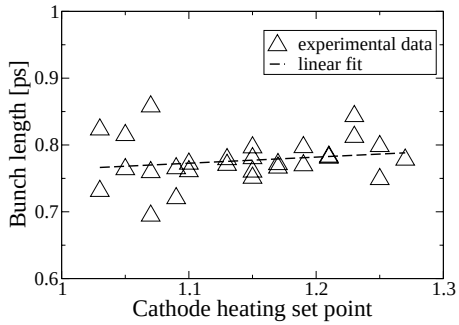

Figure 6: Bunch length vs. RF gun heating.

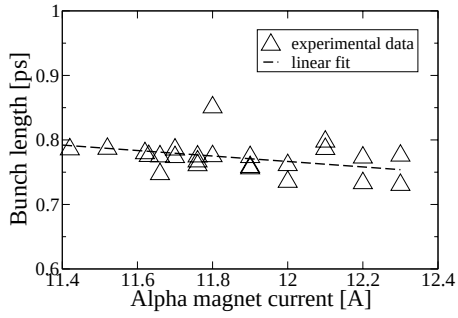

Figure 7: Dependence of electron bunch length on alpha magnet current.

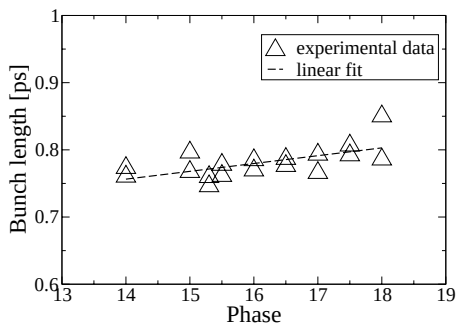

Figure 8: Dependence of electron bunch length on RF phase.

CONCLUSION

As a first stage of electron beam diagnostics using diffraction radiation, we have measured coherent DR spectrum from a slit of silicon wafer screens, and extracted the bunch length from the interferogram. We applied this diagnostic technique to the parameter study at Vanderbilt FEL linac.

We are planning to measure the electron beam transverse dimensions through the analysis of the angular distribution of incoherent DR. The total intensity of angular distribution in the normal plane has a minimum value when the beam passes through the center of slit. In practice, this property can be used to center the electron beam in the slit, and it may be a useful tool with which a cavity BPM can be centered on the beam. In order to get more accurate angular information, we plan to place two parallel slits to generate DR. The forward radiation from the first slit interferes coherently with the backward radiation from the second. Analyzing the whole angular distribution in the normal plane and fitting it to the theoretical prediction will allow us to determine the transverse dimension, the energy and emittance of the electron beam.

REFERENCES

[1] A.H. Lumpkin, N.S. Sereno, D.W. Rule,"First measurements of subpicosecond electron beam structure by autocorrelation of coherent diffraction radiation", Nucl. Inst. and Meth. A 475 (2001) 470-475;

[2] B. Feng, M. Oyamada, F. Hinode, S. Sato, Y. Kondo, Y. Shibata and M. Ikezawa,"Electron bunch shape measurement using coherent diffraction radiation", Nucl. Inst. and Meth.A 475(2001),492-497;

[3] R.B. Fiorito, D.W. Rule, "Diffraction radiation diagnostics for moderate to high energy charged particle beams", Nucl. Inst. and Meth. B 173 (2001) 67-82;

[4] M. Castellano, "A new non-intercepting beam size diagnostics using diffraction radiation from a slit", Nucl. Inst and Meth. A 394(1997)275-280;

[5] M. Castellano, V.A. Verzilov, L. Catani, A. Cianchi, G. Orlandi and M. Geitz, "Measurements of coherent diffraction radiation and its application for bunch length diagnostics in particle accelerators", Phys. Rev. E, 63 (2001) 056501-8;

[6] P. Karataev, S.Araki, R. Hamatsu, H. Hayano, T. Hirose, T. Muto, G. Naumenko, A. Potylitsyn, J. Urakawa, "Status of optical diffraction radiation experiment at KEK-ATF extraction line", Nucl. Inst and Meth. B 201 (2003) 140-152.

[7] T. I. Smith,"Instrumentation and diagnostics for free electron lasers", AIP Conference Proceeding No.252, p124, 1992.

[8] R. Lai and A. J. Sievers, Phys. Rev. E 50(1994) R3342.

[9] A. Murokh, J.B. Rosenzweig,M. Hogan, H. Suk, G. Travish, U. Happek, "Bunch length measurement of picosecond electron beams from a photoinjector using coherent transition radiation", Nucl. Inst and Meth. A 410(1998) 452-460.

SIMULATIONS OF THE NEWARK FIR FEL OPERATION

Jianjun Zheng, Ken K. Chin, NJIT, Newark, NJ 07032, USA
Eric B. Szarmes, John M. J. Madey, UH, Honolulu, HI 96816 USA

Abstract

The operation of the Newark FIR FEL is simulated for the first time using a simulation code based on the coupled Maxwell-Lorentz equations of motion. The lasing behavior is explored for a wide range of parameters. Particularly, we studied the effects of the e-beam pulse phase stability on the operation of the microtron based FIR FEL. The study shows that for even very small systematic phase slews the lasing is suppressed. However, for a random phase slew up to 7 ps/pulse centered at the nominal micropulse frequency, the laser is still capable of turning on. We estimate the tolerance for different types of phase slew and discuss the possible proper operation condition of the device.

INTRODUCTION

The Newark FEL has been under re-commissioning recently. The device was initially developed in the 1980's at AT&T Bell Laboratory under the direction of Kumar Patel and Earl Shaw[1]. The system was integrated in the late 1980's, and in 1991 it achieved first lasing at AT&T. Soon after, the device was transferred to the campus of Rutgers University (Newark)[2]. During the last decade, considerable effort was devoted to commission the system. However, the slow progress of re-commissioning suggests that there could be design and component problems. The basic design specification includes:

Electron beam parameter:
16 μs macropulse
30 Hz macropulse repetition rate
19 Mev (γ=38) nominal energy
70 mA nominal macropulse electron current
30 ps micropulse width
3 GHz micropulse repetition rate
Undulator and cavity parameters:
Helical polarization
20 cm period
50 periods
10 meter length
10 cm bore
15 meter cavity length
Laser output parameters:
Optical wavelength tunable between 100-250 μm
Micropulse length ~50 periods
Micropulse peak power ~200 kW
Macropulse length 16μs
Macropulse average power ~10 kW

If operated at its nominal specifications, the Newark FEL would closely match the performance of the Felix-1[3]. However, the Newark system had never met the design expectations. We are hereby trying to find out the reason. Investigations of the fully integrated system show that all the required components are complete. The device has no obvious design problems, although engineering errors are often hard to exclude. If the system has any prospects for further development, we must have a clear understanding of the source of the problems encountered in the commissioning of the system. To this purpose, we have initiated a diagnosis of the system based on computer simulations. Many simulation codes aimed at entire FEL systems or particular subsystems were developed in the 1980's and 1990's, each code having been designed for a specific system. Although these systems are similar to the Newark FEL in certain aspects [4, 5, 6], the simulations reported in this paper are the first to be done specifically on the Newark FEL system. The simulation code used in the present study was originally developed at Stanford University to study pulse propagation effects and system performance in the Mark III FEL[7,8], and was modified here to incorporate the helical undulator and system parameters of the Newark FEL. The lasing behavior can be explored for a wide range of parameters using this modified simulation code.

POSSIBLE SOURCES OF PROBLEMS

There are two primary problems which could possibly affect the performance of the Newark FEL:

a) Study of the first lasering behavior[2] suggests that the resonator losses are anomalous, with an observed "ring-down time" for the optical resonator indicating 6% total losses versus 1% absorption losses per round trip. This number is also consistent with the net gain observed in the early experiments[2]. A possible source of these unanticipated losses may be the hole bored through the resonator mirror, which may outcouple more loss than anticipated.

b) Traditionally, the phase of the electron pulses has not been considered an experimental variable relevant to the operation of microtrons, and hence has not been treated as a source of problems. The mechanism that makes the energy stability intrinsic to microtrons also makes the phase of the electron pulses a function of accelerating cavity voltage. Interestingly, the cathode temperature change will lead to a significant change of the accelerated electron current[9], which in turn changes the accelerating voltage and hence the phase of the electron pulses. The change in phase of the electron pulses could suppress the lasing operation of the FEL

The simulation presented in this work employs the parameters used in the first lasing experiment on the Newark FEL with more efforts concentrating on the problems mentioned above.

ASSUMPTIONS OF THE SIMULATIONS AND ANALYSIS

The simulations are restricted to the performance of the resonant cavity, disregarding physical process used to prepare the electron pulses which are fed into the undulator; we study only what happens in the optical cavity if certain operating parameters are changed. The code assumes that the undulator is ideal without fluctuation of magnetic field, and incorporates only the lowest order Gaussian mode. The e-beam pulse is assumed to have a top-hat density profile whose amplitude and profile do not change during the macropulse. In other words, all of the e-beam pulses injected into the cavity during the macropulse are statistically identical in the simulation.

The electron pulse slew imposed on the micropulse, on the time scale of the μs macropulses, is modulated in four categories:

a) Linear phase slew (first order of Taylor expansion)

$$\phi(t) = \phi_0 + \frac{d\phi}{dt}\cdot t = \phi_0 + 2\pi ft$$

where $\frac{d\phi}{dt}$ is the angular frequency $2\pi f$ evaluated at t=0, and f is the RF frequency. In practical operation of the FEL, the gun repetition rate f can assume any value as an operational parameter. However, as long as it does not change during the macropulse and remains constant over many macropulses, we can simply tune the cavity length to synchronize the electron pulses with the optical pulses, thereby maintaining good overlap between them. In other words, a linear phase slew is not a problem for the operation of the FEL.

b) Higher order systematic phase slew (i.e. the micropulse repetition rate changes during lasering)

$$\phi(t) = \phi_0 + \frac{d\phi}{dt}\cdot t + \frac{1}{2}\frac{d^2\phi}{dt^2}\cdot t^2 + \frac{1}{6}\frac{d^3\phi}{dt^3}\cdot t^3 + \cdots$$
$$= \phi_0 + 2\pi ft + c_1 t^2 + c_2 t^3 + \cdots$$

where $c_1 = \frac{1}{2}\frac{d^2\phi}{dt^2}$, $c_2 = \frac{1}{6}\frac{d^3\phi}{dt^3}$, and the derivatives are evaluated at t=0. The effect of the electron pulse on the lasing due to the c_1 and c_2 terms in the above equation can not be eliminated by tuning the cavity length. One purpose of the simulations is to determine the extent to which these systematic higher order terms will suppress the lasing of the FEL.

c) First order random phase slew

$$\phi(t) = \phi_0 + 2\pi ft + Random\_noise$$

Both uniform (i.e. square) and Gaussian distributions of the random noise are considered. Here we assume that operation frequency f does not change, and the phase fluctuates evenly around the central value within a specified range. The simulation studies are designed to reveal the noise tolerance for this type of phase slew. Previous work on the phase stability issue has been published in the last two decades, and the estimated micropulse jitter tolerance is also discussed in the literature[10], but none of these studies provides systematic experimental or simulation data that can be applied to the Newark FEL.

d) Characteristic phase slew due to cathode heating by back bombardment of the electrons (assuming both a) and b) are presented).

SIMULATION RESULTS

Parameters employed (in addition to design parameters):

Cavity length detuning = 76μm
Energy spread $\frac{\Delta\gamma}{\gamma}$ = 0.25%
Emittance $\varepsilon_x = 8\pi$ mm mrad, $\varepsilon_y = 3\pi$ mm mrad
Micropulse length 20 ps
Normalized wiggler parameter K = 1
Rayleigh range R = 288 cm (instead of 433 cm in ref. [2])
Target operation wavelength 140 μm

In simulations of the effects of cavity loss, the 6% total loss (propagation and output coupling) of the Newark FEL was sufficient to suppress lasing. The output micropulse peak power versus total loss is shown in Figure 1.

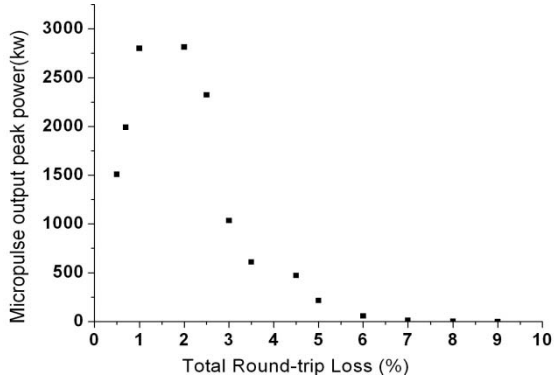

Figure 1: Loss performance

Simulations show that with an e-beam micropulse current of 2 A, lasing operation is optimized by reducing the total losses to 2%. However, if the micropulse peak current is increased from 2 A to 7 A, saturated lasing can be easily achieved even with losses up to 25%.

Simulations of higher order phase slew (i.e. systematic microwave "chirping", Figure 2) reveal that, even with a very small second order coefficient c_1 on the order of several rad/μs^2, e.g. 6 rad/μs^2, the laser could not give appreciable output, indicating that the FEL has almost zero tolerance to this kind of systematic phase slew. It is likely that third order or higher order terms give similar results.

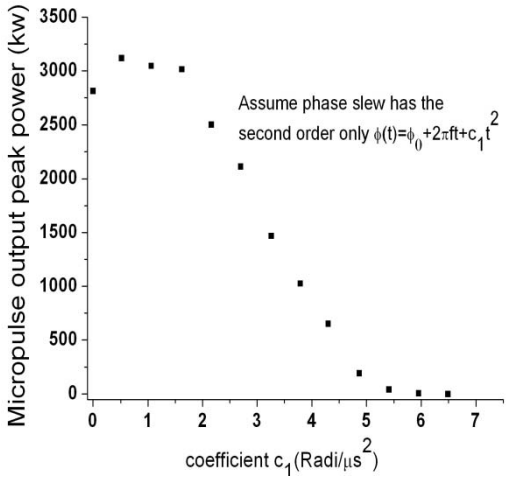

Figure 2: Effects of the second order phase slew

The real-time macropulse behavior of the FEL under this kind of phase slew (c_1>7 rad/μs^2) is shown in Figure 3. Evidently, at the early stages of oscillation, where the accumulated desynchronism between the pulses is still small, the lasing starts to build up, but it cannot continue as the phase desynchronism increases on subsequent passes in the cavity: eventually the lasing is suppressed. Simulations also show that, even with higher peak current, no lasing trend is observed, further indicating that this kind of phase slew is not permitted.

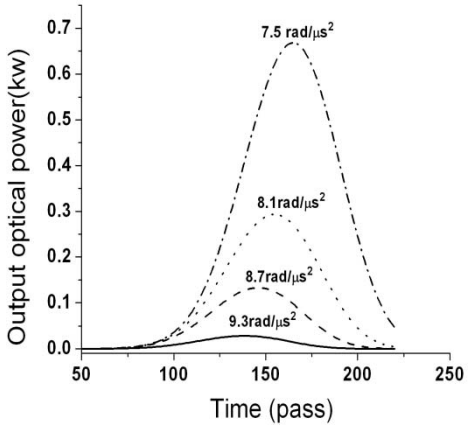

Figure 3: Lasing performances under the condition when c_1>7 rad/μs^2

This result is consistent with expectations, since the synchronization between the e-beam pulse and the optical pulse cannot be maintained for this situation and lasing is killed. To simulate the phase slew caused by random noise, two kinds of distribution are studied, uniform and Gaussian. The random noise sequence with uniform distribution is generated using the pseudo random process, which is good enough to mimic the natural random process.

The effect of the noise sequences with different standard deviations are simulated, and results show that the lasing could be achieved with relatively large electron pulse time jitters (standard deviation). Surprisingly, jitters of less than 2 ps/pulse show no effect on the laser performance, a result which is quite out of our expectations. Jitters of 7 ps/pulse are, however, sufficient to suppress the lasing. A summary of these simulations is shown in Figure 4. For the Gaussian distribution of jitter, the results appear to be indistinguishable from the results for the uniform distribution. Our simulations also demonstrate that the lasing behavior strongly depends on the noise sequence. When the averaged jitter is between 3 and 8 ps/pulse, the laser power could differ by as much as an order of magnitude depending on the specific noise sequence. The data in Figure 4 are indeed the average for different sequences with the same standard deviation.

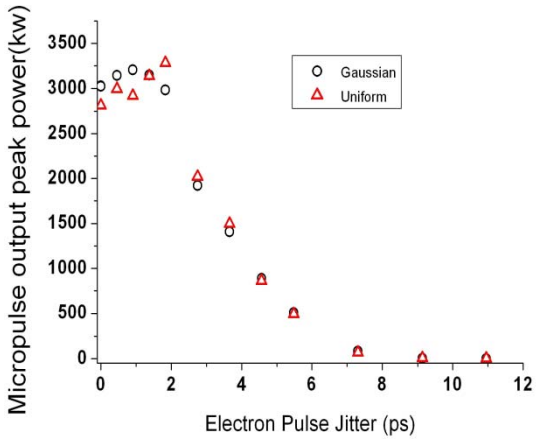

Figure 4: Effects of random electron pulse jitters on the operation of the Newark FEL

This simulation indicates that, if the e-beam pulse frequency is stable, jitters are not critical to lasing. This result can be understood in the following manner: the jitter changes the overlap between the electron and optical pulses at the beginning of the macropulse, but it does not destroy the synchronization between these pulses. Eventually, the jitter broadens the optical pulse, which in turn enhances the overlap between the electron and optical pulses. Thus, in actual operation, if the e-beam pulse is centered at one frequency, but with small fluctuations in arrival time as opposed to systematic frequency migrations, the FEL probably will produce laser output. This tolerance of 7 ps/pulse on the jitter differs

substantially from the tolerance of 0.5 ps/pulse previously estimated in the literature[10].

DISCUSSION

Simulations show that a cavity loss of 6%, corresponding to the 6cm hole used for outcoupling in the Newark FIR FEL, is sufficient to suppress lasing. For a peak micropulse current of 2 A, the optimum total loss (cavity and coupling loss) is approximately 2% per round trip. The simulation results suggest that an analysis of the hole-coupling and re-fabrication of the resonator mirrors may be beneficial.

The actual phase slew of the e-beam pulses could be more complex than we have assumed in our simulations and analysis, due to nonlinear e-beam properties originating in the injector. These non-linearities arise in the microwave cavity and gun because the real and reactive components of their shunt impedance depend on the current drawn from the cathode, and this current depends in a non-linear and non-local way on the applied RF voltage due to Schottky non-linearities in the field emission process and the induced heating of the cathode by electron back bombardment. Consequently, the emitted current increases substantially during each macropulse and yields a non-linear and systematic variation with time in both the amplitude and phase of the accelerating voltage in the cavity during each macropulse.

In addition to the systematic variations in the RF amplitude and phase described above, the non-linear and stochastic nature of electron back-heating may also introduce a degree of pulse jitter, although the relative importance with respect to the systematic variations is unknown. Thus, a combination of the systematic and random types of phase slew may be appropriate to describe the microtron pulse generator. From the record of the first lasing experiment, the e-beam current did increase with time during the macropulse, suggesting that large phase variations could possibly have suppressed the lasing operation in later efforts to commission the facility. Possible solutions to the cathode heating issue include the installation of a phase-pick off electrode, replacing the dc gun with a microwave gun[9], and designing the feed-forward compensation or feedback control system to lock the phase to the RF system master oscillator. Furthermore, since the Newark FEL shows almost zero tolerance to the systematic frequency migration, an ultra-stable RF generator is also in high demand.

CONCLUSION

The first computer simulation of the Newark FIR FEL was performed. It was found that the anomalous loss per round trip could suppress the lasing of the FEL. It also showed that the FEL has a greater tolerance for random electron pulse jitter than conventionally estimated. However, the FEL has almost zero tolerance for systematic electron pulse frequency migration. As a result, we are examining techniques to suppress or compensate these systematic variations, including installation of a phase pick-off electrode, use of a microwave gun[9], and design of feed-forward or feedback compensation to control the RF phase.

REFERENCES

[1] E.D. Shaw and C.K.N. Patel, Proc. Int. Conf. on Lasers 1980, p.53-57
[2] E.D. Shaw and R.J. Chichester, Nucl. Instr. and Meth. A318 (1992) 47
[3] P.W. van Amersfoort et al., Nucl. Instr. and Meth. A318 (1992) 42
[4] J. Blau and W.B. Colson, Nucl. Instr. and Meth. A318 (1992) 717
[5] S. Krishnagopal, M. Xie, K.J.Kim and A. Sessler, Nucl. Instr. and Meth. A318 (1992) 661
[6] G.M. Kazakevitch et al., Nucl. Instr. and Meth. A475 (2001) 599
[7] S.V. Benson et al., Nucl. Instr. and Meth., A272 (1987) 22
[8] S.V. Benson et al., Nucl. Instr. and Meth., A296 (1990) 110
[9] C.B. Mckee and J.M.J. Madey, Nucl. Instr. and Meth. A296 (1990) 716
[10] W.E. Stein, W.J.D. Johnson and J.F.Power, Nucl. Instr. and Meth. A296 (1990) 697.

MAKING AN INEXPENSIVE ELECTROMAGNETIC WIGGLER USING SHEET MATERIALS FOR THE COILS*

George H. Biallas#, Stephen V. Benson, Tommy Hiatt, George Neil, Michael Snyder, Thomas
Jefferson National Accelerator Facility, 12000 Jefferson Blvd. Newport News VA 23606, USA

Abstract

An inexpensive electromagnetic wiggler, made with twenty-eight, 8 cm periods with a K of 1 and gap of 2.6 cm was made within 11 weeks after receipt of order by an industrial machine shop. The coil design used sheet and plate materials cut to shapes using water jet cutting and was assembled in a simple stack design. The coil design extends the serpentine conductor design of the Duke OK4 to more and smaller conductors. The coils are conduction cooled with imbedded cooling plates. The wiggler features graded end pole fields, trim coil compensation for end field errors, and mirror plates on the ends to avoid three dimensional end field effects. Details of the methods used in construction and the wiggler performance are presented.

INTRODUCTION

An electromagnetic (EM) wiggler with 28, 8 cm periods and a K of 1 was manufactured for us in a very short time, 11 weeks, for a purchase cost of $176,000. Even more unusual, the magnet was made entirely using machine shop technology without the use of traditional coils. We needed the wiggler as part of multi track program to reach the goal of 10 kW from our FEL. Half of the wiggler is shown in Figure 1

Figure 1, One Half of the EM Wiggler

We needed a back-up EM Wiggler for the low energy track of our expanded effort to obtain 10 kW at the FEL Upgrade Program at Jefferson Lab[1,2]. The characteristics of the wiggler, 8 cm period, and 0.134 T rms field are in the range of a normal conducting, electromagnetic wiggler, but design and production of coils in the required three month time frame was thought to be improbable.

A lunchtime conversation led to the possibility of using a new, inexpensive approach. Make the wiggler coils out of sheet copper cut in a serpentine pattern like the undulators used in the Duke OK-4 FEL[3] that use four large, internally water-cooled, alternating orientation, serpentine conductors in each wiggler half. Since our existing power supplies are limited to 220 A, we needed many more layers of a smaller conductor. Sheet copper, 1.5 mm thick that fits in the 2 cm space between poles is a workable cross section and has acceptable power loss.

The real breakthrough came when we realized the copper sheet could be cut to high precision using newly available, water jet cutting technology. Design began in mid February, aiming at having a wiggler in 10 weeks.

DESIGN

Four Main Coil Elements

We were ready to design after setting the wiggler gap, (2.6 cm) and the number of poles, (60). The first question is: How many ampere-turns are required to excite the poles of a wiggler with serpentine conductors? Does the missing portion of the coil turn result in not creating the full field of a full turn? We didn't have time to do a 3D magnetic model of this complexity. We checked on the current used for the OK4 and there seemed to be a small effect. (Our measurements show that before any saturation effects are seen, a factor of 10% more Ampere-turns are required). We chose 24 turns per pole per half of the wiggler, about 19 % more than theoretically required by our 2D magnetic model when operating at 200 A. The power supply had 20 A additional margin.

The second most important consideration in design was coil cooling. At our selected parameters, with a current density of 6.4 A/mm^2, effective cooling is still possible. Our sheet conductor design needed cooling plates that would cool by conduction through a layer of insulation. The cooling plate has to have enough surface area to transfer the heat and enough cross section to conduct the heat to a tube of flowing cooling fluid. Early in the design process we realized that the water jet cut process gives design freedom. Our conductor didn't look like a serpent. It followed the pole tip's square corners and had three times the electrical conduction width as well as heat transfer area outside the slots. See a typical conductor shape in Figure 2. We chose cooling plates made of the same 1.5 mm sheet copper as the conductor. We used a conservative philosophy of one cooling plate for every two conductors, leading to every conductor having one surface in contact with a cooling plate through insulation. The cooling plates are cooled by tubing brazed to their outside edges beyond the outer conductor edge. See the cooling plates in Figure 3.

We chose 76 μm Kapton as the insulation between conductors and between conductors and cooling plates.

*Work supported by the US DOE Contract #DE-AC05-84ER40150, the Office of Naval Research, The Air Force Research Laboratory, the US Army Night Vision Laboratory and the Commonwealth of Virginia,
Email: biallas@jlab.org

Figure 2, Conductors

Figure 3, Cooling Plates

This is a robust insulation, with high dielectric strength, no cold flow under pressure and capable of withstanding several hundred °C in case of marginal cooling performance. An insulation sheet is shown in Figure 4.

Figure 4, Insulation Sheet

We used 6.3 mm aluminum clamp plates on the outsides of the conductor stacks to package and press the conductors, insulation and cooling plates into a unit where thermal conduction could take place reliably. A set of sixty-four 6.3 mm brass and bronze bolts and studs, run through the stacks provide uniformly distributed clamping force.

We extended our water jet cutting philosophy. We made all four of the major coil components of this complex electromagnetic wiggler very rapidly and accurately using a computer controlled water jet, the modern rendition of the jigsaw.

Simple calculations of the potential power dissipation came to 8 kW, well within the limits of the available power supply. One dimensional thermal calculations of the heat flow through the insulation, the thermal contact resistances and the heat flow through the copper conductor and cooling plate showed that temperature differences between the copper conduction strip at the center of the slot (highest temperature point) and the cooling water were limited to several degrees K.

End Complexities

We have to thank Stepan Mikhailov of the Duke University FEL Center for very constructive discussion on wiggler design at this point in the design. We copied the OK4 design's grading of end pole field's strengths, aiming for 25% field integral at the end poles and 75% at the second poles. One fourth of the conductors that serpent through the poles of the body of the wiggler end in a connection-loop around the end poles, exciting them to 25% of full field. Half of the remaining serpentine conductors end in a connection-loop around the second poles. They are excited to 75% by these turns combined with the second undulation of the quarter of the conductors looping around the end poles. The remaining one quarter of the conductors end in connection-loops around the third poles, exciting them and all subsequent poles to full field. With our chosen 24 conductors (turns) per pole in the main body of the wiggler, the ratios for end pole grading led us to stacks of 6-12-6 of the three progressively shorter serpentine conductor styles.

A simple method of connecting the 24 alternating serpentine conductors was the next design hurdle. We copied a design used on the coils of the Spreader-Recombiner Dipoles of CEBAF. At the head and tail of each serpentine conductor, we added tabs to extend the conductor termination outside the bounds of conductor/cooling plate stack. The silver plated tabs have a hole in their center and are designed to stack over one another. A series coil is formed when an insulator film is slipped between every other tab-to-tab interface and the stack of tabs is compressed to make electrical contact between the non-insulated tabs. A single bolt passing through the hole in the tabs provides the compression force. The bolt is insulated from the edges of the tab holes by an epoxy fiberglass sleeve and isolated from the end tabs by thick epoxy fiberglass washers.

The cable lug connections to the wiggler coil are made directly to the tab of a top or bottom serpentine conductor of a stack. The same bolt used to compress the tabs provides the compression force to make good electrical contact with the lug.

The grading of field in the end poles added complexity to the above connections. The stacks of tabs at each end come out of the conductor stack in three positions. The first is from the six conductors ending around the first pole. The second stack of 12 tabs is comes out at the second pole. The third stack of 6 tabs comes out at the

third pole. We added jumper strips between tab stacks to form the 24-turn coil. These stacks and connections are shown in Figure 5.

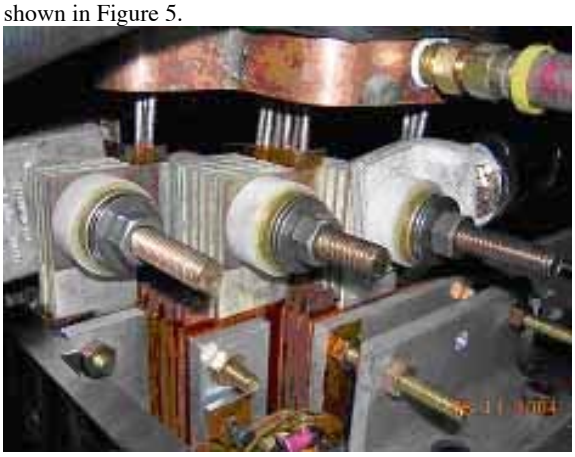

Figure 5, Lead Tabs & Bolts with Manifold

This system of tab and lug contacts and the jumpers enabled a very complex connection problem to be solved within a very small volume.

We are again indebted to Stepan Mikhailov for two additional suggestions that we adopted in our wiggler. We added trim coil sets, one set to the four end poles and a second set to the second poles. They allow us to zero out the first field integral. The second suggestion was to add mirror plates to the end of the wiggler to cancel out the 3 dimensional end field distortions.

We will run the power lead cables from or back to the power supply and to or from the opposite half of the wiggler via drops from an over-head cable tray. The pairs of opposing current cables are tied next to one another along these paths to minimize the flux lines of the 0.7 mT field created between the leads at operating current.

Cores

We planned to substitute our new wiggler for the upstream wiggler of the installed Optical Klystron (OK). We would reuse the mounting features of the common strong-back that supports both OK wigglers. This substitution requirement determined the new wiggler core's vertical dimension (10 cm thickness), the same as the core of the OK wiggler with the 20 cm periods. We reasoned that transverse field uniformity would be as good or better. We had a surplus slab of 1006 magnet steel from CEBAF's 3 m dipole program that we split in half to form the two multi poled core halves. This guaranteed identical magnetic properties in the two halves. We annealed the cores just before final machining using our standard vacuum oven, slow cool method for iron cores.

Insulation Details

We decided to forego insulating our coil packs with conventional cast epoxy-fiberglass. The chosen Kapton film is capable of holding off 30,000 V as a 2 dimensional insulation. Our challenge with this 2 dimensional insulation was to prevent arc-over to the grounded cooling plates and clamp plates from the conductor edges. These edges are found around all sixty poles, at all 64 bolt penetrations and the outer edges running the length and width of the conductor. As a design philosophy, we decided that a nominal insulation overhang of 1 mm would be applied to all such edges. Thus, at the poles, the conductors were withdrawn from the surface of the pole edge by 1 mm plus a 0.25 mm manufacturing tolerance. The Kapton film's holes to fit over the poles included only a 0.25 mm assembly tolerance. For this philosophy to succeed we would have to keep the voltage low, say below 100 V, to minimize the possibility of flash over along a surface path between conductor and ground. Fortunately, the water jet process achieved tolerances of ± 130 μm in cutting the film insulation to make the concept a reality.

The second part of the philosophy of extending 2 dimensional Kapton insulation to a 3 dimensional wiggler was to directly insulate the surfaces of the two classes of objects penetrating the conductor stacks. The pole tips are insulated with pre-formed, 76 μm Mylar sleeves and the bolts through the stacks are insulated with 50 μm Mylar tape.

To build redundancy into the insulation system, we also specified that the cores and cooling plates be coated with Sherman Williams "Clear Coat", an organic coating.

Cooling Details

We developed a compact manifold system that distributes the cooling water to the twelve parallel cooling circuits on each side of the conductor stacks and still fits within the confines of the installed strong back. The 3.2 mm outside diameter copper water tubes were bent outward in unison at the ends of the cooling plates. The manifolds are made of two parts, a pan-like vessel and a sealable cover. The pan-vessels were made with 12 holes in their bottom. The design calls for impaling the pan bottoms over the 12 tube ends and soldering the tubes into the holes from the inside of the pan while it is concave outward. Applying the sealed covers to the pan completes the manifold vessel. See figure four. This method of soldering from the front assures the small tubes are not plugged and the joints are leak free.

MANUFACTURING

We were fortunate to have a relationship with an excellent manufacturing company to make our wiggler. Process Equipment Co. (PECo) of the Dayton Ohio area machined the cores of 400 CEBAF dipoles and had performed their assembly. They were also familiar with wigglers, having machined the four core halves of the original OK Wigglers and built their strong-back. They had the additional advantage of routinely using a very good Dayton water jet company (Kerf Water Jet Co.) and a noted furnace brazing company (Wall Colmonoy).

After supplying PECo with preliminary sketches in early February followed by actual details, a contract was

placed for the Electromagnetic Wiggler on March 8 per a fixed price bid and promised 10 to 12 week delivery. This period was not our original 10 weeks from lunchtime conversation, but close to it.

We also contracted with PECo for prototype efforts of water jet cutting of both insulation and copper sheets. During this phase we transmitted CAD generated outlines of the parts directly to the water jet vendor. That vendor's software transferred the outlines into cutting code without translation error. We also funded prototype brazing of tubes to cooling plates. The prototyping gave PECo and their vendors the confidence to rapidly proceed with production once the production run materials arrived.

The production water jet cutting took about three weeks. Prototyping showed that water jet cutting forms a burr on the edges of the sheets that had to be removed. The radius left by the water jet turned out to be large enough to minimize the tear-from-an-inside-corner property of the Kapton film. This was very important; there are 240 inside corners per sheet and we only had to use tape to fix a hand full of tears. Brazing the tubes to the cooling plates took about two weeks.

As part of our contractual agreement with PECo, we designed a simple assembly tool to ease the draping of the conductors, insulation sheets and cooling plates over the 60 poles. The tool has comb like teeth. It supports the coil pieces while lowering them between the poles and can then be withdrawn. The tool was made of a sheet of polycarbonate and also cut by water jet.

Assembly took about three weeks by several skilled assembly workers and their project manager. Each coil pack was assembled twice because the first assemblies had low resistance to ground. Small chips were found embedded in the Kapton film in at least four interfaces, even though the assembly took place with extensive wiping-down in a relatively clean assembly area. They performed the second assembly in the plant's clean-room-like metrology lab.

The wiggler was received at Jefferson Lab 11 weeks after receipt of order.

RESULTS

The Jefferson Lab semi-automatic hall probe scanning table is used to measure the wiggler We removed the upper gap spacer blocks and brought the poles back to parallel using clamps. We are still qualifying the wiggler and calibrating the trim coil values vs. K. as this paper is written

Vertical scans at lower fields show excellent uniformity of the fields in the body of the wiggler. We also found that the field has a 2.5% third harmonic component that reduces the peak field for a given rms field. The new peak field for an rms K of one is 0.1850 T.

A marginally acceptable trajectory (30 μm peak to peak) for an rms K of .85 is shown in figure 6, indicating the wiggler is capable of qualification. The first trial at a trajectory for the design rms K of 1.0 is shown in Figure 7. The offset and entry angle are already quite small and the trajectory is straight to 50 microns peak to peak. In both scans, a superposed saw-tooth field along the wiggler's length, increasing at higher fields leads to the S-shaped electron trajectory. The trim coils on the first and second poles do not cancel it. We are exploring several approaches, some involving trim coils. Fortunately, we left a 3 mm space between the coil pack and the bottom of the coil slot to add the coils.

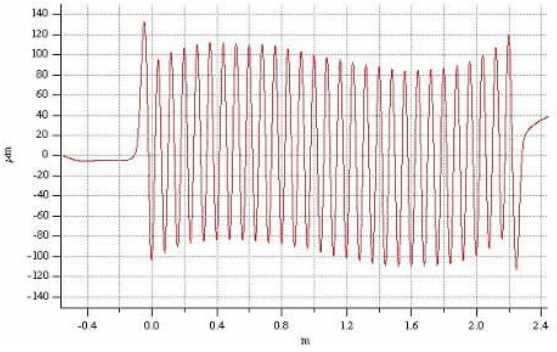

Figure 6, Trajectory for a K = 0.85

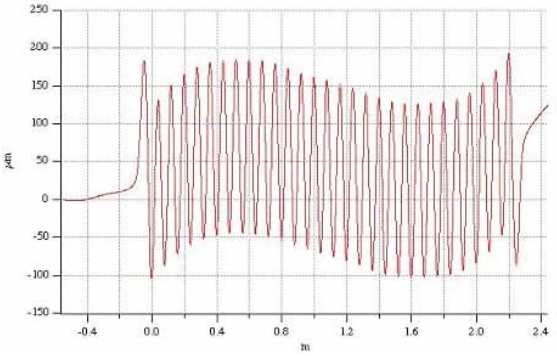

Figure 7, Trajectory for a K = 1

CONCLUSIONS

- An inexpensive wiggler may be made very rapidly using water jet cutting technology.
- Transverse field quality is not compromised by the use of serpentine conductor in this configuration.
- Field quality for this wiggler is limited by a small saturation effect - this is correctable by trim coils.
- This manufacturing method may be extended to more complicated wigglers with higher fields and shorter periods using of 3D magnetic and thermal modeling.

REFERENCES

[1] D. Douglas et.al. "A 10 kW IRFEL Design For Jefferson Lab", Proc. PAC2001, Chicago, June 2001.

[2] S. Benson et.al., High Power Lasing in the IR Upgrade FEL at Jefferson Lab, these Proceedings.

[3] G.N. Kulipanov et al, "Thee VEPP-3 Storage-Ring Optical Klystron: Lasing in the visible and ultraviolet Regions", Proc. Of the 11th FEL Conf. Naples, Fl, USA, Aug-Sept 1989.

PERFORMANCE AND MODELING OF THE JLAB IR FEL UPGRADE INJECTOR

C. Hernandez-Garcia*, K. Beard, S. Benson, G. Biallas, D. Bullard, D. Douglas, H. F. Dylla, R. Evans, A. Grippo, J. Gubeli, K. Jordan, G. Neil, M. Shinn, T. Siggins, R. Walker, B. Yunn, S. Zhang, TJNAF, Newport News, VA 23606, USA

Abstract

The JLab IR Upgrade Injector has delivered up to 9.1 mA of CW electron beam current at 9 MeV. The injector is driven by a 350 kV DC Photocathode Gun. Injector behavior and beam-based measurements are in good agreement with PARMELA simulations. The injected beam envelopes were established by measuring beam spot sizes and comparing them with those predicted by a transport matrix based model. The emittances were measured by fitting an initial trial beam matrix to the measured data. The injected bunch length was established by measuring the energy spread downstream of the Linac while operating at either side of crest.

INTRODUCTION

The injector for the Jefferson Lab 10kW Upgrade IR FEL is very similar to the 1kW IR Demo FEL [1]. The IR Demo injector has been described elsewhere [2,3]. A block diagram of the injector is shown in Figure 1. It consists of a high-DC-voltage GaAs Photocathode Gun driven by a frequency-doubled, mode-locked Nd:YLF laser, two solenoidal lenses, a room temperature buncher cavity, a 10 MeV cryounit with two CEBAF-type 5-cell superconducting cavities, a matching section composed by four quadrupoles and a bunch compressor composed by three, 20°-bending-angle dipoles. Beam diagnostics in the injector include a ceramic viewer at the entrance of the cryounit, and three optical transition radiation (OTR) profile monitors.

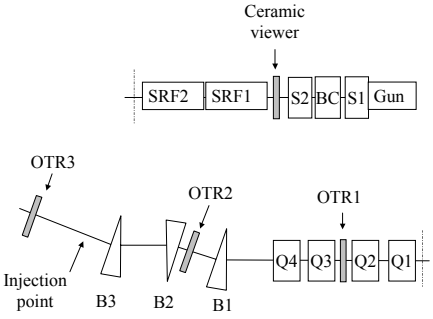

Figure 1: Block diagram of the Injector. S1 and S2 are solenoidal lenses. BC is the RF Buncher Cavity. SRF1 and SRF2 the superconducting RF cavities, Q1, Q2, Q3, and Q4 are quadrupoles, B1, B2, and B3 are dipoles.

* Corresponding author: Tel: 1-757-269-6862; fax:1-757-269-5519; E-mail address: chgarcia@jlab.org

The 10kW Upgrade IR FEL DC Photocathode Gun is an upgrade version of the 1 kW IR Demo DC Photocathode Gun, which was operated at 320 kV and achieved 5 mA of CW beam at 37.425 MHz (fortieth sub-harmonic of the accelerator rf fundamental frequency, 1.497 GHz) with 135 pC per bunch [4]. With a new 600 kV DC HVPS the current capability in the Upgrade Gun has been increased from 5 mA to 10 mA at 74.85 MHz and 135 pC/bunch, as required by the 10kW Upgrade IR FEL [5]. The 10kW Upgrade IR FEL Injector has delivered up to 9.1 mA of recirculated CW beam at 9.1 MeV with the gun operating at 350 kV and 122 pC/bunch. Pulsed operation has also been demonstrated. 8 mA/pulse in 2-16 ms-long pulses have been achieved with the drive laser operating at 75 MHz (micro-pulse frequency) and 2 Hz repetition rate. The gun routinely delivers 350 kV, 5 mA pulsed and CW beam for FEL operations. The charge extracted from the photocathode between re-cesiations is on the order of 200 C. A typical day of operations draws between 30 and 40 Coulombs from the photocathode.

MODELING

The IR FEL Demo Injector has been modeled and studied previously as a function of gun voltage [6], bunch charge [7], and number of particles [8], using a modified version of the particle-pushing code PARMELA [9] implementing the CEBAF-type SRF cavities [10]. Further modifications to the code have been recently made to incorporate overlapping of the electric field of the gun with the magnetic field of the solenoid [11]. For the Upgrade Gun, the first solenoid (S1 in Figure 1) has been shifted upstream so that now the solenoid is right against the gun's anode plate and the fields overlap. In the IR Demo Gun, the solenoid was positioned so that the magnetic field started where the electric field ended.

The design beam parameters at injection for the 10kW Upgrade IR FEL are listed in Table 1 [12,13,14].

Table 1: Beam parameters specification at injection

Transverse	Longitudinal
$\varepsilon_{N\ x,y} = 10\ \pi$ mm-mrad	$\varepsilon_{N\ z} \leq 28\ \pi$ ps-keV
$\beta_{x,y} = 10$ m	$\sigma_E \leq 15$ keV
$\alpha_{x,y} = 0$	$1.5 \leq \sigma_z \leq 2.5$ ps

The design operating voltage of the IR Demo Photocathode Gun was 500 kV (10 MV/m at the cathode), but field emission from the electrode structures encountered during its commissioning led to a decrease in the gradient at the cathode achieved by lowering the operating voltage to 320kV and by increasing the

cathode-anode gap (6 MV/m at 500 kV [15]). Simulations showed that operating the gun at lower gradient would still keep the transverse emittance within specifications [6], as measurements later proved [4].

Injector setup

The Injector modeling starts at the photocathode. Transversely, the distribution is a Gaussian truncated at $2\sigma_r$, with σ_r=2 mm. Longitudinally the distribution is Gaussian as well with σ_t =23 ps and truncated at $3\sigma_t$. The first solenoidal lens (S1 in Figure 1) strength is adjusted to focus the highly divergent electron beam following the $3\sigma_{x,y}$=beampipe-radius criterion. The buncher (BC) is a 1.497 GHz copper cavity operated at zero-crossing phase. Its gradient is set to minimize the longitudinal emittance at injection by finding the minimum energy spread at OTR2 (see Figure 1). A second solenoidal lens (S2) matches the beam transversely into the cryounit.

The cryounit accelerates the 350 keV beam to 9.1 MeV. Ideally, the solenoid (S2) strength is adjusted to position the beam waist at the middle of the first cell of the upstream (SRF1) cavity. However, this is not possible for this particular geometry due to transverse space charge effects, so the solenoid strength is set to position the beam waist as close as possible to the entrance of the SRF1 cavity. The upstream cavity (SRF1) is operated on crest, while the downstream (SRF2) cavity is operated at 20° ahead of crest for proper longitudinal beam match to the achromatic compression chicane (B1, B2, and B3). Downstream of the cryounit, four quadrupoles (Q1, Q2, Q3, and Q4) transversely match the beam to the injection point, located 1.0 m upstream of the first accelerator cryomodule (see Figure 1).

There are only two parameters that can be set in the injector and be stated as accurate, the gun voltage and the drive laser pulse length. All the rest have to be set and verified using beam-based measurements in concert with modeling results.

Code calibration

Dependencies of downstream beam parameters on a given parameter can be used to calibrate just about all the parameters. Beam-based measurements have been used to calibrate almost all of the injector parameters.

To calibrate S1, the field that produced a waist at the ceramic viewer (see Figure 1) was found by running PARMELA with the space charge option turned off. Then the same procedure was followed in the actual injector and the two field setpoints compared. It was found that the actual solenoid field is 2.24% larger than that predicted by the model.

It is difficult to calibrate the gradient value for the SRF cavities in the model against the actual setpoints, since even in EPICS there is an uncertainty of about 10%. However, the gradient ratio SRF1/SRF2 was measured by operating both cavities on crest [16]. The model was then adjusted to match the measured ratio.

There is a big discrepancy in the buncher gradient between model and the actual value reported in EPICS. The buncher setting for smallest energy spread at OTR2 corresponds in PARMELA to 0.41 MV/m, while for the actual injector is 2.5 MV/m. Therefore, the buncher gradient is set in both, model and machine, to produce the smallest energy spread at OTR2. Variations from this setpoint in the machine are translated to the model by taking the percentile increase or decrease. A careful measurement of the actual buncher gradient will be conducted later.

INJECTOR PERFORMANCE AND MODEL PREDICTIONS

Continuous feedback between PARMELA modeling and machine behavior observations proved to be an important tool during the FEL commissioning.

Longitudinal dynamics

The longitudinal match is achieved with the buncher cavity (BC), the downstream cryounit cavity (SRF2), and the downstream solenoid (S2). The buncher gradient is adjusted to minimize the energy spread at injection. The injected bunch length is adjusted with the off-crest phase on the downstream cryounit cavity (the injected bunch length is also controlled with the buncher gradient, but the energy spread grows if the buncher is not at the optimum for smallest energy spread). The downstream solenoid controls the longitudinal space charge force at the entrance of the cryounit by adjusting the beam spot size. Figure 2 shows the normalized longitudinal emittance from the cathode to the injection point.

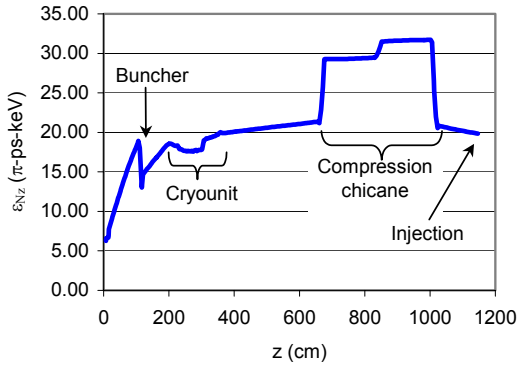

Figure 2: Normalized longitudinal emittance as a function of distance from the cathode to the injection point.

The IR Upgrade design requires an injector setup with the smallest injector energy spread. The energy spread is set using the buncher gradient, which in turn determines the injected bunch length. According to PARMELA, such a setup provides the smallest longitudinal emittance at injection (buncher gradient at 2.5 MV/m). Although the FEL lased with those settings (with the linac operating at 15° off crest), it lased better with a lower buncher gradient (2.0 MV/m) that minimized the injected bunch length.

Furthermore, the maximum Happek signal was not produced for the design buncher gradient. The optimum was a compromise between producing a small injected energy spread and a long injected bunch.

PARMELA predicts that this configuration occurs for a buncher setting 20% lower than the one that minimized the energy spread at injection. In fact this is what was observed. Measurements of the full-energy momentum spread after acceleration can be back propagated to evaluate the bunch length at injection [17]. A comparison of longitudinal phase space parameters predicted by PARMELA and those inferred *via* back-propagation is shown in Table 2.

Table 2: Model predictions at injection for two buncher settings compared to measurements inferred *via* back-propagation of energy spread measured at 80 MeV to injected energy of 9.2 MeV.

	Buncher at 2.5 MV/m	Buncher at 2.0 MV/m
PARMELA	σ_z =1.85 ps σ_E =13.2 keV ε_z =22.4 ps-keV	σ_z =0.74 ps σ_E =50 keV ε_z=36.5 ps-keV
Inferred *via* back-propagation	σ_z =1.65 ps	σ_z =0.55 ps

Note that the longitudinal emittance is much larger for the lower buncher gradient setup. The predicted longitudinal distributions at injection for the buncher gradient settings listed in Table 2 are shown in Figure 2. The energy distribution becomes the temporal distribution at the FEL and the phase distribution becomes the energy distribution. Note the large energy spread seen on the PARMELA distribution for the lower buncher gradient. This may be one of the causes for the lower FEL gain at the lower buncher setting [18].

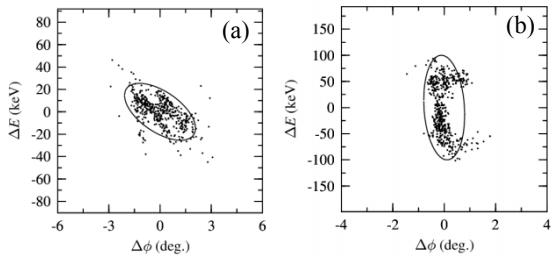

Figure 2: PARMELA longitudinal phase space at injection for: a) Buncher gradient (2.5 MV/m) optimized for smallest energy spread, and b) buncher gradient (2.0 MV/m) optimized for shortest bunch length.

For the lower buncher setting, the injected energy spread is too large and the bunch is too short. Although the injector setting with the buncher gradient that minimized the energy spread provided the design phase space at injection -a long bunch with small energy spread, it was not the best setup for lasing.

While modeling in search for an alternative injector setting, an asymmetry in the energy spread vs. linac phase and its apparent relation to bunch length were observed during the FEL commissioning. To confirm those observations, the PARMELA model was extended through the first accelerator module. The simulations confirmed the observations, indicating that the longitudinal space charge will induce what appears to be a phase-dependent asymmetry in the beam momentum spread during and after acceleration [19].

To alleviate the longitudinal space charge problem, a new injector setup was modeled to produce a longer bunch while maintaining a small energy spread. This is achieved by running the cryounit downstream cavity (SRF2) closer to crest, at 10° ahead of crest instead of the design value (20° ahead of crest). PARMELA predicts for this configuration (with the buncher gradient optimized for minimum injected energy spread) σ_z=2.4 ps, σ_E=10 keV, and ε_z =19.5 ps-keV. When the new injector configuration was implemented the injected rms bunch length inferred via back-propagation was 2.3 ps, in excellent agreement with PARMELA. Laser gain with this configuration was about as strong as the previous configuration but the peak efficiency in the detuning curve was much higher (1.25%).

Transverse Dynamics

To meet the design transverse beam envelopes at injection (see Table 1), the quadrupoles (see Figure 1) are adjusted in the model. Once a solution is found, the quadrupoles in the injector are set to the value specified by PARMELA. Then the beam transverse spot size is measured at each OTR monitor and compared to values predicted by PARMELA. The quadrupoles have not been calibrated yet against the model, but it was found that beam spots in all three OTR monitors agree with those predicted by PARMELA within 10% if the field for each quadrupole is shifted by –10 Gauss with respect to the PARMELA setpoint.

However, there is a discrepancy between the injected beam envelopes predicted by PARMELA and those established in the injector. The injected beam envelopes were established by measuring beam spot sizes after acceleration and comparing them with those predicted by a transport matrix based model. The transverse beam emittance, however agrees well with the model and it is within design specifications. The transverse emittances were measured by fitting an initial trial beam matrix to the measured data. Table 3 shows PARMELA and measured transverse beam parameters at injection with the buncher gradient set for minimum injected energy spread.

Table 3: Transverse beam parameters at injection with SRF2 cavity operating at –10 degrees off crest, buncher gradient at 2.6 MV/m, Q1=-30.5, Q2=-5, Q3=240,Q4=-248 Gauss.

	PARMELA	Established at injection
$\varepsilon_{N\_x}/\varepsilon_{N\_x}$ π mm-mrad	11.2 / 7.6	10.0 / 10.0
β_x/β_y m	14.1 / 8.4	10.7 / 6.1
α_x/α_y	-3.7 / 0.3	-0.3 / 0.4

CONCLUSIONS

The 10 kW Upgrade IR FEL Injector has demonstrated operation at 9.1 mA CW, 9.2 MeV and 122 pC/bunch. Routinely the injector delivers 5 mA pulsed and CW at 135 pC/bunch for FEL operations. In general there is good agreement between PARMELA predictions and machine behavior. The measured performance matches de model in detail.

The operational experience gained during the injector commissioning process and the constant feedback between model and machine will be very valuable for modeling and operation of future 100 mA class injectors.

ACKNOWLEDGMENTS

This work supported by The Office of Naval Research, the Joint Technology Office, NAVSEA PMS-405, the Air Force Research Laboratory, U.S. Army Night Vision Lab, the Commonwealth of Virginia, and by DOE Contract DE- AC05-84ER40150.

REFERENCES

1 S. Benson, et al., "First lasing of the Jefferson Lab IR Demo FEL", *Nucl. Inst. Meth*. A 429 (1999) 27-32.
2 P. Piot, et al., "Experimental results from an injector for an IR FEL", EPAC'98, pp. 1447-49, Stockholm, Sweden, June 1998.
3 B. C. Yunn, "Physics of the JLab FEL injector", PAC'99, pp. 2453-5, New York, April 1999.
4 T. Siggins et al., "Performance of a GaAs DC photocathode gun for the Jefferson Lab FEL", *Nucl. Inst. Meth*. A 475 (2001) 549-553.
5 D. Douglas et al., "A 10kW IR FEL Design for Jefferson Lab", PAC2001, pp. 249-52,Chicago, June 2001.
6 B. C. Yunn, "Alternative FEL Injector Setup", JLAB-TN-99-010, April 21, 1999.
7 B. C. Yunn, "High Brightness Injectors Based on Photocathode DC Gun", PAC2001, pp. 2254-6, Chicago, June 2001.
8 H. Liu, and B. C. Yunn, "A new nominal setting for the FEL injector", TJNAF TN#96-071, December 9, 1996.
9 K. Crandall and L. Young, Los Alamos National Laboratory.
10 H. Liu, et al., Nucl. Instr. And Meth., **A358** 475 (1995)
11 K. B. Beard, B. C. Yunn, and C. Hernandez-Garcia, "FEL Injector Simulation", JLAB-TN-03-28, October 2003.
12 D. Douglas, "IR Upgrade Driver Design, Rev 1.1.2", JLAB-TN-01-051, October 26, 2001.
13 D. Douglas, "Longitudinal Phase Space Management in the IR Upgrade FEL Driver", JLAB-TN-00-020, September 2000.
14 B. C. Yunn, private communication.
15 D. Engwall et al., "A high-dc-voltage GaAs photoemission gun: transverse emittance and momentum spread measurements" PAC'99, pp. 2693-5, Vancouver, May 1997.
16 S. Benson, FEL electronic logbook, entry#1193708, Feb 2, 2004.
17 D. X. Wang, et al., "Measurement of femtosecond electron buncher using rf zero-phasing method", PR E, 57, 2, 1998.
18 C. Hernandez-Garcia, S. Benson, and D. Douglas, "Qualitative behavior of the 10 kW IR Upgrade FEL Injector vs. PARMELA modeling", JLAB-TN-03-040, October 2003.
19 C. Hernandez-Garcia, et al., "Longitudinal Space Charge effects in the JLAB IR FEL SRF Linac", these proceedings.

SHORT ELECTRON BEAM BUNCH CHARACTERIZATION THROUGH MEASUREMENT OF TERAHERTZ RADIATION

S. Zhang, S. Benson, D. Douglas, M. Shinn, G. P. Williams, TJNAF, Newport News, VA23606, USA

Abstract

This paper presents measurements of sub-picosecond relativistic electron beam bunch lengths derived from an analysis of the spectra of the coherent terahertz pulses using Kramers-Kronig transformation. The results are compared with autocorrelation from a scanning polarization autocorrelator that measures the coherent optical transition radiation. The limitations of the different methods to beam characterization are discussed.

INTRODUCTION

Very high-power THz radiation has been successfully generated at Jefferson Lab[1]. The powerful short pulse THz source provides unprecedented opportunities for applications such as THz imaging and material studies. These THz pulses also carry important characteristic information about the electron bunch length which is very important to FEL and accelerator physics studies.

A measurement of the radiation spectrum will give the form factor and the electron density distribution through a Fourier Transform[2-4]. However, this always provides a symmetric distribution. By introducing a mini-phase under certain conditions, the lost phase information can be recovered and the bunch distribution asymmetry may be revealed[6]. This method requires a Kramers-Kronig transformation (KKT) analysis to calculate the mini-phase followed by an inverse Fourier transform, resulting in the expected longitudinal electron density distribution. Different from Coherent Transitional Radiation (CTR), the Coherent Synchrotron Radiation (CSR) is generated by the electrons through bending magnets and therefore requires no foils. There is no interruption to the running beam while the measurement is going on. We will use the CSR that is conveniently available form our FEL facility for the beam bunch measurement. Discussions and comparisons with other measurement methods will also be addressed.

SETUP AND MEASUREMENT

Fig.1 is an overall sketch of the Jefferson Lab 10KW upgrade FEL facility. Electrons coming from the gun are accelerated by linac and then compressed into very short bunches before traveling to the optical cavity. Synchrotron radiation is generated in several locations where the magnets bend the beam orbit. For the experiments, the primary instrument used in is a Nicolet FT-IR spectrometer. Fig.2 shows the optical layout of the experimental setup with a simplified spectrometer schematic. The THz pulses from relativistic electrons exit a diamond window through a vacuum beam port near the bending magnet that directs the 89Mev electron beam into the optical cavity and wiggler. Several silver mirrors are used to bring the THz beam into the spectrometer bench. To minimize the water absorption by THz pulses, the whole optical beam path is purged with nitrogen.

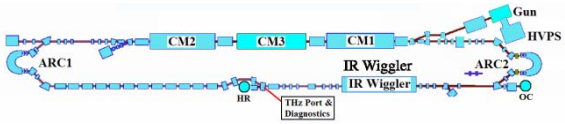

Fig.1. Layout of FEL facility and THz beam port. GUN is the photo-cathode electron source. HPVS, high-voltage power supply. CM, Linac Cryo-Module. HR, high-reflector. OC, output coupler.

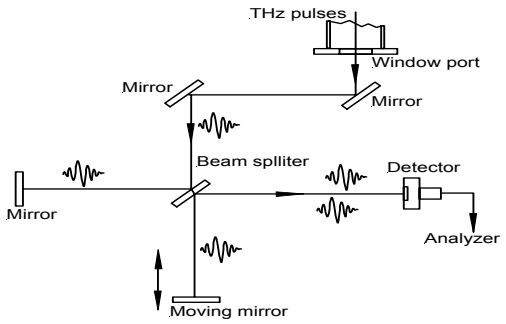

Fig.2. Schematic of the optical setup for THz spectral measurement.

RESULTS AND DISCUSSIONS

Typical spectra taken from the spectrometer are shown in Fig. 3. We used a DTGS detector with a polyethylene window. The efficiency of the detector has a spectral roll-off on the low frequency side. This can clearly be seen in the spectrum. Another major factor contributing to the low frequency cut-off is the limited diamond window aperture that restricts the diffracted beam from reaching the optical bench. Appropriate spectral fitting in the low and high frequency region is used to help reconstruct the whole spectrum and has turned out to be very effective.

Before extraction of the form factor, the spectrum was corrected by the $\omega^{2/3}$ frequency dependence of the single electron emittance. We assume that the form factor should be parabolic at low frequencies, and use $f(\omega) = 1 - a\omega^2$ as a good approximation. At

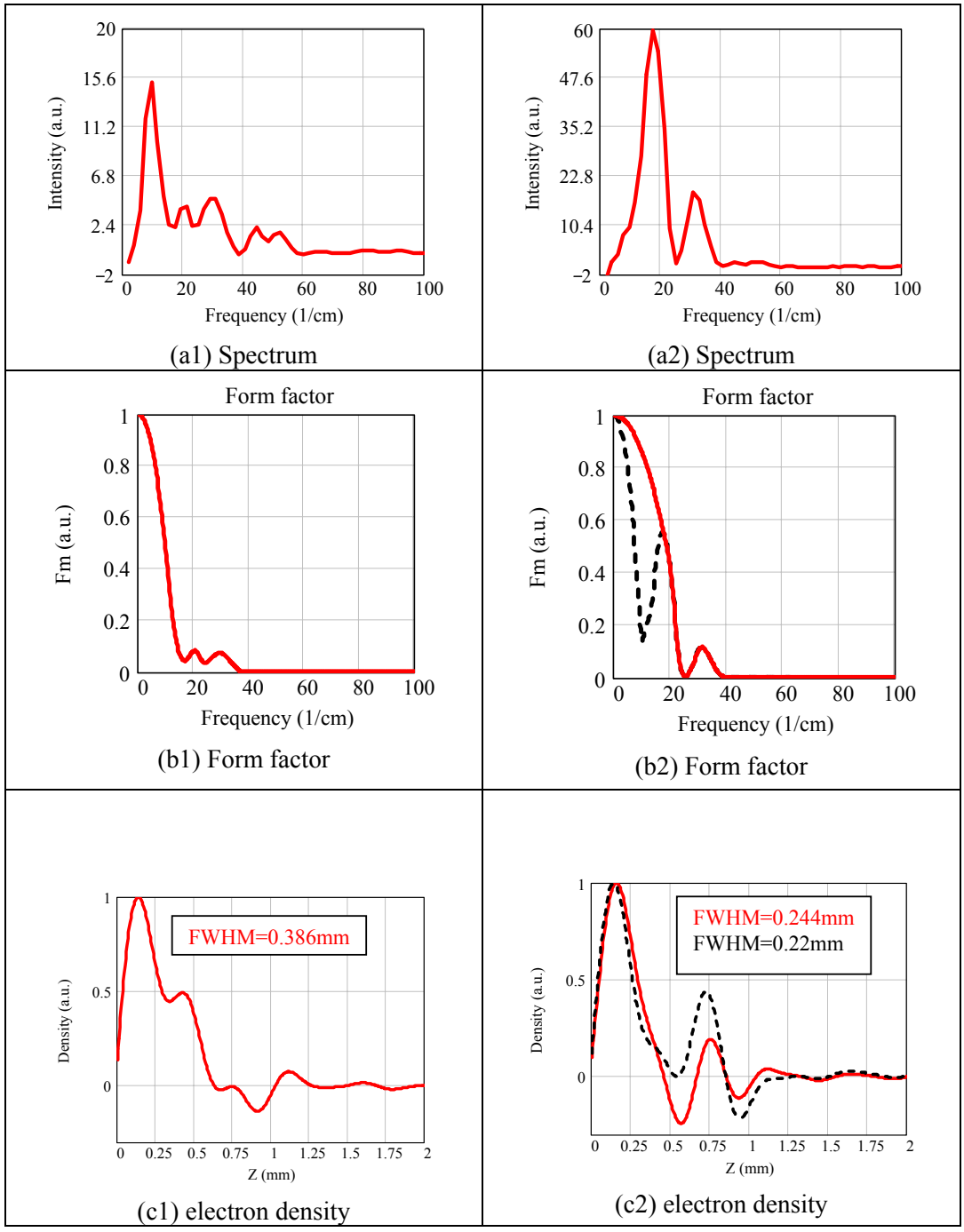

Fig.3. Two sets of measurement and analysis with different beam settings. (a) Typical THz radiation spectrum, (b) Form factor extracted from the THz spectrum, (c) Retrieved longitudinal electron density distribution. The FWHM width is 0.386mm (about 1.29ps in time duration) for in (c1) and 0.244mm (about 0.81ps) for (c2). The bunch is much shorter for the latter. The dashed curves in (b2) and (c2) are explained in text.

high frequency we use $f(\omega) = b\omega^{-4}$ (a and b are constants, depending on and decided by each specific spectral distribution). With these asymptotic attachments to each respective side, a reconstructed form factor can be obtained. Applying the KKT to the new form factor, we were able to retrieve the longitudinal electron density distribution or the beam bunch shape. Fig.3 presents the

calculated results based on two groups of measured THz spectra. The electron beam energy is 89MeV. Both profiles show clear asymmetry. The asymptotic attachment on both ends has only limited influence on the overall shape of the distribution, especially within small distances from the point where z=0[6]. Fortunately this is the region where the bunch shape and length is decided. More precise measurements at lower frequencies will lead to better determinations of the shapes of longer bunches. The negative values in the density distribution are non-physical and were partly due to the low frequency attachment. With the low frequency attachment pushed farther to the left, as shown in the dashed curves in Fig.3, the negative values in calculated density distribution are apparently reduced. The overall shape of the density distribution basically remains unchanged while a small reduction on the width can be seen.

The data in the right column of Fig.3 shows an apparently shorter bunch than that in the left. The observed higher FEL output power can also be an indication of this shorter bunch. So it is possible to get a fairly good idea about how the beam setting is by just looking at the THz spectrum while tuning the electron beams. We also did calculations on the CSR based on the experimental electron beam parameters and assuming a Gaussian beam. The spectra at different bunch lengths are shown in Fig.4. The low frequency fall-off is due to diffraction. The two sets of spectra are the same as those in Fig.3. Each of them falls into the expected bunch length range. When compared with the purely theoretical calculations, the lack of the low frequency experimental data is once again clearly evident. It can be imagined that better estimates on the bunch could be made by comparing predicted with measured data that included more low frequencies. One aspect worth mentioning is that the shorter bunch tends to push the spectrum to higher frequencies.

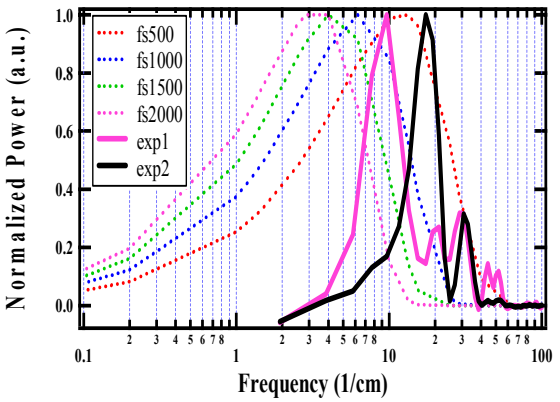

Fig.4. Comparison between the measured THz spectra and calculations with different bunch lengths. Exp1 and Exp2 correspond to the spectra shown in the left and the right column in Fig.3, respectively. The estimated bunch lengths agree with the KKT results.

Since we are dealing with THz pulses with time duration on the order of a few picoseconds or shorter, the electric field of each individual pulse only has a few cycles or less. This has been referred to as single-cycle electric field that has drawn much research interests for basic research. Compared with other ultrashort optical pulses in the visible and near IR, this type of pulse imposes certain difficulties in the determination of its temporal pulse width because of the limited number of fringes in the time window. The clear temporal intensity profile does not exist anymore and the electric field may give a better idea of the temporal characteristics. This is especially true for the measurement using polarization autocorrelation method.

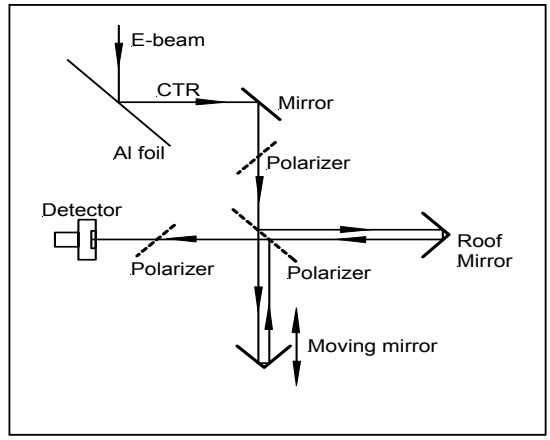

Fig.5. Simplified optical layout of a polarization autocorrelator (Martin-Pupllet interferometer). The optical pulses come from the optical transitional radiation generated by the short electron bunches interacting with a thin aluminum foil.

To have a further look at the issue, we took data from an autocorrelator, or the so-called Martin-Puplett interferometer (MPI)[7]. Fig.5 is an optical schematic of the MPI. It was set to measure the coherent optical transitional radiation (CTR) when a thin aluminum foil was inserted into the electron beam path. The MPI is a modified Michelson interferometer with thin wire grid polarizors and beam splitters. A Golay cell was used as a detector. The MPI is actually a polarization autocorrelator and the detected signal is the electric field correlation of two input replica pulses. The width of the autocorrelation traces is an indication of the input pulse width, but is not exactly the same as the width of the temporal intensity profile which is normally used for the determination of an ultrashort pulse length. In fact for a Gaussian distribution, a factor of 0.7 applies. The measured autocorrelation trace from our experiment is given in Fig.6 along with a Gaussian fitted center peak and the envelope. The FWHM values obtained from KKT method and MPI are in general agreement with each other, as can be seen from (c1) in Fig.3 and the fitted curve in Fig.6 (where data comes from

beams under same condition) . However, there are some errors which come from many factors and can be above 10%. The precision of the fitting data is primarily limited by the number of available fringes in the pulse. In the present case, there are only a few fringes and fitting is impractical. However, to obtain the fitting (blue curve) we generated the dotted curve by inverting value of the solid curve which lay below a baseline from the asymptotic limits. We note in passing, however, that in practice the central peak is frequently used as an indication of the bunch length because this peak has a clear envelope of its own which is easy to fit.

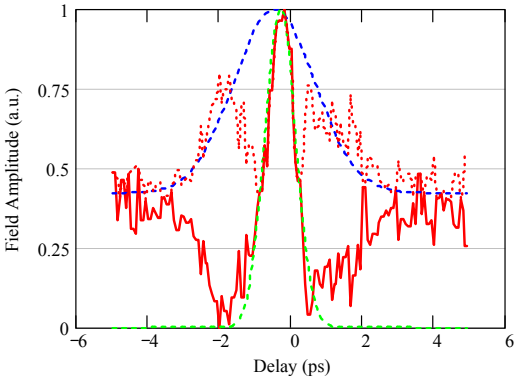

Fig.6. The red solid line is an CTR autocorrelation trace from MPI. Blue dotted curve is the fitted envelope with 1.34ps FWHM. Fitted central peak 0.71ps FWHM(green dashed line).

SUMMARY

The temporal characterization of sub-picosecond relativistic electron bunches has been performed through the measurements of THz radiation and subsequent KKT analysis. Comparisons between the CSR calculation and the result from an MPI that measures the CTR were presented. The issues with the determination of short THz pulse length are also discussed. The KKT analysis of the CSR may become a useful tool for bunch shape measurement but the precision primarily depends on the spectral measurement, especially at the lower frequency end in our case. Further studies along with a comparison with other methods such as electro-optical sampling will be helpful to clarify the above mentioned issues.

Acknowledgement

The authors would like to thank the FEL team for their assistance during the experiment and for beam operations. This work is supported by the Office of Naval Research, Research, the Joint Technology Office, NAVSEA PMS-405, the Air Force Research Laboratory, the US Army Night Vision Lab, the Commonwealth of Virginia and DOE Contract DE-AC05-84ER40150.

REFERENCES

[1] G. Carr, M. Martin, W. McKinney, K. Jordan, G. Neil, G. Williams, Nature, **420** 153-156 (2002).

[2] K.Ishi et al., Phys. Rev. **A43**, 5597 (1991).

[3] J. S. Nodvick, D. S. Saxon, Phys. Rev., **96**, 180 (1954).

[4] E. B. Blum, U. Happek,A. J. Sievers, Nucl. Instr. Meth. **A307**, 568 (1991).

[5] R. Lai, A. J. Sievers, Nucl. Instr. Meth. **A397**, 221 – 231 (1997).

[6] R. Lai, A. J. Sievers, Phys. Rev. **E52**, 4576-4579 (1995).

[7] D.Martin, Polarizing Interferometric Spectrometers for the Near and Sub-millimeter Spectra, Chpt.2, New York, Academic Press, (1982).

RF SOURCES FOR 3RD & 4TH GENERATION LIGHT SOURCES

S. Lenci, H. Bohlen, E. Wright, A. Balkcum, A. Mizuhara, CPI MPP, Palo Alto, California, USA
R. Tornoe, Y. Li, CPI Eimac, San Carlos, California, USA

Abstract

The growing number of third and fourth generation light sources has resulted in an increase of the available rf sources to power them. Single beam klystrons are the traditional power source, but the development of IOT's and multiple-beam klystrons (MBK's) in L-Band have increased the options for these machines. The Eimac division of CPI has recently built and tested a prototype L-Band IOT, which delivered 30 kW CW at 1.3 GHz. Future work includes the building of an IOT at 1.5 GHz. Meanwhile the MPP division of CPI is currently testing the prototype 10 MW peak, 1.3 GHz MBK for the TESLA x-ray free-electron laser (XFEL). Test results for these new products as well as information on all CPI products at 500 MHz, 1.3 GHz, and 1.5 GHz will be presented.

INTRODUCTION

CPI, formerly the Electron Device Group of Varian Associates, has a long history of building high-power pulsed and CW klystrons for many applications. For many years, klystrons have been the preferred RF power amplifiers for both pulsed and CW linacs at UHF and higher frequencies. Their high power capability, reasonable efficiency, stability, robustness and long life expectancy have earned them that position. Recent developments are encroaching into the klystrons dominant position. Advancements in Inductive Output Tubes (IOT) and Multiple-Beam Klystrons (MBK) make these devices very attractive in a growing number of applications.

Operation at 500 MHz provides many options at power levels below 60 kW CW. This frequency is in the UHF-TV broadcast band and can often utilize existing devices with little or no modification. Devices for L-band tend to be specifically designed for a given application, but then become available to others interested in using the developed hardware.

KLYSTRONS

Klystrons have been the traditional device for accelerators for many years. They come in a variety of power levels and frequencies. Modern design tools and the plethora of existing designs make this device easily adaptable to the needs of the accelerator community. Klystrons at 500 MHz, 1.3 GHz, and 1.5 GHz are available in many power levels, both pulsed and CW. Beam conversion to rf efficiency can exceed 65% and rf gain ranges from 40 to 55 dB.

UHF Klystrons

At 500 MHz, CPI has klystrons up to 800 kW CW. The lower power tubes are the VKP-7953 series klystron. The device is based on our UHF-TV klystron that has many years of proven service. The VKP-7953A is a slightly modified version of our UHF-TV klystron and rated for 70 kW CW and the VKP-7953B is rated for 100 kW CW. The "A" version has been in service at Taiwan's Synchrotron Radiation Research Center (SRRC) for the past 10 years. The first of higher power "B" version is presently being built. These tubes have a 5-cavity rf circuit, mod anode gun, and a single output window.

At 800 kW CW CPI has built the VKP-7957A for the Cornell Electron Storage Ring (CESR) at Cornell University and the VKP-7958A for the HERA ring at DESY. These tubes share the same rf circuit, have a single output window, and an electron gun with a modulating anode. The VKP-7957A operates horizontally with the gun in oil; the VKP-7958A operated vertically with the gun up and in air, see Figure 1.

Figure 1: VKP-7958A Klystron for DESY

Additionally there are a number of klystrons at other UHF frequencies. The VKP-7952A was developed for the APT Project and produces 1 MW CW at 700 MHz. At 805 MHz, the VKP-8291A is in production for the Spallation Neutron Source project at Oak Ridge National Lab. CPI is building 81 of these 550 kW peak pulsed devices with a beam conversion to rf efficiency in excess of 65% [1]. Additionally there is the VKP-7955 which operates at 200 kW pulsed at 1 msec at 805 MHz.

L-Band Klystrons

In this frequency band CPI has a series of low power klystrons that have been in service for a number of years. The VKL-7811 series have been reliable klystrons for a number of facilities around the world. These compact devices use diode guns, liquid cooling, and permanent magnets for focusing. The VKL-7811W was developed in the early 1990's for the Continuous Electron Beam Accelerator Facility (CEBAF) at the Thomas Jefferson

National Accelerator Facility. These tubes are rated for 5 kW CW at 1.497 GHz. Approximately 380 units were made in the original production run to populate the accelerator. Next came the VKL-7811M (5 kW CW at 1.3 GHz) for an application in Japan. Finally the VKL-7811ST (10 kW CW at 1.3 GHz) was developed for Stanford University and Forschungszentrum Rossendorf (FZR).

The VKL-7966A is a 100 kW CW klystron at 1.497 GHz that was recently built to drive the cryogenic cavities in the injector stage of the FEL Driver Accelerator at TJNAF [2]. These units were used in their experiment that achieved 10 kilowatts of infrared laser light, making it the most powerful tunable laser in the world.

In addition to these klystrons that were specifically designed for accelerator applications, CPI has tubes designed for radar that are available as well. The VA-963A is rated for 6.5 MW peak power and 10 kW of average power. It's a pulsed device that can provide 5 μseconds pulses at 1.3 GHz. The VKL-7796 is rated for 4 MW peak and 300 kW average with pulse lengths up to 130 μseconds.

Table 1: Various UHF and L-Band Klystrons

Model	Frequency	Output Power, kW	Duty
VKP-7953A	500 MHz	70	CW
VKP-7953B	500 MHz	100	CW
VKP-7957A	500 MHz	800	CW
VKP-7958A	500 MHz	800	CW
VKP-7952A	700 MHz	1000	CW
VKP-8291A	805 MHz	550	.09
VKP-7955	805 MHz	200	.002
VKL-7811M	1.3 GHz	5	CW
VKL-7811ST	1.3 GHz	10	CW
VA-963A	1.3 GHz	6500	.001
VKL-7796	1.3 GHz	4000	.075
VKL-7811W	1.497 GHz	5	CW
VKL-7966A	1.497 GHz	100	CW

MULTIPLE BEAM KLYSTRONS (MBK)

MBK technology can be separated into two categories: Fundamental Mode (FM) and Higher-Order Mode (HM) MBKs [3]. The differences between the two are the proximity of neighboring beams and the proximity of neighboring cavity modes. The primary drawback to the FM-MBK is that the clustered electron beams are constrained to fall within a circle of approximately $\lambda_0/4$ for optimum cavity interaction. The FM-MBK are generally used for applications requiring large instantaneous bandwidth. The HM-MBK electron beams can be widely separated from each other operating into higher-order-mode cavities. The HM-MBK is selected when relatively narrow bandwidths are acceptable, as with conventional single-beam klystrons, at high average power. However, for this geometry, the cathode loading is not constrained by the circuit and is instead limited by the skill of the beam-optics designer.

An equally important factor is that as a result of beam interception with and without rf, the cavity thermal loading is distributed along a relatively large surface area, increasing the average power handling capability of the HM-MBK versus the FM-MBK. A comparison of MBKs to single-beam klystrons can be seen below.

Advantages

- Lower operating voltage for a given rf power level
- Lower x-ray level due to lower operating voltage
- High efficiency vs. microperveance
- Large instantaneous bandwidths (FM-MBK)
- Compact, lightweight
- Low Noise

Disadvantages

- Difficult to focus the electron beams
- Lower average power (FM-MBK only)
- High cathode loading (FM-MBK only)

1.3 GHz MBK for TESLA

The first opportunity for CPI to build an MBK was for the TESLA project at DESY. The CPI-DESY engineering team agreed to use the HM-MBK approach. The primary reason for doing so is discussed above and worth repeating: low cathode loading combined with distributed thermal loading of the rf circuit. This HM-MBK uses six off-axis electron beams emitted from six individual cathodes. Table 2 lists the essential design parameters for this device.

Table 2: TESLA MBK Typical Operating Parameters

Parameter	**Value**	**Units**
Peak Output Power	10	MW
Average Output Power	150	kW
Beam Voltage	114	kV
Beam Current	131	A
Efficiency	65-67	%
Frequency	1300	MHz
Pulse Duration	1.5	ms
Saturated Gain	47	dB
Number of Electron Beams	6	- - -
Number of Cavities	6	- - -
Cathode Loading	~2.1	A/cm^2
Solenoid Power	4000	W, max.
Cathode Loading	~2.0	A/cm^2

TESLA MBK Prototype Test Results

Initial testing of the device has validated the basic design approach [4]. Six 120 kV electron beams of measurably identical currents of 22.9 A each have been successfully propagated through the klystron circuit with 99.5% DC beam transmission at full operating video duty and with 98.5% saturated RF transmission. A peak power of 10 MW at 1.3 GHz with 60% efficiency and 49 dB of gain have been measured. The output power versus input

power curves for varying beam voltages is shown in Figure 2. As can be seen, the curve characteristics for the MBK are substantially the same as a conventional klystron. A photo of the device is shown in Figure 3.

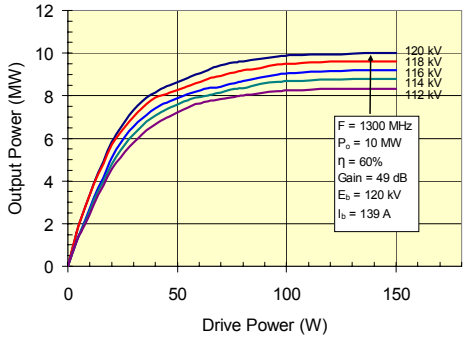

Figure 2: Measured output power versus drive power for five beam voltages

Figure 3: Prototype MBK for TESLA

Unfortunately testing was stopped due to a problem with one of the two output windows. During long pulse, high-average power testing several gas bursts were experienced, along with severe rf pulse shortening. The average power capability of the MBK degraded after these events. The problem with the window was verified. The klystron is in the process of being repaired with the target of shipping it to DESY by the end of the year.

INDUCTIVE OUTPUT TUBES (IOT)

Since the late 1980s the Inductive Output Tube (IOT) has established itself as a useful device for broadcast, applied science and industrial applications in the UHF range. Compared to a klystron, the IOT compensates for its lower gain with both superior efficiency and linearity, and it outperforms the tetrode, its next of kin, with regard to power capability and gain. However, it has long been thought that transit time effects limit the useful frequency range of IOTs to the VHF and UHF bands; 1 GHz was considered a threshold beyond which the performance of IOTs as fundamental frequency amplifiers would fall off rapidly.

Several key advantages of the IOT make them desirable for accelerator use. The salient parameters in this case are:

1. Most particle accelerator applications do not require high linearity. The IOT can be operated in class C and thus provide efficiency levels far beyond the reach of klystrons, see Figure 4.
2. The IOT does not saturate at the point of its highest efficiency like the klystron. The device does not require power back-off from optimum efficiency to allow fast feedback.
3. Since the beam current in an IOT is grid-controlled, a HV modulator is not required for pulse operation. It is sufficient to pulse the drive power.

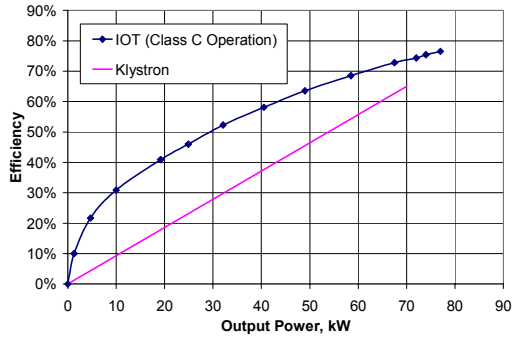

Figure 4: IOT Efficiency vs. Typical Klystron

The existing UHF-TV IOT, EIMAC K2 series, is well suited for use at 500 MHz, or anywhere within the UHF-TV operating band (470-810 MHz) and has a very positive track record in TV broadcast service (up to 130 kW peak in digital or up to 75 kW peak sync in analogue operation, respectively), as well as a CW amplifier for scientific purposes (up to 80 kW CW) with the addition of some cooling.

UHF IOTs are in CW operation in the 5 MeV CW Microtron at MELCO in Kobe, Japan. Two IOTs are combined to generate 100 kW of RF power at 500 MHz. At the FEL at the Japan Atomic Energy Research Institute, Tokai, Japan, two IOTs are used independently as RF sources for the pre-acceleration super conducting cavities (499.8 MHz). See Table 3.

Table 3: Eimac K2 IOT Operation at 500 MHz

Power Level (kW)	50	60	67	80
Beam Voltage (kV)	30	30	35	35
Beam Current (A)	2.14	2.67	2.6	2.98
Grid Current (A)	0.14	0.24	0.14	0.22
RF Drive Power (W)	190	267	275	380
Power Gain (dB)	24.2	23.5	23.9	23.2
Efficiency (%)	77.9	74.9	73.6	76.7

Eimac has delivered 15 IOTs for pulsed operation in a US government project. Each IOT delivers 80 kW peak power and operates at a different frequency in the UHF range.

The First L-band IOT design

The fundamental-frequency IOT seemed to be the single solution to maintain the well-appreciated IOT properties for an L-band version [5]. It was decided to modify EIMAC K2 as little as needed only to arrive at a 1.3 GHz version. To replace the external-cavity UHF output section with an internal 1.3 GHz resonator was a straight-forward development step. The output section consists of a standard 1-5/8 inch coaxial line, which contains an alumina window of the same type that is in use in numerous L-band klystrons. The cavity is water-cooled which serves to remove the loss energy from the cavity and provide stability against de-tuning.

Much more concern was spent on the input circuit. The input impedance of an IOT is of the order of 10 Ω only; thus the input circuit has to transform the impedance downward from that of the input line, instead of upward like in the case of a klystron. Beyond that, the input signal has to be transferred safely and reliably from ground level to the high-voltage DC potential of the electron gun. High-voltage-safe dimensions and low impedance are not easily married, but it was possible to find an elegant solution to the problem.

Apart from these two segments, almost all other elements are identical with those of the UHF version. The 1.3 GHz prototype is shown in Fig. 5.

Figure 5: 1.3 GHz IOT

L-Band Prototype Test Results

The first prototype was slightly off frequency; the second unit was slightly overcoupled. Prototype 3 was on frequency and measured data shown in Table 4.

Table 4: Prototype 3 Test Results at 1.3 GHz

Beam Voltage (kV)	Beam Current (A)	Drive Power (W)	Output Power (kW)	Gain (dB)	Effi-ciency (%)
24	0.79	208	10.0	17	52.7
25	1.10	203	15.1	19	54.9
26	1.46	183	20.6	21	54.3
32	1.35	192	25.7	21	59.5
34	1.39	253	30.2	21	63.8

Even at almost 30 kW CW the body of the IOT and its output section did not show signs of meeting any limitations. The thermal output power measurements are believed to be pessimistic because the power-absorbing bricks of the load were operating at very high temperatures and reflected a considerable part of the power back into the waveguide in the form of infrared radiation.

It is believed that these tests, performed in December of 2003 and January of 2004, mark the first time that an IOT has been operated at a frequency beyond the UHF band. The encouraging results have driven the development of a 1.5 GHz, 15 kW CW version, which is scheduled for testing in early 2005, and a 300 kW long pulse IOT at 1.3 GHz.

SUMMARY

CPI has expanded its catalogue of vacuum electron devices with the addition of the MBK and IOT. The particle accelerator community has more options in types of devices to power their machines in UHF and L-band. The klystron will remain the workhorse with the ability to cover virtually any power need. The MBK provides high efficiency at lower operating voltage while the IOT provides high efficiency over a wide range of power level. These newcomers will provide system designers lowering procurement and operating costs.

REFERENCES

[1] S. Lenci, et al., “Large Scale Production of 805-MHz Pulsed Klystrons for SNS”, Proceedings of EPAC 2004, paper TUPKF076.

[2] A. Mizuhara, “A 100 kW, 1497 MHz, CW Klystron for FEL Driver Accelerator”, Proceedings from FEL 2002 Conference, p II-27 – II-28.

[3] E. Wright, et al., “Development of a 10 MW, L-Band Multiple Beam Klystron for TESLA”, Proceedings of PAC 2003, paper TPAE029, p. 1144-1146.

[4] E. Wright, et al., “Test Results for a 10 MW, L-Band Multiple Beam Klystron for TESLA”, Proceedings of EPAC 2004, paper TUPKF077.

[5] H. Bohlen, et al., “Development of a 1.3 GHz Inductive Output Tube for Particle Accelerators”, Proceedings of Displays and Vacuum Electronics 2004 Conference, Garmisch-Partenkirchen, Germany

HIGH CURRENT ENERGY RECOVERY LINAC AT BNL*

V.N. Litvinenko#, I. Ben-Zvi, D.S. Barton, D. Beavis, M. Blaskiewicz, J.M. Brennan A. Burrill, R. Calaga, P. Cameron, X. Chang, R. Connolly, D.M. Gassner, H. Hahn, A. Hershcovitch, H.-C.Hseuh, P. Johnson, D. Kayran, J. Kewisch, R. Lambiase, W. Meng, G. McIntyre, T.C. Nehring, A. Nicoletti, D. Pate, J. Rank, T. Roser, T. Russo, J. Scaduto, K.S. Smith, T. Srinivasan-Rao, N.W. Williams, K.-C. Wu, V. Yakimenko, K. Yip, A. Zaltsman, Y. Zhao,
Brookhaven National Laboratory, Upton, NY, USA
H.P. Bluem, A. Burger, M. Cole, A. Favale, D. Holmes, J. Rathke, T. Schultheiss, A. Todd,
Advanced Energy Systems, Medford, NY, USA
J. Delayen, W. Funk, L. Phillips, J. Preble,
Thomas Jefferson National Accelerator Facility, Newport News, VA, USA

Abstract

We present the design and the parameters of a small Energy Recovery Linac (ERL) facility, which is under construction at Collider-Accelerator Department, BNL. This R&D facility has goals to demonstrate CW operation of ERL with average beam current in the range of 0.1 - 1 ampere, combined with very high efficiency of energy recovery. The possibility for future up-grade to a two-pass ERL is being considered. The heart of the facility is a 5-cell 703.75 MHz super-conducting RF linac with HOM damping. Flexible lattice of ERL provides a test-bed for testing issues of transverse and longitudinal instabilities and diagnostics of intense CW e-beam. ERL is also perfectly suited for a far-IR FEL. We present the status and plans for construction and commissioning of this facility.

GOALS OF ERL R&D PROGRAM AT BNL

The ERL R&D program is pursued by the Collider Accelerator Department (C-AD) at BNL as an important stepping-stone for 10-fold increase of the luminosity of the Relativistic Heavy Ion Collider (RHIC) [1] using relativistic electron cooling [2] of gold ion beams with energy of 100 GeV per nucleon. The system with increased luminosity and electron cooling, called RHIC II, is sketched below.

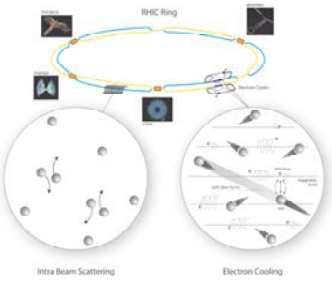

Figure 1. Electron cooling of RHIC, pictorial diagram. Electron cooling is used to reduce the emittance of an ion beam circulating in a storage ring by transferring the transverse motion (the heat) from a high emittance (hot) ion beam to a low emittance (cold) electron beam.

Furthermore, the ERL R&D program extends toward a possibility of using 10-20 GeV ERL for future electron-hadron/heavy ion collider, eRHIC [3].

The 10-fold increase of luminosity in RHIC II will extend the studies of quark-gluon plasma and QCD vacuum beyond the discovery phase towards their full characterization [1]. The ERL-based eRHIC with luminosity of 10^{34} $cm^{-2}sec^{-1}$ per nucleon will extend the capability of RHIC even further using polarized electrons to probe Colour Glass Condensate and spin structure of nuclear, to mention a few. These projects are the driving force behind the development of ampere-class ERL technology [4], which will find many applications including light sources and FELs, These programs also define the goals for the R&D ERL development:

- Test the key components of the RHIC II electron cooler
- Test the key components of the High Current Energy Recovery Linac based solely on SRF technology
  - 703.75 MHz SRF gun test with 500 mA
  - High current 5-cell SRF linac test with HOM absorbers (one turn - 500 mA, two turns - 1 A)
  - Test the beam current stability criteria for CW beam currents ~ 1 A
- Test the key components and scalability for future linac-ring collider eRHIC with
  - 10-25 GeV SRF ERL for eRHIC
  - SRF ERL based an FEL-driver for high current polarized electron gun
  - Test the attainable ranges of electron beam parameters in SRF ERL

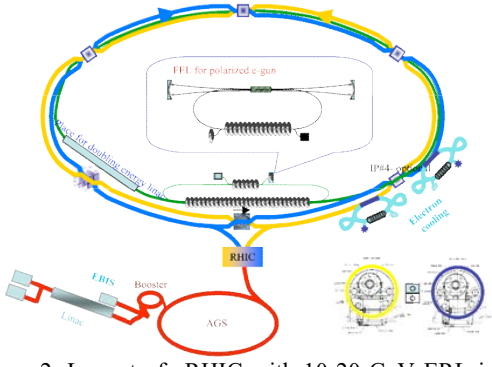

Figure 2. Layout of eRHIC with 10-20 GeV ERL in the RHIC tunnel and with circularly polarized FEL-driver for polarized electron photo-injector [3].

The plans call for construction and commissioning of the prototype ERL within 3 years. The ERL will be located in one of the spacious bays in Bldg. 912 of the RHIC/AGS complex.

Fig.3 The layout of the facility (top) and the photograph of the shielded vault for R&D ERL under construction in the bay of Bldg. 912. The bay is equipped with an overhead crane. The control room is located outside of the bay in a separate building.

Technical details of R&D ERL constitute a significant part of the 260-page ZDR (Zero's-order Design Report), for the RHIC II electron cooler, which is undergoing final polishing. The intensive R&D program geared towards the construction of the prototype ERL is under way: from development of high efficiency photo-cathodes [4] to the development of new merging system compatible with emittance compensation.

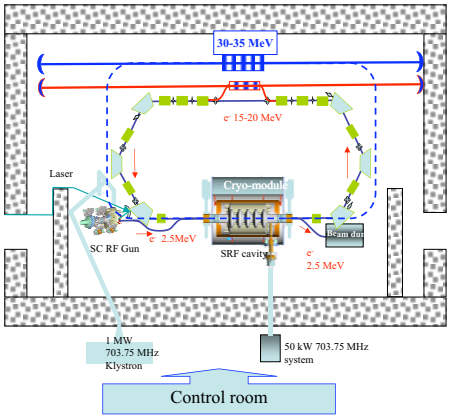

Fig. 4 Layout of the R&D linac in the shielded vault

The SRF gun is currently under design at Advanced Energy Systems with the participation of BNL. The 703.75 MHz, 1 MW CW RF system for the SRF gun is under procurement. The 5-cell SRF linac is under construction at Advanced Energy Systems and is planned to be installed and tested in Bldg. 912 in the middle of 2005. The 50 KW 703.75 MHz RF transmitter for the linac has been installed at the site and is undergoing commissioning.

The lattice of the ERL is designed and needs some final refinements to fit with the SRF injector. The main feature of the lattice is that it provides a wide range of transport matrix parameters to study both longitudinal and transverse beam break-up instability (BBU), while remaining achromatic.

In this paper we describe the current design, the main component and the expected performance of the R&D ERL.

LAYOUT AND MAIN COMPONENTS OF THE ERL

The base-line design has one turn: electrons are generated in the superconducting half-cell gun to about 2.5 MeV and injected through the merging system with emittance compensation (see below) into the main linac. Linac accelerates electrons 15-20 MeV, which pass through a one turn re-circulating loop with achromatic flexible optics (see below). The path-length of the loop provides for 180 degrees change of the RF phase, causing electron deceleration (hence energy recovery) down to 2.5 MeV. The decelerated beam separates from the higher energy beam and goes to the beam-dump. The main expected parameters of this system are listed in Table I.

Table I. Parameters of the R&D ERL in Bldg. 912

	High charge	High current
Injection energy, MeV	2.5	2.5
Maximum beam energy, MeV	20	20
Average beam current, A, up to	0.2	0.5
Bunch rep-rate, MHz	9.4	703.75
Charge per bunch, nC	~20	1.3
Normalized emittance, mm*mrad	~ 30	~1-3
Efficiency of current recovery, >	99.95%	99.95%

A description of the SRF gun and its photocathode system can be found elsewhere [4]. The maximum current from this gun will be limited to a maximum value of about 0.5 A by the RF power of 1 MW 703.75 MHz CW klystron.

Zigzag merging system

One of the novel systems we plan to use for the R&D ERL is a merging system providing achromatic conditions for the space charge dominated beam and compatible with the emittance compensation scheme [6].

The idea of the Z-system is to provide achromatic conditions for electron whose energy is changing while it propagates through the merging system. A detailed description of this mechanism will be published elsewhere [6]. Fig. 6 shows results of Parmela simulations for the R&D ERL injection system. In contrast with traditional chicane, where horizontal emittance suffers a

significant growth as result of the bending trajectory, with the Z-system the emittances are equal to each other and are very close to attainable for the straight pass.

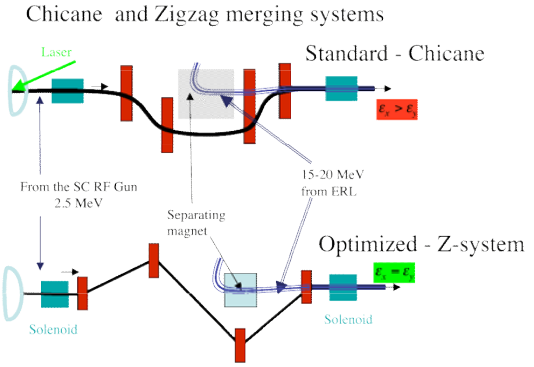

Fig. 5. Schematics of traditional chicane and Zigzag-system (Z-system) for merging system of low and high energy beams in an ERL. In contrast with chicane, which provides achromatic conditions and emittance preservation only for low-charge beams, the Z-system provide for emittance preservation and emittance compensation of e-beams with a high charge.

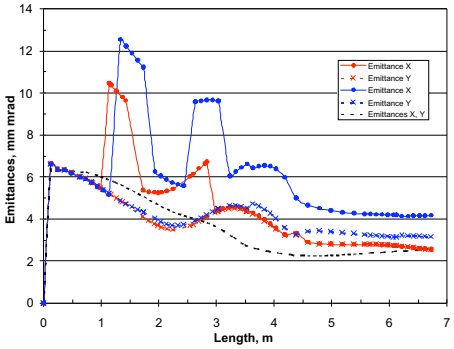

Fig. 6. Results of Parmela simulation for 1 nC e-bunch from the cathode to the end of the linac in R&D ERL: black dashed curve is for a round beam passing without bends (the baseline); blue curves are for that with a compensated chicane, red curves are for that with the Zigzag merging system.

5-cell SRF linac

The heart of the ERL facility is 5-cell SRF linac, which is designed for operating with ampere-class CW e-beams [4,5]. The main feature of this design is very large apertures of the structure which effectively couples all Higher Order Modes (HOMs) to two ferrite absorbers, which is located on both sides of the cryo-module (see Fig.7). This design provides for very low Q's for HOMs and hence very high ERL stability. Thresholds of the transverse beam break-up instability (TBBU) for ERL with one 5-cell linacs is measured in amperes (see example in Fig. 8). We plan to intentionally tune the lattice of the ERL to a special mode (see below) to test the TDBBU predictions for our SRF linac with current limited only to few hundreds of milliamps.

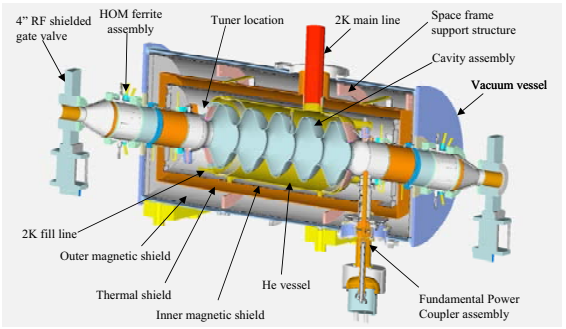

Fig. 7. The 5-cell SRF linac with HOM absorbers
© Advanced Energy System

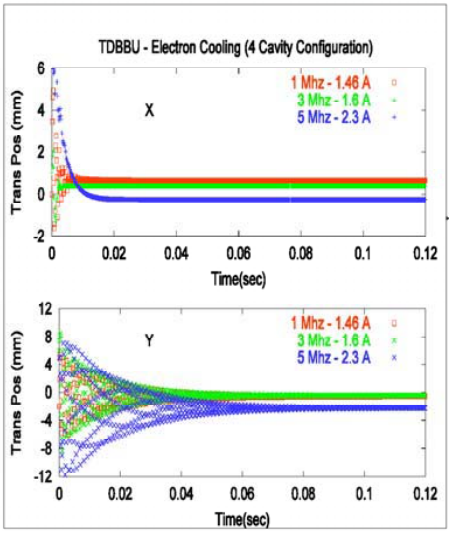

Fig. 8. Results of TBBU simulations for ERL with four 5-cell linacs [5].

Lattice of the loop

The lattice of the ERL loop controls the parameters of a symplectic transport matrix:

$$\begin{bmatrix} x \\ x' \\ y \\ y' \\ -c\delta t \\ \delta E/E \end{bmatrix}_{s2} = \begin{bmatrix} m11 & \boldsymbol{m12} & \ldots & \ldots & \ldots & D_x \\ m21 & m22 & \ldots & \ldots & \ldots & D_x' \\ \ldots & \ldots & m33 & \boldsymbol{m34} & \ldots & D_y \\ \ldots & \ldots & m43 & m44 & \ldots & D_y' \\ \ldots & \ldots & \ldots & \ldots & m55 & \boldsymbol{m56} \\ \ldots & \ldots & \ldots & \ldots & \ldots & m66 \end{bmatrix} \cdot \begin{bmatrix} x \\ x' \\ y \\ y' \\ -c\delta t \\ \delta E/E \end{bmatrix}_{s1}$$

which affect the stability and operation conditions of the ERL. The lattice of the loop is intentionally chosen to be very flexible for the R&D ERL to be a test-bed of new ampere-range of beam currents in ERL technology. The adjustable part of the lattice has two arcs and a straight section. Each arc is a three-bend achromat with adjustable longitudinal dispersion. Twelve quadrupoles in the dispersion-free straight section provides for matching of the β-function and for choosing the desirable phase advances independently in horizontal and vertical planes.

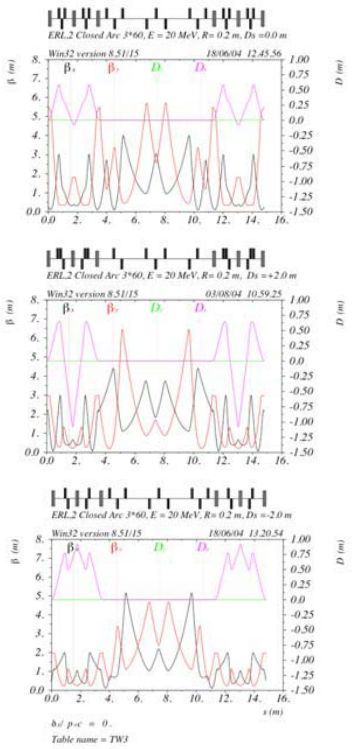

Fig. 9. Lattice β- and D- functions of the R&D ERL for the case of zero, positive (+2m) and negative (-2m) longitudinal dispersion $D_s = m_{56}$. The m_{12} and m_{34} elements are controlled independently using twelve quadrupoles in the dispersion-free straight section.

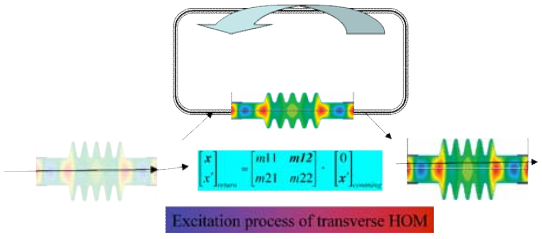

Fig. 10 A sketch of TBBU interaction in R&D ERL: injected electron beam kicked transversely by HOM passes the loop and comes to the cavity with a displacement proportional to m_{12} (for vertical - m_{34}) element of the loop matrix. The displaced beam excites the HOM, which closes the excitation loop of TBBU process.

As shown in a simple sketch below, the threshold of TBBU instability will depend on the values of m_{12} and m_{34}. Hence, we plan to increase these elements to the level of few hundreds of mA, required to observe or to reliably measure TBBU instability threshold and to compare it with the prediction based on the cavity model.

Potential up-grade of the R&D

We consider the potential extension of this facility into two turn configuration and installation of IR FEL, if funds are available. The shielded vault is designed for ERL with maximum energy of 54 MeV to accommodate these future up-grades. The loop of the ERL is designed to accommodate large energy spread of electron beam in the case of operating a high power FEL.

Table 2. Parameters of a test FEL for R&D ERL

Energy [MeV]	20	40
Wavelength [μm]	10	2.5
with micro-wiggler	*5*	*1*
Beam Power (MW)	10	20
FEL ext. efficiency	1%	1%
FEL power (kW)	100	200
Charge/bunch (nC)	1.3	1.3

CONCLUSIONS

We are designing, constructing, and commissioning a small (about 20 meters in circumference) R&D ERL to test the key issues of an amp-class CW electron accelerator with high brightness beams, required for future nuclear physics experiments at RHIC-II and eRHIC. An extensive R&D program on many novel components to be used in the ERL is under way. This facility, planned to be commissioned in 2007, will serve as the test-bet for new ranges of beam parameters whose application will extend well beyond the goals set forward by the Collider Accelerator Department at BNL.

REFERENCES

[1] http://www.bnl.gov/henp/docs/NSAC_RHICII-eRHIC_2-15-03.pdf, T. Hallman, T. Kirk, T. Roser and R.G. Milner, RHIC II/eRHIC White Paper, Submitted to the NSAC Sub-Committee on Future Facilities, February 15, 2003,

[2] Electron Cooling for RHIC, I. Ben-Zvi, et al., Proceedings of the 2001 Particle Accelerator Conference, Chicago, IL, USA, June 18-22, 2001, p.48

[3] http://www.agsrhichome.bnl.gov/eRHIC/, Appendix A, Linac-Ring Option "eRHIC, Future Electron-ion Collider at BNL", V. Ptitsyn at al., MOPLT170, Proceedings of EPAC-2004, Geneva, Switzerland, July 5-9, 2004

[4] I. Ben-Zvi at al., Ampere Average Current Photo-Injector and Energy Recovery Linac, these Proceedings.

[5] R. Calaga et al., High Current Superconducting Cavities at RHIC, TUPKF078, Proceedings of EPAC-2004, Geneva, Switzerland, July 5-9, 2004

[6] D. Kayran, V. Litvinenko, Novel merging system preserving the emittance of high brightness high charge beams in energy recovery linacs, in preparation

THERMAL AND FIELD ENHANCED PHOTOEMISSION: COMPARISON OF THEORY TO EXPERIMENT

K. L. Jensen, Naval Research Laboratory, Washington DC, USA
D. W. Feldman, N. Moody, D. Demske, P. G. O'Shea, U. of Maryland, College Park, MD, USA

Abstract

Photocathodes are a critical component of high-gain FEL's and the analysis of their emission is complex. We have developed a time-dependent model accounting for the effects of laser heating and thermal propagation on photoemission. It accounts for surface conditions (coating, field enhancement, reflectivity), laser parameters (duration, intensity, wavelength), and material characteristics (reflectivity, laser penetration depth, scattering rates) to predict current distribution and quantum efficiency. The photoemission and quantum efficiency from metals and, in particular, dispenser photocathodes, is evaluated: the later introduces complications such as coverage non-uniformity and field enhancement.

INTRODUCTION

Photoinjectors are important electron sources for Free Electron Lasers (FEL's) due to the high quality electron beams that can be achieved, and may impact synchrotron light sources, high energy linear colliders, X-ray sources, and other applications [1-4] and in particular, Naval shipboard defense systems [5]. Photo injector concepts share a drive laser (which produces short bunches of photons) and photocathode (which converts the photon bunch into short bunches of electrons). The Quantum Efficiency, emittance generated at the cathode, cathode lifetime, survivability, emission promptness and uniformity are all issues. Metallic photocathodes are rugged and have fast response times (which allows for pulse shaping), but they have low QE and require incident UV light [6]. Direct band-gap p-type semiconductors (alkali antimonides and alkali tellurides [7-8], and bulk III-V with Cesium and oxidant [9]) are the highest QE photocathodes available and operate at longer wavelengths, but they are chemically reactive and easily poisoned by, e.g., H_20 and CO_2, damaged by back ion bombardment [10], and (for NEA III-V photocathodes) insufficiently responsive for pulse shaping in an rf injector due to their long emission time (> 40 ps for GaAs).

The ideal photocathode will have a high QE at the longest possible wavelength, be capable of *in situ* repair or rehabilitation, and demonstrate good lifetime. To meet the particular needs of a megawatt (MW) class FEL, it must produce 1 nC of charge in a 10-50 ps pulse every nanosecond (ns) (100 A peak and 1 A average current) in applied fields of 10-50 MV/m and background pressures of 0.01 mTorr – and to do so for several seconds. Such a cathode is presently unavailable, and even if it were, the ability to predict its performance and the beam it generates lacks adequate emission models. Dispenser cathodes have shown to have promise as photoemitters [11,12]. They consist of a work function coating diffusing out from a porous metal base and their operation has been extensively investigated. While dispenser cathodes are the focus of our program to develop rugged photocathodes, the theory and modeling developed to describe them have wider application

In this work, we characterize various dispenser cathodes and implement models of time-dependent and spatially varying laser interactions with various materials, in which an incident laser heats the electron gas within the metal and which subsequently equilibrates with the background lattice, and use those models to examine tungsten-based dispenser photocathodes and simple metals. The present work is an integral component in the execution of the agenda to qualify dispenser photocathodes and develop a suite of simulation tools that can characterize and predicatively estimate their performance.

CURRENT AND QUANTUM EFFICIENCY

Photoemitted current is the product of several factors: (*i*) the charge of the electron q; (*ii*) the amount of incident light absorbed (1-R), where R is the reflectivity; (*iii*) the number of incident photons; (*iv*) the probability that an electron has an energy greater than the barrier height following its absorption of a photon of frequency f; and (*v*) the probability that the electron migrates to the surface without suffering a scattering event. Using the Richardson approximation, the probability of (*iv*) can be expressed as a ratio of Fowler functions $U(x)$ defined by

$$U(x) = \int_{-\infty}^{x} \ln\left(1+e^{y}\right) dy \qquad [1]$$

The probability of emission is then $U[\beta(\phi-hf)]/U[\beta\mu]$, where $\beta = 1/k_B T_e$, k_B is Boltzmann's constant, T_e is temperature, and ϕ is the barrier height above the chemical potential μ. The current density is then

$$J_\lambda(T_e, F, \Phi) = f_\lambda \frac{q}{\hbar\omega}(1-R) I_\lambda(t) \frac{U\left[\beta(\hbar\omega-\phi)\right]}{U\left[\beta\mu\right]} \qquad [2]$$

to which must be added the thermal current given by Richardson's Equation, $J_{RLD} = A\ T^2 \exp(-\beta\phi)$. From the definition of quantum efficiency (QE) as the ratio of the total emitted electrons with total incident (not absorbed) photons, it follows that

$$QE = \frac{\hbar\omega}{q} \frac{\int_{-\infty}^{\infty}\int_{0}^{\infty} J\left[F(\rho), T(\rho,t)\right] 2\pi\rho d\rho dt}{\int_{-\infty}^{\infty}\int_{0}^{\infty} I(\rho,t) 2\pi\rho d\rho dt} \qquad [3]$$

where F is the spatially varying applied field, T is the time-dependent and spatially varying electron temperature, ρ is a cylindrical coordinate, and t is time.

We shall neglect the contribution of tunneling current (though we have treated it elsewhere [13]), even though for machined dispenser cathodes, sporadic field enhancement factors can be large and contribute to dark current due to field emission [14]. Dispenser cathodes have non-uniform low work-function (Φ) coatings. Consequently, Φ is spatially varying, making the evaluation of Eq. [3], if not impossible, then very difficult. We use instead a patch model

$$\int J(x,y)\,dA = \sum_{i,j}\int_{patch} J(x,y)\,dA_{i,j} \qquad [4]$$

where A_{ij} is the area of the i,j^{th} patch on a grid, and assume that all patches are equivalent. The patch encompasses one pore from which Barium (or other coatings) dispense, and the coverage θ is assumed to vary radially from the pore like $\theta(\rho) = \{1 + \exp[(\rho-\rho_o)/\Delta\rho]\}^{-1}$. $\Phi(\theta)$ is evaluated from our version of Gyftopolous-Levine theory

$$\Phi(\theta) = \Phi_f + (\Phi_W - \Phi_f)[1 - G(\theta)]H(\theta)$$
$$H(\theta) = (1-\theta)^2(1+2\theta) \qquad [5]$$

where G is a function of atomic and covalent radii of the bulk (tungsten) and coverage (barium) atoms, and Φ_f is the work function of a monolayer of coverage [15, 16]. the performance of Eq. [5] is shown in Figure 1.

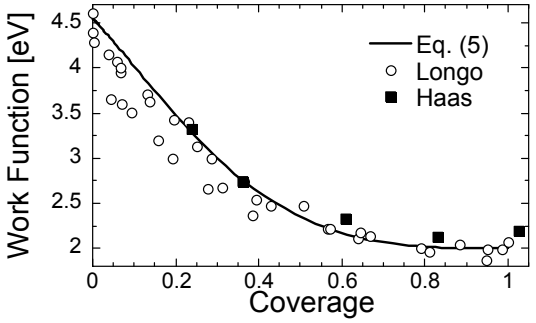

Figure 1: Work function dependence on coverage compared to experimental data [17,18] for BaO on W.

TIME DEPENDENT ELECTRON AND LATTICE TEMPERATURE EVALUATION

The Heat Diffusion Equations

Laser illumination and temperature variation for various metals have been considered extensively in the literature [19-23]. Here, we discuss the time dependent extension of procedures introduced in Ref. [5] insofar is it diverges from the steady state models therein. For those electrons not directly photoemitted, laser energy is transferred into electronic excitations. The hot electrons then come into equilibrium with other electrons via electron-electron scattering. The hot thermal Fermi-Dirac distribution comes into thermal equilibrium with the lattice via electron-phonon scattering. For laser pulse durations longer than the relaxation times associated with these processes, photons will encounter a heated electron distribution that, depending on intensity, can have temperatures significantly in excess of the bulk temperature, leading to complicating effects. In metals, a hot electron gas requires a fraction of a nanosecond to relax to its equilibrium state. The differential equations to determine electron and lattice temperatures are

$$C_e\frac{\partial}{\partial t}T_e = \frac{\partial}{\partial z}\left(\kappa\frac{\partial}{\partial z}T_e\right) - g(T_e - T_i) + G(z,t)$$
$$C_i\frac{\partial}{\partial t}T_i = g(T_e - T_i) \qquad [6]$$

where: C_e, C_i, and κ are the temperature-dependent specific heats and thermal conductivity; $G(z,t)$ governs the incident laser; and g governs the transfer of electron energy to the lattice (the notation follows Papadogiannis, *et al.*). Each term in Eq. [6] is replete with complications. The laser term is given by

$$G(z,t) = (1 - R(\theta_i))I(t)\left(\frac{e^{-z/\delta}}{\delta}\right)\left[1 - \frac{U[\beta(\hbar\omega - \phi)]}{U[\beta\mu]}\right] \qquad [7]$$

where R is the reflectivity, θ_i the incidence angle, I the laser intensity, and δ is the penetration depth. R and δ are functions of wavelength and evaluated from tabulated data of the index of refraction $n(E)$ and damping constant $k(E)$, as a function of photon energy E, from which R and δ follow [24], as in Figure 2. For normal incidence (θ_i = 0), R reduces to $R = [(n-1)^2+k^2]/[(n+1)^2+k^2]$.

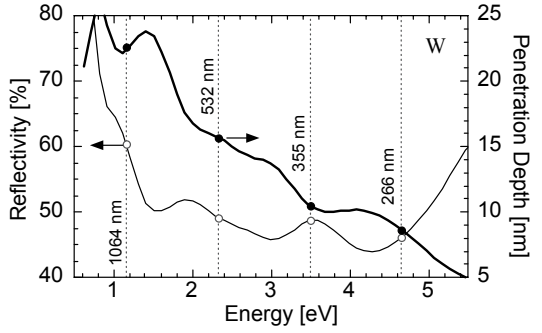

Figure 2: Reflectivity and penetration depth as a function of photon energy for normal incidence on tungsten.

The derivation of the specific heat terms for electrons and phonons follows standard solid state formulae, approximated from their exact forms in order to provide a reasonable fit over the temperature ranges we desire for numerical expedience. In these calculations, the electron number density, Debye temperature, atoms per unit cell, and sound velocity determine C_e and C_i and are calculated via a library of data for various bulk and coating materials (*e.g.,* the number of atoms per unit cell, the sound velocity, and the Debye temperature for tungsten is 0.2697, 5220 m/s, and 400 K, respectively). At high(er) temperatures, C_e and C_i are linear and constant in electron and lattice temperature, respectively.

The coefficient g and the thermal conductivity κ depend on electron-electron and electron-lattice relaxation time τ (see [5] and references therein), though now the joint relaxation time can depend on differeing T_e and T_i, as in

$$\tau\left(T_e,T_i\right)^{-1}=\tau_{ee}\left(T_e\right)^{-1}+\tau_{ph}\left(T_i\right)^{-1}$$
$$\tau_{ee}\left(T_e\right)=\frac{\hbar\mu}{A_o}\left(\frac{1}{k_BT_e}\right)^2;\tau_{ph}\left(T_i\right)=\frac{\hbar}{2\pi\lambda_o}\left(\frac{1}{k_BT_i}\right) \quad [8]$$

Thermal conductivity is an experimentally tabulated property as a function of temperature. Consequently, the dimensionless constants A_o and λ_o can be extrapolated from it and Eq. [8] – which is adequate for a many metals from room temperature to high temperatures – though tungsten contains behavior which departs from that approximation around room temprature. For dispenser cathodes, λ_o is allowed to vary slightly, reflecting that the base is an odd compilation of tungsten pellets and impregnants, and therefore not bulk material.

After an electron absorbs a photon, it is assumed to travel in a random direction and possibly suffer one or more collisions on its journey to the surface. Let any collision terminate the probability of emission (an overzealous assumption). The factor f_λ is then approximated by $f_\lambda\left(m\delta/\hbar k_o\tau\right)$ [13] where $\hbar$ is Planck's constant over 2π, k_o is the wave vector equivalent of the energy height of the barrier above the conduction band minimum, and the $f_\lambda(x)$ is defined by

$$f_\lambda\left(x\right)=\frac{1}{\pi}\int_0^{\pi/2}\frac{\cos\left(s\right)}{\cos\left(s\right)+x}ds \quad [9]$$

EXPERIMENTAL RESULTS AND COMPARISONS TO THEORY

Dispenser Cathode Quantum Efficiency

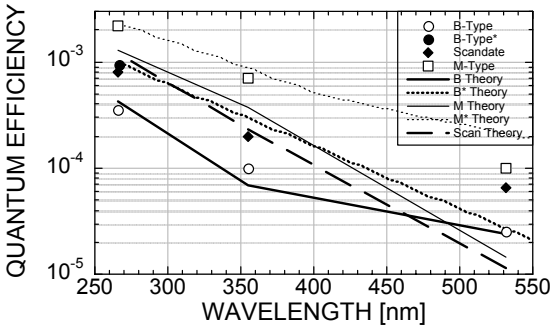

Figure 3: QE of Dispenser photocathodes. Lines are theory, points are exp. data. See text for details.

We have extensively described the experimental apparatus and conditions under which measurements were taken in previous works [5, 12]. Here, we report on intensity and field variation of emitted charge, the wavelength dependence of the quantum efficiency of both dispenser cathodes and simple metals, and their comparisons with predictions of the time dependent laser heating and photoemission modeling described above.

Theory and experimental data points for dispenser photocathodes are shown in Figure 3. The correspondence is as follows: white circle = B-type (Ref. [11]). Black circle = B-type (Ref. [25].) Black diamond: scandate. Thick solid & short dashed line: theory using Ref. [11] and Ref. [25] parameters, respectively. Thin solid and short dashed line: M-type using actual and extrapolated fields of 1.7 MV/m and 50 MV/m (a field typical of the operational environment of a MW-class FEL injector), respectively for 4.5 ns pulses and bulk temperature of 723 K. Thick long-dashed line: Scandate theory. The M-type cathodes have a coating of Osmium on the surface. It is seen that with the rather generic parameters used, theory underestimates the experimental performance of the M-type cathode by less than a factor of 2 at shorter wavelengths; at longer wavelengths, where the photon energy is comparable to the barrier height, the differences are more pronounced: a possibility is that tunneling effects may contribute more for such work functions and conditions. Both B and M-type performance vary depending on conditioning and processing of the cathode. For the scandate theory line, a smaller value of ρ_o was used in the patch model than for the field and intensity analysis (below), resulting in a smaller coverage factor of $\langle\theta\rangle = 12\%$.

Dispenser Cathode performance

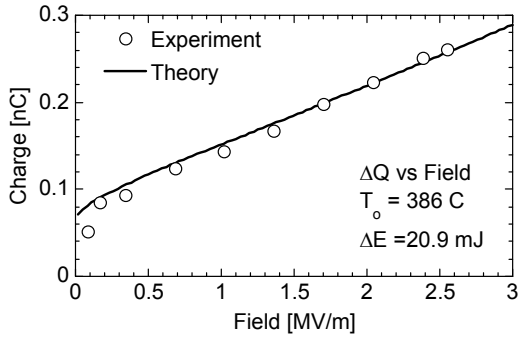

Figure 4: Emitted charge *vs.* field for scandate cathode.

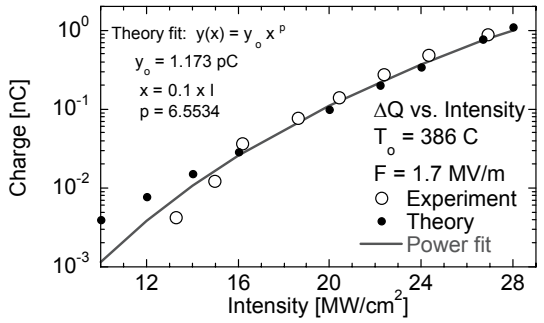

Figure 5: Same as Fig. 4, but for variation in intensity.

The modeling of Scandate dispenser cathodes using standard dispenser models is complicated by the barrier lowering mechanism, which may be more semiconductor-like band bending than patchy surface [26]. The simulations of QE for the scandate cathodes used the input data used to model the field and intensity variation: while these measurements occurred on separate occasions

and illuminating different regions of the cathode, and required $\langle\theta\rangle$=45%, and a field enhancement of 4.46, we did not separately adjust parameters when modeling intensity, using the same parameters as used for field. The field variation is shown in Figure 4 using a 4.5 ns FWHM pulse and the first harmonic (1064 nm) wavelength. Using the input data of Figure 4, the intensity dependence was calculated and compared to experiment, as shown in Figure 5.

Quantum Efficiency of Metals

Dispenser cathodes, owing to their odd constitution, induce complications that bulk metals do not. We therefore sought to compare the simulation code with quantum efficiencies for various metals determined by Srinivasan-Rao, *et al.* [27], for which gold, magnesium, and copper were selected.

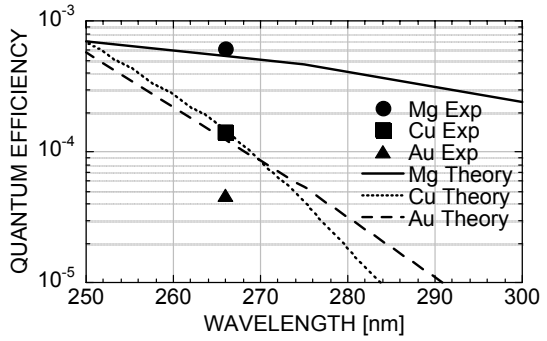

Figure 6: QE for Au, Cu, and Mg using theoretical model compared to 266 nm data from Ref. [26].

In Figure 6, all parameters were based on bulk values obtained from CRC and AIP Handbook tables, and operating conditions and parameters cited in Ref. [26]. The only adjustable parameter was field enhancement, which was set to 1.0, 2.5, and 7.0 for Au, Cu, and Mg, respectively, a range no different than that found for the dispenser cathode simulations. The performance of the model for Mg and Cu was good. The modeling performs less satisfactorily for Au, but nevertheless reasonable.

SUMMARY

We have reported on the characterization of several dispenser cathodes, and have confirmed their potentially attractive features as photoemitters, *e.g.,* low work function and high quantum efficiency, rejuvenation capabilities, and wavelength characteristics. Models were developed to simulate and predict their performance and performed well for our data as well as results for dispenser and metal photocathodes reported in the literature.

Acknowledgements

We gratefully acknowledge funding provided by the *Joint Technology Office* and the *Office of Naval Research.*

REFERENCES

[1] P. G. O'Shea, H. Freund, *Science* **292**, 1853 (2001).
[2] T. Srinivasan-Rao, J. Schill, I. Ben Zvi, M. Woodle, *Rev. Sci. Instrum*. **69**, 2292 (1998)
[3] C. Travier, G. Devanz, B. Leblond, B. Mouton, *Nucl. Inst. Meth. Phys. Res.* **A393**, 451 (1997).
[4] C. Hernandez Garcia, C. A. Brau, *Nucl. Inst. Meth. Phys*. **A483**, 273 (2002).
[5] K. L. Jensen, D. W. Feldman, M. Virgo, P. G. O'Shea, *Phys. Rev. Spec. Top.* **AB6**, 083501 (2003).
[6] J. A. Nation, L. Schächter, F. M. Mako, L. K. Len, W. Peter, C.-M. Tang, T. Srinivasan-Rao, *Proceedings of the IEEE* **87**, 865 (1999).
[7] W. E. Spicer, Phys. Rev. 112, 114 (1958); W. E. Spicer, A. Herrera-Gómez, SLAC-PUB-6306 & SLAC/SSRL-0042, Aug 1993.
[8] P. Michelato, *Nucl. Inst. Meth. Phys. Res*. **A393**, 455 (1997).
[9] T. Maruyama, R. Prepost, E. Garwin, C. K. Sinclair, B. Dunham, *Appl. Phys. Lett.* **55**, 1686 (1989)
[10] C. K. Sinclair, *Proc. 1999 Particle Accelerator Conf.,* (New York, IEEE, Piscataway, NJ, 1999) p 65.
[11] B. Leblond, *Nucl. Inst. Meth. Phys. Res.* **A317**, 365 (1992).
[12] K. L. Jensen, D. W. Feldman, P. G. O'Shea (*submitted for publication in Appl. Phys. Lett.*).
[13] K. L. Jensen, D. W. Feldman, P. G. O'Shea, *Proc. Of the Int'l. Vacuum Nanoelectronics Conference*, (Cambridge MA, July, 2004).
[14] A. H. Lumpkin, *Conference Record of the 1991 IEEE Particle Accelerator Conference,* Vol 3, 1967 (1991).
[15] J. D. Levine, E. P. Gyftopolous, *Surf. Sci.* **1**, 171 (1964); *ibid*, 225 (1964); *ibid*, 349 (1964).
[16] K. L. Jensen, Y. Y. Lau, B. Levush, *IEEE Trans. Plas. Sci.* **28**, 772 (2000).
[17] R. T. Longo, E. A. Adler, L. R.Falce, *Tech. Dig. of the IEDM*, 318 (1984).
[18] G. A. Haas, A. Shih, C. R. K. Marrian, *Appl. Surf. Sci.* **16**, 139 (1983).
[19] E. M. Logothetis, P. L. Hartman, *Phys. Rev.* **187**, 460 (1969).
[20] J. H. Bechtel, *J. Appl. Phys.* **46**, 1585 (1975).
[21] D. M. Riffe, X. Y. Wang, M. C. Downer, D. L. Fisher, T. Tajima, J. L. Erskine, R. M. More, *J. Opt. Soc. Am.* **B10**, 1424 (1993).
[22] X. Y. Wang, D. M. Riffe, Y.-S. Lee, M. C. Downer, *Phys. Rev.* **B50**, 8016 (1994).
[23] N. A. Papadogiannis, S. D. Moustaïzis, and J. P. Girardeau-Montaut, *J. Phys. D: Appl. Phys*. **30**, 2389 (1997); N. A. Papadogiannis, S. D. Moustaïzis, *J. Phys. D: Appl. Phys.* **34**, 2389 (2001).
[24] G. Haas, L. Hadley, "Chapter 6g", *AIP Handbook*, 3rd Ed, D. E. Gray (ed) (McGraw-Hill, New York, 1972).
[25] C. Travier, B. Leblond, M. Bernard, J. N. Cayla, P. Thomas, P. Georges, *Proc. Par. Accel. Conf.* (1995)
[26] J. Yater, A. Shih (NRL) (*private communication*).
[27] T. Srinivasan-Rao, J. Fischer, T. Tsang, *J. Appl. Phys.* **69**, 3291, (1990)

A MODE LOCKED UV-FEL

P. Parvin* (AUT, IR-Tehran; AEOI-RCLA, IR-Tehran), G. R. Davoud-Abadi (AUT, IR-Tehran), A. Basam (IHU, IR-Tehran), B. Jaleh (BASU, IR-Hamadan), Z. Zamanipour (AEOI-RCLA, IR-Tehran), B. Sajad (AU, IR-Tehran), F. Ebadpour (AUT, IR-Tehran)

Abstract

An appropriate resonator has been designed to generate femtosecond mode locked pulses in a UV FEL with the modulator performance based on the gain switching. The gain broadening due to electron energy spread affects on the gain parameters, small signal gain γ_0 and saturation intensity I_s, to determine the optimum output coupling as well.

INTRODUCTION

Today, there is an increasing interest in the generation of intense, tunable, coherent light in short wavelength region. Laser pulses of very short duration in UV/VUV spectrum, find applications in large number of areas, such as analysis of transit-response of atoms and molecules, non-linear optics in generation of harmonics, plasma remote sensing and range finding, induced plasma spectroscopy, time resolved UV photochemistry, diagnostic process, high speed photography, microlithography, space astronomy and the advanced research on laser induced fusion.

Short pulse phenomena in atomic and molecular lasers have been studied extensively in the last decades. These include the nonlinear phenomena of self spiking, as well as a wide range of mode-locking mechanisms and soliton formation. Mode-locked oscillation is known to be a very useful technique to get ultra short pulses in conventional laser oscillators [1-3].

The pulse duration obtained by this technique is roughly the inverse of the gain spectrum width. Using this technique, femtosecond pulses have been generated from Dye or Ti:Sa lasers, which possess the broad gain bandwidth among conventional lasers. Excimer lasers are taken into account as the most powerful commercial UV sources, whereas the UV mode-locking of those lasers do not generate a train of short pulses smaller than picosecond. Therefore, they do not resemble to be very attractive short pulse generators, mainly because of their narrow bandwidth. Among other UV lasers with mode-locking ability to generate tuneable ultra short pulses in VUV region, presently SHG Nd:YAG laser pumped THG/ FHG Ti:Al_2O_3 laser is considered as an attractive alternative.

Free-electron lasers (FELs) potentially have the ability to produce ultra short mode-locked pulses, because the gain spectrum width is inherently very wide compared to that of most conventional lasers [4]. In FEL oscillators, radiation burst and spikes have been observed in the nonlinear regime by several groups [5-10]. Although mode-locked FEL oscillators in microwave region have been formerly investigated both in theory and practice [11-12], however, a few papers are available to explain FEL mode-locking phenomena for shorter wavelengths in far-infrared and infrared range of spectrum [13, 14].

In free-electron laser operating at the FIR and IR spectral regions, using a radio-frequency accelerator for the electron beam, when the electron pulse length can be of the same order as the slippage length or even shorter, the laser emits short pulses of multimode broad-band radiation [14].

On the other hand, Storage ring FEL represents a very competitive technical approach to produce photons with these characteristics. After the first lasing of a storage ring FEL (SRFEL) in visible [15], the operation wavelength has been pushed to shorter values in various laboratories. It is based on progressive performance of particle accelerators and multilayer UV mirrors technology as to withstand the intense synchrotron radiation which damages the output coupler. An ultraviolet FEL oscillator has also been achieved using the VEPP ring at Novosobirsk [16].

Radio-frequency linacs employ a series of cavities that contain radio-frequency (r.f.) electromagnetic fields to accelerate streams of electrons. Typically time structure for a laser pulse from a FEL is based on a pulse radio-frequency linear accelerator. The laser macropulse of microsecond duration consist of a train of short micropulses which are picosecond in length. The macropulses repeat at a repetition ratio limited by the accelerator in several tens of Hz. The micropulse repetition rate can be from several MHz to several GHz.

A remarkable improvement has been obtained in recent years at various laboratories [17-21] to produce laser lights as short as 190 nm, whose wavelength is similar to ArF excimer laser as an alternative powerful VUV coherent source. In this work, we investigate a mode-locked UV-FEL at 190 nm to compare it to existing ultra short pulse lasers with gaseous and solid-state gain media.

THEORY

Depending on the current density and beam energy, FELs operate in one of three different regimes: Raman, low-gain Compton and high-gain collective regime. The Raman regime occurs at low energy and high current density. It is typical for devices that produce microwaves, whereas FELs aiming at the extreme ultraviolet, where the high reflectivity mirrors are non-existent, will necessary have to operate in the high-gain collective regime. The existing Compton FELs cover the UV wavelength range to 200 nm.

In order to design the resonator with the gain medium, the gain parameters, small signal gain γ_0 and saturation intensity I_s, are taken into account.

*Parvin@aut.ac.ir

The normalized gain function, g(υ), is a function of the parameter $\upsilon = 2\pi N_u (\omega_s - \omega)/\omega_s$, where N_u is the number of undulator periods, $\omega_s = 4\pi c\gamma^2 / [\lambda_u (1 + K^2/2)]$ is the resonant frequency and λ_u is the undulator period, and reads [22]:

$$g(\upsilon) = \frac{2 - 2\cos(\upsilon) - \upsilon\sin(\upsilon)}{\upsilon^3} \quad (1)$$

which is antisymmetric in υ.

The main positive gain region is located at υ>0 and corresponds to electrons traveling at velocities exceeding the synchronous value (υ=0). The condition υ=0 is equivalent to the synchronism condition: $\lambda_s = \lambda V_z/(c - V_z) = \lambda\beta_z/(1 - \beta_z)$ where $\beta_z = V_z/c$ and λ_s is the resonant wavelength $\lambda_s = \lambda_u (1 + K^2/2)/2\gamma^2$ being K the undulator strength. V_z is the electron velocity in the undulator direction. It should be noted that since υ depends on the optical frequency, the function g(υ) describes the frequency dependence of the gain.

The small-signal gain is directly proportional to the derivative of the spontaneous emission spectral profile. Fig. (1) depicts the spontaneous emission profile which is a sinc function in terms of detuning parameters $(\lambda - \lambda_s)/\lambda_s$, where λ_s is the emission wavelength at resonance $\lambda_s = 2\pi c/\omega_s$. Fig. (2) represents the derivative of the profile as shown in Fig (1) to express the gain versus detuning parameter. As this profile becomes rather narrow, especially for a large number of undulator periods N_u, and the constant of proportionality is small, a high-quality electron beam with small energy spread and a corresponding high current density is required. In the extreme UV, however, the demands on the transverse emittance of the beam are also very challenging.

Fig. (2) illustrates the gain of FEL with the assumption of a negligible energy spread as shown in curve 1 Fig.(3), as well, though, the electron beam is not monoenergetic in practice. Therefore, curves 2, 3, 4 represent the broadened optical gain profile due to several electron energy spreads, as to that of curve 4 is four times of curve 2 and two times of curve 3 respectively.

The sources of energy spread cause further gain broadening homogeneously and inhomogeneously. The effect of energy spread in broadening can be corrected by the terms according to Fig. (3) which illustrates the small-signal gain variation versus detuning parameter for several electron energy spread. It obviously denotes that the gain peak becomes to decrease when the corresponding gain profiles is broadened.

Small-signal gain and saturation intensity strongly depend on the broadening effects. The gain spectrum is characterized by an homogeneous width of the same order of the spontaneous spectrum. There are additional inhomogeneous broadening mechanisms related to the spread of individual electron parameters.

The electron beam itself is a source of inhomogeneous broadening, which is related

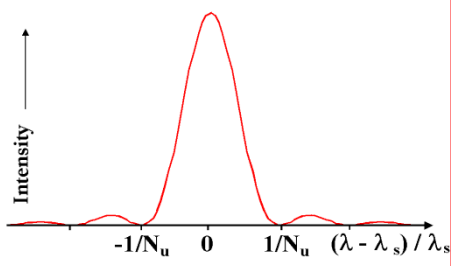

Figure 1: The spontaneous emission profile in terms of detuning parameter.

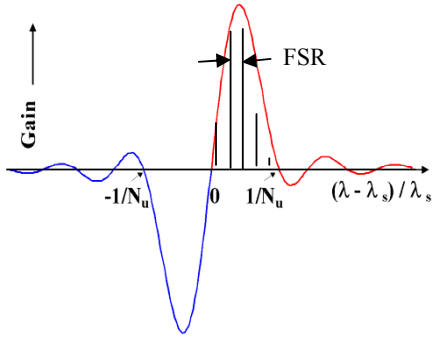

Figure 2: Gain versus detuning parameter.

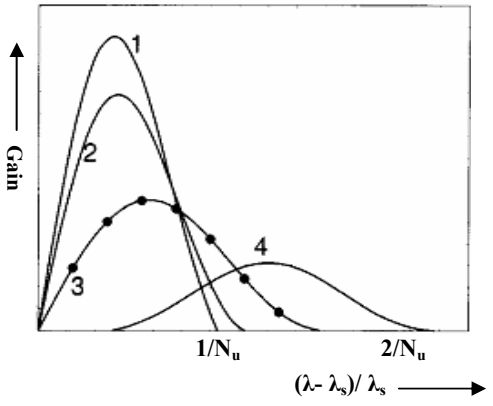

Figure 3: The effect of electron energy spread on the gain broadening of FEL. The curves 2, 3, 4 denote the relative electron energy spread [22].

to momentum spread of electrons, to the finite transverse size of the electron distribution. When the electrons enter the undulator, electrons located at different radii will experience different undulator fields and this will cause an additional inhomogeneous broadening. The undulator inhomogeneity and the energy spread of electron from the accelerator, as noted above, act to be the important inhomogeneous broadening sources accordingly. Due to the long cavity and the broad gain bandwidth, an FEL can oscillate in a very large number of cavity modes.

The homogeneous bandwidth usually exceeds the inhomogeneous one, and mode competition can cause a narrowing of the spectrum as in other lasers. The final width is determined by the quality factor of the cavity, the extending source of noise and by the duration of the pulse. For short pulses, the other effect dominates and the resulting spectrum width is to be transform limited in a FEL operating in the IR and FIR spectral regions, using a radio-frequency accelerator for the electron beam. A radio-frequency accelerator produces electrons in micropulses with a duration in the ps range. In a IR-FEL, based on such an accelerator, many modes are coupled due to the short pulse length.

The simulation of the coupling of pulses by an intracavity interferometric device, have shown that it is possible to induce coherence between independent pulses in an RF-linac based FEL. Apart from an ideal delay in the growth of the power and a gain reduction, due to absorption losses, the basic operation of the FEL is unaffected. The effect of an intracavity etalon on the spectral structure has shown that a low finess etalon suffices to suppress most of the cavity modes and to concentrate the power in modes with a much larger frequency separation. Intracavity etalons or equivalent intraferometric elements are commonly used in convetional lasers to reduce the spectral bandwidth.

The application discussed here differs in that the free spectral range of etalon is much narrower than the full gain bandwidth and a sufficient number of active modes must remain present to compose the short pulses [14].

A MODEL OF MODE-LOCKED UV FEL

Let us assume, FEL oscillating on a homogeneous or inhomogeneous transition with many modes above threshold and lasing. A general equation describing the classical electromagnetic field at a particular point in space is $e_T(t)=\sum E_n \exp j[(\omega_o + n\omega_c)t + \varphi_n]$, E_n indicates the amplitude of nth mode, which is oscillating at the frequency $(\omega_o + n\omega_c)$,where $\omega_c = 2\pi$ * FSR. It is tempting to lock each mode to a common time origin and assign each phase to be zero. It leads to short pulse occurring at a repetitive rate.

We assume a Fabry-Perot cavity for the operation of FEL as a mode-locked laser. A characteristic parameter for a FEL is the slippage length $N_u\lambda_s$ where N_u is the number of undulator period and λ_s is the optical wavelength. It gives the difference between the distance traveled by an electron and by an optical wavefront, especially, in transit time for an electron through the undulator. The homogeneous gain bandwidth of a FEL is determined by the slippage length:

$$(\Delta\upsilon)_{gain} = \frac{c}{2N_u\lambda_s} \tag{2}$$

The Fourier transform limit for the bandwidth is given by $\Delta\upsilon=1/\tau$ where τ is duration of light micropulse. For electron pulse long compared to the slippage length, the optical pulse length is almost equal to that of electron pulse. For short electron pulse, the optical pulse length is on the order of the slippage length. In that case, the transform limit is as wide as the gain bandwidth so that no further narrowing is possible. Instead of mode competition, there is mode coupling and the FEL operates as synchronously pumped mode-locked laser.

For a resonator of length L, assuming the back mirror to be high reflective with R_1 ~1, then the output coupler reflectance R_2 is directly determined. Similarly, the corresponding equations are given as below:

$$\tau_{RT}=2L/c \tag{3}$$

$$FSR=c/2L=1/\tau_{RT} \tag{4}$$

where τ_{RT}, FSR and L denote the round trip time, free spectral range and length of the resonator respectively. The number of modes n is proportional to gain bandwidth which is written as below:

$$n=(\delta\upsilon)_{gain}/FSR. \tag{5}$$

The duration of mode locked pulses τ_p is related to τ_{RT} and n according to eq (6). For simplicity, assuming the constant mode amplitudes

$$\tau_p \sim 1/(\delta\upsilon)_{gain} = \tau_{RT}/n \tag{6}$$

however, for Gaussian distribution $\tau_p \sim 0.44/(\delta\upsilon)_{gain}$ accordingly.

A typical plane Fabry-Perot cavity scheme with length L for undulator parameters L_u and N_u, is shown in Fig 4. The gain parameters are related to undulator characteristics as well. The output temporal response of the resonator includes a train of ultrashort pulses with duration τ_p and period τ_{RT} between repetitive pulses.

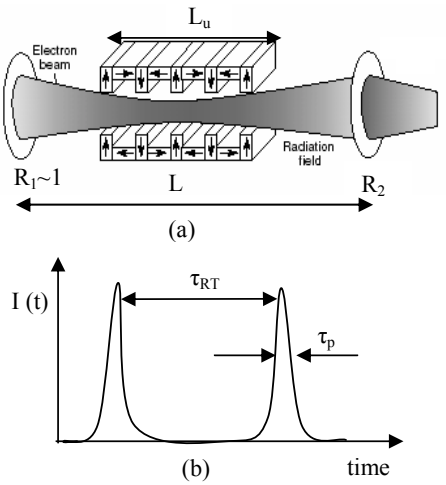

Figure 4: (a) A schematics Fabry-perot cavity
(b) Typical mode-locked output pulses, R_2 is output coupler.

According to laser amplification theory, for pulses whose shapes are sufficiently near the eigenfunction for

propagation in the homogeneous broadening, the change in the average temporal width τ of the pulse can be reasonably expected to be negligible, in such case, the effective saturation intensity is given by $I_s = h\upsilon/2\sigma_{st}\tau$, where τ is the full width at half maximum (FWHM) of the probe pulse into gain medium, if $I << I_s$, then for low input intensities the gain increases and become equal to small-signal gain and for high intensities, the gain reduces to a saturated value with an intensity increment equivalent to $I_s \gamma_o L$.

For a mode-locked laser, the small signal gain is also proportional to the population and stimulated cross-section which in turn depends on gain profile and the bandwidth. It indicates the frequency dependent γ_o and I_s as well.

Fig.4 shows a typical Fabry-Perot with gain parameters γ_o and I_s as to the axial mode width becomes relatively sharper. T_{opt} of the output coupler is given as below:

$$T_{opt}/A=(1-A- T_{opt})[\gamma_0 L +\ln(1-A - T_{opt})]/(A+ T_{opt}) \qquad (7)$$

where T_{opt} and A denote the optimum transmittance and the absorbance respectively for an optimum output coupler such that $T_{opt}=1-R_{opt}- A$.

The optimum design of mirrors in UV region of spectrum is achieved by the fabrication of pure multilayer coating of Aluminum oxide (or Halfnium oxide) on SiO_2 substrate. The gain switching for mode-locked laser requires to match the frequency of modulator to FSR (i.e. the spectral separation between the adjacent axial modes) of the resonator. In other words, the microbunching frequency should be tuned to FSR of Fabry-Perot resonator so as the repetition time of both electron micropulse and laser mode locked pulse become equal to the round trip time of the resonators τ_{RT}.

CONCLUSION

It is well understood, if the repetition time of the electron pulses is short compared to the round trip time of an optical pulse in the resonator cavity, then phase locking between successive optical pulses can be induced by an intracavity interferometer device. Moreover, for short electron pulse, the optical pulse length is in the order of the slippage length such that instead of mode competition, there is mode coupling and FEL operates as synchronously pumped mode-locked laser.

In UV region of spectrum, the slippage becomes smaller compared to that of IR region, therefore it is required to achieve shorter electron pulse length and broader gain bandwidth .

Moreover, for longer resonator cavity in UV-FEL, the resonator parameter FSR becomes relatively smaller for a given bandwidth to allow multimode operation with a great number of the active modes. In order to fulfill gain switching to generate a train of fs mode–locked pulses, the time repetition between successive pulses should be approximately equal to the round trip time of each pulse in the resonator and the gain bandwidth broadens adequately.

We have proposed a preliminary design for the resonator based on the Fabry-Perot cavity to implement a UV self mode-locked FEL according to gain switching phenomena. It is shown that effects of gain broadening on the gain parameters strongly affects on the number of the axial modes within the bandwidth of the gain profile and the output coupling of the resonator consequently. The simulation have shown that the optimum mode locking occurs when the repetition time of the electron pulses is approximately equal to the round trip time of an optical pulse in the resonator cavity with the optimum output coupling, given by eq (7) for the definite gain parameters of a UV FEL.

REFERENCES

[1] L. F. Mollenauer and R. H. Stoller, Opt. Lett., 9 (1984) 13

[2] P. G. Kryukov, and V. S. Letokhov, IEEE J. Quantum Electron. 8 (1972) 766.

[3] H. W. Mocker and R. J. Collins, Appl. Phys. Lett., 7 (1985) 270.

[4] Y. Kawamura,et al., Appl. Phys. Lett., 51 (1987) 795.

[5] R. W. Warren, B. E. Newman, and J. C. Goldestein, IEEE J. Quantum Electron.,21 (1984) 13.

[6] J. C. Goldestein, et al., Nucl. Instrum. Methods Phys. Rev.,250 (1986) 4.

[7] J. Masud, et al.,Phys. Rev. Lett., 56 (1986) 1567.

[8] J. W. Dood and T. C. Marshal, Nucl. Instrum. Methods Phys. Rev., A296 (1990) 4.

[9] B. A. R. Chman, J. M. Madey, and E. Szames, Phys. Rev. Lett., 63 (1989) 1682.

[10] E. Jerby, G. Bekefi, and S. Wurtel, IEEE J. Quantum Electron. 27 (1991) 2512.

[11] E. Jerby, G. Bekefi, and T. Hana, Nucl. Instrum. Methods Phys. Rev., A 318, (1992) 114.

[12] E. Jerby and G. Bekefi, IEEE J. Quntum Electron. 29 (1993) 2845.

[13] D. Oepts, et al., Nucl. Instr. and Meth. A,285 (1989) 204.

[14] D.Oepts and W.B Colson, IEEE J. Quantum. Electron.26(1990) 723.

[15] M. Billardon, et al., Phys. Rev. Lett.,51 (1983) 1652.

[16] G. N. Kuliapanov, et al., Nucl. Instrum and Methods Phys. Rev., A 296, (1990) 1.

[17] V. Litvinenko, et al., Nucl. Instrum. and Methods Phys. Rev., A 429 (1999) 151.

[18] K. Yamada, et al., Nucl. Instrum. And Methods Phys. Rev., A 445 (2000) 173.

[19] M.Marsi, at al. Synchrotron Radiat. News, 14 (2001) 19.

[20] A. Gatto, et al. , Nucl. Instrum. and Methods Phys. Rev., A 483 (2002) 357.

[21] M. Trovò, et. al., Nucl. Instrum. Methods Phys. Rev. A 483 (2002) 157.

[22] See e.g. G. Dattoli, A. Renieri, A. Torre, Lectures on the free electron laser theory and related topics, World Scientific, Singapore (1993)

CURRENT-ENHANCED SASE USING AN OPTICAL LASER AND ITS APPLICATION TO THE LCLS*

A.A. Zholents, W.M. Fawley†, LBNL, Berkeley, CA 94720-8211, USA
P. Emma, Z. Huang, G. Stupakov, SLAC, Stanford, CA 94309, USA
S. Reiche, UCLA, Los Angeles, CA 90095-1547, USA

Abstract

We propose a significant enhancement of the electron peak current entering a SASE undulator by inducing an energy modulation in an upstream wiggler magnet via resonant interaction with an optical laser, followed by microbunching of the energy-modulated electrons at the accelerator exit. This current enhancement allows a reduction of the FEL gain length. The x-ray output consists of a series of uniformly spaced spikes, each spike being temporally coherent. The duration of this series is controlled by the laser pulse and in principle can be narrowed down to just a single, ~ 200-attosecond spike. Given potentially absolute temporal synchronization of the x-ray spikes to the energy-modulating laser pulse, this scheme naturally makes pump-probe experiments available to SASE FEL's. We also study various detrimental effects related to the high electron peak current .

INTRODUCTION

SASE-based x-ray FEL projects continue to gather momentum at SLAC[1] and DESY[2]. Recently, Ref. [3] has proposed a technique (which we call current-Enhanced SASE or ESASE for short) to shorten the exponential gain length and provide temporal synchronization of the x-ray pulse to a master laser. Figure 1 shows a schematic of this technique as applied to the LCLS. An external, short pulse ($\sim$30-100 fs) from a high power ($\sim$1-10 GW) laser at wavelength $\lambda_L \sim 2.2\,\mu$m (*e.g.*TOPAS laser [4]) overlaps a short e-beam section at moderate energy ($\sim$4.5 GeV) in a short, appropriately-tuned wiggler (*e.g.*$\lambda_u \approx 30$ cm, $B_u \approx 1.7$ T). This induces a periodic energy modulation with relative amplitude $B \equiv \Delta\gamma/\sigma_{\gamma 0} \sim$5-10, where $\sigma_{\gamma 0}$ is the uncorrelated energy spread, but with minimal microbunching. Following final acceleration the electron beam passes through a dog-leg bend whose chromatic dispersion produces a periodic enhancement of the peak current to $\approx$20 kA. Finally, the electrons enter a long undulator and emit x-rays via the standard SASE process but with first saturation occurring by $z \approx$45-60 m. The radiation output from the current-enhanced portions will be a train of spikes at uniform spacing λ_L whose total duration is directly related to that of the upstream, energy-modulating laser. This emission will dominate SASE emission from the remainder of the e-beam if the exponential gain lengths in the current spikes have been reduced by $\approx$25% or greater.

The ESASE technique shares with other recent proposals [5, 6, 7] the common feature of employing an optical laser to induce energy modulation to produce short duration ($\tau_P \leq$500 as) output pulses from an FEL together with absolute synchronization of the x-ray probe pulse to the laser pump pulse, thus permitting pump-probe experiments. In principle, it is also related to harmonic cascade configurations [8]. However, via the use of a dispersion section to strongly enhance the current, ESASE has the additional advantage of significantly reduced gain lengths. This may allow possible relaxation of the required electron beam emittance for saturation in the "standard" LCLS undulator or (for the same base emittance) saturation at x-ray wavelengths shorter than 0.15 nm.

We now present initial "start-to-end" numerical simulation results, investigate some potential detrimental effects due to the high peak currents, and then conclude with some remarks concerning possible experimental applications.

ACCELERATOR SIMULATIONS

We initiated "start-to-end" ESASE simulations with 2×10^5 macro-particles in the *Parmela*[9] code for the RF photo-cathode gun and low-energy injector systems, up to an energy of 135 MeV. After this point, the macroparticle number is increased $10\times$, retaining all second moments and coordinate correlations, and then transported with the *Elegant*[10] code through the main linac, up to the entrance of the FEL undulator. These simulations included 2nd-order optics, accelerating structure wakefields, a model for the laser/wiggler energy modulator (EM) at 4.54 GeV, and a line-charge (1D) model of coherent synchrotron radiation (CSR) in and after the bends.

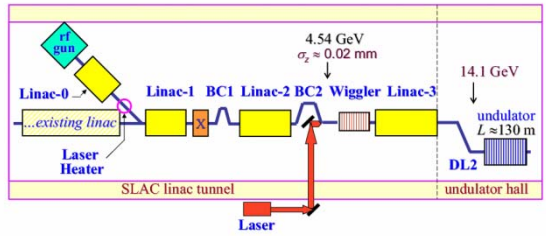

Figure 1: A schematic of ESASE as applied to the LCLS.

* Work supported in part by the Office of Science, U.S. Dept. of Energy under Contracts DE-AC03-76SF0098 and DE-AC03-76SF00515.

† WMFawley@lbl.gov

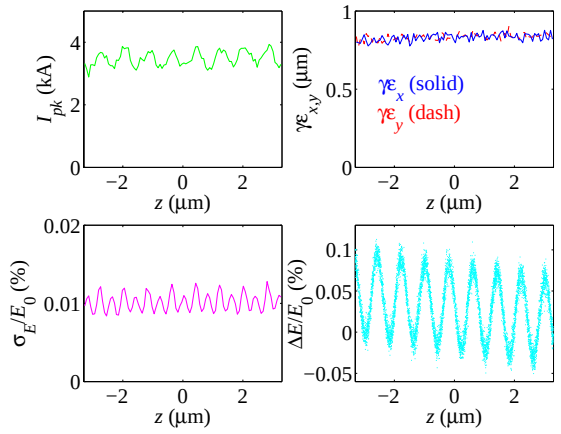

Figure 2: ELEGANT tracking results for a short section of 0.8-μm energy-modulated e^- bunch at 14 GeV, with instantaneous current, transverse emittances, rms relative energy spread, and relative energy centroid modulation plotted versus bunch coordinate z.

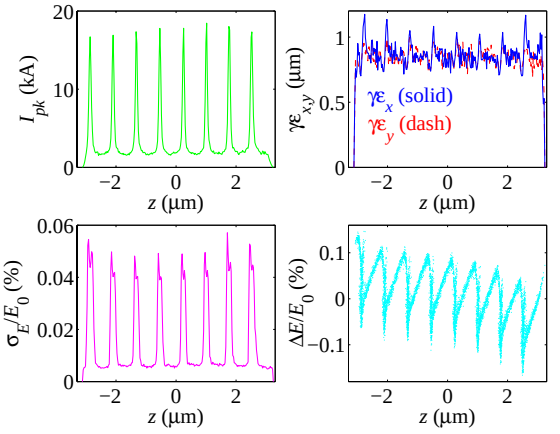

Figure 3: Same plots as in Fig. 2, but at a z-position immediately following the DL2 beamline. Strong current modulation and CSR effects are now apparent.

The EM consists of a resonant laser-electron interaction in an 2.5-m long planar wiggler located immediately after the second bunch compressor chicane where the FWHM bunch length is 65μm. The EM can easily be installed in place of one existing 3-m long accelerating structure. Table 1 gives the EM and the final buncher parameters.

Figure 2 displays the resulting current profile, transverse slice emittance, rms energy spread, and centroid energy modulation induced by an 0.8-μm wavelength EM for a short core-section of the beam at 14.1 GeV. The current profile shows weak density modulation due to the wiggler's small momentum compaction (opposite in sign to the final buncher). Similar weak modulation of σ_E is also apparent.

Following final acceleration, the beam passes through a 'dog-leg' transport line (DL2) which is used to produce a 1.25-m jog in the beamline to the south, in order to allow energy measurement and collimation. The DL2 beamline nominally has a very small momentum compaction of R_{56} ≈0.1 mm, but it can be easily increased, or even reversed in sign, by small adjustments in the gradients of three nearby quadrupole magnets. For the energy modulation shown in Fig. 2, $R_{56} = 0.30$ mm is optimum. Fig. 3 shows the beam characteristics immediately following this bend system, including CSR effects.

CSR calculations require both a large number of macroparticles and narrow bin width (∼6 nm) due to the short ESASE bunching length (≈30 nm rms). This spike length still greatly exceeds the CSR point-charge wake limit of $R/\gamma^3 \approx 0.01$ nm at 14 GeV for bends with radius $R \approx$300 m [11]. It is worth noting that the CSR in the DL2 dipoles will be partially suppressed by a combination of a non-zero R_{51} component and a relatively large transverse beam size. The projected spike length in the bends along the axis of propagation will broaden to $\sigma_x|\theta| \approx 400$ nm, where $\sigma_x \approx 45\mu$m is the rms horizontal beam size at the bend entrance and $\theta \approx 0.5°$ is the bend angle. This longer effective length, the low charge in each spike, and the weak bend angles all minimize CSR effects, although a 20% horizontal emittance growth and some phase space distortion is still evident in Fig. 3. Nonetheless, a fully 3D CSR calculation is needed to verify these 1D results.

Table 1: Energy modulator (EM) at 4.54 GeV for B=5 and two laser wavelengths (λ_L =0.8 μm and 2.2 μm).

Parameter	sym	0.8 μm	2.2 μm	unit
N wiggler periods	N_w	8	8	—
period of wiggler	λ_w	25	30	cm
peak laser power	P_{pk}	9.7	10.7	GW
laser rms waist	σ_r	0.25	0.25	mm
modulation amp.	$\Delta\gamma$	±14	±14	—
buncher R_{56}	R_{56}	0.30	0.78	mm

FEL SIMULATION RESULTS

The 6D macroparticle distributions resulting from the ELEGANT tracking studies were directly imported as input to the FEL simulation codes *GINGER*[12] and *GENESIS*[13]. We performed a number of fully time-dependent (Δt_{slice} ∼10 as) SASE runs at two different energy modulation wavelengths (0.8 and 2.2 μm) and two undulator focusing lattices ($\langle\beta\rangle$ =26 and 12 m) with the standard LCLS λ_u =30 mm undulator period. For these calculations wakefield effects were neglected. Table 2 sum-

Table 2: Simulation results from GINGER and GENESIS.

Param.	$\langle\beta\rangle = 26$ m			$\langle\beta\rangle = 12$ m		unit
λ_L	STD	0.8	2.2	0.8	2.2	μm
L_{sat}	70	58	57	44	45	m
$\langle P\rangle$	13	2.0	3.0	2.9	7.6	GW
P_{spike}	240	17	65	40	160	GW
$\omega/\Delta\omega$	1500	550	660	660	790	–

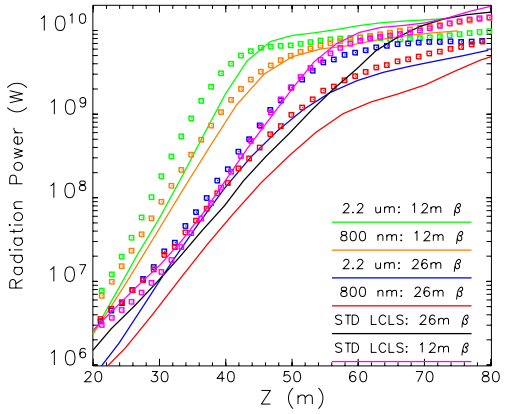

Figure 4: $\langle P \rangle$ plotted versus z for ESASE and standard LCLS configurations. The solid lines and boxes represent *GINGER* and *GENESIS* results, respectively.

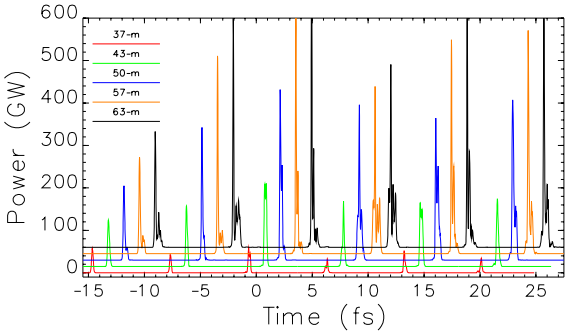

Figure 5: $P(t)$ snapshots at 5 different z-locations for a 2.2 μm-energy-modulated ESASE pulse with $\langle \beta \rangle$ =12 m, plotted with staggered offsets of 1.5 fs in time and 15 GW in power. For legibility, the z =37 m data has been multiplied by a factor of 2.0.

marizes various output parameters from the simulations. For simplicity, we have defined the saturation point as that where the normalized inverse spectral bandwidth $\omega/\Delta\omega$ reaches a maximum and P_{spike} as the average peak power of the spikes measured at $z = L_{sat}$. The ESASE results show significantly reduced saturation lengths, albeit with somewhat smaller average powers and inverse bandwidths than the "standard" LCLS configuration. In particular, if it were possible to achieve an $\langle \beta \rangle$=12 m or less, L_{sat} is reduced to less than 50 m. We believe the enhanced gain from such an ESASE configuration would allow the LCLS to operate at a somewhat larger normalized emittance than the nominal 1.2 mm-mrad or at somewhat shorter wavelengths than the nominal 0.15 nm. The time-averaged powers for both the ESASE cases and standard LCLS parameter cases ("STD") are shown in Fig. 4. Because *GENESIS* unlike *GINGER* includes non-axisymmetric modes, in the early regions of exponential gain it will tend to show a significantly higher power.

One important feature of the ESASE runs is that the instantaneous power is essentially composed of simple, uniformly-spaced spikes with effective widths $\leq$0.5 fs up to and about one-to-two gain lengths beyond L_{sat}. Between the individual spikes, the instantaneous SASE power is smaller by three orders of magnitude or greater. As predicted by Ref. [14] for SASE in the short pulse limit, the individual spikes support a single coherent longitudinal mode and their bandwidth is approximately transform-limited for $z \leq L_{sat}$ (presuming one has matched λ_L/B to approximately one coherence length). Fig. 5 shows $P(t)$ snapshots at various z-locations for a 2.2-μm laser-modulated pulse with $\langle \beta \rangle$=12 m. At z=57 m, approximately three gain lengths beyond saturation, some spikes begin to display multi-peak structure and pulse widths approaching 1-fs or greater due to slippage effects.

COLLECTIVE EFFECTS

The high peak current in the ESASE spikes raises concerns that impedance effects may induce sufficient energy spread to seriously degrade FEL performance. We now estimate the effects from three different sources.

Wakefield Effects

The longitudinal resistive wall wake of high-current spikes will be partially suppressed by the large catch up distance z_c associated with the short spike length. Indeed, for $\sigma_{\rm spike}$=30 nm and undulator pipe radius a=2.5 mm, we find $z_c = a^2/2\sigma_{\rm spike} \approx 100$ m, which exceeds the expected FEL saturation length. Due to the finite beam γ, the extension of the image charge induced on the wall by a single spike, $a/\gamma \approx$100 nm, is larger than $\sigma_{\rm spike}$. This somewhat reduces z_c. However, even without this reduction, the wake induced by a single spike inside itself is expected to be small due to the small charge of the spike ($\sim O(10)$ pC). If we take for the wake the value $w = Z_0 c/\pi a^2$ (the limit of the steady state wake for very short bunches; see, *e.g.*Ref. [15]) where Z_0=377Ω is the vacuum impedance, we estimate the induced energy spread in the spike due to this wake will be $\delta E/E \approx 4 \times 10^{-4}$ at z=100 m. This is smaller than the intrinsic energy spread σ_E of the ESASE spike and should only slightly affect FEL performance.

The total charge in the spikes is a relatively small fraction of the total charge of the bunch. This means that the average wake of multiple spikes will be dominated by the averaged smooth current distribution in the bunch. This wake is not supposed to generate excessive energy spread in the beam.

Coherent Undulator Radiation

Coherent undulator radiation (CUR) at wavelengths comparable to the spike length ($\sim$30 nm) but much longer than the resonant FEL wavelength $\lambda_r = 2\pi/k_r$ (=0.15 nm) can be an important impedance source. The CUR impedance per unit length at wavenumber k for a long

pencil beam is [16, 17]

$$Z_{CUR}^{1D}(k) = \frac{Z_0}{4\pi}\frac{K^2}{\gamma^2}\frac{k}{8}\left(2\pi + 4i\,\ln\,\frac{k_r}{k}\right), \qquad (1)$$

where K is the undulator parameter. However, long-wavelength undulator radiation is emitted primarily off-axis at an angle $\theta \approx \sqrt{2\lambda/\lambda_u} \sim 1\,\mathrm{mrad}$. Consequently, the effective radiation impedance taking into account the transverse size of the bunch is modified to

$$Z_{CUR}^{3D} \approx Z_{CUR}^{1D}\, e^{-k^2\theta^2\sigma_x^2} = Z_{CUR}^{1D}\, e^{-2kk_u\sigma_x^2}\,. \qquad (2)$$

with $k_u \equiv 2\pi/\lambda_u$. For an infinite train of ESASE bunches spaced by laser wavelength λ_L, the modulated electron current is (see *e.g.*, Ref. [8])

$$I(z) = I_0\left(1 + 2\sum_{n=1}^{\infty} J_n(nk_L R_{56} B\sigma_\delta) \times \exp\left[-n^2k_L^2R_{56}^2\sigma_\delta^2/2\right]\cos(nk_Lz)\right), \qquad (3)$$

where I_0=3.4 kA is the unmodulated beam current, J_n is the Bessel function of order n, $k_L = 2\pi/\lambda_L$, z is the longitudinal position along the bunch, and $\sigma_\delta \equiv \sigma_{\gamma 0}/\gamma$ is the normalized rms energy spread. At the optimal compression $k_L R_{56} B\sigma_\delta \approx 1$, the energy loss per unit length is

$$\frac{d(\Delta\gamma)}{ds} \approx -\frac{2I_0}{I_A}\frac{K^2}{\gamma^2}\sum_{n=1}^{\infty} J_n(n)\exp\left[-\frac{n^2}{2B^2} - 2k_nk_u\sigma_x^2\right] \times \left[\frac{\pi k_n}{4}\cos(2\pi n\bar{z}) - \frac{k_n}{2}\ln\left(\frac{k_r}{k_n}\right)\sin(2\pi n\bar{z})\right], \qquad (4)$$

where $I_A \approx 17$ kA is the Alfvén current, $k_n \equiv nk_L$ and $\bar{z} \equiv z/\lambda_L$. For B=5, λ_L=0.8μm, and $\gamma = 2.8\times 10^4$ and σ_x=33 μm in the undulator, Eq. (4) yields maximum $d(\Delta\gamma)/ds \approx 0.003\,\mathrm{m}^{-1}$, more than two orders of magnitude smaller than that obtained using the 1-D CUR impedance (*i.e.*, Eq. (1)).

Longitudinal Space Charge Effects

Another high-frequency impedance is the longitudinal space charge (LSC). Since $k_n\sigma_x/\gamma \ll 1$ (pencil beam in the rest frame) and $k_n a/\gamma \gg 1$ for all n except $n = 1$ at λ_L=0.8 μm, we use the free-space LSC impedance per unit length (see, *e.g.*, Ref. [18]):

$$Z_{LSC}(k) \approx i\,\frac{Z_0}{4\pi}\frac{k}{\gamma^2}\left(1 + 2\ln\frac{\gamma}{k\,(\sigma_x+\sigma_y)}\right). \qquad (5)$$

For B=5, λ_L=0.8 μm, and σ_x=33 μm, we find that the maximum $d(\Delta\gamma)/ds \sim 0.1\ \mathrm{m}^{-1}$. For λ_L=2.2 μm, $d(\Delta\gamma)/ds \sim 0.05\ \mathrm{m}^{-1}$. For the ≈200-m long diagnostic section between DL2 and the undulator, the space-charge-induced growth in $\Delta\gamma$ to $O(20)$ is large enough for concern. If necessary, the current bunching could be delayed by making the DL2 dogleg isochronous together with installation of a weak chicane just before the undulator. Over the 100-m length of the undulator, the space-charge-induced energy spread increase is less than that of the spikes's initial value σ_E.

CONCLUDING REMARKS

The ESASE technique allows obtaining electron beam micro-bunches with a peak current unthinkable from a standard electron bunch compressor. Our preliminary investigations suggest that the high peak currents induce only limited beam quality degradation due to collective effects such as CSR, wakefields, and space charge; nonetheless more detailed studies are needed for greater certainty. Although the exponential ESASE gain length is only somewhat shortened relative to an unmodulated beam for the standard LCLS undulator with β=26 m, there is a much shorter gain length and more rapid saturation in z for β=12 m. For this latter case, detailed "start-to-end" simulations show that the output SASE x-ray pulse will be dominated by periodic spikes of a few hundred attosecond or less duration. Consequently, the duration of the overall output envelope can be controlled by adjusting the modulating laser pulse. One can also obtain absolute synchronization between these two pulses which can be used in the pump-probe experiments for ultra-fast dynamics studies at the femtosecond time scale and beyond. We plan further studies to explore more fully the potential of ESASE techniques at the LCLS.

REFERENCES

[1] LCLS Conceptual Design Report, SLAC-R-593 (2002).

[2] TESLA Technical Design Report, DESY TESLA-FEL 2001-05 (2001).

[3] Zholents, A.A., submitted to *Phys. Rev. Lett.* (2004)

[4] http://www.lightcon.com/lc/scientific/topas.htm

[5] Zholents, A.A. and Fawley, W.M., *Phys. Rev. Lett.* **92**, 224801 (2004).

[6] Saldin, E.L, Schneidmiller, E.A., and Yurkov, M.V., *Opt. Comm*, **237**, 153 (2004)

[7] Saldin, E.L, Schneidmiller, E.A., and Yurkov, M.V., *Opt. Comm.*, in press, (2004)

[8] L.H. Yu, *Phys. Rev. A*, **44**, 5178 (1991).

[9] J. Billen, LANL Report LA-UR-96-1835 (1996).

[10] M. Borland, ANL report APS LS-287 (2000).

[11] E.L. Saldin, E.A. Schneidmiller, and M.V. Yurkov, *Nucl. Inst. Meth. A*, **398**, 373 (1997).

[12] W.M. Fawley, LBNL-49625 (2002).

[13] S. Reiche, *Nucl. Inst. Meth. A*, **429**, 243 (1999).

[14] R. Bonifacio *et al*., Phys. Rev. Lett. **73**, 70 (1994).

[15] K.L.F. Bane and M. Sands, SLAC-PUB-95-7074 (1995).

[16] E.L. Saldin, E.A. Schneidmiller and M.V. Yurkov, *Nucl. Instrum. Meth. A*, **417**, 158 (1998).

[17] J. Wu, T. Raubenheimer, G. Stupakov, *Phys. Rev. ST Accel. Beams*, **6**, 040701 (2003).

[18] A. Chao, *Physics of Collective Beam Instabilities in High Energy Accelerators* (Wiley, New York, 1993).

GENERATION OF TERAHERTZ RADIATION BY MODULATING THE ELECTRON BEAM AT THE CATHODE

J. Neumann*, R. Fiorito, H. Freund, P. O'Shea,
IREAP, Univ of MD, College Park, MD 20742, USA
G. L. Carr, H. Loos, T. Shaftan, B. Sheehy, Y. Shen, Z. Wu,
Brookhaven National Lab, Upton, NY 11973, USA

Abstract

A bunched electron beam can be used to generate coherent radiation in a particle accelerator. This experiment, a collaboration between the University of Maryland and the Source Development Laboratory at Brookhaven National Laboratory, uses a drive laser modulated at terahertz frequencies in an RF-photoinjecting electron accelerator to produce a bunched beam at the cathode. The experiment is designed to determine if such a scheme could be used to develop a compact, high power terahertz emitter. After acceleration to approximately 73 MeV, a mirror intercepts the beam. The backwards transition radiation from the mirror is measured with a bolometer. The experiment was conducted at various modulation frequencies and levels of charge.

INTRODUCTION

Shaping the profile of a laser pulse incident on a photocathode is important for many types of radiative devices. In some free electron laser applications, smoothing the profile may be necessary to prevent unwanted emission of radiation. In other cases, laser modulation can be used as a radiation source. This work explores using a modulated drive laser to produce a similarly modulated electron beam in order to generate terahertz radiation. There are many potential applications for terahertz light including exploration of vibrational modes in DNA and proteins, weapons and explosives detection, and communications. A review of some applications and available sources of terahertz radiation is given by Siegel [1].

In general, the radiation emitted by a bunch of electrons can be expressed as

$$\frac{d^2W}{d\omega d\Omega} = \frac{d^2W_1}{d\omega d\Omega}\left[N_e + N_e(N_e-1)F(\omega,\theta,\phi)\right] \quad (1)$$

where N_e is the number of electrons, and $F(\omega,\theta,\phi)$ is the form factor. The form factor is a number between zero and one that depends on the geometry of the electron beam. A tightly bunched beam (the bunches are much smaller than the wavelength separating the bunches) will yield a form factor of 1, while an unbunched beam will yield a form factor of zero.

The single particle term, $d^2W_1/(d\omega d\Omega)$ applies to any radiative mechanism, such as a wiggler, a bend magnet, or a transition radiator. While this experiment focuses on a transition radiator, injecting a prebunched beam into a wiggler causes it to reach saturation faster than an unbunched beam (Fig. 1)

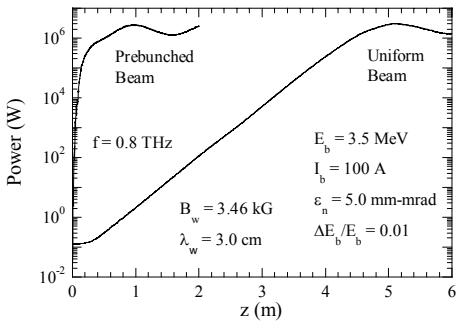

Fig. 1: Comparison of the growth of 0.8 THz radiation in WIGGLIN simulation using both prebunched and uniform beams.

This experiment, conducted at the Source Development Laboratory (SDL), at Brookhaven National Laboratory, used a modulated Ti:sapphire drive laser to produce a modulated electron beam. The electrons are accelerated to approximately 73 MeV, and transition radiation is produced by interaction of the beam with a 2cm diameter mirror placed at 45 degrees with respect to the beam direction. The terahertz light passes through a transport system to a bolometric detector. Information about the spectrum of the radiation is obtained by using various terahertz filters.

In an ideal case, a periodic train of short electron bunches would be accelerated to the radiator. One example of this type of profile is shown in Fig. 2. The expected spectrum of the terahertz radiation that could be emitted by such a beam is shown in Fig. 3, depicting cases for 1, 2, 4, and 8 bunches. Note that a single short bunch produces a broadband coherent signal, whereas the bunched cases result in a more narrow band source.

*neumann@glue.umd.edu

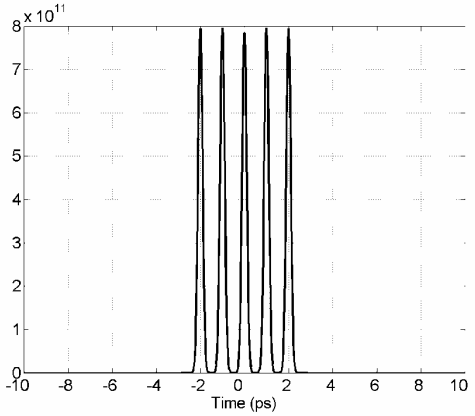

Fig. 2: "Ideal" train of short electron bunches

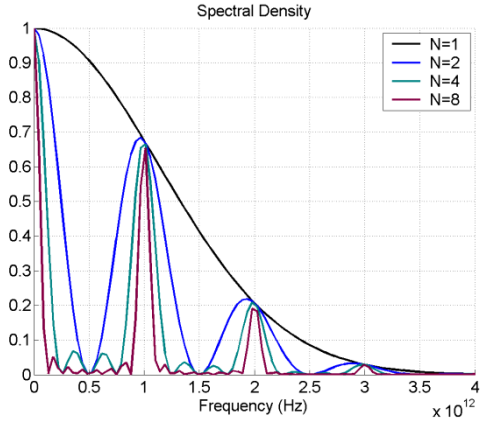

Fig. 3: Calculated spectrum for bunch train of 1,2,3 and 4 equally spaced bunches.

Assuming 1 nC of charge and a the finite metal disc in the SDL as a transition radiator, the total backwards transition radiation is calculated to be 112.2 μJ, 54.8 μJ, 25.9 μJ, and 12.1 μJ for N=1, 2, 4, and 8 respectively.

This experiment focuses on generating a narrow band source, in contrast to other electron beam-based broadband coherent terahertz sources including one demonstrated at the Source Development Laboratory [2] and the Thomas Jefferson National Laboratory [3].

DRIVE LASER MODULATION

The drive laser at the Source Development Lab is based on a commerical 800 nm Ti:sapphire laser. The system produces a 100 fs pulse. A chirped pulse amplification system increases the pulse energy, and it is frequency tripled to 266 nm. In normal operation, a multipicosecond UV laser pulse is directed to the cathode. A scanning cross correlator is used to measure the time profile of the incident laser pulse [4].

In this experiment, an interferometer was used in order to induce drive laser modulations. This technique succeeded in generating several different pulse train configurations, varying in modulation frequency and number of bunches. Two representative cross correlations of obtained UV laser pulses follow in Fig. 4.

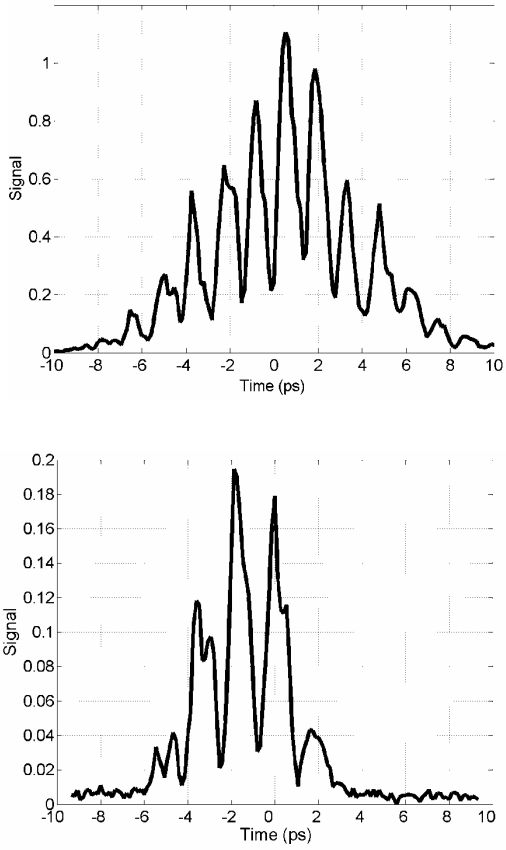

Fig. 4: Examples of UV drive laser cross correlations.

ELECTRON BEAM MEASUREMENTS

After acceleration, the electron beam longitudinal profile is measured. The measurement is made by applying an energy chirp, passing the beam through a magnetic dipole, and examining the beam on a screen. Measurements are made using the RF zero phasing technique, but it has been shown that energy modulation may appear as density modulation using this technique [5]. Varying the energy chirp allowed a tomographic reconstruction technique [6] to be applied to a series of projections in order to recover a time profile of the electron bunch.

Fig. 5 shows two examples of electron beam profiles for different charge levels. Notice that as the charge increases, the entire bunch spreads in time and each individual peak also expands. This has a corresponding effect on the spectrum of the terahertz radiation.

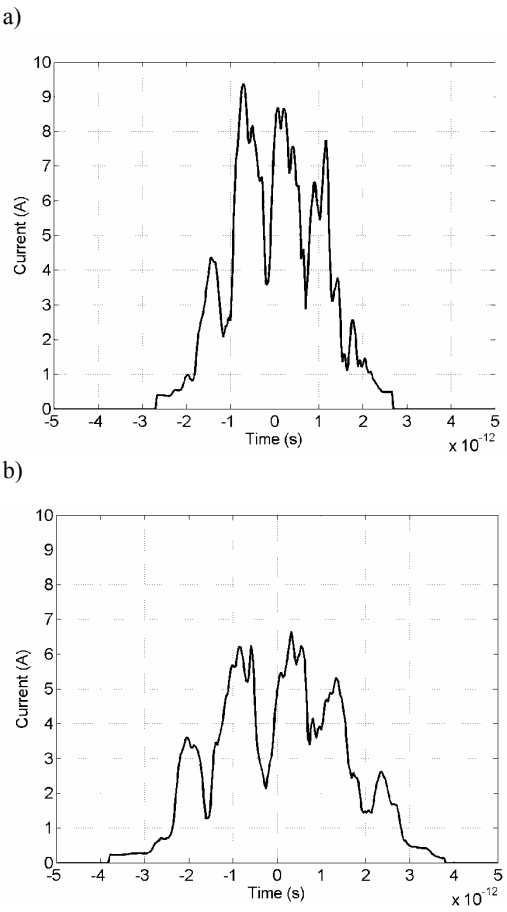

Fig. 5: Two electron beam profiles from tomographic reconstruction corresponding to the second laser pulse shown above. The total charge in (a) is 20 pC and the total charge in (b) is 65 pC.

TERAHERTZ MEASUREMENTS

As a first step for characterizing this source, it was important to determine the energy and spectrum of the terahertz light. Although the spectrum could not be measured directly, four filters were used to sample the the spectrum. The filters are a metal mesh design, and their transmission characteristics were measured on the U12 IR beamline at the National Synchrotron Light Source. The measured filter transmission curve is shown in Fig. 6.

Each of the filters is referred to by a color for convenience. For each charge and modulation setting, the transition radiation produced by the electron beam was measured with a helium cooled bolometer, and with each filter. The expected amount of energy was calculated using equation (1) to determine the expected spectral density per solid angle, taking into account losses due to absorption in air and the geometry of the transport system; the appropriate filter transmission curves were applied, and the total integrated energy was compared to the measurements at the detector. One result of such a comparison is shown in Fig. 7.

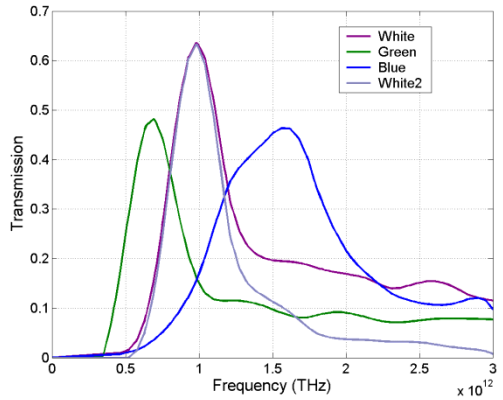

Fig. 6: Characterization of the terahertz filters

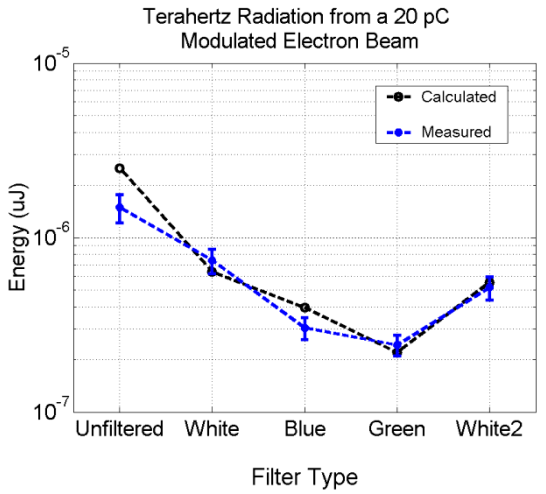

Fig. 7: Terahertz energy measured/calculated at the detector

Agreement between the experimental measurements and theoretical calculations are an indicator that the calculated spectrum is representative of the actual terahertz radiation spectrum produced by the electron beam.

Fig. 8 shows the spectral density calculated from the two electron beam profiles shown above. Note how increasing charge affects the electron beam density profile, and therefore the spectrum.

The total energy arriving at the detector for the 20 pC case was 1.5 pJ (measured) compared to 2.5 pJ (calculated). Estimation of losses in the transport system suggest that the terahertz light exiting the accelerator window is approximately 0.4 nJ. In the 65 pC case, the total energy arriving at the detector was 5.4 pC, which corresponds to 2.4 nJ at the accelerator window.

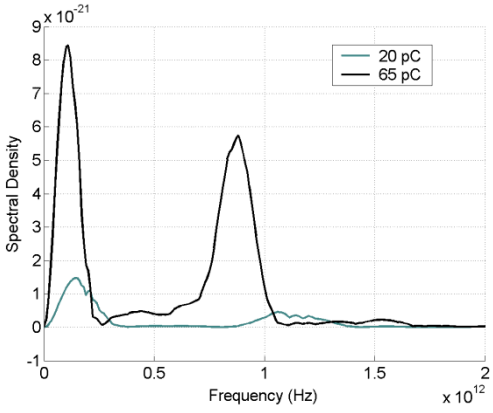

Fig. 8: Achieved Spectral Density

CONCLUSION

This experiment indicates that information from drive laser fluctuations are passed on to the electron beam and can be detected after acceleration. Although the total energy measured at the detector was small, one might achieve higher single shot terahertz pulse energy, as well as a narrower bandwidth, by implementing a better laser control system or a customized electron beam transport system in order to generate a pulse train closer to the ideal case.

One of the problems with pre-modulation of the electron beam is washout of the density modulation. It is important to note, however, that there is still evidence of the initial density modulation in the energy-time phase space even if the density modulation is washed out. This means that it may be possible to recover this density modulation through an appropriate dispersive mechanism.

ACKNOWLEDGEMENTS

This work was carried out with the support of the U.S. Department of Energy, Division of Materials Sciences and Division of Chemical Sciences, under Contract No. DE-AC02-98CH10886 and with support from NAVSEA and the JTO.

REFERENCES

[1] P.H. Siegel, IEEE Trans. Microwave Theory & Techniques 50, 910 (2002).

[2] H. Loos. Personal communication.

[3] G.L. Carr *et al*., Nature, 420, 153 (2002).

[4] H. Loos, *et al. Proc. 2002 Adv. Accel. Concepts*

[5] T. Shaftan *et al*, Proc. 2003 Particle Accel. Conf. 329 (2003).

[6] H. Loos, *et al.* Nucl. Intr. and Meth. A 528, 189 (2004).

SUPPRESSION OF MULTIPASS, MULTIBUNCH BEAM BREAKUP IN TWO PASS RECIRCULATING ACCELERATORS*

C. Tennant#, D. Douglas, K. Jordan, L. Merminga, E. Pozdeyev, TJNAF, Newport News, VA 23606
T. Smith, W.W. Hansen Experimental Physics Laboratory, Stanford, CA 94305

Abstract

Beam Breakup (BBU) occurs in all accelerators at sufficiently high currents. In recirculating accelerators, such as the energy recovery linacs used for high power FELs, the maximum current has historically been limited by multipass, multibunch BBU, a form that occurs when the electron beam interacts with the higher-order modes (HOMs) of an accelerating cavity on one pass and then again on the second pass. This effect is of particular concern in the designs of modern high average current energy recovery accelerators utilizing superconducting technology. In such two pass machines rotation of the betatron planes by 90°, first proposed by Smith and Rand in 1980 [1], should significantly increase the threshold current of the multibunch BBU. Using a newly developed two-dimensional tracking code, we study the effect of optical suppression techniques on the threshold current of the JLAB FEL Upgrade. We examine several optical rotator schemes and evaluate their performance in terms of the instability threshold current increase.

INTRODUCTION

In May of 2004 the multipass, multibunch beam breakup instability was observed at 3 mA of average beam current for the first time in the Jefferson Lab FEL Upgrade Driver. At the onset of the instability we observed HOM power levels in one particular cavity grow exponentially until the beam losses tripped off the machine (see Figure 1). With the knowledge that beam breakup is a real limitation to machine operation, the focus turns to finding a means of suppressing the instability.

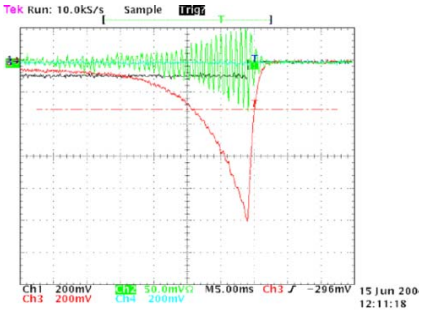

Figure 1: An oscilloscope trace from a BBU induced machine trip. The green trace is the cavity HOM voltage and the red trace is the total HOM power as measured from a Schottky diode. The time scale is 5 msec/div.

*Supported by the Office of Naval Research, the Joint Technology Office, the Commonwealth of Virginia, the Air Force Research Laboratory, and by DOE Contract DE-AC05-84ER40150
#tennant@jlab.org

The intent of this paper is to describe how BBU can be suppressed, or eliminated altogether, by modifying the recirculation transfer matrix from an unstable cavity back to itself in such a way that BBU cannot develop (or it does so at a sufficiently high average current). Applying conventional means of suppressing beam instabilities - such as beam-based feedback and HOM damping techniques - to BBU are discussed elsewhere [2]. The techniques described in this paper are applicable to any two-pass ERL machine; however, for simplicity we study the effect of applying this method to Jefferson Lab's FEL Upgrade Driver.

The Driver is an energy-recovery based linear accelerator used to condition an electron beam for high power lasing [3]. Electrons are injected at 10 MeV and are accelerated to 145 MeV through three cryomodules (each containing 8 superconducting niobium cavities). The beam is transported to a wiggler where up to 10 kW of laser power is generated. The spent electron beam is recirculated and phased in such a way that the beam is decelerated through the linac region on the second pass. Upon exiting the linac, the 10 MeV recirculated beam is extracted to a dump (see Figure 2 for a layout of the FEL).

EFFECTS OF ARBITRARY MODE POLARIZATION AND GENERALIZED TRANSPORT ON BBU

A beam bunch will excite dipole HOMs in a cavity if it passes through the cavity off-axis. The magnetic field of the excited mode then acts to deflect the following bunches. The kick produced by the mode is translated into a transverse displacement at the cavity after recirculation. Thus, the recirculated beam constitutes a feedback which can cause the voltage of the HOMs to grow. An approach based on the consideration of energy deposited by the beam into a cavity HOM was used to derive the threshold current. We consider only a single cavity and a single beam recirculation. However, instead of limiting the HOM orientations to either 0° or 90°, we allow for an arbitrary orientation angle, α, with respect to the horizontal axis. We also allow for a full 4x4 recirculation matrix (i.e. the off-diagonal 2x2 matrices need not be zero). The threshold current is then given by the following expression [4]:

$$I_{th} = -\frac{2p_b c}{ek(R/Q)Q\,M_{12}^{*}\sin(\omega T_r)} \qquad (1)$$

$$M_{12}^{*} \equiv M_{12}\cos^2\alpha + (M_{14}+M_{32})\sin\alpha\cos\alpha + M_{34}\sin^2\alpha$$

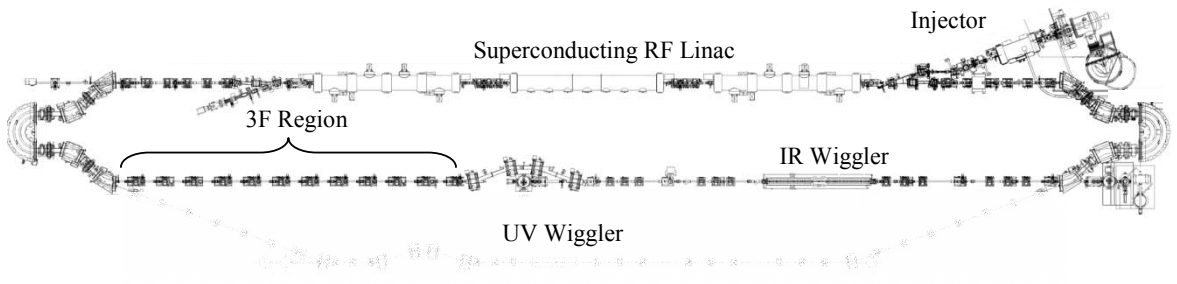

Figure 2: Layout of the JLab FEL Upgrade Driver (the UV transport line is currently being installed).

where p_b is the beam momentum at the cavity, c is the speed of light, e is the electron charge, k is the wavenumber (ω/c) of the HOM, $(R/Q)Q$ is the shunt impedance of the HOM, T_r is the recirculation time and the M_{ij} are the elements of the recirculation transport matrix from the cavity back to itself (which can describe coupled transverse motion).

OPTICAL SUPPRESSION SCHEMES

We consider two methods for beam optical control of BBU. The first method is a reflection which is most effective at suppressing BBU when the HOMs are oriented at 0° or 90°, while the second method utilizes a 90° rotation of the betatron planes in which BBU is eliminated regardless of HOM orientation.

Reflection

The transport matrix describing a reflection about a plane at 45° to the horizontal or vertical axis takes the following form, where each element represents a 2x2 matrix;

$$\begin{pmatrix} 0 & M \\ M & 0 \end{pmatrix}. \qquad (2)$$

The 2x2 sub-block transport matrix M is the same for both exchanges (x to y, y to x). Thus, such a reflector cleanly exchanges the horizontal and vertical phase spaces.

To see how a reflection can be effective in suppressing BBU, consider equations (1) and (2). Since $M_{12} = M_{34} = 0$, for a mode oriented at 0° or 90° the threshold current becomes infinity. However, if an HOM is rotated at an angle α, not equal to 0° or 90°, then the recirculated beam will not come back to the cavity with the angle ($\alpha + 90°$) and its projection on the HOM will be non-zero. To get an infinite threshold for all HOM polarizations requires that $M_{32} = -M_{14}$.

A practical implementation of a reflector using skew-quadrupoles has been non-invasively embedded in the 3F "backleg" region of the FEL Upgrade Driver (see Figure 2) [5]. Operationally, normal quadrupoles upstream and downstream of the module are used as betatron matching telescopes. These allow transverse matching of the phase spaces across the reflector, so that the 3F region, in its entirety, remains transparent to the rest of the machine - save for the exchange of horizontal and vertical emittance, the interchange of incident steering, and possible differences in phase advance, nothing is changed. While the skew-quadruples produce a reflection across the 3F region, the transport matrix of interest for suppressing BBU is from the unstable cavity back to itself. Thus, with nominal operating conditions, the effect of the embedded skew-quadrupole reflector is to produce a pseudo-reflection; a matrix similar in form to equation (2) but with the off-diagonal matrices not exactly equal to each other.

Rotation

A more robust optical scheme which suppresses BBU regardless of HOM orientation is a 90° rotation. The transport matrix describing a 90° rotation takes the following form, where as before, each element represents a 2x2 matrix;

$$\begin{pmatrix} 0 & M \\ -M & 0 \end{pmatrix}. \qquad (3)$$

Consider now equations (1) and (3). Since $M_{12} = M_{34} = 0$ and $M_{32} = -M_{14}$, the threshold current is infinity and BBU is eliminated - independent of the mode orientation. A rotation implemented in a two-pass system effectively breaks the feedback loop formed between the beam and cavity HOM so there can be no exchange of energy. The idea is conceptually simple and is illustrated in Figure 3. If on the first pass an offending mode imparts an angular deflection α, to a bunch, then on the second pass (and after a 90° rotation), the resultant displacement will be orthogonal to the deflection. Thus the bunch will be unable to couple energy to the mode that caused the deflection.

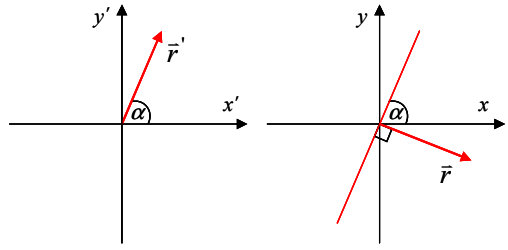

Figure 3: The effect of a 90° rotation. A deflection on the first pass (left) is transformed to a displacement which is orthogonal to the deflection which caused it (right).

One way of implementing a rotation is by the use of a solenoid. However, in high energy machines a solenoid becomes impractical because of the large magnetic field integral required. In addition, a solenoid introduces undesirable strong transverse focusing. Another way of implementing a rotation is via a reflection. An embedded reflection in the recirculator can, in principle, be made to produce a pure rotation from the unstable cryomodule back to itself [6].

DESCRIPTION OF THE TWO-DIMENSIONAL BBU SIMULATION CODE

Simulations to study the effectiveness of the optical suppression schemes described above were performed using a newly developed BBU code (yet to be named) [7]. The code was written in the Standard ANSI C++ language and the first version of the code has been tested and benchmarked. The primary motivation for developing a new code was the necessity for a correct treatment of two-dimensional transverse beam dynamics and the capability to handle HOMs with arbitrary orientations. The code works by tracking particles through a machine characterized by transfer matrices and follows the HOM energy buildups in accelerating cavities. In the present configuration, the code simulates beam dynamics in a two-pass recirculating accelerator.

The code has been used to simulate beam breakup in several one-dimensional cases including the FEL Upgrade Driver. The results are in 3% agreement with results simulated by the previous BBU simulation codes used at Jefferson Laboratory, TDBBU [8, 9] and MATBBU [10]. Because the results for two-dimensional simulations have not been compared with existing BBU codes, the results were compared to the formula given in equation (1). The simulation results for two-dimensional cases show excellent agreement with the theory [11]. In addition to the capability of handling two-dimensional transverse motion and arbitrarily oriented HOMs, the new code is faster than TDBBU and MATBBU by an order of magnitude or more depending on the particular problem.

SIMULATION RESULTS

To see the effectiveness of the two aforementioned methods for beam optical control of BBU, two-dimensional simulations were performed. The simulation model uses the FEL design optics including the RF focusing effects and uses measured data to describe the HOMs (frequencies and loaded Qs). The only unknown is the polarization of each HOM. Thus two sets of simulations were performed. The first set simulates HOMs with orientations of either 0° or 90° ("aligned modes"). A second simulation was performed with the orientations "skewed" slightly. Each mode from the first set was changed (randomly) by an amount between 1° and 15° to see the effects of different HOM orientations ("skewed modes"). For each set, three different machine optics were simulated: (1) nominal, uncoupled optics (2) pseudo-reflector optics (3) rotated optics. The results are summarized in Table 1.

	Nominal	Pseudo-Reflection	Rotation
"Aligned"	2.83 mA	288 mA	613 mA
"Skewed"	2.87 mA	18.3 mA	208 mA

Table 1: Simulation results of the BBU threshold currents.

Nominal Optics

With no suppression techniques applied, the threshold current for the case of "aligned modes" is just under 3 mA. The threshold current remains virtually unchanged for the "skewed modes" case.

Pseudo-Reflector Optics

With the modes "aligned" the threshold current is increased substantially from the nominal optics case (by a factor of ~100). The threshold is not infinite - as one might expect – since coupling between HOMs is possible due to the finite Q's and frequency separation, thus facilitating BBU at lower currents. The point of interest, however, is that due to mode orientations being "skewed", a pseudo-reflection alone does not effectively suppress BBU. The factor of 6 increase in the threshold current is consistent with a misaligned mode as given in equation (1), but is significantly less effective than with the modes "aligned" (e.g. 18.3 mA versus 288 mA). Thus, unless it is known that dangerous HOMs are oriented very nearly to 0° or 90°, a reflection scheme may not adequately suppress BBU. Figure 4 illustrates the effects of the pseudo-reflected optics as given by the BBU simulation code. Each plot shows the transverse displacement (horizontal and vertical) versus time. The average beam current for the simulations was 100 mA. In the case of "aligned modes" initial beam offsets damp down and the beam is stable. In the case of the "skewed modes" the threshold current is much lower than the current simulated and hence BBU develops and the beam offset grows exponentially.

Rotated Optics

For the case of "aligned modes" the threshold current is increased by a factor of ~200. In theory, BBU should be eliminated altogether with a pure 90° rotation of betatron planes (see equation (1)). However, the recirculation matrix used for the unstable region back to itself is not a perfect rotation (i.e. the 2x2 off-diagonal matrices are of opposite sign, but are not exactly equal). Hence BBU occurs at a finite current. With the modes "skewed", a rotation is still very effective in raising the threshold current. This is expected since, as discussed previously, a rotation suppresses BBU regardless of the mode orientations.

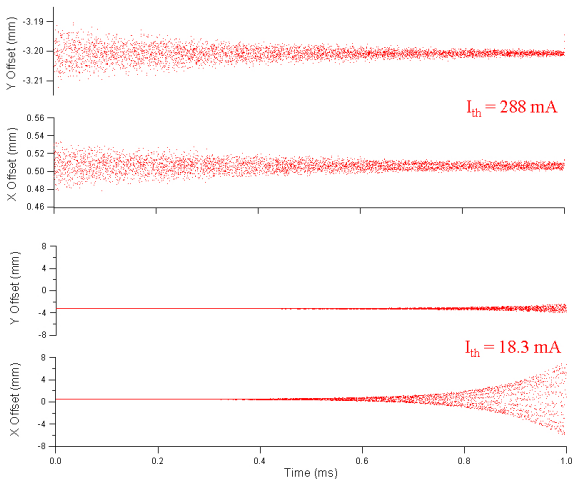

Figure 4: Transverse displacement versus time for "aligned modes" (top) and "skewed modes" (bottom) with pseudo-reflection optics. The average beam current for each simulation is 100 mA.

FIRST OPERATIONAL EXPERIENCE

Operational experience with the FEL Upgrade is consistent with this discussion of instability control. By tuning the betatron phase advances and match, it was possible to vary the BBU-driven current limit from as low as 1 mA to over 5 mA (the usual operational current). Such configurations did not always reproduce over the course of days due to irreproducibility in the transport system quadrupoles. When problematic, thresholds could be moved to acceptable levels – often without invoking adjustments in betatron phase advance – by improving betatron matching and current transmission.

We have, further, succeeded at operating at over 8 mA by use of the aforementioned skew-quadrupole reflection. When activated, we have verified this system completely cross-couples the two transverse planes. Modeling further suggests that certain choices of phase advance render the installed system a true reflection [12]. We note however that this configuration awaits operational evaluation. Though it is possible to manipulate the transfer matrix in this manner, it is not certain that the machine will perform properly, as internal mismatch can generate beam loss that limits machine performance just as surely as BBU. Conversely, it was found during FEL operation that simply matching the machine well (so as to clean up the transport, but ignoring BBU altogether) could result in a factor of 4 or 5 improvement in the threshold current.

CONCLUSIONS

The multipass, multibunch beam breakup instability has been observed at the Jefferson Lab FEL Upgrade Driver. This has prompted investigations of methods for beam optical control of BBU. From a simple, analytical model and from two-dimensional BBU simulations, it was shown that a 90° rotation of the betatron planes is the most effective means to suppress the instability in a two-pass recirculator. Experimentally, the skew-quadrupole reflector has been successfully commissioned in the FEL Upgrade Driver. A systematic and quantitative study of its effect on the threshold current has yet to be performed. However, operational experience has shown that the threshold is increased from 5 mA to over 8 mA using the reflector without any evidence of BBU induced machine trips.

REFERENCES

[1] Rand R., Smith T., *Beam Optical Control of Beam Breakup in a Recirculating Electron Accelerator*, Particle Accelerators, Vol. II, pp. 1-13 (1980).

[2] Tennant C., et al., "Methods for Measuring and Controlling Beam Breakup in High Current ERLs," Proceedings of the LINAC 2004 Conference (2004).

[3] Benson S., et al., "High Power Lasing in the IR Upgrade FEL at Jefferson Lab," these proceedings (2004).

[4] Pozdeyev E., Tennant C., "Equation for the Multipass Beam Breakup Threshold Current for a Single Mode and a 4x4 Recirculation Matrix," JLAB-TN-04-019 (2004).

[5] Douglas D., "A Skew-Quad Eigenmode Exchange Module (SQEEM) for the FEL Upgrade Driver Backleg Transport," JLAB-TN-04-016 (2004).

[6] Douglas D., "Reflections on Rotators," JLAB-TN-04-023 (2004).

[7] The BBU code was developed by E. Pozdeyev (pozdeyev@jlab.org)

[8] Krafft G., Bisognano J., "Two Dimensional Simulations of Multipass Beam Breakup," Proceedings of the 1987 Particle Accelerator Conference, p. 1356 (1987).

[9] Beard K., "TDBBU 1.6: Another Tool for Estimating Beam Breakup Due to Higher-Order Modes," JLAB-TN-02-045 (2002).

[10] Beard K., "MATBBU 2.4: A Tool to Estimate Beam Breakup Due to Higher-Order Modes," JLAB-TN-02-044 (2002).

[11] Tennant C., Pozdeyev E., "Simulation Results of Two-Dimensional Multipass Beam Breakup," JLAB-TN-04-020 (2004).

[12] Douglas D., "Operation of the FEL Upgrade with Skew Quad Reflection and Rotation," JLAB-TN in preparation (2004).

POTENTIAL USE OF eRHIC's ERL FOR FELS AND LIGHT SOURCES

Vladimir N. Litvinenko and Ilan Ben-Zvi
Brookhaven National Laboratory, Upton, NY, USA

Abstract

One of the designs of a future electron-hadron collider, eRHIC, is based on a 5-10 GeV high current energy-recovery linac (ERL) with possible extension of its energy to 20 GeV. This ERL will operate with high brightness electron beams, which naturally match requirements for X-ray FELs and other next generation light sources. In this paper we discuss possible scenarios of using the eRHIC ERL in parasitic and dedicated mode for SASE, HGHG and oscillator X-ray FELs.

INTRODUCTION

A Twenty-Year Outlook DoE document on "Facilities for the Future Science" [1] includes a new electron-hadron collider at BNL, based on the Relativistic Heavy Ion Collider (RHIC) and a new electron accelerator.

Table 1. Main parameters of eRHIC

RHIC	
Ring circumference [m]	3834
Protons: number of bunches	360
Beam energy [GeV]	26 - 250
Protons per bunch (max)	$2.0 \cdot 10^{11}$
Normalized 96% emittance [μm]	14.5
Gold ions: number of bunches	360
Beam energy [GeV/u]	50 - 100
Ions per bunch (max)	2.0 · 109
Normalized 96% emittance [μm]	6
Electrons: Beam rep-rate [MHz]	28.15
Beam energy [GeV]	5 – 20
γ, Relativistic factor	$1 - 4\ 10^4$
RMS normalized emittance [μm]	5- 50
Beam emittance @ 20 GeV [Å]	1.25-12.5
RMS Bunch length [psec]	30
Charge per bunch [nC]	1.6 -16
Average e-beam current [A]	0.45

The main goal of the eRHIC is to explore the physics at so-called "low-x", and the physics of color-glass condensate in electron-hadron collisions [2]. In response, the Collider-Accelerator Department at BNL in collaboration with Bates Laboratory at MIT issues the eRHIC ZDR (0^{th}–order design report), which includes a linac-ring eRHIC design based on 10 GeV ERL [3]. The design is based on CW linac with high current super-conducting RF (SRF) 5-cell cavities, which are under construction at BNL [4,5] and a polarized photo-injector using a dedicated 2 kW circularly polarized FEL [3]. The main parameters of the eRHIC are summarized in Table 1. The parameters of the electron beam are very impressive and it can easily be used as a next generation light source in parasitic mode.

In addition, RHIC rings operate only for about 30 weeks per year, which leaves about 4 and a half months for dedicated mode of ERL operation as a light source. In this case we suggest using a lower charge per bunch and a higher rep-rate, while keeping the same level of average e-beam current (~ 500 mA). The e-beam parameters for this mode of operation are listed in Table 2.

Table 2. Main parameters in dedicated mode

Electrons	
Beam rep-rate [MHz]	703.75
Beam energy [GeV]	5 – 20
γ, Relativistic factor	$1 - 4\ 10^4$
RMS normalized emittance [μm]	0.9
Beam emittance @ 20 GeV [Å]	0.18
Full transverse coherence λ[Å]	1.13
photon energy [keV]	11
RMS Bunch length [psec]	0.03 - 3
Charge per bunch [nC]	0.7
Average e-beam current [A]	0.5

Parameters of the electron beam in eRHIC's ERL naturally match the requirements for a next generation light source. First, let us note that the eRHIC ERL light source would have transverse coherence in the X-ray range up to 11 keV. Second, 20 GeV operation of the ERL will extend the range of spontaneous radiation from undulators and bending magnets into γ-ray range and open new possibilities for low energy nuclear physics. Third, the ERL is a perfect driver for high power (i.e. kilowatts of CW power) FELs ranging from hard X-rays to VUV. Fourth, it is also a perfect match for generating beam of very intense circularly polarized γ-rays with energies up to 12 GeV.

In this paper, we take a first look at the potential of the ERL at eRHIC as a light source. We describe two possible layouts, discuss the effects of synchrotron radiation in the ERL's arcs on the e-beam parameters and, finally, present a straw-man design of X-ray FELs based on SASE, distributed optical klystron (DOK) and optics-free oscillator schemes.

LAYOUTS OF THE ERL-based eRHIC

Fig.1 shows a possible layout for a stand-along ERL. The electron beam, generated in SRF photo-injector is accelerated to an energy of 0.5 GeV by low energy ERL, followed by two passes through high energy linacs. This layout provides for a natural use of the beam-lines installed on the 2.5, 5, 7.5 and 10 GeV arcs for a variety of sources of spontaneous radiation. After passing through the collision point, the beam is going

through the energy recovery process, which doubles the beam current in each arc (except that at 10 GeV). FEL can be installed in a straight section connecting the end of the 10-GeV arc with the linac. This scheme is limited to maximum energy of ~ 10 GeV by the size of the accelerator and the acceptable power of the synchrotron radiation.

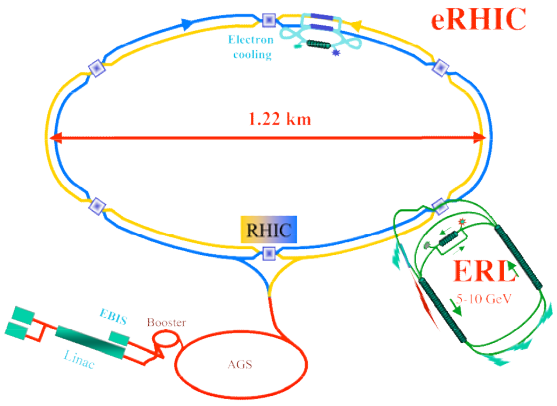

Fig. 1 Layout of eRHIC with a stand-along 10 GeV ERL.

Fig.2 shows a more attractive layout of ERL sharing a 3.8 km tunnel with two hadron storage rings (called the blue and the yellow).

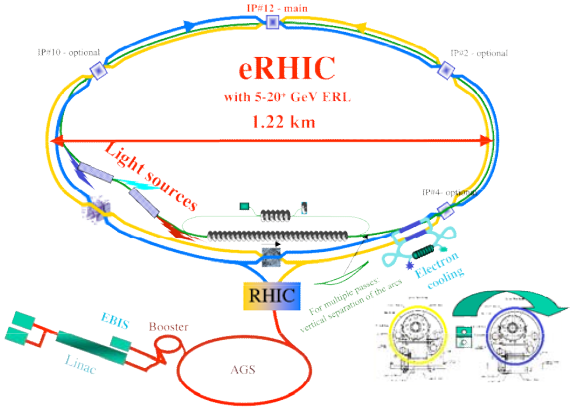

Fig. 2 Layout of the eRHIC ERL in the RHIC tunnel.

This layout provides for multiple collision points for eRHIC and also allows an increase in the energy of electron beam to 20 GeV or above while keeping power of synchrotron radiation under control (and especially keeping linear power density well below 1 kW/m). Obviously, this layout has many advantages for the light source applications. It has best emittance and hundreds of meters of free space for hard X-ray FELs.

Similarly to other ERLs, the electron beam is generated in the gun, pre-accelerated in the low energy SRF linac, then injected into the main high energy SRF linac, which it passes twice to reach maximum energy of 20 GeV. Then the beam is decelerated to recover its energy back into RF field and is finally dumped.

On the way to the final energy the electron beam passes through the arcs, where synchrotron radiation may significantly affect the e-beam parameters. Our present design is based on 150 25-meter long achromatic cells (see sketch in Fig. 3) with a bending radius of 400 m in the dipoles. The energy loss for synchrotron radiation is 35 MeV for 20 GeV electrons.

Fig. 3 A sketch of 25 meter-long achromatic cell for 10 and 20 GeV arcs in the eRHIC's ERL.

Table 3. Parameters of the 10 GeV e-beam

Energy	10	GeV	
Radius, average	610.20	m	
B, magnets	0.83	kGs	
ε_{norm}	9.50E-07	m rad	
ε	0.485	Å	
Bunchlength	from 0.1 to 2	psec	
$\Delta\varepsilon$	0.001	Å	0.10%
ε , final	0.486	Å	
RMS energy spread	4.49E-06		

Table 4. Parameters of the 10 GeV e-beam

Energy	20	GeV	
Radius, average	610.20	m	
B, magnets	1.67	kGs	
ε_{norm}	9.50E-07	m rad	
ε	0.243	Å rad	
Bunch length	from 0.1 to 2	psec	
$\Delta\varepsilon$	0.016	Å rad	6.70%
ε , final	0.259	Å rad	
RMS energy spread	2.54E-05		

The beam parameters at the end of the arc for 10 GeV and 20 GeV beams and some basic parameters of the arcs are given in Table 3 and Table 4, correspondently. In this design, synchrotron radiation determines the energy spread of both 10 GeV and 20 GeV, while contribution of the initial energy spread is negligible. In contrast, this low emittance lattice of the arc provides for essential preservation of the initial normalized transverse emittance: the horizontal emittance grows by 0.1% for 10 GeV beam and by 6.7% for 20 GeV beam. Extremely high quality of the electron beam in eRHIC's ERL provides for a natural use of its strong spontaneous radiation from its regular or *specialized* magnets (see Table below).

Table 5. Synchrotron radiation at 20 GeV.

Loss per turn	35.40	MeV
Power	17.70	MW
λ_c (regular bend)	0.28	Å
E_c (regular bend)	44.35	KeV
λ_c (10 T bend)	*0.0047*	*Å*
E_c (10 T bend)	*2661*	*KeV*

Energy of 20 GeV makes building hard X-ray sources an easy task: a wiggler with period of 2 cm will generate fundamental wavelength of ~ 0.1 Å. The range of expected spectral brightness for these sources of spontaneous radiation is shown n Fig. 5.

ERL-based FELs

Low emittance, high peak current of the 20 GeV ERL operating in dedicated mode (Table 2) make it an attractive driver for high gain X-ray FELs, which can operate in SASE [6], and HGHG [7] modes. The very low energy spread of this source makes it attractive to use a scheme of distributed optical klystron (DOK) [8], schematically shown in Fig. 4. DOK driven by a low energy spread beam has shorter gain length ($L_{G\ DOK}$) compared with that of a SASE FEL (L_G):

$$L_{G\ DOK} \cong L_G \cdot \left\{ e^{\frac{1}{4}} \cdot 2\sqrt{\frac{4\pi L_G}{\lambda_w}\frac{\sigma_\gamma}{\gamma}} / \kappa^{3/2} \right\};\ \kappa = \frac{L_w}{L_c}.$$

where σ_γ / γ is RMS energy spread of electron beam and λ_w is the wiggler period. DOK reduces the gain length X-ray FELs at eRHIC 2.2 and 5 fold at energies of 20 GeV and 10 GeV, correspondingly. Table 6 summarizes the parameters of ERL based FELs at eRHIC.

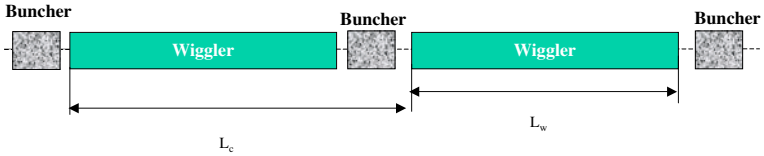

Fig. 4 A sketch of distributed optical klystron, which consists of repeating cells comprising a wiggler and a buncher. Similar to the traditional optical klystron [1], the slippage in the buncher is significantly larger that in the wiggler. This additional bunching combined with low energy spread beam enhances the FEL gain.

Table 6. Main parameters of X-ray FEL driven by ERL at eRHIC

Energy, GeV	20	20	15	15	10	10
Wavelength, Å	0.5	1	0.87	1.8	2	4
Bunch length, psec	0.2	0.2	0.27	0.27	0.4	0.4
Peak Current, kA	5	5	3.75	3.75	2.5	2.5
Wiggler period, cm	2.5	3	2.5	3	2.5	3
SASE gain length, m	**7.5**	**4.3**	**5.5**	**3.3**	**3.7**	**2.4**
SASE Saturation length, m	100	60	76	47	51	34
Saturation power, GW	7.7	19	6.4	14	4.5	9
DOK, gain length, m	**3.5**	**1.4**	**1.5**	**0.65**	**0.51**	**0.25**
DOK, saturation length, m	47	19	21	9	7	3.5

A simple use of SASE FEL combined with a very high repetition rate of ERL at eRHIC leads to extremely high average lasing power from 0.6 MW to 1.3 MW at wavelength of 1Å (photon energy 12 keV). The solution for this potential problem is either to use Fourier limited source. i.e. either HGHG FEL or optics-free FEL oscillator (OFFO) [10], the schematic of which is sketched in Fig. 6 The main ERL drives an high gain FEL amplifier with gain of ~ 10^5. Amplified light passes through a micro-wiggler with low energy, low current, low emittance e-beam used for feed-back. The feed-back-beam carries-on the modulation to the entrance of the FEL, where it radiates coherently in another micro-wiggler. This radiation is then amplified by the new electron bunch in the high energy FEL. This process closes the loop and makes this FEL an oscillator [12].

The advantage of this scheme is that this FEL is fully tunable, optics independent and has a line-width of an oscillator. This scheme would allow reducing the line-width of X-ray FEL to a *few parts per million* compared with a few parts per thousands, typical for

SASE FELs [11]. In this case, the average power of X-ray FEL at eRHIC with average spectral brightness in 10^{30} range (see Fig.5) will reduce to manageable levels of tens of hundreds of watts.

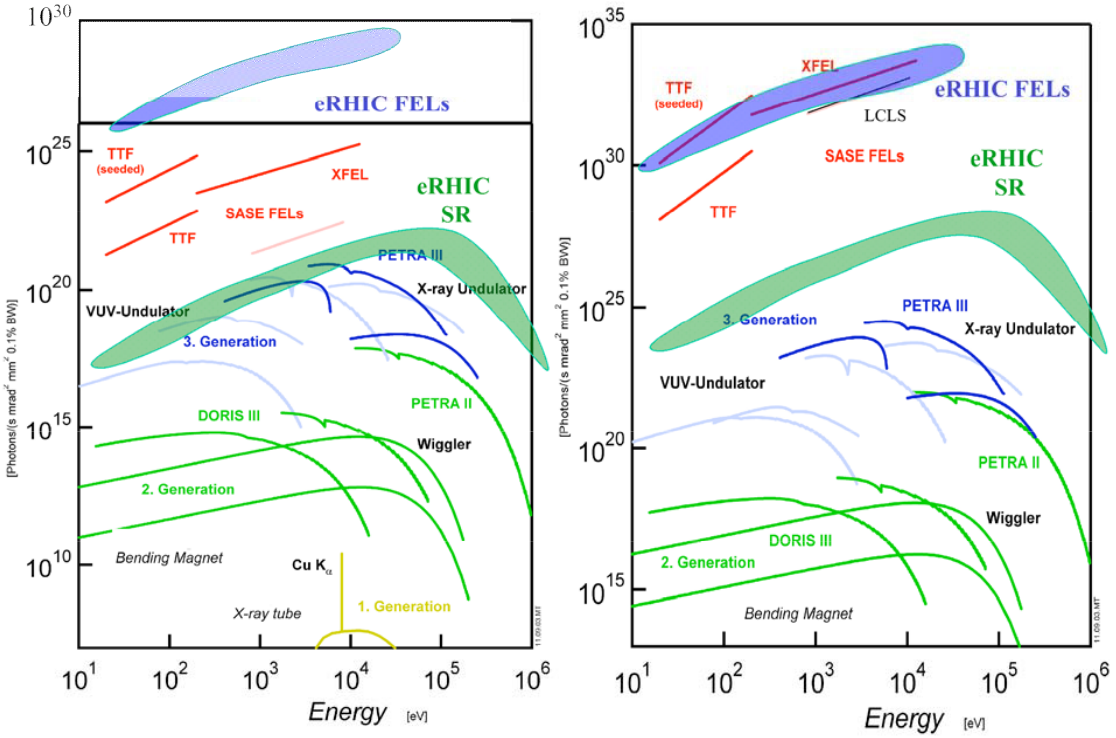

Fig.5 Average and peak spectral brightness of eRHIC light source (blue – FELs, green – spontaneous radiation) compared with other sources. While being similar to SASE FEL sources in peak spectral brightness, the average spectral brightness of eRHIC FELs would exceed the rest of the light sources (existing and proposed) by about 5 orders of magnitude.

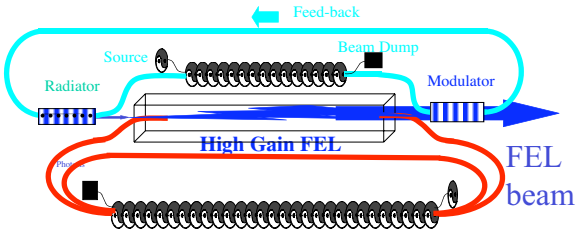

Fig. 6 Schematic of OFFO using two ERLs.

CONCLUSION

Future high current 10-20 GeV ERL for eRHIC electron-hadron collider has outstanding potential to become a next generation light source with unprecedented levels of average spectral brightness.

This work is supported by the US Department of Energy and Office of Naval Research.

REFERENCES

[1] http://www.er.doe.gov/Sub/Facilities_for_future/facilities_future.htm

[2] http://www.bnl.gov/henp/docs/NSAC_RHICII-eRHIC_2-15-03.

[3] http://www.agsrhichome.bnl.gov/eRHIC/, Appendix A, Linac-Ring Option

[4] I. Ben-Zvi at al., Ampere Average Current Photo-Injector and Energy Recovery Linac, these Proceedings.

[5] R. Calaga et al., High Current Superconducting Cavities at RHIC, Proceedings of EPAC-2004, Geneva, Switzerland, July 5-9, 2004

[6] A.M. Kondratenko, and E.L. Saldin, Particle Accelerators 10, 207 (1980); J.B. Murphy and C. Pellegrini, Nuclear Instruments, and Methods A237, 159 (1985);

[7] L.H. Yu et al, Physics Review Letters **91**, No. 7, 074801-1 (2003)

[8] V.N. Litvinenko, Nuclear Instruments and Methods **A 304**, (1991) 463

[9] N.A. Vinokurov and A.N . Preprint INP 77-59, Novosibirsk, 1977

[10] V.N. Litvinenko, Proceedings of FEL conference, August 2002, APS, Argonne, IL, Eds. K.-J.Kim, S.V.Milton, E.Gluskin, p. II-1

[11] V. Ayvazyan et al., Physics Review Letters **88**, 104802 (2002)

THE HARMONICALLY COUPLED 2-BEAM FEL

B. W. J. M^{c}Neil* and G. R. M. Robb, University of Strathclyde, Glasgow G4 0NG, UK
M. W. Poole, ASTeC, Daresbury Laboratory, Warrington WA4 4AD, UK

Abstract

A model of a Free Electron Laser amplifier operating simultaneously with two electron beams of different energy is presented. The electron beam energies are chosen so that the fundamental resonance of the higher energy beam is at an harmonic of the lower energy beam. By seeding the lower energy FEL interaction at its fundamental radiation wavelength, an improved coherence of the un-seeded higher energy FEL emission is predicted and may offer an alternative to current proposals for seeding XUV and x-ray FELs. An initial study of the effects of beam energy spread on the intearction is presented.

INTRODUCTION

It is now well established that high gain FELs operating in the SASE mode [1] are characterised by a noisy FEL output at saturation with relatively poor temporal coherence and large fluctuations [2]. The simplest conceptual method to resolve this problem is to inject a well-formed resonant coherent seed field at the beginning of the FEL interaction that dominates the intrinsic noise. The FEL output is then significantly improved over that of SASE at saturation. However, there are, as yet, no suitable seed sources available in the XUV and x-ray. Seeding at longer wavelengths can generate shorter wavelengths by using the two-wiggler harmonic method of [3]. Variations on this theme have been suggested and implemented experimantally [4]. Another self-seeding method proposes using a monochromator either at the early stages of the FEL interaction [5] or with some feedback [6] to improve temporal coherence. In this paper an alternative method of seeding, based on a two electron beam FEL interaction [7], is described and investigated in the 1-D limit. Preliminary results of the effects of electron beam quality on the two-beam FEL are also presented.

THE MODEL

A simple FEL wiggler system, of constant period λ_w, and field strength B_w, was proposed, through which two electron beams of different energy co-propogate [7]. The lower energy electron beam has a Lorentz factor of γ_1 and the higher energy γ_n. The higher energy electron beam is chosen so that its fundamental resonant wavelength is an harmonic resonant wavelength of the lower energy beam. From the FEL resonance relation, $\lambda = \lambda_w(1 + a_w^2)/2\gamma^2$, it may easily be shown that $\gamma_n = \sqrt{n}\gamma_1$. It should then be possible to seed the co-propagating electron beams with an externally injected seed radiation field at the fundamental of the lower energy electron beam. If such a seed field is significantly above the noise level then the lower energy electrons will begin to bunch at their fundamental resonant wavelength and retain the coherence properties of the seed. Such bunching at the fundamental also generates significant components of bunching at its harmonics which can also be expected to retain the coherence properties of the seed. In a planar FEL this also results in on-axis radiation emission at these harmonics. This process should couple strongly with the the co-propagating higher energy beam whose fundamental FEL interaction is at one of the lower energy beam's harmonics. This coupling between lower and higher energy FEL interactions may allow the transferal of the coherence properties of the longer wavelength seed field to the un-seeded shorter harmonic wavelength interaction.

Another coupling between the lower and higher energy electron beams, which has the potential to degrade beam quality, is the two-stream instability [8]. Using the results of [8], however, it can be shown that the instability is either below threshold or has an insignificant effect for electron beam currents ($\gtrsim 1$ kA) and energies ($\gtrsim 500$ MeV) typical to those used in the FEL interactions presented here.

The physics of the planar wiggler FEL in the 1-D Compton limit may be described by the coupled Maxwell/Lorentz equations which, under the simplifying assumptions, universal scaling and notation of [1, 9], are written:

$$\frac{d\vartheta_j}{d\bar{z}} = p_j \quad (1)$$

$$\frac{dp_j}{d\bar{z}} = -\sum_{h,odd} F_h \left(A_h e^{ih\vartheta_j} + c.c. \right) \quad (2)$$

$$\frac{dA_h}{d\bar{z}} = F_h \left\langle e^{-ih\vartheta} \right\rangle , \quad (3)$$

where $j = 1..N$ are the total number of electrons, $h = 1, 3, 5...$ are the odd harmonic components of the field and F_h are the usual difference of Bessel function factor associated with planar wiggler FELs. This set of equations (1..3) is used to describe the FEL interaction of the lower energy (γ_1) electron beam.

Strongest coupling between the lower and higher energy electron beams would be expected for the lowest harmonic interaction $h = n = 3$ so that the higher energy electron beam has energy $\gamma_3 = \sqrt{3}\gamma_1$. Higher harmonic interactions $h = n > 3$ may also be of interest, as those harmonics $h < n$ of the lower energy beam are not resonant with the higher energy beam and would not be expected to unduly disrupt the coupling to the higher harmonic.

* b.w.j.mcneil@strath.ac.uk

The equations describing the FEL interaction of the higher energy electron beam, with its fundamental resonant field only, may be written in the similar form:

$$\frac{d\varphi_j}{dz'} = \wp'_j \quad (4)$$

$$\frac{d\wp'_j}{dz'} = -F_1\left(A'_1 e^{i\varphi_j} + c.c.\right) \quad (5)$$

$$\frac{dA'_1}{dz'} = F_1\left\langle e^{-i\varphi}\right\rangle. \quad (6)$$

We shall neglect harmonics of the higher energy electron beam as these will have a weaker coupling to the lower energy beam , e.g. if $n = 3$ then the third harmonic of the higher energy beam will be the ninth harmonic of the lower energy beam.

In their universally scaled forms the two sets of equations (1..3) and (4..6) have different Pierce parameters [1], ρ, due to the different energy and current density of the electron beams. In [7], by using the usual relations between scaled and unscaled fields and lengths [1], equations (4..6) were written with the same scaling of equations (1..3) to give the final set of working equations describing the coupled FEL system. Here, we use the scaling of equations (4..6) to rescale equations (1..3). For purely notational convenience we rewrite $z' \to \bar{z}$ and $A'_h \to A_h$ in equations (1..6) after rescaling to give the final set of working equations:

$$\frac{d\vartheta_j}{d\bar{z}} = p_j \quad (7)$$

$$\frac{d\varphi_j}{d\bar{z}} = \wp_j \quad (8)$$

$$\frac{dp_j}{d\bar{z}} = -\frac{1}{c_1}\sum_{h,odd}^{n} F_h\left(A_h e^{ih\vartheta_j} + c.c.\right) \quad (9)$$

$$\frac{d\wp_j}{d\bar{z}} = -\left(F_1 A_n e^{i\varphi_j} + c.c.\right) \quad (10)$$

$$\frac{dA_h}{d\bar{z}} = S_{h\vartheta} \quad (11)$$

$$\frac{dA_n}{d\bar{z}} = S_\varphi + S_{n\vartheta}, \quad (12)$$

where

$$S_{k\vartheta} \equiv \frac{1}{c_2}F_k\left\langle e^{-ik\vartheta}\right\rangle, \quad S_\varphi \equiv F_1\left\langle e^{-i\varphi}\right\rangle \quad (13)$$

$$c_1 = \frac{1}{n^{1/4}}\left(\frac{\rho_n}{\rho_1}\right)^{3/2} = \frac{1}{n}\sqrt{\frac{I_n}{I_1}} \equiv \frac{\sqrt{R_n}}{n} \quad (14)$$

$$c_2 = n^{1/4}\left(\frac{\rho_n}{\rho_1}\right)^{3/2} = \frac{1}{\sqrt{n}}\sqrt{\frac{I_n}{I_1}} \equiv \frac{\sqrt{R_n}}{\sqrt{n}}, \quad (15)$$

and in (11) h refers to all odd harmonics $h < n$, I is the beam current and subscripts 1 (n) refers to the parameters of the lower (higher) energy beam. Note that all harmonic interactions have been assumed negligable for $h > n$ in equation (9). By assuming both beams have the same transverse cross section (or equivalently the same normalised transverse emittance in a common, matched focusing channel through the wiggler) then $\rho_{1,n} \propto I_{1,n}^{1/3}/\gamma_{1,n}$ and the second equalities of (14) and (15) are obtained in terms of the beam currents. This assumption is applied to the work presented hereafter. Note that the equations (3) and (6), describing evolution of the fields A_n and A'_1, refer to the *same* field, which, once (3) has been re-scaled, allows the two source terms to be combined into the single differential equation (12) for the harmonic field $A'_n \to A_n$.

The coupling of the low energy electrons to both fundamental and harmonic field is seen in equation (9). From equation (10), the higher energy electrons only couple to the harmonic field A_n (their fundamental) - the fields A_h are sub-harmonic to the higher energy electrons and are therefore not resonant. The fields A_h, are seen from equation (11), to be driven only by the lower energy electron beam (the higher energy electrons are not resonant with A_h.) Equation (12) demonstrates that the highest harmonic field has two driving sources, both the lower and higher energy electron beams. From these couplings it is seen that, whereas the shorter wavelength radiation field is directly coupled to both lower and higher energy electron beams, the longer wavelengths have no direct coupling with the higher energy beam. In this sense, the short wavelength harmonic interaction may be described as 'parasitic' as it may resonantly extract energy directly from both lower and higher energy electron beams, whereas the longer wavelengths may only directly extract energy from the lower energy beam.

The working equations readily yield a constant of motion corresponding to conservation of energy:

$$\sum_{h,odd}^{n}|A_h|^2 + \frac{\langle p\rangle}{\sqrt{n}} + \langle\wp\rangle. \quad (16)$$

It is seen from the definitions of the scaled electron energy parameters $p_j \equiv (\gamma_j - \gamma_1)/\rho_n\gamma_1$ and $\wp_j \equiv (\gamma_j - \gamma_n)/\rho_n\gamma_n$ that the electron beam energy relation $\gamma_n = \sqrt{n}\gamma_1$ accounts for the factor of $\sqrt{n}$ in (16).

A linear analysis of the system (7..12) was carried out using the method of collective variables [1]. Assuming resonant interactions for both electron beams, and that both beams are effectively 'cold' so that neither emittance nor energy spread have a deleterious effect upon the FEL interaction, this analysis yields a condition for the beam current ratio, $R_n \equiv I_n/I_1$, above which gain at the harmonic is greater than gain at the longer wavelength:

$$R_n > n\sqrt{n}\left(1 - \frac{n|F_n|^2}{|F_1|^2}\right). \quad (17)$$

A NUMERICAL EXAMPLE

The evolution of the coupled two-beam FEL system is demonstrated by numerically solving the working equations (7..12). Two (noiseless) electron beams were used with $n = 3$ and of current ratio $R_3 = 5$, co-propagating in

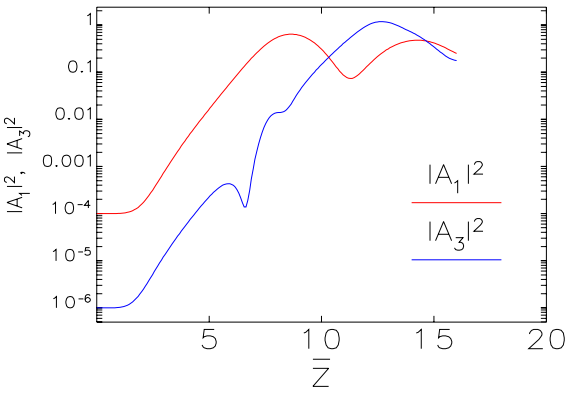

Figure 1: The scaled radiation intensities $|A_1|^2$ and $|A_3|^2$ as a function of scaled distance $\bar{z}$ through the FEL interaction region for $n = 3$, $R_3 = 5$, $\sigma_p = 0.1$ and $\sigma_\wp = 0.4$.

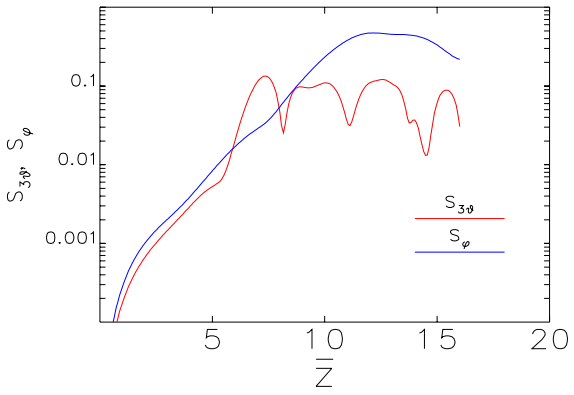

Figure 2: The source terms S_φ and $S_{3\vartheta}$ as a function of scaled distance through the FEL interaction region for $n = 3$, $R_3 = 5$, $\sigma_p = 0.1$ and $\sigma_\wp = 0.4$.

a wiggler of parameter $a_w = 2$. Both beams were given a Gaussian energy spread of scaled width in p of $\sigma_p = 0.1$, and in $\wp$ of $\sigma_\wp = 0.4$. The seed field at the longer wavelength is modelled by defining its initial scaled intensity at the beginning of the FEL interaction $|A_1(\bar{z} = 0)|^2$ to be two orders of magnitude greater than that of the harmonic. In figure (1) the scaled intensities $|A_1|^2$ and $|A_3|^2$ are plotted as a function of scaled distance, $\bar{z}$, through the FEL interaction region. The feature of interest from figure (1) is the rapid growth in the harmonic intensity $|A_3|^2$ by approximately two orders of magnitude in the interval $6.5 \lesssim \bar{z} \lesssim 8$. This period of more rapid growth (approximately $n = 3$ times the fundamental growth rate) is driven by the strong harmonic component of the bunching $|b_3|$ of the lower energy beam [9, 10, 11]. This harmonic bunching is caused, not by electrons bunching at the harmonic wavelength, but by the significant harmonic component of the strong, non-linear, bunching at the fundamental $|b_1|$ as the lower energy FEL interaction approaches its saturation at $\bar{z} \approx 8.5$. The harmonic bunching and subsequent harmonic emission of A_3 from the lower energy beam, can be expected to retain the coherence properties of the initial radiation seed field at the fundamental. This process should therefore act as a harmonic seed field with good coherence properties. Following this harmonic seeding by the lower energy electron beam it is seen that the harmonic intensity continues exponential growth by approximately another two orders of magnitude until saturation at $\bar{z} \approx 12.5$.

Further insight is gained by plotting individually the moduli of the source terms S_φ and $S_{3\vartheta}$ of the harmonic field evolution equation (12), as shown in figure (2). The contribution S_φ is due to the higher energy electron beam, and $S_{3\vartheta}$, the lower energy beam. The figure clearly shows the strong seeding phase between $6.5 \lesssim \bar{z} \lesssim 8$, as discussed above, where the harmonic field is strongly driven by the lower energy beam ($S_{3\vartheta} > S_\varphi$). This is followed by the amplification phase where the harmonic field is driven by the higher energy beam ($S_\varphi > S_{3\vartheta}$).

The above results also suggest that a hybrid HGHG scheme may be possible if the interaction is stopped at $\bar{z} \approx 8.0$ and the mildly bunched higher energy electron beam injected into another wiggler which would allow strong emission at one of its higher harmonics.

The equations have also been numerically solved, in the cold beam limit ($\sigma_p = \sigma_\wp = 0$) to demonstrate the same seeding mechanism for a fifth harmonic interaction [7]. A similar interaction to that for the above simulation was observed, except the intermediate third harmonic field had no resonant coupling with the higher energy beam. This results in the fifth harmonic having both a greater linear growth rate and saturation intensity than the third harmonic.

ENERGY SPREAD EFFECTS

An initial study of the effects of energy spread in a higher energy beam with $n = 3$, was conducted by solving the working equations for a range of values of initial Gaussian spread $\sigma_\wp$. The same lower energy beam as above ($R_3 = 5$ and $\sigma_p = 0.1$), wiggler parameter ($a_w = 2$) and initial field intensities ($|A_1(\bar{z} = 0)|^2 = 10^{-4}$ and $|A_3(\bar{z} = 0)|^2 = 10^{-6}$) were assumed. For comparative purposes, FEL evolution of the higher energy beam in the absence of the lower energy beam was also modelled by conducting a set of simulations with a large electron beam current ratio of $R_3 = 10^3$ and a reduced initial longer wavelength scaled intensity of $|A_1(\bar{z} = 0)|^2 = 10^{-16}$. With these parameters there is no effective FEL evolution of the lower energy beam and the higher energy harmonic interaction evolves as though the lower energy beam were absent.

Figure (3) plots the scaled harmonic saturation intensity, $|A_3|^2_{\text{sat}}$, for a range of Gaussian energy spread parameter $\sigma_\wp$ and figure (4) plots the corresponding scaled harmonic field sataration lengths $\bar{z}_{sat}$.

From these figures one distinguishing difference be-

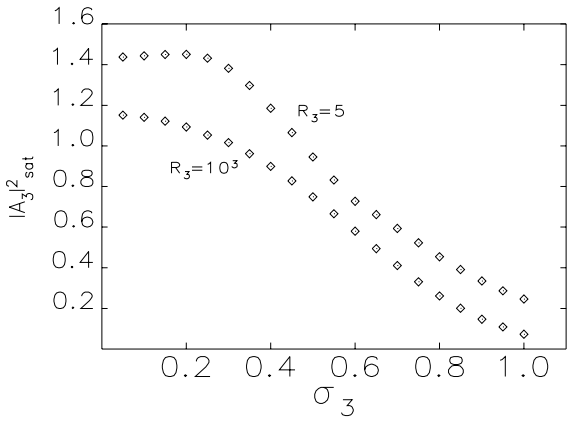

Figure 3: Saturation intensity $|A_3|^2_{\rm sat}$ as a function of energy spread $\sigma_\wp$ (σ_3 in plot) of the higher energy beam.

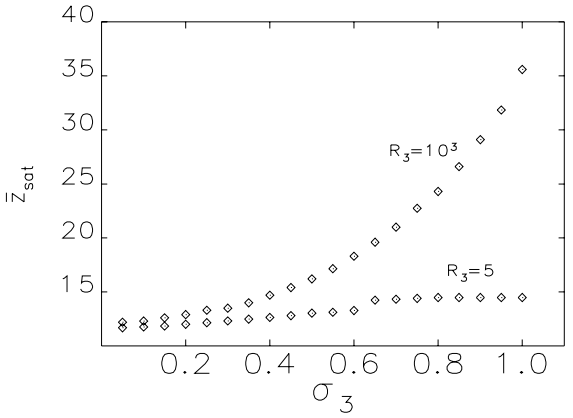

Figure 4: Scaled saturation length of harmonic intensity $\bar{z}_{sat}$ as a function of energy spread $\sigma_\wp$ (σ_3 in plot) of the higher energy beam.

tween the coupled two-beam interaction ($R_3 = 5$) and the higher energy beam only interaction ($R_3 = 10^3$) is apparent: for the coupled two-beam interaction case, both the harmonic saturation intensity$|A_3|^2_{\rm sat}$ and its sataration length are less sensative to the energy spread $\sigma_\wp$ of the higher energy beam. This encouraging preliminary result will be extended to a wider range of energy spread parameter space of the two beams in future work.

CONCLUSIONS

A simple 1-D model of a two-beam FEL has been presented. This concept introduces potentially interesting coupled FEL interactions some of which may have beneficial properties over single beam interactions. Indeed, one need not be limited to only two beams and can envisage more complex systems with more than two harmonically coupled beams - a multi-beam FEL equivalent of the cascaded HGHG scheme [4]. Such multi-beam FELs may offer the prospect of a reduction in overall length when compared with an equivalent HGHG scheme. One can also envisage possible hybrid schemes involving combinations of multi-beam FELs with HGHG. Clearly, these suggestions are speculative at this stage and will require further research.

As an illustration of the type of interactions possible, numerical simulations of the coupled two-beam FEL interaction demonstrated that a seeded lower energy beam interaction may evolve to effectively seed that of the higher energy. The conjecture was made that the improved coherence properties of the seeded interaction at the longer wavelength would be inherited by the higher beam energy, shorter wavelength, interaction. Such seeding may be of interest to proposals for FELs operating at sub-VUV wavelengths where no 'conventional' seed sources are yet available. Further analysis is required to verify any predicted improvement in the coherence properties. Any analysis will need to model a minimum of two independent variables (e.g. (z,t) or (z,ω)) and include the effects of the relative slippage between the lower and higher energy electron pulses. This relative slippage must be less than that between the lower energy beam and the radiation field.

An initial study of the effects of an electron beam energy spread on the two-beam FEL system has shown no debilitating effects. Indeed, the results encourage a more complete investigation of parameter space.

No assessment has yet been made of the importance of other factors that will effect such two-beam interactions, e.g. accelerator physics issues such as electron pulse synchronism, beam focussing and emittance, the relative energy detuning between the electron beams and transverse modes. Some of these issues will undoubtedly require the development of new simulation models.

REFERENCES

[1] R. Bonifacio, C. Pelligrini and L.M. Narducci, Opt. Commun. **50**, 373 (1984)

[2] E.L. Saldin, E. A. Schneidmiller, and M.V. Yurkov, TESLA-FEL Report No. 97-02, 1997, DESY, Hamburg, Germany.

[3] R. Bonifacio, L. De Salvo Souza, P. Pierini and E.T. Scharlemann, Nucl. Instrum. and Meth. A **296**, 787 (1990)

[4] L.-H. Yu et al, Science **289**, 932 (2000)

[5] J. Feldhaus, E.L. Saldin, J.R. Schneider, E.A. Schneidmiller and M.V. Yurkov, Opt. Commun. **140**, 341 (1997)

[6] B. Faatz, J. Feldhaus, J. Krzywinski, E.L. Saldin, E.A. Schneidmiller, and M.V. Yurkov, Nucl. Instrum. and Meth. A **429**, 424 (1999)

[7] B.W.J. McNeil, M.W. Poole and G.R.M. Robb, Phys. Rev. E, (in press)

[8] J.D. Lawson, *The Physics of Charged-Particle Beams*, (Oxford Science Publications, New York, 1988.)

[9] R. Bonifacio, L. De Salvo Souza and P. Pierini Nucl. Instrum. and Meth. A **296**, 627 (1990)

[10] H.P. Freund, S.G. Biedron, and S.V. Milton, IEEE J. Quantum Electron. **QE-36**, 275 (2000)

[11] Z. Huang and K.-J. Kim, Phys. Rev. E **62**, 7295 (2000)

LOW EMITTANCE GUN PROJECT BASED ON FIELD EMISSION

R. Ganter, J.-Y. Raguin, A. Candel, M. Dehler, J. Gobrecht, C. Gough, G. Ingold, S.C. Leemann, K.Li, M. Paraliev, M. Pedrozzi, L. Rivkin, H. Sehr, V. Schlott, A. Streun, A. Wrulich, S. Zelenika

Paul Scherrer Institut – Villigen CH 5232 - Switzerland

Abstract

The design of an electron gun capable of producing beam emittance one order of magnitude lower than current technology would reduce considerably the cost and size of a free electron laser radiating at 0.1nm. Field emitter arrays (FEAs) including a gate and a focusing layer are an attractive technology for such high brightness sources. Electrons are extracted from micrometric tips thanks to voltage pulses applied between the gate and the tips. The focusing layer should then reduce the initial divergence of each emitted beamlet. This FEA will be inserted in a high-gradient diode configuration coupled with a radiofrequency (RF) structure. In the diode part the high electric field (several hundreds of MV/m) will limit the degradation of emittance due to space-charge effects. This first acceleration will be obtained with high voltage pulses (about one megavolt in a few hundreds of nanoseconds) synchronized with the low voltage pulses applied to the FEA (~ 200 – 300V in less than one nanosecond at a frequency lower than a kilohertz). This diode part will then be followed by an RF accelerating structure in order to bring the electrons to relativistic energies.

MOTIVATION

A Free Electron Laser (FEL), driven by a single pass linear accelerator (linac), is today the most promising mechanism able to produce 0.1 nm wavelength, with pulses shorter than 100 fs. In FELs, the electron beam emittance plays a major role in the laser saturation process. For an ideal electron-photon matching, the electron beam normalized emittance must satisfy the diffraction limit [1]:

$$\varepsilon < \frac{\beta}{L_G}\frac{\lambda\gamma}{4\pi} \qquad (1)$$

Where λ is the radiated wave length, γ the relativistic factor, β the beta function, L_G the gain length and ε the normalized emittance. This relation shows that the energy of the electron beam can be decreased, together with the linac length, provided that the emittance is sufficiently small. The electron source, with its initial emittance and current, becomes thus the first master piece of the driving accelerator.

Emittances on the order of 10^{-6}m.rad, and sufficient charge to drive an FEL, are presently achieved using RF photo-cathode guns. The linac energy for such a beam is in the 15-20 GeV range, for a peak current at the undulator between 2 and 5 kA. A substantial improvement (small linac, short gain length and relaxed peak current) would be achieved with emittances below 10^{-7}m.rad. Fig. 1 presents the FEL gain length versus the undulator period for different peak magnetic fields and normalized emittances of 1.2 mm.mrad and 0.1 mm.mrad. In these computations, it was assumed that the relative energy spread was 1.10^{-4}. Fig. 2 shows the required linac energy vs. the undulator period for three different undulator peak magnetic fields, the linac energy being determined by the resonance condition:

$$\lambda = \frac{\lambda_u}{2\gamma^2}\left(1+\frac{K^2}{2}\right) \qquad (2)$$

where λ_u is the undulator period, K=0.934 B[T] λ_u [cm] is the undulator deflecting parameter and B the peak undulator magnetic field.

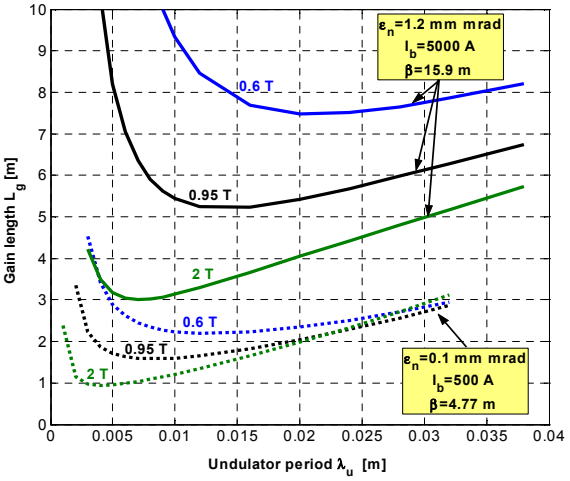

Figure 1: FEL gain length vs. undulator period for several undulator peak magnetic fields and two different electron beam emittances.

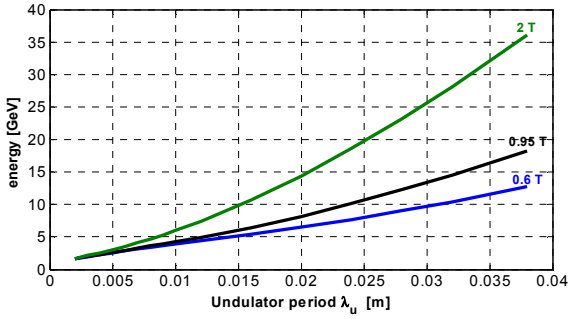

Figure 2: Beam energy vs. undulator period for several undulator peak magnetic fields.

The FEL parameters considered for these comparisons have been fixed accordingly.

As shown in Fig. 1 the required beam current and the FEL gain length can be considerably reduced by improving the electron beam properties (see also [2]). The size of the linac (Fig. 2) can be decreased as well, allowing an appreciable cost reduction of the accelerator facility.

Ultimately, the normalized transverse emittance is limited by its initial value at the cathode which can be expressed as follows:

$$\varepsilon = \gamma \frac{r_c}{2} \sqrt{\frac{E_{r,kin}}{m_0 c^2}} \qquad (3)$$

where r_c is the cathode radius and $E_{r,kin}$ the mean transverse kinetic energy just after emission. To lower the emittance one can reduce the size of the electron source (r_c) and/or the mean transverse energy of emitted electrons (roughly the initial divergence). In this project we are aiming at reducing both parameters thanks to field emission based cathodes.

CONCEPT

Most of the accelerators use either photocathodes or thermionic cathodes. An alternative technology for generating electrons is field emitters based cathode. Applications of field emitters for X-ray tubes and microwave tubes have already been explored in the past [3,4]. More recent studies report on the use of photo assisted field emission from needles for table top free electron laser applications [5]. At Paul Scherrer Institut we are studying the possibility of using field emitter tips (field emitter arrays or individual tips) for high quality beams in accelerator applications. Although the idea has already been proposed [6-8], recent progress in vacuum microelectronics and nanotechnology makes field emitters an attractive solution for new electron sources. The best advantages of field emitters on other types of cathode are probably the high achievable current density of the emission (up to 10^8 A/cm^2) and the low temperature of the emitted electrons. Field emission is a tunneling effect where electrons are emitted with energies close to the Fermi level. They follow then mainly the electric field lines [7].

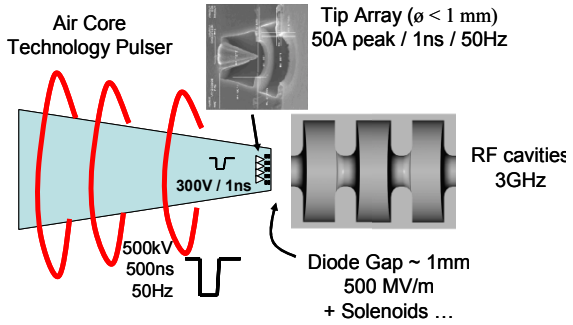

Figure 2: Schematic of the gun concept which combines diode acceleration with RF acceleration. Electrons are extracted by modulation of the gate layer and first acceleration is given by high voltage pulses (SEM picture of tip from [9])

In field emitter arrays, emission arises from tips thanks to a close spaced gate layer (see Fig. 2 and 3). In order to shape electron trajectories, FEAs can integrate a second grid layer which focus the individual beamlets produced by each tip (see Fig. 2). The tips height is about one micrometer as well as the distance apex - focusing layer. Typical emission area is about a few nanometers square per tip [10]. In such field emitter cathodes the emission bunching is achieved by pulsing the tip to gate voltage. After extracting and focusing the electrons, a high gradient acceleration is required to limit space charge effects. The FEA will be inserted in the cathode side of a diode configuration. The anode would then be the iris of an RF cavity (see Fig. 2). This combination of diode and RF acceleration is inspired from the DC photogun built at TU Eindhoven [11]. In the diode gap, we hope to reach very high values of electric field gradient. Arc probability will be considerably reduced by applying short voltage pulses (< 500 ns) between the cathode and the anode at low repetition rate. The unwanted field emitted current or dark current will be minimized thanks to various conditioning methods, electrodes geometry optimization and careful assembling. Emittance compensation schemes will also be considered.

Many problems which could affect the achievable beam emittance are not solved yet. It is the aim of this project to evaluate the beam quality that could be obtained from field emitters.

PROJECT STATUS

In order to investigate the possibility of using field emitter tips to make an improved electron gun, several activities are progressing in parallel.

Cathode Evaluation

Preliminary studies of field emitter arrays (or single tip) properties have been performed (see companion paper [12]) on commercially available field emitters. First tests concerned the maximum emitted peak current. It has been

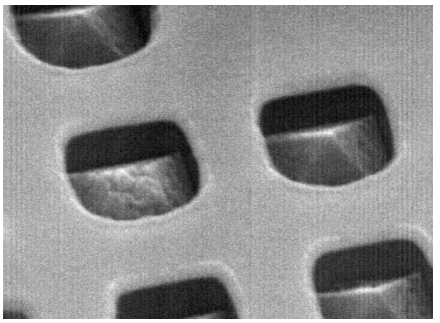

Figure 3: Scanning electron microscope picture of gated diamond tips from XDI Inc. [13].

found that emission during short pulses (~ 100 ns) at low repetition rate (few Hz) prevent tips from overheating and thus enable larger emission intensities and better stability than in DC regime. In this pulsed regime we finally reached the saturation of the FEAs at about 50 mA due to the highly resistive silicon wafer. This high silicon resistivity is required in DC operation but not for our application which use short emission pulses at low frequency. Another way to reach higher current is to increase the emission uniformity. During the fabrication of FEAs, geometric differences at the nanometric scale between tips lead to bad emission uniformity at initial turn on. Fig. 3 illustrates such differences between two neighbouring tips. A specific test stand, called SAFEM (scanning anode field emission microscope [14]) is under construction for studying non uniformities of the emission.

We also investigated characteristics from single tip in ZrC. We showed that such single tip in ZrC is capable of emitting several milliamperes during microsecond long pulses. This corresponds already to a quite high brightness between 10^{12} and 10^{13} A.(m.rad)$^{-2}$ if we take into account an emitting area of 200 nm in diameter and an initial divergence angle of 20 degrees [8]. We hope to reach even higher peak current with shorter pulses.

These preliminary tests on commercially available field emitters enable us to better understand our needs in terms of cathode development for our particular application. In parallel to collaborations with companies specialized in field emitter fabrication, we also initiated the development of field emitter arrays at the micro and nanotechnology laboratory of PSI.

High Gradient Acceleration in the Diode Gap

As described above, the electrons are extracted from the tips by a grid layer and focalized by a second grid layer one micrometer above the tip apexes. After this focusing layer, electrons enter a drift region until the iris of the radiofrequency cavity. In this gap the electric gradient must be as high as possible in order to limit space charge effects. Space charge forces have a non linear effect on beam spreading which leads to emittance growth.

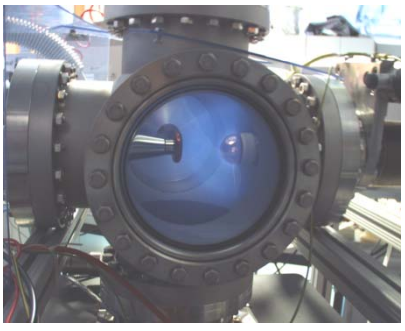

Figure 4: Picture of the high gradient test stand during helium glow discharge treatment used for cleaning / polishing the electrodes.

However, when a high electric field is applied between two massive metallic pieces, unwanted field emission is generated from all the surface defects of the cathode support [15]. This dark current must be as small as possible in order to limit his influence on the useful beam and the risks of arcs. Since dark current is also field emitted current, it depends on local field enhancement factor (roughness, dust, …) and surface work function (e.g. adsorbed contaminants). As for tips in FEAs (see companion paper [12]) it is the overheating of the dark current emitter which eventually leads to the generation of an arc. In order to prevent local dark current emitters from generating arcs we plan to apply short voltage pulses (a few hundred of nanoseconds) at low repetition rate. For this purpose, a first pulser prototype delivering pulses of 500 kV amplitude and 500ns length is currently under construction.

To limit dark current intensity (even if it does not generate arcs) very good polishing and cleaning methods for the electrodes as well as clean room conditions during assembling are required. In addition, we are also looking for some in-situ conditioning method once electrodes are sealed under vacuum. For this reason, a specific test stand has been developed in order to test the field strength between two electrodes of similar size to what is foreseen for the final gun (see Fig 4). Different in situ conditioning techniques have been investigated in order to improve the field strength. Fig. 5 represents the dark current measured between two massive copper electrodes of several square centimetres. After glow discharge treatment of the electrodes, the required electric field for 1 nA of dark current went from about 50 MV/m to 75 MV/m. Then we applied a series of 100 ns voltage pulses between electrodes with a small gap in order to draw large dark current pulses. These large current pulses tend to smooth and blunt the dark current emitters. This is a similar method to the one used for the conditioning of tips in field emitter arrays [16]. Other materials, as well as polishing and cleaning processes are under investigation in this test

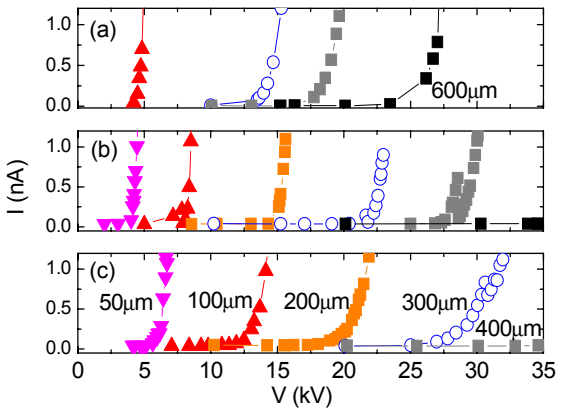

Figure 5: Dark current versus applied DC voltage. The numbers 50 to 600 indicate the electrode gaps in µm. (a) Initial situation at 10^{-9} mbar, (b) after glow discharge treatment of electrodes for several hours and (c) after pulse conditioning (100ns at 50 Hz).

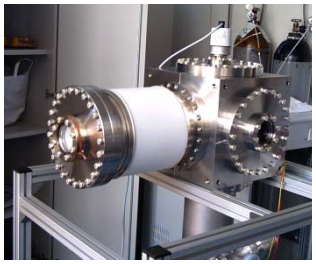

Figure 6: 100kV test stand for evaluation of beam emittance produced by field emitters.

stand in order to reduce dark current in the diode gap of the gun.

Space Charge Compensation

In addition to high-gradient acceleration, magnetic compensation schemes are also considered for emittance preservation. A 100 kV DC gun test stand (see Fig. 6) integrating several beam diagnostic tools is currently under development. This should provide preliminary measurements of beam emittance at 100 keV. This gun prototype will also be used to test various magnetic compensation schemes with solenoids. Fig 6 shows the test stand (not yet completed). This test stand will also enable comparisons with simulation results on beam dynamics.

Simulations

MAFIA simulations have been performed in order to improve the anode – cathode geometry in the 100 kV gun test stand [17]. The purpose of these simulations was to minimize emittance increase at gun exit. Further simulations including solenoid effects have been done and will be compared to measurements done in the gun test stand.

In order to simulate the granularity of the beam emitted by a matrix of thousands of tips, a full 3 dimensional Maxwell solver using particle in cell method has been developed [18]. Comparisons of this 3D PIC solver with Mafia simulation gave good agreement [17].

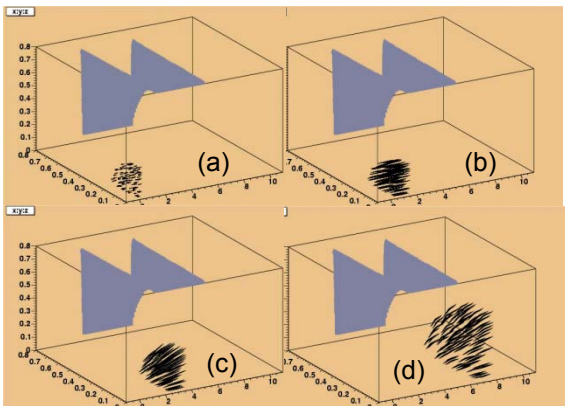

Figure 7: Time evolution of particles emitted by a matrix of individual emitters with 80 % failures. Position in the A – K gap (a), (b) and after the anode iris (c), (d).

For example, this 3D PIC code enables simulation of non uniformity of the emission from a field emitter array, when only a fraction of the total number of tips does contribute to the emission. Fig 7 illustrates the evolution of field emitted particles when only 20 % of the FEA tips are emitting (see [18] for details). This preliminary simulation shows a 20 % increases in the normalized transverse emittance when going from a uniform distribution of beamlets to this much worse case where 80 % of the tips are not emitting.

CONCLUSION

In order to achieve high quality electron beam for a free electron laser application, a research project on a field emission based gun has been initiated. This gun would combine diode and RF acceleration and the electrons would be produced by field emission cathodes. Test stands development, beam dynamic simulations as well as preliminary studies of cathode properties are currently in progress. In parallel to field emission cathode evaluation, tests of integrating such cathodes in high electric gradients are under way.

References

[1] L. H. Yu et al., NIM A 272**,** 436-441 (1988).
[2] M. Pedrozzi et al., Proc. LINAC, Luebeck - Germany, 2004.
[3] F. Charbonnier, Appl. Surf. Sci. 94/95**,** 26-43 (1996).
[4] D. R. Whaley et al., IEEE Trans. Plasma Sci. 30**,** 998-1008 (2002).
[5] C. H. Garcia et al., NIM A 483**,** 273-276 (2002).
[6] G. Bekefi et al., J. Appl. Phys. 62**,** 1564-1567 (1987).
[7] Y. Liu et al., J. Vac. Sci. Technol. B 14 (1996).
[8] K. L. Jensen et al., Appl. Surf. Sci. 111**,** 204-212 (1997).
[9] L. Dvorson et al., J. Vac. Sci. Technol. B 20**,** 53-59 (2002).
[10] W. Zhu, *Vacuum Microelectronics* (John Wiley & Sons, 2001).
[11] F. Kiewiet, Thesis, TU Eindhoven, 2003.
[12] K. Li et al., these proceedings.
[13] K. D. Jamison et al., J. Vac. Sci. Technol. B 21 (2003).
[14] L. Nilsson et al., Applied Physics Letters 76**,** 2071-2073 (2000).
[15] M. E. Cuneo, IEEE Trans. Diel. Electr. Insul. 6 (1999).
[16] P. R. Schwoebel et al., J. Vac. Sci. Technol. B 19**,** 582-584 (2001).
[17] A. Candel et al., Proc. EPAC, Luzern - Switzerland, 2004
[18] A. Candel et al., Proc. ICAP, St-Petersburg, Russia, 2004

FIELD EMITTER ARRAYS FOR A FREE ELECTRON LASER APPLICATION

K. Li, R. Ganter, J.-Y. Raguin, M. Dehler, J. Gobrecht, L. Rivkin, A. Wrulich

Paul Scherrer Institut – Villigen CH 5232 - Switzerland

Abstract

The development of a new electron gun with the lowest possible emittance would help reduce the total length and cost of a free electron laser. Recent progress in vacuum microelectronics makes field emitter arrays (FEAs) an attractive technology to explore for high brightness electron sources. Indeed, several thousands of microscopic tips can be deposited on a one millimeter diameter area. Electrons are then extracted by a first grid layer close to the tip apex and focused by a second grid layer one micrometer above the tip apex. In order to be a good candidate for a low emittance gun, field emission cathodes must provide at least the peak current, stability and homogeneity of current state of the art electron sources. Smaller initial divergence should then be achieved by the focusing grid and the intrinsic properties of the field emission process.

MOTIVATIONS

In a free electron laser undulator, the required normalized transverse electron beam emittance ε_n must satisfy the following condition:

$$4\pi\varepsilon_n < \lambda\gamma \qquad (1)$$

where λ is the radiated wavelength and γ the relativistic factor. Small normalized beam emittance would considerably reduce the required beam energy and thus the cost and size of the accelerator facility. On the other hand a smaller emittance would also reduce the required minimum peak current to efficiently drive a free electron laser. Ultimately the emittance is limited by its initial value at the cathode which can be expressed as follows:

$$\varepsilon_n = \gamma \frac{r_c}{2} \sqrt{\frac{E_{r,kin}}{m_0 c^2}} \qquad (2)$$

where r_c is the cathode radius and $E_{r,kin}$ the mean transverse kinetic energy just after emission. To lower the emittance one can reduce the size of the electron source (r_c) and/or the mean transverse energy of emitted electrons (roughly the initial divergence).

FIELD EMISSION CATHODES

Current accelerator guns use photocathodes or thermionic cathodes [1]. In both cases, the mean transverse energy of the extracted electrons is several hundred meV either due to the difference between photon energy and cathode work function or due to the cathode temperature. This already limits the minimum achievable initial transverse kinetic energy of the produced electron beam. In addition, the diameter of these cathodes is usually larger than a few millimeters. One alternative process is field emission where electrons are emitted with energies around the Fermi level and the mean transverse energy is mainly determined by the geometry of the electric field lines [2]. The achievable current density by field emission is also much higher than with other type of cathodes so that the emitting area could be smaller. Field emission cathodes are usually made with tips, either single tip or array of tips with an integrated gate layer (ie. field emitter arrays FEAs). These FEAs consist of thousands of conductive tips in the micrometer size range separated from a conductive gate layer by a one micrometer thick dielectric layer (see Fig. 3 and 4). By applying a voltage between the tips and the gate layer (V_{ge}) electrons are emitted from the tip's apexes. In order to shape electron trajectories, FEAs can integrate two grid layers. The first grid is used for extracting the electrons while the second grid provides focusing of the electrons.

Field Emitters Characteristics

To be a good candidate for free electron laser application, field emitters must achieve higher peak currents than in usual applications like flat panel displays or scanning electron microscopes. In addition we must be able to focus the field emitted beam thanks to a focusing layer deposited a few micrometers above the tips. Finally the emission must have a good uniformity and stability in time.

In a first approach we focused our work on the maximum achievable emitted current. Typically a

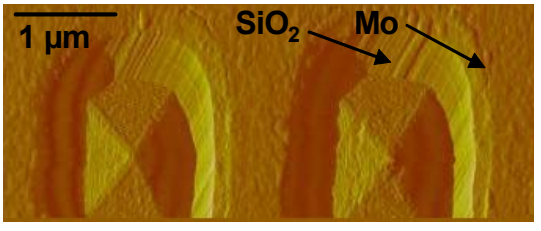

Figure 1: Top view (Atomic force microscope) of two pyramidal diamond tips (height 1 µm) from XDI Inc. Tips are separated by SiO_2 dielectric material (1 µm thick). SiO_2 is covered by a conductive Mo layer: the gate layer

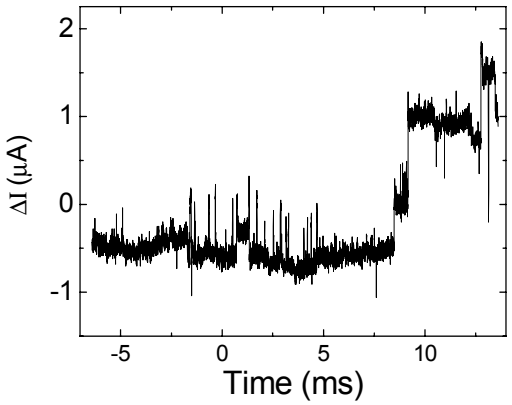

Figure 2: Fluctuations of the field emitted current versus time due to thermally induced surface changes. The DC component (200 μA) of the field emitted current has been removed.

standard gated molybdenum tip is capable of emitting a few microamperes in DC operation [3]. Above this level, the risk of overheating the tip and generate a destructive arc increases. One way to obtain higher current is to use a matrix with thousands of tips (FEAs).

For these preliminary tests, we used cathodes available on the market. The SEM pictures in Fig. 3 and 4 represent diamond tips from the company XDI Inc [4] and molybdenum tips from SRI Inc [5] respectively. XDI's cathode has around 3,000 tips distributed on a 170 μm diameter disc area. These diamond tips have a pyramidal shape due to the molding technique used for their elaboration (Fig. 1). The tip material is a mixing of diamond and graphite which is electrically conductive. Tips are surrounded by a dielectric material (SiO_2) which isolated them from the molybdenum gate layer. The typical height and base size of each tip as well as the gate aperture diameter is about one micrometer.

The FEAs from SRI support around 50,000 molybdenum tips on a 1 mm diameter disc area. The dimensions of these conical tips are close to XDI's pyramidal tips but the growing method is different. SRI Inc. has developed the so called Spindt method [3] to grow molybdenum tips in a gated structure with nanometer tolerances. In order to test the emission of these gated structures we used a triode configuration. Field emitted current is measured on a collector positively biased in respect to the gate and tip voltages. If too much electrons are directly collected on the gate, the risk of overheating the gate is too high.

In addition to gated structure, we also investigated the emission from single tips in Zr covered by a ZrC layer from the company APTech Inc. [6]. These tips are inserted in a Vogel mounting without any extracting gate layer (Fig. 6). We tested these single tips in a simple diode configuration.

Field Emission Current Instabilities

As already mentioned, the limiting factor for high current emission in DC operation is the excessive heating of the tip and the surrounding materials (gate, anode, etc.). This leads to a series of thermally induced surface changes like desorption of contaminants or surface migration. When ionized, these desorbed contaminants can also back bombard the tips. Eventually, local pressure rise can initiate destructive arcs.

These well known environmental problems are also responsible for current emission fluctuations by changing either the surface work function or the tip geometry [5]. Fig. 2 represents such typical current fluctuations observed on the emission of one XDI field emitter array. Only the variations of the current are represented, the DC component (~ 200 μA) of the signal has been removed. The amplitude of these fluctuations corresponds to a few

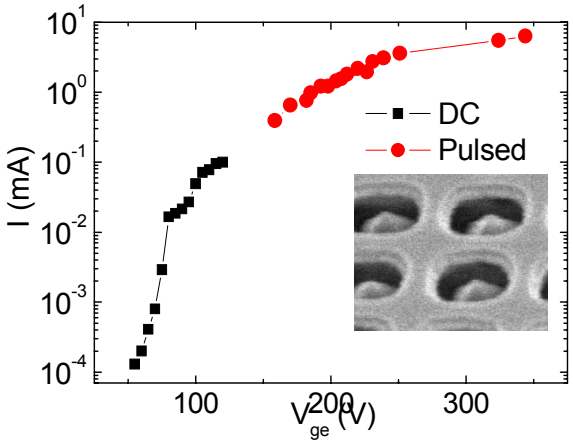

Figure 3: Current voltage characteristic in DC and pulsed regime for a FEA from the company XDI Inc (~3,000 diamond tips, ø = 170 μm). Insert: SEM picture of diamond tips.

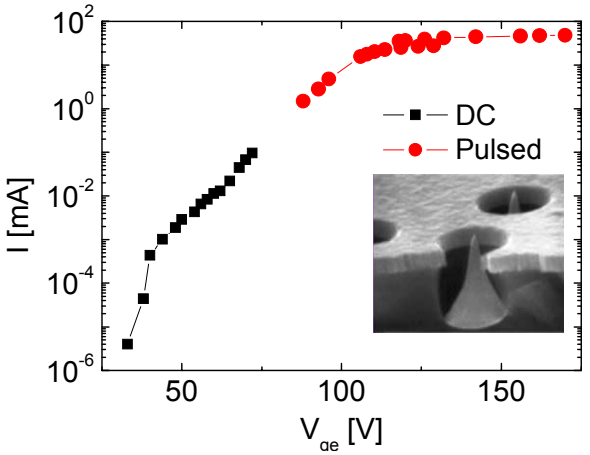

Figure 4: Current voltage characteristic in DC and pulsed regime for a FEA from the company SRI Inc (50,000 Mo Tips, ø = 1000 μm). Insert: SEM picture of conical Mo tips from SRI website [5].

percents of the total emitted current. The "steplike" behaviour of the fluctuations corresponds to instantaneous changes in the surface state due to successive adsorption, desorption and migration processes [8].

Because of the strong dependence of field emitted current on the geometry of the tip (field enhancement factor β) and his surface composition (work function Φ), even small surface changes lead to strong variations in the current intensity. This can be illustrated by Fowler-Nordheim's equation which describes the dependence of the field emitted current density on these parameters:

$$J = \frac{A}{\Phi}.(\beta.V)^2.\exp\left(\frac{-B.\Phi^{3/2}}{\beta.V}\right)$$

where A, B are constant values, V represents the applied voltage between electrodes, Φ is the work function in eV and β is the enhancement factor of the electric field due to geometrical effect.

One way to increase the total emitted current without overheating is to use a large number of tips. However the strong dependence of the field emitted current on tip geometry and surface composition makes the uniformity between tips very important. After fabrication, it is usual to observe that only a few percent of the total number of tips contributes significantly to the total emission [9]. Field emission will occur preferably from the sharpest tips. Variation of the geometry of the tip apexes at a nanometric scale can lead to non uniformity of emission between tips. Fig. 1 represents atomic force microscope measurements of two neighbouring tips from an XDI array. The nanometric roughness of the tip surface can be seen on Fig. 1. These nanoprotrusions contribute to the overall field enhancement factor and can introduce non uniformity that are not easily controlled during fabrication. Several conditioning processes have been developed in order to improve the uniformity of the emission and promising results have been achieved by scientist from SRI Inc. [7]. In fact, they found that self-heating of tips by drawing large current during short pulses, tends to smoothen and clean tips without destruction. The uniformity of electron emission could be improved by this method. This is in favour of a free electron laser application which does not require DC but only pulsed emission.

Pulse Mode of Operation

By operating the FEA with short voltage pulses at low frequency it is possible to considerably reduce the heat brought to the tips and therefore to eliminate most of the thermally induced problems. Consequently the emitted current can be increased with less risk of deterioration.

Fig. 3 represents the emitted current versus the applied tip to gate voltage for an array of about 3,000 diamond tips distributed on a 200 micrometers diameter disc area. The maximum current measured in continuous mode was about 800 µA but emission was subject to fluctuations and monotonic decay with time was observed as in [7]. However in the 50 Hz pulsed regime, with 100 ns voltage pulses it was possible to reach up to 6 mA peak current. In this mode of operation, emission was very stable and no decrease of the emitted current was observed after one day of operation. The maximum current performance was limited by the internal resistance of the field emitter array (~ 25 kΩ). This internal resistance originates from the silicon wafer on which tips are deposited. In DC applications it is preferable to have a highly resistive silicon wafer in order to protect tips from brutal current rises. In a pulsed mode, a smaller resistivity could be tolerated. This internal resistance also limits the minimum pulse length that can be applied between gate and tips by introducing a large charging time constant. Fig. 4 represents a similar current voltage characteristic but for a

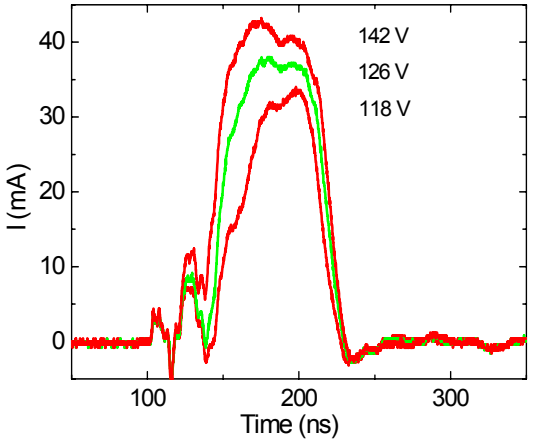

Figure 5: Current pulses emitted by a FEA with 50,000 Mo tips from the company SRI Inc. when applying square voltage pulses with amplitude of 118, 126 and 142V.

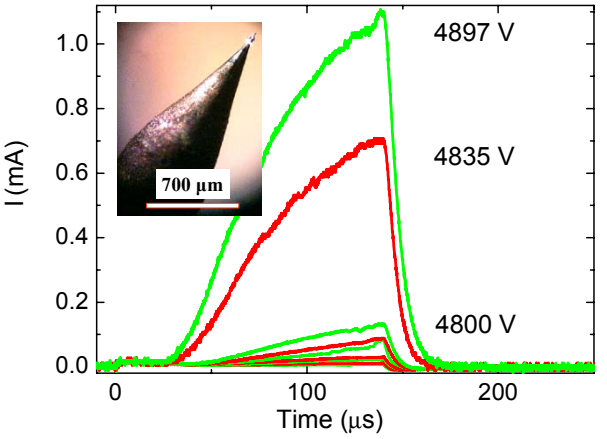

Figure 6: Current pulses emitted by a single ZrC tip from the company APTech Inc. for different square voltage amplitudes of 100 microseconds.

standard FEA from the company SRI Inc. This FEA consists of 50,000 Mo tips grown by the so called Spindt method [3] on a one millimeter diameter disc area. Again, the sensitivity to environmental conditions was much less important in the pulsed regime than in DC. The maximum current performance was limited by the silicon wafer resistance to values around 50 mA. Fig. 5 shows typical 100 ns current pulses collected from a 50,000 Mo tips FEA.

We have also tested the maximum peak current that can be emitted by a single tip in zirconium carbide (ZrC) (see Fig. 6). Since this tip does not have any gate layer a copper anode has been placed five millimeter away from the tip and large voltage pulses (kilovolts) were applied. To protect the tip from too high current values, a 10 kΩ resistor was placed in series with the tip. The effect of the resistor is the slow charging ramp on the current pulses seen in Fig. 6. More than 3 mA peak current have been measured out of such a single tip. Only the apex of the ZrC tip emits and the tip apex radius is less than one micrometer (specifications give values between 20 and 100 nm). If we assumed an emission area of one square micrometer, the corresponding current densities is as high as 10^5 A/cm^2.

CONCLUSION

Preliminary tests on commercial field emitter samples showed that higher peak current and more stable emission can be achieved when using short square voltage pulses at low frequency. For a free electron laser application such peak current values are still too small [10], but with the help of even shorter pulses and smaller internal FEA resistance we hope to reach the required current.

References

[1] Fred Kiewiet, Thesis, TU Eindhoven, 2003
[2] Y. Liu, Y. Y. Lau, J. Vac. Sci. Technol. B 14(3), 1996
[3] W. Zhu, *Vacuum Micro-electronics*, John Wiley & Sons, New York (2001)
[4] K. D. Jamison, B. G. Zollars, D.E. Patterson, R. Schueller, H. Windischmann, G. A. Mulhollan and A. Kloba, J. Vac. Sci. Technol. B 21(4), 2003
[5] http://www.sri.com/psd/microsys/
[6] http://www.a-p-tech.com/
[7] P.R. Schwoebel, C.A. Spindt, C.E. Holland and J.A. Panitz, J. Vac. Sci. Technol. B 19(3), 2001
[8] R.T. Olson, G.R. Condon, J.A. Panitz, P.R. Schwoebel, J. Appl. Phys., Vol. 87 ,4 pp. 2031 (2000).
[9] P.R. Schwoebel, C.A. Spindt, C.E. Holland and J.A. Panitz, J. Vac. Sci. Technol. B 19(2), 2001
[10] R. Ganter et al., THPOS01, in these proceedings.

UNDULATORS FOR THE BESSY SOFT-X-RAY FEL

J. Bahrdt[#], W. Frentrup, A. Gaupp, B. Kuske, A. Meseck, M. Scheer, BESSY, Berlin, Germany

Abstract

BESSY plans to build a linac based Soft-X-ray FEL facility. Three FEL lines will cover the energy range between 24eV and 1000 eV. The FELs are operated in a high gain harmonic generation scheme providing short pulses and stable operation. This paper describes the undulator systems for the FELs.

INTRODUCTION

The time structure of a high gain harmonic generation FEL is determined by the time structure of the Laser system. The FWHM of the FEL radiation is expected to be below 30 fs. Furthermore, the shot to shot intensity variations are small compared to a SASE FEL scheme. The three FELs will be operated at electron energies of 1GeV (LE-FEL) and 2.3GeV (ME-FEL and HE-FEL), respectively. They consist of 2, 3, and 4 stages with a modulator, a dispersive section and a radiator each followed by a final amplifier (table 1).

The photon energy tuning will be done via gap motion. For the HE-FEL the electron beam energy has to be modified additionally to provide the full tuning range. The last radiators and the final amplifiers will be devices with full polarization control. The other modules which are responsible for the electron beam bunching are planar undulators.

Table 1: Parameters of the BESSY Soft-X-Ray FEL. Period lengths (1st number) and section lengths (2nd number) are given in mm and m, respectively [1].

Device	LE-FEL		ME-FEL		HE-FEL	
Energy range	24-120 eV		100-600 eV		500-1000 eV	
	Modulator	Radiator	Modulator	Radiator	Modulator	Radiator
Stage 1	80 / 1.60	62 / 3.47	122 / 2.56	92 / 3.86	122 / 2.20	92 / 3.86
Stage 2	62 / 1.61	50 / 3.45	92 / 2.21	70 / 2x3.78	92 / 2.01	70 / 3x3.80
Stage 3			70 / 2.31	50 2x3.75	70 / 2.1	50 / 3x 3.1
Stage 4					50 / 2x2.65	28.5 / 2x 3.28
Final amplifier	50 / 3x3.85		50 / 3x3.85		28.5 / 5x3.65	
Total length / m	21.68		37.55		60.98	

LAYOUT OF THE UNDULATORS

Since all gaps are variable a separated function focussing scheme has been adopted. The quadrupoles of the FODO structure are located between the undulator segments. Permanent magnet phase shifters with adjustable magnetic gaps provide the correct phase adaption between the undulator segments. Correction coils, and diagnostic systems are located in the intersections as well.

A dogleg collimator with a spatial and an energy collimation stage protects the magnets from being hit by dark current electrons.

MAGNETIC DESIGN

The modulators and the first radiators will be pure permanent magnet structures. The last radiator and the final amplifier are of the APPLE III type (see figure 1) [2]. An APPLE III provides the same flexibility concerning the polarization control as an APPLE II but the maximum field is larger at the expense of a reduced access from the side. In a linac driven FEL a circular beam pipe can be used and more magnetic material can be located close to the electron beam. Side access to the magnetic structure is needed only for Hall probe measurements and for the chamber support. A minimum magnetic gap at the side of only 5.4mm can be realized still providing the space for a 10.4mm diameter tube. The magnetic field can be further enhanced by tilting the magnetization direction to 45 degrees. The reverse fields in an APPLE III structure require a more stable material compared to an APPLE II undulator and as a consequence the remanence of the material is about 6% lower. Nevertheless, the effective magnetic field is a factor of 1.4 higher than for an APPLE II with a gap of 10.4mm.

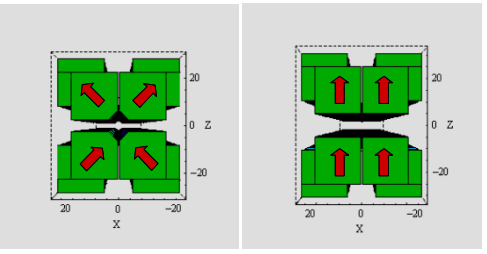

Figure 1: Magnetic structure of an APPLE III (left) compared to an APPLE II design (right).

[#]bahrdt@bessy.de

The magnetic field of an APPLE III undulator can be parametrized with:

$$B(T) = a \cdot \exp(b \cdot (gap/\lambda_0) + c \cdot (gap/\lambda_0)^2)$$

useing the parameters of table 2.

The parameters of table 2 have been evaluated with the 3D-code RADIA [3] for remanence = 1.13T and 1.19T (longitudinally and 45° magnetized blocks), block dimensions = 40x40mm^2, minimum vertical distance = 5.4mm, free aperture = 10.4mm. The parameters are valid for period lengths of 20mm $\leq \lambda_0 \leq$ 50mm.

Table 2: Field parameters of the APPLE III design

	hor. lin.	vert. lin.	circular	lin. 45°
A	2.481	2.035	2.209	1.569
B	-6.258	-6.576	-6.400	-6.392
C	0.112	0.602	0.285	0.231

The horizontal roll off of the vertical field component is larger for an APPLE III than for an APPLE II whereas the roll off of the horizontal field component is smaller (figure 2). For the HE-FEL a relative alignment accuracy of the undulator modules of ±20µm is required. The undulator segments will be mounted onto remote controlled transversely movable stages in order to meet this tight tolerance. The indication for a correct alignment will be the FEL output.

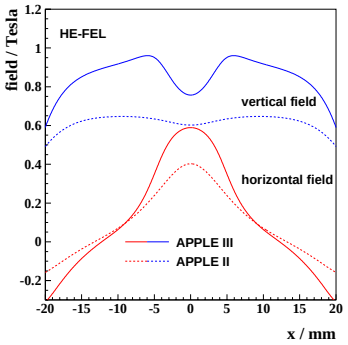

Figure 2: Comparison of the transverse field profiles of the APPLE II and the APPLE III design evaluated for the HE-FEL.

SOURCE CHARACTERIZATION

Three dimensional FEL codes provide information about the electric field distribution at the end of the final amplifier, $z=z_0$. This point is not the location of the photon beam waist. The beamline designer needs to know the exact location and the size of the photon beam waist in order to maximize the brightness at the sample. This information can be derived from the results of a longitudinal propagation of the electric field distribution. There are two ways to proceed:

1: Integration of the diffraction equation of Fresnel and Kirchhoff:.

$$\vec{E}(x',y') = \frac{1}{\lambda}\int_{-\infty}^{\infty}\int_{-\infty}^{\infty}\vec{E}(x,y)\frac{e^{i\vec{k}(\vec{r}-\vec{r}')}}{|\vec{r}-\vec{r}'|}\cos(\beta)\cdot dx\cdot dy$$

2: Application of Fourier optic methods.

A FFT yields the angle distribution of the FEL output

$$\vec{E}_0(\nu_x,\nu_y) = \int_{-\infty}^{\infty}\int_{-\infty}^{\infty}\vec{E}(x,y)\cdot e^{-2\pi i(\nu_x x+\nu_y y)}dx\cdot dy$$

This distribution is multiplied by a factor which represents a longitudinal drift of Δz.

$$\vec{E}(\nu_x,\nu_y) = \vec{E}_0(\nu_x,\nu_y)\cdot e^{2\pi i\cdot\Delta z\cdot\sqrt{1/\lambda^2-\nu_x^2-\nu_y^2}}$$

An inverse FFT provides the spatial distribution at $z=z_0+\Delta z$.

$$\vec{E}(x',y') = \int_{-\infty}^{\infty}\int_{-\infty}^{\infty}\vec{E}(\nu_x,\nu_y)\cdot e^{2\pi i\cdot(\nu_x x+\nu_y y)}\cdot d\nu_x\cdot d\nu_y$$

The second method is much faster in cases where the transverse dimension of the photon beam size does not change too much within Δz. The following results are derived with this method.

To study the development of the radiation properties within the final amplifier time dependent GENESIS simulations [4] have been performed for various lengths L of the LE-FEL final amplifier of $L=L_0$-$81\lambda_0$, L_0-$60\lambda_0$, L_0-$40\lambda_0$, L_0-$20\lambda_0$ and L_0, where L_0 is the length of the final amplifier given in table 1.The power distributions are plotted in figure 3. The corresponding electric fields have been propagated by amounts of Δz with -30m ≤ Δz ≤ +20m and the intensities have been projected onto the horizontal and the vertical plane. The first and second moments of these projections have been evaluated and the results for slice 4 are plotted in figure 4. Similar numbers have been obtained for slices 2,3 and 5.

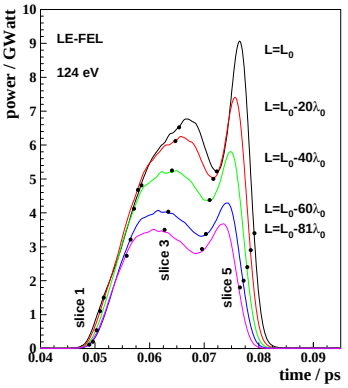

Figure 3: GENESIS simulations for different lengths L of the final amplifier. The electric fields of five slices (black circles) have been propagated.

The photon beam waist is located several meters upstream from the FEL end and this distance increases with L. As a consequence the brightness at the sample can be increased by a factor of two if the waist is focussed instead of the FEL end.

The photon beam size increases with the length of the final amplifier (figure 4). This might be partly due to the increasing electron beam size which varies between 115 and 127μm horizontally and between 105 to 130μm vertically for $L_0\text{-}81\lambda_0 \le L \le L_0$.

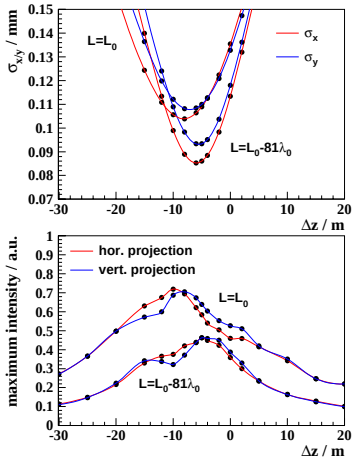

Figure 4: Photon beam size (top) and maxima of the projected intensity (bottom) versus longitudinal distance to the final amplifier end. The data of slice 4 are plotted.

The photon beam divergence decreases with L and the phase space product σσ' is nearly independent of L for slice 4 (figure 5) and also for slices 2, 3 and 5. For a diffraction limited beam we expect a product of $\sigma\sigma' = \lambda/4\pi$ = 0.8nm (124eV). Based on the GENESIS simulations we obtain for each of the slices 2, 3, 4 and 5 a product of about 1.25nm which is close to the theoretical limit.

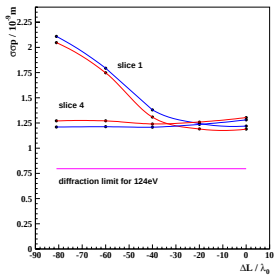

Figure 5: Phase space volume of the LE_FEL radiation for various lengths of the final amplifier.

For $L = L_0\text{-}81\lambda_0$ slice 1 is far below saturation. The waist is located close to the FEL end and moves further upstream for increasing L (figure 6). The phase space product of slice 1 is a factor of 2.5 above the diffraction limit for $L = L_0\text{-}81\lambda_0$ and approaches the value of the slices 2-5 for increasing L (figure 5).

The specific case of the LE-FEL at 124eV indicates that the location of the waist moves upstream relative to the FEL end when the FEL goes into saturation. A distance of 10m between the FEL end and the waist is significant and has to be regarded in a monochromator design. The question has to be answered whether the location of the waist moves with photon energy which would imply the necessity of a variably focussing beamline optic. Further studies for more photon energies and also for the ME-FEL and the HE-FEL are in progress.

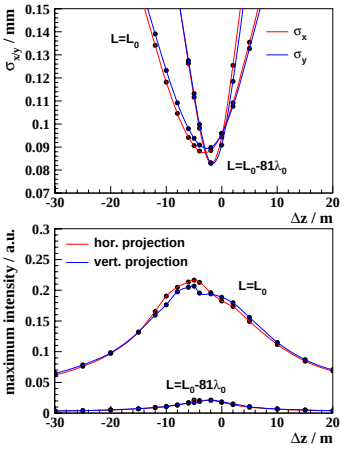

Figure 6: Photon beam size (top) and maxima of the projected intensity (bottom) versus longitudinal distance to the final amplifier end. The data of slice 1 are plotted.

FIELD OPTIMIZATION

The field tuning for the planar modulators and the radiators of the first stages is straight forward [5]. Shimming of the last radiator and the final amplifier is more complicated due to several reasons: i) Iron shims can not be used as usual because the signature changes with magnet row shift. ii) the shims do not stick by magnetic forces. iii) The shims can not be applied directly above or below the electron beam because the magnet rows are separated by a slit of 1mm. iv) The field integrals depend on the shift of the magnet rows which is due to the non unity of the magnetic permeability.

Magnet sorting techniques based on detailed field data of individual magnets are essential for these devices to reduce the work on shimming after assembly. At BESSY a precise set-up for the characterization of magnet block inhomogeneities has been developed [6]. Using the inhomogeneity data together with the Helmholtz coil data in a simulated annealing code the best magnet configuration is evaluated. It has been demonstrated at BESSY that even for devices consisting of more than 1000 individual blocks the field integrals can be predicted with an accuracy of ± 1.5Gm [6]. The prediction is based only on single block data and no further field measurement and resorting has been performed during magnet assembly. The remaining field errors can be removed in three steps:

1: Trajectory and phase errors are minimized with transverse block movements (virtual shimming).

2: The endpoles can be designed such that the field integral variation with gap is small [1] [7]. The remaining

shift dependent terms are minimized with iron shims which are glued onto the magnets.

3: Shift independent field integrals are removed with permanent magnet arrays at both ends of the device.

These techniques have been applied to several APPLE II undulators at BESSY and they are documented in detail in [6].

SUPPORT AND DRIVE SYSTEM

The support structure (cast iron) consists of a base frame carrying two C-frames. The magnetic structures will have a length of up to 4m. The magnet girders will be made from aluminum. The deflection is minimized with four supports (instead of two) using two cross bars. This design has already been implemented successfully at BESSY.

Four longitudinal drive systems give the flexibility to move each row individually. This provides full polarization control for the user. Parallel motion of two rows changes the polarization from horizontal linear to circular and to vertical linear. Anti-parallel motion tilts the linear polarization vector continuously from 0° to 90°. Sometimes, the orientation of the sample is not well known. In these cases it is useful to rotate the polarization vector by more than 90°. With 4 motors a rotation of 180° is possible.

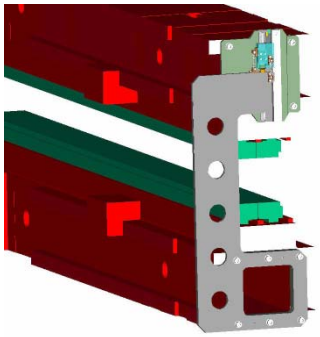

Figure 7: The new gap measurement system as implemented at the BESSY UE49 undulator.

Two servo motors provide the gap tunability. The gaps of the individual undulator sections have to be adjusted with a relative accuracy better than 3µm. This tight tolerance can not be achieved with measurement systems used so far. Rotary encoders suffer from backlash of gearboxes and linear encoders coupled to the upper and the lower I-beam do not follow Abbe's comparator principle. We have developed a new measurement system where the linear encoder is located directly above the electron beam thus following Abbe's comparator principle. The system recently installed at the BESSY APPLE II undulator UE49 (figure 7) demonstrated a gap reproducibility of ±1µm independent of the gap history (figure 8).

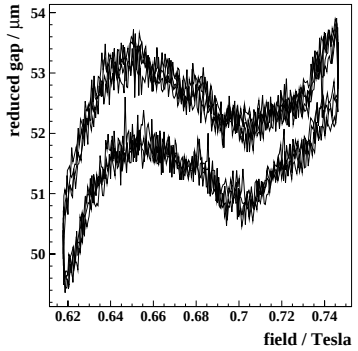

Figure 8: Measured gaps versus magnetic field for several cycles of gap opening and closing. A 4th order polynomial has been subtracted from the raw data to show the residual error.

REFERENCES

[1] The BESSY Soft-X-Ray Free Electron Laser, Technical Design Report, Berlin, Germany, March, 2004.

[2] J. Bahrdt, W. Frentrup, A. Gaupp, B. Kuske, A. Meseck, M. Scheer, "Undulators for the BESSY SASE-FEL Project", 8th International Conference on Synchrotron Radiation Instrumentation, San Francisco, Cal., 2003, AIP 0-7354-0180-2/04, p215.

[3] P. Elleaume, O. Chubar, J. Chavanne, "Computing 3D magnetic fields from insertion devices", Proc. of the 1997 PAC, Vancouver, Canada (1997) 3509-3511. O. Chubar, P. Elleaume, J. Chavanne, "A three-dimensional magnetostatics computer code for insertion devices", J. Synchr. Rad. 5 (1998) 481-484.

[4] A. Meseck, B. Kuske, these proceedings

[5] D.C. Quimby, S.C. Gottschalk, F.E. James, K.E. Robinson, J.M. Slater, A.S. Valla, "Development of a 10-meter wedged-pole undulator", Nucl. Instr. and Meth., A285 (1989) 281-289. S.C. Gottschalk, D.C. Quimby, K.E. Robinson, J.M. Slater, "Wiggler error reduction through shim tuning", Nucl. Instr. and Meth., A296 (1990) 579-587. B. Diviacco, R.P. Walker, "Recent advances in undulator performance optimization", Nucl. Instr. and Meth., A368 (1996) 522-532. J. Chavanne, P. Elleaume, "Undulator and wiggler shimming", Synchr. Rad. News, Vol.8 No.1 (1995) 18-22.

[6] J. Bahrdt, W. Frentrup, A. Gaupp, M. Scheer, "Magnetic field optimization of permanent magnet undulators for arbitrary polarization", Nucl. Instr. and Meth. A, 516 (2004) 575-585.

[7] J. Chavanne, P. Elleaume, P. Van Vaerenbergh, "End field structures for linear/helical insertion devices", Proc. of the PAC, New York, NY, USA (1999) 2665-2667.

PROPOSAL OF LASER-DRIVEN ACCELERATION WITH BESSEL BEAM

D. Li*, K. Imasaki, Institute for Laser Technology, 2-6 yamada-oka, suita, Osaka 565-0871,Japan

Abstract

A novel approach of laser-driven acceleration with Bessel beam is presented in this paper. Bessel beam, in contrast to the Gaussian beam, demonstrates "diffraction-free" characteristics in its propagation, which implies potential in laser-driven acceleration. A configuration of Bessel beam truncated by a set of annular slits makes several special regions in its travelling path, where the laser field becomes very weak and the accelerated particles are possible to receive slight deceleration as they undergo decelerating phase. Thus, multistage acceleration is realizable. With the help of numerical computation, we have shown the potential of multistage acceleration based on a three-stage model.

INTRODUCTION

The intense laser field provides an ultrastrong field gradient implying an attractive potential in particles acceleration. Laser-driven accelerator, an active current research area, has received considerable attention in recent years [1-7]. Many proposals, such as inverse free electron laser [8], plasma-wave accelerator [9], ponderomotive schemes [10], inverse Cherenkov acceleration [11], and vacuum acceleration directly by the longitudinal component of electric field [12,13] were presented and extensively studied.

In general, laser beam from a laser cavity travels in the form of Gaussian mode, exhibiting manifest transverse spreading when it is focused down to small spot size. A strongly focused Gaussian beam will show apparent divergence after it passes a short certain distance, known as Rayleigh length. Thus, even there exist schemes to keep synchronization between accelerated particles and the wave, the effective acceleration can only occur within a relative short range. In order to extend the interaction, "diffraction-free" Bessel beams are introduced to the laser driven accelerator [12,13].

Since Durnin experimentally demonstrated the nondiffracting property of Bessel beam, it has been widely studied in various applications [14-16]. Hafizi et.al analysed the vacuum beat wave accelerator with using laser Bessel beam [17], and other Bessel beam driven acceleration schemes were also discussed recently.

This paper is aimed at an innovative approach in vacuum laser-driven acceleration with using Bessel beam. We truncate the Bessel beam by a set of annular slits (hereafter, we call it slits-truncated Bessel beam), so that several special regions are formed in its propagation, where the laser field becomes rather weak, and consequently, the accelerated particles, which slide behind the wave, are possible to receive slight deceleration as they undergo the decelerating phase of the wave field by just travelling in these regions. Because of the "diffraction-free" characteristic of Bessel beam, multistage acceleration comes to be feasible.

*lidazhi@ile.osaka-u.ac.jp

BESSEL BEAM

General Theory

A solution of the Helmholtz wave equation for an azimuthally symmetric wave of frequency ω that propagates in the positive z direction gives the Bessel beam expression

$$\psi(\vec{r},t) = J_0(k\sin(\alpha)\rho)e^{i(k\cos(\alpha)z-\omega t)} \quad (1)$$

An ideal Bessel beam maintains the same radial profile over arbitrary propagation distance and has maximum amplitude on-axis and hence is called "diffraction-free". The following integral representation of Bessel function is helpful to comprehend the angle α,

$$J_0(k\sin(\alpha)\rho)e^{i(k\cos(\alpha)z-\omega t)} = \frac{1}{2\pi}\int_0^{2\pi} d\phi e^{i(k\sin\alpha x\cos\phi + k\sin\alpha y\sin\phi + k\cos\alpha z-\omega t)} \quad (2)$$

which exhibits that Bessel beam is superposition of an infinite set of ordinary plane waves making angle α with respect to the z axis [18]. And this is also the principle to generate Bessel beam, i.e., superpose plane waves with equal amplitude and a common phase that make angle α to the z axis.

A simple geometrical relation tells that, if the Bessel beam is formed at z=0 plane and to propagate a distance z, extent of $\mathbb{R}=z\tan\alpha$ at z=0. That means an ideal Bessel beam needs arbitrarily large initial radial extent and arbitrarily large energy, to retain its "diffraction-free" character over an arbitrarily large distance, which is impossible to realize in practice. The physically meaning beam is an aperture-truncated one, which possesses nearly diffraction-free properties within some axial distance. The generation of aperture-truncated Bessel beam was widely studied elsewhere [14,15].

The phase velocity of a Bessel beam relies on the angle α,i.e., $v_p = c/\cos(\alpha)$, which is larger than the light speed c. If such a beam is used for direct laser-driven acceleration in vacuum, the particle will slide behind the wave and cannot gain net energy during a wave period. Naturally, we conceive a scheme that after the particle is accelerated in the first half circle of the wave period, the laser field suddenly disappears to allow the particle avoid the following deceleration; and when the particle slides

into the next accelerating phase, the laser field takes on again. In other words, we have to make "laser-on" and "laser-off" regions alternatively appearing during laser propagation and well arrange the intervals among them to realize required phase matching.

Annular Slits-truncated Bessel Beam

A Bessel beam truncated by a set of annular slits can do the work, as schematically shown in Fig. 1, where laser

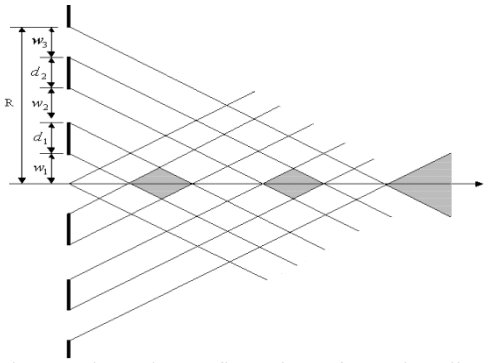

Fig. 1 schematic configuration of annular slits-truncated Bessel beam

field disappears at those shadow regions. The lengths of "laser-on" and "laser-off" regions are related to the slits' parameters, width w_i (i=1,2,3) and the interval between two slits d_i (i=1,2). Using the geometrical method we can easily work out those lengths. Actually, the "laser-off" areas are not entirely free of laser field because of the diffraction effect induced by annular slits. To precisely analysis Bessel beam diffraction, we employ scalar diffraction theory.

In the Fresnel approximation the amplitude $A(r, z)$ at a distance z can be obtained from diffraction integral. For a circularly symmetric incident amplitude A(ρ , 0), we have [19]

$$A(r,z) = \exp(ikz + \frac{ikr^2}{2z})(\frac{k}{iz}) \times \int_0^a \rho A(\rho,0) J_0(\frac{k_\rho r}{z}) \exp(\frac{ik\rho^2}{2z}) d\rho \quad (3)$$

where a is the radius of a circular aperture. For the case of Bessel beam, we have $A(\rho,0)=J_0(k\sin(\alpha)\rho)$ as the initial amplitude distribution. If the beam is truncated by a set of annular slits, e.g., for the case as shown in Fig. 1, the incident amplitude should be modified as

$$A(\rho,0) = \zeta(\rho) J_0(k \sin \alpha \rho) \quad (4)$$

and $\zeta(\rho)$ is given by

$$\zeta(\rho) = \begin{cases} 1 & (0 \le \rho < R_1) \\ 0 & (R_1 \le \rho < R_2) \\ 1 & (R_2 \le \rho < R_3) \\ 0 & (R_3 \le \rho < R_4) \\ 1 & (R_4 \le \rho < R_5) \\ 0 & (R_5 \le \rho < \infty) \end{cases}$$

where $R_1=w_1$, $R_2=R_1+d_1$, $R_3=R_2+w_2$, $R_4=R_3+d_2$, $R_5=R_4+w_3$.

Together with the initial conditions, Eq. 3 can be numerically calculated to understand the propagation properties. As an example, here we consider the on-axis case (r=0) and employ the following parameters: laser wavelength λ =1 μ m, α =1°, and w_1 =4 mm, w_2 =4 mm, w_3 =6 mm, d_1 =2 mm, d_2 =4 mm. The computation results for slits-truncated Bessel beam are illustrated in Fig. 2, and for the sake of comparison, aperture-truncated Bessel beam (with circular aperture radius of a=20 mm, summation of w_i and d_i) is also presented. The blue and grey curves represent aperture- and slits-truncated beams, respectively. It is seen that, their amplitudes characterize oscillation and decay at a finite distance ~a/tan(α). Contrast to the aperture-truncated beam, the slits-truncated one exhibits two special zones where the amplitude falls down by two orders in magnitude. With properly setting the parameters of annular slits, the injected electrons are possible to spend the decelerating phase in those regions and receive slight deceleration. The red curve is synthesized to approximate the grey curve with showing an average effect, in ignorance of the oscillation. It takes the below form, with the use of exponential functions to fit the falling and rising edges,

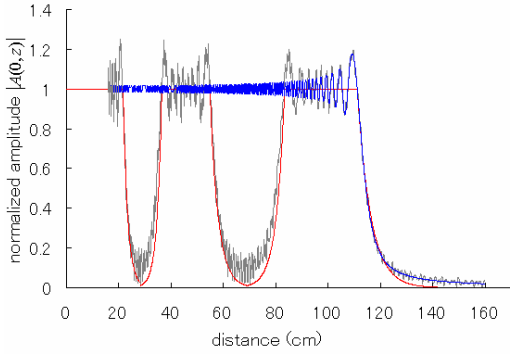

Fig. 2 Propagation of aperture-truncated (blue curve) and slits-truncated (grey curve) Bessel beam shown from z=16 cm. Synthesized function $\chi(z)$ (red curve) gives out the approximation to the grey curve

$$\begin{aligned} \chi(z) &= [H(z-0) - H(z-21.6)] \\ &+ [H(z-21.6) - H(z-28.3)]\exp(-0.056 \times (z-21.6)) \\ &+ [H(z-28.3) - H(z-36.5)]\exp(0.056 \times (z-36.5)) \\ &+ [H(z-36.5) - H(z-54.8)] \\ &+ [H(z-54.8) - \mathrm{H}(z-69.2)]\exp(-0.032 \times (z-54.8)) \\ &+ [H(z-69.2) - H(z-83.4)]\exp(0.032 \times (z-83.4)) \\ &+ [H(z-83.4) - H(z-111.2)] \\ &+ [H(z-111.2)]\exp(-0.02 \times (z-111.2)), \end{aligned} \quad (5)$$

where H is the Heaviside function.

Laser Field

All field components satisfying Maxwell's equation are derived in reference [18] for ideal Bessel beam. For the convenience, we made a summary as below,

$$E_\rho = E_0 \cot(\alpha) J_1(k_\rho \rho)\cos(\eta)$$

$$E_z = -E_0 J_0(k_\rho \rho)\sin(\eta)$$

$$B_\varphi = \frac{E_0}{c\sin(\alpha)} J_1(k_\rho \rho)\cos(\eta)$$

where E_0 is the peak amplitude, and $k_\rho = k\sin(\alpha)$ $k_z = k\cos(\alpha)$ $\eta = k_z z - \omega t$. The other components are zero. In our proposal, we directly apply the longitudinal electric field E_z to accelerating the particles.

DYNAMICS

We first consider accelerating a single electron in the slits-truncated Bessel beam field. The motion of the electron in an electromagnetic field is governed by Lorentz equation

$$d\vec{p}/dt = -e\left(\vec{E} + \vec{v} \times \vec{B}\right) \quad (6)$$

where $\vec{p} = \gamma m_0 \vec{v}$ represents the momentum, $\vec{v}$ is the electron velocity, and γ is the Lorentz factor. At first, let us see the case of on-axis acceleration. According to the above field expressions, only the longitudinal electric field exists at ρ =0, while the others are cancelled out . For a slits-truncated Bessel beam, the longitudinal field could be rewritten as

$$E_z = E_0 |A(0,z)| \sin(\eta) \quad (7)$$

where $A(0, z)$ is the combination of Eqs. (3) and (4). However, the numerical calculation of $A(0, z)$ was proven to be terrible time-consuming, leading to inconvenience in processing phase-matching optimization. In order to simplify computation, we take a function ε (z), which is in the form of χ (z), to substitute $A(0, z)$, and we therefore have

$$E_z \cong E_0 \varepsilon(z) \sin(\eta) \quad (8)$$

This approximation will not damage the essential of this acceleration approach, but only affects the details in determining slits' parameters. The concrete form of ε (z) concerning a given initial energy of an electron will be optimized and figured out as one of simulation results.

Apparently, the present approach inclines to accelerating the relativistic electrons. The static or slow electrons cannot make effective interaction with the accelerating field holding a phase velocity larger than the light speed. As an example, we assume an electron with initial energy of 150 MeV, only having axial velocity, is injected together with the laser Bessel beam by an appropriate phase at z=0. The angle α is supposed to be 0.2 degree, in order to get lower phase velocity. We choose the peak amplitude of field E_0=10^{10} *V/m*, resulting in that ~100 TW power should be contained in the central lobe of Bessel beam. After carefully optimizing the lengths of "laser-on" and "laser-off" regions, a three-stage acceleration scheme is shown in Fig. 3. From Fig. 3 (a) we know that the electron is accelerated from 150 MeV to more than 1 GeV just over ~90 cm distance. The

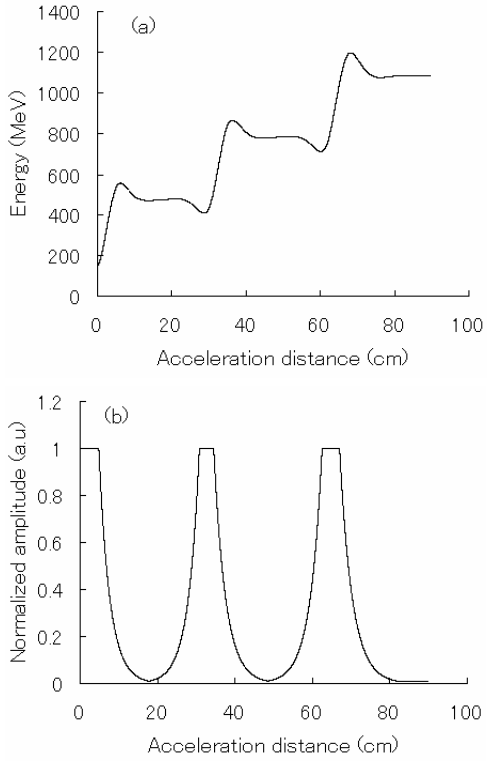

Fig. 3 Three-stage acceleration mechanism. (a) total energy of the accelerated electron shown as a function of distance, (b) corresponding ε (z) function

corresponding ε (z) function is given by Fig.3 (b), from which the slits parameters could be roughly deduced.

The radiation damping effect is not involved in above computation. Making use of the Larmor's formula

$$P = \left(2r_e/3m_0c\right)\left[\left(d\vec{p}/d\tau\right)^2 - \left(1/c^2\right)\left(d\varepsilon/d\tau\right)^2\right]$$

the instantaneous radiated power from an accelerated electron is calculable. Here r_e is the classical radius of the electron, $d\tau = dt/\gamma$, ε indicates the electron energy. For the case of Fig. 3, the total radiated energy is ~0.042 eV, which means the radiation influence is unimportant by the parameters treated in this paper.

Actually, by such an approach, acceleration with more stages is possible to reach. The maximum number of acceleration stages relies on the laser pulse length, the realizable Bessel beam propagation distance, and the technology on manufacturing annular slits.

OFF-AXIS INJECTION

Only a small fraction of the electrons in a bunch of transverse dimensions of a few microns will be interact with laser field with precisely zero initial transverse coordinates. The rest will enter the interaction region with

transverse distance from the axis. The field components E_ρ and B_ϕ lead to radial force, which probably induces transverse spreading of electron bunch during acceleration. To understand this effect, we conducted computation for off-axis injection.

We consider injecting 11 electrons with different initial radial positions: the first one is on-axis, while the others are uniformly distributed along radial direction with an interval of 1 μ m. These electrons are orderly numbered 0,1,2…10, and they have the same initial energy of 150 MeV, only with the longitudinal velocity, while the initial transverse velocity components are set to zero. The $\varepsilon(z)$ function shown in Fig. 3 (b) is adopted in this calculation, i.e., the on-axis electron is chosen for reference. The laser parameters are the same as used above.

After numerically solving the motion equation with full fields, we got the results as shown in Fig. 4. Note that the final energies of off-axis injecting electrons are lower than that of on-axis injecting one, and this therefore raises energy spread. For the case of Fig. 4a, the maximum energy deviation is ~92 MeV. Electron trajectories are depicted in Fig. 4b, which illustrates that the radius of electron bunch spreads from the original 10 μ m to the final 60 μ m. The outer electrons receive slighter acceleration than the inner ones, which is due to the transverse distribution of the longitudinal electric field, described by the zero-order Bessel function.

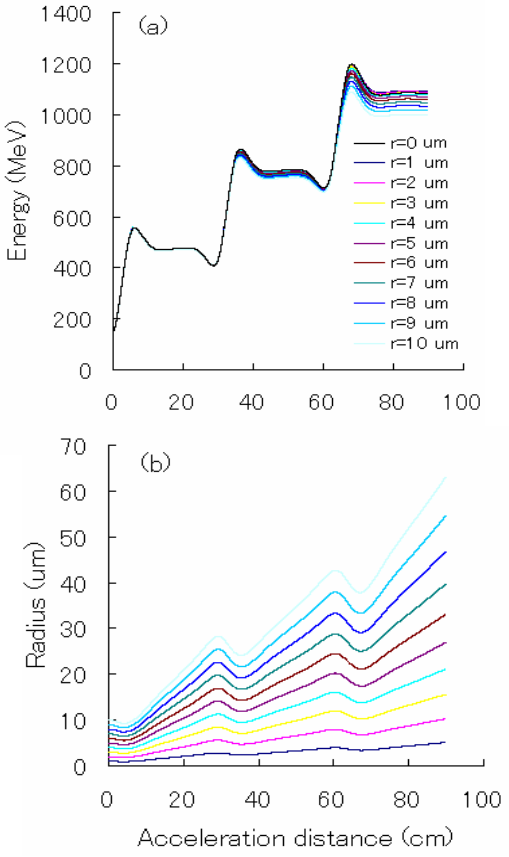

Fig. 4 Acceleration of off –axis injection electrons. (a) energy evolution, and (b) electrons' trajectories.

CONCLUSION

We proposed a novel method for laser-driven acceleration. Annular slits-truncated Bessel beam forms some special regions, where the accelerated particles are allowed to "avoid" deceleration when they slide in the decelerating phase of wave. We analysed the propagation properties of annular slits-truncated Bessel laser beam and demonstrated the acceleration mechanism by numerically solving the motion equation. The results show this method considerable potential in laser-driven acceleration.

REFERENCES

[1] A.Ting, C.I.Moore, K.Krushelnick, C.Manka, et.al, Phys. Plasmas 4 (1997) 1889
[2] P.Sprangle, E.Esarey, J.Krall, Phys. Plasmas 3 (1996) 2183
[3] Y.Liu, D.Cline, P.He, Nucl. Instrum. Methods Phys. Res. A424 (1996) 296
[4] J.A.Edighoffer, R.H.Pantell, J. Appl. Phys. 50 (1979) 6120
[5] T.B.Zhang, T.C.Marshall, M.L.Lapointe, et.al, Phys. Rev. E 54 (1996) 1918
[6] R.B.Palmer, J. Appl. Phys. 43 (1972) 3014
[7] R.H.Pantell, T.I.Smith, Appl. Phys. Lett. 40 (1982) 753
[8] C.Pellegrini, P.Sprangle, W.Zacowicz, proceedings of the 13th conference on particle acceleration, (1983) 473
[9] T.Katsouleas, J.Dawson, Phys. Rev. Lett. 51 (1983) 392
[10] L.Cicchitelli, H.Hora, R.postle, Phys. Rev. A 41 (1990) 3727
[11] G.Fontana, R.Pantell, J. Appl. Phys. 54 (1983) 4285
[12] Marlan O.Scully, M.S.Zubairy, Phys. Rev. A 44 (1991) 2656
[13] B.Hafizi, E.Esarey, P.Sprangle, Phys. Rev. E 55 (1997) 3539
[14] J.Durnin, J.J.Miceli, and J.H.Eberly, *Phys. Rev. Lett.* 58, (1987) 1499
[15] L.C. Laycock and S.C.Webster, *GEC J. Res.* 10 (1992) 36
[16] D.Li, K.Imasaki, M.Aoki, J. Nucl. Sci. Tech. 32 (2003) 211
[17] B.Hafizi, A.K.Ganguly, A.Ting, Phys. Rev. E 60 (1999) 4779
[18] http://arxiv.org/abs/physics/0006046
[19] Zhiping Jiang, Qisheng Lu, and Zejin Liu, *Appl. Opt.* 34 (1995) 7183

AMPLIFICATION OF SHORT-PULSE RADIATION FROM THE ELECTRON UNDERGOING HALF-CYCLOTRON ROTATION*

M. R. Asakawa, H. Marusaki, Y. Tsunawaki[(a)], N. Ohigashi[(b)] and K. Imasaki[(c)]
Institute of Free Electron Laser Osaka university, Tsudayamte 2-9-5, Hirakata, Osaka 573-0128, Japan

(a) Osaka Sangyo University, Nakadaito, Daito, Osaka 574-8530, Japan
(b) Department of Physics, Kansai University, Osaka 564-8680, Japan
(c) Institute of Laser Technology, Yamadaoka, Suita, Osaka 565-0871, Japan

Abstract

A novel light source which can generate an half-cycle radiation pulse is being developing at Institute of Free Electron Laser, Osaka university.

INTRODUCTION

The number of the optical cycles contained in a radiation pulse is simply determined by the number of the electron wigglings or rotations during which the electron emits the radiation pulse. Electrons passing through a bending magnet emit a radiation pulse whose phase variation is less than unity. The bending magnet radiation, thus, can be used as a broadband continuous-spectrum light source. When such radiation is confined in the optical cavity, the radiation should be amplified via the interaction with the electrons periodically injected by the accelerator. In the bending magnet, however, the interaction length is usually short and the gain, then, should be small. Based on this idea, we are developing a half-cycle light source using the electrons which undergo an half-cycle cyclotron motion in a solenoid field. As described in the following, the pulse length is approximately equal to that of the electron beam. Thus this light source can produce broadband continuous-spectrum radiation in the THz wave range, because the accelerator produces the electron beam with a pulsewidth of a few picoseconds.

THEORETICAL CONSIDERATIONS

The electric field produced by the electron passing through the solenoid field is calculated from the *Liénard-Wiechert* potential and given by

$$\mathbf{E}(\mathbf{x},t)=\frac{q}{4\pi\varepsilon_0}\left[\frac{R(t')}{s(t')^3}\left(\mathbf{n}(t')\text{-}\boldsymbol{\beta}(t')\right)\left(1\text{-}\beta(t')^2\right)+\frac{R(t')^2}{cs(t')^3}\mathbf{n}(t')\times\left(\left(\mathbf{n}(t')\text{-}\boldsymbol{\beta}(t')\right)\times\dot{\boldsymbol{\beta}}(t')\right)\right] \quad (1),$$

where q is the charge of the particle, c the light velocity, ε_0 the vacuum dielectric constant, $\dot{\boldsymbol{\beta}}$ is the normalized acceleration vector, $\mathbf{R}$ (R) is the vector (distance) from the particle to the observation point, $\mathbf{n}$ is a unit vector in the direction of $\mathbf{R}$, and s is defined as,

$$s(t')=R(t')-\frac{\mathbf{R}(t')\cdot\upsilon(t')}{c} \quad (2).$$

Quantities on right-hand-side in equation (3) are to be evaluated at the retarded time,

$$t'=t-\frac{R(t')}{c} \quad (3).$$

The magnetic field is, then, given by

$$\mathbf{B}(\mathbf{x},t)=\frac{1}{c}\mathbf{n}(t')\times\mathbf{E}(\mathbf{x},t) \quad (4),$$

and then the magnitude of the Poynting vector is given by

$$\left|S(\mathbf{x},t)\right|=\varepsilon_0 E^2 \quad (5).$$

The calculations are made for a 150MeV electron beam with pulse length of 3ps passing through the 3m-long solenoid magnetic field of 0.7T and the radiation field is shown in figure 1. A uniform electron distribution in a block, 4×4×0.9 mm^3, is assumed. The bunch length of 0.9 mm corresponds to the pulsewidth of 3 ps. The electrons are located at x_0=[-2 mm, 2mm] and y_0=[-2 mm-r_L, 2 mm-r_L], so that the centres of the circular electron motion lay in x_{c0}=y_{c0}=[-2 mm, 2mm] with the angle of θ_{0x}>0. Here r_L is the Larmor radius. The initial angle and r_L are 3 mrad and 2.6 mm in figure 1, respectively. The coordinates of the observation points, (x_{ob}, y_{ob}, z_{ob}), is (0, 0, 5 m), i.e., the centre of the resonator mirror which reflects back the spontaneous emission. The resonant wavelength is to be 65 μm, and corresponding optical period is 217 fs. During passing through the 3 m-long solenoid field, the electron with γ=300 executes a half-circulation (166 degree in phase).

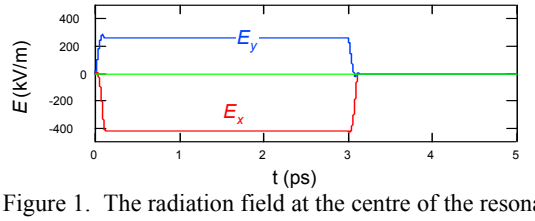

Figure 1. The radiation field at the centre of the resonator mirror produced by a 150MeV electron beam which undergoes a half cyclotron rotation in a 3m-long solenoid field.

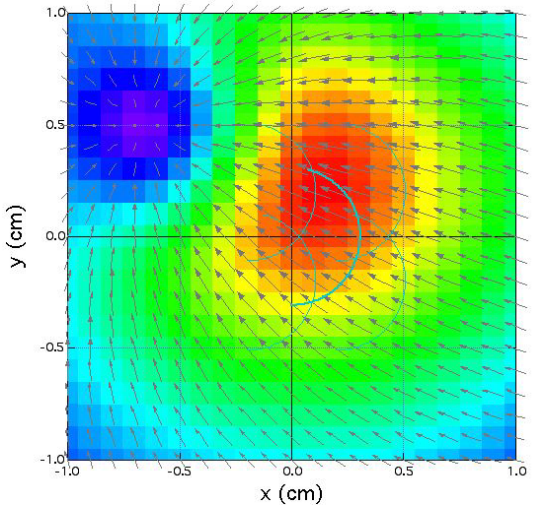

Figure 2 The energy flux distribution and the polarization of the radiation field.

The z-component of the field, E_z, is negligibly small comparing to E_x, E_y. As expected, the phases of the fields, E_x and E_y, do not vary by 2π: the field remains almost constant during its pulsewidth. It depends on the observation point that if the field starts from negative or positive value.

The distribution of the energy flux of radiation, $\int dt' \left| S\left(x,t'\right) \right|$, are shown in figure 2 for the same condition used in figure 1. Typical electron trajectories, for the centre and edge of the electron beam, are projected on the figure as the arcs. The energy flux has a peak at (0.15 cm, 0.2 cm) and falls to 10 % of the peak at a distance of 1.6 cm from the origin, i.e., the axis of the cyclotron motion and the resonator. The radiation should be confined in a radius of 2 cm on the mirror. The contours tend to be displaced from the axis toward first quadrant in the graph. This is because the electrons undergo the half-circulation mainly in the region $x>0$, and rise from fourth quadrant to first quadrant as they are passing through the solenoid field. This tendency becomes more remarkable as larger the initial electron angle is.

Note that the product of the electron velocity and the electric field, $\boldsymbol{\upsilon}_\perp \cdot \mathbf{E}_\perp$, is positive in the most of the part, especially in the region where the radiation field is intense. Thus it is possible to amplify the radiation via the successive interaction with the electron beam if the radiation can be confined in the resonator.

Figure 3 shows the distribution of energy flux for the initial angle of 1, 3, 5 and 10 mrad at z_{ob}=5 and 10 m. The electron trajectories are set so that the guiding centre of the electron beam may be located at the centre of the resonator axis in all cases. All the distributions are normalized by their peaks. The variation of the peak intensity is shown in figure 4.

It is clear that the increase in the initial angle enlarges the cross-section of the radiation field. The position of the peak flux also deviates remarkably with the large initial angle. In detail, the position of the peak is almost the same in the cases of 1mrad and 3 mrad injection, while it deviates at larger initial angles. That is, the radiation propagates unparallel to the axis of the optical cavity when initial angle is large.

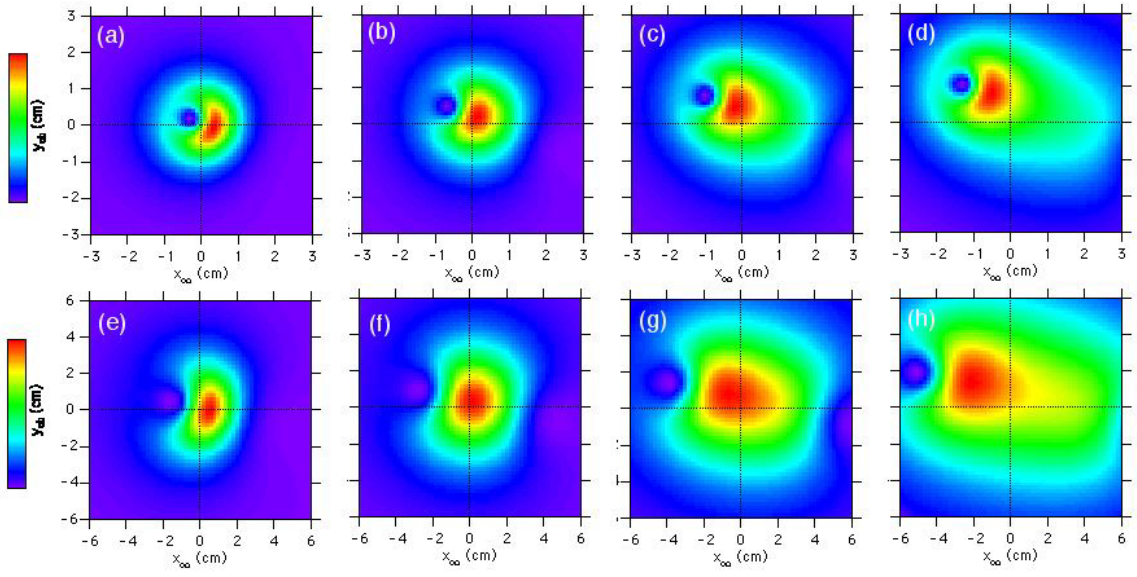

Figure 3 Dependence of the field distribution on the initial angle. (a)-(d) and (e)-(h) show the distribution at the z_{ob}=5 and 10m, respectively. The initial angle is 1mrad for (a) and (b), 3mrad for (b) and (f), 5mrad for (c) and (g), 10 mrad for (d) and (h). All distributions are normalized by their peak.

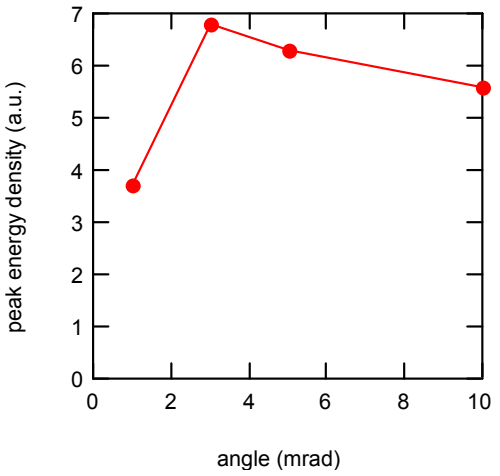

Figure 4. Dependence of the peak flux on the initial angle.

As shown in figure 4, the peak intensity rapidly increases when the initial angle is increased and then slowly decreases above 3mrad. Total energy of the radiation increases monotonically with the angle, because the cross section increases with the angle, though the angle should be chosen around 3mrad to store the radiation in the cavity.

The divergence angle in the case of 3 mrad initial angle is evaluated to be 4-5 mrad. The radiation field, therefore, can be stored in the optical resonator. Because the radiation field has negative or positive value as shown in figure 1, it can be expected that the field can be added up coherently at each round trips analogously to FEL fed by the coherent synchrotron radiation emitted by electron bunches.[1] Then this radiation source will produce broadband far-infrared radiation. The additional growth process via the interaction between the electron and the radiation, $\boldsymbol{\upsilon}_{\perp} \cdot \mathbf{E}_{\perp}$, is now being studied.

EXPERIMENT

The experiments are underway on the 150 MeV beam line, which was used for the demonstration of ultraviolet free-electron laser. A S-band rf-linac produces the electron bunch of 0.25 nC /3 ps at a repetition rate of 22.3 MHz (1/128 of S-band frequency) for 25 μs. Thus the macropulse contains 550 electron bunches. The UV undulator was replaced with 3 m-long solenoid coil wound around a drift tube with an inner radius of 8.5 mm.

This solenoid is located between two pairs of bending magnets used to detour the electron beam around the cavity mirrors. The coil is fed by a capacitor bank (0.1 F/ 500 V) and generates a magnetic field of 1.0 T with a current of 1.5 kA. The discharge time constant is 30 ms so that the change in the solenoid field is negligibly small (less than 0.2 %) during the macropulse duration of 25 μs.

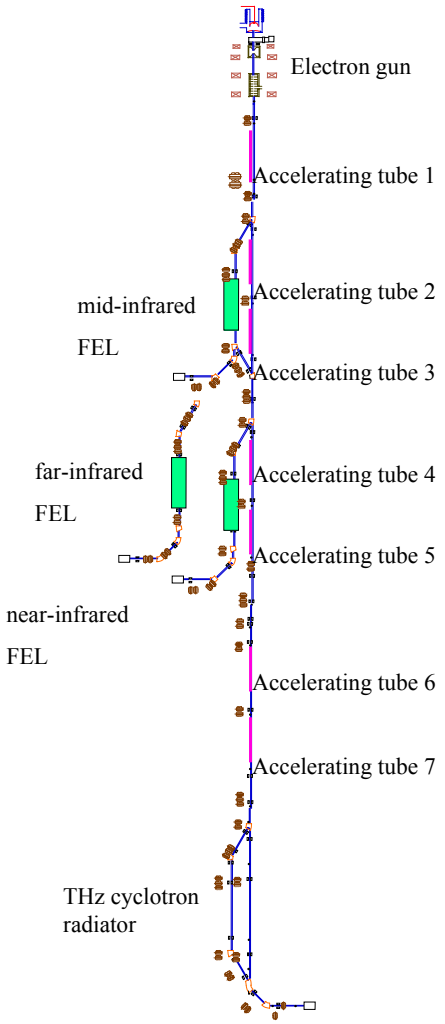

Figure 5. Accelerator system at iFEL and cyclotron radiator.

The incident angle of the bunch is controlled by a set of 'kicker coils' installed at the entrance of the solenoid. The effect of the beam emittance (10 πmm·mrad in normalized emittance) on the beam trajectory is also negligibly small, because the incident angle ranges from 1-5 mrad in the experiment. The optical resonator consists of a pair of the Au-coated concave mirrors spaced 6.72 m apart. At the 22.3 MHz bunch repetition rate, a single radiation pulse is stored in the resonator. Thus the radiation pulse can interact with the electron bunch 550 times during the macropulse.

The intensity of the spontaneous emission was measured for various field strength of the solenoid by removing the downstream cavity mirror. The cyclotron resonance condition,

$$\omega = \omega_{co} / \left(1 - \beta_z\right) \qquad (6),$$

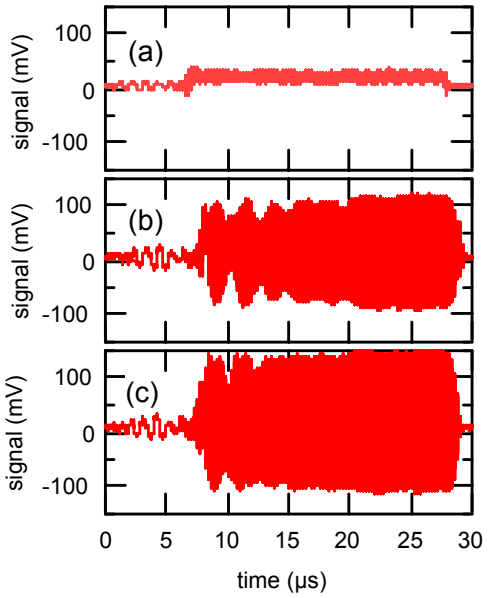

Figure 6. Time trace of the microwave diode response. The solenoid field is 0 T, 0.7 T and 1.0T for (a)-(c), respectively.

where ω_{co}, γ and β_z are the cyclotron frequency, the electron relativistic factor and the normalized axial velocity, gives a resonant frequency of 4.0 THz for typical experimental condition, an electron energy of 150 MeV, an incident angle of 5 mrad and a solenoid field of 1 T. Under these conditions, the electron undergoes a half-cyclotron rotation while it passes through the solenoid. Figure 6 shows the time traces of the response of the microwave diode with a cutoff frequency of 100 GHz. The signal involves the pulses synchronized to the electron bunches and thus appears as it is hatched in the figure. The radiation signal when the solenoid field was off, in fig. 6 (a), generated at the bending magnets. And the radiation power increased as increasing the magnetic field up to 1T. The radiation power with the solenoid field of 1 T exceeded that without the solenoid field by a factor 10.

CONCLUSION

A novel radiation source, which can generate a half-cycle radiation, is being developed at iFEL Osaka university. This source is based on the cyclotron radiation from the electron that undergoes a half-cyclotron rotation in the solenoid field. The numerical study revealed that the radiation can be stored with a certain initial pitch angle of electron. Furthermore the polarization of the radiation directs the same direction with electron cyclotron motion. Thus the radiation can be amplified by interacting with successive electron beam. Substantial power of the spontaneous emission was observed experimentally on the 180 MeV electron beam-ling of iFEL accelerator. The lasing experiment is now under way.

REFERENCES

[1] M. Asakawa, et al., Appl. Phys. Lett. 64 (1994) 1601

RESEARCHES OF THOMSON SCATTERING X-RAY SOURCE AT TSINGHUA UNIVERSITY*

CH.X. Tang, W.H. Huang*, H.B. Chen, C. Cheng, Y. Cheng, Q. Du, T.B. Du, Y.CH. Du, X.Z. He, J.F. Hua, G. Huang, Y.CH. Ge, Y.ZH. Lin, B. Xia, M.J Xu, X.D. Yuan, SH.X. Zheng

Department of Engineering Physics, Tsinghua University, Beijing 100084, PR China

Abstract

The bright and tunable short pulse X-ray sources are being widely used in various research fields. Thomson scattering is one of the most promising approaches to short pulsed x-ray. Researches on Thomson scattering x-ray sources are being carried out in Tsinghua University. Some theoretical results and the preliminary experiment on the Thomson scattering between electron beams and laser pulses are described in this paper.

INTRODUCTION

Tunable, ultrashort pulsed x-ray source are useful in various research fields, such as solid-state physics, material, chemical, biological, medical sciences and industrial applications. The x-ray can be produced with different mechanisms, such as x-ray free-electron lasers [1], electron bunch slicing in synchrotrons [2], and relativistic Thomson scattering[3,4]. The x-ray source based Thomson scattering will possibly generate ultrashort hard x-rays with comparatively low energies electron beams.

The generation of x-ray by scattering between laser light and relativistic electrons was originally proposed in 1960s. With the development of table-top-terawatt (T3) lasers, a number of experimental studies of Thomson scattering have been performed recently. It is shown that Thomson scattering is one of the most promising approaches to ultrashort pulsed x-ray. Researches on Thomson scattering x-ray sources are being carried out in Tsinghua University.

In this paper some theoretical results and the preliminary experiment setup on the Thomson scattering between electron beams and laser pulses are described.

X-RAY GENERATION VIA LINEAR THOMSON SCATTERING AT ARBITRARY INTERACTION ANGLES

To describe the kinematics of the linear Thomson scattering at arbitrary interaction angle α, we consider the frames as given in figure 1. The two frames are both laboratory frame: the electron beam is along the $+z$ axis of the electron frame and the laser beam is along the $-z'$ axis of the laser frame. We assume that the Rayleigh range of laser beam is much longer than laser pulse length, the intensity profile of laser beam satisfy the Gaussian distribution,

$$\rho_l = \frac{n_l}{(2\pi)^{3/2}\sigma_{lx'}\sigma_{ly'}\sigma_{lz'}} \times \exp\left[-\frac{(x'-x'_{l0})^2}{2\sigma_{lx'}^2} - \frac{(y'-y'_{l0})^2}{2\sigma_{ly'}^2} - \frac{(z'-z'_{l0}+ct)^2}{2\sigma_{lz'}^2}\right] \quad (1)$$

where $\sigma_{lx'}, \sigma_{ly'}, \sigma_{lz'}$ and $x'_{l0}, y'_{l0}, z'_{l0}$ are the laser beam's rms size and position offset in x', y', z' direction, respectively. n_l is the total number of laser photons in one pulse. Similarly, we assume that the envelope function of electron beam is much greater than then electron beam pulse length, the intensity of electron beam can be given by

$$\rho_e = \frac{n_e}{(2\pi)^{3/2}\sigma_{ex}\sigma_{ey}\sigma_{ez}} \times \exp\left[-\frac{(x_e-x_{e0})^2}{2\sigma_{ex}^2} - \frac{(y_e-y_{e0})^2}{2\sigma_{ey}^2} - \frac{(z_e-z_{e0})^2}{2\sigma_{ez}^2}\right] \quad (2)$$

where $\sigma_{ex}, \sigma_{ey}, \sigma_{ez}$ and x_{e0}, y_{e0}, z_{e0} are the laser beam's rms size and position offset in x, y, z direction, respectively. n_e is the total number of electrons in one pulse.

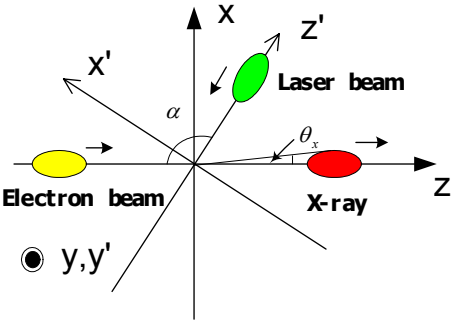

Figure 1: A schematic illustration of Thomson scattering(xyz -electron frame; $x'y'z'$ -laser frame)

The differential cross section of the relativistic Thomson scattering under the linear interaction is

$$\frac{d\Sigma}{d\Omega} = \frac{r_0^2}{2}\frac{(1+\beta^2)(1+\cos^2\theta_x) - 4\beta\cos\theta_x}{\gamma^2(1-\beta\cos\theta_x)^4} \quad (3)$$

where θ_x is emitting angle of x-ray, β is the velocity of electron, r_0 is the classical radius of electron. From equation (1)-(3), we can get the number of photons in the produced x-ray[5]

*huangwh@mail.tsinghua.edu.cn

$$\frac{dn_x}{d\Omega} = C_{off}\frac{n_e n_l}{\sqrt{2\pi}}\frac{d\Sigma}{d\Omega}\times \frac{1}{\sqrt{(\sigma_{ey}^2+\sigma_{ly'}^2)[(1-\cos\alpha)(\sigma_{ex}^2+\sigma_{lx'}^2)+(1+\cos\alpha)(\sigma_{ez}^2+\sigma_{lz'}^2)]}} \quad (4)$$

where

$$C_{off} = \exp\left(-\frac{(y_{e0}-y'_{l0})^2}{2(\sigma_{ey}^2+\sigma_{ly'}^2)} - \frac{[(z_{e0}+z'_{l0})\cos(\alpha/2)-(x_{e0}-x'_{l0})\sin(\alpha/2)]^2}{(1-\cos\alpha)(\sigma_{ex}^2+\sigma_{lx'}^2)+(1+\cos\alpha)(\sigma_{ez}^2+\sigma_{lz'}^2)}\right) \quad (5)$$

is the decrease ratio of x-ray due to the mismatch of position and time. The pulse length of the produced x-ray is

$$\sigma_T = \frac{\sigma_{ez}\sqrt{(1-\cos\alpha)(\sigma_{ex}^2+\sigma_{lx'}^2)+(1+\cos\alpha)\sigma_{lz'}^2}}{c\sqrt{(1-\cos\alpha)(\sigma_{ex}^2+\sigma_{lx'}^2)+(1+\cos\alpha)(\sigma_{ez}^2+\sigma_{lz'}^2)}} \quad (6)$$

which is consistent with the result in Ref.[6] when scattering angle $\alpha = 90°$.

PRELIMINARY THOMSON SCATTERING EXPERIMENT

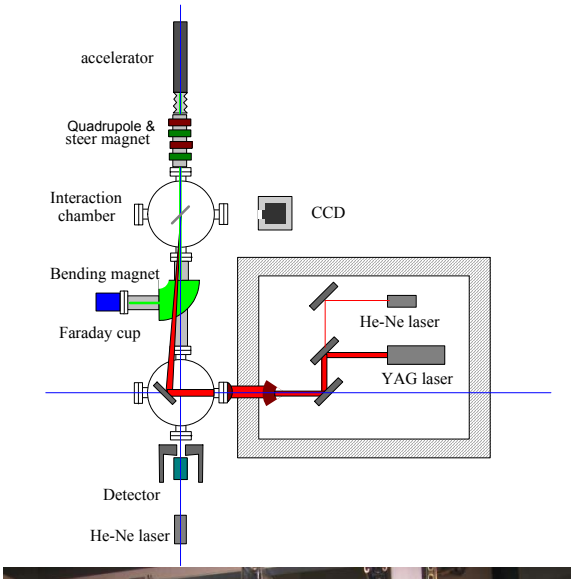

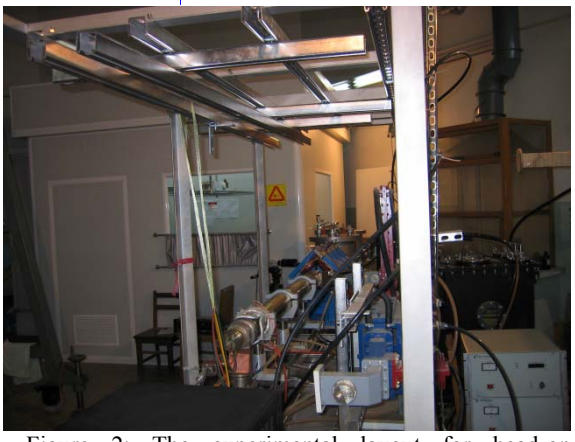

Figure 2: The experimental layout for head-on Thomson scattering

Preliminary experiments of x-ray generation through Thomson scattering are made with the backward travelling wave 16MeV electron linac[7] and the YAG laser system. The electron beams are delivered from the 2856MHz RF linac with a 4μs macrobunch duration and 35ps total microbunch duration at a repetition rate of up to 250 Hz. The YAG laser system produces ~10 ns output pulses of λ=1064 nm with an energy ~2J at a repetition rate of 10Hz. Head-on scattering geometry(177°) is adopt to get the maximum x-ray yield. Due to long duration of electron macrobunch, the need of synchronization between two beam is easily fulfilled.

The experimental layout of Thomson scattering is shown in figure 2. Laser pulses are finally focused by a mirror with a focal length of 1.5m and reflected into interaction chamber. The linac is separated with a 100μm thick titanium widow from the interaction chamber to maintain ultrahigh vacuum in the linac. The electron beams are focused by quadrupole magnets before interaction and swept off by a 45° bending magnet. The x-ray photons are detected by a CsI(Tl) scintillator that is coupled to the photomultiplier tube.

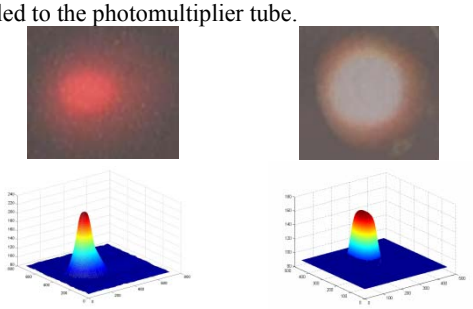

Figure 3: CCD image of electron and laser beam at interaction point(left:electron, right:laser)

Table 1: Parameters of Preliminary Thomson scattering experiments

Laser beam	
Wavelength	1064 nm
Pulse energy	2 J
Total pulse duration	~10 ns
Focal spot radius	0.5 mm
Electron beam	
Energy	16 MeV
Microbunch peak current	1.2 A
Total microbunch duration	35 ps
Macrobunch duration	4 μ s
Charge/microbunch	0.042 nC
RMS beam radius	1.25 mm
x-ray pulse	
Maximum photon energy	4.5 keV
Microbunch pulse duration	35 ps
Number of photons/microbunch	$\sim 1\times 10^3$

Due to head-on geometry and long duration of electron beam macrobunch, the laser beam will interact with several electron microbunchs, depending on the Rayleigh range of laser beam and beta function of electron beam.

This will help to increase the x-ray photon flux. Up to now, the electron beam and the laser pulse focusing have been tested at the interaction point. The focal spot of electron and laser beam at interaction point are shown in figure 3. The parameters that both laser system and linac now can provide and estimates of x-ray based on equation (4)-(5) are summarized in Table 1. Some upgrade with linac and laser system are going on. The effects of emittance, energy spread, interaction position and time mismatch of both beams are simulated by the code CAIN[8].

PROPOSAL OF A THOMSON SCATTERING X-RAY SOURCE FACILITY IN TSINGHUA UNIVERSITY

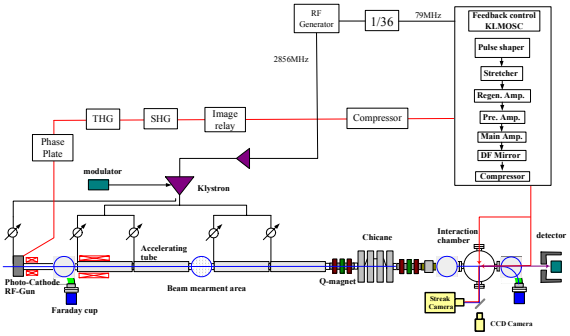

Figure 4: The schematic layout of proposed Thomson scattering x-ray source

As a next step we propose to build up a sub-picosecond hard x-ray source based on Thomson scattering between Ti:Sapphire T3 laser system and electron linac. The simplified schematic layout is shown as Figure 4. The laser pulses from oscillator are splitted into two beams after the pre-amplification: one is tripled to 266 nm after amplification to excite the photocathode RF gun; the other one is coupled into interaction chamber after chirped-pulse-amplification. The electron beam generated by the photoinjector is accelerated with four traveling wave accelerating tube up to 60~100 MeV. The electron beam from the linac is focused by quadrupole magnets and compressed by the bunch compression chicane, then interacts with laser pulse via orthogonal and head-on scattering geometry. Table 2 summarizes the design parameters of Thomson scattering x-ray source.

Table 2: Design parameters of Proposal Thomson scattering x-ray source

Laser beam	
Wavelength	800 nm
Pulse energy	500 mJ
Pulse duration	25~50 fs
Focal spot radius	~0.1 mm
Electron beam	
Energy	60~100 MeV
Bunch duration	1~10 ps
Charge/microbunch	1.0 nC
Beam radius	0.1 mm
x-ray pulse	
Photon energy	36~200 keV
Pulse duration	50~1000 fs
Number of photons	9.5×10^{5}~1.5×10^{8}

REFERENCES

[1] http:// http://www-ssrl.slac.stanford.edu/lcls/.
[2] R.W. Schoenlein, S. Chattopadhyay, H.H.W. Chong, et al., Science 287,2237 (2000).
[3] R.W. Schoenlein, W.P. Leemans, A.H. Chin et al., Science 274, 236(1996).
[4] D.J. Gibson, S.G. Anderson, P. J. Barty, et al., Phys. Plasmas, Vol. 11, No. 5, 2857(2004)
[5] W.H. Huang et al.,HEP&NP,Vol.28,No.4,446(2004) (in chinese)
[6] K.J. Kim, S. Chattopadhyay, C.V. Shank, Nucl. Instr. and Meth. A 341 (1994) 351.
[7] H.B. Chen et al, LINAC02, 623(2002).
[8] P.Chen, G. Horton-Smith, T. Ohgaki, A.W. Weidemann, and K. Yokoya, Nucl. Instr. and Meth. A 355, 107 (1995).

THE COHERENT SYNCHROTRON RADIATION INFLUENCE ON THE STORAGE RING LONGITUDINAL BEAM DYNAMICS

E.G. Bessonov*, R.M. Feshchenko, Lebedev Physical Institute RAS, Moscow, Russia
V.I. Shvedunov, Moscow state University

Abstract

We investigate influence on the storage ring beam dynamics of the coherent Synchrotron Radiation (SR) self fields produced by an electron bunch. We show that the maximum energy gain in the RF cavity must far exceed the energy loss of electrons due to the coherent SR.

INTRODUCTION

The energy ε of a particle in storage rings oscillates in the vicinity of the equilibrium energyε_s. The difference between equilibrium and nonequilibrium energies is proportional to the derivative of the particle's phase $d\varphi/dt = h(\omega_s - \omega_r)$:

$$\Delta\varepsilon = \varepsilon - \varepsilon_s = \frac{\varepsilon_s}{hK\omega_s}\frac{d\varphi}{dt}, \qquad (1)$$

where $K = -\partial \ln \omega_r/\partial \ln \varepsilon = (\alpha\gamma_s^2 - 1)/(\gamma_s^2 - 1)$ is self phasing coefficient; α, the momentum compaction factor; $\varphi = \int \omega_r(t)dt$, the particle's phase; $\gamma = \varepsilon/mc^2$, the relative energy; $\omega_r = 2\pi f$; f, the revolution frequency of a particle in the storage ring. Equilibrium values have lower index s [1-3]. The radio frequency (RF) voltage in the cavity's gap is varying as $V = V_{rf}\cos\omega_{rf}t$, where ω_{rf} is the radio frequency; h, the subharmonic number of radio frequency.

Balance of energy gained by an electron during the period of a single revolution $T = 1/f = C/c = 2\pi R(1 + \mu)/c$ in the RF cavity and lost due to synchrotron radiation and Thomson scattering defines an equation for electron phase oscillations in the storage ring:

$$\frac{d\varepsilon}{dt} = \frac{eV_{rf}\cos\varphi}{T} - < P^{rad} >, \qquad (2)$$

where $< P^{rad} >= d\varepsilon^{rad}/dt$ is the power of radiation losses averaged over the length of the orbit; C, the length of the orbit; R, the curvature radius of the particle orbit in bending magnets; $\mu = \sum_i l_i/2\pi R$, the ratio of the sum of straight intervals l_i in the storage ring to the path length in the bending magnets. The synchronous phase $\varphi_s$is defined as $d\varepsilon_s/dt = 0$ or $eV_{rf}\cos\varphi_s = \left\langle P_s^{rad}\right\rangle T$.

The spontaneous coherent SR doesn't depend on the particle energy but depends on the particle position in the longitudinal direction, the shape of the beam and on the number of particles. For the Gauss longitudinal distribution one can obtain:

$$\left\langle P_{coh}^{rad}(\varphi)\right\rangle = -\frac{3^{1/6}\Gamma^2(2/3)Ne^2c}{2^{1/3}\pi R^{2/3}\sigma_s^{4/3}(1+\mu)} *$$
$$\exp\left[-\frac{1}{2}\left(\frac{R(\varphi-\varphi_s)(1+\mu)}{h\sigma_s}\right)^2\right] *$$
$$[1 - \frac{2^{1/6}\sqrt{\pi}}{3\sqrt{3}\Gamma(2/3)}\frac{R(\varphi-\varphi_s)(1+\mu)}{h\sigma_s} -$$
$$\frac{1}{6}\left(\frac{R(\varphi-\varphi_s)(1+\mu)}{h\sigma_s}\right)^2 + \ldots]. \qquad (3)$$

It is supposed here that the phase in the center of the bunch is equal to synchronous phase φ_s, σ_s is the bunch mean square length and $\Gamma(2/3) = 1.35$ [4].

If the laser beam is homogeneous and its transversal dimensions far exceed ones of the electron beam, the powers of Thomson scattering radiation and spontaneous incoherent SR obey the simple power dependence as functions of energy$< P_{noncoh}^{rad} >=< P_{s,noncoh}^{rad} > (\varepsilon/\varepsilon_s)^{k_i}$. The difference between radiated power of synchronous and nonsynchronous particles is

$$< P_{noncoh}^{rad} > - < P_{s,noncoh}^{rad} >= \frac{d < P_{s,noncoh}^{rad} >}{d\varepsilon}\Delta\varepsilon =$$
$$k_i < P_{s,noncoh}^{rad} > \frac{\Delta\varepsilon}{\varepsilon_s}, \qquad (4)$$

where $k_i = 2$ for the Thompson backscattering, $k_i = 1$ for the Raleigh backscattering by ions and $k_i = 1 \div 1.5$ for the SR.

Subtracting the power balance equation for synchronous particles from the equation for nonsynchronous one (2) and taking into account (1), (4) we obtain equation for phase oscillations in the storage ring:

$$\frac{d^2\varphi}{dt^2} + \frac{k_i < P_{noncoh}^{rad} >}{\varepsilon_s}\frac{d\varphi}{dt} - \frac{he\omega_s^2 K}{2\pi\varepsilon_s}[V(\varphi) - V(\varphi_s)] = 0, \qquad (5)$$

where $V(\varphi) = V_{rf}\cos\varphi - 2\pi R(1+\mu)/c\left\langle P_{coh}^{rad}(\varphi)\right\rangle$. The synchronous phase is determined by the equation $U(\phi_s) = 0$.

Incoherent synchrotron radiation and Thompson scattering cause slow damping of phase oscillations (the damping time far exceeds the period of oscillations) and can be neglected in the first approximation, so equation (5) can be rewritten as:

* bessonov@x4u.lebedev.ru

$$\frac{1}{2}\frac{d}{dt}(\frac{d\varphi}{dt})^2 - \frac{he\omega_s^2 K}{2\pi\varepsilon_s}[V(\varphi) - V(\varphi_s)]\frac{d\varphi}{dt} = 0. \quad (6)$$

The first integral, determining particle phase trajectories behavior is

$$\frac{d\varphi}{dt} = \sqrt{\frac{he\omega_s^2 K}{\pi\varepsilon_s}\int [V(\varphi) - V(\varphi_s)]d\varphi}. \quad (7)$$

The coherent synchrotron radiation force acts similar to the radio frequency accelerating field. The autophasing force of the storage ring is defined by the derivative $dV(\varphi)/d\varphi$. Thus, in accordance with (5), the reaction of the coherent SR makes this force weaker. This weakening reaches maximum when the phase equals $\varphi = \varphi_s + h\sigma_s/R\,(1+\mu)$. Therefore the stability of the electron beam requires that the derivative $dV(\varphi)/d\varphi$ is negative in the interval $|\varphi - \varphi_s| < h\sigma_s/R(1+\mu)$. This phase range corresponds to the stable oscillations of the majority of particles with amplitudes $A \simeq \sigma_s$. Using the formulas for the power of the coherent SR (3) for a beam with Gauss longitudinal distribution of particles one can find:

$$V_{rf} > V_{rf,c} = \frac{2\pi R^2\,(1+\mu)^2\,P_{coh}^{rad}\,(\varphi_s)}{\sqrt{e_n}h\sigma_s}, \quad (8)$$

where $e_n \approx 2.72$ is the natural logarithm foundation. In reality the coherent SR can be neglected if the value V_{rf} is $2 \div 3$ times higher than $V_{rf,c}$ and $\sin\varphi_s \approx 1$. The maximum energy gains in the RF cavity, according to (8), must far exceed the energy loss of electrons due to the coherent SR.

If the value P_{coh}^{rad} is neglected, the equation (5) is transformed into the equation of small amplitude phase oscillations:

$$\frac{d^2\psi}{dt^2} + \frac{k_i P_{noncoh}^{rad}}{\varepsilon_s}\frac{d\psi}{dt} + \Omega^2\psi = 0, \quad (9)$$

where $\Psi = \varphi - \varphi_s << 1$ and $\Omega = \omega_s\sqrt{qhKV_{rf}\sin\varphi_s/2\pi\varepsilon_s}$.

The equation (9) has solutions that can be expressed as $\psi = \psi_m(t)\cos\Omega' t$, where $\psi_m = \psi_{m,0}\exp(-t/\tau_{ph})$ is the varying amplitude and

$$\tau_{ph} = \frac{\varepsilon_s}{P_{noncoh}^{rad}}, \quad (10)$$

the damping time, $\Omega' = \sqrt{\Omega^2 + \tau_s^{-2}}$, the frequency of small particle oscillations.

EXAMPLE

An electron storage ring has the radius R=50 cm, h=10, σ_s= 1 cm, $\mu = 1$, $N = 10^{10}$,$\sin\varphi_s \approx 1$. In this case the losses of a synchronous particle per a revolution is $V_{coh}^{rad}(\varphi_s)$= 9.25 kev, $V_{rf} > 114$ kV. Thus for the stable storage ring operation the RF cavity voltage should be much higher than the coherent radiation losses. The shielding by the vacuum chamber can weaken this requirement [5]. One should also note that the energy losses of a synchronous electron per a revolution are approximately $2^{2/3}$ times greater than average losses of electrons in the beam (see Appendix).

APPENDIX

Suppose that a beam has small angular $\Delta\theta \sim 1/\gamma$ and energy $\Delta\varepsilon/\varepsilon \sim 1/\gamma$ spread (emittance). In such a case electromagnetic fields emitted by different particles are similar to each other but have a temporal shift. The Fourier images of these fields are:$\mathbf{E}_{i,\omega} = \mathbf{E}_{1,\omega}\exp(i\Delta\varphi_i)$ i=1,2,3, ... N, where the phase difference between waves emitted by the first and the i-th particles is $\Delta\varphi = \omega(t_i' - t_1') + \mathbf{k}[\mathbf{r}(t_i') - \mathbf{r}(t_1')]$. The moments of emission t and detection t' are connected as $t = t' - R_0/c - \mathbf{nr}/c$, R_0 is the distance between the points of emission and detection, $\mathbf{k} = \omega\cdot\mathbf{n}/c$, $\mathbf{n}$ is a unit vector pointing in the direction of emission, $\mathbf{r}$ – the vector lying in the plane perpendicular to the trajectory of a particle. The time difference for ultrarelativistic particles $t_i' - t_1'$ is connected with the space distance by a simple relation $c(t_i' - t_1') = z_i - z_1$. Therefore the Fourier image of the sum of fields of N particles $\mathbf{E}_\omega = \sum_i \mathbf{E}_{i,\omega}$ can be written as (for the electrical field):

$$\mathbf{E}_\omega = N\int_{-\infty}^{\infty}\rho(z,\mathbf{r})\mathbf{E}_{1,\omega}\exp[i\Delta\varphi(z,\mathbf{r})]dzd\mathbf{r}, \quad (11)$$

where $\rho(z,\mathbf{r})$ – the density distribution of particles normalized to unity.

If the transversal dimensions of the beam are small, the integration in the equation (11) over transversal coordinate $\mathbf{r}$ can be omitted:

$$\mathbf{E}_\omega = N\cdot\mathbf{E}_{1,\omega}\int_{-\infty}^{\infty}\rho(z)\exp[i\frac{2\pi z}{\lambda}]dz. \quad (12)$$

In this case the spectra-angular distribution of the emitted energy

$$\frac{\partial^2\varepsilon^{coh}}{\partial\omega\partial o} = cR_0^2|\mathbf{E}_{1,\omega}|^2 = N^2\frac{\partial^2\varepsilon_1}{\partial\omega\partial o}s(\omega), \quad (13)$$

where ε_1 is the energy of the radiation emitted by a single particle, $s\,(\omega) = \left|\int_{-\infty}^{\infty}\rho\,(z)\exp\,[i2\pi z/\lambda]\,dz\right|^2$, the spectral radiation coherence factor, $\lambda = 2\pi c/\omega$– the wavelength of SR. The spectral energy distribution and the full emitted energy can be found by integration of (13) over angles

$$\frac{\partial\varepsilon^{coh}}{\partial\omega} = N^2\frac{\partial\varepsilon_1}{\partial\omega}s(\omega) \quad (14)$$

and over frequency

$$\varepsilon^{coh} = N^2 \int_0^\infty \frac{\partial \varepsilon_1(\omega)}{\partial \omega} \cdot s(\omega) \cdot d\omega. \qquad (15)$$

From (13) – (15) it follows that for a point-like beam $\rho(z) = \delta(z)$ and therefore $s(\omega) = 1$, $\varepsilon^{coh} = N^2 \int_0^\infty [\partial \varepsilon_1(\omega)/\partial \omega] d\omega = N^2 \varepsilon_1(\omega)$, i.e. the energy emitted by the beam is N^2 times larger than the energy emitted by a single particle.

If the beam's motion is periodical one can introduce average radiation power:$P^{coh} = f \cdot \varepsilon^{coh}$, $\partial P^{coh}/\partial \omega = f \cdot \partial \varepsilon^{coh}/\partial \omega$, $f = v/C$ – the revolution frequency, $\nu \approx c$– the particle's velocity and C is the perimeter of the orbit.

The values $\partial \varepsilon_1/\partial \omega$ and $\partial P_1/\partial \omega = f \cdot \partial \varepsilon_1/\partial \omega$ are known. In particular, the spectral power of radiation is

$$\frac{\partial P_1}{\partial \xi} = \frac{3\sqrt{3} e^2 c \gamma^4}{2RC} F(\xi), \qquad (16)$$

where $\beta = v/c$ – the relative particle velocity, $\gamma = \varepsilon/mc^2$– the relative energy, $F(\xi) = \xi \int_\xi^\infty K_{5/3}(\xi) d\xi$, $\xi = \omega/\omega_c$, $\omega_c = 3\beta\gamma^3 c/2R$ – the critical radiation frequency, R– the orbit radius in a bending magnet of the storage ring [6,7]. One can also calculate $\int_0^\infty F(\xi) d\xi = 8\pi/9\sqrt{3}$[6]. Thus the full radiation power for one particle can be expressed as:

$$P_1 = \frac{4\pi}{3} \frac{e^2 c \gamma^2}{RC}. \qquad (17)$$

In the case under consideration the radiation is coherent if the wavelength is longer than the length of the bunch i.e. $\xi << 1$, $K_{5/3}(\xi) \approx 2^{4/3} \Gamma(2/3) \xi^{-5/3}$,

$$\int_\xi^\infty K_{5/3}(\xi) d\xi = \int_0^\infty K_{5/3}(\xi) d\xi - \int_0^\xi K_{5/3}(\xi) d\xi$$

$$= \pi\sqrt{3} - \int_0^\xi K_{5/3}(\xi) d\xi, F(\xi) = 2^{2/3} \Gamma(2/3) \xi^{1/3}.$$

Now the formula (16) can be written as

$$\frac{\partial P_1}{\partial \xi} = \frac{3\sqrt{3} e^2 c \gamma^4}{2^{4/3} \pi R^2 (1+\mu)} \Gamma(\frac{2}{3}) \xi^{1/3}. \qquad (18)$$

The spectral coherence factor $s(\omega)$ is determined by the particle density distribution law $\rho(z)$ and for the Gaussian distribution

$$\rho(z) = \frac{1}{\sqrt{2\pi}\sigma_x} e^{\frac{-z^2}{2\sigma_x^2}} \qquad (19)$$

can be derived from equations (13) and (19) as $s(\omega) = \exp(-4\pi^2 \sigma_x^2/\lambda^2)$ [8,9]. The value σ_x is the mean square bunch length.

The full power of the spontaneous coherent SR, the average loss rate for a single particle and the losses over a revolution can be calculated numerically using the formula (15) and the expression $P^{coh} = f \cdot \varepsilon^{coh}$. In the special case when the coherent SR is dominated by the low frequency radiation $\xi << 1$, taking into account (18) and $\int_0^\infty k^{1/3} \exp(-k^2\sigma_x^2) dk = \Gamma(2/3)/2\sigma_x^{4/3}$, one can derive that

$$P^{coh} = c \frac{d\varepsilon^{coh}}{dt} = \frac{3^{1/6} \Gamma^2(2/3) r_e c N^2}{2\pi R^{2/3} \sigma_x^{4/3} (1+\lambda)} mc^2, \qquad (20)$$

The energy losses per a revolution are

$$\Delta\varepsilon^{coh} = \frac{d\varepsilon^{coh}}{dt} T = \frac{3^{1/6} \Gamma^2(2/3)\, r_e R^{1/3} N^2}{\sigma_x^{4/3}} mc^2$$

$$\approx 3.1 \cdot 10^{-7} R^{1/3} N^2/\sigma_x^{4/3} [eV/revolution]. \qquad (21)$$

The formula (21) matches with the results of the first work on the coherent SR [10], is $2^{1/6} \approx 1.12$ times lower than one in the reference [4] , $2^{7/3} \approx 5.04$ times lower than the value in the reference [11] and $2^{8/3} \approx 6.35$ times lower than one in the reference [12]. In the last reference the authors used formula from the work of Shiff [10] and erred in converting it to their definition of the valueσ_x. They multiplied the Shiff's formula by the $2^{4/3}$ instead of dividing by it. In the remaining references the source of errors is unclear but more probably connected with the same mistake.

The coherence factor is decreasing for the wavelengths $\lambda \geq \lambda_d = 2\pi\sigma_x$ or if $\omega \geq \omega_d = c/\sigma_x$. The expression (21) is justified if the main part of the energy of the coherent SR is emitted in the spectral range $\omega \leq \omega_d \approx \omega_c (\xi << 1)$ i.e. when $\sigma_x > \lambda_c/2\pi$, where $\lambda_c = 2\pi c/\omega_c = 4\pi R/3\gamma^3$. The expression also (21) doesn't take into consideration the shielding of the beam by the vacuum chamber, which leads to the weaker radiation for the wavelengths longer than the vacuum chamber gap.

The vast majority of the energy is emitted in the angular range $\Delta\theta \sim 1/\gamma$ relative to the direction of the particle's motion when $k \cdot r(t') << k \cdot r/\gamma$. So, the condition when one can neglect the transversal beam dimensions is $k_d \cdot r << \gamma$ or $r << (\lambda_d/2\pi)\gamma = \sigma_x \gamma$.

REFERENCES

[1] A.A. Kolomensky and A.N. Lebedev, Theory of Cyclic Accelerators. North Holland Publ., , 1966.

[2] H. Bruk, Accelerateurs Circulaires de Particules (Press Universitaires de France, 1966).

[3] C H. Wiedemann, Particle Accelerator Physics I \& II (Springer-Verlag, New York, 1993).

[4] L.V.Iogansen, M.S.Rabinovich, JETP, v.37, 118, 1959 (in Russian).

[5] J.B.Murphy, S.Krinsky, R.L.Gluckstern, Particle Accelerators, 1997, v.57, pp.9-64.

[6] D.Ivanenko, A.Sokolov, Classical Theory of field, GITTL, 1951 (in Russian).

[7] L.D.Landau, E.M.Lifshits, The classical Theory of Fields, Pergamon Press, Oxford, UK, 1975.

[8] H.Wiedemann, Particle Accelerator Physics, v.I, Springer – Verlag, NY, 1993, p.319.

[9] A.Andersson, M.Johnson, B.Nelander, Coherent synchrotron radiation in the far infrared from 1 mm electron bunch, Opt. Eng. V.39, p. 3099-3115, 2000.

[10] L.Schiff, Rev. Sci. Instr., v.17, 7, 1946.

[11] E.L.Saldin, E.A.Schneidmiller, M.V.Yurkov, TESLA FEL Report 96-14, November 1996 (corrected in Nucl. Instr. Meth. v.A398 (1997), p.373).

[12] J.S.Nodvic, D.S.Saxon, Phys. Rev., v.96, No 1, p. 180-184, 1954.

ISOCHRONOUS BEND FOR HIGH GAIN RING FEL

A.N. Matveenko, O.A. Shevchenko, N.A. Vinokurov
Budker Institute of Nuclear Physics, 11 Acad. Lavrentyev Prosp., 630090, Novosibirsk, Russia
Email:A.N.Matveenko@inp.nsk.su

Abstract

The recently proposed ring free electron laser (FEL) consists of several undulators with isochronous bends between them. Isochronous bends are necessary to preserve the beam bunching between undulators. Such FEL configuration may be used as an independent soft X-ray source or as a master oscillator for an X-ray FEL (high gain harmonic generator or other type). The lattice of the compact 500-MeV 60-degree bend for a soft X-ray (50 nm) FEL is proposed. Fundamental restrictions due to quantum fluctuations of synchrotron radiation and technically achievable fields to construct isochronous bends of a shorter wavelength ring FEL are discussed.

INTRODUCTION

A mirror-free ring Free Electron Laser (FEL) configuration consisting of several undulator sections separated by isochronous bends is considered to be a possible solution for an X-ray FEL [1, 2]. In this configuration the beam bunching grows from undulator to undulator and after a 360-degree turn radiation from the last undulator illuminates the beam in the first undulator and induces bunching in the incoming fresh beam. Such a configuration, driven by an energy recovery linac, is shown in Fig. 1.

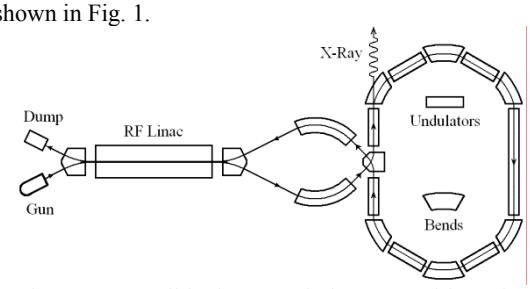

Figure 1. Possible layout of ring FEL driven by an energy recovery LINAC.

One of the critical parts of the scheme is the isochronous bend section between undulators. Their aim is to preserve the beam bunching along the ring. If we express the time delay of an electron from a reference particle moving along the design orbit in terms of the first order transport matrix *Rij* we get (planar bend is assumed)

$$c\Delta t = R_{51}x + R_{52}x' + R_{56}\frac{\Delta E}{E} \qquad (1)$$

In an isochronous bend we must make all three matrix elements in Eq. (1) equal to zero. Let $d(s)$ is the (horizontal) dispersion function with zero initial conditions at the bend entrance s = 0, s is the coordinate along the reference trajectory Then R_{52} and R_{51} are proportional to dispersion $d(L) = R_{16}$ and it's derivative $d'(L) = R_{26}$ at the bend exit $s = L$, so the bend must be achromatic in the first order. R_{56} can be expressed in terms of dispersion

$$R_{56}(0,L) \approx \int_0^L h(s)d(s)ds \qquad (2)$$

Here $h(s)$ is the orbit curvature. This matrix element can be easily made zero in a symmetric three-bend achromat.

It is worth noting, that bunching conservation in the achromatic bend for the visible wavelength range was demonstrated in [3].

In this paper we discuss two causes for bunching degradation and propose a compact 500-MeV 60-degree bend for a soft X-ray (50 nm) ring FEL. Quantum fluctuations of synchrotron radiation and second order aberrations in the lattice are taken into account. Limiting factors to construct an X-ray ring FEL are discussed further.

EFFECT OF QUANTUM FLUCTUATIONS OF SYNCHROTRON RADIATION

An electron, moving in the bending magnet, emits synchrotron radiation. In classical electrodynamics it leads to the slow change of the beam energy. But really the quantum fluctuations of radiation increase the beam energy spread. Due to the energy loss particles arrive the bend exit slightly later. If quantum nature of radiation is taken into account, the time delay spread appears*.

The delay caused by the emission of photon with energy $\varepsilon = \eta\omega$ at the point s of the trajectory and measured at the point L (exit of achromat) is

$$c\Delta t = -R_{56}(s,L)\frac{\varepsilon}{E} \qquad (3)$$

The probability of this photon emission may be expressed through the spectral power density of synchrotron radiation $dI/d\omega$

$$dp = \frac{dI}{d\omega}d\omega\frac{ds}{\varepsilon c} \qquad (4)$$

Then the square of the delay dispersion $\sigma_{c\Delta t}^2 = \left\langle (c\Delta t)^2 \right\rangle - \left\langle c\Delta t \right\rangle^2$ is the sum of contributions from different parts of the trajectory ds and frequency intervals $d\omega$

* The debunching due to quantum fluctuations was pointed out by V. N. Litvinenko.

$$\sigma_{c\Delta t}^2 = \int_0^\infty \int_0^L \left(R_{56}(s,L)\frac{\varepsilon}{E} \right)^2 \frac{dI}{d\omega}\frac{ds}{\varepsilon c} d\omega \qquad (5)$$

After the integration over frequencies it gives

$$\sigma_{c\Delta t}^2 = \frac{55}{24\sqrt{3}} \frac{r_0^2}{\alpha} \gamma^5 \int_0^L R_{56}^2(s,L) \cdot h^3(s) \cdot ds \qquad (6)$$

where r_0 is the classical electron radius, α = 1/137 is the fine-structure constant, γ is the relativistic factor. For the mirror symmetric isochronous systems $R_{56}(s,L)$=-$R_{56}(0,s)$. Then

$$\sigma_{c\Delta t}^2 = \frac{55}{24\sqrt{3}} \frac{r_0^2}{\alpha} \gamma^5 \int_0^L R_{56}^2(0,s) \cdot h^3(s) \cdot ds \qquad (7)$$

The reduction of the current Fourier harmonics at frequency $\omega = ck$ is given by the factor $\left\langle e^{i\omega\Delta t} \right\rangle$. If $k\sigma_{c\Delta t} << 1$, the current spectral density reduction after the pass through the bend may be estimated as

$$\left| \left\langle e^{ikc\Delta t} \right\rangle \right|^2 \approx \left| 1 + ik\left\langle c\Delta t \right\rangle - \frac{k^2}{2}\left\langle (c\Delta t)^2 \right\rangle \right|^2 \approx$$
$$1 - k^2 \left(\left\langle (c\Delta t)^2 \right\rangle - \left\langle c\Delta t \right\rangle^2 \right) = 1 - k^2 \sigma_{c\Delta t}^2 \qquad (8)$$

As it is seen from Eq. (8), $k\sigma_{c\Delta t} < 1$ is required to keep significant bunching after the bend.

Consider, for simplicity, a three-bend isochronous achromat. It may be shown, that the main (and uneliminable) contribution to the delay dispersion Eq. (7) is given by two side magnets. Let α_0 is the bend angle for each of these magnets, and α_0<<1. At the first magnet we have

$$R_{56}(0,s) = \frac{h^2 s^3}{6} \qquad (9)$$

and then, neglecting the contribution of the central magnet,

$$\sigma_{c\Delta t}^2 = \frac{55}{24\sqrt{3}} \frac{r_0^2}{\alpha} \gamma^5 \frac{\alpha_0^7}{126}.$$

Comparing it to $(\lambda/2\pi)^2$, we get an estimation of the maximum permissible bend angle in the system

$$\alpha_0 \sim \left(\frac{\lambda^2}{4\pi^2 r_0^2 \gamma^5} \right)^{1/7} \qquad (10)$$

It is worth noting, that this limitation does not depend on the orbit curvature h, therefore high-field superconducting magnets may be used.

If we assume the beam emittance to be a limiting factor for a short-wavelength FEL, the beam energy should be large enough, $\gamma > k\varepsilon_n$, where ε_n is the normalized beam emittance. Therefore,

$$\alpha_0 < \frac{\lambda}{2\pi} \varepsilon_n^{-5/7} r_0^{-2/7} \approx \frac{\lambda}{200\,\text{Å}} \qquad (11)$$

(ε_n=10^{-6} m·rad is taken for the estimation).

Thus, the debunching, caused by quantum fluctuations of synchrotron radiation, can be neglected for the wavelengths, larger then 200 Å. For shorter wavelengths maximal bend angle scales as λ and going deep below 100 Å can be a problem.

SHORT WAVELENGTH RING FEL ISOCHRONOUS BEND

For wavelength shorter then 100 Å the bend section can be made up of a number of isochronous bends on a smaller angle. Such a system can be thought of as a bended undulator. However, the focusing of an undulator is too weak to make its period isochronous and additional quadrupole focusing is necessary.

Total debunching in the section, consisting of N isochronous bends, is

$$(\sigma_{c\Delta t}^2)_N \sim \sigma_{c\Delta t}^2 N \qquad (12)$$

Taking N=1/α_0 for the bend section of 1 radian and comparing it to $(\lambda/2\pi)^2$ we get an estimation of the maximum permissible bend angle in the system for this case

$$\alpha_0 \sim \left(\frac{\lambda^2}{4\pi^2 r_0^2 \gamma^5} \right)^{1/6} \text{ or}$$
$$\alpha_0 < k^{-7/6} \varepsilon_n^{-5/6} r_0^{-1/3} \approx \left(\frac{\lambda}{200\,\text{Å}} \right)^{7/6} \qquad (13)$$

Making the bend angle small we can decrease the synchrotron radiation effects to a desirable level. However, the length of the bend section can become too long. The bend section total length can be estimated in the following manner. Let us denote the maximal achievable gradient of the focusing lenses G. In order to make the dispersion zero in each bend its length must be

$$l_{min} \sim 2\pi \sqrt{\frac{pc}{eG}} \qquad (14)$$

The total one-radian section length is given then by

$$L \sim l_{\min} N \sim 2\pi \sqrt{\frac{pc}{eG}} \left(\frac{4\pi^2 r_0^2 \gamma^5}{\lambda^2} \right)^{1/6} \qquad (15)$$
$$\approx \left(\frac{140\,\text{Å}}{\lambda} \right)^{5/3} m \,,$$

G = 10 kGs/cm was assumed. It is worth noting that for short wavelengths this length is much longer then the orbit curvature radius in a bending magnet, i.e. the bend section length of an X-ray ring FEL is limited by the maximal achievable field gradient.

SECOND ORDER ABERRATIONS

The finite energy spread and transverse emittances will also cause debunching. The delay longitudinal dependence for a particle is given by

$$\frac{d}{ds}c\Delta t = \frac{1}{\beta_0}\left(hx - \frac{\delta}{\gamma_0^2} - \frac{hx\delta}{\gamma_0^2} + \frac{\delta^2}{\gamma_0^2}\left(1+\frac{\beta_0^2}{2}\right) + \frac{x'^2}{2} + \frac{y'^2}{2} \right) \quad (16)$$

Here $p = p_0(1+\delta)$, and we retain only terms up to the second order in δ, x, y, and their derivatives. The first and second terms on the right are the first-order terms. Simple estimations show that the third and the fourth term contributions are negligible in comparison with the fifth and the sixth ones. These last terms give the positive contribution which can be estimated as

$$\sigma_{c\Delta t}^2 \le \frac{\varepsilon_x^2}{2}\left(\int_0^s \gamma_x(\tau)d\tau \right)^2 + \frac{\varepsilon_y^2}{2}\left(\int_0^s \gamma_y(\tau)d\tau \right)^2 \quad (17)$$

where ε_x, ε_y are the rms beam emittances, γ_x, γ_y are the Twiss parameters. This debunching can be compensated by the contribution of the first term in Eq.(16). For example, one of the second order matrix elements is

$$T_{511}(s) = \frac{1}{\beta_0}\int_0^s \left(\frac{C_x'^2}{2} + h(x\,|\,x_0^2) \right) ds' \quad (18)$$

where C_x, S_x are the basic trajectories, and $(x|x_0^2)=T_{111}$. Choosing the proper values of sextupoles one can adjust $(x|x_0^2)$ to make T_{511} zero.

ISOCHRONOUS BEND FOR 500 Å RING FEL

According to [2], the 500 Å ring FEL shall be driven by a 500MeV energy recovery LINAC. The parameters of the LINAC and the laser are shown in table 1.

Table 1. Soft X-ray ring FEL parameters.

Energy, GeV	0.5
Relative energy spread, %	0.05
Normalized rms emittance, micron	5
Peak current, kA	0.3
Undulator period, m	0.03
Undulator deflection parameter K	2
Radiation wavelength, Å	500
Undulator section length, m	12
Undulator first and last section length, m	5
Bend angle, degrees	60
Bend length, m	5

The proposed lattice of the 60° isochronous bend modeled in MAD is shown in fig.2. It consists of two 30° bending sections. Each section is essentially a symmetric isochronous three-bend achromat. Bends are proposed to be made with the field gradient in order to shorten the overall bend length. Bending sections are separated by quadruples. Sextupole correction is inserted into the negative bends of each bending section.

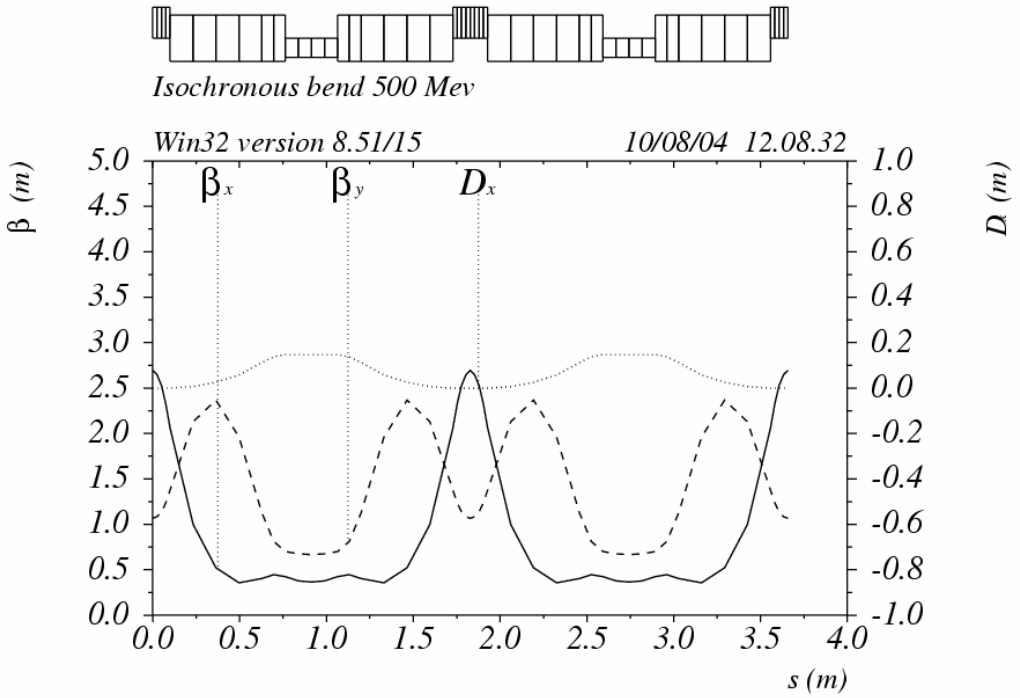

Figure 2. Linear lattice functions β_x, β_y, and D_x of the isochronous bend of the 500 Å ring FEL.

Contribution of quantum fluctuations of synchrotron radiation to the dispersion of the time of flight calculated according to Eq.(7)

$$\sigma_{c\Delta t} \sim 60\,\mathring{A} \tag{19}$$

Second order aberrations are calculated using the second order transport matrix T_{5ij} from MAD program in the following way.

$$c\Delta t^{(2)} = T_{5ij} x_i x_j \tag{20}$$

$$\sigma_{c\Delta t}^2 = \left\langle (c\Delta t)^2 \right\rangle - \left\langle c\Delta t \right\rangle^2 = T_{5ij} T_{5kl} \left(\left\langle x_i x_j x_k x_l \right\rangle - \left\langle x_i x_j \right\rangle \left\langle x_k x_l \right\rangle \right) \tag{21}$$

If we consider plane system and upright phase plane ellipses on the system entrance, the only nonzero elements remain

$$\begin{aligned} \sigma_{c\Delta t}^2 = {} & T_{511}^2 \cdot 2\beta_x^2 \varepsilon_{0x}^2 + T_{522}^2 \cdot 2\gamma_x^2 \varepsilon_{0x}^2 + T_{512}^2 \cdot 4\varepsilon_{0x}^2 + \\ & + T_{533}^2 \cdot 2\beta_y^2 \varepsilon_{0y}^2 + T_{544}^2 \cdot 2\gamma_y^2 \varepsilon_{0y}^2 + T_{534}^2 \cdot 4\varepsilon_{0y}^2 + \\ & + T_{566}^2 \cdot 2\beta_\Delta^2 \varepsilon_{0\Delta}^2 + T_{516}^2 \cdot 4\beta_x \varepsilon_{0x} \beta_\Delta \varepsilon_\Delta + T_{526}^2 \cdot 4\gamma_x \varepsilon_{0x} \beta_\Delta \varepsilon_\Delta \end{aligned} \tag{22}$$

where β, γ are the Twiss parameters at the entrance of the system, ε are the beam emittances. Indexes x, y, and Δ indicate transverse planes x and y, and longitudinal motion respectively.

For the system shown in Fig. 2.

$$\sigma_{c\Delta t} \sim 60\,\mathring{A} \tag{23}$$

Total dispersion then

$$\sigma_{c\Delta t} \sim 80\,\mathring{A} \approx \frac{\lambda}{2\pi} \tag{24}$$

CONCLUSION

The feasibility of the magnetic system for the ring FEL at the soft X-ray band is shown. Quantum fluctuations of synchrotron radiation and second order aberrations in the lattice are taken into account. The collective effects including CSR have to be considered yet.

REFERENCES

[1] N. A. Vinokurov. Nucl. Instr. and Meth. A 375 (1996), p. 264.

[2] N. A. Vinokurov and O. A. Shevchenko. Nucl. Instr. and Meth. A 528 (2004), p. 491.

[3] N.G.Gavrilov, G.N.Kulipanov, V.N.Litvinenko, I.V.Pinayev, V.M.Popik, I.G.Silvestrov, A.S.Sokolov, P.D.Vobly, and N.A. Vinokurov. IEEE J. Quantum Electron., v.27 (1991), p.2569.

[4] K.G.Steffen, High Energy Beam Optics, Interscience publishers, New York – London – Sydney, 1965.

[5] K.L.Brown, R.V.Servranckx, "First- and second-order charged particle optics", SLAC-PUB-3381

THE TWO-BEAM FREE ELECTRON LASER OSCILLATOR

N. R. Thompson, ASTeC, Daresbury Laboratory, Warrington WA4 4AD, UK*
B. W. J. M^{c}Neil, University of Strathclyde, Glasgow G4 0NG, UK

Abstract

A one-dimensional model of a free-electron laser operating simultaneously with two electron beams of different energies [1] is extended to an oscillator configuration. The electron beam energies are chosen so that an harmonic of the lower energy beam is at the fundamental radiation wavelength of the higher energy beam. Potential benefits over a single-beam free-electron laser oscillator are discussed.

INTRODUCTION

A one-dimensional model of a single pass high-gain free-electron laser operating with co-propagating electron beams of different energies has been described elsewhere [1, 2]. The resonant beam energies are chosen such that the nth harmonic radiation wavelength of the lower energy beam is at the fundamental radiation wavelength of the higher energy beam. It was suggested that this concept may have certain advantages over a single beam FEL amplifier. For example, it may be possible to seed the lower energy beam at the fundamental wavelength and use the coupled interaction between the two beams to transfer the coherence properties of the seed field to the harmonic radiation field. In this paper the model is extended to a one-dimensional steady-state oscillator configuration. Numerical studies are done of the evolution of the system and the properties of the model are explored, including the effect of different energy spreads in the higher energy beam.

THE MODEL

The evolution of the two-beam system is given by a set of coupled equations whose derivation and underlying assumptions are outlined elsewhere [1]. For convenience the working equations are repeated here in their final form, specialised to the case where $n = 3$:

$$\frac{\mathrm{d}\vartheta_j}{\mathrm{d}\bar{z}} = p_j \tag{1}$$

$$\frac{\mathrm{d}\varphi_j}{\mathrm{d}\bar{z}} = \wp_j \tag{2}$$

$$\frac{\mathrm{d}p_j}{\mathrm{d}\bar{z}} = -\frac{1}{c_1}\sum_{h,odd}^{3} F_h(A_h e^{ih\vartheta_j} + c.c.) \tag{3}$$

$$\frac{\mathrm{d}\wp_j}{\mathrm{d}\bar{z}} = -(F_1 A_3 e^{i\varphi_j} + c.c.) \tag{4}$$

$$\frac{\mathrm{d}A_1}{\mathrm{d}\bar{z}} = S_\vartheta \tag{5}$$

$$\frac{\mathrm{d}A_3}{\mathrm{d}\bar{z}} = S_\varphi + S_{3\vartheta}. \tag{6}$$

Here p and ϑ represent the energy detuning and phase of the low energy electrons and $\wp$ and φ refer to the high energy beam. For resonant beams $p = \wp = 0$. The variable $j = 1 \ldots N$ where N is the total number of sample electrons in each beam and F_1 and F_3 are the usual difference of Bessel function factors for planar wigglers. Also

$$S_{k\vartheta} \equiv \frac{1}{c_2} F_k \langle e^{-ik\vartheta} \rangle, \quad S_\varphi \equiv F_1 \langle e^{-i\varphi} \rangle \tag{7}$$

$$c_1 = \frac{\sqrt{R_3}}{3}, \quad c_2 = \frac{\sqrt{R_3}}{\sqrt{3}} \tag{8}$$

where R_3 is the ratio of currents in the high energy and low energy beams I_3/I_1.

In these equations the universal scaling is via the FEL parameter ρ_3 related to the higher energy beam. Hence the explicit appearance of the additional scaling factors R_3 and $n = 3$ via c_1 in equation (3), and via c_2 in equation (7). By changing the value of R_3 we assume the current of the lower energy beam is altered whereas that of the higher energy beam remains constant.

An important feature of the system is expressed in (6) - the harmonic field has two source terms S_φ and $S_{3\vartheta}$ which derive from the high and low energy beams respectively. This feature is exploited in the work in this paper to allow either beam to be 'switched off' by setting the appropriate source term to zero. This is useful when comparing the behaviour of the two-beam system to the behaviour with one or the other beam alone. An equivalent way of 'switching off' the lower energy beam is by setting $R_3 \gg 1$ making the low energy beam current negligibly small. From (8) and (7) it can be seen that this reduces the source term $|S_{3\vartheta}| \ll 1$.

The oscillator model is very simple. At the end of each pass the radiation intensities within the cavity are reduced by appropriate factors depending on the mirror reflectivities then used as the input intensities for the next pass. We assume mirror reflectivities r_1 and r_3 which can be varied independently for the two radiation wavelengths. We also assume that any other cavity losses are zero so that the outcoupled intensities are given by

$$|A_i|^2_{\mathrm{out}} = (1 - r_i)|A_i|^2, \quad i = 1, 3. \tag{9}$$

* n.r.thompson@dl.ac.uk

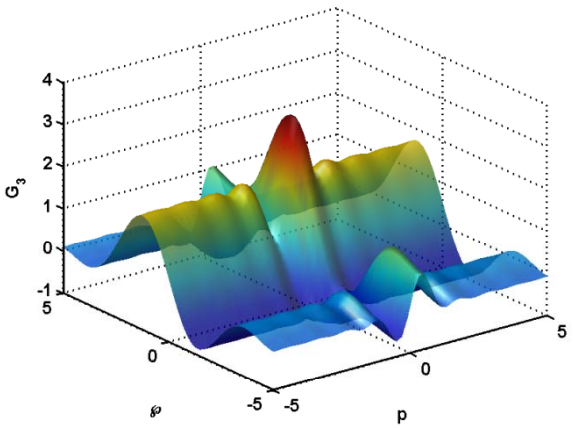

Figure 1: Both beams: third harmonic gain G_3 as a function of beam detunings in p and $\wp$. The current ratio R_3=5, so that the lower energy beam has one fifth the current of the higher energy beam: $G_{3,\mathrm{peak}} \approx 3.1$.

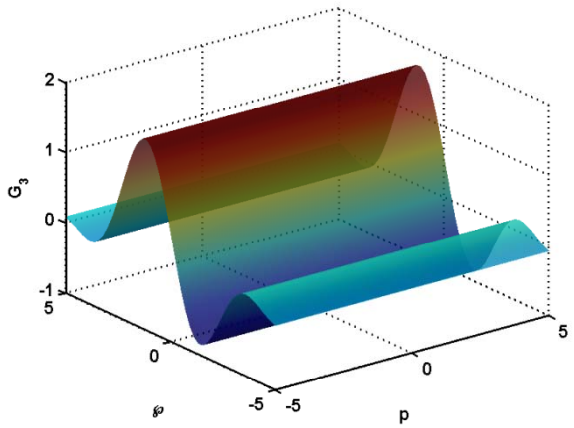

Figure 2: Low energy beam 'switched off': third harmonic gain G_3 as a function of detunings in p and $\wp$. There is now no p-dependence as expected. $G_{3,\mathrm{peak}} \approx 1.7$.

NUMERICAL METHODS

The system equations (2–6) were solved numerically using MATLAB and Fortran codes. The MATLAB code used a variable step size intrinsic integration method and the Fortran code used the standard fixed step size 4th-order Runge-Kutta method. The codes were benchmarked against each other and agreed well.

NUMERICAL INVESTIGATIONS

In a high-gain 2-beam amplifier, and assuming cold, resonant beams, linear analysis gives a threshold condition in the beam currents for the harmonic gain to be greater than that of the fundamental [1]:

$$R_3 > 3\sqrt{3}\left(1 - \frac{3\,|F_3|^2}{|F_1|^2}\right). \qquad (10)$$

Here this gives the condition $R_3 > 2.13$ for the chosen wiggler parameter a_w=2. Although an intermediate gain of $\bar{z} = 2$ is assumed, and therefore the system is not high-gain, a current ratio of $R_3 = 5$ was chosen and this is subsequently shown in the following section to similarly result in a greater gain in the harmonic field than the fundamental.

Model Optimisation

The optimum beam detunings, $p(\bar{z} = 0)$ and $\wp(\bar{z} = 0)$, were determined by a numerical scan of the single pass gain at the third harmonic G_3. The result is shown in Fig. 1 where the peak gain is ≈ 3.1 (310%) at $(p, \wp) \approx (0.4, 1.2)$. For comparison the scan was repeated for the high energy beam only (Fig. 2), where the peak gain was found to be $\approx$ 1.7, and the low energy beam only (Fig. 3) where the peak gain was found to be ≈ 0.9.

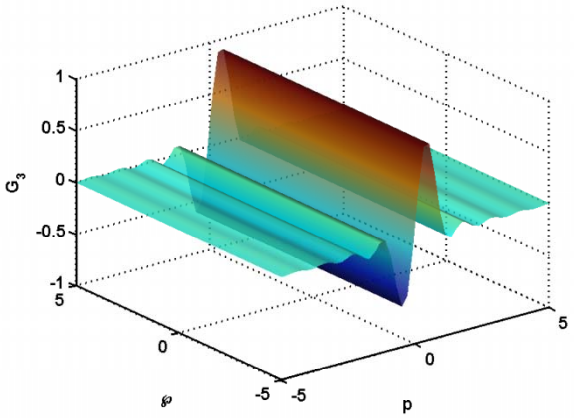

Figure 3: High energy beam 'switched off': third harmonic gain G_3 as a function of beam detunings in p and $\wp$. There is now no $\wp$-dependence. $G_{3,\mathrm{peak}} \approx 0.89$.

The gain for the two-beam system is greater than the sum of the gains due to the individual beams, even though the current in the lower energy beam is only one fifth the current in the higher energy beam. A similar scan was carried out for $\bar{z} = 0.5$ and it was found that in this linear small signal gain regime the gain for the two-beam system was the sum of the individual gains. The small enhancement in the nonlinear ($\bar{z} = 2$) regime is due to the non-linear coupling between the two beams, there being no such coupling in the small signal/small gain regime.

It is clear from Fig. 1 that the gain is sensitive to the relative detuning between the two beams. Away from the maximum at $(p, \wp) \approx (0.4, 1.2)$ the coupling decreases and the surface evolves into a Madey gain curve as a function of the low energy beam detuning p and a more asymmetric higher gain curve as a function of the higher energy beam detuning $\wp$. These curves are seen more clearly in Fig. 2

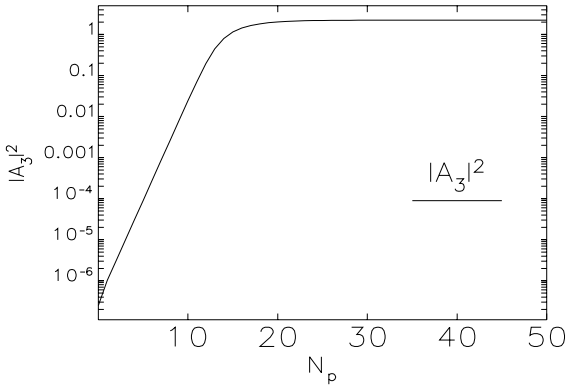

Figure 4: Evolution of harmonic radiation field intensity $|A_3|^2$. Current ratio $R_3 = 5$, $\bar{z} = 2$.

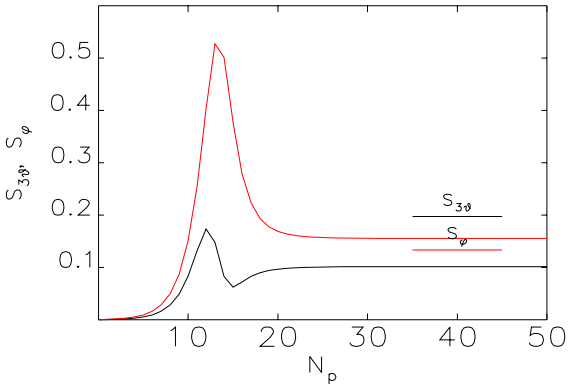

Figure 5: Evolution of harmonic radiation field source terms S_φ and $S_{3\vartheta}$. Current ratio $R_3 = 5$, $\bar{z} = 2$.

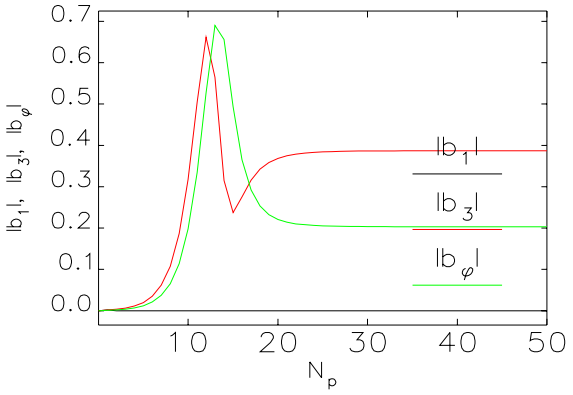

Figure 6: Evolution of electron beam bunching parameters $|b_1|$, $|b_3|$ and $|b_\varphi|$. Current ratio $R_3 = 5$, $\bar{z} = 2$.

and Fig. 3 where the low and high energy beams respectively are 'switched off'.

The mirror reflectivities r_1 and r_3 were optimised via numerical scans to maximise the saturation intensity of the third harmonic, $|A_3|^2_{\rm sat}$.

The optimum reflectivity at the fundamental was found to be $r_1 < 0.45$, i.e. below threshold for the fundamental ($G_1 <$ cavity losses). Thus bunching of the lower energy beam at the fundamental disrupts its coupling to the harmonic field.

The optimum reflectivity for the harmonic was determined to be $r_3 \approx 0.7$.

For all further simulations the following values were therefore adopted: $r_1 = 0.0$, $r_3 = 0.7$. Thus the fundamental resonant field of the lower energy beam A_1 is not stored in the cavity and so has little effect upon the coupled interaction.

NUMERICAL EXAMPLES

A two-beam oscillator FEL with the above optimised parameters was simulated. A minimal gaussian energy spread of $\sigma_p = \sigma_\wp = 0.1$ was assumed. Fig. 4 shows the evolution of the harmonic output intensity over 50 passes. The fundamental shows no growth due to the zero reflectivity at that wavelength and so is not shown. The harmonic field saturates after around 20 passes. The steepest growth in the harmonic field (i.e. the maximum increase in intensity over a single pass) occurs around pass 12. It can be seen from Fig. 5 and Fig. 6 that this coincides with peaks in the evolution of the source terms S_φ and $S_{3\vartheta}$ and peaks in the bunching terms $|b_3|$ and $|b_\varphi|$. These latter terms are measures of the bunching in the lower energy beam at its third harmonic wavelength and in the higher energy beam at its fundamental wavelength. The harmonic radiation field is clearly being driven here by both electron beams with the lower current, lower energy beam being the dominant contribution. The simulation was repeated twice more, each time with one of the beams 'switched off'. For the low energy beam only the source term is $S_{3\vartheta}$, the other source term S_φ having been set to zero, and *vice versa* for the case of the high energy beam only. The total source terms for the three cases are shown in Fig. 7. It is seen that for the coupled interaction the source term of the harmonic field is significantly greater than for either of the two beams individually.

EFFECT OF ENERGY SPREAD

The equations (2–6) were solved numerically with the same parameters as before, but now with a variation in the higher energy beam energy spread $\sigma_\wp$. This was done both for the case of the higher energy beam alone (by setting $R_3 = 1000$) and for the coupled two-beam oscillator, with $R_3 = 5$ as before. The results are shown in Fig. 8 and Fig. 9 respectively. The significance of the results is illustrated by considering first the performance due to the single electron beam, and then the change in performance by adding a lower energy beam of one fifth the current. For a minimal energy spread in the higher beam, $\sigma_\wp = 0.1$, the saturation intensity $|A_3|^2_{\rm sat}$ is increased by 18% from 1.9 to

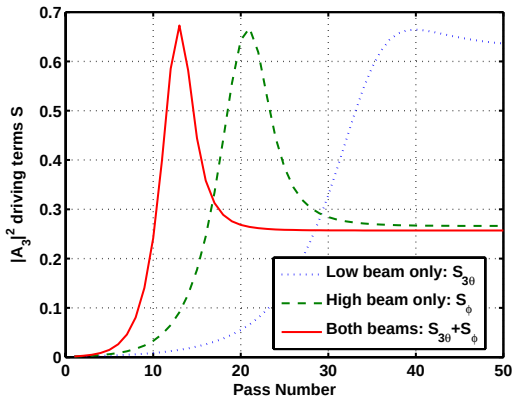

Figure 7: Source terms for the two beam oscillator and for the low energy and high energy beams individually.

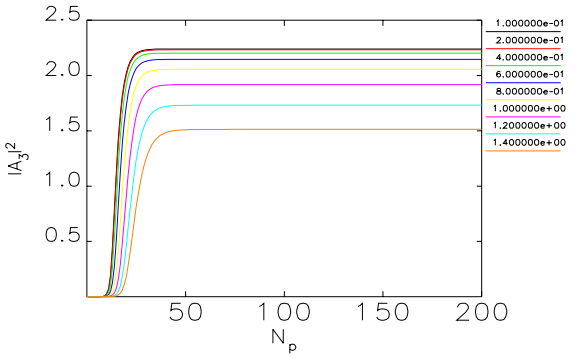

Figure 8: Evolution of the harmonic intensity in the two-beam oscillator for varying gaussian energy spreads $\sigma_{\wp}$ in the higher energy beam.

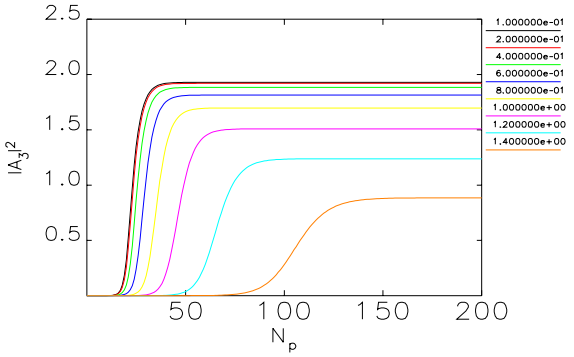

Figure 9: Evolution of the harmonic intensity with the lower energy beam switched off, for varying gaussian energy spreads $\sigma_{\wp}$ in the higher energy beam.

		$\sigma_{\wp} = 0.1$	$\sigma_{\wp} = 1.4$
$\|A_3\|^2_{\rm sat}$	High beam only	1.9	0.8
	Two beams	2.25	1.5
	Increase	18%	87%
$N_{\rm sat}$	High beam only	50	150
	Two beams	30	50
	Decrease	40%	66%

Table 1: Changes in saturation intensity $|A_3|^2_{\rm sat}$and saturation time $N_{\rm sat}$ due to the introduction of a lower energy beam of one fifth the current, for different energy spreads $\sigma_{\wp}$ in the higher energy beam.

2.25 and the number of passes to saturation, $N_{\rm sat}$, reduced by 40% from 50 passes to 30 passes. However as the energy spread in the higher beam is increased the effect of adding the lower energy beam becomes more significant—for $\sigma_{\wp} = 1.4$ the saturation intensity $|A_3|^2_{\rm sat}$ is increased by 87% from 0.8 to 1.5 and $N_{\rm sat}$ reduced by 66% from 150 passes to only 50 passes. These figures are summarised in Table 1.

These preliminary results examining the effect of energy spread in the higher energy beam deserve more study but give an initial indication of the the potential benefit of adding a smaller current, lower energy beam to the higher energy beam.

CONCLUSION

A model of a one-dimensional two-beam oscillator free-electron laser has been presented and investigated numerically in the steady-state regime for the case where the current in the lower energy beam is one-fifth of the current in the higher energy beam. It has been seen that in the mildly nonlinear regime of $\bar{z} = 2$ considered here, the gain of the coupled two-beam system is enhanced slightly over that obtained from a summation of the gains obtained from the individual beam interactions. It is seen that in the amplification phase before saturation the increase in intensity of the third harmonic is driven by both electron beams simultaneously. The effect of energy spread in the higher energy beam has been investigated and there is evidence that a two-beam oscillator may allow for a reduction in the beam quality requirements.

Further analysis is required over a wider range of the multi-parameter space defining the system before any definitive statements can be made as to whether the two-beam FEL oscillator offers real prospects of improvement over that available from a single beam interaction only.

REFERENCES

[1] B. W. J. McNeil, M.W. Poole and G.R.M. Robb, these proceedings.

[2] B. W. J. McNeil, G. R. M. Robb and M.W. Poole , Phys. Rev. E (in press)

HARMONIC CASCADE FEL DESIGNS FOR LUX, A FACILTY FOR ULTRAFAST X-RAY SCIENCE*

J. Corlett, W. Fawley†, G. Penn, W. Wan, and A. Zholents, LBNL, Berkeley, CA 94720-8211, USA
M. Reinsch and J. Wurtele, Univ. Calif. Berkeley, Berkeley, CA 94720, USA

Abstract

LUX is a design study to develop concepts for future ultrafast x-ray facilities. Presently, LUX is based on an electron beam accelerated to ∼3-GeV energy in a superconducting, recirculating linac. Included in the design are multiple free-electron laser (FEL) beamlines which use the harmonic cascade approach to produce coherent XUV & soft X-ray emission beginning with a strong input seed at ∼200-nm wavelength obtained from a "conventional" laser. Each cascade module generally operates in the low-gain regime and is composed of a radiator together with a modulator section, separated by a magnetic chicane. The chicane temporally delays the electron beam pulse in order that a "virgin" pulse region (with undegraded energy spread) be brought into synchronism with the radiation pulse. For a given cascade, the output photon energy can be selected over a wide range by varying the seed laser wavelength and the field strength in the undulators. We present numerical simulation results, as well as those from analytical models, to examine certain aspects of the predicted FEL performance. We also discuss lattice considerations pertinent to harmonic cascade FELs, somesensitivity studies and requirements on the undulator alignment, and temporal pulse evolution initiated by short input radiation seeds.

INTRODUCTION

In the past decade, there has been an increasingly strong interest in developing intense sources of tunable, coherent radiation at extreme ultraviolet and soft x-ray wavelengths. While much of this effort has been concentrated upon SASE-based FEL's, there is an alternative "harmonic cascade" FEL approach [1][2] which begins with a temporally and transversely coherent input signal from a "conventional" laser in the ultraviolet region (*e.g.* $\lambda_{in} \sim 240\,\mathrm{nm}$). This input is then effectively frequency-upshifted via resonant electron-radiation interaction in a series of FEL undulators to produce a short wavelength (*e.g.* $\lambda_f \sim 1$ nm) final signal with excellent transverse and temporal coherence.

LUX is a design study underway at LBNL to develop concepts for future ultrafast x-ray facilities with emphasis on parameters complementary to SASE-based projects. Concepts have been developed for an integrated system of ultrafast x-ray techniques and lasers, using laser-seeded harmonic cascade FEL's, rf- and laser-based electron-bunch manipulation, x-ray compression, high-brightness high-repetition rate electron sources, and with timing and synchronization systems as fundamental elements. This paper follows on previous conference contributions [3][4] which have given details of possible cascade layouts together with expected performance and sensitivity to various e-beam and input laser parameters. Here we want to present some additional work that has been performed at LBNL on the LUX concept such as an analytic model for cascade performance, a design for an isochronous bend which would preserve microbunching exiting a modulator at short wavelength scales, some results concerning sensitivity to undulator alignment and tilt, and the temporal evolution of a short input pulse.

ANALYTICAL RESULTS FOR CASCADE PERFORMANCE

An analytic theory for seeded beams (please see [5] for much greater detail) has been developed which allows for the rapid numerical evaluation and optimization power output in low gain harmonic cascades. A key *ansatz* of the theory holds that the "preferred" output mode from the radiator is that which maximizes the output power for a given set of undulator and modulated electron beam parameters. For the first stage, when seeded by a radially-large external laser, the theory predicts that the optimal power output, P, from the radiator scales at wavelength λ as

$$P \approx 4.12\, Z_0\, I^2 N_U\, \zeta\, [J_0(\zeta) - J_1(\zeta)]^2\, J_n^2(j'_{n,1}) \times F_\gamma^2\left(\frac{j'_{n,1}\sigma_\gamma}{\Delta\gamma_M}\right)\left(1 + 4\,\frac{\beta}{L}\frac{\varepsilon_N/\gamma}{\lambda/4\pi}\right)^{-1} . \quad (1)$$

Here, $Z_0 = 377\,\Omega$, I and ε_N are the beam current and normalized emittance, respectively, N_U is the number of radiator undulator periods, n is the harmonic number, $\zeta \equiv a_U^2/2(1+a_U^2)$, $j'_{n,1}$ is the first zero of the derivative of J_n, $\Delta\gamma_M$ is the energy modulation produced by the upstream modulator, and the function F depends on the energy distribution and decreases with increasing argument. At this optimum, the Rayleigh length will be $Z_R \approx 0.15L + 2\pi\sigma_e^2/\lambda$, where L is the radiator length and σ_e is the electron beam size. Quantitative comparison of the analytic theory predictions (as evaluated via a Mathematica script) with numerical simulations with the GENESIS code show agreement of 20% or better for LUX cascade parameters. Consequently, we believe that the above

* Work supported in part by the Office of Science, U.S. Dept. of Energy under Contract DE-AC03-76SF0098
† WMFawley@lbl.gov

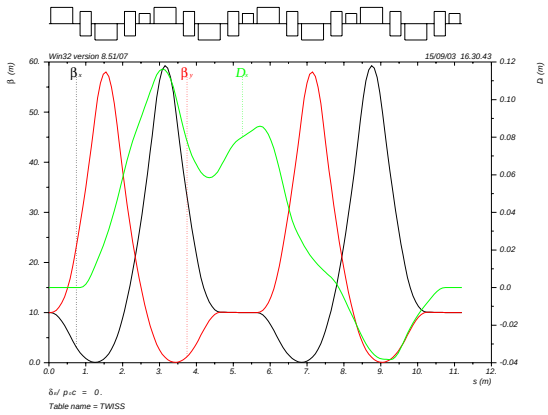

Figure 1: Plots of the bend lattice functions

mentioned ansatz has been confirmed, at least in the LUX operational regime.

BEND SECTION DESIGN

The present design of LUX ([3, 6, 7, 8]) has included the option of bending the electron beam immediately following the exit of each modulator. The purpose here was to allow easy access to the radiation beam for experimentalists. However, various colleagues have raised the issue as to whether it is possible to design a bend which would retain the microbunching (and especially that at the higher harmonic wanted for good radiator output) without undue degradation. In the past year we have examined in detail a bending section design to satisfy these concerns.

Type	Length (cm)	Field at 1.5 cm (kG)
Bend (B1)	30	12.7375
Bend (B2)	30	-6.6243
Quad (QF)	60	-2.5513
Quad (QD)	60	2.5423
Sextupole (S1)	60	0.7297
Sextupole (S2)	60	1.5768
Sextupole (S3)	30	-3.6514

Table 1: List of magnets (trims not included), along with their lengths and strengths

First of all, the microbunching length scale of 1 nm is at least an order of magnitude shorter than that examined in any previous study ([9, 10]). There is no doubt that all second order aberrations in time-of-flight will need to be corrected. It remains to be seen whether higher order aberrations are small enough to be effectively ignored. One efficient way of achieving this goal is to take full advantage of the four cell achromat first systematically studied and applied in realistic design by K. Brown ([11]). The basic result of that work was that a beamline is an achromat if it consists of 4 identical FODO cells with 90 degree phase advance in both planes. To the first order, time-of-flight depends on momentum only ($R_{56} \neq 0$). If 2 families of sextupoles are added to correct chromaticity, to the second order, the time-of-flight depends on momentum only ($T_{566} \neq 0$). To maintain bunch structure at the 1 nm level, both R_{56} and T_{566} have to be under control, which means that one extra knob each on the first and second order optics. It is certain that at 2.5 GeV, the knob to adjust T_{566} has to be a sextupole. Yet there are at least two options to cancel and adjust R_{56}. To cancel R_{56}, or to make R_{56} very small, which is the case here, either negative dispersion has to be created or reverse bends must be used. Generally speaking, using reverse bends requires weaker quadrupoles. It was found that third order aberrations are too large if negative dispersion is used to cancel R_{56}. To adjust R_{56}, one option is to use an additional family of quads; this was not adopted due to the concern of the cost and the length of the beamline. Instead, the scheme used here is the redistribution of bending (keeping the total bending angle fixed). As a result, the bending section consists of 4 identical cells. Each cell contains 2 dipole, 2 quadrupole and 3 sextupole magnets. The total bending angle of the beamline is 5 degrees. It turns out that, at sub-micron level, adjusting R_{56} does not affect focusing, making it an independent knob. To shorten the length further, two families of sextupoles are placed inside the quads. The spacing between magnets is 10 cm, except that, after each quad, an extra 10 cm is reserved for BPM and correct/skew quad coils. The key parameters of all main magnets are listed in Table 1 and the lattice functions are shown in Fig. 1.

Preliminary tracking study for the last section (λ=1 nm) has been done to evaluate the performance of the beamline. The initial distribution of electrons was taken directly from a *GINGER* [12] FEL simulation of the LUX harmonic cascade through to the end of the 4-nm modulator. The energy of the electron beam was 2.5 GeV, the normalized transverse emittance (round beam) is 3π mm-mrad and the peak to peak energy modulation is 5 MeV. First, the effect of the remaining aberrations beyond the second order is examined, with fringe field included. The result is that there is no net change in the bunch length.

The effect of errors is simulated through a computer-generated random Gaussian distribution. Up to now, only static errors have been included, which are the setting errors of the dipoles, quadrupoles and sextupoles, the sextupole component in dipoles and quadrupoles, tilt and misalignment of quadrupoles and sextupoles. In order to ensure success in operation, dipole, quadrupole (normal and skew) and sextupole correctors are included in the design. Trim coils are envisioned in each quad and two families of sextupoles that are inside the quads. A 10-cm slot downstream of each quad is reserved for a BPM and a set of dipole corrector/skew quad coils. The currents of the main dipoles are used to restore R_{56} to the optimal value. Specifically, there are 8 horizontal dipole correctors and 8 vertical correctors, all of which are individually powered. The trim

quads, skew quads and trim sextupole are grouped into 2 families. In one family, the elements are powered symmetrically about the midpoint of the beamline and, in the other family, they are powered anti-symmetrically. The two currents of the main dipoles are grouped into one family, keeping the difference fixed, hence the total bending angle unchanged. The conclusion is that, with typical errors in accelerators, bunch compression can be restored when trim quads, skew quads, and trim sextupoles are turned on and the dipole correctors are off. Without orbit correction, both trim and skew quads must be energized to maintain the short bunches. On the other hand, practical implementation remains an outstanding issue. A practical scheme is yet to be developed to tune up the beamline and maintain stable operating conditions over time.

UNDULATOR MISALIGNMENT SENSITIVITY

We have conducted a survey study of the sensitivity of radiator output to undulator misalignments and tilts using the *GENESIS* [13] simulation code. For wavelengths as short at 1 nm, offsets of up to 10 microns do not lower the output power by more than 15%. For 20-micron offsets, at 2- and 1-nm wavelengths the power drops by 25% and 40%, respectively. Offsets of 40 mcirons essentially eliminate the power at the shortest wavelengths and reduce it by 40% at 10-nm. Simple angular tilts of up to 2 μrad do not appreciably reduce the output whereas there is a $\approx$40% loss for a 4-μrad tilt; increasing the tilt to 8 μrad essentially turns off the device at wavelengths 2.0-nm and shorter. These results suggest reasonably careful (but not absurdly intricate) alignment will be necessary for operation below 10-nm wavelength.

SHORT PULSE EVOLUTION

Some user applications may require output radiation pulse durations much shorter than the nominal $\approx$ 200 fs adopted in our sample design for LUX. For a *high gain* FEL cascade initiated with a Gaussian temporal profile, Saldin *et al.*[14] have predicted that the rms radiation pulse duration will tend to shrink by a factor $\sqrt{M}$ from one stage to the next where M is the harmonic ratio between the modulator resonant wavelength and that of the radiator immediately downstream. A high power, low gain design cascade is less sensitive to input power variations and one therefore expects less shrinkage. Moreover, in the extreme limit where the radiation pulse duration is quite short, one expects that slippage effects will place a lower limit on the output pulse duration from each stage.

To study these phenomena, we initiated a LUX cascade with a Gaussian temporal profile seed pulse with σ_t =5 fs (11.2-fs FWHM) and examined the downstream $P(t)$. *GINGER* simulations were done in full time-dependent mode and included shot noise effects. In order to obtain sufficient energy modulation in the first stage, the peak input power was increased to 2.5 GW from the nominal time-steady value of 1.0 GW. Figure 2 shows the temporal output power profiles from each radiator stage. The FWHM temporal duration first increases to $\approx$15 fs at λ=48 nm, presumably because τ_{slip}=24 fs, but then shrinks back to a nearly constant $\approx$11 fs in the next 3 stages, in strong contrast to the scaling observed in [14]. Since the slippage is less than 3 fs in the 4- and 1-nm stages, the lack of additional pulse shrinkage must be due the design features of a low gain, high power configuration. Some noise modulation appears on the 1-nm output $P(t)$ but the pulse remains nearly completely temporally coherent.

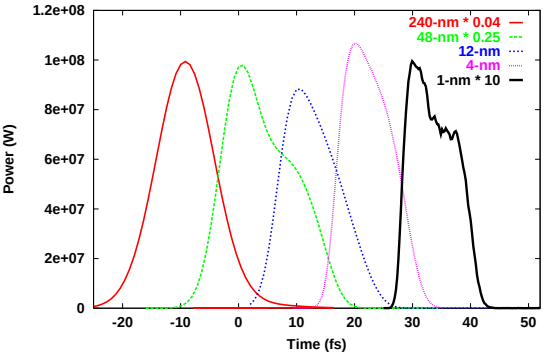

Figure 2: Predicted $P(t)$ profiles at different stages for a LUX cascade initiated with a Gaussian profile pulse with a 5-fs RMS duration. Each curve has been scaled by the indicated factor to fit on the plot.

REFERENCES

[1] L.H. Yu, *Phys. Rev. A*, **44**, 5178 (1991).

[2] R. Bonifacio *et al.*, *Nucl. Inst. Meth. A*, **296**, 787 (1990).

[3] W.M. Fawley *et al.*, *Proc. 2003 Particle Accel. Conf.*, **IEEE 03CH37423**, 923 (2003).

[4] G. Penn *et al.*, *EPAC2004*, Paper MOPKF074 (2004).

[5] G. Penn, J. Wurtele and M. Reinsch, "Analytic Model of harmonic Generation in the Low-Gain FEL Regime", Paper MOPOS57, these proceedings.

[6] J. Corlett *et al.*, LBNL report LBNL-51766 (2002).

[7] J. Corlett *et al.*, *Proc. 2003 Particle Accel. Conf.*, **IEEE 03CH37423**, 186 (2003).

[8] A. A. Zholents *et al.*, *Beam Transport Lattice in a Cascaded Harmonic FEL* LBNL CBP Tech Note-281 (2003).

[9] S. Chattopadyay *et al.*, LBNL report LBNL-39788 (1997).

[10] A. Zholents, M. Zolotorev and W. Wan, *Proc. 2001 Particle Accel. Conf.*, **IEEE 01CH37268**, 723 (2001).

[11] K. L. Brown, *IEEE Trans. Nucl. Sci.*, **NS-26**, 3490 (1979).

[12] W.M. Fawley, LBNL report LBNL-49625 (2002).

[13] S. Reiche, *Nucl. Inst. Meth. A*, **429**, 243 (1999).

[14] E.L. Saldin, E.A. Schneidmiller, and M.V. Yurkov, *Opt. Comm.*, **202**, 169 (2002).

NOVEL METHOD FOR PHASE-SPACE TOMOGRAPHY OF RAPIDLY EVOLVING E-BEAMS

K. Chalut, Duke University, Department of Physics, Durham, NC 27708, U.S.A,
V.N. Litvinenko, I.V. Pinayev, Brookhaven National Laboratory, Upton, NY 11973, U.S.A.

Abstract

In this paper, we describe a new method for phase-space tomography. This method allows one to restore phase space density using a small number of projections covering a limited angle of rotation or another linear transformation in the phase space. Practical applications of this method for phase-space tomography are discussed.

INTRODUCTION

Traditional methods of phase-space tomography, such as the Radon transform, require multiple, evenly spaced projections of exactly a 180° rotation angle in the phase-space in order to reconstruct a frozen picture [1]. It means that reconstruction of the longitudinal phase space of the e-beam with Radon transforms require the evolution of the e-beam to be slow (adiabatic) on the time scale of synchrotron oscillations. Radon transforms also apply only to rotations, i.e. to a very small sub-group of linear transformations and projections used in accelerator physics and, generally, in imaging.

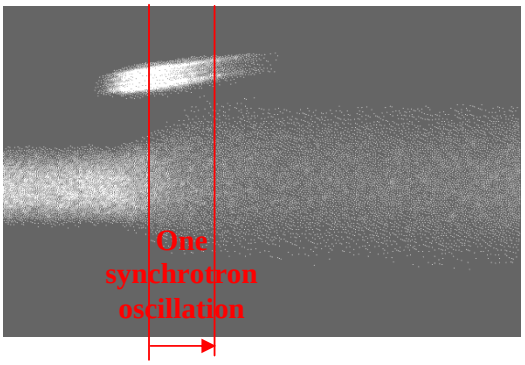

Figure 1: Dual-sweep streak camera image of giant pulse. The camera recorded the time structure of the intensity of the light generated by the e-beam on multiple turns. The vertical sweep, which is synchronized with the revolution of the e-beam, is fast and has the full scale of 1.6 nsec. The horizontal sweep is slow and has the full scale of 500 μsec. The trace seen at top is the FEL light. The main image is that of the spontaneous radiation of electron beam, which is identical to the beam time profile.

In the giant pulse process in a storage ring FEL [2], the electron beam evolves dramatically and its energy spread increases by up to a factor of three within one synchrotron oscillation. For the giant pulse process, and other processes that evolve quickly, a new method of reconstruction is needed. We investigate two new methods of reconstruction that are not limited by observation angle, and work for any linear process, not just rotation. The only requirement is that we have some known set of linear projections.

METHOD DESCRIPTION

Projection matrix

Suppose we have an arbitrary distribution of particles $F(\vec{X}_n,\vec{P}_n)$ in an N^D phase space (*D* is its dimension), described by its spatial $(\vec{X})$ and momentum $(\vec{P})$ coordinates, it follows that there is a projection operator $\hat{P}(\alpha)$ which, when acting upon the distribution, will give us a set of linear projections (images) $I(\vec{x}_m,\alpha)$ where

$$I(\vec{x}_m,\alpha)=\hat{P}(\alpha)\otimes F(\vec{X}_n,\vec{P}_n). \qquad (1)$$

$\vec{x}_m$ is the sub-set of spatial coordinates in the projection (image) space. Typical projection space used for imaging beam of charged particles has one or two dimensions. The projection matrix depends only upon the parameter α, which we use to identify projection.

In our specific example we used a dual sweep streak camera (hence one dimensional images) for reconstruction of an evolution of electron beam density (*F*) in longitudinal phase space (two dimensions). But the method is applicable of any process with linear transformations and projections [3].

The longitudinal phase space of electron beam in a storage ring can described by two dimensionless coordinates $\varepsilon=(E-E_0)/\sigma_{E0}$ and $\zeta=(t-t_0)/\sigma_{t0}$, where *E* and *t* are the energy and arrival time of an electron, E_o and t_o are, respectively, the energy and time of the synchronous electron, σ_{E0} and σ_{t0} are corresponding RMS spreads of a stationary beam. Electron bunches under study are very short and the unperturbed motions of electrons in the longitudinal phase space can be presented as a simple rotation in which the angle is the synchrotron phase advance φ:

$$\begin{bmatrix}\varepsilon\\ \zeta\end{bmatrix}_n=\begin{bmatrix}\cos\varphi_n & \sin\varphi_n\\ -\sin\varphi_n & \cos\varphi_n\end{bmatrix}\cdot\begin{bmatrix}\varepsilon\\ \zeta\end{bmatrix}_o;\varphi_n=n\cdot 2\pi Q_s \quad (2)$$

where $Q_s << 1$ is synchrotron tune [4] and *n* is the turn number. The rotation causes a transformation of the phase space density governed by the Liouville theorem:

$$F_n(\zeta,\varepsilon)=F_0(\zeta\cdot\cos\varphi_n-\varepsilon\cdot\sin\varphi_n,\varepsilon\cdot\cos\varphi_n+\zeta\cdot\sin\varphi_n) \quad (3)$$

At each turn of the e-beam around the ring the dual sweep streak camera records the time profile of the beam, i.e. the projection of the phase space density F(E,ζ) onto the time coordinate:

$$I(\zeta\cdot\sigma_{to})_{\varphi}=P(\varphi)\otimes F_o(\zeta,\varepsilon)=\int_{-\infty}^{\infty}F(t/\sigma_{to},\varepsilon)\cdot d\varepsilon= \int_{-\infty}^{\infty}F_o(\zeta\cdot\cos\varphi_n-\varepsilon\cdot\sin\varphi_n,\varepsilon\cdot\cos\varphi_n+\zeta\cdot\sin\varphi_n)\cdot d\varepsilon \quad (4)$$

Hence in our case the projection operator is completely defined by the synchrotron phase φ. This is still a description using continuous functions and coordinates. To make the problem computer friendly we must translate this problem into arrays and bits of information. Let's consider that we have a distribution function defined on an *N x N* grid in the phase space, $F=[F_{ij}]$. Our goal is now to find a way to extract information about the array F from the finite number of projections.

We get our full set of linear projections from a dual-sweep streak camera [5], which captures the synchrotron light from the electrons. A CCD camera digitizes the images from the streak camera. Let's select a sub-set of *J* projections (along vertical lines in Fig. 1), which cover a small portion of a synchrotron period, and use *M* pixels from each image. The information contained in these projections has $J \times M$ bits. As long as $J \times M > N^2$ we have a chance to extract the information about the distribution function $F=[f_{ij}]$.

The matrix form of equation (1) takes following form:

$$[I]_u=[P]_{u,v}\cdot[F]_v;\quad u=N^{2D};v=M\cdot J \quad (5)$$

where array *I* is a combination of ordered J projections, *F* is the array of ordered F_{ij}, and ***P*** is the projection matrix, specific appearance of which we define later. In the case of the giant pulse process in a storage ring FEL, the relevant parameter for the projection matrix is the synchrotron phase, and knowing the synchrotron frequency and the time of each projection provides us with that knowledge.

The problem is now reduced to a robust way of solving equation (1) and finding F with reasonable accuracy. The projection matrices are typically very large, non-square and singular, which makes singular value decomposition (SVD) method a natural choice for solving equation (1).

SVD

There is a wealth of information concerning SVD (see for instance [6]), but it is, in brief, the decomposition which, when inverted, satisfies the least-squares minimum criteria for the function

$$\Phi=\left\|I-P\cdot F\right\|^2 \quad (6)$$

One decomposes a matrix $P\rightarrow UDV^T$, where the columns of U are the eigenvectors of PP^T, the columns of V are the eigenvectors of P^TP, and D is a diagonal matrix comprising the singular values (square root of the eigenvalues) of PP^T. U and V are, by definition, orthogonal. This decomposition can be inverted (pseudoinverse) as $P^+=VD^+U^T$, where the diagonal of D^+ is made up of the inverse of each of the singular values of D, in descending order, so long as the singular value in question is not zero. If the singular value of D is zero, then the corresponding element of D^+ is also zero. If we assume ***P*** is a $u\times v$ matrix, then as *u* increases, some diagonal elements of D^+ can be very large, and undue emphasis can be put on the corresponding singular values. This may cause a very high sensitivity of the method to errors and noise. Fortunately, SVD allows us to truncate the series at any desirable number of eigen values (which are all positive, or zero, and are numerated in descending order) with any $K \le min\ (u,v)$:

$$P^+=\sigma_1E_1+\ldots\sigma_KE_K=\sum_{k=1}^{K}\sigma_kE_k;\ E_k=\left|U_k\right\rangle\left\langle V_k\right|. \quad (7)$$

Truncation provides for robustness of this method and makes it less sensitive to the errors in the knowledge of projection matrix as well as to the noise in the images. The projection matrix is defined both by the type of projection (for example the angle of rotation), the size of the pixel in the image array and the type of discrete representation of a continuous distribution. Here we present two simple discrete models representation: pillbox and Gaussian.

Pillbox representation

This is a simple representation of the distribution by *NxN* pillboxes with F_{ij} height located on an evenly spaced 2D-grid.

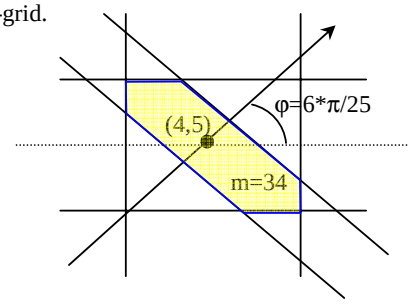

Figure 2: Element of projection matrix $P_{634,31}$ of grid-box (4,5) on the 34th pixel when the grid is rotated on the angle of φ =6*π/25 around the origin is equal to the area of the intersection shaded in light yellow.

The elements of the projection matrix are equal to the area of intersection of a box located on (i,j)-grid node with the lines indicating the boundaries of the m[th] pixel. The grid rotates around the origin according to the angle φ of given projection. Figure 2 shows a specific example of such a cross-section:

$$P_{m,j,i,l}=P_{634,35}=Area_{ovelap} \quad (8)$$

The pillbox representation has the advantage of giving the exact projection matrix, but the sharp corners inherent in the method do not provide for a smooth reconstruction. Hence, these sharp corners can be exaggerated in the presence of errors or/and noise.

Gaussian representation

It is a more elegant representation of a distributed function by a set of *NxN* Gaussians centered at the evenly spaced 2d-grid - see equation (9a). Each Gaussian has individual height (F_{ij} for (i,j)th node) and a common r.m.s. width σ_r, which plays the role of an adjustable parameter.

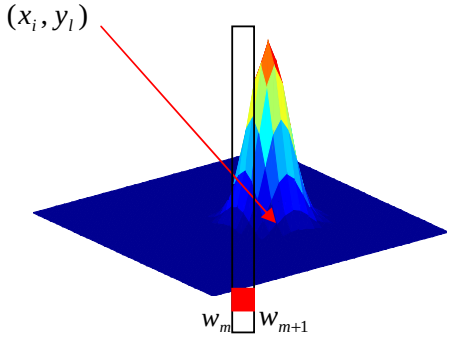

Figure 3: The projection of a pixel onto a Gaussian node in the phase-space.

The projection matrix is then found by projecting each Gaussian mode onto each pixel using eq. (4) and the pixel width (w_m,w_{m+1}):

$$(a)\ F(x,y)=\sum_{i,l}F_{i,l}*e^{-\frac{1}{2\sigma_r^2}(-(x-x_i)^2-(y-y_l)^2)}$$
$$(b)\ P_{m,i,j,l}=\sqrt{2\pi}\sigma_{rep}\int_{w_m}^{w_{m+1}}e^{-\frac{1}{2\sigma_r^2}(x_i\cos\varphi_j+y_l\sin\varphi_j-u)}du \qquad (9)$$

Solution

When projection matrix is pseudo-inverted for a given choice of K (i.e. cut-off number of eigen vectors used in reconstruction) using eq. (7), the $P^+(K)$ gives the resulting elements of F_{il} as:

$$[F]=[P^+(K)]\cdot[I]. \qquad (7')$$

In pillbox case these are the heights of the boxes on the grid with discontinuities on each grid edge. For Gaussian representation, the result is a smooth function (9a), whose scale of variations can be limited by increasing of σ_r. Increase of σ_r to or above a size of a grid size will also lead to the reduction of the accuracy of the representation. Hence, there is an optimum σ_r (depending of the errors and the noise level), which provides a smooth but reasonable accurate representation of the real distribution function.

THEORETICAL COMPARISON

In order to study the theoretical aspects of the two representations, we created a theoretical construction, wherein we may compare a known function with our reconstruction. Here we present few selected results with the trial function a Gaussian with unit height, located off-origin and having r.m.s. width of 2 grid size. Both representations were using 13x13 2D-drid with using grid size. Theoretical projections are 117 pixels for each image (an arbitrary number). We then use the SVD method described above for both representations. We evaluated the accuracy of reconstruction by subtracting the theoretical numbers from the reconstruction on the grid and comparing the norm of the difference with the norm of original function:

$$Error[\%]=\frac{norm(reconstruction-baseline)}{norm(baseline)}*100$$

Figure 4 shows results of preliminary studies of the methods accuracy as function of the number of projections (spaced 10° apart).

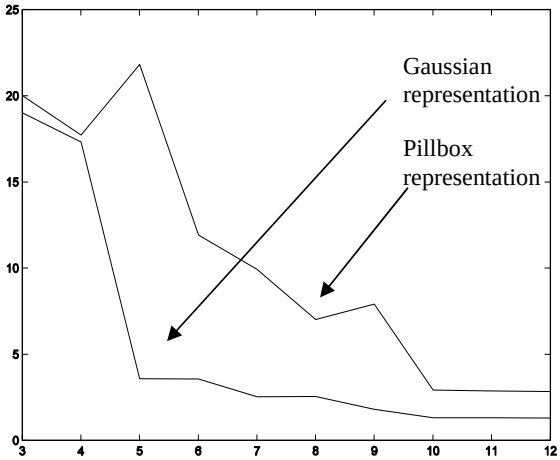

Figure 4: Error of reconstruction vs. # projections for pillbox and Gaussian representations.

We did not succeed so far in accurate reconstructing of the trial functions using two projections and limited number of pixels ~ 100 - the errors are too large. We attribute it either to a need for a better image resolution (M >> 100) or to a possible "small bugs" in our programs. It is clear from our preliminary studies that the Gaussian representation provides a better reconstruction for smooth functions than the pillbox representation. We continue the studies of the analytical features of the method, including reconstruction of distributions with complex topology.

ANALYSIS OF GIANT PULSES

Figure 1 shows one of many measured dual sweep streak camera images of electron beam evolution in the Duke OK-4 storage ring FEL during the giant pulse process. During the above measurement the synchrotron frequency was 24.3 kHz, and the image shows evolution of the longitudinal distribution of the electron beam over

approximately 12 synchrotron oscillations. One can see that there is a transition region, where the length if the e-bunch is evolving rapidly, and dramatically, in less than one synchrotron oscillation.

The self-consistent theory of giant pulses [7] predicts strongly asymmetric, snail-like distribution [8] generated in the giant pulse process. Out new method allows us to reconstruct distributions from a limited number of projections, to observe the details of phase space dynamics during the giant pulse and to compare them with the theory. Preliminary results look promising, as seen in the pictures below.

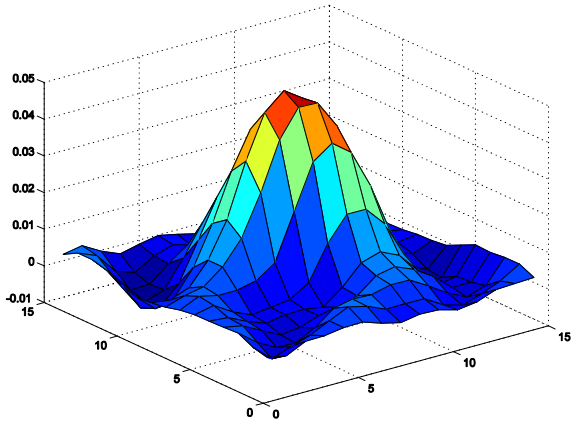

Figure 5: Reconstruction of e-beam distribution in equilibrium (before lasing) using 8 projections, 6.82° apart. Scale is arbitrary.

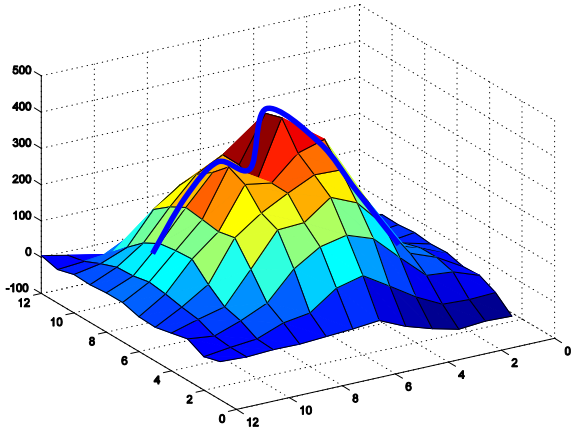

Figure 6: A reconstruction using 8 projections, 6.81° apart, of the transition region. Noticeable double-hump is remarkably similar to the profile predicted by the theory [7,8].

The pictures in Figures 5 and 6 were reconstructed using the Gaussian representation. The reconstructions using the pillbox representation had many jagged peaks.

The reconstructed distribution shown in Fig. 6 qualitatively agrees with the theoretical prediction [7,8]. Clearly, there is room for more studies and comparisons. We plan to finish detailed comparison of a giant-pulse simulation using #vuvfel code [8] (with beam parameters taken from experimental runs) and to compare the simulated electron distributions with the reconstructions we get from dual-sweep streak camera images. The reconstruction passes the eye test, but the next step is to do a quantitative comparison. We stress that only 8 projections, space 6.82° apart, were used to complete this reconstruction, for a total observation angle of 47.8°. There is reason to believe some improvements can be made on the code so that we can get a better reconstruction with an even smaller set of projections.

CONCLUSIONS

We developed a novel method of phase-space tomography, which theoretically requires only a full set of two or more linear projections. Currently, we are improving the model to see how low the limit can be pushed. Theoretical models indicate that, with limited resolution, we can get a good reconstruction (<5%) with a set of five projections. Perhaps we could get better reconstruction using greater resolution. We used experimental data from giant-pulse measurements at the Duke storage ring FEL to test the model, and saw some promising results.

It is important that this method works for any linear projections, not only for rotations [3]. It has potential applications of this method for accelerator physics, medicine, military, and astronomy. Future work will be to further improve the model, compare it to giant-pulse simulations, and apply the method to other problems.

REFERENCES

[1] S.R. Deans, The Radon Transform and Some of Its Applications, Wiley & Sons, 1983.

[2] I.V. Pinayev et al., Nucl. Instr. and Meth. A475 (2001), pp. 222-228

[3] SVD-based tomography, K.Chalut, V.N. Litivinenko. in preparation

[4] see for example, “The Principles of circular Accelerators and Storage Rings”, Philip J.Briant and Kjell Johnsen, Cambridge University Press, 1993, p.156

[5] A.H. Lumpkin et al., Nucl. Instr. and Meth. A407 (1998), pp. 338-342.

[6] P.E.Gill et al, Numerical Linear Algebra and Its Optimization, Addison-Wesley, 1989.

[7] V.N. Litvinenko, Proceedings of FEL conference, August 2002, APS, Argonne, IL, Eds. K.-J.Kim, S.V.Milton, E.Gluskin, p. II-1

[8] V.N. Litvinenko et al., Nucl. Instr. and Meth. A358 (1995), pp. 334

ACCELERATION OF ELECTRONS IN A DIFFRACTION DOMINATED IFEL

P. Musumeci, S. Ya. Tochitsky, S. Boucher, A. Doyuran, R. J. England,
C. Joshi, C. Pellegrini, J. Ralph, J. B. Rosenzweig, C. Sung, G. Travish, R. Yoder
University of California at Los Angeles, CA 90095, USA
A. Varfolomeev, S. Tolmachev, A. Varfolomeev Jr., T. Yarovoi, RRCKI, Moscow, Russia

Abstract

We report on the observation of energy gain in excess of 20 MeV at the Inverse Free Electron Laser Accelerator experiment at the Neptune Laboratory at UCLA. A 14.5 MeV electron beam is injected in a 50 cm long undulator strongly tapered both in period and field amplitude. A CO_2 10.6 μm laser with power $>$ 300 GW is used as the IFEL driver. The Rayleigh range of the laser ($\sim$ 1.8 cm) is shorter than the undulator length so that the interaction is diffraction dominated. Few per cent of the injected particles are trapped in stable accelerating buckets and electrons with energies up to 35 MeV are detected on the magnetic spectrometer. Three dimensional simulations are in good agreement with the electron energy spectrums observed in the experiment and indicate that substantial energy exchange between laser and electron beam only occurs in the first 25-30 cm of the undulator. An energy gradient of $>$ 70 MeV is inferred. In the second section of the undulator higher harmonic IFEL interaction is observed.

INTRODUCTION

Inverse Free Electron Laser (IFEL) schemes to accelerate particles have been proposed as advanced accelerators for many years [1, 2]. Recent successful proof-of-principle IFEL experiments have shown that along with acceleration [3, 4] this scheme offers the possibility to manipulate and control the longitudinal phase space of the output beam at the laser wavelength. First among other laser accelerator schemes, the Inverse Free Electron Laser has in fact experimentally demonstrated microbunching [5], phase-dependent acceleration of electrons [6], phase locking and multi-stage acceleration [7] and control of final energy spread [8]. Up to now, though, only modest energy gains and gradients have been achieved in an IFEL accelerator mostly because of the relatively low peak laser power employed in the experiments carried out so far.

The Inverse Free Electron Laser experiment at the Neptune laboratory at UCLA accelerated electrons from 14.5 MeV up to more than 35 MeV utilizing a CO_2 laser beam with a peak power ($\sim$ 0.4 TW), one order of magnitude greater than any other previous IFEL experiment had used. To maintain the resonant condition with the accelerating electrons, the 50 cm long undulator is strongly tapered both in period and magnetic field amplitude. An important point of the Neptune IFEL configuration is that the Rayleigh range of the laser beam is much shorter than the undulator length and the Inverse Free Electron Laser interaction is diffraction dominated.

EXPERIMENTAL SETUP

In Table 1 we report the design parameters of the Inverse Free Electron Laser experiment at the Neptune Laboratory.

In Fig. 1 it is shown the experimental layout for the IFEL experiment. An electron beam of 300 pC at 14.5 MeV is delivered to the experimental region by the Neptune rf photoinjector [9]. Final focus quadrupoles with large aperture to avoid clipping of the copropagating laser beam were installed on the beamline and focused the electron beam to the nominal spot size of 120 μm rms in the middle of the undulator. A TW-class CO_2 laser system [10] is used to drive the IFEL. The high power laser beam is brought in vacuum through a NaCl lens that has both the function of producing the correct focusing geometry and serves as a vacuum window. The laser is made collinear to the e-beam utilizing a plane copper mirror with a hole. The beams are aligned on the probe in the midplane of the undulator with an accuracy of $<$ 100 μm and the angular misalignment is kept below 1 mrad using the screens located before and after the undulator. After the interaction region, the e-beam is energy analyzed by the magnetic spectrometer and the laser beam is sent to the streak camera for timing measurements.

The undulator for the IFEL experiment at the Neptune Laboratory was built at the Kurchatov Institute [11]. It is a unique magnet because of the very strong variation of the undulator parameters (wiggling period and magnetic field amplitude) along the axis, carefully tailored to maintain the resonance condition of the IFEL interaction between the CO_2 photons and the quickly accelerating electrons. The undulator parameters are reported in Table 2.

Synchronization between electrons and photons is the

Electron beam	
energy	14.5 MeV
charge	0.3 nC
emittance	5 mm-mrad
pulse length (rms)	3 ps
CO_2 laser	
Power	400 GW
Wavelength	10.6 μ m
pulse length (rms)	100 ps
spot size	340 μ m

Table 1: Electron beam and CO_2 Laser parameters at the Neptune Laboratory

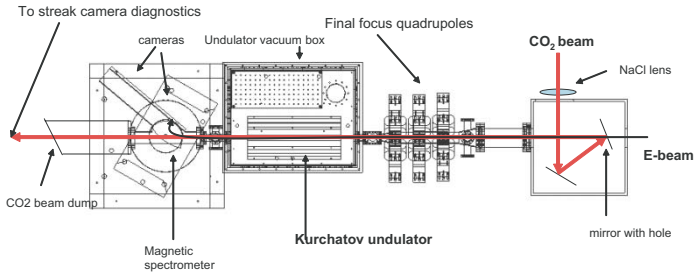

Figure 1: Layout of Neptune IFEL experiment

key for every laser accelerator with an externally injected electron beam and it is even more delicate in an IFEL experiment. In this kind of interaction in fact, there is no resonant medium (or cavity) where the accelerating electromagnetic wave is resonating and can live independently than the laser beam. The accelerator is virtually turned on only at the time the laser pulse goes through the undulator and the ponderomotive gradient that accelerates the electrons depends on the instantaneous power felt by the electrons.

At the Neptune laboratory, the electron pulse ($\sim$ 15 ps FWHM) and the longer CO_2 laser pulse ($\sim$ 240 ps FWHM) have been synchronized in the past with a cross-correlation method that was based on the e-beam controlled transmission of CO_2 through a Germanium sample. This technique [12] constituted the first step of the synchronization procedure also in the IFEL experiment. On the other hand, the cross-correlation measurement is conducted with the unamplified laser pulse propagating through the final triple passed, 2.5 m long multiatmosphere CO_2 amplifier with no inversion of population and has an intrinsic systematic error due to the different group velocity of the laser pulse within the inverted medium of the final amplifier in comparison with no-gain conditions. Moreover, fluctuations in laser power (gain in the final amplifier) $\pm$ 50 % cause fluctuations in the time of arrival of $\pm$ 50 ps. This jitter is intrinsic in the laser amplification system and could not be eliminated. In order to get very accurate information on the relative timing between the electrons and the amplified pulse on each shot, we set up a new streak camera based timing diagnostics.

In Fig. 2, it is shown a typical picture of the streak camera output. In the bottom left corner there is the reference green pulse from the photocathode drive laser that is representative of the electron timing. On the upper right side there is the streak of the CO_2 pulse. The delay (1170 ps) shown in Fig. 2 corresponds to the optimal timing and it was found maximizing the output IFEL energy as a function of delay. Utilizing the streak camera diagnostics, we were able to determine for each laser shot the pulse length (and so the peak power) of the CO_2 beam and which part of the laser pulse intensity profile the electron beam sampled with an accuracy of $\pm$ 10 ps.

The optical geometry used in the experiment to focus and control transversely the laser beam size is of particular importance. In the original design, a 2.56 m focal length NaCl lens focused the laser in the middle of the undulator to a spot size of 340 μm with a Rayleigh range of 3.5 cm to increase as much as possible the extent of the region where the beam is more intense. The resulting peak intensity is $2 \cdot 10^{14}$ W/cm^2 in the laser focus, about two orders of magnitude more than any previous IFEL experiment used [7, 8]. Dealing with this very high laser intensities on the other hand had some disadvantages.

Experimentally, in fact, we were limited by damage threshold on the last optical elements of the CO_2 transport line and we could not increase the f-number of the optical geometry as we planned. For our typical pulse lengths of 200 ps, we observed damage on the copper mirrors for fluences above 3J/cm^2 and on the single crystal NaCl optics for fluences above 2J/cm^2. In the end, we measured a spot size of 240 μm and Rayleigh range of 1.8 cm that, respect to the original design geometry, implied a stronger varia-

	initial	final
Undulator period	1.5 cm	5 cm
Magnetic field amplitude	0.16 T	0.65 T
K	0.2	2.8
Resonant energy	14.5 MeV	52 MeV

Table 2: RRCKI IFEL undulator parameters

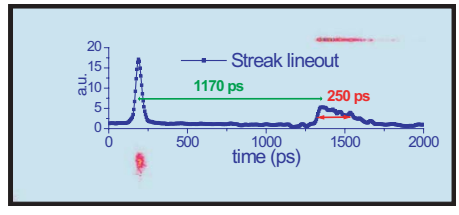

Figure 2: Streak camera picture of photocathode driver reference (lower-left corner) and CO2 pulse. The screen calibration gives a measurement of the laser pulse length and of the optimum delay between the reference and the CO2

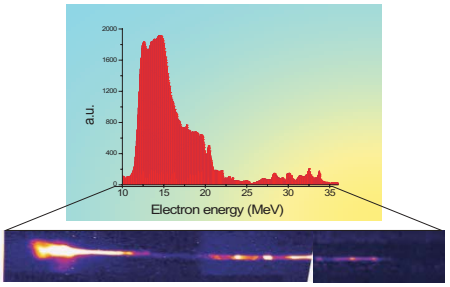

Figure 3: Single shot spectrum of the Inverse Free Electron Laser accelerator. More than 5 % of particles are accelerated to 35 MeV with 150 % energy gain

tion of the beam size along the interaction region, and with the same nominal focus position at the mid-point of the undulator, a larger and less intense beam at the entrance and exit of the undulator.

To trap and accelerate particles along the design resonant orbit, the ponderomotive IFEL gradient generated by the laser electric field has to match the designed tapering gradient. If this is not the case, no trapping or acceleration are possible. Because of the differences between nominal and measured Rayleigh range, it was found out necessary to move the laser focus upstream from the nominal position to increase the intensity at the undulator entrance above the trapping threshold and start the acceleration process early in the undulator. Of course that would also cause the particles to fall out of resonance soon after the mid point of the undulator because of lack of enough ponderomotive force to sustain the acceleration along the designed orbit. It was found that the optimum position of the laser focus for the power levels available, was 2 cm (one Rayleigh range) upstream of nominal focus position.

EXPERIMENTAL RESULTS AND SIMULATIONS

The electrons were detected by a phosphorous screen observed by CCD cameras. The screen was attached to the thin mylar window at the exit slit of the spectrometer. Different neutral density filters were applied to each cameras to get unsaturated images of the output slit. A postprocessing application that takes into account the different filters and scales the horizontal axis of the images with energy, reconstructed the single shot spectrum of the electron beam out of the IFEL accelerator for each laser shot. A typical image of a dispersed electron beam is presented in Fig. 3 along with a reconstructed spectrum.

The energy spectrum shows more than 5 % of particles trapped and accelerated up to 35 MeV with a 150 % energy gain. The measured power in the CO_2 pulse for this IFEL shot was 400 GW of power and the laser was focused upstream of the nominal position by 2 cm.

The code that was used to simulate the experiment at the design phase is a 4th-order Runge-Kutta integrator that solved the Lorentz equation for the particle motion in the combined fields of the undulator magnet and laser beam (TREDI[13]). The same code was used to understand the experimental results reproducing the experimental condition, and, once we put the correct laser intensity profile along the undulator, agree quite well with the experiment.

In Fig. 4 the simulated longitudinal phase-spaces at two different distances along the undulator are shown. The histograms on the left of the graphs are the projection of the phase-spaces on the energy axis. The simulation results allowed us to draw several conclusions.

First of all (Fig. 4a) that the IFEL acceleration mostly takes place in the first section of the undulator (first 25 cm). Few cm after the mid-point the laser intensity has decreased below the trapping threshold and the designed tapering is too strong for the particles too follow. That allows us to infer an accelerating gradient of > 70 MeV/m.

Secondly, Fig. 4b shows the structure of the high energy side of the spectrum observed in the experiment. This structure is particularly interesting because experimentally it was reproducible shot to shot, ruling out the possibility of micro-structures present in the e-beam or the laser beam. Instead, the structure is due to a different kind of IFEL interaction that takes place in the second section of the undulator.

We know that efficient energy exchange between the transverse EM wave and the particles wiggling in the undulator can only take place when the resonant condition is satisfied, and so the energy of the particles is such that in the electron's rest frame the wiggling induced by the undulator has the same frequency of the wiggling induced by the laser. On the other hand, it is known that particles of a fixed energy going through an undulator interact not only with the fundamental resonant frequency, but also with the radiation harmonics [14]. From another point of view, particles of different energy $\gamma_{r,n}$ can interact with the same laser frequency, because they see the EM wave as a higher harmonic of the fundamental frequency that they are resonant with. In other words, for a given laser and undulator,

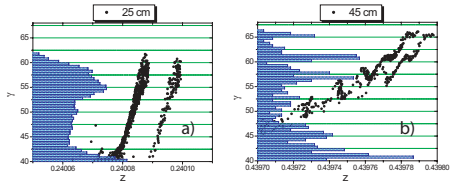

Figure 4: Simulations of IFEL longitudinal phase space at different points along the z axis. a) Longitudinal phase space at the undulator mid-point. The energy gain has already taken place in 25 cm. b) Energy modulation due to second harmonic interaction in the second section of the undulator. The structure in the simulated spectrum corresponds to the one in the measured spectrum

there are multiple resonant energies

$$\gamma_{r,n} = \sqrt{\frac{\lambda_w \cdot \left(1 + \frac{K^2}{2}\right)}{2\lambda \cdot n}} \quad (1)$$

In Fig. 5, we show the first three resonant energy curves for the Neptune IFEL undulator. In the experiment the particles fall out of the accelerating bucket from the resonant curve (red) because of the mismatched laser intensity distribution. At some point later in the undulator the particles energy is $1/\sqrt{2}$ times the resonant energy, at this point the electrons can exchange energy with the 10.6 μm photons mediated by the second harmonic IFEL interaction.

The equations for the Higher Harmonics IFEL interaction are the standard IFEL equation, with the coefficient JJ for the first harmonic interaction replaced by the appropriate JJ_n coupling coefficient [15].

$$\mathrm{JJ}_n = \sum_{m=-\infty}^{+\infty} J_m(\xi) \cdot (J_{2m+n+2}(\sigma) - J_{2m+n}(\sigma)) \quad (2)$$

with dependence on the undulator K factor hidden in $\xi = K^2/(4+2K^2)$, the usual Bessel function argument, and in $\sigma = K/(\gamma k_w w)$ where k_w is the undulator wave number and w is the laser spot size.

The parameter σ taking a closer look, is the ratio of the particles wiggling amplitude to the laser spot size, and it can be viewed as a quantitative measure of how three-dimensional the interaction is. We note that the even harmonics interaction should be suppressed as a consequence of the known fact that the on-axis spectrum of a planar undulator has only the odd harmonics. This is reflected by the behavior of the coupling coefficients for even harmonics (i.e. $\mathrm{JJ}_n \rightarrow 0$ when $\sigma \rightarrow 0$. for even n). In other words σ determines the strength of the IFEL coupling to the even harmonics [16].

In the Neptune experiment, the trajectory wiggling amplitude increases along the undulator and it becomes comparable to the laser beam size around the focus region. The σ parameter reaches relatively large values (~ 0.5) and the second harmonic IFEL coupling is not negligible. Moreover, in this region of the undulator the CO_2 laser is still very intense, so that a significant amount of energy can be transferred to the e-beam. The longitudinal modulation induced by HHIFEL interaction that appears in the simulated phase space is washed out after a short drift propagation, because of the large energy spread. On the other hand, the deep energy structure resulting from this kind of interaction remains imprinted on the experimental beam energy spectrum. The energy exchange is not as efficient for the third harmonic IFEL interaction that could take place at the end of the undulator. Here, regardless of the strength of the coupling constant, the laser field is just not intense enough to perturb significantly the electron energy spectrum.

The higher harmonic interaction is the origin of the energy modulation seen reproducibly in the output spectrum of the experiment.

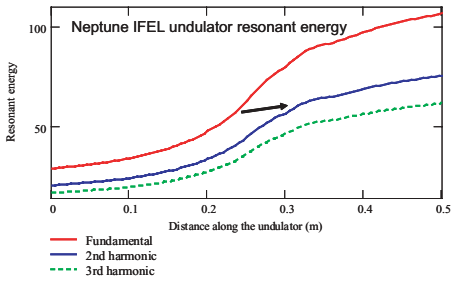

Figure 5: Neptune IFEL undulator different resonant energies.

CONCLUSION

We report on the observation of $>$ 20 MeV energy gain (150 %) at the Inverse Free Electron Laser experiment at the Neptune Laboratory. An energy gradient of $>$ 70 MeV/m is inferred. The fraction of self-trapped particles exceeded 5 % of the injected bunch. The acceleration gain reported is to date the highest obtained with an IFEL accelerator. Self-trapping of particles in a stable accelerating bucket from a not-prebunched initial distribution was demonstrated. The effects of the laser diffraction were analyzed in the design phase and studied experimentally. Finally, for the first time higher harmonic IFEL (HH-IFEL) interaction was observed in the second section of the undulator. The HH-IFEL adds a degree of freedom (the harmonic coupling number n) in the design of magnetic systems capable of coupling lasers and electron beams. This work is supported by U.S. Dept. of Energy grant DE-FG03-92ER40693

REFERENCES

[1] R.B. Palmer. *J. Applied Physics*, 43:3014, 1972.

[2] E. D. Courant, C. Pellegrini, and W. Zakowicz. *Phys. Rev. A*, 32:2813, 1985.

[3] I. Wernick and T. C. Marshall. *Phys. Rev. A*, 46:3566, 1992.

[4] A. Van Steenbergen et al. *Phys. Rev. Lett.*, 77:2690, 1996.

[5] Y. Liu et al. *Phys. Rev. Lett.*, 80:4418, 1998.

[6] R. B. Yoder, T. C. Marshall, and J. L. Hirshfield. *Phys. Rev. Lett.*, 86:1765, 2001.

[7] W. Kimura et al. *Phys. Rev. Lett.*, 86:4041, 2001.

[8] W. Kimura et al. *Phys. Rev. Lett.*, 92:054801, 2004.

[9] S. G. Anderson et al. *AIP Conf. Proc.*, 569:487, 2000.

[10] S. Ya. Tochitsky et al. *Opt. Lett.*, 24:1717, 1999.

[11] S. Tolmachev et al. these proceedings

[12] S. Ya. Tochitsky et al. *Phys. of Plasmas*, 11:2875, 2004.

[13] L. Giannessi, P. Musumeci, M. Quattromini *Nucl. Instr. Meth. A*, 436:443, 1999.

[14] Z. Huang and K. J. Kim. *Phys. Rev. E*, 62:7295, 2000.

[15] P. Musumeci et al. 2004. to be submitted for publication.

[16] M. J. Schmidt and C. J. Elliot *Phys. Rev. A*, 34:4843, 1986.

ADVANCES IN THE PHYSICAL UNDERSTANDING OF LASER SURGERY AT 6.45 MICRONS

M. Shane Hutson*, Department of Physics & Astronomy, Vanderbilt University, Nashville, TN 37235, USA
Glenn S. Edwards, Free Electron Laser Laboratory and Department of Physics, Duke University, Durham, NC 27708, USA

Abstract

We previously presented a model that attributes the wavelength-dependence of FEL tissue ablation to partitioning of absorbed energy between protein and saline. This energy-partitioning subsequently influences the competition between protein denaturation and saline vaporization. The original model approximated cornea as a laminar material with a 50:50 saline-to-protein volume ratio. We have now refined the microscopic geometry of the model in two ways: (1) cornea is represented as a saline bath interpenetrated by a hexagonal array of protein fibrils; (2) the volume ratio is matched to the measured value, 85:15. With this volume fraction, the specific absorption coefficient for protein is much larger than previously reported. Thus, the fibril array model magnifies the differences between wavelengths that target saline versus protein. We will discuss: (1) the consistency of this model with previous, seemingly conflicting, experimental data; (2) predictions of the model, with a particular emphasis on the role of laser intensity; and (3) the experiments needed to test these predictions.

INTRODUCTION

Early on in the development of surgical applications for free-electron lasers (FELs), the tunability of FELs was exploited to investigate the wavelength-dependence of tissue removal [1]. In the mid-IR, wavelengths near 6.45 μm proved remarkably adept at removing defined volumes of soft tissue with very little collateral damage. In fact, tuned to this wavelength, the Vanderbilt Mark-III FEL has been used successfully in both neurological and ophthalmic surgeries on human patients [2-4]. However, due to cost and size constraints, it seems unlikely that such FELs will ever find widespread use in patient care. We now face the challenge of translating the surgical successes of mid-IR FELs to cost-effective, compact, and dedicated medical laser systems.

Several 6.45-μm sources have already been evaluated, including a Sr vapor laser and a picosecond OPA system [5-6]. Unfortunately, the surgical performance of both sources was unacceptable. These failures highlight a key point: *the surgical performance of a laser system is not determined by wavelength alone, but by a combination of wavelength, intensity and pulse structure*. If a tabletop system matched the Mark-III FEL in all these characteristics, then one could be reasonably assured of its success. Unfortunately, such an exact match is unlikely given the complex pulse structure of a Mark-III FEL (i.e. 2-6 μs long superpulses, repeated at 1-30 Hz, with each superpulse containing a 2.856 GHz train of picosecond pulses) [7]. Guidance on how to relax these pulse constraints has and will come from a better understanding of the dynamics governing mid-IR tissue ablation.

It should be noted that 6.45 μm is not an obvious choice for FEL tissue ablation. Soft tissues absorb mid-infrared light most strongly at the water absorption bands of 3.0 and 6.1 μm; however, wavelengths near 6.45 μm were superior for surgical applications [1-4]. This anomalous wavelength-dependence was attributed to partitioning of the absorbed energy between the aqueous components of a tissue and its protein matrix. Thermodynamic arguments suggested that wavelengths targeting the protein matrix (like 6.45 μm) could reduce collateral damage [1]. Subsequently, we reported a dynamic model that confirms the plausibility of this argument [8]. The dynamic model attributes the observed wavelength-dependence to the influence of energy-partitioning and nanoscale thermal diffusion on two competing thermal processes: protein denaturation and explosive vaporization of saline.

This dynamic model has also been used to investigate the role of FEL pulse structure. As a photothermal model, it suggested that the characteristics of FEL tissue ablation should not depend on high peak intensity in an FEL's picosecond pulses [8]. Pulse-broadening experiments have recently confirmed that expanding the picosecond pulses to widths in excess of 100 ps has little effect on the ablation threshold and efficiency [9-10].

The model instead suggested a key role for high average intensity within a superpulse. By investigating a wide range of incident intensities and pulsewidths, we delineated regions of parameter space, or "sweet spots", within which the model predicts a reduced degree of collateral damage [11]. Importantly, each of the wavelengths investigated (3.0, 6.1 and 6.45 μm) had such a region, but the sweet spot for 6.45 μm was much larger and encompassed much higher intensities. In collaboration with industry (PASSAT Inc, Linthicum, MD, USA), these predictions have guided the design specifications of a new 6.45-μm laser source (several mJ of energy in 12-15 ns pulses) [12]. This laser is currently under development.

Our previous computational investigations of FEL ablation were performed on a laminar model, in which corneal stroma was approximated as alternating, 30-nm layers of saline and protein [8,11]. Although the laminar model gets the characteristic distance for nanoscale heat

*shane.hutson@vanderbilt.edu

diffusion correct, it underestimates the temperature rise in the protein component. This underestimate arises because the laminar model is equivalent to a tissue with a 50:50 volume ratio of saline:protein. However, the measured ratio for corneal stroma is 85:15 [13]. Thus, the light absorbed by protein is actually confined to a much smaller volume than in the laminar model, yielding higher energy densities and larger temperature rises.

Here we expand our computational efforts to investigate mid-infrared laser ablation in two important ways. First, we use a geometry that more closely approximates the heterogeneous structure of corneal stroma. Results for 6.45 and 3.0-μm irradiation are very similar to the previous laminar model. However, results for wavelengths near 6.1 μm are qualitatively different. Most interestingly, the sweet spot at this wavelength actually splits in two. Second, we isolate the role of energy-partitioning by investigating the five mid-infrared wavelengths for which the tissue absorption coefficient is matched to that at 6.45 μm. The computational results from this matched set help explain previous experimental results and suggest new experiments to test the predictions of our model.

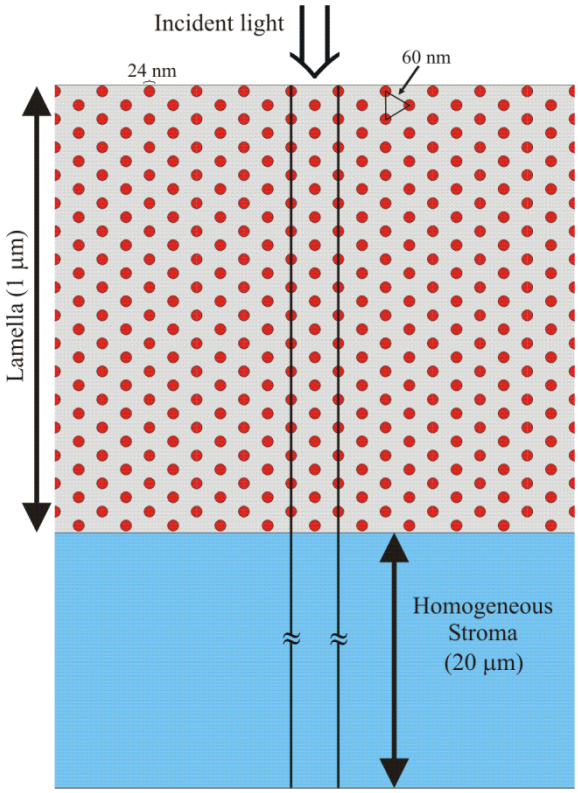

Figure 1. Geometry used to model laser heating in corneal stroma. The microstructure of one lamella is modeled as a hexagonal array of collagen fibrils (**red**) immersed in a saline bath (**grey**). Beyond the first lamella, the stroma is treated as a homogeneous material (**blue**).

METHODS

Corneal stroma consists of hundreds of lamellae, each 1-2 μm thick, where each lamella contains a quasi-hexagonal array of collagen fibrils [14]. The collagen fibrils within a lamella are nearly parallel, whereas those in adjacent lamellae are crossed. Based on this ultrastructure, we model corneal stroma with two layers. The first layer is a single heterogeneous lamella (1-μm thick) composed of a hexagonal array of collagen fibrils in a saline bath. The interfibrillar spacing is 60 nm and the fibril diameter is 24 nm. These distances are consistent with cross-sectional transmission electron micrographs of stroma, [14] and yield a volume fraction ratio of 85:15. We model the remainder of stroma as a 20-μm thick homogeneous layer. A graphical representation of this geometry is shown in Figure 1.

The symmetries and length scales of the geometry allow us to simplify the model. Since we are modeling irradiation with spot diameters of 100 μm or more, heat diffusion in the direction parallel to the tissue surface and parallel to the fibrils is negligible for times less than ~10 ms [15]. However, the onset of material removal in FEL ablation occurs within 10's to 100's of nanoseconds. Thus, we may reduce the geometry to a single plane. A similar argument applies to long-range heat diffusion in the direction parallel to the surface and perpendicular to the fibrils. To maintain a proper consideration of short-range heat diffusion in this direction, we (1) reduce the geometry to the width of a unit cell in the hexagonal lattice and (2) apply a zero heat flux boundary condition on the lateral edges of this section (vertical solid lines).

Laser heating and heat diffusion within this thin strip of stroma is described by Fourier's equation, [16]

$$\rho c_p \frac{\partial T}{\partial t} = \kappa \nabla^2 T + Q \qquad (1)$$

where ρ is the density, c_p is the specific heat at constant pressure and κ is the thermal conductivity. Saline, protein and homogeneous regions are assigned specific ρ, c_p and κ [13]. The heat source term, Q, represents the absorption of laser energy. A Neumann insulating boundary condition is applied to the air-tissue interface and a Dirichlet boundary condition (zero temperature rise) is applied to the rear of the homogeneous stroma layer.

To compute the specific heat source terms for each component, we measured mid-infrared spectra of porcine corneal stroma and saline. These spectra were measured in attenuated total reflectance (ATR) with a Bruker IFS-66 Fourier-Transform Infrared (FTIR) spectrometer and a single-bounce ZnSe crystal. After correction for the 1/λ dependence of the sampling depth, the saline absorbance spectrum was interactively subtracted from the stroma absorbance spectrum to minimize the water association band centered at 4.7 μm. The resultant spectrum represents the absorbance spectrum of the protein component of stroma. The difference between this result and the original stroma spectrum is the absorbance spectrum of the saline component.

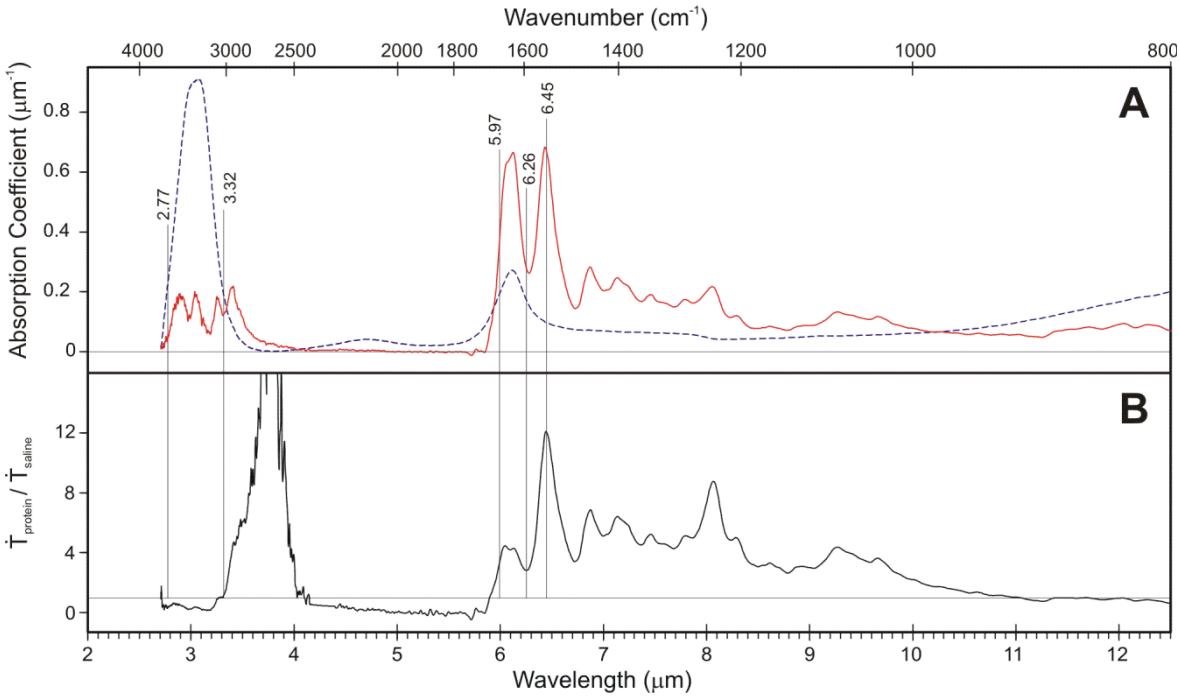

Figure 2. Component-specific absorption of light by the two major components of corneal stroma. **A.** Absorption coefficients for the protein (**red solid**) and saline (**blue dashed**) components based on stroma that is 85% saline by volume. The ratio of these spectra represents the relative laser energy density deposited in each. **B.** Using the respective heat capacities, one can calculate a ratio of the heating rates in the absence of heat diffusion.

A ratio of the component absorbance spectra reflects how the total incident energy is partitioned. However, for thermal modeling, we need the magnitudes of the heat sources, i.e. the deposited *energy density*. To convert the absorbance spectra, A, to the appropriate absorption coefficients, α, we must consider the fraction of stromal volume, f_v, occupied by each component. Based on a stroma that is 80% water by weight and the respective densities of saline and protein, the volume fraction ratio of stroma is 85:15 (water-to-protein) [13]. Following a simple Beer-Lambert law, the absorbance of each component is related to its absorption coefficient by:

$$f_v l\alpha = A\ln 10 . \qquad (2)$$

The unknown sampling depth, l, is found by forcing the absorption coefficient of the 6.1-μm saline peak to 0.27 μm^{-1} [17]. The resulting absorption coefficients are shown in Figure 2.

The local heat source term is then given by

$$Q = (1-R)I\alpha_i e^{-z\alpha_{stroma}} \qquad (3)$$

where R is the reflection coefficient for the air-tissue interface, I is the incident intensity of the laser, α_i represents the component-specific absorption coefficient, and z is depth into the tissue. Using this heat source term and the geometry described above, Fourier's equation was solved numerically on a 2D triangular mesh using a finite element model running under Matlab (The MathWorks Inc., Natick, MA). Solutions were calculated for 181 logarithmically spaced times from 10^{-12} to 10^{-3} s.

From these thermal histories, the accumulated protein denaturation was calculated by integrating an Arrhenius formulation [8,13]. Explosive vaporization of saline was treated as a threshold event at the superheat limit of saline, 575 K [18]. Note that the validity of this thermal model only extends to the wavelength and intensity-dependent onset of vaporization.

RESULTS

The component-specific absorption coefficients for corneal stroma reveal that the energy density deposited into protein exceeds that deposited into saline for a wide range of wavelengths (3.4-4 and 6-10 μm). This region includes the amide I, II and III, as well as the CH-stretch absorption bands of protein. Since the heat capacity of protein is less than saline, the heating rate ratio is greater than one (i.e. protein is always hotter than saline) over an even wider wavelength range. In Table 1, the penetration depths ($1/\alpha$) and heating rate ratios are reported for the three strongest mid-infrared absorption bands of soft tissues (3.0, 6.1 and 6.45 μm). Note that these penetration depths reflect the measured volume fractions in cornea and thus differ from those reported previously [11]. Also included in Table 1 is a set of five wavelengths whose overall absorption matches that at 6.45 μm. The heating rate ratio varies more than a factor of 40 over this set.

Table 1. Component-specific penetration depths of corneal stroma based on an 85:15 saline:protein volume fraction. The last two columns give the relative rates at which the energy density and temperatures of each component would rise due to laser heating (in the absence of heat diffusion).

	Penetration Depths (μm)			Power Density Ratio (p:s)	Heating Rate Ratio (p:s)
λ (μm)	δ_{stroma}	$\delta_{protein}$	δ_{saline}		
2.77	5.5	30.3	4.8	0.16	0.28
3.32	5.5	8.1	5.2	0.64	1.12
5.97	5.5	4.1	5.8	1.41	2.47
6.26	5.5	3.7	6.0	1.63	2.83
6.45	5.5	1.5	10.3	6.93	12.08
12.5	5.5	14.4	5.0	0.34	0.60
3.0	1.3	8.5	1.1	0.13	0.23
6.1	3.1	1.5	3.7	2.41	4.20

We first compared laser-heating calculations with the hexagonal array and laminar models for 3.0 and 6.45 μm [8]. For an intensity of 7.3 x 10^7 W/cm^2 (corresponding to the superpulse intensity at the center of a Gaussian beam, with a 1/e^2 spot radius of 50 μm, and a picosecond pulse energy of 1 μJ), the temperature profiles at the superheat limit differ as expected (not shown). At 3.0 μm, the hexagonal array model predicts a protein temperature rise that still trails that of saline, but the temperature difference is smaller. At 6.45 μm, the protein temperatures exceed those of saline by even more than in the laminar model. Both effects arise because the laminar model underestimated the temperature rise in the protein regions. The laminar model also predicted an exacerbated temperature difference between the surface layers. This surface effect is still present in the hexagonal array model, but at a slightly reduced extent. In general, for wavelengths that strongly target either saline or protein, the results of the hexagonal array and laminar models are qualitatively similar.

As a next step, we constructed "sweet spot" plots for each of the above wavelengths. These plots, shown in Figure 3, consist of three curves in the parameter space of intensity versus pulsewidth: (1 – green/dashed) the power density necessary to superheat saline, i.e. to ensure that energy deposition outpaces energy consumption from the growth of pre-existing vapor bubbles; (2 – solid/red) for a given intensity, the time required for the saline to reach the superheat limit; and (3 – dotted/blue) for a given intensity, the time required to accumulate 1% denaturation of protein. The sweet spot (yellow/shaded areas) represents the area of parameter space for which the structural integrity of protein is compromised (via 1% denaturation) before the onset of explosive vaporization. Graphically, this is any intensity for which curve 2 lies to the right of curve 3. For intensities that meet this criterion, the minimum pulsewidth lays on curve 2 and the maximum on curve 1. We expect laser ablation in this region to be more efficient and to cause less collateral damage.

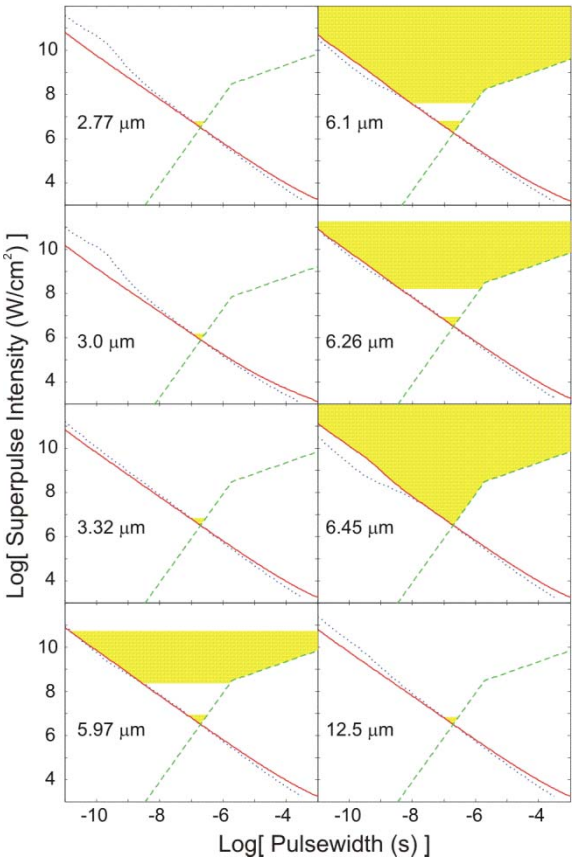

Figure 3. Sweet spot plots for laser ablation of corneal stroma at mid-IR wavelengths. The three curves in each plot represent the following: (**green/dashed**) power density necessary to superheat saline; (**red/solid**) combination of time and intensity required to reach the onset of explosive vaporization; (**blue/dotted**) combination of time and intensity required to accumulate 1% denaturation in the surface protein regions. The sweet spot (**shaded area**) is the set of intensities and pulsewidths for which explosive vaporization occurs after the protein matrix as been compromised by denaturation.

When compared to similar plots constructed with the laminar model [11], those for 3.0 and 6.45 μm are similar, but the plot for 6.1 μm is qualitatively different. Just as in the previous report, the very small sweet spot for λ= 3.0 μm stands in stark contrast to the enormous acceptable parameter range for 6.45 μm. In fact, the upper limit of the 6.45-μm sweet spot now lies outside the range of our model calculations. For 6.1 μm, the sweet spot actually encompasses two regions of parameter space. In our previous laminar model calculations, the uppermost region was not included. For this wavelength, the model predicts that intensities between 10^7 to 10^8 W/cm^2 would cause more collateral damage than either higher or lower intensities.

When we expand the calculations to include a larger set of wavelengths, we find that the sweet spot plots fall into

three classes. For wavelengths that largely target saline absorption (power density ratio less than one, e.g. 2.77, 3.0, 3.32, 12.5 μm), the sweet spot is very small. For wavelengths that moderately target protein (power density ratio of one to three, e.g. 5.97, 6.1, 6.26 μm), the sweet spot splits into a large high-intensity region and small low-intensity region that is only slightly larger than the sweet spots of saline-targeting wavelengths. Finally, if the power density ratio is very large (6.45 μm), the two regions merge into a single large sweet spot.

We have constructed these sweet spots on the somewhat arbitrary choice of requiring 1% denaturation to occur before the onset of vaporization. The 10% and 0.1% denaturation curves are only slightly displaced (approximately a line width) from that of 1%. However, that small difference is enough to change the constructed sweet spots. If we increased the requirement to 10%, then even 6.45 μm would exhibit a split sweet spot. On the other hand, if we decreased the requirement to 0.1%, then the two sweet spots for 5.97, 6.1 and 6.26 μm would merge into one.

As a more robust way to look at the interplay of protein and saline dynamics, we calculated the fractional denaturation at vaporization (FDV), i.e. the amount of denaturation accumulated in the surface protein regions when the saline reaches the superheat limit. In Figure 4A, we compare FDV versus superpulse intensity for the set of six wavelengths with matched stromal absorption coefficients. At very low intensities ($<10^5$ W/cm^2), the laser heating process is slow enough that vaporization commences after almost all of the protein has denatured. At slightly higher intensities, FDV decreases for all six wavelengths. In this regime, the time required to reach the superheat limit decreases to less than 1 μs, limiting the accumulation of denatured protein. All six wavelengths behave similarly because the intensity is not yet high enough to overcome nanoscale thermal diffusion. Thus, the temperature differences between protein and saline regions are negligible. This situation changes as the intensity increases further ($>3 \times 10^6$ W/cm^2). For wavelengths that target saline, FDV continues to decline. However, for wavelengths that target protein, the trend reverses and FDV begins to increase with intensity. The minimum FDV attained in this region depends on how strongly the wavelength targets protein. The intensities are now large enough to outpace thermal diffusion and large wavelength-dependent temperature differences may arise between protein and saline regions. If the protein is substantially hotter than saline, the exponential dependence of the denaturation rate on temperature can overcome the shorter times. Finally, at very high intensities ($>10^9$ W/cm^2), the protein-saline temperature differences have been maximized and further increases in intensity serve only to decrease the time available for denaturation. Thus, FDV again decreases with intensity. Note that this is not yet apparent for 6.45 μm within the range of our calculations.

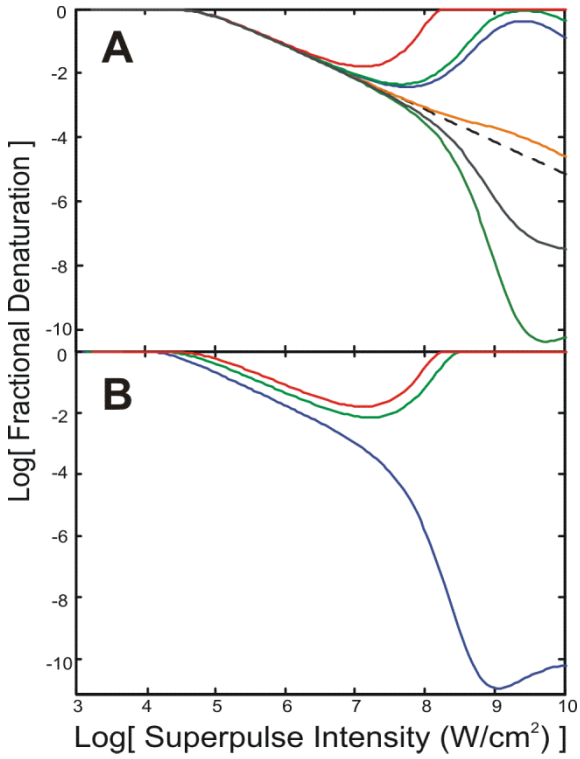

Figure 4. Fractional denaturation accumulated prior to vaporization in the surface protein regions. **A.** Mid-IR wavelengths with stromal absorption coefficients matched to that at 6.45 μm. From top to bottom, the solid curves are for wavelengths of 6.45, 6.26, 5.97, 3.32, 12.5 and 2.77 μm. The dashed curve represents a hypothetical wavelength for which there is no difference between protein and saline absorption. **B.** Peaks in the mid-IR spectra of soft tissues. From top to bottom, the curves are for 6.45, 6.1 and 3.0 μm.

In Figure 4B, we compare FDVs for the three major mid-IR absorption peaks of soft tissues. In this case, the stromal absorption coefficients are not matched and the FDV versus intensity curves do not overlap at low intensities. For a given intensity, a larger absorption coefficient implies a faster heating rate and less time prior to vaporization. Thus the FDV curve for 3.0 μm is always below those of 6.1 and 6.45 μm. The curves are roughly parallel until ~3×10^6 W/cm^2. They begin to diverge as the heating rate becomes sufficient to overcome nanoscale thermal confusion. At this point, FDV begins to increase with intensity for both 6.1 and 6.45 μm. Although the very strong protein targeting of 6.45 μm ensures that its FDV never drops below 1%, the slightly weaker targeting of 6.1 μm allows its FDV to drop slightly below this limit.

DISCUSSION

Can these computational results shed light on previous experimental investigations of FEL tissue ablation? Although the original study reported an anomalous

wavelength-dependence [1], subsequent studies found that the ablation efficiency and threshold followed the mid-IR spectra quite closely [19-20]. Interestingly, the superpulse intensities used by Edwards et al ranged from of 4-8 x 10^7 W/cm^2 [1]. In contrast, subsequent ablation efficiency studies at FELIX and Vanderbilt were conducted between 1-3 x 10^6 W/cm^2 [19-20]. For ablation threshold studies, the intensities are even lower (order of 10^5 W/cm^2) [20]. The model calculations presented here suggest that FEL ablation metrics should follow a simple wavelength-dependence, i.e. one that does not depend on the degree of protein targeting, until the superpulse intensity exceeds ~3 x 10^6 W/cm^2. This is consistent with the available experimental results on ablation efficiency and threshold. However, there are reports of secondary ablation metrics (e.g. the size of ejected particulates in the plume) that do show a low-intensity dependence on the dominant chromophore [19]. Thus, the model presented here may explain some of the previous experimental discrepancies, but additional mechanisms must also contribute.

What sort of experiments should tell us whether the degree of protein targeting, as modeled here, plays a significant role in the wavelength-dependence of FEL ablation? We suggest investigations of how the ablation metrics vary with superpulse intensity. This is straightforward for ablation efficiency and collateral damage. Complementary information should be available from measurements of how the ablation threshold fluence varies with superpulse width. For such measurements on cornea, at wavelengths with matched stromal absorption, our model predicts that the thresholds should diverge below 100 ns.

What about tissues besides cornea? For wavelengths that strongly targeted saline or protein, the laminar and hexagonal array models agreed quite well. This agreement implies that the form factor introduced by a specific geometry is not as important as the characteristic length for nanoscale diffusion. This length scale is the key parameter for evaluating the role of energy-partitioning in other tissues. For collagenous tissues, the relevant length is the diameter of collagen fibrils. The relevant length in non-collagenous (e.g. neural) tissues is not clear.

What do these new calculations predict for the performance of the 6.45-μm tabletop source currently under development? Assuming this laser will be focused to similar spot sizes as the FEL, its pulse intensity will lie in the range of 10^9 W/cm^2 [12]. According to the model calculations, this intensity is high enough to drive truly remarkable protein-saline temperature differences, yielding an FDV of order one. While the prospects for this 6.45-μm source are very promising, we must caution that this range of intensities has not yet been explored experimentally.

Because of their wavelength-tunability and relatively long pulse length, FELs are excellent prototyping tools. FELs can be used to investigate wide swaths of parameter space to find optimal operating conditions for a specific application. The challenge, that we hope to repeatedly face, is to then find a more economical source, dedicated to the application of interest.

ACKNOWLEDGEMENTS

This work was supported by grants FA9550-04-1-0045 and F49620-00-1-0370 from the DOD MFEL Program.

REFERENCES

[1] G. Edwards, R. Logan, M. Copeland, L. Reinisch, J. Davidson, J.B. Johnson, R. Maciunas, M. Mendenhall, R. Ossoff, J. Tribble, J. Werkhaven and D. O'Day, Nature (London) 371 (1994) 416.

[2] G.S. Edwards et al, Rev. Sci. Instr. 74 (2003) 3207.

[3] M.L. Copeland, R.J. Maciunas and G.S. Edwards, In *Neurosurgical Topics: Advanced Techniques in Central Nervous System Metastases*, R.J. Maciunas, Ed. (The American Association of Neurological Surgeons, Park Ridge, IL, 1998), Chap. VII.

[4] K.M. Joos, J.H. Shen, D.J. Shetlar and V.A. Cassagrande, Lasers Surg. Med. 27 (2000) 191.

[5] M.A. Mackanos, E.D. Jansen, A.N Soldatov, R.A. Haglund and B. Ivanov, Proc. SPIE 5319 (2004) 201.

[6] G. Edwards, M.S. Hutson, S. Hauger, J. Kozub, J. Shen, C. Shieh, K. Topadze and K. Joos, Proc. SPIE 4633 (2002) 194.

[7] J.M.J. Madey, J. Appl. Phys. 42 (1971) 1906.

[8] M.S. Hutson, S.A. Hauger and G.S. Edwards, Phys. Rev. E 65 (2002) 061906.

[9] M.A. Mackanos, J.A. Kozub, E.D. Jansen, Proc. SPIE 5319 (2004) 209.

[10] J.A. Kozub, M.A. Mackanos, M.H. Mendenhall, E.D. Jansen, Proc. SPIE 5340 (2004) 87.

[11] G.S. Edwards and M.S. Hutson, J. Synchrotron Rad. 10 (2003) 354.

[12] A.I. Makarov, G.A. Pasmanik, A.A. Shilov, A.G. Spiro, L.R. Tiour and G.S. Edwards, Presented at Solid State and Diode Laser Technology Review (2004) Albuquerque, NM, USA.

[13] J. Kampmeier, B. Radt, R. Birngruber and R. Brinkmann, Cornea 19 (2000) 355.

[14] K.M. Meek and N.J. Fullwood, Micron 32 (2001) 261.

[15] M.J.C. van Gemert and A.J. Welch, In *Optical-Thermal Response of Laser-Irradiated Tissue* (Plenum Press, New York, 1995), Chap. XIII.

[16] L.D. Landau and E.M. Lifshitz, *Fluid Mechanics*, 2nd Ed. (Pergamon Press, Oxford, 1987), Chap. V.

[17] G.M. Hale and M.R. Querry, Appl. Opt. 12 (1973) 555.

[18] V.P. Skripov, *Thermophysical Properties of Liquids in the Metastable (Superheated) State* (Gordon & Breach, New York, 1988).

[19] J.M. Auerhammer, R. Walker, A.F.G. van der Meer and B. Jean, Appl. Phys. B 68 (1999) 111.

[20] S.R. Uhlhorn, Ph.D. Thesis, Vanderbilt University, April 2002.

PROPOSALS FOR PUMP-PROBE EXPERIMENTS IN THE GAS PHASE USING THE TTF2-FEL

M. Meyer, L.U.R.E., Centre Universitaire Paris-Sud, Bâtiment 209D, F-91898 Orsay Cedex, France

Abstract

A selection of experiments is discussed, which will make use of the combination between VUV photon pulses produced by the TTF2-FEL in Hamburg (Germany) and pulses of an optical laser for studying atomic and molecular samples. By applying a two-photon pump-probe excitation scheme, the proposed investigations and the expected results will enable us, on the one hand, to characterize the FEL pulses and, on the other hand, to gain new insight in the dynamics of the electronic interaction in the electronic clouds of excited atoms as well as of the molecular dissociation processes.

INTRODUCTION

Many processes induced by the interaction of XUV light with free atoms and molecules take place on a very short time scale. Photoexcitation of a core-electron to the ionization continuum or to a resonant state will, in general, be followed by fast electronic relaxation through autoionization or Auger process on a sub-picosecond time scale. The temporal width of the soft X-Ray pulses from the TTF2-FEL (100-300 fs) and of the synchronized, tunable optical laser (about 150 fs) will therefore be ideally suited to gain insight into the dynamics of these processes. By using time-resolved pump-probe techniques it will be possible to investigate the temporal evolution of a variety of processes, like electronic relaxation of autoionization states, coupling between two autoionization states, wave-packet formation of higher Rydberg states, coupling between electronic and nuclear motion in molecular systems, fast dissociation of molecules upon inner- and outer-shell photoexcitation, coherent population of fragment states etc.

First experiments have of course also to serve for characterizing the FEL pulses themselves, in particular the intensity, frequency and time structure of the individual pulses, since these values are only estimated on the basis of theoretical simulations. A powerful tool to obtain information about the shape of femtosecond pulses is given by cross correlation experiments [1-3]. This two-color method has been successfully applied to characterize the short X-Ray pulses generated by the generation of higher harmonics in an intense laser in a gas jet of rare gas atoms. It uses the measurement of the ionization signal induced by a XUV photon in the presence of a strong infrared beam (Figure 1). The latter induces sidebands on both sides of the main line in the photoelectron spectrum. The shape, intensity and position of the sidebands are directly correlated to the shape of the pulses and their time delay. At low photon energies, i.e. in the region between 15 and 50 eV, the ionization of the outer Xe 5p or Ar 3p shell can be studied. At higher energies more tightly bound electrons can be excited, e.g. Xe 4d at about 65 eV or Kr 3d at 90 eV.

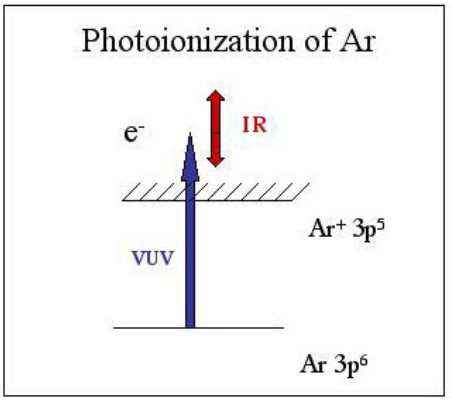

Figure 1: Schematic representation of the photoionization process of atomic Ar by a VUV photon in the presence of a strong IR laser field.

In addition, after excitation of a core electron it will also be possible to measure the corresponding Auger spectrum, where the dressing laser will give rise to the same type of side bands [4,5]. The spectra will be influenced by the interaction between different ionization continua (one-photon and two-photon ionization) and the resonantly excited state, which is characterized by an Auger lifetime of the same order as the exciting femtosecond photon pulses.

CHARACTERIZATION OF FEL-PULSES

In order to select suitable systems for measuring and controlling the temporal delay between the FEL and the optical laser pulses and to find out the potentiality of the cross correlation method, we have performed a series of measurements [3] using the femtosecond laser system at the Laser Center (LLC) in Lund (Sweden). The XUV pulses are produced in Ar gas by generation of the higher harmonics (HHG) nof an intense (about 1 mJ at a 1 kHz repetition rate) 800 nm laser system giving 50 fs pulses [6]. The XUV pulses are used to ionize in the experimental chamber a sample of rare gas atoms and the photoelectron spectrum is recorded using a magnetic bottle spectrometer. The cross correlation measurements have been performed with part of the fundamental 800 nm beam, which is separated before entering the chamber for the production of the higher harmonics. In the presence of the strong IR laser pulse (dressing beam) the photoelectron spectra shows clearly some side-bands,

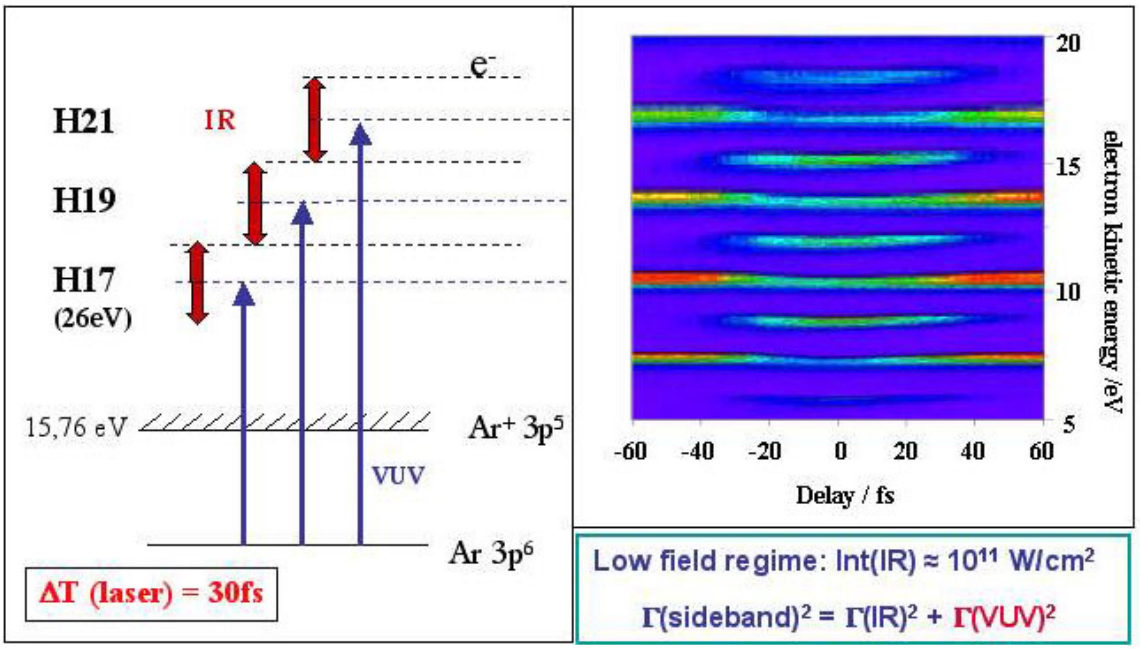

Figure 2: Schematic representation showing the photoionization of Ar atoms by VUV photons, which are produced through generation of higher harmonics of an intense IR laser, in the presence of the same IR laser in the interaction region (left-hand side). The resulting photoelectron spectra as a function of the time delay between the VUV and the IR pulses are given on the right-hand side of the figure.

which are due to an absorption or emission of an IR photon during the ionization process (Figure 2). The intensity, precise energy position and peak-shape of the electron lines strongly depend on the spatial and, more importantly, temporal overlap between the VUV and IR pulses as well as on the intensity of the dressing beam.

Due to the expected temporal jitter between the individual FEL pulses, the possibility to record single-shot spectra will be envisaged for the experiments at the TTF2-FEL. Simulations show (Figure 3) that that it is possible to determine the width and the relative position of the VUV pulses when the IR pulses are characterized providing a temporal resolution of better than 10fs. A precise analysis of the peak-shape allows in addition to determine the width of the VUV pulses. Since the IR pulses introduce a temporally non-uniform field the ionization conditions for different parts of the VUV pulses are also different, which results in an asymmetric, but characteristic lineshape. In this way the synchronization between fs-pulses can be analyzed and eventually also controlled.

In the experiments using the HHG source, spectra were recorded by averaging over 30 000 shots. This was mainly related to the intensity of the source providing about 10^6-10^7 photons/pulse, which corresponds to about 3 electrons per pulse. With the projected FEL output of ~10^{13} photons/pulse it can be estimated that cross correlation spectra are achievable with a single shot, if the IR laser can deliver ~0.5mJ. With the expected ~0.1mJ energy of the IR laser, the low field measurements yielding the phase shift will be possible at a 100 µm spot of the FEL. For measuring also the profile (10TW/cm^2) the experiment has to be performed with a 10µm diameter of the FEL in the interaction region. Problems might arise from space charge effect in the source volume when a huge amount of electrons are produce by the same FEL pulse. Simulations of the expected effects on the photoelectron spectra, in particular on the achievable kinetic energy resolution are under progress.

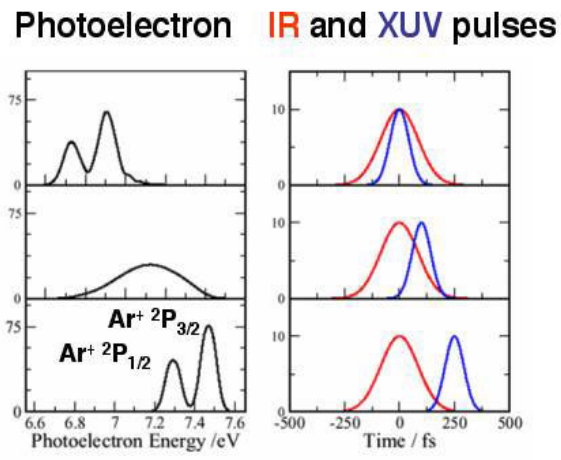

Figure 3: Simulation of the position and the shape of the Ar 3p photoelectron spectrum for different position of the VUV pulse with respect to the IR dressing pulse.

In general, the performed test experiments have demonstrated that the cross correlation measurements can be used to measure precisely the temporal parameters of a VUV pulse with respect to a well-characterized IR pulse.

APPLICATIONS TO ATOMES

Depending on the final characteristics of the FEL with respect to photon energy range and tuneability, the pump-probe experiments will be extended to a large number of further experiments on atomic or molecular samples. To list just a few of them three examples are given:

(i) The investigations of resonances with same parity as the ground state, e.g. Xe* $4d^9 5s^2 5p^6 nd$, ms. Due to dipole selection rules, these states can only be excited either by a direct two-photon one-color excitation or by a two-photon two-color excitation via an intermediate resonant state, like the strong Xe* $4d^9$ 6p resonance ($h\nu$ (FEL) = 65.1eV). The short lifetime of the Xe* $4d^9$ 6p resonance (Γ=0.11eV, ΔT=6fs) necessitates the combination and synchronization of fs-pulses (XUV + Visible). Resonant Auger spectroscopy will be used here to study the relaxation dynamics and additionally the influence of alignment of the intermediate state when the polarization of the two photon beams are changed in a controlled way. The results will extend and complete conventional studies using one-photon excitation and will provide a new and important basis for the theoretical treatment of electronic interaction and correlation in atomic multi-electron systems.

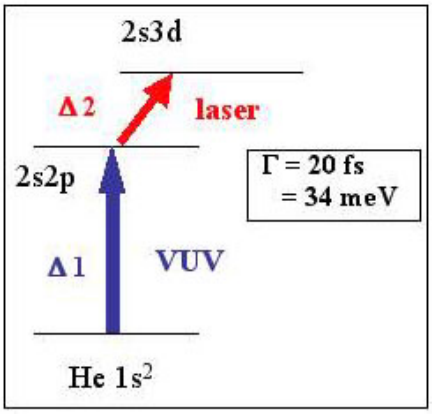

Figure 4: Excitation scheme for the coupling of autoionization resonances in He.

(ii) Coupling of autoionization states by a strong laser field. Similar to the above example, the FEL and a second synchronized fs-laser are used in a pump-probe arrangement to excite and to couple two autoionizing resonances, like He* 2s2p ^{1}P and 2s3d ^{1}D (at photon energies $h\nu$ (FEL) of about 60eV) (Figure 4). The profile of the resonances, being strongly asymmetric for He* 2s2p ^{1}P [7], will strongly depend on the intensity of the two laser beams and on small changes in the relative time delay of the pulses and the photon energy of the second laser (detuning). Theoretical treatments [8,9] predict a pronounced and characteristic splitting in the resonance profile for laser intensities of 1GW/cm^2, which will be accessible in the planned experimental configuration.

APPLICATIONS TO MOLECULES

(iii) Coherent population of excited states by fast dissociation: The photodissociation of H_2 or HCl in the photon energy region $h\nu$ (FEL)>17eV leads to the production of excited hydrogen atoms, in particular to the excited states with principal quantum number n = 2 or 3. Observation of the radiative decay of these states can separate the contributions from 2s and 2p as well as 3s, 3p and 3d levels by their different lifetimes (several nanoseconds). In a pump-probe experiment the FEL can be used to induce the dissociation process and the external laser to ionize the excited hydrogen atoms. The use of femtosecond pulses will allow the time resolution to be increased significantly and to observe quantum beats on the decay curve. The coherent population of the different fine-and hyperfine levels, which are energetically separated by 1 - 10 GHz, will induce a beat structure with a period of about 10 - 100ps (e.g. [10, 11]). For different resonant excitations different dissociation mechanisms are expected, which would lead to different, but characteristic quantum beats patterns of the decay curve.

CONCLUSION

The given examples for experiments using the FEL pulses in combination with a synchronized optical fs-laser are part of working program, which has been proposed by a European collaboration including experimental groups at HASYLAB (Germany), Lund Laser Center and MAX-Lab (Sweden), Dublin City University (Ireland), Max-Born Institute for Nonlinear Optics and Short-Pulse Spectroscopy (Germany), and LURE (France). First experiments are schedules for spring 2005.

REFERENCES

[1] A. Bouhal et al., J. Opt. Soc. Am **14**, 950 (1998)
[2] E.S. Toma et al., Phys. Rev. A **62**, 061801(R) (2000)
[3] P. O'Keeffe et al., Phys. Rev. A **69**, 051401(R) (2004)
[4] J.M. Shins et al., Phys. Rev. A **52**, 1272 (1995)
[5] T.E. Glover, R.W. Schoenlein, A.H. Chin, and C.V. Shank, Phys. Rev. Lett. **76**, 2468 (1996)
[6] R. Lopez-Martens et al., Eur. Phys. J. D **26**, 105 (2003)
[7] M. Domke, G. Remmers, and G. Kaindl, Phys. Rev. Lett. **69**, 1171 (1992)
[8] H. Bachau, P. Lambropoulos, and R. Shakeshaft, Phys. Rev. A **34**, 4785 (1986)
[9] A.I. Magunov, I. Rotter, and S.I. Strakhova, J. Phys. B **32**, 1489 (1999)
[10] C.C. Havener, N. Rouze, W.B. Westerveld, and J.S. Risley, Phys. Rev. A **33**, 276 (1986)
[11] M. Motzkus, S. Pedersen, and A.H. Zewail, J. Phys. Chem. **100**, 5620 (1996).

PICKED FEL MICROPULSE FOR NANO-SECOND INTERACTION WITH BIO-MOLECULE

S. Y-Suzuki*, T. Kanai, K. Ishii, Y. Naito, K. Awazu, Institute of Free Electron Laser, Graduate School of Engineering, Osaka Univ., 2-9-5 Tsuda-yamate , Hirakata, Osaka 573-0128, Japan

Abstract

Laser pulse duration is a very important parameter to determine the threshold between thermal and nonthermal effects in laser surgery of biomedical tissue. Free Electron Laser (FEL) at Osaka University, Japan, has a pulse structure in which a macropulse (pulse width: 15 μs) consists of equally separated micropulses, whose width and interval are approximately 5 ps and 44.8 ns, respectively. A precisely controlled of micropulse train may establish fast optic processes because thermal relaxation time in tissue is about 1μs. A pulse-picking system was designed in order to extract a single or a few micropulses from an entire macropulse using an acousto-optic modulator (AOM) in which the light path can be transiently diffracted by an external gate signal. The extracted micropulse train was monitored by a mercury-cadmium-telluride (MCT) photodetector with ~1 ns response time and recorded on a digital oscilloscope. A single micropulse was extracted as a result of adjusting the duration of the gate signal to 50 ns which is nearly equal to the micropulse interval. Investigation of a fast interaction between FEL and tissue using this system is expected.

INTRODUCTION

Many bio-molecules absorb mid-infrared (MIR) light strongly due to molecular vibration. Exciting a specific molecular vibration selectively using MIR pulse laser gives various medical treatment effects on a level of molecules.

In laser surgery, controlling thermal effects is important. The thermal and nonthermal effects are generally classified according to the thermal relaxation time (τ_{therm}) of a biomedical tissue. If the interaction time (τ_{int}) which depends on the pulse width and frequency of laser is longer than the thermal relaxation time ($\tau_{int} > \tau_{therm}$), the heat spreads over the entire biomedical tissue and produces macroscopic thermal effects. For example, a surgical laser incision and coagulation in tissue using the thermal effect. However, the thermal effect has an influence on normal tissue due to diffusion, and the selective interaction by bio-molecular vibration is not expectable. In the case of $\tau_{int} < \tau_{therm}$, because a particular molecule is excited within τ_{therm}, the selective interaction is caused faster than diffusion.

Biomedical applications have been studied using a free electron laser (FEL). FEL at iFEL, Osaka University in JAPAN, is tunable from 5 μm to 22 μm in mid-infrared (MIR) region, which is high peak power and short pulse operation. The FEL has a unique double pulse structure; the structure consists of a train of macropulses, and each macropulses contains an ultrashort 300-400 micropulses. The width of a macropulses is about 15 μs and repetition rate is 10 Hz. The width of a micropulse is shorter than 10 ps and the separation between micropulses is 44.8 ns. Therefore, precise control of micropulses is required in order to evaluate FEL irradiation effects on the bio-molecule without thermal effects.

There is a number of technologies for switching the laser beam, e.g. Pockels cell (PC) [1, 2] or acousto-optic modulator (AOM). PC switches the polarization direction of laser beam rapidly by high-voltage switching. Becker *et al*. have achieved switch out from 80ns to the full 6 μs duration of the FEL macropulse [1]. AOM can transiently diffract the light path with an external gate signal. The switching speed of AOM is slower than PC, but has a higher switching efficiency. We have chosen AOM control micropulse train.

A micropulse-picking apparatus was designed to switch-out a short micropulse train from an entire macropulse by a deflection of the light path using a germanium acousto-optic modulator (Ge-AOM). We will discuss the nano-second interaction with bio-molecul tissue sample.

PULSE-PICKING SYSTEM

Principle of the acousto-optic modulator

The basic principle of the acousto-optic modulator (AOM) is shown in figure 1. All AO devices are based on a crystalline material whose one side is bonded to a piezo-electric transducer. When radio frequency (RF) signal is applied to the transducer, an acoustic wave (AW) is produced by the inverse piezoelectric effect and travels in the crystal. The wave of condensation and rarefaction in the crystal is acted as a diffraction grating. An incident beam to the crystal is diffracted into many orders during the formation of the AW. If the angle of incidence is set to the Bragg angle, the majority of the diffracted light appears in the first order. This is the optimal setting in most practical application.

The Bragg angle (θ_B) is determined by wavelength of incident laser λ_i and RF drive frequency f_c.

$$\theta_B = \frac{\lambda_i f_c}{2 \cdot v} \qquad (1)$$

, here v is velocity of AW into the crystal.

* suzuki@fel.enf.osaka-u.ac.jp

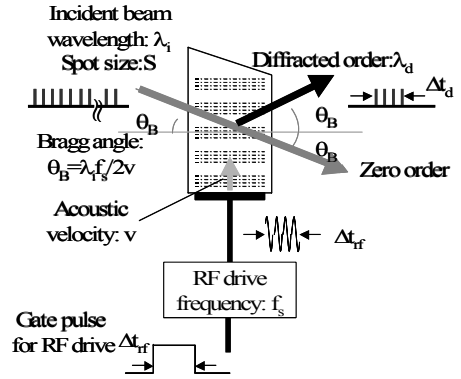

Figure 1: Basic principle of the acousto-optic modulator

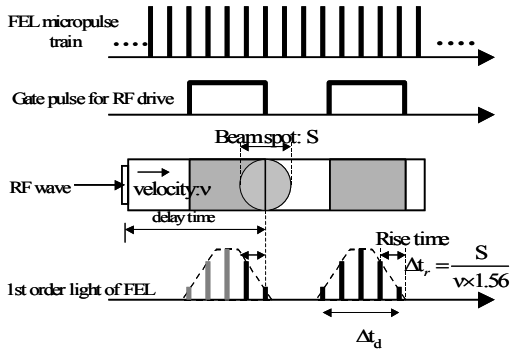

Figure 2: Time chart of pulse diffraction

Figure 2 shows a time chart and image of the pulsed diffraction. The diffracted light is produced while the pulsed AW passes the whole incident light spot. In other words, an adjustment of the gate pulse for the RF driver (Δt_{rf}) can control the micropulse train which is extracted from a macropulse. The minimum temporal window of the diffracted light (Δt_d) is limited by the rise / fall time (Δt_r) which depends on the AW velocity (v) and light spot size (S).

$$\Delta t_r = \frac{S}{v \times 1.56} \qquad (2)$$

(1.56=a correction factor for large beam size)

Designs

The setup for diffraction of FEL beam is shown in figure 3. As the crystalline material of AOM, we chose a germanium (Ge-AOM) which has a high transmission and allowable input energy at MIR wavelength region. Table 1 shows the specification and the ba performance of the Ge-AOM (AGM-402A1, IntraCation CO.) and RF driver (GE-4010, IntraCation CO.) used in our experiments. We chose the Ge-AOM with anti-reflection (AR) coatings limited to 5.7~7.0 μm in order to eliminate the Fresnel reflection on the Ge surface.

In order to extract a signal or a few micropulses from an entire macropulse, the incident FEL beam spot size needs to be about 250 μm which is estimated from the equation (2) as equivalent to Δt_d =50 ns. The focusing of FEL beam on AOM causes various problems; for example, damage to Ge and decrease in the diffraction efficiency. Therefore, the incident beam to AOM is better to be collimated.

The FEL beam which was focused with two ZnSe convex lenses (f1 = 50 cm, f2 = 3cm) entered the Ge-AOM at the Bragg angle (θ_B= 38.5 mm radian). The polarization direction of the incident beam was vertical to the diffraction grating in the operating AOM. If the polarization is parallel to the gating, the diffraction efficiency is significantly reduced by the consequence of Maxwell equations. The diameter of incident beam is about 1 mm; it is too large to extract a single micropulse. However, it is possible to evaluate an interaction without the thermal effect in bio-medical tissue. Although the beam is not collimated, it is equivalent to the parallel light within the AOM because the beam divergence at an angle of 7 mm radian is smaller enough than the Bragg angle.

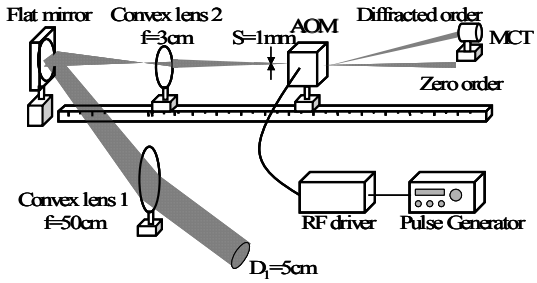

Figure 3: The setup for micropulse-picking

Table 1: specification and the basic performance of AOM and RF drive

Acousto-optic modulator (AGM-402A1)	
Acousto-optic material	Germanium
Acoustic Velocity (v)	5.5 mm/μsec
RF Center Frequency	40 MHz
Optical Insertion Loss	< 7 percent
Optical wavelength	10.6 μm
Beam Separation	77 mm radian
Bragg Angle	38.5 mm radian
Diffraction Efficiency	70 percent

RF driver (GE-4010)	
Oscillator Frequency	40 MHz
RF Output Power	10 watts
Rise/Fall Time	30 nsec

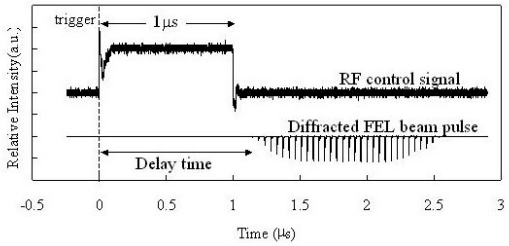

Figure 4: Experiment result of micropulse train extracted with the control signal of 1μs.

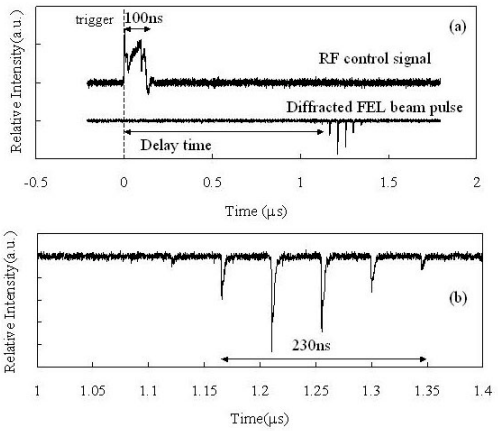

Figure 5: Experiment result of micropulse extracted with the control signal 100ns (a) and expansion of extreacted micropulse (b).

RESULTS OF MICROPULSE EXTRACTION

Figure 4 and 5 show the results of the experiment for examination of the pulse-picking system using Ge-AOM. The temporal window for the micropulse-picking depends on the gate pulse for the RF driver. Figure 4 confirmed that about 30 micropulses (44.8 ns * 30 = ~1.3 μs) are extracted from an entire macropulse by the gate pulse of Δt_{rf}=1μs. The diffracted light was detected about 1.2 μs after the rising edge of the gate pulse. This delay time is caused by the response time (30ns) of the RF driver and the travel time of AW in the crystal. Figure 5 shows the micropulse train extracted by the gate pulse of Δt_{rf}=100 ns. Figure 5 (b) is the enlarged view. Five micro pulses (44.8 ns * 5 = ~230 ns) are found to be extracted and the picking temporal window Δt_d is different from Δt_{rf}. The window is limited to the rise time (t_r) of the AOM. In the case of the incident beam of 1 mm in diameter t_r=116 ns is estimated from the equation (2). Therefore, a micropulse train of less than 232 ns cannot be extracted. Furthermore, in the case of Δt_d < 232 ns, the diffracted light intensity decreased because the pulsed AW became not able to cover the entire incident beam spot and a portion of the incident light was diffracted. This system can adjust the micropulse train in the range from 5 to 335 micropulses (macropulse width: 232 ns - 15 μs).

Figure 6 shows the optical insertion loss of wavelength 5~12 μm. The loss in the AR coatings wavelength region is about 7%, which agrees with the specification values. The loss in the region out of the AR coating wavelength (< 10 μm) is also low; it is less than 30%. The diffraction efficiencies at the FEL wavelength of 6.3 μm and 9.4μm are 65~70%, also agree with specification value (see table 1).

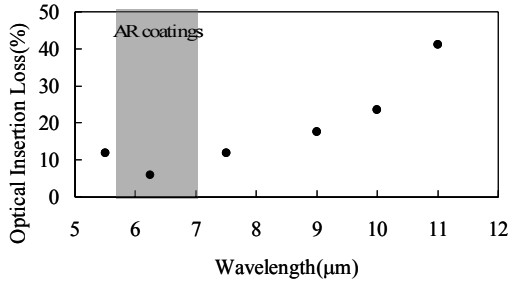

Figure 6: Optical insertion loss as a function of wavelength.

APPLICATIONS OF PICKING SYSTEM

Interaction with biomedical tissue

We have researched various interactions between biomedical tissues and MIR-FEL, for example the selective removal of cholesterol ester (5.75 μm), the surface modification of tooth dentin (9 μm band) and the control of dephosphorylation (9 μm band). Control of thermal effects is important to lead to these processes effectively.

We showed that the infrared absorption peak of the phosphate group is reduced after the FEL wavelength 9.4 μm irradiation (average power density 8.6 W/cm^2) [3]. The thermal effect on the interaction between a critical tissue and the controlled micropulse train was investigated. The length of the micropulse train was varied by the pulse-picking system while the average irradiation power density was adjusted to be constant. polyacrylic acid without phosphorylation was used as the sample in the primary experiment. polyacrylic acid is used as a model of a biomechanical material because chemical structure is simplicity and handling is easy. The sample was irradiated with FEL (wavelength 9.4 μm) of macropulse width of 15us and 2us respectively. Each irradiation effect is estimated by comparing the absorption spectra measured by Fourier Transform Infrared Spectrometer (FT-IR).When an entire macropulse is irradiated (15 μs), the polyacrylic acid dissolved remarkably. In contrast, the decrease in micropulse train (~2 μs) reduces thermal effect and the cemical structure is kept. Evaluate of interaction which controlled thermal effect is expected.

Matrix-assisted laser desorption/ionization using UV laser and FEL

Matrix-assisted laser desorption/ionization (MALDI) is a powerfull and robust technique for protein identification [4]. We have developed a novel MALDI method based on a simultaneous irradiation of a UV laser and FEL (UV/FEL-MALDI). The UV laser and FEL can create electronically and vibrationally excited states on a sample in parallel. The results provided analyses of macromolecules and insoluble proteins which are not amenable to the conventional measurement [5, 6].

The typical pulse width for MALDI has been reported to be ~100 ns, however neither of macropulse nor micropulse of our FEL has a suitable time scale. To achieve the optimum irradiation condition, the FEL micropulse train and the timing of electronic and vibration excitation need to be adjusted arbitrarily.

Figure 8 shows a schematic diagram of UV/FEL-MALDI time-of-flight mass spectrometer (TOF-MS) with a micropulse picking system. The irradiation of the UV laser and FEL is controlled by synchronous trigger signals. Figure 9 shows the timing chart of the irradiation event. This result confirms that the diffracted FEL micropulse train and UV laser pulse are irradiated simultaneously. The UV/FEL-MALDI with the micropulse picking system which is extracts a short micropulse train can synchronize precisely the UV and FEL laser pulses and is expect to elucidate the ion generation mechanism and to improve the efficiency of ionization.

CONCLUSIONS

In order to control the FEL micropulse train for classifying thermal and non-thermal effects on biomedical tissue, we designed a micropulse picking system using Ge-AOM in which the light path can be diffracted to extract a few micropulses from an entire macropulse. The pulse-picking system achieved to control the diffracted micropulse train from 232 ns to 15 μs. The diffraction efficiency reached to 65~70%.

The thermal effect related to the interaction between a micropulse train and phosphrylate acrylamide was verified. The result obtained by the controlled micropulse train, whose length was varied at the constant average power, confirmed that limiting the micropulse train decreases the thermodiffusion in a critical tissue. The UV/FEL-MALDI equipped with the picking system can control the timing of electronic and vibration excitation precisely, and many achieve the optimum irradiation condition for protein identification. The picking system is expected to give many information about interaction between laser and biomedical tissue.

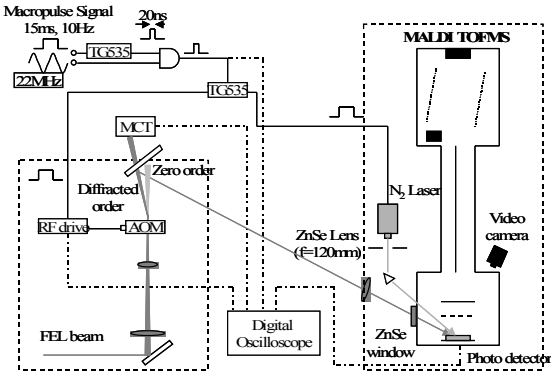

Figure 8: UV/FEL-MALDI TOFMS required micropulse-picking system.

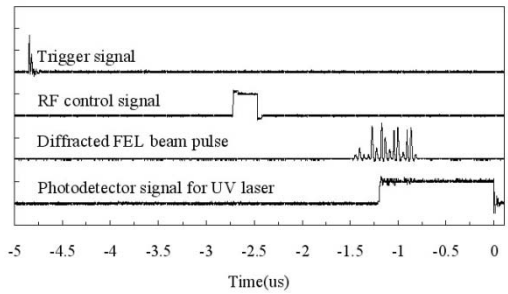

Figure 9: Experiment result of timing control on a simultaneous irradiation of a UV laser and FEL.

ACKNOWLEDGMENTS

We are grateful to Mr. Kuma, Mr. Marusaki and Mr. Teranishi, operational staff of iFEL graduate school of engineering, Osaka University.

This study was supported by a research budget of the Intellectual Cluster Project from Senri Life Science Foundation / the Ministry of Education, Culture, Sports, Science and Technology of Japan.

REFERENCES

[1] K. Becker et al., Rev. Sci. Instrum. 65(5), 1496(1994).
[2] A. V. V. Nampoothiri et al., Rev. Sci. Instrum. 69(3), 1240(1998).
[3] K. Ishii et al., Nucl. Instrum and Math. Phys. Res. A, 528, 614, (2004).
[4] K. Tanaka et al., Rapid Commun. Mass Spectrun 2, 151(1998)
[5] Y. Naito et al., Nucl. Instrum and Math. Phys. Res. A, 528(1-2), 609,(2004).
[6] S. Y. Suzuki et al., Rev. Laser Engineering, 31(12), 835(2003).

COHERENT PROTEIN DYNAMICS EXPLORED AT FELIX

R. Austin, Princeton University, Aihua Xie, Oklahoma State University
B. Redlich, Lex van der Meer, FOM Institute for Plasma Physics

Abstract

We have used extremely narrow (1-2 cm^{-1}), high energy pump-probe time domain spectroscopy to probe the heterogenously broadened amide I band in several proteins. We find that the short wavelength side of the amide I band can give rise to very large (50%) bleaching signals, indicating a very long dephasing time of at least 20 ps to the internal amino acid amide I stretch band.

INTRODUCTION

At a recent conference, we heard an eminent theorist refer to the "original sin" committed in a talk. The theoretical talk was about self-localization of vibrational (not electronic) energy and the generation of solitons in a biopolymer, in this case DNA. It was a good talk, very clear and carefully presented. What then was the sin? The critic was convinced that relevant biological motions in biology are all overdamped and therefore diffusive in nature. If they are overdamped, then (perhaps) issues of energy self-localization and solitons are simply irrelevant at least at the picosecond time scale. So, our critic's point was: if you don't address head-on issues of overdamping times in biological vibrational dynamics you do commit an original sin: everything after that is tainted.

There is an additional issue that wasn't mentioned in the charge of original sin, that of dephasing time. Using the language of NMR and the Bloch equations, there are two parameters that characterize an excited state: the longitudinal relaxation time T_1 which is a measure of the lifetime of an excited state, and the transverse relaxation time (pure dephasing time) T_2^*, which is a measure of how long the system remains in phase [1]. It could be, as we discuss below, that the dephasing time of any coherently excited vibrations can be much shorter than the excited state relaxation times and determine the linewidths of the transition. In that case, it is almost as great a sin to ignore a short T_2^* as ignoring T_1, for many non-linear effects need the coherence times of the excitations to be long as well to be effective. A short T_2^* can be as destructive as a short T_1 for a beautiful theory of non-linear effects in biology.

The determination of the T_1 and T_2^*'s of a state starts with the static spectroscopy of the state. If a particular transition is not heterogeneously broadened, the static lorentzian linewidth Γ_o of the transition (in energy units of wavenumbers, cm^{-1}) is given by [1]:

$$\Gamma_o = \frac{1}{c}\left[\frac{1}{\pi T_2^*} + \frac{1}{2\pi T_1}\right] \quad (1)$$

The classic problems in proteins is of course is that by static spectroscopy it is not possible to disentangle T_1 from T_2^* by static spectroscopy alone, and further that the vibrational lines in the IR spectra of a protein are inhomogenously broadened due to complex energy landscape of a protein [2]. It is possible that within this distribution of lines that there exist a set of states that are both spectrally narrow and have long dephasing times. In order to discover these states it is necessary to probe their dynamics by some form of site-selective spectroscopy.

STATIC SPECTROSCOPY

In fact, there is evidence from static spectroscopy at least that there exists a distribution of relatively narrow states within the broad envelope of amide I modes in proteins. We take as our example Mb, but other proteins show similar evidence (data not shown). Fig. 1 shows the spectrum IR spectra of myoglobin in a D_2O-d-glycerol buffer as a function of temperature. If we concentrate on the amide-I band, it is clear that the short wavelength side of the amide I band shows little temperature dependence, while the long wavelength (red) side shows the appearance of a new band as temperature is decreased, indicative of increasing hydrogen bond strength with decreasing temperature [3]. The amide I mode is due to the C=O stretch of the amide group, and is moderated by a weak hydrogen bond with neighboring hydrogen atoms of the primary amine groups, and with hydrogens of water if they are accessible to the amino acids. Those amino acid groups which are are buried within the protein and not in contact with the surface or the solvent would be expected to not have this temperature-dependent change in the amide-I frequency, thus we identify the blue-side part of the amide-I band with the internal amino acids, and the red-side amide-I band with the external, solvent exposed amino acids.

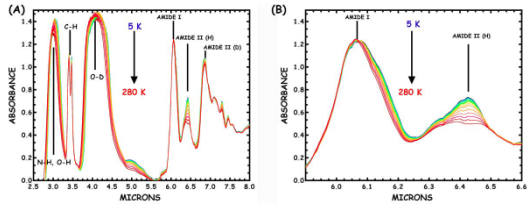

Figure 1: (A). The infrared absorption spectrum of sperm whale myoglobin as a function of temperature from 5 K to 300 K, from 2.8 to 8.0 microns. (B) The spectrum from 5.9 to 6.6 microns

We can make a further observation: the Debye-Waller factor S, a measure of the variance of the positions of atoms in a lattice [4], is also a function of the position of the amino acid in a protein. S is defined by: $S =< x^2 >$, where

$< x^2 >$ is the variance of the position x of atoms in the protein crystal. As a general rule, the interior parts of the protein have small S while those at the surface of the protein have large S. Thus, not only do the internal amino acids have small Debye-Waller factors but they also show less interactions with the solvent. One might then imagine that these internal amino acids have unusual dynamical properties compared to the amino acids at the protein surface which are held less tightly in place than the interior.

PUMP-PROBE MEASUREMENTS

At FELIX it turns out that the pulse width can be made as long as 10 picoseconds, giving rise to a linewidth of about 2 cm^{-1}, while still retaining about 1 microjoule of energy delivered to a 100 micron spot size. Further, at FELIX it is possible to deliver this pulse as a single pulse, since as we have painfully shown delivering too much energy via a series of micropulses at a rate higher than the diffusional cooling rate only leads to damaging the protein and introduction of complications [6]. Fig. 2 shows the heterodyne mixing signal of a long pulse from FELIX. This pulse has a duration of 10 ps and hence a spectral linewidth of 0.01 microns or 2 cm^{-1}. When such a long pulse is scanned across the amide I+II spectral region of Mb, from 5.8 to 6.5 microns, a remarkable thing happens. While ordinarily when pulses of duration 1 ps or shorter are used the typical transmission change observed for 1 uJ pulses focussed to 100 micron spot sizes is about 1% or less, if the spectral width is narrowed the signal enormously increases, by a factor of 50! Fig. 3 shows an example of the signals observed as a narrow pulse is scanned across the amide I+II region. Note that the huge enhancement is seen only for the amide I band, and only on the blue side of the amide I band.

This blue-side signal enhancement could be due to excitation of chromophore bands which lie within the amide I band of the protein, but this is probably not the case. Fig.4 shows a scan of the amide I region of lysozyme, an enzyme which has no chromophores. Not only does this scan show that a similar anomalous enhancement of the pump-probe signal occur on the blue side of the amide I band of this protein, it also shows that the shape of this enhanced signal depends on the protein. Of course, narrowing the spectral width has its costs in that the time resolution decreases. Fig. 5 shows what happens as the pulse width is changed to the time-domain response of the sample. When the pulse width is long the response of the protein, in this case myoglobin, looks like the autocorrelation of the pulse with no obvious lifetime. As the pulse is shortened, exciting more modes and putting less energy into each mode, the shape of the response qualitively changes with a clear lifetime effect coming in at longer times but less amplitude to the pulse. If the pulses are made as long as possible and the signal is observed at the spectral peak of the response, then varying the energy of the pulse by use energy attenuators shows that the transmission change is proportional to the energy of the

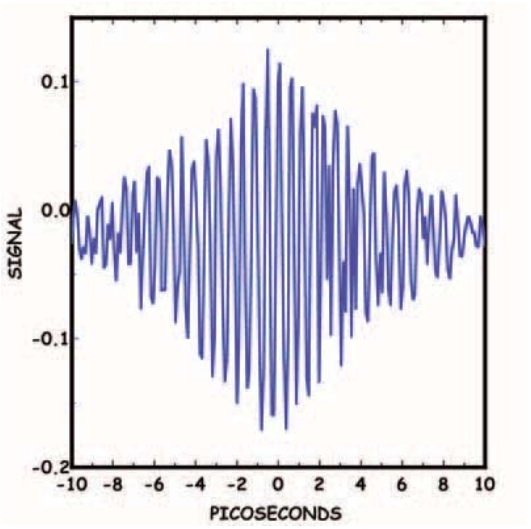

Figure 2: Heterodyne mixing of the pump and probe pulse used for these experiments.

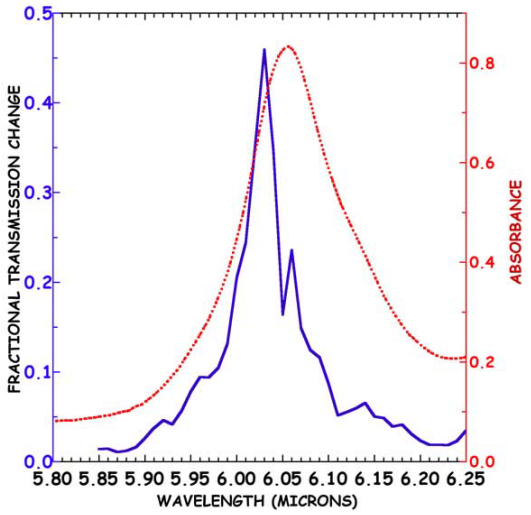

Figure 3: Wavelength scan of the transmission change vs. wavelength of the pump-probe signal seen for Mb in a 75% d-glycerol/25% D_2O solvent at room temperature (solid line). We have superposed the measured absorbance of this sample (dashed line).

pulse. Finally, the polarization of the pump pulse can be rotated with respect to the polarization of the probe pulse, these measurements shown in Fig. 6 reveal that the pump polarization must be parallel to the probe polarization for maximum signal.

It is difficult in this brief communication to reveal succinctly all of the data we have required, even more difficult to explain what is happening. We have already discussed how the heterogeneous broadening of the amide I

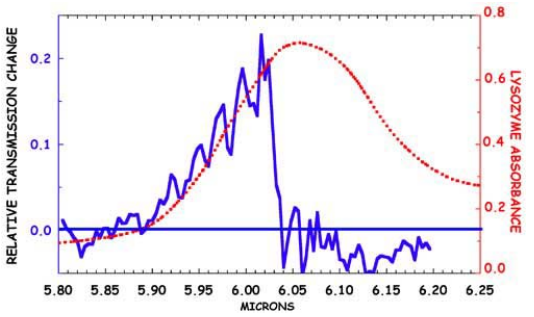

Figure 4: Scan of the pump-probe signal observed for the enzyme lysozyme (solid line). The absorbance of the sample is given by the dashed line.

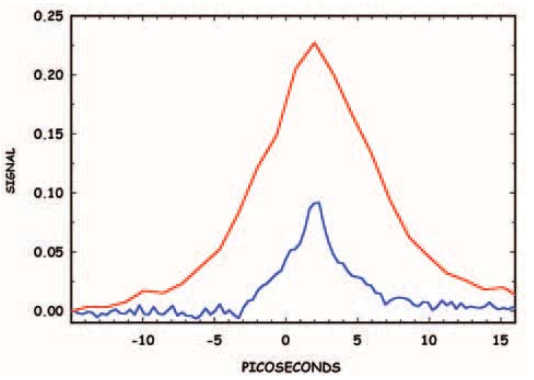

Figure 5: A time scan of the Mb signal at 6.04 microns as the pump pulse is scanned via the delay line over the probe pulse. The two traces are for a 10 ps and a 2 ps wide pulse.

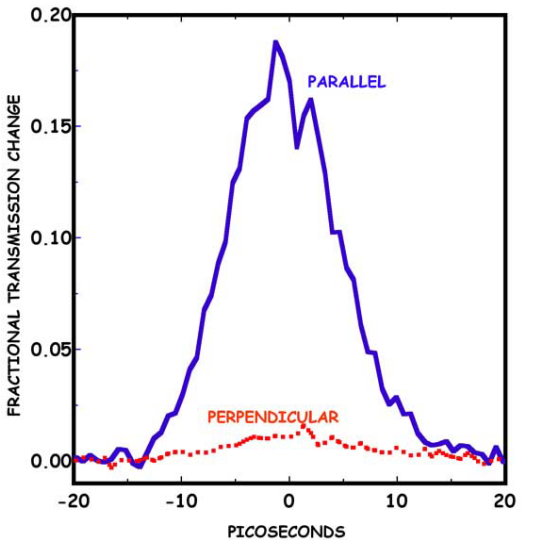

Figure 6: A time scan of the Mb signal at 6.04 microns as a function of the relative polarization between the pump and probe.

band can be roughly split into a blue side distribution of buried amino acids not in contact with the solvent and a red side distribution of solvent exposed amino acids. We also speculated that perhaps the blue side, buried amino acids with their small Debye-Waller factors might have long coherence times T_2^*. How can we begin to draw a quantitative connection between coherence dephasing times and the amplitude of these strange signals? The simplest model, which does require phase coherence of the excited state, is the phenomena called Rabi flopping [1]. In Rabi flopping a 2 level system is driven by a resonant electromagnetic wave with electric field strength E. We denote the strength of the electric dipole transition moment to be μ. Somewhat counter-intuitively, when such a two level system is driven coherently the population of the ground state $\rho_1(t)$ and the excited state $\rho_2(t)$ oscillates as:

$$P_1(t) = \frac{[\cos(\chi t) + 1]}{2} \qquad (2)$$

where $\chi = \frac{\mu E}{\hbar}$ is the Rabi flopping frequency. The surprising aspect of Rabi Flopping is of course the fact that a population can completely invert with time if driven resonantly and if the dephasing time T_2^* is much longer than χ. It is possible to characterize a pulse of such resonant light by an angle $\theta = \int \chi dt$ which represents for example the population change it creates. For example, a $\pi/2$ pulse would the equalize the ground and excited state populations. Such a pulse would of course result in a huge bleaching signal because there would be no net absorbance changes.

It is possible to estimate θ and hence the extent of transmission change possible. The FEL pump pulse had an energy of 1 microjoule, a pulse duration of 5 ps, and a focused diameter of 100 microns. This yields an optical electric field E of about 10^8 V/m. The amide I band is a strongly allowed transition, we assume the electric dipole moment is approximately 1e-Å. We compute then that a π pulse should take about 1 ps, IF the coherence time T_2^* is on the order of the longitudinal relaxation time T_1. Of course, dont know dipole moment, so this is just a guess but it does indicate that if a narrow state with long T_2^* exists, its population can be inverted. We can guess how the intensity of the observed bleaching signal signal will vary with θ. Since the potential transmission change in our case is about 1000% (a ten-fold increase in transmission since the sample has an optical density of about 1 at the maximum wavelength). Since we observe at most 50% changes the actual value of θ must be much less than 1 radian. Thus, we can expand the $\cos(\theta)$ term in Eq. 2 yielding:

$$P_1(\tau) \sim 1 - \frac{[(\mu E \tau/\hbar)^2}{4}] \sim 1 - \mathcal{E}_{pump}\frac{[\mu/\hbar]^2}{4} \qquad (3)$$

where we measure the response at the midpoint of pump-pulse, τ and $\mathcal{E}_{pump}$ is the energy of the pump pulse. The prediction then is that the transmission change which is proportional to $P_1 - 1$ would be proportional to the energy of the pump $\mathcal{E}$. In Fig. 7 we show that in fact the signal

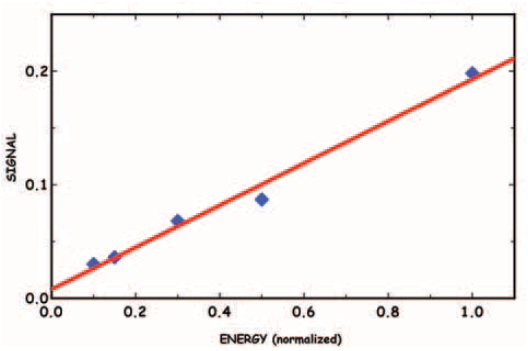

Figure 7: The dependence of the peak in the transmission signal with pump pulse energy for Mb.

is linearly proportional to the pump energy as predicted by Eq. 3.

We come back to the issue of Original Sin. We suggest that the T_2^*, the dephasing times, of the deeply buried amino acid band is very long, at least 20 ps. IIf so, then this part of the protein is an inherently quantum mechanical, strongly coupled anharmonic system. system. Perhaps we are addressing one aspect of the Original Sin problem in protein dynamics.

ACKNOWLEDGEMENTS

We would like to thank the staff of the FOM Laserphysics facility FELIX for their dedicated help, Profs. Warren Warren and Marlon Scully of Princeton University for discussions, Lorand Kellerman for assistance in the FTIR spectra and the Office of Naval Research for their financial support.

REFERENCES

[1] P.W. Milonni, and J.H. Eberley, **Lasers**. John Wiley and Sons, NY, 1988.

[2] R.H. Austin, K.Beeson, L.Eisenstein, H.Frauenfelder, I.Gunsalus and V.Marshall, Dynamics of Ligand Binding to Myoglobin, Biochemistry 14, 5355-5373 (1975)

[3] G.A. Jeffrey, An Introduction to Hydrogen Bonding; Oxford University Press: New York, 1997.

[4] D. Mermin, J. Math. Phys. 7 (1966) 1038.

[5] H. Frauenfelder, G.A. Petsko, and D. Tsernoglou, Nature 280 (1979) 563.

[6] R.H. Austin and A. Xie, Nuc. Instru. and Meth. Physics. Res. A (1998) 504

PREPARATION FEMTOSECOND LASER PREVENTION FOR THE COLD-WORKED STRESS CORROSION CRACKINGS ON REACTOR GRADE LOW CARBON STAINLESS STEEL*

Eisuke J. Minehara, Akihiko Nishimura*, and Takashi Tsukada**
Free-Electron Laser laboratory at Tokai, *High Peak Power Laser Laboratory at Kizu,
**Research Group for Reactor Structural Materials at Tokai, JAERI, Tokai, Naka, Ibaraki 319-1195 JAPAN

Abstract

Femto-second (fs) lasers like low average power, Ti:Sapphire lasers, the JAERI high average power free-electron laser excimer laser, fiber laser and so on could peel off and remove two stress corrosion cracking (SCC) origins of the cold-worked (CW) and the cracking susceptible material, and residual tensile stress in hardened and stretched surface of low-carbon stainless steel cubic samples for nuclear reactor internals as a proof of principle experiment except for the third origin of corrosive environment. Because it has been successfully demonstrated that the fs lasers could clearly remove the two SCC origins, we could resultantly prevent the cold-worked SCC in many fields near future.

INTRODUCTION

We first reported the novel method that femto-second (fs) lasers of the low average power Ti: Sapphire one, the JAERI high average power free-electron laser, excimer laser, fiber laser and so on [1,2] could peel off and remove both stress corrosion cracking (SCC) origins of the cold-worked (CW) and very crack-susceptible material, and residual tensile stress in the hardened surface of low-carbon stainless steel cubic samples for nuclear reactor internals as a proof of principle experiment except for the last and third origin of corrosive environment. Because it has been successfully demonstrated that the fs lasers could clearly remove the two SCC origins, we could resultantly prevent the cold-worked SCC in many field near future.

The SCC is a well known phenomenon [3, 4, 5, 6] in modern material sciences, technologies, and industries, and defined as an insidious failure mechanism that is caused by the corrosive environment, and the crack-susceptible material and the surface residual tensile stress simultaneously. There are a large number of famous SCC examples for damaging stainless steels, aluminium alloys, brass and other alloy metals in many different cases. In many boiling light-water reactor (BWR) nuclear power plants and a few pressurized light water reactor (PWR) ones in Japan and the world [3, 4, 5, 6, 7] up to now, a large number of the deep and wide cracks have been recently found in the reactor-grade low-carbon stainless steel components of core shroud, control-blade handle, re-circulating pipes, sheath and other internals in the reactor vessel under very low or no applied stresses. These cracks have been thought to be initiated from the crack-susceptible like very small-sized cracks, pinholes, concentrated dislocation defects and so on in the hardened surface, which were originated from cold-work machining processes in reactor manufacturing factories, and to be insidiously penetrated widely into the deep inside under the residual tensile stress and corrosive environment, and under no applied stress during a much shorter term operation. Most people had thought to be unavoidable that Japanese economy would be damaged more or less because most of the nuclear power plants near Tokyo were shut-down during the last summer because of the CWSCC failures. As it was fortunately a cold summer last year because of global climate disorder, Japan and the Japanese domestic electric power companies could have a narrow escape from a large scale black-out in many prefectures near Tokyo and Tokyo metropolitan area.

SAMPLE PREPERATIONS

The low-carbon type 316, 304 and other austenitic stainless steel materials commonly used in nuclear reactor internals were prepared and cold-worked to introduce high residual tensile stress, crack-susceptibility and hardening in the one side using a conventional multi-purpose milling machine before the cutting, characterizing the cold-worked surface hardness, susceptibility and tensile stress, and fs laser peeling-off. As a lot of the reactor core shrouds and others have been found to be damaged by CWSCC during their operation and to be manufactured and cold-worked to finish by a disk-sander and a bite of a huge turning mill in the factories, the same stainless steel material with them and the multi-purpose milling machine were used to simulate or to reproduce their cold-work processes like breaking-down surface grains and lattice microstructures.

FS LASER PEELING OFF

After the stainless steel material sheet was cut into about one centimeter cubic samples of several tens, typical depth of the hardened surface zone was measured to be about several tens to a hundred micrometer. Each cube of them was used as a standard test sample being prepared in the same manner to compare with each other in different peeling-off and testing conditions. The laser typically irradiated to peel off about 2mm by 2mm square area in the depth of 0.05-0.75mm without any heat effects around the central part of the cold-worked, hardened and tensioned one in air atmosphere. Each of the irradiated samples was cut into 2 pieces by a sharp and thin ceramic

disc to have a rectangular 2mm by 1mm peeled-off strip area under water-spraying and cooling. One of the half pieces was used to measure hardness distribution along the depth, and another of them used to measure the residual stress strength and direction of compressing or tensioning in the peeled-off strip and hardened side.

The half piece sample for the hardness testing was polished carefully to peel off the damaged surface layer spraying water and diamond powder. Then, the cross-sectional surface of the half was electrochemically etched to get rid off the damaged layer by 10% oxalic acid solution. The etched surface was used to measure hardness distribution along the depth from the cold-worked surface to the deep inside by a Vickers type micro hardness testing machine [8]. Results of the hardness distribution measurements have shown that the fs laser completely peeled off the susceptible and the hardened zone.

RESIDUAL TENSILE STRESS

A commercially-available small area X-ray diffractometer [9] was used to analyze residual stress in the peeled-off strip, and to confirm no effective residual stress in it. As typically measured in the diffractometry, the residual tensile stress which was introduced to range from 500 to 600 MPa by the cold-work were removed from the fs laser peeled-off strip.

HARDNESS TESTINGS

The typical value shows that the hardness one near the surface was measured to be very high, around 470 kg/mm^2, and the artificially-introduced residual stress by the milling and other cold workings measured to be tensioned along the surface. In contrast with the high hardness values, the measured hardness ones around the fs laser peeled-off area of about 2mm by 2mm square were as low as the original low-carbon stainless steel austenitic material deep inside, and the fs laser peeling-off could remove the cold-worked and hardened one and make no additional hardened zone on the strip surface.

SUMMARY

The novel method of the fs laser-peeling off two SCC origins of the susceptible zone and residual tensile stressed ones without additional heat effects in the stainless steel except for the corrosive and environmental was firstly demonstrated utilizing a half watt or less Ti-Sapphire fs laser [1] as the proof-of principle experiment to evaluate a feasibility utilizing tens kW class fs free-electron laser (FEL) peeling and finishing. A $MgCl_2$ SCC test [10] for the samples has shown to be no crack of the CWSCC and a few tens of other shallow cracks in the peeled-off strip, and clearly indicates successful removal of the two origins.

All of the commercially-available fs ultra-fast lasers of Ti-Sapphire laser, excimer laser, fiber laser and so on[7] except for high power fs FELs have intrinsically no capability and no future possibility to produce a fs and kW high average power [1]. It is thought that the high average power and fs FEL[2] has only and enough capability to peel off the two SCC origins and to prevent their damages of the nuclear reactor pressure vessel internals like the core shroud, pipes, and other structural components for realizing at least several times longer interval than current life expectation spans of the nuclear reactor safely, easily and quickly in low cost near future. There is a large possibility that we could apply the novel fs laser removal method with a large number of the similar boiling and steam generating plants or devices which were made of stainless steel and other iron alloys, and other metal alloys like Aluminium one, Brass and other ones to prevent their CWSCC damages near future if the same or the similar origins will govern their CWSCC failure processes.

ACKNOWLEDGEMENTS

The authors would like to express our sincere thanks to Drs. S. Saito, T. Iwamura and T. Kimura for their continuous supports and encouragements, also special thanks to all members of the research group for reactor structural materials and FEL laboratory at Tokai Research Establishment, JAERI for their critical helps and supports in the work. The work is partially supported by JAERI internal supporting funds No.20030412, and 20030413

REFERENCES

[1]C. Momma et.al., Optics Comm.129, 134(1996).
[2]N. Nishimori et. al., Physical Review Letters, vol86, No.25, p.5707-5710 (2001).
[3]R.M.Horn et. al., Nuclear Engineering and Design, 174(1997)313-325.
[4]O. Wacher and G. Brummer, Nuclear Engineering and Design, 168(1997)35-52.
[5]R. A. Mulford et.al., Corrosion-NACE, 39-4(1983)132-143.
[6]Bushan, Bharat, and B.K. Gupta, Handbook of Tribology. McGraw Hill Inc. New York.1991.
[7]T. Tsukada et. al., JAERI-Conf 2003-014(2003)119-131.
[8]Harry Chandler, Hardness Testing, ISBN0871706407, ASM International, 2nd edition (December 15, 1999).
[9]Victor E. Buhrke, Ron Jenkins, and Deane K. Smith, A Practical Guide for the Preparation of Specimens for X-Ray Fluorescence and X-Ray Diffraction Analysis, ISBN0471194581, Wiley-VCH、(November 7, 1997).
[10]Japanese Standard Association, JIS G0576, Stress corrosion Cracking Test for Stainless Steels, Ferrous Materials and Metallurgy I-2004 pp.1142-1149, ISBN4542136175, (April 20, 2001).

THZ IMAGING BY A WIDE-BAND COMPACT FEL

Young Uk Jeong, Hyuk Jin Cha, Seong Hee Park, Byung Cheol Lee, KAERI, Daejon, Korea
Grigori M. Kazakevitch, BINP, Novosibirsk, Russia

Abstract

We have developed a laboratory-scale users facility with a compact terahertz (THz) free electron laser (FEL). The FEL operates in the wavelength range of 100–1200 μm, which corresponds to 0.3–3 THz. THz radiation from the FEL shows well collimated Gaussian spatial distribution and narrow spectral width of $\Delta\lambda/\lambda \sim 0.003$, which is Fourier transform limited by the estimated pulse duration of 20 ps. The main application of the FEL is THz imaging for bio-medical researches. We are developing THz imaging techniques by 2-dimensional (2-D) scanning, single pulse capturing with the electro-optic method, and 3-D holography. High power, coherent, and short-pulsed feature of the FEL radiation is expected to show much better performance in advanced THz imaging of 3-D tomography. The coherent length of the FEL micropulse is measured to be 8-12 mm. In this paper we will show and discuss the main results of THz imaging with the different methods by using the KAERI compact FEL.

INTRODUCTION

T-ray which means THz radiation imaging technology was selected as one of '10 emerging technologies that will change your world' by a magazine named MIT's Technology Review of January 31, 2004. If we see the other selected technologies, e.g. universal translation, synthetic biology, and so on, the potentiality of the THz radiation technology might go beyond the usual understanding of us. THz radiation has several remarkable advantages for imaging compared with other conventional sources, such as safe energy range without ionization to the materials, foot-print spectral region of most chemicals and bio-materials, and relatively high spatial resolution for medical imaging.

There are several kinds of THz radiation sources [1–5]. Table-top THz sources generated by conventional lasers have been developed and used for various applications in the THz range [6–8]. However, advanced THz imaging such as tomography of living species requires much more power of the radiation to get information with better S/N ratio and higher speed of data acquisition. Inexpensive and compact THz FEL [5,9] can play the important role of encouraging the advanced THz applications due to its higher power and spectral brightness compared to the table-top sources.

We have developed a THz users facility based on a compact FEL [10]. The wavelength range of the FEL is 100-1000 μm and we could construct a users experimental stage for the wavelength of 100–300 μm. The THz FEL beam shows good performance in pulse-energy stability, polarization, spectrum and spatial distribution. We could get the 2-D imaging of various materials with the THz FEL beam. The measured coherence length of the THz FEL micropulses is 8-12 mm, which corresponds to 25-40 ps. The main idea for 3-D coherent THz tomography with the coherent pulse is proposed and discussed in this paper.

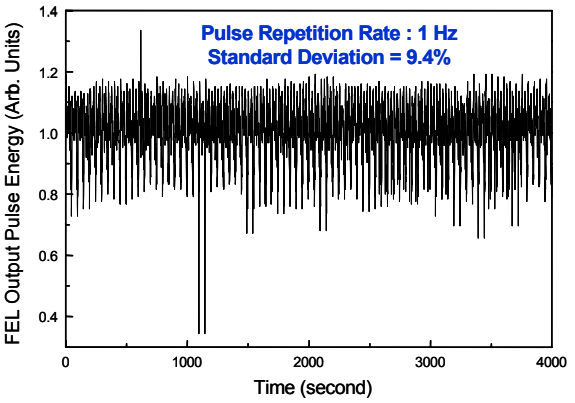

Figure 1: Measured fluctuation of the THz pulse energy depending on time.

THZ FEL BEAM CHARACTERISTICS FOR IMAGING

The stability of the radiation pulse energy was improved by keeping cooling water and air temperature of the system and laboratory within 0.1 and $1^{O}C$, respectively. Figure 1 shows the measured fluctuation of the THz pulse energy depending on time. The repetition rate of the FEL macropulse was 1 Hz during the measurement. We could not observe any drift of average value of the FEL pulse energy and the fluctuation of the pulse energy is less than 10% in r.m.s value. If we monitor and normalize the pulse energy fluctuation of the FEL beam, the measuring error is decreased to be less than 1%. With the stable THz pulses, we could measure 2-D scanned imaging, interference patterns, or spectroscopic information of species with high resolution.

The polarization of the THz FEL beam has been measured by using a metal-wire polarizer having 20 μm spacing, which is shown in Fig. 2. The FEL beam is highly polarized with a linear component of more than 98% due to wiggling motion of the electron beam inside a planar undulator. We could understand that the polarization of the FEL beam is not disturbed by the long distance (~10 m) propagation with more than 10 pieces of mirrors, windows and lens.

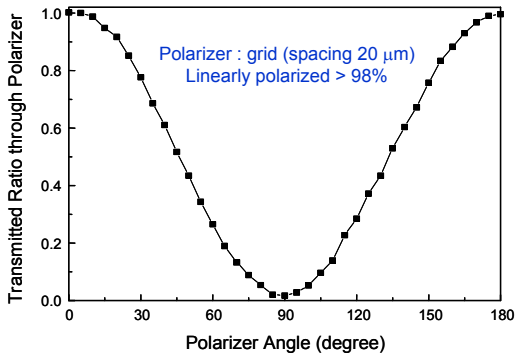

Figure 2: Measured polarization of the THz FEL beam by using a metal-wire polarizer having 20 μm spacing.

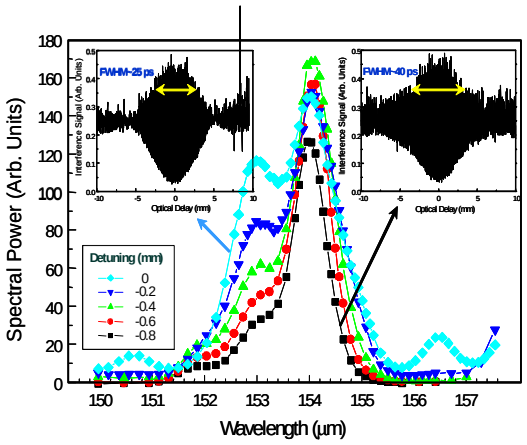

Figure 3: Measured FEL beam spectra depending on detuning lengths of the FEL cavity. Measured results of the coherence lengths of the FEL micro-bunches for the detuning lengths of 0 and -0.8 mm from the resonance position of the FEL optical cavity are shown in left and right insets of the figure, respectively.

Spectra of the FEL beam have been measured by a high resolution spectrometer having resolution of 10^{-4}. And the results were compared by the measured value of the coherence length of the FEL micropulses. Coherent length of the FEL micropulse could be measured by the Michelson configuration of the interferometer. Figure 3 shows measured FEL beam spectra depending on detuning lengths of the FEL cavity. Measured results of the coherence lengths of the FEL micro-bunches for the detuning lengths of 0 and -0.8 mm from the resonance position of the FEL optical cavity are shown in left and right insets of the figure, respectively. The FWHM of the FEL line width is between 0.7 μm to 2 μm, which corresponds to 0.4-1.2% of the wavelength. The measured coherence length from the interferogram is between 10 mm to 16 mm in FWHM, which corresponds to the FEL bunch length of 25-40 ps (8-12 mm, FWHM) in the case of the Gaussian-shaped pulse. The bunch length from the coherence length measurement agrees well with the estimation of the FEL bunch length from the calculated value of the electron beam bunch.

The spatial distribution of the FEL beam was measured on the experimental stage as shown in Ref. [10]. The results show the distribution of the THz FEL beam is near Gaussian shape. We have focused the beam having spot size of 7 mm and wavelength of 110 mm with a parabola mirror (F/2). The focal length of the mirror is 50 mm. The measured beam waist at the focal point is 0.3 mm, which is close to value of the diffraction limitation from the 7-mm-diameter THz FEL beam.

We could understand that our THz FEL beam has excellent performance in power stability, polarization, spectral width, spatial distribution and wavefront. We hope that the THz radiation could be used for the advanced application of THz imaging for 3-D coherence tomography.

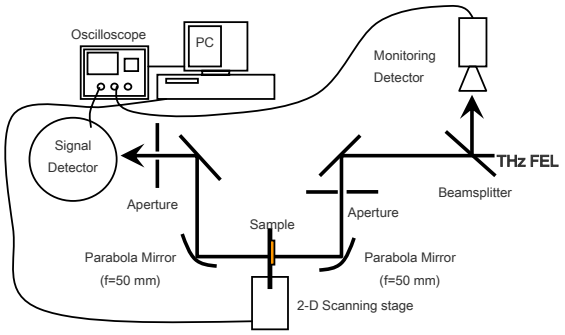

Figure 4: Schematics of the experimental setup for THz transmitted imaging with 2-D scanning of the samples.

2-D THZ IMAGING

Figure 4 shows schematics of the experimental setup for THz transmitted imaging with 2-D scanning of the samples. The 2-D scanning and data acquisition are automatically performed by a personal computer with a controller. For the first experiment on the THz imaging, we did not perform spectral study on the sample. Therefore the used wavelength for the THz imaging experiment was not optimised.

The first sample of 2-D THz imaging with our FEL was a microchip as shown in Fig. 5. From the experiment we could find the dynamic range of the THz imaging is much bigger than that of the usual vision recognition by human eyes. Even the dark part of the THz imaging inside the chip contains information on its structure. Figure 6 shows a transmitted THz imaging through an invisible paper box containing metal and silicon rings. We could see the shape of the rings clearly. Additionally the density information inside the silicon ring could be measured by the THz radiation, which means that the big dynamic

range is very useful to recognize the nature of sample with THz spectral information. Without any additional processing of the imaging data, we could get the dynamic range of 10^5 for the measurements.

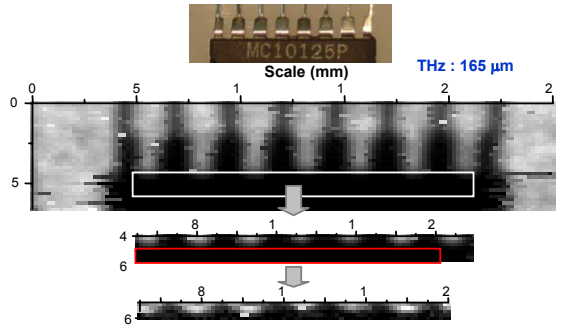

Figure 5: 2-D THz imaging of a microchip. From the experiment we could find the dynamic range of the THz imaging is much bigger than that of the usual vision recognition by human eyes. Even the dark part of the THz imaging inside the chip contains information on its structure.

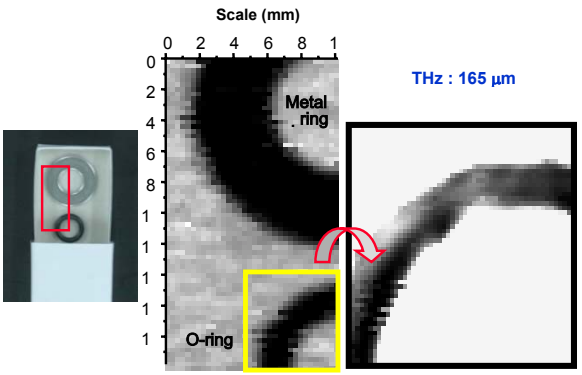

Figure 6: Transmitted THz imaging through an invisible paper box containing metal and silicon rings

Figure 7 shows a THz imaging of a gingko leaf, which is compared with a visible transmitted imaging. You can see the difference between the visible and THz imaging clearly. The main difference is caused by 10^3-10^4 times difference in absorption coefficient of liquid water between the two frequencies.

We are constructing a fast imaging system with a single micropulse of the THz beam by using the electro-optic (EO) detection and switching method. The linearly polarized visible or IR laser beam is collinearly incident to the EO crystal with the THz beam. The image of the THz beam is transferred to the visible or IR laser beam and the transferred image can be captured by an intensified CCD camera.

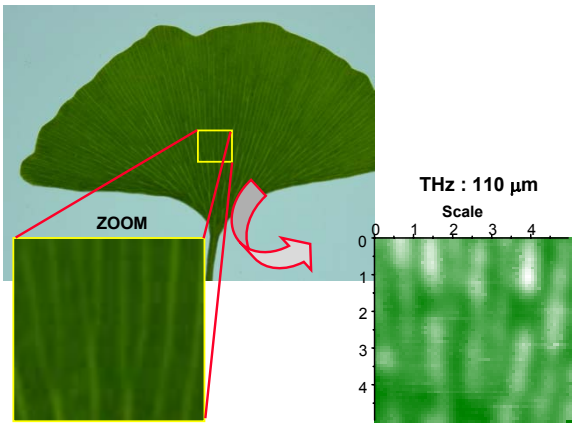

Fig. 7. Transmitted THz imaging of a gingko leaf, which is compared with a visible transmitted imaging.

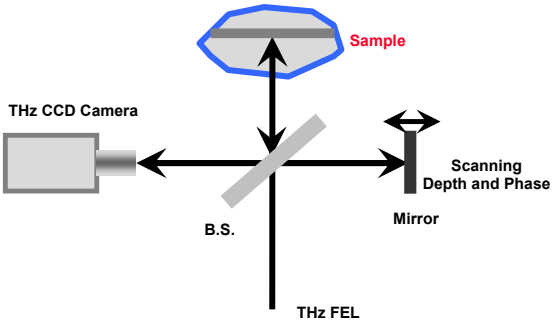

Figure 8: Schematics of the coherent THz tomography.

PROPOSAL FOR COHERENT 3-D THZ TOMOGRAPHY

The main difficulty of the THz tomography for medical application is the huge absorption of the radiation by liquid water which is the major constitution of human body. To get the information from inner part of living sample, we should remove the relatively strong signal scattered from the surface or near the surface of the sample. The most simple and effective way to get weak signal from strong background is to modulate the amplitude of the signal with the frequency which we can measure.

We have proposed a coherent 3-D THz tomography technique by using the method of holography. Figure 8 shows schematics of the coherent THz tomography. The THz FEL beam is divided into illuminating and reference beams. By using the short-pulsed feature of the THz FEL beam and controlling the optical path of the reference beam, we can select a certain cross-section inside the

sample to make a hologram. By changing the optical path of the reference beam minutely, we can get modulating signal at fixed point of the hologram.

The idea is similar with optical coherence tomography (OCT) which uses optical range source. But in this technique, the light source has broad-band spectrum to reduce the resolution in depth up to ~μm. The light is focused on a point. And by modulating the path difference of reference beam, the absolute distance of depth is measured by the interference of the white light. Usually they get imaging information by scanning through x, y, and z. As you can see the detailed phase information of the interference is not important in the OCT technique. In our case, the THz FEL is narrow-band coherent source. The coherence length of the FEL beam is same as the pulse length, which is 8-12 mm as shown in Fig. 3. If we make and measure hologram with the beam, we could get the information of the depth less than the coherence length. With THz range light, it is much easier to get the phase information of the interference. And we do not need to get the full phase information through the coherence length because we only need the relative phase information among the points in imaging plane. If we have high power, coherent source of the THz light and sensitive measuring 2-D device for the THz light, we could get 3-D tomography of the living species with THz spectroscopic information.

CONCLUSION

We have developed a compact THz FEL and the main activity of its application for THz imaging is introduced in this paper. The FEL beam showed good performance in pulse-energy stability, polarization, spectrum and spatial distribution. We could get the 2-D imaging of various materials with the THz FEL beam. To perform spectroscopic imaging, we will develop a Fourier transform spectrometer for THz range. The main idea for 3-D coherent THz tomography is proposed and discussed briefly. We hope to develop the technique for bio-medical application or non-destructive inspection.

ACKNOWLEDGEMENTS

This work was supported by Korea Research Foundation Grant (KRF-2003-042-D00195).

REFERENCES

[1] Rudeger Kohler, et al., Nature, 417 (2002) 156.
[2] Kodo Kawase, et al., Appl. Phys. Lett. 78 (2001) 2819.
[3] Q. Wu and X.-C. Zhang, Appl. Phys. Lett. 67, (1995) 3523.
[4] M. Abo-Bakr, et al., Phys. Rev. Lett. 88 (2003) 254801.
[5] Y.U. Jeong, et al., Nucl. Instr. and Meth. A 475 (2001) 47.
[6] D.M. Mittleman, et al., Appl. Phys. B 68 (1999) 1085.
[7] K. Kawase, et al., Opt. Express 11 (2003) 2549.
[8] T. Loffler, et al., Opt. Express 9 (2001) 616.
[9] Y.U. Jeong, et al., Nucl. Instr. and Meth. A 507 (2003) 125.
[10] Y.U. Jeong, et al., Nucl. Instr. and Meth. A 528 (2004) 88.

THE PRESENT APPLICATIONS OF IR FEL AT PEKING UNIVERSITY *

Yizhuang Xu[a], Limin Yang[b†], Yunlan Su[a], Jinguang Wu[a†], Kui Zhao[b], Jia'er Chen[b], Mingkai Wang[c],
[a] College of Chemistry and Molecular Engineering, Peking University, Beijing 100871, China,
[b] Institute of Heavy Ion Physics, Peking University, Beijing 100871, China, [c] Institute of High Energy Physics, Chinese Academy of Sciences, Beijing 100080, China

Abstract

In this study the sections of human tissues were treated under 9.5 μm FEL in the BFEL based on previous vibrational spectroscopic investigations that significant differences occur between normal and malignant tissues. Under the defocus condition, one part of the tissue section is burned while another part remains unchanged, suggesting that the FEL can selectively destroy some parts of the tissue. Vibrational spectroscopic and microscopic methods have shown that the FEL can induce decomposition of malignant tissues. The application of FEL whose wavelength is on the characteristic bands of malignant tissues may provide a new method to kill cancer cells with higher selectivity. For understanding the interactions between FEL and biological tissues, structure changes of substances under irradiation by FEL of about 9.4 and 11 μm were measured using FTIR spectroscopy. The samples include ATP, ADP, AMP, and D-ribose, etc. The FTIR spectra of the molecules before and after irradiation of FEL indicate molecular structure variations of the samples after irradiation of FEL, especially the rearrangement of their hydrogen bond networks, which may be caused by multiple photons process induced by FEL.

INTRODUCTION

Infrared laser, which stimulates vibrational levels of specific chemical groups in molecules and induces a variation of chemical reaction that can not occur by conventional thermal treatment, is regarded as "alchemy in chemistry" and received extensive investigation since 1970. However, the selection of wavelength in conventional infrared laser is limited. This hampers the understanding of the nature of the interaction between infrared laser and molecules.

Free Electron Lasers (FEL), as a powerful tool, are used for researches in material science, photochemistry, chemical technology, biophysical science, medical applications and surface studies, etc. [1-4]. The advent of FEL makes infrared laser with continuous tunable wavelength possible. This brings abundant opportunity for further understanding on the nature of the interaction between infrared laser and molecules. Especially the investigation on the changes of structures of bio-molecules induced by FEL provides information for the various biomedical applications [5-12].

The BFEL (Beijing Free Electron Laser, constructed by the Institute of High Energy Physics, CAS), whose wavelengths cover the fingerprint region of bio-molecules/organic molecules, provides a powerful tool for modification of molecular structure at chemical bonds, conformation as well as crystalline lattice levels. Recently, we take advantage of the mid-infrared light outputted by BFEL and FTIR to investigate on the sections of human tissues and some organic substances. The sections of human tissues were treated under 9.5 μm FEL in the BFEL due to the significant spectroscopic differences found between normal and malignant tissues [13]. For understanding the interactions between FEL and biological tissues, structure changes of substances under irradiation by about 9.4 and 11 μm FEL were measured using FTIR spectroscopy. Taking the sorts of benzoic acid as examples, after irradiation under some specified condition of FEL, the samples are characterized before and after irradiation with FTIR (Fourier Transform Infrared) spectroscopy, which indicate that some changes are observed [5]. In this work, significant structural variations of ATP, ADP, AMP, tRNA, cholic acid, deoxycholic acid, sodium cholate and sodium deoxycholate, D-ribose and its metal complex were observed in their FT-IR spectra upon the irradiation of FEL.

EXPERIMENTAL

The principal laser used in these experiments was BFEL, which has a complex pulse structure that consists of a train of macropulses, each containing a train of ultra short micropulses. The time structure of laser pulse is shown in the reference [5]. The width of the macropulses is 4 μs and the repetition rate is ca. 3 Hz. The separation between micropulses is 350 ps. The width of the micropulses is 4 ps.

The sections of human stomach tissues obtained from the third hospital, Peking University were treated under 9.5 μm FEL. The samples, analytical reagents from commercial source, including ATP, ADP, AMP, tRNA, cholic acid, deoxycholic acid, sodium cholate, sodium deoxycholate, ribose and a metal-saccharide complex were put under the FEL exposure in air at room temperature. The exposure time to the sample surface is 30 min. The size of light spot FEL was unfocused and controlled around 1 mm in diameter. The light parameters of irradiation are listed in Table 1. The FEL was tuned at

* Supported in part by Chinese Ministry of Science and Technology under the National basic Research Projects (No.2002CB713600 and 2002CCA01900)

† *E-mail*: wjg@chem.pku.edu.cn; yanglm@pku.edu.cn

the wavelength regions about 9, 6 and 11 μm. FT-IR spectra of the samples before and after irradiation of FEL were measured using micro IR method on a Nic-plan Nicolet Magna IR 750-II spectrometer at 4 cm^{-1} resolution and 128 scans.

Table 1: The light parameters of irradiation

	Irradiation wavelength (μm)	Energy (mJ)	Time of irradiation (min)
AMP	11.04	1.56	30
ADP	11.02	1.5	30
ATP	11.06	1.62	30
tRNA	9.32	2.35	30
cholic acid	9.3	2.4	30
deoxycholic acid	9.4	2.2	30
NaC	9.3	2.4	30
Na(DC)	9.4	2.2	30
D-Ribose	9.92	2.8-3	30
$SmCl_3$-D-ribose	6.72	2.9-3	30

RESULTS AND DISCUSSION

The application of FEL on cancer treatment [6]

The sections of human stomach tissues were treated under 9.5 μm FEL in the BFEL because significant differences occur between normal and malignant tissues. The power of FEL is strong enough to destroy malignant tissues (Fig. 1(a)). Thus application of FEL whose wavelength is on the characteristic bands of malignant tissues may provide a new method to kill cancer cells with higher selectivity. In addition, combination of FEL with fiber optic techniques into endoscope may provide surgeons a powerful tool to perform minor-trauma surgery process to improve the surviving rate of terminal cancer patients. Under the defocus condition, one part of the tissue section is burned, but another part remains unchanged, suggesting that the FEL can selectively destroy some part of tissue. The photo was shown in Fig. 1 (b). Vibrational spectroscopic and microscopic methods have shown that the FEL can induce decomposition of malignant tissues. If this approach is feasible, then the FT-IR spectroscopic studies of cancer will come into a new era. The methods will extent from diagnosis cancer at molecular level into cure cancer at molecular level. The characteristic bands of malignancy tissue provide us an alternative selectivity. It can be imaged that surgical treatment of cancer in the future is performed by the interactive combination of spectroscopic diagnosis and spectroscopic treatment. The malignant and peripheral region are scanned by FEL laser, spectroscopic diagnosis information from each spot of the region are used as feedback that controls the laser power, so that it is possible to destroy malignant tissue as much as possible and protect normal tissue as much as possible. The application of fiber optics renders the surgical operation to be of minor trauma. For understanding the interactions between FEL and biological tissues, the interactions between FEL and biomolecules were investigated. The structure changes of substances under irradiation by FEL of about 9 and 11 μm were measured using FTIR spectroscopy.

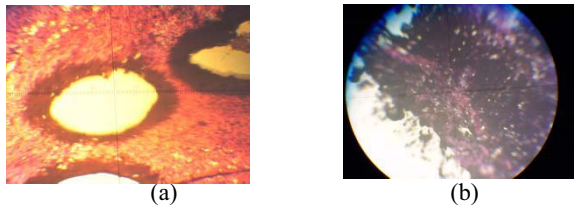

(a) (b)

Fig.1 (a) The malignant tissue destroyed by FEL (b) Under the de-focus condition, one part of the tissue section is burned and another part remains unchanged, suggesting that the FEL can selective destroy some part of the tissue.

FTIR spectra of AMP, ADP, ATP and tRNA before and after FEL irradiation [7]

Adenosine 5'-phosphate (AMP), Adenosine 5'-diphosphate (ADP), Adenosine 5'-triphosphate (ATP) and transfer RNA (tRNA) are important bio-molecules. The four samples were irradiated at different wavelengths of free electron laser (FEL) obtained by Beijing Free Electron Laser (BFEL), and they were characterized with FT-IR spectroscopy before and after irradiation. The light parameters of irradiation are listed in Table 1. The FTIR spectra of AMP before and after irradiation of FEL are shown in Fig. 2. The characteristic frequencies in the FTIR spectra of AMP, ADP, ATP and tRNA before and after irradiation of FEL are listed in Table 2.

For AMP and ATP, some changes were observed in the region of 3500-3000 cm^{-1} with the OH stretching bands become even broader after irradiation. It also indicated that irradiation of FEL has great influence on P=O and P-O-C. The stretching band of P=O in both AMP and ATP splits into two bands. For AMP, the P=O stretching band is a broad band at 1234 cm^{-1}, while after irradiation it divides into two sharp bands at 1218 cm^{-1} and 1205 cm^{-1}; For ATP, the irradiation of FEL induces the P=O stretching band to split from 1248 cm^{-1} to 1261 cm^{-1} and 1221 cm^{-1}. These results indicate that the hydrogen bond networks are dissociated partly and rearranged with the irradiation of FEL. Considering the obvious variation in 1100 cm^{-1} and 1010 cm^{-1} of P-O-C and C-O vibration, it is suggested that the molecular skeletons of AMP and ATP vary after irradiation. However, for ADP, only minor changes in skeleton vibration can be observed in FT-IR spectra after irradiation. For tRNA, interesting change can be observed after irradiation. That is, the variation of intensity rate of peaks at 1085 cm^{-1} and 1073 cm^{-1}. Before irradiation the intensity rate is 0.965, while after irradiation, the rate is 1.083. Considering the P=O band from 1234 cm^{-1} to 1236 cm^{-1}, the irradiation of FEL induces the conformational variation of lecithoid group. The same phenomenon can also be observed in AMP. The

intensity rate of peaks at 1085 cm^{-1} and 1065 cm^{-1} is 1.167 before irradiation, after irradiation the rate of peaks at 1084 cm^{-1} and 1058 cm^{-1} is 0.875. Considering the irradiation wavelength of FEL at tRNA is 9.32 μm that is 1073 cm^{-1}, which is near the stretching band of P-O-C, at AMP and ATP the irradiation wavelengths of FEL are 11.04 μm and 11.06 μm respectively, which are about 909 cm^{-1}. We can get the conclusion that the irradiation induced the conformation change of the biomolecules with lecithoid group.

Table 2: The characteristic frequencies in the FTIR spectra of AMP, ADP, ATP and tRNA

Sample	Original	After FEL irradiation	Assignment
AMP	3333,3208	3388,3094	OH
	1693	1685	
	1234	1218,1205	P=O
	1085,1065	1084,1058	P-O-C, C-O
ADP	3339	3335	OH
	1660	1659	
	1223	1222	P=O
	1081	1079	P-O-C, C-O
ATP	3347,3151	3344,3154	OH
	1698	1716	
	1248	1261,1221	P=O
	1104,1051 ,1018,965	1101,998,9 70	P-O-C, C-O
tRNA	3360,3238	3336,3244	OH
	1686,1650	1688,1651	
	1234	1236	P=O
	1085,1073	1085, 1073	P-O-C, C-O

FTIR spectra of cholic acid, deoxycholic acid and their sodium salts before and after FEL irradiation [8]

As the predominant ingredients of bile, bile salts are one of the most important bio-surfactants in vivo. Cholic acid, deoxycholic acid and their sodium salts were irradiated using FEL about 9.4 μm and characterized with FT-IR spectroscopy before and after irradiation. Their FTIR spectra are shown in Fig. 3. The frequencies are listed in Table 3. For cholic acid and deoxycholic acid, the fine structures in OH stretching region (3000-3700 cm^{-1}) disappear, and the CH stretching bands become even broader after irradiation. For cholic acid, the C=O of COOH stretching band is a sharp band at 1715 cm^{-1}, while after irradiation it becomes a broad band at 1708 cm^{-1}. For deoxycholic acid, the COOH stretching bands are two sharp bands at 1714 cm^{-1} and 1695 cm^{-1}, while after irradiation they appear a broad band at 1709 cm^{-1}. These results indicate that the hydrogen bond networks are dissociated and rearranged after irradiation. Considering the obvious variation in skeleton vibration, it is suggested that the molecular skeletons of these two bile

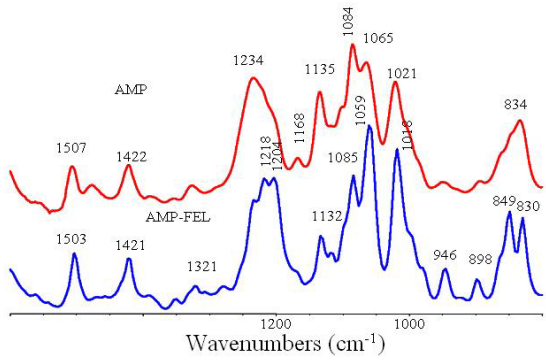

Fig. 2 IR spectra of AMP before and after irradiation (1600-800 cm^{-1})

acids vary after irradiation. However, for sodium cholate and sodium deoxycholate, there is no obvious alternation in FTIR spectra after irradiation. Only minor changes in skeleton vibration can be observed. In conclusion, for cholic acid and deoxycholic acid, the interaction of FEL can induce the dissociation and rearrangement of H-bond structure. However, the effect of FEL to sodium cholate and sodium deoxycholate is not so obvious.

For above molecules, a mechanism of multiple photons process induced by FEL is suggested. FT-IR spectra of the samples treated with FEL represent stable/meta-stable structures of the samples and FEL provide energy to help the molecular system to overcome the energy barrier on the potential surface and reach a stable/meta-stable structure. When FEL makes the molecules reach their excited states, vibrational energy rapidly flow and have rapid redistribution, then have stable/meta-stable structures. The variation of the FT-IR spectra of the molecules proves that the spectral variations of the samples induced by FEL are closely related to hydrogen bond networks.

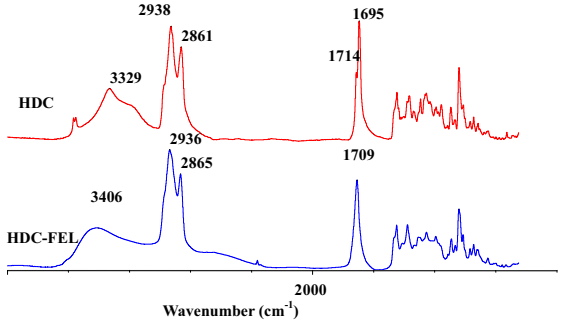

Fig. 3 The FTIR spectra of HDC before and after FEL irradiation

Table 3: The characteristic frequency data of FTIR spectra of HC and HDC before and after FEL irradiation

	HDC		HC	
	Original (cm^{-1})	After FEL (cm^{-1})	Original (cm^{-1})	After FEL (cm^{-1})
OH	3567, 3553, 3329	3406	3523, 3321, 3192	3405
CH	2928, 2861	2936, 2865	2966, 2935, 2872	2935, 2868
COOH	1714, 1695	1709	1715	1708

FTIR spectra of D-ribose and its metal complex before and after FEL irradiation

The above results indicate that hydrogen bond networks rearrange after irradiation of FEL. Carbohydrates are important biomolecules and often used as model systems to study hydrogen bonds, therefore, the structure changes of carbohydrates after irradiation of FEL were investigated. The FTIR spectra of D-ribose and $SmCl_3$-D-ribose complex before and after irradiation of FEL are shown in Fig. 4 and Fig. 5. The results indicate that the fine structures disappeared and hydrogen bond networks were broken and rearranged for $SmCl_3$-D-ribose complex ($SmCl_3 \cdot C_5H_{10}O_5 \cdot 5H_2O$) after irradiation of FEL. The bands of OH and CH vibrations become broader after irradiation. Two sharp bands at 1634 and 1619 cm^{-1}, corresponding to the deformation vibrations of water molecules, become a broad band located at 1639 cm^{-1} after irradiation of FEL. In the 1500-900 cm^{-1} region the bands also become broad, which indicate that the hydrogen bond networks formed by hydroxyl groups of D-ribose, chloride ions and water molecules broken and rearranged after irradiation of FEL. For D-ribose, the OH stretching vibrations also have shifts about 10 cm^{-1}. Most of the bands in the 1500-650 cm^{-1} region have differences in peak positions before and after irradiation of FEL, which indicate the changes of the structure. The different changes for D-ribose and $SmCl_3$-D-ribose complex may be caused by the different excited wavelength of FEL.

CONCLUSIONS

The H-bond networks of a series of molecules, including ATP, ADP, AMP, tRNA, cholic acid, deoxycholic acid, sodium cholate, sodium deoxycholate, D-ribose and $SmCl_3$-D-ribose complex exhibit significant re- arrangement upon the irradiation of FEL at both about 9.4 and 11 μm. Free electron lasers provide a powerful tool for modification of molecular structure at chemical bonds, conformation as well as crystalline lattice levels. Structure changes were observed after irradiation of FEL for some molecules, which indicate that FEL may be used to control reactions. The results show that FELs would have extensive applications in the fields of chemistry and biology.

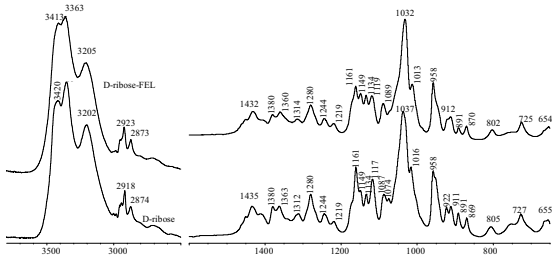

Figure 4: The FTIR spectrum of D-ribose in the 3800-2500 and 1600-650 cm^{-1} region before and after irradiation of 9.92 μm FEL.

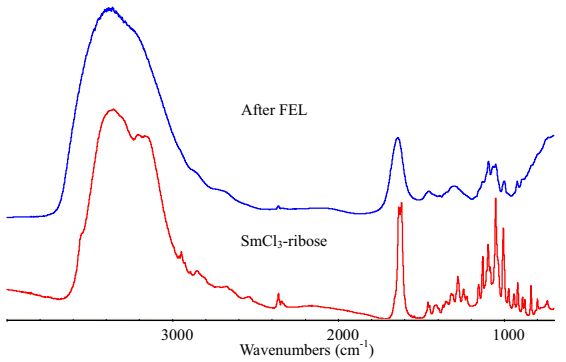

Figure 5: The FTIR spectra of $SmCl_3$-D-ribose before and after irradiation of 6.72 μm FEL.

REFERENCES

[1] P. G. O'Shea, et al., Science, 292 (2001) 1853.
[2] S. C. J. Meskers, et al., Phys. Rev. B, 61(15) (2000) 9917.
[3] D. van Heijnsbergen, et al., Chem. Phys. Lett., 364 (2002) 345.
[4] C. W. Rella, et al., Phys. Rev. Lett., 77(8) (1996) 1648.
[5] Y. Li, et al., Spectrosc. Spect. Anal., 22 (2002) 384.
[6] J. G. Wu, et al., Proceedings of PITTCON 2002, 1105.
[7] J. G. Wu, et al., Proceedings of PITTCON 2002, 2242p.
[8] J. G. Wu, et al., Proceedings PITTCON 2002, 1103.
[9] J. G. Wu, et al., Proceedings of PITTCON 2002, 1658p.
[10] J. G. Wu, et al., Proceedings of PITTCON 2002, 2081p.
[11] J.G. Wu, et al., Proceedings of PITTCON 2002, 2242p.
[12] Y. Zhao, et al., Proceedings of PITTCON 2002, 2086p.
[13] J. G. Wu, et al., Biopolymers, 62 (2001) 185.

INTERACTION OF INTENSE ULTRASHORT XUV PULSES WITH DIFFERENT SOLIDS – RESULTS FROM THE TESLA TEST FACILITY FEL PHASE I

Jacek Krzywinski, Marek Jurek, Dorota Klinger, Robert Nietubyc, Jerzy Pelka, Andrzej Wawro, IP/PAS, Warsaw, Poland

Marcin Sikora, AGH University of Science and Technology, Krakow, Poland

Evgeny Saldin, Evgeny Schneidmiller, Barbara Steeg, Rolf Treusch, Mikhail V. Yurkov, HASYLAB/DESY, Hamburg, Germany

Michal Bittner, Dagmar Chvostova, Libor Juha, Vit Letal, Vladimir Vorlicek, IP/ASCR, Prague, Czech Republic

Andrzej Andrejczuk, Henryk Reniewicz, University of Bialystok, Bialystok, Poland

Ryszard Sobierajski, Warsaw University of Technology, Warsaw, Poland

Anna Kauch, Warsaw University, Warsaw, Poland

Abstract

Key results of a study of irreversible changes induced at surfaces of metals, semiconductors, and insulators by ultrashort XUV pulses generated at the TTF FEL facility are reported and discussed. Energy spectra of ions ejected from the irradiated surfaces are also reported. Special attention is paid to a difference in the ablation behavior of (semi)conductors and insulators that we have observed. The difference is dramatic while the absorption coefficients are similar for all materials at the TTF1 FEL wavelength.

INTRODUCTION

Before the FELIS [1] experiments were performed at TTF1 FEL in 2001-2002, the shortest wavelengths at which laser ablation had been investigated were 46.9 nm and 125 nm. The 46.9-nm radiation was emitted from a capillary-discharge Ne-like Ar XUV laser [2] and the 125-nm radiation was generated by four-wave-sum-frequency mixing (FWSFM) of a 626-nm dye laser and its second harmonics in Hg vapor [3]. The pulse duration in both cases was in the nanosecond range. A few papers (for a review see [4]) have reported ablation induced at even shorter wavelengths (i.e. in the soft X-ray region) but the radiation used was not coherent. In the present study, not only the laser wavelength is short (< 100 nm) but also the pulse duration is very short (typically 50-100 fs) [5]. The short wavelength and ultrafast coherent beam represent a unique combination. The ablation behavior of a wide variety of materials has been investigated under these irradiation conditions.

In this contribution, key results of a study of irreversible changes induced at surfaces of metals, semiconductors, and insulators by ultrashort XUV pulses generated at the TTF1 FEL facility are reported and discussed. We also report the mass, energy, and spectra of ions ejected from the irradiated surfaces.

Special attention is paid to a difference in the ablation behavior that we have observed for (semi)conductors and insulators. The difference is dramatic while the absorption coefficients are similar for all the materials at the TTF1 FEL wavelength.

Ablation characteristics, i.e. thresholds, etch (ablation) rates, and ablated structure quality, often differ dramatically with conventional UV-Vis-IR lasers, depending on whether the radiation energy is delivered to the material surface in short (typically nanosecond) or ultra-short (typically femtosecond) pulses [6,7]. The FELIS experiment, together with ablation experiments utilizing plasma-based XUV lasers, makes it possible to investigate how ablation characteristics depend on the pulse duration in the XUV spectral region ($\lambda < 100$nm).

EXPERIMENTAL

The samples were irradiated by the SASE-FEL beam emitted by the Tesla Test Facility (TTF) at HASYLAB/DESY in Hamburg [5]. The wavelength was tuned between 85 and 98 nm. Spectral and energy characteristics of the laser beam were measured using photon diagnostics described in details elsewhere [8]. The beam was focused by an elliptical mirror into the interaction chamber as shown in Fig. 1. For more details, see [9].

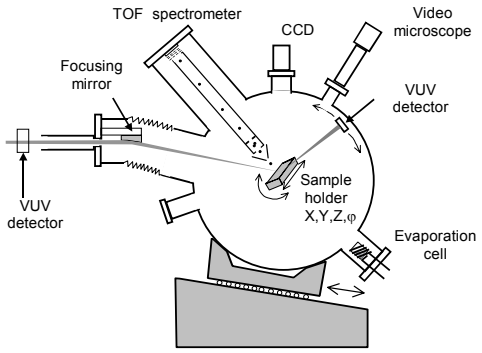

Figure 1: Schematic of the FELIS chamber [9].

Morphological changes at the surface of the exposed samples were investigated by Nomarski, conventional optical, scanning electron, and atomic force (AFM) microscopy. Raman spectra were made with a laser microbeam in the usual backscattering geometry, which enables probing chosen locations on the sample surface. Ion energies and mass spectra were measured using a time-of-flight (TOF) spectrometer equipped with high pass energy filter.

Samples

A number of different samples were irradiated by the focused FEL beam. The bulk samples were: Au, Si, PMMA, Ce:YAG, and SiO_2. We have also irradiated Si crystals polished to optical quality and covered with thin films: 15-nm Au (Au-15), 10-nm and 40-nm amorphous carbon (a-C-10 and a-C-40).

RESULTS

Surface damage

Modification of silicon surfaces exposed to FEL pulses of increasing fluences and recorded by Nomarski microscope is presented in Fig. 2. Each spot was irradiated with 11 shots. The first changes seen are due to modification of the refractive index. An imprinted interference pattern,

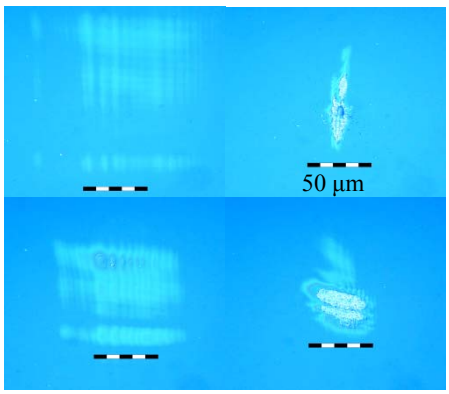

Figure 2: Modification of monocrystalline-Si surfaces imaged by Nomarski microscopy. The fluence increases counterclockwise and is equal to 0.015, 0.04, 0.3, and 1.8 J/cm^2 , respectively.

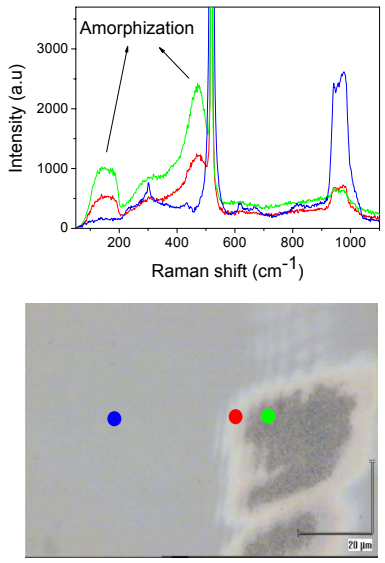

Figure 3: Raman spectra measured at different places on an FEL-irradiated sample of monocrystalline Si.

which is due to diagnostics that were installed in front of the focusing mirror and to slope errors of the mirror surface, is clearly seen. The AFM and TOF measurements do not indicate any morphological changes or ion emission, respectively. Raman spectra however show signs of an amorphous phase in the modified region. The Raman spectra measured at three different locations of the excitation-micro-beam spot are shown in Fig. 3. The amorphous fraction increases towards the center of the crater. The first observable changes were recorded at a fluence of 0.005 J/cm^2.

In Table I we present two different fluence thresholds at which we start to record modifications of the irradiated surface. The first (ΦI) is the fluence at which we notice a change of the refractive index and the second (ΦII) is the fluence at which deformation of the surface is indicated by the AFM. It can be seen that, except for Au-10 and PMMA, the ΦII values oscillate about 0.03 J/cm^2. This is of the order of the fluence, F_c, at which the absorbed energy per atom is equal to the cohesive energy, E_c,

$$F_c = E_c n / \alpha,$$

Table 1: TTF1-FEL surface modification thresholds

Material	ΦI [J/cm^2]	ΦII [J/cm^2]
Au	0.02	0.02
Au-15	0.01	0.01
a-C-40	0.01	0.03
Si	0.005	0.04
SiO_2	0.03	0.03
Ce:YAG	0.02	0.02
PMMA	0.01	0.01

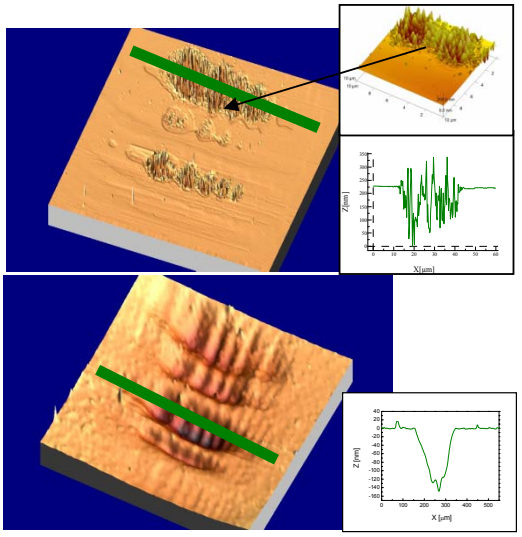

Figure 4: AFM measurements of the silicon (upper) and quartz (lower) samples. Irradiation conditions were similar (fluence $\sim 0.04\,\mathrm{J/cm^2}$). The insets are the crater profiles along the green lines.

where n is atomic density and α is the absorption coefficient. For typical values $E_c \sim 3$ eV/at, $n \sim 5 \times 10^{22}$ at/cm^3, and $\alpha \sim 10^6$ cm^{-1}, $F_c \approx 0.025$ J/cm^2, which corresponds to the values shown in Table 1.

Difference in ablation behavior between (semi)conductors and insulators

Results of the AFM investigations carried out for the crystalline Si and SiO_2 samples are presented in Fig 4. The samples were irradiated with 11 shots at an average fluence of 0.04 J/cm^2. One can notice a dramatic difference in the morphology of both craters. The silicon crater is covered by columnar structures. The peaks of the columns are located above the sample's surface. In the case of crystalline SiO_2 (quartz), the interior of the crater is very smooth and the interference pattern is clearly imprinted into the sample's surface. Exposure of all investigated insulator samples to multiple shots leads to very similar surface pattern when the distance between the sample and the focal spot is the same. Both the morphology of the irradiated surface and the crater depth do not depended on the FEL beam intensity. These features indicate that intense ultra-short pulses of XUV radiation can be used for nano- and micro-machining of insulators.

The ion spectra measured for the Si and SiO_2 samples are presented in Fig. 5. Multiple charged ions were recorded for high-intensity irradiation of Si. The kinetic energy of the ions increases with charge state and reaches the keV range for highly charged ions. Again, there is a clear difference between Si and SiO_2. The high charge states and energetic ions shown for Si are typical of all (semi)conductors. Only singly charged, low-energy ions (~50 eV) were detected for the insulator SiO_2 under all irradiation conditions. Other insulators investigated

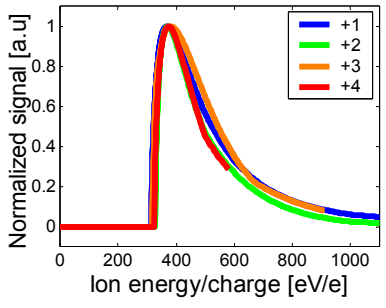

(a)

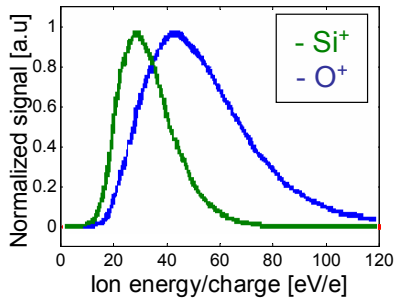

(b)

Figure 5: The energy spectra of ions taken with the TOF spectrometer for the silicon (a) and quartz (b) samples. Signals have been normalized. The energy scale has been divided by the ions charge state.

exhibited similar behavior. An interesting feature of the ion spectra observed for all (semi)conductors is that the measured values can be normalized to one curve if the energy of the ion is divided by its charge. This suggests a field emission mechanism.

It is very interesting to notice that the difference in ablation behavior between (semi)conductors and insulators is very pronounced although the absorption coefficients are similar for all the materials at the TTF1 FEL wavelength.

FEL-induced periodic surface structures

Although laser-induced periodic surface structures (LIPSS) were discovered in the middle of the 1960s [10], they remain a subject of extensive research (for a review see [11,12]). According to the nature of their origin, two kinds of LIPSS can be distinguished on laser-irradiated surfaces. In the initial stage of research, most LIPSS observed were ripples, with a spatial period related to the laser wavelength. The ripples, which are called LIPSS of the first kind (LIPSS-I), are created by the interference of the incident laser beam with a wave diffracted by periodic features in the materials' surface. The spatial periods of LIPSS of the second kind (LIPSS-II), however, depend more on laser intensity than on wavelength and are significantly longer than the laser wavelength when a short-wavelength laser is used for irradiation. On the material surfaces irradiated by the focused TTF1-FEL beam, LIPSS-I have been found at the rim of a few of the craters created in a-C and PMMA by 98-nm and 86-nm radiation

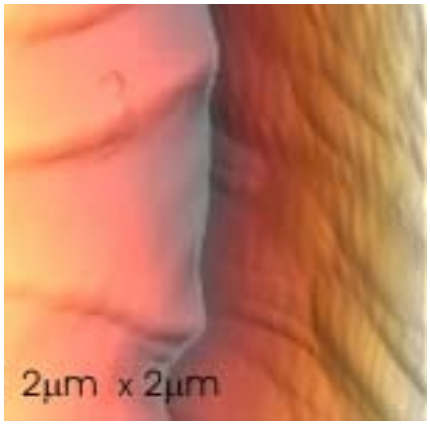

Figure 6: AFM image (tapping mode) of LIPSS at the rim of a crater ablated in PMMA by the tightly focused beam of the TTF1 FEL (λ = 86 nm, ϕ = 0.5 J/cm^2; 11 accumulated pulses, 55^o incidence)

respectively [1,13,14]. In Fig. 6, ripples of 70-nm periodicity can be seen on the right side. Currently, 86-nm FEL radiation represents the shortest-wavelength radiation used for production of well-developed LIPSS-I. According to our best knowledge, the shortest wavelength at which LIPSS-I had previously been produced was that of the157 nm F_2 excimer laser [12].

LIPSS-I have not yet been observed on the surfaces of Si, Ce:YAG, or SiO_2 (quartz) irradiated by TTF1 FEL. How might this be explained? Although a possible explanation was discussed in [14], the problem remains unsolved. Contrary to the scarcity of LIPSS-I, LIPSS-II have been found on almost all FEL-irradiated surfaces. LIPSS-II can be attributed to capillary (surface tension) and surface acoustic waves, fixed in laser-melted near-surface material by its re-solidification, and also to Rayleigh-Taylor and Helmholtz-Kelvin instabilities, relaxation of stress, and similar phenomena. All of these processes are expected to be very common at FEL irradiated surfaces, so that the observed high abundance of LIPSS-II is not surprising.

SUMMARY

Results of the study of irreversible changes induced at surfaces of metals, semiconductors, and insulators by ultrashort XUV pulses generated at the TTF1 FEL facility have been reported and discussed. A distinct difference between the behaviors of (semi)conducting materials and insulators was observed. In the case of inorganic insulators, the morphology of the irradiated surface and the crater depth hardly depended on the beam intensity. In contrast, the irradiated silicon surface becomes very rough when the intensity exceeds the damage threshold. There is also a clear difference between insulators and (semi)conducting materials with respect to the spectra of ejected ions. Highly-charged, energetic ions (~ a few keV) were typical for (semi)conductors. Only singly-charged, low-energy ions (~50 eV) were detected for insulators under all irradiation conditions. LIPSS-I have been found at the rim of a few craters created in a-C and PMMA by 98-nm and 86-nm radiation, respectively. LIPSS-II have also been found. Their spatial periods depend more on laser intensity than wavelength and are significantly longer than the laser wavelength, for short-wavelength lasers.

REFERENCES

[1] R. Sobierajski, et al.,: "Structural changes at solid surfaces irradiated with femtosecond, intense XUV pulses generated by TTF-FEL", Proceedings of the 24th International Free Electron Laser Conference & 9th FEL Users Workshop, Argonne, IL, September 9-13, 2002 pp. II77-78 (2003).
[2] B. R. Benware et al., Opt. Lett. 24 (1999) 1714.
[3] D. Riedel and M. C. Castex, Appl. Phys. A69 (1999) 375.
[4] L. Juha et al., Surf. Rev. Lett. 9 (2002) 347.
[5] V. Ayvazyan et al., Eur. J. Phys. D20 (2002) 149.
[6] R. Srinivasan et al.: Appl. Phys. Lett. 51 (1987) 1285.
[7] S. Küper and M. Stuke: Appl. Phys. B44 (1987) 199.
[8] R. Treusch et al., Nucl. Instrum. Meth. Phys. Res. A 467-8 (2001) 30.
[9] A. Andrejczuk, et al., HASYLAB Annu. Rep. (2001) 117.
[10] M. Birnbaum: J. Appl. Phys. 36 (1965) 3688.
[11] A. E. Siegman and P. M. Fauchet: IEEE J. Quant. Electron. QE-22 (1986) 1384.
[12] P. E. Dyer et al.: Appl. Surf. Sci. 96-97 (1996) 537.
[13] B. Steeg et al.: Appl. Phys. Lett. 84 (2004) 657.
[14] L. Juha et al.: HASYLAB Annual Rep. 2003 Part I (2003) 763.

EXPLORING THE SPATIAL RESOLUTION OF THE PHOTOTHERMAL BEAM DEFLECTION TECHNIQUE IN THE INFRARED REGION

W. Seidel, H. Foerstendorf, Forschungszentrum Rossendorf, 01314 Dresden, Germany
F. Glotin, J.M. Ortega, R. Prazeres, LURE, 91898 Orsay Cedex, France

Abstract

In photothermal beam deflection (PTBD) spectroscopy generating and detection of thermal waves occur generally in the sub-millimeter length scale. Therefore, PTBD provides spatial information about the surface of the sample and permits imaging and/or microspectrometry. Recent results of PTBD experiments are presented with a high spatial resolution which is near the diffraction limit of the infrared pump beam (CLIO-FEL).

INTRODUCTION

The PTBD technique is based on the theory of photothermal spectroscopy which describes the conversion of absorbed energy of a light beam incident on a sample into heat by nonradiative de-excitation processes [1]. The distribution of this induced, exponentially decaying, thermal field is given by the solution of the heat equation with a source term of a Gaussian beam [2]. In typical PTBD experiments the magnitude of the signal is proportional to the slope of the induced displacement of the sample surface. Additionally, it can be shown that there is a direct proportionality between the observed signal and the absorption coefficient of the material under investigation [2]. Therefore, a direct access to absorption spectra is provided [3]. The detection limit is expected to be extremely low since absorptions as low as 10^{-6} to 10^{-8} have been measured in the visible region by this method [4].

In typical PTBD experiments a solid sample is irradiated by a modulated beam of monochromatic light produced by a tunable infrared laser and a probe beam (*e.g.* a HeNe laser) which is reflected from the sample (Fig. 1). Depending on the modulated intensity of the pump beam the photoinduced displacement of the probe beam changes periodically and thus a different reflection angle is observed by the use of a high resolution position detector. The resulting beam deflection signals are shown in Fig. 2.

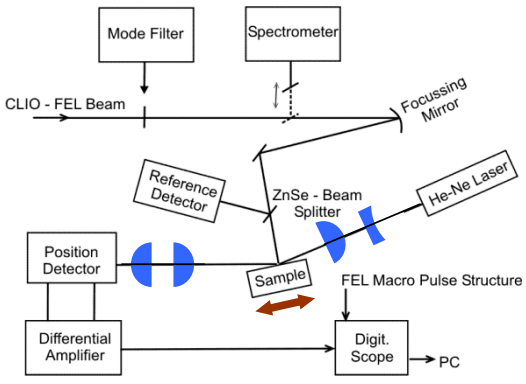

Figure 1: Layout of the PTBD experiment setup used at CLIO for microspectrometry.

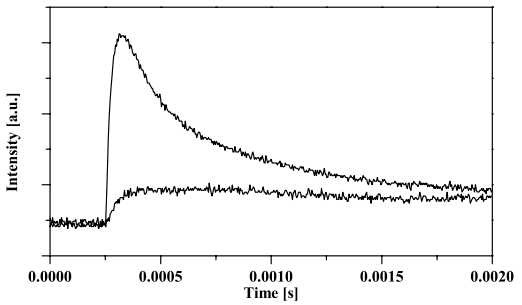

Figure 2: Time-resolved beam deflection signals of a strong absorbing (upper trace) and a nearly transparent sample (lower trace).

We investigated O^+-implanted and untreated regions of germanium substrates serving as model surfaces. The different areas of the surfaces can be distinguished by optical absorption (*i.e.* the amplitude of the deflection signal) at $\lambda = 11.6$ µm of the germaniumoxide produced during the implantation process (Fig. 3).

RESULTS

Simple Border Range

We investigated the border range of O^+-implanted and untreated regions of a germanium substrate serving as a model surface. The different areas of the surface can be distinguished by optical absorption (*i.e.* the amplitude of

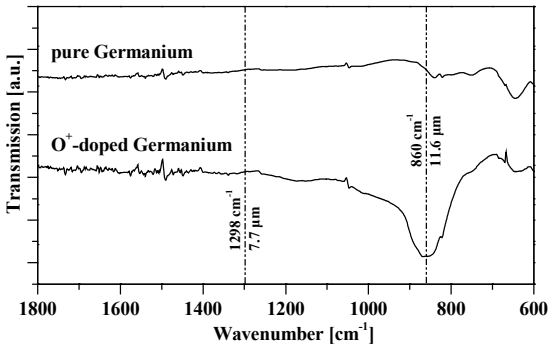

Figure 3: FT-IR transmission spectra of a Ge-substrate of O^+-implanted and untreated regions.

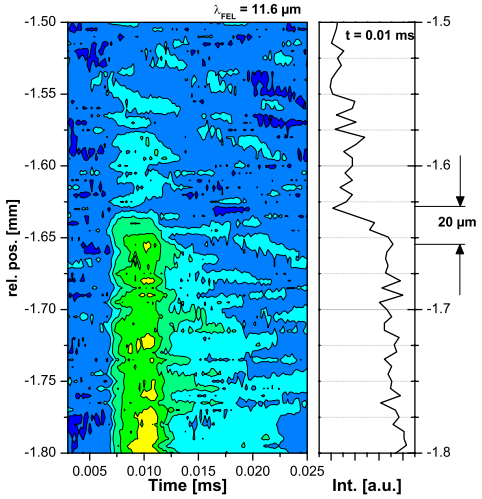

Figure 4: Mapping plot of the set of time curves of the deflection signal at distinct sample positions and the extracted absorption profile of the border range between O^+-doped and pure germanium (extracted at t = 10 µs and at λ = 11.6 µm).

the deflection signal) at λ = 11.6 µm of the germaniumoxide produced during the implantation process (Fig. 3). From the set of time curves (Fig. 2) recorded at distinct positions of the surface of the sample profiles can be obtained reflecting the distribution of the implanted oxygen in the substrate as it is shown in Fig. 4.

The transition between an O^+-doped and an untreated region of the substrate was investigated. The HeNe laser probe beam was focused in front of the surface of the sample to about 15 µm. This leads to an enhancement of the spatial resolution up to about 20 µm as it can be seen around 1.65 mm rel. pos. (Fig. 4, right panel).

Revcovery of More Complex Structures

In the next series of our experiments we investigated a sample showing a distinct pattern of implanted regions which was achieved by a special stainless steal mask in front of the substrate during the implantation process. The dimensions of the mask are given in Fig. 5A. Additionally, the implanted regions are indicated as grey stripes throughout Figs. 5 B-D.

The profiles presented in Fig. 5B clearly reproduce the structure of the implanted regions generated by the mask.

In Fig. 5C an enlarged range of five thin implanted regions were detected at high resolution of positioning (step width: 2 µm). Again, the recovery of the pattern of implantation is of excellent quality. For demonstration that the deflection signal is solely caused by optical absorption the same sample area was recorded at a wavelength of 7.7 µm where no absorption occurs (Fig. 3). This is demonstrated in Fig. 5D.

It is noteworthy, that all profiles shown in this work were obtained with only one macropulse for each sample position. A significantly higher signal-to-noise ratio can be expected when the deflection curves are averaged over several FEL pulses. This will probably facilitate the reproduction of more complex structures by PTBD-FEL microspectrometry.

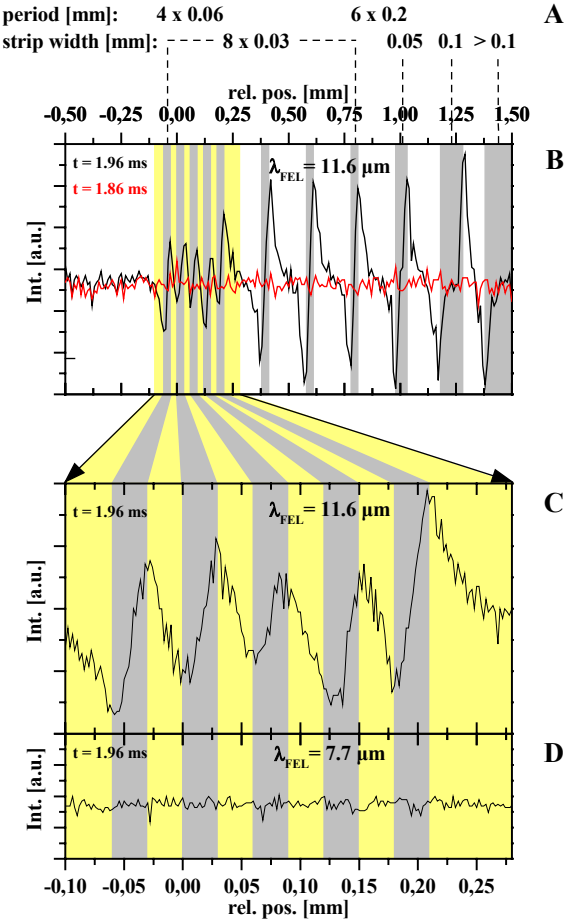

Figure 5: Dimensions of the implantation pattern for the preparation of the Ge-substrate with O^+-ions (A). Extracted absorption profiles (B-D): Profiles (step width: 10 µm) of the whole implanted structure at different times after the FEL pulse (black line: time of max. deflection, red line: time before deflection occur) (B). Profiles (step width: 2 µm) of five thin lines at different wavelengths (C-D). 11.6 µm: max. absorption (C), 7.7 µm: no absorption (see Fig. 3) (D).

References

[1] A. Rosencwaig and A. Gersho, J. Appl. Phys. 47 (1976) 64.
[2] M.A. Olmstead et al., Appl. Phys. A 32 (1983) 141.
[3] W. Seidel et al., Eur. Phys. J - Appl. Phys. 25 (2004) 39.
[4] A. Mandelis, Physics Today 53 (2000) 29.

EXPERIMENTS ON THE SYNCHRONIZATION OF AN ULTRAFAST CR:LISAF LASER WITH THE ELETTRA STORAGE RING AND FEL PULSES

M. Ferianis, M. B. Danailov, G.De Ninno, B. Diviacco, M. Trovò, ELETTRA, 34012 Trieste, ITALY
M. Coreno, CNR-IMIP, 34012 Trieste, ITALY, G. E. Afifi, NILES, Cairo, EGYPT

Abstract

The techniques for synchronizing ultra fast lasers to external radio frequency reference sources are well established and characterized in the literature. However, data lack on the minimum light-to-light jitter that can be achieved in different synchrotron operation modes when an external laser is locked to the storage ring master clock. Here we present first results for the synchronization of an ultra fast Cr:LiSAF laser with electromagnetic radiation coming from the Elettra storage ring in four bunch and multi-bunch mode. In addition, data on the synchronization of the same laser with the Elettra FEL pulses, both in free running and Q-switching regime, are reported. In our experiments, laser-to-RF locking was continuously monitored using a built-in phase detection. The laser light to storage ring light locking was characterized by simultaneous acquisition of two/three pulse trains by a streak camera. In addition, pulse jitter was determined by processing of the signal of fast photodiodes monitoring the different light beams.

INTRODUCTION

During the last decade, remarkable progress has been obtained in the establishment and full-potential operation of Third Generation Synchrotron light sources. At the same time, impressive peak powers (Terawatts) have been achieved by continuous advances in laser techniques; femto-second pulse duration is now available from commercial equipments. Current projects of fourth generation sources in the X-ray spectral range, X-ray Free Electron Lasers (X-FELs) integrate accelerator and laser based technologies [1]. This process has started also at the ELETTRA Laboratory, where the Storage Ring Free-Electron Laser SR-FEL [2] is in operation and the fourth generation light source [3] FERMI@ELETTRA is now ready to go.

As the synchronization of fs-lasers to the electron bunches is crucial for the optimum operation of these new sources, we performed some synchronization experiments using the currently available sources.

RADIATION SOURCES AT ELETTRA

Different radiation sources can be used simultaneously at ELETTRA for "time resolved" experiments. Beside the well-known Undulator and Bending magnet radiation, whose temporal structure directly reflects the Storage Ring filling pattern, the Storage Ring Free Electron Laser (SR-FEL) is now becoming available. Furthermore, table top laser oscillators can be used when the wavelength or the energy per pulse of a specific experiment is not fulfilled by the ELETTRA sources. In Table 1 the temporal structures of these sources are reported.

Table 1: Temporal structure of the radiation sources.

Source type	Pulse length t_{FWHM}	Repetition Frequency
Bending/ Undulator	50÷120ps 60ps	MB: 500MHz 4B: 4.26MHz
SR-FEL, free run	15ps	4.64MHz, pulsed
SR-FEL, Q-switch	15ps	10Hz
Table top fs laser Ti:Sa, Cr:LiSAF	≈110fs	≈100MHz

Synchrotron radiation

During user shifts the machine is operated in:

- multi bunch mode (MB), the standard user mode
- four-bunch mode (4-B), the SR-FEL mode

In MB mode, the 90% of the available buckets are filled consecutively, with 2ns spacing between bunches. This mode is used by those beam lines that rely on the average photon flux and do not exploit the time structure of the radiation. Typical electron energies are ranging from 2 to 2.4GeV, with a maximum average current of 330mA. Synchrotron radiation pulses have duration of typically $60ps_{FWHM}$ in MB operation; recently using the Third Harmonic super-conducting cavity, this value raised up to $120ps_{FWHM}$. The temporal structures of different sources are listed in Table 1.

The four bunch (4-B) mode is used by the SR-FEL, at 1GeV, and by the Users carrying out "time resolved" experiments, mostly at 2GeV as the photon beam is brighter. In this mode, four bunches are evenly distributed in four storage ring buckets and the interval between them results to be 216ns.

Storage Ring Free Electron Laser

In a SR-FEL, a relativistic electron beam interacts with an electromagnetic field as it passes through a periodic magnetic structure forcing particles to move along sin-like trajectories and, consequently, to emit radiation. The ELETTRA SR-FEL is the first and only one installed on a third-generation synchrotron light source. As a consequence, its performance profit from a relative low

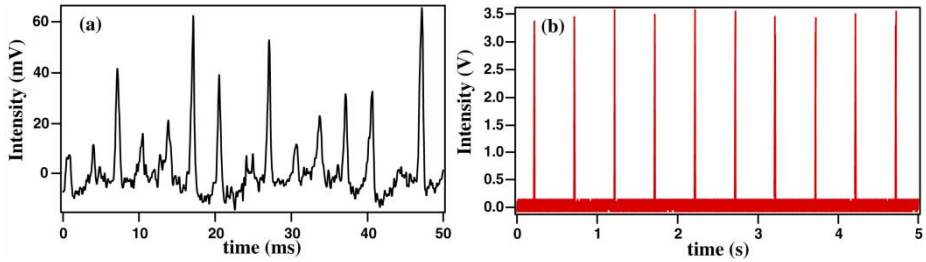

Figure 1: Example of the different macro-temporal structures displayed by the ELETTRA FEL when operated in standard (Figure 2a) or Q-switching (Figure 2b) mode.

emittance and short duration of the electron bunch and from a longer interacting region (this resulting in a higher gain with respect to similar devices). ELETTRA holds the world record of the shortest wavelength ever reached using an oscillator FEL (190 nm). The time duration of a single pulse from the SR-FEL can be as low as $15ps_{FWHM}$. The repetition rate of the SR-FEL pulses varies according to the operation mode of the SR-FEL: free running (fig. 1 left) and Q-switch (fig. 1 right), where the FEL power is "concentrated" into a series of giant pulses. In this case, the peak power is considerably enhanced (one to few orders of magnitude). The giant-pulse operation on a SR-FEL can be obtained by means of a radio frequency (RF) modulation, or using a gain-switching technique [4].

Table top fs laser oscillator

The laser system used for the experiments is a home-made femtosecond Cr:LiSAF laser. The laser construction has been optimized in order to decrease the intrinsic noise and increase stability. The active material is a 3% doped 3mm long Brewster cut Cr:LiSAF crystal (with temperature stabilization at 18°C by a Peltier cooler), which is pumped at 670nm by a 350mW diode. The phase locking to an external reference is based on the well-established technique using a feedback loop acting on the cavity length [5]: we have used a commercially available instrument (CLX1100, Time Bandwidth Products) which implements this approach. The necessary laser frequency reference signal is provided by an avalanche photodiode illuminated by a small fraction of the laser output beam.

EXPERIMENT SET-UP

The objectives of the experiments were:

- to synchronize the fs laser to the machine RF
- to acquire in a single shot all three sources: synchrotron bending, SR-FEL and fs laser
- to measure the jitter between the sources
- to observe their stability on the long-term time scale, compared to the duration of the pulses

A pre-requisite for the experiment was to have all three sources available at the same location to allow their simultaneous acquisition. This configuration has been easily achieved in the Optical Laboratory of the Instrumentation Group where the synchrotron radiation (UV-VIS-NIR) generated by the storage ring bending magnet S12.2 is made available for diagnostic purposes. Furthermore, the back-end of the SR-FEL is conveniently located in the close vicinity of the same laboratory where the installed Streak Camera is routinely used for measuring both the synchrotron radiation pulses and the SR-FEL pulses. The accelerating voltage radio frequency (RF) has been routed to the Optical Laboratory to feed the streak camera timing system. Therefore, to perform the experiment it was sufficient to move the Cr:LiSAF fs laser to the Optical Laboratory and to synchronize it to the same RF signal by means of a low-jitter electronic module.

Electron beam operating conditions

The experiments have been carried out in both MB and 4-B modes. As the fs laser normally operates at a repetition frequency of 100MHz, to synchronize it to the MB beam it was sufficient to tune the length of its optical cavity to obtain f_{rep1}= 99.9308MHz. The reference signal at this frequency has been obtained by division modulo-5 of the RF, as indicated in Table 2.

Table 2: Different frequencies used for the experiments.

Symbol	div. modulo N	Frequency [MHz]	period [ns]
f_{RF}	1	499.654	2.0
f_{rep_1}	5	99.9308	10.0
f_{rep_2}	6	83.2756	12.0
$f_{4\text{-BUNCH}}$	108	4.626	216.1
$108/6=18 \Rightarrow f_{rep_2}=18^{th}$ harmonic (f_{4bunch})			

In 4-B mode, being the synchrotron radiation repetition rate equal to $f_{4\text{-BUNCH}}$=4.626MHz, to lock the fs laser pulses to the synchrotron radiation ones at each revolution, the fs laser repetition frequency has been changed to f_{rep_2}=83.2756MHz. In doing so, each synchrotron radiation pulse had a laser pulse locked to it, one out of 18 as f_{rep_2} has been selected to be the 18^{th} harmonic of $f_{4\text{-BUNCH}}$.

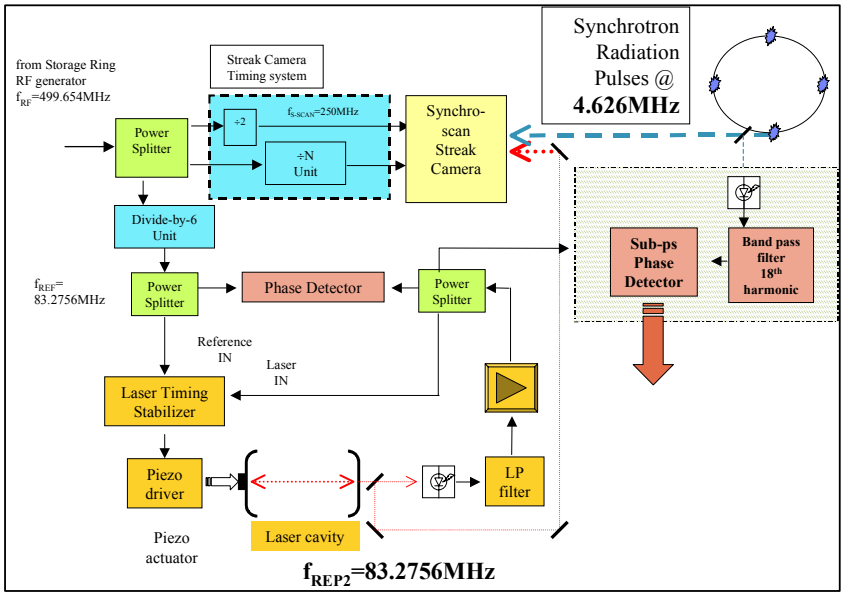

Figure 2: Block diagram of the Synchronization experiment

Description of the block diagram

The block diagram is reported in figure 2. In the upper left part, the low –jitter division-by-6 module can be seen. In the lower part, the Cr:LiSAF fs laser is visible with the lock-in equipment. Finally, in the right hand part of the block diagram, the light-to-light jitter measurement device is shown.

Before acquiring these different sources with the streak camera, they had to be precisely aligned onto the streak camera input pinhole (D=50÷200μm) and separately attenuated, using Neutral Density filters, due to their rather different intensities.

JITTER MEASUREMENTS

With the term jitter, here we intend the amplitude of the short-term time fluctuations of a signal with respect to its reference. When dealing with signals of the same frequency (i.e. frequency locked) the jitter turns out to be the phase noise of a signal to its reference.

The fs laser is equipped with its Timing Stabilizer unit that locks the repetition frequency of the laser to a reference by controlling the length of the optical cavity using a piezoelectric actuator. The Timing Stabilizer unit outputs the phase noise instantaneous values on a front panel display that is very useful for the fs laser set-up.

As the phase noise is a key parameter to know in our experiment, we implemented a redundant phase noise measurement beside the Timing Stabilizer unit. We adopted the Amplitude and Phase Detector AD8302 from Analog Devices [6] that performs amplitude ratio and phase difference measurements on two signals, from DC up to 2.7GHz and with a bandwidth of 30MHz. The two measurements have been cross-checked in both the time and frequency domain. In figure 3, the phase oscillations of the fs laser with respect to its reference, and due to a kick applied to the laser table, are shown. The upper trace shows the AD8302 output, the lower one the Timing Stabilizer output: there is a very good agreement with a higher sensitivity on the AD8302. Same results have been obtained with spectral observations in the range 10Hz to 1MHz, showing no major laser phase noise components above 1kHz.

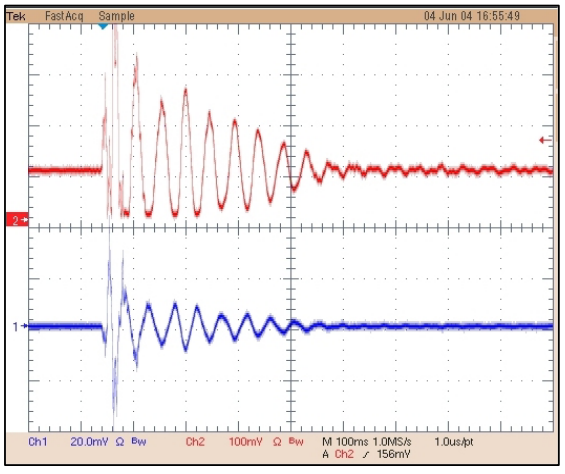

Figure 3: Phase oscillations of fs laser to reference after applying an external kick to the laser table. Upper trace: AD8302 phase output, 100mV/div. Lower trace: Timing Stabilizer output, 20mV/div. Hor. Scale 100ms/div.

STREAK CAMERA ACQUISITIONS

Several streak camera measurements have been carried out during the experiments. The aim was not the measurement of the fs laser pulse duration, well beyond streak camera resolution, but rather the characterization of the jitter and the long-term stability of the synchronized sources. The synchro-scan streak camera with its double sweep capability is well suited for this measurement as it can acquire up to 70ms of light pulses while keeping the resolution of few picoseconds. The synchro-scan acquisitions of the ELETTRA streak camera show the fast time axis horizontally and the slow one vertically, from the bottom to the top of the picture.

In the following figures, some examples of streak camera acquisitions are shown with simultaneous acquisitions of the fs laser pulses and synchrotron light pulses, even overlapping on the same fast sweep (duration 440ps or 880ps), like in figure 4. In this acquisition the fs laser pulse really "seats" on the synchrotron light pulse. The duration of the fs laser pulses is greatly increased by the limited streak camera resolution (<$2ps_{FWHM}$). Synchrotron pulses are 2ns apart

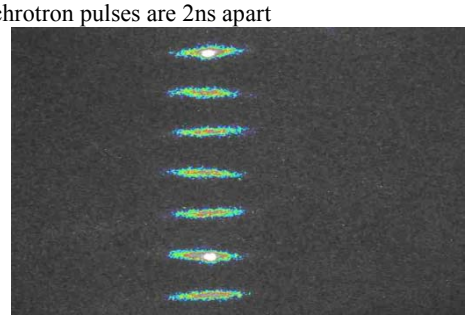

Figure 4: Fast synchro-scan acquisition (VERT=13ns, HOR=880ps) of seven synchrotron light pulses (MB beam) and two overlapping fs laser pulses at f_{rep1} (10ns apart).

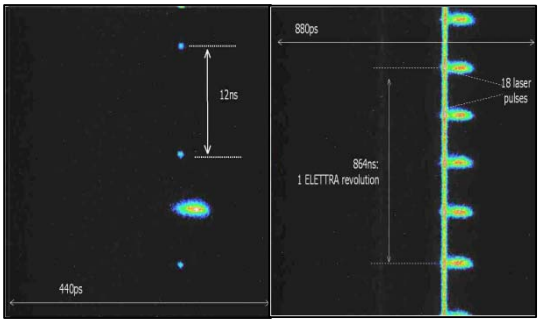

Figure 5, LEFT: fast synchro-scan acquisition (VERT=34ns, HOR=440ps) of one ELETTRA bunch (4-B mode) surrounded by three fs laser pulses. The laser now operates at f_{rep2} 12ns period). RIGHT, same beam but slower vertical axis (VERT=1380ns, HOR=880ps): six ELETTRA bunches captured with 18 laser pulses in between each pair, here shown as a solid line.

In figure 5 LEFT, one bunch of the ELETTRA beam in 4-B mode has been captured with three surrounding fs laser pulses. Now the light pulses have been "streaked" on different sweeps. In figure 5 RIGHT, a longer synchro scan acquisition is shown with the same 4-B beam as fig. 5 LEFT: the laser-to-synchrotron jitter has been estimated to be ≤$1ps_{RMS}$. In figure 6, all three sources have been captured on a long-time scale (VERT=6.7ms; HOR=880ps) acquisition. The fs laser and the synchrotron pulses appear as solid lines, whereas the SR-FEL is operating free running (pulsed): the stability between the sources can be estimated.

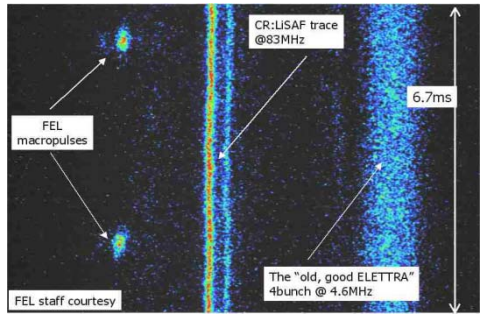

Figure 6: all three sources on a single synchro scan acquisition (VERT=6.7ms, HOR=880ps). The fs laser and synchrotron light pulses appear as continuous lines, the SR-FEL is in free running mode i.e. pulsed.

LIGHT TO LIGHT JITTER MONITOR

As previously shown (fig. 1), a direct light to light jitter monitor is proposed here based on the AD8302 phase detector. Relying on the integer multiplying factor (N=18) between the 4-B beam repetition frequency and the fs laser operating at f_{rep2} (83.2756MHz), a narrow-band band pass filter can be adopted to extract the 18^{th} harmonic from a beam signal (pick-up or photo-diode). The two sinusoidal signals (fs laser rep. rate and filtered beam signal) can be, then, phase-compared using an AD8302, in a 30MHz bandwidth and with a resolution better than 0.01deg. We call it light to light, real-time, on-line jitter monitor: reliminary measurements are encouraging.

REFERENCES

[1] G. Dattoli, A. Renieri, NIM A **507** (2003) 464
[2] G. De Ninno et al., Nucl. Instr. and Meth. A, 507 (2003) 274
[3] R. Bakker et al. "FERMI at ELETTRA: 100 nm - 10nm Single Pass FEL User Facility", EPAC2004 conference Proceedings
[4] I. V. Pinayev et al., Nucl. Instr. and Meth. A, 475 (2001) 222
[5] M.J.W.Rodwell et al, IEEE J.Quantum Electron. **25** (1989), 817
[6] LF-2.7GHz RF/IF Gain and Phase detector AD8302, P.O. Box 9106, Norwood, MA, USA.

LASER COMPTON SCATTERING GAMMA RAY INDUCED PHOTO-TRANSMUTATION

D. Li*, K. Imasaki, ILT, 2-6 yamada-oka, suita, Osaka 565-0871,Japan
S. Miyamoto, S. Amano, T. Mochizuki, LASTI, 3-1-2 Koto, Kamigori, Hyogo 678-1201, Japan

Abstract

High brightness beams of gamma rays produced in the means of laser Compton scattering have the potential to induce photo-transmutation through (γ , n) reaction, which implies an efficient method to dispose long-lived fission products. Preliminary investigations have been carried out in understanding the feasibility of developing transmutation facility to repose nuclear waste. A laser Compton scattering setup has been built on NewSUBARU storage ring and worked steadily to generate gamma-ray beams for studying the relevant nuclear physics. This paper aims at exploring the dependency of nuclear transmutation efficiency on target dimensions and gamma ray features with employing ^{197}Au target. The experimental results are in agreement with the theoretical estimations.

INTRODUCTION

To repose long-lived fission products effectively is an attractive issue in management and disposal of nuclear waste. Recently a number of methods have been presented and discussed [1,2], involving transmutation by bombardment with neutrons from a reactor or a particle accelerator, and laser-driven gamma generation for photo-transmutation [3]. However, nuclear transmutation through photonuclear reaction induced by high brightness gamma ray generated from a storage ring based laser Compton scattering facility is considered by us as a promising alternative [4][5]. In accordance to the conceptual scheme, we carried out relevant researches both on laser Compton scattering to produce high brightness gamma ray and photonuclear reaction through nuclear giant resonance. We have reported the laser Compton scattering setup built on NewSUBARU storage ring elsewhere [6][7].

In this paper, we concentrate on exploring the nuclear transmutation efficiency and its dependency on target geometrical dimensions and properties of laser Compton scattering gamma rays, which is a key point for realization of nuclear transmutation facility.

LASER COMPTON SCATTERING GAMMA RAY

Our laser Compton scattering setup was built on one of the straight section of NewSUBARU storage ring, which provides 1GeV electron beam with average current up to 200 mA. A laser light of 1.064 μ m wavelength from Nd:YAG laser was guided into the vacuum chamber to collide with the electron beam in a head-to-head manner, and scattered gamma ray photons with maximum energy of 17.6 MeV. The gamma ray goes along the incident electron moving direction in a forward cone of angle $1/\gamma$, where γ is the relativistic factor of electron, namely, 0.5 mrad in our experiment for the 1 GeV electron beam. The interaction point was designed at the center of the straight section, where both the electron beam and laser transverse profiles were focused to the minimum.

The gamma ray generated from our laser Compton scattering setup is polarized, and its polarization is changeable with inserting a wave plate in the laser light path [4].

ESTIMATION OF TRANSMUTATION EFFICIENCY

When a beam of gamma rays strikes on a target, the photonuclear reaction rate (1/sec/m^3) is given by

$$R = N_0 \sigma_g(E) I(E,z) \quad (1)$$

where N_0 is the number of atom per volume, $\sigma_g(E)$ is the nuclear giant resonance cross section, and $I(E, z)$ is the gamma ray intensity, which is a function of photon's energy E and penetrating depth z in a target.

According to the fact that laser Compton scattering gamma ray features a circular transverse profile, we considered a cylindrical target with radius of a and length of b, and the integration of volume gives the total reaction rate

$$\widetilde{R} = \int R dV = N_0 \int \sigma_g(E) I(E,z) dV \quad (2)$$

The gamma ray intensity could be expressed as

$$I(E,z) = \xi \sigma_L(E) e^{-\mu z} \quad (3)$$

where ξ relates to the properties of electron beam and laser light for collision, $\sigma_L(E)$ is the laser Compton scattering cross section, and μ is the total linear attenuation coefficient given by

$$\mu = \mu_{PE}(E) + \mu_C(E) + \mu_{PP}(E) + \mu_{PN}(E) \quad (4)$$

where $\mu_{PE} = \sigma_{PE}(E) N_0$, $\mu_C = \sigma_C(E) Z N_0$, $\mu_{PP} = \sigma_{PP}(E) N_0$, $\mu_{PN} = \sigma_{PN}(E) N_0$, Z is the atomic number, $\sigma_{PE}(E)$, $\sigma_C(E)$, $\sigma_{PP}(E)$ and $\sigma_{PN}(E)$ represent cross sections of photoelectron, Compton, pair production and photonuclear reactions, respectively. Consequently, Eq. (2) could be rewritten as

$$\widetilde{R} = N_0 \xi \int_0^b \int_0^a \sigma_L(E) \sigma_g(E) e^{-\mu z} \cdot 2\pi\rho d\rho dz \quad (5)$$

*lidazhi@ile.osaka-u.ac.jp

And we also have the following expressions to determine the energy of laser Compton scattering gamma photons [8]

$$E = \frac{E_m}{1+(\frac{\theta}{\theta_0})^2} \qquad \theta = \arctan(\frac{\rho}{L}) \tag{6}$$

$$E_m = \frac{x}{1+x}E_b \quad \theta_0 = \frac{mc^2}{E_b}\sqrt{x+1} \quad x = \frac{4E_b\upsilon_0}{m^2c^4}$$

where E_m is the maximum gamma ray energy, L is the distance from the interaction point to the front surface of target, E_b is the electron's energy, and υ_0 is the laser photon's energy.

The total injected gamma photons should be written as

$$F = \int I(E,0)ds = \xi\int_0^a \sigma_L(E)\cdot 2\pi r dr \tag{7}$$

Then, we achieved the expression for the transmutation efficiency defined as the quantity of transmuted nuclei by per photon,

$$\eta = \frac{\widetilde{R}}{F} = \frac{N_0\int_0^b\int_0^a \sigma_L(E)\sigma_g(E)e^{-\mu z}\cdot 2\pi r dr\,dz}{\int \sigma_L(E)\cdot 2\pi r dr} \tag{8}$$

From Eq.(8) we understand that the efficiency depends on not only the parameters of the target itself, such as target species, radius and length, but also the characteristics of laser Compton scattering setup including the electron beam energy, the laser photon's energy and even the distance from interaction point to the target.

Calculations and pictorial illustrations of transmutation efficiency are made for a gold (^{197}Au) target, positioned on axis 15.35 m away from the interaction point. $\sigma_L(E)$ can be derived from klein-nishina formula [8], $\sigma_{PE}(E)$, $\sigma_C(E)$, $\sigma_{PP}(E)$ and $\sigma_{PN}(E)$ are same as in reference [5].The dependency of efficiency on target length is shown in Fig. 1, depicting

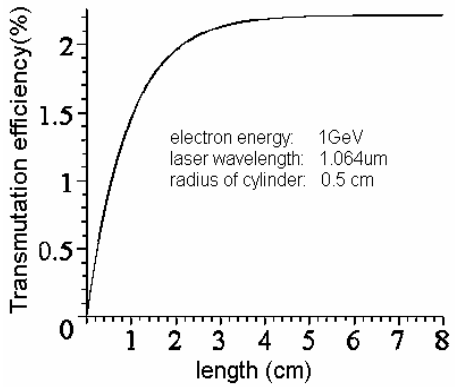

Fig. 1 Transmutation efficiency vs. the length of target

that the efficiency approaches constant when the length is longer than 5 cm. That is because all injecting gamma photons are absorbed after they travel such long a distance in target. The optimum radius of cylinder is about 0.5 cm as shown in Fig. 2, resulting in a maximum efficiency of 2.2%. And the efficiency falls

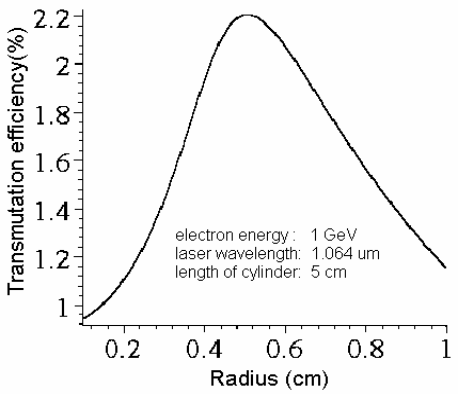

Fig. 2 Transmutation efficiency vs. radius of target

down when the radius continues growing, because a lot of low energy gamma photons are involved, which contributes little to the photonuclear reaction. Furthermore, the efficiency is sensitive to the electron beam energy as shown in Fig. 3, and the optimal energy is 950 MeV to make a peak of ~2.5%.

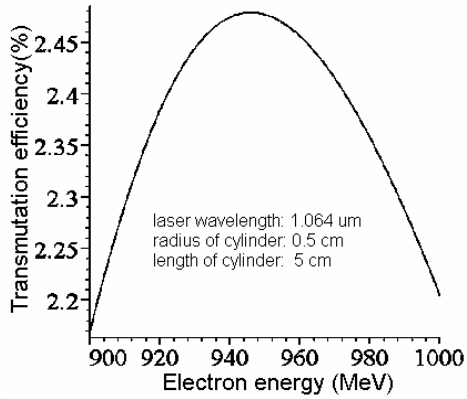

Fig. 3 Transmutation efficiency vs. electron beam energy

EXPERIMENT

Transmutation Efficiency

We use ^{197}Au samples for the nuclear transmutation experiment. The target was placed on axis receiving gamma ray irradiation, 15.35 m away from the interaction point, in front of a Germanium detector. In experiment, the Germanium detector was used to estimate the absorption ratio of gamma ray by the target. An example

of measured energy spectra is shown in Fig. 4, where the

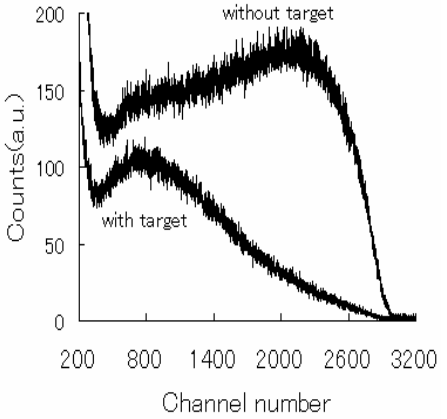

Fig. 4 Laser Compton scattering gamma ray energy spectrum with and without target, respectively.

difference between those two signals depicts the absorbed portion of gamma photons. Thus, one can deduce the total absorbed gamma photons in the duration of irradiation.

The ^{197}Au nucleus releases a neutron to undergo transmutation to ^{196}Au when absorption of gamma photons leads to (γ, n) reaction. ^{196}Au is unstable, and eventually transmuted to ^{196}Pb and ^{196}Hg in the way of radioactive decay. The transmutation from ^{196}Au to ^{196}Pb predominates and emits gamma ray of energy 355.73 KeV, which was able to be measured by a NaI(TI) detector. Through the measurement of radioactivity of irradiated target, the number of transmuted nucleus at the moment of end of irradiation can be deduced according to decay law

$$N_0 = \frac{\Delta N e^{\lambda t}}{1 - e^{-\lambda \Delta t}},$$

where N_0 is the number of undecayed nuclei, ΔN is the number of decays in the duration of Δt, λ is the decay constant, and t is the time interval from the end of irradiation to the beginning of activity measurement.

Two samples of cylinder gold target were employed in our experiment, with 5 cm long and radius of 0.25 cm and 0.5 cm, respectively. Both of them were irradiated with duration of 8 hours, and were processed with activity measurement separately. An example of emission spectrum was given in Fig. 5, showing the gamma ray rising from the decay process. The loss of the radioactivity inside the target was estimated by using EGS4 code [9]. And after data processing, we achieved the transmutation efficiency shown in Fig. 6, together with the calculation curve. The experimental results illustrate a little higher than the calculation, which might be the reason of secondary transmutation induced by electron-gamma showers occurring inside target. The errors come from the loss evaluation and statistical process, and with the promotion of our detecting system more precise measurement will be reached in the future.

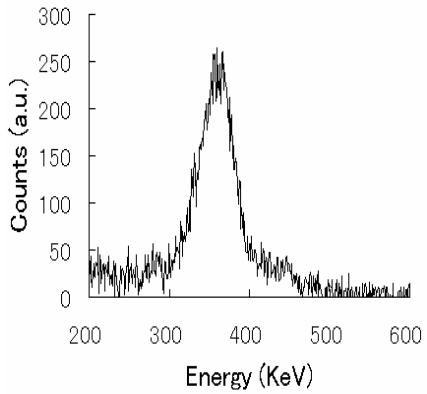

Fig. 5 Gamma ray energy spectrum of radioactivity of irradiated target

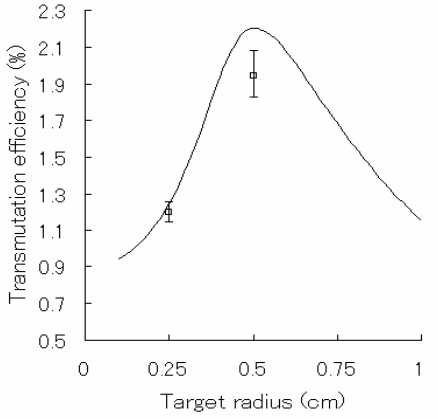

Fig. 6 Comparison of transmutation efficiency for experimental data and calculation curve

Secondary Gamma Ray

The interaction of high energy photons with matters raises secondary gamma rays, which is from the Compton scattering, bremsstrahlung and else effects. We performed experiments on measuring the secondary gamma rays.

A Germanium detector, with crystal measuring 64.3 mm in diameter and 60 mm in length, exhibiting 45% efficiency, was positioned 4 cm away the target, vertical to the beam line. The measurement was conducted for two targets, with radius of 0.5 cm and 0.25 cm, respectively. Their energy spectra (removed background) are shown in Fig. 7. It is known that the secondary gamma ray yield is small, especially the high energy photons. Generally speaking, the photonuclear reaction is induced by the photons with energy spanning from 8 MeV to 30 MeV,

therefore, the secondary gamma ray will not contribute to the photo-transmutation.

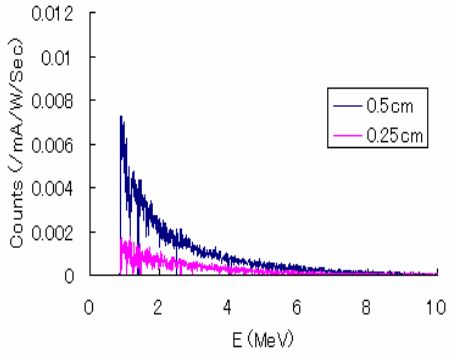

Fig. 7 Secondary gamma ray energy spectrum for target with radius of 0.5 cm and 0.25 cm, respectively.

CONCLUSION

Transmutation efficiency concerned with characteristics of target and gamma ray was studied experimentally with a storage ring based laser Compton scattering system, in order to investigate the feasibility of developing an efficient nuclear transmutation scheme to dispose the long-lived radioactive waste. We carefully analyzed the reaction rate of gamma ray with the nuclear giant resonance, and gave out the relation of transmutation efficiency with target dimensions and gamma ray properties. ^{197}Au rod target was used in irradiation experiments for demonstration, and the experimental results are close to the analytical estimations.

REFERENCE

[1] S. Matsuura ,Nucl. Phys. A 654 (1999) 417c
[2] W. Gudowski, Nucl. Phys. A 654 (1999) 436c
[3] K.W.D. Ledingham, J. Magill, P.Mckenna, et.al, J. Phys. D: Appl. Phys. 36 (2003) L79
[4] K. Imasaki , A. Moon, SPIE 3886 (2000) 721
[5] D. Li, K. Imasaki, M. Aoki, J. Nucl. Sci. and Tech. 39 (2002) 1247
[6] D. Li, K. Imasaki, M.Aoki, etal, Int. J. Infrared Milli. 24 (2003) 1301
[7] D. Li, K.Imasaki, S.Miyamoto et.al, The Review of Laser Engineering, 32 (2004) 211
[8] V. Telnov, Nucl.Instr. and Meth. A 355, (1995) 3
[9] W.R. Nelson, H. Hirayama, W.O. Roger, The EGS4 code system, SLAC-Report, 265 (1985)

DEVELOPMENT OF A PUMP-PROBE SYSTEM USING A NON-COATED ZnSe BEAM SPLITTER CUBE FOR AN MIR-FEL

M. Heya*, K. Ishii, S. Suzuki, K. Awazu, and H. Horiike, Institute of Free Electron Laser, Graduate School of Engineering, Osaka Univ., 2-9-5 Tsuda-yamate, Hirakata, Osaka 573-0128, Japan

Abstract

A reliable pump-probe technique is essential to gain a proper understanding of the interaction of lasers with tissue and similar materials. Our pump-probe system divides an incident s-polarized MIR-FEL (Mid-Infrared Free Electron Laser) into two beams of equal intensity, and simultaneously crosses the two beams. One beam acts as a pump beam, while the other as a probe beam with an additional time delay. Time-resolved absorption spectroscopy using this technique provides us with information about the vibrational dynamics of molecules. We have developed this system using a non-coated ZnSe beam splitter cube. The beam splitter cube is composed of two ZnSe prisms in the shape of a trapezoid. Two pulses with equal intensity are generated due to Fresnel reflection/transmission at the boundary between the two prisms, which then simultaneously illuminate the same position around the point of intersection of the two divided beams. We have conducted a proof-of-concept experiment for this system using the MIR-FEL. We showed that this system requires no complicated or time-consuming optical alignment, and that it is applicable for a broad MIR waveband (5~11 μm).

INTRODUCTION

In order to properly understand the interaction of lasers with tissue and other materials, a pump-probe technique is required. Conventional pump-probe techniques using a Michelson interferometer split an incoming pulse into two beams; a pump beam and a probe beam with a variable time delay relative to the pump beam. In this technique the two beams must simultaneously illuminate the same position, so it requires complicated and time-consuming optical alignment. Additionally, optical alignment for invisible mid-infrared (MIR) light is technically difficult.

From the above point of view, we have proposed and designed a new pump-probe system for a tunable MIR-FEL (Free Electron Laser) using a non-coated ZnSe beam splitter cube. Since one beam splitter cube divides an incoming pulse into two pulses with equal intensity, complicated and time-consuming optical alignment is no longer requied. We adopted the use of Fresnel reflection/transmission and total internal reflection to equally divide the incident MIR-FEL pulse into the two pulses. Since AR coating severely limits the applicable waveband range, no AR coating was used. In this article, we describe the principles and features of this pump-probe system. In order to confirm the performance of a trial pump-probe system, we have conducted its proof-of-concept experiment using an MIR-FEL. Since the FEL user facility at Osaka Univ. can provide an MIR-FEL within the range of λ = 5~12 μm [1], we designed the ZnSe beam splitter cube for λ = 7.5 μm. The refractive index of ZnSe is 2.421 at λ = 7.5 μm.

PRINCIPLES

Figure 1(a) shows the principles of our pump-probe technique involving the ZnSe splitter cube. The ZnSe splitter cube consists of two non-coated ZnSe prisms in a trapezoidal configuration. An air layer with a thickness of 50 μm exists between the two ZnSe prisms. The incident MIR-FEL beam is s-polarized. The incoming MIR-FEL pulse divides the two pulses (Beams A and B) at the boundary between the ZnSe prisms (point C). The reflected and transmitted beams are reflected due to total internal reflection, and then each beam crosses simultaneously outside the beam splitter at point D. In order to generate two pulses A1 and B1 with equal intensity, the angle θ_3 must be set at 20.4 deg, leading to reflectance R = 0.382, as shown in Fig. 1(b). Multiple Fresnel reflection occurs at point C. If we let the intensity

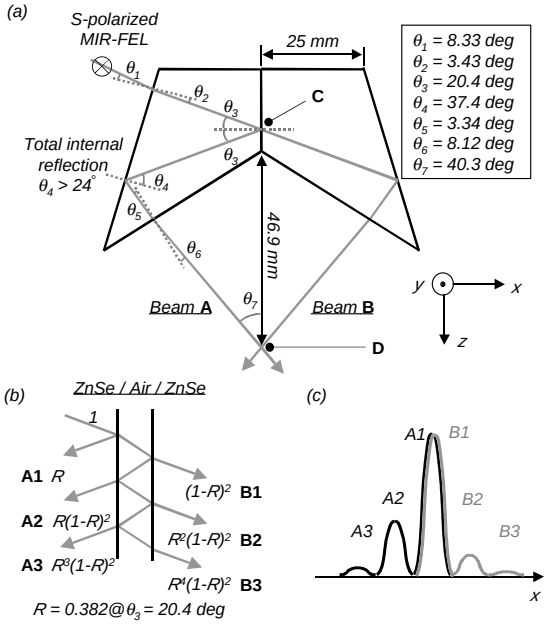

Figure 1: Principles of the pump-probe system using a non-coated ZnSe beam splitter cube. (a) Configuration of this system. The definitions of the *x*-, *y*-, and *z*-axes are also shown. (b) Generation of Beams A1 and B1 with equal intensity at the boundary between the two prisms (point C). (c) Typical profiles of Beams A and B along the *x*-axis at the point of intersection (point D).

*heya@fel.eng.osaka-u.ac.jp

of the incident beam at point C be unity, then the intensities for the respective divided beams are as follows: $I_{A1} = 3.82\times10^{-1}$, $I_{A2} = 1.46\times10^{-1}$, $I_{A3} = 2.13\times10^{-2}$, $I_{B1} = 3.82\times10^{-1}$, $I_{B2} = 5.57\times10^{-2}$, and $I_{B3} = 8.13\times10^{-3}$. Here we neglected the forth reflection/transmission and higher. As shown in Fig. 1(c), we can simultaneously illuminate a target at point D by using the two pulses (Beams A1 and B1) of equal intensity. Beams A1 and B1 can be used as either a pump or a probe beam. Note that the intensities for Beams A1 and B1 are ~0.3 (=0.382×(1−0.3)) times the incident MIR-FEL, since the total reflectance loss at the first and final boundaries is ~0.3.

Figure 2 shows the configuration of a typical pump-probe experimental set-up. The sample is located at point D. In this case, an optical window, whose material has good transmission characteristics for MIR-FEL, is inserted to the beam line for Beam B1, which is used as a probe beam. The optical window (such as CaF_2 and MgF) acts as a time delay relative to Beam A1, which acts as the pump beam. The time delay can be arbitrarily varied within the range 1~20 ps by changing the thickness of the optical window. The intensity of the transmitted probe beam is time-resolved by an MCT detector. This time-resolved signal, $S(t)$, gives us information about the vibrational dynamics of molecules during MIR-FEL irradiation.

The main features of this pump-probe technique are as follows.

(1) Since one beam splitter cube divides two pulses with equal intensity and crosses them over, optical alignment of this system is simple and not time-consuming.

(2) ZnSe prisms have good transmission characteristics over both the MIR and the visible spectrum, which enables us to use He-Ne lasers as the guide laser for optical alignment.

(3) The variation of the refractive index for ZnSe is less than 1% over a broad waveband of 2~11 μm [2]. In addition, non-coated ZnSe prisms are used. This means that tunable lasers can be utilized.

(4) This system is composed of transmittive optics. The use of ultra-fast pulse lasers is not possible due to group velocity dispersion within the system. This system is applicable for picosecond MIR-FELs, since the effects on the group velocity dispersion become significant in the femtosecond range.

(5) The time delay is constrained by the thickness of the MIR windows and is less than a few tens of picoseconds.

(6) The reflectance of the MIR windows is about 3~5%, leading to a slight difference in intensity between the two pulses.

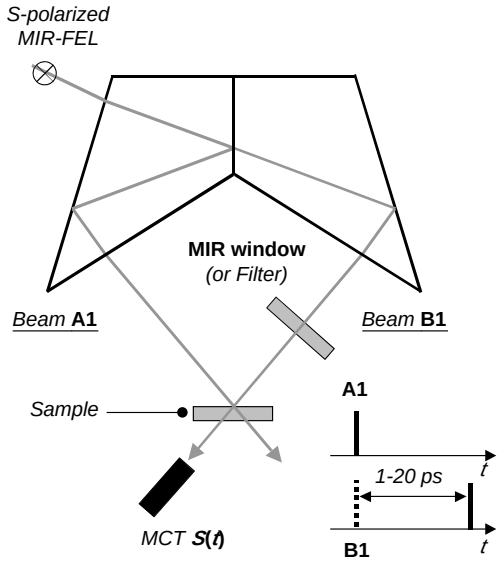

Figure 2: Typical configuration of the pump-probe experimental set-up. In this case, Beam A1 is the pump beam, while Beam B1 is the probe beam. The MIR window acts as an optical delay.

PROOF-OF-CONCEPT EXPERIMENT

We have conducted a proof-of-concept experiment using a tunable MIR-FEL in order to confirm the following performances of this system: (1) the division into two pulses (A1 and B1) with equal intensity over λ = 5~11 μm and (2) the focusability of the two pulses onto the same position.

Division

When the intensity of Beam A1 is exactly equal to that of Beam B1, the intensity ratio of Beam A to Beam B is 1.23 (as shown in Fig. 1(b)), where Beam A (B) generally terms multiple beams A1~A3 (B1~B3). The intensity ratio can be controlled by the incident angle of the MIR-FEL, θ_1. We measured the average powers for Beams A and B while adjusting θ_1. As a result, we confirmed that the intensity ratio can be set at 1.23 with a possible error of $\pm$10% over λ = 5~11 μm by only adjusting θ_1. Therefore, we can easily generate two pulses (A1 and B1) with equal intensity within an error of $\pm$10%. This error causes due to the uncertainty of the measurement of an average power.

Focusability

We examined the focusability of the two pulses onto the same position using heat sensitive papers, which were located at the point of intersection (point D). We obtained burn patterns on the papers by MIR irradiation while moving the target along the z direction. Note that this experiment was carried out after adjustment of the intensity ratio as described previously.

Figure 3 shows the burn patterns on the paper observed with an optical microscope after MIR-FEL irradiation. The wavelength and average power of the incident MIR-FEL were 9.4 μm and ~25 mW, respectively. An increase in z means a backward movement away from the beam splitter. We can see three burn patterns for Beams A1, A2, and B1. Patterns for the other beams were not observed because of their weaker intensities. As z increases, the

burn patterns of A1 and A2 gradually become closer to that of B1. Around z = 0.5 mm, patterns A1 and B1 overlap with each other, and then they separate again with an additional increase in z.

From Fig. 3, we can obtain data for the optical paths of Beams A1 and B1. When z is changed from 0 to 0.2 mm, the x-position of the center of Beam B1 shifts laterally by Δx = ~150 μm. We first experimentally estimated θ_7' from these data using the expression: $\theta_7' = \tan^{-1}(\Delta x/\Delta z)$, resulting in θ_7' = 36.9 deg. The specification of θ_7 is 40.3 deg (Fig. 1 (a)). This disagreement gives us the difference in path length between Beams A1 and B1. This difference in path length, ΔL, can be roughly evaluated by using the equation: $\Delta L = L_{total}(1-\cos(|\theta_7-\theta_7'|))$, resulting in ΔL = 0.206 mm. This difference leads to the time difference between the both beams, Δt (< 1 ps in this case). Δt is considerably shorter than the pulse duration of our MIR-FEL and is negligible. Here L_{total} is the total path length from the first ZnSe surface to point D, and was about 117 mm.

Secondly, we estimated the positional difference between both beams in the y direction. The distance between the centers of the both beams in the y direction is seen to be ~100 μm from the topmost image in Fig. 3. A positional difference should be reduced down to less than one-tenth the spot size of each beam at point D.

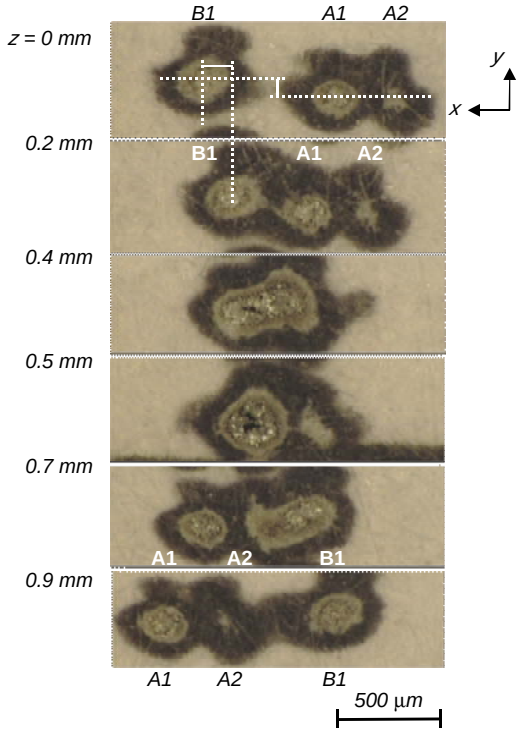

Figure 3: Observed burn patterns by MIR-FEL irradiation as a function of z. The definitions of the x-, y-, and z-axes are similar to those used in Fig. 1(a).

From these observations, the following can be derived.

(1) The pump-probe technique using the ZnSe beam splitter cube does not require complicated and time-consuming optical alignment and is applicable for a tunable MIR-FEL system. Especially, we can divide two pulses with equal intensity by only adjusting the incident angle of the MIR-FEL even over a broad waveband (λ = 5~11 μm).

(2) The time difference between both pulses was less than 1 ps and can be neglected.

(3) The positional difference in the y direction was ~100 μm, meaning that the spot size of the beams should be set at 1000 μm or more at point D.

CONCLUSIONS

In order to establish a useful pump-probe technique using a ZnSe beam splitter cube, we have designed it and have carried out its proof-of-concept experiment using an MIR-FEL. We demonstrated that this pump-probe technique is a wavelength-independent system and is applicable for a broad MIR waveband.

We will further measure the dynamic absorption properties [4] of soft tissue using this pump-probe technique. The dynamic absorption properties are those during laser irradiation and strongly dominate the extent of the heating, coagulation, and cutting of tissue. For non-invasive and predictable laser surgery, a knowledge of the dynamic absorption coefficients is essential.

ACKNOWLEDGEMENTS

The authors thank A. Ueguchi at Sumitomo Electric Industries, Ltd. for many useful discussions. We also give thanks for excellent technical support from all staff at the Institute of Free Electron Laser, Osaka Univ.

REFERENCES

[1] K. Awazu, M. Asakawa, and H. Horiike, "Status report and biomedical applications of the Institute of FEL, Osaka University," Nucl. Instr. and Meth. in Phys. Res. A, **507**, 2003, p. 547.

[2] H. Landolt and R. Bornstein, "Landolt-Bornstein numerical data and functional relationships in science and technology," Springer, Berlin, 1982, p. 147.

[3] Y. Ishida, T. Yajima, and A. Watanabe, "A simple monitoring system for single subpicosecond laser pulses using an SH spatial autocorrelation method and a CCD image sensor," Opt. Commun., **56**, 1985, p. 57.

[4] J. P. Cummings and J. T. Walsh Jr., "Erbium laser ablation: The effect of dynamic optical properties," App. Phys. Lett., **62**, 1993, p. 1988.

MEDICAL APPLICATION OF FREE ELECTRON LASER TRANSMITTANCE USING HOLLOW OPTICAL FIBER

S. Y-Suzuki*, K. Ishii, K. Awazu, Institute of Free Electron Laser, Graduate School of Engineering, Osaka University, 2-9-5 Tsuda-yamate, Hirakata, Osaka 573-0128, Japan

Abstract

Mid-infrared Free Electron Laser (FEL) is expected as new application for biomedical surgery. However, delivery of MIR-FEL into the body is difficult because the common glass optical fibers have strong absorption at MIR region. A good operational and flexible line for FEL is required at medical field. A Hollow optical fiber is developed for IR laser and high-power laser delivery. We evaluated the fiber for FEL transmission line. This fiber is coated with cyclic olefin polymer (COP) and silver thin film on the inside of glass capillary tube. It is 700 μm-bore and 1 m in length. The fiber transmission loss of the measured wavelength region of 5.5 μm to 12 μm is less than 1 dB/m when the fiber is straight and 1.2 dB/m when bent to radius of 20 cm. In additionally, the output beam profile and the pulse structure is not so different form incidence beam. In conclusion, the fiber is suitable for delivery of the FEL energy for applications in medical and laser surgery.

INTRODUCTION

A bio-molecule that constitute of the protein has strong absorption coefficient due to molecule vibration in infrared region. A free electron laser (FEL) is expected as selective and low-invasive treatments because the FEL which is able to tune in a wide wavelength range of infrared region excite molecule vibration selectively.

An atherosclerosis is caused by accumulation of cholesterol ester which is ester bond of cholesterol and fatty acid. We have reported that the wavelength of 5.75 μm corresponding to C=O stretching vibration of ester band resolves only cholesterol ester selectively [1]. The effect was confirmed on the *in-vitro* which used the cholesteryl oleate, the rabbit and the human blood vessel arteriosclerosis part section [2] [3]. Since the technique is the potential a low-invasive laser surgery in blood vessel compared a conventional method, an in-vivo experiment is expected. However, there is no guide line for transmitting infrared FEL. The FEL beam is usually guided by ZnSe lenses and mirrors to target materials but is difficult to deliver to small target in a narrow space and/or in the body. The common medical devices are used articulated manipulator or grass optical fiber for laser transmission. However, the articulated manipulators are unusable *in-vivo* surgery. The common glass optical fibers with IR absorption are also difficult to transmit enough energy. Therefore, the FEL beam transmission line is required good operationally and flexibility at medical field.

The FEL transmittance loss using chalcogenaide NSEG fiber have been reported by Awazu *et al* [4]. The transmittance could not exceed 70%. The fiber was fabricated with GeAsSeTe glass for the core and GeAsSe glass for the cladding is also harmful to human, thus it is not suitable for medical applications. A Hollow optical fiber which is developed by Miyagi and Matsuura is suitable for delivery IR laser beam and high-power laser such as CO_2 laser and Er:YAG laser which is in practical use [5] [6]. It is a thin tube composed of the air core and the dielectric with high refractive index or metal cladding, and loss in the core is practically nought. Transmission loss of wavelength 6.45 μm FEL at Vanderbilt University has reported by Matsuura *et al* [7]. The 1000 μm bore fiber, 1 m in length, gave transmission loss of 0.46 dB. In addition, the hollow optical fiber is used for some medical application using infrared laser. For example, Shen *et al* [8] reported that the hollow optical fiber is suitable for delivering the IR FEL for intraocular microsurgical procedures.

We have researched various interactions between biomedical tissues and FEL, beside the selective removal of cholesterol (5.75 μm), such as the surface modification of tooth dentin using FEL wavelength 9 μm bands and the ablation of soft tissue using FEL 6.05 μm.

This article reports the FEL transmission loss of wavelength from 5 μm to 12 μm using hollow optical fiber of 700 μm-bore, the guide system in a blood vessel using the hollow optical fiber is discussed.

EXPERIMENT

We tested the FEL power transmission of the hollow optical fibers with 700 μm-bore and 320 μm -bore, respectively. Both the hollow fibers are coated with cyclic olefin polymer (COP) and silver thin film on the inside of glass capillary tube. Figure 1 shows the IR absorption of the fiber measured using Fourier transform infrared spectroscopy (FTIR). The large peak at around 7.0 μm and the broad peak at 7-8 μm are due to absorption of the COP film. However, we need the transmission line which can be broadly covered in a mid infrared region. In addition, 6 μm and 9 μm bands used for our research such as surface modification and/or soft tissue ablation has little absorption.

The setup for the FEL power transmission experiments is shown Figure 2. The length of both the fibers is 1m. A FEL at Institute of FEL (iFEL), Osaka University in JAPAN, is tunable from 5 μm to 22 μm in mid-infrared (MIR) region, which is high peak power and short pulse

* suzuki@fel.eng.osaka-u.ac.jp

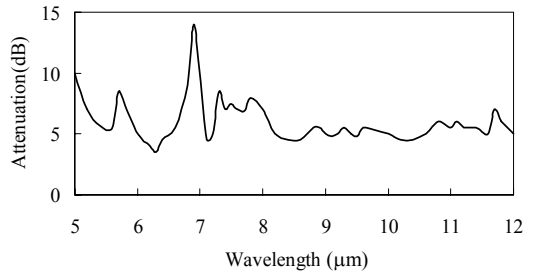

Figure1: Typical absorption spectrum of hollow optical fiber.

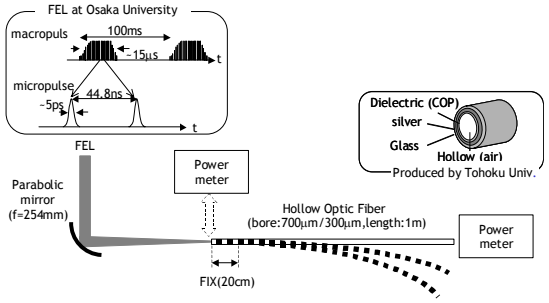

Figure 2: Experiment setup for the power transmission of the FEL.

operation. The FEL has a unique double pulse structure; the structure consists of a train of macropulses, and each macropulses contains train 300-400 ultrashort micropulses. The width of the macropulses is about 15 μs and repetition rate is 10 Hz. The width of micropulses is shorter than 10 ps and the separation between micropulses is 44.8 ns. The FEL beam focused using parabolic mirror (f = 254 mm) and enter an input end of hollow optical fiber. The mirror with a long focus reduces the coupling loss. The diameter of a beam is small enough to the input end of the fibers, and the input end of the fiber is not damage.

We measured the FEL average power at input end and output end of the fiber using the power meter (LaserStar 2A-SH, OPHIR) and calculate the power loss.

TRANSMISSION CHARACTERISTICS

Transmittance loss

The FEL transmission loss of wavelength from 5.5 μm to 12.0 μm in each fiber is shown in Figure 3. The transmission loss is not dependent on wavelength and is not influenced by IR absorption of COP. In the 700 μm -bore fiber, the transmittance loss at 5.5-12.2 μm is less than 1.2dB/m, which corresponds to over 80 % power transmission. The result shows that the 700 μm -bore hollow optical fiber is low loss and is enough as the guide line of FEL. In contrast, the 320 μm -bore fiber have the large loss exceeding 3dB/m, which corresponds to 50 % power transmission, because the diameter of FEL beam is no focus attention on less than 320 μm.

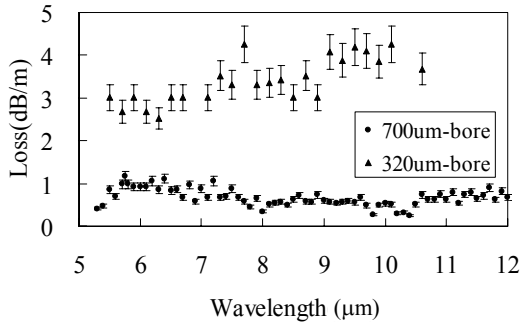

Figure3: Transmittance loss as a function of wavelength. The bore diameter is 700 mm and 320 mm, respectively and each fibers length is 1m.

Bending loss

Figure 4 shows the bending loss of FEL wavelength 5.75, 6.0, 9.4 10.6 and 12.0 μm, which are effective in bio-molecular such as ester band [1][2], phosphoric group and amide bond. The bending loss was increased from straight state (0 m^{-1}). The max bending loss in curvature 4.5 m^{-1} is 1.2 dB/m. The hollow optical fiber has losses sufficiently low for MIR-FEL transmittance.

Output beam profile

FEL beam spectrum and pulse structure after transmission are estimated. Figure 6 (a), (b), (c) shows beam profile of points which is distant from output end 2, 5, 10 mm, respectively. The estimated divergence angle is 2-3 degree. The form of these output beams are the same Gaussian as an input beam form. The distributed of light in Figure 6 (c) may be due to propagation mode but it is no problem because fiber come in contact with treated area in a blood vessel.

Figure 7 shows the pulse structure of before entering fiber and after transmission using MCT detector (R005, Vigo System). There is not much difference between before and after entering fiber.

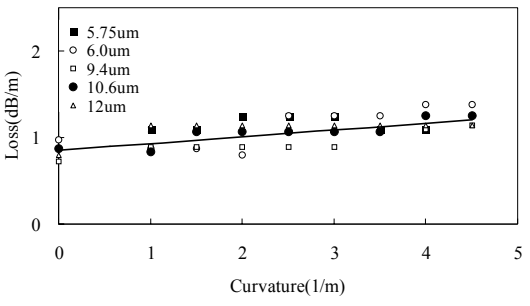

Figure 4: Bending losses of FEL wavelength 5.75 μm, 6.0 μm, 9.4 μm, 10.6 μm and 12 μm.

DISCUSSION AND CONCLUSIONS

We verified the hollow optical fiber as guiding line for transmitting FEL. The transmission efficiency achieved

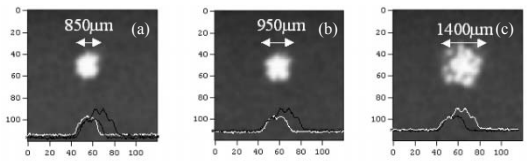

Figure 6: Beam profile of output end. Each point is distant fram output end (a) 2 mm, (b) 5 mm, (c)10 mm.

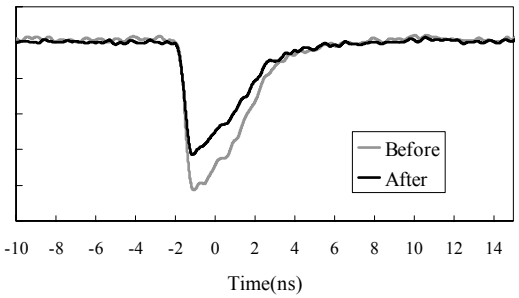

Figure 7: Pulse form of before entering fiber and after transmission using MCT detector

over 80 % in the case of bore diameter of 700 μm. The form and profile of beam passed in the fiber is like incident beam. These results confirmed that the fiber which developed CO_2 laser is applicable to the FEL with a unique pulse structure.

We have proposed the medical treatment in a blood vessel of atherosclerosis using the hollow optical fiber. In a previous report, we showed that the optimal power density which removes cholesterol ester selectively is 16 W/cm^2 [3]. Figure 8 shows the relation of the FEL average power to the diameter of beam required in order to give the power density of 16W/cm. When using the fiber of 700 μm-bore, the FEL average power exceeding 60mW is needed, but in iFEL, it is less than 50 mW. The scale factor of the fiber of 320 μm-bore to 700 μm-bore is 4.7, thus the fiber of 300 μm-bore obtains a necessary requirement for removes cholesterol ester by 15 mW average power. However, the loss of 320 μm-bore fiber is not the optimal in order to exceed 3dB by coupling loss (see Figure 3). In addition, the guide of the light in a blood vessel has a problem about the structure of the hollow optical fiber. Since the core of the fiber is an air hole, the blood flows in the fiber and blocks transmission of laser beam. We are developing the fiber cap like lens. The material of lens cap uses a diamond which has little absorption at MIR region and is harmless to humans.

In the future we are going to evaluate about the fiber with lens cap and to apply to clinical. Establishment of the technique is only the guiding light in blood vessel, but is also possible to transmit at region which it is not possible to focus by lens and/or mirror such as vacuum region, is useful to the FEL application.

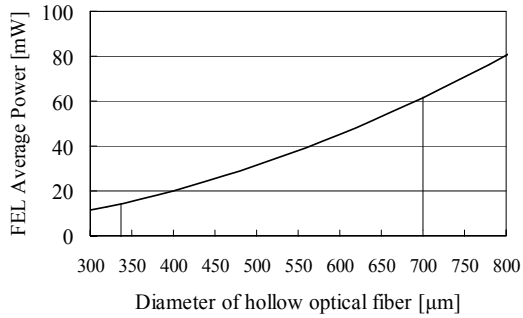

Figure 8: the relation of the FEL average power to the diameter of beam required in order to give the power density for removes cholesterol ester (16W/cm).

ACKNOWLEDGMENTS

We are grateful to Mr. Kuma, Mr. Marusaki and Mr. Teranishi, operational staff of iFEL graduate school of engineering, Osaka University.

Gratitude is expressed to Dr. Matsuura at Tohoku University, Japan, for providing the hollow optical fiber.

REFERENCES

[1] Kunio Awazu, Akio Nagai and Katsuo Aizawa, Selective Removal of Cholesterol Esters in an Arteriosclerotic Region of Blood Vessels with a Free-Electron Laser, Laser on Surgery and Medicine, 23, 233-237, 1998

[2] Kunio Awazu and Yuko Fukami, Selective removal of cholesteryl oleate through collagen films by MIR FEL, Nuclear Instruments and Methods in Physics Research A 475 (2001) 650-655.

[3] Katsunori Ishii, Kouichi Iwatuki, Toshiki Yoshimine, Kunio Awazu, The selective Removal of cholesterol oleate in the human carotid artety by infrared free electron lasers, The review of laser engineering, 30, 12 (2002) 742-746.

[4] Kunio Awazu, Seiji Ogino, Akio Nagai, and Takio Tomimasu, Midinfrared free electron laser power delivery through a chalcogenide grass fiber, Rev. Sci. Instrum., 68 (12), December 1997, 4351-4352

[5] Yuji Matsuura and Mitsunobu Miyagi, Hollow fibers for high-power lasers, The proceedings of SPIE conference, 3609 (1999) 251-255

[6] Yuji Matsuura, Todd Abel and James A. Harrington, Optical properties of small-bore hollow grass waveguides, Applied optics, 34, 30 (1995) 6842-6847.

[7] Yuji Matsuura, Kaori Matsuura and James A. Harrington, Power delivery of free electron laser light by hollow grass waveguides, Applied optics, 35, 27 (1996) 5395-5397

[8] J. H. Shen, K. M. Joos, J. A. Harrington, D. M. O'Duy, and G. S. Edwards: proc. SPIE 3262 (1988) 130.

MODIFICATION OF HYDROXYAPATITE CRYSTAL USING IR LASER

S. Satoh*, R&D Center, Saga University, Japan
A. Danjyo, M. Goto, Y. Yamaguchi, Faculty of Medicine, Saga University
C. Yamabe, N. Hayashi, S. Ihara, W. Guan, Fac. Sci. & Eng. Saga University

Abstract

To remineralize the dental surface, infrared (IR) laser was applied. The purpose of this experiment was concentrating to investigate crystal structure change of hydroxyapatite (HAp) before and after laser irradiation. The wavelength of incident laser beam is matching the characteristic absorption peak of HAp which ranging around 10μm. As a preliminary study for Free Electron Laser (FEL) application in biological field, the results we have got with the 10μm irradiation indicated that the FEL's capability of precisely deliver energy over a wide band of infrared makes it an attractive tool for further ameliorating of hydroxyapatite crystallization.

INTRODUCTION

The first application of laser technology to dentistry was for the removal of caries infected material and preparation of cavities [1]. However, ever since reports of laser application on improvement of dental surface were emerged, much attention has been focused on the laser's potential to enhance enamel's hardness and resistance to acid [2], [3], [4].

Although many attempts have been made to alter the tooth structure in order to increase its resistance to dental caries, little understanding on the physicochemical mechanisms involved has been achieved [5]. This research has pursued the photochemical phenomenon occurred during laser irradiation on artificial and biological HAp. In order to find a creative method to remineralize the demineralized enamel or the exposed coronal of dentine, the authors developed a novel procedure during laser irradiation [6].

Free electron laser (FEL) application is also intended primarily to realize the same purpose. The micro-pulse structure and duration of FEL laser was expected to be suitable to modify dental surface efficiency [7], [8].

In this study, slice samples of sound molar and artificial HAp pellet were irradiated with 10.6 μm CO_2 laser separately. Various laser parameter and chemical condition were applied in the experiment. There series of samples covered with saturation calcium ion solution ($Ca(OH)_2$ and $CaHPO_4$) and their combination were compared after irradiation. To investigate the micro-crystal morphology of the samples, X-ray Diffraction (XRD) pattern were surveyed. The comparison of XRD result shows that the chemical coating effected the irradiation process evidently.

EXPERIMENTAL PROCEDURE

Experimental layout

Experimental setup shows Figure 1. A transversely excited atmospheric pressure (TEA) CO2 laser, which works at pulse width τ=1μs (FWHM) and wave length λ=10.6μm was employed. This equipment permits the selection of the pulse energy from 60mJ to 500mJ, and of the repetition rare from 0.2Hz to 1Hz. The laser output beam was focused by a plano-nonvex ZnSe lens on the front side of the samples to spot sizes of the order of 10^{-2} cm^2, which corresponding energy density of 9J/cm^2. Laser pulse energy was measured with an energy meter (Gentec, Model ED-500L) prior to and after tissue irradiation and pulse-to-pulse stability of the CO2 laser was 23%. Some experiments show that the fluence threshold at this parameter are 0.3J/cm^2 and 0.6J/cm^2 for dentin and enamel respectively. For our experiment, the ablation threshold was estimated approximately 1J/cm^2. The teeth samples used in this experiment are obtained from the Department of Oral and Maxillofacial Surgery, Faculty of Medicine, Saga University. Extracted sound human molars were conserved in a physiologic serum to avoid cracking due to dryness and then embedded into polyester resin and cut into slices less than 1mm thick by a diamond saw microtome. After sliding, the slide discs were polished with a series of water-lubricated SiC papers up to 5000. Thus, enamel and dentine region were prepared flat and accessible to laser treatment.

Additionally, artificial HAp pellet was chosen as the target material for comparison. The Ca/P molar ratio value of the HAp pellet (PANTAX, Japan) was 1.67, which confirms the stoichiometric value. The HAp pellet samples present a high crystallinity as it was demonstrated by X-ray diffraction.

In the irradiation experiments, the specimen was mounted on a motorized x-y-z translation stage and positioned perpendicular to the direction of laser incidence. All experiments have been performed in air. The incidence area was constantly changed to avoid carbonization.

* e-mail : 1952sato@cc.saga-u.ac.jp

The specific experimental conditions concerned in this experiment are following;

(1) XRD survey of original and CO_2 laser irradiated artificial HAp.
(2) XRD survey of dentine and enamel before and after CO_2 laser irradiation.
(3) XRD survey of enamel covered with saturated chemical solution film after CO_2 laser irradiation.

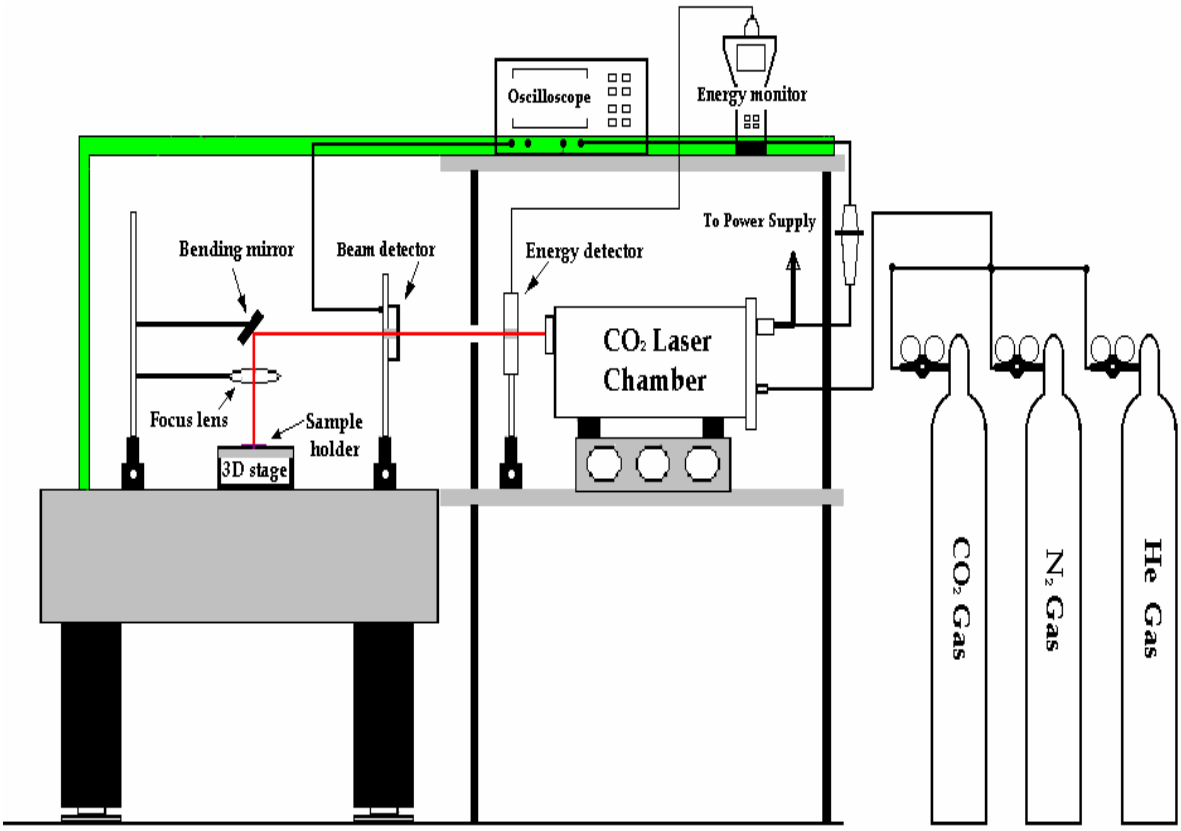

Figure 1: The scheme of irradiation experiment

The XRD analysis

The X-ray diffraction of the profile breadth and relative intensity date were collected from the samples on X-ray diffractomerter using Cu(Kα) radiation (RINT1100, Rigaku, Japan). The divergence slit was 1° and the receiving slit was 0.3mm. The scan range for relative intensities was from 20º to 70º (2θ), and scan rate was 4º (2θ/min)

RESULT AND DISCUSSION

Compared with artificial HAp sample shown in Figure 2, the (213) and (202) reflection intensity of dentine was not so intense. After irradiation with $CaHPO_4$ solution film shown in Figure 3, the reflection (202) appeared. And ten relative intensity peaks of artificial HAp pellet sample, (002), (202), (222) was modified. Most of the characteristic peaks of HAp were decreased.

Through the result we can suppose that HAp may be decomposed due to the thermal effect of laser irradiation [8], while as the product of decomposed HAp also exists in the dentine and enamel as amorphous calcium phosphate phase. The general reaction of HAp infused with chemical solution under the photo-thermal effect condition is considered as following.

$$3Ca_3(PO_4)_2 + Ca(OH)_2 \rightarrow Ca_{10}(PO_4)_6(OH)_2 + 2H_2O + 4CO_2 \quad (1)$$

Due to the thermal effect during photo ablation process, the temperature of the interaction surface should raise instantaneously. HAp may be decomposed through the reaction as formula (2).

$$Ca_{10}(PO_4)_6(OH)_2 \rightarrow 3Ca_3(PO_4)_2 + CaO + H_2O \quad (2)$$

And CaO is easy to react with water, and the produce tricalcium phosphate and heat.

The potential reaction under the irradiation with $Ca(OH)_2$ and $CaHPO_4$ mixed saturation solution film was considered as following.

$$4\ Ca(OH)_2 + 6\ CaHPO_4 \rightarrow Ca_{10}(PO_4)_6(OH)_2 + 6\ H_2O \quad (3)$$

As $CaHPO_4$ is easy to react with $Ca(OH)_2$ to produce various calcium phosphate formations. At the same time, the reaction will release amount of heat. This may delay the heat transmittal and decrease the thermal threshold of hard tissue during irradiation. The apparent amorphous regions of XRD patter were considered to be connecting with this mechanism.

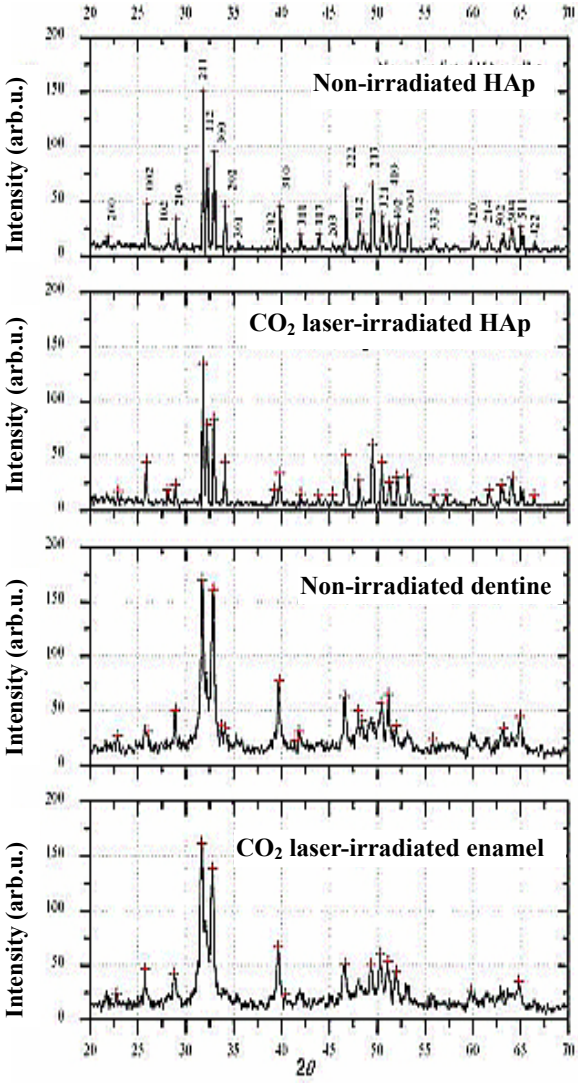

Figure 2: Comparison of CO_2 laser irradiation on artificial HAp and dentine sample

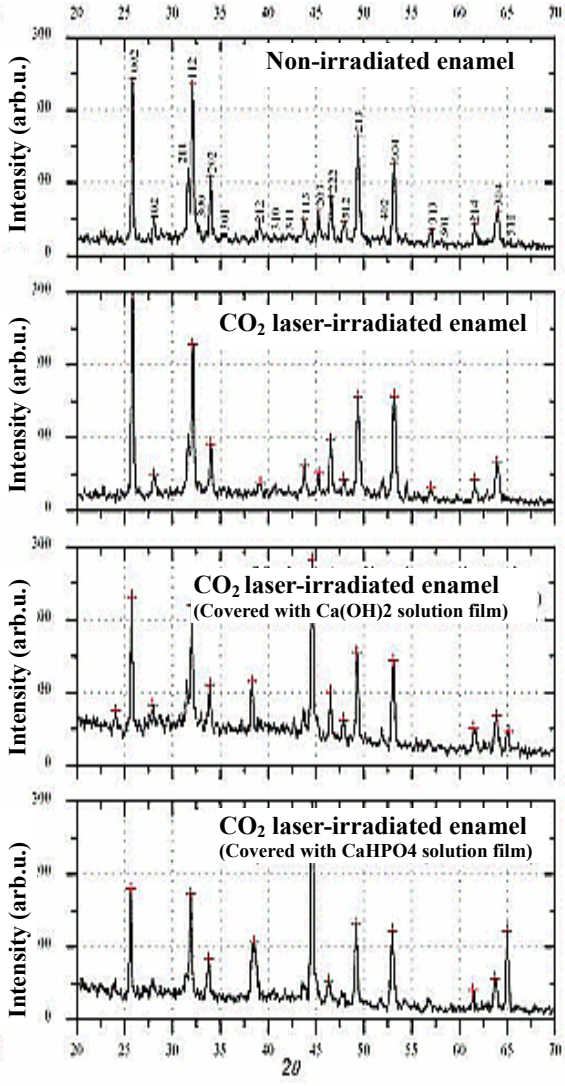

Figure 3: Comparison of CO_2 laser irradiation on enamel sample, with and without chemical solution

CONCLUSION

After CO_2 laser irradiation, the (002) reflection was increased significantly. It indicates the crystal growth in c-axis. On the other hand the (222) reflection was reduced both in HAp and dentine. It was considered relating to the thermal effect during high-energy irradiation.

The intense band in the spectrum around 2θ=45° (fig.3) is not a HAp band, but a strong metal reflection most possibly caused by aluminum. In the some observation, this band has been erroneously assigned as a HAp band in the XRD spectra of phosphates. In the spectrum of irradiated samples, the crystal phase show very broad peaks and high background. This may indicate the presence of very small crystallites, which will result in broad peaks.

The broadening of spectrum was assumed to be caused mainly by crystallite (domain) and lattice strain (within the domain). At the same time, we can see the new peaks, which indicate HAp did not dissociate, but is transformed to a new ablated form about 1000 degree. Phase transition in $Ca_3(PO_4)_2$ from a tricalcium phosphate type to a HAp type structure, which also occurs at the similar conditions, did not induce the dissociation of HAp. However, we were failed to assign the new peaks to these structures. Alternatively, the diffraction peaks of a new HAp polymorph can be indexed by an orthorhombic cell with lattice parameter a=b=9.43nm, c=0.688nm.

REFERENCE

[1] M. Myers, "The effect of laser irradiation on oral tissues", J Prothet Dent, 66 (1991) 395.
[2] S. Kantola, "Laser-induced defects on the tooth structure", Acta Odontol Scand, 30(1972)475.
[3] J. Melcer, "Latest treatment in dentistry by means of the CO_2 laser beam", Lasers Surg Med, 6(1986)396.
[4] L. Miserendin, "The laser apicoectomy: endodontic application of the CO_2 laser in apical surgery", Oral Surg Oral Med Oral Pathol, 66(1988)615.
[5] M. Gonzalez, et al, "Particle-induced X-ray emission and scanning electron microscopic analyses of the CO_2 laser irradiation on dental structure", J. Dentistry, 27(1999)595.
[6] W. Guan, et al, "Modification of hydroxyapatite crystallization using IR laser", Program and Abstracts of MAPEES'04, (2004)112.
[7] S. Ogino, et al, "The Effect of Free Electron Laser Irradiation on Dentine", J. Jpn. Soc. Laser Dent, 7(1996)67.
[8] M. Tanaka, et al, "Surface Modification of Tooth Dentine Irradiated by a 9.45μm CO_2 laser", J. Jap. Soc. Laser Dent, 11(2000)104.

VIBRATIONAL EXCITATION OF AMMONIA MOLECULES BY FEL-SUT

Y. Ogi*, K. Tsukiyama, Tokyo Univ. of Science, 1-3 Kagurazaka, Shinjuku, Tokyo 162-8601, Japan

Abstract

Free Electron Laser at Tokyo University of Science (FEL-SUT) was employed for exciting single vibrational modes of ammonia molecules. FEL is tuned to 10.5 μm, corresponding to the X $^1A_1'$ $2^1 \leftarrow 2^0$ transition of NH_3. The population of the vibrationally excited states is probed by the (2 + 1) resonance enhanced multiphoton ionization (REMPI) technique via the B $^1E''$ Rydberg state. Excitation efficiency of the $2^1 \leftarrow 2^0$ transition was about 30 %. Rotational analyses of the spectra revealed that vibrational ladder climbing up to X 2^2 in NH_3 was realized for the first time. IR-FEL excitation spectra were also recorded.

INTRODUCTION

For chemical physicists, the most serviceable advantage of the infrared free electron laser (IR-FEL) over conventional laser light sources is its spectral range. Since the mid infrared (MIR) spectral region falls in the range of excitation energy of a specific molecular vibrational mode, IR-FEL is considered to be a powerful tool for spectroscopic study in the MIR region and bond-selective photochemistry. Our group [1] reported on vibrational excitation of CO molecules as the first result of experiment on gas-phase molecules employing IR-FEL at Tokyo University of Science (FEL-SUT). The 4.7-μm FEL, corresponding to the X $^1\Sigma^+$ $v'' = 1 \leftarrow 0$ transition of CO, generated vibrationally excited CO molecules which were probed by (2 + 1) resonance-enhanced multiphoton ionization (REMPI) technique via B $^1\Sigma^+$ state. We found that ~10 % of the population in $v'' = 0$ was excited to $v'' = 1$, but no sequential excitation to the $v'' \geq 2$ vibrational levels was observed.

As a next stage, this paper describes preliminary results on vibrational excitation of ammonia (NH_3) molecules. Ammonia and its isotopomers are one of the most representative small gas-phase molecules. From the view point of vibrational excitation, Akagi et al. [2] reported bond-selective dissociation of partially deuterased ammonia excited to the overtone state of N-H or N-D stretching mode. When the $5\nu_{NH}$ overtone state (excited by 650-nm visible laser) of NHD_2 was photodissociated by UV laser, the NH dissociation cross section was ~5 times as large as the ND dissociation cross section per bond. Report on the vibrational excitation of single quantum has also been made by Ying et al. employing FEL at Vaderbilt University [3]. Their main purpose was to observe absorption spectrum corresponding to X $^1A_1''$ $2^1 \leftarrow 2^0$. In the current study we attempted to generate a large amount of the vibrationally excited ammonia molecules and to investigate whether the ladder climbing exists or not. We employed (2 + 1) REMPI schemes via the B $^1E''$ Rydberg state to detect vibrationally excited ammonia, because the observation of the B $^1E''$ using REMPI schemes has been thoroughly studied [4-8].

EXPERIMENT

The experiment was performed at laboratory III in IR-FEL Research Center at Noda campus of Tokyo University of Science. The status of the FEL-SUT facility was reported elsewhere [9-11]. Figure 1 displays a schematic diagram of the experimental system. The system consists of a reflectron-type time-of-flight spectrometer (Jordan D-651) with a pulsed valve (Jordan C-211AL), a beam duct and several mirrors for the guidance of the FEL beam to the TOF system, a nanosecond dye laser (Continuum ND6000) pumped by a Q-switched YAG laser (Lotis TII), and a microcomputer unit for data storage and control of the dye laser wavelength. A main chamber is evacuated by two turbo molecular pumps (SHIMADZU TMU1500 and TMU 150): The background pressure is below 10^{-7} Torr. The pulsed valve with a skimmer nozzle produces a supersonic molecular beam with 60 μs duration. Molecular beam is supplied with 5 % NH_3 in Ar at the back pressure of 1 atm. This molecular beam is intersected by two counterpropagating laser lights. Both laser beams are focused with a lens (f = 30 cm; BaF_2 for IR and quartz for UV). The polarization plane of the IR-

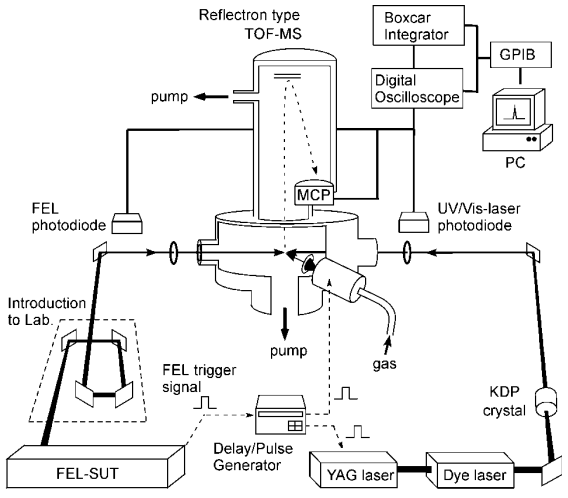

Figure 1: Experimental apparatus.

*ogi@rs.kagu.tus.ac.jp

FEL is parallel to the TOF axis and the UV laser polarization is perpendicular to them.

The synchronization among the pulsed molecular beam, FEL macropulse and YAG-laser pulse was controlled electrically by the use of several digital delay generators (SR DG535). The repetition rates of macropulse and micropulse are 5 and 2856 MHz, respectively. As long as the dye laser pulse is sitting in a macropulse of ~ 2 μs duration, the dye laser pulse of 3 ns duration contains several micropulses which have 350 ps interval. Because a fast detector for MIR radiation is not available, we monitored the temporal profile of visible harmonics with a photodiode (Electro-Optics Technology, ET-4000).

The wavelength of FEL was tuned around 10.5 μm, corresponding to the X $^1A_1$" $2^1 \leftarrow 2^0$ transition of NH_3. Typical bandwidth of the IR laser, monitored by using monochromator and a HgCdTe detector, was ~0.16 μm (~14 cm^{-1}, FWHM). In front of the window of the main chamber, the macropulse energy at this wavelength was measured to be 8-15 mJ which is several times greater than that in the earlier experiment [1]. On the other hand, 315-340 nm light required for (2 + 1) REMPI via the B ^{1}E" state of NH_3 was obtained as a second harmonic of the dye laser output. The output of the dye laser was frequency doubled in a KDP crystal. The UV pulse energy was measured to be ~1 mJ.

RESULTS AND DISCUSSION

The B ← X REMPI excitation spectrum obtained by scanning UV wavelength in the range of 315-340 nm was governed by the vibronic progression of ν_2 as seen in earlier reports [4-8]. This fact is based on the large change of equilibrium geometry. Whilst the ground state is pyramidal (point group C_{3v}) the Rydberg states are all planar (point group D_{3h}).

Figure 2a) shows a portion of the REMPI excitation spectrum corresponding to the B ← X 2^1_0 transition without introduction of IR-FEL. Rotational assignments are performed using known molecular constants [4]. The B ← X two-photon transition belongs to the perpendicular band and the selection rule for K is $\Delta K = \pm 1$. The $^rS_0(0)$ and $^pR_1(1)$ lines cannot be resolved by our laser bandwidth. Missing of the transition from the $J_K = 1_0$ level is explainable as follows. Due to the inversion doubling, each ν_2 state in the ground state has s and a components having A_1' and A_2" vibronic symmetry, respectively. In the B state, the vibronic symmetry is either E" or E', for even or odd ν_2 level, respectively. Two-photon transitions connect lower and upper states according to the schemes E" ← A_1'(s) and E' ← A_2"(a). Owing to the nuclear spin statistics, the A_1' component in the X state has only odd-numbered J for $K = 0$. Inversely, the A_2" component has only even-numbered J for $K = 0$. For B ← X 2^1_0 transition, the lower state doesn't have $J_K = 1_0$ level since the vibronic symmetry is A_2".

Figure 2a) could be reproduced consistently by a simulation taking into account rotational line strengths [12], rotational degeneracy, rotational temperature, and nuclear spin statistics in the ground state. Rotational temperature was found to be ~8 K. This calculation indicated that over 99 % of population was fell in the $J_K = 0_0$ and 1_1 in the X(a) state.

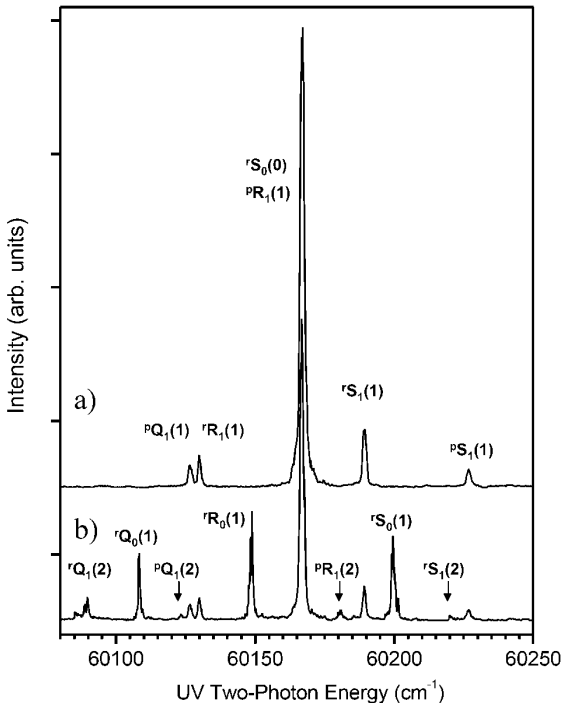

Figure 2: REMPI spectra in the region of the B ← X 2^1_0 two-photon transition of NH_3 a) without and b) with irradiation of the IR-FEL (10.5 μm). Rotational assignments added in traces a) and b) belong 2^1_0 and 2^2_1 bands, respectively.

Figure 2b) is the REMPI spectrum obtained by the irradiation of both the IR-FEL and UV laser. The center wavelength of the IR-FEL was fixed to 10.5 μm (952 cm^{-1}). Newly appeared peaks were assigned to the rotational lines in the B ← X(s) 2^2_1 two-photon transition, demonstrating that the vibrational excitation of NH_3 corresponding to the X(s) $2^1 \leftarrow$ X(a) 2^0 transition in the ground state was achieved. Simultaneous observation of rovibronic transitions from the X(s) 2^1 $J_K = 1_0$ and 2_1 levels indicate that the broad spectral width of IR-FEL covers the transition energies of the $a^qR_0(0)$ (951.78 cm^{-1}) and $a^qR_1(1)$ (971.88 cm^{-1}) [13]. Note that the selection rules for the rovibrational transition are A_1'(s) - A_2"(a) and $\Delta K = 0$ (parallel band).

Efficiency of the vibrational excitation was estimated comparing Fig. 2a) and b). The intensity of the each peak in Fig. 2a) apparently decreased in Fig. 2b). Average of the decrease in peak intensities for $^pQ_1(1)$, $^rR_1(1)$, $^rS_1(1)$, and $^pS_1(1)$ peaks suggests that 30 % of the total population in the X(a) 2^0 $J_K = 1_1$ was pumped to the X(s) 2^1 $J_K = 2_1$. Here the strongest peak constructed by two rotational lines was not involved in the calculation.

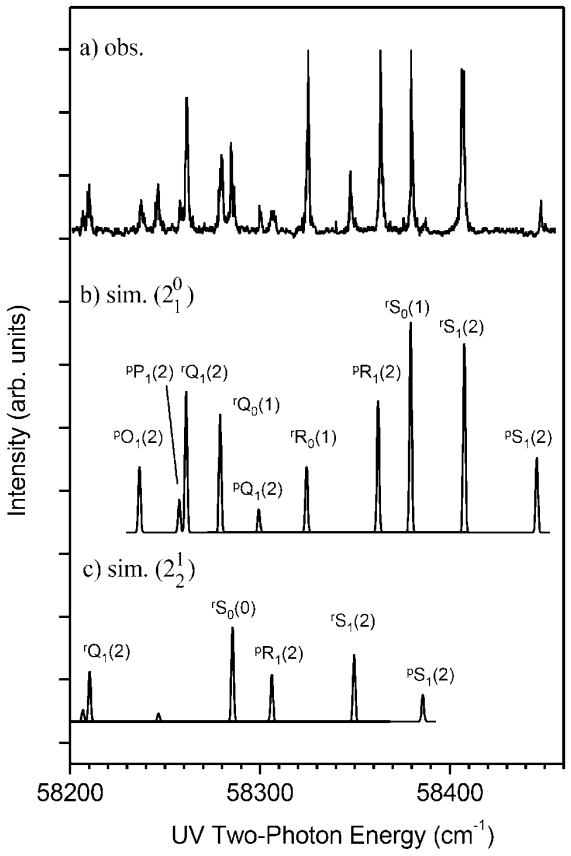

Figure 3: REMPI spectra in the region of the B ← X 2^0_1 and 2^1_2 two-photon transition of NH_3. a) Observed spectrum with irradiation of both the IR-FEL (10.5 μm) and UV laser. b)c) Simulation for B ← X b) 2^0_1 and c) 2^1_2 transitions.

Figure 3a) displays REMPI spectra in the region of the B ← X 2^0_1 and 2^1_2 two-photon transition of NH_3 obtained with irradiation of both the IR-FEL and UV laser. Since this energy region is below the B ← X band origin (~59300 cm^{-1}), no signal appeared without the IR-FEL. Figure 3b) represents the calculated spectrum corresponding to the B ← X 2^0_1 transition. This trace reproduces ten peaks in Fig. 3a) almost perfectly. The disagreement of their intensities is mainly caused by the fluctuation of the FEL macropulse intensity. The rotational levels in the X 2^1 state are identified to be J_K = 1_0 and 2_1, showing that the rotational lines in the X(s) 2^1 ← X(a) 2^0 band are $^qR_0(0)$ and $^qR_1(1)$, as same in Fig. 2.

Additionally, the signals corresponding to the B ← X 2^1_2 transition appeared in this region. The calculated spectrum displayed in Fig. 3c) clearly shows that the X(a) 2^2 J_K = 0_0 and 2_1 levels are populated. These two levels are excited from the X(s) 2^1 J_K = 1_0 and 2_1 through the $^qP_0(1)$ (929.61 cm^{-1}) and $^qQ_1(2)$ (947.88 cm^{-1}) branches, respectively. This observation demonstrates for the first time that the ladder climbing up to ν_2 = 2 was realized in the NH_3 system. The complete paths of the vibrational excitations are written as (i) X(a) 2^2 J_K = 0_0 ← X(s) 2^1 J_K = 1_0 ← X(a) 2^0 J_K = 0_0, and (ii) X(a) 2^2 J_K = 2_1 ← X(s) 2^1 J_K = 2_1 ← X(a) 2^0 J_K = 1_1. No signals could be observed corresponding to the subsequent climbing to X(s) 2^3: the transition energy of the X(s) 2^3 ← X(a) 2^2 band (~ 500 cm^{-1}) is far from the IR-FEL wavenumber used.

Figure 4 shows the examples of IR-FEL excitation spectra recorded by scanning IR-FEL wavelength. The UV laser frequencies are fixed to the a) $^qR_0(1)$ and b) $^pR_1(1)$ branches of the B ← X 2^0_1 transitions; the probed levels by the UV laser are X(s) 2^1 J_K = 1_0 and 1_1, respectively. These two levels were pumped through the $a^qR_0(0)$ and $a^qQ_1(1)$ branches of the X(s) 2^1 ← X(a) 2^0 vibrational band. Though the spectral features are very broad owing to the condition of FEL-SUT, the spectral positions are consistent with the transition energies (calculated from ref. [14]) indicated by down arrows.

In summary, we succeeded in detecting vibrationally hot NH_3 molecules populated by light pulses from FEL-SUT. MIR FEL was tuned to 10.5 μm which corresponds

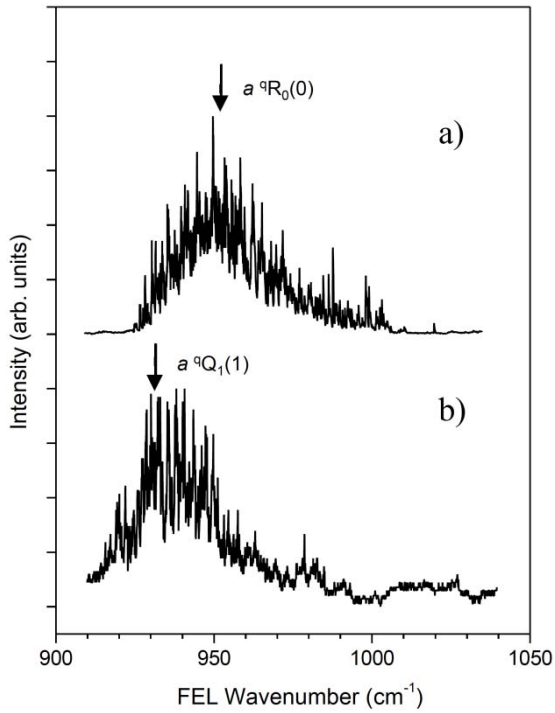

Figure 4: IR-FEL excitation spectra corresponding to the X(s) 2^1 ← X(a) 2^0 of NH_3. The UV laser frequencies are fixed to the $^qR_0(1)$ and b) $^pR_1(1)$ branches of the B ← X 2^0_1 transition. Down arrows represent the known transition energies.

to the X $2^1 \leftarrow$ X 2^0 band. The population of the vibrationally excited state was probed by (2 + 1) REMPI method. Efficiency of the vibrational excitation of the X 2^1 state is as large as 30 %. Spectral assignments revealed that vibrational ladder climbing up to $\nu_2 = 2$ in NH_3 was realized for the first time. Experiment on the vibrational excitation of the ν_4 vibrational mode of NH_3 molecules is under way.

ACKNOWLEDGEMENTS

The authors gratefully acknowledge the skillful supports by the FEL-SUT staffs. The experiments were done with the help of Mr. M. Kawashita and the other students in our laboratory.

REFERENCES

[1] Y. Ogi, T. Endo, K. Tsukiyama, H. Kondoh, K. Tono, Y. Ogawa, Y. Hamada, T. Ohta and H. Kuroda J. Electr. Spectrosc. Relat. Phenom. 128 (2003) 67.
[2] H. Akagi, K. Yokoyama, A. Yokoyama, J. Chem. Phys. 120 (2004) 4696.
[3] Z.C. Ying, A.S. Lahamer, O. Yavas, R.F. Haglund Jr. and R.N. Compton, Chem. Phys. Lett. 282 (1998) 268.
[4] M.N.R. Ashfold, R.N. Doxpn, N. Little, R.J. Stickland, and C.M. Western, J. Chem. Phys. 89 (1988) 1754.
[5] M.N.R. Ashfold, R.N. Dixon, R.J. Stickland, C.M. Western, Chem. Phys. Lett. vol. 138 (1987) 201.
[6] B.D. Kay, A.J. Grimley, Chem. Phys. Lett. 127 (1986) 303.
[7] J. Bentley, B.J. Cotterell, A. Langham, and R.J. Stickland, , Chem. Phys. Lett. 332 (2000) 85.
[8] W.E. Conaway R.J.S. Morrison, and R.N. Zare, Chem. Phys. Lett. vol. 113 (1985) 429.
[9] M. Kawai, H. Kuroda, in: Free Electron Lasers, Proceedings of the 21st international FEL conference and 6th FEL application workshop II-67 (1999).
[10] M. Yokoyama, F. Oda, A. Nakayama, K. Nomaru, H. Koike, M. Kawai, H. Kuroda, Nucl. Instr. and Meth. A 445 (2000) 379.
[11] M. Yokoyama, F. Oda, K. Nomaru, H. Koike, M. Sobajima, M. Kawai, H. Kuroda, K. Nakai, Nucl. Instr. and Meth. A 507 (2003) 261.
[12] K. Chen, E.S. Yeung, J. Chem. Phys. 69 (1978) 43.
[13] S. Urban, V. Špirko, D. Papousek, R.S. McDowell, N.G. Nereson, S.P. Belov, L.I. Gershstein, A.V. Maslovskij, A.F. Krupnov, J. Curtis, K.N. Rao, , J. Mol. Spectrosc. 79 (1980) 455.
[14] S. Urban, R. D'Cunha, K. N. Rao, and D. Papousek, Can. J. Phys. 62 (1984) 1775.

PHOTO-ACOUSTIC SPECTROSCOPY WITH INFRARED FEL

M. Yasumoto*, H. Ogawa, N. Sei, K. Yamada
Research Institute of Instrumentation Frontier, National Institute of Advanced Industrial Science and Technology (AIST), AIST Tsukuba Central 2, Tsukuba, Ibaraki, 305-8568, Japan

Abstract

We are proposing a new photo acoustic spectroscopy (PAS) method with an infrared free electron laser (FEL). The FEL-PAS, using the infrared FEL as the light source, can be applied in various samples with high sensitivity, because the FEL has continuous tunability in the infrared wavelength range. We measured the photo-acoustic spectrum of a polyethylene terephtarate (PET) film using the FEL-PAS method and confirmed a high level of agreement as compared to the absorption spectrum by a Fourier transform infrared (FTIR) spectroscope. In addition, we constructed an imaging system of the FEL-PAS. The imaging system can make a map of the PAS signal with a high spatial resolution that is a diffraction limit of the IR-FEL.

INTRODUCTION

Free-electron laser (FEL) is a useful laser having two advantages: continuously coverage of a wide wavelength range from infrared (IR) to ultra violet (UV); very short pulse duration. The FEL in the IR wavelength region is expected to be applied in various researches because there are few lasers that can cover a wide range of wavelengths continuously. The 5 ~ 15-μm wavelength range, known as the molecular fingerprint region, is especially useful because it corresponds to the unique absorption features of various molecular structures. Thus, the IR-FEL of the wavelength range has been applied to research using excitation of specific molecular vibration [1].

We applied the IR-FEL to the photo acoustic process, known as photo acoustic spectroscopy (PAS). In ordinary PAS, a modulating laser beam at a wavelength that overlaps with a spectral feature of the target molecule excites the target molecule by absorption of the incident radiation. The excited molecule is deactivated via collisions during which the absorbed radiation energy is converted into periodic local heating at the modulation frequency. We then monitor the resulting acoustic waves with a microphone. In this study we used the IR-FEL as the modulating laser radiation. The IR-FEL irradiation excites the target molecule more efficiently than an ordinary laser pulse by matching the photon energy of the IR-FEL to the excitation energy. In addition the sensitive PAS method can be developed to make a PAS image by micro-spectroscopy. Thus, we measured the PA spectrum of a polymer sample for the preliminary experiment of the new PAS method and constructed the PAS imaging system in this paper.

*m.yasumoto@aist.go.jp

PHOTO ACOUSTIC SPECTROSCOPY WITH FREE ELECTRON LASER

The PAS is a sensitive method of measuring the absorbance of various samples [2]. In the PA process, the conversion of heat input from the incident laser radiation into acoustic waves is described in the following equation 1.

$$\nabla^2 p - \frac{1}{c^2}\frac{\delta^2 p}{\delta^2 t} = -\frac{(\gamma - 1)}{c^2}\frac{\delta H}{\delta t} \qquad (1)$$

where p is the pressure, H is the generated heat, and γ is the ratio of specific heat.

The heat will be modulate, if the laser radiation is modulated ($\delta p/\delta t$ is not 0). The magnitude of the photo acoustic signal is described in the following equation 2.

$$S = CPN\ \Delta t \sigma S_m \qquad (2)$$

where C is a cell specific constant, P is the incident laser power, N is the number density of absorbing molecules, σ is absorption cross section of the transition that is being interrogated, Δt is the cycle period of the modulated radiation and S_m is the sensitivity of the microphone.

The signal magnitude (S) is proportional to the absorption cross section (σ) of the transition. Carbon dioxide (CO_2) lasers have long been used in the laboratory because of the ability to produce discrete wavelengths that are effectively absorbed by a variety of molecules. CO_2 lasers have approximately 120 discrete wavelengths between 9 μm and 11 μm with high output power. They have nearly coincident with one of the target spectral line, because the CO_2 lasers are not a continuous tunable laser. On the other hand, the IR-FEL is a continuous tunable laser and can be matched perfectly with the absorption line of the target molecule. Thus, the PAS with the IR-FEL is a more highly-sensitive method than ordinary PAS methods.

In this study we used MIR-FEL at the FEL user facility of Osaka University in Japan as the infrared FEL. The MIR-FEL is one of the four FEL machines (MIR-, NIR-, UVV-, FIR-FEL) at the facility and that covers the wavelength range of 5 ~ 18 μm [3, 4]. The wavelength range corresponds to the fingerprint region. Table 1 shows the specifications of the MIR-FEL.

Another advantage of the MIR-FEL is short pulse duration with high power. The MIR-FEL has a double micropulse structure of ~3-ps duration and a macropulse

of ~20-μs duration. The short duration pulse is sensitive to the surface of the sample.

Table 1: Specifications of the MIR-FEL.

Wavelength	5 ~ 20 μm
Peak power	~3 MW
Average power	~20 mW
Pulse duration	~3 ps (micropulse) ~20 μs (macropulse)
Pulse repetition rate	22.3 MHz (micropulse) 10 Hz (macropulse)

Although many kinds of PAS methods using other spectroscopic lights such as the Fourier Transform Infrared (FTIR), the synchrotron infrared radiation are proposed in the past, the FEL-PAS proposed in this paper has other advantages.

(1) The FEL-PAS has a sensitivity of the sample surface comparing with the synchrotron radiation (SR) in the infrared wavelength region, because the pulse duration of the FEL is much shorter than one of the SR.

(2) In the FEL-PAS method the PAS spectrum can be measured in a short time, although in the FTIR-PAS the enough time is needed for storing the data. Thus, the FEL-PAS enables real-time diagnosis of the sample.

FEL-PAS SPECTRA OF POLYMER FILM

We measured a FEL-PAS spectrum of the polyethylene terephtarate (PET) film to show the feasibility of the FEL-PAS. The spectrum was detected by a developed PA cell with a microphone. The output signal from the microphone was recorded by a digital oscilloscope under the FEL irradiation. The PA cell has a transparent window (ZnSe) for introducing the IR-FEL to the sample. The irradiation power of the IR-FEL is ~5mW. The PA signals were detected from 9.2 to 12.2 μm by 0.1-μm steps. Figure 1 shows the normalized PA signals of the PET with the IR-FEL and the normalized absorption spectrum measured by the FTIR (Nicolet 750). The film thickness was about 100 μm. The FEL-PA signals almost correspond to the curve of the FTIR spectrum.

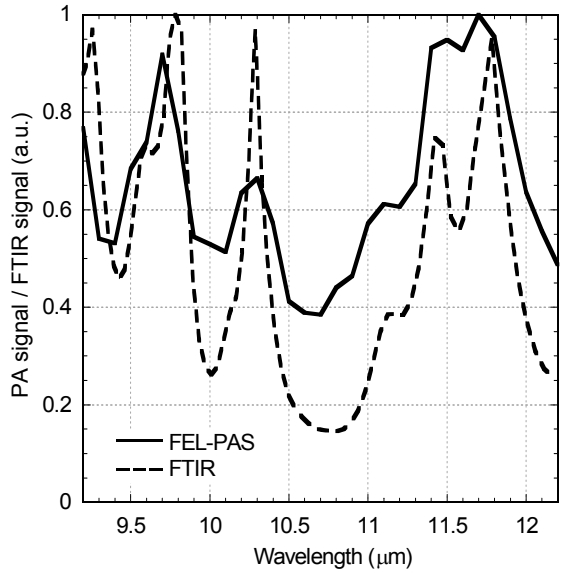

Figure 1: Spectra of PAS signal and FTIR signal from the PET film. The solid line and the dashed line are the PAS spectrum and the FTIR spectrum, respectively. Both are normalized with the maximum value.

FEL-PAS IMAGING SYSTEM

We constructed a new FEL-PAS imaging system with the IR-FEL. The new FEL-PAS imaging system is designed for making a PAS image with the infrared FEL. The FEL-PAS imaging system takes a full infrared PA spectrum at each point on the sample. A spatial resolution is limited to the diffraction limit of the IR-FEL, approximately equal to the wavelength. The spatial resolution of the system is one of the important parameters for making PA image. Samples are precisely scanned by a XY-stage for producing magnitude maps of the PA signal corresponding to the absorption coefficient of the wavelength.

The FEL-PAS imaging system consists of an optical microscope, a PA cell and a focusing mirror of the IR-FEL shown in Figure 2. The sample cell has a microphone to detect the PA signal and placed on the XY-stage. The focusing mirror, an off-axis parabolic mirror, is placed upon the PA cell. After observation of the measuring area using the optical microscope, we can irradiate the sample using the parabolic mirror. The sample can be moved with the raster scanning. Simultaneously, the PAS signal from the irradiated points can be detected by the microphone. The signal value can be reformed to the PAS image of the sample. Elimination of the mirror aberrations leads to better confinement of the beam and the spot size is almost equal to the diffraction limit of the IR-FEL.

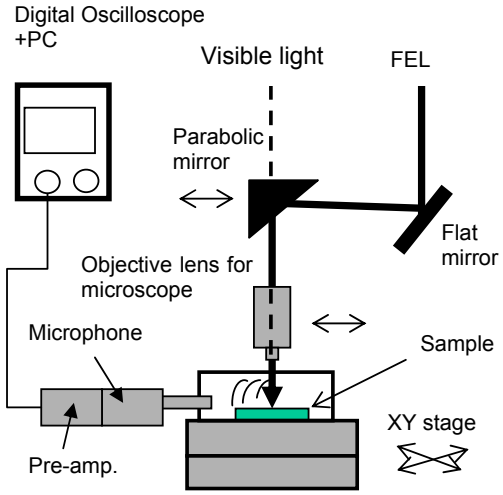

Figure 2: Schematic of optical path inside the FEL-PAS system. A parabolic mirror is removed and the objective lens is installed, when observed with microscope.

SUMMARY

We have proposed a new PA spectroscopy with the IR-FEL (FEL-PAS) in this paper. The FEL-PAS offers unique capabilities that allow analysis of very broad range of sample types with high sensitivity. In the case of a PET film, the signals from the FEL-PAS are good agreement with absorption spectra from the FTIR between 9.2 μm and 12.2 μm. In addition, the FEL-PAS imaging system is also described. The FEL-PAS imaging system is useful for microscopic analysis of a sample surface. The spatial resolution is more or less limited by the wavelength of the IR-FEL. Although the PET sample is stable in time, the FEL-PAS will be especially useful in time resolved analysis of the sample because of its high power during short pulse duration. Thus, the FEL-PAS is expected to play an important role in the field of bio-medical research and semiconductor research.

ACKNOWLEDGEMENTS

We would like to thank all staff of the FEL user facility (*i*FEL) at Osaka University for their efforts in maintaining an excellent FEL beam quality.

REFERENCES

[1] Proceedings of AFEL97, Osaka, Jan. 1997.
[2] A. Rosencwaig, Rev. Sci. Instrum. 48 (1977) 1133.
[3] T. Tomimasu et al. Nucl. Instrum. And Meth. B144 (1998) 1.
[4] H. Horiike et al., Jpn. J. Appl. Phys. 41 (2002) Suppl.41-1, 10.

FREE ELECTRON LASERS IN 2004

W. B. Colson* and B. W. Williams
Physics Department, Naval Postgraduate School, Monterey CA 93943 USA

Abstract

Twenty-seven years after the first operation of the free electron laser (FEL) at Stanford University, there continue to be many important experiments, proposed experiments, and user facilities around the world. Properties of FELs operating in the infrared, visible, UV, and x-ray wavelength regimes are listed and discussed.

INTRODUCTION

The following tables list existing (Table 1) and proposed (Table 2) relativistic free electron lasers (FELs) in 2004. Each FEL is identified by a location or institution, followed by the FEL's name in parentheses; references are listed in Tables 3 and 4.

The first column of the table lists the operating wavelength λ, or wavelength range. The large range of operating wavelengths, six orders of magnitude, indicates the flexible design characteristics of the FEL mechanism. In the second column, σ_z is the electron pulse length divided by the speed of light *c*, and ranges from almost CW to short sub-picosecond pulse time scales. The expected optical pulse length can be 3 to 5 times shorter or longer than the electron pulse depending on the optical cavity *Q*, the FEL desynchronism, and the FEL gain. If the FEL is in an electron storage-ring, the optical pulse is typically much shorter than the electron pulse. Most FEL oscillators produce an optical spectrum that is Fourier transform limited by the optical pulse length.

The electron beam energy *E* and peak current *I* provided by the accelerator are listed in the third and fourth columns. The next three columns list the number of undulator periods *N,* the undulator wavelength λ_0, and the undulator parameter $K=eB\lambda_0/2\pi mc^2$ where *e* is the electron charge magnitude, *B* is the rms undulator field strength, and *m* is the electron mass. For an FEL klystron undulator, there are multiple undulator sections as listed in the *N*-column. Note that the range of values for *N*, λ_0, and *K* are much smaller than for the other parameters, indicating that most undulators are similar. Only a few of the FELs use the klystron undulator at present, and the rest use the conventional periodic undulator. The FEL resonance condition, $\lambda=\lambda_0(1+K^2)/2\gamma^2$ where γ is the relativistic Lorentz factor, provides a relationship that can be used to derive *K* from λ, *E*, and λ_0. The middle entry of the last column lists the accelerator type (RF for Radio Frequency Linear Accelerator, MA for Microtron Accelerator, SR for Storage Ring, EA for Electrostatic Accelerator), and the FEL type (A for FEL Amplifier, O for FEL Oscillator, S for SASE FEL, H for a high-gain high harmonic HGHG FEL). Most of the FELs are oscillators, but recent progress has resulted in short wavelength FELs using SASE (Stimulated Amplification of Spontaneous Emission).

For the conventional undulator, the peak optical power can be estimated by the fraction of the electron beam peak power that spans the undulator spectral bandwidth, *1/4N*, or $P\approx EI/4eN$. For the FEL using a storage ring, the optical power causing saturation is substantially less than this estimate and depends on ring properties. For the high-gain FEL amplifier, the optical power at saturation can be substantially greater. The average FEL power is determined by the duty cycle, or spacing between electron pulses, and is typically many orders of magnitude lower than the peak power. The TJNAF IRFEL has now reached an average power of 10 kW with the recovery of the electron beam energy in superconducting accelerator cavities.

In the FEL oscillator, the optical mode that best couples to the electron beam in an undulator of length $L=N\lambda_0$ has Rayleigh length $z_0\approx L/12^{1/2}$ and has a mode waist radius of $w_0\approx N^{1/2}\gamma\lambda/\pi$. The FEL optical mode typically has more than 90% of the power in the fundamental mode described by these parameters.

ACKNOWLEDGMENTS

The authors are grateful for support from ONR, NAVSEA, and the JTO.

* Corresponding Author: 831-656-2765, Colson@nps.edu

Table 1: Free Electron Lasers (2004)

EXISTING FELs	λ (μm)	σ_z(ps)	E(MeV)	I(A)	N	λ_0(cm)	K(rms)	
Italy (FEL-CAT)	760	15-20	1.8	5	16	2.5	0.75	RF,O
UCSB (mm FEL)	340	25000	6	2	42	7.1	0.7	EA,O
Novosibirsk (RTM)	120-180	70	12	10	2x33	12	0.71	RF,O
Korea (KAERI-FEL)	97-1200	25	4.3-6.5	0.5	80	2.5	1.0-1.6	MA,O
Himeji (LEENA)	65-75	10	5.4	10	50	1.6	0.5	RF,O
UCSB (FIR FEL)	60	25000	6	2	150	2	0.1	EA,O
Osaka (ILE/ILT)	47	3	8	50	50	2	0.5	RF,O
Osaka (ISIR)	40	30	17	50	32	6	1	RF,O
Tokai (JAERI-FEL)	22	2.5-5	17	200	52	3.3	0.7	RF,O
Bruyeres (ELSA)	20	30	18	100	30	3	0.8	RF,O
Osaka (FELI4)	18-40	10	33	40	30	8	1.3-1.7	RF,O
UCLA-Kurchatov	16	3	13.5	80	40	1.5	1	RF,A
LANL (RAFEL)	15.5	15	17	300	200	2	0.9	RF,O
Stanford (FIREFLY)	15-80	1-5	15-32	14	25	6	1	RF,O
UCLA-Kurchatov-LANL	12	5	18	170	100	2	0.7	RF,A
Maryland (MIRFEL)	12-21	5	9-14	100	73	1.4	0.2	RF,O
Beijing (BFEL)	5-20	4	30	15-20	50	3	1	RF,O
Dresden (ELBE1)	3-22	10	40	8	2x34	2.73	0.3-0.8	RF,O
Korea (KAERI HP FEL)	3-20	10-20	20-40	30	30x2	3.5	0.5-0.8	RF,O
Newport News (IR demo)	3, 6, 10	0.2	160	270	25	20	4.5	RF,O
Darmstadt (FEL)	6-8	2	25-50	2.7	80	3.2	1	RF,O
BNL (HGHG)	5.3	6	40	120	60	3.3	1.44	RF,A
Osaka (iFEL1)	5.5	10	33.2	42	58	3.4	1	RF,O
Tokyo (KHI-FEL)	4-16	2	32-40	30	43	3.2	0.7-1.8	RF,O
Nieuwegein (FELIX)	3-250	1	50	50	38	6.5	1.8	RF,O
Duke (MARKIII)	2.7-6.5	3	31-41.5	20	47	2.3	1	RF,O
Stanford (SCAFEL)	3-13	0.5-12	22-45	10	72	3.1	0.8	RF,O
Orsay (CLIO)	3-53	0.1-3	21-50	80	38	5	1.4	RF,O
Vanderbilt (FELI)	2.0-9.8	0.7	43	50	52	2.3	1.3	RF,O
Osaka (iFEL2)	1.88	10	68	42	78	3.8	1	RF,O
Nihon (LEBRA)	0.9-6.5	<1	58-100	10-20	50	4.8	0.7-1.4	RF,O
UCLA-BNL (VISA)	0.8	0.5	70.9	250	220	1.8	1.2	RF,S
BNL (ATF)	0.6	6	50	100	70	0.88	0.4	RF,O
Dortmund (FELICITAI)	0.42	50	450	90	17	25	2	SR,O
BNL NSLS (DUVFEL)	0.1	0.7	300	500	256	3.9	0.7	RF,SH
Orsay (Super-ACO)	0.3-0.6	15	800	0.1	2x10	13	4.5	SR,O
Osaka (iFEL3)	0.3-0.7	5	155	60	67	4	1.4	RF,O
Okazaki (UVSOR)	0.2-0.6	6	607	10	2x9	11	2	SR,O
Tsukuba (NIJI-IV)	0.2-0.6	14	310	10	2x42	7.2	2	SR,O
Italy (ELETTRA)	0.2-0.4	28	1000	150	2x19	10	4.2	SR,O
Duke (OK-4)	0.193-2.1	0.1-10	1200	35	2x33	10	0-4.75	SR,O
ANL (APSFEL)	0.13	0.3	399	400	648	3.3	2.2	RF,S
DESY (TTF1)	0.08-012	0.04	250	3000	492	2.73	0.81	RF,S

Table 2: Proposed Free Electron Lasers (2004)

PROPOSED FELs	λ(μm)	σ_z(ps)	E(MeV)	I(A)	N	λ_0(cm)	K(rms)	
Tokyo (FIR-FEL)	300-1000	5	10	30	25	7	1.5-3.4	RF,O
Netherlands (TEUFEL)	180	20	6	350	50	2.5	1	RF,O
Rutgers (IRFEL)	140	25	38	1.4	50	20	1	MA,O
Novosibirsk (RTM1)	3-20	10	50	20-100	3x33	6	2	RF,O
Dresden (ELBE)	30-750	1-5	10-40	30	45	5	0.4-1.6	RF,O
Daresbury (4GLS-IRFEL)	5-100	0.2-1	50	100	100	4	2	RF,O
Novosibirsk (RTM)	2-11	20	98	100	4x36	9	1.6	RF,O
Frascati (SPARC)	0.533	0.1	142	500	6x71	3	1.3	RF,S
TJNAF (UVFEL)	0.25-1	0.2	160	270	60	3.3	1.3	RF,O
Hawaii (FEL)	0.3-3	2	100	500	84	2.4	1.2	RF,O
Harima (SUBARU)	0.2-10	26	1500	50	33,65	16,32	8	SR,O
Shanghai (SDUV-FEL)	0.5-0.088	1	300	400	400	2.5	1.025	RF,O
Frascati (COSA)	0.08	10	215	200	400	1.4	1	RF,O
Daresbury (4GLS-VUV)	0.4-0.1	0.1-1	600	300	150	5	2	RF,O
Daresbury (4GLS-XUV)	0.1-0.01	0.1-1	600	2000	1000	2	1	RF,S
Duke (OK-5,VUV)	0.03-1	0.1-10	1200	50	4x32	12	3	SR,O
DESY (TTF2)	0.006	0.17	1000	2500	981	2.73	0.9	RF,S
Italy (SPARX)	0.0015	0.1	2500	2500	1000	3	1.2	RF,S
BESSY (Soft X-ray)	0.0012	0.08	2300	3500	1450	2.75	0.9	RF,S
Trieste (FERMI)	0.001-0.1	0.1	3000	2500	570-1140	3.5	1.2	RF,S
RIKEN (SPring8 SCSS)	0.00036	0.5	1000	2000	1500	1.5	1.3	RF,S
MIT (Bates X-Ray FEL)	0.0003	0.05	4000	1000	1500	1.8	2	RF,S
SLAC (LCLS)	0.00015	0.07	14350	3400	3328	3	3.7	RF,S
DESY (TESLA)	0.0001	0.08	30000	5000	4500	6	3.2	RF,S
Pohang (PAL X-FEL)	0.0003	0.1	3000	4000	6000	1.5	1.1	RF,S

Table 3: References and Websites for Existing FELs

EXISTING FELs	Internet Site or Reference
ANL (APSFEL)	J. W. Lewellen et. al., NIM **A483**, 40 (2002).
Beijing (BFEL)	http://bfel.ihepa.ac.cn
BNL NSLS (DUVFEL)	http://www.nsls.bnl.gov/organization/Accelerator/DUVFEL
BNL (ATF)	K. Batchelor et. al., NIM **A318**, 159 (1992).
BNL (HGHG)	A. Doyuran et. al., NIM **A475**, 260 (2001).
BNL (VISA)	A. Tremaine et. al., NIM **A483**, 24 (2002).
Bruyeres (ELSA)	P. Guimbal et. al., NIM **A341**, 43 (1994).
Darmstadt (FEL)	http://linaxa.ikp.physik.tu-darmstadt.de/richter/fel
DESY(TTF1)	http://www-hasylab.desy.de/facility/fel
Dortmund (FELICITAI)	http://www.delta.uni-dortmund.de/pub/fel/FEL.html
Duke (MARKIII)	http://www.fel.duke.edu/lightsources/mk3.html
Duke (OK-4)	http://www.fel.duke.edu
Himeji (LEENA)	http://www.lasti.himeji-tech.ac.jp/NS/LEENA/LEENA_HP.html
Italy (ELETTRA)	http://www.elettra.trieste.it/projects/euprog/fel
Italy (FEL-CAT)	A. Doria et. al, Phys. Rev. Lett. **80**, 2841 (1998).
Korea (KAERI HP FEL)	http://www.kaeri.re.kr/fel/index.php
Korea (KAERI-FEL)	http://www.kaeri.re.kr/fel/index.php
LANL (RAFEL)	http://www.lanl.gov/orgs/ibdnew/usrfac/userfac03.html
Maryland (MIRFEL)	http://www.ireap.umd.edu/FEL
Newport News (IR demo)	http://www.jlab.org/FEL
Nieuwegein (FELIX)	http://www.rijnh.nl/n4/n3/f1234.htm
Nihon (LEBRA)	http://www.lebra.nihon-u.ac.jp
Novosibirsk (RTM)	http://www.inp.nsk.su
Okazaki (UVSOR)	http://uvsor-ntserver.ims.ac.jp
Orsay (CLIO)	http://www.lure.u-psud.fr/CLIO.HTM
Orsay (Super-ACO)	M. E. Couprie et. al., NIM **A407**, 215-220 (1998).
Osaka (FELI4)	T. Takii et. al., NIM **A407**, 21-25 (1998).
Osaka (iFEL1)	http://www.fel.eng.osaka-u.ac.jp/english/index_e.html
Osaka (iFEL2)	http://www.fel.eng.osaka-u.ac.jp/english/index_e.html
Osaka (iFEL3)	http://www.fel.eng.osaka-u.ac.jp/english/index_e.html
Osaka (ILE/ILT)	N. Ohigashi et. al., NIM **A375**, 469 (1996).
Osaka (ISIR)	http://www.ei.sanken.osaka-u.ac.jp
Stanford (FIREFLY)	K. W. Berryman and T. I. Smith, NIM **A375**, 6 (1996).
Stanford (SCAFEL)	H. A. Schwettman et. al., NIM **A375**, 662 (1996).
Tokai (JAERI-FEL)	R. Hajima et. al., NIM **A507**, 115 (2003).
Tokyo (KHI-FEL)	M. Yokoyama et. al., NIM **A475**, 38 (2001).
Tsukuba (NIJI-IV)	K.Yamada et. al., NIM **A475**, 205 (2001).
UCLA-Kurchatov	http://pbpl.physics.ucla.edu
UCLA-Kurchatov-LANL	http://pbpl.physics.ucla.edu
UCSB (FIR FEL)	http://sbfel3.ucsb.edu
UCSB (mm FEL)	http://sbfel3.ucsb.edu
Vanderbilt (FELI)	http://www.vanderbilt.edu/fel

Table 4: References for Proposed FELs

PROPOSED FELs	References for Proposed FELs
BESSY (Soft X-ray)	M. Abo-Bakr et. al., Nucl. Inst. and Meth. **A483**, 470 (2002); Tsukuba Mo-P-07,Mo-P-08,We-P-51 (Sept 2003).
Daresbury (4GLS)	M. W. Poole and B. W. J. McNeil, Nucl. Inst. and Meth. **A507**, 489 (2003).
DESY (TESLA)	R. Brinkmann et. al., Nucl. Inst. and Meth. **A393**, 86 (1997); TESLA Technical Design Report.
DESY (TTF2)	W. Brefeld et. al., Nucl. Inst. and Meth. **A375**, 295 (1996).
Dresden (ELBE)	F. Gabriel et. al., Nucl. Inst. and Meth. **B161**, 1143 (2000).
Dresden (ELBE1)	F. Gabriel et. al., Nucl. Inst. and Meth. **B161**, 1143 (2000).
Duke (OK-5,VUV)	V. N. Litvinenko et. al., Nucl. Inst. and Meth. **A358**, 369 (1995).
Frascati (COSA)	F. Ciocci et. al., A. Torre, IEEE J.Q.E. **31**, 1242 (1995).
Frascati (SPARC)	A. Renieri et. al., Nucl. Inst. and Meth. **A507**, 507 (2003).
Harima (SUBARU)	S. Miyamoto et. al., Report of the Spring-8 International Workshop on 30 m Long Straight Sections, Kobe, Japan (August 9, 1997).
Italy (SPARX)	A. Renieri et. al., Nucl. Inst. and Meth. **A507**, 507 (2003).
MIT (Bates X-Ray FEL)	W.S. Graves et. al., Nucl. Inst. and Meth. **AXXX**, xx (2004); Twenty-Fifth International Free Electron Conference, Tsukuba, Japan (Mo-P-49, Sept 2003).
Netherlands (TEUFEL)	J. I. M. Botman et. al., Nucl. Inst. and Meth. **A341**, 402 (1994).
Novosibirsk (RTM)	N. G. Gavrilov et. al., Status of Novosibirsk High Power FEL Project, SPIE Proceedings, vol. **2988**, 23 (1997); N. A. Vinokurov et. al., Nucl. Inst. and Meth. **A331**, 3 (1993).
Novosibirsk (RTM1)	V. P. Bolotin et. al., Nucl. Inst. and Meth. **A475**, II-37 (2001).
Pohang (PAL X-FEL)	pal.postech.ac.kr/kor
RIKEN (SPring8 SCSS)	T. Shintake et. al., Nucl. Inst. and Meth. A507, 382 (2003); Tsukuba We-P-59 (Sept 2003).
Rocketdyne/Hawaii (FEL)	R. J. Burke et al, Proc. SPIE: Laser Power Beaming, Los Angeles, Jan. 27-28, 1994, Vol **2121**.
Rutgers (IRFEL)	E. D. Shaw et. al., Nucl. Inst. and Meth. **A318**, 47 (1992).
Shanghai (SDUV-FEL)	Z. T. Zhao et. al, Nucl. Inst. and Meth. **AXXX**, xx (2004); Twenty-Fifth International Free Electron Conference, Tsukuba, Japan (We-P-65, Sept 2003).
SLAC (LCLS)	M. Cornacchia, Proc. SPIE 2998, 2-14 (1997); LCLS Design Study Report, SLAC R-521 (1998).
TJNAF (UVFEL)	S. Benson et. al., Nucl. Inst. and Meth. **A429**, 27-32 (1999).
Tokyo (FIR-FEL)	H. Koike et. al., Nucl. Inst. and Meth. **A483**, II-15 (2002).
Trieste (FERMI)	C. J. Bocchetta et. al., Nucl. Inst. and Meth. **A507**, 484 (2003); Tsukuba We-P-53 (Sept 2003).

Author Index

Author Index

***Bold** paper codes mean primary author.*

D

E

F

G

H

I

J

K

L

M

N

O

P

Q

R

S

T

U

V

W

X

Y

Z

Index of Paper ID’s

Index of Paper ID's

Producing the Conference Proceedings

The Proceedings of the 2004 edition of the FEL Conference have been produced thanks to the long experience and deep knowledge matured among the Joint Accelerators Conference Website's "working group" (JACoW – see `http://www.JACoW.org`).

The JACoW collaboration has recently developed the SPMS, a new Open Source tool that aims to automate as many tasks a conference like this requires to perform. This includes full abstracts treatment (collecting, accepting, editing, etc.), generic conference management (sessions, speakers, posters, etc.) and production of final proceedings.

This SPMS, achronym that means "Scientific Programme Management System" has been adopted by and customised for FEL 2004: being founded on a back-end database with a web interface, it has recorded all the proposed abstracts (pure text plus simple formulæ), helped put them into sessions, produced the Abstract Booklet, kept all the information about the scientific contributions and produced the proceedings.

Every single contribution has been submitted to the SPMS in Adobe PostScript (PS) format and, for most of the cases, in 'source' format (mostly Microsoft Word files and LaTeX): a well-motivated and extremely effective group of persons from Sincrotrone Trieste, during and after the conference, has then checked the files for fonts/graphics (un-)readability and adherence to proposed conference templates, hence transforming all the contributions in Adobe Portable Document Format (PDF) files.

With all the metadata (titles, list of authors and related institutes, etc.) in a database and all the accepted PDF files on a server, going to the production of the Proceedings was very easy. A novel package in the SPMS, developed for this conference, permitted to generate a LaTeX source file that, when compiled, merged all the contribution files into one and in the proper order, inserted running page numbers, inserted different headings and footers for different pages, created the Table Of Contents and various other indexes. As a result, one PDF file has been produced to print this book, together with several HTML and PDF files to publish on the web and on the CD.

Commercial software was only needed to create the PDF's (Acrobat Distiller), touch up the PDF's (Adobe Acrobat and Enfocus PitStop – see `http://www.enfocus.com`), seldom to change the source files (if generated by Microsoft Word). All the other steps have been performed using Open Source tools: LaTeX, pdfTeX with the `pdfpages`, `fancyhdr` and `multind` packages, `vim` for editing (`http://www.vim.org`), `Perl` scripts for a couple of global changes in PDF files, GNU/Linux for the Operating System. Even if the SPMS is currently based on Oracle, its code has been released under the GNU General Public License (see `http://www.gnu.org/licenses/licenses.html`).

I hope that this information will be of use to future conference organisers.

Ivan Andrian, *Nov. 2004*
`<ivan.andrian@elettra.trieste.it>`

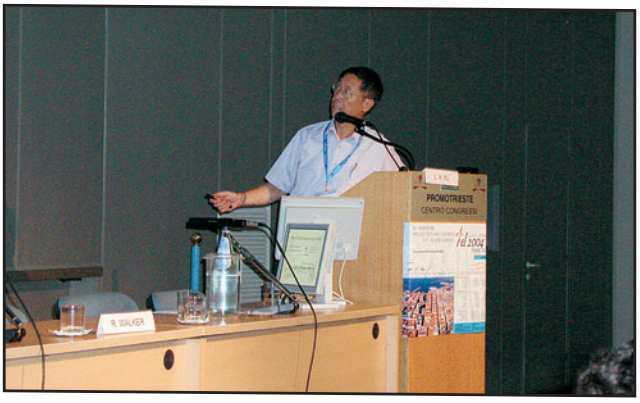
PROMOTRIESTE
CENTRO CONGRESSI
R. WALKER


TRIESTE
PROMOTRIESTE
CENTRO CONGRESSI
Fel 2004
Trieste, Italy


PROMOTRIESTE
CENTRO CONGRESSI


C. RIZZUTO
TRIESTE
PROMOTRIESTE
CENTRO CONGRESSI
Fel 2004
Trieste, Italy


R. BAKKER
PROMOTRIESTE
CENTRO CONGRESSI
Fel 2004


Welcome to
Fel 2004
Trieste, Italy


R. COSOLINI
TRIESTE
PROMOTRIESTE
CENTRO CONGRESSI
Fel 2004

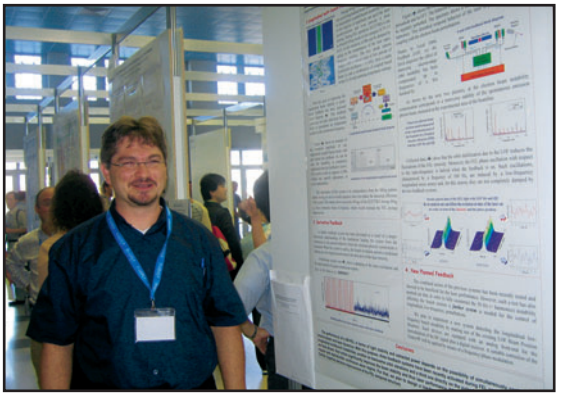

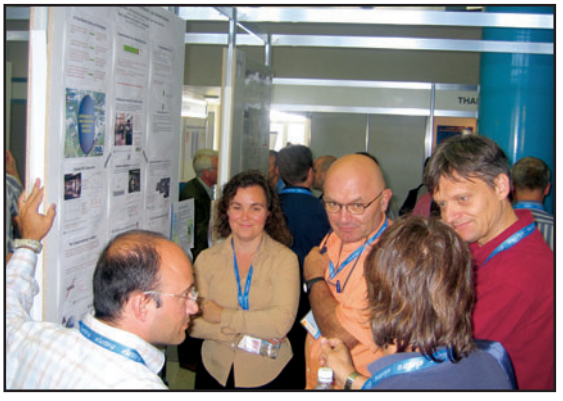

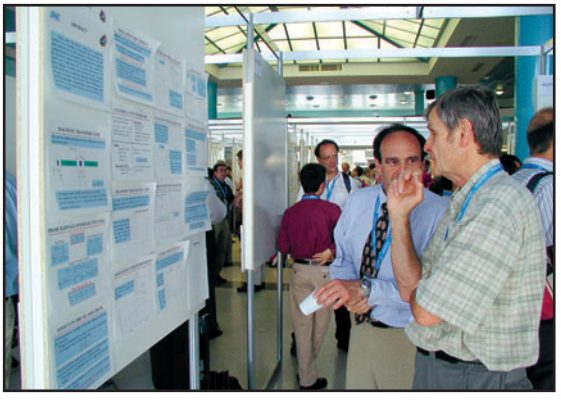

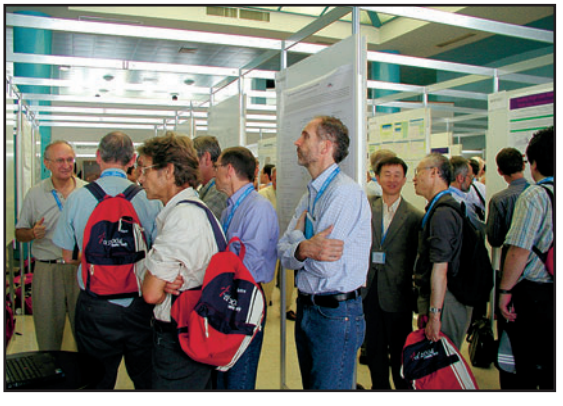

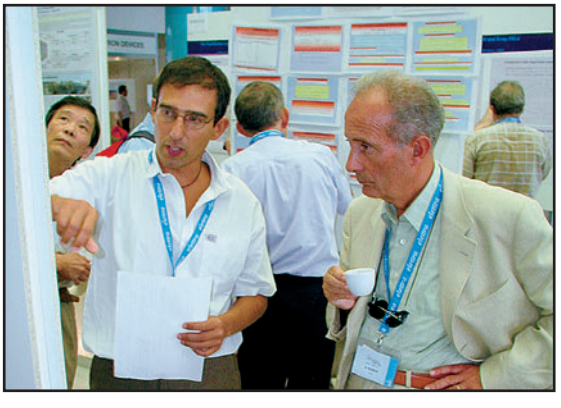


Fel 2004
Trieste


Fel


26TH INTERNATIONAL
FREE ELECTRON LASER CONFERENCE
& 11TH FEL USERS WORKSHOP
Fel 2004
Trieste, Italy